POLYTECHNIQUE MONTRÉAL

affiliée à l'Université de Montréal

Improving the seismic robustness of Conventional Construction concentrically braced steel frames by mobilizing the gravity load framing system

THIERRY BÉLAND

Département des Génies Civil, Géologique et des Mines

Thèse présentée en vue de l'obtention du diplôme de *Philosophiae Doctor*

Génie Civil

Décembre 2019

© Thierry Béland, 2019.

POLYTECHNIQUE MONTRÉAL

affiliée à l'Université de Montréal

Cette these intitulée:

Improving the seismic robustness of Conventional Construction concentrically braced steel frames by mobilizing the gravity load framing system

Présentée par **Thierry BÉLAND**

en vue de l'obtention du diplôme de *Philosophiae Doctor*

a été dûment acceptée par le jury d'examen constitué de :

Bruno MASSICOTTE, président

Robert TREMBLAY, membre et directeur de recherche

Larry A. FAHNESTOCK, membre et codirecteur de recherche

Pierre LÉGER, membre

Matthew EATHERTON, membre externe

DEDICATION

To Joel

ACKNOWLEDGEMENTS

I would like to take this opportunity to express my deepest gratitude to Professor Robert Tremblay and Professor Larry Fahnestock, whose support and advice has made this work possible. I would also like to thank the members of the evaluation committee, Professors Matthew Eatherton, Pierre Léger and Bruno Massicotte for agreeing to review this thesis. I would also like to thank the staff of the Structures Laboratory of Polytechnique Montreal, Jonathan Auger, Romain Siguier, David Ek, Patrice Bélanger, Xavier Willem and Martin Leclerc for their involvement in the experimental programs conducted and the countless hours spent in the Laboratory on this project. I also take this opportunity to thank Ali Davaran, Jessalyn Nelson, Cameron Bradley and Joshua Sizemore who provided assistance in developing the testing programs.

The funding of this research is also acknowledged: The study was supported by the Natural Sciences and Engineering Research Council of Canada (Canada Research Chair Program, Grant no. 219924), the National Science Foundation (Grant No. CMMI-1207976) and the American Institute of Steel Construction. I would also like to thank SSEF of the Canadian Institute of Steel Construction for granting the 2015 G.J. Jackson Fellowship for this research and the CEISCE for allowing me to spend five months at the University of Illinois at Urbana-Champaign.

I am also thankful to my officemates who became my friends, Morteza Deghani, Poulad Daneshvar, Fabien Eddy Lagier, Ali Imanpour, Yasaman Balazadeh Minouei, Marie-Ève Gagné and Ivana Jurcova. I would also like to acknowledge the unconditional support provided by my parents Christian and Lucie. Finally, this endeavor would not have been possible without the constant support, encouragement and patience of my loving partner Joel Morissette.

RÉSUMÉ

Au Canada, le processus de conception de systèmes de reprise des charges sismiques (SRFSs) en acier de faible ductilité de type Constructions Conventionnelles (Type CC) ne demandent pas de conception par capacité et la majorité de la conception peut être effectuée rapidement avec des résultats d'analyses élastiques. Cette méthode de conception simple et rapide représente un grand incitatif aux ingénieurs de conceptions pour choisir ce système. La ductilité limitée de ce système provient de la ductilité inhérente à l'acier et au glissement des connexions pour accommoder les déformations inélastiques et dissiper l'énergie sismique. Le manque de contrôle sur la réponse inélastique et sur la hiérarchie de plastification peut créer des mécanismes de ruine indésirables comme un étage faible ou des ruptures fragiles dans le SRFS.

L'effet de cadre rigide provenant de la rigidité rotationnelle et de la force des connexions gravitaires poutres-colonnes peuvent fournir une résistance et une rigidité additionnelle pour créer un système de capacité de réserve qui peut améliorer la robustesse de la structure. L'élaboration d'une simple connexion poutre-colonne partiellement rigide (PR) qui peut développer une grande résistance latérale et une grande rigidité tout en montrant une capacité de déformation stable et plastique sous un chargement cyclique inélastique consiste en une avenue prometteuse pour augmenter la performance de cadres rigides de Type CC tout en limitant les coûts et les modifications aux pratiques courantes actuelles. Parmi plusieurs connexions examinées dans des études passées, les doubles cornières d'âmes avec cornières aux semelles de la poutres (2L-TS) semblent être un choix excellent par sa simplicité et sa grande capacité en ductilité. La résistance et la rigidité de la connexion dépend des paramètres géométriques des cornières. La conception des connexions peut ainsi être ajustée pour optimiser la capacité de réserve et peut-être ajustée au bâtiment, soit existant ou nouveau. Par contre, l'influence de ces paramètres doit être caractérisé méthodiquement.

Pour pallier ce problème, un programme expérimental a été entrepris à l'École Polytechnique de Montréal sur des cornières boulonnées simples dans ce projet d'études doctorales. Un total de 139 tests a été réalisés sur 19 géométries de cornières. L'influence de l'épaisseur des cornières, de la position des boulons de la colonne, des conditions de chargement et des conditions de boulonnage ont été caractérisés. De plus, les résultats des essais monotoniques ont été utilisés pour déterminer

les paramètres d'un modèle mathématique établi afin de prédire la réponse non-linéaire des cornières.

En général, le comportement non-linéaire des cornières boulonnées a montré une grande ductilité et une grande résistance, ce qui peut se traduire par une capacité de dissipation d'énergie substantielle sous des conditions sismiques. Par contre, des études antérieures ont mentionné de grandes différences entre le comportement des cornières observé dans des essais de connexions à échelle réelle et des essais en traction simplifiés, comme ceux réalisés dans ce programme expérimental.

Pour résoudre ce problème, un deuxième programme d'essais sur des connexions poutres-colonnes à échelle réelle et sollicitées simultanément en cisaillement et en flexion a été réalisé à l'École Polytechnique de Montréal pour caractériser le comportement global non-linéaire des connexions boulonnées. Un total de 8 tests sur des doubles cornières d'âme et 15 tests sur des connexions 2L-TS a été réalisé.

Généralement, le comportement non-linéaire des cornières boulonnées démontrait une grande ductilité, ce qui se traduit par une grande capacité de dissiper de l'énergie sous des charges sismiques. De plus, l'ajout de deux cornières aux semelles de la poutre augmente considérablement la capacité en flexion de la connexion. Ainsi, l'utilisation de cornières boulonnées dans les connexions gravitaires peut être bénéfique puisque leur grande redondance combinée à leur substantielle capacité de dissiper l'énergie peut améliorer la capacité de réserve du bâtiment et ainsi mitiger la rupture dans les cadres contreventés de Type CC.

Les paramètres requis pour recréer les résultats des essais monotoniques sur les cornières avec le matériau Steel02 de OpenSees ont été déterminés. Par contre, certaines erreurs entre le comportement hystérétique obtenu des essais expérimentaux et du matériau Steek02 de OpenSees ont été identifiés. Pour régler ces divergences, quelques modifications sont proposées au modèle mathématique pour améliorer sa précision et pour recréer le comportement hystérétique spécifique aux cornières boulonnées. Les paramètres intrants de ce modèle mathématique proposé ont été déterminés pour chaque essai cyclique du programme expérimental sur les cornières boulonnées. Des équations empiriques basées sur les propriétés géométriques et de matériaux sont proposées pour recréer le comportement hystérétique de n'importe laquelle des configurations.

Ce modèle a également été implanté dans OpenSees en tant que matériau Uniaxial. Le comportement hystérétique obtenu des essais à échelle réelle de connexions poutre-colonnes ont été précisément recréées avec une approche basée sur le comportement des composantes.

De plus, une approche de dimensionnement est proposée pour améliorer la capacité de réserve de bâtiments de Type CC utilisant des connexions robustes 2L-TS dans le système gravitaire. Des lignes directrices sont proposées pour obtenir une réponse sismique adéquate pour les bâtiments en acier de Type CC fait de cadres contreventés en chevrons, tout en minimisant les changements apportés aux procédures de dimensionnement des autres éléments de la structure comme les poutres et poteaux gravitaires. La relaxation du critère de force augmentée pour les connexions entre les diagonales et les goussets est évaluée. Un exemple de dimensionnement d'un bâtiment de 3 étage situé à Montréal a été réalisé. Cet exemple a ensuite été modélisé sur OpenSees pour évaluer la réponse dynamique du bâtiment avec des connexions améliorées.

Somme toutes, les connexions améliorées n'ont pas une influence significative sur le cisaillement à la base ou sur la période fondamentale du bâtiment non-fracturé. Par contre, les déplacements inter-étages maximaux obtenus au premier étage étaient améliorés avec les connexions PR. Le déplacement inter-étage maximal avec les connexions améliorées était limité à 3%, ce qui est en-deçà de la limite de 3% anticipée lors du processus de conception. De plus, la présence de connexions améliorées réduit le moment développé dans la colonne de gravité. Finalement, le modèle de connexion montre un comportement ductile lors des modélisations numériques.

ABSTRACT

In Canada, the design process of steel low-ductility Conventional Construction (Type CC) seismic force resisting systems (SFRSs) does not require capacity design and most of the design can be performed quickly based on elastic analysis results. This quick and simple design procedure represents a strong incentive to design engineers for selecting this type of SFRSs. The limited ductility of this system is provided by the inherent ductility of steel and slip in connections to accommodate inelastic deformations and dissipate the seismic energy. The lack of control on the inelastic response and yielding hierarchy can lead to undesirable failure mechanisms such as a soft story or brittle failures in the SFRS.

The frame action resulting from the rotational stiffness and strength of gravity beam-column connections can provide additional lateral strength and stiffness to form a reserve capacity system that can significantly enhance the seismic robustness of the structure. Developing a simple partially-restrained (PR) beam-column connection that can exhibit high lateral strength and stiffness while exhibiting stable plastic deformation capacity under inelastic cyclic loading is a promising avenue for enhancing the seismic performance of Type CC braced frames with limited cost increase and changes to current practice. Among the several connections examined in past studies, the double angle connections with top and seat angle (2L-TS) seems to be an excellent choice because of its simplicity and high ductility capacity. The connection stiffness and strength depend on geometrical parameters of the angle components. The design of the connection can thus be adjusted to optimize the reserve capacity and be adjusted to the requirements of the building, either existing or new. However, the influence of these parameters needs to be characterized carefully.

To resolve this issue, an experimental program was conducted at École Polytechnique de Montreal on bolted angle components in this doctoral research program. A total of 139 tests were performed on 19 different bolted angle geometries. The influence of the angle thickness, the column bolt position, the loading conditions and the fastening conditions were characterized. Furthermore, the results from the monotonic tests were used to determine the parameters of an established power model which can be used to predict the monotonic nonlinear response of the angle.

In general, the nonlinear behaviour exhibited by bolted angles showed large ductility and resistance, which can translate into a substantial energy-dissipation capacity under seismic loading conditions. However, some previous studies mentioned large discrepancies between the angle behaviour observed in full-sized beam-column connections and simple pull tests, as the ones performed in this experimental campaign.

To resolve this problem, a second experimental program on full-scale beam-column connections loaded simultaneously in shear and rotational demand has been conducted at École Polytechnique de Montreal to characterize the global nonlinear behaviour of bolted angle connections. A total of 8 tests on double web angle connections and 15 tests on 2L-TS connections were performed.

In general, the nonlinear behaviour exhibited by bolted angle connections showed large ductility, which translated into a substantial energy-dissipation capacity under seismic loading conditions. Furthermore, the addition of top and seat angles allows a significant increase of the connection moment capacity. Therefore, the use of bolted angles for gravity framing connections can be beneficial as their large redundancy combined with their significant energy-dissipation capacity can enhance the reserve capacity of the building and thus mitigate the building collapse of Type CC braced frames.

The parameters required to recreate the results of the bolted angle monotonic tests with the *Steel02* material of OpenSees were determined. However, some discrepancies between the hysteretic behaviour obtained form the experimental tests and the *Steel02* material of OpenSees were identified. To mitigate these divergences, some modifications have been proposed to the mathematical model to increase the model precision to recreate the hysteretic behaviour specific to bolted angles. The input parameters of this proposed mathematical model were determined for each cyclic test of the bolted angle experimental program. Empirical equations based on geometrical and material properties were proposed to recreate the hysteretic behaviour of any bolted angle configuration.

This mathematical model was also implemented in OpenSees as a Uniaxial material. The hysteretic behaviour obtained in the full-scale beam-column connection experimental program were accurately recreated with a simple component-based modeling approach.

Furthermore, a design approach was proposed to improve the reserve capacity of Type CC buildings using enhanced 2L-TS connections in the gravity frame. Guidelines were proposed to achieve adequate seismic response for steel building structures with Type CC chevron braced frames, while minimizing changes to design procedures of other building components such as gravity beams and columns. Relaxation of the increased brace connection strength requirement was also investigated. A design example of a 3-storey building located in Montreal was performed. This design example was then modeled in OpenSees to assess the dynamic response of the building with enhanced connections.

Overall, the enhanced connections do not have a significant influence on the maximum base shear or the fundamental period of the unfractured building. However, the maximum first storey drift experienced by the models with enhanced connections was smaller than the one experienced by the model with the pinned connections. The maximum storey drift of the building with the enhanced connection was limited to 3% which is smaller than the one anticipated during the design process. Furthermore, the presence of enhanced connections reduced the moment developed at the top of the gravity column. Finally, the component-based model of the connection exhibited a ductile behaviour as expected during the numerical modeling.

TABLE OF CONTENTS

DEDICATION III

ACKNOWLEDGEMENTS IV

RÉSUMÉ V

ABSTRACT VIII

TABLE OF CONTENTS XI

LIST OF TABLES XX

LIST OF FIGURES XXIII

LIST OF SYMBOLS AND ABBREVIATIONS XXXIV

CHAPTER 1 INTRODUCTION 1

1.1 Background 1

1.2 Objectives 4

1.3 Research methodology 6

1.4 Organization of the thesis 6

CHAPTER 2 LITTERATURE REVIEW 9

2.1 Design requirements of low-ductility steel buildings in Canada 9

2.1.1 Minimum seismic load 9

2.1.1 Equivalent static force procedure of NBCC 13

2.1.2 Dynamic spectral analysis procedure of NBCC 15

2.1.3 Seismic design requirements for steel SFRS of the Conventional Constructions category 16

2.1.4 Comparison with ASCE7 20

2.2 Lateral reserve capacity of steel buildings 21

2.2.1 Reserve capacity from gravity beam-column connections 22

2.2.2 Reserve capacity from column continuity....25
2.2.3 Residual capacity of braced frames....28
2.3 Beam-column connections....31
2.3.1 Flexible connections....33
2.3.2 Partially restrained top and seat angle connections....39
2.3.3 Top and seat with double web angles connections....49
2.4 Building modeling with OpenSees....54
2.4.1 Hysteretic behavior of Giuffré and Pinto (1970) and Menegotto and Pinto (1973)....54
2.4.2 Fatigue damage accumulation with partial cycles....60
CHAPTER 3 METHODOLOGY....64
3. METHODOLOGY....64
3.1 General....64
3.2 Literature review....65
3.3 Experimental characterization of bolted angles....66
3.3.1 Introduction and objectives....66
3.3.2 Experimental setup....67
3.3.3 Experimental instrumentation....68
3.3.4 Test matrix....69
3.3.5 Testing procedures....73
3.3.6 Test data analysis....82
3.4 Experimental characterization of angle material....82
3.4.1 Coupon types....83
3.4.2 Test procedures....85
3.4.3 Test data analysis....87

3.5 Experimental characterization of full-scale bolted angle beam-column connections....88
3.5.1 Introduction and objectives....88
3.5.2 Experimental setup....89
3.5.3 Experimental instrumental setup....95
3.5.4 Test matrix....104
3.5.5 Testing procedures of beam-column tests....107
3.5.6 Test data analysis....110
3.6 Characterizing the hysteretic behaviour with a proposed mathematical model....111
3.7 Enhanced gravity connection design procedure....113
3.7.1 Parametric study defining the influence of the reserve capacity stiffness on the dynamic response....113
3.7.2 Development of the enhanced connection design procedure....118
CHAPTER 4 ARTICLE 1: EXPERIMENTAL PARAMETRIC CHARACTERIZATION OF BOLTED ANGLE CONNECTION BEHAVIOR....121
4.1 Introduction....122
4.2 Experimental Program....123
4.2.1 Test setup....123
4.2.2 Angle specimens....124
4.2.3 Experimental procedures....126
4.2.4 Procedure for low-cycle fatigue tests....128
4.3 Test Results....128
4.3.1 Monotonic tests....128
4.3.1 Cyclic tests....133
4.3.1 Seismic tests....135

4.3.2 Low-cycle fatigue tests....137
4.4 Failure modes....137
4.4.1 Column leg fracture....138
4.4.2 Beam leg fracture....140
4.4.3 Bolt fracture....141
4.4.4 Net section fracture near the column bolts....141
4.5 Influence of design parameters....142
4.5.1 Influence of bolt gage....142
4.5.2 Influence of angle thickness....144
4.5.3 Influence of the aspect ratio g_2/t....144
4.5.4 Influence of bolt grade....146
4.5.5 Influence of bolt pretension....147
4.5.6 Influence of loading conditions....148
4.6 Conclusions....152
4.7 Data Availability Statement....153
4.8 Acknowledgments....153
CHAPTER 5 ARTICLE 2: EVALUATING THE ROTATIONAL CAPACITY OF BOLTED DOUBLE WEB ANGLE BEAM-COLUMN GRAVITY CONNECTIONS WITH FULL-SCALE EXPERIMENTAL TESTING....157
5.1 Introduction....158
5.2 Experimental Program....160
5.2.1 Test setup....160
5.2.2 Beam-column connection specimens....161
5.2.3 Loading procedures....162

5.3 Experimental results 165
5.3.1 Nonlinear behavior of double web angle connections with rotational shear 165
5.3.1 Nonlinear behavior of double web angle connections with seismic gravity shear .. 166
5.4 Nonlinear characterization of the moment-rotation backbone curve 168
5.5 Influence of geometrical and loading parameters 170
5.5.1 Influence of seismic gravity shear load 170
5.5.2 Influence of design shear excursions 172
5.5.3 Influence of beam depth 173
5.5.4 Influence of asymmetric loading conditions 175
5.6 Conclusions and recommendations 177
5.7 Data Availability Statement 178
5.8 Acknowledgments 178
CHAPTER 6 ARTICLE 3: FULL-SCALE CYCLIC ROTATION AND SHEAR LOAD TESTING OF DOUBLE WEB WITH TOP AND SEAT ANGLE BEAM-COLUMN CONNECTIONS 183
6.1 Introduction 184
6.2 Experimental Program 186
6.2.1 Test setup 186
6.2.2 Instrumentation setup 187
6.2.3 Beam-column connection specimens 190
6.2.4 Loading procedures 192
6.3 Experimental results 195
6.3.1 Nonlinear behavior of connections with rotational shear 195
6.3.2 Nonlinear behavior of connections with seismic gravity shear 196

6.4 Nonlinear characterization of the moment-rotation envelope curve 199
6.5 Influence of geometrical and loading parameters 202
6.5.1 Influence of seismic gravity shear load 203
6.5.2 Influence of beam depth 205
6.5.3 Influence of top and seat angle geometry 206
6.5.4 Influence of column section 207
6.5.5 Influence of asymmetric loading conditions 208
6.6 Conclusions and recommendations 209
6.7 Data Availability Statement 210
6.8 Acknowledgments 210
CHAPTER 7 NUMERICAL MODELING OF BOLTED ANGLE HYSTERETIC BEHAVIOUR BASED ON EXPERIMENTAL TESTING 215
7.1 Context 215
7.2 Comparison between the cyclic bolted angle experimental results and *Steel02* model 217
7.2.1 Test data base 217
7.2.2 Modeling monotonic response of bolted angles with *Steel02* 219
7.2.3 Modeling hysteretic behaviour of bolted angles with the *Steel02* material 220
7.3 Proposed *SteelAngles* model 224
7.3.1 Modification scheme 224
7.3.2 Modeling the compressive yield force 227
7.3.3 Modeling of the unloading response 228
7.3.4 Modeling of the reloading response 231
7.3.5 Calculating the total load 233

7.4 Calibration of the *SteelAngles* model 236
7.4.1 Input parameters defining the Bauschinger effect and isotropic hardening 236
7.4.2 Input parameters of the compressive yield strength 237
7.4.3 Input parameters of the unloading and reloading response 237
7.4.4 Correspondence between the test data and the SteelAngles model 239
7.5 Implementing low-cycle fatigue and strength degradation 242
7.5.1 Fatigue damage counting method developed by Uriz and Mahin 242
7.5.2 Constant amplitude fatigue test data 245
7.5.3 Fatigue parameters for other angle geometries 246
7.6 Empirical definition of input parameters 248
7.7 Modeling bolted angle beam-column connections 252
7.8 Summary 257
CHAPTER 8 GRAVITY CONNECTION DESIGN FOR ENHANCING THE SEISMIC CAPACITY OF TYPE CC CHEVRON BRACED FRAME BUILDINGS 258
8.1 Design approach for enhanced gravity beam-column connections 258
8.1.1 Step 1: Required lateral stiffness for the gravity frame 260
8.1.2 Step 2: Required rotational stiffness for the PR connections 261
8.1.3 Step 3: Connection strength limits 265
8.1.4 Step 4: Contribution of the web angles to the connection strength 266
8.1.5 Step 5: Geometry of the top and seat angles 269
8.2 Application and validation of the proposed design method 270
8.2.1 Design of the steel building structure 270
8.2.2 Design of the reserve lateral capacity system 273
8.3 Validation of the proposed design approach 281

8.3.1 Numerical model of the structure studied 281
8.3.2 Modeling of the frame members 282
8.3.3 Modeling of the PR beam-column connections 284
8.3.4 Seismic loading 289
8.3.5 Response of the studied structure 290
8.4 Summary 303
CHAPTER 9 GENERAL DISCUSSION 305
9.1 Introduction 305
9.2 Influence of the storey stiffness reduction on the dynamic properties of buildings 305
9.2.1 Parametric study of dynamic response 306
9.2.2 Numerical validation with the building example 311
9.3 Angle material testing results 314
9.3.2 Test results of ASTM Standard 316
9.3.3 Results of tensile tests on subsize coupons 322
9.3.4 Results of tensile tests on strips coupons 324
9.3.5 Conclusions on the angle material testing 330
9.4 General discussion on the hypotheses and limitations of the research project 331
9.4.1 Limitations of the connection modeling 331
9.4.2 Limitations of the design procedure 334
CHAPTER 10 CONCLUSION AND RECOMMANDATIONS 337
10.1 Conclusions 337
10.1.1 Bolted angle component behaviour 337
10.1.2 Bolted angle beam-column connection behaviour 339
10.1.3 Bolted angle hysteretic behaviour mathematical model 340

10.1.4 Enhanced gravity connection design approach 341
10.2 Original contribution 341
10.3 Recommendations 344
10.3.1 Design recommendations 344
10.3.2 Recommendations for future work 345
BIBLIOGRAPHY 348
APPENDICES 361

LIST OF TABLES

Table 2.1. Reduction factors Rd and Ro for steel SFRSs 10

Table 2.2. Values of acceleration dependent factor *F* (NBCC 2015) 12

Table 2.3. Values of higher mode effect coefficient M_v (NBCC 2015) 14

Table 2.4. Spectral accelerations for several Canadian cities and class sites 19

Table 3.1. Dimensions of each bolted angle test cases 72

Table 3.2. Loading protocol based on storey drift ratio (AISC 2010) 74

Table 3.3. Geometrical properties of beam-column joints 78

Table 3.4. Displacement demands for the fatigue tests 80

Table 3.5. Summary of tests conducted on each angle configuration 81

Table 3.6. Test matrix of beam-column connection tests 105

Table 3.7. Design plastic moment and shear resistance of sections and specimens 106

Table 3.8. Summary of tests conducted on beam-column specimens 108

Table 3.9. Member sections of buildings 116

Table 3.10. Member sections of example 120

Table 4.1 Key response parameters from monotonic tests at a strain rate of 100 με/s. 130

Table 4.2 Key response parameters from monotonic tests at a strain rate of 600 με/s. 131

Table 4.3 Key response parameters from monotonic tests at a strain rate of 750000 με/s. 131

Table 4.4 Key-response parameters of monotonic tests with ASTM F3125 grade A325 bolts 133

Table 4.5 Key-response parameters of monotonic tests with snug-tight column bolts 133

Table 4.6 Key response parameters of cyclic tests. 135

Table 4.7 Key response parameters from seismic tests. 136

Table 4.8 Key response parameters from low-cycle fatigue tests. 137

Table 4.9. Failure mode occurrence. 138

Table 5.1. Shear and moment-rotation key response parameters of beam-column connections . 168

Table 5.2. Nonlinear backbone curve characterization of beam-column connections 170

Table 6.1. Geometrical properties, loading procedures and design resistance of the connection specimens 191

Table 6.2. Material properties of the connection specimen components. 192

Table 6.3. Shear and moment-rotation key response parameters of beam-column connections. 200

Table 6.4. Nonlinear envelope curve characterization of beam-column connections 202

Table 7.1. Calibrated parameters of *Steel02* model with monotonic tests 220

Table 7.2. Calibration parameters of cyclic tests considering a theoretical W310 beam 238

Table 7.3. Calibration parameters of cyclic tests considering a theoretical W410 beam 238

Table 7.4. Calibration parameters of the hysteretic behaviour of Time-History tests 239

Table 7.5. Number of cycles of fatigue tests at fracture 245

Table 7.6. Low-cycle fatigue degradation parameters of cyclic and time-history tests 247

Table 7.7. Normalized yield stress ratio and effective width of each angle configuration 249

Table 7.8. Summary of empirical input parameters of the SteelAngles model 250

Table 7.9. Input parameters of the *SteelAngles* model in the beam-column connection numerical model 255

Table 8.1. Summary of empirical input parameters of the *SteelAngles* model 268

Table 8.2. Seismic ang gravity loads in the example building 271

Table 8.3. Member sections of example prototype 272

Table 8.4. required secondary lateral stiffness for the first storey of the design example 274

Table 8.5. Gravity frame stiffness calculation of the first storey 275

Table 8.6. Rotational stiffness and strength limits calculations of the first storey connections. . 276

Table 8.7. Calculations of the web angle contribution to the strength of the bolted angle connections in the first storey. 277

Table 8.8. Calculations of the top and seat angle dimensions in the first storey. 279

Table 8.9. Final design of the top and seat angles in the first storey. 281

Table 8.10. *Steel02* material properties (Mazzoni et al. 2006). 283

Table 8.11. Geometrical and input parameters used in the *SteelAngles* material in OpenSees ... 286

Table 8.12. Vibration periods of the undamaged two models including P-delta effects. 290

Table 8.13. Failure modes observed and peak first storey drift (δ_1) to target drift (δ_{Target}) ratio for each ground motion with and without enhanced gravity connections 299

Table 9.1. Member sections of buildings 307

Table 9.2. Period shifts after brace failure with and without enhanced gravity connections 313

Table 9.3. Material data from ASTM Standard coupons 317

Table 9.4. Material data for ASTM Subsize specimens 323

Table 9.5. Material data from Strip coupons 326

LIST OF FIGURES

Figure 2.1. Deformation of partially restrained element along a) translational degree of freedom b) rotational degree of freedom (Nethercot et al. 1988) 23

Figure 2.2. Median and 84th percentile of storey drift vs. backup frame stiffness ratio for a) 4-storey building b) 12-storey building (Xie 2008) 24

Figure 2.3. Plan and elevation views of 8-storey models with a) levelled splices b) staggered splices (Flores et al. 2014). 26

Figure 2.4. Pushover curves for a) 4-storey and b) 8-storey SMF buildings (Flores et al. 2016)..27

Figure 2.5. Hysteresis of base shear vs. total frame drift for a) OCBF and b) R = 3 CBF (Bradley et al., 2017)..... 30

Figure 2.6. Geometric properties of a chevron braced frame and force-deformation behaviour of a typical storey (Tremblay 2018). 31

Figure 2.7. Flexural stiffness classification method of Eurocode 3 (European Standard 1993)....32

Figure 2.8. Moment-rotation hysteretic behaviour of a a) 3-row b) 4-row c) 6-row test (Astaneh-Asl et al. 1989) 34

Figure 2.9. Bolt configuration of specimens tested by Ricles and Yura (1983) 35

Figure 2.10. Failure mode observed by Ricles and Yura (1983) 35

Figure 2.11. Moment-rotation hysteresis curves of a) Bolted-Bolted and b) Bolted-Welded connections (Abolmaali et al. 2003) 37

Figure 2.12. Moment vs. rotation response with and without slab (Liu and Astaneh-Asl 2000) ..38

Figure 2.13. Schematic view of the Wind Moment Frame method (Leon and Kim 2004) 40

Figure 2.14. a) Top and seat angle deformation b) Experimental setup (Shen and Astaneh-Asl 1999) 41

Figure 2.15. Failure modes (Shen and Astaneh-Asl 1999) 42

Figure 2.16. Effective width according to Faella et al. (1998)..... 45

Figure 2.17. Cyclic deformations of bolted top and seat angle connections (Kukreti and Abolmaali 1999).....46

Figure 2.18. Moment-rotation curves of top and seat angles with varying bolt pretension Citipitioglu et al. (2002).....48

Figure 2.19. Hysteretic behaviour of Giuffré and Pinto (1970) and Menegotto and Pinto (1973) mathematical model and load reversal parameters 56

Figure 2.20. Cyclic degradation of the Giuffré and Pinto (1970) and Menegotto and Pinto (1973) model enhanced by Filippou et al. (1983).....57

Figure 2.21. Isotropic hardening of the Giuffré and Pinto (1970) and Menegotto and Pinto (1973) model enhanced by Filippou et al. (1983).....58

Figure 2.22. Partial unloading error of Menegotto and Pinto (1973) model enhanced by Filippou et al. (1983) 59

Figure 2.23. Typical stress-cycle or strain-cycle curve of low-cycle fatigue 60

Figure 2.24 Low-cycle fatigue damage index algorithm flow chart (Uriz and Mahin 2008).....63

Figure 3.1. a) Typical deformation of a beam-column joint made of bolted angles b) Simplified experimental setup.....67

Figure 3.2. Sketch of experimental setup.....68

Figure 3.3. Instrumentation and angles setup.....69

Figure 3.4. Test Matrix of angles experimental program.....70

Figure 3.5. Flexural span of the column leg g_2 71

Figure 3.6. Schematic representation of angles with a) low g_2/t b) high g_2/t.....71

Figure 3.7. Dimensions of bolted angles.....72

Figure 3.8. Time history of storey drift demand (AISC 2010) 74

Figure 3.9. Plan and elevation view of the typical building considered in determining the cyclic loading procedure (Bradley 2016).....75

Figure 3.10. Simplified structural system for the joint displacement calculation 76

Figure 3.11. Displacement demand signal for Time-History tests 79

Figure 3.12. Dimensions of ASTM Standard coupons 83

Figure 3.13. a) Dimensions and b) Position on angle leg of ASTM Subsize coupons 84

Figure 3.14. a) Dimensions and b) Position on angle legs of Strips coupons 84

Figure 3.15. Loading frame and instrumentation used for the ASTM Standard material testing .. 86

Figure 3.16. Setup used for the ASTM Subsize and Strips coupons and coupons before, during and after testing 87

Figure 3.17. Sketch of beam-column connection experimental setup 90

Figure 3.18. Attachment to the beam specimen detailing for a) top actuator and b) bottom actuator 92

Figure 3.19. Picture of beam-column connection experimental setup 93

Figure 3.20. Shear force, bending moment and rotation sign convention a) for a typical beam-column connection in a building b) for the experimental specimens 94

Figure 3.21. Connection displacement sign convention and axes a) for a typical beam-column connection in a building b) for the experimental specimens 95

Figure 3.22. Rotation measurement setup 96

Figure 3.23. Slip measurement setup 98

Figure 3.24. String potentiometers setup 100

Figure 3.25. Free body diagram of beam specimen 101

Figure 3.26. Rotation measurement setup using a W250x67 column specimen 102

Figure 3.27. Optical system setup for the specimens using W250x67 column 103

Figure 3.28. Paint treatment required on the specimen components for the optical system 104

Figure 3.29. Storey drift demand for a) Cyclic tests b) Cyclic test with design shear excursions c) Near fault (-) tests d) Near fault (+) tests 110

Figure 3.30. Configurations and dimensions of a) 3x3-, b) 4x4-, c) 5x5- and d) 6x6-bay buildings. 114

Figure 3.31. Response acceleration spectra of a) Vancouver b) Montreal. 115

Figure 3.32. Excel spreadsheet developed to design the buildings. 115

Figure 3.33. 3-DDOF system after the failure of the primary seismic load resisting system, with their stiffness and mass matrices including P-delta effects. 117

Figure 3.34. Excel spreadsheet developed to determine the fundamental period of the building with varying residual stiffness. 118

Figure 3.35. Example building geometry 119

Figure 4.1. Experimental setup. 124

Figure 4.2. Test matrix. 125

Figure 4.3. Loading protocols: a) AISC story drift-based demand for cyclic tests; b) Angle deformations for seismic tests. 127

Figure 4.4. Force-deformation behavior from: a) Monotonic test with plastic phase only (TC16-1); b) Monotonic test with hardening (TC4-1); c) Monotonic test with softening (TC6-1); d) Monotonic test with softening and hardening (TC18-1); e) Comparison between monotonic experimental test and calibrated 4-parameter power model (TC16-1); f) Comparison between monotonic 129

Figure 4.5. a) Monotonic test (TC12-1) and cyclic test with softening (TC12-4); b) Monotonic test (TC4-1) and cyclic test with hardening (TC4-4); c) Monotonic test (TC4-1) and Seismic test (TC4-6); and d) Monotonic test (TC9-1) and Low-cycle fatigue test (TC9-11). 134

Figure 4.6. Observed behavior: a) Column leg fracture in monotonic test (TC10-2); b) Column leg fracture in cyclic test (TC10-4); c) Beam leg fracture in monotonic test (TC14-2); d) Beam leg fracture in cyclic test (TC5-5); e) Bolt fracture (TC18-6); and f) Net section tension fracture (TC10-4). 139

Figure 4.7. Influence of column bolt gage g_c on the force-deformation response in monotonic tests for specimens with thickness of a) 7.9 mm; b)9.5 mm; c) 12.7 mm; d) 15.9 mm; and e) 19.1 mm. 143

Figure 4.8. Influence of angle thickness t on the force-deformation response in monotonic tests for specimens with column gage of a) 63.5 mm; b) 76.2 mm; c) 88.9 mm; 101.9 mm; and 114.3 mm. 145

Figure 4.9. Influence of the aspect ratio g_2/t on: a) Initial stiffness K_i; b) Yielding force F_Y; c) Plastic to initial stiffness ratio K_P/K_i; and d) Softening and hardening to initial stiffness ratios K_S/K_i; K_H/K_i. 146

Figure 4.10. a) Impact of column bolt grade and pretension on the force-deformation relationship (TC10, g_2/t = 4.38). b) Impact of column bolt grade and pretension on the initial stiffness. 147

Figure 4.11. Influence of strain rate in monotonic tests: a) Impact on global force-deformation relationship (TC10, g_2/t = 4.38). b) Impact on initial stiffness. 149

Figure 4.12. a) Compressive yield force F_Y^- in cyclic tests (TC4-4); b) Influence of the aspect ratio g_2/t on the compressive yield force to yield force ratio; c) Energy-dissipation in the cyclic tests; d) Pinching response in seismic test (TC4-6); e) Relationship between deformation demand and number of cycles to failure in low-cycle fatigue tests; and f) Relationship between energy dissipated and number of cycles to failure in low-cycle fatigue tests. 151

Figure 5.1. Beam-column connection test setup. 161

Figure 5.2. Beam-column connection details and loading procedures. 162

Figure 5.3. Beam-column connection loading protocols for a) cyclic tests; b) Cyclic tests with design shear excursions; c) Negative asymmetric near-fault tests; d) Positive asymmetric near-fault tests. 163

Figure 5.4. Deformation pattern of double web angle connections with rotational shear (Specimen 2C): a) Lateral view of the connection b) Front view of the connection c) Column leg fracture d) Deformed angle at fracture. 165

Figure 5.5. Deformation pattern of double web angle conections with seismic gravity shear and design shear excursions (Specimen 2B): a) Lateral view of the connection b) Front view of the connection c) Beam leg fracture and column leg rotation d) Deformed angle at fracture. 167

Figure 5.6. Free-body diagram of a web angle component in the connection. 167

Figure 5.7. Numerical modeling of moment-rotation backbone curve: a) with seismic gravity shear (Specimen 2A) and b) with rotational shear (Specimen 2C). 170

Figure 5.8. Influence of seismic gravity shear load on the connection hysteretic behavior: a) W310 beam and b) W410 beam. 171

Figure 5.9. Influence of design shear load excursions on the connection hysteretic behavior: a) W310 beam and b) W410 beam. 172

Figure 5.10. Transverse displacement (Z): a) without shear excursions (2A) and b) with shear excursions (2B). 173

Figure 5.11. Influence of beam depth on the connection hysteretic behavior: a) with seismic gravity shear b) with rotational shear c) with seismic gravity shear and normalized with the beam plastic moment and d) with rotational shear and normalized with the beam plastic moment. 175

Figure 5.12. a) Influence of asymmetric loading protocol on the connection hyteretic behavior b) Transverse displacement (Z) of the negative asymmetric test (2D) c) Transverse displacement (Z) of the positive asymmetric test (2E). 176

Figure 6.1. Beam-column connection test setup. 188

Figure 6.2. a) Instrumentation setup for measuring the connection rotation; b) Captors position on the specimen; c) Instrumentation setup for measuring the angle vertival and horizontal displacement; d) String attachment detail to the top and seat angles. 189

Figure 6.3. Beam-column connection parameters. 190

Figure 6.4. Beam-column connection loading protocol for a) cyclic tests; b) cyclic tests with design shear excursions; c) Asymetric near-fault tests; d) Shear loading. 194

Figure 6.5. Specimen 1C: a) overall deformation pattern without shear; b) top angle deformation; c) seat angle fracture. 196

Figure 6.6. Specimen 1A: a) overall deformation with W360x347 column and shear; b) top angle fracture; c) top angle beam leg rotation. 197

Figure 6.7. Transverse displacement (Δ_Z) with shear load; a) Specimen 2A; b) Specimen 2D…198

Figure 6.8. Specimen 4D; a) overall deformation pattern with W250x49 column and shear; b) web angle deformation; c) top angle cracking; d) column flange yielding and top angle beam leg rotation. 199

Figure 6.9. Numerical modeling of moment-rotation envelope curves: a) Specimen 3A, with shear load; b) Specimen 3C, without shear load.....202

Figure 6.10. Influence of shear: a) influence of shear load on the connection hysteretic behavior (Specimens 3A and 3C); b) influence of shear load excursions on the connection hysteretic behavior (Specimens 3A and 3B).....203

Figure 6.11. Influence of shear load on the free body diagram of top and seat angles.....204

Figure 6.12. Influence of beam depth on the connection hysteretic behavior: a) Specimens 1A and 3A; b) Specimens 2A and 4A; c) Normalized connection moment with the beam plastic moment for specimens 1A and 3A; d) Normalized connection moment with the beam plastic moment for specimens 2A and 4A.....205

Figure 6.13. Influence of the top and seat angle geometry on the connection hysteretic behavior: a) Specimens 1A and 2A; b) Specimens 3A and 4A.....207

Figure 6.14. Influence of the column section on the connection hyteretic behavior: a) Specimens 2A and 2D; b) Specimens 4A and 4D.....207

Figure 6.15. Influence of asymmetric loading protocol on the connection hyteretic behavior (Specimen 2D).....209

Figure 7.1. a) Top and seat with double web angle beam-column connection detailing b) Moment-rotation response of proposed models.....215

Figure 7.2. Potential bolted angle connection types to model with the *SteelAngles* model.....217

Figure 7.3. Sketch of experimental setup 218

Figure 7.4. Test Matrix of angles experimental program 219

Figure 7.5. Modeling bolted angle monotonic response with Steel02 model 220

Figure 7.6. a) Hysteretic behaviour of the *Steel02* material b) Cyclic degradation of the *Steel02* material c) Strain-hardening and d) Partial reloading error associated to the strain hardening of the *Steel02* material 222

Figure 7.7. a) Comparison between monotonic and cyclic tests (TC4-1 & TC4-4) b) discrepancies between the Steel02 model and experimental results (TC4-4) 223

Figure 7.8. Modifications to the Steel02 model to create the SteelAngles model a) for the unloading response b) for the reloading response, c) Decomposition of the Steel02 model at small cycles, d) Decomposition of the Steel02 model at large cycles, e) Decomposition of the SteelAngles model at small cycles, f) Decomposition of the SteelAngles model at large cycles 226

Figure 7.9. a) Compressive yield force of a typical cyclic test (TC4-5) b) Increase of the transition load between the initial and secant stiffness of the negative excursions (TC4-5) 228

Figure 7.10. Flowchart of the proposed mathematical model algorithm 235

Figure 7.11. Comparison between experimental response and SteelAngles model of a) static cyclic test (TC4-5) b) Time-History test (TC4-7) c) Hysteretic pinching d) Partial excursion error e) Energy-dissipated in a static cyclic test (TC4-5) f) Energy-dissipated in a Time-History test 241

Figure 7.12. Flowchart of low-cycle fatigue damage index calculation (Uriz and Mahin 2008) 244

Figure 7.13. a) Typical fatigue test failure (TC9-11) b) Relationship between deformation demand and number of cycles of low-cycle fatigue tests. 245

Figure 7.14. Numerical model a) without fatigue degradation b) with fatigue degradation 247

Figure 7.15. Effective width calculation (Faella et al. 1998) 248

Figure 7.16. Correlation between the best fit and the empirically estimated parameters a) positive yield force F_0^+, b) initial stiffness K_i^+, c) positive plastic stiffness K_P^+, d) unloading to initial

stiffness ratio e_N, e) fatigue deformation parameter Δ_c and f) Energy-dissipated in the tests and the model with the empirical parameters and fatigue degradation. 251

Figure 7.17. Numerical modeling of: a) 2L connections; b) 2L-TS connections. 252

Figure 7.18. Numerical modeling of : a) 2L connections with W310 beam; b) 2L connections with W410 beam; c) 2L-TS connections with W310 beam and angle thickness of 9.5 mm; d) 2L-TS connections with W410 beam and angle thickness of 9.5 mm; e) 2L-TS connections with W310 beam and angle thickness of 19.1 mm; f) 2L-TS connections with W410 beam and angle thickness of 19.1 mm; 256

Figure 8.1. a) Spring representation of the building reserve capacity; b) Parameters for residual braced frame stiffness; c) Parameters for gravity column stiffness; d) parameters for gravity beam stiffness; e) Parameters for gravity beam-column connection stiffness. 264

Figure 8.2. Connection secant stiffness range respecting the strength limits 266

Figure 8.3. Schematic contribution of the web in the connection strength 269

Figure 8.4. Example building geometry 272

Figure 8.5. Web angle detailing of gravity connections for: a) exterior beams; and b) interior and braced beams. 273

Figure 8.6. Displacement spectrum of Montreal Soil type C expressed in storey drift. 274

Figure 8.7. Angle yield force by effective width F_0^+/b_{eff} varying with the column leg flexural span g_2 for different angle thickness t. 280

Figure 8.8. Building detailing a) Prototype building modeling; b) Residual stress pattern in the columns (Galambos and Ketter 1958); c) Out-of-plumbness and element discretization of columns and braces. 282

Figure 8.9. Numerical modeling of: a) gusset-beam-column connections; and b) gravity beam-column connections. 285

Figure 8.10. Force-displacement behaviour of : a) 1 mm-strip web angle; b) Angle geometry A; c) Angle geometry B; d) Angle geometry C; e) Elastic No-tension material. 287

Figure 8.11. Hysteretic moment-rotation behaviour of a) Angle geometry A with W250x49 beam; b) Angle geometry A with W310x60 beam; c) Angle geometry B with W250x49 beam; d) Angle geometry B with W310x60 beam; e) Angle geometry C with W250x49 beam. 288

Figure 8.12. Response spectra of: a) M6.0 ground motions; and b) M7.0 ground motions. 289

Figure 8.13 Hysteretic brace force of: a) Pinned connection model; b) Enhanced connection model. 291

Figure 8.14 Building deformation at: a) Point A; b) Point B. 291

Figure 8.15 Time-history of a) Base shear; b) 1st storey drift; c) 2nd storey drift; d) 3rd storey drift. 294

Figure 8.16 Time-history of a) Right brace force; b) Left brace force; c) Moment at the top of interior gravity column; d) Moment in an interior connection attached to a strong axis column. 296

Figure 8.17. Moment distribution in the columns of the gravity frame with enhanced connections. 297

Figure 8.18. Hysteretic response of a connection joining a W310x60 beam to an interior column on its strong axis during Ground Motion 9. 297

Figure 8.19. Base shear versus first storey drift for every ground motion, with pinned and enhanced gravity connections 300

Figure 9.1. NBCC 2015 design spectra for: a) Vancouver; b) Montreal. 306

Figure 9.2. Configurations and dimensions of a) 3x3-, b) 4x4-, c) 5x5- and d) 6x6-bay buildings. 308

Figure 9.3. 3-DOF system after the failure of the primary seismic load resisting system, with their stiffness and mass matrices including P-delta effects. 309

Figure 9.4. Influence of the loss in storey stiffness variability on the fundamental period of the buildings located in: a) Vancouver; and b) Montreal. 310

Figure 9.5. Influence of the loss in storey stiffness variability on the spectral acceleration of the buildings located in: a) Vancouver on site class C; b) Montreal on site class C; c) Vancouver on site class E; and d) Montreal on site class E. 311

Figure 9.6. Dimensions of ASTM Standard coupons 314

Figure 9.7. a) Dimensions and b) Position on angle leg of ASTM Subsize coupons 315

Figure 9.8. a) Dimensions and b) Position on angle legs of Strips coupons.....315

Figure 9.9. Typical stress-strain curve obtained from a tensile test: a) Entire curve; b) Close-up of the elastic and yield plateau regions of the curve.....317

Figure 9.10. Typical stress-strain curve of ASTM Subsize and Strips specimens.....322

Figure 9.11. Yield stress distribution along angle legs for the L4x4x5/16 (TC19) angles. 329

Figure 9.12. Yield stress distribution along angle legs for the L4x6x3/8 (TC1) 329

Figure 9.13. Yield stress distribution along angle legs for the L6x8x1/2 B (TC4 & TC16) 329

Figure 9.14. Yield stress distribution along angle legs for the L6x8x3/4 A (TC13 & TC14) 330

Figure 9.15. Envelope response of a connection with a concrete slab (Liu and Astaneh 2004)..332

Figure 9.16. *Joint2D* element definition (Mazzoni et al. 2006).....333

Figure 9.17. a) Modeling of fiber material in series; b) bolt slip model (Shen and Astaneh 2000). 334

LIST OF SYMBOLS AND ABBREVIATIONS

Abbreviations

2L	Double web angle connection
2L-TS	Double web angle with top and seat angles connection
NBCC	National Building Code of Canada
PR	Partially restrained
SFRS	Seismic force resisting system
Type CC	Conventional Construction Category
Type D	Ductile SFRS
Type LD	SFRS of limited ductility
Type MD	SFRS of moderate ductility
WWF	Welded wide flange
LVDT	Linear variable differential transformer
AISC	American Institute of Steel Constrution
CISC	Canadian Institute of Steel Constrution
CSA	Canadian Standard Association
ASCE	American Society of Civil Engineers
ASTM	American Society of Testing and Materials
FEMA	Federal Emergency Management Agency
LP	Linear potentiometer
SP	String potentiometer
DDOF	Dynamic degree of freedom
DOF	Degree of freedon
CBF	Concentrically braced frame
SMF	Steel moment frame
BRBF	Buckled-restrained braced frame
SDA	Storey drift angle
OCBF	Ordinary concentrically braced frame
EBF	Eccentric braced frame
WMF	Wind moment frame
OpenSees	Open System for Earthquake Engineering Simulation
SD	Standard deviation
COV	Coefficient of variation

AF Amplification factor

Symbols

α	Stiffness reduction factor resulting in the residual stiffness
α	Rayleigh damping parameter
α_1, α_1	Unitless parameter defining the compressive isotropic hardening
a_2, a_2	Unitless parameter defining the compressive isotropic hardening
a_3, a_3	Unitless parameter defining the tensile isotropic hardening
a_4, a_4	Unitless parameter defining the tensile isotropic hardening
AB	Initial distance between the inclined SP and the horizontal SP
A_{bb}	Braced frame beam area
A_{brace}	Brace area
AC	Initial distance between the inclined SP and the measured point
AC'	Measured distance between the inclined SP and the measured point
A_{eff}	Effective area of the angle leg section
B	Beam leg length
b	Ratio between the plastic and initial stiffness
b^-	ratio between the negative initial and plastic stiffness of the backbone curve
b^+	ratio between the positive initial and plastic stiffness of the backbone curve
b_1	Unitless parameter defining the compressive isotropic hardening
b_1	Plastic stiffness ratio of the first power curve
b_2	Unitless parameter defining the tensile isotropic hardening
b_2	Ratio between the backbone plastic stiffness and the secant stiffness
BC	Initial distance between the horizontal SP and the measured point
BC'	Measured distance between the horizontal SP and the measured point
b_{eff}	Effective angle width
b_{secant}	ratio between the secant stiffness and the initial stiffness
C	Column leg length
C_f	Compressive load on the column
$C_{f\text{-}E}$	Seismic brace compression force
c_{r1}	Unitless parameter defining the degradation rate
c_{r2}	Unitless parameter defining the degradation rate
d_b	Bolt diameter
d_{beam}	Beam depth
d_c	Column depth
DF	Damage factor
d_{hb}	Bolt head diameter (Faella et al. 1998)
DI	Damage index
d_L	Distance between the bottom flange of the beam and the lower fiber of the web angles
d_N	Distance between the North linear potentioneters
D_{nx}	Building dimension perpendicular to the lateral loading direction
d_S	Distance between the South linear potentioneters

d_U	Distance between the bottom flange of the beam and the upper fiber of the web angles
e	Bolt edge distance
E	Steel Elastic modulus
ε	Strain
ε^*	Normalized strain
ε_0	strain at which the element can sustain only one full cycle in low-cycle fatigue
ε_0	Strain of the intersection point between the asymptotes of the initial stiffness and the plastic stiffness
e_h	Hardening strain
$\varepsilon_{M\alpha\xi-}$	Maximum strain experienced in compression
$\varepsilon_{M\alpha\xi+}$	Maximum strain experienced in tension
eN	Ratio between the negative and positive initial stiffness
ε_ρ	Strain at the load reversal
e_{rupt}	Strain at rupture
e_y	Yield strain
F	Acceleration and velocity factor (Chapter 2)
F	Bolt head width (Chapter 3)
F	Force
f	frame increment
F^*	Force ratio
F_0	Force at the intersection between the initial and plastic stiffness
F_0^-	Compressive yield force
F_0^+	Tensile yield force
$F_{0\text{-}1}$	Force at the intersection between the initial and plastic stiffness of the first power curve
$F_{0\text{-}2}$	Force at the intersection between the initial and plastic stiffness of the second power curve
$F_{0\text{-}3}$	Force at the intersection between the initial and plastic stiffness of the third power curve
F_1	Force obtained from the first power curve
F_1^*	Force ratio of the first power curve
F_2	Force obtained from the second power curve
F_2^*	Force ratio of the second power curve
F_3	Force obtained from the third power curve
F_3^*	Force ratio of the third power curve
F_{angle}	Force in the angle
F_i	Total force
F_{IH}	Target load including hardening
F_L	Force obtained from the linear curve
f_L	Force at the lower fiber of the web angles
F_{max}	Maximum force
fN	Ratio between the negative and positive yield force
$F_{pj,T}$	Force in the top angle at the anticipated storey drift

F_R	Force at load reversal
$F_{R\text{-}1}$	Force at the load reversal of the first power curve
$F_{R\text{-}2}$	Force at the load reversal of the second power curve
$F_{R\text{-}3}$	Force at the load reversal of the third power curve
F_{st}	Force gain from strain-hardening
F_t	Seismic load at the top of the building
F_T	Target force
F_T^*	Relative target force
F_U	Ultimate force
F_u	Ultimate stress (Chapter 9)
f_U	Force at the upper fiber of the web angles
$_{FV1000}$	Load applied by the 1000 kN actuator
F_{V500}	Load applied by the 500 kN actuator
F_x	Seismic load at the level x
F_Y	Yield force
F_y	Steel yield stress
F_Y^-	Compressive yield force
$F_{y\ -\ Static\ avg}$	Average static yield stress
$F_{y,0.2\%}$	Yield stress at a strain offset of 0.2%
F_Y^+	Tensile yield force
$F_{y\text{-}Standard}$	Yield stress of standard ASTM coupon
$F_{y\text{-}static}$	Static yield stress
$F_{y\text{-}Strip}$	Yield stress of strip coupon
g	Gravitational acceleration (9.81 m/s^2)
g_2	Column leg flexural span
g_c	Column bolt gage
h_n	Building height
h_s	Storey height
h_x	Height of the storey x
I_b	Beam section column of inertia
I_c	Column section moment of inertia
I_E	Earthquake importance factor
I_{eff}	Effective moment of inertia of the angle leg section
i	Storey increment
I_{mb}	Beam moment of inertia
I_{nc}	Column moment of inertia
k	Fillet width
K'_{Br}	Residual stiffness of the braced frame
$K_{b,\,f}$	Stiffness of the beams for frame f
$K_{c,\,f}$	Stiffness of the columns for frame f
K_H	Hardening stiffness
K_i	Initial stiffness
K_i^-	Initial stiffness of negative backbone
$K_{i\ -\ 100me/s}$	Initial stiffness of test at 100 me/s
$K_{i\ -\ 600me/s}$	Initial stiffness of test at 600 me/s

$K_{i\ -\ 750000me/s}$	Initial stiffness of test at 750000 me/s
$K_{i\ -\ A325}$	Initial stiffness of A325 bolt tests
$K_{i\ -\ A490}$	Initial stiffness of A490 bolt tests
$K_{i\ -\ Pretensionned}$	Initial stiffness of pretensionned bolt tests
$K_{i\ S\text{-}T}$	Initial stiffness of snug-tight bolt tests
K_i^+	Initial stiffness of positive backbone
$K_{j,\ fi}$	Stiffness of the joints for frame f at storey i
K_L	Linear plastic stiffness
K_p^-	Plastic stiffness of negative backbone
K_P^-	Negative plastic stiffness
K_p	Plastic stiffness
K_p^+	Plastic stiffness of positive backbone
k_q	Connection flexural stiffness
K_R	Residual stiffness
K_S	Softening stiffness
$K_{sj,f}$	Rotational stiffness of the joint
K_{Target}	Target lateral stiffness
L	Total width of the angles
$L/T_{\ Fu}$	Longitudinal to transversal ultimate stress ratio
$L/T_{\ Fy}$	Longitudinal to transversal yield stress ratio
L_b	Beam length
L_c	Column length
LP_{NE}	North-East linear potentiometer measurement
LP_{NW}	North-West linear potentiometer measurement
LP_{SE}	South-East linear potentiometer measurement
LP_{SW}	South-West linear potentiometer measurement
L_{V1000}	Distance between the column flange and the 1000 kN actuator
L_{V500}	Distance between the column flange and the 500 kN actuator
L_W	Web angle length
M	Flexural moment in the connection
m	Slope defining the low-cycle fatigue degradation
M	Moment
m	Beam increment
M_A	Moment in the connection causing a rotation of q_b
M_{fx}	Maximum imposed moment on the column in its strong axis
M_{fy}	Maximum imposed moment on the column in its weak axis
M_j	Moment in the joint
M_{max}	Maximum moment
M_{min}	Minimum moment
M_p	Moment plastique
M_{pb}	Beam plastic moment
M_{pc}	Column plastic moment
M_{pj}	Joint plastic moment
M_{pj}	Plastic moment of the connection
$M_{pj,w}$	Moment created by the web angles

$M_{q\,max}$	Moment at maximum rotation
$M_{q\,min}$	Moment at minimum rotation
M_{rb}	Beam resisting moment
$M_{sj,fi}$	Maximum moment required in the connection at the target storey drift
μ_T	Building period-based ductility (FEMA P695)
M_v	Higher mode factor
M_Y	Yield moment
M_y^-	Yield moment of negative backbone
M_y^+	Yield moment of positive backbone
n	Number of storeys
N	Number of cycles
n	Column increment
N_b	Number of beams in frame f
N_c	Number of columns in frame f
N_f	Number of moment frames in the buildings created by the gravity frame
N_{fj}	Number of cycles to failure
N_j	Number of joint in frame f
p	Distance between the bolts perpendicular to the loading direction
PGA	Peak ground acceleration
PGA_{ref}	Reference peak ground acceleration
P_1	Compressive load on the column of the first storey
P_{Slip}	Friction load between the fastened elements
θ	Brace angle (Chapter 8)
$\theta_{M\alpha\xi}$	Maximum rotation
$\theta_{M\iota\nu}$	Minimum rotation
$\theta_{M-M\alpha\xi}$	Rotation at maximum moment
$\theta_{M-M\iota\nu}$	Rotation at minimum moment
θ_b	Joint rotation
$\theta_{\varphi,\,\phi\iota}$	Joint rotation at target storey drift
R	American seismic reduction factor (ASCE7 2015)
r	Fillet width (Faella et al. 1998)
R	Coefficient defining the transition between the initial and plastic stiffness
R^-	Transition parameter of negative backbone
R^+	Transition parameter of positive backbone
R_0	Initial coefficient defining the transition between the initial and plastic stiffness
R_2	Transition parameter of the second power curve
R^2	Determination coefficient
R_d	Ductility seismic force reduction factor
r_{eff}	Effective radius of gyration of the angle leg section
R_o	Overstrength seismic force reduction factor
R_y	Factor to account for the probable yield stress in the structure
σ	Stress
S	Spectral ordinate
s	Joint increment

$S(T_a)$	Design spectral response acceleration of the building
σ^*	Normalized stress
σ_0	Stress of the intersection point between the asymptotes of the initial stiffness and the plastic stiffness
s_1	Unitless parameter representing the increase in transition force during unloading
s_2	Unitless parameter representing the increase in transition force during unloading
s_3	Unitless parameter representing the increase in transition force during reloading
s_4	Unitless parameter representing the increase in transition force during reloading
S_a	Spectral acceleration
σ_ρ	Stress at the load reversal
$\sigma_{st,\ Compression}$	Stress shift caused by isotropic hardening in compression
$\sigma_{st,\ Tension}$	Stress shift caused by isotropic hardening in tension
T	Fundamental lateral period of vibration of the building
t	Angle thickness
$T1$	First vibration period
$T2$	Second vibration period
$T3$	Third vibration period
T_a	Design fundamental lateral period
T_{emp}	Empirical period
$T_{f\text{-}E}$	Seismic brace tensile force
T_i	Fundamental lateral period of vibration of the initial building
T_r	Fundamental lateral period of vibration of the residual building
T_x	Static torsional moment in storey x
V	Shear load in the connection
V_A	Lateral load causing the moment M_A
V_{base}	Design base shear
V_d	Design base shear
V_e	Base shear determined with the design spectra
V_{ed}	Design elastic base shear
V_{Max}	Maximum shear load
V_{Min}	Minimum shear load
V_r	Base shear calculated with fractured period
V_x	Storey shear in storey x
W	Seismic load of the building
W_o	overstrength factor (FEMA P695)
W_x	Seismic load of the storey x
x	Level of the building
β	Rayleigh dampin parameter
ξ	Equivalent stiffness
ξ	Deformation ratio
Z	Plastic modulus

Δ	Displacement
Δ^*	Deformation ratio
Δ_0	Initial displacement
Δ_0	Deformation at the intersection between the initial and plastic stiffness
Δ_0^-	initial yield deformation in compression
Δ_0^+	Initial yield deformation in tension
$\Delta_{0\text{-}1}$	Deformation at the intersection between the initial and plastic stiffness of the first power curve
$\Delta_{0\text{-}2}$	Deformation at the intersection between the initial and plastic stiffness of the second power curve
$\Delta_{0\text{-}3}$	Deformation at the intersection between the initial and plastic stiffness of the third power curve
Δ_1^*	Deformation ratio of the first power curve
Δ_2^*	Deformation ratio of the second power curve
Δ_3^*	Deformation ratio of the third power curve
Δ_A	Amplitude of low-cycle fatigue tests
Δ_{Angles}	Angle displacement
$\Delta_{b,fi}$	Displacement caused by the beam flexure
Δ_{Beam}	Frame lateral displacement caused by the beam rotation
Δ_C	Amplitude at which a single cycle leads to the fracture
$\Delta_{c,fi}$	Displacement caused by the column flexure
Δ_{Column}	Frame lateral displacement caused by the column flexural deformations
δ_{Drift}	Storey drift
δ_{Slip}	Cumulative gap between the bolt and the fastened elements
Δe	Strain amplitude
Δ_{FMax}	Displacement at maximum force
Δ_H	Displacement at the start of the hardening phase
Δ_i	Applied deformation
$\Delta_{j,fi}$	Displacement caused by the joint rotation
Δ_{Joint}	Frame lateral displacement caused by the joint rotation
Δ_L	Displacement at the lower fiber of the web angles
Δ_{max}^-	Maximum deformation in compression
Δ_{max}^+	Maximum deformation in tension
$\Delta_{pj,T}$	Force in the top angle at the anticipated storey drift
Δ_R	Deformation at load reversal
$\Delta_{R\text{-}1}$	Deformation at the load reversal of the first power curve
$\Delta_{R\text{-}2}$	Deformation at the load reversal of the second power curve
$\Delta_{R\text{-}3}$	Deformation at the load reversal of the third power curve
ΔS	Stress amplitude
Δ_S	Displacement at the start of the softening phase
Δ_{Storey}	Total frame lateral displacement
Δ_T	Target deformation
Δ_T^*	Relative target deformation
δ_1	Peak first storey drift
δ_{Target}	Target storey drift

Δ_U	Ultimate displacement
Δ_U	Displacement at the upper fiber of the web angles
$\Delta_{U\text{-}cyclic}$	Ultimate displacement experienced by the angle specimen in cyclic tests
Δ_x	Horizontal displacement in the beam-column tests
Δ_z	Vertical displacement in the beam-column tests
φ	design factor

LIST OF APPENDICES

Appendix A Angle component test summary 361

Appendix B Full-scale connection testing results 501

Appendix C SteelAngles uniaxial material code.....550

CHAPTER 1 INTRODUCTION

1.1 Background

In the National Building Code of Canada (NBCC) 2015 (NRCC 2015), earthquakes are considered as rare events for design and the design seismic data is determined for a probability of exceedance of 2% in 50 years. Consequently, the main objective of the NBCC seismic provisions is to provide life safety for building occupants, while allowing permanent inelastic deformations in the structure. Ductile structures can resist strong seismic ground motions through inelastic deformations, and it is therefore possible to design ductile seismic force resisting systems (SFRSs) of buildings with seismic design loads that are reduced as a function of the expected inherent ductility of the system. In the NBCC, design seismic loads are reduced from the expected elastic force level by the ductility-related force modification factor R_d which can take a value between 1.0 and 5.0 depending on the SFRS ductility. The NBCC also includes an overstrength-related force modification factor R_o that accounts for the difference between the design seismic loads and the probable lateral resistance that can be mobilised by the SRFS during rare seismic events of the design earthquake (Mitchell et al. 2003).

Clause 27 of the CSA S16 standard for design of steel structures in Canada (CSA 2014) outlines the provisions for the seismic design of structural steel buildings to achieve the expected inelastic behaviour. Generally, the seismic design requirements for members and connections of structures relying on a high level of ductility (designed with higher R_d values) are stricter. Those stringent provisions, along with capacity design requirements for non-ductile SFRS components, are needed to ensure that the intended SFRS yielding mechanism and energy dissipation can be achieved while maintaining structural integrity during a strong earthquake. Overall, the design of a ductile SFRS requires numerous verifications and rigorous detailing which lengthen and complicate the design process and increase construction costs.

NBCC and CSA-S16-14 include provisions for steel SRFSs of the Conventional Construction (Type CC) category, i.e. SFRSs that essentially rely on the inherent ductility of steel and slip in connections to accommodate inelastic deformations and dissipate the input seismic energy. In the NBCC, Type CC SFRSs, which are also referred to as low-ductility SRFSs, must be designed with an R_d factor of 1.5 in view of their limited inelastic deformation capacity. However, seismic design

requirements for these SFRSs are minimal and much simpler. For instance, capacity design is not required and most of the design can be performed quickly based on elastic analysis results. This represents a strong incentive for selecting SFRSs of the Type CC category rather than a more ductile system, in spite of the higher design seismic loads (low R_d factor). For this reason, a large portion of the steel buildings in Canada are designed with Type CC SFRSs, most of them being concentrically braced steel frames because of their simplicity and high efficiency for resisting lateral loads.

However, strict limitations are imposed for this system category in the NBCC and CSA S16 to compensate for the limited ductility and the lack of control on the inelastic response and yielding hierarchy that can lead to undesirable failure mechanisms such as a soft story or brittle failures in the SFRS. In the NBCC, the system is limited to 15 m in height for structures located in regions of moderate and high seismic hazard. For these structures, CSA S16 requires that the design seismic loads for the SFRS connections be increased by 1.5 (i.e. corresponding to $R_d = 1.0$) if the governing failure mode of the connections is not ductile. This increased required strength can result in very large, uneconomical connections. A possible solution could be to design the brace connections without amplified loads and to rely on the lateral resistance of the gravity system to prevent building collapse in case of brace connection failure. Lateral resistance can be obtained in the gravity frame by forming moment frames by introducing partially-restrained (PR) connections between beams and columns. This approach may also reduce the seismic loads induced in the braced frames and thereby the likelihood of failure in braced frame members and connections other than the brace connections.

Typically, in design of Type CC braced steel frames, the entire lateral load is considered to be resisted by the braced frames only and the contribution of other structural components is neglected. However, the frame action resulting from the rotational stiffness and strength of gravity beam-column connections (Shen and Astaneh-Asl 2000, Wang et al. 2006, Yang and Tan 2013, Flores and Charney 2014, Elkady and Lignos 2015, Hwang and Lignos 2017, Del Carpio et al. 2019) and the fixity of column base-to-foundation connections (Maan and Osman 2002, Aviram et al. 2010, Kanvinde et al. 2012, Zareian and Kanvinde 2013), can provide the building with additional lateral strength and stiffness which is usually not accounted for in the building design. The lateral stiffness of a singular element can indeed be neglected compared to that of a braced frame, but because of

their large number, they can form a reserve capacity system that can significantly enhance the seismic robustness of the structure (Hines et al. 2009). Therefore, a design that ensures minimum lateral strength, stiffness and ductility from the gravity system can increase considerably the redundancy and seismic collapse capacity of the structure, especially if a failure occurs in the primary SRFS. This reserve capacity can also provide the structure with sufficient resistance and robustness to withstand aftershocks that can be expected after the main seismic event. Structural robustness can be defined as the ability of a structure to withstand extreme loading such as earthquakes, explosions and impacts without experiencing disproportionate damage (Baker et al. 2008). This characteristic is usually defined by the structural redundancy and ductility.

To date, several studies were carried out to characterize the cyclical response of partially restrained (PR) and rigid connections for use in steel moment frames, at both the column base (Picard and Beaulieu 1985, Picard et al. 1987, Fafard et al. 1990, Dumas et al. 2006, Kanvinde et al. 2013, Kanvinde et al. 2014) and beam-column joints (Astaneh-Asl et al. 1989, Chen and Kishi 1989, Kishi and Chen 1990, Shen and Astaneh-Asl 1999, Liu and Astaneh-Asl 2000, Liu and Astaneh-Asl 2004, Pirmoz et al. 2009, Gong 2014).

Lately, the role of simple beam-column gravity connections in the mitigation of progressive collapse or improving resistance against blast loading has attracted interest in research community in the United States (Tyas et al. 2012, Yang and Tan 2013, Mander et al. 2014). However, limited studies have been performed to investigate the possible contribution of these connections to increase the seismic resistance of entire steel buildings (e.g. Flores et al 2014, Elkady and Lignos 2015, Hwang and Lignos 2017, Del Carpio et al. 2019). Therefore, data available is not sufficient to fully exploit the gravity frame potential lateral capacity to ease the seismic design of or relax limitations currently imposed to Type CC braced frames in Canada. For instance, by incorporating a properly designed reserve capacity with sufficient strength and stiffness in the gravity system, strict design requirements for Type CC frames, such as designing brace connections for amplified seismic loads, may no longer be required.

The characterization of the lateral capacity of a gravity frame to seismic resistance depends on several parameters related to the building geometry and detailing:

1. Type of gravity beam-column connection (eg: shear tab, double web angle, single web angle, top and seat angles, top and seat with double web angles);
2. Detailing of the beam-column connections (eg: concrete slab, bolt position, component thickness);
3. Detailing of the column base plate (eg: size, thickness, position of anchor rods);
4. Building dimensions (eg: number of storeys, number of bays in each directions);
5. Braced frame configuration (eg: chevron bracing, X-bracing, Split-X bracing);
6. Column continuity over several storeys; and
7. Orientation of and sections used for the columns.

Among these parameters, it is believed that developing a simple PR beam-column connection that can develop high lateral strength and stiffness while exhibiting stable plastic deformation capacity under inelastic cyclic loading is the most promising avenue for enhancing the seismic performance of Type CC braced frames with limited cost increase and changes to current practice. Among the several connections examined in past studies, the double angle connections with top and seat angle (2L-TS) seems to be an excellent choice because of its simplicity and high ductility capacity (Azizinamini 1982, Azizinamini 1985, Elnashai et al. 1998, Shen and Astaneh-Asl 1999, Calado et al. 2000, Garlock et al. 2003, Yang and Tan 2013, Gong 2014). This connection can also be easily implemented as a retrofit solution for seismically deficient existing structures as the top and seat angles can be bolt connected to the existing beams and columns. The connection stiffness and strength also depend on geometrical parameters of the angle components. The design of the connection can thus be adjusted to optimize the reserve capacity and be adjusted to the requirements of the building, either existing or new. Although the addition of these enhanced connections may increase the design, fabrication and construction costs, it is expected that the proposed approach will improve the seismic response and robustness of Type CC braced frames.

1.2 Objectives

The general objective of this Ph.D. project is to evaluate the possible contribution of the gravity framing system to the seismic robustness of SFRSs of the Conventional Construction category

using enhanced beam-column connections. As indicated, among the several parameters that can influence the contribution of gravity system to the lateral resistance, the most promising avenue is the development and characterization of a double web bolted angle (2L) gravity beam-column connection enhanced with top and seat angles aiming at improving the building reserve capacity. The research project focuses on chevron brace configuration buildings because this configuration is widely used. Also, it was shown that the beam flexural response in chevron bracing results in beneficial residual reserve capacity after failure of a brace connection (Sizemore 2017, Tremblay 2018). In line with the main research objective, the following specific objectives are defined:

1. Investigate experimentally the influence of geometrical and material parameters on the nonlinear hysteretic response of bolted angle components;
2. Develop numerical models that can reproduce accurately and efficiently the nonlinear hysteretic response of bolted angle connections using a component-based modeling approach;
3. Validate the new modeling approach with full-scale experimental test data for bolted angle connections;
4. Investigate experimentally the influence of geometrical parameters on the nonlinear behaviour of full-scale bolted angle gravity connections under simultaneous shear and flexural moment loading;
5. Improve the beam-column connection contribution to the building reserve lateral capacity by using simple yet ductile top and seat angle beam-column connections in the gravity frame;
6. Develop connection design guidelines to reduce the required brace connection strength of type CC buildings with chevron brace configurations; and
7. Validate these guidelines with a design example supported by numerical simulations to assess the contribution of the gravity system to the seismic resistance.

1.3 Research methodology

Comprehensive experimental and analytical work has been conducted in this doctoral research. The following steps were taken to fulfill the aforementioned objectives:

1. Characterize the bolted angles as a connection component:
    a. the influence of the geometrical parameters of the angles was investigated experimentally to characterize the behaviour of simple bolted angle loaded in tension;
    b. a material testing campaign was also conducted to determine the material properties of the bolted angles;
    c. a mathematical model was proposed to define the hysteretic behaviour of bolted angles as a connection component, including the low-cycle fatigue effect.
2. Evaluate the nonlinear behaviour of the gravity connections under simultaneous shear and flexural moment:
    a. the moment-rotation behaviour of bolted angle connections loaded with simultaneous shear was evaluated by means of a full-scale experimental program;
    b. the mathematical model proposed to define the hysteretic behaviour of an angle component was validated using the connection experimental results;
3. Propose a gravity connection design procedure which can reduce the required brace connection strength when considering an enhanced gravity frame system:
    a. a design procedure was developed to design top and seat angle connections to enhance the behaviour and reserve lateral capacity of the gravity frame;
    b. the contribution of the enhanced connections on the seismic behaviour of a building is illustrated and validated through a design example.

1.4 Organization of the thesis

This dissertation is divided into 10 chapters and three appendices. Chapter 1 is the introduction, outlining the background, objectives and methodology of the research project. A literature review

is presented in Chapter 2 on the seismic design requirements for low-ductility steel braced frames in Canada, the seismic reserve capacity of buildings and the nonlinear behaviour of flexible and partially restrained beam- column connections. Chapter 3 focuses on the methodology of the research, detailing the experimental programs performed. This chapter also contextualizes the experimental programs with respect to the analytical work that was carried out. The results of these experimental programs are presented in three articles that have been submitted for publication in scientific journals. These articles, which are presented in Chapters 4 to 6, are:

1. Beland, T., Bradley, C. R., Nelson, J., Sizemore, J. G., Davaran, A., Hines, E. M. Fahnestock, L. A. (2019). "Experimental parametric characterization of bolted angle connection behavior". *Accepted for publication to ASCE Journal of Structural Engineering on December 9th 2019.*
2. Beland, T., Tremblay, R., Hines, E. M., Fahnestock, L. A., (2019b). "Evaluating the rotational capacity of bolted double web angle beam-column gravity connections with full-scale experimental testing." *In Review. Submitted to ASCE Journal of Structural Engineering on April 27 2019.*
3. Beland, T., Tremblay, R., Hines, E. M., Fahnestock, L. A., (2019c). "Full-scale cyclic testing with shear load of double web with top and seat angle beam-column connections". *In review. Submitted to ASCE Journal of Structural Engineering on April 27 2019.*

The mathematical model proposed to represent the hysteretic behaviour of a bolted angle component is detailed in Chapter 7. Chapter 8 presents a design procedure to account for enhanced gravity connections made of top and seat with double web angle beam-column connections for chevron braced frames. Chapter 9 presents complementary research results on angle material testing not included in the articles. Finally, Chapter 10 summarizes the conclusions and the recommendations for future research.

The results of the tests performed on bolted angle components are also presented in detail in Appendix A. These results are analyzed in detail in Chapter 4. The results of the full-scale tests on bolted angle connections are each presented in Appendix B, while these results are analyzed in Chapter 5 and 6 for the double web angle connections and the connections with top and seat angles

respectively. The code programmed to integrate the proposed mathematical model in OpenSees (Mazzoni et al. 2006) is transcribed in Appendix C.

CHAPTER 2 LITTERATURE REVIEW

The lateral reserve capacity depends greatly on the design of the building. To situate the addressed problematic in the context of Canadian steel buildings, the design requirements for low-ductility buildings in Canada are summarized in this chapter. Then a review of previous studies performed to assess the lateral reserve capacity of steel buildings is presented, with a focus on the contribution of the gravity beam-column connections. The nonlinear behaviour of these connections was widely studied experimentally and numerically. A summary of these studies is presented for flexible and partially restrained bolted angle connections. Finally, an overview of building modeling procedures with the finite element analysis software OpenSees (Mazzoni et al. 2006) is presented, with an emphasis on the numerical modeling of nonlinear hysteretic and low-cycle fatigue behaviour.

2.1 Design requirements of low-ductility steel buildings in Canada

2.1.1 Minimum seismic load

The NBCC provides two methods to design the SFRSs: the dynamic analysis and the equivalent static force procedure. The latter is generally preferred by practicing engineers for its simplistic and quick procedure.

Numerous dynamic analyses showed that a linear and a nonlinear structure with the same initial stiffness and loaded with the same ground motion present similar maximum displacements when their natural period is significantly higher than the dominant period of the ground motion (Veletsos and Newmark 1964). This concept, referred to as the equal displacement principle, is widely used in seismic codes and the NBCC is no exception. Permanent inelastic damage is allowed in the structure and the design force of the SFRS is reduced based on the system's expected ductility. This ductility is represented by the factor R_d (Mitchell et al. 2003). To ensure sufficient ductility during a seismic event, the yielding mechanism of the structural system must be controlled by concentrating the inelastic behavior in the most ductile elements. Alternatively, the other elements must comply with the capacity design principles to avoid potential brittle failure modes.

Additionally, the NBCC estimates explicitly the probable lateral capacity of the SRFS during a seismic event with the factor R_o (Mitchell et al. 2003). This overstrength comes from:

a) the size choices or rounded up dimensions of the minimal required sections;

b) the difference between nominal and factored resistances;

c) the difference between the nominal and actual yield strengths;

d) the material strain hardening; and

e) the capacity mobilization required to form a complete collapse mechanism.

Both the R_d and R_o factors are used to reduce the seismic design base shear V_{base} on the structure according to Equation 2.1. $S(T_a)$ is the design spectral response acceleration for the building design fundamental lateral period of vibration T_a, M_v is the higher mode effect factor, I_E is the earthquake importance factor and W is the seismic load of the building. The seismic load corresponds to the dead load and 25% of the design snow load. The R_d and R_o values for steel buildings are given in Table 2.1.

$$V_{base} = \frac{S(T_a)M_v I_E W}{R_d R_o} \leq max\left(\frac{2}{3}\frac{S(0.2)I_E W}{R_d R_o}; \frac{S(0.5)I_E W}{R_d R_o}\right) \quad (2.1)$$

Table 2.1. Reduction factors Rd and Ro for steel SFRSs

SFRS Type	R_d	R_o
Ductile moment resisting frame (Type D)	5.0	1.5
Moderately ductile moment resisting frame (Type MD)	3.5	1.5
Limited-ductility moment resisting frame (Type LD)	2.0	1.3
Moderately ductile concentrically braced frame (Type MD)	3.0	1.3
Limited-ductility concentrically braced frame (Type LD)	2.0	1.3
Ductile eccentrically braced frame (Type D)	4.0	1.5
Ductile buckling restrained braced frame (Type D)	4.0	1.2
Ductile plate wall (Type D)	5.0	1.6
Limited-ductility plate wall (Type LD)	2.0	1.5
Conventional construction (Type CC)	1.5	1.3

The NBCC gives the spectral accelerations S_a of every important municipalities in Canada based on a probabilistic exceedance of 2% in 50 years (2475 years return period) for periods of 0.2 s, 0.5 s, 1.0 s, 2.0 s, 5 s and 10 s considering a 5% damping (Mitchell et al. 2010). To account for local site conditions, the spectral acceleration $S_a(T)$ is modified by an acceleration and velocity related factor, F. The design spectral acceleration $S(T)$ is dependent on the fundamental lateral period of vibration of the building T and is obtained by interpolation between the equations presented in Equation 2.2.

$$S(T) = \begin{cases} \max\left(F(0.2)S_a(0.2), F(0.5)S_a(0.5)\right) & if\ T \leq 0.2s \\ F(0.5)S_a(0.5) & if\ T = 0.5s \\ F(1.0)S_a(1.0) & if\ T = 1.0s \\ F(2.0)S_a(2.0) & if\ T = 2.0s \\ F(5.0)S_a(5.0) & if\ T = 5.0s \\ F(10.0)S_a(10.0) & if\ T \geq 10.0s \end{cases} \quad (2.2)$$

Those factors account specifically for the soft soil amplification observed in previous seismic event such as the 1985 Mexico City earthquake (Mitchell et al. 1986), the 1989 Loma Prieta earthquake (Bruneau 1990, Mitchell et al. 1990a) and the 1988 Saguenay earthquake (Mitchell et al., 1990b). The amplification factor depends on the reference peak ground acceleration PGA_{Ref} of the site. The reference peak ground acceleration PGA_{Ref} is obtained from Equation 2.3 and depends on the ratio between the 0.2 s spectral acceleration and the PGA given by NBCC for the building location.

$$PGA_{Ref} = \begin{cases} 0.8PGA & if\ \dfrac{S_a(0.2)}{PGA} < 2.0 \\ PGA & if\ \dfrac{S_a(0.2)}{PGA} \geq 2.0 \end{cases} \quad (2.3)$$

The amplification factor *F* is given in Table 2.2, along with a general description of the ground profile for each site class. NBCC includes a site class F, which incorporates all other types of soil. For this particular category, a geological study is required to evaluate the amplification factor for the specific location of the building. The value of *F(T)* must be interpolated on the correct value of the reference peak ground acceleration PGA_{Ref}. With these values, the design spectrum accounting the site class of the building can be established with Equation 2.2.

The equivalent static force procedure is a simple alternative to the dynamic analyses and allows a quick design of the SFRS. However, NBCC specifies that the structure must respect at least one of the following criteria for the application of this simplified method:

a) The factored short period acceleration $I_E F_a S_a(0.2)$ is lower than 0.35g;

b) The structure is regular, its height h_n is smaller than 60 m and its fundamental lateral period T_a is smaller than 2 s in both directions; and

c) The structure is irregular, except in torsion (Type 7), its height h_n is smaller than 20 m and its fundamental lateral period T_a is smaller than 0.5 s in both directions.

Table 2.2. Values of acceleration dependent factor *F* (NBCC 2015)

T	Site class	Ground profile	F(T) for PGA_{Ref}				
(s)			**≤ 0.1**	**= 0.2**	**= 0.3**	**= 0.4**	**≥ 0.5**
0.2	A	Hard rock	0.69	0.69	0.69	0.69	0.69
0.5			0.57	0.57	0.57	0.57	0.57
1.0			0.57	0.57	0.57	0.57	0.57
2.0			0.58	0.58	0.58	0.58	0.58
5.0			0.61	0.61	0.61	0.61	0.61
10.0			0.67	0.67	0.67	0.67	0.67
0.2	B	Rock	0.77	0.77	0.77	0.77	0.77
0.5			0.63	0.63	0.63	0.63	0.63
1.0			0.63	0.63	0.63	0.63	0.63
2.0			0.63	0.63	0.63	0.63	0.63
5.0			0.64	0.64	0.64	0.64	0.64
10.0			0.69	0.69	0.69	0.69	0.69
0.2	C	Very dense soil & soft rock	1.00	1.00	1.00	1.00	1.00
0.5			1.00	1.00	1.00	1.00	1.00
1.0			1.00	1.00	1.00	1.00	1.00
2.0			1.00	1.00	1.00	1.00	1.00
5.0			1.00	1.00	1.00	1.00	1.00
10.0			1.00	1.00	1.00	1.00	1.00
0.2	D	Soft soil	1.24	1.09	1.00	0.94	0.90
0.5			1.47	1.30	1.20	1.14	1.10
1.0			1.55	1.39	1.31	1.25	1.21
2.0			1.57	1.44	1.36	1.31	1.27
5.0			1.58	1.48	1.41	1.37	1.34
10.0			1.49	1.41	1.37	1.34	1.31
0.2	E	Soft soil	1.64	1.24	1.05	0.93	0.85
0.5			2.47	1.80	1.48	1.30	1.17
1.0			2.81	2.08	1.74	1.53	1.39
2.0			2.90	2.24	1.92	1.72	1.58
5.0			2.93	2.40	2.14	1.96	1.84
10.0			2.52	2.18	2.00	1.88	1.79

For the buildings that do not meet any of these requirements, the simplifications inherent to the static equivalent force method do not provide a representative load distribution along the height of

the buildings. Therefore, dynamic analyses are required to assess the building seismic response with higher mode effects and its structural irregularities (Heidebrecht 2003).

2.1.1 Equivalent static force procedure of NBCC

When using the static load equivalent method, the fundamental lateral period of steel buildings can be determined with the empirical equations of Equation 2.4, depending on the height of the building h_n and the type of SFRS used in the structure. The fundamental lateral period T_a can also be determined numerically, without being larger than 1.5 times the empirical period T_{emp} of Equation 2.4 for moment frames and 2.0 times the empirical period of Equation 2.4 for braced frames and shear walls.

$$T_{emp} = \begin{cases} 0.085(h_n)^{3/4} & \text{For moment frames} \\ 0.025h_n & \text{For braced frames} \\ 0.05(h_n)^{3/4} & \text{For shear walls \& other SFRS} \end{cases} \quad (2.4)$$

The higher mode effect is considered in the static equivalent force method in two ways. First, the seismic base shear V is increased with a coefficient M_v. This coefficient, presented in Table 2.3, depends on the ratio of the 0.2 s and 5.0 s design spectral accelerations at the specific building site. The type of SFRS used in the building and its fundamental lateral period of vibration T_a are also considered in the higher mode effect coefficient.

Also, the higher mode effect is considered in the lateral seismic force distribution along the height of the building. If the fundamental lateral period of the building Ta is larger than 0.7 s, a lateral force F_t, given by Equation 2.5, is applied at the top of the building. The remaining force is then distributed along the height of the building according to Equation 2.6, where x is the storey for a total of n storeys. The effects of accidental torsion must also be accounted for in the design procedure. A torsional moment of $\pm 0.10 D_{nx} F_x$ is thus applied at each level x, where D_{nx} is the building dimension perpendicular to the lateral loading direction. F_x is the seismic load at each level determined with Equation 2.6.

$$F_t = 0.07 T_a V_{base} \leq 0.25V \quad (2.5)$$

$$F_x = (V_{base} - F_t)\, W_x h_x \Big/ \sum_{i=1}^{n} W_i h_i \quad (2.6)$$

Table 2.3. Values of higher mode effect coefficient M_v (NBCC 2015)

$\frac{S_a(0.2)}{S_a(2.0)}$	SFRS Type	Values of M_v			
		$T_a \leq 0.5$ s	$T_a = 1.0$ s	$T_a = 2.0$ s	$T_a \geq 5.0$ s
5	Moment-Resisting Frame	1	1	1	1
20		1	1	1	1
40		1	1	1	1
65		1	1	1.03	1.03
5	Coupled Walls	1	1	1	1
20		1	1	1	1.08
40		1	1	1	1.30
65		1	1	1.03	1.49
5	Braced Frames	1	1	1	1
20		1	1	1	1
40		1	1	1	1
65		1	1.04	1.07	1
5	Walls, Wall Frame Systems	1	1	1	1.25
20		1	1	1.18	2.30
40		1	1.19	1.75	3.70
65		1	1.55	2.25	4.65
5	Other Systems	1	1	1	1
20		1	1	1.18	1.18
40		1	1.19	1.75	1.75
65		1	1.55	2.25	2.25

To calculate deflections, the fundamental lateral period T_a of the building determined through numerical analysis may be used. Therefore, the upper limits of 1.5 times the empirical period T_{emp} of Equation 2.4 for moment frames and 2.0 times the empirical period of Equation 2.4 for braced frames and shear walls imposed on the period to determine the seismic loads do not apply in the deflection evaluation. However, the fundamental lateral period shall not exceed 4.0 s for walls and wall-frame systems, and 2.0 s for moment-resisting frames, braced frames and other systems. Furthermore, the anticipated storey drifts are determined by multiplying the elastic displacements obtained with the reduced factored load of Equation 2.1 with R_dR_o/I_E. These anticipated storey drifts shall be limited to $0.01h_s$ for post-disaster buildings, $0.02h_s$ for high importance category buildings and $0.025h_s$ for all other buildings.

2.1.2 Dynamic spectral analysis procedure of NBCC

In the cases where the equivalent static force procedure is not applicable, a dynamic analysis is required by the NBCC. Generally, a linear dynamic spectral analysis is performed with a numerical model of the building. The equivalent static force procedure, although not applicable, can provide a sense of the seismic load in the building to obtain the preliminary design. Such preliminary design is required to assess numerically the fundamental lateral period of the building, T_a, and the base shear V_e, with the design spectra of Equation 2.2. a preliminary design must be performed.

The design elastic base shear V_{ed} is then determined with Equation 2.7. This equation aims at limiting the base shear with the spectral acceleration limits used in the equivalent static force procedure of Equation 2.1. The design base shear V_d is then obtained from Equation 2.8. However, for regular structures and irregular structures that can be designed with the equivalent static force procedure, the design base shear V_d can be no less than $0.8V_{base}$, and no less than V_{base} for irregular structures requiring dynamic analysis. In these lower limits, V_{base} is the base shear determined from the equivalent static force method with the lateral fundamental period T_a determined with the numerical model.

$$V_{ed} = V_e \times \max\left(\frac{2}{3}\frac{S(0.2)}{S(T_a)}; \frac{S(0.5)}{S(T_a)}\right) \leq V_e \tag{2.7}$$

$$V_d = \frac{V_{ed} I_E}{R_d R_o} \tag{2.8}$$

The effects of accidental torsion must be accounted for in the building model in one of two ways:

a) A torsional moment of $\pm 0.10 D_{nx} F_x$ is applied at each level x, where D_{nx} is the building dimension perpendicular to the lateral loading direction. F_x is the seismic load at each level, either determined through a elastic dynamic analysis, or with Equation 2.5 times $R_d R_o / I_E$;

b) If the building is not sensible to the torsion (Type 8 irregularity), a three-dimensional dynamic analysis can be performed with each level center of gravity shifted of $-0.05 D_{nx}$ and $+0.05 D_{nx}$.

The scale factor V_d/V_e, where V_e is the base shear obtained from the linear dynamic spectral analysis, is the applied on the elastic storey shear, storey forces, member forces and deflections obtained from the linear dynamic spectral analysis including the accidental torsion. From these scaled results, the preliminary building design can then be adjusted and validated by applying the same procedure.

The anticipated interstorey deflections are determined by multiplying the elastic displacements obtained from the linear dynamic spectral analysis with R_dR_o/I_E. These anticipated storey displacements shall be limited to $0.01h_s$ for post-disaster buildings, $0.02h_s$ for high importance category buildings and $0.025h_s$ for all other buildings.

2.1.3 Seismic design requirements for steel SFRS of the Conventional Constructions category

The Canadian standard for design of steel structure CSA-S16-14 includes provisions for the seismic design of steel buildings, to assure the anticipated ductility of the SFRS. A system with a high R_d is expected to dissipate energy through inelastic deformations of specific members. To ensure that plastic mechanism occurs as anticipated during a seismic event, CSA-S16-14 requires capacity design and includes numerous strict requirements for elements such as columns, beams and brace connections. Those requirements decrease along with the system ductility.

The SFRS must offer sufficient lateral resistance to the building, but also provide adequate lateral stability against P-delta effects and initial out-of-plumbness. Therefore, clause 27.1.8 (CSA 2014) stipulates that notional loads and P-delta effects shall be included when sizing the SFRS. Design forces in the braced frames should also account for accidental torsion effects by considering the static torsional moments T_x equal to the seismic load V_x times 10% of the perpendicular building dimension D_{nx}. In dynamic analyses, masses can be displaced by 5% in the numerical model.

For Type CC systems, with a ductility reduction factor R_d of 1.5 and an overstrength reduction factor R_o of 1.3, seismic provisions are practically nonexistent for low-rise buildings. The only design criterion concerns the connections which need to exhibit a ductile failure mode or be designed for seismic loads amplified by 1.5. This amplified load corresponds to the design load with an R_d of 1.0. The braced frame can be designed according to standard gravity design and

construction practices. However, past earthquakes have shown the higher vulnerability of multi-storey compared to low-rise buildings (Castonguay 2009). These observations, along with a lack of knowledge on the seismic performance of low-ductility multi-storey buildings, have led to some restraints concerning the conventional construction category. The CSA-S16-14 specifies that for assembly occupancy buildings, which includes stadiums, museums, theatres and classrooms, the building height shall not exceed 15 m. For other types of buildings, when the specified short-period spectral acceleration ratio $I_E F_a S_a(0.2)$ is greater or equal than 0.35g, a structure may exceed a height of 15 m if the following conditions are met:

a) The factored seismic loads are increased linearly by 2% per metre of height above 15 m, without exceeding the forces calculated with $R_d R_o$ of 1.3;

b) The height does not exceed 40 m when $I_E F_a S_a(0.2)$ is greater than 0.75g or $I_E F_v S_a(1.0)$ is greater than 0.30g;

c) The height does not exceed 60 m when $I_E F_a S_a(0.2)$ is greater or equal than 0.35g, but less or equal than 0.75g;

d) The Dynamic Analysis Procedure detailed in the NBCC is used to determine the seismic forces and deformations;

e) Clauses 27.1.3 to27.1.8 are satisfied. The design must then include the probable yield stress $R_y F_y$ and the effects of notional loads and P-delta effects;

f) All members of the SFRS are Class 1 or Class 2 sections;

g) The width-to-thickness ratio of flat elements of member cross-sections satisfy the limits imposed by Clause 27.6.3.2, in accordance with Clause 27.5.3.2;

h) The columns are designed to resist in compression the effects of gravity loads combined with 1.30 times the member factored seismic force. The seismic induced axial loads for columns that are part of two or more intersecting SFRS are obtained from analyses of the structure independently in any two orthogonal directions for 100% of the earthquake loads applied in one direction plus 30% of the earthquake loads in the perpendicular direction;

i) Connections are designed to resist the smaller of the gross section strength of the section using the probable yield stress R_yF_y or the gravity loads combined with 1.30 times the member factored seismic forces;

j) Connections are designed and detailed such that the governing failure mode is ductile when the gross section strength does not govern the design load;

k) The factored seismic forces for diaphragms are determined for forces corresponding to R_oR_d of 1.3; and

l) Members of the SRFS that intersect at an unbraced location are designed for an additional out-of-plane transverse force equal to 10% of the axial load carried by the compression members at that intersection point.

Table 2.4 presents the spectral accelerations $I_EF_aS_a(0.2)$ and $I_EF_vS_a(1.0)$ for class sites A to E in major Canadian cities. Blue values represent buildings of normal importance (I_E = 1.0) limited to a height of 60 m, while red values are limited to 40 m. For buildings higher than 15 m with a bold short period spectral acceleration value $I_EF_aS_a(0.2)$ on Table 2.4, either underlined or not, are subjected to the specific conditions of the CSA-S16-14 (CSA 2014) presented above.

Castonguay (2009) and Guilini-Charette (2010) evaluated the seismic response of 2-, 4-, 6-, 8- and 10-storey conventional constructions located in Montreal and Vancouver, with class sites C and E. The objective of this study was to assess the validity of the 15 m limit above which ductile connections are required. The load demand on the connection was thus compared to the load amplified by a factor of 1.5 required for non-ductile connections.

Table 2.4. Spectral accelerations for several Canadian cities and class sites

City		Montréal	Québec	Ottawa	Toronto	Vancouver	Victoria
$S_a(0.2)$		**0.64**	**0.55**	**0.64**	**0.22**	**0.94**	**1.20**
$S_a(1.0)$		**0.14**	**0.15**	**0.14**	**0.07**	**0.33**	**0.38**
$I_E F_a S_a(0.2)$	**A**	**0.48**	**0.40**	**0.48**	0.15	**0.75**	**0.96**
	B	**0.55**	**0.45**	**0.55**	0.18	**0.92**	**1.20**
	C	**0.64**	**0.55**	**0.64**	0.22	**0.94**	**1.20**
	D	**0.73**	**0.65**	**0.73**	0.29	**1.03**	**1.22**
	E	**0.79**	**0.74**	**0.79**	**0.46**	**0.89**	**1.08**
$I_E F_v S_a(1.0)$	**A**	0.07	0.08	0.07	0.03	0.17	0.22
	B	0.09	0.10	0.09	0.04	0.24	**0.30**
	C	0.14	0.15	0.14	0.07	**0.33**	**0.38**
	D	0.19	0.20	0.19	0.09	**0.39**	**0.43**
	E	0.29	**0.31**	0.29	0.14	**0.61**	**0.66**

The load demand was smaller than the required capacity for the buildings of 2 and 4 storeys (height smaller than 15 m) located in Montreal on a site class C. The height limit of 15 m is thus adequate for these buildings. However, for the 2- and 4-storey buildings located in Vancouver on a site class C, the amplification factor applied to obtain an elastic response of the non-ductile connections should be increased from 1.5 to 2.2. The connection load demand for 6-, 8- and 10-storey buildings on site class C and for 2-, 4-, 6-, 8- and 10-storey buildings on site class E in Montreal and Vancouver also exceeded the prescribed capacity. In these cases, the amplifications factor should generally be increased from 1.5 to 1.9 for buildings in Montreal and to 2.8 for buildings in Vancouver. Castonguay (2009) and Guilini-Charette (2010) observed smaller connection deformations in chevron-braced buildings compared to their Split-X equivalent. Also, the ratio between the connection load demand to capacity was generally larger at the top storeys, which indicate that the spectral analyses could not predict accurately the upper brace axial forces, especially in tall buildings.

Some concerns were raised concerning the lack of capacity design in brace connections, which may limit the ductile behaviour of the braced frame (Gryniuk 2008, Carter 2009). The braced frame beams and columns are only designed to resist the lateral and gravity loads, without considering the unbalanced loading pattern created after brace buckling. Therefore, unwanted yielding may occur in these structural elements and lead to a loss gravity load bearing capacity and frame

instabilities (Gryniuk 2008). Castonguay (2009) reported a large reduction of column axial load demand when ductile brace connections were considered compared to non-ductile connections.

In summary, the CSA-S16-14 provides, with the conventional constructions, a simple and quick SFRS option for buildings smaller than 15 m. The several requirements applicable for taller buildings can no longer provide a quick and simplistic design procedure for this low-ductility SFRS.

2.1.4 Comparison with ASCE7

The Canadian Type CC category is situated between two steel frame systems described in ASCE7: The Steel system not specifically detailed for seismic resistance, excluding cantilever column systems (R = 3) and the Ordinary Concentrically Braced Frame (OCBF, R = 3.25). The former does not require any seismic design, while the latter must respect capacity design provisions for braced frame beams, columns and brace connections.

For both R = 3 and Type CC concentrically braced frames (CBFs), capacity design procedures and seismic detailing for the beams, columns and connections of the braced frames are not required. The ductility and overstrength reduction factors of the Type CC category result in a total reduction factor of 1.95. However, the Canadian Type CC category is allowed anywhere in the country, with some restrictions depending on the location spectral accelerations previously mentioned. On the other hand, the American R = 3 system is only allowed in low and moderate seismic regions.

The Canadian code requires the connections of Type CC systems to be ductile or designed with a strength corresponding to 1.5 (R_d) times the brace design load. This increased load specification aims at designing the connections to remain elastic during a seismic event, and thus prevent premature failure in the braced frame. This specification is not included in ASCE7-16 for R = 3 systems, where the design strength is the same for every element of the braced frame (Chu 2017, Sizemore 2017). The gusset connections may thus not have sufficient strength and deformation to accommodate the brace yielding and buckling, which may result in brittle fracture of the connection (Chu 2017, Sizemore 2017).

On the other hand, a similar clause is included in the design requirements of the OCBF (R = 3.25) system, where the connection must be designed to resist the brace capacity. While the amplified

load is only applied for brace connection design for Type CC systems, the OCBF also includes local slenderness limits for braces, increased seismic loads for the braced frame beams and columns (Chu 2017, Sizemore 2017). The OCBF system can be used without height limit in low and moderate seismic regions. An height limit of 10.668 m (35') is imposed on buildings in high seismic regions.

Furthermore, neither Canadian nor American standards include provisions to limit beam yielding caused by unbalanced loading in the post-buckling state of the braces. Because of the reduced beam span in chevron or Split-X configurations, the section size is generally significantly smaller and may experience significant yielding (Chu 2017, Sizemore 2017).

2.2 Lateral reserve capacity of steel buildings

The 1994 Northridge earthquake induced significant damage to steel moment frame buildings. In some cases, extensive failure was observed in 75% of the moment connections of the buildings, but the structure experienced relatively small inter-story drift (Hajjar et al. 1995, O'Sullivan et al. 1998). The gravity system beam-column connections, combined with the concrete slab, created composite partially-restrained (PR) connections (Leon 1998; Liu and Astaneh-Asl 2000). The moment frame action resulting from these PR connections in the gravity frame mitigated the damage to the building and allowed structural rehabilitation (O'Sullivan et al. 1998).

The gravity frame can thus influence the seismic behavior and robustness of steel structures. The gravity frame can act as a back-up lateral load resisting system in case of failure of the primary system through a moment frame action. Although gravity beam-column connections were designed to resist only shear loads, their inherent rotational stiffness can have beneficial impacts on the seismic behavior of the building: mitigate drifts and P-delta effects (Ji et al. 2009; Flores et al. 2014, Flores et al. 2016) and increase the building collapse prevention (Owens and Moore 1992, Gupta and Krawinkler 2000, Lee and Foutch 2002, Callister and Pekelnicky 2011, Stoakes and Fahnestock 2011, Jarrett et al. 2015, Judd et al. 2015, Elkady and Lignos 2015, Shen et al. 2015, Sizemore et al. 2017, Hwang and Lignos 2017). Further considerations such as the column continuity (Tremblay and Stiemer 1994, MacRae et al. 2004, Ji et al. 2009, Flores et al. 2014, Chu 2017) and the residual capacity of braced frames (Rahgozar and Humar 1998, Hines et al. 2009,

Stoakes and Fahnestock 2011, Davaran et al. 2014, Bradley et al. 2017, Sizemore et al. 2017, Chu 2017, Sizemore 2017) after failure can also contribute to the reserve capacity of the building.

2.2.1 Reserve capacity from gravity beam-column connections

The variability of lateral stiffness provided by a range of different types of beam-column connections have been acknowledged since at least 1917 (Wilson and Moore 1917). The connections can be categorized based on their flexural stiffness (k_θ) as either flexible (pinned, $k_\theta = 0.0$) fully rigid (fixed, $k_\theta = \infty$) or a partially restrained (PR) ($0 < k_\theta < \infty$). For the latter category, the flexural stiffness can reduce the maximum moment of a beam under gravity loads. They also reduce the effective length and creates bending moments in the columns which modifies their load-carrying capacity (Morris and Packer 1987). Ang and Morris (1984) proposed a method to account for those effects, by introducing modification factors to the local stiffness matrix of beam and column elements. Those factors are based on the connection rotational stiffness obtained from experimental results. Also, an iterative process analysis is required to account for geometrical and material nonlinearities.

Frye and Morris (1975) and Nethercot et al. (1988) also suggested a mathematical method to develop the stiffness matrix considering partially restrained connections. A rational approach was proposed by considering the total node rotation as the sum of the beam and of the joint rotations. Figure 2.1 shows those two separate rotations along a) a translational and b) a rotational degree of freedom. This approach considers the flexural stiffness of the beam and of the connections in series, and the connection stiffness is derived from experimental results. The rotation experienced by the connection elements and by the beam can be determined numerically through an iterative process analysis to account for geometrical and material nonlinearities. Considering the connection behaviour as separated from the beams and columns also simplify the modeling of shear and axial deformations of the connections (Li et al. 1995).

More recently, Elkady and Lignos (2015) performed numerical studies of 2-, 4- 8- 12- and 20-storeys steel moment frames (SMF) considering shear tab gravity connections with concrete slab composite action. Those two considerations increased the base shear by an average of 50% compared to the bare SMF alone. The overstrength factor Ω_o, calculated according to FEMA P695 (FEMA 2009), also increased between 40 and 60% for the 20- and the 2-storeys respectively.

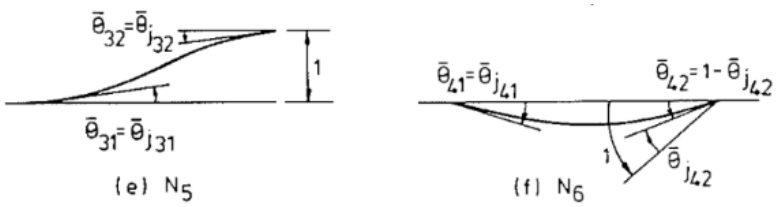


Figure 2.1. Deformation of partially restrained element along a) translational degree of freedom b) rotational degree of freedom (Nethercot et al. 1988)

Flores et al. (2014) performed pushover analyses of 2-, 4- and 8-storeys special SMFs considering the continuity of gravity columns as well as the stiffness of beam-column connections of the gravity frame. The flexural stiffness of those connections was modeled as equal to the beam stiffness, but the moment capacity was assigned as 0, 35, 50 and 70% of the gravity beam plastic moment. The base shear and the overstrength Ω_o capacity of the buildings experienced an increase of up to approximately 60% However, its period-based ductility μ_T reduced of up to 30%.

These studies, along with several others (Ariyaratana and Fahnestock 2011, Sahoo and Chao 2015, Sizemore et al. 2014, Shen et al. 2015) highlight the influence of the gravity connections in the seismic resistance and dynamic behavior of a steel building. However, most studies only approximated the stiffness of PR connections based on the beam capacity or on few experimental results. Such estimations cannot be realistically achieved in a design process without clearly stating the connection capacity beforehand.

These numerical investigations were aimed at characterizing the impact of the gravity frame in the seismic behavior of steel building for collapse mitigation. ASCE7 includes a similar SFRS category, the Type E, which is defined as a dual system with intermediate moment frame capable of resisting at least 25% of the prescribed seismic forces (ASCE7 2016). The total lateral resistance is to be provided by the moment frames and shear walls or braced frames in proportion to their stiffness. However, AISC-341 (AISC 2016) does not provide any guidelines for the design of such backup systems.

Numerical studies showed that the integration of such dual systems in buckled-restrained braced frames (BRBF) were able to reduce the maximum storey drift by approximately 10 to 15%, and the residual storey drift up to around 60% (Whittaker et al. 1989, Kiggins and Uang 2006, Sahoo

and Chao 2015). Xie (2008) performed numerical parametric studies by varying the stiffness ratio of the backup system on 4- and 12-storey buildings. The author noted that even a small stiffness ratio can reduce significantly the maximum storey drift angle (SDA) as well as the storey drift concentration, as shown in Figure 2.2. The improvement of collapse resistance attributed to the gravity framing reserve capacity is more significant in shorter buildings (Carter 2009).

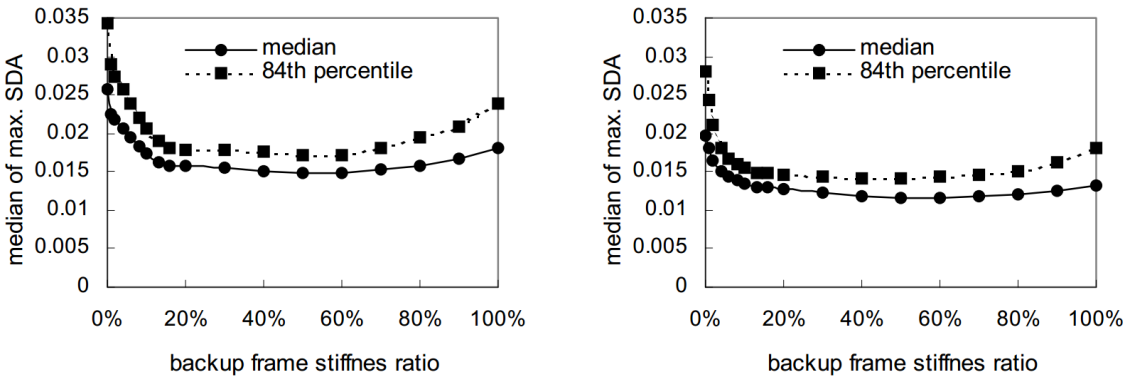


Figure 2.2. Median and 84th percentile of storey drift vs. backup frame stiffness ratio for a) 4-storey building b) 12-storey building (Xie 2008)

Mohsenzadeh and Wiebe (2018) evaluated the gravity frame contribution of 3-, 6- and 12-storey braced frame buildings with pinned connections and shear tabs gravity beam-column connections calibrated by Elkady and Lignos (2015) on the experimental results of Liu and Astaneh (2000). Modeling the gravity frame reduced the peak storey drifts over the height, which resulted in a significant increase of the lateral capacity and a change in the plastic mechanism of the braced frames. The gravity system also improved the load redistribution after brace failure over the height of the building. The authors proposed a minimum lateral stiffness in the gravity columns of 1.5% of the braced frame stiffness.

Del Carpio et al. (2019) conducted hybrid simulations to evaluate the response of a 4-storey SMF building and its gravity framing. The subassembly of a half-scale 1 ½-bay by 1 ½-storey of the gravity frame first storey was tested experimentally, while the rest of the building was modeled numerically. The physical and numerical models were loaded with several ground motions through hybrid simulations. The beam-column connections of the building were shear-tabs with a light-weight concrete slab over a steel deck. The authors observed an elastic stiffness in the gravity frame

larger than expected. Fracture of the gravity connections were not observed during the tests, unlike the results from conventional shear tab connection tests (Liu and Astaneh 2000). The authors attributed this contradiction to the difference in beam depth and the absence of inelastic cumulative damage inherent to symmetric loading protocols. Furthermore, the concrete slab, steel columns and the panel zones did not experience significant damage, whereas the gravity column base connections suffered significant plate yielding and anchor bolt fracture.

2.2.2 Reserve capacity from column continuity

Gravity loads acting on building structures reduce their lateral stiffness by amplifying horizontal deformations with the second order effect P-delta. In inelastic structures, if this stiffness reduction is greater than the strain hardening of the elements, the system reaches a state of structural instability and collapse is imminent (Gupta and Krawinkler 2000). In the building design process, gravity framing columns are assumed pinned between each floor. However, for practical and economic reasons, columns are usually continuous over several storeys and can contribute to avoid structural instability through bending response (Tremblay and Stiemer 1994).

The benefits of considering column continuity have been investigated through several inelastic pushover and dynamic time history analyses (Flores et al. 2014, Ji et al. 2009, MacRae et al. 2004, Tremblay and Stiemer 1994). This contribution was proven proportional to the combined flexural stiffness of braced frame and gravity columns. It can mitigate soft storey collapse by creating a more uniform storey drift distribution along the building height. Also, the additional stiffness provided by column continuity helped the system to deform along its first mode. However, this additional stiffness results in a shorter period of vibration which increases the inertial forces on the structure (Flores et al. 2014).

For Type MD braced frames, CSA-S16-14 specifies that braced frame and gravity columns shall be continuous and of constant cross-section over a minimum of two storeys. Columns in braced bays shall meet the requirements of Class 1 or 2 and shall be designed to resist an additional bending moment of $0.2ZF_y$ in combination with the computed bending moments and axial loads. Also, gravity columns must meet the requirements of Class 1, 2 or 3 of flexural members. More stringent restrictions apply for Type MD tension-only braced frames. Indeed, the columns must be continuous and of constant cross section over the entire building height, which is limited to 20 m

for this type of SFRS. Tension-only braced frames of Type LD require all columns to be continuous and of constant cross-section over a minimum of three storeys. For Type CC SFRSs, no such restriction exists.

Usually, the severity of drift concentration in one particular story increases along with the height of the building (Ji et al. 2009, MacRae 2011). Since a small building of 2 or 3 storeys has already a relatively constant storey drift along its height, continuous columns can be significantly beneficial for tall buildings. Column continuity can be realistically achieved over 3 storeys, otherwise splices are required. Previous pushover analyses have been performed on 4- and 8-storey models with and without column splices (Flores et al. 2014). The influence of levelled and staggered splices was also investigated, as illustrated in Figure 2.3. Results showed a reduction of stiffness in the models with column splices, thus decreasing the efficiency of column continuity. Also, levelled and staggered splices displayed similar behaviors. The observed stiffness reduction is directly dependent on the moment capacity of the splice.

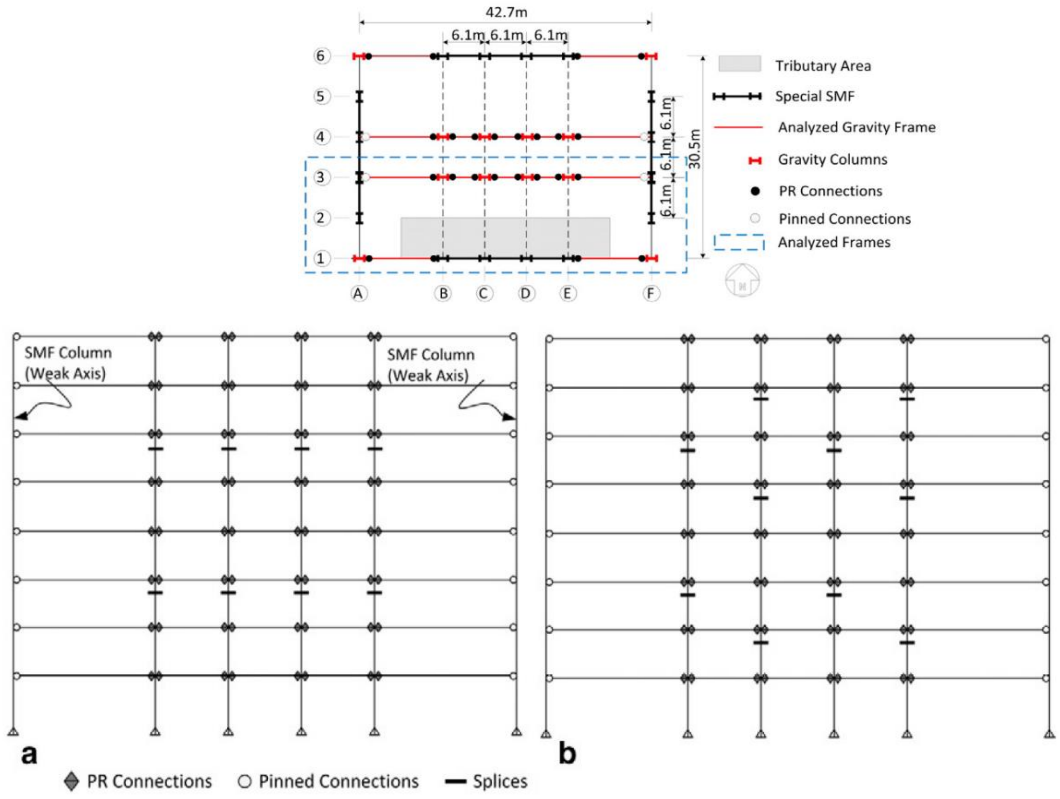


Figure 2.3. Plan and elevation views of 8-storey models with a) levelled splices b) staggered splices (Flores et al. 2014).

Moreover, the global stiffness of continuous columns has been investigated through 2-, 4- and 8-storeys SMF buildings (Flores et al. 2016). The lateral stiffness of the gravity system is expressed as a ratio of the SMF column stiffness, varying from 10% to 100%. Figure 2.4 shows the pushover curves of the 4- and 8-storey buildings. In those models, gravity columns are considered pinned at their base and continuous over their full height, with simply supported beams. Hence, they are only contributing to the post-yield stiffness and the maximum base shear corresponds to the capacity of the moment frame. Figure 2.4 illustrates that an increase in gravity column stiffness translates into an increase of the building's lateral ductility. Also, the impact of the gravity system on the structural behavior is greater in taller buildings (Flores et al. 2014), which are subjected to larger second order effects, although the results presented do not consider column splices.

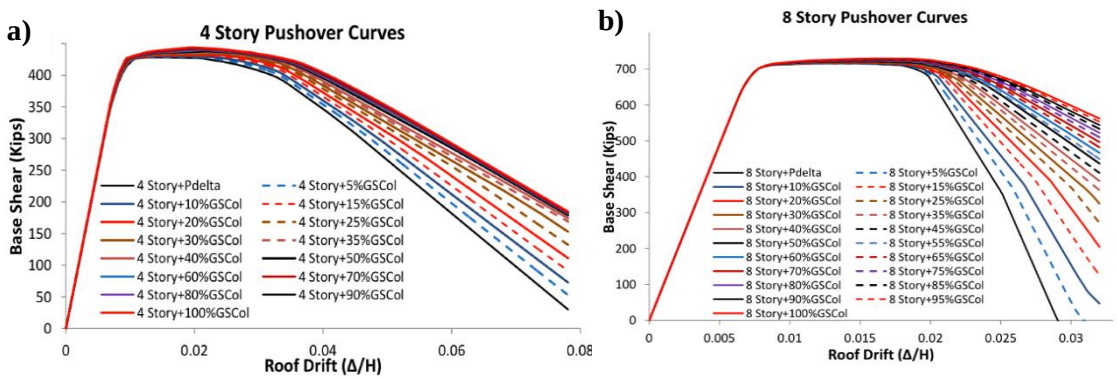


Figure 2.4. Pushover curves for a) 4-storey and b) 8-storey SMF buildings (Flores et al. 2016).

Finally, nonlinear dynamic analyses performed on 3-storey CBF buildings with continuous gravity columns have identified a vulnerability of drift concentration in the first storey (Ji et al. 2009). This mechanism is caused by a more important gravity load on the columns, which reduces their flexural capacity, as well as a larger storey shear. Thus, the members are more loaded laterally and possess a smaller lateral stiffness, which leads to a soft first storey collapse mechanism.

The lateral capacity of the first storey is highly dependent on the boundary conditions at its base. Nonlinear dynamic analyses were also performed considering continuous columns with pinned and fixed bases (Ji et al. 2009). Logically, the fixed columns increased drastically the lateral capacity of the building, while not necessarily preventing a first storey mechanism. However, both pinned

and fixed connections are unrealistic assumptions, particularly for gravity columns, and no studies were performed with partially restrained column bases.

2.2.3 Residual capacity of braced frames

During the braced frame design, the overstrength of the system is accounted for by the R_o reduction factor. This overstrength relies on the difference between the nominal and probable material properties, on the selection of member sizes from a discrete list and from the internal load redistribution due to redundancy and ductility (Rahgozar and Humar 1998). To assess the building reserve strength, Rahgozar and Humar (1998) performed pushover analyses on X and chevron braced frames from 2 to 30 storeys. The main parameter controlling the reserve strength is the slenderness ratio of the braces. The global reserve strength of the building is governed by the critical storey, but the height of the building and number of storeys had little influence on the behaviour of the system. The authors also observed a larger reserve capacity in frames with the chevron configuration than X configuration. The authors explain this observation by the gravity load carried by the chevron braces, which prematurely causes yielding of the compression brace but delays the yielding of the tension brace.

Hines et al. (2009) performed a numerical study of 3-, 6-, 9- and 12-storey chevron braced frames under 14 different ground motions. Each configuration was designed with a ductility reduction factor R of 2, 3 and 4, with no seismic detailing, but accounting for some lateral capacity in the gravity system. The frames were designed for Boston, Massachusetts according to ASCE7 (2005). The authors attributed the collapse prevention of $R = 3$ concentrically braced frames more to the inherent reserve capacity of the building rather than its ductility. Changing the ductility reduction factor R from 3 to 2 or 4 without any changes to the design process did not significantly modify the building behavior and collapse resistance. With this study, the authors prone a design philosophy emphasised on collapse prevention in low and moderate seismic regions, rather than potential economic loss in high seismic regions. This design philosophy tends to acknowledge a greater role of the lateral reserve capacity in the seismic behavior and may lead to more economic buildings. Moreover, the authors found a great sensitivity to ground motion variations in low-ductility braced frame buildings (Appel 2008).

Bradley et al. (2017) performed two full-scale testing on a two-storey R = 3.25 split-X ordinary concentrically braced frame (OCBF) and a R = 3 chevron concentrically braced frame (CBF). Both frames were designed with the AISC seismic provisions (AISC 2005) for a building located in the moderate seismic region of Boston, Massachusetts. These two types of frames were chosen because of the little variation in their reduction factor R, but the large difference in their design process.

The columns and connections of the OCBF were designed with a system overstrength factor, Ω_o, of 2.0, as prescribed by the AISC seismic provisions (AISC 2005). Furthermore, the fundamental period of the OCBF was assumed as the upper limit allowed by the ASCE 7 (2005) standard, 0.555 s. On the other hand, the R = 3 CBF was designed using the approximate period T_a allowed by ASCE7 (2016) of 0.347 s and the connection design loads were not amplified with the overstrength factor. The difference in the fundamental period, along with the slight ductility reduction factor difference, resulted in seismic design base shear of 858 kN for the OCBF and 1490 kN for the R = 3 system.

Figure 2.5a) presents the base shear versus total frame drift of the R = 3.25 OCBF. The base shear reached a maximum value of 2564 kN, which is approximately three times the design base shear. The ductile regime, starting at a drift of approximately 0.3% was mostly controlled by the buckling of the braces and plastic hinges forming in the gusset plates. The OCBF reached a total drift of approximately 1.5% before a significant loss of capacity resulting from a brace-to-gusset weld fracture in the second storey. Because of the Split-X configuration, the weld fracture did not affect significantly the system capacity under negative drift excursions, until the occurrence of another brace-to-gusset weld fracture at a drift of -1.62%. The frame still reached its maximum drift of 2.98% after the weld fracture, with a capacity of 219 kN. This reserve capacity was created by the contact between the compressive brace and the gusset, creating a brace reengagement. Furthermore, the beam-column connections in the frame created a moment frame action, which also contributed to the frame reserve capacity.

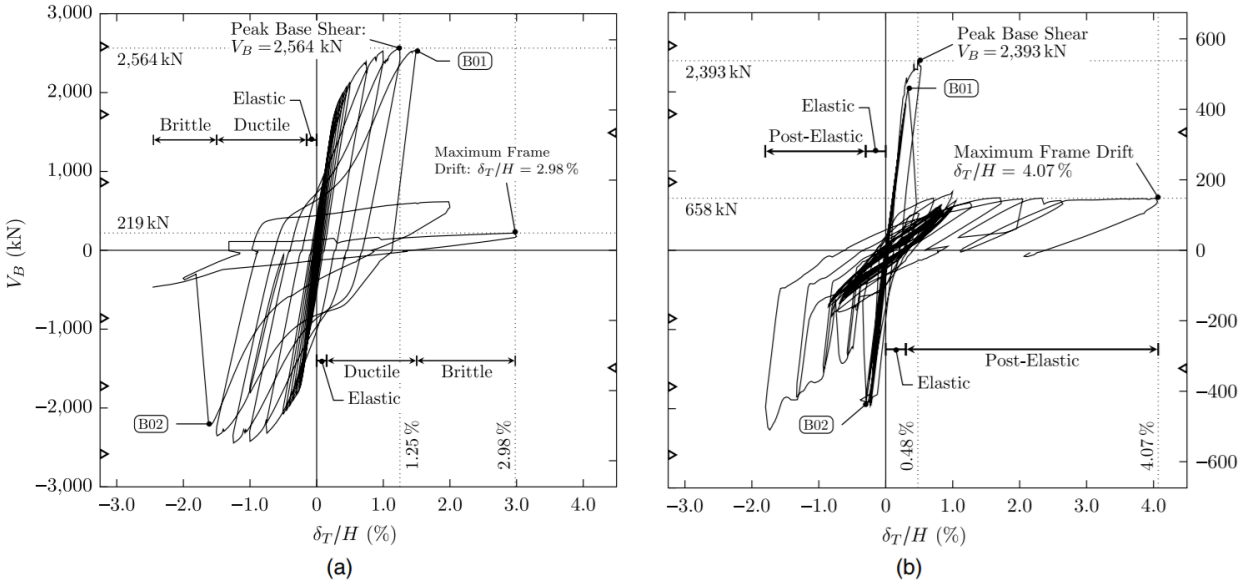


Figure 2.5. Hysteresis of base shear vs. total frame drift for a) OCBF and b) R = 3 CBF (Bradley et al., 2017)

Figure 2.5b) presents the base shear versus total frame drift of the *R* = 3 CBF. The second storey braces buckled globally and locally at a drift of approximately 0.35%. The local buckling in the braces created a plastic hinge at the center of the member, thus reducing the system lateral capacity and stiffness significantly. The system exhibited little ductility before a brace-to-gusset weld failure occurred in the first storey at a drift of 0.48%. However, after the weld fracture, the frame adopted a behaviour similar to a long-link eccentric braced frame, thus creating a lateral reserve capacity of 658 kN. This capacity was kept constant until a maximum drift of 4.07% was obtained. During the negative drift excursions, the fractured brace entered in contact with the gusset plate, thus creating a brace reengagement and contributing more significantly to the building lateral capacity.

Sizemore et al. (2017) recreated numerically the test results with finite element modeling. These models were then used to evaluate the relative influence of the system type (*R* = 3.25 OCBF and *R* = 3 CBF) and the system configuration (Split-X and chevron). The system configuration impacted the failure mechanism forming in the frame and thus affected the inherent reserve capacity. Split-X configuration only mobilized the column capacity and created multi-storey mechanisms which are prone to instability. On the other hand, the chevron configuration resulted in better performances of the system after a primary SFRS failure, as it mobilized both the beams

and columns in bending. The beams in chevron configurations also increased the reserve capacity as the long-link eccentric braced frame (EBF) behavior created after a brace fracture was more significant. Tremblay (2018) proposed Equation 2.9 to evaluate the post-failure stiffness of this long-link EBF system. The geometric properties of the frame are presented in Figure 2.6, along with the force-deformation behavior of the storey.

$$k_s' = \frac{V'}{\left(\frac{L}{2EA_b} + \frac{L}{2EA_d\,cos^3\,\theta} + \frac{L^3\,tan^2\,\theta}{48EI_b}\right)} \geq \frac{P}{h_s} \tag{2.9}$$

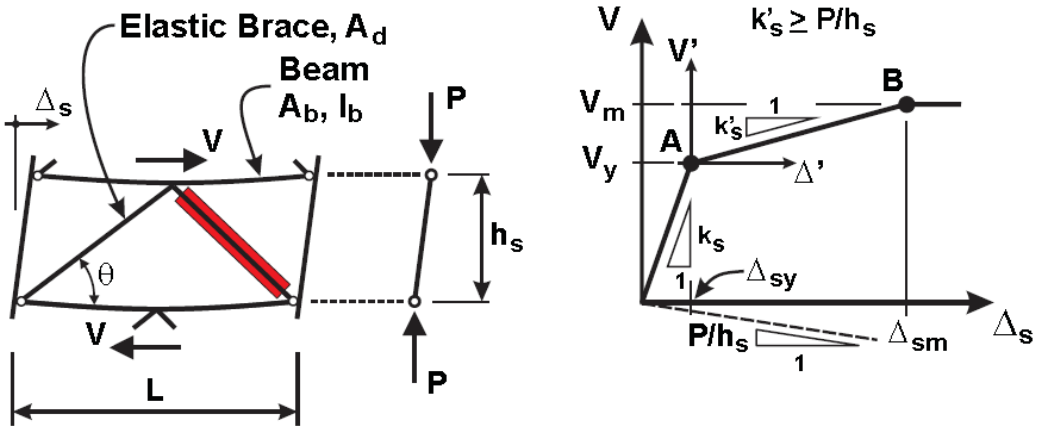


Figure 2.6. Geometric properties of a chevron braced frame and force-deformation behaviour of a typical storey (Tremblay 2018).

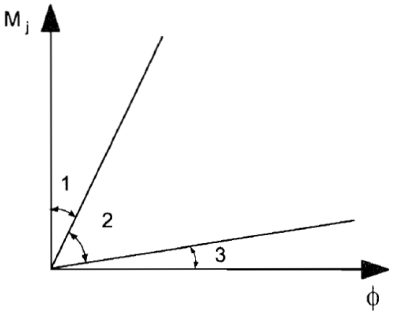
The system type influenced mainly the ductility obtained in the braced frames. Since the design provisions of the *R* = 3.25 OCBF require the columns and the connections to be capacity designed with an amplification factor (AISC 2005), the system can develop more ductility in the braces (Sizemore et al. 2017). The simple connection design required for the *R* = 3 CBF may lead to a brittle fracture, which limits the ductility of the system. If such failure occurs, the reserve capacity of the building becomes essential to sustain the forces created by the rest of the ground motion and to mitigate the P-delta effects (Sizemore et al. 2017).

2.3 Beam-column connections

The rotational capacity of a connection depends on its type (e.g. shear tab, end plate, top and seat angles) and its geometry (Frye and Morris,1975, Morris and Packer 1987, Morris 1989, Dubina et

al, 2001). Beam-column connections have mostly been categorized qualitatively (Frye and Morris 1975, Morris and Packer 1987, Bjorhovde et al. 1990, Kishi and Chen 1990, Wong et al. 1995) into three groups: flexible, fully restrained (or fixed, rigid) and PR (or semi-rigid).

However, the Eurocode 3-8 (European Standard 1993) classifies connections quantitatively based on their moment resistance or their flexural stiffness, depending on the type of analysis performed. The strength classification is used in elastic-plastic and plastic analyses. It defines a joint as fully restrained if its plastic moment M_{pj} is greater than the beam M_{pb} or twice the column $2M_{pc}$. For connections at the roof, the latter condition is reduced to once the column plastic moment M_{pc}. Connections assumed pinned by the designer are defined as flexible and all others are characterized as partially restrained. The flexural stiffness classification, summarized in Figure 2.7, is used in elastic and elastic-plastic analyses. This method defines joints as flexible if their stiffness is less than $0.5EI_b/L_b$ and fully restrained if their stiffness is greater than $8EI_b/L_b$ and the bracing system reduces the lateral displacement by at least 80%. If the latter condition is not achieved, fully restrained joints must have a flexural stiffness greater than $25EI_b/L_b$ and the ratio between the mean values of I_b/L_b and I_c/L_c must exceed 10% for every storey. All other joints are classified as PR. For the purpose of the literature review, a qualitative approach will be used.



Zone 1: rigid, if $S_{j,ini} \geq k_b EI_b / L_b$

where:

$k_b = 8$ for frames where the bracing system reduces the horizontal displacement by at least 80 %

$k_b = 25$ for other frames, provided that in every storey $K_b/K_c \geq 0,1$ *)

Zone 2: semi-rigid

All joints in zone 2 should be classified as semi-rigid. Joints in zones 1 or 3 may optionally also be treated as semi-rigid.

Zone 3: nominally pinned, if $S_{j,ini} \leq 0,5 EI_b / L_b$

*) For frames where $K_b/K_c < 0,1$ the joints should be classified as semi-rigid.

Key:

K_b is the mean value of I_b/L_b for all the beams at the top of that storey;
K_c is the mean value of I_c/L_c for all the columns in that storey;
I_b is the second moment of area of a beam;
I_c is the second moment of area of a column;
L_b is the span of a beam (centre-to-centre of columns);
L_c is the storey height of a column.

Figure 2.7. Flexural stiffness classification method of Eurocode 3 (European Standard 1993)

2.3.1 Flexible connections

Flexible connections are very common in steel constructions for their low construction cost and fast erection (Koduru and Driver 2014). The most common connections are shear tabs, shear tees, and double web angles connections. They are designed to sustain only the gravity loads of the frame through direct shear and their moment resistance is considered negligible. Thus, those types of gravity joints are considered pinned. However, several studies were aimed at defining clearly their rotational capacity (Astaneh-Asl et al. 1993, Liu and Astaneh Asl 2000, Crocker and Chambers 2004, Liu and Astaneh-Asl 2004, Weigand and Berman 2014).

Double web angle connections generally show larger rotational capacity and larger shear capacity compared to shear tabs (Liu et al. 2012). An overview of the impact of geometrical parameters, of the presence of a concrete slab and of the column flanges present in double web angle connections on the nonlinear behavior of flexible joints is presented.

2.3.1.1 Influence of the horizontal bolt rows and angle length

Astaneh-Asl et al. (1989) performed cyclic tests on six full-scale double angle connections welded to the beam web and bolted to the column flange to investigate the influence of the number of horizontal bolt rows on the moment-rotation of the connection. This parameter studied was correlated with the angle length and the beam depth. Additionally, the angle thickness and the bolt type (ribbed vs. high-strength A325) were studied. Bolts of 19.1 mm and a W250x101 column were used for all tests. Also, a weld size of 6.4 mm between the beam web and the angle leg was kept constant throughout the tests.

The authors observed hysteretic pinching which was attributed to the development of the gap between the angles and the column flange in the tensile zone of the connection. This gap grew larger due to the permanent deformation of angles and bolt elongation. In rib-bolted specimens, large yielding of the engaged threads resulted in large bolt elongation, more severe pinching and eventually failed by stripping off the bolt threads. Connections with A325 bolts showed a more ductile behaviour and failed through excessive cracking in the angles near the fillet.

The number of horizontal bolt row influenced significantly the initial stiffness of the connection, as well as its ultimate moment and rotational capacity. Figure 2.8 a), b) and c) presents the moment-

rotation curve of a 3-, 4- and 6-row double web angle connection respectively. The ultimate moment capacity increases from 33.9 kN-m (25 kips-ft) for the 3-row to 54.2 kN-m (40 kips-ft) for the 4-row and up to 142.4 kN-m (105 kips-ft) for the 6-row connection. Meanwhile, the ultimate rotational capacity decreases from 0.06 rad to 0.045 rad and as low as 0.015 for the 3-, 4- and 6-bolt row connections respectively.

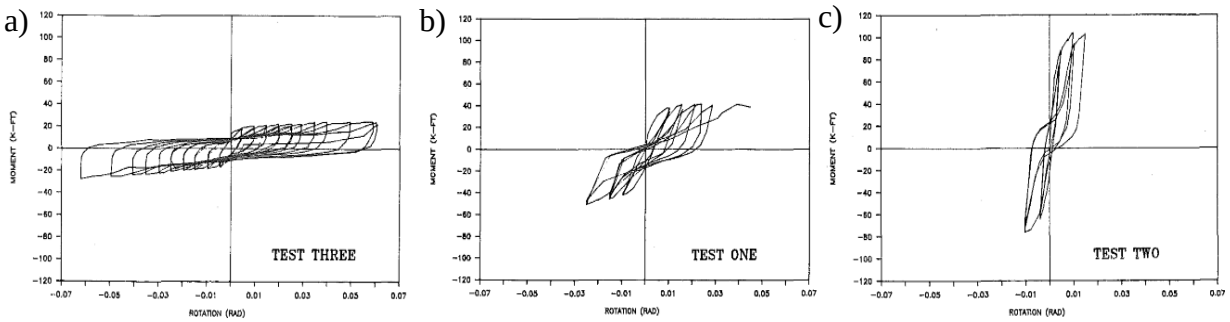


Figure 2.8. Moment-rotation hysteretic behaviour of a a) 3-row b) 4-row c) 6-row test (Astaneh-Asl et al. 1989)

These trends are attributed to the position of the connection neutral axis being farther from the most loaded bolt in tension in a connection with a greater number of bolt rows. Indeed, when this distance is larger, the tensile demand on the farther bolt is larger, thus increasing the moment capacity. However, the farther bolt and the angle in this region are also more loaded in tension, resulting in bolt stripping or angle cracking at smaller connection rotations. De Stefano et al. (1994) obtained similar observations through numerical and analytical modeling.

2.3.1.2 Influence of two vertical bolt rows

Ricles and Yura (1983) investigated the influence of several geometrical parameters on the behaviour of double web angle connections with two vertical bolt rows on the beam web. The studied parameters were the effect of coped beam, the horizontal *H* and vertical *V* edge distances of the first bolt row, the number of bolts in each row and the impact of long-slotted holes. Figure 2.9 illustrates the bolt configurations of the specimens tested. The load was applied at 610 mm (24”) from the connection, creating a large shear load, but also a small flexural demand on the connection.

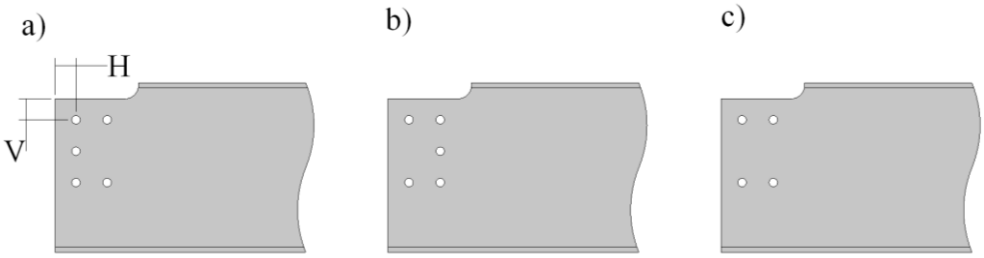


Figure 2.9. Bolt configuration of specimens tested by Ricles and Yura (1983)

All specimens showed a similar failure pattern, initiated by the fracture of the web along the bottom horizontal bolt line and web yielding between the fracture line and the top flange, as illustrated in Figure 2.10. Aside from the bottom bolt line, no hole elongation was observed, thus implying that the shear load did not distribute uniformly among the bolts. In four test cases, web buckling at the cope was observed after the fracture of the bottom bolt line. The presence of the upper beam flange reduced significantly the web yielding, but eventually yielding developed in the compression flange.

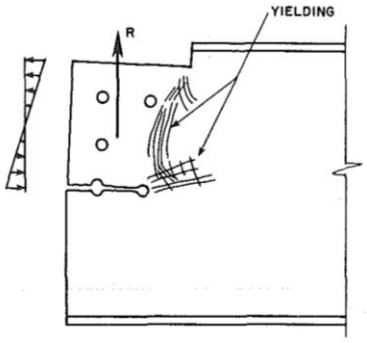


Figure 2.10. Failure mode observed by Ricles and Yura (1983)

The edge distances, both horizontal *H* and vertical *V*, affected the ultimate shear capacity, as well as the vertical displacement of the connection. The shear and deformation capacity of the connection increased proportionally with the edge distances, as the load required to produce the fracture at the bottom bolt line was larger. An increase of the horizontal edge distance *H* from 25 mm (1") to 51 mm (2") translated into an 18% increase in shear capacity. However, the same increase in the vertical edge distance only resulted in a shear capacity increase of 9%. The presence of long slotted holes caused a significant drop of capacity when fracture occurred and reduced the shear capacity, since the net section was reduced. The bolt configuration had no significant impact

on the connection behaviour, since the connection length remained constant throughout the testing program.

2.3.1.3 Influence of bolted vs. welded angles

Abolmaali et al. (2003) performed 20 full-scale cyclic tests on double web angle connections, among which 12 were bolted to both the beam web and the column flange (BB) and 8 were bolted to the column flange and welded to the beam web (BW). The authors investigated the impact of the type of connection to the beam web (bolted vs. welded), as well as the angle thickness t, the bolt size d_b, the distance between the column bolt line and the angle corner g_c, the number of bolt rows and the beam depth.

The authors identified two failure modes for the bolted-bolted angle connections: excessive rotation due to yielding of the angle and beam web bearing failure. The former was observed in test cases with a thickness equal or smaller than 10 mm, while the latter occurred in cases with a thickness larger than 10 mm. The overall behaviour of bolted-bolted angles exhibited a large capacity at dissipating energy and a significant moment transferred to the column. The authors noted that an increase of the number of bolts rows and consequently of the beam depth increased the moment capacity but decreased the ultimate rotational capacity of the connection. Those observations are consistent with the ones reported by Astaneh-Asl et al. (1989) and presented previously.

For the bolted-welded connections, the two failure modes observed were excessive rotation caused by angle yielding and bolt fracture. Bolt fracture occurred in tests 1BW and 3BW, where the distance between the column bolt line and the corner of the angle g_c are small with respect to the angle thickness. The other specimens failed by excessive angle yielding. The authors noted a significant decrease of stiffness as the column bolt gauge g_c grows larger, but an increase in rotational capacity. The bolt size obviously impacted the bolt capacity and thus controlled the failure mode of bolt fracture, but also contributed slightly to the rotational capacity through bolt elongation. The bolt size also modified the effective flexural stiffness of the column leg through the width of the bolt head and consequently impacted the initial stiffness. The overall hysteresis behaviour of a double web angle connection is therefore attributed to a highly nonlinear interaction of several geometric parameters. Also, the energy dissipation capacity of the connections can be enhanced by optimizing their geometric parameters (Abolmaali et al. 2009).

The influence of the beam leg boundary condition is illustrated in Figure 2.11. The bolt slip and hole elongation in the bolted beam leg resulted in a more flexible connection with severe pinching, identified as a flat region by the authors. This flat region, which was more pronounced in specimens with thicknesses larger than 10 mm that failed in web bearing, provided a larger rotational capacity to the bolted-bolted connections. However, their flexural stiffness was significantly reduced, which resulted in a lesser ultimate moment than their bolted-welded counterparts.

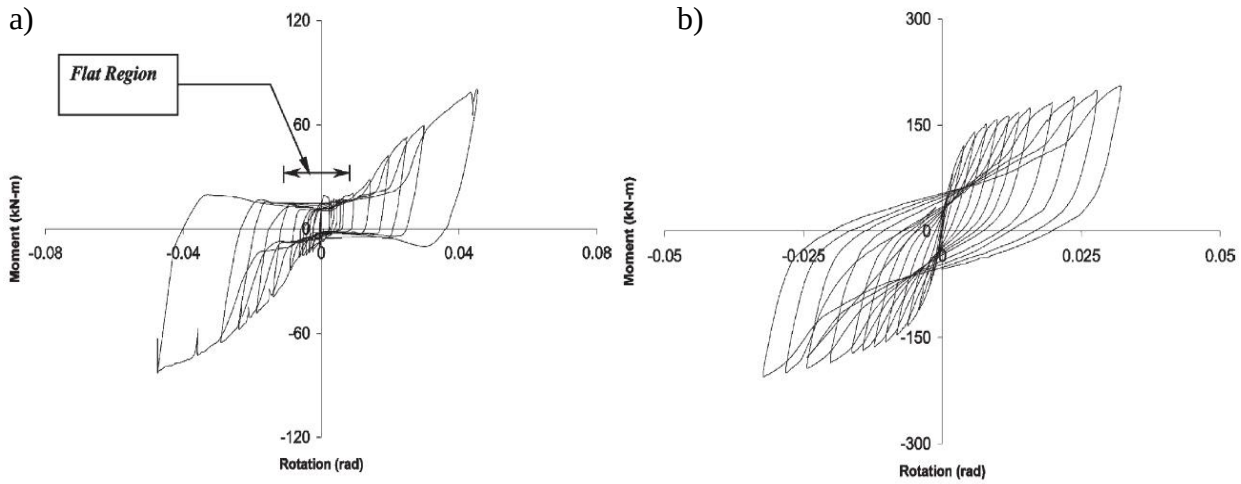


Figure 2.11. Moment-rotation hysteresis curves of a) Bolted-Bolted and b) Bolted-Welded connections (Abolmaali et al. 2003)

To summarize, several full-scale experimental programs have been conducted on double web angle connections. The nonlinear behaviour of the connection is greatly dependent on the connection geometry. Astaneh-Asl et al. (1989) investigated the influence of the angle thickness as well as the number of bolt rows on connections made of double web angles bolted to the column flange and welded to the beam web. A connection with more bolt rows showed a larger ultimate moment, but a smaller rotation. A similar general trend can also be formulated for the angle thickness.

Additionally, Ricles and Yura (1983) performed full-scale tests on coped beams with variable bolt configurations and edge distances. The authors observed a positive correlation between the edge distance and the shear capacity of the connection, but the bolt configuration did not significantly impact the joint resistance.

Abolmaali et al. (2003) investigated the influence of the angle thickness, the column bolt position, the bolt diameter, the beam depth and the number of bolt rows in connections made of double web

angles bolted to the column flange and either welded or bolted to the beam web. The interaction between the investigated parameters is highly nonlinear and the connections can be optimised based on the capacity and ductility design requirements.

2.3.1.4 Influence of concrete slab

Liu and Astaneh-Asl (2000, 2004) performed an experimental study on shear tab connections with the effect of a concrete slab. A numerical model to predict the moment-rotation capacity was also developed to evaluate the role of shear tabs with the effect of slab in the seismic resistance of a welded steel moment frame building. A total of 16 tests, separated in 2 series, were conducted (Liu and Astaneh-Asl 2000, Liu and Astaneh-Asl 2004) and several parameters were studied, such as the presence of slab, the concrete type and reinforcement level and the number of bolts in the shear tab connections.

The presence of a slab increases drastically the moment capacity of the connection, up to a rotation of 0.04 rad, where the concrete starts to crack and lose its integrity, as shown in Figure 2.12 (Liu and Astaneh-Asl 2000). From 0.04 rad until fracture, at roughly 0.14 rad, the contribution of the floor slab increased the moment capacity of the connection by a factor of approximately 2.0. Also, the concrete slab offers a lateral support to the top flange of the beam which improves the resistance against local and torsional buckling of the section (Civjan et al. 2000, Civjan et al. 2001, Zhang and Ricles 2006).

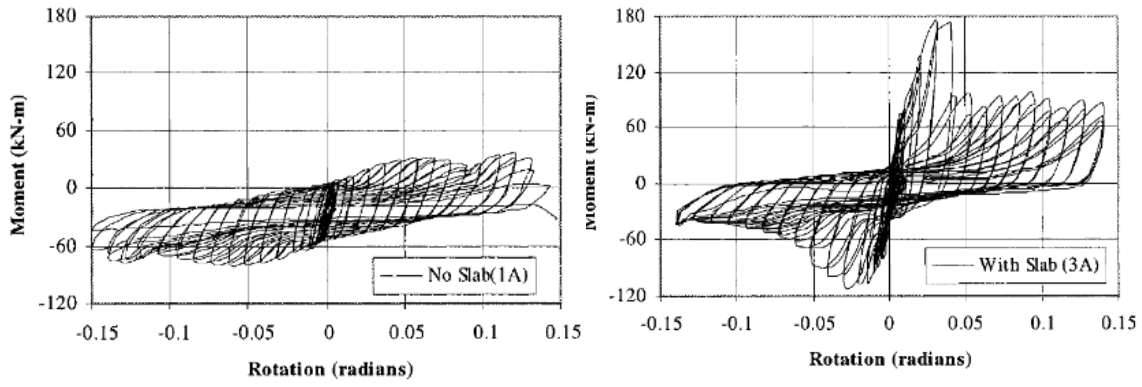


Figure 2.12. Moment vs. rotation response with and without slab (Liu and Astaneh-Asl 2000)

However, the presence of the concrete slab results in a shift of the neutral axis position. This change affects the negative excursion, since more material is loaded in compression and the concrete has

no tensile capacity. With the concrete loss of integrity, the neutral axis slowly shifts towards the center of the steel beam and the composite action loses its effect on the negative moment capacity of the connection. Therefore, the slab effect has a significant impact on the global stiffness of shear tabs and on the contribution of the gravity framing in the lateral load resistance, especially under small rotations (Liu and Astaneh-Asl 2000).

To increase the moment capacity of the connection in negative bending, a seat angle has been added to a specimen (Liu and Astaneh-Asl 2000). This addition resulted in a 50% increase of negative moment capacity, but the angle fractured at a rotation of 0.09 rad, which is significantly less than the 0.14 rad of a shear tab with composite action. Experimental results have shown that neither the type of concrete nor the concrete reinforcement ratio have a significant effect on the composite shear tab behavior (Liu and Astaneh-Asl 2000). The authors also propose a numerical model to evaluate the composite action between the concrete slab and the steel connection (Liu and Astaneh-Asl 2004).

The influence of a floor slab has been studied on several kind of beam-column connections either partially-restrained (e.g. Braconi et al. 2007, Green et al. 2004) or fully restrained (e.g. Leon et al. 1998, Hajjar et al. 1998, Civjan et al. 2000, Civjan et al. 2001, Jones et al. 2002, Zhang and Ricles 2006). Similar behavior as the one described previously were observed in those studies.

2.3.2 Partially restrained top and seat angle connections

Top and seat angle connections are usually used to transfer shear loads to the columns and maintain the beam stability (Chen and Kishi 1989). Although those connections are not usually used to transfer moments to the columns, they are qualitatively considered as PR, and thus, several studies were aimed at characterizing the moment-rotation behaviour of such connections.

2.3.2.1 Wind moment frames

Historically, American steel design codes have permitted a simplified design procedure for moment frames subjected to gravity and wind loads called the Wind Moment Frame (WMF) method that is still allowed (Kim 2003). The Wind Moment Frame design methodology was developed when the analysis of partially restrained connections was a complex endeavor, without the current computer-

based modeling and design tools available. This procedure assumes pinned connections under gravity loads and fixed connections under wind loads, as schematically presented in Figure 2.13.

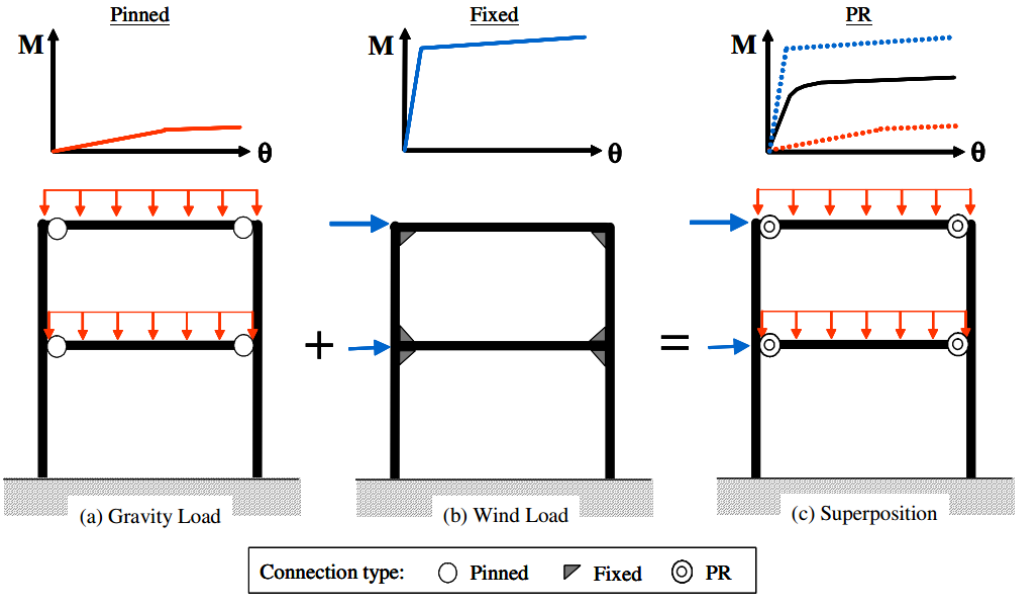


Figure 2.13. Schematic view of the Wind Moment Frame method (Leon and Kim 2004)

While the connection stiffness is actually an intermediate between those assumptions, the beams and columns are designed to resist the combined flexural moments and axial loading from the two conditions (Kim 2003, Kim and Leon 2007, Leon and Kim 2004). This methodology, generally applied to every connection in the building, usually results in a conservative design of beams and columns and a significantly weaker connection. Still, the method offers a reasonable design for regular frames with strong connections subjected to moderate lateral loads (Ackryod 1985). A similar procedure is also included in the Eurocode 3 (Hensman and Nethercot 2001, Anderson 2006). Pushover analyses of 4-, 6- and 8-storey Wind Moment Frames designed for the American Midwest were performed by Leon and Kim (2004). These buildings were stable until a 0.04 rad drift ratio, after which large plastic deformations in the lower storeys lead to the building collapse.

2.3.2.2 Influence of angle thickness

Shen and Astaneh-Asl (1999) studied the nonlinear behaviour of 8 bolted angles specimens and the influence of several geometrical parameters such as the angle thickness, the bolt diameter and the column bolt distance to the angle corner, as well as the loading conditions.

In a beam-column connection, the imposed rotation of a seismic event induces a moment at the column face which can be decomposed into a tensile and a compressive force in top and seat angles, as shown in Figure 2.14a). In the compressive angle, the force is transferred through contact, which provides large stiffness. However, the behaviour of the tensile angle needs to be characterized experimentally, as its behaviour depends greatly on several geometrical parameters. Therefore, to simplify the test setup and procedure, the experimental setup was only constituted of angles loaded in tension under monotonic protocols and tension-compression under cyclic loading, as illustrated in Figure 2.14b).

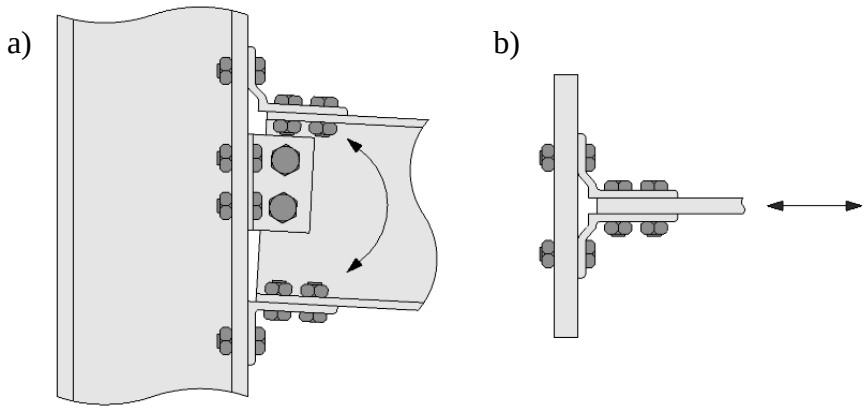


Figure 2.14. a) Top and seat angle deformation b) Experimental setup (Shen and Astaneh-Asl 1999)

The authors observed an ultimate strength 2 to 3 times larger than the yielding strength due to the combined effect of material strain hardening and large deformations. Also, a thickness increase from 10 mm to 13 mm (Specimens 1 and 2) resulted in doubling the yield and ultimate loads of the angles. However, changing the thickness from 13 mm to 19 mm (Specimens 5 and 6) only increased the yield strength of 30% and the ultimate load of 70%. This relatively low increase of yield strength is attributed to the different deformation patterns and failure modes observes between specimens 5 and 6. Thus, the thickness of the angle is the most influent parameter, as it defines the nonlinear behaviour and the failure mode experienced by the angles (Shen and Astaneh-Asl 1999).

Indeed, the first failure mode, presented in Figure 2.15, was observed mostly in angles with a small thickness. It is characterized either by fracture near the fillet in the column leg of the angle, or bolt shear failure of the beam bolts with cracking in the column leg near the fillet. The second failure

mode was observed mainly in thick angles and is defined by either fracture near the fillet in the beam leg of the angle, or net section fracture of the angle at the location of the beam bolts accompanied by cracking near the fillet in the beam leg.

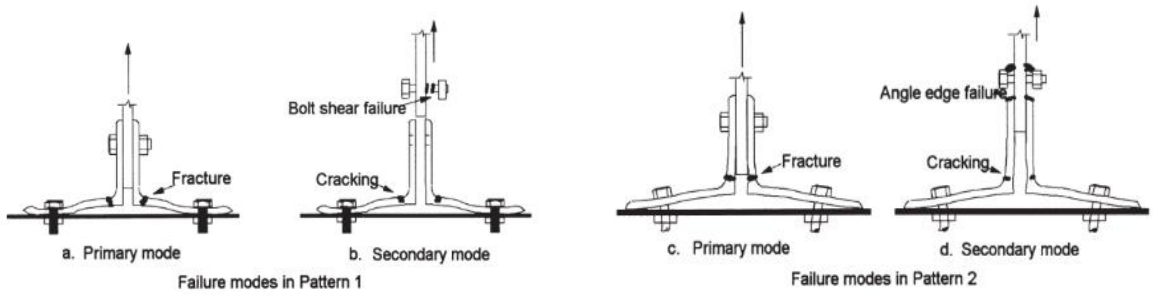


Figure 2.15. Failure modes (Shen and Astaneh-Asl 1999)

The authors reported a significantly smaller ultimate displacement under cyclic loading compared to monotonic conditions, in the tests where the first failure mode was observed. The ductility of the specimens that failed according to the second failure mode was not as sensitive to the loading conditions. In some tests where the column bolts were subjected to a large demand, the hysteretic behaviour of the angles was characterized by significant pinching, caused by the plastic bolt elongation accentuated by a large prying action.

Shen and Astaneh-Asl (2000) proposed a trilinear model to determine the nonlinear behaviour and the hysteretic envelope of bolted angles. This model is based on solid mechanics and gave a reasonable approximation of the behaviour for the 8 tests performed, as long as the failure mode is clearly identified. However, this model does not account for the prying action on the column bolts, which can be quite significant and can cause bolt tensile failure (Komuro et al. 2006).

Azizinamini (1985) performed an experimental investigation on two full-scale top-and-seat bolted angles connections, as well as two simple pull tests of back-to-back angles. The angle thicknesses were 9.5 mm (3/8”) and 12.7 mm (1/2”) for the specimens of both tests types. The connection tests showed that thicker top and seat angles result in larger initial stiffness and ultimate moment. However, the ultimate beam rotation obtained was similar in both tests notwithstanding the angle thickness.

Yang and Tan (2013) performed 14 experimental tests on bolted angles to characterize the behaviour of the connection component, using a test setup similar to Shen and Astaneh-Asl (1999).

The specimens consisted of monotonically loaded back to back bolted angles with three rows of bolts and varying angle thickness and distance between the column bolts and the angle corner. The authors reported Two angle fracture modes: net section fracture at the position of the column bolts, and gross section fracture of the column leg neat the heel of the angles. Important yielding of bolts was also observed in stiff specimens, and bolt failure occurred in one specimen. In every test, plastic hinges were formed near the heel of the angle on both the column and beam leg, as well as near the column bolts. The position of the hinge near the column bolts varied with the angle stiffness, as flexible angle legs tended to yield near the bolt head, on the side of the angle heel, whereas the plastic hinge of stiff angles formed in the opposite side of the bolt head, closer to the edge. For angles with an average, the plastic hinges formed around the bolt centerlines. This parametric study showed that an increase of angle thickness resulted in an increase of ultimate resistance of bolted angles, but a decrease in ultimate displacement. On the other hand, a larger distance between the column bolt and the angle corner increased the angle flexibility, thus creating a larger ultimate displacement, but a smaller ultimate load. The authors also proposed a mechanical model of bolted angle connections based on the experimental tests performed. This model included the effect of the column bolt gage, the angle thickness, the bolt size and material properties. The material and geometric nonlinearities at large deformation were also included in the model, as well as the bolt slip.

2.3.2.3 Influence of the column leg flexural span

Garlock et al. (2003) performed 7 tests on bolted angles similar to the tests performed by Shen and Astaneh-Asl (1999). This experimental campaign aimed to simulate the tensile excursion of top and seat angles subjected to a flexural moment, in a test setup similar to the one presented in Figure 2.4. The specimens had varying thicknesses and distances between the column bolts and the angle corner. For three specimens of different thicknesses, the column bolt gage was determined in order to keep the g_2/t ratio constant at a value of 4.00, where g_2 is defined as the distance between the edge of the column bolt washer and the beginning of the corner fillet. Every specimen was loaded under cyclic conditions.

The authors reported a common yield mechanism of three plastic hinges in all specimens. A plastic hinge formed on each leg adjacent to the fillet and another near the column bolts. A decrease in

stiffness was observed following the formation of this yield mechanism, to obtain a nearly linear post-yield stiffness made of a combination of geometric and material hardening. The authors also suggested the presence of a Bauschinger in the cyclic behaviour, but no isotropic hardening was observed.

Three distinctive failure modes were also reported. The first one occurred at the location of the beam leg plastic hinge adjacent to the fillet and was preceded by necking. The second and most common failure mode was the full fracture of the column leg near the fillet. Finally, the third mode was characterized by the failure of the column bolts. The failure surface of the bolts indicated a failure by low-cycle fatigue (Garlock et al. 2003).

A positive correlation was reported between the angle thickness and both the initial stiffness and the strength of the specimen. On the other hand, as the distance between the column bolts and the angle corner increased, the initial stiffness and the ultimate strength decreased, while the displacement capacity remained proportional to this geometrical parameter. Also, for a specific displacement of the angle, a specimen with the column bolts closer to the fillet showed larger strain values. Therefore, the angles accumulated plastic strain more rapidly, thus leading to earlier low-cycle fatigue failure.

Furthermore, the specimens with a smaller value of g_2/t were able to dissipate more energy for a given angle displacement due to their larger strength capacity. However, their smaller ductility made those specimens less resistant to low-cycle fatigue. Therefore, the authors suggested that the g_2/t ratio of the top and seat angles should be carefully determined by the designer to consider the stiffness, strength, ductility and energy dissipation requirements of the connection. Similar observations were reported by Gong (2014) and Smitha and Babu (2013).

2.3.2.4 Effective width of bolted angles

On all the tested specimens of Azizinamini (1985), strain gages were applied on both the column and beam leg, halfway between the heel of the angle and the bolt line. Along the angle width, the strain gages were aligned with the bolts and at the center of the angle, halfway between the bolts.

The results from those strain gages showed that, at small displacements, the strains below the bolts and in the middle of the angle were similar in both angle legs. When the angle started to yield, the

strains in the column leg below the bolt started to increase faster than the ones between the bolts, to reach values of approximately two times larger.

Meanwhile, the strains in the beam leg remained comparable between the two positions, at values much smaller than the ones recorded in the column leg. Therefore, the bolt position of column leg is more critical than the beam leg. The strains recorded in the beam leg of the connection specimens were significantly more important than the ones recorded in the simple pull test specimens. This difference can be explained by the rotation of the beam leg present in the connection test that was absent in the pull test, as the beam leg remained horizontal.

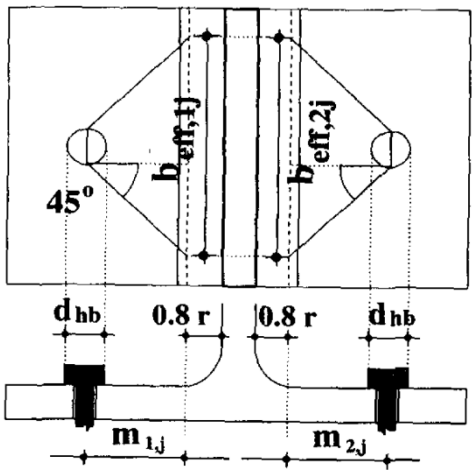


Figure 2.16. Effective width according to Faella et al. (1998)

Faella et al. (1998) also investigated the effective width of bolted T-stubs sections through an experimental campaign of 16 tests. The authors proposed a method to determine the effective width of each bolt row b_{eff} based on the bolt head diameter d_{hb}, the radius of the fillet r and the column bolt gauge m, as illustrated in Figure 2.16. The load flow is assumed to follow an angle of 45° to determine the effective width of the column leg. This method also assumes that the plastic hinges are forming in the fillet, at $0.8r$ from the beam leg, and at the centerline of the column bolts, under the bolt head. Therefore, since the effective width near the column bolts is significantly smaller than the one near the fillet, the first plastic hinge should be observed near the column bolts.

2.3.2.1 Influence of the beam depth

Kukreti and Abolmaali (1999) performed a parametric study on 12 specimens of full-scale beam-column connections with top and seat angles. This investigation was aimed at characterizing the

influence of the beam depth and distance between the column bolt and the angle corner on the initial rotational stiffness and ultimate moment of the connections. The other parameters studied were the angle thickness, the column leg length and the bolt diameter.

The authors reported tensile bolt failure in 6 specimens, while the 6 others failed through excessive rotation of the connection. The authors qualified the latter failure mode as a specimen reaching a rotation of 0.045 rad, at which point the large angle yielding resulting from the excessive rotation caused a significant loss in stiffness.

Also, the authors reported that all but one specimen exhibited pinching. During a typical cycle loading as shown in Figure 2.17, the seat angle, acting as the rotation point, is compressed to the column flange, while the top angle is loaded mainly in tension (point A). During the load reversal, the seat angle starts to deform in tension while the top angle is slowly being compressed. Before contact is made between the top angle and the column flange, the gap caused by the inelastic deformations experienced by the angle has to be closed, which results in a very flexible portion of the hysteresis, thus creating the pinching (point B). Once contact is established, a significant stiffness gain is observed (point C) and the hysteretic loop reaches the envelope curve of the connection.

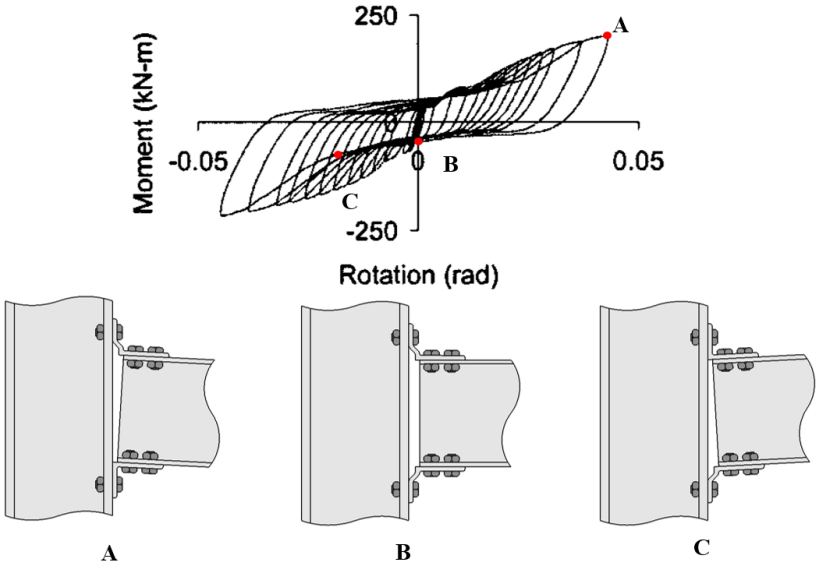


Figure 2.17. Cyclic deformations of bolted top and seat angle connections (Kukreti and Abolmaali 1999)

The authors reported that an individual increase in either the angle thickness or the bolt size resulted in a significant increase of the initial stiffness, as well as of the ultimate moment. Also, a variation of the distance between the column bolts and the angle heel causes an inversely proportional variation of the initial stiffness and of the ultimate moment. Also, it was observed that the length of the angle leg did not affect the behaviour of the connection. Finally, the beam depth has a proportional influence to the initial stiffness of the connection, but its effect on the ultimate moment is small. The authors recommend a more detailed study to investigate the individual and coupled impact of geometric parameters on the nonlinear behaviour of top and seat angle connections.

Smitha and Babu (2013) investigated numerically the influence of beam depth on the response of top and seat angle connections. The authors reported an increase in rotational stiffness and in rotational capacity as the beam depth increases.

2.3.2.2 Influence of bolting conditions

Citipitioglu et al. (2002) used a finite element analysis software to perform a numerical parametric study investigating the influence of bolt pretension, and bolt slip. The results of this numerical investigation showed that an increase of bolt pretension increased the ultimate moment of the connection significantly, as shown in Figure 2.18. However, the impact of the pretension on the initial rotational stiffness of the connection was minimal.

The authors also performed a finite element analysis to investigate the difference between simple pull tests and actual beam-column rotation of top and seat angle connections under monotonic loading conditions. The force-displacement F_{Angle}-Δ_{Angle} responses of the pull tests were converted into moment-rotation M_j-θ_j by assuming the relationships presented by Equations 2.10 and 2.11, where d_{beam} is the beam depth.

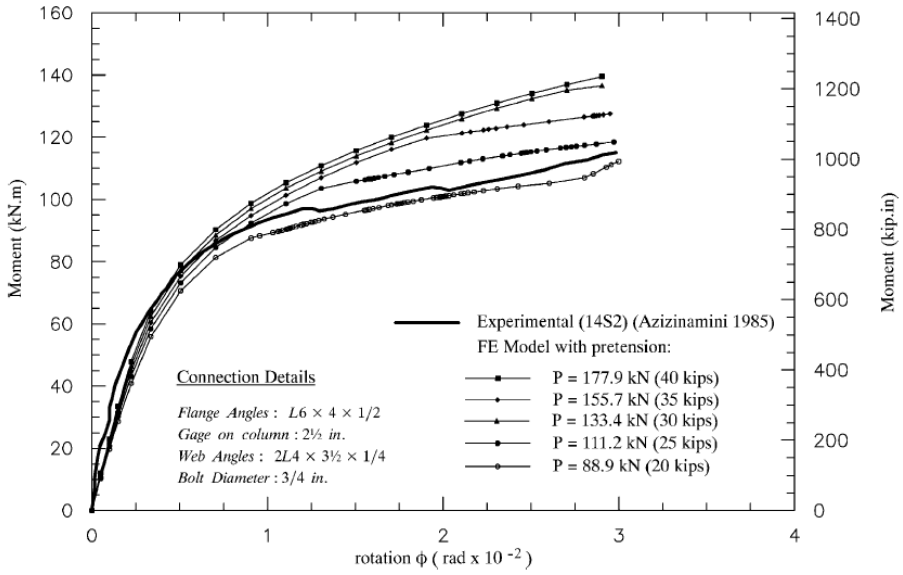


Figure 2.18. Moment-rotation curves of top and seat angles with varying bolt pretension Citipitioglu et al. (2002)

$$M_j = F_{Angle} \times d_{beam} \tag{2.10}$$

$$\theta_j = arctan\left(\frac{\Delta_{Angle}}{d_{beam}}\right) \tag{2.11}$$

It was observed that the moment-rotation behaviour of the connection was similar to the response based on the force-displacement curves of simple pull tests under elastic deformations. Therefore, the initial stiffness of the connection is mainly governed by the top angle geometry. However, the two behaviours started to diverge as the plastic deformations increased. The pull tests systematically underestimated the moment-rotation behaviour of the connections, making them less representative of full-scale models under large rotations. The plastic strains have also been compared between a full top and seat connection model and a simple pull test. The authors reported plastic strains in the pull test model larger than the ones in the connection under 0.03 rad, at which point the strains in the connection angle became higher. This observation was attributed to the rotation of the angle beam leg in the connection model, which added more strains, whereas the angle in the pull test remained constrained to a horizontal displacement.

Pirmoz and Danesh (2009) also performed finite element analyses to evaluate the influence of the seat angle on the moment-rotation behaviour of top and seat angle connections. They suggested that the underestimation of the moment-rotation behaviour of the pull tests resulted from the absence of seat angle. This connection element is used to transfer the shear load from the beam to the column but can also contribute to the flexural stiffness under large deformations (Pirmoz et al. 2009).

To summarize, several experimental and numerical studies have been performed on top and seat bolted angle connections. Those studies indicated that the most influential parameters on the nonlinear behaviour of the angles are the thickness and the distance between the column bolts and the angle corner.

Shen and Astaneh-Asl (1999) used an experimental setup simplifying the top and seat angle deformation in a connection into an angle loaded axially, to characterize the influence of several geometrical parameters on the angle component level. Similar experimental setups have been used by Azizinamini (1985), Garlock et al. (2003), Yang and Tan (2013) and Gong (2014).

On the other hand, Kukreti and Abolmaali (1999), as well as Azizinamini (1985) performed tests on full-scale top and seat angle beam-column connections. The plastic strains developed in the pull tests were consistently smaller than the ones in the full-scale test, because of the absence of the beam leg rotation (Azizinamini 1985). Citipitiogli et al. (2002) compared numerical models of full-scale beam-column specimens to simple pull test models. The two setups showed similar responses at small deformations, but the pull tests underestimated systematically the moment-rotation behaviour under large deformations. Pirmoz and Danesh (2009) suggested that this underestimation of the pull tests is a result of the lack of seat angle.

2.3.3 Top and seat with double web angles connections

Top and seat connections can also be combined with flexible shear connections such as double or single web angles and shear tabs. Those composed joints combine the stiffness of both kind of connection in parallel (Kishi and Chen 1990, Lee and Moon 2012). Therefore, the previously mentioned mathematical models used to determine the moment-rotation behaviour of top and seat connections and of shear connections can be joined in parallel. The added benefits of top and seat

connections come mainly from their large inherent ductility and their capacity can be adjusted with geometrical parameters to avoid column or beam yielding, while the double web angle connections offer a large shear load capacity. The larger rotational stiffness provided by the top and seat angles generally governs the behaviour of these connections (Chen and Kishi 1989, Kishi and Chen 1990). Mathematical models are proposed to evaluate the rotational stiffness and moment-rotation behavior of top and seat with double web angle connections (Kishi and Chen 1990, Lee and Moon 2012, Kong and Kim 2017).

In addition to the simple pull tests and top and seat connections tests, Azizinamini (1982, 1985) also conducted an investigation program consisting of 43 full-scale bolted top and seat with double web angles connections. Among those, 18 tests were performed under monotonic static loading conditions, 16 specimens were loaded cyclically with a constant amplitude and 7 were loaded cyclically with increasing amplitudes. The varying parameters of the study were the beam size, the top and seat angle thickness, the bolt diameter, as well as the distance between the column bolt and the heel of the angle of the top and seat angles.

The cyclic tests showed generally stable hysteresis loops throughout the tests. The author explained this stability by the plastic strain variation along the width of the column leg of the top and seat angles. Indeed, the maximum plastic strains were recorded below the bolts along the width, whereas the minimum strains were located at the center of the angle width, halfway between the bolts. These observations are consistent with the observations reported previously on the effective width of bolted angles (Faella et al. 1998). As the region in the vicinity of the bolts started to lose its capacity due to excessive yielding and cracking, the region between the bolts compensated this loss by a greater contribution. Therefore, this load redistribution along the angle width allowed a stable behaviour throughout the test. Also, the cyclic tests all failed through angle fracture on the column leg adjacent to the fillet and the crack initiation was reported to take place below the column bolts, where the largest plastic strains were measured.

The author reported that the initial stiffness and moment-rotation behaviour of the connection were mainly governed by the following geometrical parameters: the beam depth, the top and seat angle thickness and the column bolt gage of the top and seat angles. The change in bolt diameter did not significantly affect the initial stiffness, but the plastic behaviour of the specimens with larger bolts was stiffer, resulting in a larger ultimate moment.

The displacement demand of the top and seat angles was proportional to the beam depth. Therefore, the force developed in each angle increased with the beam depth, which in turn increased the moment capacity of the connection. However. The larder displacement demand indicated that the ultimate displacement of the top and seat angles was reached at a smaller rotational demand on the connection. The rotational capacity of the top and seat with double web angle was therefore inversely proportional to the beam depth. These observations are consistent with the ones expressed on the bolted top and seat angle connections.

2.3.3.1 Influence of top and seat angle thickness

Abdalla et al. (2015) conducted a parametric study through finite element modeling of top and seat with double web angle connections. Numerical models with varying top and seat angle thickness were developed. The impact of the friction coefficient in the modeling of the contact interfaced throughout the connection, as well as the level of bolt pretensioning were also investigated. The modelled connections were loaded through an incremental monotonic load applied at the extremity of a rigid beam, thus creating a moment at the beam-column connection. The displacement of the beam end was then used to calculate the connection rotation, in order to compute the moment-rotation behaviour of the connection.

The results of the parametric study showed that an increasing top and seat angle thickness lead to overall larger connection stiffness and strength. However, the larger prying action associated with the thicker angle could result in excessive yielding of the bolts, beam flange and column flange. Therefore, the authors recommended that the thickness of the top and seat angles should be carefully selected during the design process. Similar results were observed by Brunesi et al. (2013).

As of the bolt pretensioning, the authors reported only a slight increase in the connection strength as the pretension load applied increased. However, as the moment on the connection increased, the top angle deformed more and the prying forces grew larger to a point where the total tensile force in the bolts were similar, with no dependency to the applied bolt pretensioning. Therefore, the gain in strength related to the pretensioning is present at small deformations, but gradually reduces as the connection load increases.

2.3.3.2 Influence of the initial rotational stiffness

Elnashai et al. (1998) experimentally investigated the behaviour of restrained and partially restrained beam-column connections in two-storey frames under cyclic loading and pseudo-dynamic ground-motions. The goal of this study was to evaluate the seismic response of a frame constituted of bolted top and seat with double web angles, considered as partially restrained. 6 tests were performed on such connections, with varying top and seat angle dimensions and loading conditions. Those results were then compared to the response of fully welded beam-column connections, considered as fully restrained.

The authors found that the bolted connections displayed a ductile and stable moment-rotation behaviour under cyclic loading, which was also reflected through the overall frame response. However, the pseudo-dynamic testing showed that the response of the frame is highly dependent on the dynamic characteristics of the frame itself and on the input ground-motion. The smaller elastic stiffness of the partially restrained connections resulted in a more flexible frame, with a stiffness decrease of up to 30%. This stiffness reduction translated into a larger period of vibration of the frame and thus a different response to the same ground-motion. Therefore, the PR frame may, depending on the input ground-motion, exhibit a better behaviour than the fully restrained connections. Thus, bolted top and seat with double web angle connections may be used effectively for seismic design. However, attention should be brought to the storey drift, as the PR connections created a more flexible frame, thus more vulnerable to lateral instability.

Brunesi et al. (2013) proposed an empirical method to evaluate the rotational stiffness of bolted top and seat with double web angle connections. This method was developed with a numerical parametric study investigating the influence of the bolt pretension, the prying action and the relative component slippage on the moment-rotation behaviour of the connection. The rotational stiffness proposed by Brunesi et al. (2013) increases along with the column flange thickness, the angle thickness, the beam depth and the bolt size. Mathematical models are also proposed to evaluate the rotational stiffness and moment-rotation behavior of top and seat with double web angle connections (Kishi and Chen 1990, Lee and Moon 2012, Kong and Kim 2017).

2.3.3.3 Influence of the shear load

Danesh et al. (2007) conducted a numerical investigation to determine the impact of the connection shear force on the initial rotational stiffness of top and seat with double web angle connections. The experimental results of full-scale connections tested by Azizinamini (1985) were chosen to validate the finite element modeling approach. Then, 5 different connection geometries, with several beam depth and angle thicknesses, were loaded by a constant shear force at the connection throughout the numerical analysis, but with a different value than the other models. The connection was then monotonically loaded by imposing an increasing vertical load at the extremity of the beam in order to obtain the monotonic moment-rotation behaviour of the connection.

The authors reported a reduction of up to 49% of the elastic rotational stiffness of the connection when large shear forces were applied. Also, at larger shear forces, earlier bolt slippage and yielding were observed, thus creating additional losses of initial stiffness and smaller energy dissipation capacity. However, a slight increase in plastic stiffness was observed as the shear force increased.

Furthermore, this study indicated that some geometrical parameters of the connection had an important effect on the moment capacity of the connection, such as the top and seat angle thickness, but a relatively small impact on the shear capacity. On the other hand, the web angle thickness was not determinant in the moment capacity of the connection but played an important role in the shear capacity of the connection. Indeed, the Von Mises stress distributions of the angle connection showed that an increasing shear force translated into an important stress increase in the double web angle, while some additional yielding of lesser magnitude were also observed in the top and seat angles. The shear load was therefore mainly sustained by the web angles. The authors also observed a positive correlation between the rotational stiffness reduction of the connection and the ratio between the applied load and the web angle shear capacity.

In general, the addition of top and seat angles to double web angle connections seems a viable option to enhance the flexural behaviour of the connection while keeping a large shear capacity. Indeed, the shear load is mainly resisted by the double web angles (Danesh et al. 2007), while the top and seat angles increase significantly the moment capacity and the flexural stiffness of the joint (Kishi and Chen 1990). The top and seat with double web angle connection can offer significant lateral stiffness through moment frame action (Elnashai et al. 1998). Therefore, using such

connections in the gravity framing system can contribute significantly to the mitigation of unwanted failure mechanism for American R = 3 and Canadian Type CC braced frames.

However, several geometrical parameters influence the behaviour of bolted angle connections. Geometrical parameters of the connection itself, such as the number of bolts and consequently the beam depth and angle length, seems to dictate the flexural behaviour and shear resistance of double web angles (Ricles and Yura 1983, Astaneh-Asl et al 1989, Abolmaali et al 2003). On the other hand, the nonlinear behaviour of top and seat angle connections is mostly governed by the parameters of the angle itself: the thickness and the distance between the column bolts and the corner of the angle (Azizinamini 1985. Shen and Astaneh-Asl 1999, Garlock et al. 2003, Danesh et al. 2007, Gong 2014), but the influence of these parameters remained vague.

2.4 Building modeling with OpenSees

The Open System for Earthquake Engineering Simulation (OpenSees) (McKenna 1997, Mazzoni et al. 2006, McKenna and Fenves 2016) is a finite element, object-oriented, open source software. This platform is used in research to simulate the seismic response of structural and geotechnical systems. The object-oriented framework of the platform offer versatility in modeling structural systems by allowing the user to combine a large array of material behaviour, element behaviour, solution methods and data processing procedures (McKenna 1997). The following sections summarize the behaviour of material modules used to model steel components (*Steel02*) and the low-cycle fatigue behaviour (*Fatigue*) in the OpenSees framework (Mazzoni et al. 2006).

2.4.1 Hysteretic behavior of Giuffré and Pinto (1970) and Menegotto and Pinto (1973)

The stress-strain relationship proposed by Giuffré and Pinto (1970) and Menegotto and Pinto (1973) is presented in Equation 2.12. The stress σ is evaluated at each strain demand ε imposed on the material. The parameters σ_0 and ε_0 correspond to the yield stress and strain, b is the ratio between the plastic and initial stiffness and R is a coefficient defining the transition between the initial and plastic stiffness. These parameters are defined by the user and remain constant for each stress evaluation. Equation 2.12 can be transposed into the force-displacement F-Δ relationship of Equation 2.13. The latter corresponds exactly to the power model proposed by Kishi and Chen

(1990), where K_i and K_p are the initial and plastic stiffness, F_0 is the yield force and R is the transition coefficient.

$$\sigma = \sigma_0 \left(\frac{(1-b)\frac{\varepsilon}{\varepsilon_0}}{\left[1 + \left(\frac{\varepsilon}{\varepsilon_0}\right)^R\right]^{\frac{1}{R}}} + b\frac{\varepsilon}{\varepsilon_0} \right) \tag{2.12}$$

$$F = \frac{(K_i - K_P)\Delta}{\left[1 + \left(\frac{\Delta}{F_0/K_0}\right)^R\right]^{\frac{1}{R}}} + K_P\Delta \tag{2.13}$$

To characterize the hysteretic behavior, the stress-strain relationship of Equation 2.12 must be updated at each load reversal. This update allows the model to consider the stress and strain values at the load reversal, by reformulating the relationship of Equation 2.12 into Equation 2.14, with the normalized stress σ^* and strain ε^* defined by Equations 2.15 and 2.16 respectively. In these equations, σ_r and ε_r are the stress and strain at the load reversal, but also the initial stress and strain of the next excursion. σ_0 and ε_0 represent the stress and strain values of the intersection point between the asymptotes of the initial stiffness and the plastic stiffness of the next excursion. The graphical representations of these values are presented in Figure 2.19 for the first two load reversals. In this figure, the stress and strain values to use in Equations 2.15 and 2.16 for each load reversal are indicated by the subscript.

$$\sigma^* = \frac{(1-b)\varepsilon^*}{(1 + (\varepsilon^*)^R)^{\frac{1}{R}}} + b\varepsilon^* \tag{2.14}$$

$$\sigma^* = \frac{\sigma - \sigma_r}{\sigma_0 - \sigma_r} \tag{2.15}$$

$$\varepsilon^* = \frac{\varepsilon - \varepsilon_r}{\varepsilon_0 - \varepsilon_r} \tag{2.16}$$

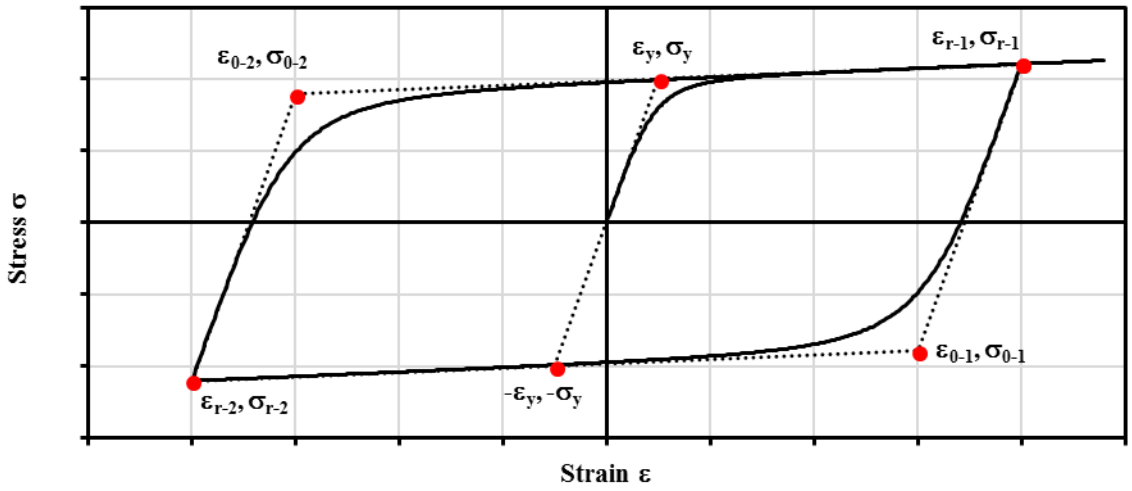


Figure 2.19. Hysteretic behaviour of Giuffré and Pinto (1970) and Menegotto and Pinto (1973) mathematical model and load reversal parameters

The updating of the stress-strain relationship at each load reversal is exploited by the model to acknowledge the deterioration of the cyclic curvature caused by the Bauschinger effect. This cyclic deterioration depends on the maximum strain experienced by the angles. Thus, this value is known at each step of the loading and is updated with the stress-strain relationship defining the next excursion. The model developed by Giuffré and Pinto (1970) and Menegotto and Pinto (1973) proposed to consider the cyclic deterioration by updating the transition parameter R with Equation 2.17. In this equation, the unitless parameters c_{r1} and c_{r2} define the degradation rate and should be calibrated based on experimental results. The strain ratio ξ is given by the maximum plastic strain range experienced by the angles with respect to the initial yield strain ε_0, as defined by Equation 2.18. Figure 2.20 presents the ξ ratio for the first two cycles, as well as typical hysteretic curves with and without cyclic degradation.

$$R = R_0 - \frac{c_{r1}\xi}{c_{r2} + \xi} \tag{2.17}$$

$$\xi = \frac{\varepsilon^{+}_{\mathrm{Max}} - \varepsilon^{-}_{\mathrm{Max}}}{2\varepsilon_0} \tag{2.18}$$

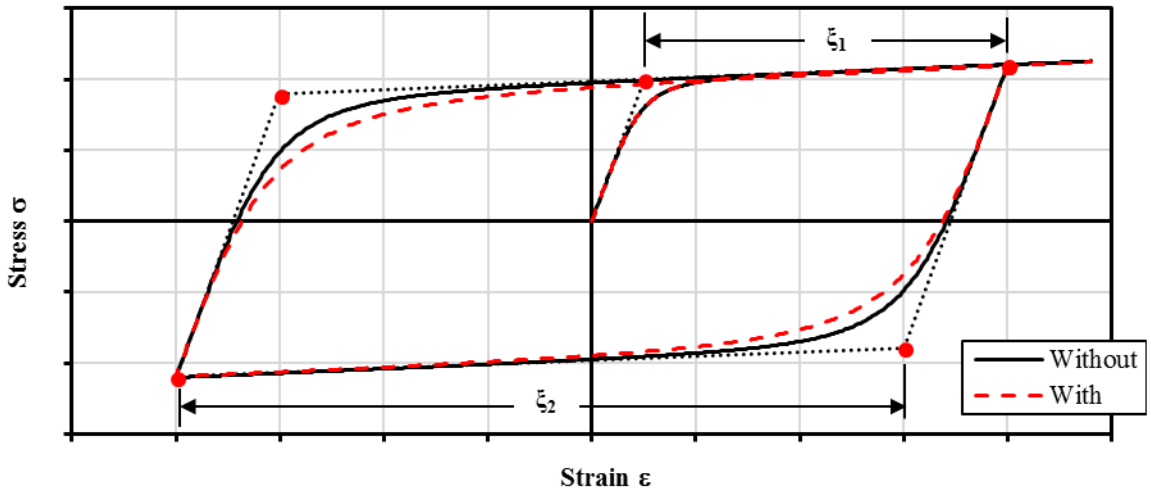


Figure 2.20. Cyclic degradation of the Giuffré and Pinto (1970) and Menegotto and Pinto (1973) model enhanced by Filippou et al. (1983)

The stress-strain relationship proposed by Giuffré and Pinto (1970) and Menegotto and Pinto (1973) was enhanced by Filippou et al. (1983) to account for the isotropic hardening of the steel rebars in reinforced concrete structures. This improvement exploits the updating character of the numerical model. The isotropic hardening depends on the maximum strain experienced by the angles and is revaluated at each load reversal, during the update of the stress-strain curve of the next excursion. Filippou et al. (1983) proposed Equation 2.19 to characterize the stress shift σ_{st} caused by the isotropic hardening, without distinction for the compressive and tensile stress shift. Figure 2.21 presents this stress increase by comparing typical hysteretic curves with and without the isotropic hardening.

$$\frac{\sigma_{st}}{\sigma_0} = \alpha_1 \left(\frac{\varepsilon_{Max}}{\varepsilon_0} - \alpha_2 \right) \tag{2.19}$$

However, In the *Steel02* material of OpenSees (Mazzoni et al. 2006), a distinction was made between the hardening during the compressive and tensile excursions. Furthermore, in the source code of the *Steel02* material (McKenna et al. 2006), the stress shift σ_{st} rather follows the formulation proposed by Lanning and Uang (2014) and transcribed in Equations 2.20 and 2.21 for the compressive and tensile excursions respectively.

The unitless parameters α_1 and α_2 are associated with the compressive excursion, while the hardening of the tensile excursions uses the parameters α_3 and α_4. These unitless parameters should be calibrated based on experimental results. Figure 2.21 presents the influence of the isotropic hardening on a cyclic excursion. Also, in the source code of the *Steel02* material (McKenna et al. 2006), the parameters b_1 and b_1 were both set at 0.8.

$$\sigma_{st,Compression} = \alpha_1 \left(\frac{\xi}{\alpha_2}\right)^{b_1} \sigma_0 \tag{2.20}$$

$$\sigma_{st,Tension} = \alpha_3 \left(\frac{\xi}{\alpha_4}\right)^{b_2} \sigma_0 \tag{2.21}$$

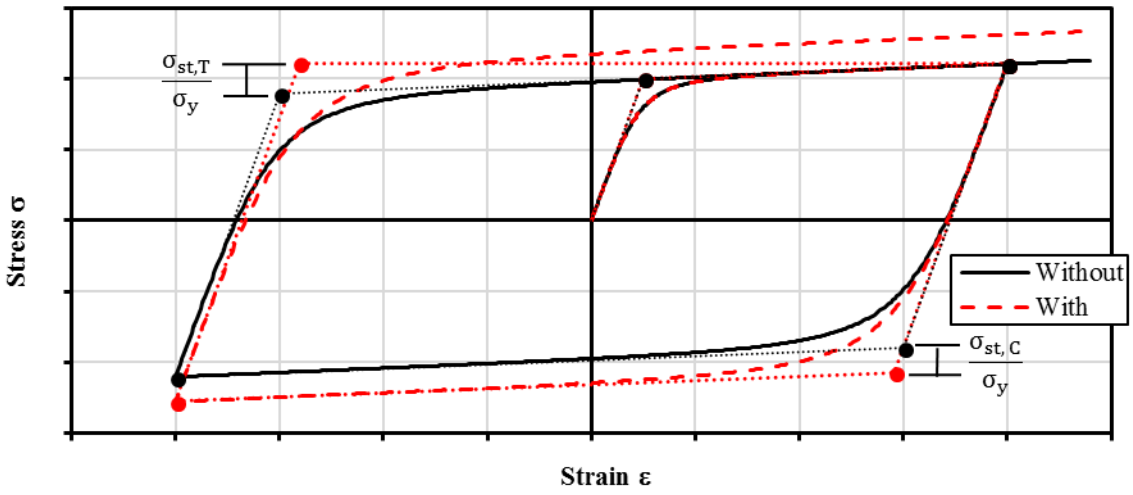


Figure 2.21. Isotropic hardening of the Giuffré and Pinto (1970) and Menegotto and Pinto (1973) model enhanced by Filippou et al. (1983)

The mathematical model of Menegotto and Pinto (1973) and enhanced by Filippou et al. (1983) needs to keep the loading history of the test in memory to accurately predict the material hysteretic behavior. However, keeping the data from the entire test is computationally impractical when creating an efficient numerical model such as the *Steel02* material in OpenSees (Mazzoni et al. 2006). Therefore, Filippou et al. (1983) proposed the storage of only a few values, namely:

a) The monotonic envelope parameters, K_i, K_p, P_0, R_0 (User defined);
b) The hysteretic behavior parameters, C_{r1}, C_{r2}, α_1, α_2, α_3, α_4, (User defined);
c) The maximum strains experienced in tension and compression, ε_{Max+} & ε_{Max-}; and

d) The stress and strain values at which the last load reversal occurred σ_r and ε_r.

However, some concerns (Orakcal et al. 2006, Kunnath et al. 2009) were raised on the overshooting of the stress estimated by the model after partial reloading. The stress-strain relationship is still revaluated with the degradation of cyclic curvature after partial excursions. This reevaluation may overestimate the target load σ_0 corresponding to the intersection between the initial stiffness and the plastic stiffness. Figure 2.22 shows such discrepancy with partial unloading in negative and positive excursions.

The second excursion, starting at ε_{r-2}, σ_{r-2}, was a positive strain increment excursion, but did not reach plastic strains. This excursion ended at ε_{r-3}, σ_{r-3}, which also corresponded to the start of a negative strain increment excursion. At this load reversal, the stress-strain relationship was updated, along with the strain hardening. Therefore, the point defining the transition of the excursion, ε_{0-3}, σ_{0-3} was slightly superior to its realistic value, the end of the prior negative strain increment, ε_{r-2}, σ_{r-2} (Orakcal et al. 2006). Figure 2.22 also shows the same discrepancy with a partial negative strain increment excursion. At the load reversal of the partial negative excursion, ε_{r-6}, σ_{r-6}, the initial to plastic transition point ε_{0-6}, σ_{0-6} was also superior to its realistic value, as the plastic portion was realistically the continuity of the prior positive excursion (Orakcal et al. 2006).

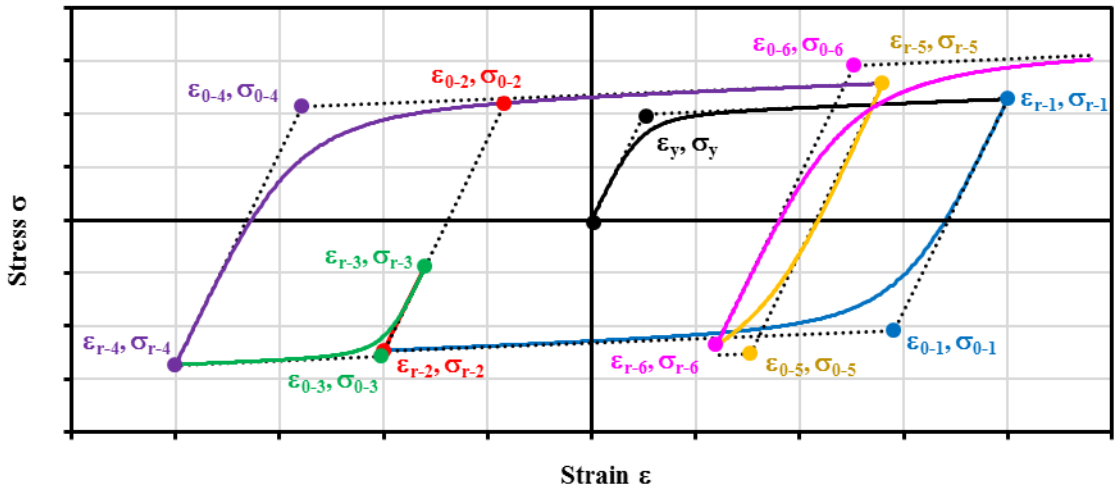


Figure 2.22. Partial unloading error of Menegotto and Pinto (1973) model enhanced by Filippou et al. (1983)

2.4.2 Fatigue damage accumulation with partial cycles

Steel structures have a finite fatigue lifespan that depend on the stress or strain amplitudes imposed on the material and its intrinsic resistance to fatigue. Low-cycle fatigue is characterized by plastic deformations, which cause failure at a much lower number of cycle than high-cycle fatigue. Although the fatigue behaviour is relative to the material of the structural component, it is closely related to the yielding mechanism occurring in the component. Therefore, fatigue behavior is generally considered on an element level, rather than at the material level (Uriz and Mahin 2008).

To characterize the fatigue lifespan of a component, the stress-cycle (S-N) or strain-cycle (ε-N) curves are generally determined experimentally (ASTM E606 2012, ASTM E466 2015, ASTM E739 2015). The test consists of loading the component with a constant stress or strain demand amplitude, $\Delta\sigma$ or $\Delta\varepsilon$, and counting the cycles N until fracture. The applied load must create plastic deformations in the component to estimate its low-cycle fatigue properties. This test is then repeated at several stress or strain amplitudes and the stress-cycle (S-N) or strain-cycle (ε-N) curves are drawn. These relationships are linear in the logarithmic domain, as shown in Figure 2.23.

Ballio et al. (1997) and Bernuzzi, et al. (2000) performed several data analyses of fatigue tests on connections and beams, in order to determine the appropriate parameters for those structural components when using the stress-cycle (S-N) relationship. It was shown that a slope m ranging from -0.50 to -0.33 in the logarithmic domain is considered ductile under fatigue loading.

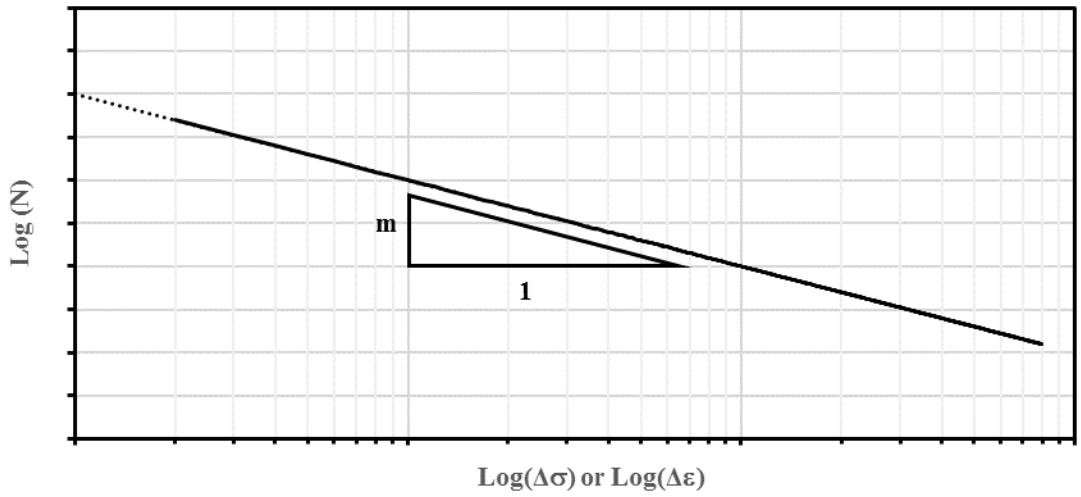


Figure 2.23. Typical stress-cycle or strain-cycle curve of low-cycle fatigue

The stress-cycle (S-N) or strain-cycle (ε-N) curves allow the estimation of the fatigue life under a constant stress or strain demand. However, under variable stress amplitudes, the number of cycles to failure also vary. A cumulative damage rule has thus been proposed by Miner (Miner 1945) to estimate the mobilization of each stress or strain amplitude to the fatigue life. This rule, presented in Equation 2.22, consists of summing the ratio between the applied number of cycles, N_j, to the number of cycle to failure, N_{fj}, of each amplitude. The latter is estimated with the stress-cycle (S-N) or strain-cycle (ε-N) curves for each amplitude. When the summation reaches a value of 1.0, the fatigue life is considered exhausted, and thus failure occurs.

$$\sum \frac{N_j}{N_{fj}} = 1 \tag{2.22}$$

Under seismic loading, the assessment of the low-cycle fatigue life requires a cycle-counting procedure to convert the irregular time-history cycles into an equivalent number of uniform cycles. The rainflow cycle counting, developed by Matsuishi and Endo (1968) has been generally recognized as an adequate procedure for irregular cycle counting (ASTM E1049 2017).

However, in order to accurately apply the rainflow counting procedure developed by Matsuishui and Endo (1968), the entire loading history must be analyzed. Such analysis is incoherent when evaluating the fatigue life of a structural component under a seismic event, Indeed, the stress or strain amplitudes applied on the studied component depend on the behaviour and the fatigue life of its surrounding elements. Also, the computational power required to evaluate the entire loading history for every component is extremely high. These issues render the rainflow counting process impractical for finite element analyses.

To palliate to these difficulties with the fatigue life evaluation, Uriz and Mahin (2008) proposed a simplified version of the rainflow counting. This simplified procedure only requires the last 4 load reversal points to assess the remaining fatigue life of the element, thus reducing considerably the required computational power of an analysis. The simplifications create an intrinsic error on the fatigue life of the element with respect to the rainflow counting method developed by Matsuishi and Endo (1968).

Figure 2.24 presents the low-cycle fatigue damage index (DI) algorithm proposed by Uriz and Mahin (2008). The damage index (DI) depends on the four previous load reversals experienced by

the elements (peaks A, B, C and D). The stress amplitudes X and Y define the damage incurred by the element. The value *m* corresponds to the strain-cycle ε-N slope of the element, while ε_0 corresponds to the strain at which the element can sustain only one full cycle.

The simplified method proposed by Uriz and Mahin (2008) can easily be applied in a finite element model to assess the fatigue life of the elements. The algorithm presented in Figure 2.24 was added into the OpenSees source code as the *Fatigue* material (Mazzoni et al. 2006). Furthermore, the damage index *DI* could also be used in a material model to integrate a fatigue deterioration parameter (Uriz and Mahin 2008). Such degradation was not implemented in the *Fatigue* material of OpenSees (Mazzoni et al. 2006).

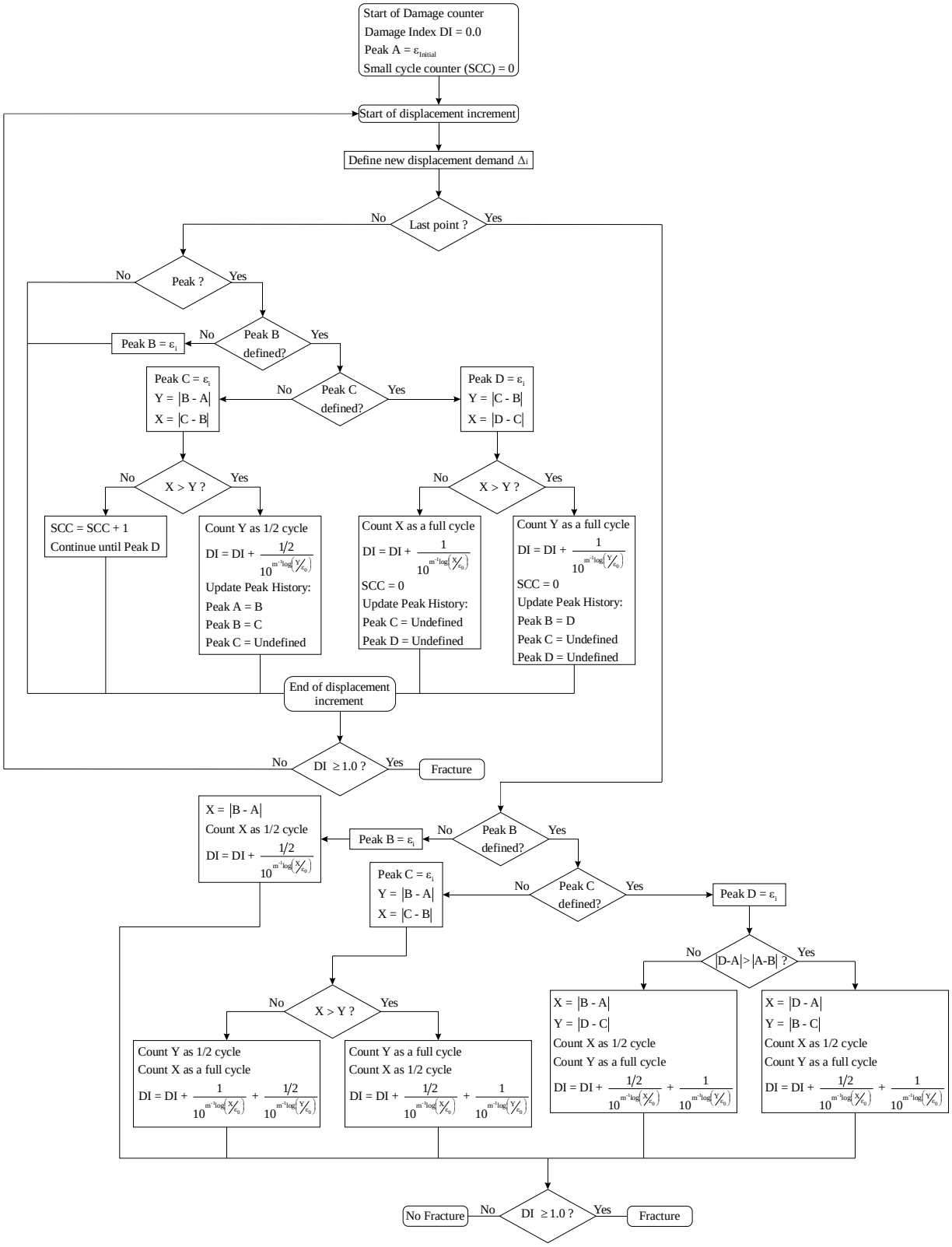


Figure 2.24 Low-cycle fatigue damage index algorithm flow chart (Uriz and Mahin 2008)

CHAPTER 3 METHODOLOGY

3.1 General

At Ecole Polytechnique Montreal, research on the behaviour of low-ductility braced frame buildings (Type CC) started in 2009 (Richard 2009) to validate the seismic provisions of the Canadian Standards for industrial buildings. Wider studies were then performed on conventional construction buildings (Guilini Charette 2010). Concerns were raised on braced frame connection details and a typical detail is proposed and tested experimentally (Castonguay 2009). Further experimental studies were then performed on the center connections of X braced frames to assess its influence on the bracing system stability (Gelinas 2013). These experimental results were then validated numerically (Decaen 2015). These studies focused on the seismic behavior of the braced frame systems and showed the importance of connection detailing in the seismic response of Type CC buildings. This vulnerability in the connections may lead to non-ductile connections designed with a load increased by a factor of 1.5. However, this seismic provision may be too conservative when the reserve capacity of the building is considered.

To assess the reserve capacity of low-ductility steel buildings, an interinstitutional project between École Polytechnique Montreal, Tufts University and the University of Illinois at Urbana-Champaign was developed. This project aimed at evaluating the overall reserve capacity of the building developed in 1) the fractured braced frame (Bradley 2019, Bradley et al. 2017, Sizemore 2017) and 2) the gravity system. Within this project, the subject of the PhD program of the author focuses on the gravity system reserve capacity.

Preliminary studies and a literature review revealed that the gravity connections should provide sufficient lateral stiffness and strength to contribute significantly to the building reserve capacity. These two criteria can be achieved with several types of connections, either completely made of steel components or made of a composite action between steel components and a concrete slab. However, the hysteretic behaviour of the connection needs to be well defined to assess its contribution in the reserve capacity. For the purpose of this study, the connections are limited to 2L-TS bolted angles only. To assess lateral stiffness of gravity connections, the following research plan is developed:

1. Characterize the bolted angles as a connection component:
    a. The influence of the geometrical parameters of the angles is investigated experimentally to characterize the behaviour of simple bolted angle loaded in tension;
    b. A material testing campaign is also conducted to determine the material properties of the bolted angles;
    c. A mathematical model is proposed to define the hysteretic behaviour of bolted angles as a connection component, including the low-cycle fatigue effect.
2. Evaluate the nonlinear behaviour of the gravity connections under simultaneous shear and flexural moment:
    a. The moment-rotation behaviour of bolted angle connections loaded with simultaneous shear is evaluated with a full-scale experimental program;
    b. The mathematical model proposed to define the hysteretic behaviour of an angle component is validated with the connection experimental results;
3. Propose a gravity connection design procedure which can reduce the required brace connection strength when considering an enhanced gravity frame system:
    a. A design procedure is developed to design top and seat angle connections to enhance the behaviour and reserve capacity of the gravity frame;
    b. The contribution of the enhanced connections on the seismic behaviour of a building is validated with a design example.

3.2 Literature review

Past research on the lateral reserve capacity of buildings and of beam-column connections are reviewed. The focus on the reserve capacity is put on three elements: 1) the gravity beam-column connections, 2) the column continuity and 3) the braced frame residual capacity. Then, several past studies on beam-column connections with top and seat angles are reviewed. The literature review is presented in Chapter 2. A review of the seismic provisions for the Conventional Construction type, as well as a summary of two material modules of the OpenSees software are also presented.

3.3 Experimental characterization of bolted angles

3.3.1 Introduction and objectives

Adding bolted TS angles to a 2L angle connection can increase significantly the flexural stiffness of the joint and the lateral resistance of the structure, while keeping the constructability simple and minimizing the additional expanses. Using such connections in gravity frames can enhance significantly the reserve capacity. However, limited information is available on the inelastic behaviour of those bolted angles connections and the influence of several geometrical parameters. To resolve this situation, an extensive experimental investigation has been conducted to characterize the nonlinear behaviour of bolted angles as a component of beam-column connections. More precisely, the following specific objectives have been expressed for this parametric investigation:

1. Characterize the influence of geometrical parameters on the angle behaviour:
   a. Column bolt gage; and
   b. Angle thickness.
2. Characterize the influence of different loading conditions on the angle behaviour:
   a. Strain rate of loading;
   b. Static cyclic loading;
   c. Dynamic time-history loading; and
   d. Low-cycle fatigue loading.
3. Characterize the influence of bolt detailing parameters on the angle behaviour:
   a. The grade of the column bolts (A490 or A325); and
   b. The column bolt pretension.

These parameters are investigated through monotonic and cyclic loadings, with 19 different angle geometries, for a total of 139 tests conducted at École Polytechnique Montreal from June to October 2013 and March to July 2014. The results of this experimental program and the influence of the parameters studied are the subject of a first scientific article presented Chapter 4. This chapter also presents an overview of the experimental setup, instrumentation, specimens and testing

procedures. However, a more detailed description of these subjects is herein presented, along with the data postprocessing procedures.

3.3.2 Experimental setup

The moment frame action under lateral loading is characterized by a rotation of the beam and a flexural moment developing at the connection. This moment translates into a tensile force in an angle and a compressive force in the other, as shown in Figure 3.1a. Since the compressive force is transferred to the column through direct contact, the experimental program focuses only on the inelastic behaviour of the angle loaded in tension. In order to create a similar behaviour, the experimental setup has been simplified to an angle bolted to a plate, which is in turn bolted to the actuator. The actuator is then used to load the angle in tension to create a displacement demand similar to the one caused by the beam rotation, as seen in Figure 3.1b). To avoid any flexural effect resulting from the setup asymmetry and the eccentricity between the column bolts and the plate, a second angle has been added under the plate. Similar testing setups have been widely used in previous experimental investigations (Azizinamini 1985, Shen and Astaneh-Asl 1999, Garlock et al. 2003, Yang and Tan 2013 Gong 2014). The setup was simplified to increase the total number of specimens tested. This simplified test setup assumes that the rotation of the beam leg has a negligible impact on the nonlinear behaviour of the bolted angles. A sketch of the complete experimental setup is presented in Figure 3.2. The angles are bolted to their column leg to a stocky custom-built welded-wide-flange (WWF) section, which is in turn attached to a rigid frame anchored to the strong floor of the laboratory.

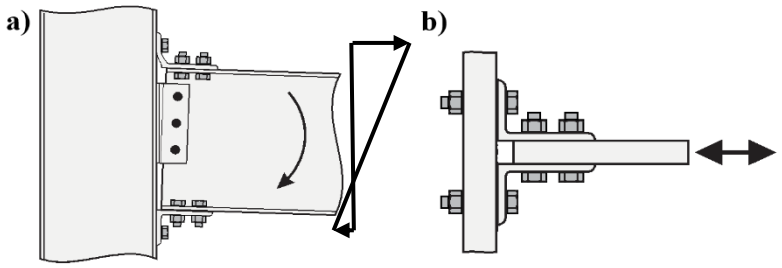


Figure 3.1. a) Typical deformation of a beam-column joint made of bolted angles b) Simplified experimental setup

The depth of the WWF section is 510 mm, to provide enough space for the bolting process and the flange thickness is chosen at 64 mm, to avoid significant flange deformation during loading. The dimensions of the WWF custom-built section are also presented in Figure 3.2. An intricate hole pattern on the flanges of the WWF column section allowed, with minimal changes to the setup, the testing of multiple column bolt positions, with 5 different distances between the column bolts and the angle corner and 19.1 and 25.4 mm-diameter bolts.

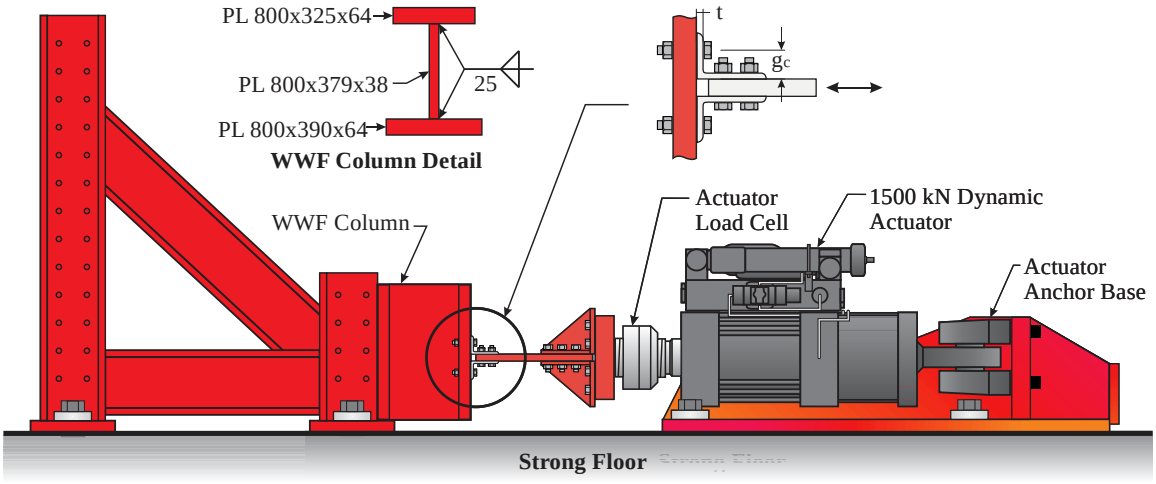


Figure 3.2. Sketch of experimental setup

The angles are also bolted on their beam leg to a loading plate. The 7.9 mm and 9.5 mm thick angles are bolted to a 19.1 mm-thick plate, while the angles with thicknesses of 12.7, 15.9 and 19.1 mm are bolted to a 51 mm-thick loading plate. These thicknesses are selected to provide sufficient axial stiffness, while avoiding significant axial deformation and bearing of the bolt holes, to avoid any failure mode in the loading plate and to reuse it throughout the experimental program. The loading plates are also bolted to a 1500 kN actuator capable of dynamic loading, with a maximum stroke of ± 125 mm.

3.3.3 Experimental instrumentation

The angle deformations are measured with 2 Linear Variable Differential Transformers (LVDTs) attached to the WWF section. Those instruments measured the displacement of the angles between the setup column and two small plates welded to the side of each specimen. Those plates are attached near the edge of the beam leg, where the local material alterations caused by the welding

process did not influence the angle material properties and behaviour. The LVDT measurements correspond to the real displacement of the angles, without considering the elastic elongation of the loading plate under large tensile force, or the bolt slip occurring in the beam bolts, between the angles and the loading plate. During the tests, slip was visually observed, but was not measured.

All the angle displacement values correspond to the average of the two LVDT measures. Figure 3.3a and b shows the instrumental setup of a typical test in a plan and elevation view respectively. A picture of a typical setup of the angles at the beginning of a test with the instrumentations is also presented in Figure 3.3c. Furthermore, the applied force on the angles is measured by a loading cell integrated in the actuator itself. It is assumed that the load applied during the test is resisted equally by the two back-to-back angles. Therefore, the force values considered for each angle is obtained by dividing by two the recorded force.

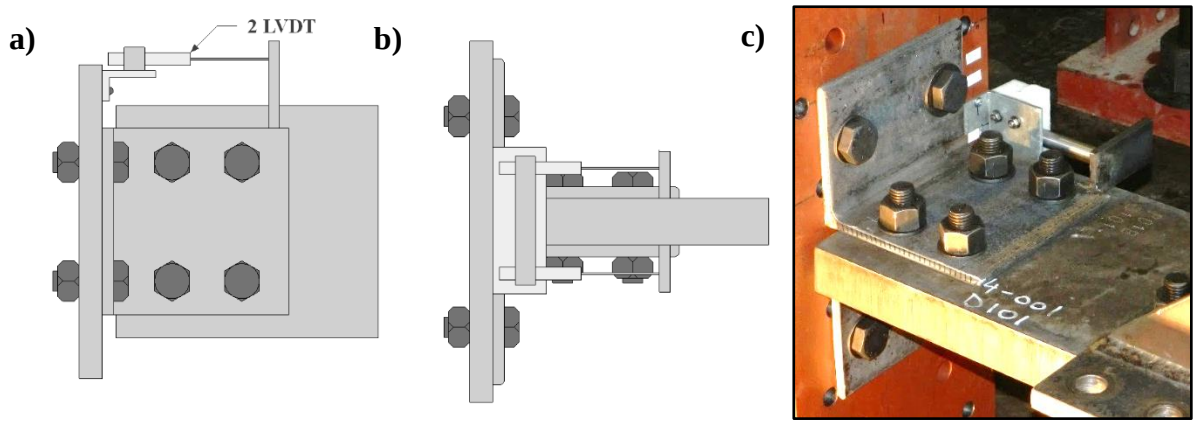


Figure 3.3. Instrumentation and angles setup

3.3.4 Test matrix

The inelastic behaviour of bolted angles depends greatly on various geometric parameters such as the distance between the corner of the angles and the column bolts and the angles thickness (Azizinamini 1985, Kukreti and Abolmaali 1999, Shen and Astaneh-Asl 1999, Abolmaali et al. 2003, Garlock et al. 2003, Yang and Tan 2013, Gong 2014). Therefore, this experimental study aimed to characterize the influence of those parameters. The parametric study is established by varying the thickness t of the angles from 7.9 to 19.1 mm (5/16” to 3/4”) and the tensile bolt gage g_c from 63.5 to 114.3 mm (2.5” to 4.5”). A test matrix of 19 test cases with different angle geometries has been assembled and is presented in Figure 3.4.

Since the parametric study tries to characterize the behaviour of the angles until rupture, the bolts are overdesigned to avoid bolt failure and to develop the ultimate capacity of the angles. All the 7.9 mm- and 9.5 mm-thick angles used A325 bolts with a diameter of 19.1 mm (3/4”). The other angle configurations used A490 bolts with a 25.4 mm (1”) diameter, except for some specimens where the bolt grade influence is studied. Furthermore, all the bolts are pretensioned according to the article 23.8.1 of CSA S16-14, except for some specific tests where the impact of bolt pretension is investigated.

Most of the displacements are expected to occur in the column leg of the angles, between the bolt and the corner. This part of the angle is characterized by the flexural span g_2, which corresponds to the distance between the end of the fillet and the edge of the bolt head, as illustrated in Figure 3.5, where the fillet width is defined by k and the bolt head flat width is given by F. To establish a unitless comparative basis between the several test cases, the ratio of g_2/t is used. As shown in the test matrix presented in Figure 3.4, those ratios vary from 1.25 to 8.00 for the different angle configurations studied.

g_c (mm) \ t (mm)	7.9	9.5	12.7	15.9	19.1
63.5	TC19 3.80 L 102 x 102 x 7.9	TC1 2.67 L 102 x 152 x 9.5	TC3 1.38 L 102 x 203 x 12.7		
76.2		TC2 4.00 L 152 x 152 x 9.5	TC4 2.38 L 152 x 203 x 12.7	TC5 1.70 L 152 x 203 x 15.9	TC6 1.25 L 152 x 203 x 19.1
88.9		TC7 5.33 L 152 x 152 x 9.5	TC9 3.38 L 152 x 203 x 12.7	TC11 2.50 L 152 x 203 x 15.9	TC13 1.92 L 152 x 203 x 19.1
101.6		TC8 6.67 L 152 x 152 x 9.5	TC10 4.38 L 152 x 203 x 12.7	TC12 3.30 L 152 x 203 x 15.9	TC14 2.58 L 152 x 203 x 19.1
114.3		TC15 8.00 L 152 x 152 x 9.5	TC16 5.38 L 152 x 203 x 12.7	TC17 4.10 L 152 x 203 x 15.9	TC18 3.25 L 152 x 203 x 19.1

Legend:
Test Case ID
g_2/t
Angle section
$g_2/t < 2.00$
$2.00 \leq g_2/t < 3.00$
$3.00 \leq g_2/t < 4.00$
$4.00 \leq g_2/t < 5.00$
$5.00 \leq g_2/t < 6.00$
$6.00 \leq g_2/t$

Figure 3.4. Test Matrix of angles experimental program

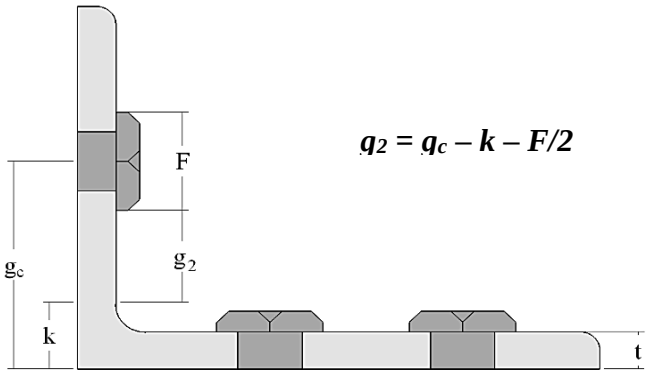


Figure 3.5. Flexural span of the column leg g_2

In general, an angle with a low g_2/t ratio indicates that the column bolts are close to the angle corner and the angles are quite thick, as shown in Figure 3.6a. The flexural span of the column leg is then short, and the angle behaviour is expected to be stiffer. Alternatively, an angle with a large g_2/t ratio has a much smaller thickness and larger column bolt gage, which translates in a more flexible expected behaviour, as illustrated in Figure 3.6b.

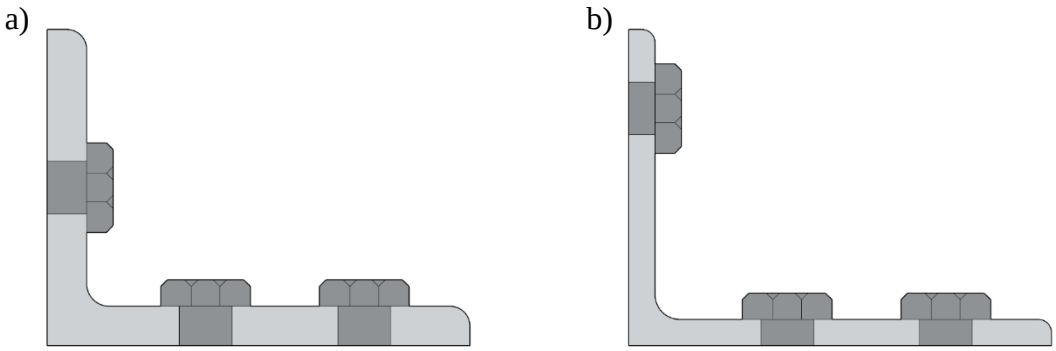


Figure 3.6. Schematic representation of angles with a) low g_2/t b) high g_2/t

However, in the test matrix presented in Figure 3.4, the test cases are color-coded based on their aspect ratio to highlight the fact that a similar ratio can be obtained with significantly different angles, such as TC19, with a thickness of 7.9 mm and a column gage of 63.5 mm which results in a g_2/t ratio of 3.80, and TC18, with a g_2/t ratio of 3.25 obtained from a 19.1 mm thick angle and a column gage of 114.3 mm. The dimensions of each 19 different geometries are detailed in Table 3.1, along with the g_2/t aspect ratio. The dimensions of the angles and the bolts are presented in this table. These dimensions are also shown in the side and front views of a typical angle specimen

depicted in Figure 3.7. In this table, d_b corresponds to the bolt diameter, g_b corresponds to the beam bolt gage, the edge distance to the bolt centerline is given by e and the distance between the bolts perpendicular to the loading direction is given by p. The beam leg and the column leg length are given by B and C respectively, while the total width of the angle corresponds to L.

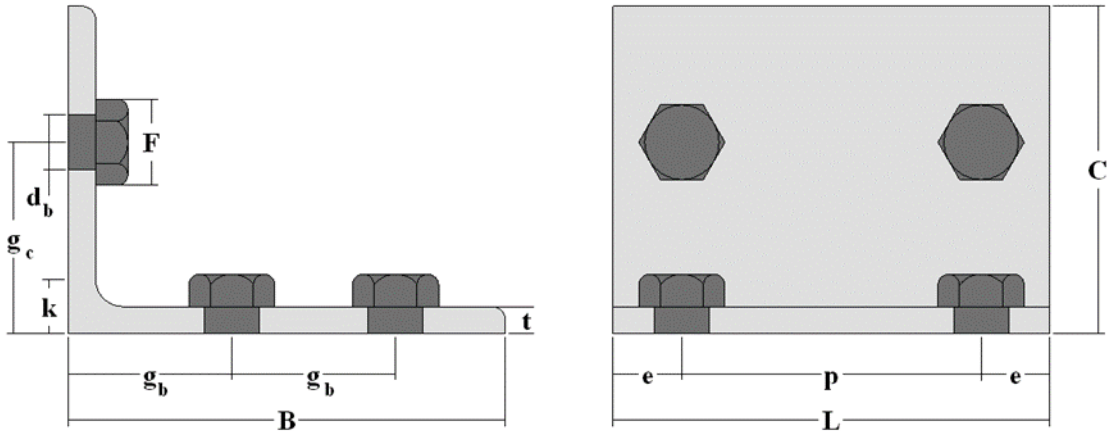


Figure 3.7. Dimensions of bolted angles

Table 3.1. Dimensions of each bolted angle test cases

Test ID	t	B	C	g_c	d_b	F	k	g_b	g_2/t
	mm	mm	mm	mm	mm	mm	mm	mm	-
TC1	9.5	152	102	63.5	19.1	31.8	22.2	57.2	2.68
TC2	9.5	152	152	76.2	19.1	31.8	22.2	57.2	4.01
TC3	12.7	203	102	63.5	25.4	41.3	25.4	76.2	1.38
TC4	12.7	203	152	76.2	25.4	41.3	25.4	76.2	2.38
TC5	15.9	203	152	76.2	25.4	41.3	28.6	76.2	1.70
TC6	19.1	203	152	76.2	25.4	41.3	31.8	76.2	1.24
TC7	9.5	152	152	88.9	19.1	31.8	22.2	57.2	5.35
TC8	9.5	152	152	101.6	19.1	31.8	22.2	57.2	6.69
TC9	12.7	203	152	88.9	25.4	41.3	25.4	76.2	3.38
TC10	12.7	203	152	101.6	25.4	41.3	25.4	76.2	4.38
TC11	15.9	203	152	88.9	25.4	41.3	28.6	76.2	2.49
TC12	15.9	203	152	101.6	25.4	41.3	28.6	76.2	3.29
TC13	19.1	203	152	88.9	25.4	41.3	31.8	76.2	1.91
TC14	19.1	203	152	101.6	25.4	41.3	31.8	76.2	2.57
TC15	9.5	152	152	114.3	19.1	31.8	22.2	57.2	8.02
TC16	12.7	203	152	114.3	25.4	41.3	25.4	76.2	5.38
TC17	15.9	203	152	114.3	25.4	41.3	28.6	76.2	4.09
TC18	19.1	203	152	114.3	25.4	41.3	31.8	76.2	3.24
TC19	7.9	102	102	63.5	19.1	31.8	17.6	57.2	3.80
For each test case: L = 203 mm; e = 32 mm; p = 140 mm									

3.3.5 Testing procedures

Several specimens were planned for each angle geometry to investigate the impact of the strain rate and the monotonic or cyclic conditions of the load applied. The strain rate was studied by comparing results from different monotonic tests. However, the rationale to define the loading conditions varied for monotonic, cyclic, time-history and fatigue tests.

3.3.5.1 Procedure for monotonic tests

For each angle geometry, three monotonic tests were performed to determine the influence of the strain rate on the inelastic behaviour of the angles, but also to obtain some repetitiveness in the experimental results. The strain rates studied were kept roughly constant for all the angle geometries at respectively 100 με/s and 600 με/s for the first two tests. The relationship between the strain and the angle displacement was determined based on spring and beam-column element models developed on OpenSees for all of the geometries. The strain rates were then translated into displacement rates through this relationship. Since no strain gauge was applied on the specimen to determine the exact rate of each test, the values given are only an approximation based on the numerical models and could not be validated experimentally.

The first two tests of each angle configuration were conducted at a strain rate of approximately 100 με/s and 600 με/s respectively. Since the loading speeds of those tests were quite slow, they are considered static. The results of these tests were used to determine the loading protocol of the cyclic and time-history tests, as well as a comparative basis for evaluating the impact of the various parameters investigated in this experimental program. The results of the second tests were used to validate the behaviour observed in the first one, while investigating a slight increase in strain rate.

The third test of each test case consisted of creating a displacement demand on the specimens equal to the maximal displacement of the first two tests, in one second. Therefore, the strain rate corresponding to this demand averaged around 750000 με/s. This loading protocol is considered dynamic. The main objective of those tests was thus to investigate the influence of dynamic loading on the behaviour of bolted angles.

Moreover, some additional monotonic tests have been performed on some test cases. Those tests aimed at investigating the influence of bolts related parameters, such as the bolt grade and the bolt

pretension. Four tests have been conducted using A325 bolts instead of the A490 commonly used in the experimental program. Also, ten tests were performed to observe the effect of snug-tight bolts instead of fully pretensioned, as requested in the article 23.8.1 of CSA S16-14 for bolts acting in tension. Those changes in the bolt parameters were only applied to the bolts in tension, connecting the angles to the column. Those additional tests were performed using the exact same loading protocol as the first static monotonic test conducted, with a strain rate averaging 100 με/s.

3.3.5.2 Procedure for cyclic tests

The loading protocol used for cyclic tests is based on the storey drift demand proposed by AISC (2010) for the experimental characterization of beam-column joints in moment frames. This loading protocol is detailed in Figure 3.8, as well as in Table 3.2.

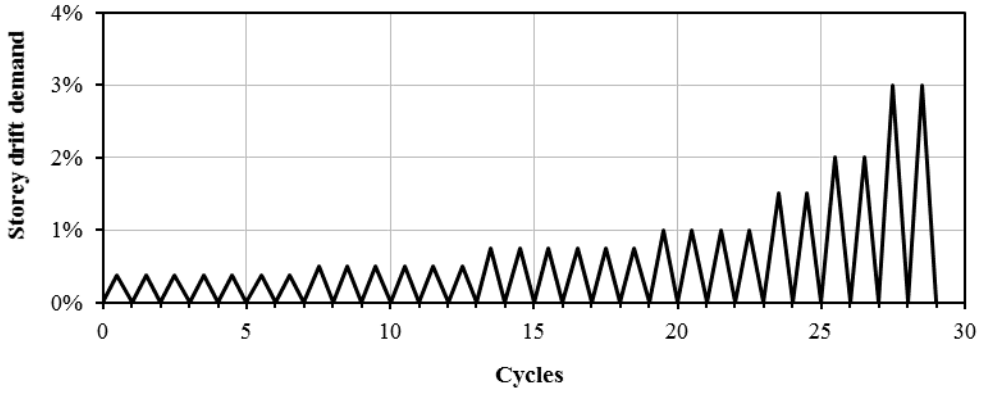


Figure 3.8. Time history of storey drift demand (AISC 2010)

Table 3.2. Loading protocol based on storey drift ratio (AISC 2010)

Loading increment	Storey drift δ_{drift} (rad)	Cycles
1	0.00375	6
2	0.005	6
3	0.0075	6
4	0.01	4
5	0.015	2
6	0.02	2
7	0.03	2
8	0.04	2
…	…	…
+1	+0.01	2

Since the loading procedure proposed by AISC (2010) specifies a storey drift ratio demand, a typical building situated in Boston is considered to determine the contribution of the bolted joints in this displacement demand. Plan and elevation views of this building are shown in Figure 3.9.

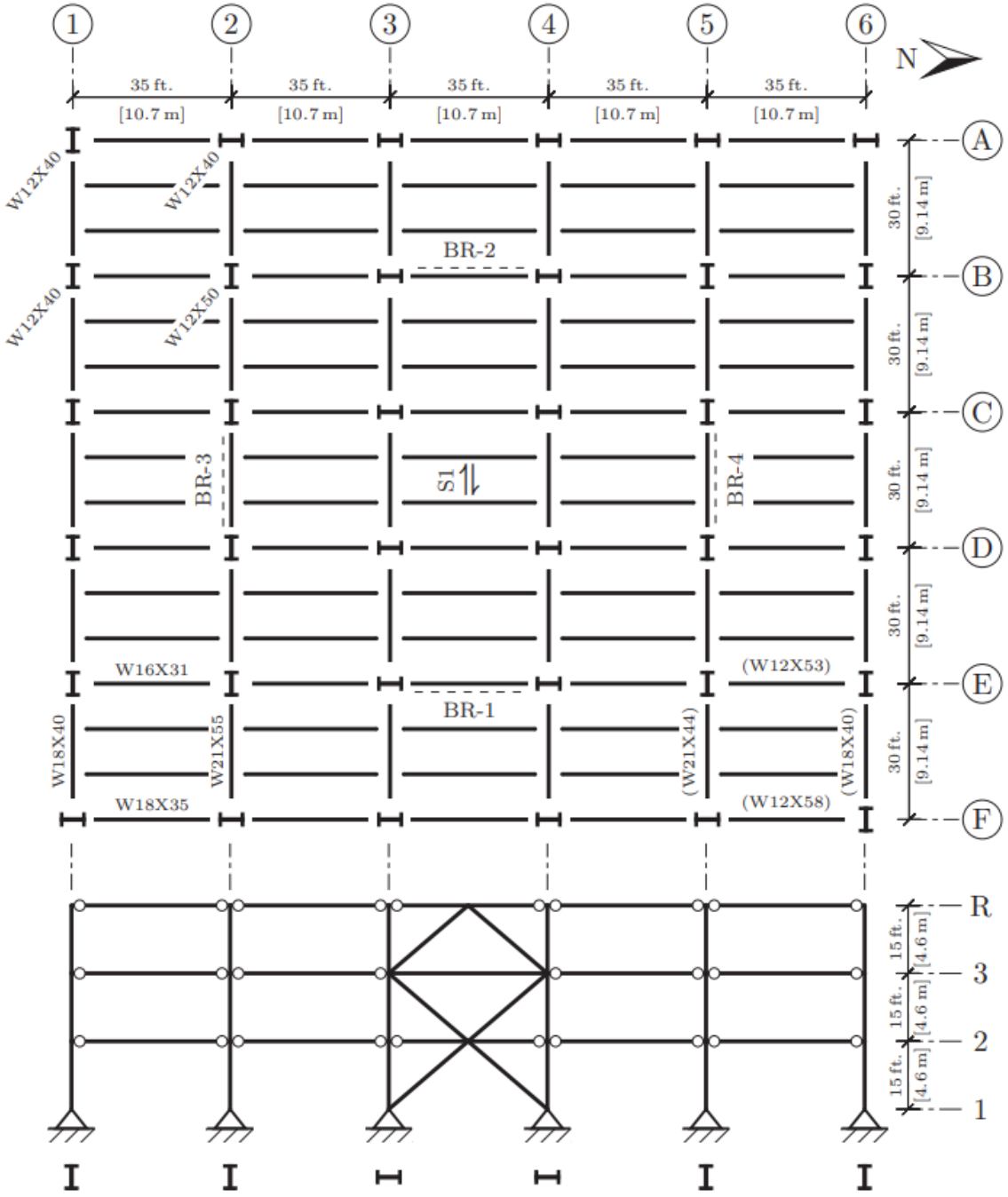


Figure 3.9. Plan and elevation view of the typical building considered in determining the cyclic loading procedure (Bradley 2016).

The height of all the stories is 4572 mm (15’). The lateral load resisting system is designed according to ASCE 7 (2005), with R = 3. This building was used as the prototype building for full-scale experimental tests performed at Lehigh University (Bradley et al. 2017, Sizemore et al. 2017) that are included in the interinstitutional project. These tests aimed to assess the failure mechanisms and residual stiffness of the braced frame after failure (Bradley et al. 2017). For consistency within the interinstitutional project, the same prototype building is used for the bolted angle loading protocols. The design procedure of the prototype building is detailed by Bradley (2016).

The contribution of the bolted beam-column joint in the storey drift can be determined by simplifying the building into a simple frame, where the beams and columns are deforming in double curvature. Therefore, the inflexion points, which are characterized by a moment of zero, are supposed at the mid-span of the beams and at the mid-height of the columns. Those inflexion points are then substituted by hinges, which allows the simplification of the system into an isostatic cruciform frame, as depicted in Figure 3.10.

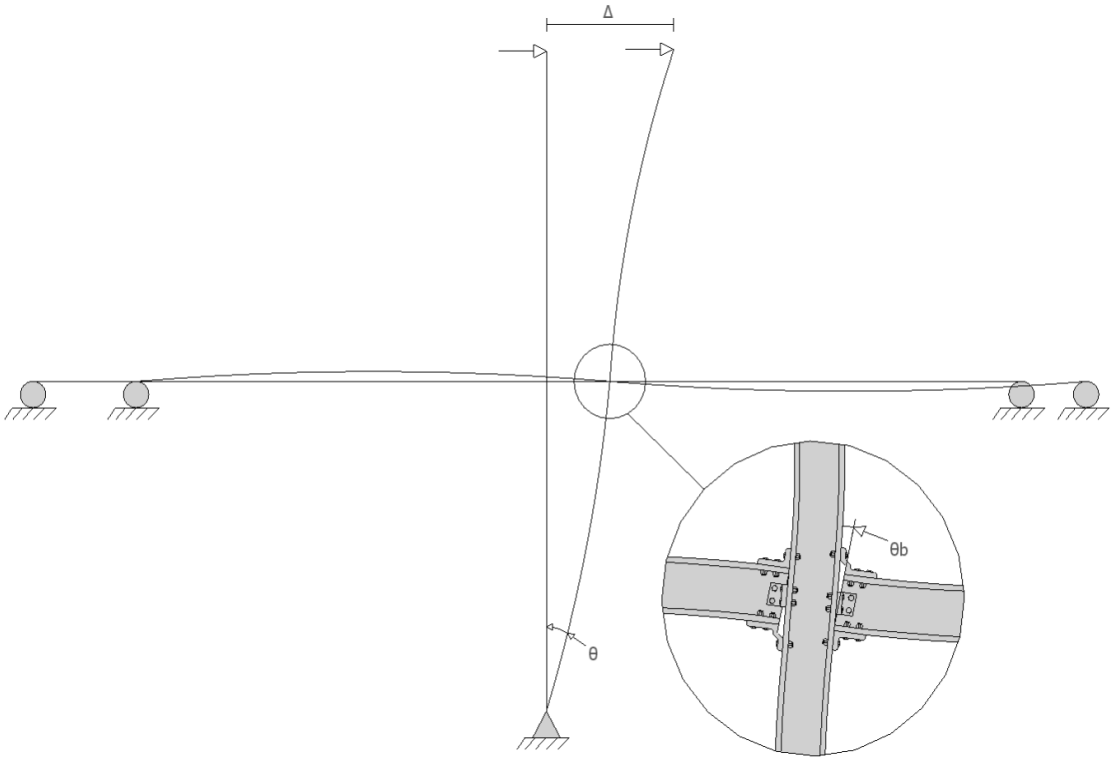


Figure 3.10. Simplified structural system for the joint displacement calculation

The flexural moment in the beam transferred to the column by the joint causes inelastic displacements in the angles loaded in tension. Those deformations can be translated into a rotation of the joint θ_b, with respect to the opposite edge of the beam section as the center of rotation, as shown in Figure 3.10. The amplitude of those displacement is influenced mainly by the joint configuration, but also by the beam depth.

This joint rotation acts, as the beam rotation, on the storey drift by inducing an additional rotation in the columns at the floor levels. The storey drift of the frame can be obtained with Equation 3.1, where h_s is the height of the storey. The displacement contribution of each element can be determined based on its own flexibility, as expressed by Equations 3.2 to 3.4, while the total displacement of the storey is given by Equation 3.5. In these equations, θ_b is the joint rotation under the flexural moment M_A given by Equation 3.6, where d_C is the depth of the column section and L_b is the beam length. V_A corresponds to the lateral load creating the storey displacement Δ_{Storey}.

$$\Delta_{Storey} = \delta_{Drift} h_s \tag{3.1}$$

$$\Delta_{Column} = \frac{V_A h_s^3}{12 E I_C} \tag{3.2}$$

$$\Delta_{Beam} = \frac{V_A h_s^2 L_b}{12 E I_b} \tag{3.3}$$

$$\Delta_{Joint} = \theta_b h_s \tag{3.4}$$

$$\Delta_{Storey} = \Delta_{Column} + \Delta_{Beam} + \Delta_{Joint} \tag{3.5}$$

$$M_A = \frac{V_A h_s}{L_b}\left(\frac{L_b}{2} - \frac{d_C}{2}\right) \tag{3.6}$$

The relation between the flexural moment M_A and the joint rotation θ_b is determined based on the Force-Displacement curve of the monotonic tests. The rotation is obtained by dividing the displacement by the depth of the beam d_{beam}, while the moment in the joint is obtained by multiplying the tensile force with the beam depth.

For each amplitude in the storey drift demand presented at Table 3.2, the shear load V_A which causes a displacement equal to the demand is evaluated by iterations. With this load, the final displacement demand on the top angle can be evaluated with the Equation 3.7.

$$\Delta_{Angles} = \theta_b d_{beam} \quad (3.7)$$

Based on this equation, for a same joint rotation, the displacement demand on a top angle is increasing as the depth of the beam increases. In the typical building illustrated in Figure 3.8, there are two types of beam-columns connections in the typical joint considered: 1) a joint connects a W310x33 (W12x26) beam to the W310x67 (W12x45) column in its strong axis, 2) another joins a W410x67 (W16x45) girder to the W310x67 (W12x45) column in its weak axis. Two cyclic tests were performed on each test case to investigate the influence of the beam depth on the inelastic behaviour of the angles.

Also, the first 18 cycles (up to a storey drift of 0.0075 rad) are mostly loading the angles elastically. Hence, most of the storey drift corresponded to the frame deformation, especially in the connection with the W310x67 column in its weak axis and the W410x67 girder. But as soon as the displacement demand reached inelastic deformations in the angles, the storey drift is then concentrated in the connection, because of the low post-yielding stiffness of the angles compared to the other elements. This frame behaviour translated in the loading protocol used for the cyclic tests. Table 3.3 summarizes the several geometrical properties of the previously mentioned joints. The loading rate for those cyclic tests is quite slow, the loading is thus assumed static.

Table 3.3. Geometrical properties of beam-column joints

Beam	I_b	L_b	I_c	h_s	d_{beam}
	106 mm4	mm	106 mm4	mm	mm
W310x33	85.1	10668	144	4572	310
W410x67	246	9144	20.4	4572	410

3.3.5.3 Procedure for Time-History tests

The main goal of this experimental program is to characterize the inelastic behaviour of bolted angles connection under seismic loading. For this purpose, a test simulating a seismic loading has been conducted on each test case. The time-history signal used for these tests has been developed by Ali Davaran, a member of the interinstitutional project, by isolating a joint rotational demand

in a building model under seismic loading in OpenSees. The rotational demand of the joint is then translated into a displacement demand variable in time, shown in Figure 3.11, using Equation 3.7 with a beam depth of 410 mm.

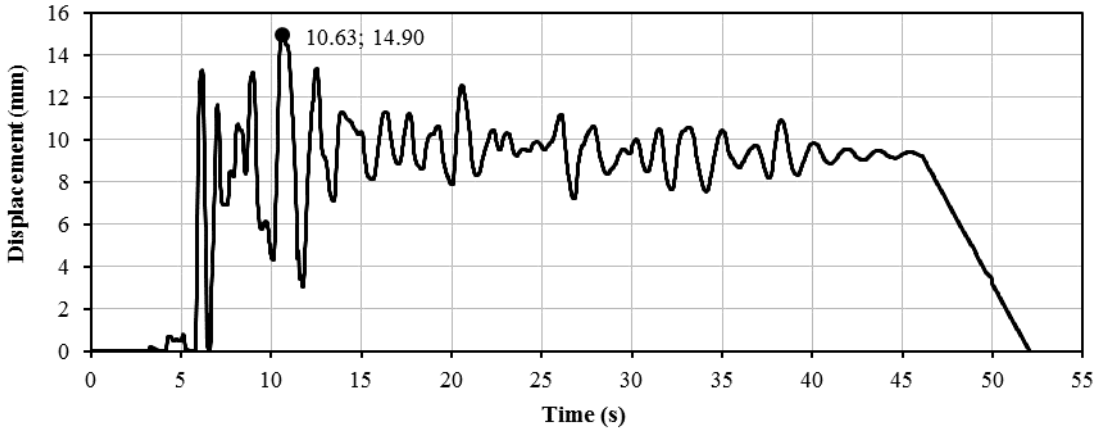


Figure 3.11. Displacement demand signal for Time-History tests

This signal is applied three times on the same specimens, with different scale factors, in order to simulate different ground motion intensities. Since the cyclic inelastic stiffness of the angles is determined by the maximum displacement experienced by the angles and because large displacement demands are imposed on the angles at the beginning of the signal, the yielding experienced by previous specimens only affected a small part of the inelastic behaviour.

The scale factors were determined from the ultimate displacement recorded in static cyclic tests ($\Delta_{U\text{-cyclic}}$). The first signal aimed at representing a moderate earthquake causing yielding of the connection. The maximum displacement of this excursion was then taken as 33% of $\Delta_{U\text{-cyclic}}$. The second earthquake represented a major earthquake causing large plastic damage without initiating the fracture of the connection. The signal of this earthquake was then scaled to obtain an ultimate displacement of 66% of $\Delta_{U\text{-cyclic}}$. Finally, the last earthquake represented an extreme earthquake causing the connection fracture. The maximal displacement of this excursion corresponded to 120% of $\Delta_{U\text{-cyclic}}$.

At the end of the signal, the angles were brought back to their initial position. However, since the specimens experienced inelastic behaviour, this initial position was characterized by a compressive force acting on the angles. To avoid any undesirable effect due to this preloading in the following signal, the angles were unloaded before each reloading. The plastic deformation associated with

this unloading was considered as the new reference and did not affect the displacement amplitude of the following signal. Since the loading of those tests was mimicking an earthquake, the loading is considered dynamic.

3.3.5.4 Procedure for fatigue tests

Finally, some low-cycle fatigue tests were performed on two test cases, TC9 and TC14. Those tests were used to create simple numerical models for which the angle behaviour and the cyclic degradation follow the hysteretic curve obtained from fatigue tests. The maximal displacements for those tests were determined based on the static cyclic Force-Displacement curves translated into Moment-Rotation, considering a 410 mm deep beam.

The smaller amplitude is taken as the end of the transition portion between the elastic and plastic behaviour. The larger amplitude is defined as 60% of the ultimate rotation of the static cyclic test. This level of 60% is chosen to induce large plastic deformations in the angles, while maintaining a resistance for some cycles. The middle amplitude corresponded to the average between the smaller and the larger amplitudes.

The displacement demands for those three amplitudes are presented in Table 3.4, in both rotations and displacements. For each amplitude and each test case, two tests are performed to validate the cyclic behaviour of the angles.

Table 3.4. Displacement demands for the fatigue tests

TC 9		**TC 14**	
θ_b	Δ_{Angles}	θ_b	Δ_{Angles}
rad	**mm**	**rad**	**mm**
0.01	4.1	0.01	4.1
0.03	12.3	0.0175	7.2
0.05	20.5	0.025	10.3

3.3.5.5 Summary of the tests performed

Table 3.5 presents a summary of the different tests conducted on each test case. The Snug-Tight and A325 tests are performed on the angle geometries where additional specimens are available. For some test cases, reducing the bolt pretension or changing the bolt grade would have provoked bolt failure. As this failure mode is not the focus of the study, those tests are not performed.

Also, the 3/4" diameter bolts used for test cases with angle thickness of 7.9 mm (5/16") and 9.5 mm (3/8") are already initially of grade A325. For this reason, only the Snug-Tight tests are additionally performed. Finally, some problems in the specimen fabrication lead to only 5 available specimens for TC17. Thus, no Time-History test is performed on this test case.

A total of 139 tests are performed on bolted angles, among which 71 are performed under monotonic, 56 under cyclic and 12 under low-cycle fatigue loading conditions. 19 different angle geometries are tested with varying angle thickness and column bolt gage. This extensive experimental campaign aimed at observing the influence of these two geometric parameters on the nonlinear behaviour of the bolted angles.

Table 3.5. Summary of tests conducted on each angle configuration

Test Case	Monotonic Static	Monotonic Dynamic	Monotonic Snug-Tight	Monotonic A325	Cyclic Static	Time-History	Fatigue	Total
TC1	2	1	1-	-	2	1	-	7
TC2	2	1	1	-	2	1	-	7
TC3	2	1	-	-	2	1	-	6
TC4	2	1	1	-	2	1	-	7
TC5	2	1	-	-	2	1	-	6
TC6	2	1	-	-	2	1	-	6
TC7	2	1	-	-	2	1	-	6
TC8	2	1	-	-	2	1	-	6
TC9	2	1	1	1	2	1	6	14
TC10	2	1	1	1	2	1	-	8
TC11	2	1	1	1	2	1	-	8
TC12	2	1	1	1	2	1	-	8
TC13	2	1	-	-	2	1	-	6
TC14	2	1	-	-	2	1	6	12
TC15	2	1	1	-	2	1	-	7
TC16	2	1	1	-	2	1	-	7
TC17	2	1	-	-	2	-	-	5
TC18	2	1	-	-	2	1	-	6
TC19	2	1	1	-	2	1	-	7
	38	**19**	**10**	**4**	**38**	**18**	**12**	**139**

3.3.6 Test data analysis

The tests performed on bolted angle connections created a large database from which valuable information could be harvested on the influence of geometrical parameters. From these tests, the following steps, detailed in Chapter 4, were taken to characterize their behaviour:

1. The failure mode and failure mechanism of each test was determined;
2. The force-displacement of each specimen was determined and defined with key response parameters;
3. To define mathematically the yielding phase of each angle geometry, the mathematical model proposed by Filippou et al. (1983) was calibrated with each monotonic test;
4. The low-cycle fatigue tests are analyzed to determine the parameters for defining Miner's S-N damage relationship (Miner 1945);
5. The influence of several design parameters were qualitatively evaluated by comparing the force-deformation response of the specimens:
    a. The bolt gage;
    b. The angle thickness;
    c. The aspect ratio g_2/t;
    d. The fastening parameters (bolt grade and pretension);
    e. The loading conditions (strain rate, cyclic loading, low-cycle fatigue loading).

Furthermore, the results of the 139 angle specimens are presented individually in Appendix A.

3.4 Experimental characterization of angle material

To accurately characterize the response of the angles, information on the specimen material are also required. To characterize these material properties, an experimental campaign has been developed on coupon specimens obtained from 610 mm-long angle pieces of the same steel material than the angle specimens. Three types of coupons have been prepared by Usinage Proto Concept Inc. and tested in the Structures Laboratory of École Polytechnique de Montreal between August and October 2015.

3.4.1 Coupon types

3.4.1.1 ASTM Standard

The first category of coupons corresponds to the Standard Plate-Type specified by ASTM8 (2000). Three coupons were produced from each angle leg, resulting in 6 standard coupons per material, and 66 in total. The specific dimensions of a standard coupon are presented in Figure 3.12. These types of coupons were used to determine the yield stress and strain, as well as the maximum stress and ultimate strain of the angle material. The deformation at which the hardening of the steel begins was also identified.

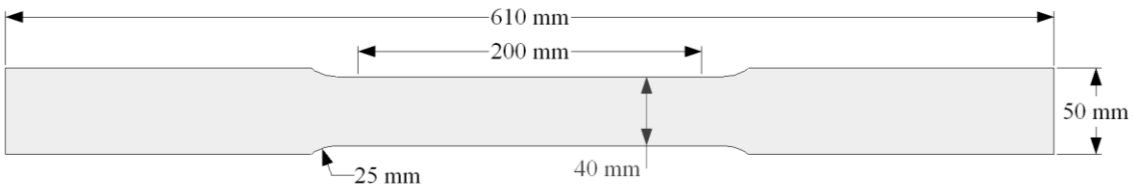


Figure 3.12. Dimensions of ASTM Standard coupons

3.4.1.2 ASTM Subsize

Another category of coupons tested corresponds to the Subsize type of ASTM8 (2000), whose dimensions are illustrated in Figure 3.13a. Four coupons are taken from each angle leg, two of which are parallel (longitudinal) to the angle fillet and the rolling process, whereas the two others are transversal to the fillet, as shown on Figure 3.13b. Since the direction of loading in the angle testing program was in the transversal direction, but the characterization of the material properties was performed longitudinally, the goal of the subsize specimens is to evaluate the impact of the loading direction on the yield and ultimate stresses.

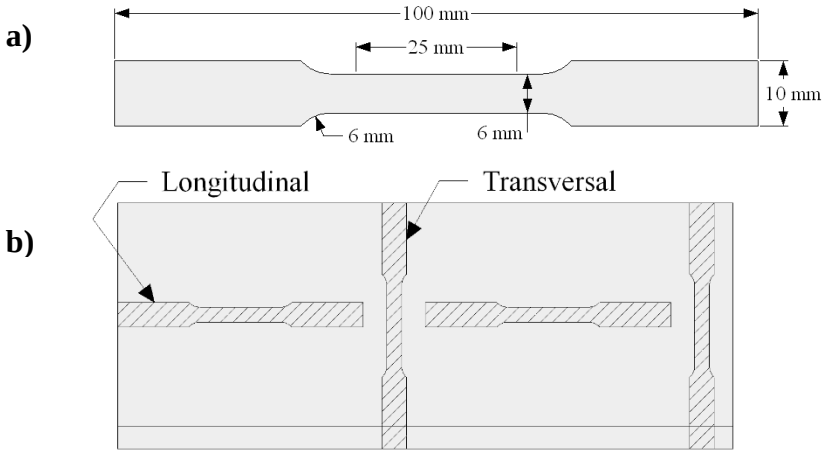


Figure 3.13. a) Dimensions and b) Position on angle leg of ASTM Subsize coupons

3.4.1.3 Strips coupons

The goal of the third type of coupons is to observe the variation in yield and ultimate stresses along the leg of the angles due to the rolling and cooling processes. To achieve this goal, several thin strips of non-standardized dimensions shown in Figure 3.14a have been taken from each angle leg, as illustrated in Figure 3.14b. The number of coupons for each angle dimension depended on the angle size. The fillet portion of the angle, as well as the edge of the legs were not transformed into strips due to the rounded section that rendered impossible an accurate measurement of the section area.

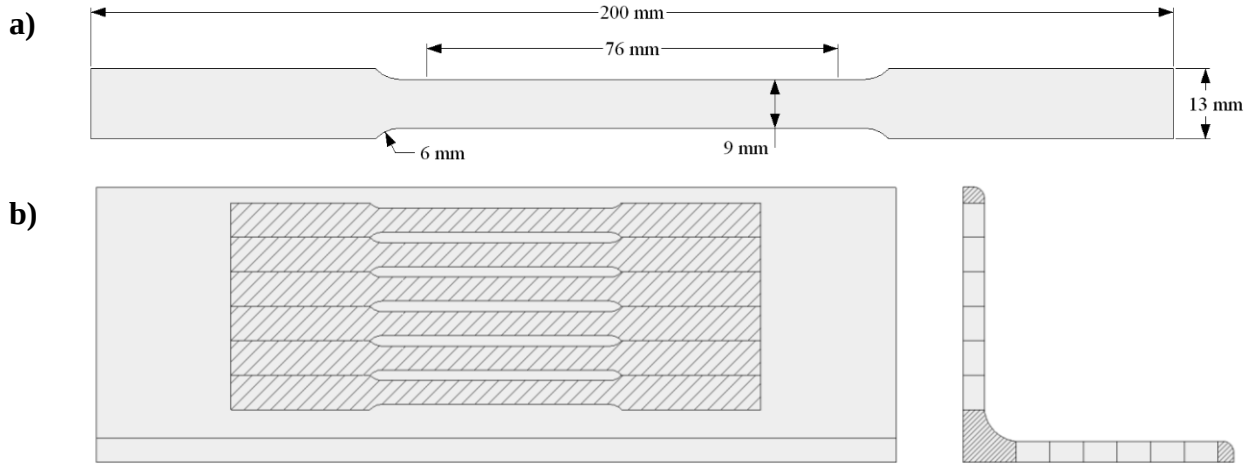


Figure 3.14. a) Dimensions and b) Position on angle legs of Strips coupons

3.4.2 Test procedures

Presented herein are some brief descriptions of the procedure followed during each material test performed. Some information related to the equipment and instrumentation used during the testing campaign are also included.

3.4.2.1 ASTM Standard

The ASTM Standard coupons have been tested in the Instron loading frame of the Structures Laboratory of École Polytechnique Montreal. The length of the coupons allowed them to be inserted into the grips of the loading frame directly, as shown in Figure 3.15a. The elongation of the coupon was measured through an extensometer placed on the reduced section of the specimen. Figure 3.15b shows a side view of the extensometer with a fractured specimen.

Every dimension of the coupon was determined using a caliber and the width and thickness of the reduced area is determined by averaging the measures taken at five different locations of the reduced cross-section.

The specifications given by ASTM8 (2000) concerning the testing procedure have been followed for the ASTM Standard coupons. Each test was performed by controlling the displacement of the loading frame with the extensometer measurement. A strain rate of $4x10^{-5}$ ε/s is applied during the elastic and plateau portions of the curve. This strain rate translated into a stress rate varying between 7.28 MPa/s and 12.02 MPa/s.

As proposed by FEMA (1997), the loading of the ASTM Standard coupons have been stopped three times during the steel plateau in order to keep the strain constant for two minutes. The stress average of these three values was then taken as the static yield stress of the steel material. Also, as the material hardening was observed during the test, the strain rate on the reduced section was gradually increased over one minute to $5x10^{-4}$ ε/s, as allowed by ASTM8 (2000).

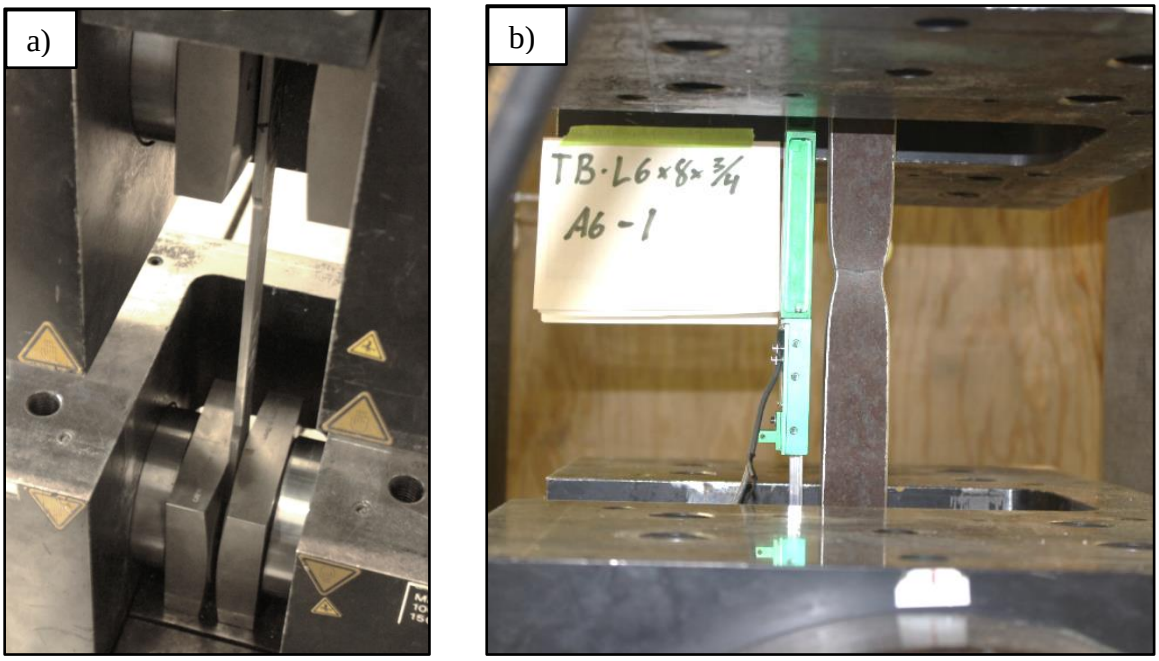


Figure 3.15. Loading frame and instrumentation used for the ASTM Standard material testing

3.4.2.2 ASTM Subsize and Strips coupons

The ASTM Subsize coupons have also been tested in the Instron loading frame of the Structures Laboratory of École Polytechnique Montreal. However, because of their short length, the use of smaller grips was required, as shown in Figure 3.16a. Also, a shorter extensometer able to fit on the reduced section of the coupons was not available. Therefore, the elongation experienced by specimens was determined through two LVDTs measuring the displacement between the two grips, as pictured in Figure 3.16a.

However, some slip between the grips and the specimen were observed and introduced in the displacement measured by the two LVDTs. This slip lead to important uncertainly in the strain and Young modulus calculations of the ASTM Subsize coupons. Therefore, only the results of yield and ultimate stress are presented in the following sections. Every dimension of the coupons was determined using a caliber and the width and thickness of the reduced area is determined by averaging the measures taken at five different locations of the reduced cross-section.

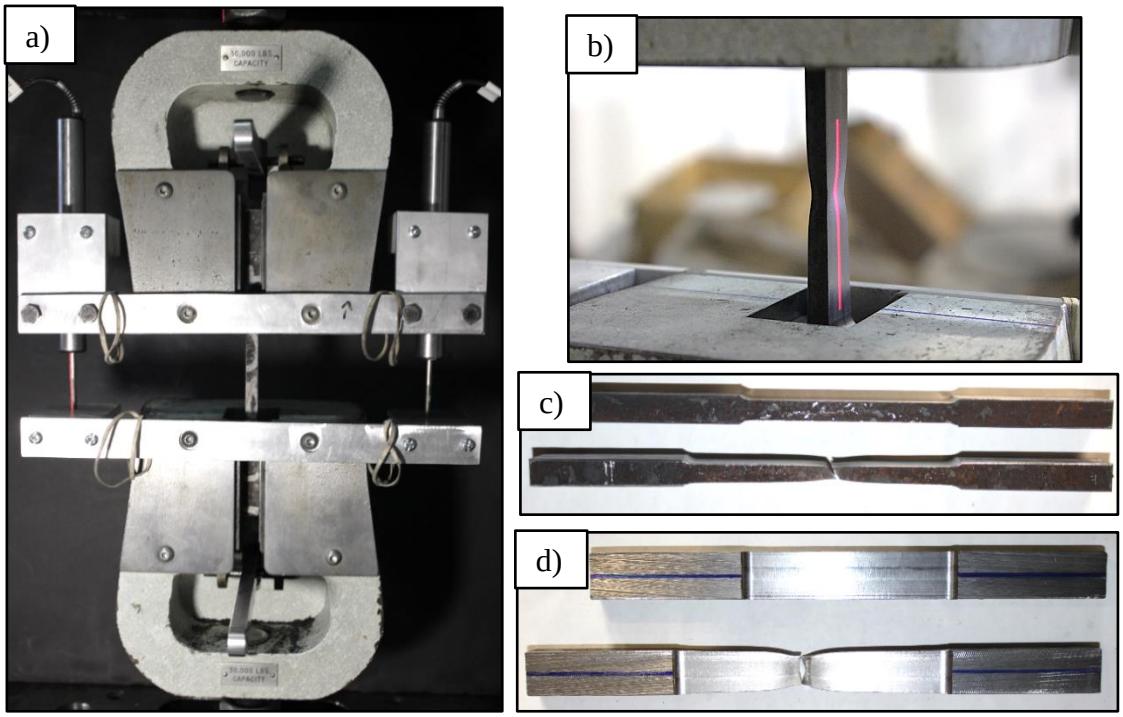


Figure 3.16. Setup used for the ASTM Subsize and Strips coupons and coupons before, during and after testing

The tests were performed through a displacement control of the LVDTs, in order to keep the stress rate in the allowed range of 1.15 to 11.5 MPa/s specified by ASTM8 (2000). Similar to the ASTM Standard coupons, once the hardening of the material was observed, the displacement rate was increased manually to reach the maximum load and eventually the fracture of the specimen occurred. The behaviour of the ASTM Subsize and Strips coupons were similar to the ASTM Standard specimens. Indeed, the expected behaviour of necking was observed, as illustrated on Figure 3.16b). Figure 3.16c and d illustrate the plastic deformation experienced by a fractured Strip coupon by comparing it to an untested specimen. Those figures also show a typical tensile fracture characterized by necking in the reduced section, as exhibited in a normalized material test.

3.4.3 Test data analysis

The force-deformation response of each coupon specimen was transformed into stress-strain behaviour. Generally, the 6 tests performed on the ASTM Standard coupons of the same angle batch gave similar results, which lead to confidence in the validity of the results presented in Chapter 9. However, an uncalibrated extensometer was inadvertently used in most tests, which

translated into some doubtful measurements of the yield and ultimate strains, and it also explains the abnormally large elastic modulus *E* obtained in several tests.

The material investigation with the subsize coupons showed no significant difference between the transversal and longitudinal results for either the yield or ultimate stresses. Therefore, it can be safely stated that the hot rolling process and the residual stresses in the angles do not affect significantly the isotropic properties of the material.

The strips coupons showed that the yield stress near the fillet stayed within a 2% difference of the average ASTM standard coupons, except for the L4x6x3/8 (TC1) angle where the first strip is up to 15.8% larger. Also, the stress along the length of the angle leg generally stayed within the same 2% difference, up to 25 mm from the edge of the leg. At this point, the stress gradually increased to reach a value 5% larger than the average yield stress from ASTM Standard coupons. These variations in the material properties along the section of the angles thus remained generally small. Their influence on the angle characterization is thus omitted.

The values obtained from the ASTM Standard coupons are used to estimate empirically the parameters of the proposed mathematical model representing the hysteretic behaviour of bolted angles presented in Chapter 7. However, the subsize and strips coupon results are not used further in the study. These results are nevertheless presented in detail in Chapter 9 as complementary research work.

3.5 Experimental characterization of full-scale bolted angle beam-column connections

3.5.1 Introduction and objectives

The experimental program on bolted angle components showed a stable and ductile hysteretic behaviour with large tensile strength in every cyclic test performed. This response is expected to translate into strong and ductile beam-column connections with significant energy-dissipation capacity. However, these observations made on bolted angle components were obtained from a simplified setup which neglected several parameters such as the beam leg rotation, the shear load, and the presence of a 2L connection. To resolve this situation, an extensive experimental

investigation has been developed to characterize the global nonlinear behaviour of bolted angle connections. More precisely, the test program has the following specific objectives:

1. Characterize the influence of top and seat angles on the connection behaviour;
2. Characterize the influence of geometrical parameters on the connection behaviour:
    a. Beam depth of 310 and 410 mm;
    b. Top and seat angles thickness and column gage; and
    c. Column section.
3. Characterize the influence of shear loading on the angle behaviour.

These objectives were investigated through 6 different connection geometries, with up to 5 specimens per geometry, for a total of 23 tests performed. The tests were conducted at the Structural Engineering Laboratory of Polytechnique Montreal from December 2015 to March 2017. The results from the 2L connections are presented in Chapter 6, while the results from the 2L-TS connections are presented in Chapter 7. In both these chapters, the experimental setup, the instrumentation, the specimens and the testing procedures are described. However, these subjects are herein presented in more detail.

In typical buildings, a concrete slab also participates to the gravity connection rotational capacity. This component is not included in the experimental program. The program rather focuses on the behaviour of connections made solely of bolted angles. Further discussion on the concrete slab is presented in section 9.4.

3.5.2 Experimental setup

The testing program on beam-column connections aims at characterizing the hysteretic behaviour and rotational capacity of bolted angle connections loaded under both rotational demand and shear loading. To achieve such loading conditions and simplify the specimen installation process in the Structures Laboratory of École Polytechnique Montreal, the considered connection have been rotated by 90°. Therefore, the beam became the vertical component while the horizontal column was anchored to the strong floor of the laboratory, as depicted in Figure 3.17. This rotated setup introduced axial loads in the connection from the beam weight. Combined with the transversal displacement of the connection, this eccentric axial load created a larger moment in the connection,

but given the relatively small axial load compared to the shear load imposed and the small displacements measured, this moment increase is not considered to have a significant influence on the failure mechanism.

Also, to apply the loading conditions on the beam specimens, three actuators attached to the reaction wall were required. The top actuator, with a force capacity of 500 kN in both compression and tension and a maximum stroke of ± 375 mm, was located at 3442 mm of the column flange. This distance was set to allow a sufficient rotational demand to characterize the nonlinear moment-rotation behaviour. This actuator was displacement-controlled, with a constant displacement rate. The change in direction was programmed to occur when the connection rotation reached its target for the current cycle.

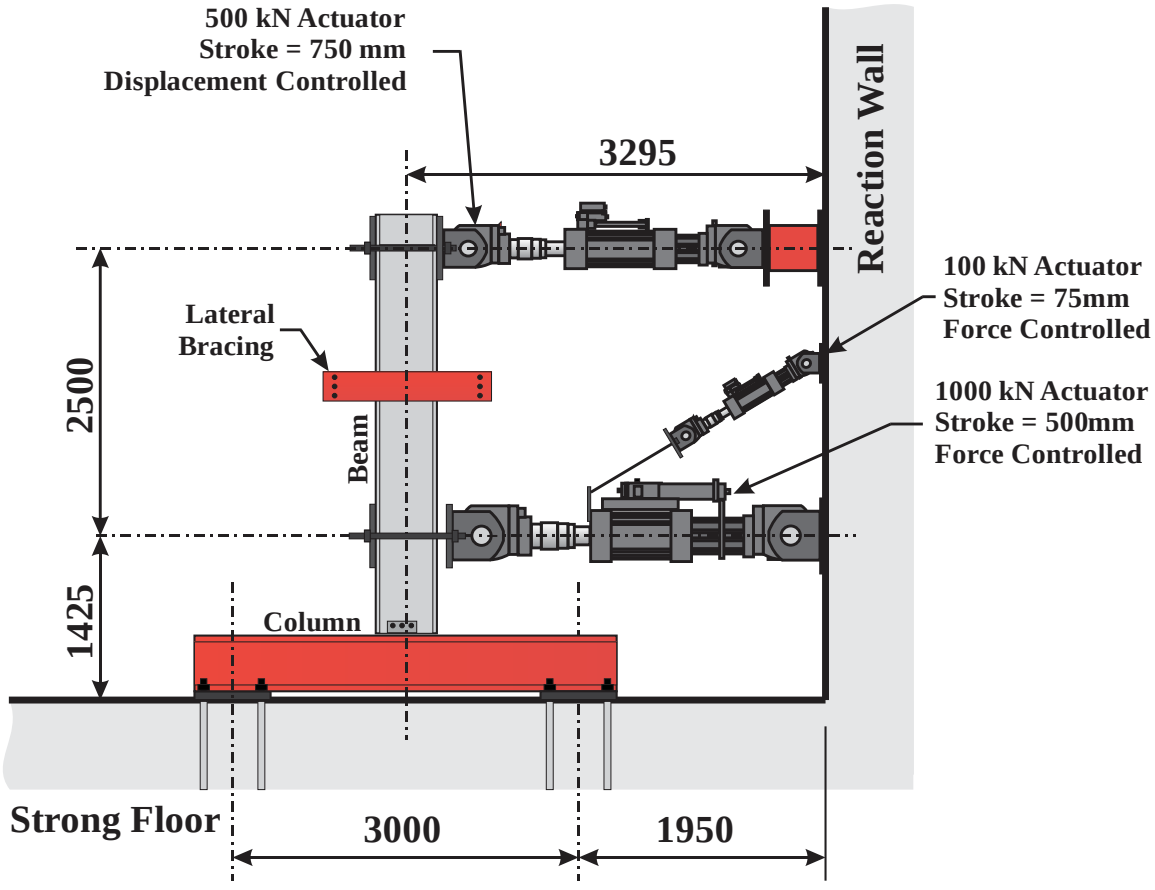


Figure 3.17. Sketch of beam-column connection experimental setup

The bottom actuator was located at a distance of 942 mm of the column flange, with a force capacity of 1000 kN in tension and compression and a maximum stroke of ± 250 mm. This actuator was

located closer to the column; therefore, its impact on the moment and the rotational demand of the connection was smaller. Its main role thus consisted in applying the shear demand on the connection.

The beam specimen in the experimental setup presented in Figure 3.17 acts similarly to a cantilever beam with two concentrated loads, rather than the simply supported beam with a continuous load, as typically considered in buildings. Therefore, the test configuration could not recreate the same moment and shear loading combinations expected simultaneously in a building and the choice to apply a constant shear load at the face of the column was made. To achieve such loading conditions, the bottom actuator was force-controlled, and its command was dependent on the load applied by the top actuator. Indeed, the lower actuator was programmed as a slave whose force command was obtained by the difference between the target shear load in the connection and the load in the master top actuator. Since the shear load applied on the connection specimen represented the gravity loads of the building, the lower actuator was always loaded in the same direction.

3.5.2.1 Actuator attachment to the beam specimens

The beam specimens were attached with two 660x660x51mm steel plates, of which one was bolted to the actuator, and two post-tensioned 51 mm diameter anchor rods as depicted in Figure 3.18a. To further concentrate the load in the beam specimen, which reduced the uncertainty of the flexural moment, two 12 mm-thick and 51 mm-wide plates were welded to the flanges of every specimen and acted as the contact point between the plates of the actuator and the specimen.

In the first three tests performed, the same setup shown in Figure 3.18a was also used for the bottom actuator. However, the small rotational stiffness of the third connection tested, which was the first specimen tested made only of 2L connections, revealed a flaw in the experimental setup. The friction inherent to the hinge of the bottom actuator was larger than the moment capacity of the connection and created false data on the moment calculation at the flange of the column.

To mitigate this error, another hinge was mechanically created outside of the actuator system and in the attachment to the beam. Since the bottom actuator was always loaded in tension, the contact surface between the outer plate and the flange of the beam was replaced into the system presented in Figure 3.18b. This system consists of a concave surface attached to the top beam flange in contact with a smaller convex surface attached to the steel plate, which was in turn attached to the actuator

with the same anchor rods. However, those anchor rods were not post-tensioned since a gap was required between the bottom flange of the beam and the plate attached to the actuator, to allow the free rotation of the beam without entering in contact with the actuator. Thus, the load of the bottom actuator was only transmitted to the beam through contact of those several components.

Furthermore, some displacements along the longitudinal axis of the beam was expected in the connection. To allow the bottom actuator to follow this displacement, a third smaller actuator was added between the two others, as shown in Figure 3.17. This third actuator, with a capacity of 100 kN and a stroke of ± 325 mm, was force-controlled with a command to keep its force equal to the weight of the bottom actuator. It allowed the bottom actuator to follow the connection displacement along the longitudinal axis of the beam.

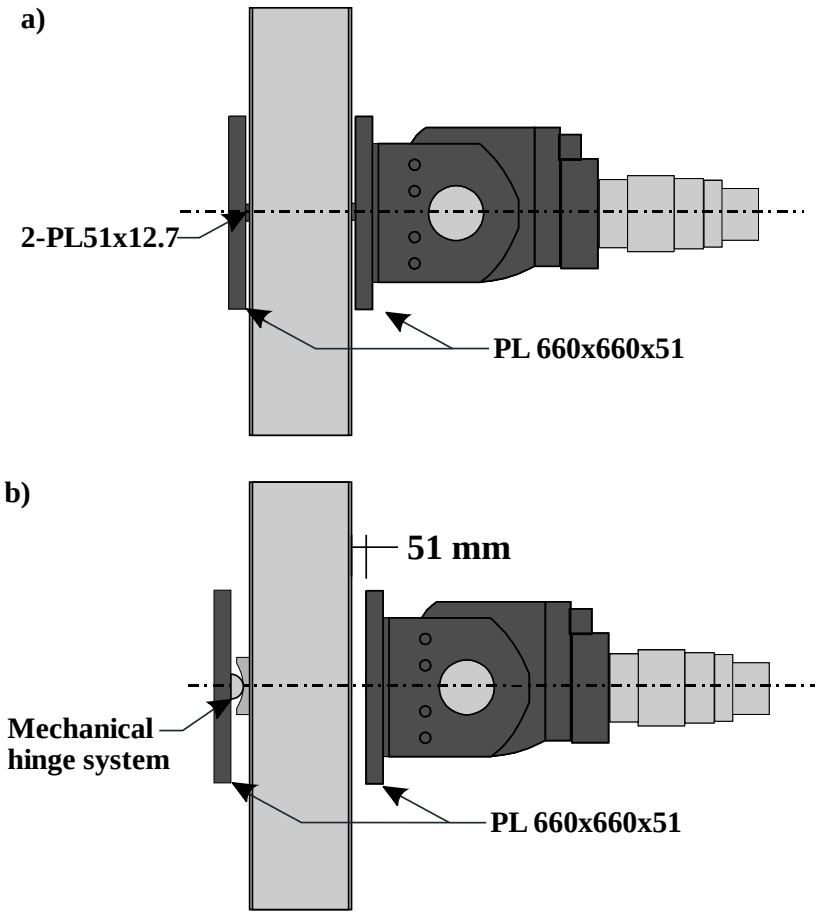


Figure 3.18. Attachment to the beam specimen detailing for a) top actuator and b) bottom actuator

Additionally, two lateral supports were installed on the beam to avoid lateral-torsional buckling. The bottom lateral support, situated at 750 mm above the bottom actuator, as illustrated in Figure 3.17, consisted of two large 254x254x8.0 HSS members attached with four 25.4 mm diameter threaded rods. One of the HSS was bolted to a W section which was in turn attached to the reaction wall behind the setup. The beam specimen was situated between these two tubular sections lined with Teflon to minimize the friction.

In the first test performed, the exact same lateral setup was also used near the top actuator. However, the large displacement demand imposed on the actuator resulted in elastic lateral-torsional buckling of the beam specimen above the lateral support. Therefore, the setup was modified at the second test to support laterally the two 660x660x51 steel plates used in the attachment of the beam specimen to the actuator. The final experimental setup with the three actuators and the two lateral supports is shown in Figure 3.19.

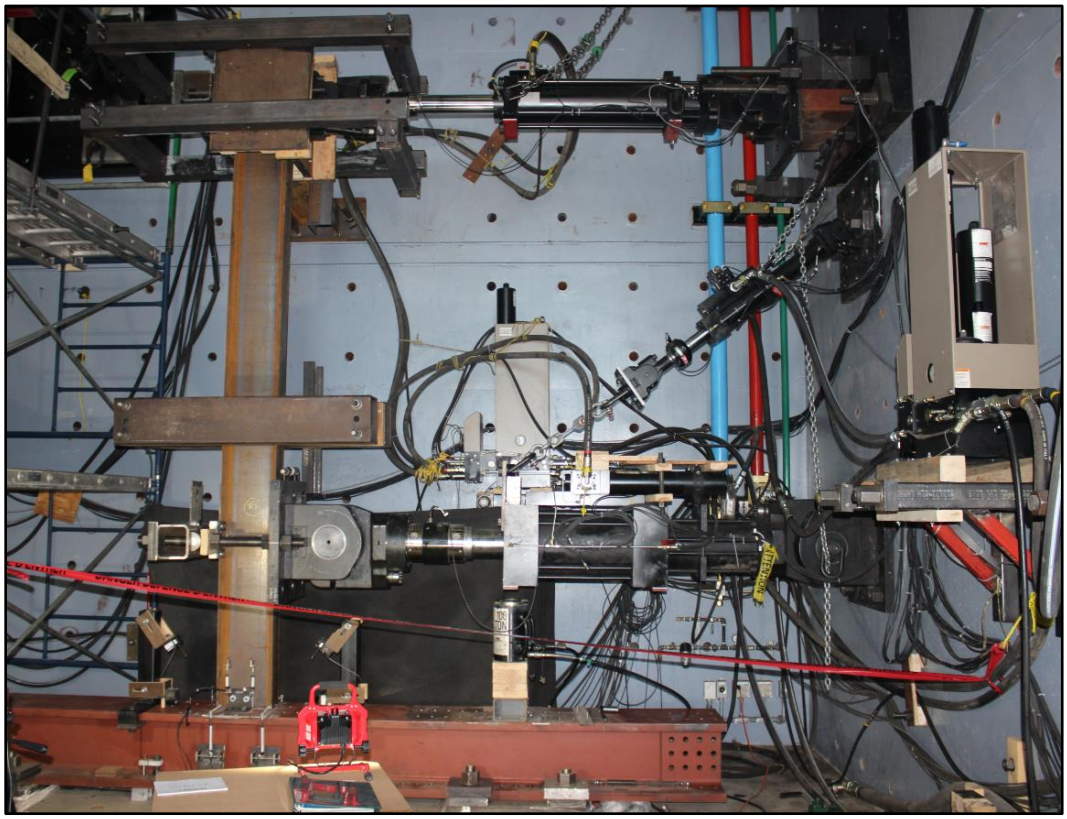


Figure 3.19. Picture of beam-column connection experimental setup

3.5.2.2 Sign convention and reference axes

The sign convention used during the loading procedures and in the current document is presented in Figure 3.20. A negative shear value is assumed in the same direction as the gravity load of the prototype building. Therefore, the constant shear applied on the connection specimens are all negative, as pictured in Figure 3.20a. Additionally, such negative shear load creates a negative bending moment as the beam rotates downwards. Therefore, the bending moment and rotation signs are identified in Figure 3.20a under both a positive and negative rotational demand. Figure 3.20b shows the shear load direction, bending moment and rotation signs on the connection specimens under both negative and positive rotational demand, as the setup is rotated by 90°.

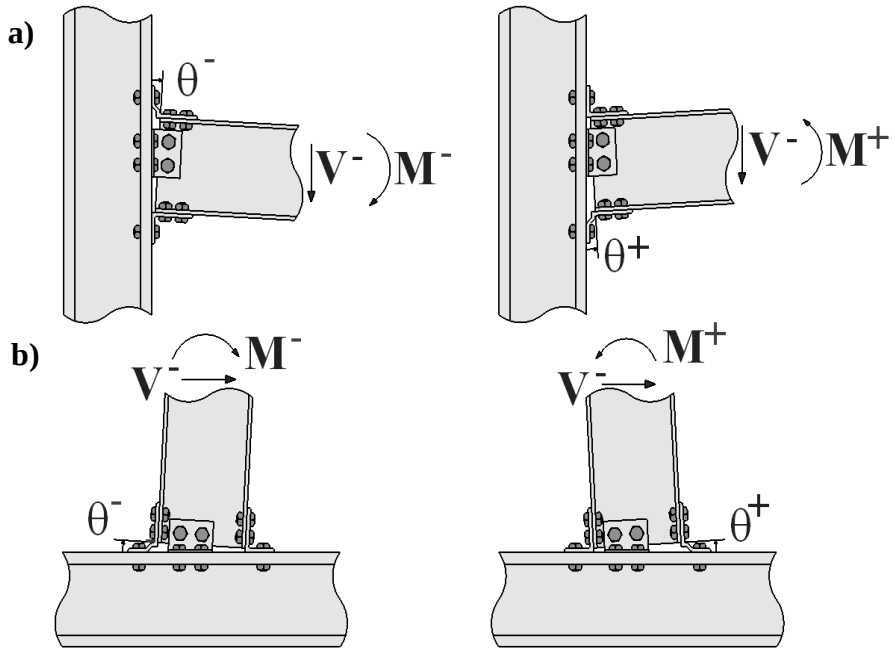


Figure 3.20. Shear force, bending moment and rotation sign convention a) for a typical beam-column connection in a building b) for the experimental specimens

Similarly, Figure 3.21a presents the displacement reference axes for a typical connection in a building. The X axis is defined as longitudinal to the beam local axis, whereas the Z reference axis corresponds to the transversal axis. Since the setup is rotated by 90°, the displacement reference axes are also rotated. The directions of the displacements measured on the experimental specimens are also presented in Figure 3.21b, along with the sign convention associated with the measured displacements.

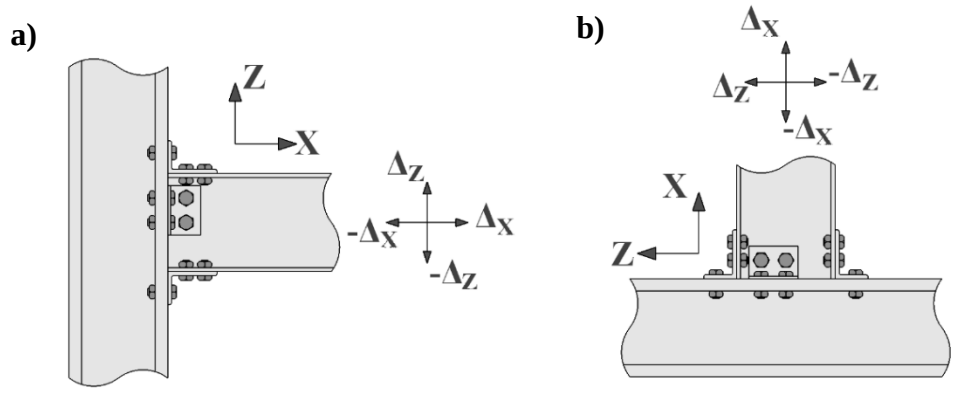


Figure 3.21. Connection displacement sign convention and axes a) for a typical beam-column connection in a building b) for the experimental specimens

3.5.3 Experimental instrumental setup

Several captors are installed on the beam-column connection specimens to accurately characterize the rotation of the joint, but also the slip between the angles and the beam and column members, as well as the overall displacement of the connection. Furthermore, the actuator internal load cell allowed the calculation of the applied shear and moment at the connection. A review of each captor installed is herein presented.

3.5.3.1 Rotation measurement of beam-column connection specimens

The rotation of the beam-column connection specimens are used in the testing procedure as the control parameter. Once the connection rotation reached the target for the current cycle, the change in loading direction of the upper actuator is triggered.

This rotation is calculated from the measurement of four linear potentiometers (LPs) of ± 50 mm attached to the edge of the beam member with square nuts welded to the interior side of the flanges and threaded rods. On the other end, the captors are attached to the lower flange of the column, as illustrated in Figure 3.22a. Therefore, the rotation obtained corresponded to the one of the connections only, since the position of the captors did not allow the measurement of the beam or of the column rotation. Figure 3.22b presents a plan view of the connection along with the nomenclature of the captors.

The rotation θ_b is obtained with Equation 3.8, given as the difference in the average of the LPs measurements at the top and bottom of the connection. This difference is then divided by the average distance between the instruments d_S and d_N to obtain the connection rotation θ_b.

$$\theta_b = \frac{\frac{LP_{NW} + LP_{SW}}{2} - \frac{LP_{NE} + LP_{SE}}{2}}{\frac{d_S + d_N}{2}} \tag{3.8}$$

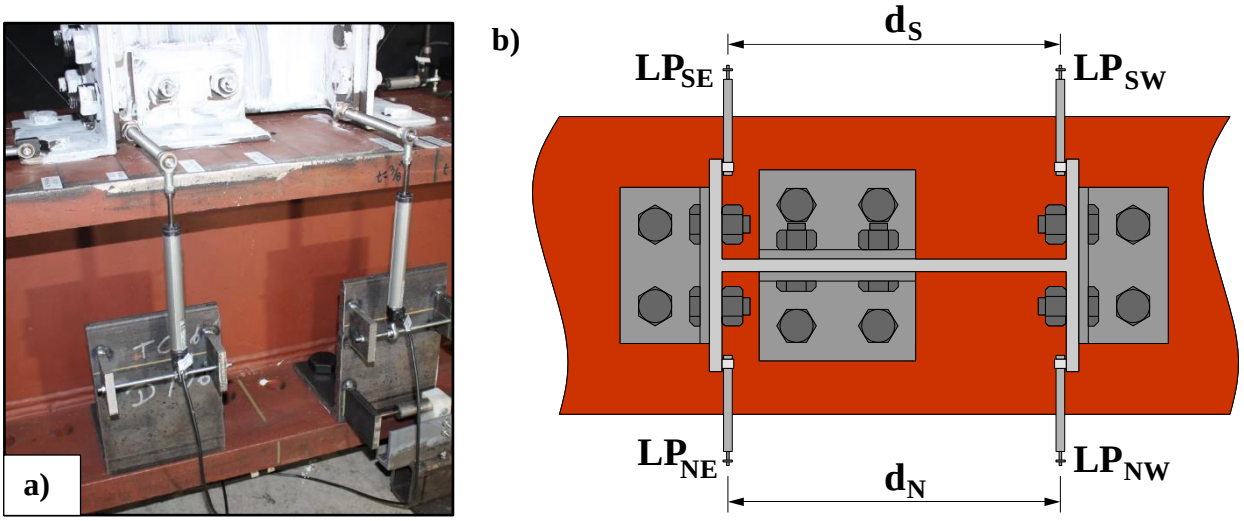


Figure 3.22. Rotation measurement setup

3.5.3.2 Slip measurement between the connection specimen components

Four LPs of ± 12.5 mm were attached to the connection to measure the slip between the connection components during the test. Therefore, the slip between the column flange and the angle leg was measured for the top and seat angle, along with the slip between beam flange and the other angle leg. The positions of these captors on the connection specimen are presented in Figure 3.23a. A small attachment plate was welded at the extremity of both angle legs to minimize the impact of local alteration in the material properties due to the welding process on the angle behaviour. Additional plates were welded to each beam flange, to which the beam-angle slip LPs were attached, as illustrated in Figure 3.23b. For the column-angle slip LPs, a plate with a small threaded rod was clamped to the column flange to attach the instrument, as presented in Figure 3.23c.

For the specimens made only of 2L angles, slip was instead measured on the top and bottom side of the angle beam leg. Therefore, the two instruments were installed with the same welded plate method as the beam-angle slip, as shown in Figure 3.23e. This measurement allowed the observation of the differential slip between the top and bottom side of the connection depending on the rotational demand throughout the test. This differential slip can translate into a large difference between the beam rotation and the angle rotation in the connection.

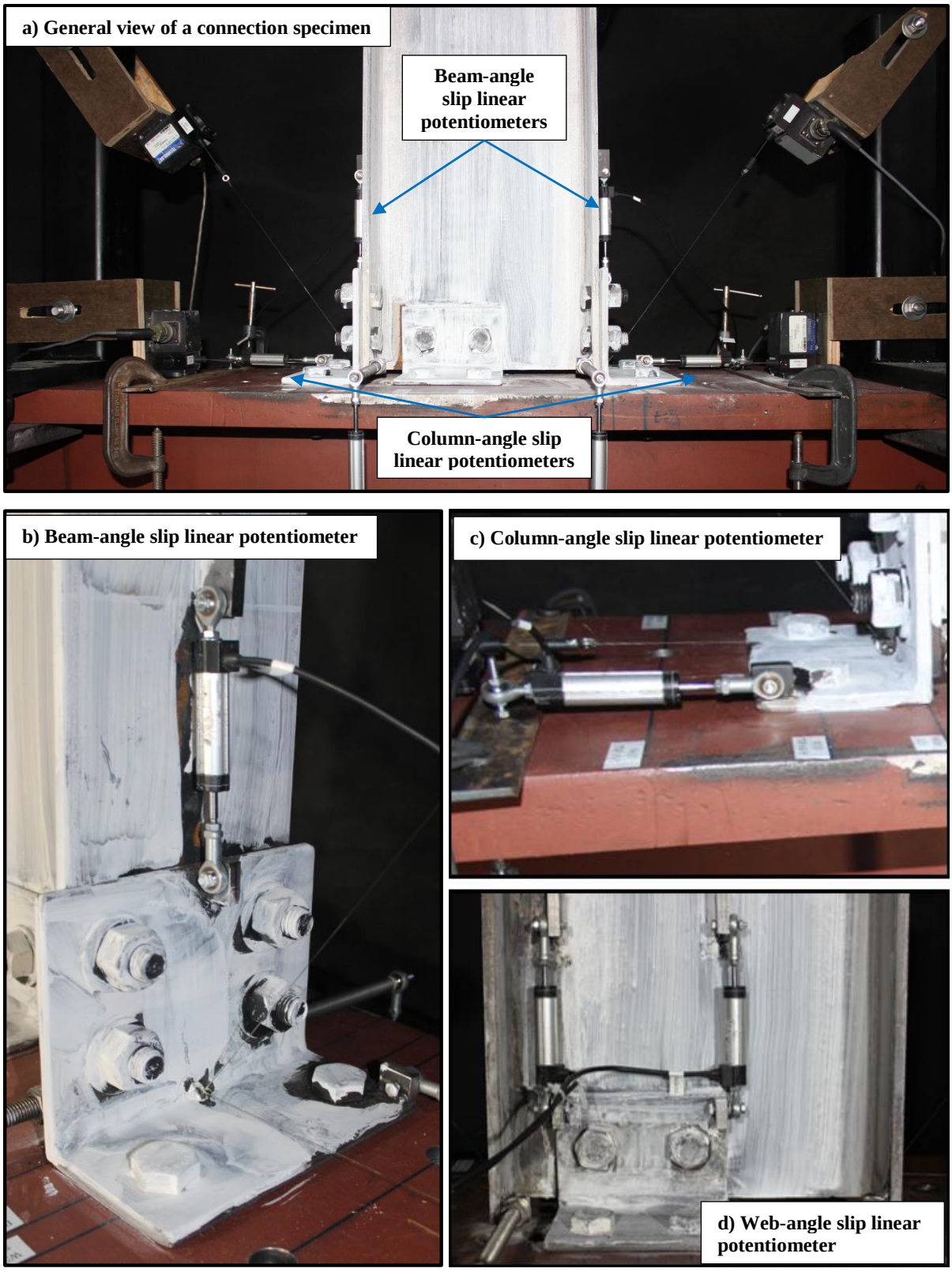


Figure 3.23. Slip measurement setup

3.5.3.3 Displacement measurement of the connection specimens

Furthermore, the horizontal and vertical displacements of the top and seat angles were calculated from the measurement of two string potentiometers (SPs) each. The captors were clamped to the column flange with a steel support as shown in Figure 3.24a. A set made of a horizontal and an inclined SP, both vertically aligned, were used to calculate the angle displacement through triangulation. This setup is pictured in Figure 3.24b.

The strings of the captors were attached to a small washer welded in the center of the angle fillet, as presented in Figure 3.24c. This type of attachment was preferred since it allowed an accurate measurement of the angle corner displacement. The material property alterations resulting from the welding only affected the local area near the weld. Since the plastic hinges were observed at the edge of the fillet in both the column and beam legs during the angle testing program and not in the fillet itself, the local material alterations are assumed to be negligible on the plastic mechanism of the top and seat angles.

For the specimens made only of 2L angles, the small washers were welded at the center of the beam flange, as illustrated in Figure 3.24d. This setup allowed the measurement of the horizontal and vertical displacement of the beam flanges.

Figure 3.24e presents the reference point positions used to calculate the horizontal Δ_z and vertical Δ_x displacements, where points A, B and C represent respectively the inclined SP, the horizontal SP and the welded washer on the specimen. The horizontal and vertical displacements are obtained by triangulation with Equations 3.9 and 3.10 respectively. The distances AB, AC and BC are measured prior to the test, while AC' and BC' are obtained by the sum of the initial distance and the instrumentation measurements. The value AB represents the distance between both captors and remained constant throughout the test.

$$\Delta_z = \frac{AC'^2 - BC'^2 + AB^2}{2AB} - \frac{AC^2 - BC^2 + AB^2}{2AB} \tag{3.9}$$

$$\Delta_x = \frac{\sqrt{2AB^2AC'^2 + 2AB^2BC'^2 + 2AC'^2BC'^2 - AB^4 - AC'^4 - BC'^4}}{4AB^2} - \frac{\sqrt{2AB^2AC^2 + 2AB^2BC^2 + 2AC^2BC^2 - AB^4 - AC^4 - BC^4}}{4AB^2} \tag{3.10}$$

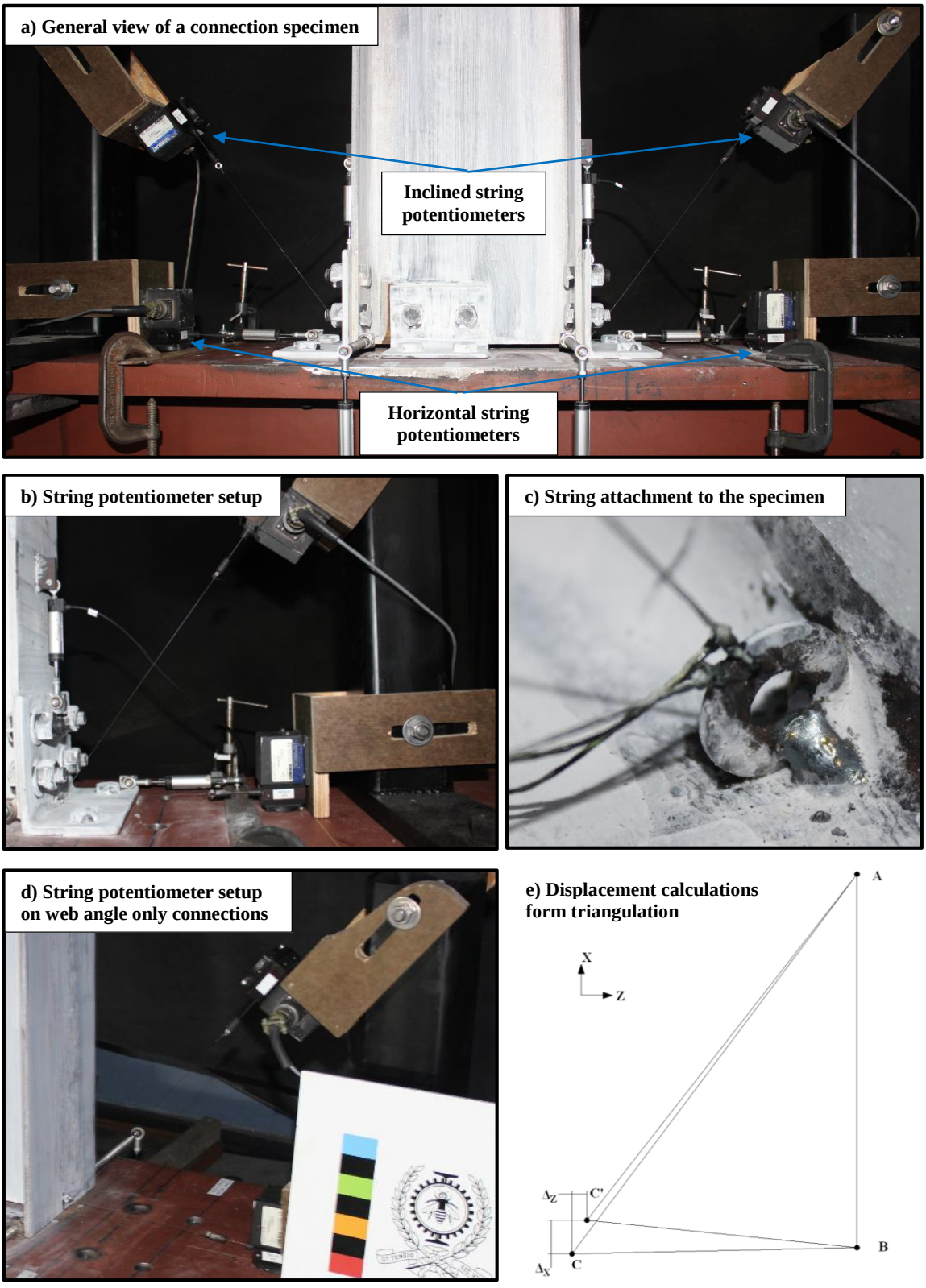


Figure 3.24. String potentiometers setup

3.5.3.4 Actuator load cells

The force of each actuator was measured with their own load cells. These values were used to calculate the shear force as well as the moment at the connection. Figure 3.25 presents the free body diagram of the beam specimen. The values of L_{V500} and L_{V1000} representing the distance between the column flange and the centerline of the upper and lower actuators respectively are measured for every specimen before the test. The values of L_{V500} varied between 3439 and 3445 mm, while L_{V1000} varied between 939 and 943 mm. The shear force and flexural moment at the connection is given by Equations 3.11 and 3.12 respectively.

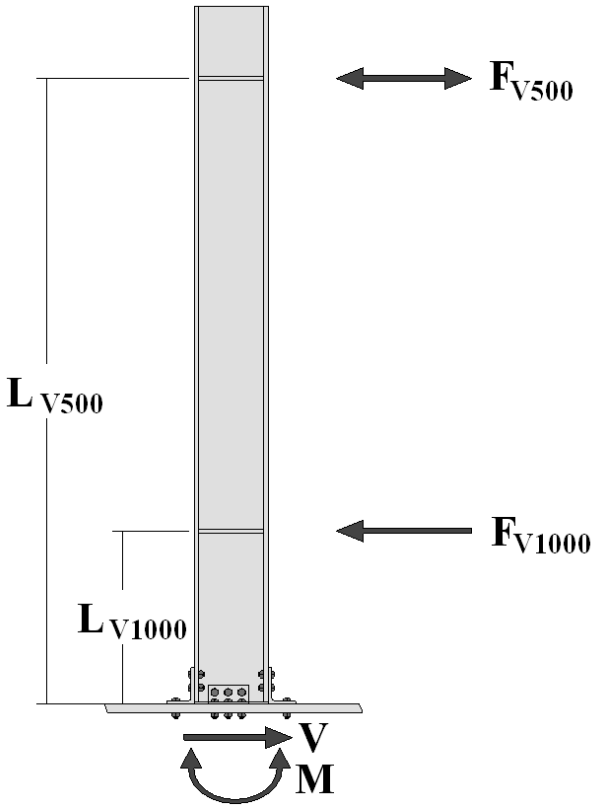


Figure 3.25. Free body diagram of beam specimen

$$V = F_{V500} + F_{V1000} \tag{3.11}$$

$$M = F_{V500} \times L_{V500} + F_{V1000} \times L_{V1000} \tag{3.12}$$

3.5.3.5 Column rotation measurement for the W250x67 column specimens

Two tests are preformed using a slenderer W250x67 column instead of the stiff W360x347 section used in the other tests. For these two specimens, a significant rotation of the column section was expected and thus, instrumentation have been installed to measure the column rotation. For these tests, the rotation of the beam-column connection specimens was still used in the testing procedure as the control parameter. Once the connection rotation reached the target for the current cycle, the change in loading direction of the upper actuator is triggered.

The same procedure described in section 3.5.2.1 was used to measure the beam rotation. Only, in the specimens with a W250x67 column, the captors were attached to a support fixed to the ground, thus obtaining the absolute rotation of the beam section, whereas the specimens using a stiffer column were fixed to the bottom flange of the column. This modification was brought to the instrumentation setup to avoid the potential impact of local plastic deformation in the column section on the beam rotation measurement. Alternatively, the rotation of the column is evaluated by measuring the displacement at the centerline of the column section with 4 LPs of ± 25 mm also attached to the strong floor of the laboratory. Figure 3.26 pictures the instruments position on the beam and column sections for the tests using a W250x67 column.

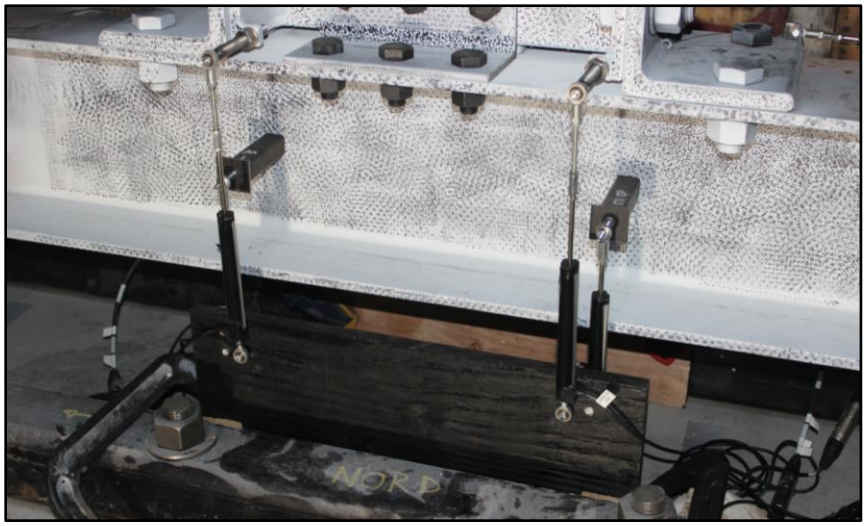


Figure 3.26. Rotation measurement setup using a W250x67 column specimen

The rotation of the connection itself was determined as the difference between the absolute rotation of the beam and the rotation measured from the column centerline. Using this definition, the

connection rotation included the deformations caused by the yielding of the angles but also the local plastic deformations that could occur in the bolted column flange and the bolt bearing deformations experienced by the beam section.

3.5.3.6 Optical system for the W250x67 column specimens

Additionally, in the two tests performed with a slenderer W250x67 column, a new optical system acquired by the laboratory was used on the specimens to test the system. This optical system consists of two high definition cameras positioned at equal distance from the specimen and offering two distinct viewpoints of the same specimen face. The position of the two cameras with respect to the specimen are presented in Figure 3.27. Furthermore, a white coat of paint was required on the specimen components, on top of which was applied a random speckle of dark points. The speckle applied on the specimen components is shown in Figure 3.28.

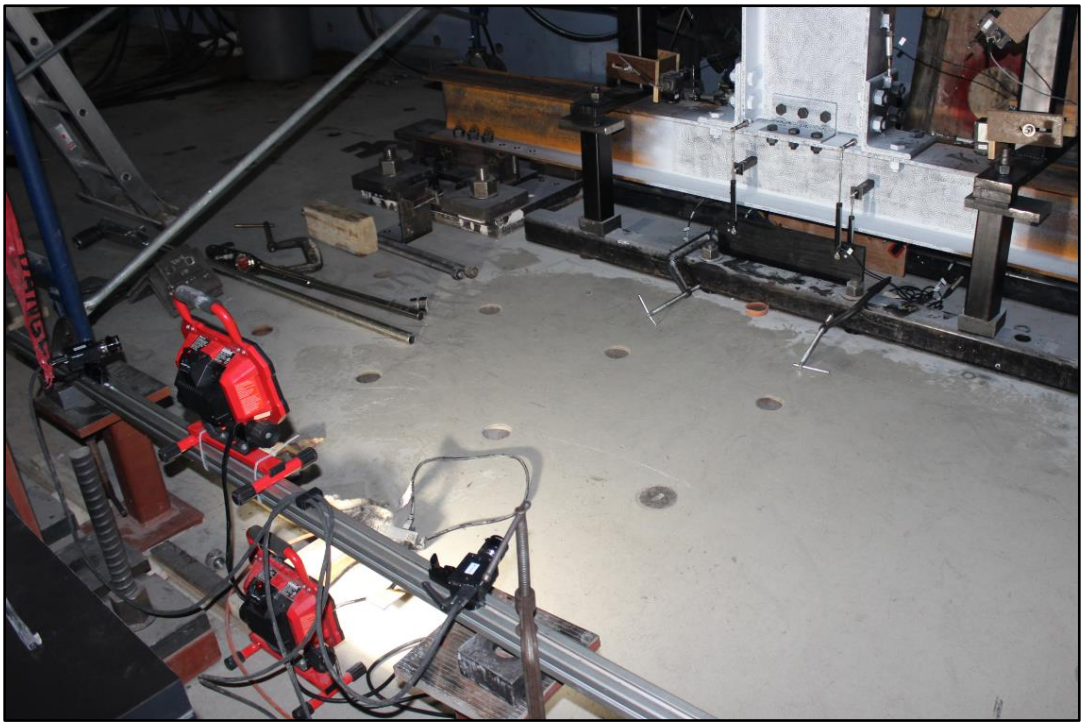


Figure 3.27. Optical system setup for the specimens using W250x67 column

During the test, the cameras took pictures of the specimen at the exact same moment, at a frequency of 0.5 Hz. From those pictures offering two distinct perspective of the specimen, the software Optical Solutions discretized the speckle on the connection into small distinguishable parts. The

software was then able to retrace every part of the speckle on the specimen and output its three-dimensional displacements with a frequency of 0.5 Hz from the triangulation obtained from the two pictures. Therefore, the results obtained from the optical system offers a global image of the displacements experienced by the entire specimen and can determine the deformation of a specific element accurately, with respect to its six degrees of freedom, at every moment of the test.

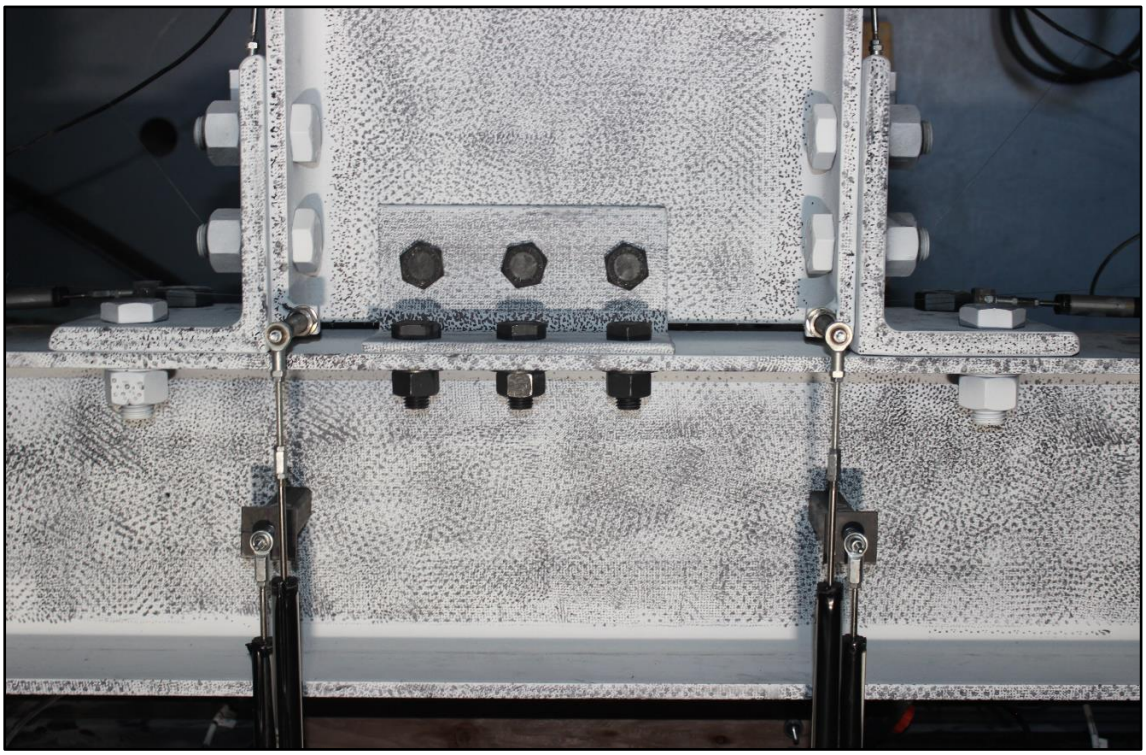


Figure 3.28. Paint treatment required on the specimen components for the optical system

However, the quality of the results obtained depend greatly on the quality of the speckle applied on the specimen. If the ratio of dark point to white background is too large or too small, the software is unable to retrace the specific speckle surrounding one point and cannot offer a reasonable precision on the obtained results. This issue was encountered in some parts of the specimen.

3.5.4 Test matrix

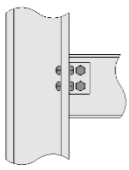
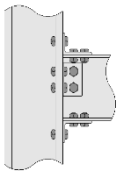
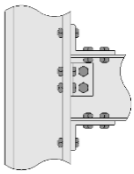
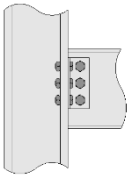
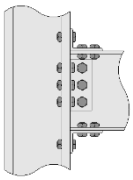
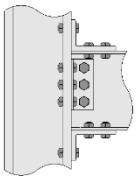
The testing program on the beam-column connections consisted of 6 distinctive connection geometries, with either a W310x39 (W12x26) or a W410x67 (W16x45) and a stiff W360x289

column. Two connection geometries (1 & 4) consisted of 2L angles only, while TS angles were added for the four other connections.

The column gage and the thickness of the TS angles added also varied. Two connection configurations (2 & 5) were composed of L102x152x9.5 angles attached to the column at 63.5 mm from the angle corner with 19.1 mm bolts, which corresponds to the TC1 (g_2/t of 2.67) angle geometry of the angle testing campaign previously performed.

Finally, the 2 other beam-column connection configurations (3 & 6) were made with the TC14 (g_2/t of 2.58) angle geometry of the angle testing campaign, which corresponds to L152x203x19.1 angles attached to the column at 101.6 mm from the angle corner with 25.4 mm bolts. These two angle geometries are chosen because of their large difference in thickness and column bolt gage, but similar aspect ratio g_2/t. These geometrical characteristics are summarized in the test matrix presented in Table 3.6.

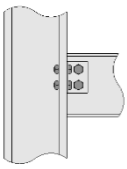
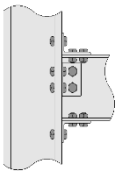
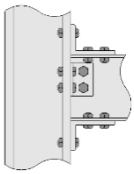
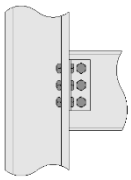
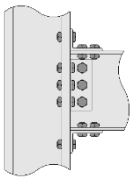
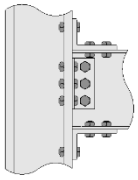
Table 3.6. Test matrix of beam-column connection tests

	1	**2**	**3**	**4**	**5**	**6**
Test						
Beam	W310x39			W410x67		
Column	W360x347		W360x347 W250x67	W360x347		W360x347 W250x67
Top & Seat	-	L102x152x9.5 g_c : 63.5 d_b : 19.1	L152x203x19.1 g_c : 101.6 d_b : 25.4	-	L102x152x9.5 g_c : 63.5 d_b : 19.1	L152x203x19.1 g_c : 101.6 d_b : 25.4
Web angles	L102x102x7.9 L_w : 140 mm g_c : 63.5 mm d_b : 19.1 mm			L102x102x7.9 L_w : 216 mm g_c : 63.5 mm d_b : 19.1 mm		

The design plastic moment of the beam and column sections, as well as the design shear resistance of the connection are presented in Table 3.7. This table also presents the limit state controlling the design shear resistance of the connection.

For the two geometries made of 2L angles only, the limit state controlling the design shear resistance of the connection correspond to the bolt shear resistance, whereas the beam shear resistance controls the resistance of the connection for the specimens where TS bolted angles are added to the double web angles.

Table 3.7. Design plastic moment and shear resistance of sections and specimens

	1	**2**	**3**	**4**	**5**	**6**
Test						
Beam	W310x39			W410x67		
Column	W360x347		W360x347 W250x67	W360x347		W360x347 W250x67
Top & Seat	-	L102x152x9.5 g_c : 63.5 d_b : 19.1	L152x203x19.1 g_c : 101.6 d_b : 25.4	-	L102x152x9.5 g_c : 63.5 d_b : 19.1	L152x203x19.1 g_c : 101.6 d_b : 25.4
Web angles	L102x102x7.9 L_w : 140 mm g_c : 63.5 mm d_b : 19.1 mm			L102x102x7.9 L_w : 216 mm g_c : 63.5 mm d_b : 19.1 mm		
Design resistance of connection						
M_P Beam	189 kN-m			422 kN-m		
M_P Column	2217	2217	2217 kN-m (W360x347) 280 kN-m (W250x67)	2217 kN-m	2217 kN-m	2217 kN-m (W360x347) 280 kN-m (W250x67)
V_r	320 kN	368 kN	368 kN	479 kN	739 kN	739 kN
Shear Limit State	Bolt shear resistance	Beam shear resistance	Beam shear resistance	Bolt shear resistance	Beam shear resistance	Beam shear resistance

3.5.5 Testing procedures of beam-column tests

Each beam-column connection geometry was loaded under several loading procedures. Table 3.8 presents each test conducted on the beam-column specimens of the experimental program. The first test performed on the 2L angles only specimen (1A) revealed major concerns about the friction inherent to the setup of the lower actuator. Because of this problem, some changes were brought to the setup to minimize the lower actuator friction, but the results obtained from this test were not realistic. It was thus discarded and performed a second time on another specimen with an improved experimental setup.

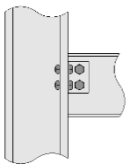
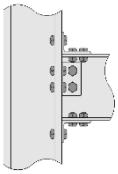
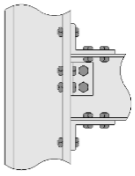
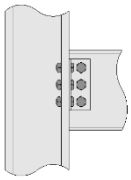
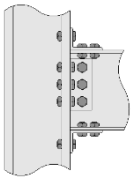
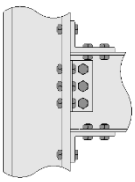
Each specimen was loaded cyclically with the top actuator while the bottom actuator kept a constant shear load in the connection, either -94 kN for W310x39 or -282 kN for W410x67 beam specimens. These shear values were defined as the seismic shear and correspond to the load combination of 1.0D + 1.0 E + 0.5L of the NBCC. These values also correspond, with a difference of ± 1%, the load combination of 1.2D + 1.0 E + 0.5L of ASCE7.

The application of this shear load was performed before the cyclic loading, by gradually increasing the force demand in the bottom actuator, while the top actuator remained at its initial position. Once the shear load was reached, the control mode of the lower actuator was changed to become a slave of to top actuator force with the command defined by Equation 3.13, where *V* is the target shear load in the connection.

$$F_{V1000} = V - F_{V500} \tag{3.13}$$

During the loading of the bottom actuator, a force developed in the top actuator, as its command was to keep its initial position. This force, along with the one applied by the bottom actuator, created a moment in the connection. Before starting the cyclical loading, this moment was brought back to 0 kN-m by adjusting gradually the top actuator position. This adjustment created a displacement of the top actuator and a small initial rotation in the connection. In order to apply the accurate rotation rotational demand on the connection, a reset of the rotation instrumentation was performed once to start the cyclic loading with a moment of 0 kN-m and a rotation of 0 rad.

Table 3.8. Summary of tests conducted on beam-column specimens

	1	2	3	4	5	6
Test						
Beam	W310x39			W410x67		
Top & Seat	-	L102x152x9.5 g_c : 63.5 d_b : 19.1	L152x203x19.1 g_c : 101.6 d_b : 25.4	-	L102x152x9.5 g_c : 63.5 d_b : 19.1	L152x203x19.1 g_c : 101.6 d_b : 25.4
Web angles	L102x102x7.9 L_w : 152			L102x102x7.9 L_w : 229 mm		
Loading procedures of each tests :						
A	~~Cyclic seismic gravity~~	Cyclic seismic gravity	Cyclic seismic gravity	Cyclic seismic gravity	Cyclic seismic gravity	Cyclic seismic gravity
B	Cyclic seismic gravity shear New setup	Cyclic seismic gravity & design shear excursions	Cyclic seismic gravity & design shear excursions	Cyclic seismic gravity & design shear excursions	Cyclic seismic gravity & design shear excursions	Cyclic seismic gravity & design shear excursions
C	Cyclic seismic gravity & design shear excursions	Cyclic rotational shear	Cyclic rotational shear	Cyclic rotational shear	Cyclic rotational shear	Cyclic rotational shear
D	Cyclic rotational shear	Near fault (-) & seismic gravity	Cyclic seismic gravity W250x39 column	Near fault (-) & seismic gravity	-	Cyclic seismic gravity W250x39 column
E	-	-	-	Near fault (+) & seismic gravity	-	-

Five different types of loading procedures were applied on the connection specimens. The first one consists of a gradually increasing cyclic story drift demand obtained from FEMA (2000), combined with a constant shear load on the connection. The storey drift demand of this loading protocol is presented in Figure 3.29a. This type of loading was also applied for the two specimens with the slenderer W250x39 column specimens.

The second type of loading performed on the beam-column specimens was similar to the first one. The same loading protocol provided by FEMA (2000) was used. However, in the second type of loading, the cyclic loading was held constant at each 0.01 rad increment to perform some shear excursions when a moment of 0 kN-m was reached. Such moment value was obtained during the unloading of the positive excursion, when the connection specimen exhibited significant plastic deformations. The approximate position of these momentary load increase on the time-history of the story drift demand are illustrated on Figure 3.29b. During these shear excursions, the command of the top actuator was modified to keep its position. The load was then increased in the bottom actuator to reach a connection shear of -152 kN and -456 kN for the specimens with a W310x39 and a W410x67 beam respectively. These shear values, identified as the design shear, correspond to the load combination of 1.25D + 1.5L of the NBCC and 1.2D + 1.6L of the ASCE7. These shear excursions were maintained for 2 minutes, after which the connection shear was brought back to either -94 kN or -282 kN and the cyclic loading was resumed. The excursions aimed as verifying the connection capacity to sustain large shear demands even after significant yielding and rotational demand from a seismic event.

The third loading protocol also uses the story drift demand proposed by FEMA (2000) and presented in Figure 3.29a. However, this test was loaded without a shear load applied on the connection. Therefore, the bottom actuator was not attached to the beam specimen and the top actuator was used to apply the rotational demand on the connection. The force required in the top actuator to create this demand was the only shear load in the connection and is identified as the rotational shear. This test aimed at evaluating the influence of the shear load on the connection behaviour.

The fourth and fifth type of loading protocol consisted of the storey drift demand proposed by FEMA (2000) for a near-fault seismic event. This loading protocol is presented in Figure 3.29c and d for the excursions occurring mainly in negative and positive rotational demands respectively. These loading protocols were applied along with the constant shear load. The whole story drift time-history was applied up to 7 times to try to provoke a low-cycle fatigue fracture in the bolted angles composing the connection. After those multiple load application cycles, the rotational demand on the connection was increased manually by gradually increasing the top actuator

displacement until connection fracture occurred or the maximum displacement allowed by the experimental setup was reached.

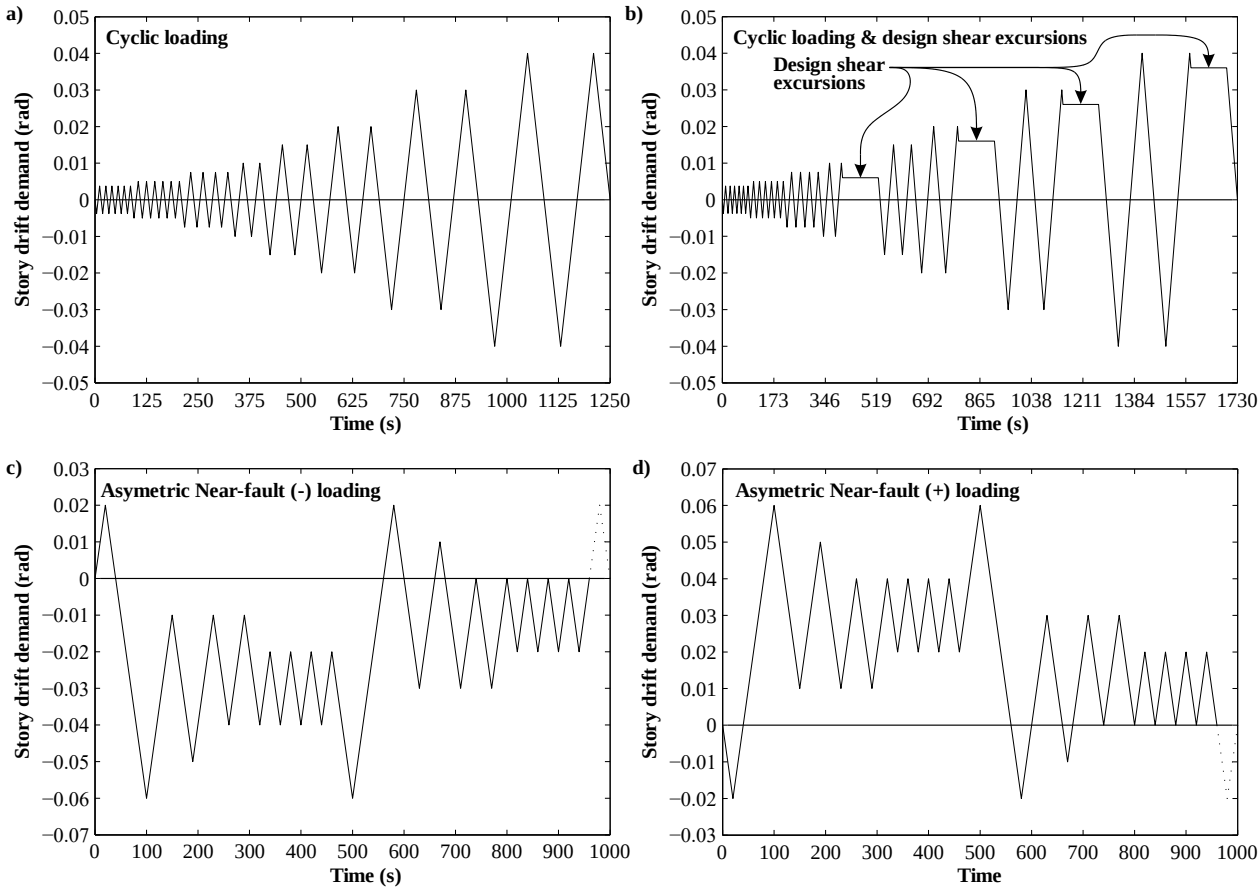


Figure 3.29. Storey drift demand for a) Cyclic tests b) Cyclic test with design shear excursions c) Near fault (-) tests d) Near fault (+) tests

3.5.6 Test data analysis

The tests performed on the connection specimens created a database from which valuable observations can be drawn on the influence of geometrical parameters and loading conditions. From these tests, the connection hysteretic behaviour of the 2L angle specimens are detailed in Chapter 5, while the 2L-TS connections are detailed in Chapter 6. The following steps were taken to characterize the behaviour of these connections:

1. The failure mode and failure mechanism of each test were determined;
2. The moment-rotation behaviour of each specimen was determined and defined with key response parameters;
3. The backbone curve of the moment-rotation behaviour was defined mathematically with the model proposed by Filippou et al. (1983).
4. The influence of several design parameters was qualitatively evaluated by comparing the moment-rotation response of the specimens:
    a. The influence of shear load and shear excursions;
    b. The beam depth;
    c. The presence of top and seat angles;
    d. The top and seat angle geometry;
    e. The column section;
    f. The loading conditions (symmetric, asymmetric).
5. Additionally, the moment-rotation response of the specimens was recreated with the proposed mathematical model characterizing the hysteretic behaviour of bolted angles and presented in Chapter 7. This model validation is also presented in Chapter 7.

Furthermore, the results of the 24 beam-column specimens are detailed individually in Appendix B.

3.6 Characterizing the hysteretic behaviour with a proposed mathematical model

The 71 monotonic tests of the angle component experimental program were used to calibrate the mathematical model of Filippou et al. (1983). This calibration process aimed to recreate the bolted angle behaviour with a single equation. The mathematical model of Filippou et al. (1983), originally developed to represent the hysteretic behaviour of steel rebars in concrete, is widely used to model the steel stress-strain behaviour in OpenSees with the *Steel02* Uniaxial material (Mazzoni

et al. 2006). It can thus be used to represent the hysteretic behaviour and was compared to the results of the cyclic and time-history tests performed.

This mathematical model can represent accurately the hysteretic behaviour of the steel material. However, some discrepancies were observed between the mathematical model and the bolted angle cyclical response. Therefore, modifications to the mathematical model were proposed to define more accurately the hysteretic behaviour specific to bolted angle components. This proposed model is detailed in Chapter 7. To define and validate this model, the following steps were taken:

1. The hysteretic behaviour of the mathematical model proposed by Filippou et al. (1983) was compared to the results of the cyclic tests.
2. Modifications were proposed to the mathematical model developed by Filippou et al. (1983) to more accurately represent:
    a. The unloading response;
    b. The reloading response;
    c. The low-cycle fatigue damage and strength degradation using the method developed by Uriz and Mahin (2008).
3. The proposed mathematical model was calibrated with the results of each cyclic tests;
4. Empirical equations based on the geometrical parameters of the angles were then developed to determine the input parameters of the proposed mathematical model and to predict the hysteretic behaviour of bolted angles;
5. The proposed mathematical model was programmed and integrated in the OpenSees framework, as the *SteelAngles* uniaxial material. For the purpose of this project, the software including the proposed material was compiled by the author. The code added to the software is presented in Appendix C.

This proposed mathematical model thus allowed the accurate modeling of bolted angle components. The hysteretic behaviour of beam-column connections was then recreated with the proposed mathematical model following a component-based modeling approach. This approach is detailed in Chapter 7. To define and validate this approach, the following steps were taken:

1. The hysteretic behaviour of each angle component was created with the empirical equations previously established;
2. Fiber sections are created, and the proposed model was assigned to the fibers;
3. Experimental results were recreated with the fiber sections to validate the approach;

In the development of the mathematical model, integrating the interaction between the shear load and the moment-rotation response was investigated. However, representing this behaviour in a numerical model with OpenSees is a complicated process demanding significant energy. Furthermore, the benefits of implementing this interaction behaviour seemed limited. For these reasons, this aspect of the beam-column connection behaviour was omitted in the numerical modeling and in the proposed mathematical model.

3.7 Enhanced gravity connection design procedure

First, a parametric study was performed to define the influence of the reserve capacity stiffness on the dynamic response this parametric study is presented in Chapter 9 as complementary research work. Then, a design procedure to determine the required bolted angle geometrical parameters to provide sufficient reserve capacity to the gravity frame was developed.

3.7.1 Parametric study defining the influence of the reserve capacity stiffness on the dynamic response

This parametric study aimed at defining the fundamental period and the design base shear of the buildings after brace failure. Indeed, the reserve capacity acts as a secondary system which influences the structural behavior of the building after the failure of the primary SFRS.

for Vancouver and Montreal, on soil type C and E, as prescribed by NBCC. The buildings consisted of 3-, 4-, 5- and 6-bays of 9144 mm (30') in both direction and 3 storeys of 4572 mm (15') height. Plan and elevation views of the buildings are presented in Figure 3.30. The prototype buildings used in this parametric study were designed with the design spectra presented in Figure 3.31. The design of the prototype buildings was performed using an Excel spreadsheet developed by the author. This spreadsheet is presented in Figure 3.32. The braced frames were designed according to the Conventional Construction (R_d of 1.5 and R_o of 1.3) provisions of CSA S16-14. Although

the gravity system contribution to the lateral load resistance was evaluated, the columns and beams were designed to resist only gravity loads. Table 3.9 summarizes the section dimensions used in the building.

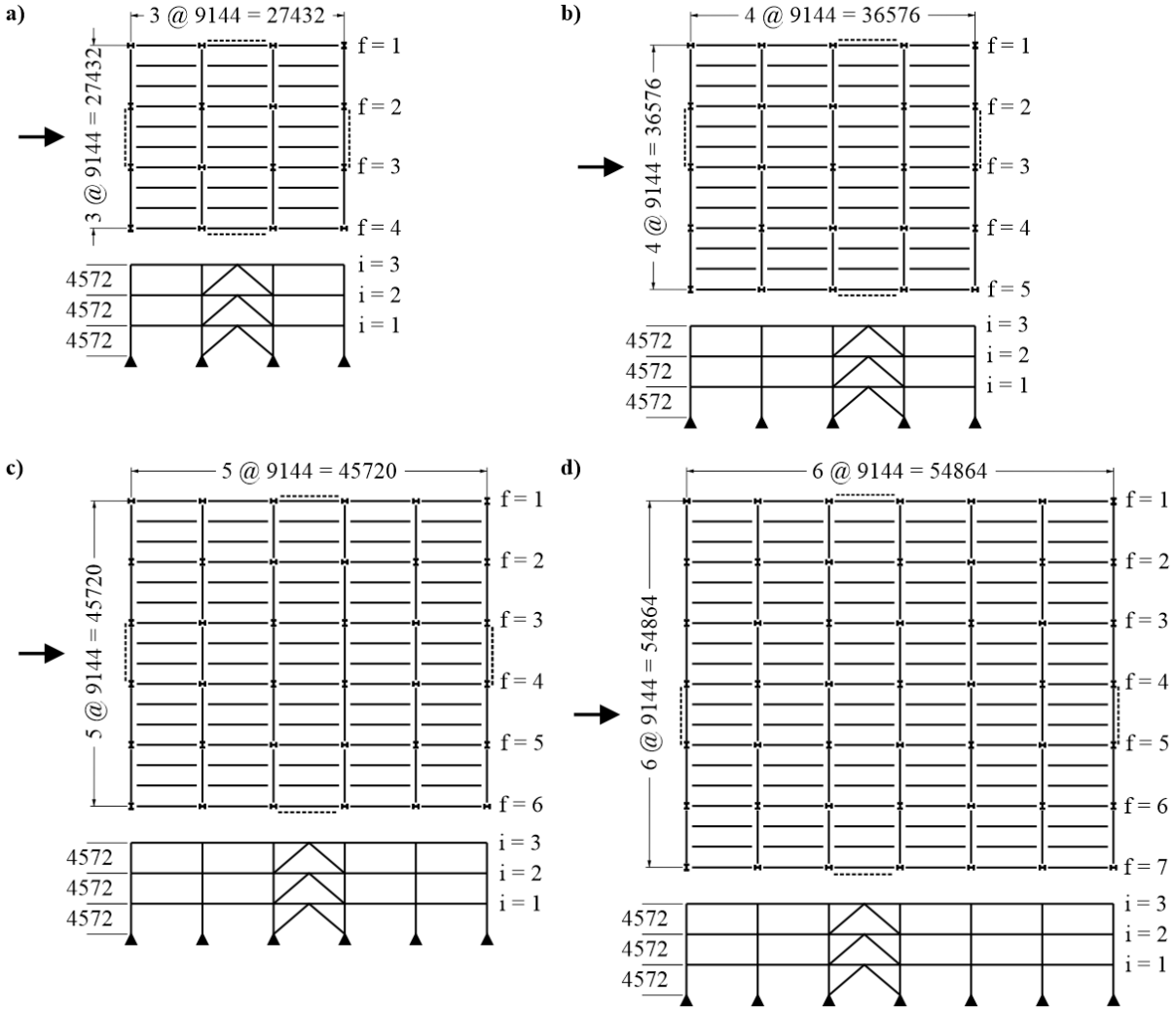


Figure 3.30. Configurations and dimensions of a) 3x3-, b) 4x4-, c) 5x5- and d) 6x6-bay buildings.

The buildings were simplified into 3-DDOF systems and a factor α varying between 0 and 1 was applied to the stiffness of the first storey. This process was then repeated with a stiffness reduction at the second and third storey. The stiffness and mass matrices of each system are presented in Figure 3.32. The stiffness matrices of Figure 3.32 vary mostly with the brace design of the building and include the P-delta effect, while the mass matrices depend only on the dimensions of the building (number of bays). With these matrices, the natural period of the building was calculated

with an Excel spreadsheet presented in Figure 3.33. in this spreadsheet, the period of the 3-DDOF system was determined for every 0.01 increment of α.

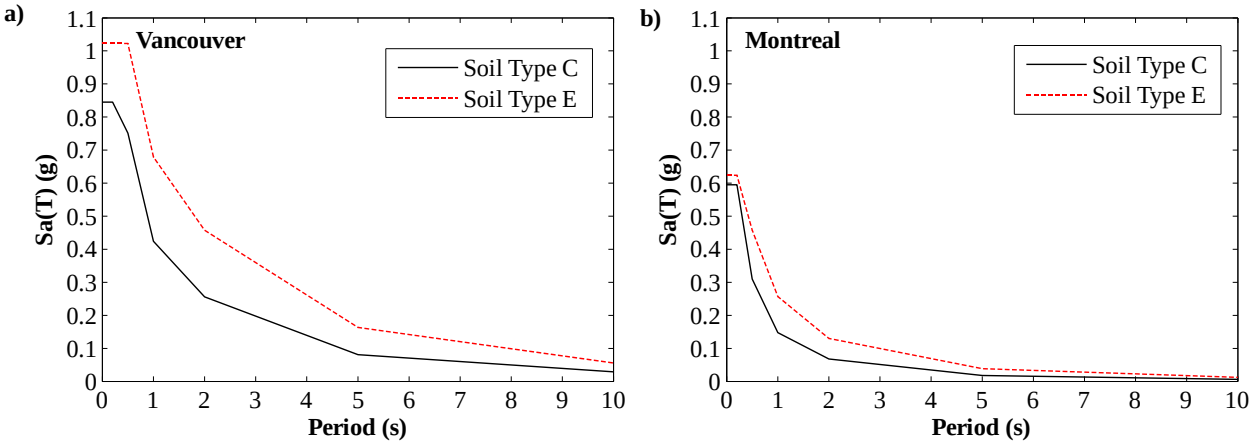


Figure 3.31. Response acceleration spectra of a) Vancouver b) Montreal.

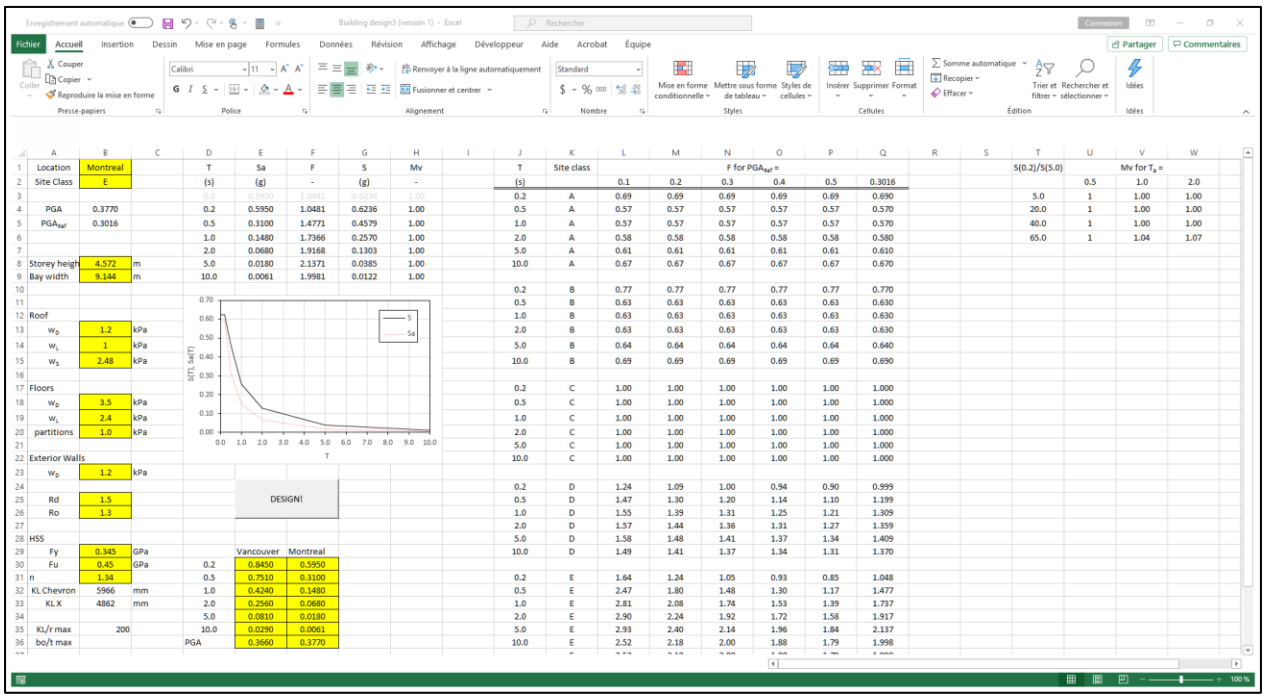
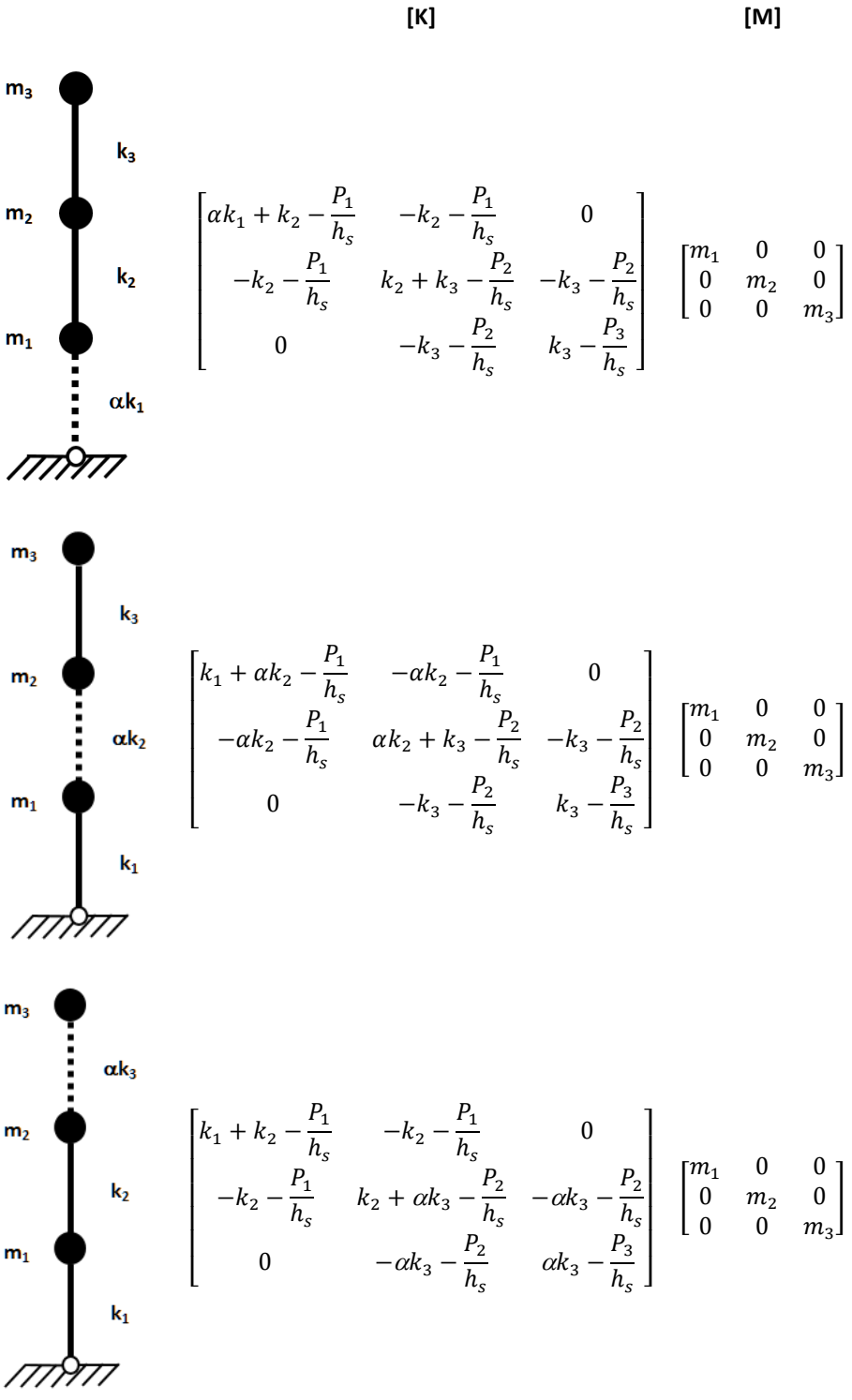


Figure 3.32. Excel spreadsheet developed to design the buildings.

Table 3.9. Member sections of buildings

	Building	Storey	Vancouver		Montreal	
			C	E	C	E
			Braced frame			
Braces	3X3	3	HSS140X140X6.4	HSS178X178X6.4	HSS114X114X4.8	HSS127X127X6.4
		2	HSS178X178X7.9	HSS203X203X7.9	HSS152X152X6.4	HSS178X178X6.4
		1	HSS203X203X7.9	HSS229X229X9.5	HSS178X178X6.4	HSS178X178X7.9
	4X4	3	HSS178X178X6.4	HSS178X178X7.9	HSS127X127X6.4	HSS152X152X6.4
		2	HSS229X229X7.9	HSS254X254X9.5	HSS178X178X7.9	HSS203X203X7.9
		1	HSS254X254X9.5	HSS254X254X12.7	HSS203X203X7.9	HSS229X229X7.9
	5X5	3	HSS203X203X7.9	HSS229X229X7.9	HSS152X152X6.4	HSS178X178X6.4
		2	HSS254X254X12.7	HSS254X254X15.9	HSS203X203X7.9	HSS229X229X9.5
		1	HSS254X254X15.9	HSS356X356X12.7	HSS203X203X12.7	HSS254X254X9.5
	6X6	3	HSS229X229X7.9	HSS254X254X9.5	HSS178X178X6.4	HSS203X203X7.9
		2	HSS254X254X15.9	HSS356X356X15.9	HSS229X229X9.5	HSS254X254X12.7
		1	HSS356X356X12.7	HSS406X406X15.9	HSS254X254X9.5	HSS254X254X15.9
Beams	3X3	3	W310X38.7	W360X44	W250X32.7	W200X35.9
		2	W250X58	W360X64	W310X44.5	W250X49.1
		1	W360X64	W310X79	W360X51	W250X58
	4X4	3	W310X44.5	W250X49.1	W200X35.9	W310X38.7
		2	W360X72	W310X79	W360X57.8	W310X60
		1	W310X79	W410X100	W250X58	W360X72
	5X5	3	W250X58	W310X67	W310X38.7	W250X49.1
		2	W310X86	W310X107	W360X64	W250X73
		1	W410X100	W310X117	W360X72	W310X79
	6X6	3	W360X64	W250X73	W250X49.1	W250X58
		2	W310X101	W310X129	W250X73	W310X86
		1	W310X117	W310X158	W310X79	W360X101
Columns	3X3	-	W250X73	W250X73	W250X73	W250X73
	4X4	-	W250X80	W410X100	W250X73	W250X73
	5X5	-	W250X101	W310X107	W250X73	W310X86
	6X6	-	W310X107	W310X143	W250X80	W250X101
			Gravity frame			
			Interior roof	**Exterior roof**	**Interior floor**	**Exterior floor**
Beam			W250x49.1	W250x49.1	W310x60	W250x49.1
Girder			W410X100	W360x64	W610X101	W360x72
Corner columns			W200x35.9			
Interior columns			W250x49.1			
Exterior columns			W250x73			



$$\begin{bmatrix} \alpha k_1 + k_2 - \frac{P_1}{h_s} & -k_2 - \frac{P_1}{h_s} & 0 \\ -k_2 - \frac{P_1}{h_s} & k_2 + k_3 - \frac{P_2}{h_s} & -k_3 - \frac{P_2}{h_s} \\ 0 & -k_3 - \frac{P_2}{h_s} & k_3 - \frac{P_3}{h_s} \end{bmatrix} \quad \begin{bmatrix} m_1 & 0 & 0 \\ 0 & m_2 & 0 \\ 0 & 0 & m_3 \end{bmatrix}$$

$$\begin{bmatrix} k_1 + \alpha k_2 - \frac{P_1}{h_s} & -\alpha k_2 - \frac{P_1}{h_s} & 0 \\ -\alpha k_2 - \frac{P_1}{h_s} & \alpha k_2 + k_3 - \frac{P_2}{h_s} & -k_3 - \frac{P_2}{h_s} \\ 0 & -k_3 - \frac{P_2}{h_s} & k_3 - \frac{P_3}{h_s} \end{bmatrix} \quad \begin{bmatrix} m_1 & 0 & 0 \\ 0 & m_2 & 0 \\ 0 & 0 & m_3 \end{bmatrix}$$

$$\begin{bmatrix} k_1 + k_2 - \frac{P_1}{h_s} & -k_2 - \frac{P_1}{h_s} & 0 \\ -k_2 - \frac{P_1}{h_s} & k_2 + \alpha k_3 - \frac{P_2}{h_s} & -\alpha k_3 - \frac{P_2}{h_s} \\ 0 & -\alpha k_3 - \frac{P_2}{h_s} & \alpha k_3 - \frac{P_3}{h_s} \end{bmatrix} \quad \begin{bmatrix} m_1 & 0 & 0 \\ 0 & m_2 & 0 \\ 0 & 0 & m_3 \end{bmatrix}$$

Figure 3.33. 3-DDOF system after the failure of the primary seismic load resisting system, with their stiffness and mass matrices including P-delta effects.

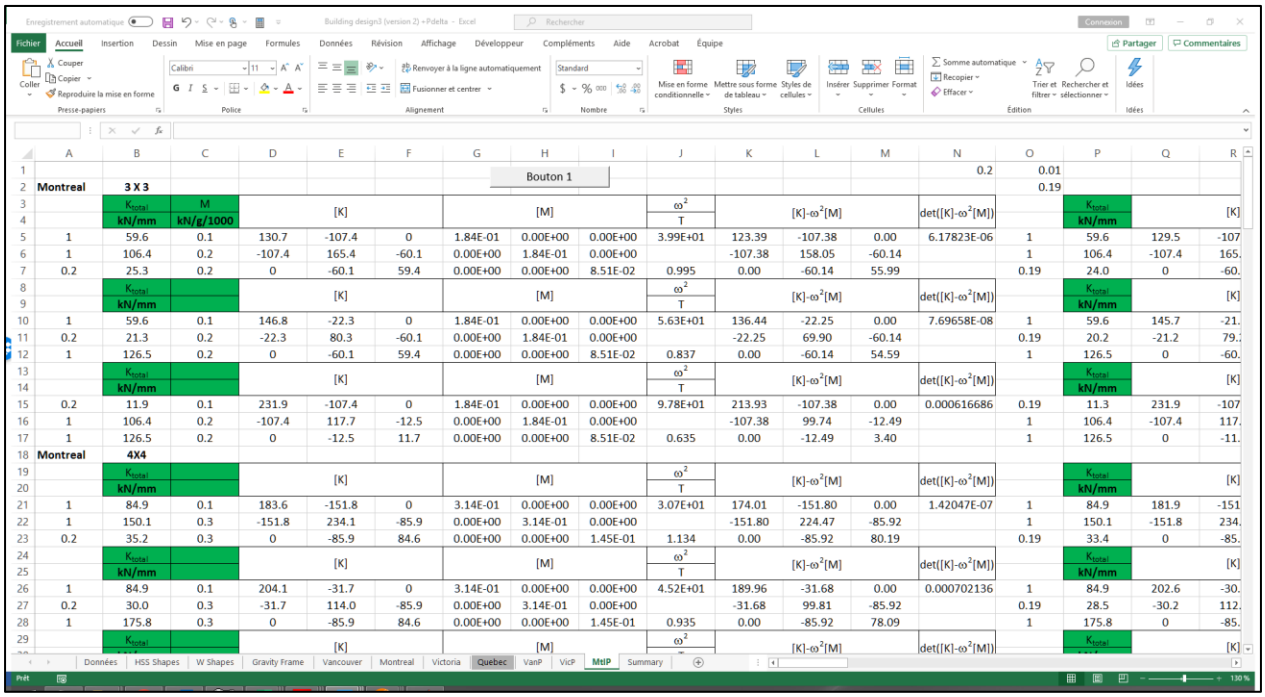


Figure 3.34. Excel spreadsheet developed to determine the fundamental period of the building with varying residual stiffness.

3.7.2 Development of the enhanced connection design procedure

Finally, a design procedure to determine the geometrical parameters of the top and seat angle connections required to enhance the reserve capacity and achieve adequate seismic response for steel building structures with Type CC chevron braced frames was established. This design procedure is developed to provide the gravity frame with sufficient stiffness and energy dissipation capacity to prevent structural collapse in case of the failure of brace connections at any level of the structure. Therefore, the amplified seismic load requirement for the design of brace connections is not required with enhanced connection. To develop this design procedure, the following steps were taken:

1. Define design guidelines to limit the influence of the enhanced connections on the original design of the building;
2. Develop a simple method allowing the evaluation of the building lateral stiffness including the braced frame post-failure residual stiffness and the gravity frame stiffness with springs in series and parallel;

3. Estimate the required rotational stiffness of the connection, the contribution of the web angles and the tensile stiffness and strength requirements of the top and seat angles;
4. Develop an iterative method to determine the top ang seat angle geometrical parameters;
5. Validate the design procedure with the numerical modeling of a design example.

An design example is presented in Chapter 8 to highlight the steps and methodology of the proposed design approach. The building used in this example is designed for Montreal, on soil type C, according to the design spectra prescribed by NBCC. The building consists of 5 bays of 9144 mm (30') in both direction and 3 storeys of 4572 mm (15') height. The geometry of the building is presented in Figure 3.35. The braced frames are designed according to the Conventional Construction (R_d of 1.5 and R_o of 1.3) provisions of CSA S16-14. Although the gravity system contribution to the lateral load resistance is evaluated, the columns and beams are stiff designed to resist only gravity loads. Table 3.10 summarizes the section dimensions used in the building. The web angles are also designed to resist only the gravity loads.

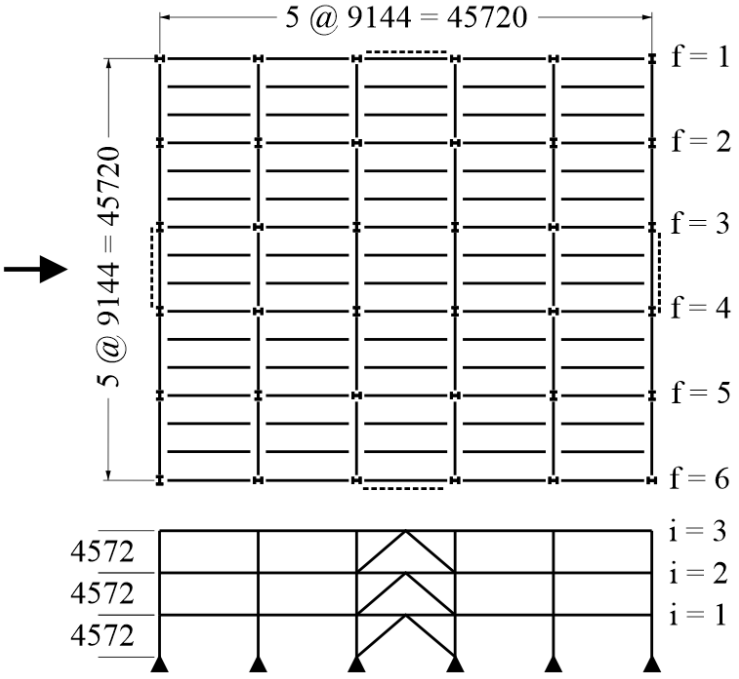


Figure 3.35. Example building geometry

Table 3.10. Member sections of example

Braced frame				
Storey	**Braces**	**Beams**		**Columns**
3	HSS152.4x152.4x6.4	W310x52		W310x97
2	HSS203.2x203.2x7.9	W310x74		
1	HSS203.2x203.2x12.7	W310x79		
Gravity system				
	Interior roof	**Exterior roof**	**Interior floor**	**Exterior floor**
Beam	W250x49.1	W250x49.1	W310x60	W250x49.1
Girder	W410X100	W360x64	W610X101	W360x72
Corner columns	W200x35.9			
Interior columns	W250x49.1			
Exterior columns	W250x73			

Half of this building was modeled in OpenSees to validate the seismic behaviour of the structure under 11 ground motions. This model included the beam-column connections of the gravity frame modeled with the component-based modeling approach and the proposed mathematical model presented in Chapter 7. As a comparative basis, the same building was also modeled with pinned gravity connection, to estimate the contribution of the gravity connections to the reserve capacity and on the dynamic response of the building.

Additionally, modal analyses were performed on the same two buildings to assess the influence of the reserve capacity on the fundamental period of the building supposing one and two fractured braces at each storey individually. These periods were calculated with the initial stiffness of the connections to present a qualitative assessment. The results of these analyses are presented in Chapter 9.

Finally, a general discussion highlighting the conclusions of the study and recommendations for future research work are proposed in chapter 10.

CHAPTER 4 ARTICLE 1: EXPERIMENTAL PARAMETRIC CHARACTERIZATION OF BOLTED ANGLE CONNECTION BEHAVIOR

Thierry Béland
École Polytechnique de Montréal, Montreal, Québec H3C 3A7, Canada
thierry.beland@polymtl.ca

Cameron R. Bradley
Tufts University, Medford, Massachusetts 02155, USA
cameron.bradley@tufts.edu

Jessalyn Nelson
Walter P. Moore, Houston, Texas 77010, USA
jnelson@walterpmoore.com

Joshua G. Sizemore, P.E., A.M.ASCE
Degenkolb Engineers, Seattle, Washington 98101, USA
jsizemore@degenkolb.com

Ali Davaran
École Polytechnique de Montréal, Montreal, Québec H3C 3A7, Canada
Ali.Davaran@polymtl.ca

Robert Tremblay
École Polytechnique de Montréal, Montreal, Québec H3C 3A7, Canada
robert.tremblay@polymtl.ca

Eric M. Hines, P.E., F.SEI
Tufts University, Medford, Massachusetts 02155, USA
eric.hines@tufts.edu

Larry A. Fahnestock, P.E., F.SEI
University of Illinois at Urbana-Champaign, Urbana, Illinois 61801, USA
fhnstck@illinois.edu

Paper submitted to *ASCE Journal of Structural Engineering*,
Submitted April 27th, 2019
Accepted for publication December 9th, 2019.

ABSTRACT:

This article describes an extensive experimental program that was conducted to characterize comprehensively the nonlinear sectional force-displacement response of bolted steel angle semi-rigid connections. A total of 139 tests were performed to investigate the influence of angle

thickness, position of the column bolts, bolt grade, and bolt pretension. The effect of loading sequence was also examined by applying static and dynamic monotonic and cyclic loading conditions. The observed behavior and failure modes are described. Key parameters defining the load-deformation response of the specimens are quantified, including the yield strength, initial stiffness, sharpness of the transition between initial and yielding phases, post-yielding stiffness properties, peak forces and deformations at failure. Monotonic test results were used to define a four-parameter power model that reproduces the force-deformation response of the angles. The influence of each geometric parameter, the bolt type and the loading protocols on the behavior of the bolted angles is also described. The tests showed that strength and stiffness increased when angle thickness increased and decreased when the distance between the heel and the column bolt is increased. The force-deformation response of monotonic tests can be used to predict the backbone of the cyclic and seismic responses. The angles subjected to cyclic and seismic tests however developed stable hysteretic response characterized by gradual softening, strength degradation, and smaller ultimate deformations compared to those subjected to monotonic loading.

KEYWORDS: Bolted Angle Connections; Full-Scale Tests; Steel Buildings; Seismic Response.

4.1 Introduction

Beam-column connections with double web angles and top and seat angles (2L-TS) can represent simple and cost-effective alternatives to conventional full strength, rigid moment connections for seismic applications (Elnashai et al. 1998, Shen and Astaneh-Asl 1999, Calado et al. 2000). These bolted connections are usually classified as partial strength semi-rigid connections (Chen and Kishi 1989, Kishi et al. 1997, Elnashai et al. 1998, Shen and Astaneh-Asl 1999). Their inherent flexibility translates into a larger deformation capacity in the connection components and thus, a larger connection ductility. Therefore, a compromise between stiffness and ductility can be achieved to optimize the connection behavior under seismic demands. A minimum stiffness is necessary to create moment frame action under lateral loading, but the connection should also sustain sufficient deformations to meet the energy dissipation objectives of the building design.

The stiffness and rotational capacity of bolted angle connections vary with several geometrical parameters: beam depth, web angle length (Abolmaali et al. 2003, Azizinamini 1985), angle thickness and column bolt position (Azizinamini 1982, 1985, Garlock et al. 2003, Shen and

Astaneh-Asl 1999, Yang and Tan 2013, Gong 2014). The bolt spacing also influences the effective width of the angles, their stiffness and deformation capacity (Azizinamini 1982, Faella et al. 1998). The bolt size, grade and pretension also influence the angle response, as the prying action takes an important part in the nonlinear behavior (Swanson and Gao 2000, Gong 2014). These influential parameters create a complex nonlinear behavior but offer the potential to achieve the optimal balance of connection stiffness and ductility. To date, however, influence of these parameters on the inelastic behavior of bolted angles connections has lacked systematic definition based on a comprehensive experimental program.

This paper presents an experimental investigation that has been conducted to generate a consistent and comprehensive data set on the nonlinear behavior of bolted angles with varying column bolt gage, angle thickness, column bolt grade and bolt pretension. These parameters were characterized under different loading conditions: static and dynamic monotonic tests, as well as cyclic, seismic and low-cycle fatigue tests. The monotonic response parameters investigated are the initial stiffness, yield strength, post-yield stiffness and the sharpness transition parameter. These parameters can be used to reproduce the force-deformation response with a four-parameter power model expressed in terms of load and deformation of the angles (Giuffre and Pinto 1970, Menegotto and Pinto 1973, Richard and Abott 1975). For the cyclic tests, the compressive yield force and the dissipated energy were also studied.

4.2 Experimental Program

4.2.1 Test setup

In a moment frame seismic force-resisting system (SFRS), flexural demand at a connection is resisted by tension-compression couples at the beam and column flanges where they meet at the beam-column joint. In a 2L-TS connection, the flange forces are transferred by angles (Figure 4.1). On the compressive side of the connection, the force is transferred from the beam flange to the column flange through bearing, whereas on the tension side of the connection, the force is transferred from the beam flange to the column flange through bending of the angle leg. Thus, the experimental program sought to replicate this condition and characterize the inelastic behavior of angles as shown in Figure 4.1. The experimental setup was simplified into two angles (to remove

asymmetry) bolted to a plate, which was bolted to a 1500 kN dynamic actuator with a maximum stroke of ± 125 mm. The actuator loaded the angle to replicate the displacement demand caused by a beam flange tension force. Similar testing setups were successfully used in prior studies (Azizinamini 1985, Garlock et al. 2003, Shen and Astanel-Asl 1999, Yang and Tan 2013, Gong 2014), although this simplified setup neglects the influence of the beam leg rotation on the angle behavior. The angle specimens were bolted to a stocky custom-built welded-wide-flange (WWF) column section, which was attached to a rigid reaction frame anchored to the strong floor. The angle deformations were measured with two LVDTs attached to the WWF section and small plates welded on the angle side, as shown in Figure 4.1. The LVDTs recorded only the angle displacement and the average displacement was used to define the specimen behavior. The applied force was measured by the actuator load cell and was assumed to be resisted equally by the two back-to-back angles. The force defining each specimen behavior thus correspond to half the recorded force.

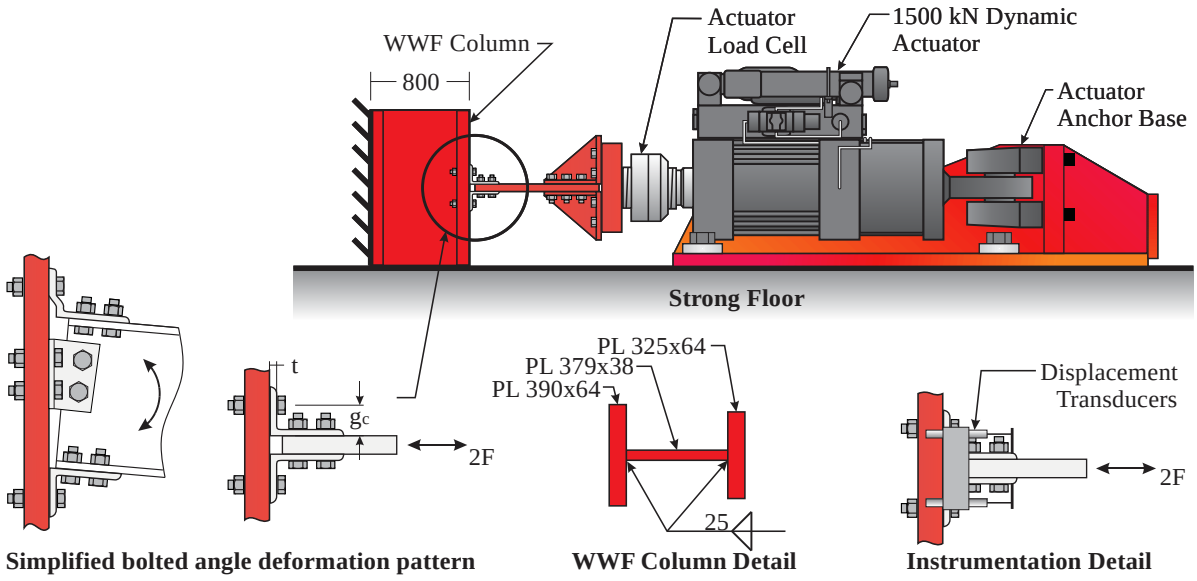


Figure 4.1. Experimental setup.

4.2.2 Angle specimens

Figure 4.2 shows the test matrix and the key geometric parameters used in the study: the column bolt gage, g_c, which corresponds to the distance between the heel of the angle to the center of the column leg bolts; the flexural span, g_2, equal to the distance between the top of the fillet and the bottom edge of the bolt head; and the angle thickness, t. The parametric study was established by

varying the angles thickness (t) from 7.9 to 19.1 mm (5/16 to 3/4 in.) and the bolt gage (g_c) from 63.5 to 114.3 mm (2.5 to 4.5 in.). In total, 19 test cases were considered. In Figure 4.2, the test case identification, the ratio g_2/t and the angle size are given for each of the test cases.

g_c (mm) \ t (mm)	7.9	9.5	12.7	15.9	19.1
63.5	**TC19** 3.80 L102x102x7.9	**TC1** 2.67 L102x152x9.5	**TC3** 1.38 L102x203x12.7		
76.2		**TC2** 4.00 L152x152x9.5	**TC4** 2.38 L152x203x12.7	**TC5** 1.70 L152x203x15.9	**TC6** 1.25 L152x203x19.1
88.9		**TC7** 5.33 L152x152x9.5	**TC9** 3.38 L152x203x12.7	**TC11** 2.50 L152x203x15.9	**TC13** 1.92 L152x203x19.1
101.6		**TC8** 6.67 L152x152x9.5	**TC10** 4.38 L152x203x12.7	**TC12** 3.30 L152x203x15.9	**TC14** 2.58 L152x203x19.1
114.3		**TC15** 8.00 L152x152x9.5	**TC16** 5.38 L152x203x12.7	**TC17** 4.10 L152x203x15.9	**TC18** 3.25 L152x203x19.1
g_b (mm)	57.2		76.2		
d_b (mm)	19.1		25.4		
e (mm)	32				
L (mm)	203				

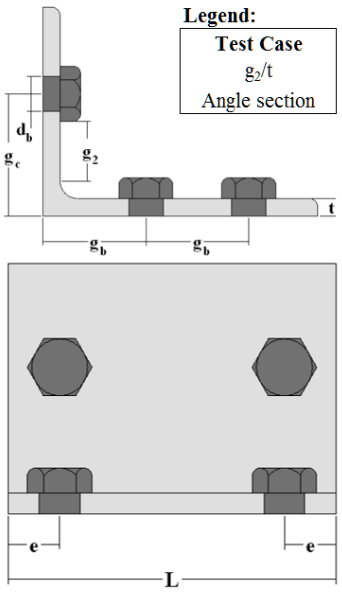


Figure 4.2. Test matrix.

Since most of the deformation was expected to occur in the flexural span g_2 in the column leg, between the bolt and the fillet, the ratio g_2/t was used as a key parameter. This ratio varied from 1.25 to 8.0, where stiffness increases as the ratio decreases. In all specimens, two bolts were used for the column leg. In every test case but TC19, the beam leg was attached with two bolt rows with a distance of g_b between the centerlines, to avoid bolt shear failure. For TC19, the beam leg of 102 mm allowed only one bolt row. Bolt sizes and grades were selected to ensure that failure would develop in the angles for all specimens: ASTM F3125 grade A325 19.1 mm bolts for angle thickness of 9.5 mm and lower, and ASTM F3125 grade A490 25.4 mm bolts for the thicker angles. All bolts were pretensioned with the turn-of-the-nut method, according to the requirements of CSA-S16-14 (CSA 2014). For some test cases with thick angles, additional specimens were tested with ASTM F3125 grade A325 bolts instead of ASTM F3125 grade A490 bolts to examine the effects of the bolt grade. Tests were also performed on specimens with snug tight bolts to investigate the impact of bolt pretension. These bolt condition variations were only applied to the column bolts.

4.2.3 Experimental procedures

Each of the 19 angle geometries were tested under monotonic static, monotonic dynamic, cyclic static, and dynamic seismic loading signals. For test cases TC9 and TC14, constant amplitude low-cycle fatigue tests were performed to investigate further the resistance to fatigue under inelastic cyclic demand. Each test was performed under displacement control conditions until failure of one angle specimen occurred.

4.2.3.1 Procedure for monotonic tests

For each test case, three monotonic tests were performed at three different strain rates to determine the influence of this parameter on the inelastic behavior and to obtain some repetitiveness in the experimental results. The first two tests performed were conducted under static strain rates of approximately 100 με/s and 600 με/s respectively. For each angle size, these strain rates were transformed into displacement rates using the relationship between displacements and strains obtained from an analysis of the angle modeled with fiber-based beam-column elements using OpenSees (Mazzoni et al. 2006). The third monotonic test aimed at investigating the influence of dynamic loading on the angle behavior. For each angle size, the imposed displacement rate was set to reach in 1 second the average ultimate deformation measured in the previous two specimens. The resulting strain rate was back calculated from the applied displacement using the OpenSees model. On average for all specimens, that strain rate was equal to 750000 με/s. In the tests, the strain rates were not measured using strain gages and the results are presented using the target values which may differ slightly from the actual strains experienced by the angles. For each test case, the results from the first test at 100 με/s was used as the reference for evaluating the impact of the other parameters investigated. The additional tests on specimens with different bolt grades and bolts in the snug tight condition were performed under monotonic loading at 100 με/s only.

4.2.3.2 Procedure for cyclic tests

The loading protocol used for cyclic tests was based on the protocol specified in the AISC Seismic Provisions (AISC 2010) for the qualification testing of beam-column joints in moment frames and detailed in Figure 4.3a. A prototype frame was used to transform the story drift from AISC to the displacement to be imposed on the specimens. Two beam-column connection sizes taken from the

prototype building studied by Hines et al. (2009) were considered for this transformation: a joint connecting a W310x33 beam to a W250x67 column bent about its strong axis, and a joint between a W410x67 girder and a W310x67 column bent about its weak axis. A structural model consisting of a cruciform beam-column assembly was used to determine connection rotations resulting from imposed story drifts. The rotations were then used to calculate the deformations sustained by the top and seat angles of the connections. For each test case, the semi-rigid connection properties of the angles in the model were those obtained from the first monotonic angle test. For each test case, one cyclic test was performed for each of the beam sizes of the prototype building. In the tests, the displacements were imposed slowly to represent static loading condition.

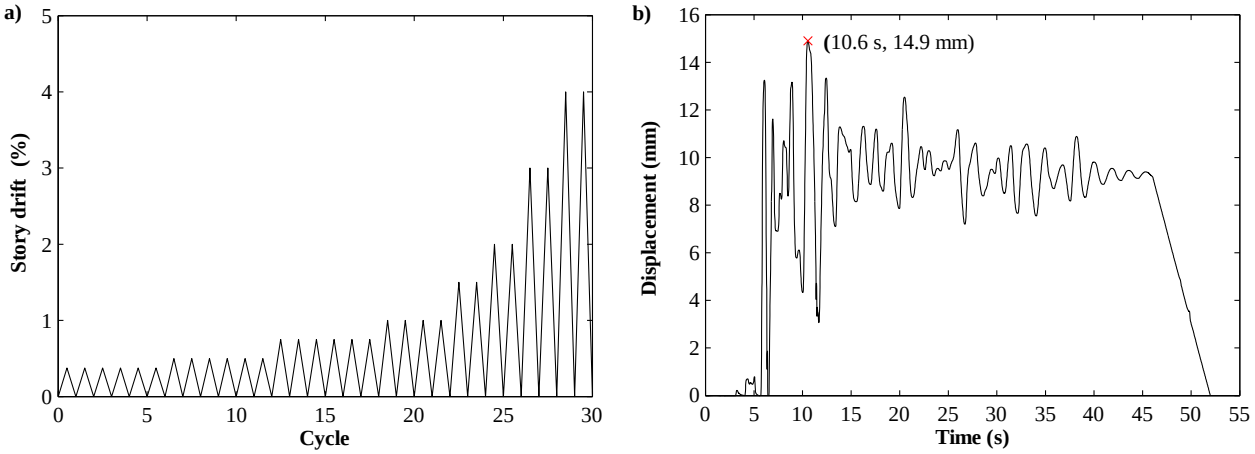


Figure 4.3. Loading protocols: a) AISC story drift-based demand for cyclic tests; b) Angle deformations for seismic tests.

4.2.3.3 Procedure for seismic tests

A test simulating dynamic seismic loading was performed for each test case. The time-history signal used for these tests was determined from the joint rotational demand computed for a three-story building model subjected to a seismic ground motion using OpenSees (Mazzoni et al. 2006). The joint rotation demand was then translated into the displacement demand shown in Figure 4.3b. For each specimen, this signal was applied three times, with gradually increasing scaling factors, to simulate ground motions of increasing intensities. The scale factors were determined from the angle ultimate deformation measured in the static cyclic tests. The first signal represented the demand from a moderate earthquake causing yielding of the connection, whereas the second one represented a major event imposing large plastic deformations without causing fracture. The third

signal represented an extreme earthquake causing fracture of the angle. At the end of the first two signal applications, the actuator force was reduced to zero and the residual deformation was used as the starting point for the signal of the subsequent test.

4.2.4 Procedure for low-cycle fatigue tests

For the two test cases where low-cycle fatigue was evaluated, a total of six tests were performed – two identical tests at three different amplitudes. The smaller amplitude was taken as the end of the yielding transition and the start of the mostly linear plastic phase described in the next section. The larger amplitudes corresponded to 60% of the angle ultimate deformation capacities measured in the static cyclic tests. The middle amplitude equaled the average between the two other amplitudes.

4.3 Test Results

4.3.1 Monotonic tests

The monotonic force-deformation response can be divided into two, three or four main phases that are illustrated in Figure 4.4. The first phase is referred as the yielding phase, characterized by an initially linear elastic response that progressively softens as yielding initiates and propagates in the angle legs. The second portion of the monotonic response is the plastic phase during which the specimens exhibit a nearly linear response characterized by a post-yielding, or plastic stiffness K_P.

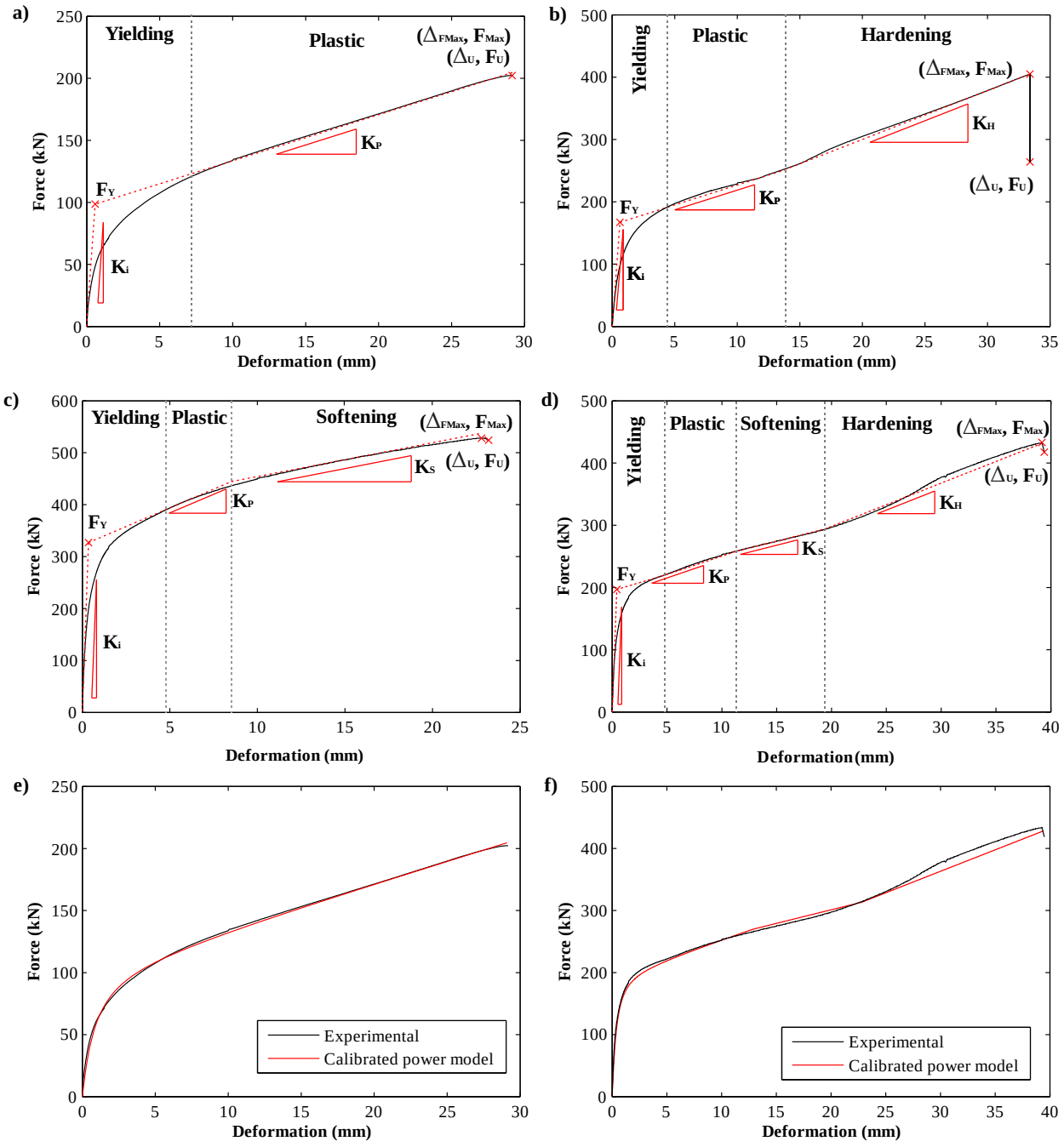


Figure 4.4. Force-deformation behavior from: a) Monotonic test with plastic phase only (TC16-1); b) Monotonic test with hardening (TC4-1); c) Monotonic test with softening (TC6-1); d) Monotonic test with softening and hardening (TC18-1); e) Comparison between monotonic experimental test and calibrated 4-parameter power model (TC16-1); f) Comparison between monotonic

For all specimens, the response in the yielding and plastic phases can be reproduced with the four-parameter power model expressed in terms of force and deformation of the angles (Giuffre and Pinto 1970, Menegotto and Pinto 1973, Richard and Abott 1975):

$$F = \frac{(K_i - K_P)\Delta}{\left[1 + \left(\frac{\Delta}{F_Y/K_i}\right)^R\right]^{\frac{1}{R}}} + K_P\Delta \qquad 4.1$$

The values of the initial stiffness, K_i, yield force, F_0, and progressive yielding transition parameter R were determined from test data using a least square calibration method. The plastic stiffness, K_P, was determined from a linear regression of the measured load-deformation values in the plastic phase. These values are presented in Tables 4.1, 4.2 and 4.3 for the 100 με/s, 600 με/s and 750000 με/s strain rate tests respectively.

Table 4.1 Key response parameters from monotonic tests at a strain rate of 100 με/s.

Test	F_0	K_i	R_0	K_P	K_S	Δ_S	K_H	Δ_H	$F_{F\,Max}$	$\Delta_{F\,Max}$	F_U	Δ_U
Case	kN	kN/mm	-	kN/mm	kN/mm	mm	kN/mm	mm	kN	mm	kN	mm
TC1	100	113	1.518	3.9	-	-	6.3	10.3	197	21.3	197	21.3
TC2	75	91	1.541	4.6	-	-	5.5	13.3	207	33.5	207	33.5
TC3	177	436	1.716	12.9	10.2	6.0	-	-	282	9.7	282	9.7
TC4	167	267	1.490	6.7	-	-	7.9	14.3	405	33.4	405	33.4
TC5	246	647	1.304	9.7	7.5	9.0	9.4	14.0	503	30.2	463	31.7
TC6	327	909	1.393	14.1	5.9	9.6	-	-	528	22.8	524	23.2
TC7	81	64	1.401	3.2	-	-	5.2	15.2	177	26.7	166	27.5
TC8	63	39	1.676	2.8	-	-	4.1	15.6	162	33.6	134	35.7
TC9	134	170	1.759	4.3	-	-	7.2	11.0	327	34.1	327	34.1
TC10	107	137	1.551	4.2	-	-	5	13.6	255	32.4	255	32.4
TC11	218	417	1.106	7.0	5.7	8.5	-	-	305	15.4	305	15.4
TC12	192	318	1.050	6.1	4.2	9.7	8.8	18.2	317	22.9	317	22.9
TC13	260	790	0.999	9.9	6.4	10.6	11	16.4	473	24.6	464	25.5
TC14	249	617	0.892	9.9	6.9	7.7	-	-	339	13.2	339	13.2
TC15	48	25	1.611	1.6	-	-	3.5	16.9	172	45.4	172	45.4
TC16	105	107	1.170	3.6	-	-	-	-	202	29.1	202	29.1
TC17	139	283	1.439	5.5	-	-	-	-	408	49.8	408	49.8
TC18	197	465	1.411	5.8	4.4	11.3	7.4	19.2	433	39.4	418	40.4
TC19	66	86	1.825	3.0	-	-	4.1	12.4	149	27.5	149	27.5

Table 4.2 Key response parameters from monotonic tests at a strain rate of 600 με/s.

Test Case	F_Y kN	K_i kN/mm	R_0 -	K_P kN/mm	K_S kN/mm	Δ_S mm	K_H kN/mm	Δ_H mm	$F_{F\,Max}$ kN	$\Delta_{F\,Max}$ mm	F_U kN	Δ_U mm
TC1	98	107	1.418	4.0	-	-	5.9	10.9	191	19.7	191	19.7
TC2	82	87	1.495	4.0	-	-	5.2	9.7	208	26.9	209	26.9
TC3	179	405	2.022	13.0	9.7	6.0	-	-	324	13.4	324	13.4
TC4	170	284	1.341	6.9	-	-	8.0	11.4	333	22.8	333	22.8
TC5	234	697	1.443	11.0	7.1	8.6	10.5	16.1	502	29.6	498	31.1
TC6	304	1011	1.497	17.2	6.3	8.5	-	-	541	25.4	539	25.7
TC7	85	58	1.305	2.9	-	-	5.9	17.4	198	30.1	148	34.8
TC8	64	41	1.592	2.9	1.7	10.5	4.7	17.4	176	35.4	150	36.9
TC9	132	164	1.665	4.9	-	-	6.8	16.4	334	35.8	334	35.8
TC10	104	132	2.228	4.6	-	-	-	-	278	39.6	278	39.6
TC11	220	460	1.405	8.6	5.9	8.3	-	-	312	13.3	312	13.3
TC12	191	342	1.260	5.9	4.3	10.9	5.3	16.5	288	19.6	288	19.6
TC13	300	723	0.975	11.9	7.3	7.5	-	-	402	12.1	402	12.1
TC14	253	574	0.976	9.5	6.1	9.1	-	-	368	16.8	368	16.8
TC15	48	22	2.121	1.6	-	-	3.3	16.2	161	43.7	161	43.7
TC16	90	102	1.550	4.0	-	-	-	-	212	31.5	212	31.5
TC17	138	262	1.535	4.8	-	-	5.9	16.8	416	49.8	416	49.8
TC18	197	408	1.385	6.0	4.3	10.9	8.6	23.9	439	40.9	429	41.6
TC19	71	79	1.575	3.0	-	-	3.8	12.0	155	26.6	155	26.6

Table 4.3 Key response parameters from monotonic tests at a strain rate of 750000 με/s.

Test Case	F_Y kN	K_i kN/mm	R_0 -	K_P kN/mm	K_S kN/mm	Δ_S mm	K_H kN/mm	Δ_H mm	$F_{F\,Max}$ kN	$\Delta_{F\,Max}$ mm	F_U kN	Δ_U mm
TC1	97	348	1.118	4.5	-	-	6.5	11.0	231	25.4	231	25.4
TC2	79	310	1.114	4.8	-	-	6.2	17.0	251	32.2	229	32.4
TC3	189	903	1.803	15.4	8.2	7.2	-	-	381	17.9	381	17.9
TC4	168	546	1.451	7.5	-	-	8.0	14.1	463	39.2	463	39.2
TC5	255	2181	1.625	10.1	7.3	9.7	10.0	14.4	559	33.8	535	34.9
TC6	375	1987	1.311	8.2	5.3	15.7	-	-	561	27.1	557	27.6
TC7	80	144	1.314	3.5	-	-	5.4	13.9	224	33.1	189	34.1
TC8	75	139	0.939	2.2	-	-	4.8	16.9	194	33.6	157	35.6
TC9	151	378	1.687	5.0	-	-	7.1	15.8	409	40.9	389	45.7
TC10	113	398	1.751	4.9	-	-	5.3	9.7	282	32.9	280	33.0
TC11	213	898	1.211	9.5	6.4	8.1	-	-	325	14.7	325	14.7
TC12	181	959	1.218	7.5	4.9	10.3	6.0	15.1	374	35.5	374	35.7
TC13	282	1695	0.895	13.1	6.3	8.7	11.4	18.0	465	19.9	465	19.9
TC14	232	1252	1.079	12.6	5.8	8.2	10.0	19.5	421	22.1	421	22.1
TC15	49	71	1.179	2.2	-	-	3.8	18.7	197	48.4	190	48.4
TC16	97	367	1.218	4.3	-	-	4.6	28.4	262	38.1	262	38.1
TC17	150	749	1.492	4.9	-	-	6.1	16.1	437	49.7	437	49.7
TC18	207	990	1.526	5.4	4.4	12.8	8.6	22.8	471	42.8	454	43.5
TC19	66	259	1.433	3.0	-	-	4.2	14.3	166	31.8	166	31.8

In 13% of the tests, the plastic phase extended up to fracture of the specimens, as shown in Figure 4.4a. The force-deformation relationship of the remaining specimens exhibited a third phase characterized by either a hardening (Figure 4.4b) or a softening (Figure 4.4c) behavior. The former was observed in 48% of the monotonic tests, mostly on specimens with larger g_2/t ratios. For these angles, hardening was observed until failure. For the specimens showing a softening third phase, softening continued up to failure for a sub-group representing 18% of the tested angles, usually those with smaller g_2/t ratios. For the remaining specimens, the softening third phase was followed by a fourth phase during which hardening took place before failure occurred, as illustrated in Figure 4.4d. Average softening and hardening stiffness values K_S and K_H in the third and fourth phases, as applicable, were evaluated through linear regression and the values are presented in Tables 4.1 to 4.3 for the three loading rates. The start of these phases are defined by Δ_S and Δ_H respectively. Explanations for these observed softening and hardening behaviors are provided in the last section of the article. Figure 4.4e shows that the yielding and plastic portion of the experimental response can be reproduced mathematically with the calibrated four-parameter power model (Giuffre and Pinto 1970, Menegotto and Pinto 1973, Richard and Abott 1975). The behavior of the softening and hardening phases can be represented by linearly adding the stiffnesses to Equation 4.1 and creating Equation 4.2. Figure 4.4f compares the experimental response with the calibrated four-parameter power model (Giuffre and Pinto 1970, Menegotto and Pinto 1973, Richard and Abott 1975) and the softening and hardening stiffnesses.

$$F = \begin{cases} \dfrac{(K_i - K_P)\Delta}{\left[1 + \left(\dfrac{\Delta}{F_Y/K_i}\right)^R\right]^{\frac{1}{R}}} + K_P\Delta & \text{for } \Delta \le \Delta_S \\ \dfrac{(K_i - K_P)\Delta}{\left[1 + \left(\dfrac{\Delta}{F_Y/K_i}\right)^R\right]^{\frac{1}{R}}} + K_P\Delta + (K_S - K_P)(\Delta - \Delta_S) & \text{for } \Delta_s < \Delta \le \Delta_H \\ \dfrac{(K_i - K_P)\Delta}{\left[1 + \left(\dfrac{\Delta}{F_Y/K_i}\right)^R\right]^{\frac{1}{R}}} + K_P\Delta + (K_S - K_P)(\Delta - \Delta_S) + (K_H - K_P)(\Delta - \Delta_H) & \text{for } \Delta > \Delta_{\mathrm{H}} \end{cases} \quad 4.2$$

Tables 4.4 and 4.5 present the key response parameters for the A325 and snug-tightened column bolts tests respectively. In the vast majority of the tests, failure occurred in the column or beam leg, depending on the angle geometry. Failure modes will be described in detail in the next section. In most tests, the maximum force, F_{max}, was reached just prior to failure; in other tests, the specimens

exhibited limited strength degradation before failure, resulting in force capacity at ultimate deformation, F_U, smaller than F_{max}. Tables 4.1 to 4.5 present deformation and force values when maximum force was reached (Δ_{FMax}, F_{Max}) and ultimate deformation before failure (Δ_U, F_U).

Table 4.4 Key-response parameters of monotonic tests with ASTM F3125 grade A325 bolts.

Test	F_Y	K_i	R_0	K_P	K_S	Δ_S	K_H	Δ_S	$F_{F\,Max}$	$\Delta_{F\,Max}$	F_U	Δ_U
Case	kN	kN/mm	-	kN/mm	kN/mm	mm	kN/mm	mm	kN	mm	kN	mm
TC9	139	193	1.776	5.9	-	-	6.6	12.9	422	43.5	422	43.5
TC10	111	141	1.643	4.2	-	-	5.1	14.2	250	30.7	245	34.3
TC11	211	548	1.204	8.2	6.4	8.7	9.1	16.2	368	21.1	368	21.1
TC12	182	436	1.227	7.5	5.5	8.8	6.7	16.0	318	21.5	318	21.5

Table 4.5 Key-response parameters of monotonic tests with snug-tight column bolts.

Test	F_Y	K_i	R_0	K_P	K_S	Δ_S	K_H	Δ_S	$F_{F\,Max}$	$\Delta_{F\,Max}$	F_U	Δ_U
Case	kN	kN/mm	-	kN/mm	kN/mm	mm	kN/mm	mm	kN	mm	kN	mm
TC1	95	90	2.099	5.0	-	-	-	-	187	19.5	187	19.5
TC2	75	67	1.795	4.6	-	-	5.0	11.6	217	29.9	217	29.9
TC4	148	84	2.583	7.3	-	-	10.3	13.7	326	23.3	326	23.6
TC9	118	84	2.020	6.6	-	-	-	-	330	34.3	330	34.3
TC10	94	54	2.680	5.3	-	-	-	-	271	40.9	257	44.2
TC11	191	105	1.819	8.2	-	-	9.8	11.5	371	22.3	371	22.3
TC12	180	86	2.137	7.2	5.7	9.6	-	-	272	16.5	272	16.5
TC15	42	18	1.879	2.1	-	-	3.3	17.4	146	46.2	146	46.2
TC16	82	51	2.051	4.2	-	-	-	-	210	32.9	210	32.9
TC19	56	69	3.400	3.8	-	-	-	-	138	26.4	138	26.4

4.3.1 Cyclic tests

Each cyclic test exhibited yielding and plastic phases, similar to the monotonic tests. In 12 of the 19 test cases, representing 47% of the cyclic tests, the specimens exhibited a softening of the backbone curve, as shown in Figure 4.5a. This softening response was therefore more common under cyclic loading compared to monotonic loading, likely because of the strength degradation due the to the cyclic nature of the loading. Alternatively, hardening of the backbone curve was observed in 26% of the cyclic tests, mostly in specimens with a large g_2/t ratio (Figure 4.5b). Hardening response in the cyclic tests occurred only in test cases for which hardening had been observed under monotonic loading.

In Figure 4.5a and b, the cyclic behavior of the specimens shows steep and constant unloading stiffness after reaching the cycle target displacement. When the load is reversed from tension to compression, the stiffness gradually decreases such that the resistance reaches a force value at zero deformation that remains nearly constant regardless of the number of cycles. This point is referred

to as the compressive yield force of the hysteretic response. Upon reloading, the angles show a high stiffness until the load is reversed from compression to tension. Beyond that point, the stiffness gradually reduces as tension force is increased. This portion of the hysteresis is characterized by a progressive stiffness reduction as the maximum imposed displacement is increased. However, all specimens exhibited no, or very little degradation in the second cycle of a given amplitude. Towards the end of the test, fracture initiated in the legs, which led to strength degradation.

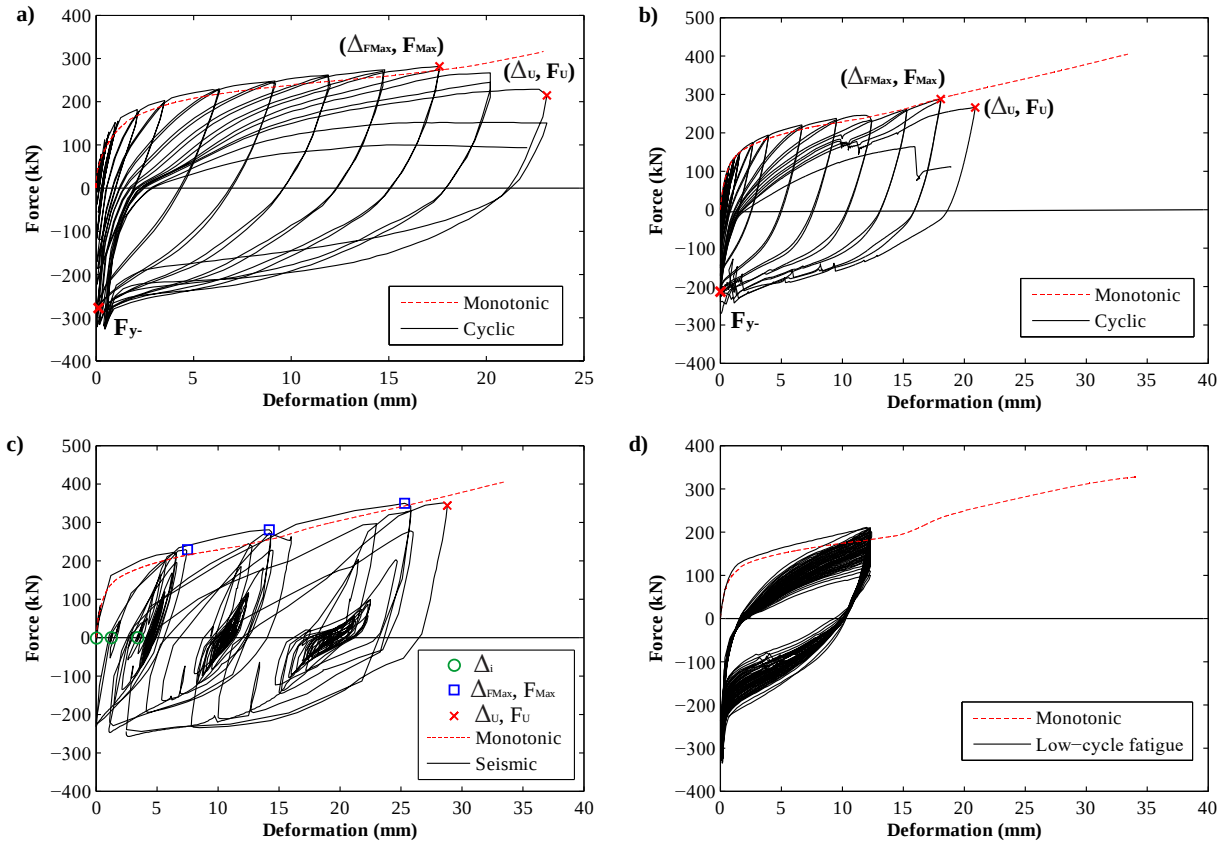


Figure 4.5. a) Monotonic test (TC12-1) and cyclic test with softening (TC12-4); b) Monotonic test (TC4-1) and cyclic test with hardening (TC4-4); c) Monotonic test (TC4-1) and Seismic test (TC4-6); and d) Monotonic test (TC9-1) and Low-cycle fatigue test (TC9-11).

The cyclic behavior of bolted angles was characterized by several key response parameters. Figure 4.5a and 5b show that a good representation of the cyclic backbone curve can be obtained from the monotonic curve. Therefore, Equation 4.1 with the values presented in Tables 4.1 to 4.5 offers an acceptable estimate of the cyclic backbone curve. However, Figure 4.5b shows that the deformation capacity is significantly reduced under cyclic loading as opposed to the monotonic response. Three

key response parameters, shown in Figure 4.5a and b can be used to characterize the cyclic behavior: the maximum load F_{Max} and the ultimate deformation Δ_U and the compressive yield force F_Y^-, characterizing the force at which the compressive excursions tend to converge. These values are presented in Table 4.6. In 92% of the cyclic tests, the cycle at which F_{Max} was recorded did not correspond to the one where the ultimate deformation occurred, as shown in Figure 4.5a and 5b. Therefore, the angles suffered progressive damage due to the cyclic loading.

Table 4.6 Key response parameters of cyclic tests.

Test case	W310 prototype beam					W410 prototype beam				
		Max. Force		Ultimate			Max. Force		Ultimate	
	F_Y^-	F_{Max}	$\Delta_{F\,Max}$	F_U	Δ_U	F_Y^-	F_{Max}	$\Delta_{F\,Max}$	F_U	Δ_U
	kN	kN	mm	kN	mm	kN	kN	mm	kN	mm
TC1	-110	162	19.2	144	22.1	-110	166	21	154	21.2
TC2	-90	161	22.1	135	25.2	-89	167	23.8	165	27.7
TC3	-331	301	11.5	264	17.2	-322	305	12.4	260	15.9
TC4	-297	288	18	266	20.8	-283	287	21.3	245	21.4
TC5	-529	377	16.5	241	22	-585	438	21.7	289	21.8
TC6	-794	494	15.1	424	18.1	-720	505	18.9	499	19
TC7	-85	142	22.5	93.9	25.6	-86	148	22.5	140	26
TC8	-69	124	26	73.2	28.8	-70	125	27.2	30.1	30.7
TC9	-186	244	18.6	199	18.7	-179	259	19.3	62.5	26
TC10	-145	195	21.9	169	24.8	-153	201	24.4	125	28.1
TC11	-449	315	13.1	168	20.3	-520	298	9.3	238	20.5
TC12	-372	282	17.6	215	23.1	-358	283	17.1	161	23.5
TC13	-783	430	13.6	429	14.3	-730	457	23.3	457	23.3
TC14	-642	370	16.5	323	19.4	-601	378	20.8	271	21.2
TC15	-49	112	29	109	32.4	-49	114	29.9	100	30
TC16	-110	180	22.3	172	22.7	-107	184	24	184	24
TC17	-322	279	29.7	253	30	-335	283	29.6	283	29.6
TC18	-602	341	26.2	143	29.2	-625	350	27.9	332	28.2
TC19	-72	100	16.6	67	22.9	-76	106	19.6	76	23.1

4.3.1 Seismic tests

All specimens sustained the first two seismic test signals without failure except for TC17-6, which failed during the second signal. As expected, all the remaining specimens failed during the third loading signal during which the monotonic ultimate deformation was reached and exceeded. Figure 4.5c shows the response of a specimen subjected to the three seismic signals with increasing

amplitudes. The specimens exhibited similar hysteretic response compared to the ones obtained in cyclic tests. Because the maximum amplitudes vary between cycles and the angles do not return to their undeformed position within cycles, it is possible to see pinching hysteretic behavior. Also, the reloading stiffness in tension is governed by the peak load and deformation reached in a previous cycle. The key response parameters characterizing the three different loadings are shown in Figure 4.5c: the initial deformation Δ_0 and the maximum force F_{Max}. The ultimate deformation Δ_U of the specimens is also presented. These key response parameters are presented in Table 4.7, along with the amplification factors of each loading.

Table 4.7 Key response parameters from seismic tests.

Test Case	Increment 1				Increment 2				Increment 3					
	AF 1	Δ_0	Max. Force		*AF 2*	Δ_0	Max. Force		*AF 3*	Δ_0	Max. Force		Ultimate	
			F_{Max}	$\Delta_{F\,Max}$			F_{Max}	$\Delta_{F\,Max}$			F_{Max}	$\Delta_{F\,Max}$	F_U	Δ_U
	%	mm	kN	mm	%	mm	kN	mm	%	mm	kN	mm	kN	mm
TC1	65	0	132	9.6	130	1.2	180	20.7	220	3.1	201	27.8	96	36
TC2	70	0	123	10.3	140	1.8	159	22.5	230	4.4	218	34.5	188	38.8
TC3	66	0	272	6.4	125	0.8	313	11.6	200	1.2	324	15.1	245	21.1
TC4	50	0	229	7.3	100	1.2	282	14.4	175	2.6	352	28.5	342	28.8
TC5	50	0	318	7.1	100	0.8	391	15.6	175	2.2	480	28.1	467	28.3
TC6	50	0	422	7.2	100	1	493	15.5	175	2.5	569	25.1	501	28.6
TC7	100	0	113	9.8	200	1.6	142	19.7	350	2.4	193	30.4	30	35
TC8	100	0	94	11.2	200	2	121	21.1	350	3	178	33.7	31	43.9
TC9	65	0	198	9.5	130	1.7	259	21	230	3.7	311	33.6	262	38.1
TC10	75	0	168	11	150	1.6	216	19.6	250	3.6	209	28.2	57	41
TC11	60	0	287	7.7	120	0.9	353	16.9	200	3.1	366	26.8	337	33
TC12	65	0	253	9.1	130	1.4	307	20.6	230	3.3	312	25	199	37.6
TC13	60	0	360	8.5	120	1.1	449	18.4	200	2.4	533	28.4	502	32.4
TC14	60	0	336	8.5	120	1	392	16.6	-	-	-	-	-	-
TC15	85	0	68	12.5	170	2.4	112	27.6	285	5.9	130	30.6	37	31.2
TC16	100	0	158	14.7	125	2.1	171	20.7	210	4.7	231	32.1	171	32.4
TC17	-	-	-	-	-	-	-	-	-	-	-	-	-	-
TC18	75	0	263	10.6	150	1.7	330	23.9	260	4	433	37.9	297	43
TC19	65	0	90	9.5	130	1.2	118	18	200	2.8	92	23.1	32	35.7

4.3.2 Low-cycle fatigue tests

Low-cycle fatigue tests were performed for two test cases: TC9 (g_2/t = 3.38) and TC14 (g_2/t = 2.58). In each case, 6 tests were performed (2 tests x 3 amplitudes). The number of cycles prior to fracture are presented in Table 4.8 for each test, along with the displacement amplitudes imposed. Figure 4.5d shows a typical hysteretic curve from a low-cycle fatigue test. In the first excursion of the test, the behavior was similar to the one of the monotonic test, while the hysteretic behavior coincides with the observations of the cyclic tests. However, as the test progressed, the maximum force gradually decreased in both the reloading and unloading phases of the hysteretic curve. The final strength degradation was more significant in tests with a larger number of cycles before fracture. The degradation towards the end of the test was caused by crack initiation near the bolts and, subsequently progression of cracks that reach the full width of the angle legs.

Table 4.8 Key response parameters from low-cycle fatigue tests.

Test	g_2/t	Amplitude	Cycles	
		mm	Test 1	Test 2
TC9	3.38	4.1	424	360
		12.3	41	44
		20.5	12	8
TC14	2.58	4.1	259	322
		7.2	81	81
		10.3	44	46

4.4 Failure modes

Three primary failure modes have been observed during the testing program: beam leg fracture, column leg fracture and bolt fracture. Additionally, net section fracture at the column bolt line was observed in some specimens. This latter failure mode was only partial and did not result in a significant loss of strength capacity or stiffness. It is therefore considered as a secondary failure mode. For each angle, the failure mechanism was mainly governed by its geometric parameters, g_2/t and the loading protocol. Table 4.9 presents the occurrence of each failure mode for the monotonic, cyclic, seismic and low-cycle fatigue tests performed.

Table 4.9. Failure mode occurrence.

Test Case	g_2/t	Monotonic			Cyclic		Time-History			Fatigue	
		Beam	Colum	Bolt	Beam	Colum	Beam	Colum	Bolt	Beam	Colum
TC1	2.67	2	3	-	1	1	1	-	-	-	-
TC2	4.00	-	4	1	2	-	1	-	-	-	-
TC3	1.38	4	-	-	2	-	1	-	-	-	-
TC4	2.38	1	4	-	2	-	-	-	-	-	-
TC5	1.70	-	-	3	2	-	1	-	-	-	-
TC6	1.25	-	-	3	2	-	1	-	-	-	-
TC7	5.33	-	3	-	-	2	-	1	-	-	-
TC8	6.67	-	3	-	-	2	-	1	-	-	-
TC9	3.38	3	3	-	-	1	-	1	-	1	5
TC10	4.38	1	3	-	-	2	-	1	-	-	-
TC11	2.50	3	2	-	2	-	-	1	-	-	-
TC12	3.30	1	4	-	-	2	-	1	-	-	-
TC13	1.92	2	-	1	1	1	1	-	-	-	-
TC14	2.58	2	2	-	1	1	-	1	-	6	-
TC15	8.00	-	4	-	-	2	-	1	-	-	-
TC16	5.38	-	3	-	-	2	-	1	-	-	-
TC17	4.10	-	3	-	-	2	-	-	-	-	-
TC18	3.25	-	-	3	-	2	-	-	1	-	-
TC19	3.80	-	4	-	1	1	-	1	-	-	-
Total	-	19	45	11	16	21	6	10	1	7	5

4.4.1 Column leg fracture

Among the monotonic tests, 60% of the angles fractured in the column leg, of which 76% occurred in angles with an aspect ratio g_2/t larger than 3.0. Column leg fracture was also observed in 57% of the specimens loaded with cyclic, seismic and low-cycle fatigue procedures. The angles with a g_2/t ratio larger than 3.0 represent 86% of the column leg fracture occurrences observed in these tests. Therefore, the column leg fracture is expected to occur in slender angles with a large flexural span.

Figure 4.6a presents the deformation at fracture of typical bolted angles loaded monotonically. The beam leg uplift from the pull plate observed in this figure created a rotation of the fillet which reduced the rotational demand on the section of the column leg near the fillet. This behavior was not systematically observed in all monotonic tests but occurred in the more flexible specimens. In

cyclic tests, fillet rotation was also observed, along with the beam leg uplift, but to a lesser extent, as shown in Figure 4.6b.

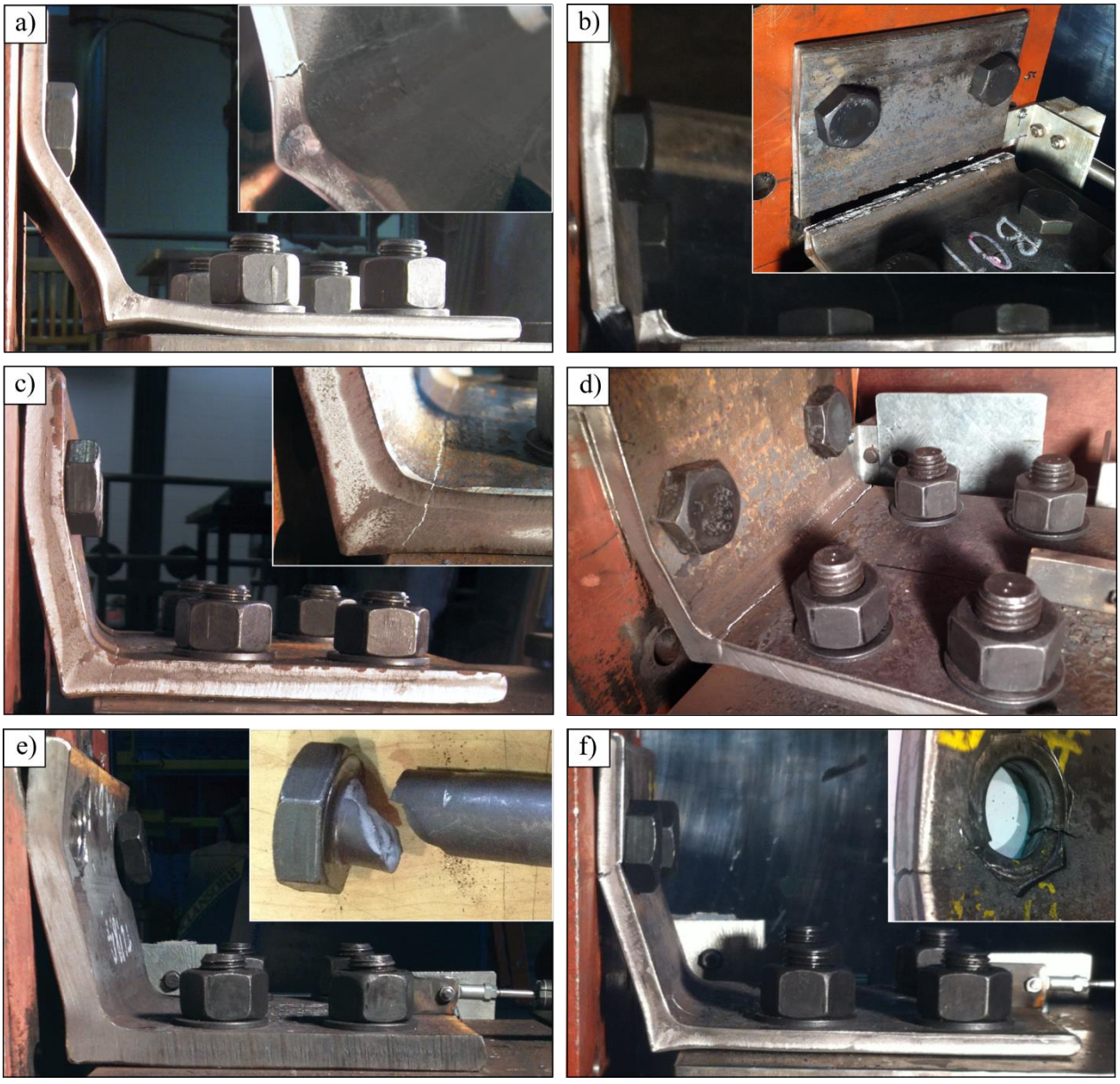


Figure 4.6. Observed behavior: a) Column leg fracture in monotonic test (TC10-2); b) Column leg fracture in cyclic test (TC10-4); c) Beam leg fracture in monotonic test (TC14-2); d) Beam leg fracture in cyclic test (TC5-5); e) Bolt fracture (TC18-6); and f) Net section tension fracture (TC10-4).

The cracks in the Figure 4.6b initiated at the surface of the column leg near the fillet. These small cracks indicate that the column leg fracture is mostly caused by large rotational demand in the plastic hinge region above the fillet. In most monotonic tests, the cracks propagated through the thickness of the leg on one edge of the angle, causing a fracture over a part of the angle width. This point marked the end of the test. The angles still exhibited a residual strength capacity after fracture. A similar cracking initiation was observed in the cyclic tests. However, the failure of the column leg generally occurred on the entire width of the angle, causing a complete fracture. Since the rotational demand at the column leg plastic hinge was constant along the width of the angles, the damage caused by the low-cycle fatigue was more uniformly distributed. Once the cumulated damage was sufficient, fracture occurred over the whole width of the specimen, unlike the behavior observed in monotonic tests.

4.4.2 Beam leg fracture

The beam leg fracture near the fillet was observed mainly in stockier angles, at relatively small ultimate deformations. In the monotonic tests, 25% of the angles experienced beam leg fracture, of which 74% were observed in specimens with an aspect ratio g_2/t smaller than 3.0. In the cyclic tests, the beam leg failure mode was observed in 43% of the tests, among which 67% occurred in angle specimens with a g_2/t ratio smaller than 3.0. Hence, the plastic hinge forming in the beam leg is more vulnerable to low-cycle fatigue, as most of these failures were observed under cyclic conditions.

Figure 4.6c presents a typical beam leg fracture under monotonic loading. The fillet tends to rotate along with the column leg, reducing the rotation demand in the column leg plastic hinge, but concentrating the rotation in the beam leg plastic hinge. The flexural moment transferred from the column leg through the fillet, combined with a large tensile load, provoked the beam leg fracture. These specimens did not show significant cracking prior to fracture. However, a continuous fracture along the entire width and over the full thickness was observed in most specimens. This cracking pattern is attributed to the large axial load and resulted in a significant loss of strength capacity.

In the cyclic tests, low-cycle fatigue resulted in a progressive cracking along the width of the angles prior to fracture, as shown in Figure 4.6d. This cracking started in the plastic hinge region, over a

length approximately corresponding to the bolt edge distance, and progressively spread across the angle width up to fracture. This behavior resulted in a progressive loss of strength capacity between the cycles.

4.4.3 Bolt fracture

This failure mode was observed in 15% of the tests, in angles with either a large thickness of 19.1 mm (TC6, TC13 & TC18), or a small column gage (g_c) of 76.2 mm (TC2, TC5 & TC6). These geometrical parameters created a significant prying action in the column bolts which, combined with the large angle load capacity, caused bolt tension failure.

Figure 4.6e presents this failure mode. Because the bolts failed first in these connections, no significant damage were observed in the angles, aside from large inelastic deformations. The fracture occurred in the bolt shank, near the head. This failure mode occurred in angles that developed large tensile loads, either due to the high stiffness of the angle, or the large geometric hardening. These large forces were amplified by important prying action. Plastic rotation also occurred in the angle leg under the bolt head, which created flexural demand in the bolt shank. The combination of these effects caused the bolt fracture.

4.4.4 Net section fracture near the column bolts

Net section fracture is defined by a partial fracture of the angle leg between the column bolt holes and the edge of the angle, as presented in Figure 4.6f. In some cases, the fracture also extended between the two column bolts, although complete net section fracture was not observed. This fracture generally did not influence significantly the stiffness or strength capacity of the specimens.

Net section fracture was observed in 12 of the 19 different test cases, with various angle thicknesses, column gages, and g_2/t ratios ranging from 1.38 to 6.67. Of the 51 tests where this secondary failure mode was observed, 27%, 39%, 22% and 12% occurred in monotonic, cyclic, seismic and low-cycle fatigue tests respectively. Furthermore, 72% of the net section fracture cases were associated with a column leg fracture as a primary mode, while the beam leg fracture mode coexisted with net section fracture in only 28% of these tests. Consequently, net section fracture is more likeky to occur in more flexible specimens, where the column bolt plastic hinge experiences larger rotational demands.

4.5 Influence of design parameters

4.5.1 Influence of bolt gage

A primary objective of the current study was to characterize the influence of the bolt gage g_c, i.e. the distance between the column leg bolts and the angle heel. Five different column bolt gages were considered, ranging from 63.5 to 114.3 mm (2.5 to 4.5 in.). Figure 4.7a to e present the influence of the column bolt gage for each angle thickness tested, varying from 7.9 to 19.1 mm (3/8 in. to ¾ in.) on the monotonic force-deformation response.

Every bolted angle specimen exhibited ductile behavior. However, the initial stiffness and the force causing the yielding increased as g_c decreased. A smaller distance between the column bolts and the angle corner translated into a shorter flexural span g_2 in the column leg. Therefore, larger stiffness values, both elastic and plastic, were observed in specimens with smaller bolt gages for a constant angle thickness. The ultimate deformation generally increased along with the bolt gage g_c, because a larger deformation is required to reach the ultimate plastic hinge rotation with a longer distance between plastic hinges.

The specimens with larger g_c developed more pronounced geometric hardening at large deformations. This behavior is caused by a combination of tension and flexural resistances that are mobilized in the column leg. However, the hardening begins at a larger deformation when g_c is increased. In monotonic tests this geometric hardening was amplified by the beam leg uplift.

As described previously, some specimens exhibited softening at large deformations before or instead of hardening. This softening was mainly observed in thicker angles with a short column gage g_c. In these specimens, the rotational demand near the fillet was mostly concentrated in the beam leg, as the fillet rotated along with the column leg. The bending moment created by this rotational demand, combined with the large axial load in the beam leg, resulted in a progressively decreasing plastic stiffness, thus softening.

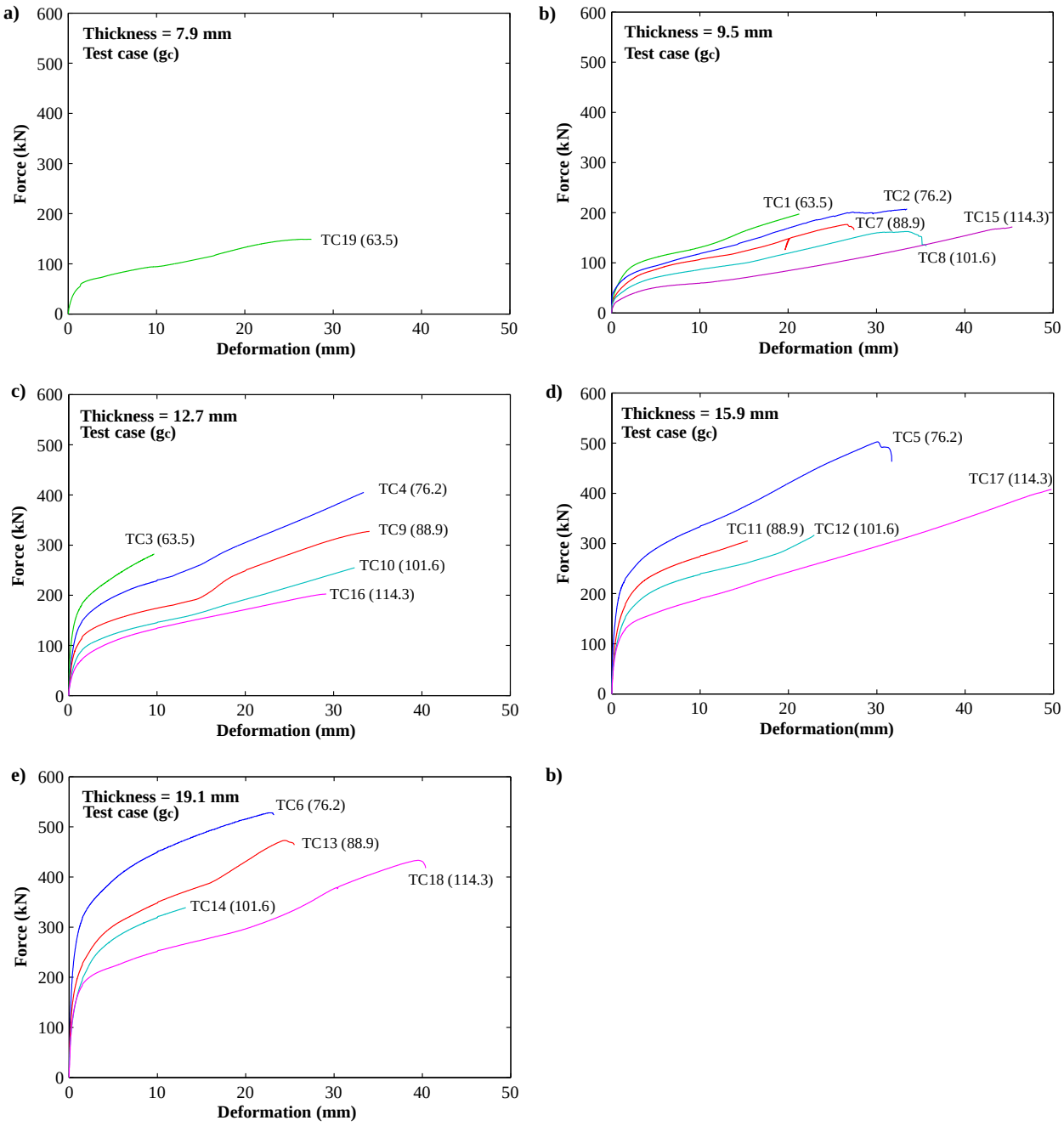


Figure 4.7. Influence of column bolt gage g_c on the force-deformation response in monotonic tests for specimens with thickness of a) 7.9 mm; b)9.5 mm; c) 12.7 mm; d) 15.9 mm; and e) 19.1 mm.

4.5.2 Influence of angle thickness

A second main objective of the study was to characterize the influence of the angle thickness on their nonlinear behavior. Five thicknesses were considered ranging from 7.9 to 19.1 mm (5/16 to 3/4 in.). Figure 4.8a to e illustrate the influence of the angle thickness on the monotonic load-deformation behavior for each column bolt gages g_c, ranging from 63.5 mm to 114.3 mm respectively.

In general, the initial stiffness, the yield force and the plastic stiffness increased along with the angle thickness, because of its importance in the flexural stiffness and strength of the angle legs. However, as the angle thickness increases, the ultimate deformation capacity of the angle decreases. Assuming a linear strain distribution across the angle leg thickness, the thicker angles reach the ultimate strain of the steel material at a smaller rotation in the plastic hinge, thus causing fracture at a smaller deformation.

4.5.3 Influence of the aspect ratio g_2/t

The influences of the column gage and thickness were evaluated independently in the previous sections. In design, the use of a third parameter, g_2/t, that reflects the ratio of the two studied parameters can also be useful to obtain optimized angle properties to meet specific design objectives for the connections.

As shown in Figure 4.9a and 9b, the initial stiffness K_i and yield strength F_Y both are inversely proportional to the aspect ratio g_2/t and their effects are more pronounced when the thickness increases. Therefore, the thickness has a dominant influence on the angle stiffness and strength for the entire non-linear behavior. From the perspective of beam-column connections made with angles, which could contribute to seismic collapse resistance, a high g_2/t ratio would provide some energy dissipation through yielding while limiting the moment transmitted to the column due to the angle flexibility. This behavior combination is beneficial since the moment limitation could prevent column plastic hinge formation, which may result in a story collapse mechanism. The plastic, softening and hardening stiffnesses were also found to depend on the geometrical properties of the angles. Figure 4.9c presents the influence of the aspect ratio g_2/t on the stiffness ratio K_P/K_i.

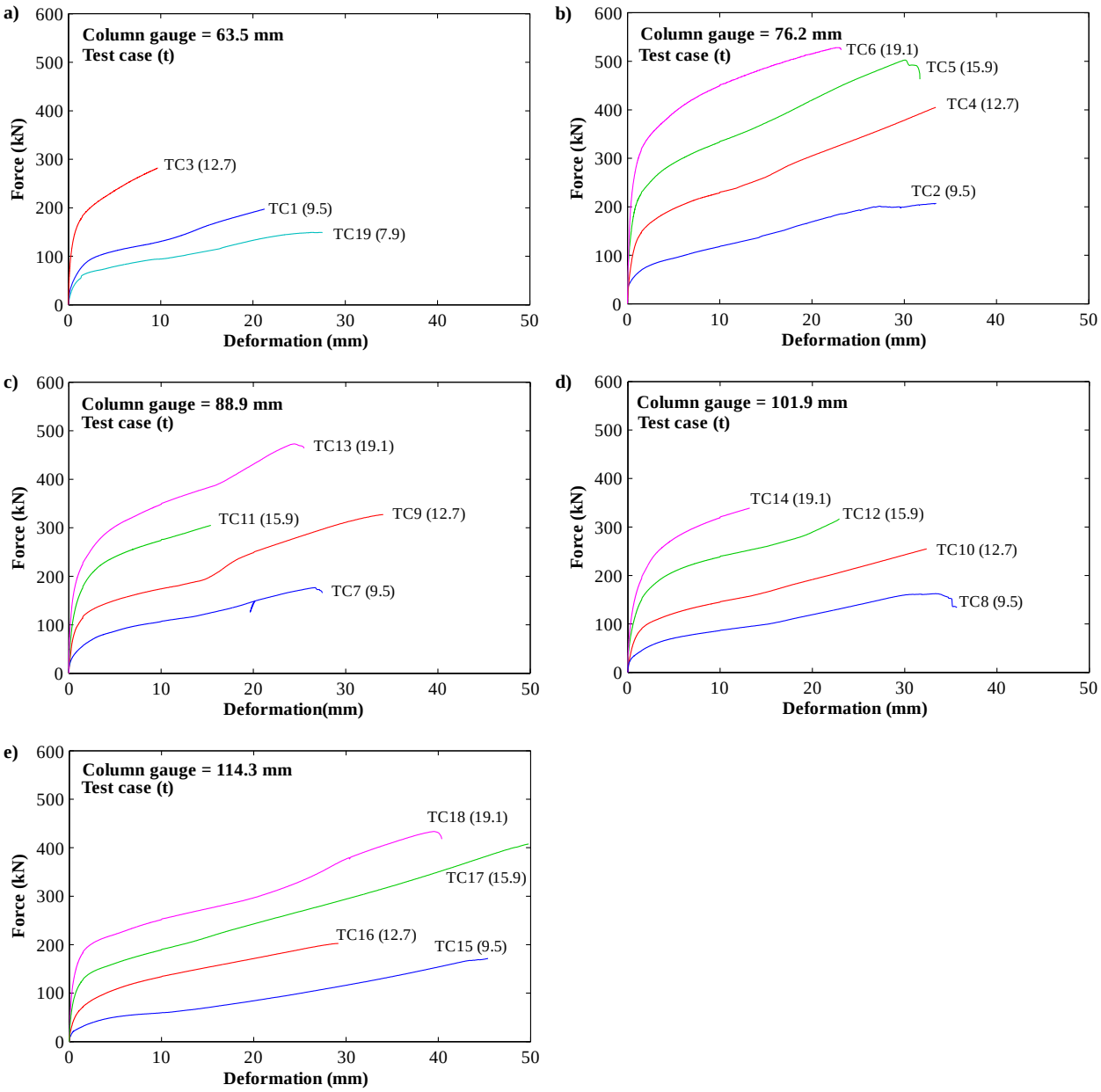


Figure 4.8. Influence of angle thickness *t* on the force-deformation response in monotonic tests for specimens with column gage of a) 63.5 mm; b) 76.2 mm; c) 88.9 mm; 101.9 mm; and 114.3 mm.

The aspect ratio does not significantly influence the stiffness ratio K_p/K_i for the thick specimens, as it averaged 1.5% for every 19.1 mm-thick specimens. A larger K_p/K_i ratio can be obtained by selecting a larger g_2/t ratio with a smaller thickness. The impact of the g_2/t ratio on the softening and hardening ratios, K_S/K_i and K_H/K_i respectively, are illustrated in Figure 4.9d. The softening

ratio K_S/K_i is generally small with an average of 1.0% and does not vary with the g_2/t ratio. Conversely, the stiffness ratio K_H/K_i varies significantly with the aspect ratio g_2/t, ranging from 1.4% up to 14.8%. In this case, a higher hardening ratio, if required, can be achieved by increasing the g_2/t ratio and keeping thinner angles.

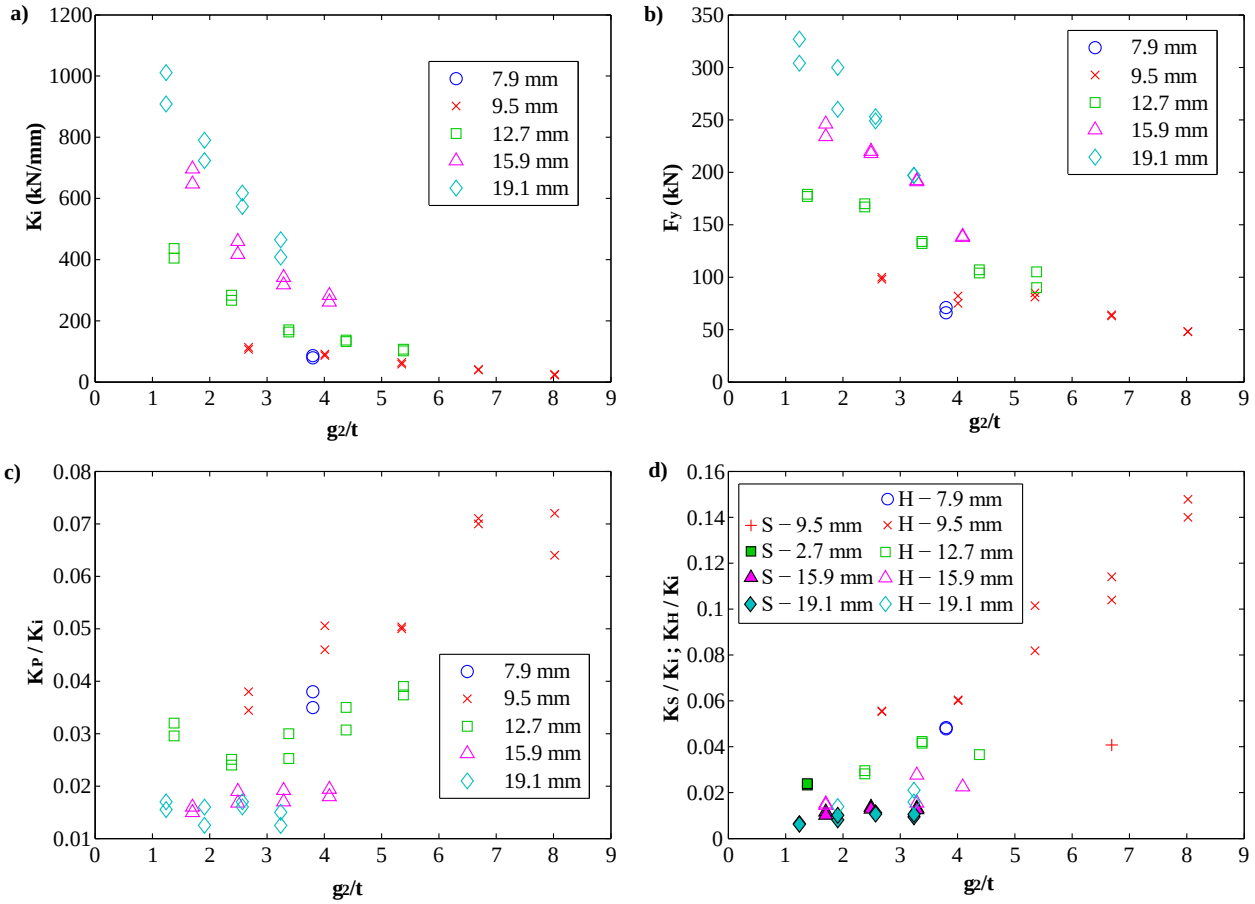


Figure 4.9. Influence of the aspect ratio g_2/t on: a) Initial stiffness K_i; b) Yielding force F_Y; c) Plastic to initial stiffness ratio K_P/K_i; and d) Softening and hardening to initial stiffness ratios K_S/K_i; K_H/K_i.

4.5.4 Influence of bolt grade

The influence of the bolt grade used for the column bolts was studied with four test cases. Figure 4.10a shows a comparison between the behavior of the test case TC10 (g_2/t = 4.38) with 25.4 mm diameter ASTM F3125 grade A490 and ASTM F3125 grade A325 bolts. The global nonlinear behavior of both tests are similar. However, a larger initial stiffness as well as a smaller transition

portion between the initial and plastic stiffnesses is observed in the A325 bolt test. Figure 4.10b shows the initial stiffness ratio between the specimens with ASTM F3125 grade A325 and ASTM F3125 grade A490 bolts. This increase averaged 21%, with a stiffness variation of 8% and 34% for the 12.7 mm- and 15.9 mm-thick angles.

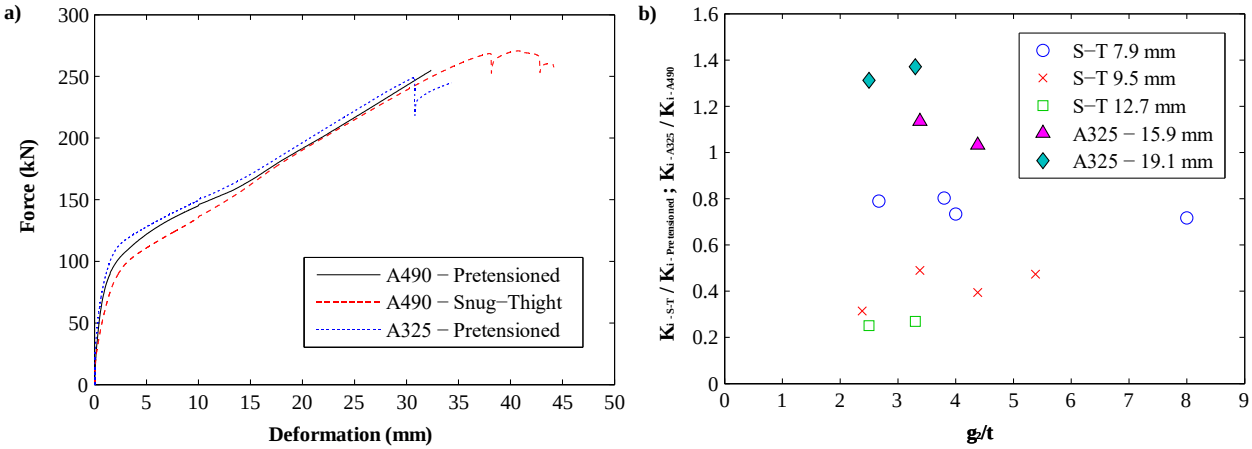


Figure 4.10. a) Impact of column bolt grade and pretension on the force-deformation relationship (TC10, g_2/t = 4.38). b) Impact of column bolt grade and pretension on the initial stiffness.

This increase results from the higher pretension required for the ASTM F3125 grade A490 bolts, which created higher through thickness compressive stresses in the column leg near the bolts. According to the Von Mises yield criterion, the required stress to reach yielding from the column leg flexion is thus smaller for stronger bolts and the net leg flexural capacity is reduced. Aside from this difference in the elastic portion, the general behavior of the angles using ASTM F3125 grade A325 and ASTM F3125 grade A490 bolts were similar.

4.5.5 Influence of bolt pretension

10 tests were conducted using ASTM F3125 grade A490 25.4 mm- or ASTM F3125 grade A325 19.1 mm-diameter column bolts only snug-tightened by hand with a standard wrench. Figure 4.10a presents a comparison between the typical behavior of pretensioned and snug-tightened specimens. This figure shows a stiffer behavior with pretensioned bolts especially at smaller deformations. A decrease in initial stiffness averaging 24% was observed on specimens with a thickness of 9.5 mm, with ASTM F3125 grade A325 19.1 mm-diameter bolts, as shown in Figure 4.10b. With the A490 25.4 mm-diameter bolts, the initial stiffness decreased to 58% and 74% for the 12.7 mm- and 15.9

mm-thick specimens respectively. Because of pretension, the bolt region of the angle leg is highly compressed against the column flange which gives a shorter flexural span compared to the snug-tight specimens. As discussed previously, a decreasing flexural span leads to a stiffer and stronger behavior. At larger deformations after yielding of the leg, the force-deformation response of the snug-tight specimens converges towards the response of the pretension ones. The maximum force, ultimate deformation and fracture mode were generally similar.

4.5.6 Influence of loading conditions

Loading effects were investigated through monotonic tests with varying strain rates and cyclic tests with varying histories.

4.5.6.1 Influence of strain rate

Three monotonic tests were performed for each test cases at target strain rates of 100με/s, 600με/s and 750000με/s. The first two were considered static loading, while the latter was dynamic. Figure 4.11a shows the force-deformation relationships at the three different strain rates. The nonlinear behaviors of the two static tests (100με/s and 600με/s) were almost identical. Figure 4.11b also shows initial stiffness ratio of nearly 1.00 between the two static tests. However, the angles subjected to a dynamic loading exhibited an elastic stiffness between 2.0 and 3.5 times larger than the stiffness of the static tests. Figure 4.11b presents the ratio between the initial stiffness of the 750000με/s test and the 100 με/s test, plotted against the aspect ratio g_2/t. The initial stiffness ratio averaged 2.67 for the 750000 με/s, without significant influence from the aspect ratio or the angle thickness.

In Figure 4.11a, the strain rate did not influence significantly the nonlinear behavior of the bolted angles after yielding. The plastic and hardening stiffness remained similar to the one observed in the 100 με/s test, regardless of the strain rate. However, the ultimate deformation and the maximum force in the dynamic tests are generally larger than the ones of the statically loaded angles. Previous studies on the strain rate effect (Chang and Lee 1987, Soroushian and Choi 1987, Wakabayashi et al. 1984) showed that the yield plateau, the ultimate stress and the ultimate strain increase along with the strain rate, which is consistent with the test observations.

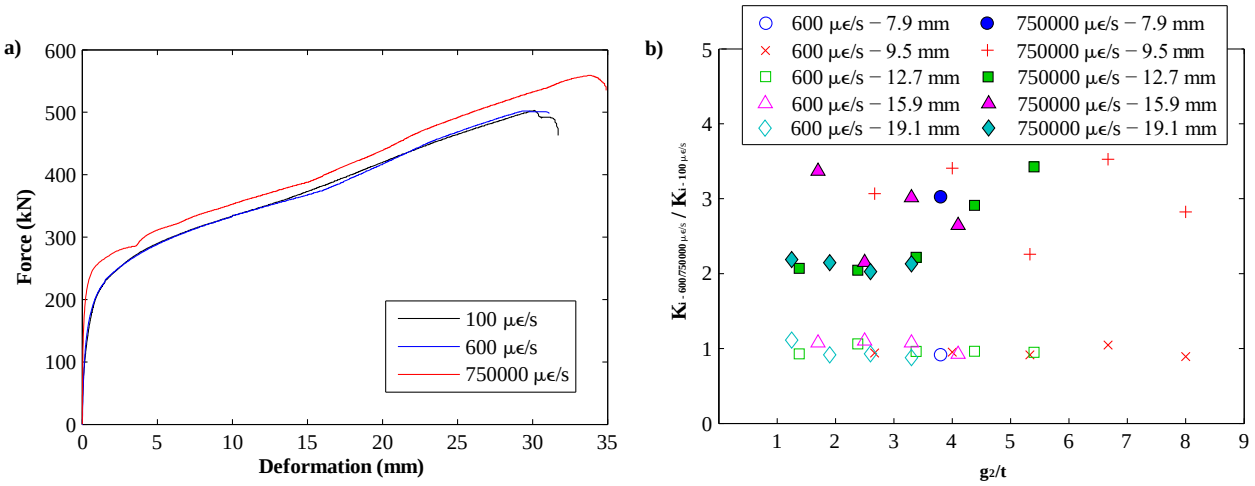


Figure 4.11. Influence of strain rate in monotonic tests: a) Impact on global force-deformation relationship (TC10, g_2/t = 4.38). b) Impact on initial stiffness.

4.5.6.2 Cyclic loading

All cyclic tests were performed under static cyclic loading conditions. Figure 4.12a shows that the monotonic test offers a good approximation of the cyclic backbone curve. As discussed previously, the hysteretic response under cyclic tests are characterized by a point which corresponds to the compressive force F_Y^- required to restore the contact between the column leg and the column flange in each cycle, as illustrated in Figure 4.12a. Figure 4.12b indicate that this compressive force varies between 1.36 and 2.11 times the yield force used in Equation 1 from the monotonic tests. In spite of this difference, the response observed in Figure 4.12a shows a similar inelastic response in unloading and reloading excursions, which results in high energy dissipation capacity. Figure 4.12c presents the total energy dissipated by the cyclically loaded specimens as a function of the aspect ratio g_2/t. As shown, the influence of the aspect ratio is limited for a given thickness, as the total energy that can be dissipated by the plastic hinges only depends on the accumulated plastic rotational capacity of the hinges, which does not depend on distance between these hinges. However, as expected, the total energy dissipated generally increases with the thickness.

The hysteretic behavior of the angle follow a backbone curve similar to the monotonic tests and the reloading excursions aim towards the maximum load and displacement experienced by the angles. However, several small amplitudes in the seismic tests result in a strength and stiffness

decrease due to low-cycle fatigue. These two behaviors create a pinching response as shown in Figure 4.12d, which result in a decrease in dissipated energy.

4.5.6.3 Low-cycle fatigue loading

The low-cycle fatigue behavior of bolted angles was studied for 2 test cases with 12 specimens. Figure 4.12e presents the relationship between the imposed displacement amplitude of each test Δ and the number of cycles N sustained by the angles up to fracture. Those relationships, in the logarithmic scale are linear, as already observed by Ballio et al. (1997) and Bernuzzi et al. (2000). Bernuzzi et al. (2000) also performed several data analyses of fatigue tests on connections and beams, in order to determine the parameters for those structural components when using Miner's S-N damage relationship (Miner 1945). Their study showed that ductile fatigue failure is characterized by a slope ranging from -0.50 to -0.33 in the logarithmic scale. In this test program, values of -0.44 and -0.48 were obtained for TC9 and TC14 respectively, which means the behavior of those angles can be qualified as ductile.

Figure 4.12f presents the relationship between the energy dissipated by the angles and the number of cycles sustained by the specimen until failure, in the logarithmic domain. For both test cases, the energy dissipation capacity of the angles increases proportionally with the number of cycles prior to fracture. Therefore, an angle subjected to smaller displacement amplitude cycles will sustain more cycles and dissipate more energy compared to the same angle subjected to larger displacement cycles. This observation suggests that larger displacement cyclic demands create relatively more damage and decreases the total energy dissipation capacity of angles. Nevertheless, the test shows that the bolted angles possess significant energy dissipation capacity through yielding, which makes bolted top and seat angles a viable option for beam-column connections to enhance lateral load resistance for seismic collapse prevention.

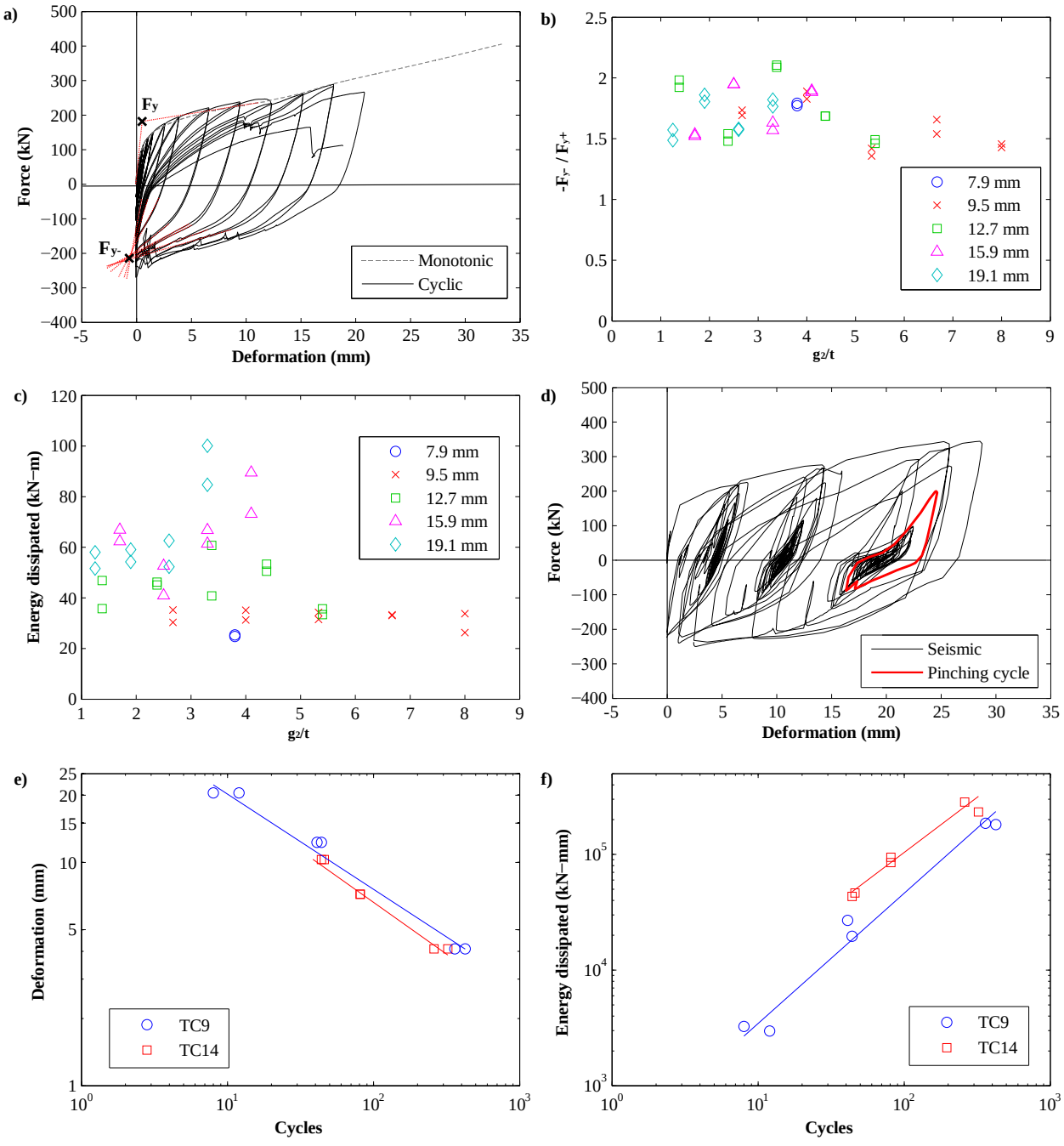


Figure 4.12. a) Compressive yield force F_Y^- in cyclic tests (TC4-4); b) Influence of the aspect ratio g_2/t on the compressive yield force to yield force ratio; c) Energy-dissipation in the cyclic tests; d) Pinching response in seismic test (TC4-6); e) Relationship between deformation demand and number of cycles to failure in low-cycle fatigue tests; and f) Relationship between energy dissipated and number of cycles to failure in low-cycle fatigue tests.

4.6 Conclusions

This article described a test program that studied the inelastic response of bolted top and seat angles for beam-column connections. This program included 139 tests performed on 19 different test cases to characterize the influence of geometric parameters and loading conditions on the nonlinear behavior of angles. In all tests, the specimens exhibited stable and predictable response characterized by large ductility, dependable resistance and substantial energy-dissipation capacity. The results from the monotonic tests were used to determine the parameters of an established power model, which can be used to predict the nonlinear connection response. From this study, the following conclusions can be drawn:

- Decreasing the column bolt gage g_c resulted in stiffer and stronger angles, exhibiting reduced deformation capacity.
- Increasing angle thickness also resulted in stiffer and stronger angle, with lesser deformation capacity.
- The thickness has a larger impact on the angle stiffness than the column leg flexural span g_2.
- At large deformations, geometric hardening was observed in more flexible angles, whereas stiffer angles exhibited a reduced plastic stiffness.
- Angles with a g_2/t ratio larger than 3.0 are more likely to fail in the column leg, whereas beam leg failure is expected when g_2/t ratio smaller than 3.0.
- Column bolt failure was observed in thick angles because of the higher tension forces amplified with the prying action.
- The static monotonic curve can predict well the backbone curve for static cyclic tests.
- In seismic tests, a pinching response developed as a result of stiffness degradation.
- Under low-cycle fatigue, the angles subjected to a smaller deformation were able to sustain more cycles and dissipate more energy prior to fracture.
- The plastic hinge forming in the beam leg was more vulnerable to low-cycle fatigue failure.

- Partial net section fracture near the column bolts was more common under cyclical loading.

Broadly, the nonlinear experimental behavior of the bolted angles in this study demonstrated large ductility and substantial energy dissipation capacity. These parameters are critical for favorable seismic response and illustrate the potential for inexpensive and common connection components to contribute to seismic stability. In particular, the use of bolted angles for gravity framing connections is a promising strategy to enhance the reserve (secondary) capacity of a building and mitigate seismic collapse, particularly when the primary lateral system has low ductility and experiences significant earthquake-induced damage.

4.7 Data Availability Statement

The following data, models, or code generated or used during the study are available from the corresponding author by request:

- Information on the experimental setup;
- Experimental measurements;
- Processed data; and
- Calibrated models of the monotonic tests.

4.8 Acknowledgments

This study was partially supported by the National Science Foundation (Grant No. CMMI-1207976) and the American Institute of Steel Construction. Patrice Bélanger, Jonathan Auger and David Ek of the Structures Laboratory of Polytechnique Montreal provided valued assistance to conduct the experimental tests. The opinions, findings, and conclusions in this paper are those of the authors and do not necessarily reflect the views of those acknowledged here.

REFERENCES

Abolmaali, A., Kukreti, A.R., Razavi, H. (2003). “Hysteresis behavior of semi-rigid double web angle steel connections.” *J. Constr. Steel. Res*. 59(8): 1057-1082.

AISC. (2010). *AISC 341-10, Seismic provisions for structural steel buildings*., American Institute of Steel Construction, Chicago, IL.

Azizinamini, A. (1982). *Monotonic response of semi-rigid steel beam to column connections,* M. Sc. Thesis, College of Engineering, University of South Carolina, Ann Arbor, MI.

Azizinamini, A. (1985). *Cyclic characteristics of bolted semi-rigid steel beam to column connections*, Ph.D. Thesis, College of Engineering, University of South Carolina, Ann Arbor, MI.

Ballio, G., Calado, L., Castiglioni, C.A. (1997). "Low cycle fatigue behaviour of structural steel members and connections." *Fatigue Fract. Eng. Mater. Struct.* 20(8): 1129-1146.

Bernuzzi, C., Calado, L., Castiglioni, C.A. (2000). "Low-cycle fatigue of structural steel components: A method for re-analysis of test data and a design approach based on ductility." *ISET J. of Earthquake Tech.* 37(4): 47-63.

Bjorhovde, R., Colson, A., Brozzetti, J. (1990). "Classification System for Beam-to-Column Connections." *J. Struct. Eng*. 116(11): 3059-3076.

Calado L., De Matteis G., and Landolfo, R. (2000) "Experimental response of top and seat angle semi-rigid steel frame connections." Materials and Structures, 33(232), 499-510.

Chang, K.C., Lee, G.C. (1987). "Strain Rate Effect on Structural Steel under Cyclic Loading." *J. of Eng. Mech.* 113(9): 1292-1301.

Citipitioglu, A.M., Haj-Ali, R.M., White, D.W. (2002). "Refined 3D finite element modeling of partially-restrained connections including slip." *J. Constr. Steel. Res.* 58(5-8): 995-1013.

CSA. (2014). *CSA-S16-14, Design of steel structures.* Canadian Standard Association, Mississauga, ON, Canada.

Danesh, F., Pirmoz, A., Daryan, A.S. (2007). "Effect of shear force on the initial stiffness of top and seat angle connections with double web angles." *J. Constr. Steel. Res.* 63(9): 1208-1218.

Elnashai, A.S., Elghazouli, A.Y., and Denesh-Ashtiani, F.A. (1998) "Response of semirigid steel frames to cyclic and earthquake loads." J. Struct. Eng. 124(8): 857-867.

Faella, C., Piluso, V., Rizzano, G. (1998). "Experimental Analysis of Bolted Connections: Snug versus Preloaded Bolts." *J. Struct. Eng.* 124(7): 765-774.

Garlock, M., Ricles, J., Sause, R. (2003). “Cyclic Load Tests and Analysis of Bolted Top-and-Seat Angle Connections.” *J. Struct. Eng.* 129(12): 1615-1625.

Giuffre, A. and Pinto, P. E. (1970). “Il comportamento del cemento armato per sollecitazioni cicliche di forte intensita.” *Giornale del Genio Civile,* 5, 391-408.

Goldberg, J. and Richard, R.H. (1963). “Analysis of nonlinear structures.” *J. of the Struct. Div.*, 89(4), 333-352.

Gong, Y. (2014). “Ultimate tensile deformation and strength capacities of bolted-angle connections.” *J. Constr. Steel. Res.* 100(6): 50-59.

Kishi, N., Hasan, R., Chen, W.F., Goto, Y. (1997). “Study of Eurocode 3 steel connection classification.” *Eng. Struct.* 19(9): 772-779.

Kulak, G.L., Fisher, J.W., Struik, J.H.A. (2001). *Guide to design criteria for bolted and riveted joints*. American Institute of Steel Construction, Chicago, IL.

Mazzoni, S., McKenna, F., Scott, M.H., Fenves, G.L. (2006). *OpenSees Command Language Manual.* Pacific Earthquake Engineering Research Center, University of California Berkeley.

Menegotto, M., Pinto, P.E. (1973). *Method of analysis for cyclically loaded R.C. plane frames including changes in geometry and non-elastic behaviour of elements under combined normal force and bending*. Edited by I.r.o.t.w. commissions, Rome, Italy. p. 9.

Miner, M.A. (1945). Cumulative damage in Fatigue. *J. of Appl. Mech.* 67: 5.

Nakashima, M., Inoue, K., Tada, M. (1998). “Classification of damage to steel buildings observed in the 1995 Hyogoken-Nanbu earthquake.” *Eng. Struct.* 20(4-6): 10.

Shen, J., Astaneh-Asl, A. (1999). “Hysteretic behavior of bolted-angle connections.” *J. Constr. Steel. Res.* 51(3): 201-218.

Soroushian, P., Choi, K.B. (1987). “Steel Mechanical Properties at Different Strain Rates.” *J. Struct. Eng.* 113(4): 663-672.

Swanson, J. A., Gao, X. (2000). “Strength determination of heavy clip-angle connection components.” *Proc. 4th Int. Workshop on Connections in Steen Struct*, Roanoke, Virginia, US. pp 234-243.

Richard, R.M., and Abbott, B.J. (1975). “Versatile Elastic-Plastic Stress-Strain Formula.” *J. Eng. Mech. Div.*, 101(4), 511-515.

Wakabayashi, M., Nakamura, T., Iwai, S., Hayashi, Y. (1984). “Effect of strain rate on the behavior of structural members subjected to earthquake force.” *Proc., 8th World Conf. on Earthquake Eng. (8WCEE)*, San Francisco, California, US. pp. 491-498.

Yang, B., Tan, K. (2013). “Robustness of bolted-angle connections against progressive collapse: Mechanical modelling of bolted-angle connections under tension.” *Eng. Struct.* 57: 153-168.

CHAPTER 5 ARTICLE 2: EVALUATING THE ROTATIONAL CAPACITY OF BOLTED DOUBLE WEB ANGLE BEAM-COLUMN GRAVITY CONNECTIONS WITH FULL-SCALE EXPERIMENTAL TESTING

Thierry Béland
École Polytechnique de Montréal, Montreal, Québec H3C 3A7, Canada
thierry.beland@polymtl.ca

Robert Tremblay, Ph.D.
École Polytechnique de Montréal, Montreal, Québec H3C 3A7, Canada
robert.tremblay@polymtl.ca

Eric M. Hines, Ph.D., P.E., F.SEI
Tufts University, Medford, Massachusetts 02155. USA
eric.hines@tufts.edu

Larry A. Fahnestock, Ph.D., P.E., F.SEI
University of Illinois at Urbana-Champaign, Urbana, Illinois 61801, USA
fhnstck@illinois.edu

Paper submitted to *ASCE Journal of Structural Engineering*,
Submitted April 27th, 2019
Accepted for publication December 5th, 2019.

ABSTRACT:

Double web angle beam-column connections are used extensively for gravity framing in steel buildings. Although they are designed to resist shear and to allow rotation, they still possess moment capacity that may contribute to lateral resistance, particularly in extreme-load scenarios. To characterize the nonlinear hysteretic behavior of bolted angle connections subjected to simultaneous gravity shear and rotational demand from the moment frame action, a comprehensive test program was conducted at Ecole Polytechnique Montreal. Eight full-scale beam-column sub-assemblages of 2 different geometries were tested to characterize their hysteretic behavior and failure modes in relationship to the following parameters: angle geometry, beam and column section properties, gravity shear load and loading history. The backbone curve of each test was calibrated numerically to reproduce the connection behavior. Double web angle connections exhibited large rotational capacity and stable hysteretic behavior. Their stable hysteretic behavior

in a reserve capacity perspective may be of interest as it can provide sufficient rotational capacity to the gravity frame and mitigate the building collapse in low-ductility braced frames.

KEYWORDS: Bolted-Angle Connections; Experimental tests; Steel buildings; Cyclic response.

5.1 Introduction

Beam-column connections that are part of the gravity load system in steel buildings are typically assumed to behave as pinned connections and to provide no contribution to resisting lateral loads. However, many connections designed to resist shear and to allow rotation have non-negligible moment capacity. Although this connection moment-rotation capacity does not affect global building response during service-level conditions, it may become important during an extreme-load scenario such as a large earthquake, which causes failure in the primary lateral force-resisting system of a building. In such a scenario, the secondary moment frame action of the gravity system may become important for seismic stability. However, for these connections to contribute to seismic stability, they must accommodate the building lateral displacement during a seismic event by exhibiting ductile behavior with sufficient rotational capacity.

Secondary moment frame action enhances seismic stability by controlling drifts and mitigating P-delta effects (Ji et al. 2009; Flores et al. 2014; Flores et al. 2016; Gupta and Krawinkler 2000; Lee and Foutch 2002; Callister and Pekelnicky 2011; Hines et al. 2009, Stoakes and Fahnestock 2011; Jarrett et al. 2014; Judd and Charney 2015; Elkady and Lignos 2015; Sizemore et al. 2017; Hwang and Lignos 2017). However, the contribution of secondary moment frame action has historically been difficult to quantify due to the lack of comprehensive data on connections and connection components tested to large inelastic deformation demands consistent with seismic response.

The moment-rotation behavior of gravity connections is strongly influenced by angle geometric properties such as the thickness and the column bolt position. (Astaneh et al. 1989, De Stefano et al. 1994, Shen and Astenah-Asl 1999, Shen and Astaneh-Asl 2000, Abolmaali et al. 2003, Gong 2014, Beland et al. 2019a). The beam depth, the web angle length and the number of bolt rows also influence the connection hysteretic behavior (Astaneh et al. 1989, Kishi and Chen 1990, De Stefano et al. 1994, Abolmaali et al. 2003, Guravich and Dawe 2006, Oosterhof and Driver 2012, Liu et al. 2012, Yang and Tan 2013, Weigand and Berman 2016, Matthews and Arjomandi 2017). These

parameters have an important role in the stiffness, moment and rotational capacity of bolted angle connections, and thus on the lateral stiffness and ductility of the gravity frame. Including the effect of the concrete slab in the connection resistance increases significantly the resisting moment until the concrete starts to crack and lose its integrity (Liu and Astaneh-Asl 2000, Liu and Astaneh-Asl 2004, Braconi et al. 2007).

After double web angle connections have been mobilized to resist lateral loads, they must still fulfill their initial role of supporting the gravity loads, and therefore must retain sufficient gravity connection capacity resist the shear loading. Previous experimental studies on double web angle (2L) beam-column connections focused on the nonlinear behavior during a column removal scenario (Guravich and Dawe, Oosterhof and Driver 2012, Liu et al. 2012, Yang and Tan 2013, Weigand and Berman 2016). These investigations addressed an important issue relative to the moment-rotation behavior of gravity connections subjected to combined shear and moment. However, these studies did not investigate the hysteretic behavior of the connections under cyclic loading.

An experimental program was developed at École Polytechnique Montreal to define the hysteretic nonlinear behavior of bolted angle connections under shear and rotational demands. The study focused on the behavior of the bolted angles; the beneficial but more complex influence of the concrete slab was thus omitted. The first phase of the experimental program aimed at characterizing the behavior of 2L connections. 8 full-scale beam-column specimens were tested to assess the influence of the shear load and the beam depth. The specimens were tested under a symmetric cyclic rotational demand with and without additional gravity shear. They were also tested under an asymmetric rotational demand. A second phase of the experimental program aimed at evaluating the behavior of top and seat with double web angles connections is documented separately (Beland et al. 2019b). In the present paper, the nonlinear behavior of 2L connections, their deformation patterns and the failure modes observed are detailed. The influence of geometrical parameters and loading conditions on the hysteretic moment-rotation behavior of the connections are also assessed.

5.2 Experimental Program

5.2.1 Test setup

The testing program aimed to characterize the hysteretic behavior and rotational capacity of gravity beam-column connections made of bolted web double angles. To achieve realistic loading conditions, the specimens were loaded with a large shear force representing the gravity load acting on the connection, simultaneously with the rotational demand. In the Structures Laboratory of École Polytechnique Montreal, the connection specimen was rotated by 90° as illustrated in Figure 5.1, where the vertical component is the beam and the horizontal column is anchored to the strong floor. To create the combination of shear and rotational demand at the connection, two hydraulic actuators were used simultaneously. A 500 kN capacity actuator created the rotational demand on the connection. This actuator was located at 3442 mm from the connection and acted in displacement-control with a constant displacement rate.

The connection shear load was generated by the 1000 kN capacity actuator at a distance of 942 mm from the connection. The shear load at the face of the column was kept constant to simplify the loading procedure. The 1000 kN actuator was force-controlled and its command was obtained by the difference between the connection target shear load and the load induced in the 500 kN displacement-controlled actuator. The 1000 kN actuator was always applying force in the same direction. To reduce the axial load in the beam specimen, a third 100 kN actuator was used to support the weight of the 1000 kN actuator. This setup still allowed the connection to experience longitudinal displacements along the beam local axis, as the actuator could move along with this movement. The longitudinal and transversal displacements of the beam flanges were recorded throughout the tests with string potentiometers, along with the bolt slip and bearing deformations between the beam web and the angle legs.

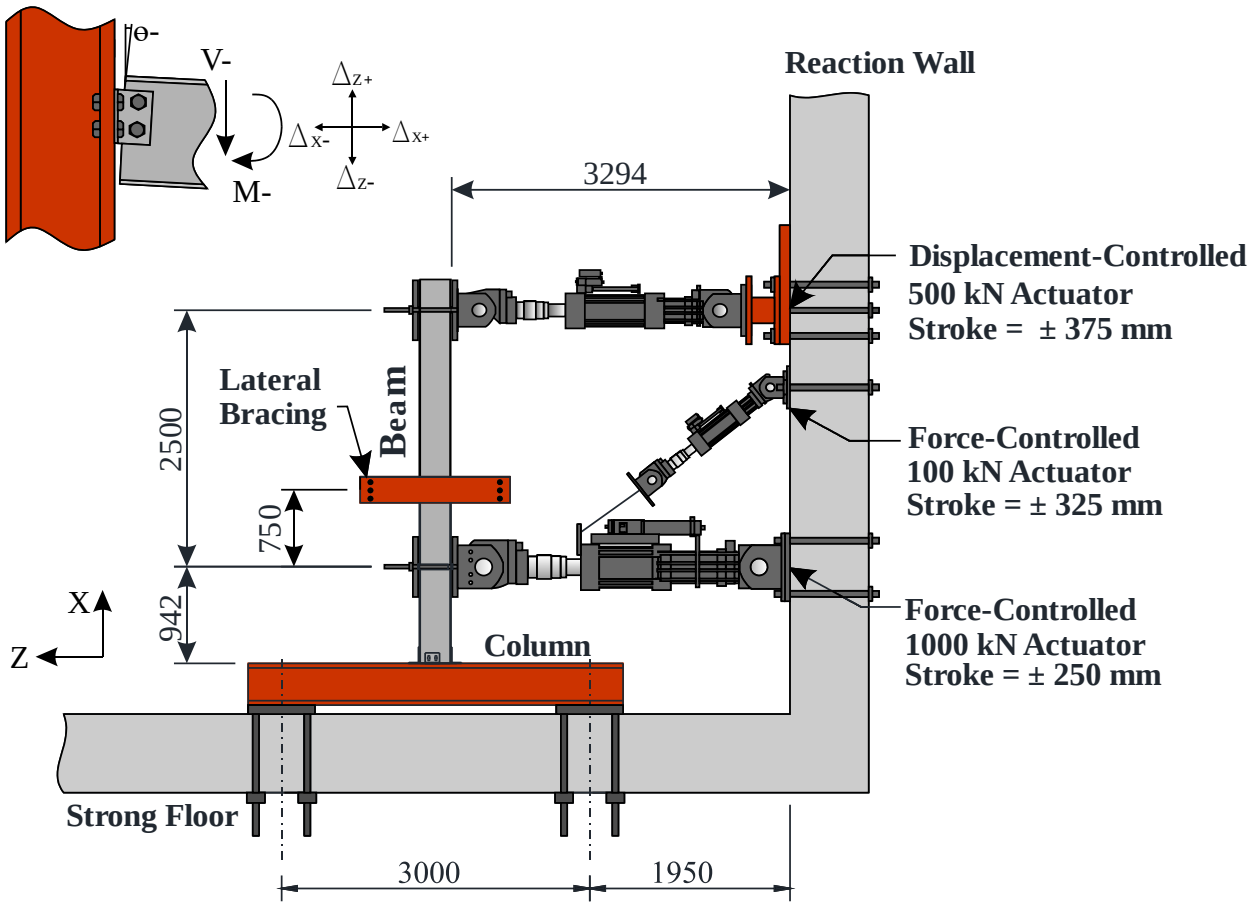


Figure 5.1. Beam-column connection test setup.

5.2.2 Beam-column connection specimens

The testing program on the beam-column connections consisted of two connection geometries, with either a W310x39 (W12x26) or a W410x67 (W16x45) beam and a stiff W360x289 (W14x193) column. The connections consisted of 2L102x102x7.9 (2L4x4x5/16) web angles with 2 and 3 bolt rows for the W310 and W410 beam specimens respectively. The length of the web angles L_w was 140 mm and 216 mm for the W310 and the W410 beam specimens respectively. The bolts used were A325 with a diameter d_b of 19.1 mm (3/4”). The column bolts were located at a distance from the angle corner g_c of 63.5 mm. The flexural span of the column leg g_2, given by the distance between the edge of the bolt head and the angle fillet, corresponded to 30 mm. With a thickness t of 7.9 mm, the web angles thus corresponded to the TC19 (g_2/t of 3.80) angle geometry of the related angle component testing campaign (Beland et al. 2019a). The geometrical

characteristics of each specimen are presented in Figure 5.2. The design plastic moment M_p of the beam and column sections and the connection design shear resistance are also presented in Figure 5.2. For the two connections, the bolt shear resistance controlled the connection design shear. The design values shown in Figure 5.2 include a design factor φ of 0.9.

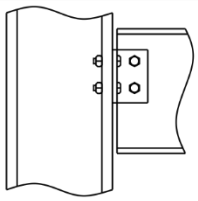
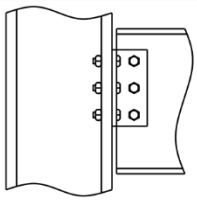
Test	1 	2 
Beam	**W310x39**	**W410x67**
Column	**W360x347**	
Web angles	**2L102x102x7.9** **L_w :** 140 mm **g_c:** 63.5 mm **d_b:** 19.1 mm	**2L102x102x7.9** **L_w :** 216 mm **g_c:** 63.5 mm **d_b:** 19.1 mm
Design resistance of connexion (φ = 0.9)		
M_p Beam	189 kN-m	422 kN-m
M_p Column	2217 kN-m	
Limit state	Bolt shear resistance 320 kN	Bolt shear resistance 479 kN
Loading procedures of each test:		
A	Cyclic + seismic gravity shear	Cyclic + seismic gravity shear
B	Cyclic + seismic gravity & design shear excursions	Cyclic + seismic gravity & design shear excursions
C	Cyclic + rotational shear	Cyclic + rotational shear
D		Near fault (-) + seismic gravity shear
E		Near fault (+) + seismic gravity shear

Figure 5.2. Beam-column connection details and loading procedures.

5.2.3 Loading procedures

Figure 5.2 presents the loading procedure for each connection geometry, for a total of eight tests performed. Five different protocols (A-E) were applied on the connection specimens to assess the influence of loading parameters. To determine the loading conditions, a prototype frame with story

heights of 4572 mm (15') and bay width of 9144 mm (30') was considered. The rotational demand on the connection was determined by imposing the story drift demand proposed by AISC 2010 for evaluating moment-frame connections. The drift contribution of the beam and column were determined by supposing an elastic behavior, while the connection behavior was simplified into a parallel spring element using the experimental results of (Beland et al. 2019a). The connection shear forces were -94 kN and -282 kN for the W310x39 and W410x67 beam specimens, respectively. These values correspond, with a ± 1% difference, to the beam shears obtained with the load combinations 1.2D + 1.0E + 0.5L in ASCE 7-16 (ASCE 2016) and 1.0D + 1.0E + 0.5L of the National Building Code of Canada (NBCC 2015). These shear loads are referred as the seismic gravity shear.

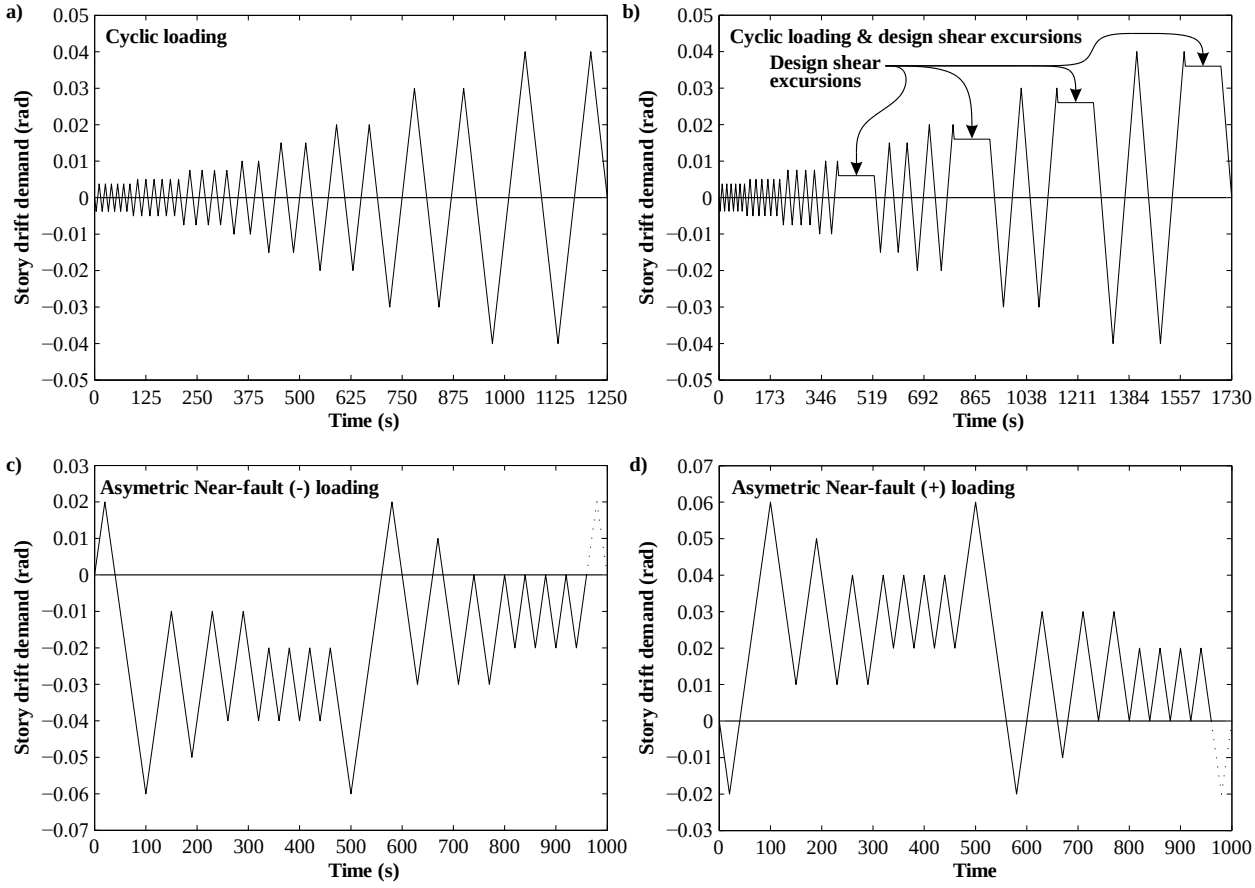


Figure 5.3. Beam-column connection loading protocols for a) cyclic tests; b) Cyclic tests with design shear excursions; c) Negative asymmetric near-fault tests; d) Positive asymmetric near-fault tests.

The first loading procedure (A) was applied on both geometries and consisted of a symmetrical amplitude cyclic rotational demand increase, as pictured in Figure 5.3a. This rotational demand was combined with a constant shear demand. The specimen was loaded cyclically with the 500 kN actuator while the 1000 kN actuator applied and maintained a constant shear load equal to the seismic gravity shear.

The same gradual cyclic rotational demand was used in the second loading procedure (B) but the cyclic demand was held constant for a period of 2 minutes during which the connection shear demand was increased. These interruptions happened at each 0.01 rad increment in the theoretical frame rotational demand, when a moment of zero was reached during the unloading of the positive excursion. The shear load was then increased to the design shears -152 kN and - 456 kN on specimens 1B and 2B, respectively. The design shear loads correspond to the factored 1.2D + 1.6L load combinations in ASCE 7-16 (ASCE 2016) and 1.25D + 1.5L in the NBCC (2015). The applications of these increased shear loads are presented in Figure 5.3b. After each application, the connection shear was brought back to the seismic gravity shear value and the cyclic loading was resumed. These design shear excursions aimed at verifying the connection capacity to sustain their design shear strength after significant yielding and rotational demand from a seismic event.

The third loading protocol (C) used the same rotational demand presented in Figure 5.3a, without additional gravity shear load applied on the connection. Therefore, the only shear demand in the connection resulted from the force required in the 500 kN actuator to create the rotational demand, which is referred as the rotational shear. This protocol aimed at evaluating the influence of the shear load on the connection behavior by comparing the behavior with the previous tests.

The fourth and fifth loading procedures were based on the story drift demand proposed by AISC (2010) for a near-fault seismic event with a negative or a positive rotational demand, respectively, as presented in Figure 5.3c and 5.3d. These loading protocols were applied with the constant seismic gravity shear demand of -282 kN on the specimens 2D and 2E. The whole rotational demand time-history was applied up to 7 times to try to provoke a low-cycle fatigue fracture in the connection. However, fracture was finally obtained by manually increasing the connection rotational demand.

The seismic gravity shear load at the connection was applied prior to the start of the cyclical rotational demand. During the application of the shear load, small rotations were measured at the connection. However, a reset of the instrumentation was performed prior to the start of the cyclical loading. The rotation values defining the connection behavior are thus resulting from the cyclic loading and the shear-moment interaction in the connection only.

5.3 Experimental results

5.3.1 Nonlinear behavior of double web angle connections with rotational shear

The deformation pattern and failure mode observed on Specimen 2C under rotational shear demand are presented in Figure 5.4a. Under large rotational demand, crack initiation was observed in the column leg of the angle, as illustrated by Figure 5.4c on the bottom side of the angle component.

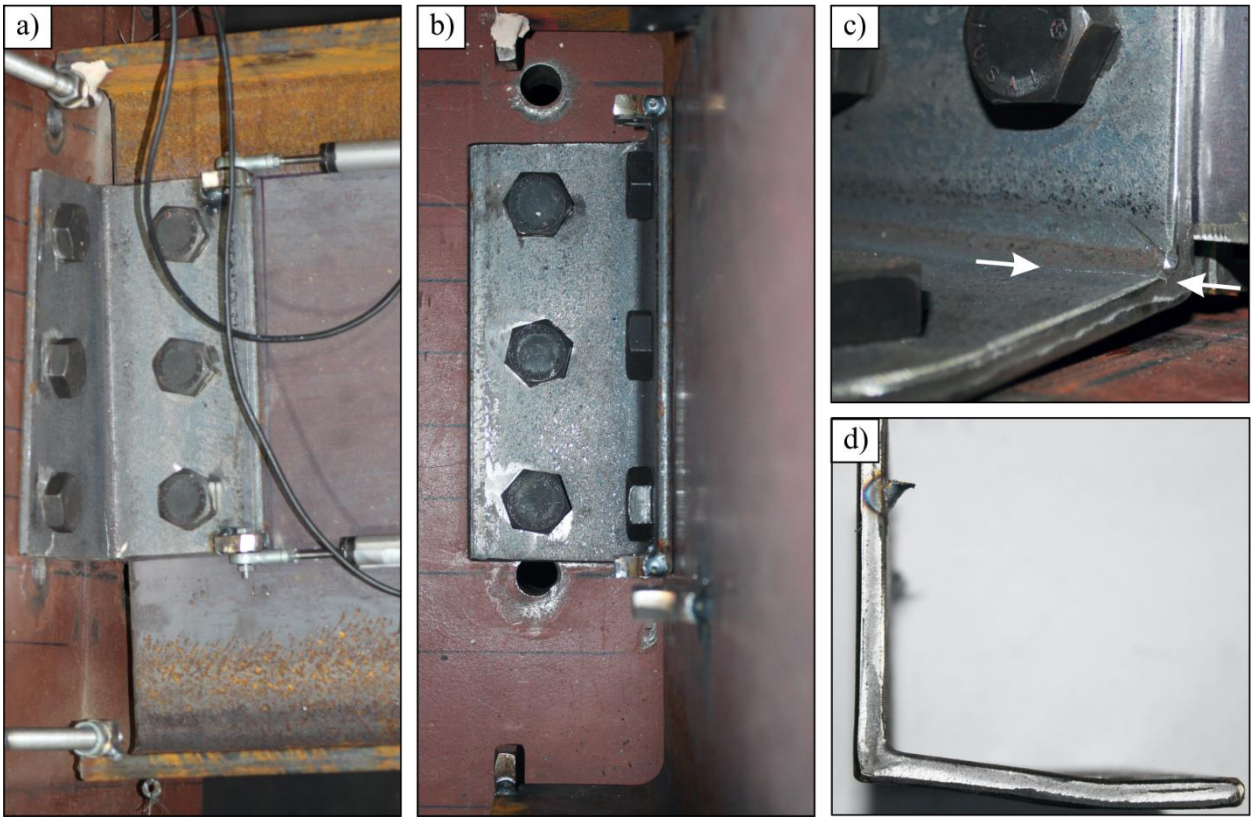


Figure 5.4. Deformation pattern of double web angle connections with rotational shear (Specimen 2C): a) Lateral view of the connection b) Front view of the connection c) Column leg fracture d) Deformed angle at fracture.

The maximum displacement demand on the angles remained relatively small even at large rotational demands, because of the outer fiber proximity to the neutral axis, as illustrated by Figure 5.4d. The specimens loaded with rotational shear only did not exhibit significant transverse deformations (Figure 5.4b). Furthermore, the slip measured between the angle beam legs and the beam web itself varied between 0.58 mm and -0.31 mm for most specimens. These small recorded values indicate that the bolted angles mostly followed the beam rotation with minimal bolt slip. For specimen 4D, slip displacements varying between -2.18 mm and -1.58 mm were observed, which reduced significantly the angle deformation required to reach the connection rotation.

5.3.1 Nonlinear behavior of double web angle connections with seismic gravity shear

Of the six specimens subjected to simultaneous flexural moment and seismic gravity shear load, five fractured in the beam leg near the fillet, while only one failed in the column leg. These fracture all occurred on the top side of the connection, as represented by a typical test in Figure 5.5a. The constant seismic gravity shear load applied on the 2L connections created large shear deformations in the column legs, as illustrated by Figure 5.5b. The eccentricity between the shear load transferred from the beam to the angle by the web bolts and from the angles to the column by the column leg bolts created an in-plane torsional moment in the column leg. This eccentricity, corresponding to the column bolt gauge g_c, created an in-plane torsional moment between the shear forces developed in the column and beam legs, as presented in Figure 5.6. With the formation of plastic hinges near the angle fillet and the column bolts, the column leg was particularly vulnerable as each of its boundaries eventually yielded.

The in-plane rotation of the column leg is observed in Figure 5.5b, where the edge of the column leg did not remain parallel to the beam leg. This rotation is also observed in Figure 5.5c, where the bottom sides of the web angles were pulled away from the beam web. On their top side, the web angle fillets were pushed under the beam web, leading to premature contact between the web and the connection components under positive moments. Eventually, fracture occurred at the top side of the angle beam leg as shown in Figure 5.5d. This failure is due to the combination of excessive yielding and a stress concentration resulting from the premature contact with the beam web under positive moments.

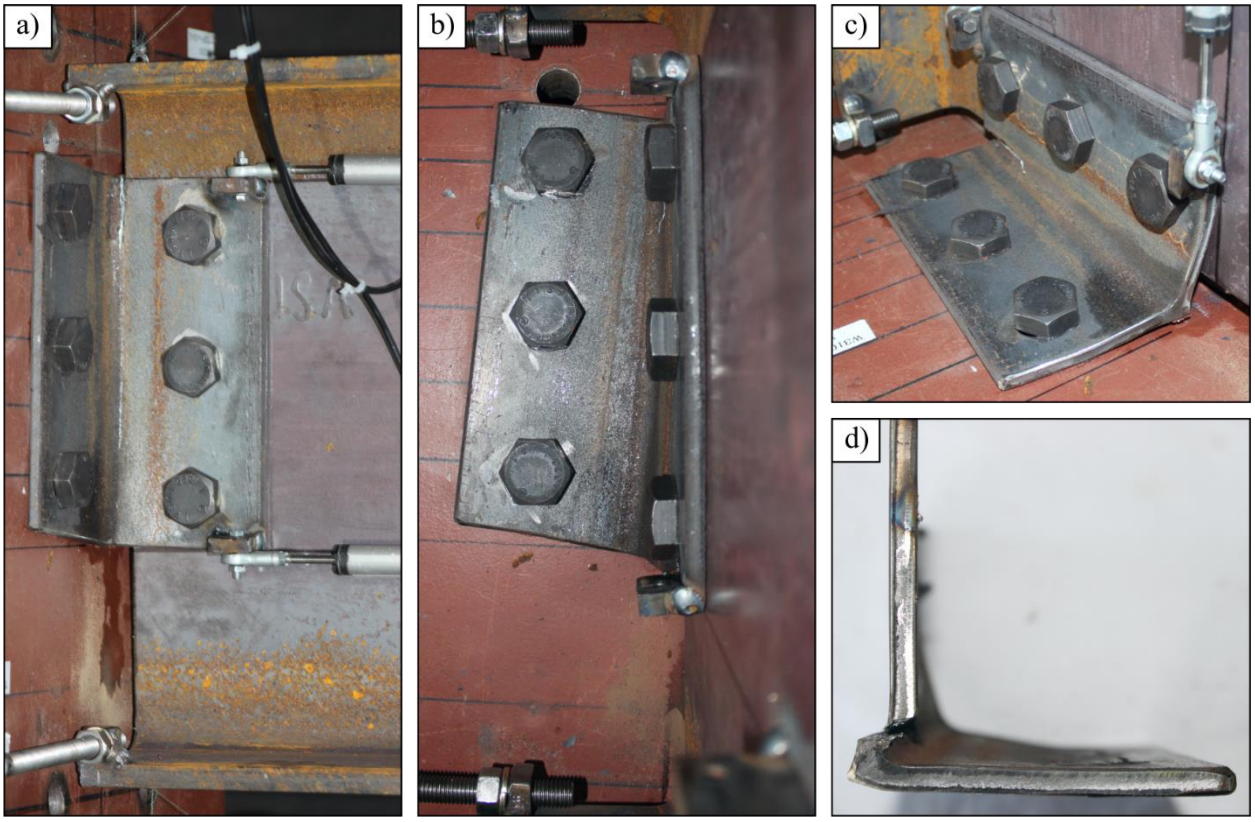


Figure 5.5. Deformation pattern of double web angle conections with seismic gravity shear and design shear excursions (Specimen 2B): a) Lateral view of the connection b) Front view of the connection c) Beam leg fracture and column leg rotation d) Deformed angle at fracture.

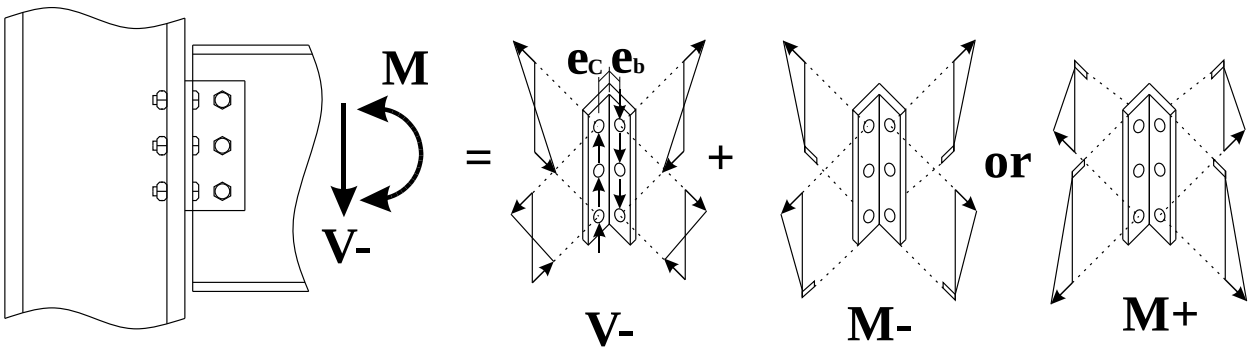


Figure 5.6. Free-body diagram of a web angle component in the connection.

5.4 Nonlinear characterization of the moment-rotation backbone curve

Table 5.1 summarizes the moment capacity of each specimen, both positive (M_{Max}) and negative (M_{Min}), with their corresponding rotational demands, $\theta_{M\text{-}Max}$ and $\theta_{M\text{-}Min}$ respectively. This table also includes the ultimate rotational demands, both positive (θ_{Max}) and negative (θ_{Min}), and their corresponding moments, $M_{\theta\text{-}Max}$ and $M_{\theta\text{-}Min}$ respectively. The loading procedure applied on each test and the minimum and maximum shear loads, V_{Min} and V_{Max}, experienced by the connection specimen are included. To provide a tool for representing the nonlinear behavior of beam-column connections made of bolted angles, a numerical model has been calibrated for the moment-rotation backbone curves of the positive and negative excursions of each test.

Table 5.1. Shear and moment-rotation key response parameters of beam-column connections

Test ID	Loading Type	V_{Min}	V_{Max}	θ_{Max}	$M_{\theta max}$	θ_{Min}	$M_{\theta min}$	$\theta_{M\text{-}Max}$	M_{max}	$\theta_{M\text{-}Min}$	M_{min}
		kN	kN	Rad	kN-m	Rad	kN-m	Rad	kN-m	Rad	kN-m
1A	Cyclic + seismic gravity	-94	-94	0.075	9	-0.075	-4	-0.045	15	-0.027	-5
1B	Cyclic + design shear	-152	-94	0.074	13	-0.070	-9	-0.019	21	-0.070	-9
1C	Cyclic + rotational shear	-2.3	1.9	0.075	7	-0.075	-8	0.075	7	-0.075	-8
2A	Cyclic + seismic gravity	-283	-283	0.070	27	-0.070	-16	0.033	34	-0.015	-19
2B	Cyclic + design shear	-465	-283	0.070	30	-0.070	-14	0.021	33	-0.070	-14
2C	Cyclic + rotational shear	-6.1	6.1	0.070	21	-0.070	-21	0.070	21	-0.070	-21
2D	Asymmetric NF (-) + Seismic gravity shear	-283	-283	0.014	21	-0.078	-9	-0.005	28	0.001	-9
2E	Asymmetric NF (+) + Seismic gravity shear	-283	-283	0.070	21	-0.017	-12	0.070	21	-0.017	-12

The moment-rotation envelope of each test has been characterized with the mathematical model proposed by Menegotto and Pinto (1973). Equation 5.1 presents the stress-strain relationship proposed by Menegotto and Pinto (1973), where σ_0 and ε_0 correspond to the yield stress and strain, b is the ratio between the plastic and initial stiffness and R is a coefficient defining the transition between the initial and plastic stiffness. This formulation is transposed into the moment-rotation relationship of Equation 5.2. The latter corresponds exactly to the power model proposed by Kishi et al. (1990), where K_i and K_p are the initial and plastic stiffness, M_Y is the yield moment and R is the transition coefficient. This observation acts as a validation to use this model to characterize the connection envelope.

$$\sigma = \sigma_0 \left(\frac{(1-b)\frac{\varepsilon}{\varepsilon_0}}{\left[1+\left(\frac{\varepsilon}{\varepsilon_0}\right)^R\right]^{\frac{1}{R}}} + b\frac{\varepsilon}{\varepsilon_0} \right) \quad (5.1)$$

$$M = \frac{(K_i - K_P)\theta}{\left[1+\left(\frac{\theta}{M_Y/K_i}\right)^R\right]^{\frac{1}{R}}} + K_P\theta \quad (5.2)$$

The numerical model was calibrated to the experimental data envelope for each test using the least square method. The initial rotational stiffness K_i, the plastic rotational stiffness K_P, the yielding moment M_Y and the shape parameter R were defined with this calibration process. The calibrated parameters are presented in Table 5.2. Since the hysteretic moment-rotation behavior was asymmetrical, the negative and positive backbone curves have been calibrated separately. The coefficient of determination R^2 was also included to offer some insight on the representativeness of the calibrated numerical model. The positive and negative backbone curve of each experimental test can thus be recreated using the calibrated parameters of Table 5.2 in Equation 5.2.

Figure 5.7a presents the hysteretic behavior, the backbone curve and the numerical model of specimen 2A, which behaved typically for a 2L connection with seismic gravity shear load. In this test the negative stiffness characterizing the hysteretic behavior of the connection at large displacement translated as a negative plastic stiffness in the numerical model. Because of this discrepancy and the loss of moment capacity at each cycle, the 2L connection specimens with seismic gravity shear loading obtained the least representativeness between the experimental behavior and the numerical model. Still, with a determination coefficient $R^2$of 0.746 the numerical model offered a good approximation of the connection backbone behavior. The symmetrical and stable behavior of 2L angle connections with rotational shear was better characterized by the numerical model, with a determination coefficient R^2 of at least 0.905. Figure 5.7b presents the nonlinear representation of a typical 2L connection with rotational shear, specimen 2C.

Table 5.2. Nonlinear backbone curve characterization of beam-column connections

Test ID	Positive backbone					Negative backbone				
	K_i^+	M_y^+	R^+	K_p^+	R^2	K_i^-	M_y^-	R^-	K_p^-	R^2
	kNm/rad	kNm	-	kNm/rad	-	kNm/rad	kNm	-	kNm/rad	-
1A	10688	14	0.868	-32	0.746	2155	-6	0.608	-3	0.819
1B	10609	15	0.912	-25	0.944	3937	-8	0.927	-7	0.878
1C	7323	8	0.552	4	0.922	6410	-9	0.639	4	0.905
2A	10688	34	1.278	-40	0.821	11155	-20	1.161	-52	0.844
2B	11688	35	1.312	-62	0.903	7273	-18	0.932	-46	0.847
2C	11976	17	1.026	67	0.988	9817	-15	0.951	99	0.954
2D	8156	17	0.976	75	0.970	11149	-9	1.185	-33	0.944
4E	11602	18	1.470	33	0.935	5835	-6	0.843	38	0.886

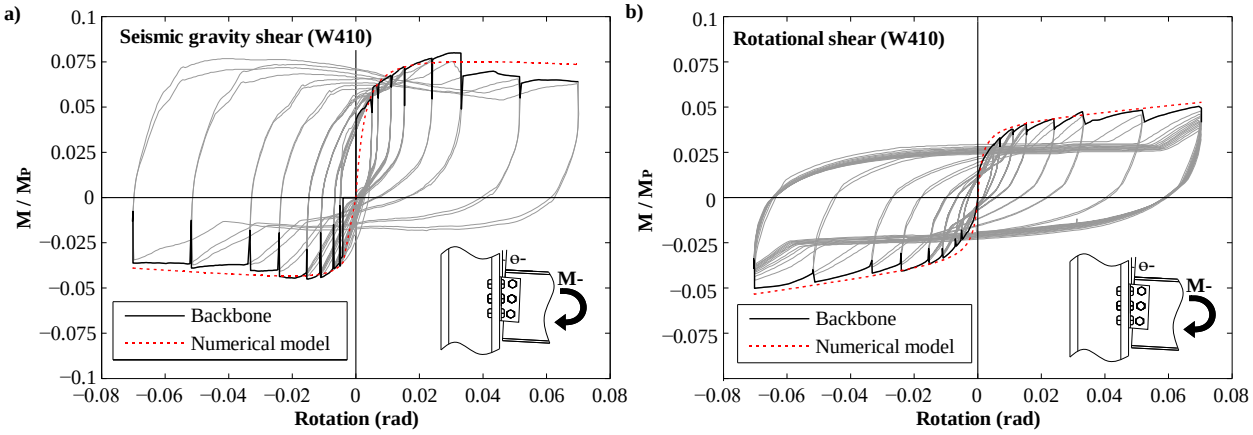


Figure 5.7. Numerical modeling of moment-rotation backbone curve: a) with seismic gravity shear (Specimen 2A) and b) with rotational shear (Specimen 2C).

5.5 Influence of geometrical and loading parameters

The influence of several parameters on the hysteretic behavior of beam-column connections made of bolted angles were investigated. The tests performed on the specimens with a cyclic rotational demand and a constant seismic gravity shear load were established as the comparative basis.

5.5.1 Influence of seismic gravity shear load

The deformation pattern for the specimens tested with rotational shear and with seismic gravity shear demand influenced significantly the hysteretic behavior of the bolted connections, as

presented in Figure 5.8. Overall, the hysteretic behavior remained symmetrical under rotational demand only. The addition of seismic gravity shear load had a significant impact on the specimen behavior by increasing the positive moment capacity and decreasing the maximum negative moment capacity. However, the shear load did not affect the rotational capacity of the connection. The asymmetric deformation pattern of 2L connections with seismic gravity shear demand resulted in an asymmetric hysteretic behavior. The maximum moment capacity developed during a positive excursion was significantly larger than during the corresponding negative excursion. The in-plane torsional moment developed in the column legs due to the applied shear load resulted in a constant tensile loading on the top side of the web angle, as illustrated in Figure 5.6. The force resulting from the torsional moment reduced the capacity mobilized by negative moment and thus reduced the connection moment capacity under negative bending.

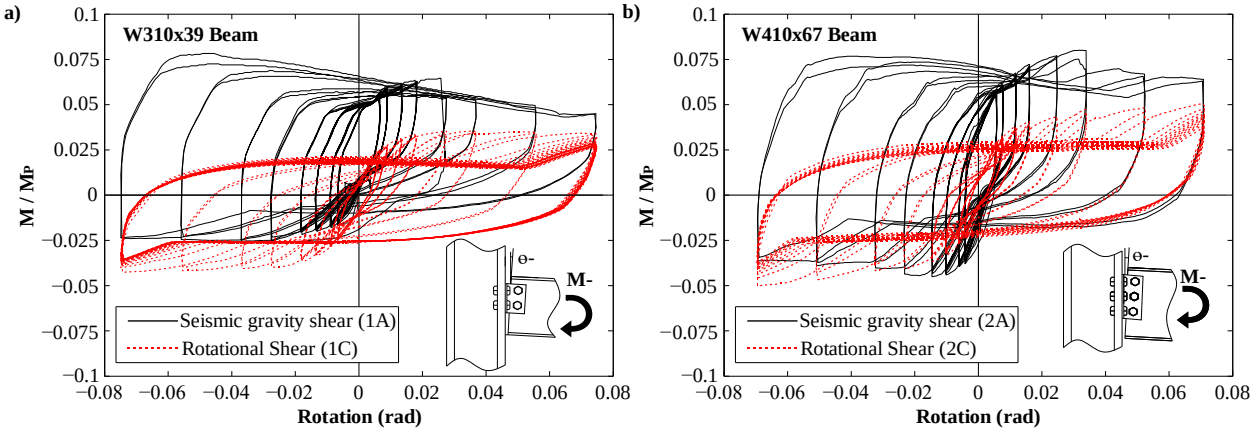


Figure 5.8. Influence of seismic gravity shear load on the connection hysteretic behavior: a) W310 beam and b) W410 beam.

The same torsional moment created a counteracting force on the bottom side of the web angles illustrated in Figure 5.6. Under positive bending, the force couple created by the torsional moment opposed the force developed by the flexural moment, which increased the connection positive moment capacity. The maximum positive moment was obtained just after the load reversal, when the beam web entered in contact with the top side of the web angle fillet. As the angles deformed inelastically, the moment capacity gradually decreased until contact was achieved between the web angle fillet and the column flange. This contact created a positive plastic stiffness. Adding shear demand on the beam-column connections resulted in a larger positive moment capacity increase

than the decrease of negative moment capacity. Therefore, the addition of seismic gravity shear loading increased the overall connection energy-dissipation capacity by inducing additional localized inelastic response in the angles.

5.5.2 Influence of design shear excursions

Specimens 1B and 2B were loaded with the same cyclic rotational demand as specimens 1A and 2A, but the protocol was paused intermittently to increase the applied connection shear to the design shear. These excursions aimed at verifying the connection capacity to sustain the design shear demand after significant yielding and rotational demand from a seismic event.

The two specimens loaded with this pattern sustained their design shear load, even after large rotational demands. The connections failures did not occur during the design shear excursions, but rather during the cyclic rotational demand combined with the gravity loads associated with a seismic event. Figure 5.9 presents the hysteretic behavior of the specimens tested with the shear excursions compared to the tests without the excursions. The design shear excursions did not affect the rotational capacity of the connections but slightly increased the effects of the shear load. This augmentation is particularly observed in specimen 1 with the W310 beam, where the positive moment capacity is significantly increased. This specimen is more sensitive to the shear demand as the connection is more flexible.

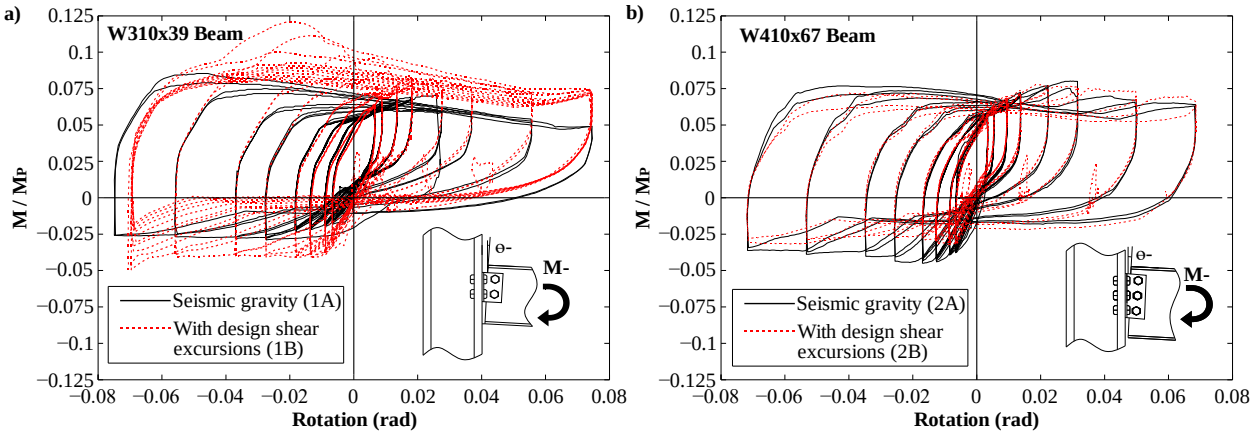


Figure 5.9. Influence of design shear load excursions on the connection hysteretic behavior: a) W310 beam and b) W410 beam.

Figure 5.10 compares the displacement transverse to the beam local axis (Z) for a specimen with seismic gravity shear, without (2A) and with (2B) the design shear excursions. During the seismic gravity shear load application, before the cyclic loading, the transverse displacement of the connections reached -3.3 mm and -4.1 mm respectively. Then, the transverse displacement (Z) increased gradually with the accumulated rotational demand, to reach a maximum of -14.3 mm and -17.0 mm respectively. The intermittent design shear excursions increased the transverse displacement significantly as illustrated in Figure 5.10b. The displacement measurements shown in Figure 5.10 include the shear deformation of the angle beam leg as well as the transverse displacement resulting from the in-plane rotation of the column leg.

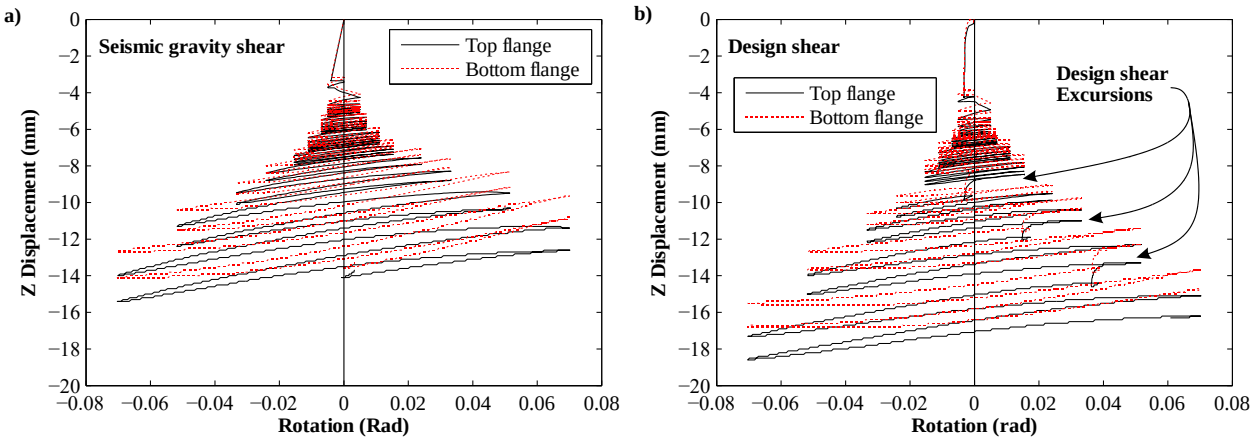


Figure 5.10. Transverse displacement (Z): a) without shear excursions (2A) and b) with shear excursions (2B).

5.5.3 Influence of beam depth

The beam depth is an important geometrical parameter for the design of beam-column connections, as it generally determines the length of double web angle components required to offer a sufficient lateral support to the beam. For this purpose, the 2L lengths were 140 mm and 216 mm for the connections with a W310 and a W410 beam, respectively. Additionally, the larger design shear load on the W410 connection required 3 bolt rows in the beam web instead of the 2 rows required for the W310 connection. These differences translated into significant moment capacity increases for the 2L connections in the deeper beam, as presented in Figure 5.11a and b. An increase in the angle length of 54% resulted in moment capacities approximately 3 times larger. The negative plastic stiffness associated with the shear load influence was also reduced by an increase of the

angle length. Furthermore, both specimens reached significant rotational demand, up to 0.075 rad in both directions. If gravity connections are to be employed for lateral resistance contributing to seismic stability, deeper connections are desirable since this translates into an increase in the moment capacity and a more stable hysteretic behavior. Nevertheless, the normalized moment capacity with respect to the beam plastic moment M_p remains similar in both connection geometry tested, as presented in Figure 5.11c and d. Since the angle length is generally determined from the beam depth to provide enough lateral support, the maximum negative and positive moments developed in the connection averaged -5% and 7.5% of M_p respectively for the connections subjected to seismic gravity shear. The connections with rotational shear reached approximately 5% of M_p in both negative and positive bending. Therefore, 2L connections still remain the most flexible element and will not initiate unwanted yielding in the column and beams of the gravity frame.

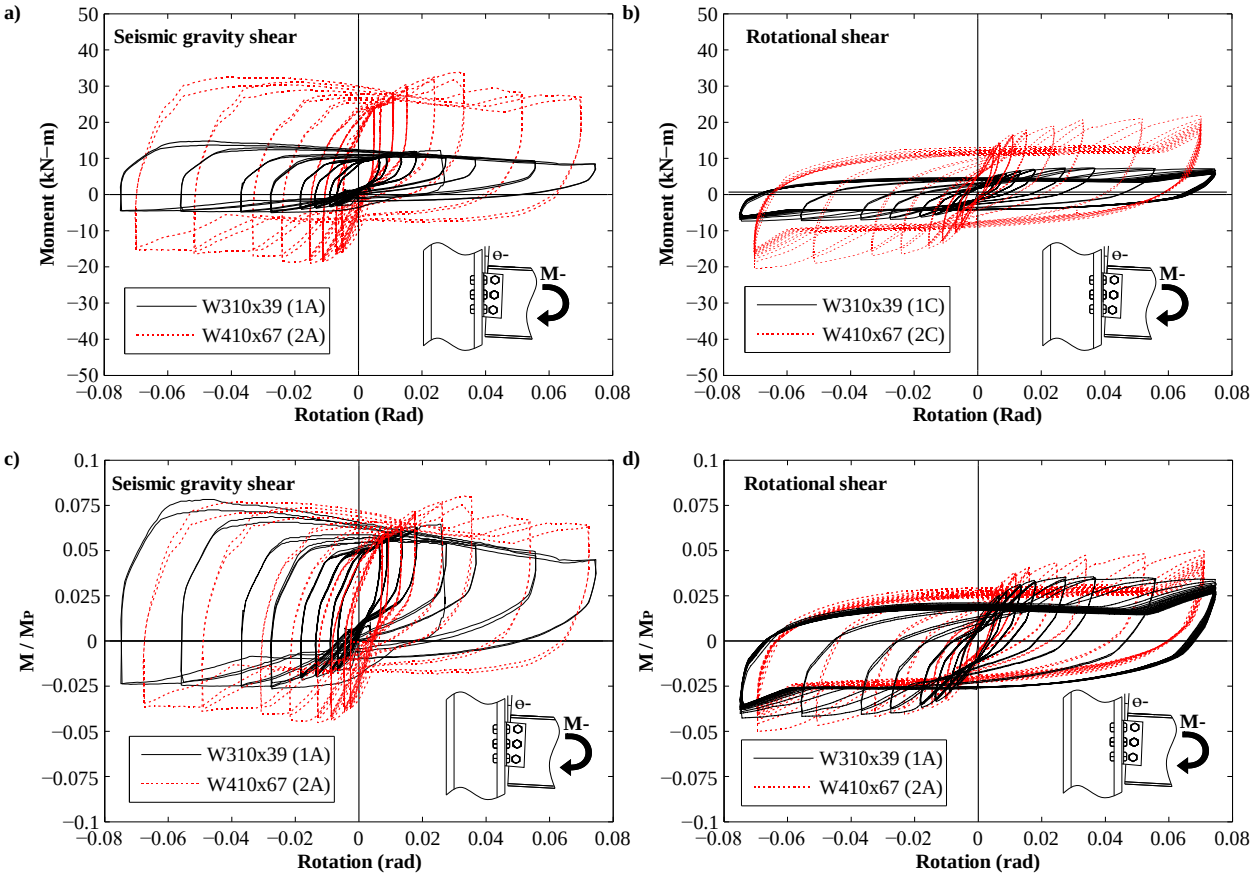


Figure 5.11. Influence of beam depth on the connection hysteretic behavior: a) with seismic gravity shear b) with rotational shear c) with seismic gravity shear and normalized with the beam plastic moment and d) with rotational shear and normalized with the beam plastic moment.

5.5.4 Influence of asymmetric loading conditions

In a related prior study (Beland et al. 2019a), the force-displacement hysteretic behavior of bolted angle components was found to follow a secant stiffness behavior, where the reloading stiffness depended directly on the maximum displacement already experienced by the angle. To observe the influence of this component behavior on the connection hysteresis, the influence of the rotational demand history was investigated with asymmetric loading protocols, where the rotational demand did not reach a new maximum value at each cycle.

Specimens 2D and 2E were tested with an asymmetric loading protocol imposing predominantly negative rotational demands in one and positive rotational demands in the other. These tests are presented in Figure 5.12a, along with the symmetrical hysteretic behavior obtained from specimen 2A. All three specimens were subjected to a constant seismic gravity shear load of -282 kN. The behavior observed in the asymmetric tests also followed a behavior where the reloading stiffness depended on the maximum rotation and moment previously reached by the angles. The lesser rotational demand imposed on the angles reduced the in-plane torsional deformations in the column legs. Figures 5.12b and 5.12c present the transverse (Z) displacement measured at the beam flanges of specimens 2D and 2E respectively. Large displacements were measured during the gravity shear load application and during the first few cycles. However, the vertical displacements remained small during the asymmetric loading. This observation indicates that the influence of the column leg in-plane torsional deformations on the moment capacities was less pronounced in the asymmetric tests. The positive moment capacity increase was reduced by approximately 30% because of the smaller contact forces developed between the angle fillets and the beam web.

Additionally, the connection develops most of its negative moment capacity once the bottom side of the web angles enters in contact with the column flange. In the asymmetric tests, the first cycle of the loading protocol reached the maximum rotations imposed on the connection in both directions. Therefore, in the following cycles, the web angles reach their maximum deformations and the connection reaches its moment capacity only when the maximum imposed rotation is

reached. Furthermore, in specimen 4D, loaded in predominantly with negative rotational demand, significant bolt slip between the angles and the beam web was observed during the first negative excursion. This bolt slip reduced the required deformation experienced by the angles to reach the target rotational demand, thus reducing the maximum negative moment in the connection. Indeed, the negative moment capacity was reduced by approximately 50%. Although the moment capacities of the asymmetric tests were smaller than those of the symmetric test, the rotational capacities of the specimens remained similar. The reduced cumulative rotational demand imposed during the asymmetric test allowed the specimen 2D to reach a negative rotational capacity 12% greater than the symmetric test (2A). However, the same rotational capacity was obtained in both the positive asymmetric test (2E) and the symmetric test (2A).

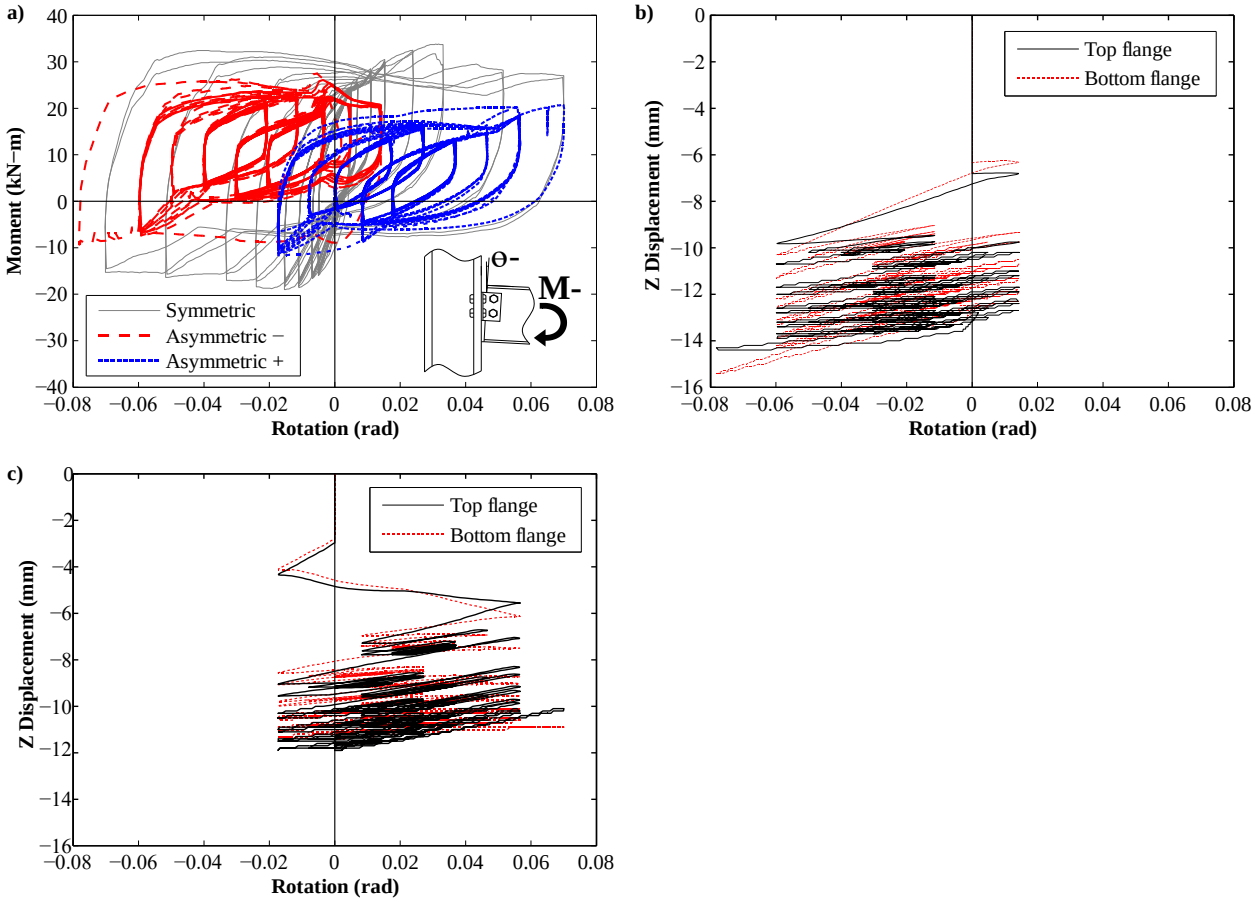


Figure 5.12. a) Influence of asymmetric loading protocol on the connection hyteretic behavior b) Transverse displacement (Z) of the negative asymmetric test (2D) c) Transverse displacement (Z) of the positive asymmetric test (2E).

5.6 Conclusions and recommendations

Since gravity framing in steel buildings has the potential to contribute to seismic stability after damage has occurred in the primary lateral force-resisting system, an experimental program was developed to characterize the global nonlinear behavior of bolted double angle shear connections under simultaneous shear and rotational demand. Each of the eight tests performed were characterized with key response parameters and visual observations. So that this connection type can be represented in simulations, the mathematical model proposed by Menegotto and Pinto (1973) was calibrated with the positive and negative envelopes of each test.

The specimens were subjected to both symmetrical and asymmetrical loading protocols, and several shear loading conditions were explored. From these tests, the following conclusions are drawn:

- The deformation patterns were not significantly influenced by the beam depth and the column section;
- The specimens with the larger beam depth exhibited a larger moment capacity, without significant influence on the rotational capacity;
- Increased shear load created a complex deformation pattern resulting in a highly nonlinear hysteretic behavior;
- Every connection sustained the design shear load, even after experiencing large rotational demands and plastic deformations.

In general, the nonlinear behavior exhibited by bolted angle connections showed large ductility, stable moment-rotation hysteresis, and reliable shear capacity even at high rotation demands, which can translate into stable behavior under seismic loading conditions. Therefore, bolted angles for gravity framing connections could be reliably assessed as part of the reserve capacity of the building system. Considering the large redundancy and stable behavior of these connections, a simple numerical assessment of approximately $0.05M_p$ for each connection, where M_p refers to the design beam plastic moment capacity, can provide designers with an initial read on the gravity system's inherent capacity to help mitigate the building collapse in low-ductility braced frames.

5.7 Data Availability Statement

The following data, models, or code generated or used during the study are available from the corresponding author by request:

- Information on the experimental setup;
- Experimental measurements;
- Processed data; and
- Calibrated model of the envelope curves.

5.8 Acknowledgments

This study was supported by the Natural Sciences and Engineering Research Council of Canada (Canada Research Chair Program, Grant no. 219924), the National Science Foundation (Grant No. CMMI-1207976) and the American Institute of Steel Construction. The first author received the SSEF G.J. Jackson Fellowship of the Canadian Institute of Steel Construction for this research. Ali Davaran, Jessalyn Nelson, Cameron Bradley and Joshua Sizemore provided assistance in developing the testing program described in this paper. Jonathan Auger, Romain Siguier and Patrice Bélanger of the Structures Laboratory of Polytechnique Montreal provided valued assistance to conduct the experimental tests. The opinions, findings, and conclusions in this paper are those of the authors and do not necessarily reflect the views of those acknowledged here.

REFERENCES

Abolmaali, A., Kukreti, A. R., and Razavi, H. (2003). “Hysteresis behavior of semi-rigid double web angle steel connections.” *J. Constr. Steel Res.*, 59, 1057–1082.

AISC. (2010). “Seismic provisions for structural steel buildings.” *AISC341-10*, Chicago.

Astaneh, A, Nader, M. N., Malik, L. (1989). “Cyclic behavior of double angle connections.” *J. Struct. Eng.*, 115(5), 1101-1118.

Beland, T., Bradley, C. R., Nelson, J., Sizemore, J. G., Davaran, A., Hines, E. M. Fahnestock, L. A. (2019a). “Experimental parametric characterization of bolted angle connection behavior”. *In Review.*

Beland, T., Tremblay, R., Hines, E. M., Fahnestock, L. A., (2019b). “Full-scale cyclic testing with shear load of double web with top and seat angle beam-column connections”. *In review.*

Braconi, A., Salvatore, W., Tremblay, R., and Bursi, O. S. (2007). “Behaviour and modelling of partial-strength beam-to-column composite joints for seismic applications.” *Earthquake Eng. Struct. Dyn.* 36(1), 142-161.Callister, J. T., Pekelnicky, R. G. (2011). “Seismic Evaluation of an existing low ductility braced frame building in California.” *Proc. ASCE Structures Congress 2011*, 2756-2767.

Citipitioglu, A. M., Haj-Ali, R. M., White, D. W. (2002). “Refined 3D finite element modeling of partially restrained connections including slip.” *J. Constr. Steel. Res.*, 58, 995-1013.

Danesh, F., Pirmoz, A., Daryan, A. S., (2007) “Effect of shear force on the initial stiffness of top and seat angle connections with double web angles.” *J. Constr. Steel. Res.*, 63, 1208-1218.

De Stefano, M., De Luca, A., Astaneh-Asl, A. (1994). “Modeling of cyclic moment-rotation response of double-angle connections.” *J. Struct. Eng.*, 120(1), 212-229.

Elkady, A., Lignos, D. G. (2015). “Effect of gravity framing on the overstrength and collapse capacity of steel frame buildings with perimeter special moment frames.” *Earthquake Eng. Struct. Dyn.*, 44(8), 1289–1307.

Filippou, F. C., Popov, E. P., Bertero, V. V. (1983). *Effect of bold deterioration on the hysteretic behavior of reinforced concrete joints*. National Science Foundation, Earthquake Engineering Research Center, Berkeley, CA.

Flores, F. X., Charney, F. A., Lopez-Garcia, D. (2014). “Influence of the gravity framing system on the collapse performance of special steel moment frames.” *J. Constr. Steel. Res.*, 101, 351-362.

Flores, F. X., Charney, F. A., Lopez-Garcia, D. (2016). “The influence of gravity column continuity on the seismic performance of special steel moment frame structures.” *J. Constr. Steel. Res.*, 118, 217-230.

Gong, Y. (2014). “Ultimate tensile deformation and strength capacities of bolted-angle connections.” *J. Constr. Steel. Res.*, 100, 50-59.

Gupta, A., Krawinkler, H. (2000). “Behavior of ductile SMRFs at various seismic hazard levels.” *J. Struct. Eng.*, 126(1), 98-107.

Guravich, S. J., Dawe, J. L. (2006). “Simple beam connections in combined shear and tension”. *Can. J. Civ. Eng.* 33. 357-372.

Hines, E. M., Appel, M. E., Cheever, P. J. (2009). “Collapse performance of low-ductility chevron braced steel frames in moderate seismic regions”. *AISC Eng. J.*, 3rd Quarter, 149-180.

Hwang, S.-H., Lignos, D. G. (2017). “Effect of modelling assumptions on the earthquake-induced losses and collapse risk of steel-frame buildings with special concentrically braced frames.” *J. Struct. Eng.*, 143(9).

Jarrett, J. A., Judd, J. P., Charney, F. A. (2015). “Comparative evaluation of innovative and traditional seismic-resisting systems using the FEMA P-58 procedure.” *J. Constr. Steel. Res.*, 105, 107-118.

Ji, X., Kato, M., Wang, T., Hitaka, T., Nakashima, M. (2009). “Effect of gravity columns on mitigation of drift concentration for braced frames.” *J. Struct. Steel. Res.*, 65, 2148-2156.

Judd, J. P., Charney, F. A., Pryor, S. E. (2015). “Retrofit of steel-frame buildings using enhanced gravity-frame connections.” *Proc. 2nd ATC & SEI Conf. on improving the seismic performance of existing buildings and other structures,* 132-143.

Kishi, N., Chen, W.-F. (1990). “Moment-rotation relations of semirigid connections with angles.” *J. Struct. Eng.*, 116(7), 1813-1834.

Lee, K., Foutch, D. A. (2002). “Performance evaluation of new steel frame buildings for seismic loads.” *Earthquake Eng. Struct. Dyn.*, 31, 653-670.

Liu, J., Astaneh-Asl, A. (2000). “Cyclic testing of simple connections including effects of slab”. *J. Struct. Eng.*, 126(1), 32-39.

Liu, J., and Astaneh-Asl, A. (2004). “Moment-rotation parameters for composite shear tab connections.” *J. Struct. Eng.-ASCE* 130(9), 1371-1380.

Liu, J., Main, J., Sadek, F. (2012). “Modleing of double-angle shear connections for evaluation of structural robustness.” *Proc. Forensic Engineering 2012*. 1081-1090.

Matthews, J., Arjomandi, K. (2017). “Improved ductility of bolted double-angle shear connections.” *Pract. Period. Struct. Des. Constr.*, 22(3).

Mazzoni, S., McKenna, F., Scott, M. H., Fenves, G. L. (2006). *OpenSees command language manual*. Pacific Earthquake Engineering Research Center, University of California Berkeley, Berkeley, CA.

Menegotto, M., Pinto, P. E. (1973). “Method of analysis for cyclically loaded R.C. plane frames including changes in geometry and non-elastic behaviour of elements under combined normal force and bending”. *IABSE reports of the working commissions*. Zurich, Switzerland.

NBCC. (2015) *National Building Code of Canada*. National Research Council Canada, Ottawa, ON.

Oosterhof, S. A., Driver, R. G., (2012). “Performance of steel shear connections under combined moment, shear and tension.” *Proc. Structures Congress 2012*. 146-157.

Pirmoz, A., Daryan, A. S., Mazaheri, A., Darbandi, H. E. (2008). “Behavior of bolted angle connections subjected to combined shear force and moment”. *J. Constr. Steel Res.*, 64, 436-446.

Radziminski, J. B., Bradburn, J. H. (1984) “Experimental investigation of semi-rigid steel beam-column connections”. *Proc. 8th World Conference on Earthquake Engineering,* 169-176.

Shen, J., Astaneh-Asl, A. (1999). “Hysteretic behavior of bolted-angle connections.”, *J. Constr. Steel. Res.*, 51, 201-218.

Shen, J., Astaneh-Asl, A. (2000). “Hysteretic model of bolted-angle connections.”, *J. Constr. Steel. Res.*, 54, 317-343.

Sizemore, J. G., Fahnestock, L. A., Hines, E. M., Bradley, C. R. (2017) “Parametric study of low-ductility concentrically braced frames under cyclic static loading.” *J. Struct. Eng.*, 143(6).

Stoakes, C. D., Fahnestock, L. A. (2011). “Cyclic flexural testing of concentrically braced frame beam-column connections.” *J. Struct. Eng.*, 137, 739-747.

Weigand, J. M., Berman, J. W. (2016). “Integrity of bolted angle connections subjected to simulated column removal.” *J. Struct. Eng.*, 142(3).

Yang, B., Tan, K. H. (2013). “Robustness of bolted-angle connections against progressive collapse: Mechanical modelling of bolted-angle connection under tension.” *Eng. Struct.*, 57, 153-168.

CHAPTER 6 ARTICLE 3: FULL-SCALE CYCLIC ROTATION AND SHEAR LOAD TESTING OF DOUBLE WEB WITH TOP AND SEAT ANGLE BEAM-COLUMN CONNECTIONS

Thierry Béland
École Polytechnique Montréal, Montreal, Québec H3C 3A7, Canada
thierry.beland@polymtl.ca

Robert Tremblay
École Polytechnique de Montréal, Montreal, Québec H3C 3A7, Canada
robert.tremblay@polymtl.ca

Eric M. Hines, P.E., M.ASCE
Tufts University, Medford, Massachusetts 02155. USA
eric.hines@tufts.edu

Larry A. Fahnestock, P.E., M.ASCE
University of Illinois at Urbana-Champaign, Urbana, Illinois 61801, USA
fhnstck@illinois.edu

Paper submitted to *ASCE Journal of Structural Engineering*,
Submitted April 27th, 2019.

ABSTRACT:

Partially restrained beam-column connections such as bolted double web with top and seat angle connections can be used in the gravity load system of steel buildings to develop secondary moment frame action and enhance seismic collapse prevention. To assess the gravity beam-column connection role in lateral reserve capacity, a comprehensive test program was conducted at Ecole Polytechnique Montreal to characterize the nonlinear hysteretic behavior of bolted angle connections subjected to simultaneous gravity shear and rotational demand from the moment frame action. Fifteen full-scale beam-column sub-assemblages of four different geometries were tested to characterize their deformation pattern and failure modes. The influence of the following critical parameters on the connection hysteretic behavior was investigated: the top and seat angle geometrical parameters, the beam and column sections, the gravity shear load and the loading history. The envelope curve of each test was mathematically characterized to numerically reproduce the connection behavior. The tested connections exhibited large ductility and significant moment capacity, which translated into a substantial energy dissipation capacity. The use of bolted

angles for gravity framing connections could thus be beneficial by enhancing the reserve capacity and providing lateral resistance to mitigate seismic building collapse.

KEYWORDS: Bolted-Angle Connections; Experimental tests; Cyclic response; Steel buildings; Seismic stability.

6.1 Introduction

During the 1994 Northridge earthquake, some steel-framed buildings experienced fracture in many of their moment frame welded connections, but the structures survived and even experienced relatively small story drift (Hajjar et al. 1995, O'Sullivan et al. 1998). The gravity system single plate shear connections, combined with the concrete slab, created composite partially-restrained (PR) connections (Leon 1998), which mitigated the building damage through moment frame action (O'Sullivan et al. 1998). These observations from post-earthquake evaluation illustrate the beneficial effect that the gravity frame can have on seismic response. The gravity frame serves as a back-up (secondary) lateral force-resisting system (LFRS), which is critical in case of failure of the primary system. Although gravity beam-column connections are designed to resist only shear loads, their inherent rotational stiffness creates moment frame action that reduces drifts and destabilizing effects of gravity (Ji et al. 2009; Flores et al. 2014, Flores et al. 2016) and increases the building collapse resistance (Gupta and Krawinkler 2000; Lee and Foutch 2002; Callister and Pekelnicky 2011; Hines et al. 2009, Stoakes and Fahnestock 2011; Jarrett et al. 2014; Judd and Charney 2015; Elkady and Lignos 2015; Sizemore et al. 2017; Hwang and Lignos 2017, Del Carpio et al. 2019).

In a steel-framed building with I-shaped beams and columns, double-angle web connections are commonly used for the gravity system. As indicated above, web-only beam column connections can mobilize frame action but enhancing the connection with top and seat angles is a relatively simple way to increase connection stiffness and strength and improve seismic response (Bjorhovde et al. 1990; Kishi et al. 1997; Nethercot et al. 1998; Astaneh-Asl et al. 1998; Krawinkler and Seneviratna 1998, Callister and Pekelnicky 2011). These connections must also exhibit sufficient ductility to sustain the rotational demand that will occur at relatively large story drifts after significant damage to the primary system. For engineers to use double web angle connections with top and seat angles (2L-TS) connections as part of a secondary lateral system, the nonlinear

connection behavior must be clearly understood through large-scale experimental tests and then characterized with accurate but relatively simple models.

Several geometrical parameters influence the moment-rotation relationship of 2L-TS connections, such as the beam depth and the web angle length (Azizinamini 1985, Azizinamini and Radziminski 1989, Fleischman et al. 1991, Abolmaali et al. 2003). These parameters play an important role in the stiffness, moment and rotational capacity of 2L-TS connections. The geometrical parameters of the top and seat angles also significantly influence the moment-rotation behavior of the connection, particularly the angle thickness, the column bolt distance and the angle length (Azizinamini 1982, Radziminski and Bradburn 1984, Azizinamini 1985, Mander et al. 1994, Mander et al. 1995, Kukreti and Abolmaali 1999, Calado et al. 2000, Abdalla et al. 2014, Ghineda et al. 2015, Liu et al. 2015).

Experimental investigations focused on the influence of several geometrical parameters on the nonlinear behavior of bolted angles on a component level (Azizinamini 1982, Azizinamini 1985, Shen and Astaneh-Asl 1999, Shen and Astaneh-Asl 2000, Garlock et al. 2003, Yang and Tan 2013, Gong 2014, Beland et al. 2019). These investigations characterized the monotonic and cyclic behavior of bolted angles and identified the angle thickness and the column bolt position as the most influential parameters on the nonlinear behavior of the angle.

Past experimental investigations have provided valuable data on individual angle behavior, but they were performed using simplified test setups, loading the angles only in tension. Although such simplification is reasonable to comprehensively study a broad range of angle parameters (Beland et al. 2019), this tension loading condition ignores the beam leg rotation present in the deformation of the angle in a beam-column connection (Azizinamini 1985, Citipitioglu et al. 2003, Danesh et al. 2007). This rotation decreases the ultimate displacement capacity of the top and seat angles in a complete connection test.

The connections of the gravity frame can provide secondary lateral resistance through a moment frame action, but the gravity frame must still fulfill its primary role of supporting the gravity loads. Part of the gravity connection capacity must then be mobilized to resist the beam end shear reactions. Through finite element analyses, Danesh et al. (2007) observed an initial rotational stiffness reduction up to 55% due to this partial mobilization of the connection shear capacity.

Pirmoz et al. (2008) proposed an analytical model to represent this stiffness decrease due to the shear demand. These numerical investigations addressed an important issue relative to the realistic moment-rotation behavior of gravity connections subjected to combined shear and moment. However, these observations were not validated experimentally. Tests on 2L-TS beam-column subassemblies were performed to characterize their moment-rotation response (Azizinamini and Radziminski 1989, Kukreti and Abolmaali 1999, Calado et al. 2000, Abdalla et al. 2015, Ghindea et al. 2015) and their monotonic moment-rotation behavior with simultaneous shear and tension demand in the context of progressive collapse (Yang and Tan 2013, Liu et al. 2015). The hysteretic response of beam-column connections under simultaneous shear and rotational demand has not yet been addressed experimentally. The connection capacity to sustain the gravity shear load after large flexural yielding caused by a seismic event must be validated.

An experimental program was thus conducted at Ecole Polytechnique Montreal to validate this capacity and define the hysteretic nonlinear behavior of 2L-TS connections under shear and rotational demands. The influence of the shear load, the beam depth, the column section, the top and seat angles thickness and column bolt position were investigated through 15 tests performed on full-scale beam-to-column specimens. Specimens were tested with a symmetric cyclic rotational demand with and without gravity shear, as well as an asymmetric rotational demand. The moment-rotation envelope of each test was characterized with the mathematical model proposed by Kishi and Chen (1990).

The nonlinear behavior, deformation patterns and failure modes observed throughout the experimental program are detailed in this paper. The influence of geometrical parameters and loading conditions on the nonlinear behavior of bolted angle connections are also presented. More specifically, the influence of top and seat angles, their thickness and column bolt distance, the beam depth and the column section are investigated.

6.2 Experimental Program

6.2.1 Test setup

This testing program characterized the hysteretic behavior and rotational capacity of bolted angle beam-column connections subjected to combined rotational demand and shear loading. Figure 6.1

illustrates the test setup in the Structures Laboratory of École Polytechnique Montreal, where the beam is the vertical component and the horizontal column is anchored to the strong floor. Two actuators were used to create the loading conditions. The 500 kN capacity actuator, located at 3442 mm from the connection, created the rotational demand on the connection. This actuator was displacement-controlled, with a constant displacement rate. The 1000 kN capacity actuator, was used to apply the shear load on the connection at a distance of 942 mm from the connection. The shear load at the face of the column was held constant to simplify the loading procedure. The 1000 kN actuator was thus force-controlled and its command was dependent on the load applied by the 500 kN actuator. The force command was obtained by the difference between the connection target shear load and the load in the 500 kN displacement-controlled actuator. The height of the 500 kN actuator was set to reach the beam plastic moment M_p with a load in the actuator smaller than the target shear load. Therefore, the target shear load could never be reached with the top actuator only and the load from the 1000 kN actuator was always applied in the same direction.A third actuator (100 kN) was used to support the weight of the 1000 kN actuator. This setup minimized the axial load in the beam specimen, while allowing the connection to experience longitudinal displacements along the beam local axis.

6.2.2 Instrumentation setup

The rotation of the beam-column connection specimens is used in the testing procedure as the control parameter. Once the connection rotation reached the target for the current cycle, the change in loading direction of the upper actuator is triggered.

This rotation is calculated from the measurement of four linear potentiometers (LPs) of ± 50 mm attached to the edge of the beam member with square nuts welded to the interior side of the flanges and threaded rods. On the other end, the captors are attached to the lower flange of the column, as illustrated in Figure 6.2a. Figure 6.2b presents a plan view of the connection along with the nomenclature of the captors.

The rotation θ is obtained with Equation 6.1, given as the difference in the average of the LPs measurements at the top and bottom of the connection. This difference is then divided by the average distance between the instruments d_S and d_N to obtain the connection rotation θ_b.

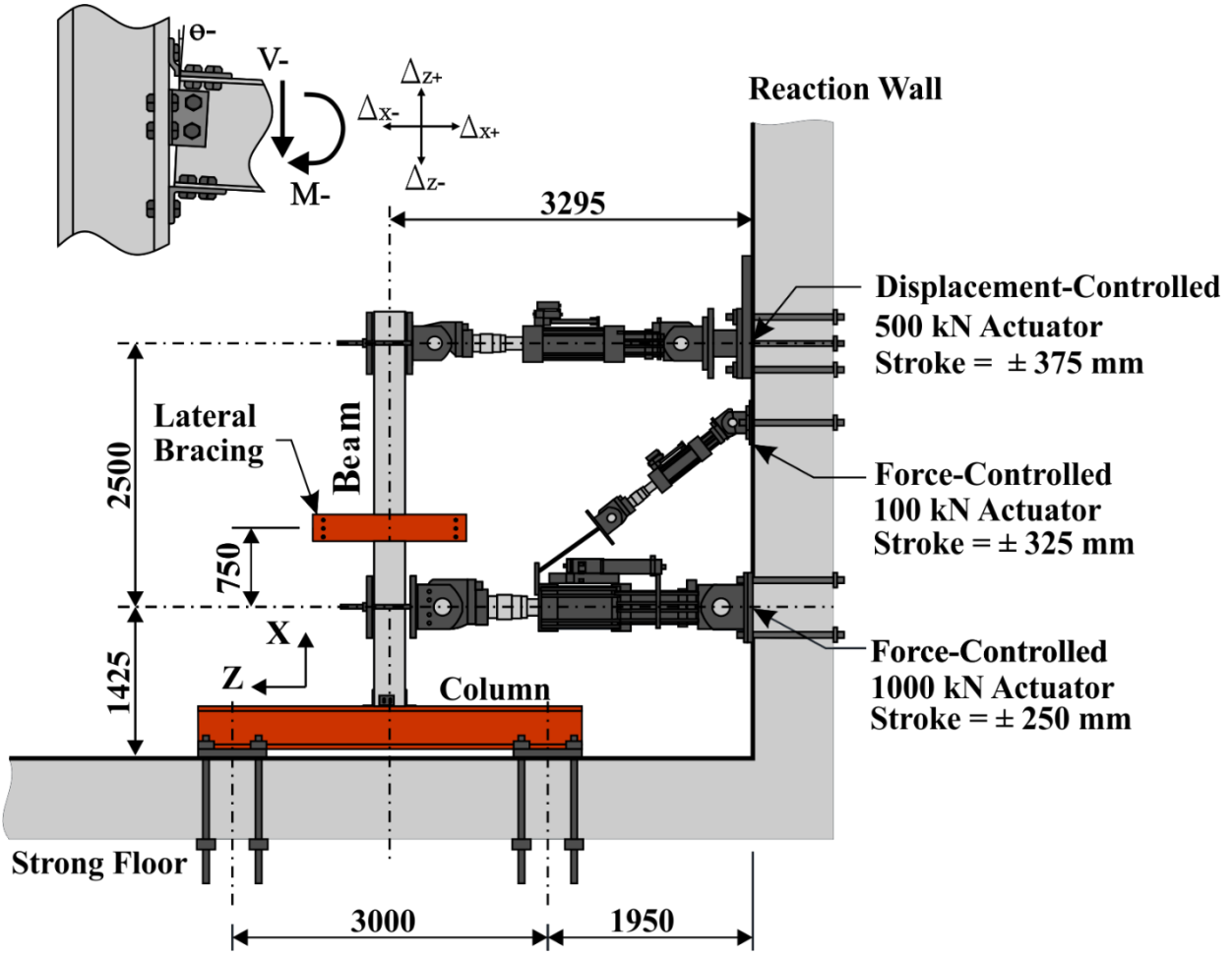


Figure 6.1. Beam-column connection test setup.

$$\theta = \frac{\frac{LP_{NW} + LP_{SW}}{2} - \frac{LP_{NE} + LP_{SE}}{2}}{\frac{d_S + d_N}{2}} \tag{6.1}$$

The loads in the 1000 kN and 500 kN actuators, F_{V1000} and F_{V500} respectively, are recorded by the load cells in the actuators. These values are used to determine the moment M at the connection, with Equation 6.2. In this Equation, L_{V500} correspond to the distance between the column flange and the top actuator, 0.942 m, while L_{V1000} correspond to the distance between the column flange and bottom actuator, 3.442 m.

$$M = F_{V500} \times L_{V500} + F_{V1000} \times L_{V1000} \tag{6.2}$$

Furthermore, the horizontal and vertical displacements of the top and seat angles were calculated from the measurement of two string potentiometers (SPs) each. The captors were clamped to the column flange with a steel support as shown in Figure 6.2c. A set made of a horizontal and an inclined SP, both vertically aligned, were used to calculate the angle displacement through triangulation. This setup is pictured in Figure 6.2c.

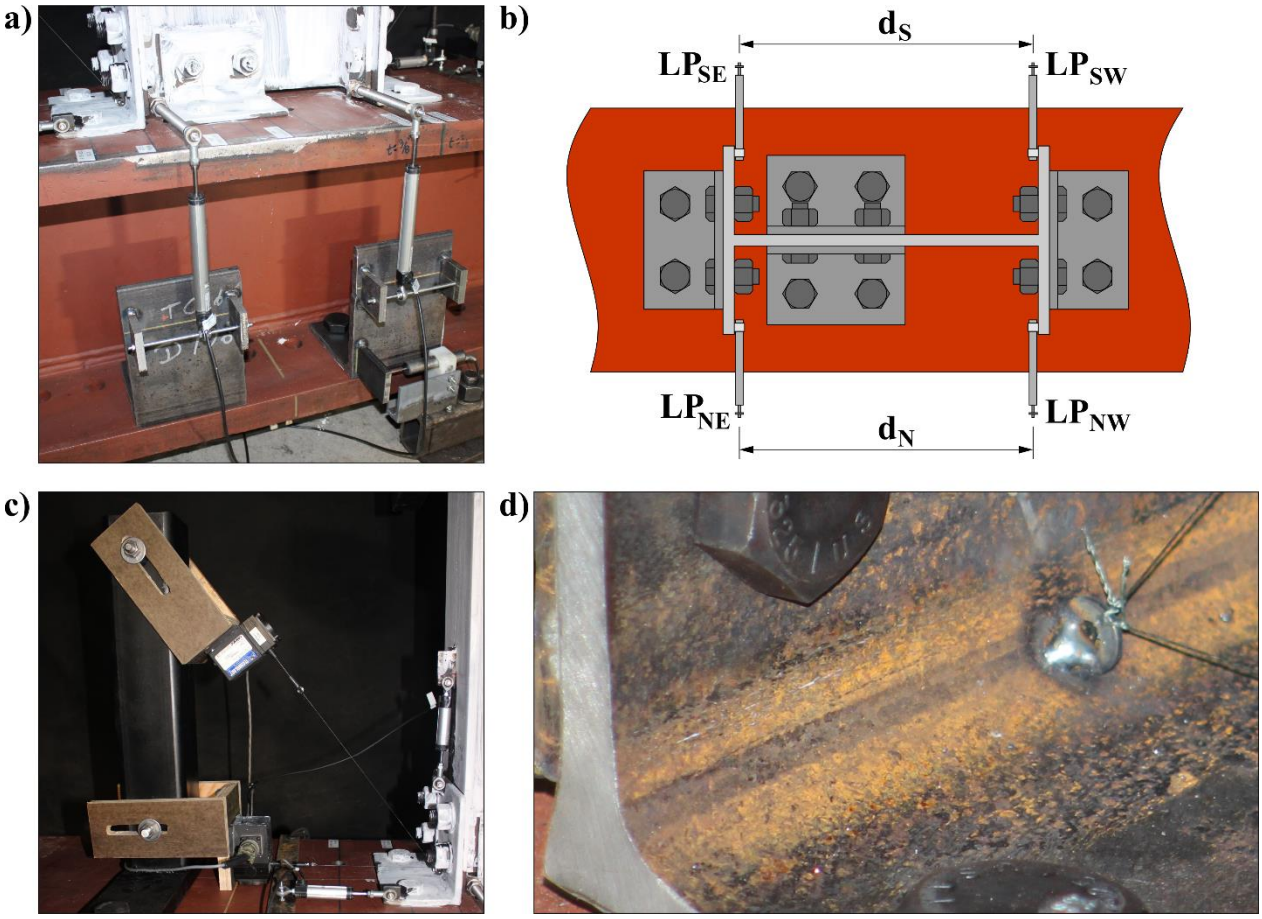


Figure 6.2. a) Instrumentation setup for measuring the connection rotation; b) Captors position on the specimen; c) Instrumentation setup for measuring the angle vertival and horizontal displacement; d) String attachment detail to the top and seat angles.

The strings of the captors were attached to a small washer welded in the center of the angle fillet, as presented in Figure 6.2d. This type of attachment was preferred since it allowed an accurate measurement of the angle corner displacement. The material property alterations resulting from the welding only affected the local area near the weld. Since the plastic hinges were observed at the edge of the fillet in both the column and beam legs during the angle testing program and not in the

fillet itself, the local material alterations are assumed to be negligible on the plastic mechanism of the top and seat angles.

6.2.3 Beam-column connection specimens

The testing program on the beam-column connections consisted of four connection geometries (Table 6.1), with either a W310x39 (W12x26) or a W410x67 (W16x45) beam and a W360x289 (W14x193) or a W250x49 (W10x45) column. The global connection layout is presented in Figure 6.3. The connection geometries consisted of L102x102x7.9 (L4x4x5/16) double web angles with top and seat angles. The length of the web angles L_w was 140 mm and 216 mm with 2 or 3 bolt rows for the W310 and the W410 beam specimens respectively. The bolts were ASTM A325 with a diameter d_b of 19.1 mm (3/4”). The column bolts were located at a column gage g_c, defined as the distance between the bolt centerline and the angle corner, of 63.5 mm. The flexural span of the column leg g_2, given by the distance between the edge of the bolt head and the angle fillet, corresponded to 30 mm. The distance between the beam bolts and the angle corner g_b for the top and seat angles, and the distance e between the beam top flange and the web angles are presented in Table 6.1.

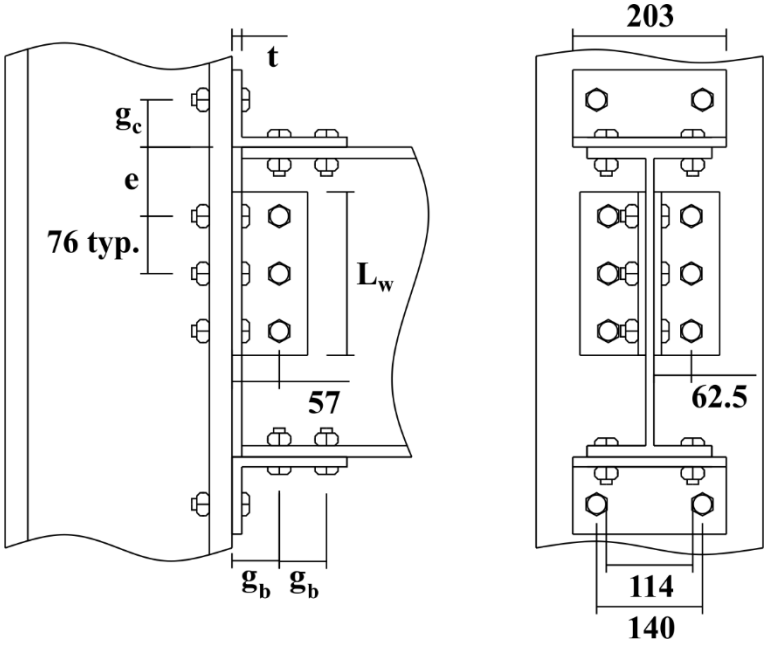


Figure 6.3. Beam-column connection parameters.

Table 6.1. Geometrical properties, loading procedures and design resistance of the connection specimens

Specimen	**1**	**2**	**3**	**4**
Beam	W310x39 e = 76 mm		W410x67 e = 100 mm	
Column	W360x347	W360x347 W250x49	W360x347	W360x347 W250x49
Top & Seat	L152x102x9.5 g_c : 63.5 mm g_b : 57 mm d_b : 19.1 mm	L203x152x19.1 g_c : 101.6 mm g_b : 76 mm d_b : 25.4 mm	L152x102x9.5 g_c : 63.5 mm g_b : 57 mm d_b : 19.1 mm	L203x152x19.1 g_c : 101.6 mm g_b : 76 mm d_b : 25.4 mm
Web angles	L102x102x7.9 L_w : 140 mm, d_b : 19.1 mm		L102x102x7.9 L_w : 216 mm, d_b : 19.1 mm	
Loading procedures of each tests				
A	Cyclic + seismic gravity shear	Cyclic + seismic gravity shear	Cyclic + seismic gravity shear	Cyclic + seismic gravity shear
B	Cyclic + seismic gravity + design excursions shear	Cyclic + seismic gravity + design excursions shear	Cyclic + seismic gravity + design excursions shear	Cyclic + seismic gravity + design excursions shear
C	Cyclic + rotational shear	Cyclic + rotational shear	Cyclic + rotational shear	Cyclic + rotational shear
D	Near fault (-) + seismic gravity shear	Cyclic + seismic gravity shear, W250x39 column	-	Cyclic + seismic gravity shear, W250x39 column
Design resistance of connection φ = 0.9				
M_p	189 kN-m	189 kN-m	422 kN-m	422 kN-m
M_{pc}	2217 kN-m	2217 kN-m (W360x347) 280 kN-m (W250x49)	2217 kN-m	2217 kN-m W360x347) 280 kN-m (W250x49)
V_r	368 kN		739 kN	

The column bolt gage g_c, defined as the distance between the column bolts and the corner of the angles, and thickness t of the top and seat angles also varied. Two connection configurations (1 and 3) used L152x102x9.5 (L6x4x3/8) angles attached to the column at distance g_c 63.5 mm from the angle corner with 19.1 mm ASTM A325 bolts. The two other beam-column connection configurations (2 and 4) were made of L203x152x19.1 (L8x6x3/4) angles with a column gage g_c of 101.6 mm and 25.4 mm ASTM A490 bolts. The two angle geometries used as the top and seat components were chosen because of their large difference in thickness and column bolt gage g_c, but similar aspect ratio g_2/t. The beam and column design plastic moments M_p and M_{pc} respectively and the connection design shear resistance V_r are presented in Table 6.1. These limit states are determined with the Canadian Standard CSA S16-14 (CSA 2014) with a reduction factor φ of 0.9.

The beam shear resistance was the design limit state of all the specimens. Furthermore, the yield and ultimate stresses and the maximal elongation of the connection components obtained from mill tests, F_y, F_u and ε_u respectively, are presented in Table 6.2. The W360x347 column was previously used in a loading setup at the Structures Laboratory of École Polytechnique Montreal and material data could not be found. However, this component was chosen for its large rotational stiffness and strength to isolate the connection behavior. No yielding or significant deformations are expected in this member.

Table 6.2. Material properties of the connection specimen components.

Component	F_y	F_u	ε_u
	MPa	**MPa**	**%**
Web angles L102x102x7.9	366	530	23.1
Top and seat angles L152x102x9.5	396	534	24.6
Top and seat angles L203x152x19.1	357	469	25.0
W310x39 beam	376	473	23.3
W410x67 beam	379	496	26.0
W250x49 column	399	493	23.7
W360x347 column	-	-	-

6.2.4 Loading procedures

Each beam-column connection geometry was subjected to several loading procedures based on the established protocol proposed by AISC (2010). Table 6.1 presents the procedure performed on each connection geometry, for a total of 15 tests. Four different types of loading protocols were applied on the connection specimens to assess the influence of loading parameters. The beam-column connection rotation was defined as the control parameter in the testing procedure. Once the connection rotation reached the current cycle target, the change in loading direction of the upper actuator was triggered.

AISC (2010) proposes a story drift demand to evaluate moment-frame connections. This story drift demand must be transformed into a rotational demand on the connection. To determine this rotational demand, a prototype frame consisting of a 9.144 m (30') W310x39 beam or a 10.668 m (35') W410x67 girder attached to the strong axis of 4.572 m (15') W250x49 columns was used. This prototype frame was taken from the building designed by Bradley et al. (2014) and used for a large-scale testing of low-ductility concentrically braced frames. The rotational demand on the

connection was determined by imposing the story drift demand proposed by AISC (2010) for evaluating moment-frame connections. The drift contribution of the beam and column were determined by assuming elastic member behavior, while the connection behavior was simplified into a parallel spring element using the experimental results of Beland et al. (2019). The shear demand applied was -94.3 kN and -282 kN for the W310x39 and W410x67 beam specimens, respectively. These values correspond within 1% to the beam shear for the load combinations 1.2D + 1.0E + 0.5L in ASCE 7-16 (ASCE 2016) and 1.0D + 1.0E + 0.5L in the National Building Code of Canada (NBCC 2015). This load corresponds to the gravity load during a seismic event and is referred as the seismic gravity shear. The shear load was applied before the start of the cyclic loading by gradually increasing the load of the 1000 kN actuator, while the top actuator kept the beam in its original position. During the application of the shear load, a small moment developed in the connection. Once the seismic gravity shear was reached and the 1000 kN force-control command dependent on the 500 kN force was implemented, the connection in the moment was removed by adjusting the top actuator load.

To verify that the connection specimen is able to sustain the gravity shear load during and after large flexural yielding, the connections were loaded with a quasi-static symmetrical rotational demand. The first loading procedure (A), consisted of gradually increasing the cyclic rotational demand, as pictured in Figure 6.4a, combined with a constant shear condition. The specimen was loaded cyclically with the 500 kN actuator while the 1000 kN actuator was used to maintain the seismic gravity shear during the test. This loading procedure was also applied for the specimens 2D and 4D with a W250x49 column.

The second loading procedure (B) was similar to the first one (A), with the exception that the cyclic rotational demand was stopped to increase the connection shear demand at discrete times. At each 0.01 rad increment in the theoretical frame demand, the shear load was increased when a moment of zero was reached during the unloading of the positive excursion. The increased shear load corresponded to the design factored shear load of -152 kN and - 456 kN for the specimens with a W310x39 and a W410x67 beam respectively. These values were obtained from the load combinations 1.2D + 1.6L in ASCE 7-16 (ASCE 2016) and 1.25D + 1.5L in NBCC (2015). The times of application of these design shears are shown in Figure 6.4b. The increased shear was maintained for two minutes, after which the connection shear was brought back to either -94.3 kN

or -282 kN and the cyclic loading was resumed. The shear excursions were intended to verify the connection capacity to sustain the design shear demand after significant yielding and rotational demand from a seismic event. The shear load applied on the connection is presented in Figure 6.4d, for the specimens with a W310x39 and a W410x67, with and without the design shear excursions.

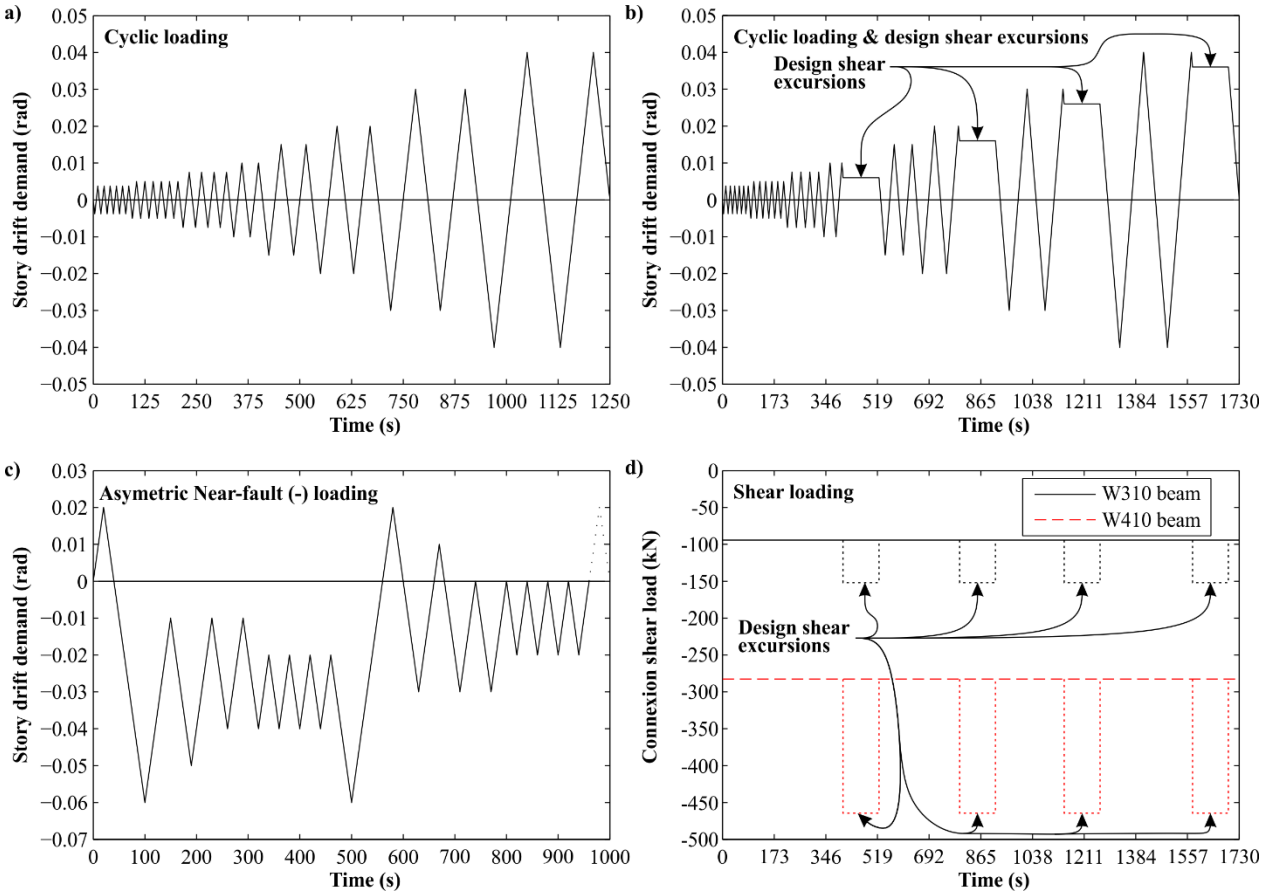


Figure 6.4. Beam-column connection loading protocol for a) cyclic tests; b) cyclic tests with design shear excursions; c) Asymetric near-fault tests; d) Shear loading.

The third loading protocol (C) used the same rotational demand presented in Figure 6.4a, without additional shear load applied on the connection. Therefore, only the force required in the 500 kN actuator to create the rotational demand was transferred as a shear demand in the connection. This protocol was intended to evaluate the influence of the shear load on the connection behavior and the shear load in this protocol is referred as the rotational shear.

The fourth type of loading protocol was based on the story drift demand proposed by the SAC venture (Krawinkler et al. 2000) for a near-fault seismic event with a dominant negative rotational

demand, as presented in Figure 6.4c. This story drift demand is transformed into a rotational demand on the connection using the same procedure and prototype building as the symmetric cyclic tests. This loading protocol was applied with the constant seismic gravity shear shear of -94.3 kN to specimen 1D. The whole rotational demand time-history was applied 6 times attempting to induce a low-cycle fatigue fracture in the connection. However, fracture was finally obtained only by manually increasing the rotational connection demand.

6.3 Experimental results

6.3.1 Nonlinear behavior of connections with rotational shear

As a baseline, four tests were performed on 2L-TS with rotational shear load, among which three fractured in the seat angle, while one fractured in the top angle. All failures occurred in the beam leg and significant cracking was observed on the other leg.

Figure 6.5a presents a global view of specimen 1C at the end of the test. The fracture occurred during a positive rotation excursion, when the seat angle was in tension. Figure 6.5c shows the seat angle deformation, where fracture occurred across the width of the component, in the beam leg, near the fillet region.

Under negative rotational demand, the top angle was in tension and cracking was observed in the beam leg, as presented in Figure 6.5b. This cracking was similar to the one observed in the seat angle, which indicates a symmetrical deformation pattern for top and seat angle connections. Under positive rotation, where the top angle was in compression, extensive cracking was observed on the beam leg.

The smaller distance between the web angles and the connection center of rotation reduced significantly the displacement demand on these components. The web angles experienced plastic deformations varying along the length of the connection with respect to their position of the center of rotation, as shown in Figure 6.5a. However, cracking was not observed in these components.

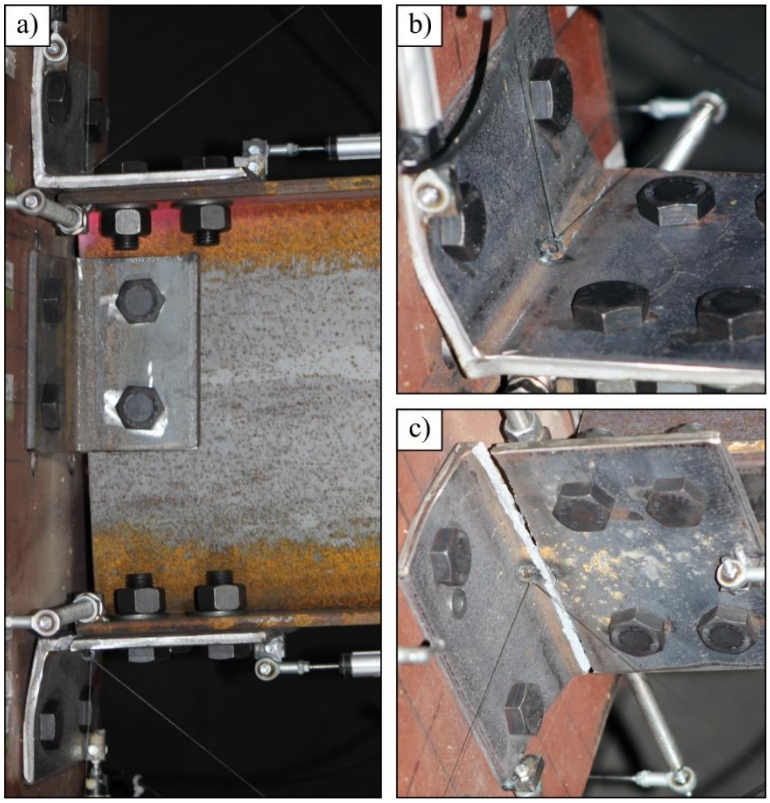


Figure 6.5. Specimen 1C: a) overall deformation pattern without shear; b) top angle deformation; c) seat angle fracture.

6.3.2 Nonlinear behavior of connections with seismic gravity shear

The presence of additional shear load influenced significantly the deformation pattern of the connections. Additionally, connection to the stiff W360x347 column allowed the characterization of the connection behavior itself, whereas the more flexible W250x49 column sections experienced plastic deformations. A distinct deformation pattern was observed for the specimens with a more flexible column.

6.3.2.1 Specimens with a W360x347 column

Out of the nine tests performed on the connections attached to a W360x347 column and subjected to shear load, seven fractured in the top angle beam leg, while two failed in the seat angle beam leg. Most specimens showed extensive cracking at both positions prior to fracture.

Figure 6.6a presents the specimen 1A, which has a typical deformation pattern and failure mode. The entire connection experienced a transverse displacement Δ_Z in the same direction as the gravity load, created by the shear load applied during the test. In the top angle, this displacement resulted from the beam leg rotation illustrated by Figure 6.6c. The maximum transverse displacement recorded was -3.2 mm for the top angle. However, the transverse displacement experienced by the seat component reached -9.8 mm and was mostly exhibited through extensive bolt slip between the column flange and the angle leg. Figure 6.7a shows the transversal displacement of the angles at their fillet. The combined flexural and axial response created by the rotational demand and the shear load lead to fracture at the top angle beam leg plastic hinge, as illustrated in Figure 6.6b and 6c. In contrast, because of their proximity with respect to the connection center of rotation, the web angles experienced smaller displacement demands than the top and seat angles. Aside from the variable yielding along their length presented in Figure 6.6d, the displacements of these components were not critical in the connection deformation pattern.

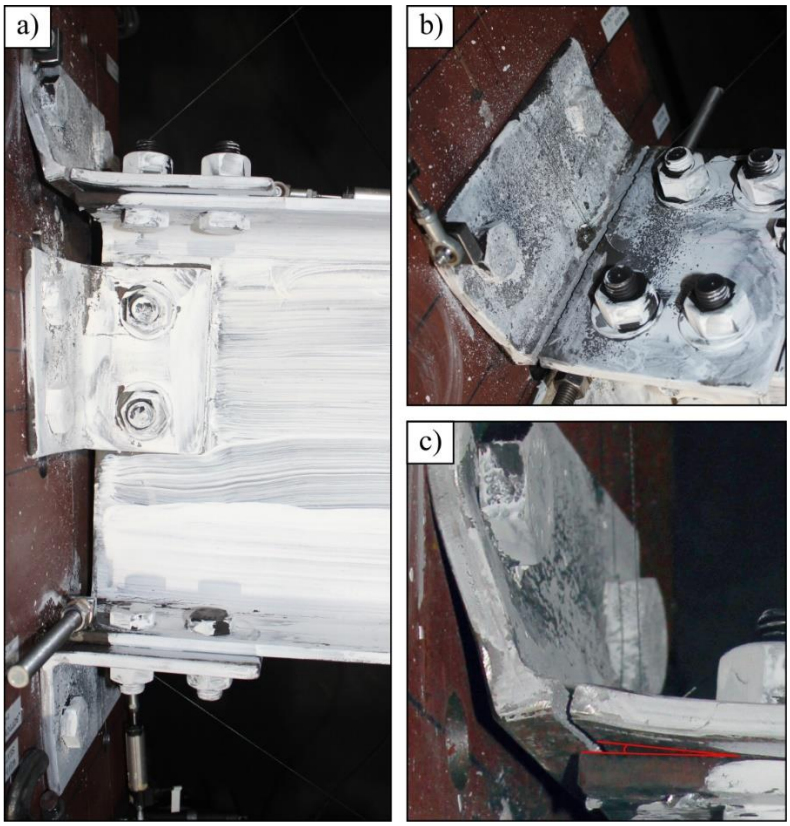


Figure 6.6. Specimen 1A: a) overall deformation with W360x347 column and shear; b) top angle fracture; c) top angle beam leg rotation.

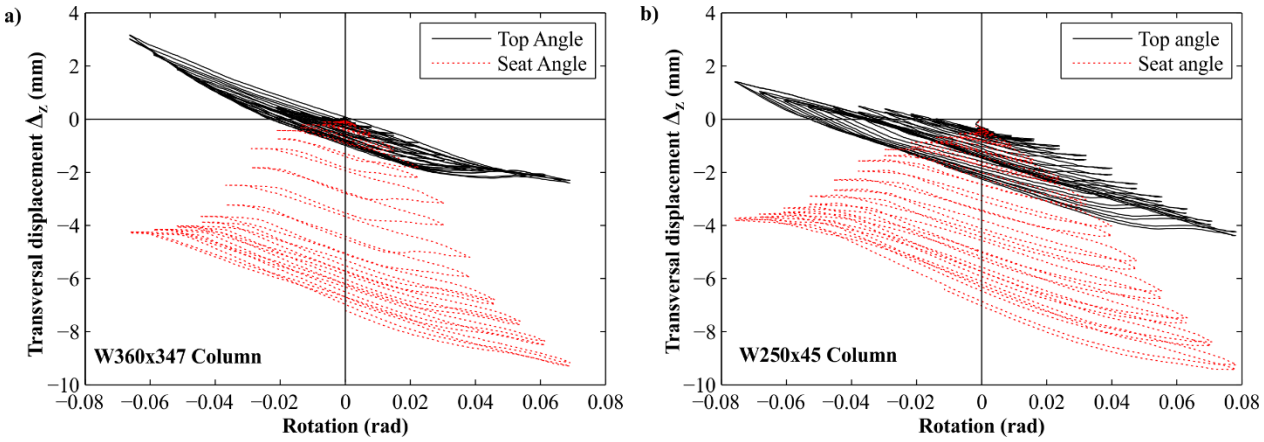


Figure 6.7. Transverse displacement (Δ_Z) with shear load; a) Specimen 2A; b) Specimen 2D.

6.3.2.2 Specimens with a W250x49 column

The deformations observed in beam-column connections with a W250x49 column remained consistent with the observations made for the connections using a W360x347 column. However, some additional local plastic deformations were observed in the slenderer column flanges near the bolts of the top and seat angles, as illustrated by Specimen 2D (Figure 6.8a). The top and seat angle thickness of 19.1 mm was larger than the column flange thickness of 15.7 mm, so both the angle and the column flange experienced large plastic deformations and the global rotational stiffness of the connection was reduced. However, this reduced stiffness did not change the failure mode observed in the connection, and the fracture still occurred in the beam leg of the top angle, as pictured in Figure 6.8c.

Shear deformations were also observed with the in-plane rotation of the web angle column leg, illustrated in Figure 6.8b. This observation is confirmed by the transverse displacement (Z) measurements presented in Figure 6.7. The displacements reached -4.3 mm and -9.4 mm for the top and seat angles respectively. These measurements are larger than the ones measured on the same connection geometry with the stiff 360x347 column (Specimen 3D): -2.4 mm and -9.3 mm for the top and seat angles, respectively. These increased displacements include the larger hole elongation and bolt rotation resulting from the column flange yielding, but the deformation pattern observed in the angles remained similar. The transverse (Z) displacement was concentrated in the beam leg of the top angle, as pictured in Figure 6.8d, and in the bolt slip of the seat angle.

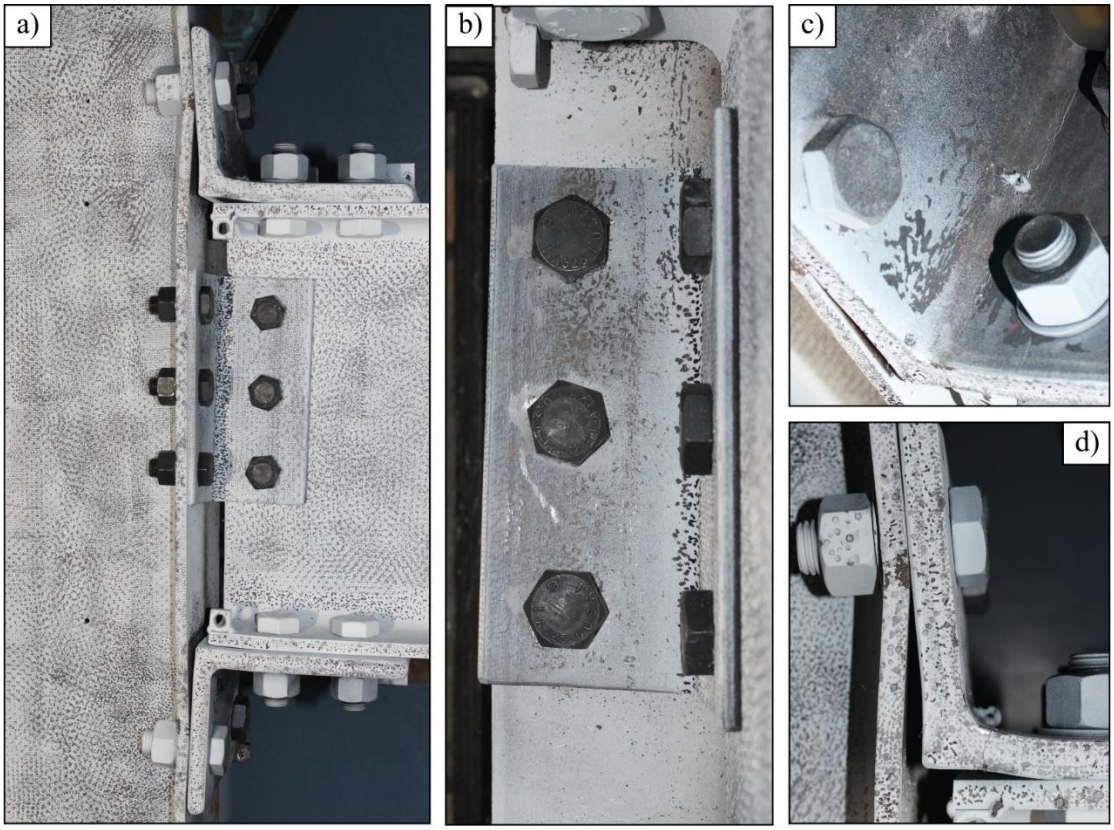


Figure 6.8. Specimen 4D; a) overall deformation pattern with W250x49 column and shear; b) web angle deformation; c) top angle cracking; d) column flange yielding and top angle beam leg rotation.

6.4 Nonlinear characterization of the moment-rotation envelope curve

Each of the 15 tests performed on beam- column connections during the experimental program has been characterized by key response parameters obtained from the moment-rotation hysteretic behaviors. Table 6.3 summarizes the moment capacity of each specimen, both positive (M_{Max}) and negative (M_{Min}), with their rotational demands, $\theta_{M\text{-}Max}$ and $\theta_{M\text{-}Min}$ respectively. Additionally, Table 6.3 includes the ultimate rotational demands, both positive (θ_{Max}) and negative (θ_{Min}), and their corresponding moments, $M_{\theta\text{-}Max}$ and $M_{\theta\text{-}Min}$, respectively. The loading procedure applied on each test and the minimum and maximum shear loads, V_{Min} and V_{Max}, experienced by the connection specimen are also included.

The maximum rotational demand of each specimen satisfied the moment frame connection ductility criterion for a Special Moment Frame (SMF), as specified by AISC 341 (2017). The story drift must reach 0.04 rad to fulfill the ductility requirement. The story drift is comprised of the beam flexural deflection, the column flexural deflection and the connection rotation. By itself, the maximum connection rotation was larger than the 0.04 rad requirement in every specimen. However, the strength criterion of developing a moment in the connection corresponding to at least 80% of the beam plastic moment M_{pb} at a storey drift of 0.04 rad was respected by only one specimen. At this rotation, the specimens with L203x152x19.1 top and seat angles and a W310 and a W410 beam reached 84% and 51% of M_{pb}, respectively. The specimens with L152x102x9.5 top and seat angles and a W310 and a W410 beam reached 44% and 34% of M_{pb}, respectively. Therefore, only the geometry of specimen 3 fulfills the strength and ductility requirements of SMF connections according to AISC 341 (2017).

Table 6.3. Shear and moment-rotation key response parameters of beam-column connections.

Test ID	Loading Type	V_{Min}	V_{Max}	θ_{Max}	$M_{\theta max}$	θ_{Min}	$M_{\theta min}$	θ_{M-Max}	M_{max}	θ_{M-Min}	M_{min}
		kN	kN	Rad	kN-m	Rad	kN-m	Rad	kN-m	Rad	kN-m
1A	Cyclic + seismic gravity	-94.3	-94.3	0.067	113	-0.067	-86	0.067	113	-0.067	-86
1B	Cyclic + design shear	-152	-94.3	0.054	100	-0.067	-72	0.054	100	-0.051	-104
1C	Cyclic + rotational shear	-24.1	19.0	0.054	58	-0.052	-83	0.045	66	-0.052	-83
1D	Asymmetric (-) + seismic gravity	-94.3	-94.3	0.011	46	-0.075	-93	0.011	46	-0.075	-93
2A	Cyclic + seismic gravity	-94.3	-94.3	0.068	134	-0.066	-174	0.068	134	-0.066	-174
2B	Cyclic + design shear	-152	-94.3	0.068	134	-0.058	-164	0.068	134	-0.066	-156
2C	Cyclic + rotational shear	-47.9	40.9	0.061	141	-0.066	-165	0.061	141	-0.066	-165
2D	Cyclic + seismic gravity - W250x49	-94.3	-94.3	0.075	108	-0.074	-137	0.075	108	-0.074	-137
3A	Cyclic + seismic gravity	-283	-283	0.045	96	-0.04	-145	0.044	123	-0.04	-145
3B	Cyclic + design shear	-465	-283	0.043	125	-0.051	-148	0.043	125	-0.051	-148
3C	Cyclic + rotational shear	-38.3	-31.3	0.050	108	-0.047	-123	0.050	108	-0.041	-132
4A	Cyclic + seismic gravity	-283	-283	0.044	182	-0.048	-177	0.044	182	-0.042	-218
4B	Cyclic + design shear	-465	-283	0.050	177	-0.048	-233	0.043	189	-0.048	-233
4C	Cyclic + rotational shear	-62.4	-56.9	0.050	196	-0.048	-215	0.050	196	-0.048	-215
4D	Cyclic + seismic gravity - W250x49	-283	-283	0.050	156	-0.055	-203	0.050	156	-0.055	-203

To characterize the nonlinear behavior of the beam-column connections tested in this program, a numerical model has been calibrated for the moment-rotation envelope curves of the positive and negative excursions of each test. The power model proposed by Kishi et al. (1990), which

represents the full range of nonlinear monotonic behavior with a single equation, was used to calibrate these envelope curves. This model was chosen to assess the initial stiffness, K_i, the plastic stiffness K_p and the yield moment M_Y of the positive and negative excursions. The moment-rotation, M-θ, relationship is given by Equation 6.3, where R is the transition coefficient between the initial and plastic stiffness K_i and K_p.

$$M = \frac{(K_i - K_P)\,\theta}{\left[1 + \left(\frac{\theta}{M_Y/K_i}\right)^R\right]^{\frac{1}{R}}} + K_P\,\theta \tag{6.3}$$

To obtain the best fit between the numerical model and the experimental data envelope, a calibration was performed for each test. The initial rotational stiffness K_i and the plastic rotational stiffness K_p were determined based on linear regressions of the elastic and the post-yield behavior of the envelope curves. The yielding moment M_Y correspond to the intersection between these regression curves. With these values, the shape parameter R was defined with an iterative process to determine the best fit value with the least square method. These calibrated values are presented in Table 6.4. This table also contain information about the connection components and the loading protocol performed on each specimen. The coefficient of determination R^2 was also included to quantify the accuracy of the calibrated numerical model. The positive and negative envelope curve of each experimental test can thus be recreated by using the calibrated parameters of Table 6.4 in Equation 6.3. The numerical model offered a good approximation for the tests performed with and without shear load. The coefficient of determination R^2 obtained for these connections remained larger than 0.9, which indicates a good fit. Figure 6.9a and 6.9b present the numerical approximation of the envelope curve for typical connections with seismic gravity shear (Specimen 3A) and rotational shear (Specimen 3C), respectively.

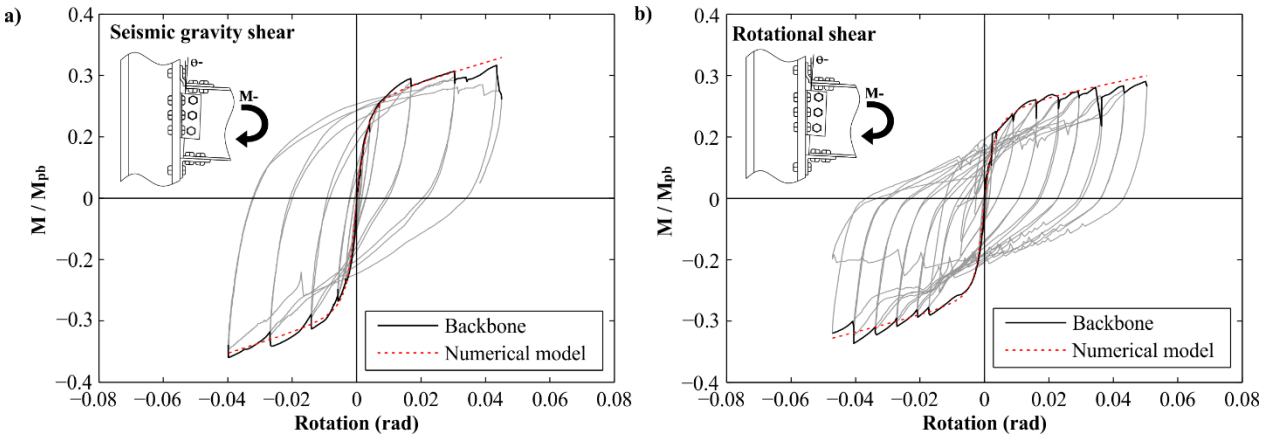


Figure 6.9. Numerical modeling of moment-rotation envelope curves: a) Specimen 3A, with shear load; b) Specimen 3C, without shear load.

Table 6.4. Nonlinear envelope curve characterization of beam-column connections.

Test ID	Beam	Positive envelope					Negative envelope				
		K_i^+	M_y^+	R^+	K_p^+	R^2	K_i^+	M_y^-	R^-	K_p^-	R^2
		kNm/rad	kNm	-	kNm/rad	-	kNm/rad	kNm	-	kNm/rad	-
1A	W310x39	40684	92	0.694	492	0.999	40589	-67	0.853	415	0.992
1B		49145	85	0.800	384	0.964	47663	-102	0.671	393	0.981
1C		48230	59	0.820	204	0.902	42004	-78	0.674	341	0.984
1D		30683	72	0.546	309	0.984	40055	-69	1.026	345	0.982
2A		58353	131	0.697	437	0.951	57923	-165	0.760	419	0.982
2B		52673	133	0.753	267	0.997	56759	-170	0.692	396	0.989
2C		59909	154	0.683	219	0.951	58076	-184	0.672	309	0.993
2D		27011	112	0.672	202	0.993	37084	-117	0.780	479	0.975
3A	W410x67	24152	95	2.030	868	0.942	36956	-108	1.743	911	0.975
3B		23574	93	1.601	987	0.958	42085	-114	1.891	819	0.940
3C		23511	86	1.660	605	0.929	33858	-94	1.799	759	0.987
4A		101772	166	0.768	917	0.963	135063	-197	0.792	894	0.998
4B		97012	181	0.703	741	0.951	121573	-209	0.755	901	0.987
4C		88877	176	0.886	672	0.980	86394	-189	0.914	690	0.991
4D		72205	157	0.625	589	0.989	76155	-172	0.811	757	0.981

6.5 Influence of geometrical and loading parameters

The influence of key parameters on the hysteretic behavior of the tested connections was investigated. The tests performed on the specimens loaded with a cyclic rotational demand and constant shear were viewed as the baseline.

6.5.1 Influence of seismic gravity shear load

Although the addition of seismic gravity shear load did not significantly affect the connection rotational capacity, several influences were observed (Figure 6.10). The hysteretic behavior of the connections with the rotational shear only remained symmetrical when subjected to rotational demand. Generally, the addition of seismic gravity shear load increased the positive moment capacity but decreased the negative moment capacity. The flexural stiffness exhibited by the shear-loaded specimen also increased significantly during the positive moment excursions. The shear load created a compressive force in the seat angle and a tensile force in the top angle, as pictured in the free-body diagram of Figure 6.11. These forces acted in the same direction as the ones created by a negative moment on the connection but were opposed to the forces under positive moment. These opposing forces created an increase in the moment capacity and flexural stiffness of the connection under positive bending. However, under negative bending, the tensile capacity mobilized by the rotational demand was reduced, thus reducing the negative moment capacity of most specimens. Adding shear on the beam-column connections resulted in a larger positive moment capacity increase than the decrease of negative moment capacity. Therefore, the addition of shear loading increased the overall connection energy-dissipation capacity.

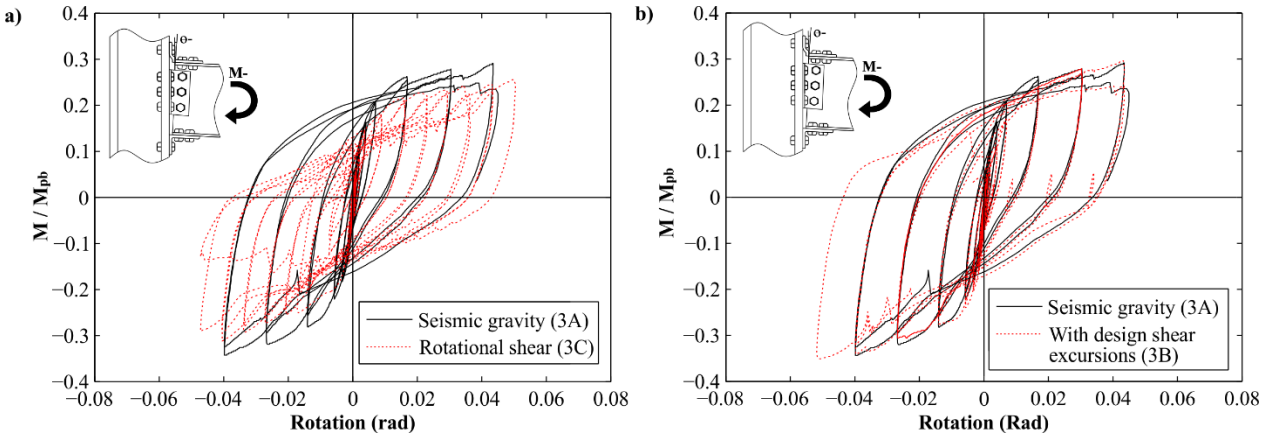


Figure 6.10. Influence of shear: a) influence of shear load on the connection hysteretic behavior (Specimens 3A and 3C); b) influence of shear load excursions on the connection hysteretic behavior (Specimens 3A and 3B).

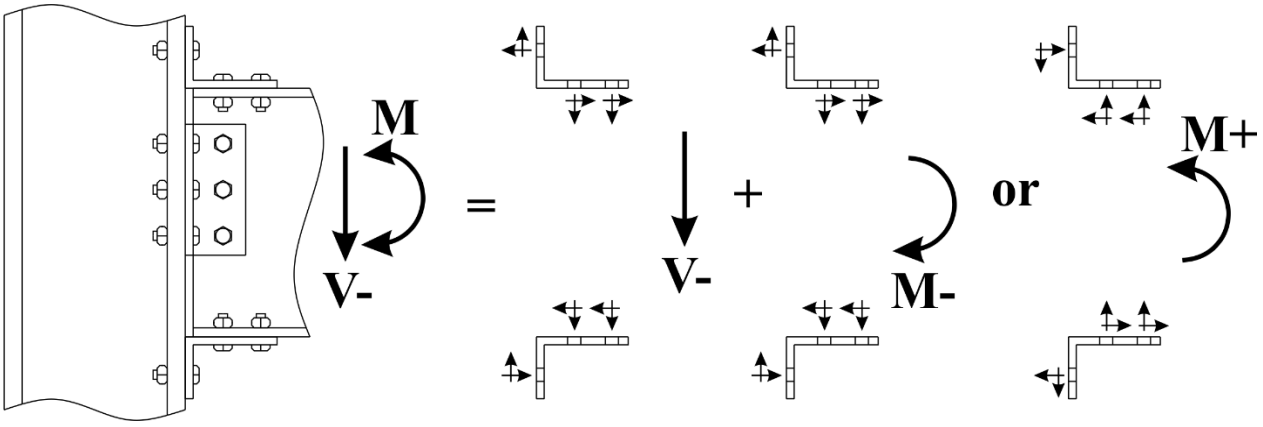


Figure 6.11. Influence of shear load on the free body diagram of top and seat angles.

For some connections, the cyclic rotational demand protocol was paused at predetermined locations to increase the connection shear demand to the design shear load. At each 0.01 rad increment, when the unloading of the positive excursion reached a moment of zero, the shear load on the connection was increased to -152 kN and -456 kN as described previously. The design shear was maintained for 2 minutes, after which the connection shear was brought back to the seismic gravity shear of either -94.3 kN or -282 kN to resume the cyclic loading. These excursions were intended to verify the connection capacity required to sustain the design shear load after significant yielding and rotational demand from a seismic event. Each specimen sustained the design shear load, even after large rotational demands. The connections failures were observed during the cyclic rotational demand combined with the seismic gravity loads. Figure 6.10b presents the moment rotation hysteretic behavior and illustrates that the design shear excursions did not affect the rotational capacity of the connections and had little influence on the moment capacity of the connections.

Even with this significant increase to the design shear load, the shear demand still remained at approximately 40 and 60% of the connection shear capacity presented in Table 6.3 for the W310 and W410 specimens respectively. Because the increased shear demand remained well under the connection shear capacity and no rotational demand was applied on the connection simultaneously, no significant influence of the design shear excursions on the deformation pattern was observed. Therefore, 2L-TS connections can sustain a large shear force demand, even after experiencing large plastic deformations, without compromising the integrity of the connection.

6.5.2 Influence of beam depth

The beam depth is an important geometrical parameter for the design of beam-column connections, as it generally determines the length of double web angle components required to offer a sufficient lateral support to the beam. The double web angle length were 140 mm and 216 mm for the connections with a W310 and a W410 beam respectively. Additionally, the larger design shear load on the W410 connection required 3 bolt rows in the beam web instead of the 2 rows required for the W310 connection. These differences translated into significant moment capacity increases of the double web angle connections, as presented in Figure 6.12a and b.

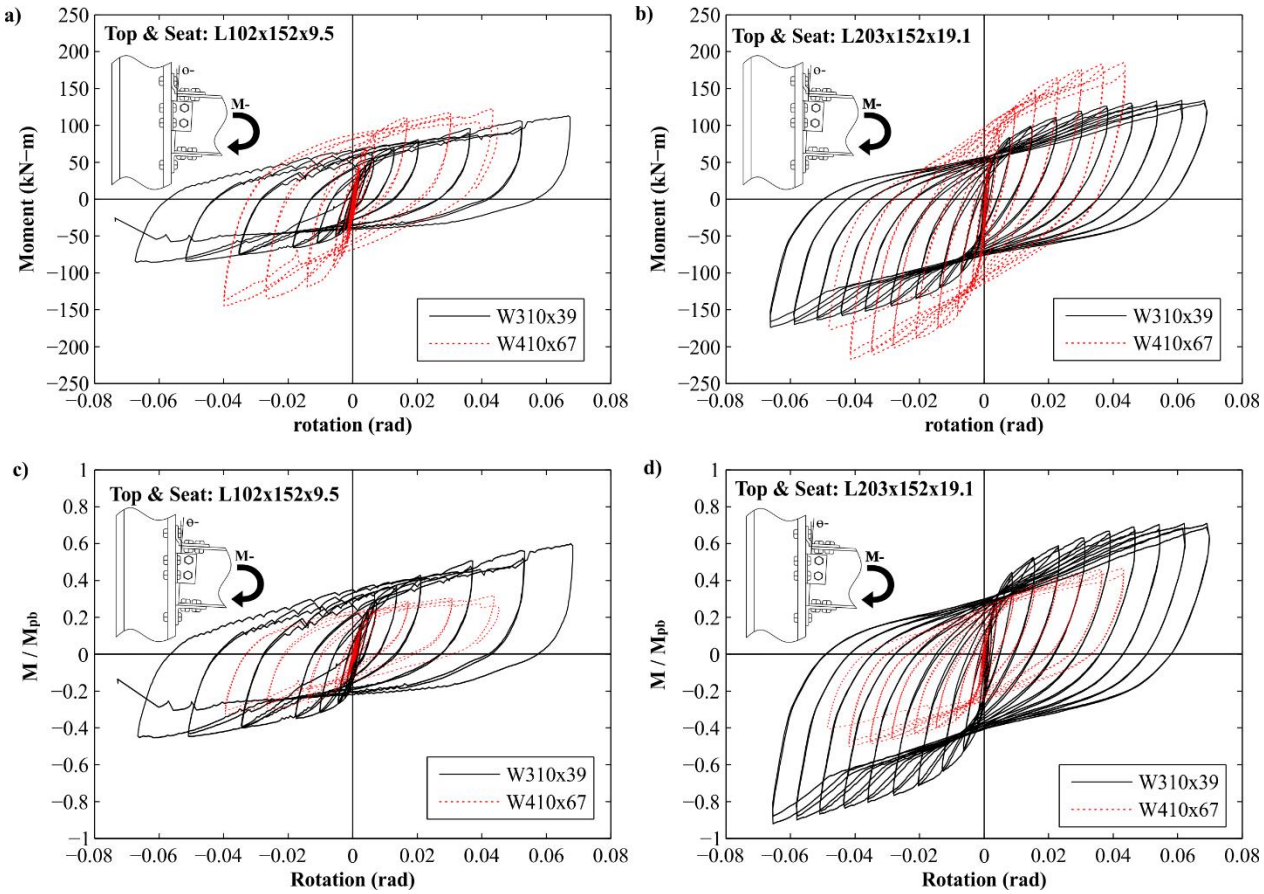


Figure 6.12. Influence of beam depth on the connection hysteretic behavior: a) Specimens 1A and 3A; b) Specimens 2A and 4A; c) Normalized connection moment with the beam plastic moment for specimens 1A and 3A; d) Normalized connection moment with the beam plastic moment for specimens 2A and 4A.

The beam depth increase translated into a larger displacement demand on the angle subjected to tension for a given rotation. The larger force developed in the angle, because of this increased displacement demand, combined with a larger moment arm between the tensile angle and the center of rotation, resulted in a significant moment capacity increase. The moment capacity increases averaged 1.31, which corresponds to the beam depth ratio of the specimens. The moment capacity increase is therefore approximately linearly proportional to the beam depth increase. However, the connection moment capacity represents a smaller ratio of the beam plastic moment as the beam depth increases, as pictured in Figure 6.12c and d.

The larger displacement demand on the angle loaded in tension resulted in angle fracture at a smaller ultimate rotation. Increasing the beam depth therefore resulted in a moment capacity increase, but a decrease of rotational capacity, as illustrated in Figure 6.12.

6.5.3 Influence of top and seat angle geometry

The ratio between the column leg flexural span and the angle thickness, g_2/t, was used previously (Beland et al. 2019) to characterize the behavior of bolted angle components in beam-column connections. The top and seat angle geometries used in the experimental program were defined with an aspect ratio g_2/t of 2.67 and 2.58 respectively.

Although their aspect ratios were similar, the angle thickness played a more important role in the stiffness behavior of the angles on a component level. An increase in moment capacity was observed for the specimens with L203x152x19.1 top and seat angles. Figure 6.13 presents the hysteretic behavior of the connections with W310 and W410 beam sections.

The change in top and seat angle section increased significantly the moment capacity of the connection along with its initial rotational stiffness. A moment capacity increase of approximately 55% was observed with the changes of the top and seat angle section. However, the ultimate rotational capacity, the deformation pattern and the global hysteretic behavior of the connection remained similar. Therefore, adding top and seat angles to a double web angle connection created a stable hysteretic behavior. The scale of these changes depended on the geometrical properties of the components added, mostly the angle thickness, but also the distance between the column leg and the angle corner.

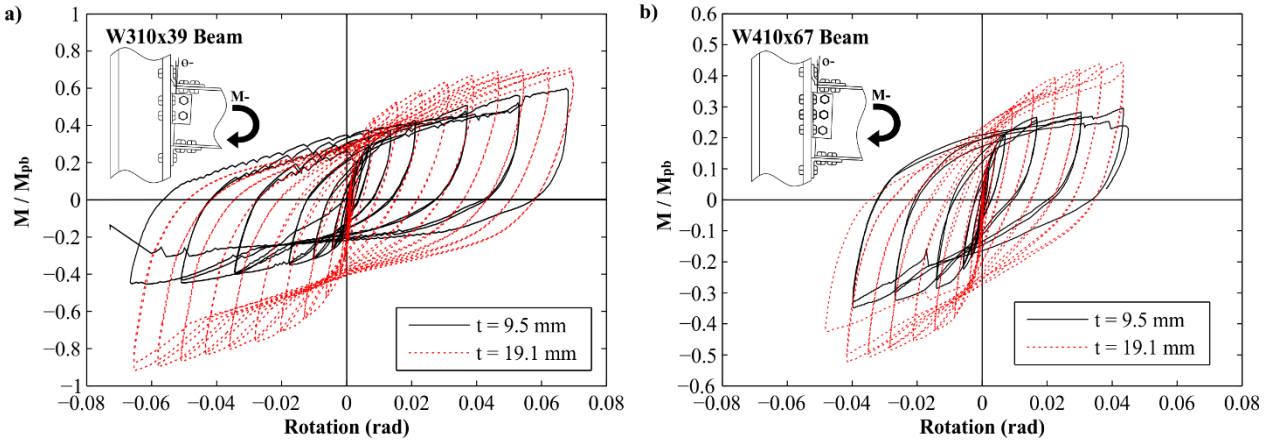


Figure 6.13. Influence of the top and seat angle geometry on the connection hysteretic behavior: a) Specimens 1A and 2A; b) Specimens 3A and 4A.

6.5.4 Influence of column section

The influence of the column section was investigated by comparing L203x152x19.1 top and seat angles connections connecting the beam sections with a stiff W360x347 and a flexible W250x45 column. Plastic deformations were observed in the W250x45 flanges near the top and seat angle bolts. These deformations occurred in series with the angles deformations and thus resulted in a more flexible behavior of the connection. Figure 6.14 shows the hysteretic behavior of the bolted joints connecting the W310x39 and W410x67 beams to each column sections.

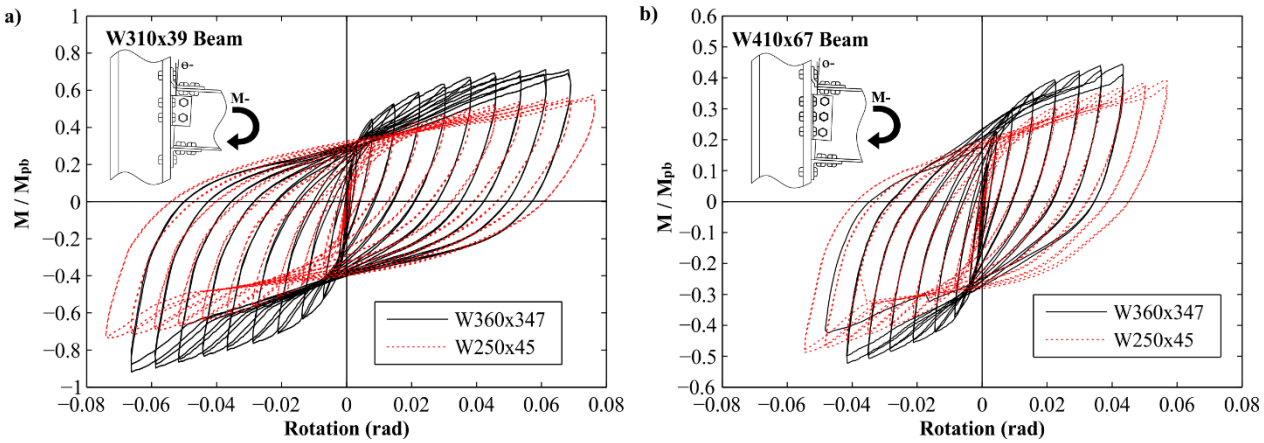


Figure 6.14. Influence of the column section on the connection hyteretic behavior: a) Specimens 2A and 2D; b) Specimens 4A and 4D.

The flexibility of the W250x45 column translated into a more flexible connection behavior, where the ultimate moment capacity was reduced by up to 21%. The moment capacity decrease was similar for both positive and negative moment capacity. The plastic deformations of the column flange contributed significantly to the moment capacity decrease. However, the column flange displacement was also included in the connection rotation. Therefore, the maximum displacement capacity of the top and seat angles was reached at a larger rotation. The rotational capacity was increased by approximately 13%.

6.5.5 Influence of asymmetric loading conditions

The force-displacement hysteretic behavior of bolted angle components followed a secant stiffness (or peak-oriented) behavior, where the reloading stiffness depended directly on the maximum displacement already experienced by the angle (Beland et al. 2019). Therefore, the influence of the rotational demand history has been investigated with an asymmetric loading protocol, where the rotational demand did not reach its maximum value at each cycle. One specimen, 1D, was loaded under this condition, with a constant seismic gravity shear load of -93.4 kN.

Figure 6.15 compares the asymmetric test performed on specimen 2D with the symmetric test of specimen 2A. This connection geometry consisted of 2L-TS attaching the W310x39 beam to the W360x347 column. The envelope curve obtained from the asymmetric test was similar to the one of the symmetric tests. The connection followed a reloading behavior similar to the individual behavior of the connection component observed by Beland et al. (2019), where the reloading stiffness depended directly on the maximum moment previously experienced by the connection.

The smaller positive rotational demand reached during the asymmetric test limited the maximum moment reached during the first positive excursion, and every subsequent excursion, which affects the energy dissipated by the connection. However, the initial reloading stiffness remained similar in both tests. The lesser cumulative rotational demand imposed during the asymmetric test allowed the connection to reach a negative rotational capacity 12% greater, while the negative moment capacity also increased by 8%.

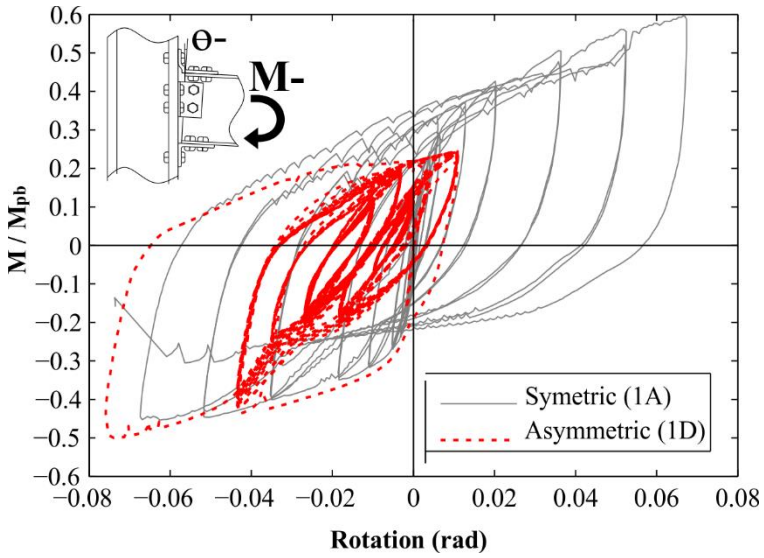


Figure 6.15. Influence of asymmetric loading protocol on the connection hyteretic behavior (Specimen 2D).

6.6 Conclusions and recommendations

Steel beam-column connections with bolted double angle web connections enhanced with top and seat angles economically provide flexural stiffness, strength and rotation capacity. This connection configuration can be used to develop moment frame action that serves as a secondary lateral system for seismic collapse prevention. Considering this application, an experimental investigation was developed to characterize the global nonlinear behavior of bolted angle connections under simultaneous shear and rotational demand. Fifteen tests performed on four connection configurations were characterized with key response quantities of the moment-rotation hysteretic behavior and the effects of critical parameters were examined. The mathematical model proposed by Kishi and Chen (1990) was calibrated to represent the positive and negative envelope of each test performed. From these tests, the following conclusions are drawn:

- The deformation patterns were not significantly influenced by the beam depth and the column section;
- The specimens with the larger beam depth exhibited a larger moment capacity, but a smaller rotational capacity;

- The more flexible column section exhibited local yielding near the top and seat angle bolts, which reduced global rotational stiffness and moment capacity;
- The additional seismic gravity shear load caused large deformations to occur in the beam leg plastic hinge of the top angle and eventually lead to fracture at this position;
- Every connection tested could sustain the design shear load, even after experiencing large rotational demands and plastic deformations.

In general, the nonlinear behavior exhibited by bolted angle connections showed large ductility, which translated into a substantial energy dissipation capacity, which is a critical parameter related to favorable seismic response. Therefore, the use of bolted angles for gravity framing connections could be beneficial as their large redundancy combined with their significant energy dissipation capacity can enhance the reserve capacity of a building and mitigate building collapse, particularly if the primary lateral system has low ductility.

6.7 Data Availability Statement

The following data, models, or code generated or used during the study are available from the corresponding author by request:

- Information on the experimental setup;
- Experimental measurements;
- Processed data; and
- Calibrated model of the envelope curves.

6.8 Acknowledgments

This study was supported by the Natural Sciences and Engineering Research Council of Canada (Canada Research Chair Program, Grant no. 219924), the National Science Foundation (Grant No. CMMI-1207976) and the American Institute of Steel Construction. The first author received the SSEF G.J. Jackson Fellowship of the Canadian Institute of Steel Construction for this research. Ali Davaran, Jessalyn Nelson, Cameron Bradley and Joshua Sizemore provided assistance in developing the testing program described in this paper. Jonathan Auger, Romain Siguier and Patrice Bélanger of the Structures Laboratory of Polytechnique Montreal provided valued

assistance to conduct the experimental tests. The opinions, findings, and conclusions in this paper are those of the authors and do not necessarily reflect the views of those acknowledged here.

REFERENCES

Abdalla, K. M., Drosopoulos, G. A., Stavroulakis, G. E. (2014). "Failure behavior of a top and seat angle bolted steel connection with double web angles." *J. Struct. Eng*., 141(7).

Abolmaali, A., Kukreti, A. R., and Razavi, H. (2003). "Hysteresis behavior of semi-rigid double web angle steel connections." *J. Constr. Steel Res*., 59, 1057–1082.

AISC. (2017). "Seismic provisions for structural steel buildings." *AISC341-17*, Chicago, IL.

ASCE 7. (2016). "Minimum design loads for buildings and other structures." *ASCE 7*, Reston, VA.

Astaneh-Asl, A., Modjtahedi, D., McMullin, K., Shen, J.-H., D'Amore, E. (1998). "Stability of damaged steel moment frames in Los Angeles." *Eng. Struct*., 20(4), 433-446.

Azizinamini, A. (1982). *Monotonic response of semi-rigid steel beam to column connections*. M.S. Dissertation, University of South Carolina, Columbia, SC.

Azizinamini, A. (1985). *Cyclic characteristics of bolted semi-rigid steel beam to column connections*. Ph.D Thesis, University of South Carolina, Columbia, SC.

Azizinamini, A., Radziminski, J. B., (1989), "Static and cyclic performance of semirigid steel beam-to-column connections.", *J. Struct. Eng.*, 115(12), 2979-2999.

Beland, T., Bradley, C. R., Nelson, J., Sizemore, J. G., Davaran, A., Hines, E. M. Fahnestock, L. A. (2019). "Experimental parametric characterization of bolted angle connection behavior". *In Review*.

Bjorhovde, R., Colson, A., Brozzetti, J. (1990). "Classification system for beam-to-column connections.", *J. Struct. Eng.*, 116(11), 3059-3076.

Bradley, C., Sizemore, J., Nelson, J., Tremblay, R., Hines, E. M., Fahnestock, L. A. (2014). "Large-scale testing of low-ductility concentrically braced frames." *Proc. ASCE Structures Congress 2014*.

Calado, L., De Matteis, G., Landolfo, R. (2000). "Experimental response of top and seat angle semi-rigid steel frame connections". *Mat. And Struct.*, 33(10), 499-510.

Callister, J. T., Pekelnicky, R. G. (2011). "Seismic Evaluation of an existing low ductility braced frame building in California." *Proc. ASCE Structures Congress 2011*, 2756-2767.

Citipitioglu, A. M., Haj-Ali, R. M., White, D. W. (2002). “Refined 3D finite element modeling of partially restrained connections including slip.” *J. Constr. Steel. Res.,* 58, 995-1013.

Danesh, F., Pirmoz, A., Daryan, A. S., (2007) “Effect of shear force on the initial stiffness of top and seat angle connections with double web angles.” *J. Constr. Steel. Res.,* 63, 1208-1218.

Del Carpio, M., Mosqueda, G., Lignos, D. G. (2019) “Experimental investigation of steel building gravity framing system under strong earthquake shaking.” *Soil Dyn. and Earthquake Eng.* 116, 230-241.

Elkady, A., Lignos, D. G. (2015). “Effect of gravity framing on the overstrength and collapse capacity of steel frame buildings with perimeter special moment frames.” *Earthquake Eng. Struct. Dyn.,* 44(8), 1289–1307.

Fleischman, R. B., Chasten, C. P., Lu, L.-W., Driscoll, G. C. (1991). “Top-and-seat-angle connections and end-plate connections: Snug vs. fully pretensioned bolts.” A*ISC Eng. J.*, 28, 18-28.

Flores, F. X., Charney, F. A., Lopez-Garcia, D. (2014). “Influence of the gravity framing system on the collapse performance of special steel moment frames.” *J. Constr. Steel. Res.,* 101, 351-362.

Flores, F. X., Charney, F. A., Lopez-Garcia, D. (2016). “The influence of gravity column continuity on the seismic performance of special steel moment frame structures.” *J. Constr. Steel. Res.,* 118, 217-230.

Garlock, M. M., Ricles, J. M. Sause, R. (2003). “Cyclic load tests and analysis of bolted top-and-seat angle connections.” *J. Struct. Eng*., 129(12), 1615-1625.

Ghindea, M., Catarig, A., Ballok, R. (2015). “Behavior of beam-to-column connections with angles. Part 1-Experimental investigations”. *J. App. Eng. Sci.,* 5(18), 21-28.

Gong, Y. (2014). “Ultimate tensile deformation and strength capacities of bolted-angle connections.” *J. Constr. Steel. Res*., 100, 50-59.

Gupta, A., Krawinkler, H. (2000). “Behavior of ductile SMRFs at various seismic hazard levels.” *J. Struct. Eng*., 126(1), 98-107.

Hajjar, J. F., O’Sullivan, D. P., Leon, R. T., Gourley, B. C. (1995). “Evaluation of the damage to the Borax corporate headquarters building as a result of the Northridge earthquake.”

Technical Report: *Case Studies of Steel Moment Frame Building Performance in the Northridge Earthquake of January 17, 1994*. SAC 95-07.

Hines, E. M., Appel, M. E., Cheever, P. J. (2009). "Collapse performance of low-ductility chevron braced steel frames in moderate seismic regions". *AISC Eng. J.*, 3rd Quarter, 149-180.

Hwang, S.-H., Lignos, D. G. (2017). "Effect of modelling assumptions on the earthquake-induced losses and collapse risk of steel-frame buildings with special concentrically braced frames." *J. Struct. Eng*., 143(9).

Jarrett, J. A., Judd, J. P., Charney, F. A. (2015). "Comparative evaluation of innovative and traditional seismic-resisting systems using the FEMA P-58 procedure." *J. Constr. Steel. Res*., 105, 107-118.

Ji, X., Kato, M., Wang, T., Hitaka, T., Nakashima, M. (2009). "Effect of gravity columns on mitigation of drift concentration for braced frames." *J. Struct. Steel. Res*., 65, 2148-2156.

Judd, J. P., Charney, F. A., Pryor, S. E. (2015). "Retrofit of steel-frame buildings using enhanced gravity-frame connections." *Proc. 2nd ATC & SEI Conf. on improving the seismic performance of existing buildings and other structures*, 132-143.

Kishi, N., Chen, W.-F. (1990). "Moment-rotation relations of semirigid connections with angles." *J. Struct. Eng.*, 116(7), 1813-1834.

Kishi, N., Hasan, R., Chen, W.-F., Goto, Y. (1997). "Study of Eurocode 3 steel connection classification". *Eng. Struct.*, 19(9), 772-779.

Krawinkler, H., Seneviratna, G. D. P. K. (1998). "Pros and cons of a pushover analysis of seismic performance evaluation." *Eng. Struct*., 20(4), 452-464.

Krawinkler, H., Gupta, A., Medina, R., and Luco, N., 2000-a. "*Development of Loading Histories for Testing of Steel Beam-to-Column Assemblies*." SAC Background Report SAC/BD-00/10.

Kukreti, A. R., Abolmaali, A. S. (1999). "Moment-rotation hysteresis behavior of top and seat angle steel frame connections." *J. Struct. Eng*., 125(8), 810-820.

Lee, K., Foutch, D. A. (2002). "Performance evaluation of new steel frame buildings for seismic loads." *Earthquake Eng. Struct. Dyn*., 31, 653-670.

Leon, R. T. (1998). "Composite connections." *Progress Struct. Eng. Mat*., 1(2), 159-169.

Liu, C., Tan, K. H., Fung, T. C. (2015). “Investigations of nonlinear dynamic performance of top-and-seat with web angle connections subjected to sudden column removal”, *Eng. Struct.,* 99, 449-461.

Mander, J. B., Chen, S. S., Pekcan, G. (1994). “Low-cycle fatigue behavior of semi-rigid top-and-seat angle connections.” *AISC Eng. J*., 31, 111-122.

Mander, J. B., Pekcan, G., Chen, S. S. (1995). “Low-cycle variable amplitude fatigue modeling of top-and-seat angle connections.” *AISC Eng. J.,* 32, 54-62.

NBCC. (2015) *National Building Code of Canada*. National Research Council Canada, Ottawa, ON.

Nethercot, D. A., Li, T. Q., Ahmed, B. (1988). “Unified classification system for beam-to-column connections”. *J. Constr. Steel Res.*, 45(1), 39-65.

O’Sullivan, D. P., Hajjar, J. F., Leon, R. T. (1998). “Repairs to mid-rise steel frame damaged in Northridge Earthquake.” *J. Perform. Constr. Facilities*, 12(4), 213-220.

Pirmoz, A., Daryan, A. S., Mazaheri, A., Darbandi, H. E. (2008). “Behavior of bolted angle connections subjected to combined shear force and moment”. *J. Constr. Steel Res.*, 64, 436-446.

Radziminski, J. B., Bradburn, J. H. (1984) “Experimental investigation of semi-rigid steel beam-column connections”. *Proc. 8th World Conference on Earthquake Engineering,* 169-176.

Shen, J., Astaneh-Asl, A. (1999). “Hysteretic behavior of bolted-angle connections.”, *J. Constr. Steel. Res.,* 51, 201-218.

Shen, J., Astaneh-Asl, A. (1999). “Hysteretic model of bolted-angle connections.”, *J. Constr. Steel. Res.,* 54, 317-343.

Sizemore, J. G., Fahnestock, L. A., Hines, E. M., Bradley, C. R. (2017) “Parametric study of low-ductility concentrically braced frames under cyclic static loading.” *J. Struct. Eng.*, 143(6).

Stoakes, C. D., Fahnestock, L. A. (2011). “Cyclic flexural testing of concentrically braced frame beam-column connections.” *J. Struct. Eng.*, 137, 739-747.

Yang, B., Tan, K. H. (2013). “Robustness of bolted-angle connections against progressive collapse: Mechanical modelling of bolted-angle connection under tension.” *Eng. Struct.*, 57, 153-168.

CHAPTER 7 NUMERICAL MODELING OF BOLTED ANGLE HYSTERETIC BEHAVIOUR BASED ON EXPERIMENTAL TESTING

7.1 Context

Several analytical models have been proposed to characterize the moment-rotation behaviour of bolted top and seat with double web angles, either trilinear (Shen and Astaneh-Asl 1999, Pirmoz et al. 2009), polynomial (Azizinamini and Radziminski 1989), hyperbolic (Kong and Kim 2017) or power models (Kishi and Chen 1990). However, for the same connection presented in Figure 7.1a, these models do not agree on the moment-rotation response, as pictured in Figure 7.1b. Only the trilinear model proposed by Shen and Astaneh-Asl (1999) offered an evaluation of the ultimate rotation of the connection.

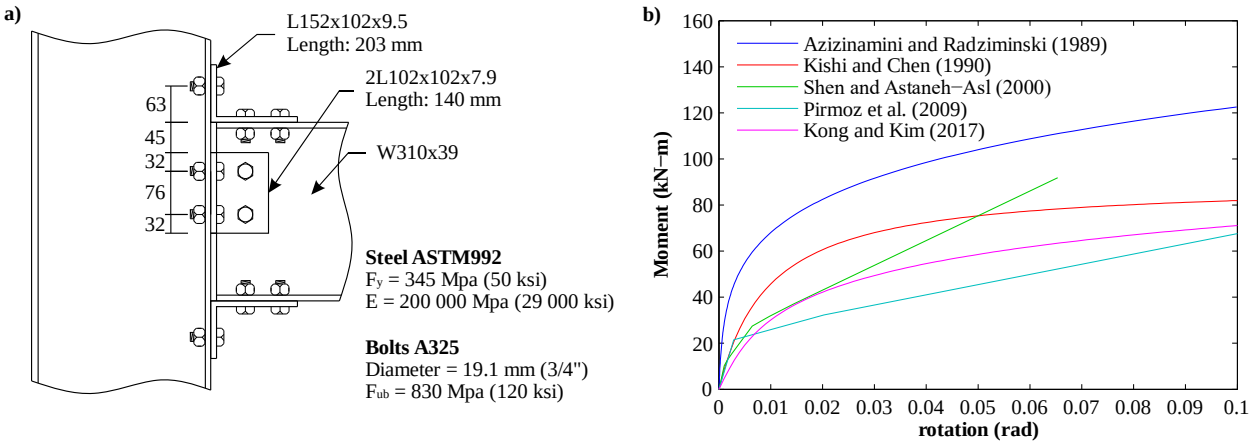


Figure 7.1. a) Top and seat with double web angle beam-column connection detailing b) Moment-rotation response of proposed models.

These discrepancies between the models result from the differences between the experimental campaigns on which the models are developed and calibrated. Such differences may include variations in the setup procedures, the loading protocols and the instrumentation. Furthermore, the complex nonlinear behaviour of bolted angles may also be influenced by parameters varying between experimental campaigns, but not characterized in the models, such as the bolt pretension, the bolt grade and the bolt spacing.

To acknowledge the influence of these geometrical parameters, a model is required to represent the inelastic behaviour of bolted angle connections. The development of this model is performed after

an extensive experimental investigation conducted to create an array of data with limited variation in the testing conditions. This investigation aimed at defining the influence of the column bolt gauge, the angle thickness, the column bolt grade and pretension load. These parameters were characterized through 139 tests under different loading conditions: Quasi-static and dynamic, as well as monotonic and cyclic loading. Among those 139 tests, 71 were performed under monotonic loading conditions, while 38 tests were loaded with a cyclic static protocol and 18 under asymmetric cyclic dynamic protocol. 12 tests aimed at characterizing the low-cycle fatigue behaviour of the bolted angles.

The model developed by Menegotto and Pinto (1973) and enhanced by Filippou et al. (1983) is widely used with the OpenSees software (2006) through the *Steel02* material to represent the stress-strain behaviour of steel. This model represents the hysteretic behaviour of steel including the isotropic hardening and Bauschinger effect. In OpenSees (2006), The *fatigue* material using the formulation developed by Uriz and Mahin (2008) can be applied to the *Steel02* material to represent the low-cycle fatigue damage and rupture in the material. For the monotonic tests, the input parameters of the *Steel02* material were obtained to represent the force-deformation behaviour of the tested specimens.

However, for the cyclic tests, the procedure adopted by the *Steel02* material cannot represent the complex behaviour of the bolted angles hysteresis. The limitations and of the *Steel02* model are presented along with the discrepancies observed when trying to represent the hysteretic nonlinear behaviour of bolted angles. The discrepancies, concerning the unloading portion, reloading portion and compressive yield strength are addressed by proposing modifications to the *Steel02* model. These modifications aim at creating a new model to represent accurately the nonlinear behaviour of bolted angle components. This proposed model, referred to as the *SteelAngles* model, includes the fatigue cycle counting method developed by Uriz and Mahin (2008) to offer a prediction on the fracture of the component and assess the strength loss caused by low-cycle fatigue. The input parameters of the *SteelAngles* model are determined for the 38 tests loaded with a cyclic static protocol and the 18 tests asymmetric cyclic dynamic protocol. Finally, the *SteelAngles* is used to model four top and seat with double web bolted angle beam-column connections and the moment-rotation behaviour is compared to experimental results. Although tests showed an influence of the shear load on the rotational behaviour of the connection, the proposed model does not include an

interaction between the shear and the moment capacity of the connection. The implications of this simplification are discussed in detail in section 9.4. The *SteelAngles* model could also be extended to other type of connections, for example the double web angle connections, beam-column to gusset connections and column base plates pictured in Figure 7.2.

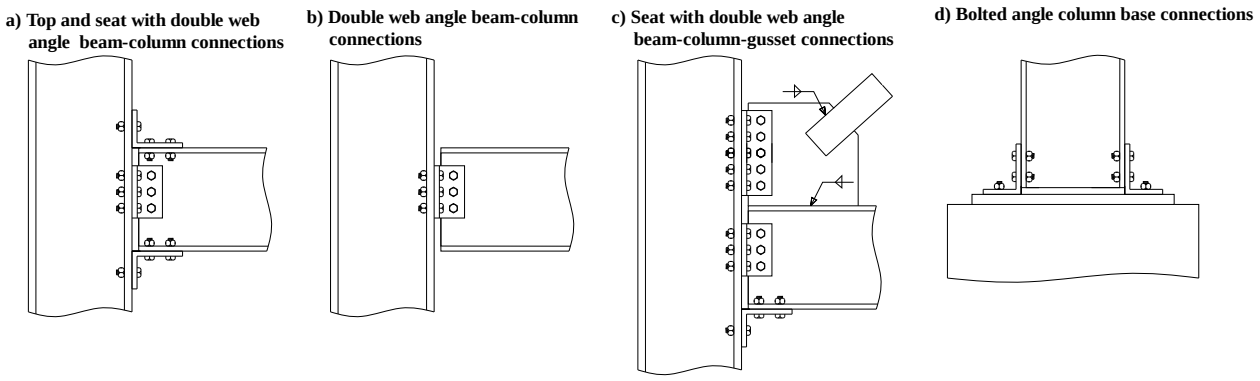


Figure 7.2. Potential bolted angle connection types to model with the *SteelAngles* model.

7.2 Comparison between the cyclic bolted angle experimental results and *Steel02* model

7.2.1 Test data base

The experimental program conducted on bolted angle components aimed at characterizing the angles on a component level and providing a wide array of angle geometries. A simple setup was privileged to test a wider range of thickness and column bolt gauge. The angle specimens were bolted to a stocky custom-built welded-wide-flange (WWF) column section, which was in turn attached to a rigid reaction frame anchored to the strong floor. The specimens were also bolted on their beam leg to the loading plate. The plate was in turn bolted through steel grips to a 1500 kN dynamic actuator, with a maximum stroke of ± 125 mm. A second angle was added under the plate to avoid flexural effects resulting from the setup asymmetry. The complete experimental setup is presented in Figure 7.3. Similar testing setups were previously used (Azizinamini 1985, Shen and Astaneh-Asl 1999, Garlock et al. 2003, Yang and Tan 2013, Gong 2014).

The parametric study was established by varying the angles thickness (t) from 7.9 to 19.1 mm (5/16” to 3/4”) and the column bolt gauge (g_c) from 63.5 to 114.3 mm (2.5” to 4.5”). The test matrix

presented in Figure 7.4 consists of 19 test cases with different angle geometries. Most of the deformations were expected to occur in the column leg, between the bolt and the fillet. This part of the angle is represented by the flexural span g_2, which corresponds to the distance between the end of the fillet and the edge of the bolt head. To establish a unitless comparative basis between the test cases, the ratio of g_2/t was used. This ratio varied from 1.25 to 8.00, as shown in the test matrix of Figure 7.4, where a small ratio is generally associated to a stiff specimen and a large ratio represents a flexible angle.

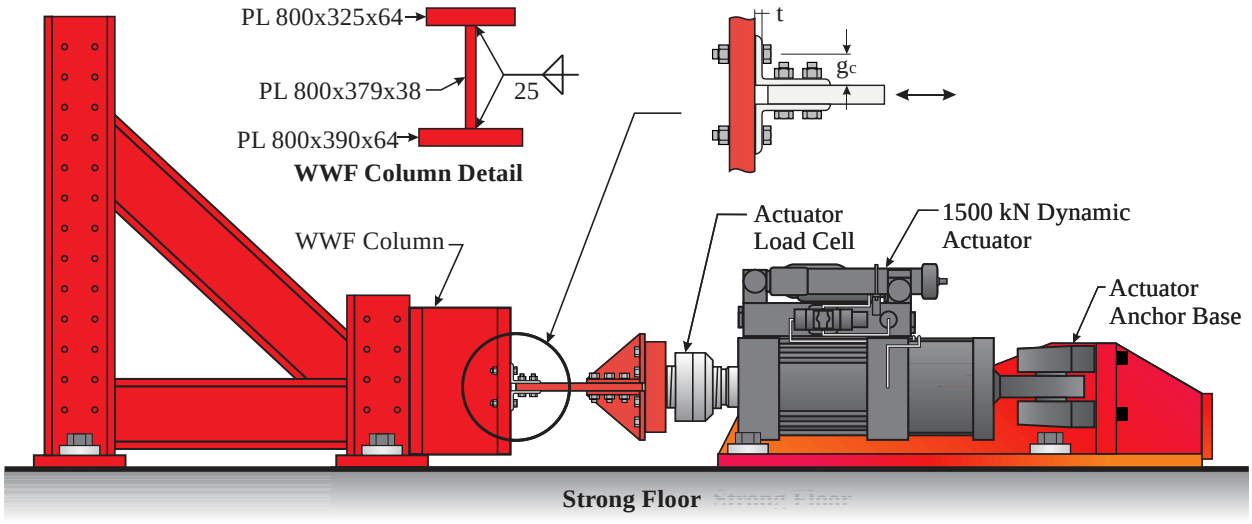


Figure 7.3. Sketch of experimental setup

g_c (mm) \ t (mm)	7.9	9.5	12.7	15.9	19.1
63.5	**TC19** 3.80 L 102 x 102 x 7.9	**TC1** 2.67 L 102 x 152 x 9.5	**TC3** 1.38 L 102 x 203 x 12.7		
76.2		**TC2** 4.00 L 152 x 152 x 9.5	**TC4** 2.38 L 152 x 203 x 12.7	**TC5** 1.70 L 152 x 203 x 15.9	**TC6** 1.25 L 152 x 203 x 19.1
88.9		**TC7** 5.33 L 152 x 152 x 9.5	**TC9** 3.38 L 152 x 203 x 12.7	**TC11** 2.50 L 152 x 203 x 15.9	**TC13** 1.92 L 152 x 203 x 19.1
101.6		**TC8** 6.67 L 152 x 152 x 9.5	**TC10** 4.38 L 152 x 203 x 12.7	**TC12** 3.30 L 152 x 203 x 15.9	**TC14** 2.58 L 152 x 203 x 19.1
114.3		**TC15** 8.00 L 152 x 152 x 9.5	**TC16** 5.38 L 152 x 203 x 12.7	**TC17** 4.10 L 152 x 203 x 15.9	**TC18** 3.25 L 152 x 203 x 19.1

Legend:

Test Case ID
g_2/t
Angle section

Figure 7.4. Test Matrix of angles experimental program

7.2.2 Modeling monotonic response of bolted angles with *Steel02*

The force-deformation behaviour of monotonic tests has been calibrated with the stress-strain *Steel02* model, translated into a force-deformation relationship. This model allowed the representation of the force-deformation *F-Δ* behaviour with the single formulation of Equation 7.1.

$$F = \frac{(K_i - K_P)\Delta}{\left[1 + \left(\frac{\Delta}{F_0/K_i}\right)^{R_0}\right]^{\frac{1}{R_0}}} + K_P\Delta \qquad (7.1)$$

The values of the yield force F_Y, of the initial stiffness K_i and of the initial to plastic transition parameter R_0 were determined to obtain the best fit possible with the least square method. The plastic stiffness K_P was determined through linear regression of the plastic behaviour. Table 7.1 summarizes the calibration parameters obtained for each of the 19 angle configurations. Figure 7.5 shows a good representation of the monotonic nonlinear experimental behaviour with the *Steel02* model. However, hardening and softening were not considered in the cyclic tests because these behaviours were not observed systematically in all cyclic tests.

Table 7.1. Calibrated parameters of *Steel02* model with monotonic tests

Test Case	g_c	t	g_2/t	F_0	K_i	R_0	K_P
	mm	mm	-	kN	kN/mm	-	kN/mm
TC1	63.5	9.5	2.67	100	113	1.518	3.9
TC2	76.2	9.5	4.00	75	91	1.541	4.6
TC3	63.5	12.7	1.38	177	436	1.716	12.9
TC4	76.2	12.7	2.38	167	267	1.490	6.7
TC5	76.2	15.9	1.70	246	647	1.304	9.7
TC6	76.2	19.1	1.25	327	909	1.393	14.1
TC7	88.9	9.5	5.33	81	64	1.401	3.2
TC8	101.6	9.5	6.67	63	39	1.676	2.8
TC9	88.9	12.7	2.38	134	170	1.759	4.3
TC10	101.6	12.7	3.38	107	137	1.551	4.2
TC11	88.9	15.9	2.50	218	417	1.106	7.0
TC12	101.6	15.9	3.30	192	318	1.050	6.1
TC13	88.9	19.1	1.92	260	790	0.999	9.9
TC14	101.6	19.1	2.58	249	617	0.892	9.9
TC15	114.3	9.5	8.00	48	25	1.611	1.6
TC16	114.3	12.7	5.38	90	107	1.430	4.0
TC17	114.3	15.9	4.10	139	283	1.439	5.5
TC18	114.3	19.1	3.25	197	465	1.411	5.8
TC19	63.5	7.9	3.80	66	86	1.825	3.0

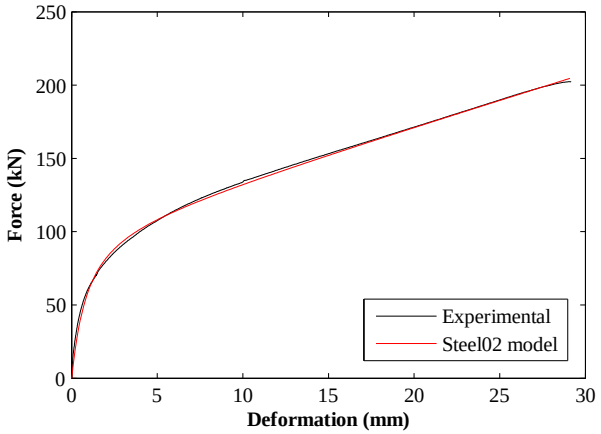


Figure 7.5. Modeling bolted angle monotonic response with Steel02 model

7.2.3 Modeling hysteretic behaviour of bolted angles with the *Steel02* material

For cyclic response, the *Steel02* model is established by Equation 7.2 and the relative deformation and force, Δ^* and F^* are defined in Equations 7.3 and 7.4. These unitless ratios allow the model to account for the initial position of the load reversal, Δ_i and F_i, as well as the point characterizing the

transition between the initial and plastic stiffness, Δ_0 and F_0, as identified in Figure 7.6a. These two points are redefined at each load reversal, but the general equation of the model, Equation 7.2, remain valid.

$$F^* = b\Delta^* + \frac{(1-b)\Delta^*}{\left(1+(\Delta^{*R_0})\right)^{\frac{1}{R_0}}} \tag{7.2}$$

$$\Delta^* = \frac{\Delta - \Delta_R}{\Delta_0 - \Delta_R} \tag{7.3}$$

$$F^* = \frac{F - F_R}{F_0 - F_R} \tag{7.4}$$

At each load reversal, the force-deformation relationship is updated to define the behaviour of the upcoming excursion and some parameters are revaluated to assess the cyclic degradation and the strain-hardening. First, the deterioration of the cyclic curvature caused by the Bauschinger effect is acknowledged, as illustrated in Figure 7.6b. This cyclic deterioration depends on the maximum positive and negative deformation experienced by the angles and is considered by updating the transition parameter R with Equation 7.5. The unitless parameters c_{r1} and c_{r2} define the degradation rate. The deformation ratio ξ is given by the maximum plastic deformation range experienced by the angles, Δ_{max}^{+} and Δ_{max}^{-}, with respect to the positive and negative initial yield deformation Δ_0^{+} and Δ_0^{-}, as defined by Equation 7.6.

$$R = R_0 - \frac{c_{r1}\xi}{c_{r2} + \xi} \tag{7.5}$$

$$\xi = \frac{\Delta_{Max}^{+} - \Delta_{Max}^{-}}{\Delta_0^{+} + \Delta_0^{-}} \tag{7.6}$$

Filippou et al. (1983) added the strain-hardening evaluation to the model proposed by Menegotto and Pinto (1973) pictured in Figure 6c. The *Steel02* material uses the formulation of Lanning and Uang (2014) to characterize the force gain F_{st} defined by Equation 7.7. The unitless parameters a_1 and a_2 characterize the compressive hardening rate and define the compressive force gain F_{st}, while a_3 and a_4 characterize the tensile hardening rate and its force gain F_{st}. This method to consider the strain-hardening may lead to some discrepancies in cycles characterized by partial reloading as illustrated in Figure 7.6d.

$$F_{st} = \begin{cases} a_1 \left(\frac{\xi}{a_2}\right)^{0.8}, & \text{in compression} \\ a_3 \left(\frac{\xi}{a_4}\right)^{0.8}, & \text{in tension} \end{cases} \tag{7.7}$$

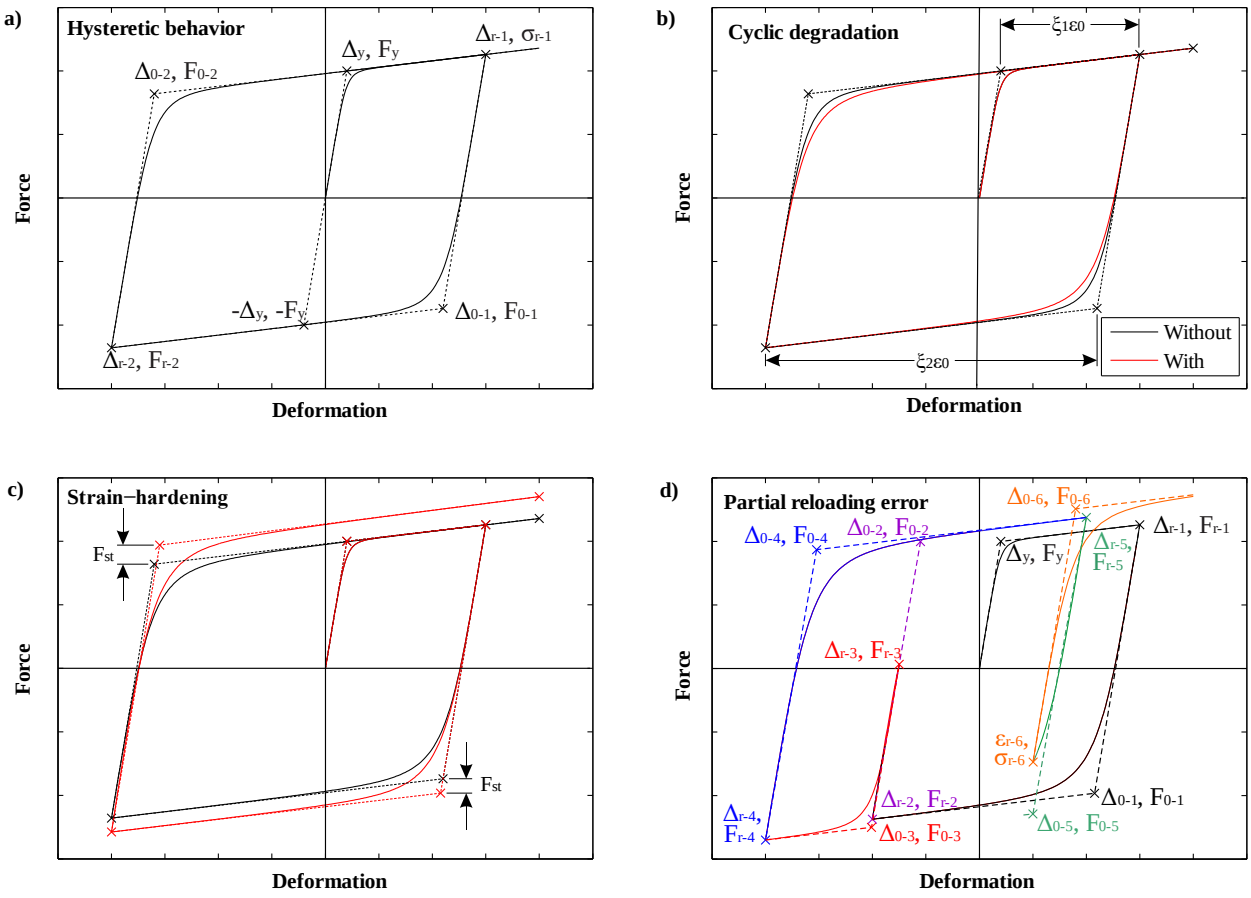


Figure 7.6. a) Hysteretic behaviour of the *Steel02* material b) Cyclic degradation of the *Steel02* material c) Strain-hardening and d) Partial reloading error associated to the strain hardening of the *Steel02* material

The experimental static monotonic curves give a good approximation for the backbone curve of the cyclic tests, as shown in Figure 7.7a. Therefore, the input parameters determined by are valid for characterizing the backbone behaviour of the cyclic tests. However, the intrinsic hysteretic characterization of the *Steel02* model, when using the parameters calibrated from the monotonic tests, does not agree with the experimental results of the cyclic tests. Figure 7.7b compares these two hysteretic behaviours. As shown in this figure, the parameters obtained from the monotonic test calibration offers an accurate estimation of the cyclic backbone curve. However, the *Steel02*

material did not accurately estimate the unloading and reloading behaviours of bolted angles, as well as the compressive yield strength.

First, the unloading stiffness of the experimental results is smaller than its initial stiffness. However, the *Steel02* model considers the same value for both part of the hysteretic behaviour. This discrepancy, identified as the unloading error in Figure 7.7b, leads to an overestimation of the unloading stiffness and of the energy dissipated by the plastic mechanism.

Also, during the unloading excursions, the bolted angles tend to adopt a stiffness projecting towards a constant compressive force value larger than the tensile yield force. This behaviour is not accurately represented through the numerical model, where the unloading behaviour tend towards the yield force in compression. The energy dissipation capacity of the angle is thus underestimated as illustrated by the compressive yield force error of Figure 7.7b.

Finally, the reloading behaviour obtained from the *Steel02* model tend to reach and follow the backbone curve. However, the experimental adopt a stiffness projecting towards the maximum load and deformation experienced by the angle. The stiffness and force capacity of the angles are largely overestimated by the numerical model during the reloading, which overestimates the energy-dissipation capacity of the angles as represented by the reloading error in Figure 7.7b.

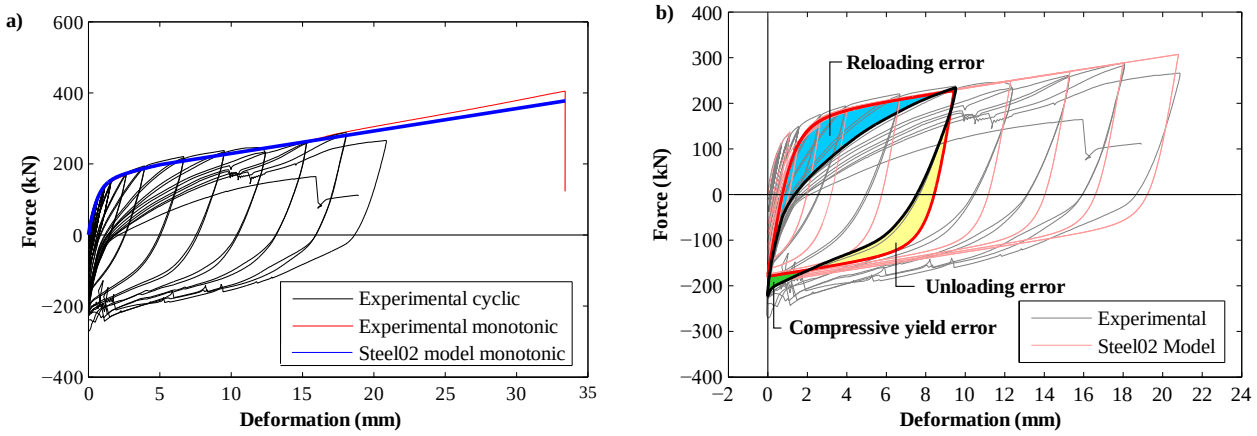


Figure 7.7. a) Comparison between monotonic and cyclic tests (TC4-1 & TC4-4) b) discrepancies between the Steel02 model and experimental results (TC4-4)

7.3 Proposed *SteelAngles* model

To mitigate those discrepancies, a new model based on the *Steel02* model has been developed to more accurately represent the nonlinear hysteretic behaviour specific to bolted angles. The proposed *SteelAngles* model can also account for low-cycle fatigue deterioration and fracture as it incorporates the modified rainflow method proposed by Uriz and Mahin (2008). In an effort to increase the *SteelAngles* model versatility, the contact between the angle and the column flange is not represented and large inelastic compressive excursions are allowed in the model. Such behaviour was however not observed in the tests as the angle reached contact to the column flange when returning to its initial position. This contact is integrated separately by introducing an *Elastic No-tension* material in parallel during the connection modeling. Furthermore, bolt slip was observed in the tests, but it is not included in the *SteelAngles* model.

7.3.1 Modification scheme

To address the compressive yield strength, unloading and reloading discrepancies of the *Steel02*, the formulation of the force-deformation relationship has been modified to create the *SteelAngles* model. The force-deformation relationship of the *Steel02* model is comprised of two components: a power equation representing the initial stiffness and transition portion and a linear equation representing the plastic stiffness. To create the *SteelAngles* model, the equations defining the unloading and reloading responses are revisited, as pictured in Figure 7.8a and b respectively. Two power curves are added to represent the secant stiffness behaviour and to follow the backbone curve of the angles. The plastic stiffness is also defined by a linear equation. The proposed *SteelAngles* model thus consists of the sum of 4 distinct curves:

1- A linear curve representing the plastic stiffness behaviour;
2- A power curve representing the initial stiffness response;
3- A power curve representing the secant stiffness response; and
4- A power curve following the backbone curve.

The contribution of each curve in the total force calculation is conditional to the deformation demand imposed on the angle and the previous deformation history. Figure 7.8c and 7.8d present

the decomposition of the *Steel02* model at small and large cycles respectively. The behaviour of each curve is not dependent on the maximum deformation previously experienced by the angles.

Alternatively, in Figure 7.8e, the first cycle occurs during the backbone transition between the initial and plastic backbone stiffnesses. In this case, the secant stiffness aiming towards the larger force-deformation experienced by the angle is similar to the initial stiffness. Therefore, the reloading phase is mainly dominated by the secant stiffness curve and the initial stiffness curve has no significant contribution. After the maximum load experienced by the angle is reached, the backbone curve allows the force-deformation relationship to continue the transition between the initial and plastic backbone stiffness. On the other hand, in Figure 7.8f, the unloading occurs after the backbone transition. Therefore, the contribution of the backbone curve is null, and the initial and secant stiffness curves contribute significantly to the force-deformation relationship.

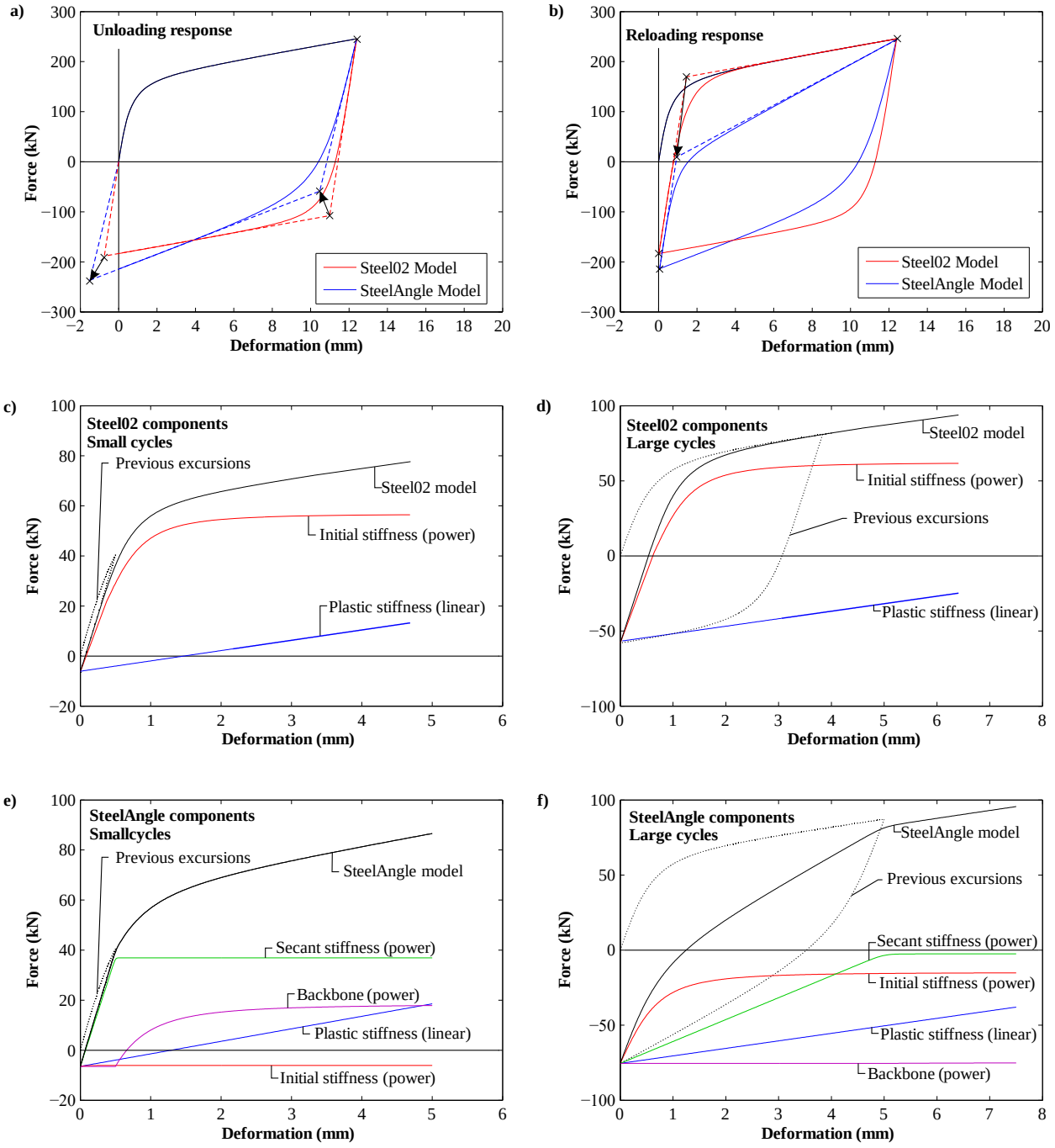


Figure 7.8. Modifications to the Steel02 model to create the SteelAngles model a) for the unloading response b) for the reloading response, c) Decomposition of the Steel02 model at small cycles, d) Decomposition of the Steel02 model at large cycles, e) Decomposition of the SteelAngles model at small cycles, f) Decomposition of the SteelAngles model at large cycles

The characteristics of the *Steel02* model to define the isotropic hardening, the Bauschinger effect and the initial stress remain in the *SteelAngles* model. Four input parameters are added in the *SteelAngles* model to characterize accurately the transition between the initial and secant curves, while three parameters are added to assess the compressive force error and two others allow the definition of the low-cycle fatigue behaviour.

At each load reversal, the force-deformation relationship is updated to define the behaviour of the upcoming excursion. This update consists of a revaluation of the transition points of each of the 3 power curves of the proposed model. The set of equations used to evaluate these points depends if the deformation increment is positive (reloading excursion) or negative (unloading excursion).

However, some parameters are updated at each load reversal regardless of the loading direction. First, the deterioration of the cyclic curvature caused by the Bauschinger effect is acknowledged following the procedure used in the *Steel02* and presented by Equations 7.5 and 7.6. No changes were brought to the cyclic degradation.

The proposed mathematical model can also account for low-cycle fatigue deterioration. At each load reversal, the damage index *DI* is calculated based on the modified rainflow method proposed by Uriz and Mahin (2008) and presented in section 7.5. The damage factor *DF* applied in certain equations of the proposed mathematical model is defined by Equation 7.8. This equation was chosen for its simplicity and it provided a relatively good fit for most tests. Other equations could be applied to consider differently the damage strength loss in the model.

$$DF = 1 - 0.5DI^2 \tag{7.8}$$

7.3.2 Modeling the compressive yield force

To palliate to the compressive yield force error, two new input parameters are introduced in the model: the compressive yield force and the compressive initial stiffness. As presented by Figure 7.9a, the unloading excursions of the bolted angles tend towards the same point, defined by a deformation Δ_0^- and a force F_0^-. This point is defined as the anchor load and is required to accurately define the hysteretic behaviour of bolted angles. The compressive initial stiffness K_0^- is derived from this point with Equation 7.9. This stiffness is also used to more accurately define the

unloading initial stiffness behaviour and reduce the unloading error. A third input parameter defining the negative plastic stiffness ratio b^- is also added to the model to increase its versatility.

$$K_i^- = F_0^- / \Delta_0^- \tag{7.9}$$

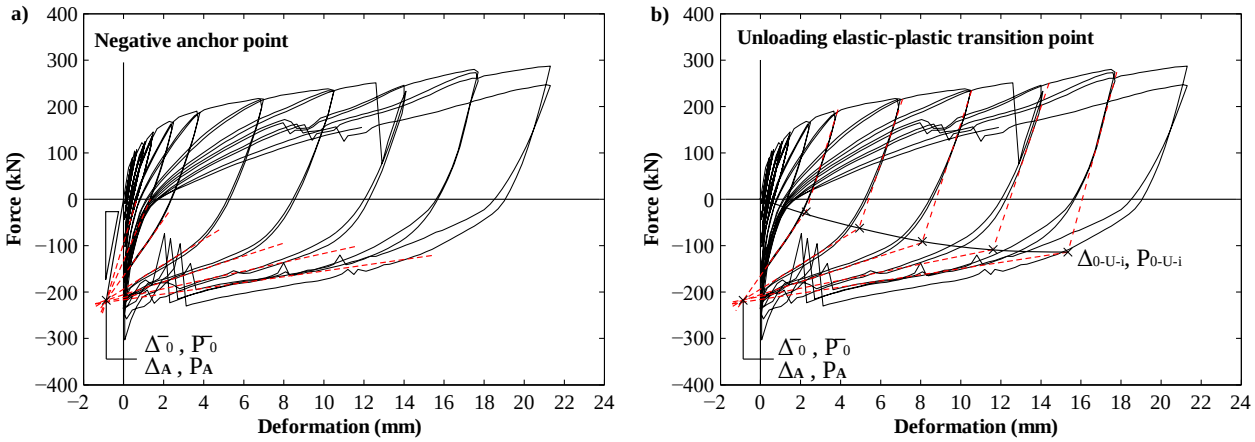


Figure 7.9. a) Compressive yield force of a typical cyclic test (TC4-5) b) Increase of the transition load between the initial and secant stiffness of the negative excursions (TC4-5)

7.3.3 Modeling of the unloading response

The unloading response if determined after the first excursion following the backbone curve. At the load reversal, the deformation and load defining the start of the new excursion Δ_R and F_R are defined. If the deformation reached during the previous positive increment is larger than the maximum positive deformation experienced by the angles, the value of Δ_{Max}^+ is updated. The deformation and load Δ_R and F_R correspond to the start of the first power curve defining the initial unloading, Δ_{R-1} and F_{R-1}.

As observed in Figure 7.9b, the transition load between the initial and secant stiffness obtained from linear regression increases along with the deformation demand on the bolted angles. To represent this increase, a set of parameters, s_1 and s_2 were added to the *SteelAngles* model. These unitless parameters act similarly as the a_1 and a_2 parameters used by Filippou et al. (1983) to account for the steel material hardening. The formulation developed by Lanning and Uang (2014) was used to characterize the transition load of the first power curve, F_{0-1}, defined by Equation 7.10.

The corresponding deformation, $\Delta_{0\text{-}1}$, is then defined with Equation 7.11. Finally, the plastic stiffness ratio of the first power curve b_1 is taken as the input parameter b^-.

$$F_{0-1} = F_0^- s_1 \left(\frac{\xi}{s_2}\right)^{0.8} DF \tag{7.10}$$

$$\Delta_{0-1} = \Delta_R + \frac{F_{0-1} - F_R}{K_i^-} \tag{7.11}$$

The second power curve define the secant stiffness of the unloading excursion aiming towards the maximum negative deformation experienced by the angles Δ_{Max}^- and its corresponding load. However, before defining the secant stiffness and the target load must be defined by including the hardening load, F_{IH}, as defined by Filippou et al. (1983). This hardening load depends on the values of the unitless parameters a_1 and a_2 and is obtained wit Equation 7.12.

$$F_{IH} = F_0^- a_1 \left(\frac{\xi}{a_2}\right)^{0.8} \tag{7.12}$$

The load corresponding to the maximum negative deformation experienced by the angles, Δ_{Max}^-, is located on the backbone curve. The backbone parameters defined by the user are thus used. Equation 7.13 define the relative target deformation on the backbone curve, Δ_T^*, while Equation 7.14 define the corresponding relative target load, F_T^*.

$$\Delta_T^* = \frac{\Delta_{Max}^-}{\Delta_0^-} \tag{7.13}$$

$$F_T^* = b^- \Delta_T^* + \frac{(1 - b^-)\Delta_T^*}{[1 + (\Delta_T^*)^{R_0}]^{\frac{1}{R_0}}} \tag{7.14}$$

The target deformation and load, Δ_T and F_T, are then defined by Equation 7.15 and 7.16 respectively to account for the low-cycle degradation and the hardening behaviour of the bolted angles. This point also corresponds to the transition point of the second power curve between the secant stiffness and the backbone curve, defined as $\Delta_{0\text{-}2}$ and $F_{0\text{-}2}$.

$$\Delta_{0-2} = \Delta_T = \Delta_{Max}^- + \frac{F_{IH} DF}{K_0^-} \tag{7.15}$$

$$F_{0-2} = F_T = (F_T^* F_0^- + F_{IH}) DF \tag{7.16}$$

The secant stiffness b_{secant} is obtained as the slope between this point and the transition point of the first power curve, defined by the deformation and load, $\Delta_{0\text{-}1}$ and $F_{0\text{-}1}$, as defined by Equation 7.17.

The plastic stiffness must then be revaluated with respect to the secant stiffness according to Equation 7.18. Finally, the point corresponding to the start of the second power curve, characterized by the deformation and load Δ_{R-2} and F_{R-2}, is defined with Equations 7.19 and 7.20.

$$b_{secant} = \frac{F_{0-2} - F_{0-1}}{\Delta_{0-2} - \Delta_{0-1}} \times \frac{1}{K_i^-} \tag{7.17}$$

$$b_2 = \frac{b^-}{b_{secant}} \tag{7.18}$$

$$F_{R-2} = F_{0-1} - b_{secant} K_i^- (\Delta_{0-1} - \Delta_R) \tag{7.19}$$

$$\Delta_{R-2} = \Delta_R \tag{7.20}$$

The third power curve aims at following the backbone curve after the maximum negative deformation has been reached. The use of this curve in the calculation of the total load is conditional on the deformation demand previously imposed on the angle. The backbone curve is updated based on the hardening defined with Equation 7.12 and the low-cycle fatigue degradation factor established by Equation 7.5. The transition point of the backbone curve is defined by the deformation and load Δ_{0-3} and F_{0-3} obtained with Equations 7.21 and 7.22 respectively. The starting point of the third power curve is obtained with Δ_{R-3} and F_{R-3} determined by Equations 7.23 and 7.24.

$$F_{0-3} = (F_0^- + F_{IH})DF \tag{7.21}$$

$$\Delta_{0-3} = \Delta_0^- DF + \frac{F_{IH} DF}{K_i^-} \tag{7.22}$$

$$F_{R-3} = F_{0-2} - b^- K_i^- \Delta_{0-2} DF \tag{7.23}$$

$$\Delta_{R-3} = \Delta_{0-2} \tag{7.24}$$

Finally, the stiffness of the linear plastic curve, K_L corresponds to the plastic stiffness defined by the user for the negative backbone, K_P^-. The calculation of the total load is presented in section 7.3.5.

7.3.4 Modeling of the reloading response

The procedure applied for a reloading response is similar to the unloading excursion, but the parameters used in the set of equations are different. Following the load reversal, the deformation and load defining the start of the new excursion Δ_R and F_R are redefined. If the deformation reached during the previous negative increment is larger than the maximum negative deformation experienced by the angles, the value of Δ_{Max}^- is also updated. These parameters also correspond to the start of the initial reloading power curve, Δ_{R-1} and F_{R-1}.

The parameters, s_3 and s_4 were added to the mathematical model to define the transition load between the initial and secant stiffness. These unitless parameters act similarly as the a_3 and a_4 parameters used by Filippou et al. (1983) to account for the steel material hardening. The formulation developed by Lanning and Uang (2014) was used to characterize the transition load of the first power curve, F_{0-1}, defined by Equation 7.25. The corresponding deformation, Δ_{0-1}, is defined by Equation 7.26. The plastic stiffness ratio of the first power curve b_1 is taken as the user defined value b^+.

$$F_{0-1} = F_0^+ s_3 \left(\frac{\xi}{s_4}\right)^{0.8} DF \tag{7.25}$$

$$\Delta_{0-1} = \Delta_R + \frac{F_{0-1} - F_R}{K_i^+} \tag{7.26}$$

The second power curve defining the secant stiffness of the unloading excursion aims towards the maximum positive deformation experienced by the angles, Δ_{Max}^+, and its corresponding load. This load includes the additional load created by the hardening F_{IH}, as defined by Filippou et al. (1983) and obtained by Equation 7.27. This load depends on the values of unitless parameters a_3 and a_4.

$$F_{IH} = F_0^+ a_3 \left(\frac{\xi}{a_4}\right)^{0.8} \tag{7.27}$$

The load corresponding to the maximum positive deformation experienced by the angles, Δ_{Max}^+, is located on the backbone curve and is obtained with Equation 7.28 and 7.29.

$$\Delta_T^* = \frac{\Delta_{Max}^+}{\Delta_0^+} \tag{7.28}$$

$$F_T^* = b^+ \Delta_T^* + \frac{(1 - b^+)\Delta_T^*}{[1 + (\Delta_T^*)^{R_0}]^{\frac{1}{R_0}}} \tag{7.29}$$

The target deformation and load, Δ_T and F_T, are then defined by Equation 7.30 and 7.31 respectively and correspond to the transition point of the second power curve between the secant stiffness and the backbone curve, defined as $\Delta_{0\text{-}2}$ and $F_{0\text{-}2}$.

$$\Delta_{0-2} = \Delta_T = \Delta_{Max}^{+} + \frac{F_{IH}DF}{K_i^{+}} \tag{7.30}$$

$$F_{0-2} = F_T = (F_T^{*}F_0^{+} + F_{IH})DF \tag{7.31}$$

The secant stiffness, b_{secant}, is obtained as the slope between this point and the transition point of the first power curve, defined by the deformation and load, $\Delta_{0\text{-}1}$ and $F_{0\text{-}1}$, as defined by Equation 7.32. The plastic stiffness must then be revaluated with respect to the secant stiffness according to Equation 7.33. Finally, the point corresponding to the start of the second power curve, characterized by the deformation and load $\Delta_{R\text{-}2}$ and $F_{R\text{-}2}$, is defined with Equations 7.34 and 7.35.

$$b_{secant} = \frac{F_{0-2} - F_{0-1}}{\Delta_{0-2} - \Delta_{0-1}} \times \frac{1}{K_i^{+}} \tag{7.32}$$

$$b_2 = \frac{b^{+}}{b_{secant}} \tag{7.33}$$

$$F_{R-2} = F_{0-1} - b_{secant}K_i^{+}(\Delta_{0-1} - \Delta_R) \tag{7.34}$$

$$\Delta_{R-2} = \Delta_R \tag{7.35}$$

The third power curve aims at following the backbone curve after the maximum positive deformation has been reached. The use of this curve is conditional on the deformation demand previously imposed on the angle. The backbone curve is updated based on the hardening defined with Equation 7.27 and the low-cycle fatigue degradation factor established by Equation 7.5. The transition point of the updated backbone curve is defined by the deformation and load $\Delta_{0\text{-}3}$ and $F_{0\text{-}3}$ defined by Equations 7.36 and 7.37 respectively. The starting point of the third power curve is obtained with $\Delta_{R\text{-}3}$ and $F_{R\text{-}3}$ determined by Equations 38 and 39 respectively.

$$F_{0-3} = (F_0^{+} + F_{IH})DF \tag{7.36}$$

$$\Delta_{0-3} = \Delta_0^{+}DF + \frac{F_{IH}DF}{K_i^{+}} \tag{7.37}$$

$$\mathrm{F_{R-3}} = \mathrm{F_{0-2}} - \mathrm{b^{+}K_i^{+}\Delta_{0-2}DF} \tag{7.38}$$

$$\Delta_{\mathrm{R-3}} = \Delta_{0-2} \tag{7.39}$$

Finally, the stiffness of the linear plastic curve, K_L is taken as the plastic stiffness defined by the user for the positive backbone, K_P^+.

7.3.5 Calculating the total load

Once the parameters defining the three power curves and the linear plastic stiffness have been defined at a load reversal, the total force capacity of the bolted angles is determined for the applied deformation Δ_i. The set of equations used to this end, Equations 7.40 to 7.50, should be applied to each deformation increment imposed on the bolted angles. Equations 7.10 to 7.24 or 7.25 to 7.39 are only used to evaluate the next negative or positive excursion at a load reversal. The values defined by these set of equations are valid until the next load reversal.

To assess the load resulting from each of the power curve, the relative deformation and force ratios developed by Menegotto and Pinto (1983) and presented in Equations 7.3 and 7.4 are used.

Equations 7.40 to 7.42 evaluate the load associated with the initial reloading or unloading power curve, F_1. Equation 7.40 is only valid when the initial deformation of the excursion $\Delta_{R\text{-}1}$ is not equal to the deformation of the transition between the initial and secant stiffnesses $\Delta_{0\text{-}1}$. If this condition is not verified, the force F_1 associated to the initial loading power curve should be neglected. Similarly, Equations 7.43 to 7.45 determine the load created by the secant stiffness power curve, F_2. Equation 7.43 is only valid when the initial deformation $\Delta_{R\text{-}2}$ is not equal to the deformation of the transition between the secant and plastic stiffnesses $\Delta_{0\text{-}2}$. If this condition is not verified, the force F_2 should be neglected. In Equation 7.44, a value of 20 is proposed for the transition form parameter of the secant stiffness power curve, R_2, to obtain a smaller transition portion and a better fit.

(1) Initial loading power curve: (if $\Delta_{0\text{-}1} \neq \Delta_{R\text{-}1}$)

$$\Delta_1^* = \frac{\Delta_i - \Delta_{R-1}}{\Delta_{0-1} - \Delta_{R-1}} \tag{7.40}$$

$$F_1^* = \frac{(1 - b_1 - b_{secant})\Delta_1^*}{[1 + (\Delta_1^*)^R]^{\frac{1}{R}}} \tag{7.41}$$

$$F_1 = F_1^*(F_{0-1} - F_{R-1}) \tag{7.42}$$

(2) Secant stiffness power curve: (if $\Delta_{0\text{-}2} \neq \Delta_{R\text{-}2}$)

$$\Delta_2^* = \frac{\Delta_i - \Delta_{R-2}}{\Delta_{0-2} - \Delta_{R-2}} \tag{7.43}$$

$$F_2^* = \frac{(1 - b_2)\Delta_2^*}{[1 + (\Delta_2^*)^{R_2}]^{\frac{1}{R_2}}} \tag{7.44}$$

$$F_2 = F_2^*(F_{0-2} - F_{R-2}) \tag{7.45}$$

The load created by the third power curve representing the backbone behaviour of the angle is dependent on the deformation demand Δ_i and the previous maximum deformation experienced by the angles. The role of this power curve is to ensure the nonlinear behaviour follows accurately the backbone curve in the initial to plastic transition during subsequent loadings. Once the transition part is experienced by the angles, the load capacity resulting from this portion of the mathematical model is negligible. This load capacity is assessed with Equations 7.46 to 7.48.

(3) Secant stiffness power curve:

(if [$\Delta_i - \Delta_{i\text{-}1} \geq 0$ & $\Delta_i \geq \Delta_{0\text{-}2}$] OR if [$\Delta_i - \Delta_{i\text{-}1} \leq 0$ & $\Delta_i \leq \Delta_{0\text{-}2}$])

$$\Delta_3^* = \left|\frac{\Delta_i}{\Delta_{0-3}}\right| \tag{7.46}$$

$$F_3^* = \frac{(1 - b_1)\Delta_3^*}{[1 + (\Delta_3^*)^R]^{\frac{1}{R}}} \tag{7.47}$$

$$F_3 = F_3^*(F_{0-3} - F_{R-3}) \tag{7.48}$$

Finally, the load created by the linear plastic stiffness is defined by Equation 7.49, while the total force capacity of the bolted angles is given by Equation 7.50. This total force is simply the result of the summation of the loads obtained from the three power curves, the linear curve and the starting load of the excursion, F_R.

(4) Plastic stiffness linear curve:

$$F_L = K_L(\Delta_i - \Delta_R) \tag{7.49}$$

(5) Total force:

$$F_i = F_1 + F_2 + F_3 + F_L + F_R \tag{7.50}$$

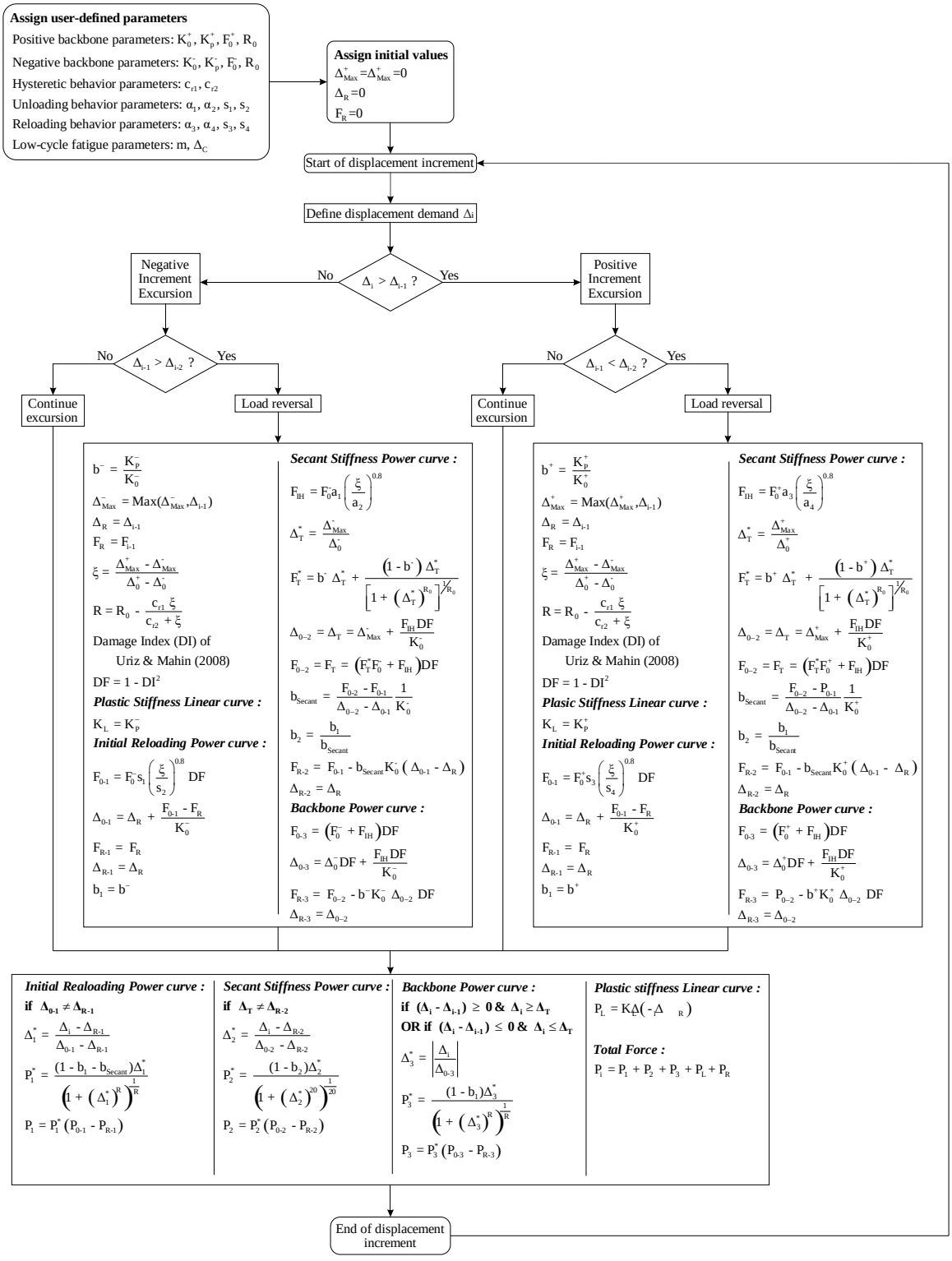


Figure 7.10. Flowchart of the proposed mathematical model algorithm

This new mathematical model is summarized in the flowchart presented in Figure 7.10. It can be added as a uniaxial material into the finite element analysis software OpenSees (2006). Such material can recreate the hysteretic behaviour of the bolted angles with only one fiber element. This new material constitutes a useful tool in the creation of full connection models, since each component of the connection can be modeled independently and assembled into the connection section, with minimal element, and thus minimal computing time.

7.4 Calibration of the *SteelAngles* model

The input parameters obtained from the calibration of the *Steel02* material in OpenSees (2006) for the monotonic test was used to define the backbone behaviour of the cyclic tests using the *SteelAngles* model. These input parameters, presented in Table 7.1, are:

1. The tensile yield force F_0^+;
2. The initial tensile stiffness K_i^+;
3. The tensile plastic stiffness ratio b^+;
4. The transition parameter between the initial and plastic stiffnesses R_0.

7.4.1 Input parameters defining the Bauschinger effect and isotropic hardening

The parameters defining the Bauschinger effect and the isotropic hardening are used in the *SteelAngles* model in the same manner as in the *Steel02*. Cr_1 and Cr_2 represent dimensionless parameters characterizing the impact of the maximum deformation experienced by the angle on the transition parameter R_0. These two values are used conjointly to calibrate the same nonlinear behaviour of the force-deformation curve. To simplify the calibration process and the application of the model, the value of Cr_2 was set to 1.0 for all the tests. The variation of the transition parameter with respect to the plastic deformation thus depended on the value of Cr_1, which was determined from the least square method to offer the best fit.

The parameters a_1 and a_2 are used to define the hardening effect of the maximum deformation on the force given by the intersection of the asymptotes of the initial stiffness and the secant stiffness for the unloading excursions according to Equation 7.12. Similarly, a_3 and a_4, have the same meaning for the reloading excursions, used in Equation 7.27. The bolted angles tested did not

significantly exhibit hardening. Therefore, to simplify the calibration process and the model application, the values of a_1 and a_3 were taken as 0.0, while a_2 and a_4 were taken as 1.0.

7.4.2 Input parameters of the compressive yield strength

The least square method was used to optimize the accuracy of the proposed mathematical model in order to characterize through a set of parameters the hysteretic behaviour of the experimental cyclic tests. The first parameter consists of defining the ratio f_N between the compressive and the tensile yield force of the angle F_0^- / F_0^+. This ratio allows to define the force towards which each of the unloading phase of the hysteretic behaviour converges, as represented in Figure 7.5a. Similarly, the second parameter calibrated is the ratio e_N between the unloading stiffness and the initial stiffness of the backbone curve obtained form the monotonic results, K_i^-/K_i^+.

7.4.3 Input parameters of the unloading and reloading response

Finally, the point defining the start of the secant stiffness was defined based on the unitless values of the parameters s_1 and s_2 in Equation 10 for the negative increment excursions and s_3 and s_4, used in Equation 25, for the positive increment excursions. Again, two parameters were used to define one aspect of the nonlinear behaviour and to simplify the calibration and application of the mathematical model, the values of s_2 and s_4 were set to 1.0 for all the tests. Therefore, the start of the secant stiffness with respect to the plastic deformation only depended on the value of s_1 and s_3, for the negative and positive increment excursions respectively.

Each of these parameters were calibrated for every specimen loaded cyclically to accurately characterize their nonlinear behaviour. The values obtained are presented in Table 7.2 and 7.3 for the specimens loaded cyclically considering a theoretical W310 and a W410 beam respectively. These tables also recalled the parameters used to define the backbone curve.

The determination coefficient R^2 is presented in these tables for each test to indicate the accuracy between the proposed mathematical model and the experimental results. The determination coefficients were larger than 0.885 for each specimen tested, indicating a good representativeness of the proposed mathematical model.

Table 7.2. Calibration parameters of cyclic tests considering a theoretical W310 beam

Test Case	g_2/t	F_0^+	K_0^+	R_0	K_P^+	F_0^+/F_0^-	K_i^+/K_i^-	Cr_1	s_1	s_3	R^2
	-	kN	kN/mm	-	kN/mm	-	-	-	-	-	-
TC1	2.67	99	113	1.518	3.8	1.684	0.896	-0.489	-0.187	0.086	0.962
TC2	4.00	75	91	1.541	4.6	1.884	0.829	-0.512	-0.221	0.049	0.945
TC3	1.38	177	436	1.716	12.9	1.878	0.535	-0.475	-0.209	0.064	0.944
TC4	2.38	167	267	1.490	6.7	1.611	0.563	-0.502	-0.191	0.046	0.985
TC5	1.70	245	647	1.304	9.7	1.643	0.463	-0.424	-0.089	0.028	0.954
TC6	1.25	327	909	1.393	14.1	1.614	0.412	-0.492	-0.071	0.029	0.936
TC7	5.33	82	64	1.401	3.4	1.684	0.967	-0.448	-0.252	0.109	0.965
TC8	6.67	68	48	1.676	2.8	1.768	0.990	-0.434	-0.224	0.057	0.971
TC9	3.38	153	170	1.759	4.3	1.864	0.823	-0.418	-0.162	0.066	0.889
TC10	4.38	121	137	1.551	4.8	1.674	0.832	-0.489	-0.196	0.048	0.952
TC11	2.50	218	417	1.106	7.0	1.841	0.486	-0.470	-0.142	0.039	0.966
TC12	3.30	192	348	1.050	6.1	1.692	0.516	-0.430	-0.191	0.036	0.979
TC13	1.92	281	790	0.999	9.9	2.049	0.359	-0.494	-0.161	0.037	0.975
TC14	2.58	249	617	0.892	9.9	1.714	0.388	-0.529	-0.124	0.021	0.968
TC15	8.00	48	31	1.611	1.6	1.814	0.986	-0.514	-0.221	0.096	0.941
TC16	5.38	90	107	1.430	4.3	1.744	0.816	-0.497	-0.202	0.061	0.980
TC17	4.10	139	283	1.439	5.5	1.976	0.432	-0.512	-0.112	0.021	0.958
TC18	3.25	197	465	1.411	5.7	1.967	0.327	-0.507	-0.109	0.025	0.952
TC19	3.80	66	86	1.825	3.0	1.748	0.913	-0.427	-0.194	0.042	0.935

Table 7.3. Calibration parameters of cyclic tests considering a theoretical W410 beam

Test Case	g_2/t	F_0^+	K_0^+	R_0	K_P^+	F_0^+/F_0^-	K_i^+/K_i^-	Cr_1	s_1	s_3	R^2
	-	kN	kN/mm	-	kN/mm	-	-	-	-	-	-
TC1	2.67	99	113	1.518	3.8	1.729	0.903	-0.418	-0.171	0.073	0.949
TC2	4.00	76	91	1.541	4.6	1.929	0.843	-0.445	-0.219	0.044	0.929
TC3	1.38	177	436	1.716	12.9	1.982	0.549	-0.454	-0.221	0.057	0.965
TC4	2.38	167	267	1.490	6.7	1.729	0.590	-0.437	-0.177	0.044	0.977
TC5	1.70	245	647	1.304	9.7	1.713	0.419	-0.442	-0.128	0.030	0.962
TC6	1.25	327	909	1.393	14.1	1.702	0.454	-0.485	-0.079	0.036	0.938
TC7	5.33	82	64	1.401	3.4	1.873	0.953	-0.462	-0.261	0.111	0.964
TC8	6.67	68	48	1.676	2.8	1.785	0.973	-0.446	-0.219	0.063	0.942
TC9	3.38	153	170	1.759	4.3	1.894	0.855	-0.464	-0.154	0.045	0.962
TC10	4.38	121	137	1.551	4.8	1.848	0.790	-0.507	-0.197	0.073	0.965
TC11	2.50	218	417	1.106	7.0	1.793	0.419	-0.441	-0.138	0.037	0.948
TC12	3.30	192	348	1.050	6.1	1.711	0.536	-0.447	-0.164	0.046	0.982
TC13	1.92	281	790	0.999	9.9	2.032	0.385	-0.527	-0.111	0.031	0.976
TC14	2.58	249	617	0.892	9.9	1.755	0.414	-0.501	-0.132	0.041	0.968
TC15	8.00	48	31	1.611	1.6	1.873	0.973	-0.510	-0.244	0.107	0.963
TC16	5.38	90	107	1.430	4.3	1.729	0.843	-0.436	-0.196	0.061	0.981
TC17	4.10	139	283	1.439	5.5	2.071	0.415	-0.504	-0.102	0.023	0.978
TC18	3.25	197	465	1.411	5.7	1.913	0.315	-0.418	-0.128	0.021	0.964
TC19	3.80	66	86	1.825	3.0	1.873	0.873	-0.454	-0.191	0.073	0.885

7.4.4 Correspondence between the test data and the SteelAngles model

An important parameter for seismic analyses consists of the stiffness variation caused by yielding of the material. This parameter directly influences the inertial forces caused by the ground motion in the building. To numerically represent realistic yielding, the stiffness of the element should follow the same stiffness variation of the experimental angles. Figure 7.11a also shows a good correspondence between the stiffness of the experimental curve and the numerical model.

The parameters used to define the backbone curve of the time-history tests were taken from the calibration of the *Steel02* model based on the results of the dynamic monotonic tests. These values are transcribed in Table 7.4, along with the various calibration parameters required to characterize the hysteretic behaviour of the bolted angles. The determination coefficient R^2 showing the accuracy of the numerical model in representing the experimental data is also presented in Table 7.4.

Table 7.4. Calibration parameters of the hysteretic behaviour of Time-History tests

Test Case	**g_2/t**	**F_0^+**	**K_0^+**	**R_0**	**K_P^+**	**F_0^+/F_0^-**	**K_i^+/K_i^-**	**Cr_1**	**s_1**	**s_3**	**R^2**
	-	**kN**	**kN/mm**	**-**	**kN/mm**	**-**	**-**	**-**	**-**	**-**	**-**
TC1	2.67	97	348	1.118	4.5	1.634	0.312	-0.422	-0.138	0.052	0.905
TC2	4.00	79	310	1.114	4.8	1.772	0.343	-0.420	-0.113	0.045	0.870
TC3	1.38	189	903	1.803	15.4	1.733	0.302	-0.446	-0.152	0.043	0.931
TC4	2.38	168	546	1.451	7.5	1.692	0.361	-0.434	-0.119	0.042	0.936
TC5	1.70	255	1281	1.625	10.1	1.653	0.231	-0.427	-0.091	0.039	0.888
TC6	1.25	376	1987	1.311	8.2	1.536	0.212	-0.426	-0.077	0.027	0.839
TC7	5.33	80	144	1.314	3.5	1.876	0.531	-0.486	-0.196	0.069	0.924
TC8	6.67	75	139	0.939	2.2	1.620	0.423	-0.456	-0.123	0.062	0.819
TC9	3.38	151	378	1.687	5.0	1.874	0.319	-0.432	-0.168	0.046	0.927
TC10	4.38	113	398	1.751	5.0	1.658	0.332	-0.395	-0.103	0.033	0.903
TC11	2.50	213	898	1.211	9.5	1.949	0.281	-0.491	-0.107	0.038	0.881
TC12	3.30	181	749	1.218	7.5	1.716	0.273	-0.412	-0.101	0.027	0.916
TC13	1.92	281	1695	0.895	13.1	1.876	0.243	-0.414	-0.118	0.018	0.845
TC14	2.58	232	1252	1.079	12.6	1.894	0.212	-0.428	-0.108	0.034	0.932
TC15	8.00	50	71	1.179	1.9	1.547	0.531	-0.512	-0.208	0.072	0.895
TC16	5.38	97	367	1.218	4.2	1.721	0.272	-0.474	-0.094	0.019	0.909
TC17	4.10	-	-	-	-	-	-	-	-	-	-
TC18	3.25	207	990	1.526	5.4	1.743	0.173	-0.422	-0.079	0.017	0.874
TC19	3.80	66	259	1.433	3.0	1.793	0.312	-0.421	-0.114	0.028	0.903

According to the determination coefficient R^2 presented in Table 7.4 and ranging between 0.819 and 0.936, the proposed mathematical model offers a reasonable approximation of the hysteretic

behaviour of the time-history tests. Figure 7.11b shows that the time-history experimental behaviour can be reasonably modeled with the proposed procedure.

The larger discrepancies between the proposed model and the time-history tests compared to the cyclic tests resides in the more dominant low-cycle fatigue inherent to the loading. The multiple load reversals applied on the angle through the time-history signal created a significant pinching effect identified in Figure 7.11c. This pinching is not accounted for in proposed model, where only the secant stiffness behaviour is represented.

Furthermore, the angles were loaded by some cycles of small amplitudes, where the transition portion between the initial and plastic stiffness of the excursion was not reached in both the experimental curve and the mathematical model, as highlighted by the darker lines in Figure 7.11d. After the load reversal, the experimental curve followed the unloading stiffness back to the point where the small amplitude cycle started and followed the curve of the precedent cycle. However, this behaviour was not captured in the proposed model. This discrepancy is inherent to the procedure used in the proposed model. The deformation of the last load reversal is considered in evaluating the relative deformations Δ_1^*, Δ_2^* and Δ_3^* used to create the force-deformation relationship of the angles. Therefore, the deformation of the load reversal acts as the initial deformation of the current excursion and remains constant until the next load reversal, notwithstanding the amplitude of the excursion. However, this consideration does not allow a good representation of the experimental results when the amplitude of the hysteretic loop is small, as shown in Figure 7.11d.

Nevertheless, the energy dissipated by the model follows closely the test data, as shown in Figure 7.11e and 7.11f for a typical static cyclic test and a Time-History test respectively. The main source of error in the energy dissipation comes from the fatigue damage inherent to the loading which reduces the angle strength. To minimize this error, strength degradation due to low-cycle fatigue has been implemented in the model. Figure 7.11e and 7.11f also show the influence of this effect on the energy dissipated by the model.

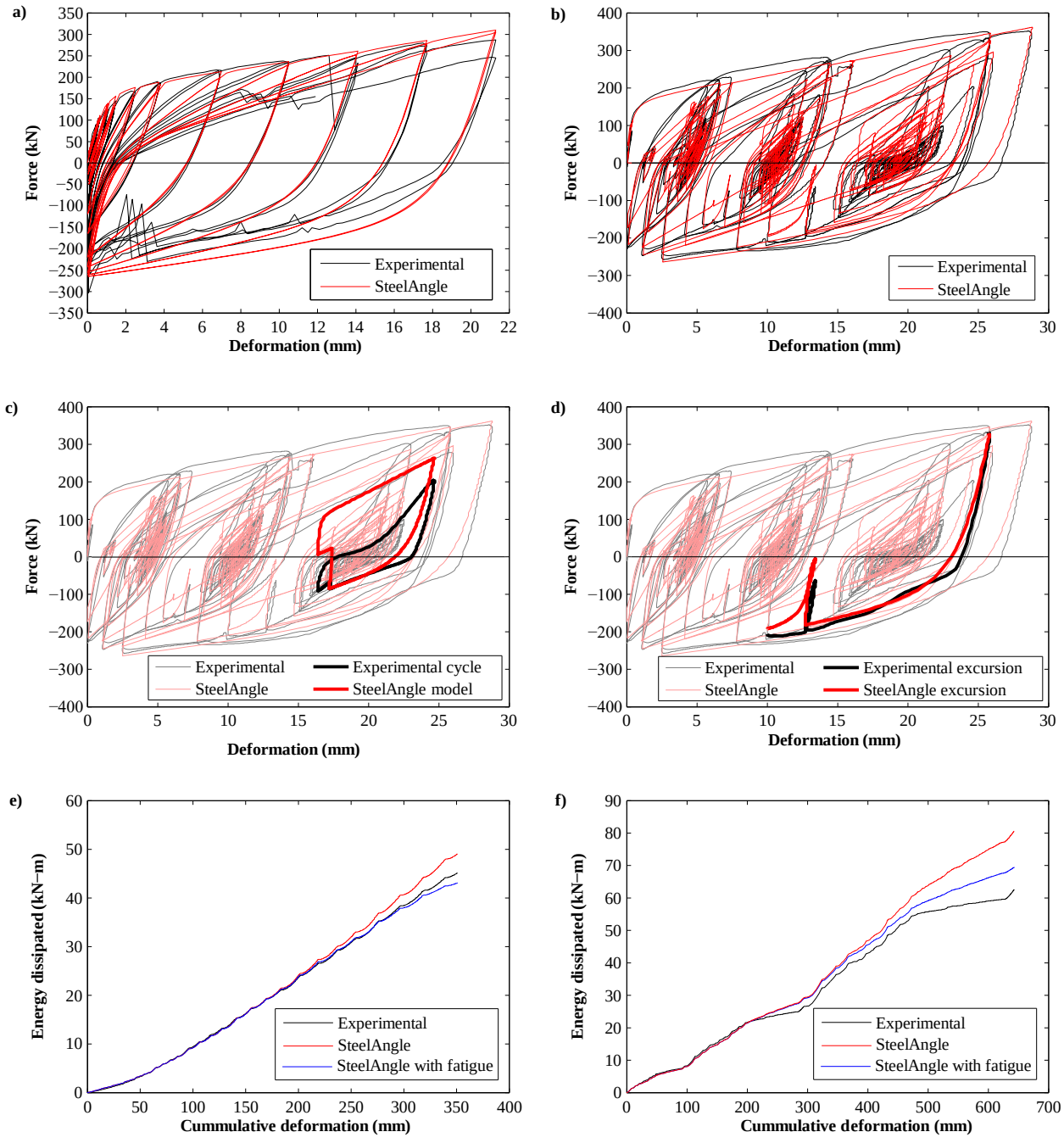


Figure 7.11. Comparison between experimental response and SteelAngles model of a) static cyclic test (TC4-5) b) Time-History test (TC4-7) c) Hysteretic pinching d) Partial excursion error e) Energy-dissipated in a static cyclic test (TC4-5) f) Energy-dissipated in a Time-History test

7.5 Implementing low-cycle fatigue and strength degradation

7.5.1 Fatigue damage counting method developed by Uriz and Mahin

Under variable amplitudes, such as seismic loading, the number of cycles to failure also vary. The assessment of the low-cycle fatigue life thus requires a cycle-counting procedure to convert the irregular time-history cycles into an equivalent number of uniform cycles. The rainflow cycle counting (Matsuishi and Endo 1968) has been generally recognized as an adequate procedure for irregular cycle counting (ASTM E1049 2017). However, in order to accurately apply this procedure, the entire loading history must be analyzed (Matsuishi and Endo 1968). Such analysis is incoherent when evaluating the fatigue life of a structural component under a seismic event, as the stress or strain amplitudes applied on the studied component depend on the behaviour and the fatigue life of its surrounding elements. Also, the computational power required to evaluate the entire loading history for every component is extremely high. These issues render the rainfow counting process impractical for finite element analyses.

To palliate to these difficulties with the fatigue life evaluation, Uriz and Mahin (2008) proposed a simplified version of the rainflow counting. This simplified procedure only requires the last four load reversal points to assess the remaining fatigue life of the element, thus reducing considerably the required computational power of an analysis. The simplifications create an intrinsic error on the element fatigue life with respect to the rainflow counting (Matsuishi and Endo 1968) which is considered acceptable.

This method consists of calculating the damage index (*DI*) based on the four previous load reversals experienced by the element. This index starts at a value of 0 and increases gradually to a value of 1, which corresponds to the element failure. The damage incurred by the element is established from the strain-cycle ε-N slope m, while ε_0 corresponds to the strain at which the element can sustain only one full cycle. This algorithm was added into OpenSees as the *Fatigue* material. Uriz and Mahin (2008) also proposed to use the damage index *DI* in a material model to integrate a fatigue deterioration parameter. Such degradation was not implemented in the *Fatigue* material of OpenSees (Mazzoni et al. 2006). The low-cycle fatigue damage index calculation proposed by Uriz and Mahin (2008) has been added to the *SteelAngles* material in *OpenSees* to account for a strength

degradation based on the damage index. The calculation algorithm incorporated to the model is presented in Figure 12. The low-cycle fatigue degradation was however programmed as an optional parameter in the *SteelAngles* algorithm.

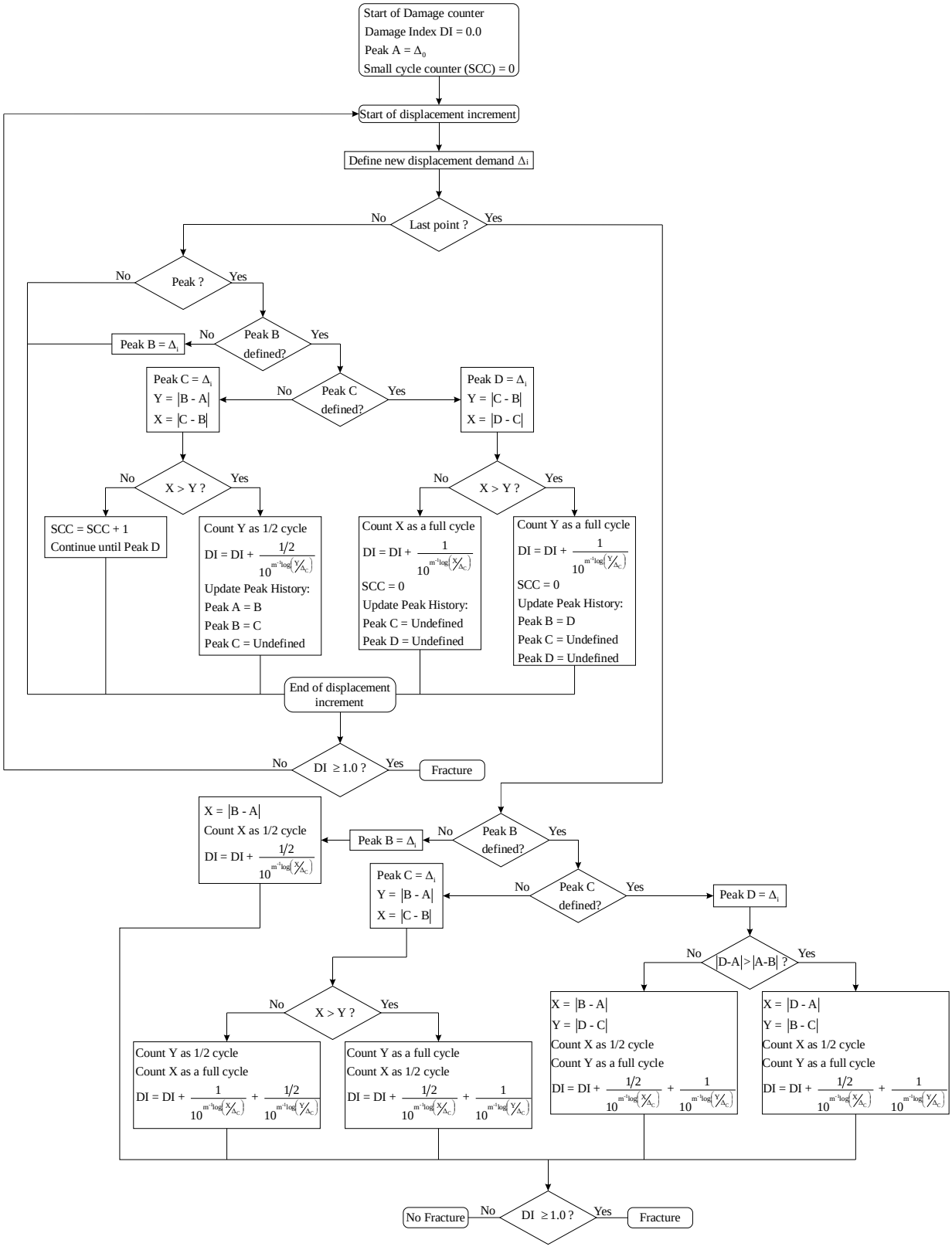


Figure 7.12. Flowchart of low-cycle fatigue damage index calculation (Uriz and Mahin 2008)

7.5.2 Constant amplitude fatigue test data

Constant amplitude low-cycle fatigue test data was available on two angle geometries: TC9 (g_2/t = 3.38) and TC14 (g_2/t = 2.58). Three different deformation amplitudes were imposed for each angle geometry and then repeated for a second test on a different specimen to validate the results. The number of cycles prior to fracture were recorded and presented in Table 7.5 for the 12 tests performed. This table also include the deformation amplitudes imposed. In the tests, the fracture occurred in flexion near the angle fillet as pictured in Figure 7.13a. Fracture occurred in both leg as shown in Figure 7.13a, where the top angle failed in the beam leg and the bottom angle failed in the column leg.

Table 7.5. Number of cycles of fatigue tests at fracture

Test case	g_2/t	Amplitude Δ_A	Cycles N	
		mm	Test 1	Test 2
TC9	3.38	4.1	424	360
		12.3	41	44
		20.5	12	8
TC14	2.58	4.1	259	322
		7.2	81	81
		10.3	44	46

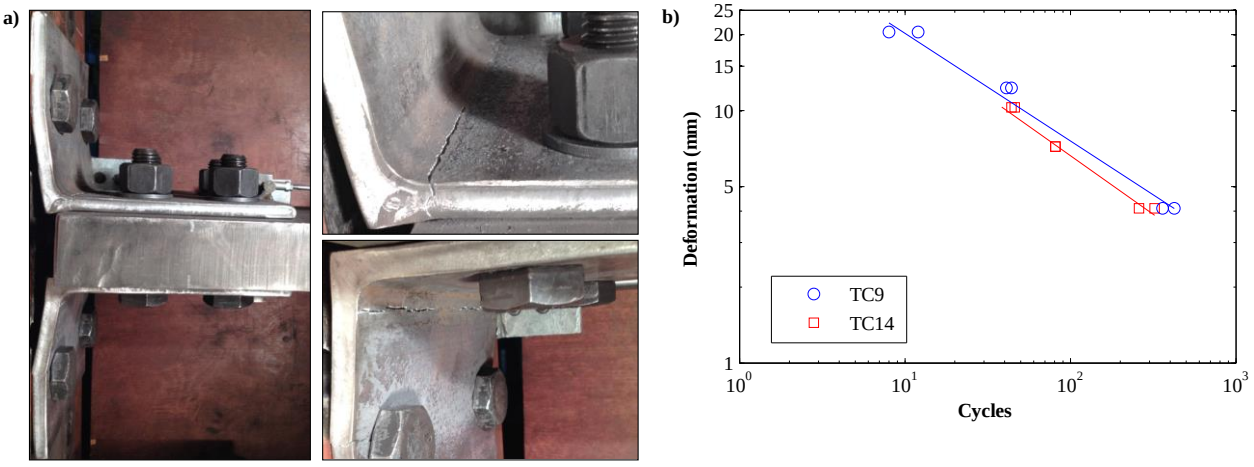


Figure 7.13. a) Typical fatigue test failure (TC9-11) b) Relationship between deformation demand and number of cycles of low-cycle fatigue tests.

To characterize the fatigue lifespan of a component, the stress-cycle (S-N) or strain-cycle (ε-N) curves are generally determined experimentally (ASTM E466 2015, ASTM E606 2012, ASTM E739 2015). The deformation-cycle Δ-N curve can also be determined with the same logic. These relationships are linear in the logarithmic domain (Ballio et al. 1997, Bernuzzi et al. 2000). Figure 7.13b respectively present the relationships of TC9 and TC14 between the deformation demand Δ and the number of cycles N sustained by the angles until fracture in logarithmic domain. These slopes of -0.4383 and -0.4837 respectively correspond to the input parameter m in the low-cycle fatigue degradation model developed by Uriz and Mahin (2008). The other input parameter corresponds to the amplitude at which a single cycle leads to the fracture. This deformation Δ_C is given by the intercept of the slope and corresponds to 58.4 mm and 62.9 mm for the TC9 and TC14 specimen respectively. These values are larger by 67% and 319% respectively to the maximum deformation measured during the monotonic tests. The complicated behaviour of the connection, where the sections are loaded with axial loads and flexural moments, does not provide a physical meaning to the Δ_C parameter, unlike typical fatigue test where this parameter indicate the maximum deformation where fracture is observed after a single cycle.

7.5.3 Fatigue parameters for other angle geometries

To include the damage index DI in the mathematical model developed to estimate the hysteretic nonlinear behaviour of bolted angles, two parameters are required: the slope m and the maximum deformation of a virgin cycle Δ_C. The damage index DI is then used to define the damage factor DF, which incorporates low-cycle fatigue damage into the mathematical model with Equation 7.8. Failure of the angles occur when the damage index reaches a value of 1.

The slope value m was taken as the average of the two slopes obtained experimentally; a value of -0.46 was thus applied to the m parameter of every test case. The parameter Δ_C was determined by a calibration process using the least-square method, to obtain the best fit between the mathematical model and the experimental data. The values of Δ_C for each test performed are presented in Table 7.6. The parameters defining the global hysteretic behaviour of Tables 7.2 to 7.4 still remain valid. The values obtained from this calibration vary between 25 and 77 mm. the values obtained for TC9 and TC14 differ by 17% and 41% respectively from the experimental data obtained from the constant amplitude fatigue tests. Figure 7.14a and b shows a comparison between the hysteretic

behaviour modeled with and without the cyclic degradation respectively, while Figure 7.8c shows the energy dissipated by the angle with and without fatigue.

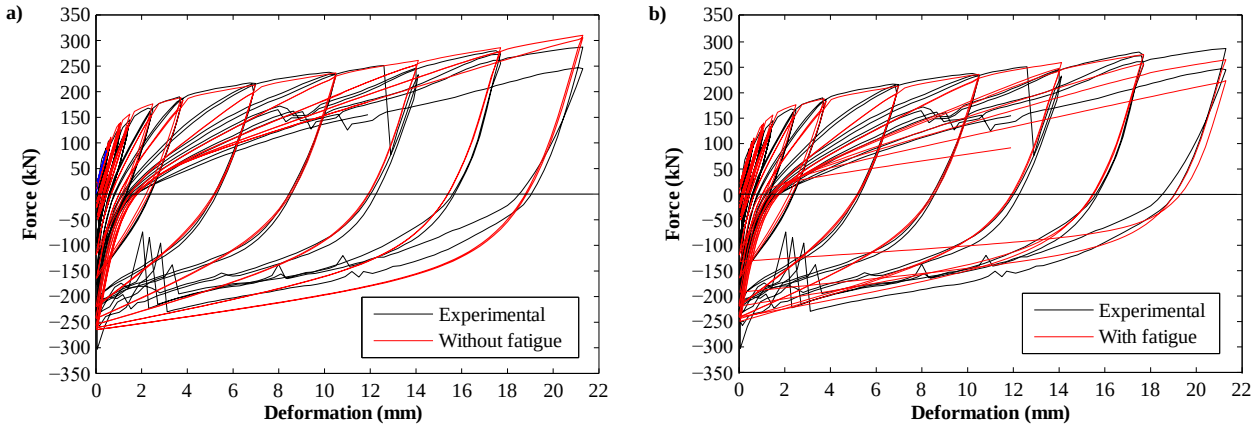


Figure 7.14. Numerical model a) without fatigue degradation b) with fatigue degradation

Table 7.6. Low-cycle fatigue degradation parameters of cyclic and time-history tests

Test Case	g_2/t	Δ_C (mm)		
	-	W310	W410	Time-History
TC1	2.67	45.8	40.0	53.3
TC2	4	50.7	51.2	56.7
TC3	1.38	31.3	25.7	32.9
TC4	2.38	38.1	39.4	42.1
TC5	1.7	41.6	41.0	42.0
TC6	1.25	33.8	27.0	44.4
TC7	5.33	56.2	53.3	42.2
TC8	6.67	61.6	61.6	63.1
TC9	3.38	38.6	51.6	54.9
TC10	4.38	53.5	53.0	57.2
TC11	2.5	36.1	28.8	50.4
TC12	3.3	48.6	47.8	55.2
TC13	1.92	26.3	33.4	51.6
TC14	2.58	37.3	40.2	24.6
TC15	8	77.7	62.5	38.9
TC16	5.38	46.1	45.6	49.3
TC17	4.1	70.2	62.1	-
TC18	3.25	68.8	57.8	52.0
TC19	3.8	47.4	44.5	52.3

7.6 Empirical definition of input parameters

The large array of test data used to determine the input parameters allow the definition of an empirical set of equations. The main goal of these equations is to provide to the user a method to determine the input parameters based on the angle geometry, without having to refer to test data. First, some parameters have an influence on the response but that were not evaluated in the parametric study. The longitudinal distance between the bolts influence the nonlinear response of the bolted angles and should thus be considered in the definition of the parameters. Faella et al. (1998) proposed a method to determine the effective width of each bolt row b_{eff} based on the bolt head diameter d_{hb}, the radius of the fillet r and the column bolt gauge m, as illustrated in Figure 7.15. The load flow is assumed to follow an angle of 45° to determine the effective width of the column leg. This method also assumes that the plastic hinges are forming in the fillet, at *0.8r* from the beam leg, and at the centerline of the column bolts, under the bolt head. Some parameter influenced by the effective width have been expressed as a variable of this geometrical parameter. Table 7.7 presents the effective width of each angle configuration. Additionally, the initial stiffness and the load characterizing the transition between the initial and plastic stiffnesses vary with respect to the yield stress of the angle material. These parameters are also presented in Table 7.7 for each of the 19 test cases.

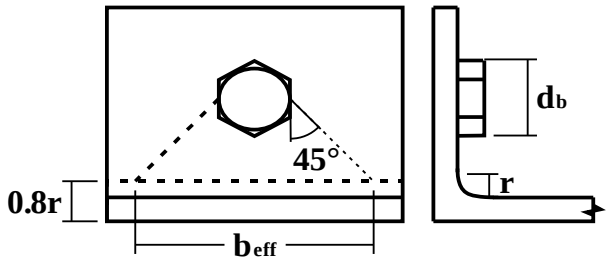


Figure 7.15. Effective width calculation (Faella et al. 1998)

Some values varied slightly between each test, but no significant trend could be established based on a geometric parameter of the angle specimens or because of lack of additional data. The remaining parameters are determined through empirical equations. Table 7.8 summarizes the input parameters, with a description and their recommended values. These empirical equations only hold within the range of parameters tested. Figure 7.16a to 7.16e presents the correlation between the

calibrated data and the empirically estimated values of each parameters. These plots show a good correlation between the suggested values obtained with the equations presented in Table 7.8 and the data obtained from the calibration process.

Table 7.7. Normalized yield stress ratio and effective width of each angle configuration

Test Case	**g_c**	**t**	**g_2/t**	**F_Y**	**b_{eff}**
	mm	**mm**	**-**	**kN**	**mm**
TC1	63.5	9.5	2.67	376	170.2
TC2	76.2	9.5	4.01	371	195.6
TC3	63.5	12.7	1.38	358	170.2
TC4	76.2	12.7	2.38	342	195.6
TC5	76.2	15.9	1.70	354	189.2
TC6	76.2	19.1	1.24	370	182.9
TC7	88.9	9.5	5.35	396	203.2
TC8	101.6	9.5	6.69	396	203.2
TC9	88.9	12.7	3.38	363	203.2
TC10	101.6	12.7	4.38	363	203.2
TC11	88.9	15.9	2.49	360	203.2
TC12	101.6	15.9	3.29	360	203.2
TC13	88.9	19.1	1.91	340	203.2
TC14	101.6	19.1	2.57	340	203.2
TC15	114.3	9.5	8.02	371	203.2
TC16	114.3	12.7	5.38	342	203.2
TC17	114.3	15.9	4.09	354	203.2
TC18	114.3	19.1	3.24	370	203.2
TC19	63.5	7.9	3.80	374	173.4

The *SteelAngles* uniaxial material should be inputted in OpenSees (Mazzoni et al. 2006) using the following syntax, where the *tag* is a unique material identification and the parameter *b* is given by the ratio between the tensile plastic stiffness and the tensile initial stiffness:

uniaxialMaterial SteelAngless $tag $F0 $K0 $b $fN $eN $bN $R0 $cR1 $cR2 $a1 $a2 $a3 $a4 $s1 $s2 $s3 $s4 <$m $eC>

where the low-cycle fatigue parameters *m* and Δ_C (*eC*) are optional.

Table 7.8. Summary of empirical input parameters of the SteelAngles model

	Description	Value	Units
tag	Unique tag identification of the material	-	-
F_0^+	Yield force in tension	$F_0^+ = \frac{1.6F_y(b_{eff}t^2/4)}{g_2}$	kN
K_i^+	Initial stiffness in tension	$K_0^+ = \begin{cases} 35\sqrt{\frac{g_2}{g_c}}\left(\frac{EI_{eff}}{g_c^3}\right) & (Static) \\ 75\sqrt{\frac{g_2}{g_c}}\left(\frac{EI_{eff}}{g_c^3}\right) & (Dynamic) \end{cases}$	kN/mm
K_p^+	Plastic stiffness in tension	$K_p^+ = 0.0005\left(\frac{EA_{eff}}{g_2}\right)$	kN/mm
f_N	Ratio between compressive and tensile yield force F_0^-/F_0^+	1.80	-
e_N	Ratio between compressive and tensile initial stiffness K_i^-/K_i^+	$e_N = \begin{cases} 1.3 - 2\sqrt{r_{eff}/g_2} & (Static) \\ 0.55 - 0.75\sqrt{r_{eff}/g_2} & (Dynamic) \end{cases}$	-
b_N	Ratio between compressive and tensile plastic stiffness K_p^-/K_p^+	1.00	-
R_0	Transition parameter between the initial and plastic backbone stiffness	1.40	-
C_{r1}	Transition degradation parameter	-0.46	-
C_{r2}	Transition degradation parameter	1.00	-
a_1	Isotropic hardening parameter of compressive envelope	0.00	-
a_2	Isotropic hardening parameter of compressive envelope	1.00	-
a_3	Isotropic hardening parameter of tensile envelope	0.00	-
a_4	Isotropic hardening parameter of tensile envelope	1.00	-
s_1	Force transition parameter between the initial and secant stiffness in unloading response	-0.14	-
s_2	Force transition parameter between the initial and secant stiffness in unloading response	1.00	-
s_3	Force transition parameter between the initial and secant stiffness in unloading response	0.05	-
s_4	Force transition parameter between the initial and secant stiffness in unloading response	1.00	-
m	Coffin-Manson fatigue degradation slope	-0.46	-
Δ_C	Coffin-Manson fatigue degradation displacement parameter (eC)	$\Delta_C = 4.2\frac{g_2}{t} + 32$	mm
I_{eff}	Effective moment of inertia of the angle leg section	$\left(b_{eff}t^3\right)/12$	mm^4
A_{eff}	Effective area of the angle leg section	$b_{eff}t$	mm^2
r_{eff}	Effective radius of gyration of the angle leg section	$\sqrt{I_{eff}/A_{eff}}$	mm

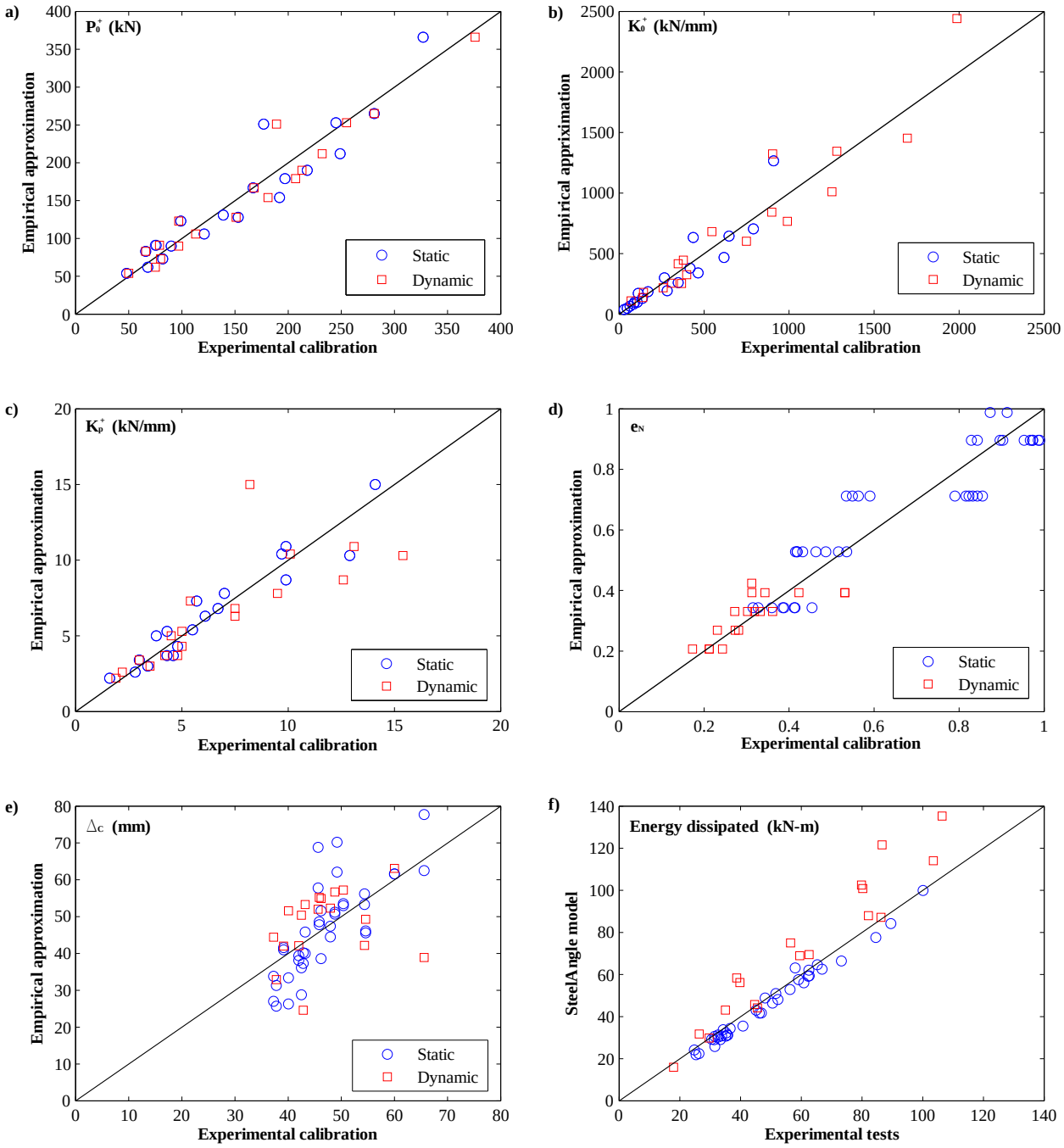


Figure 7.16. Correlation between the best fit and the empirically estimated parameters a) positive yield force F_0^+, b) initial stiffness K_i^+, c) positive plastic stiffness K_P^+, d) unloading to initial stiffness ratio e_N, e) fatigue deformation parameter Δ_c and f) Energy-dissipated in the tests and the model with the empirical parameters and fatigue degradation.

7.7 Modeling bolted angle beam-column connections

The proposed numerical model aims at creating a reasonably accurate beam-column model. It was therefore implemented as a uniaxial material in OpenSees (2006) The code added to the OpenSees framework is presented in Appendix C.

This material is used to model the connections using a component-based approach. and assigned to fibers in a *zerolengthSection* element (2006). Figure 7.17a and b present the disposition of the fibers in each section for 2L and 2L-TS connections respectively.

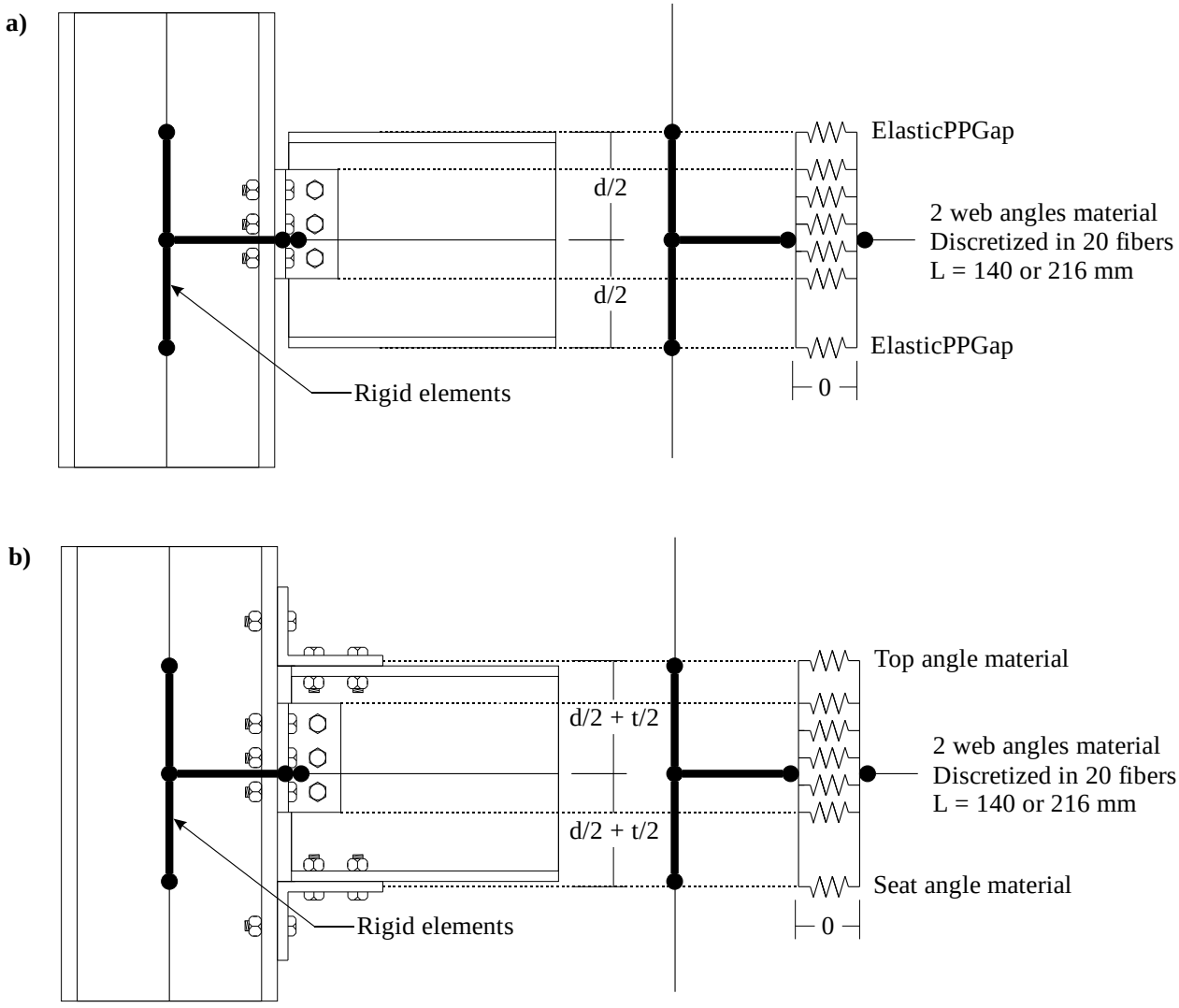


Figure 7.17. Numerical modeling of: a) 2L connections; b) 2L-TS connections.

The load in the web angle fiber depends on its position along the height of the connection and relative distance to the neutral axis. These components are thus discretized into 20 fibers as shown in Figure 7.17a. The angle geometry of the web angle corresponds to TC19. The values calculated from the empirical set of equations presented in Table 7.8 for the input parameters of the web angle material model are defined for a unitary width (b_{eff} = 1 mm). The area assigned to each fiber thus correspond to the effective width of the component. The values used in the numerical model are presented in Table 7.9. This material was modeled in parallel to an extremely stiff Elastic No-Tension (*ENT*) material (Mazzoni et al. 2006) to represent the contact between the angle leg and the column flange. Also, for the 2L connections, two fibers were modeled at the edge of the beam flange with an Elastic-Perfectly-Plastic Gap (*ElasticPPGap*) material to represent the beam flange in contact with the column flange. This contact is achieved when a gap of 12.7 mm (1/2") is filled by the rotation of the beam.

The fiber section of the connection was aggregated with a stiff material in its transversal direction, to avoid large vertical deformations. Therefore, the use of a fiber section to represent the connection complicates significantly the modeling of the interaction between the moment-rotation response and the shear load. For this reason, this interaction is omitted in the connection model.

The modeling of the 2L-TS connections is similar. However, instead of ElasticPPGap material at the beam flange, the top and seat angles are each represented by a single fiber. Figure 7.17b shows the section of this connection. The material assigned to the top and seat angles correspond to the *SteelAngles* material with the input properties defined in Table 7.8. These input properties are presented in Table 7.9. The material properties of the top and seat angles are calculated with their effective width; therefore, the fiber area is set to 1.0. The *SteelAngles* material was also modeled in parallel to an extremely rigid Elastic No-Tension (*ENT*) material to represent the contact between the angle column leg and the column flange.

Rigid elements were added between the column neutral axis and the column flange where the connection is located. The length of these rigid elements corresponds to half of the column depth and aims at modeling the connection on the flange of the column. By modeling the beam depth with rigid elements, the panel zone deformation of the column web is neglected in this modeling scheme. The implications of this simplification are discussed in detail in section 9.4.

Figure 7.18 presents the numerical modeling of two 2L connections and four 2L-TS connections tested during the full-scale connection experimental program. The tests compared with the numerical model are the ones where no gravity shear was applied on the connection. These tests were chosen because their behaviour was not further complicated with the interaction between the shear and the rotational deformations. The connection properties are also presented in Table 7.9.

The numerical model generally shows a good agreement with the experimental results. The best representations are achieved with the thicker top and seat angles, where their contribution to the moment-rotation behaviour is more dominant over the web angles. The modeling of web angles showed some discrepancy, especially when the web angle length is short. Nevertheless, a simple component-based model can accurately represent the nonlinear behaviour of bolted angle connections when using the *SteelAngles* material.

Table 7.9. Input parameters of the *SteelAngles* model in the beam-column connection numerical model

Angle geometry		**TC19 Web angles**	**TC1**	**TC14**
Geometrical parameters				
t	mm	7.94	9.53	12.7
gc	mm	64	64	70
g2	mm	27.1	25.5	28.5
$\mathbf{b_{eff}}$	mm	1	170.2	203.2
E	GPa	200	200	200
$\mathbf{F_y}$	GPa	0.345	0.345	0.345
Input parameters				
$\mathbf{F_0^+}$	kN	0.321	83.7	158.7
$\mathbf{K_0^+}$	kN/mm	0.725	206.9	451.7
$\mathbf{K_p^+}$	kN/mm	0.029	6.36	9.05
$\mathbf{b^+}$	-	0.040	0.031	0.020
$\mathbf{f_N}$	-	1.80	1.80	1.80
$\mathbf{e_N}$	-	0.718	0.643	0.583
$\mathbf{b_N}$	-	1.00	1.00	1.00
$\mathbf{R_0}$	-	1.40	1.40	1.40
$\mathbf{C_{r1}}$	-	-0.46	-0.46	-0.46
$\mathbf{C_{r2}}$	-	1.00	1.00	1.00
$\mathbf{a_1}$	-	0.00	0.00	0.00
$\mathbf{a_2}$	-	1.00	1.00	1.00
$\mathbf{a_3}$	-	0.00	0.00	0.00
$\mathbf{a_4}$	-	1.00	1.00	1.00
$\mathbf{s_1}$	-	0.04	0.04	0.04
$\mathbf{s_2}$	-	1.00	1.00	1.00
$\mathbf{s_3}$	-	0.05	0.05	0.05
$\mathbf{s_4}$	-	1.00	1.00	1.00
m	-	-0.46	-0.46	-0.46
$\mathbf{\Delta_0}$	mm	46.34	43.24	41.43
$\mathbf{I_{eff}}$	mm^4	41.714	12276	34686
$\mathbf{A_{eff}}$	mm^2	7.940	1622	2581
$\mathbf{r_{eff}}$	mm	2.29	2.75	3.67

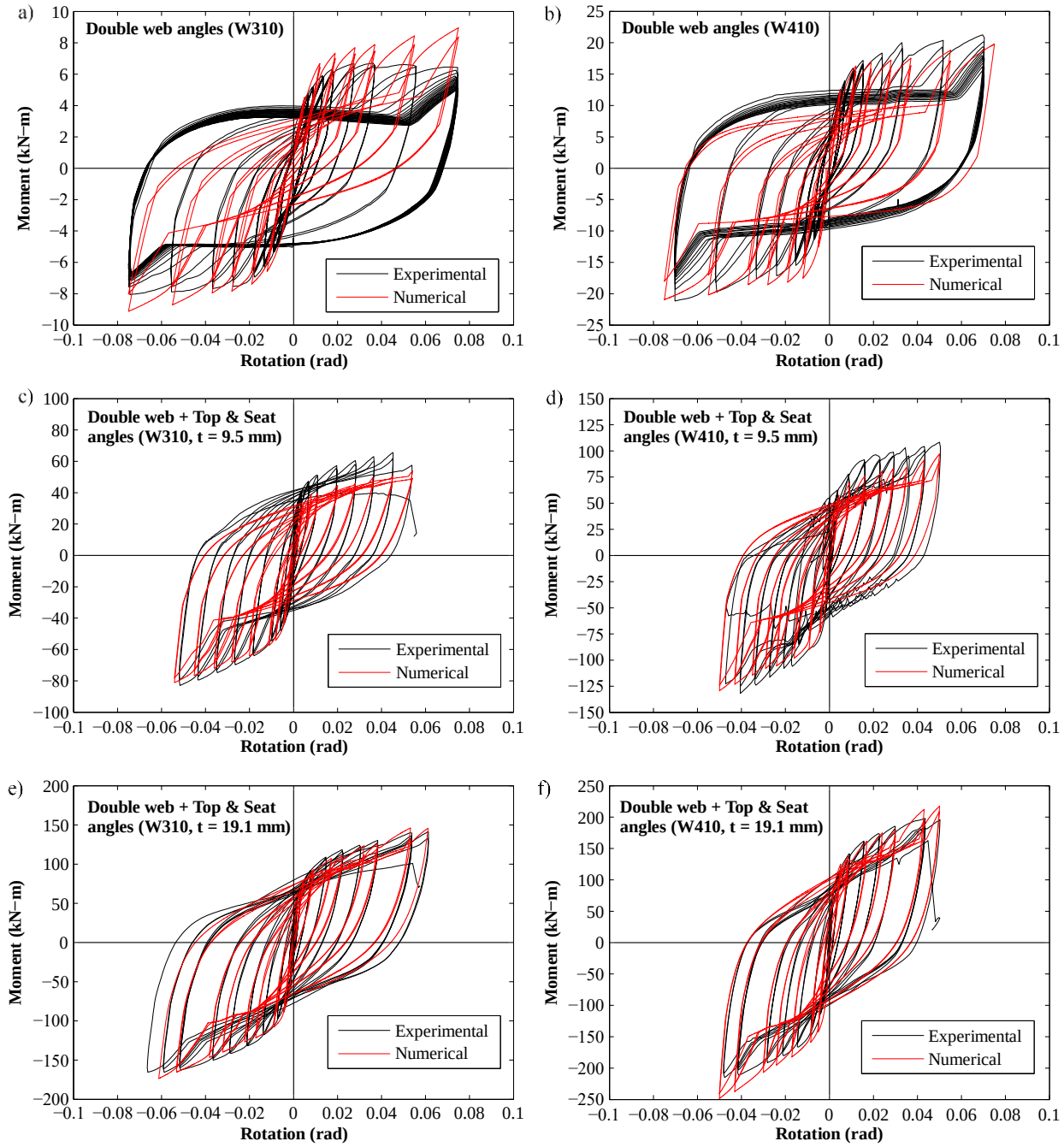


Figure 7.18. Numerical modeling of : a) 2L connections with W310 beam; b) 2L connections with W410 beam; c) 2L-TS connections with W310 beam and angle thickness of 9.5 mm; d) 2L-TS connections with W410 beam and angle thickness of 9.5 mm; e) 2L-TS connections with W310 beam and angle thickness of 19.1 mm; f) 2L-TS connections with W410 beam and angle thickness of 19.1 mm;

7.8 Summary

The contribution of the gravity frame as a secondary lateral load resisting system depends on the rotational stiffness of the beam-column connections. To accurately assess the role of the gravity frame in the reserve capacity, the nonlinear behaviour of the connection must be characterized.

A total of 139 tests data were used to characterize the bolted angle hysteretic behaviour and develop a numerical model. This model was based on the *Steel02* model developed by Menegotto and Pinto (1973) and enhanced by Filippou et al. (1983). The modifications brought to create the new model aimed to characterize the hysteretic behaviour of bolted angles and include a cumulative damage as a failure criterion.

The proposed *SteelAngles* model was calibrated on the experimental results. The calibrated parameters are presented, and an empirical set of equations was developed to determine the input hysteretic parameters based on the geometrical properties of the angles alone. The numerical model with the empirical equations offered a good agreement with the experimental behaviour.

The proposed model can also be used to characterize the hysteretic behaviour of bolted angle connections in steel buildings. The modeling approach in Opensees (2006) for a top and seat with double web angle connection has been presented. Four beam-column connections tested experimentally were modeled. A good agreement was observed between the numerical model and the experimental results.

CHAPTER 8 GRAVITY CONNECTION DESIGN FOR ENHANCING THE SEISMIC CAPACITY OF TYPE CC CHEVRON BRACED FRAME BUILDINGS

The first part of the Chapter presents a methodology that is proposed to design the partially-restrained (PR) connections of the gravity frame to achieve adequate seismic response for steel building structures with Type CC chevron braced frames. When adopting this procedure, brace connections need not be designed for the amplified seismic loads. The gravity frame will possess sufficient stiffness and energy dissipation capacity to prevent structural collapse in case of the failure of brace connections at any level of the structure.

In the second part of the Chapter, an application of the proposed design methodology is presented for a three-storey building located in Montreal, QC. The seismic response of the structure is then examined though nonlinear dynamic analysis to validate the design approach. The response of the structure without the reserve capacity contributed by the gravity frame is also investigated to demonstrate the need for such reserve capacity system for Type CC structures.

8.1 Design approach for enhanced gravity beam-column connections

Chevron brace configuration was chosen to develop the connection design approach because it provides significant reserve capacity after brace failure (Sizemore et al. 2019). After SFRS failure, the chevron CBF acts as a long-link EBF mobilizing the flexural capacity of the beam to contribute to the reserve capacity. The proposed design procedure has the following objectives:

1. Form moment frames in gravity framing system of the building structure to obtain a reserve lateral capacity system for the building to prevent structural collapse after failure of one brace connection in the braced frames. This is achieved by introducing PR beam-column connections made of 2L-TS bolted angles that have been investigated in this thesis at the beam-column joints of the gravity frame.
2. Keep the design procedure simple, based on hand calculations and with limited iterative processes. This objective aims at reflecting the Type CC design philosophy.
3. Take advantage of the period lengthening from brace connection fracture, which translated into reduced seismic loads.

The following specific design bases and criteria should be respected:

1. Brace connections in the braced frames are designed for load combinations including seismic loads determined with R_d = 1.5; *The building ductile behavior is to be supplied by the enhanced reserve lateral capacity of the gravity system in case of a brace connection failure in the braced frames;*
2. The beam and column sections of the gravity frame are designed to resist the gravity load only. *Adding the PR connections should not modify these sections;*
3. The 2L angles must be designed to resist vertical shear from gravity load only, using the design method for regular simple shear connections *Adding the PR connections should not modify the design of these elements;*
4. In any storey and along each direction, the TS angles used to form the PR connections in the gravity frame must satisfy the following requirements assuming that failure has occurred in one brace connection of all braced frames in that storey:
    a. The PR connections must have sufficient flexural stiffness in the nonlinear range such that the storey shear stiffness of the structure exceeds the negative stiffness from P-delta effects and limit the storey drift to an acceptable value.
    b. The PR connections must have a flexural resistance at the maximum anticipated storey drift such that inelastic rotation will be limited to the PR connections and will not develop in the beams and columns of the of the gravity frame.

Furthermore, the following assumptions are taken in the design procedure methodology:

1. Fracture is assumed to occur in the first storey:
    a. The first storey experience larger storey shear. Connections are expected to be more vulnerable because of their non-ductile behaviour and their design load calculated with a R_d of 1.5;
    b. The axial load on the storey is larger, which introduces larger P-delta effects;
    c. The top and seat angle design is calculated for the first storey and applied to the upper storeys;
2. Fracture occurs in every braced frame of the storey. No torsional effect resulting in the fracture of only one braced frame is considered;

3. Braced frames and brace connections are designed for a seismic load with a R_d of 1.5 and a R_o of 1.3;
4. The connection stiffness is assumed as a secant stiffness. This assumption is similar to the design of nonlinear systems;
5. The proposed method is only developed for chevron brace configuration. After the failure of one braced frame, the other brace forms a long-link EBF system that mobilizes the braced beam flexural stiffness.

To achieve these objectives, the following methodology is proposed:

- Step 1: Determine the required residual lateral stiffness for the gravity frame;
- Step 2: Determine the required rotational stiffness for the angle connections;
- Step 3: Define the connection strength limits based on the column resistance;
- Step 4: Define the contribution of the web angles to the connection strength;
- Step 5: Design the geometry of the top and seat angles to achieve the required connection strength.

The following subsections present in detail each of these steps.

8.1.1 Step 1: Required lateral stiffness for the gravity frame

The gravity frame must provide sufficient lateral stiffness to counteract the negative stiffness created by P-delta effects and limit the storey drift to an acceptable value in the storey where brace connection failure took place. The target storey drift δ_{Target} is determined by the engineer to ensure that the integrity of the structure can be maintained in the braced frame and gravity frame when that drift occurs in the storey where brace connection failure took place. This displacement should remain close to 2.5% h_{s1} limit currently specified in the NBCC as this limit aims at preventing structural instability. It can also be determined to prevent yielding of the braced frame beams acting as a long EBF link after brace connection failure, or excessive inelastic rotations in the PR connections. With the target storey drift δ_{Target} determined by the engineer and the displacement spectrum for the building site, the fundamental period of the structure after brace connection failure, T_r is determined. The assumption is made that the first storey is the most critical since the storey shear and the P-delta effects are larger. The gravity connection design is thus performed for

the first storey and applied to the upper storeys. Although this simplification does not optimize the design of the connections, it is applied to keep a simplified design procedure, which is in line with the Type CC design philosophy.

The seismic base shear V_R can then be determined using the Equivalent static force procedure of NBCC using the spectral acceleration of the fractured building period T_r. In this calculation, the R_d and R_o factors of 1.5 and 1.3 are not considered in the seismic response. The required lateral stiffness of the gravity frame can then be determined using Equation 8.1.

$$K_R \geq K_{Target} = \frac{V_R}{\delta_{Target}} + \frac{\sum P_1}{h_s} \qquad \text{[kN/mm]} \quad (8.1)$$

8.1.2 Step 2: Required rotational stiffness for the PR connections

The reserve lateral capacity of the building is schematized in Figure 8.1a. At the first level of the structure, the N_f moment frames that are created in the gravity system must resist the lateral load in parallel with the damaged braced frames. The residual storey shear stiffness K_R is the sum of the residual storey stiffness of the braced frame, K'_{Br}, and the lateral stiffness provided by the gravity frame with the PR connections, is given by Equation 8.2. The residual stiffness of the braced frame K'_{Br} is given in Equation 8.3. It depends on the axial stiffness of the beam, the axial stiffness of the brace with intact brace connections and the flexural stiffness of the beam, as adapted from Tremblay (2018). The geometrical properties influencing this stiffness are identified in Figure 8.1b.

The stiffness of each gravity frame *f* is calculated as the resulting stiffness from the columns ($K_{c,f}$), beams ($K_{b,f}$) and beam-column joints ($K_{j,f}$) acting in series. These gravity frame component stiffnesses are presented in Equations 8.4, 8.5, and 8.6, respectively, using the equations developed by Stafford-Smith and Coull (1991). These equations assume that the beams and columns bend in double curvature, except for the columns at the first storey. Therefore, a point of inflection is considered at the half-length of each beam and column. The first-storey columns are assumed to be pin-connected at their bases and, therefore, deform in single curvature. These hinges create a simplified isostatic system that can be evaluated manually. This assumption relies on the flexural stiffness of the columns to resist lateral loads similarly to the concept of the column continuity. The geometrical properties used in the calculation of these stiffnesses are presented in Figure 8.1c,

1d and 8.1e respectively. The flexural stiffness of the braced frame column is considered, but the braced beam flexural stiffness is not included in the gravity frame calculation. This stiffness is already included in Equation 8.3 determining the residual stiffness of the braced frame. Using Equations 8.2 to 8.6, the joint rotational stiffness K_{sj} is determined through an iterative process until the storey residual stiffness K_R is larger than the target lateral stiffness K_{Target} as stated in Equation 8.1. Depending on the building configuration and the brace design, the post-fracture residual stiffness of the braced frame given by Equation 8.3 may be sufficient by itself to provide the required lateral stiffness. In this case, enhanced connections are not required.

$$K_R = K'_{Br} + \sum_{f=1}^{N_f} \left(\frac{1}{\frac{1}{K_{c,f}} + \frac{1}{K_{b,f}} + \frac{1}{K_{j,f}}} \right) \quad \text{[kN/mm]} \quad (8.2)$$

$$K'_{Br} = \sum_{u=1}^{N_{Br}} \frac{1}{\frac{L}{4EA_{bb}} + \frac{L}{2EA_{Brace}\cos^3\theta} + \frac{L^3\tan^2\theta}{48EI_{bb}}} \quad \text{[kN/mm]} \quad (8.3)$$

$$K_{c,f} = \sum_{n=1}^{N_c} \frac{3EI_{nc}}{h_s^3} \quad \text{[kN/mm]} \quad (8.4)$$

$$K_{b,f} = \sum_{m=1}^{N_b} \frac{12EI_{mb}}{L_{mb}} \times \frac{1}{1.5(h_s)^2} \quad \text{[kN/mm]} \quad (8.5)$$

$$K_{j,f} = \sum_{s=1}^{N_j} \frac{K_{sj,f}}{1.5(h_s)^2} \quad \text{[kN/mm]} \quad (8.6)$$

These equations are simplified and based on simple models in which the drift is concentrated in the first storey. Fixed-end conditions are assumed for the beams, which implies double curvature. In reality, the PR connections does not provide such boundary conditions to the beams and the actual deformed shape of the beam differs from the one assumed in the model. Refinement of these equations could be made in future work to lead to a better schematic representation of the building behaviour. The model could also be improved to represent the behaviour of buildings experiencing

fracture in the upper storeys. Furthermore, the frame stiffness considers PR connections in the both the column strong and weak axes. However, the experimental program performed in this doctoral project only focused on strong axis column behaviour. Connection tests on weak axis columns are thus recommended to generate moment-rotation response that could be used in analyses. To avoid this limitation, the designer could however adopt a modeling strategy where PR connections are only located on strong axis columns.

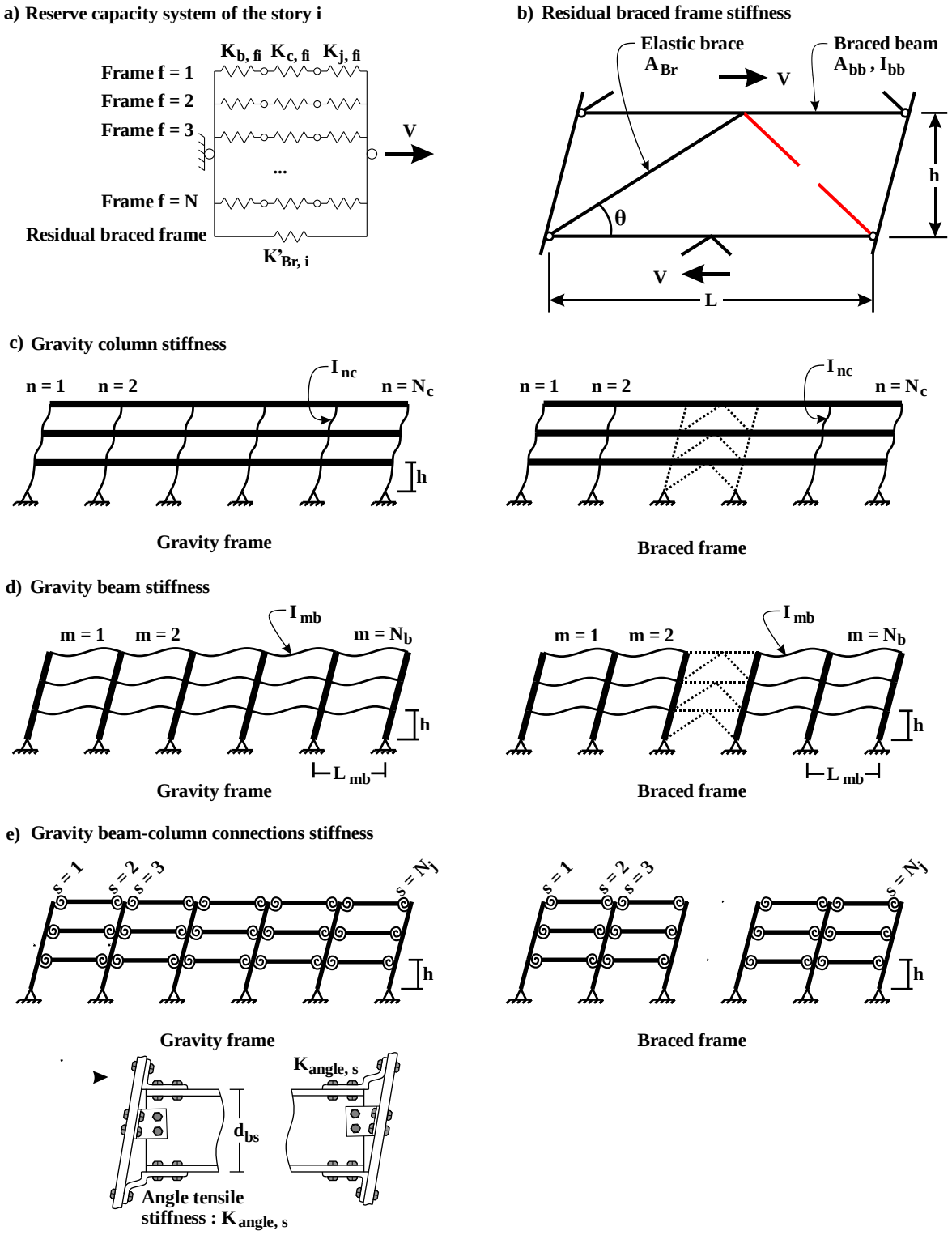


Figure 8.1. a) Spring representation of the building reserve capacity; b) Parameters for residual braced frame stiffness; c) Parameters for gravity column stiffness; d) parameters for gravity beam stiffness; e) Parameters for gravity beam-column connection stiffness.

The total lateral displacement of each storey Δ_{Target} is determined with Equation 8.7. Once the rotational stiffness of the connections $K_{sj,f}$ is determined, the lateral displacements created by the beam, column and joint can be calculated with Equations 8.8 to 8.10 respectively. Additionally, the connection rotation $\theta_{j,f}$ at the target storey drift is obtained with Equation 8.11. The assumption that each connection in a given frame experiences the same rotation is made to simplify the design process.

$$\Delta_{Target} = \delta_{Target} h_s \quad \text{[mm]} \quad (8.7)$$

$$\Delta_{c,f} = \frac{\Delta_{Target}}{\frac{1}{K_{c,f}} + \frac{1}{K_{b,f}} + \frac{1}{K_{j,f}}} \frac{1}{K_{c,f}} \quad \text{[mm]} \quad (8.8)$$

$$\Delta_{b,f} = \frac{\Delta_{Target}}{\frac{1}{K_{c,f}} + \frac{1}{K_{b,f}} + \frac{1}{K_{j,f}}} \frac{1}{K_{b,f}} \quad \text{[mm]} \quad (8.9)$$

$$\Delta_{j,f} = \frac{\Delta_{Target}}{\frac{1}{K_{c,f}} + \frac{1}{K_{b,f}} + \frac{1}{K_{j,f}}} \frac{1}{K_{j,f}} \quad \text{[mm]} \quad (8.10)$$

$$\theta_{j,f} = \frac{\Delta_{j,f}}{h_s} \quad \text{[mm]} \quad (8.11)$$

8.1.3 Step 3: Connection strength limits

Adding the top and seat angles to the connection should not modify the column or web angle design. Therefore, the angle thickness and bolt location, which influence significantly the connection moment capacity and rotational stiffness, should be designed according to the capacity of the columns. The gravity columns are designed for a compression load only, but the added flexural moment caused by the presence of the PR connection should still satisfy the axial-moment interaction design check prescribed by CSA S16 and given in Equation 8.12. For this check, the compressive load C_f on the connection is given by the load combination 1.0D + 1.0E + 0.5L + 0.25S (NBCC 2015). Therefore, the plastic moment of the connection M_{pj} is limited by the maximum imposed moment on the column, M_{fx} or M_{fy}. The connection moment transferred to the column is assumed to be equally distributed between in the column above and below the floor. Since two connections are present on interior columns, the capacity of each

connection thus corresponds to the column flexural capacity. The connection plastic moment should also be smaller than the beam flexural capacity M_{rb}.

The connection moment should still provide sufficient strength to the gravity frame to limit the storey drift to δ_{Target}, as pictured in Figure 8.2. Therefore, the connection moment should satisfy the conditions of Equation 8.13.

$$\frac{C_f}{C_r} + \frac{0.85U_{1x}M_{fx}}{M_{rx}} + \frac{\beta U_{1y}M_{fy}}{M_{ry}} \leq 1 \tag{8.12}$$

$$\theta_{j,fi}K_{sj,fi} = M_{sj,fi} \leq M_{pj} \leq \min(M_{fx}\ or\ M_{fy}, M_{rb}) \quad \text{[kNmm]} \tag{8.13}$$

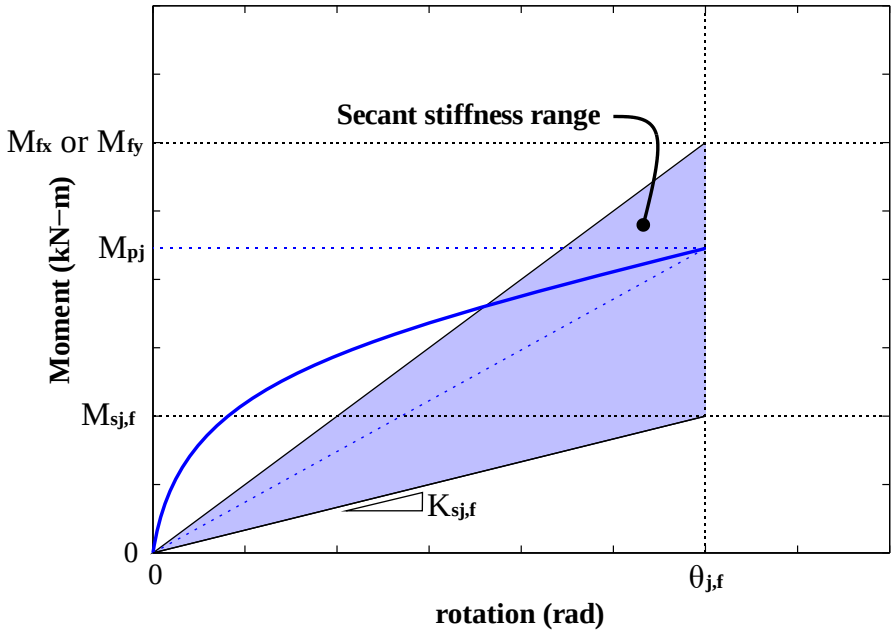


Figure 8.2. Connection secant stiffness range respecting the strength limits .

8.1.4 Step 4: Contribution of the web angles to the connection strength

As mentioned in the guidelines of the proposed approach, the geometry of the web angles should not be modified by the addition of the top and seat angles. Therefore, their geometry is determined only to transfer the design gravity shear load to the column. However, under seismic load, the web angles contribute to the connection rotational stiffness and strength. Because the 2L are designed as normal gravity connections, they are expected to be situated closer to the top flange of the beam. Their contribution to the connection moment capacity is thus larger under negative rotation than

positive rotation, as their moment arm is larger. To accommodate the strength limit defined in Step 3, the TS are designed by considering the largest contribution of the 2L. Therefore, the design procedure is only performed under negative rotation, for the top angle. The same design will then be applied for the seat angle.

A set of empirical equations and parameters are proposed in Chapter 7 to model the hysteretic behavior of bolted angles. The set of equation of the mathematical model is transcribed in Table 8.1, along with a description of the parameters. These variables are then used in the characterization of the force-deformation *F-Δ* behavior on a bolted angle connection component using Equation 8.4 The input parameters required to use this mathematical model are the web angle thickness *t*, the bolt column gage g_c and the column leg flexural span g_2, given as the distance between the edge of the bolt head and the angle fillet. The effective width b_{eff} obtained by the method proposed by Faella et al. (1998) is also used as an input parameter in the mathematical model. These methods are summarized in Chapter 7. Therefore, the nonlinear behavior of the 2L can be determined with this mathematical model.

$$F = \frac{(K_i^+ - K_p)\Delta}{\left[1 + \left(\frac{\Delta}{F_0^+ / K_i^+}\right)^{R_0}\right]^{\frac{1}{R_0}}} + K_p\Delta \qquad \text{[kN]} \qquad (8.14)$$

Table 8.1. Summary of empirical input parameters of the *SteelAngles* model

	Description	Value
$\mathbf{F_0^+}$	Yield force in tension	$F_0^+ = \frac{1.6F_y(b_{eff}t^2/4)}{g_2}$
$\mathbf{K_i^+}$	Initial stiffness in tension	$K_i^+ = \begin{cases} 35\sqrt{\frac{g_2}{g_c}}\left(\frac{EI_{eff}}{g_c^3}\right) & (Static) \\ 75\sqrt{\frac{g_2}{g_c}}\left(\frac{EI_{eff}}{g_c^3}\right) & (Dynamic) \end{cases}$
$\mathbf{K_p^+}$	Plastic stiffness in tension	$K_p^+ = 0.0005\left(\frac{EA_{eff}}{g_2}\right)$
$\mathbf{f_N}$	Ratio between compressive and tensile yield force F_0^-/F_0^+	1.80
$\mathbf{e_N}$	Ratio between compressive and tensile initial stiffness K_i^-/K_i^+	$e_N = \begin{cases} 1.3 - 2\sqrt{r_{eff}/g_2} & (Static) \\ 0.55 - 0.75\sqrt{r_{eff}/g_2} & (Dynamic) \end{cases}$
$\mathbf{b_N}$	Ratio between compressive and tensile plastic stiffness K_p^-/K_p^+	1.00
$\mathbf{R_0}$	Transition parameter between the initial and plastic backbone stiffness	1.40
$\mathbf{C_{r1}}$	Transition degradation parameter	-0.46
$\mathbf{C_{r2}}$	Transition degradation parameter	1.00
$\mathbf{a_1}$	Isotropic hardening parameter of compressive envelope	0.00
$\mathbf{a_2}$	Isotropic hardening parameter of compressive envelope	1.00
$\mathbf{a_3}$	Isotropic hardening parameter of tensile envelope	0.00
$\mathbf{a_4}$	Isotropic hardening parameter of tensile envelope	1.00
$\mathbf{s_1}$	Force transition parameter between the initial and secant stiffness in unloading response	0.04
$\mathbf{s_2}$	Force transition parameter between the initial and secant stiffness in unloading response	1.00
$\mathbf{s_3}$	Force transition parameter between the initial and secant stiffness in unloading response	0.05
$\mathbf{s_4}$	Force transition parameter between the initial and secant stiffness in unloading response	1.00
m	Coffin-Manson fatigue degradation slope	-0.46
$\mathbf{\Delta_C}$	Coffin-Manson fatigue degradation displacement parameter	$\Delta_C = 4.2\frac{g_2}{t} + 32$
$\mathbf{I_{eff}}$	Effective moment of intertia of the angle leg section	$\left(b_{eff}t^3\right)/12$
$\mathbf{A_{eff}}$	Effective area of the angle leg section	$b_{eff}t$
$\mathbf{r_{eff}}$	Effective radius of gyration of the angle leg section	$\sqrt{I_{eff}/A_{eff}}$

At a rotation of $\theta_{j,f}$ in the connection, the deformation of web angle at the lower and upper fibers, Δ_L and Δ_U, are given by Equation 8.15a and b respectively, where d_L and d_U are the distance between the lower and upper fibers respectively and the center of rotation of the connection, as pictured in Figure 8.3a. As shown in Figure 8.3b, the force developed in the web angles is distributed over the length of the web angle L_w. The distributed force f_L and f_U at the extreme fibers of the web angles are obtained for a single web angle with Equation 8.14, using the parameters of Table 8.1. To obtain the distributed force, the effective width of the angles b_{eff} in the equations is rather taken as the ratio between the effective width and the actual length of the angles b_{eff}/L_w. The moment created by the web angles, $M_{pj,w,}$ can then be determined with Equation 8.16, as illustrated in Figure 8.3c.

$$\Delta_L = \theta_{j,f} d_L \quad \text{[mm]} \quad (8.15a)$$

$$\Delta_L = \theta_{j,f} d_U = \theta_{j,f}(d_L + L_w) \quad \text{[mm]} \quad (8.15b)$$

$$M_{pj,w} = (2 f_L L_w) \times \left(d_L + \frac{L_w}{2}\right) + \left(2\frac{(f_U - f_L)}{2} L_w\right) \times \left(d_L + \frac{2L_w}{3}\right) \quad \text{[kNmm]} \quad (8.16)$$

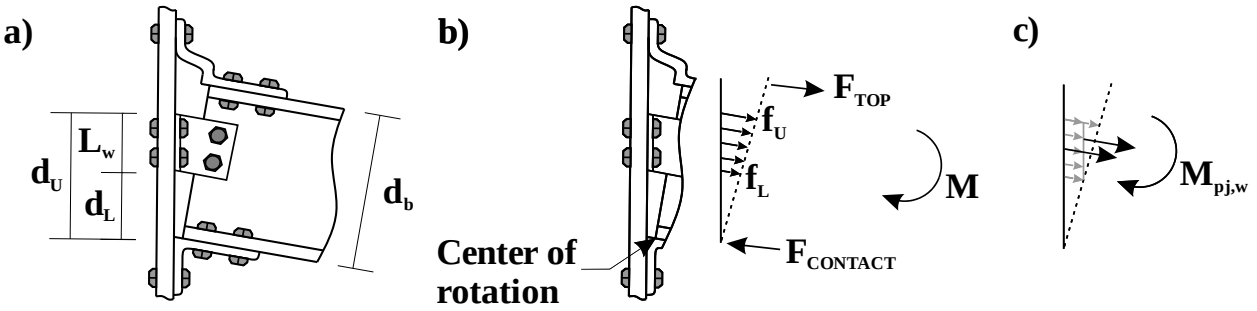


Figure 8.3. Schematic contribution of the web in the connection strength

8.1.5 Step 5: Geometry of the top and seat angles

As mentioned previously, the design procedure is only performed under negative rotation. Therefore, the top angle is designed, and the same detailing is applied to the seat angle. Once the contribution of the web angle in the moment capacity of the connection is evaluated, the moment created by the top angle can be determined with Equation 8.17. Furthermore, the force F_{pj} and the deformation $\Delta_{pj,T}$ of the top angle should respect the conditions stated in Equation 8.18 and 8.19 respectively to limit the moment developed in the column. In these equations, d_{bj} is the beam depth

at the connection. The web angle thickness t, the bolt column gage g_c, the column leg flexural span g_2 and the effective width b_{eff} can then be determined to respect these two conditions and additional geometrical limits of the connection with an iterative process.

$$M_{pj,T} \leq M_{pj,w} - M_{pj,w} \quad \text{[kNmm]} \quad (8.17)$$

$$F_{pj} \leq \frac{M_{pj,T}}{d_{bj}} \quad \text{[kN]} \quad (8.18)$$

$$\Delta_{pj,T} \leq \theta_{j,f} d_{bj} \quad \text{[kN/mm]} \quad (8.19)$$

8.2 Application and validation of the proposed design method

In this section, the proposed design methodology is applied and validated for a 3-storey building example. The design of the structure including the braced frame is shown in Section 8.2.1. The design of the PR connections is illustrated in Section 8.2.2. The numerical simulations that are carried out to verify the performance of the structure with the lateral reserve capacity system are presented in Section 8.2.3.

8.2.1 Design of the steel building structure

The building used in this example is designed for Montreal, on site class C (firm ground). The geometry of the building structure is presented in Figure 8.4. It consists of five 9144 mm (30') wide bays in both directions and 3 storeys having each 4572 mm (15') in height. A slab extension of 1' is also included on the perimeter of each floor. Beams and columns are ASTM A992 shapes (F_y = 345 MPa) whereas Braces are ASTM A500, grade C, square tubing (F_y = 345 MPa). Because of the concrete slab, lateral buckling of the beams is not considered.

The design gravity loads at the roof level are: D = 1.2 kPa; S = 2.48 kPa, L = 1.0 kPa. At the floor levels, the gravity loads are: D = 3.5 kPa and L = 2.4 kPa. The 1.0 kPa of partitions is also considered in the dead load, while only 0.5 kPa is included in the seismic weight of the storey W_i. The seismic weights and total gravity loads (ΣP_i) at every level are given in Table 8.2. The gravity load is determined with the combination 1.0D + 0.5L + 0.25S and is applied on each column to consider the destabilizing effects P-delta and P-δ on the column element. The live load reduction

factor was applied in this load combination and was based on column tributary area at each storey. The total gravity loads in Table 8.2 correspond to the sum of these loads for each storey. The storey shear V_i and brace seismic force $T_{f\text{-}E}$ or $C_{f\text{-}E}$ are also presented in this table. The braced frames are designed in accordance with the seismic provisions of the 2015 NBCC and CSA S16-14 for the Conventional Construction category. The seismic loads were determined using the equivalent static force procedure of the 2015 NBCC with force modification factors R_d = 1.5 and R_o = 1.3. The period T_a used to determine the seismic load was determined with the empirical equations proposed by NBCC and corresponded to 0.69s. The resulting base shear for the entire building is 2951 kN (0.128W). In this example, accidental in-plane torsion effects were included in the design of the braces. Each frame was designed for 60% of the total seismic loads. At the first storey, the brace axial compressive loads due to gravity loads and seismic loads are equal to 1282 kN and 104 kN, respectively, which gives a design factored compression load of 1802 kN.

Table 8.2. Seismic ang gravity loads in the example building

Storey *i*	**Seismic weight *W***	**Storey shear V_i**	**Brace seismic force $T_{f\text{-}E}$, $C_{f\text{-}E}$**	**Gravity loads ΣP_i**
	kN	**kN**	**kN**	**kN**
3	4410	952	404	4481
2	9592	2332	989	15271
1	9592	3022	1282	25970

As per the proposed design methodology, the columns and beams of the gravity frame are designed to resist gravity loads only. Table 8.3 gives the steel sections that were selected for the structure members. All column members extend over the three storeys. As also specified in the proposed design approach, the web angles are also designed to resist gravity loads only. The dimensions of these components are presented in Figure 8.5a and b for the exterior beams and the interior and braced beams connections.

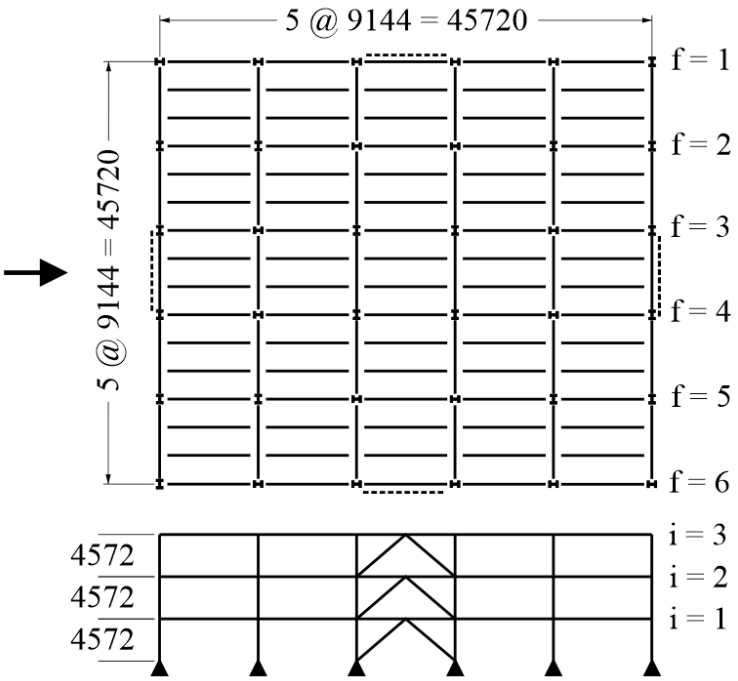


Figure 8.4. Example building geometry

Table 8.3. Member sections of example prototype

Braced frame				
Storey	**Braces**	**Beams**		**Columns**
3	HSS152.4x152.4x6.4	W310x52		W310x97
2	HSS203.2x203.2x7.9	W310x74		
1	HSS203.2x203.2x12.7	W310x79		
Gravity system				
	Interior roof	**Exterior roof**	**Interior floor**	**Exterior floor**
Beams	W250x49.1	W250x49.1	W310x60	W250x49.1
Girders	W410X100	W360x64	W610X101	W360x72
Corner columns	W200x35.9			
Interior columns	W250x73			
Exterior columns	W250x49.1			

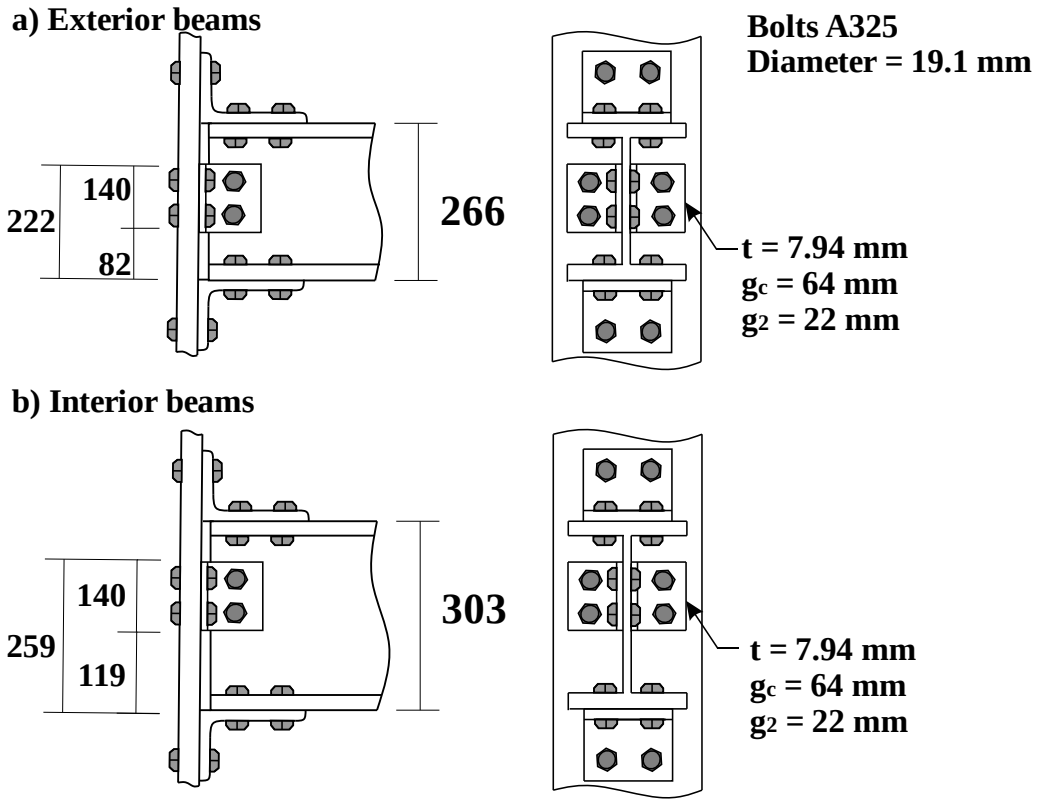


Figure 8.5. Web angle detailing of gravity connections for: a) exterior beams; and b) interior and braced beams.

8.2.2 Design of the reserve lateral capacity system

8.2.2.1 Step 1: Required lateral stiffness for the gravity frame

The first step consists at defining the required lateral stiffness of the gravity frame to create a reserve capacity able to resist the P-delta effects with acceptable storey drift determined by the engineer. For this example, a storey drift of 3% is selected, resulting in a lateral displacement δ_{Target} of 137.2 mm. Beyond this storey drift, a plastic hinge is expected to form in the beams of the braced frames acting as long EBF links after failure of the brace connections in one of the two braces. Results from the cyclic tests preformed on the 2L-TS connections in Chapter 5 showed that the connections can exhibit stable hysteretic response without strength degradation at rotations of up to 0.07 rad. A storey drift of 0.03 therefore seems as an acceptable target drift for this building. The period of vibration of the fractured building T_R required to limit the drift to 3% is determined as 7.9 s, From the displacement spectrum for Montreal on soil type C presented in Figure 8.6. With

this secondary period, the required strength of the gravity frame V_R can be determined using the Equivalent Static Force Method defined by NBCC. The target stiffness of the gravity frame K_{Target} is determined with Equation 8.1. These values are presented in Table 8.4 for the studied building.

Table 8.4. required secondary lateral stiffness for the first storey of the design example

Storey *i*	$\sum \frac{P_1}{h_s}$	**Required strength V_R**	δ_{Target}	K_{Target}
	kN/mm	**kN**	**mm**	**kN/mm**
1	2.84	128	137.2	3.49

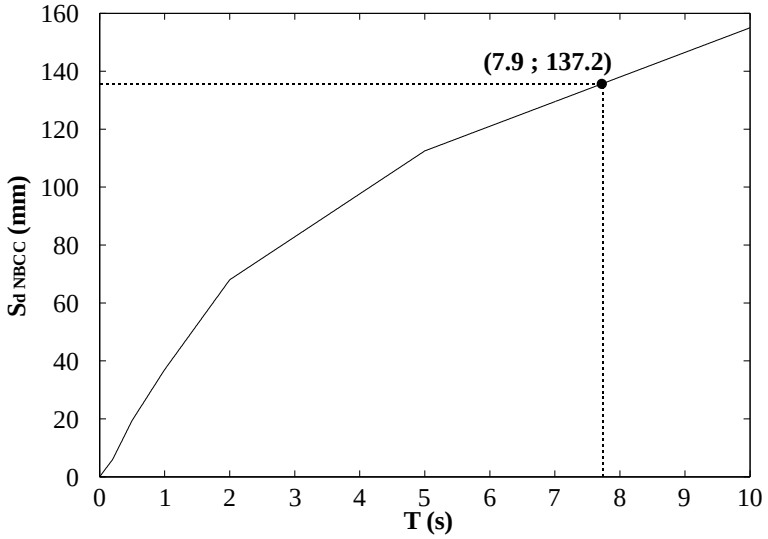


Figure 8.6. Displacement spectrum of Montreal Soil type C expressed in storey drift.

8.2.2.2 Step 2: Required rotational stiffness for the PR connections

For each frame of the first storey, the residual stiffness of the braced frame $K'_{Br,i}$, and the column stiffness, the beam stiffness and the joint stiffness are calculated. Table 8.5 summarizes these calculations. The rotational stiffness of the joints are determined through an iterative process until the total system stiffness $K_{R,i}$ of each storey reached the target stiffness. In this design example, the residual stiffness from the braced frame $K'_{Br,i}$ of the third storey possess a stiffness larger than the one required to counteract the P-delta effects. Therefore, no top and seat angles are required for this storey. Only the first two storeys require 2L-TS connections with a rotational stiffness of at least $2.98^{E}6$ and $3.95^{E}5$ N-mm/rad respectively.

Table 8.5. Gravity frame stiffness calculation of the first storey

frame		1	2	3
E	**Gpa**		200	
h_s	**mm**		4572	
L	**mm**		9144	
K'Br,i		$K'_{Br,i} = \sum_{u=1}^{N_{Br}} \frac{1}{\frac{L}{4EA_{bb}} + \frac{L}{2EA_{Brace}\cos^3\theta} + \frac{L^3\tan^2\theta}{48EI_{bb}}}$		
A_{bb}	**mm²**		10100	
A_{brace}	**mm²**		8430	
θ	**°**		45	
I_{bb}	**mm⁴**		177E6	
K'Br	**kN/mm**		2.18	
	$K_{c,f}$		$\sum_{n=1}^{N_c} \frac{3EI_{nc}}{h_s^3}$	
ΣI_{nc}	**mm⁴**	627.2E6	333.8E6	317.2E6
$K_{c,f}$	**kN/mm**	3.94	2.10	1.99
	$K_{b,f}$		$\sum_{m=1}^{N_b} \frac{12EI_{mb}}{L_{mb}} \times \frac{1}{1.5(h_s)^2}$	
ΣI_{mb}	**mm⁴**	282.4E6	640.0E6	640.0E6
$K_{b,f}$	**kN/mm**	2.36	5.36	5.36
	$K_{j,f}$		$\sum_{s=1}^{N_j} \frac{K_{sj}}{1.5(h_s)^2}$	
k_{sj}	**kNmm/rad**		2980261	
$K_{j,f}$	**kN/mm**	0.76	0.95	0.95
	$K_{R,i}$		$K_{R,i} = K'_{Br,i} + \sum_{f=1}^{N_f} \left(\frac{1}{\frac{1}{K_{c,fi}} + \frac{1}{K_{b,fi}} + \frac{1}{K_{j,fi}}} \right)$	
$K_{R,f}$	**kN/mm**	0.50	0.58	0.57
$K_{R,i}$	**kN/mm**		3.84	
Δ_{Total}	**mm**	137.16	137.16	137.16
$\Delta_{c,\,fi}$	**mm**	17.48	38.14	39.56
$\Delta_{b,\,fi}$	**mm**	29.13	14.92	14.71
$\Delta_{j,\,fi}$	**mm**	90.55	84.10	82.89
$\theta_{j,\,fi}$	**rad**	0.0198	0.0184	0.0181

8.2.2.3 Step 3: Limit on the flexural strength of the PR connections

Connection strength limits are imposed on the enhanced connections to avoid the formation of plastic hinges in the columns. By designing the connections to be more flexible and less resistant than the columns, inelastic response will develop only in the PR connections rather than in the columns, thus avoiding a soft storey mechanism. The calculations of these limits are presented in Table 8.6 for the first storey. The maximum moment required in the connection at the target storey drift, $M_{sj,fi}$, is also presented in this Table.

Table 8.6. Rotational stiffness and strength limits calculations of the first storey connections.

Column		**Corner**		**Exterior**		**Interior**		**Braced**	
Section		**W200x36**		**W250x49**		**W250x73**		**W310x97**	
Axis		**Strong**	**Weak**	**Strong**	**Weak**	**Strong**	**Weak**	**Strong**	**Weak**
Seismic strength criterion		$M_{sj,fi} = \theta_{j,fi} K_{sj}$							
$\theta_{sj,fi}$	**rad**	0.020	0.020	0.020	0.018	0.018	0.018	0.020	0.018
$M_{sj,fi}$	**kNmm**	59028	59028	59028	54032	54032	54032	59028	54032
Column strength criterion		$\frac{C_f}{C_r} + \frac{0.85 U_{1x} M_{fx}}{M_{rx}} + \frac{\beta U_{1y} M_{fy}}{M_{ry}} \leq 1$							
C_f	**kN**	259	259	518	518	1036	1036	1353	1353
C_r	**kN**	531	531	934	934	1860	1860	2820	2820
U_{1x}	-	1.00	-	1.00	-	1.00	-	1.00	-
M_{rx}	**kNmm**	92450	-	157000	-	292000	-	447000	-
U_{1y}	-	-	1.00	-	1.00	-	1.00	-	1.00
M_{ry}	**kNmm**	-	43800	-	46600	-	144000	-	148000
β	-	-	0.85	-	0.85	-	0.85	-	0.85
M_{pj}	**kNmm**	55714	26395	82267	24418	152187	75051	273571	90578
$M_{pj} > M_{sj}$		No	No	Yes	No	Yes	Yes	Yes	Yes

The column strength criterion is larger than the seismic strength criterion for the corner columns in their strong and weak axes and for the exterior columns in their weak axis. In these cases, the connection between the beam and the weak axis columns should not be stronger than the column moment capacity. Each connection to the corner column is present only once in the considered half building, while the exterior column weak axis connections are present four times. The overstrength and redundancy of the other connections in the building should provide sufficient strength and stiffness to the gravity frame to mitigate these weaker connections. For the second and third storeys, the lesser compressive force on the columns allows a larger flexural capacity in the column.

Furthermore, the destabilizing P-delta effects will also be less important because of the reduced lateral load.

8.2.2.4 Step 4: Contribution of the web angles to the connection strength

The contributions of the web angles are determined in their deformed position, at a rotation of $\theta_{j,fi}$. The lower and upper fibers of the web angles are thus deformed by Δ_L and Δ_U under loads f_L and f_U respectively. The moment generated by the web angles are then calculated in Table 8.7 for the first storey. This moment reaches 24% and 35% of the minimum required moment $M_{sj,fi}$ to limit the storey drift to the anticipated value of 3% for the W250x49 and W310x60 beams respectively.

Table 8.7. Calculations of the web angle contribution to the strength of the bolted angle connections in the first storey.

Column		**Corner**		**Exterior**		**Interior**		**Braced**	
Section		**W200x36**		**W250x49**		**W250x73**		**W310x97**	
Axis		**Strong**	**Weak**	**Strong**	**Weak**	**Strong**	**Weak**	**Strong**	**Weak**
d_L	**mm**	75				119			
d_U	**mm**	215				259			
L_W	**mm**	140				140			
Δ_L	**mm**	1.49	1.49	1.49	2.16	2.16	2.16	2.36	2.16
Δ_U	**mm**	4.26	4.26	4.26	4.70	4.70	4.70	5.13	4.70
Loads in the web angle extreme fibers		$F = \frac{(K_i^+ - K_p)\Delta}{\left[1 + \left(\frac{\Delta}{F_0^+/K_i^+}\right)^{R_0}\right]^{\frac{1}{R_0}}} + K_p\Delta$							
g_c	**mm**	63.5							
t	**mm**	7.9							
F	**mm**	31.75							
b_{eff}	**mm**	1							
F_y	**GPa**	0.345							
g_2	**mm**	30							
g_2/t	**-**	3.80							
K_i^+	**kN/mm/mm**	0.772							
F_0^+	**kN/mm**	0.287							
R_0	**-**	1.4							
K_p	**kN/mm/mm**	0.026							
Δ_0	**mm**	0.371							
f_U	**kN/mm**	0.291	0.291	0.291	0.318	0.318	0.318	0.325	0.318
f_L	**kN/mm**	0.383	0.383	0.383	0.395	0.395	0.395	0.407	0.395
Moment generated in the web angles		$M_{pj,w} = (2f_L L_w) \times \left(d_L + \frac{L_w}{2}\right) + \left(2\frac{(f_U - f_L)}{2} L_w\right) \times \left(d_L + \frac{2L_w}{3}\right)$							
$M_{Pj,w}$	**kNmm**	13975	13975	13975	19123	19123	19123	19643	19123
$M_{Pj,w} / M_{sj,fi}$		24%	24%	24%	35%	35%	35%	33%	35%

8.2.2.5 Step 5: Geometry the top and seat angles

The design of the top and seat angle geometry is an iterative process. The section and bolt location must be chosen to provide a considerable lateral stiffness to the system while avoiding the formation of plastic hinges in the columns. The maximum moment $M_{pj,T}$ that can be developed by the top angle at a displacement of Δ_{pj} is calculated in Table 8.8 for each connection type. From these values, the maximum force that can be developed in the top angle F_{pj-max} is determined.

The effective width of the angles, b_{eff} may then be determined by the designer. The choice of this dimension depends on architectural and physical constraints such as the beam or column flange width and the required spacing for the bolting procedure. To determine the thickness and the column gage of the required angle, the yield force F_0^+ for an angle strip of 1 mm-wide has been plotted against the flexural span of the column leg g_2 for several angle thickness. These curves are presented in Figure 8.7. The maximum allowable load in the top angle, $F_{pi\text{-}max}$ occurs in the plastic phase of the angles. Therefore, the yield force of the angle F_0^+ should be significantly smaller than the maximum allowable load. For this reason, a factor of 0.6 was applied to $F_{pi\text{-}max}$ for the first design iteration. This reduced load was divided by the previously determined effective width b_{eff} in order to choose the thickness t and flexural span g_2 of the first design iteration with Figure 8.7.

Table 8.8. Calculations of the top and seat angle dimensions in the first storey.

Column		**Corner**		**Exterior**		**Interior**		**Braced**	
Section		**W200x36**		**W250x49**		**W250x73**		**W310x97**	
Axis		**Strong**	**Weak**	**Strong**	**Weak**	**Strong**	**Weak**	**Strong**	**Weak**
Beam		**W250x49**				**W310x60**		**W250x49**	**W310x60**
d_b	**mm**	266				303		266	303
$M_{Pj,w}$	**kNmm**	14512	14512	14512	20027	20027	20027	20458	20027
		$M_{pj,T} \leq M_{pj,w} - M_{pj,w}$							
$M_{pj,T}$	**kNmm**	41202	11883	67755	4392	132161	55025	253113	70552
$F_{pj\ -\ max}$	**kN**	155	45	255	17	436	182	952	233
Δ_{pj}	**mm**	5.98	5.98	5.98	6.38	6.38	6.38	5.98	6.38
b_{eff} **choice**	**mm**	150	150	150	150	150	150	150	150
$0.6F_{pj}/b_{eff}$	**kN/mm**	0.58	0.17	0.94	0.17	0.97	0.62	3.16	0.79
t	**mm**	9.53	7.94	12.7	7.94	12.7	9.53	15.9	9.53
g_2	**mm**	22	49	26	60	25	26	21	22
F	**mm**	31.75	31.75	31.75	31.75	31.75	31.75	31.75	31.75
g_c	**mm**	60	86	67	97	66	64	65	60
K_i^+	**kN/mm**	211	53	366	68	378	183	710	211
F_0^+	**kN**	85	27	128	32	134	72	249	85
R_0	**-**	1.4	1.4	1.4	1.4	1.4	1.4	1.4	1.4
K_p	**kN/mm**	6.50	2.43	7.33	2.90	7.62	5.50	11.36	6.50
Δ_0	**mm**	0.40	0.50	0.35	0.47	0.35	0.39	0.35	0.40
F_{pj}	**kN**	120	39	168	33	178	104	310	123

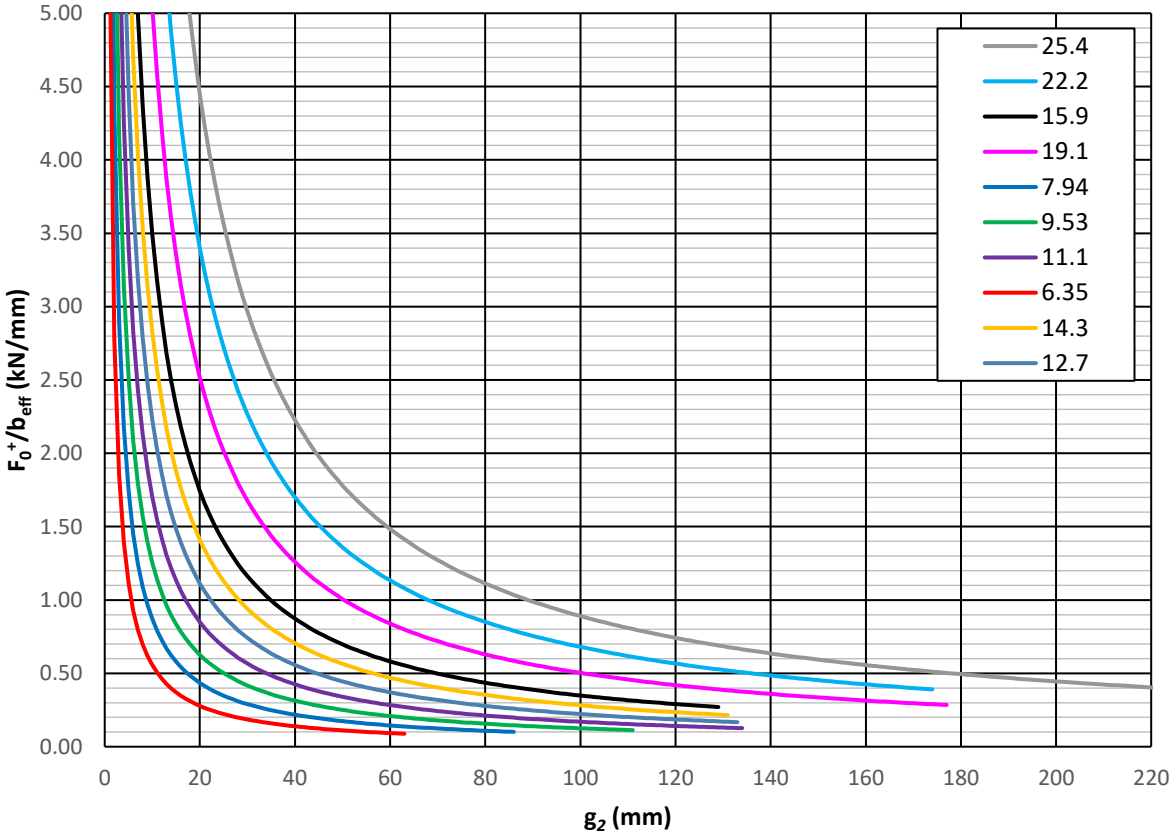


Figure 8.7. Angle yield force by effective width F_0^+/b_{eff} varying with the column leg flexural span g_2 for different angle thickness t.

With the thickness t and the flexural span g_2 of the first iteration, the properties defining the force-displacement behaviour of the angle can be determined with the empirical equations presented in Table 8.1. With this equation, the force F_{pi} of the designed angle at the maximum displacement Δ_{pj} is determined. The dimensions of the angle can then be adjusted with subsequent iterations to determine the required dimensions that can develop the largest force F_{pi} in the top angle without surpassing the maximum allowable force $F_{pi\text{-}max}$. These final dimensions are presented in Table 8.9 for every type of gravity connection in the first storey. The dimensions are determined individually for each type of connections, 8 different angles are thus obtained. The designer can however simplify the fabrication process by using a single design on several types of beam-column connections. The connections in the building example can be simplified into three top and seat angle dimensions as presented in Table 8.9:

- **Geometry A:** t = 9.53 mm; g_c = 64 mm (Corner column - Strong Axis, Interior column – Weak axis and Braced column – Weak axis);
- **Geometry B:** t = 12.7 mm; g_c = 70 mm (Exterior column - Strong Axis, Interior column – Strong axis and Braced column – Strong axis).
- **Geometry C:** t = 7.94 mm; g_c = 89 mm (Corner column - Weak Axis and Exterior column – Weak axis);

Table 8.9. Final design of the top and seat angles in the first storey.

Column		**Corner**		**Exterior**		**Interior**		**Braced**	
Section		**W200x36**		**W250x49**		**W250x73**		**W310x97**	
Axis		**Strong**	**Weak**	**Strong**	**Weak**	**Strong**	**Weak**	**Strong**	**Weak**
Beam		**W250x49**				**W310x60**		**W250x49**	**W310x60**
b_{eff}	**Mm**	150	150	150	150	150	150	150	150
t	**mm**	9.53	7.94	12.7	7.94	12.7	9.53	12.7	9.53
g_2	**mm**	25.5	52.5	28.5	52.5	28.5	25.5	28.5	25.5
F	**mm**	31.75	31.75	31.75	31.75	31.75	31.75	31.75	31.75
g_c	**mm**	64	89	70	89	70	64	70	64
K_i^+	**kN/mm/mm**	186	48	337	48	337	186	337	186
P_0^+	**kN/mm**	74	25	117	25	117	74	117	74
R_0	**-**	1.4	1.4	1.4	1.4	1.4	1.4	1.4	1.4
K_p	**kN/mm/mm**	5.61	2.27	6.68	2.27	6.68	5.61	6.68	5.61
Δ_0	**mm**	0.40	0.52	0.35	0.52	0.35	0.40	0.35	0.40
Δ_{pj}	**mm**	5.98	5.98	5.98	6.38	6.38	6.38	5.98	6.38
F_{pj}	**kN/mm**	104	37	153	38	156	106	153	106
Geometry		A	C	B	C	B	A	B	A

8.3 Validation of the proposed design approach

8.3.1 Numerical model of the structure studied

Half of the example building structure is represented in the numerical model. To assess the gravity frame contribution in the lateral resistance, the gravity frames are modeled in parallel to the braced frame, as pictured in Figure 8.8a. The lateral displacement of the braced frame was also imposed to the interior frames with joint constraints at each storey. The gravity load applied on each column

allowed the consideration of P-delta effects in the model. To simplify the model, the gravity loads were applied on the columns and at the center of the braced frame instead of the beams. This simplification was chosen to increase the computing time and model efficiency. However, the moment developed in the PR connections by the gravity loads on the beams and the braced beam yielding were not represented with this simplification.

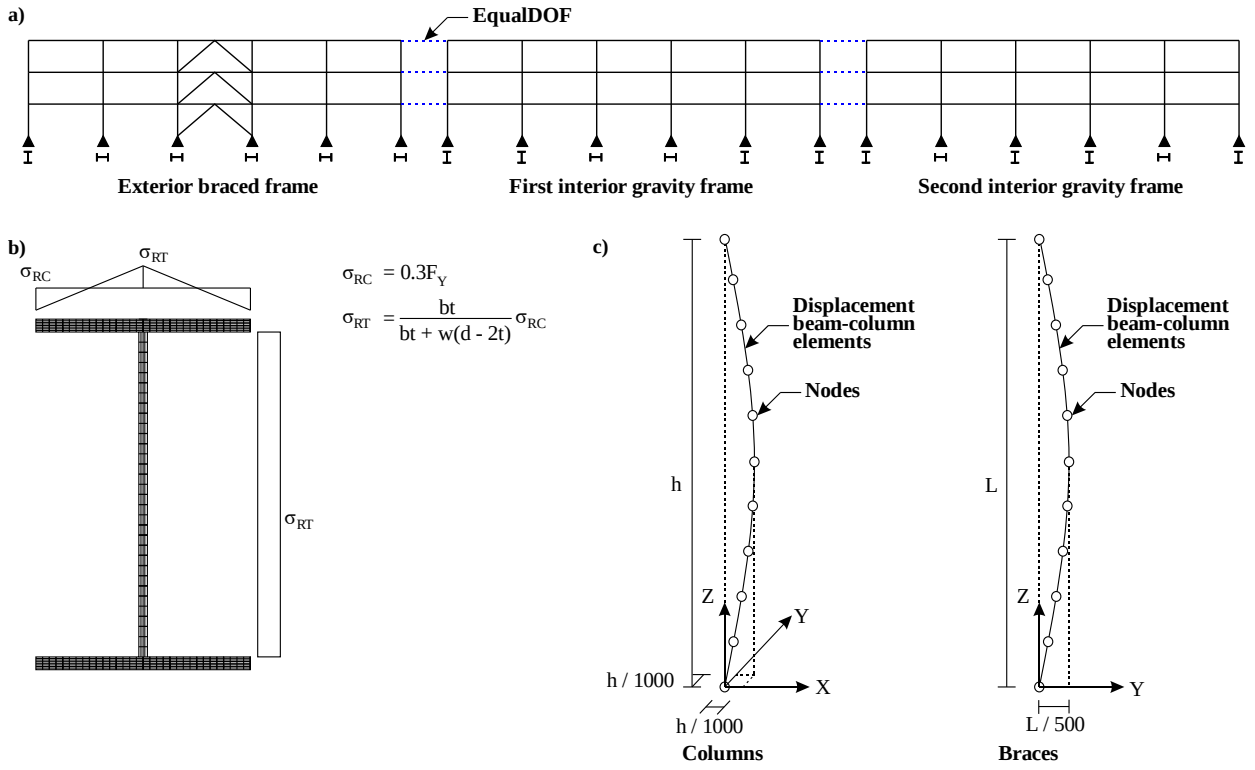


Figure 8.8. Building detailing a) Prototype building modeling; b) Residual stress pattern in the columns (Galambos and Ketter 1958); c) Out-of-plumbness and element discretization of columns and braces.

8.3.2 Modeling of the frame members

All columns of the structure were modelled using displacement-based nonlinear beam-column elements with fiber discretization of the cross-sections. The Steel02 material, which can account for combined kinematic and isotropic hardening responses, was assigned to the cross-section fibers with the properties presented in Table 8.10. The value of F_y corresponds to the probable yield stress R_yF_y as specified in CSA S16 for the beams and columns and HSS sections. Column flanges were modelled with 5 fibers over the flange thickness, 10 fibers over the flange width, 5 fibers over the

web thickness and 10 fibers over the web width. The flange width was discretized to account for the residual stresses in the section and because some columns were positioned along their weak axis. The residual stresses were considered to the material assigned to the column fibers. The pattern proposed by Galambos and Ketter (1958), presented in Figure 8.8b, was used as a modeling assumption.

Table 8.10. *Steel02* material properties (Mazzoni et al. 2006).

	F_y	E	b	R_0	C_{r1}	C_{r2}	a_1	a_2	a_3	a_4
	GPa	**GPa**	**-**	**-**	**-**	**-**	**-**	**-**	**-**	**-**
Beams & Columns	0.385	200	0.004375	18	0.925	0.15	0.0	1.0	0.0	1.0
Braces	0.460	200	0.00575	18	0.925	0.15	0.0	1.0	0.0	1.0

The columns were discretized in 10 elements over their length to allow reproducing buckling response. Initial out-of-straightness was assigned in both orthogonal directions with a half-sine function having a maximum amplitude of $h_s/1000$, as shown in Figure 8.8c. Column continuity was also considered in the numerical model. Each column was modeled with a pinned connection at their base.

The beams of the braced frame were also modelled with displacement-based nonlinear beam-column elements. The model was identical to that of the columns except that no out-of-plumbness was included for the beams. The beams were thus not discretized into several elements as was performed for the columns.

The bracing members were also modelled using displacement-based nonlinear beam-column elements. For the braces, the probable yield stress is taken as 460 MPa, as specified by CSA S16-14 (CSA 2014). The braces are also discretized in 10 elements to consider a half-sine function for the out-of-plumbness at a maximum of L/500 in the out-of-plane direction, as pictured in Figure 8.8c.

The effective length of the brace corresponds to 90% of the centerline distance, which assumes a gusset plate length corresponding to 5% of the brace length at each end, as illustrated in Figure 8.9a. Clause 27.11 of the Canadian Standard CSA S16-14 (CSA 2014) does not require ductile detailing for the gusset plate; the out-of-plane rotational behavior of the gusset was therefore not included in the model. A field-welded slotted HSS connection was assumed. The welds between

the gusset and the braces were modeled as a *zerolength* element (Mazzoni et al. 2006) with an extremely stiff material in all 6 DOF. The braces were thus considered fixed to the gusset plate. A tensile and compressive limit modeled with a *MinMax* uniaxial material was assigned to the translational axial DOF of the *zerolength* element. The *MinMax* uniaxial material force limit was set equal to 1.3 times the design brace force C_f to account for the connection overstrength which was assumed to be the same as the overstrength-related factor R_o of the system. The limit of the *MinMax* element was reached at a value of 1489 kN. Once this limit is reached, the *zerolength* element is removed from the model, thus disconnecting the brace to the gusset plate. The beams in the gravity frames were expected to deform elastically. To limit the analysis time, these elements were modelled using elastic-beam members.

8.3.3 Modeling of the PR beam-column connections

The beam-column connection was created with a *zerolengthSection* element (Mazzoni et al. 2006). The top and seat angles of the connections are each represented by a single fiber and the web angles are discretized into several fibers, as pictured in Figure 8.9b. The position of these fibers in the section correspond to the position of the angle with respect to the beam neutral axis. The proposed *SteelAngles* uniaxial material detailed in Chapter 7 is created for each angle geometry. The geometrical parameters and the input parameters used for each of these geometries are presented in Table 8.11. To represent the contact between the angle and the column flange under compression loading, an *ElasticNoTension* uniaxial material (Mazzoni et al. 2006) was added in parallel to the *SteelAngles* material. Figure 8.10a to e presents the hysteretic behaviour of the angle components. This new combined material is then assigned to the corresponding fibers to represent the angle component behaviour of each angle. The composed section is then aggregated with a rigid material to minimize the vertical shear deformations of the connection. The rigid material is thus assigned to the V_y DOF using the *Section Aggregator* (Mazzoni et al. 2006).

Rigid elements are added to the connection detailing to represent the eccentricity between the connection and the column neutral axis. This rigid link corresponds to half of the column depth for the Strong axis columns and half of the column web thickness for the weak axis columns. The hysteretic moment-rotation behaviour of each connection in the example building are presented in Figure 8.11.

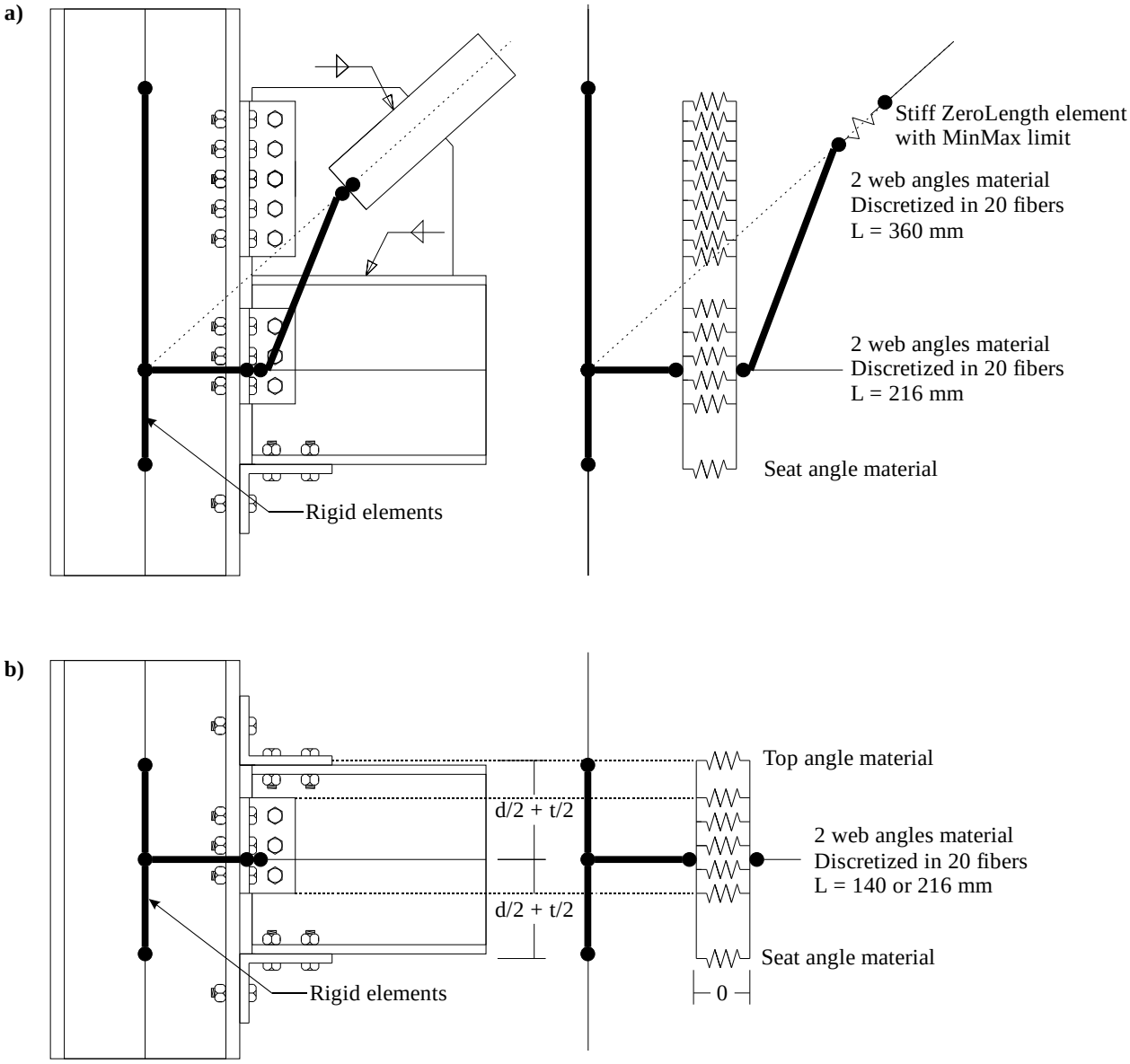


Figure 8.9. Numerical modeling of: a) gusset-beam-column connections; and b) gravity beam-column connections.

Table 8.11. Geometrical and input parameters used in the *SteelAngles* material in OpenSees

Angle geometry		**Web angles**	**A**	**B**	**C**
Geometrical parameters					
t	mm	7.94	9.53	12.7	7.94
g_c	mm	64	64	70	89
g_2	mm	27.1	25.5	28.5	52.5
b_{eff}	mm	1	150	150	150
E	GPa	200	200	200	200
F_y	GPa	0.345	0.345	0.345	0.345
Input parameters					
F_0^+	kN	0.321	74	117	25
K_i^+	kN/mm	0.741	182	333	48
K_p^+	kN/mm	0.0293	5.61	6.68	2.27
b^+	-	0.0396	0.031	0.020	0.048
f_N	-	1.8	1.8	1.8	1.8
e_N	-	0.718	0.64	0.58	0.88
b_N	-	1.00	1.00	1.00	1.00
R_0	-	1.40	1.40	1.40	1.40
C_{r1}	-	-0.46	-0.46	-0.46	-0.46
C_{r2}	-	1.00	1.00	1.00	1.00
a_1	-	0.00	0.00	0.00	0.00
a_2	-	1.00	1.00	1.00	1.00
a_3	-	0.00	0.00	0.00	0.00
a_4	-	1.00	1.00	1.00	1.00
s_1	-	0.04	0.04	0.04	0.04
s_2	-	1.00	1.00	1.00	1.00
s_3	-	0.05	0.05	0.05	0.05
s_4	-	1.00	1.00	1.00	1.00
m	-	-0.46	-0.46	-0.46	-0.46
Δ_0	mm	46.3	43.2	41.4	59.8
I_{eff}	mm^4	42	10819	25605	6257
A_{eff}	mm^2	8	1430	1905	1191
r_{eff}	mm	2.29	2.75	3.67	2.29

Furthermore, the response of the same building with pinned beam-column gravity connections and gusset-beam-column connections was numerically evaluated in OpenSees. This response is obtained as a comparative basis to evaluate the influence of the enhanced gravity connections in

the seismic response of the buildings and in the reserve capacity. It represents the current practice standard when designing Type CC braced frames.

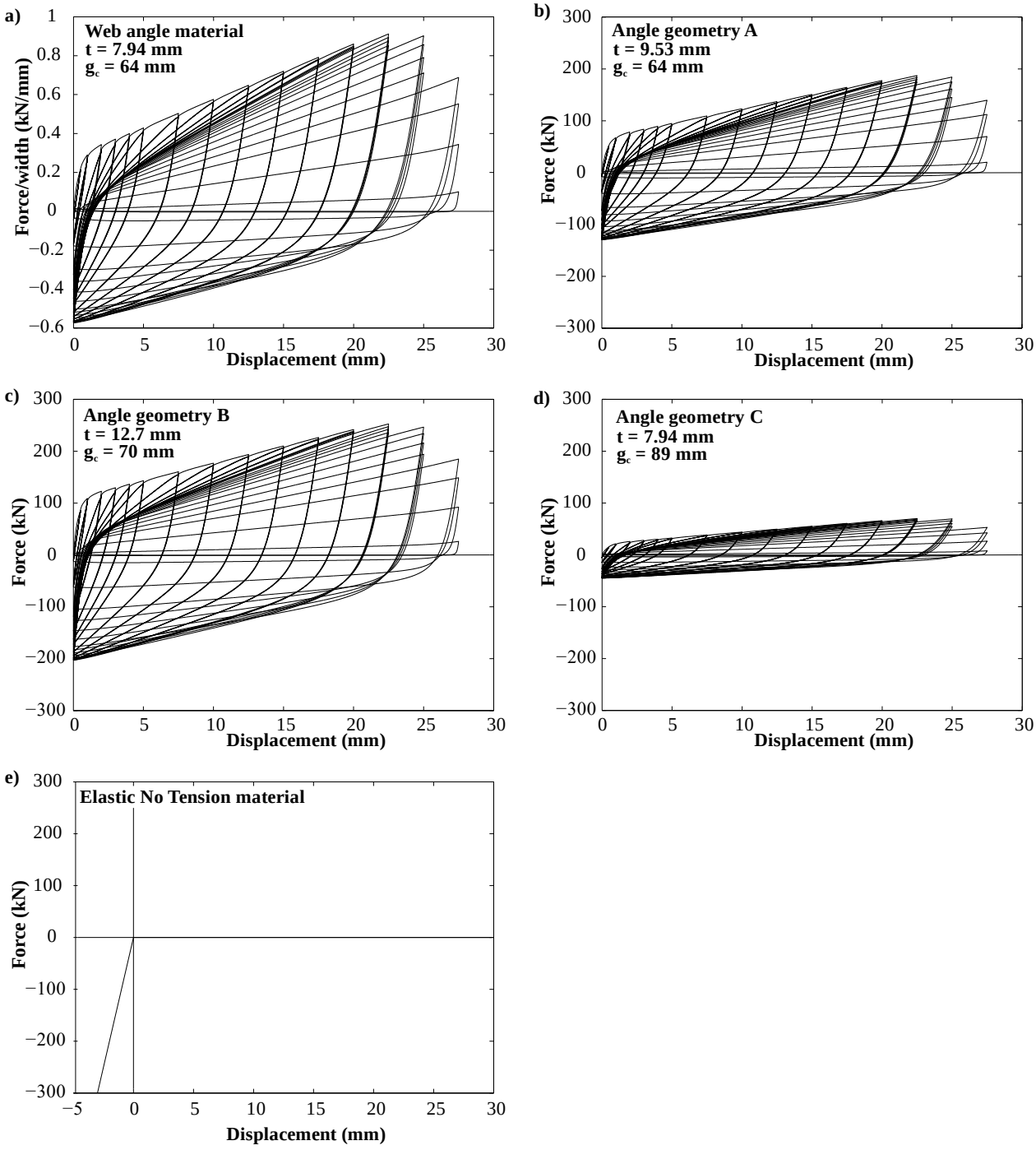


Figure 8.10. Force-displacement behaviour of : a) 1 mm-strip web angle; b) Angle geometry A; c) Angle geometry B; d) Angle geometry C; e) Elastic No-tension material.

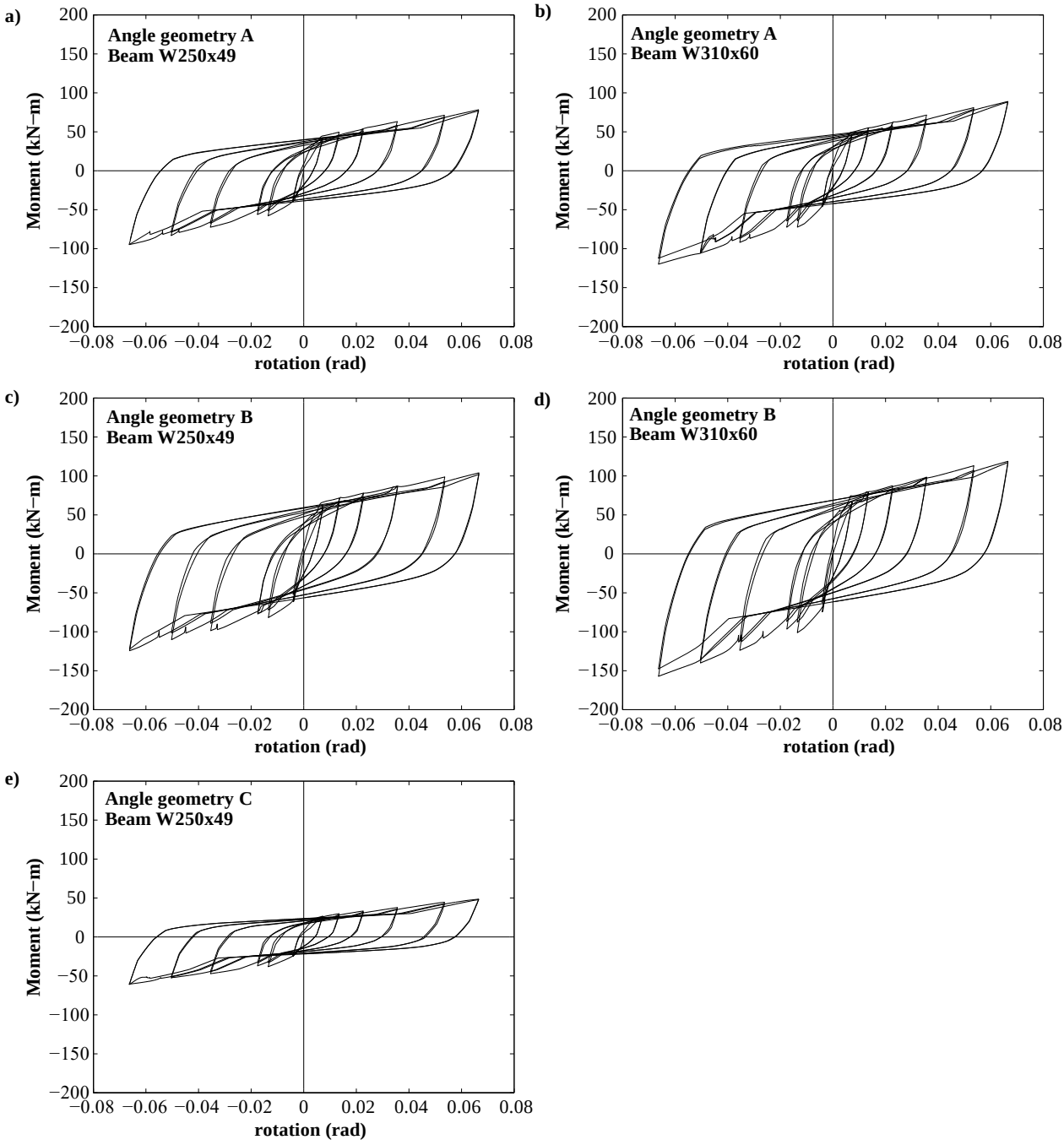


Figure 8.11. Hysteretic moment-rotation behaviour of a) Angle geometry A with W250x49 beam; b) Angle geometry A with W310x60 beam; c) Angle geometry B with W250x49 beam; d) Angle geometry B with W310x60 beam; e) Angle geometry C with W250x49 beam.

8.3.4 Seismic loading

In the analysis, gravity loads corresponding to D+0.5L+0.25S were applied to the structure prior to performing the modal analysis and applying the ground motions. Columns, braces and beams were assigned co-rotational geometric transformation to account for P-delta effects in the analyses.

Rayleigh damping was used in the time history analyses. This type of damping varies with the stiffness of the structure. After brace failure, lengthening of the vibration period is observed and the Rayleigh damping can consider this dynamic behaviour. An equivalent damping ξ of 2% was considered on the first two modes to calculate the parameters α and β used in the formulation of the Rayleigh damping. This formulation is expressed in Equation 8.20 with the calculated parameters.

$$[C] = 0.258[M] + 0.00129[K] \tag{8.20}$$

Both models are loaded with 11 ground motions, 5 of magnitude 6.0 and 6 of magnitude 7.0. These ground motions are scaled and factored for Montreal site C. The response spectra of the 11 ground motions are presented in Figure 8.12.

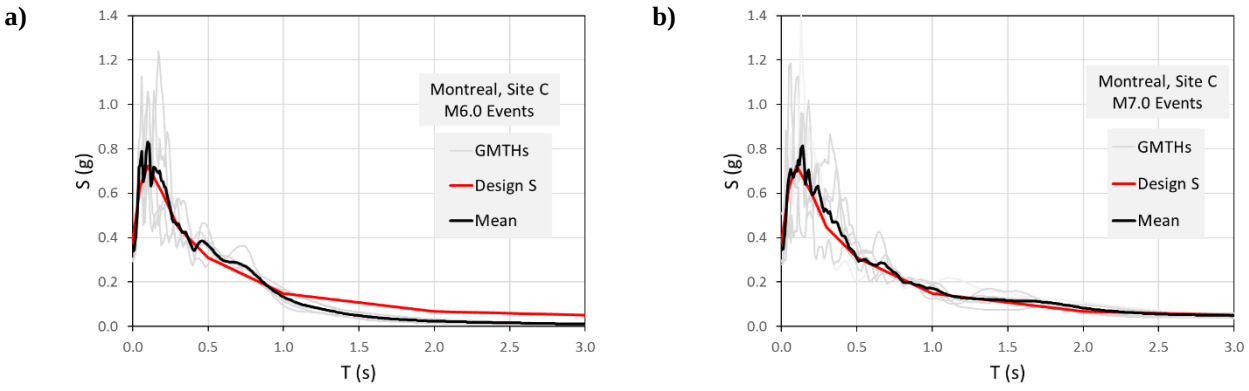


Figure 8.12. Response spectra of: a) M6.0 ground motions; and b) M7.0 ground motions.

8.3.5 Response of the studied structure

8.3.5.1 Detailed response of the two models under GM9

The computed periods of the undamaged structure in the three translational modes, including P-delta effects, for the two models are presented in Table 8.12. The presence of enhanced connections in the building modifies slightly the building periods. However, these modifications do not have a significant impact on the dynamic response of the buildings. The braced frame stiffness is very large compared to the gravity connection stiffness, the behaviour of the unfractured building is still controlled by the braced frames.

Table 8.12. Vibration periods of the undamaged two models including P-delta effects.

Period (s)	Pinned connections	Enhanced connections
T1	0.686	0.680
T2	0.289	0.309
T3	0.201	0.217

The hysteretic response of the braces in the pinned and enhanced building are presented in Figure 8.13a and b respectively. The two models exhibited a similar elastic behaviour. However, the building with the enhanced connections showed signs of yielding in the cycle prior to fracture at point A on Figure 8.11b. This yielding is attributed to the gusset-beam-column connection of the second storey, where the first storey braced beam is attached, as pictured in Figure 8.12a. This connection is loaded with the braced beam axial load combined with the brace load, thus creating a large axial load on the connection and initiating yielding. Furthermore, the yielding of the angles attaching the gusset to the column occur at small connection rotations since the distance between the angle fiber and the beam centerline is large. Moreover, the connection detailing was not included in the pinned building, the yielding is thus not observed in the hysteretic response.

Brace connection fracture occurred in the right brace at a compression force of 1799 kN and 1814 kN for the building with the pinned and enhanced connections respectively, which correspond to point B on Figure 8.13a and b. These loads are close to the expected values of 1802 kN specified by R_yC_f and assigned to the *MinMax* material.

After failure, the left brace remained attached, but the SFRS lost its integrity. The brace force in the left brace was thus reduced. The secondary stiffness obtained in the long-link EBF behaviour

of the braced beam and left brace is observed in Figure 8.14b. Since the beam connections were pinned in the pinned building, this behaviour is not observed on Figure 8.13a. The stiffness of the braced frame after failure correspond to 2.44 kN/mm, which is slightly larger than the computed value of 2.18 kN/mm. This larger value can be attributed to the gusset-beam-column stiffness contributing to the lateral stiffness of the long-link EBF. This connection is very stiff, because of the angles between the gusset and the column, thus improving the flexural stiffness of the braced beam. Even if the connection started to yield, its behaviour remains similar to the elastic behaviour. The plastic deformations experienced by the angles were limited, as the storey drift of the building remained below 0.5%. The angles thus adopt a secant stiffness behaviour, which is similar to the initial stiffness when small plastic deformations are imposed.

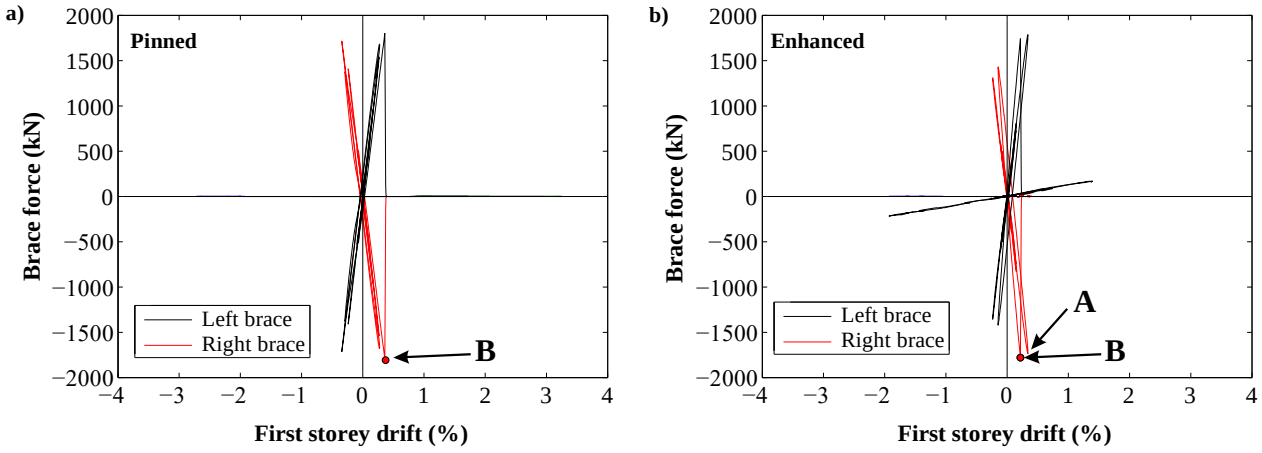


Figure 8.13 Hysteretic brace force of: a) Pinned connection model; b) Enhanced connection model.

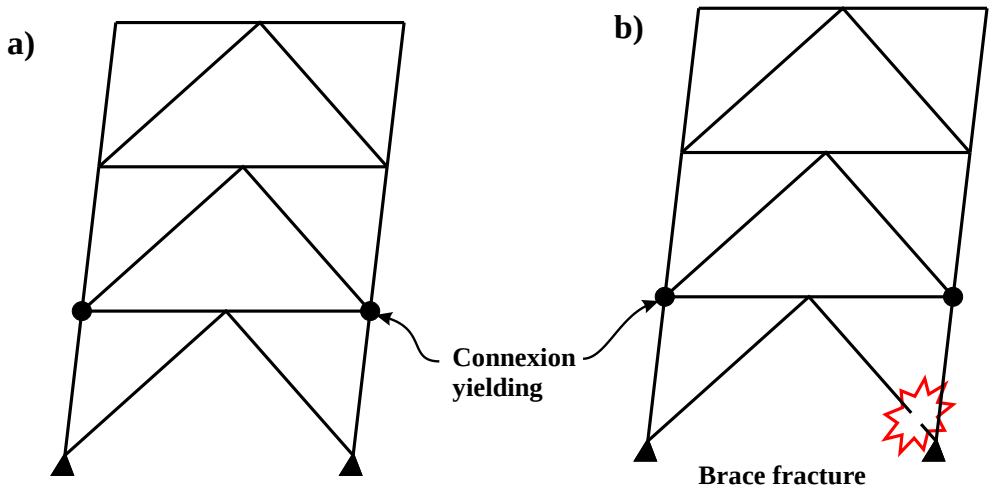


Figure 8.14 Building deformation at: a) Point A; b) Point B.

The Base shear variation during ground motion GM9 is presented in Figure 8.15a for the two buildings. Both building exhibited a similar dynamic response during the first cycles of the ground motion. However, the building with the enhanced connection failed before the building with the pinned connections, at a base shear of 2630 kN. This difference in behaviour is explained by the yielding in the gusset-beam-column connections of the second storey, which modified slightly the dynamic response of the building. The building with enhanced connections experienced larger inertial forces during an excursion which caused rupture of the brace connection. The fracture in the pinned building occurred at the same location during the following cycle, at a base shear of 2534 kN. After the brace connection fracture, the base shear of the building decreased drastically in both cases. The response of the fractured building is given by the reserve capacity. For the building with enhanced connections, this reserve capacity is formed by the braced frame residual stiffness and the moment-frame action in the gravity frame. The pinned connection building only has the column continuity to provide reserve lateral stiffness. Both buildings were able to survive the ground motion.

The storey drift in the first, second and third storey are given in Figure 8.15b, c and d respectively. As expected, the largest storey drift occurred in the first storey, where the brace connection occurred. The presence of the enhanced connections mitigated the storey drifts. Indeed, the pinned building experienced maximum storey drifts of 3.3% (148 mm), 0.45% (20 mm) and 1.77% (81 mm) for the first, second and third storey respectively, while the enhanced connections building exhibited a storey drift of 1.93% (88 mm), 0.78% (35ù mm) and 0.65% (30 mm) for the first, second and third storey respectively. The building with enhanced connection thus exhibits a storey drift in the first storey smaller than the target drift of 3% defined during the design process. This observation validates the design procedure to limit the design procedure to the anticipated value.

The right and left brace forces are presented in Figure 8.16a and b respectively. These figures also show similar response between the two models in the first cycles. The right brace fracture occurred at a load of 1799 kN and 1814 kN for the pinned and enhanced connection building. At fracture, the load developed in the left brace corresponded to 1778 kN and 1784 kN for the pinned and enhanced connection building connection. Once failure occurred, the SFRS integrity was compromised and the force developed in the left brace was drastically reduced. An axial load still

remained in the left brace of the building with the enhanced connections because of the long-link EBF system developing after the loss of a brace.

The moment in an interior gravity column is presented in Figure 8.16c. During the first few cycles, the moment developed in the connection remain small in both cases. However, after fracture in the SFRS, the flexural capacity of the gravity columns is mobilized. For the pinned connection building, the flexural stiffness of the gravity columns contributes to the lateral capacity through the column continuity. However, the moment developed in the columns reaches 262 kN-m. This moment is significantly larger than the maximum allowable moment of 152 kN-m which causes yielding of the column section according to the axial-moment interaction of CSA-S16 and presented with Equation 8.12. This moment of 152 kN-m is calculated with the factored resistance of the element and the nominal material properties. The moment obtained in the pinned connection model is nevertheless larger than the allowable maximum moment in the design process. This larger moment is caused by the column continuity acting as the only available lateral stiffness in the model. Therefore, the column flexural stiffness is completely mobilized, which can cause plastic hinges at the top of the columns and a soft storey mechanism.

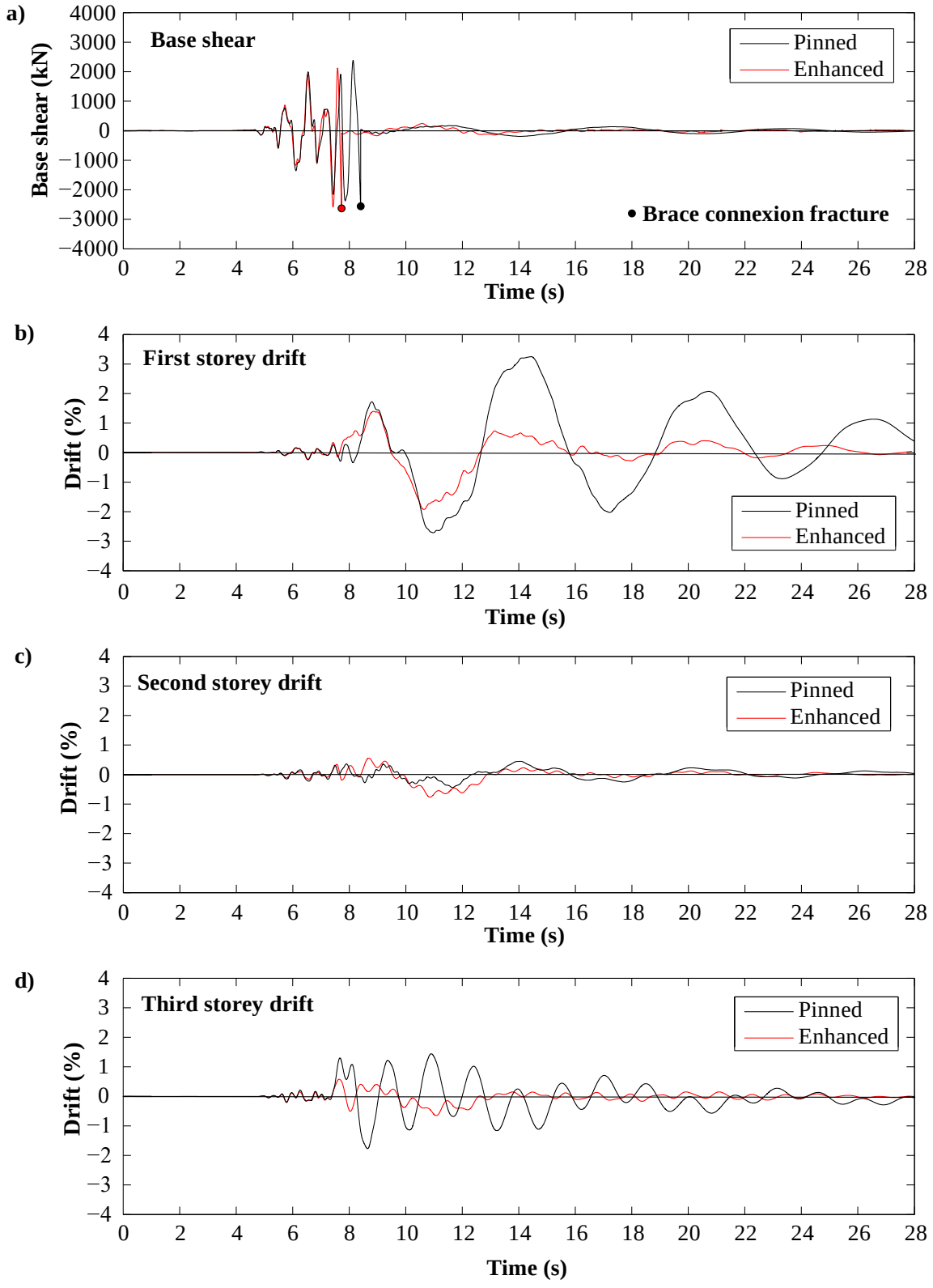


Figure 8.15 Time-history of a) Base shear; b) 1st storey drift; c) 2nd storey drift; d) 3rd storey drift.

On the other hand, the moment developed in the interior column with the enhanced connection is limited to 134 kN-m, which is smaller than the maximum allowable value of 152 kN-m imposed during the design process. This smaller moment is caused by the fact that the columns are part of a moment-frame action, where the global stiffness is shared between the columns, the beams and the connections. Therefore, the beams and connections will experience deformations which will reduce the ones imposed on the column and thus reduce the flexural moment in the element. This behaviour is beneficial since it avoids the formation of a plastic hinge in the column, as expected in the design process. However, the moment distribution in the gravity columns rather follows the pattern observed in a soft-storey mechanism rather than that of a moment frame, as pictured in Figure 8.17. The deformation occurring in the columns is thus larger than expected.

The variation of the moment in a gravity connection along the length of the ground motion is presented in Figure 8.16d. As expected, the enhanced gravity connection did not experience significant rotational demand at the beginning of the test. During this part, the connection remained elastic with a maximum moment of approximately 20 kN-m. The connections were however mobilized once brace connection fracture occurred. The connection reached a maximum moment of 42 kN-m and exhibited a ductile behaviour as expected. The hysteretic response of a connection joining a W310x60 beam to an interior column on its strong axis is presented in Figure 8.18.

This connection, attaching an interior beam to a strong-axis column, was designed to resist a moment $M_{sj,fi}$ of at least 54 kN-m and could not exceed a moment of 152 kN-m. The maximum moment experienced by the angle remained below these values. Furthermore, the maximum allowable connection rotation, $\theta_{sj,fi}$, was determined as 0.0184 rad. The maximum rotation experienced by the connection corresponded to 0.004 rad, which respects the limit set during the design process.

Furthermore, after the brace connection fracture, the building period increases significantly, and the dynamic response becomes more flexible. This change in dynamic behaviour results in fewer cycles with larger asymmetric displacements. This behaviour, combined with the fact that the plastic behaviour of the connections is mobilized only for the end of the test, result in small low-cycle fatigue degradation during the seismic event.

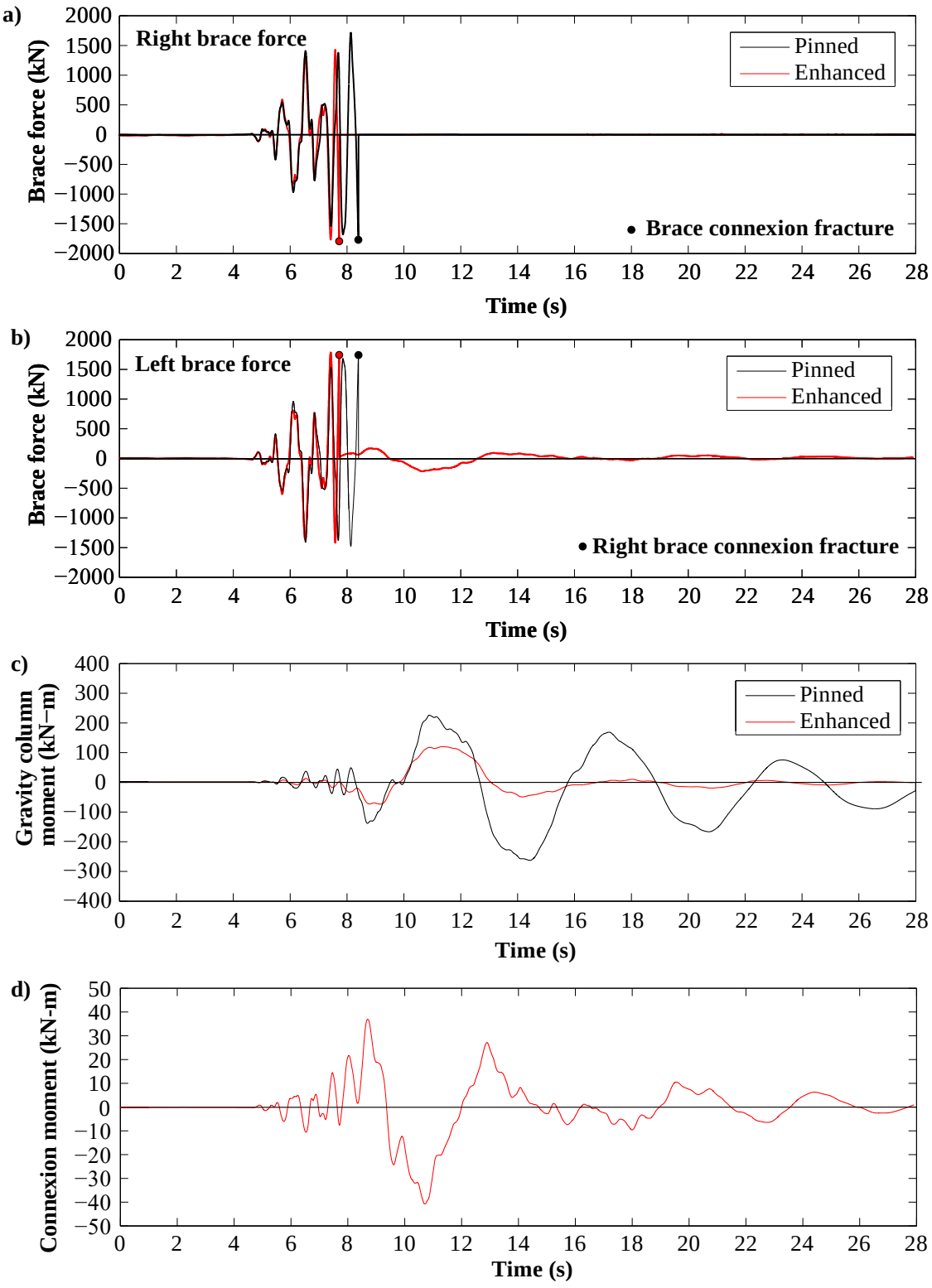


Figure 8.16 Time-history of a) Right brace force; b) Left brace force; c) Moment at the top of interior gravity column; d) Moment in an interior connection attached to a strong axis column.

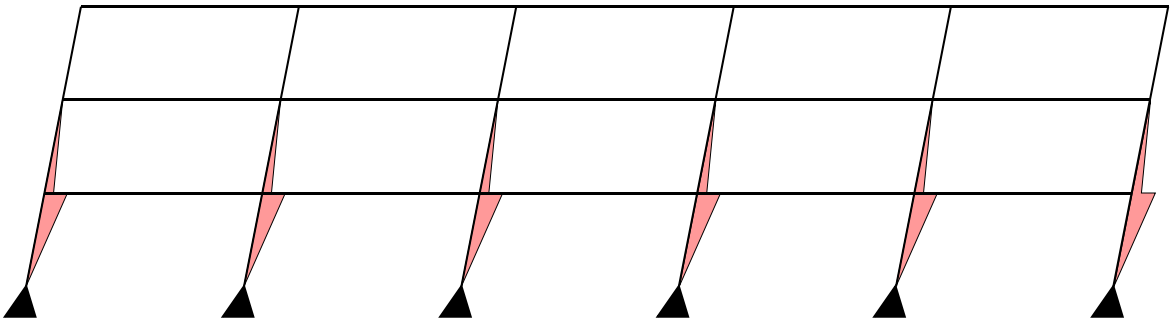


Figure 8.17. Moment distribution in the columns of the gravity frame with enhanced connections.

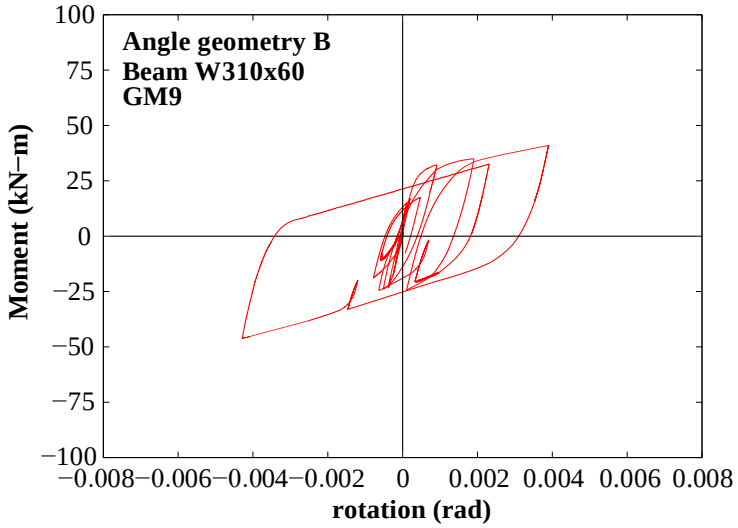


Figure 8.18. Hysteretic response of a connection joining a W310x60 beam to an interior column on its strong axis during Ground Motion 9.

8.3.5.2 General observations

The two building models are loaded with 11 ground motions factored and scaled for the NBCC 2015 design spectra of Montreal on a soil type C. The failure mode and global nonlinear behaviour of each building with each ground motions are summarized in Table 8.13. This table also presents the maximum first storey drift ratio with respect to the 3% limit defined as the maximum target drift. The following general observations can be drawn:

1. Because the brace connections are not designed with the brace capacity, but rather with the design seismic load, fracture of the brace connection was the first failure mode encountered. This failure mode is brittle and marked the start of the reserve capacity mobilization to resist the ground motion;

2. The brace connection fracture only occurred in the first storey;
3. In buildings with pinned gravity connections, 2 out of 11 models did not experience brace connection failure. The building remained generally elastic, with limited yielding in the braced frame beam. This behaviour was observed in 5 buildings with gravity connections. In these cases, yielding was also observed in gravity beam-column connections and gusset-beam-column connections; and
4. In buildings with pinned gravity connections, 2 out of 11 models experienced a soft storey mechanism following the loss of a brace connection. This behaviour was not observed in the buildings with enhanced gravity connections.

The most vulnerable storey of the example building is the first one because all brace occurrences of brace connection failure were observed in that storey. The base shear of the building is plotted against the first storey drift in Figure 8.18 for every ground motion. In this figure, the buildings with pinned connections are presented in black on the left side, whereas the response of the buildings with enhanced connections are presented in red on the right side. From this figure, the following observations can be drawn:

1. The enhanced connections do not have a significant influence on the maximum base shear. This observation supports the results obtained from the modal analyses presented in Chapter 9. Indeed, the enhanced connections do not modify significantly the fundamental period of the unfractured building, the dynamic response thus remain similar;
2. In every case, the maximum first storey drift experienced by the models with enhanced connections is smaller than the one experienced by the model with the pinned connections. The maximum storey drift of the building with the enhanced connection was limited to 3% and the buildings with enhanced connections respected that limit. The smaller storey drift may result in less damage to non-structural elements, thus reducing the economical loss caused by the seismic event;
3. The stiffness of the gravity frame is larger with the enhanced connection. This observation supports the fundamental basis of the connection enhancement.

Table 8.13. Failure modes observed and peak first storey drift (δ_1) to target drift (δ_{Target}) ratio for each ground motion with and without enhanced gravity connections

Ground motion	Gravity connection	Failure mode observed	$\frac{\delta_1}{\delta_{Target}}$
GM1	Pinned	Fracture of one first storey brace connection	120%
	Enhanced	Fracture of one first storey brace connection	68.4%
GM2	Pinned	Fracture of one first storey brace connection & soft storey mechanism	Collapse
	Enhanced	Gravity beam-column & gusset-beam-column connection & braced frame beam yielding	11.7%
GM3	Pinned	Fracture of one first storey brace connection	104%
	Enhanced	Gravity beam-column & gusset-beam-column connection & braced frame beam yielding	10.8%
GM4	Pinned	Fracture of one first storey brace connection	135%
	Enhanced	Fracture of one first storey brace connection	73.9%
GM5	Pinned	Fracture of one first storey brace connection	84.9%
	Enhanced	Fracture of one first storey brace connection	32.9%
GM6	Pinned	Braced frame beam yielding	7.7%
	Enhanced	Gravity beam-column & gusset-beam-column connection & braced frame beam yielding	7.9%
GM7	Pinned	Fracture of one first storey brace connection	56.7%
	Enhanced	Gravity beam-column & gusset-beam-column connection & braced frame beam yielding	8.2%
GM8	Pinned	Fracture of one first storey brace connection	106%
	Enhanced	Fracture of one first storey brace connection	79.5%
GM9	Pinned	Fracture of one first storey brace connection	108%
	Enhanced	Fracture of one first storey brace connection	94.4%
GM10	Pinned	Braced frame beam yielding	10.1%
	Enhanced	Gravity beam-column & gusset-beam-column connection & braced frame beam yielding	8.7%
GM11	Pinned	Fracture of one first storey brace connection & soft storey mechanism	Collapse
	Enhanced	Fracture of one first storey brace connection	50.5%

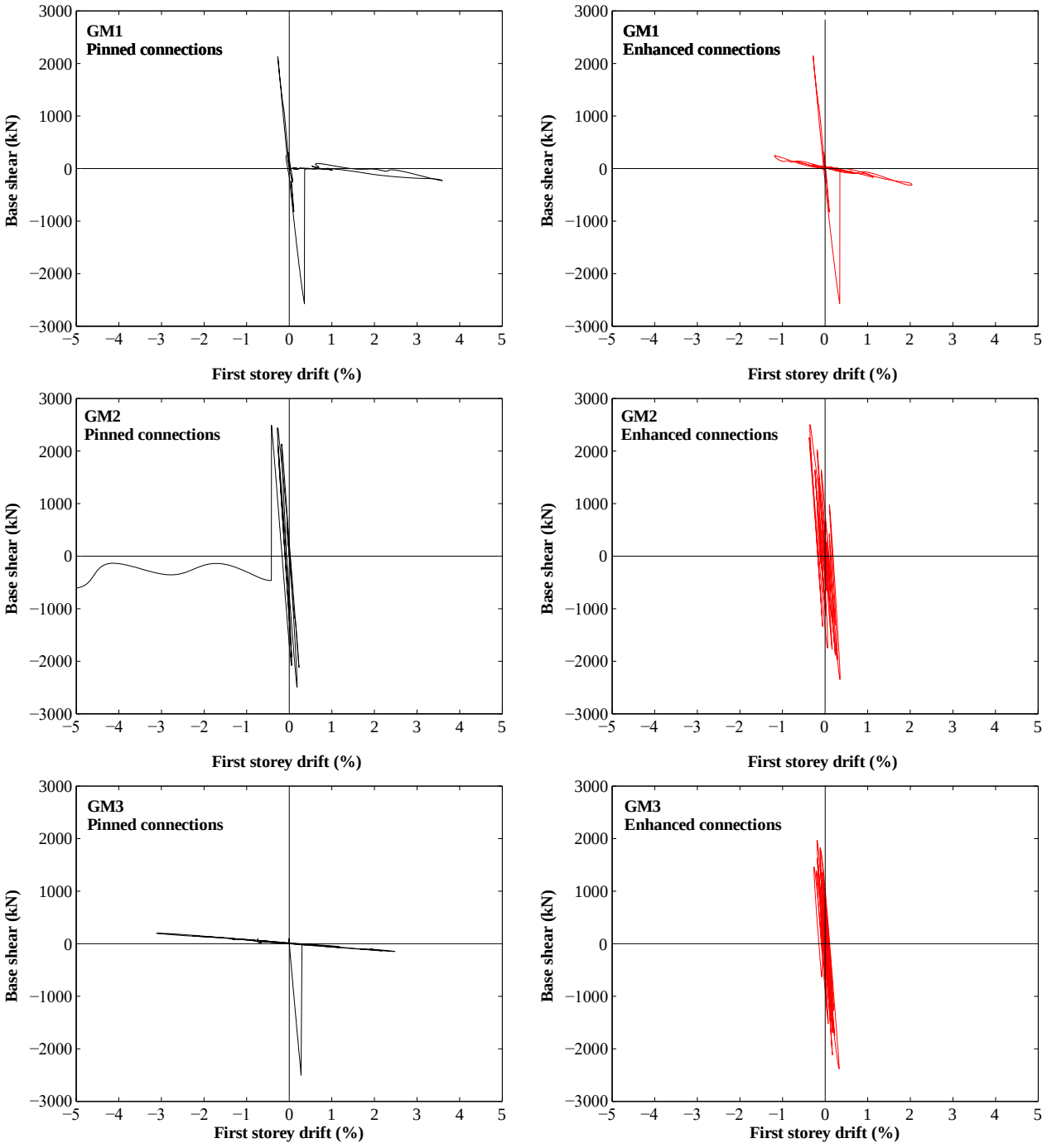


Figure 8.19. Base shear versus first storey drift for every ground motion, with pinned and enhanced gravity connections

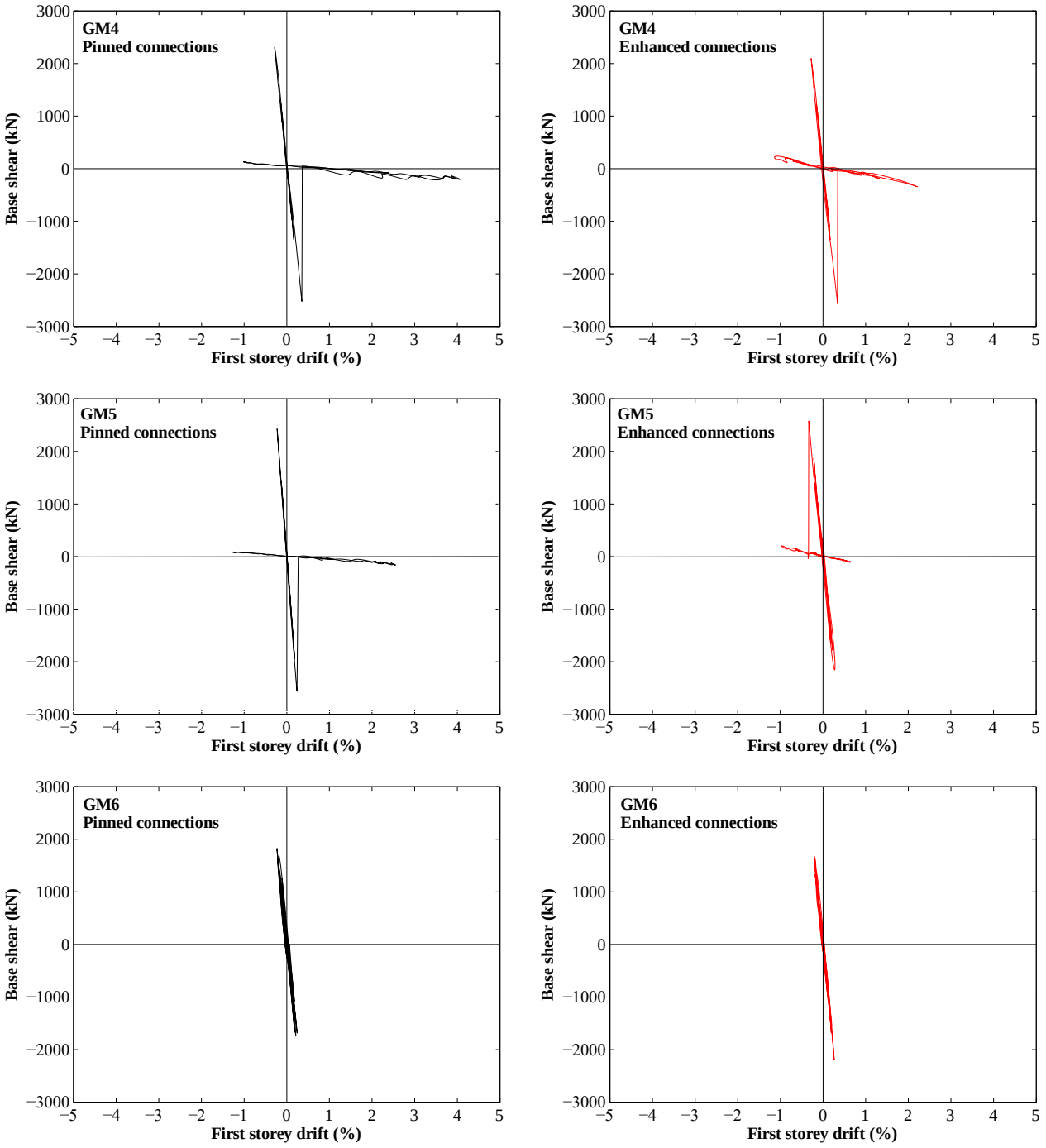


Figure 8.19. Base shear versus first storey drift for every ground motion, with pinned and enhanced gravity connections (Continuing)

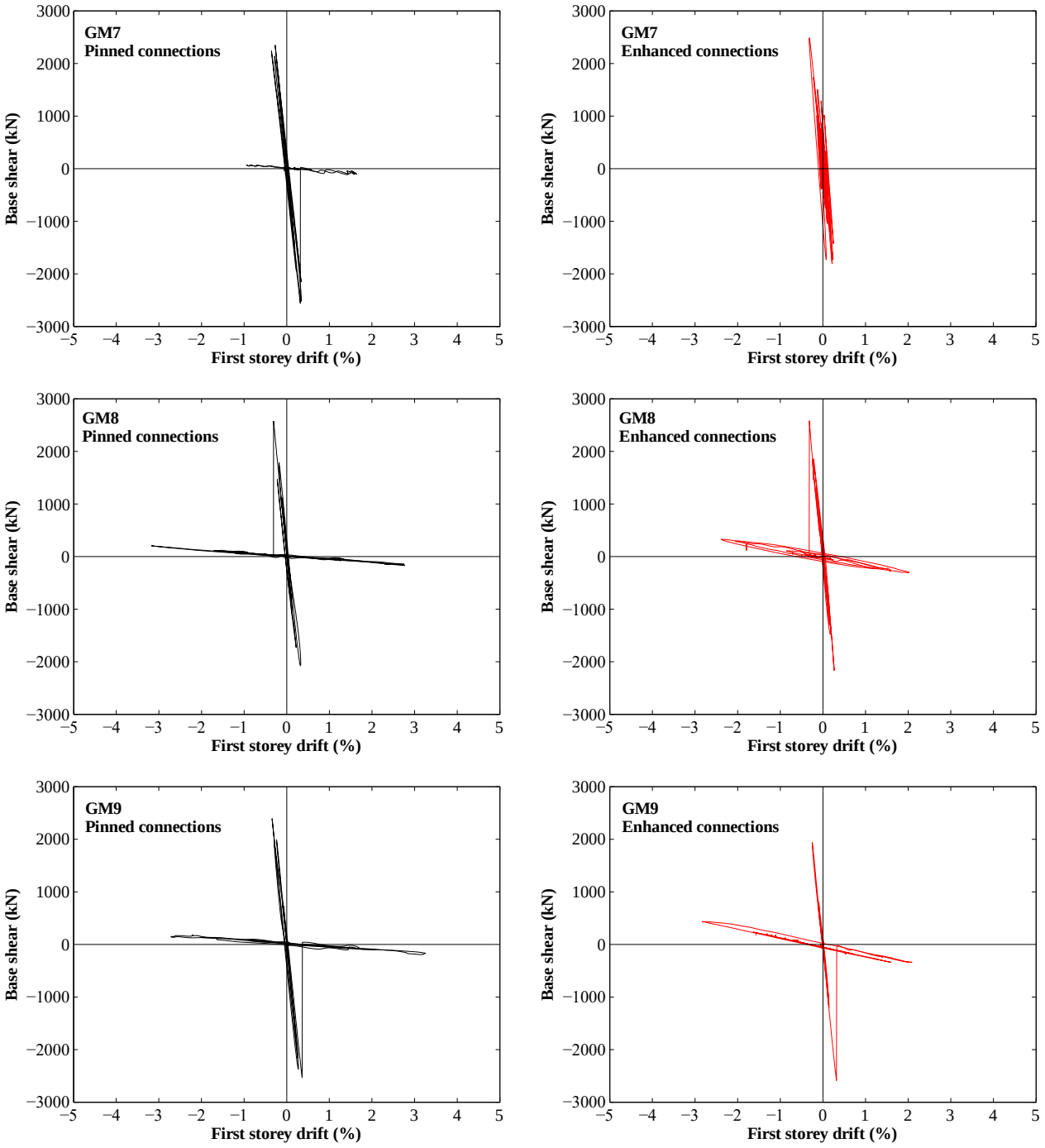


Figure 8.19. Base shear versus first storey drift for every ground motion, with pinned and enhanced gravity connections (Continuing)

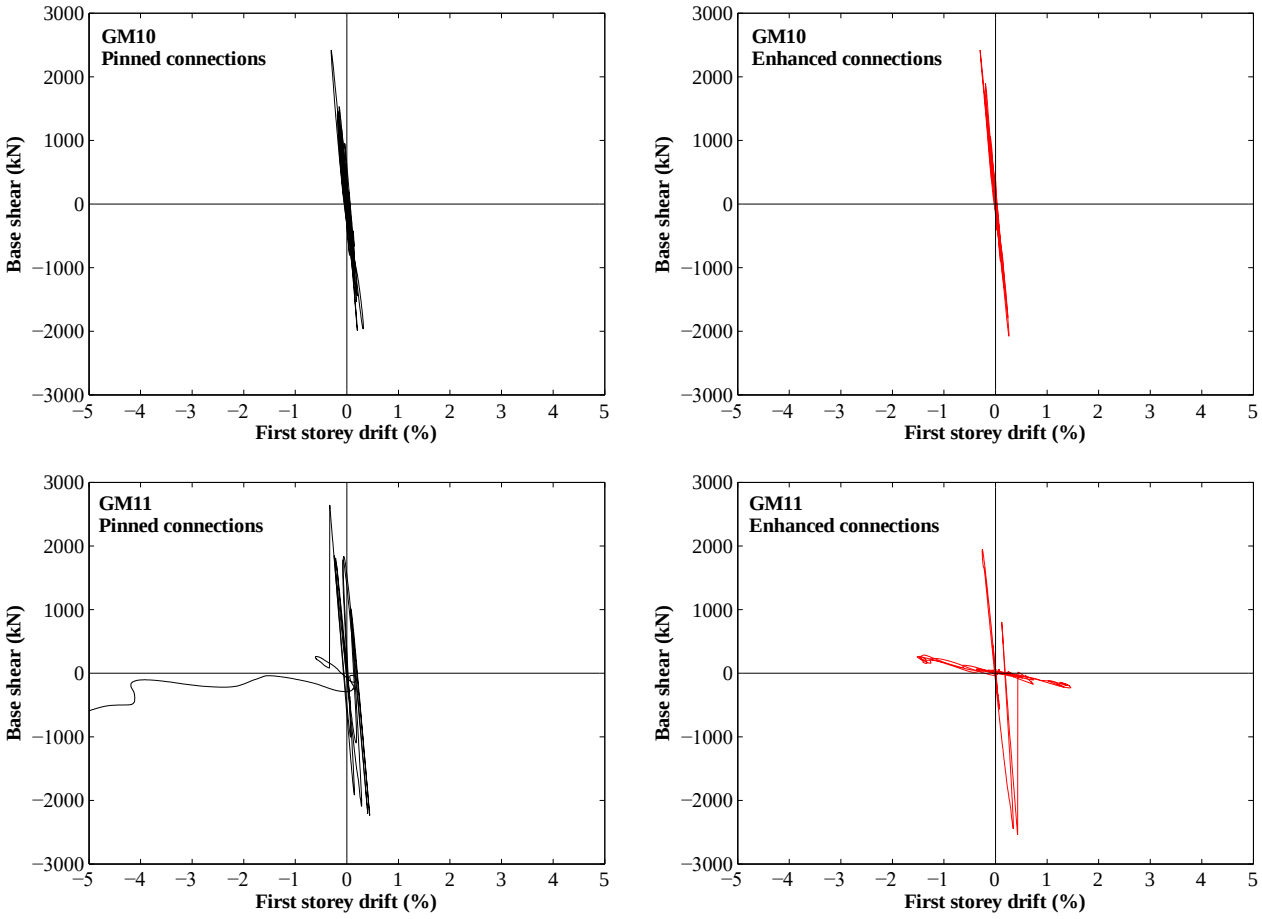


Figure 8.19. Base shear versus first storey drift for every ground motion, with pinned and enhanced gravity connections (End)

8.4 Summary

Through a moment frame action, the gravity frame of typical steel constructions can prevent collapse and mitigate P-delta effects after failure of the primary seismic load resisting system. The contribution of the gravity frame as a secondary lateral load resisting system depends on the rotational stiffness of the beam-column connections and bolted 2L-TS connections can offer significant stiffness and ductility with limited additional cost. Geometrical parameters and loading variations of the bolted angles create a complex nonlinear behavior but offer the potential to achieve the optimal compromise between the stiffness and ductility of the connection.

A rational approach is proposed to enhance the lateral reserve capacity of low-ductility steel buildings in Canada (R_d = 1.5, R_o = 1.3) by increasing the lateral load resistance of the gravity

frame with PR connections made of double web with top and seat bolted angles. With this approach, relaxations of brace connection design requirements are investigated since the building ductile behavior is insured by the enhanced reserve capacity in case of a brittle failure in the braced frame.

The proposed design procedure is then detailed with a 3-storey building located in Montreal on a soil of type C. This example building was then validated through numerical modeling in OpenSees and compared to a building without enhanced gravity connections. The following conclusions were drawn from these numerical models:

1. Fracture of the brace connection in the first storey was the first failure mode encountered. This failure mode is brittle and marked the start of the reserve capacity mobilization to resist the ground motion;
2. In buildings with pinned gravity connections, 2 out of 11 models did not experience brace connection failure. The building remained generally elastic, with limited yielding in the braced frame beam. This behaviour was observed in 5 buildings with gravity connections. In these cases, yielding was also observed in gravity beam-column connections and gusset-beam-column connections;
3. In buildings with pinned gravity connections, 2 out of 11 models experienced a soft storey mechanism following the loss of a brace connection. This behaviour was not observed in the buildings with enhanced gravity connections;
4. The enhanced connections do not have a significant influence on the maximum base shear;
5. The presence of enhanced connections reduced the moment developed at the top of the gravity column;
6. The maximum first storey drift experienced by the models with enhanced connections is smaller than the one experienced by the model with the pinned connections. The maximum storey drift of the building with the enhanced connection was limited to 3%. This storey drift is smaller than the one anticipated during the design process; and
7. The component-based model of the connection exhibited a ductile behaviour as expected during the numerical modeling.

CHAPTER 9 GENERAL DISCUSSION

9.1 Introduction

This chapter reports on two topics that were examined in the course of this thesis but that was not presented in the articles and previous chapters. The first topic is the determination of the period of a multi-storey chevron braced frame after faire has occurred in a given storey. This information is used in the design example presented in Chapter 8. In the second part of the Chapter introduces and presents the results of the test program that was conducted to characterize the yield strength properties of angles in the direction perpendicular to rolling and as a function of the position in the cross-section. Finally, a general discussion on the hypotheses and limitations of the research project is presented.

9.2 Influence of the storey stiffness reduction on the dynamic properties of buildings

The reserve capacity acts as a secondary system which influences the structural behavior of the building after the failure of the primary seismic force resisting system. In a three-storey building, the primary system failure may occur in any of the storeys. The loss of stiffness resulting from the failure changes the dynamic properties of the building and its response to the seismic loading. The stiffness loss lengthens the natural period of the building and reduces the seismic force demand on the reserve capacity. This reduction varies with the reserve capacity stiffness and the storey masses.

Section 9.2.1 presents a parametric study that has been performed to assess the impact of the residual stiffness on the periods and the seismic force demand for three-storey steel buildings with Type CC chevron braced frames. The parameters varied are the building size, the location and site class condition considered in design, the level of stiffness reduction, and the storey where brace connection failure has occurred.

In Section 9.2.2, the effect of brace connection failure on the structure periods is investigated for the three-storey braced frame building examined in Chapter 8. In this study, the storey where connection took place is varied and the variation in periods is studied for the building structure with and without the reserve lateral capacity system.

9.2.1 Parametric study of dynamic response

The buildings studied are designed for Vancouver and Montreal, on site classes C and E. The design spectra prescribed in NBCC 2015 for the two locations and site conditions are presented in Figure 9.1. The plan views and elevations of the buildings are presented in Figure 9.2. As shown, buildings having 3, 4, 5 and 6 9144 mm (30') wide bays in both directions were examined. The 3 storeys are 4572 mm (15') high. The chevron braced frames were designed in accordance with the provisions of CSA S16-14 for the Conventional Construction category, with $R_d = 1.5$ and $R_o = 1.3$). According to the design methodology described in Chapter 8, the columns and beams of the gravity system forming the reserve capacity were designed to resist gravity loads only. Table 9.1 summarizes the section dimensions used in the building.

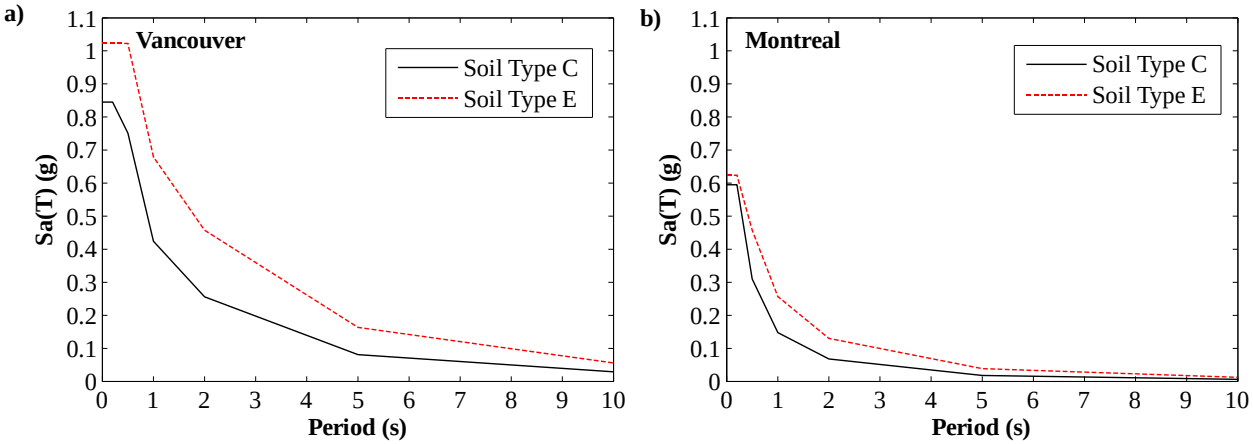


Figure 9.1. NBCC 2015 design spectra for: a) Vancouver; b) Montreal.

Table 9.1. Member sections of buildings

	Building	Storey	Vancouver		Montreal	
			C	E	C	E
			Braced frame			
Braces	3X3	3	HSS140X140X6.4	HSS178X178X6.4	HSS114X114X4.8	HSS127X127X6.4
		2	HSS178X178X7.9	HSS203X203X7.9	HSS152X152X6.4	HSS178X178X6.4
		1	HSS203X203X7.9	HSS229X229X9.5	HSS178X178X6.4	HSS178X178X7.9
	4X4	3	HSS178X178X6.4	HSS178X178X7.9	HSS127X127X6.4	HSS152X152X6.4
		2	HSS229X229X7.9	HSS254X254X9.5	HSS178X178X7.9	HSS203X203X7.9
		1	HSS254X254X9.5	HSS254X254X12.7	HSS203X203X7.9	HSS229X229X7.9
	5X5	3	HSS203X203X7.9	HSS229X229X7.9	HSS152X152X6.4	HSS178X178X6.4
		2	HSS254X254X12.7	HSS254X254X15.9	HSS203X203X7.9	HSS229X229X9.5
		1	HSS254X254X15.9	HSS356X356X12.7	HSS203X203X12.7	HSS254X254X9.5
	6X6	3	HSS229X229X7.9	HSS254X254X9.5	HSS178X178X6.4	HSS203X203X7.9
		2	HSS254X254X15.9	HSS356X356X15.9	HSS229X229X9.5	HSS254X254X12.7
		1	HSS356X356X12.7	HSS406X406X15.9	HSS254X254X9.5	HSS254X254X15.9
Beams	3X3	3	W310X38.7	W360X44	W250X32.7	W200X35.9
		2	W250X58	W360X64	W310X44.5	W250X49.1
		1	W360X64	W310X79	W360X51	W250X58
	4X4	3	W310X44.5	W250X49.1	W200X35.9	W310X38.7
		2	W360X72	W310X79	W360X57.8	W310X60
		1	W310X79	W410X100	W250X58	W360X72
	5X5	3	W250X58	W310X67	W310X38.7	W250X49.1
		2	W310X86	W310X107	W360X64	W250X73
		1	W410X100	W310X117	W360X72	W310X79
	6X6	3	W360X64	W250X73	W250X49.1	W250X58
		2	W310X101	W310X129	W250X73	W310X86
		1	W310X117	W310X158	W310X79	W360X101
Columns	3X3	-	W250X73	W250X73	W250X73	W250X73
	4X4	-	W250X80	W410X100	W250X73	W250X73
	5X5	-	W250X101	W310X107	W250X73	W310X86
	6X6	-	W310X107	W310X143	W250X80	W250X101
			Gravity frame			
			Interior roof	**Exterior roof**	**Interior floor**	**Exterior floor**
Beam			W250x49.1	W250x49.1	W310x60	W250x49.1
Girder			W410X100	W360x64	W610X101	W360x72
Corner columns			W200x35.9			
Interior columns			W250x49.1			
Exterior columns			W250x73			

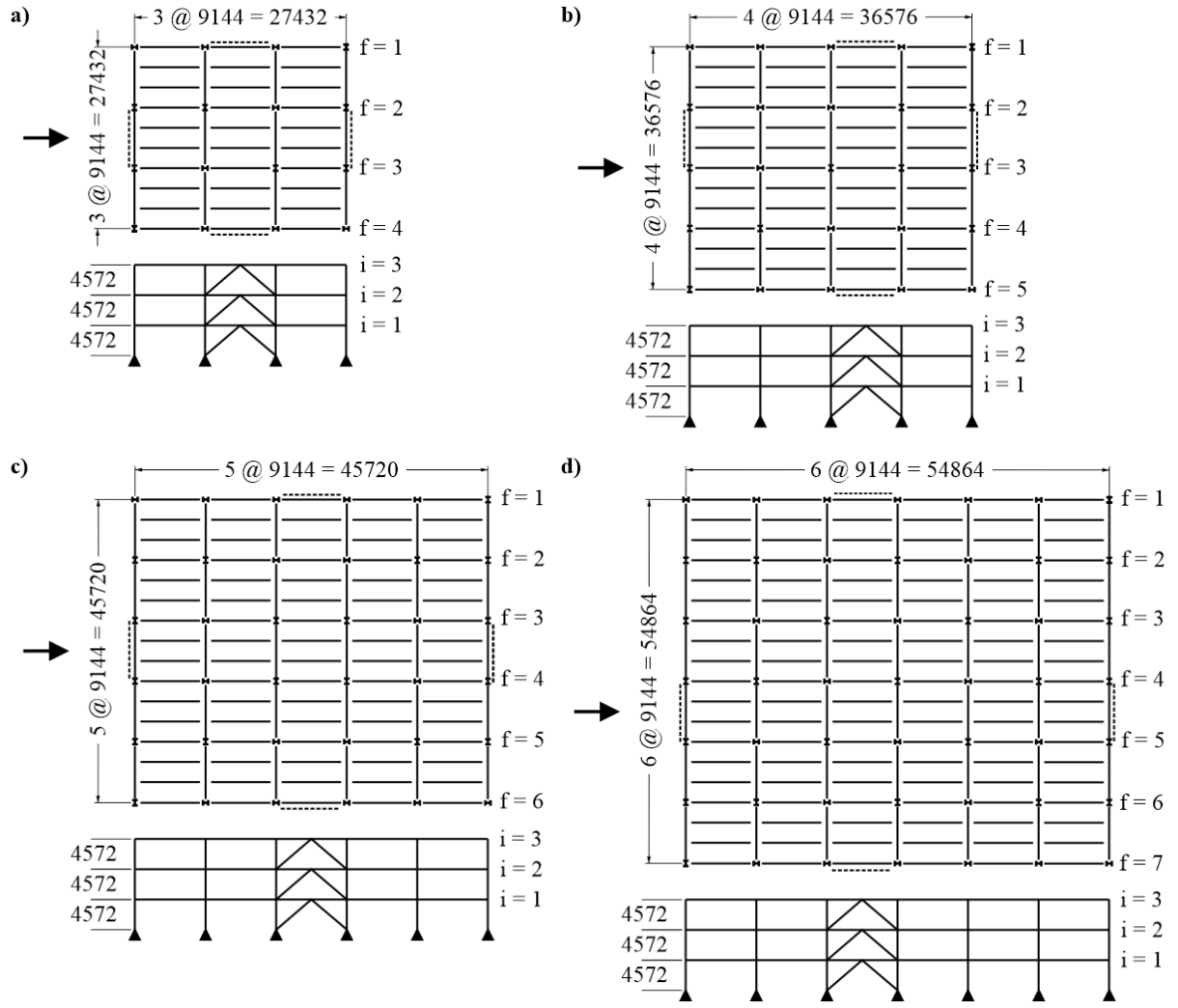
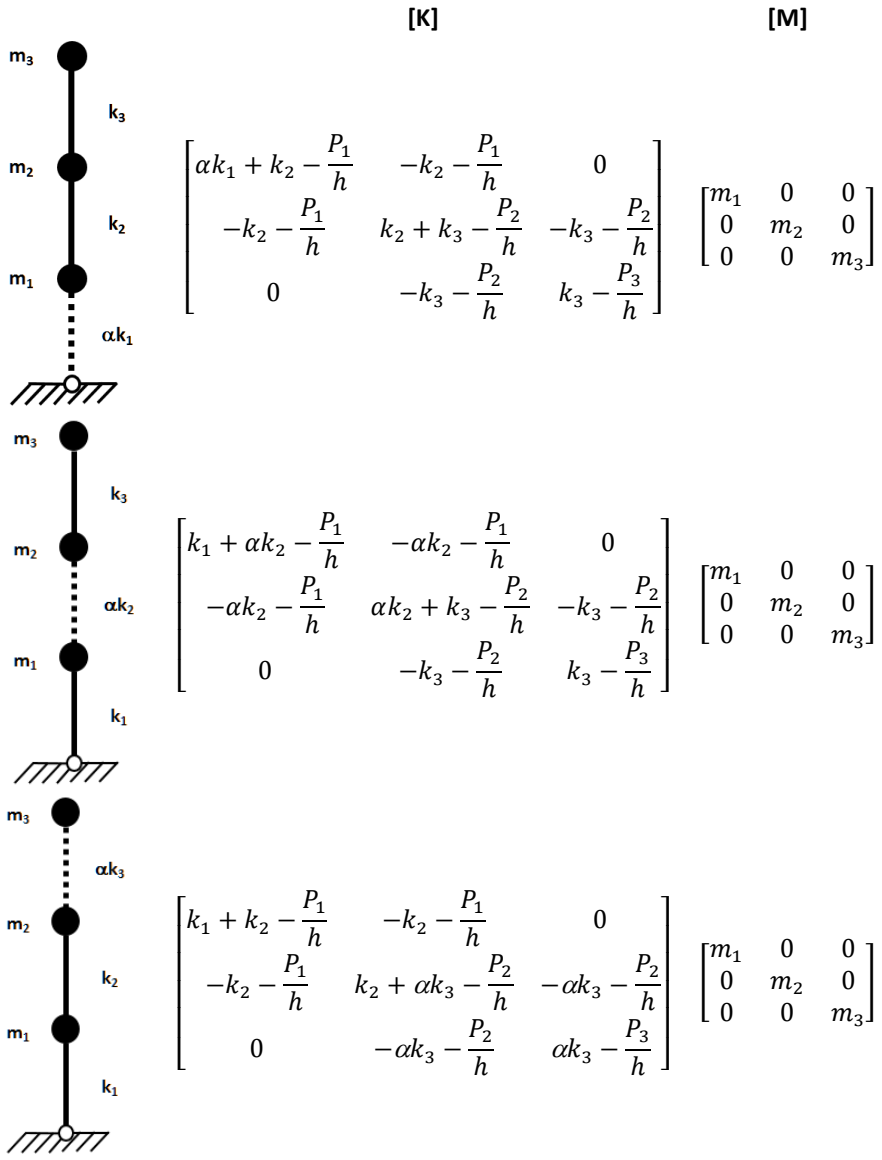


Figure 9.2. Configurations and dimensions of a) 3x3-, b) 4x4-, c) 5x5- and d) 6x6-bay buildings.

To perform this parametric study, the structures were modelled using simplified 3-DOF systems as illustrated in Figure 9.3. The stiffness and mass matrices of each system are also presented in the figure. At every level, the mass m_i corresponds to the total seismic weight at that level and the stiffness k_i corresponds to the storey shear stiffness at the level. The stiffness values were determined with a theoretical method by calculating the axial stiffness of the braces of the beam and of the column in series. (Stafford-Smith and Coull 1991) To simulate the effect of a brace connection failure in a given storey, a stiffness reduction factor α varying between 0.0 and 1.0 was applied to the stiffness value of that storey. As shown in Figure 9.3, the process was repeated for each storey.



$$\begin{bmatrix} \alpha k_1 + k_2 - \frac{P_1}{h} & -k_2 - \frac{P_1}{h} & 0 \\ -k_2 - \frac{P_1}{h} & k_2 + k_3 - \frac{P_2}{h} & -k_3 - \frac{P_2}{h} \\ 0 & -k_3 - \frac{P_2}{h} & k_3 - \frac{P_3}{h} \end{bmatrix} \quad \begin{bmatrix} m_1 & 0 & 0 \\ 0 & m_2 & 0 \\ 0 & 0 & m_3 \end{bmatrix}$$

$$\begin{bmatrix} k_1 + \alpha k_2 - \frac{P_1}{h} & -\alpha k_2 - \frac{P_1}{h} & 0 \\ -\alpha k_2 - \frac{P_1}{h} & \alpha k_2 + k_3 - \frac{P_2}{h} & -k_3 - \frac{P_2}{h} \\ 0 & -k_3 - \frac{P_2}{h} & k_3 - \frac{P_3}{h} \end{bmatrix} \quad \begin{bmatrix} m_1 & 0 & 0 \\ 0 & m_2 & 0 \\ 0 & 0 & m_3 \end{bmatrix}$$

$$\begin{bmatrix} k_1 + k_2 - \frac{P_1}{h} & -k_2 - \frac{P_1}{h} & 0 \\ -k_2 - \frac{P_1}{h} & k_2 + \alpha k_3 - \frac{P_2}{h} & -\alpha k_3 - \frac{P_2}{h} \\ 0 & -\alpha k_3 - \frac{P_2}{h} & \alpha k_3 - \frac{P_3}{h} \end{bmatrix} \quad \begin{bmatrix} m_1 & 0 & 0 \\ 0 & m_2 & 0 \\ 0 & 0 & m_3 \end{bmatrix}$$

Figure 9.3. 3-DOF system after the failure of the primary seismic load resisting system, with their stiffness and mass matrices including P-delta effects.

Eigenvalue analysis of the 3-DOF systems of Figure 9.3 was performed for all structures and for values of α between 0. and 1.0. The ratios of the elongated fundamental periods T_r obtained with α less than 1.0 to the initial fundamental period with = 1.0 are presented in Figure 9.4. The eigenvalue analysis was performed for each building size and site class (C and E) and these buildings gave similar results. In Figure 9.4, the envelope of the minimum and maximum period ratio is plotted as a range in gray, red and blue for the first, second and third storey respectively.

The average determined from the period ratio of the buildings with varying sizes and site class (C and E) is also plotted in Figure 9.4a and b for Vancouver and Montreal respectively.

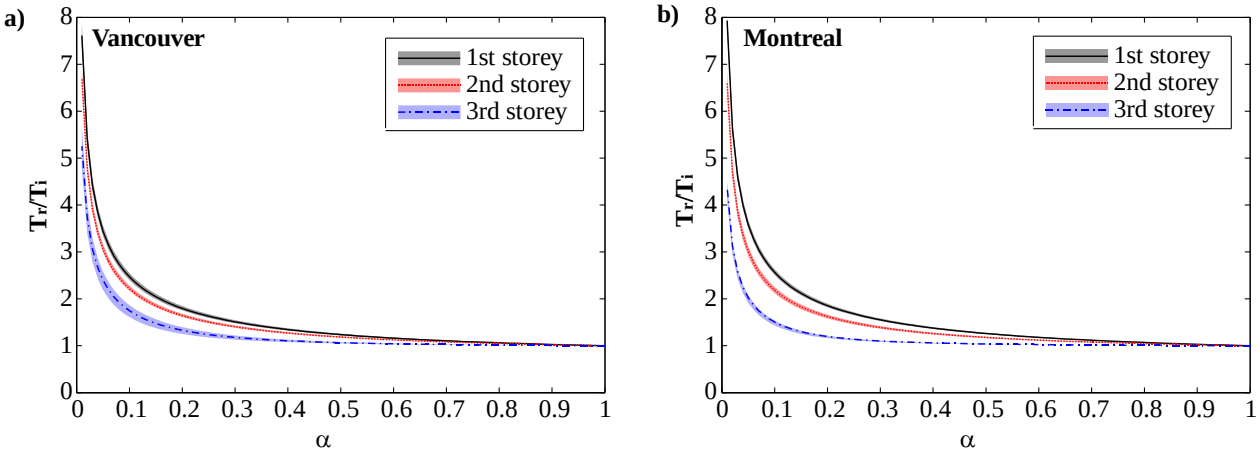


Figure 9.4. Influence of the loss in storey stiffness variability on the fundamental period of the buildings located in: a) Vancouver; and b) Montreal.

As shown in the figure, a reduction in the lateral stiffness in the first storey has a more pronounced effect on the fundamental period than the same reduction in the upper storeys. For all buildings at both locations, significant lengthening of the fundamental period, for example doubling of the fundamental period, is observed at values of α equal to approximately 0.17 in the first storey and 0.06 in the third storey.

The changes in seismic loads due to the reduction in storey stiffness was also examined. This is done by comparing the ratio of the design spectral ordinates, *S*, at the period T_r, $S(T_r)$, and at the initial period T_i, $S(T_i)$. The results are presented in Figure 9.5 using the same format as in Figure 9.4. As shown, the variation in force demand is more pronounced at the Montreal location as the drop in design spectral accelerations with period is steeper than in Vancouver. The larger lengthening of the period at the first storey result observed in Figure 9.4 result in a larger decrease in spectral acceleration.

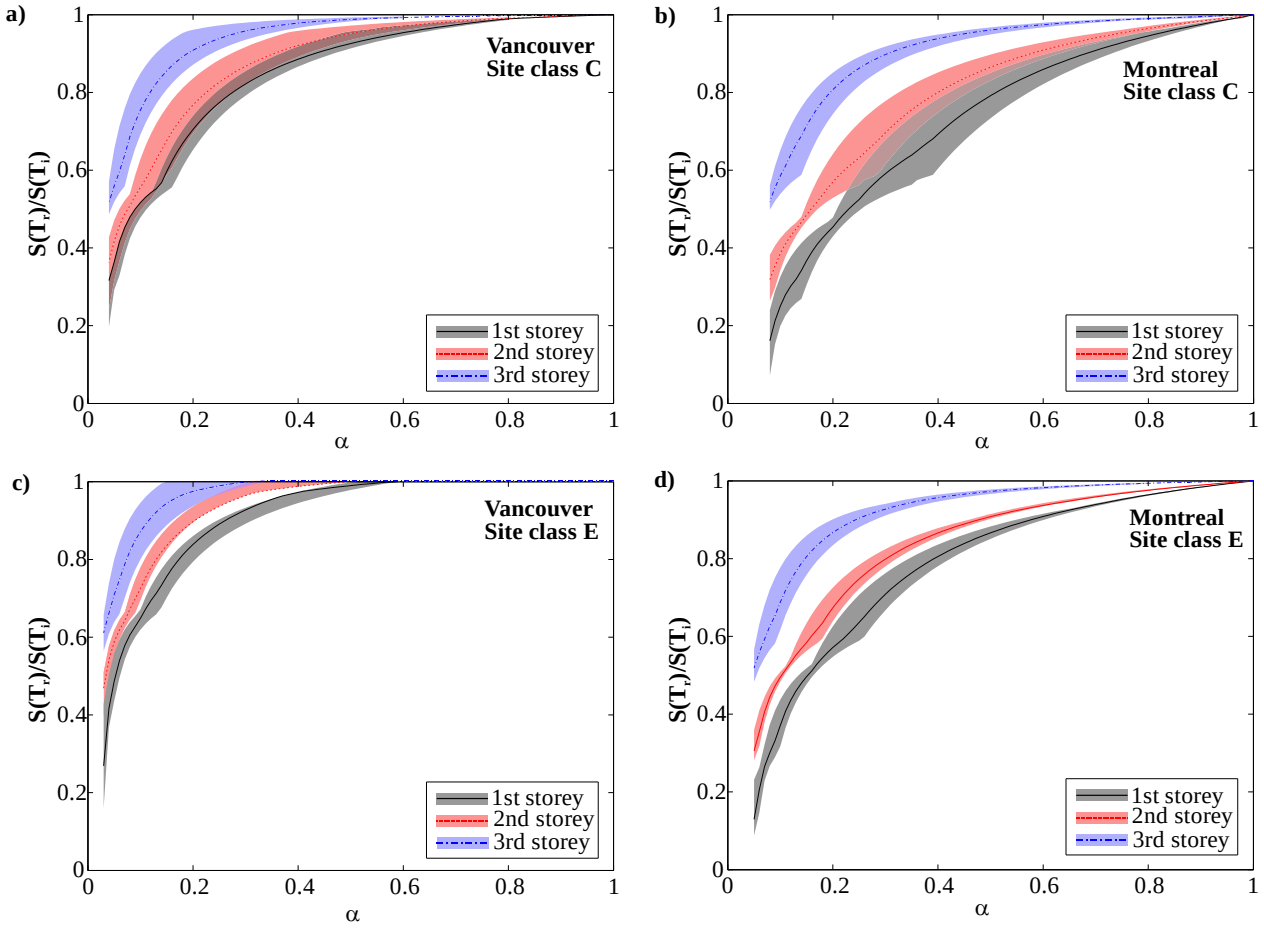


Figure 9.5. Influence of the loss in storey stiffness variability on the spectral acceleration of the buildings located in: a) Vancouver on site class C; b) Montreal on site class C; c) Vancouver on site class E; and d) Montreal on site class E.

9.2.2 Numerical validation with the building example

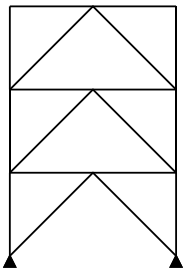
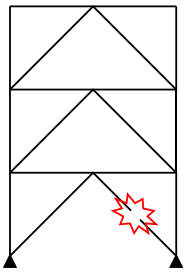
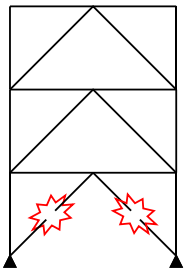
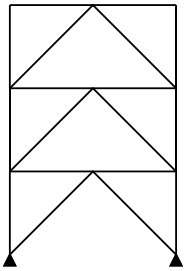
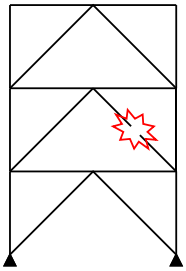
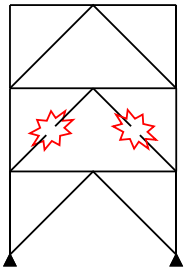
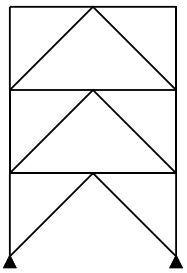
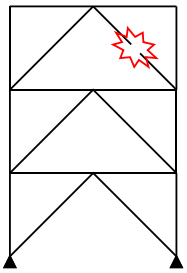
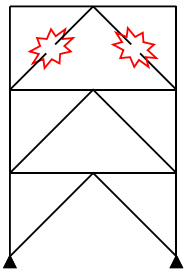
Modal analyses were also performed for the building example studied in Chapter 8 to quantify the shift in periods caused by brace connection failures in that building. In this section, the influence of stiffness reduction on building periods was performed for both cases: the structure with PR connections in the gravity frame (with a reserve capacity system) and the structure with pinned beam-column connections in the gravity frame (without a reserve capacity system). In Chapter 8, PR connections were only added between beams and columns at the first storey of the gravity frame. Modal analyses were performed with the OpenSees models of the structure by removing the bracing members with a failed connection. The periods in the first three modes of vibration of the

structure were calculated for the following 6 scenarios: brace connection failure in one brace and in two braces in any of the three storeys. For the structure with PR connections, the PR connections are those that were designed in Chapter 8. In the modal analyses of the structure with PR connections, it must be noted that the PR connection stiffness considered in the analyses is the initial connection stiffness, not the secant stiffness at a given storey drift.

The periods computed for each case are presented in Table 9.2. The period lengthening for each case is also given on the form of the ratio between the periods with failed brace connections and the periods with no brace connection failure. For the structures with pinned connections, brace connection failure results in significant lengthening in the fundamental period of the structure. As expected, this change is more important when connection failure occurs at the first storey and when connection failure occurs in both braces. For the later, more critical case, the fundamental period increases by 8.67 due to the fact that the residual stiffness in the first storey is only due to continuity of the structure columns. When brace connection fails in only one brace in the first storey, the first-storey stiffness also includes the contribution from the long link EBF response in the braced frame, which results in the lower period lengthening ratio of 5.11. Variations in second and third more periods are significantly less important with ratios varying between 0.98 and 1.67. The second and third mode periods are more affected when brace connection failure occurs in the third and second storeys, respectively.

For all cases considered, smaller variations in the fundamental period due to brace connection failure are observed when enhanced connections are implemented in the structure gravity frame. For instance, period lengthening ratios of 3.14 and 5.32 were obtained in the first mode due to brace connection failure in one and two braces at the first storey of the structure with a reserve capacity system, compared to 5.11 and 8.67, respectively, when the structure has pinned connections in the gravity frame. This beneficial effect of the PR connections on the change in first mode periods is also observed when brace connection failure occurs in the upper levels. However, the presence of the PR connections has limited influence on the increase in second and third mode periods, for all brace connection failure scenarios.

Table 9.2. Period shifts after brace failure with and without enhanced gravity connections

		Period (s)	Ratio	Period (s)	Ratio	Period (s)	Ratio
Gravity connections							
Pinned	T1	0.686	-	3.504	5.11	5.945	8.67
	T2	0.311	-	0.365	1.17	0.366	1.18
	T3	0.218	-	0.215	0.99	0.216	0.99
Enhanced	T1	0.680	-	2.136	3.14	3.617	5.32
	T2	0.309	-	0.352	1.14	0.376	1.22
	T3	0.217	-	0.216	1.00	0.234	1.08
							
Pinned	T1	0.686	-	1.758	2.56	1.996	2.91
	T2	0.311	-	0.304	0.98	0.306	0.98
	T3	0.218	-	0.267	1.22	0.268	1.23
Enhanced	T1	0.680	-	1.257	1.85	1.429	2.10
	T2	0.309	-	0.316	1.02	0.317	1.03
	T3	0.217	-	0.285	1.31	0.292	1.35
							
Pinned	T1	0.686	-	1.424	2.07	1.712	2.48
	T2	0.311	-	0.513	1.65	0.520	1.67
	T3	0.218	-	0.218	1.00	0.218	1.00
Enhanced	T1	0.680	-	1.087	1.60	1.150	1.69
	T2	0.309	-	0.506	1.64	0.505	1.63
	T3	0.217	-	0.224	1.03	0.219	1.01

9.3 Angle material testing results

The material properties of the angle specimens tested during the experimental program detailed in Chapter 4 were determined experimentally. Three types of coupons were tested to assess several properties of the material. The testing procedures were detailed in Chapter 3. A summary of the coupon types is presented with the results obtained from this complementary experimental program.

9.3.1.1 Coupon types

9.3.1.1.1 ASTM Standard

The first category of coupons corresponds to the Standard Plate-Type specified by ASTM8 (2000). Three coupons of 200 mm gauge were produced from each angle leg, resulting in 6 standard coupons per material, and 66 in total. The specific dimensions of a standard coupon are presented in Figure 9.6. These types of coupons were used to determine the yield stress and strain, as well as the maximum stress and ultimate strain of the angle material. The deformation at which the hardening of the steel begins was also identified.

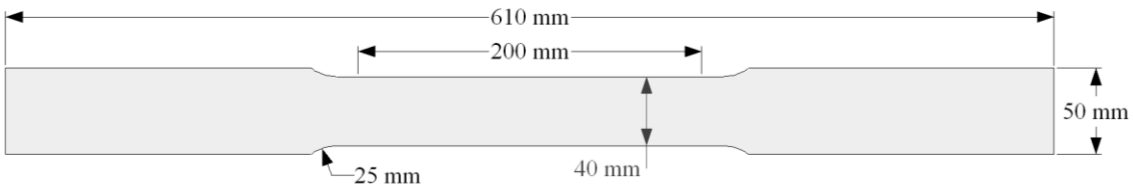


Figure 9.6. Dimensions of ASTM Standard coupons

9.3.1.1.2 ASTM Subsize

Another category of coupons tested corresponds to the Subsize type of ASTM8 (2000), whose dimensions are illustrated in Figure 9.7a. Four coupons are taken from each angle leg, two of which are parallel (longitudinal) to the angle fillet and the rolling process, whereas the two others are transversal to the fillet, as shown on Figure 9.7b. Since the direction of loading in the angle testing program was in the transversal direction, but the characterization of the material properties was performed longitudinally, the goal of the subsize specimens is to evaluate the impact of the loading direction on the yield and ultimate stresses.

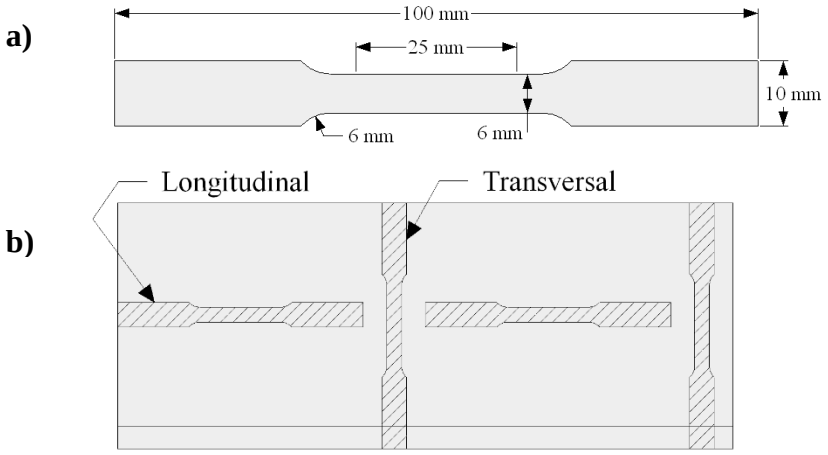


Figure 9.7. a) Dimensions and b) Position on angle leg of ASTM Subsize coupons

9.3.1.1.3 Strips coupons

The goal of the third type of coupons is to observe the variation in yield and ultimate stresses along the leg of the angles due to the rolling and cooling processes. To achieve this goal, several thin strips of non-standardized dimensions shown in Figure 9.8a have been taken from each angle leg, as illustrated in Figure 9.8b. The number of coupons for each angle dimension depended on the angle size. The fillet portion of the angle, as well as the edge of the legs were not transformed into strips due to the rounded section that rendered impossible an accurate measurement of the section area.

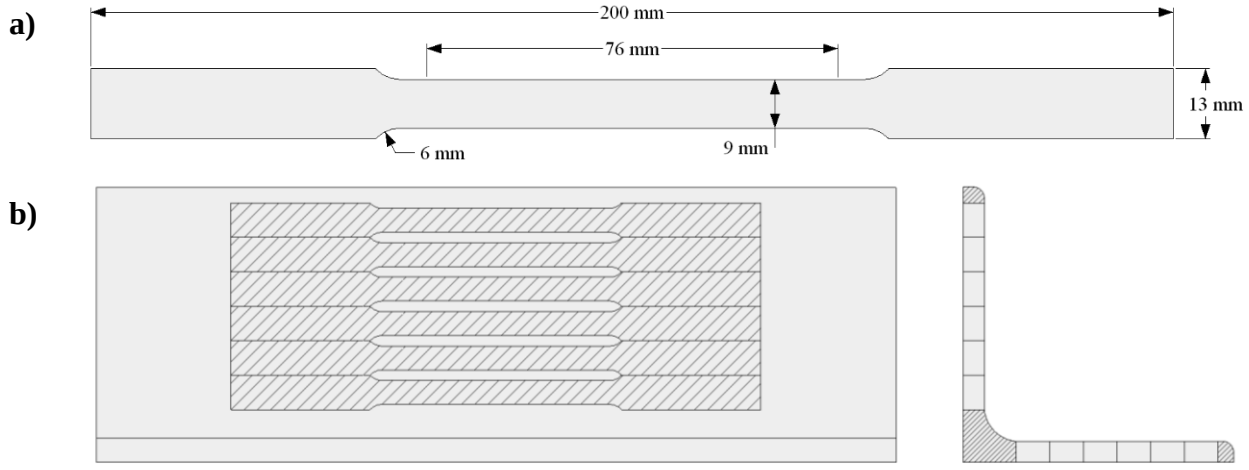


Figure 9.8. a) Dimensions and b) Position on angle legs of Strips coupons

9.3.2 Test results of ASTM Standard

Each specimen was identified by the angle leg dimensions from which it was sampled, preceded by the order in which the test was performed. For example, Specimen 2-4" of the L4x6x3/8 (TC1) batch of angles was the second specimen taken from the 4" long column leg of the angle. For this angle batch, Specimen 2-6" was taken from the beam leg. For angles with equal leg lengths, L4x4x5/16 (TC19), L6x6x3/8 A (TC7 & TC8) and L6x6x3/8 B (TC2 & TC15), three coupons were also sampled and tested for each leg but there was no distinction regarding which leg they were taken from (coupons were only numbered sequentially from 1 to 6, regardless of the leg).

These coupon specimens were used to determine the yield stress F_y and yield strain ε_y of the steel material. The 0.2% offset method described in ASTM8 (2000) was used to determine the yield stress. This method consisted of tracing a line parallel to the elastic portion of the measured stress-strain curve with an intercept with the strain axis at 0.2%. The stress at which this line intersected the stress-strain curve was taken as the yield stress $F_{y,0.2\%}$. The yield strain was taken as the strain value at the intersection of a horizontal line with an ordinate equal to the yield stress and the projection of the elastic portion of the measured stress-strain curve. These parameters are illustrated in Figure 9.9b.

Table 9.3 presents the so-obtained $F_{y\ 0.2\%}$ and ε_y values for each specimen, as well as the elastic modulus *E*. Figure 9.9a illustrates a typical stress-strain curve and the position of the relevant values characterizing the steel material.

During the test, values of the strain at the initiation of strain hardening, ε_h, ultimate tensile stress, F_u, and the strain at rupture, ε_{rupt}, were also measured. These parameters are illustrated in Figure 9.9a, and the values are given in Table 9.3.

During the tests, the imposed displacement was also paused three times for two minutes in the yield plateau, $\varepsilon_y - \varepsilon_h$ range, to measure the static yield stress, $F_{y\text{-}static}$. This static yield stress was lower than the stress measured upon imposing displacements, as pictured in Figure 9.9b. The average values of the three static values, $F_{y\ -\ Static\ avg.}$, are also given in Table 9.3. The average, standard deviation (SD) and coefficient of variation (COV) are also calculated for the three tests performed

on each angle leg. For the angles with equal legs, these data are given for the 6 tests performed. These values are also presented in Table 9.3. The ratio between the average value of each leg is also given for sections with unequal legs.

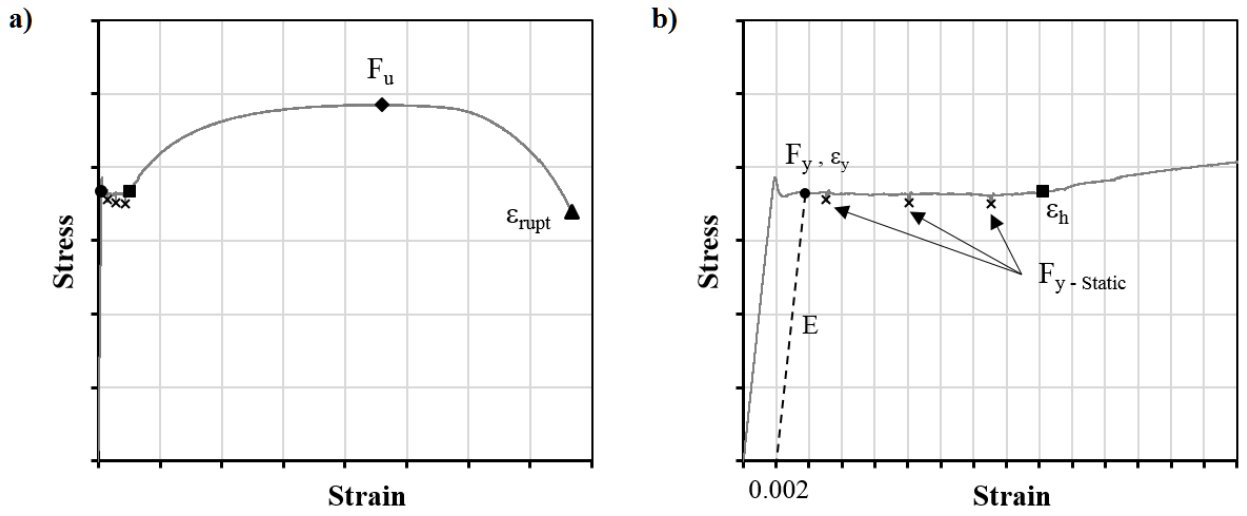


Figure 9.9. Typical stress-strain curve obtained from a tensile test: a) Entire curve; b) Close-up of the elastic and yield plateau regions of the curve.

Table 9.3. Material data from ASTM Standard coupons

Specimen	$F_{y,0.2\%}$	ε_y	$F_{y\text{ - Static avg.}}$	ε_h	F_u	ε_{rupt}	E
	MPa	-	MPa	-	MPa	-	MPa
L4x4x5/16 (TC19)							
1	377	0.0018	358	0.0205	511	0.2306	214411
2	373	0.0017	357	0.0202	502	0.2483	222162
3	371	0.0017	358	0.0182	506	0.2434	220036
4	372	0.0017	360	0.0191	505	0.2466	270436
5	378	0.0017	366	0.0219	516	0.2354	219617
6	373	0.0017	362	0.0209	511	0.2449	220331
Average	374	0.0017	360	0.0201	508	0.2415	227832
SD	2.83	0.0000	3.37	0.00	5.09	0.01	21033
COV	0.76%	0.00%	0.94%	0.00%	1.00%	4.14%	9.23%

Table 9.3. Material data from ASTM Standard coupons (Continuing)

Specimen	$F_{y,0.2\%}$	ε_y	$F_{y\text{ - Static avg.}}$	ε_h	F_u	ε_{rupt}	E
	MPa	-	MPa	-	MPa	-	MPa
L4x6x3/8 (TC1)							
1-4"	375	0.0017	366	0.015	537	0.234	219369
2-4"	377	0.0018	365	0.0135	537	0.229	213887
3-4"	382	0.0018	371	0.0152	542	0.245	216309
Average	378	0.0018	367	0.0146	539	0.236	216522
SD	3.61	0.0001	3.21	0.0009	2.89	0.008	2747
COV	0.95%	3.27%	0.88%	6.38%	0.54%	3.53%	1.27%
1-6"	375	0.0016	363	0.0167	537	0.243	230825
2-6"	374	0.0017	364	0.0178	537	0.2347	218118
3-6"	373	0.0019	361	0.0163	536	0.2375	196534
Average	374	0.0017	363	0.017	537	0.238	215159
SD	1.00	0.0002	1.53	0.0008	0.58	0.004	17336
COV	0.27%	8.81%	0.42%	4.59%	0.11%	1.77%	8.06%
4”/6”	1.011	1.059	1.011	0.859	1.004	0.992	1.006
L4x8x1/2 (TC3)							
1-4"	373	0.0018	363	0.015	517	0.2468	271105
2-4"	374	0.0019	361	0.0135	511	0.2327	197820
3-4"	373	0.0017	363	0.0156	518	0.2388	224412
Average	373	0.0018	362	0.0147	515	0.2394	231112
SD	0.58	0.0001	1.15	0.0011	3.79	0.0071	37099
COV	0.15%	5.56%	0.32%	7.36%	0.73%	2.95%	16.05%
1-8"	340	0.0016	327	0.0164	497	0.2613	232983
2-8"	344	0.0016	330	0.0166	497	0.2625	210891
3-8"	345	0.0016	330	0.0172	499	0.2651	240516
Average	343	0.0016	329	0.0167	498	0.2630	228130
SD	2.65	0.0000	1.73	0.0004	1.15	0.0019	15397
COV	0.77%	0.00%	0.53%	2.49%	0.23%	0.74%	6.75%
4”/8”	1.087	1.125	1.100	0.880	1.034	0.910	1.013
L6x6x3/8 A (TC7 & TC8)							
1	391	0.0018	380	0.0162	563	0.2289	235310
2	400	0.0017	389	0.0161	571	0.2319	228873
3	395	0.0018	385	0.0169	565	0.2256	245415
4	402	0.0018	386	0.0162	570	0.229	218031
5	395	0.0018	386	0.0158	566	0.2257	246468
6	395	0.0018	383	0.015	565	0.2306	218206
Average	396	0.0018	385	0.016	567	0.229	232051
SD	3.98	0.0000	3.06	0.0006	3.14	0.003	12613
COV	1.01%	2.29%	0.80%	3.88%	0.55%	1.12%	5.44%

Table 9.3. Material data from ASTM Standard coupons (Continuing)

Specimen	$F_{y,0.2\%}$	ε_y	$F_{y\text{ - Static avg.}}$	ε_h	F_u	ε_{rupt}	E
	MPa	-	MPa	-	MPa	-	MPa
L6x6x3/8 B (TC2 & TC15)							
1	369	0.0017	357	0.0174	514	0.2441	232873
2	370	0.0017	358	0.0167	516	0.2401	236653
3	370	0.0017	357	0.0178	516	0.2409	242825
4	374	0.0017	365	0.018	527	0.2355	218735
5	368	0.0017	360	0.0177	517	0.2496	231024
6	372	0.0017	360	0.017	520	0.2416	237568
Average	371	0.0017	360	0.017	518	0.242	233280
SD	2.17	0.0000	3.02	0.0005	4.68	0.005	8218
COV	0.59%	0.00%	0.84%	2.87%	0.90%	1.93%	3.52%
L6x8x1/2 A (TC9 & TC10)							
1-6"	363	0.0016	352	0.0173	522	0.2486	226559
2-6"	368	0.0017	354	0.0163	527	0.2496	213435
3-6"	363	0.0017	353	0.0168	522	0.2531	213645
Average	365	0.0017	353	0.0168	524	0.250	217880
SD	2.89	0.0001	1.00	0.0005	2.89	0.002	7517
COV	0.79%	3.46%	0.28%	2.98%	0.55%	0.94%	3.45%
1-8"	362	0.0017	351	0.0172	517	0.2505	233019
2-8"	361	0.0016	349	0.0181	516	0.2521	227851
3-8"	361	0.0017	350	0.0175	517	0.2549	211467
Average	361	0.0017	350	0.018	517	0.253	224112
SD	0.58	0.0001	1.00	0.0005	0.58	0.002	11252
COV	0.16%	3.46%	0.29%	2.60%	0.11%	0.88%	5.02%
6"/8"	1.011	1.000	1.009	0.933	1.014	0.988	0.972
L6x8x1/2 B (TC4 & TC16)							
1-6"	343	0.0015	335	0.0172	504	0.2598	222336
2-6"	343	0.0016	333	0.0181	500	0.2647	237299
3-6"	344	0.0016	332	0.0178	500	0.2618	230120
Average	343	0.0016	333	0.0177	501	0.262	229918
SD	0.58	0.0001	1.53	0.0005	2.31	0.002	7484
COV	0.17%	3.69%	0.46%	2.59%	0.46%	0.94%	3.25%
1-8"	346	0.0016	334	0.018	499	0.2654	212293
2-8"	337	0.0016	329	0.0176	496	0.2542	216125
3-8"	341	0.0016	331	0.0189	497	0.266	216503
Average	341	0.0016	331	0.018	497	0.262	214974
SD	4.51	0.0000	2.52	0.0007	1.53	0.007	2329
COV	1.32%	0.00%	0.76%	3.67%	0.31%	2.54%	1.08%
6"/8"	1.006	1.000	1.006	0.983	1.008	1.000	1.070

Table 9.3. Material data from ASTM Standard coupons (Continuing)

Specimen	$F_{y,0.2\%}$	ε_y	$F_{y\text{ - Static avg.}}$	ε_h	F_u	ε_{rupt}	E
	MPa	-	MPa	-	MPa	-	MPa
L6x8x5/8 A (TC11 & TC12)							
1-6"	364	0.0017	352	0.0199	474	0.277	217918
2-6"	359	0.0016	350	0.0209	474	0.2632	218569
3-6"	365	0.0017	355	0.0176	478	0.2687	217908
Average	363	0.0017	352	0.0195	475	0.270	218132
SD	3.21	0.0001	2.52	0.0017	2.31	0.007	379
COV	0.89%	3.46%	0.71%	8.69%	0.49%	2.58%	0.17%
1-8"	358	0.0017	346	0.0201	472	0.2744	212953
2-8"	355	0.0017	344	0.0214	468	0.2742	213624
3-8"	360	0.0016	348	0.0189	475	0.2696	226478
Average	358	0.0017	346	0.020	472	0.273	217685
SD	2.52	0.0001	2.00	0.0013	3.51	0.003	7622
COV	0.70%	3.46%	0.58%	6.21%	0.74%	1.00%	3.50%
6”/8”	1.014	1.000	1.017	0.975	1.006	0.989	1.002
L6x8x5/8 B (TC5 & TC17)							
1-6"	359	0.0016	347	0.0174	477	0.2701	228694
2-6"	360	0.0016	350	0.0197	479	0.2695	240929
3-6"	358	0.0017	348	0.0195	478	0.2657	211865
Average	359	0.0016	348	0.0189	478	0.268	227163
SD	1.00	0.0001	1.53	0.0013	1.00	0.002	14592
COV	0.28%	3.53%	0.44%	6.75%	0.21%	0.89%	6.42%
1-8"	350	0.0016	340	0.0183	473	0.2724	217020
2-8"	354	0.0016	343	0.0183	476	0.2704	234900
3-8"	345	0.0016	339	0.0175	472	0.2562	238753
Average	350	0.0016	341	0.018	474	0.266	230224
SD	4.51	0.0000	2.08	0.0005	2.08	0.009	11596
COV	1.29%	0.00%	0.61%	2.56%	0.44%	3.32%	5.04%
6”/8”	1.026	1.000	1.021	1.050	1.008	1.008	0.987
L6x8x3/4 A (TC13 & TC14)							
1-6"	341	0.0016	348	0.0091	524	0.2518	228148
2-6"	340	0.0016	329	0.0096	516	0.2533	219119
3-6"	336	0.0017	329	0.0098	516	0.265	199549
Average	339	0.0016	335	0.0095	519	0.257	215605
SD	2.65	0.0001	10.97	0.0004	4.62	0.007	14620
COV	0.78%	3.53%	3.27%	3.80%	0.89%	2.82%	6.78%
1-8"	337	0.0016	328	0.0099	513	0.2667	210621
2-8"	340	0.0016	330	0.011	516	0.2616	212749
3-8"	345	0.0018	329	0.0109	514	0.2567	194919
Average	341	0.0017	329	0.011	514	0.262	206096
SD	4.04	0.0001	1.00	0.0006	1.53	0.005	9738
COV	1.19%	6.93%	0.30%	5.74%	0.30%	1.91%	4.73%
6”/8”	0.994	0.941	1.018	0.864	1.010	0.981	1.046

Table 9.3. Material data from ASTM Standard coupons (End)

Specimen	$F_{y,0.2\%}$	ε_y	$F_{y\text{ - Static avg.}}$	ε_h	F_u	ε_{rupt}	E
	MPa	-	MPa	-	MPa	-	MPa
L6x8x3/4 B (TC6 & TC18)							
1-6"	373	0.0019	361	0.0204	486	0.2411	198560
2-6"	372	0.0017	360	0.0211	485	0.2782	213924
3-6"	372	0.0018	361	0.0176	487	0.2551	204817
Average	372	0.0018	361	0.0197	486	0.258	205767
SD	0.58	0.0001	0.58	0.0019	1.00	0.019	7726
COV	0.16%	5.56%	0.16%	9.40%	0.21%	7.26%	3.75%
1-8"	370	0.0018	357	0.0209	483	0.2642	206420
2-8"	365	0.0018	357	0.0211	485	0.2683	199834
3-8"	367	0.0018	353	0.0182	485	0.2728	208441
Average	367	0.0018	356	0.020	484	0.268	204898
SD	2.52	0.0000	2.31	0.0016	1.15	0.004	4501
COV	0.69%	0.00%	0.65%	8.07%	0.24%	1.60%	2.20%
6”/8”	1.014	1.000	1.014	0.985	1.004	0.963	1.004

The results presented in Table 9.3 show that the values from the 6 tensile tests gave consistent results. Standard deviations of the $F_{y,0.2\%}$ values stress for a given angle batch are generally below 1.3%, while the ultimate stress F_u remained below 1% of the average values. For all equal leg angles, the standard deviation for the 6 tests varied from 0.59% to 1.01%. For the specimens with unequal legs, the average yield stress $F_{y,0.2\%}$ of the column (shorter) leg was generally higher than the corresponding value for the beam leg. For all specimens, the ratio ranged between 0.994 and 1.087. The difference was highest for the L4x8x1/2 (TC3) batch, where mean value of F_y obtained for the 4” leg differed significantly from the value measured for the 8” leg: 373 vs 343 MPa.

Furthermore, an uncalibrated extensometer was inadvertently used in most tests, which translated into some doubtful measurements of the yield and ultimate strains, and it also explains the abnormally large elastic modulus E obtained in several tests.

For all specimens, the ratio between the average static yield stress $F_{y\text{ – Static avg.}}$ and the $F_{y,0.2\%}$ yield stress values averaged 97% with a COV of 0.9%. From all test, the measured values of $F_{y,0.2\%}$ vary between 1.17 and 0.97 times the minimum specified value of 345 MPa. On average, this ratio is equal to 1.06 with a COV of 4.5%.

9.3.3 Results of tensile tests on subsize coupons

For four angle batches, tensile tests were also performed using ASTM A370 subsize coupons to examine the differences in the yield and ultimate tensile stresses as a function of the loading direction. In this test programs, coupons were taken from both angle legs for both directions: parallel to rolling (longitudinal) and perpendicular to rolling (transversal). These additional tests were motivated by the fact that angles in the 2L-TS connections are bent in the direction perpendicular to rolling and the tensile tests presented in the previous section characterized the steel properties in the direction of rolling.

Each specimen was identified by the direction, either longitudinal or transversal, and the angle leg size from which it was carved out. For each direction and angle leg, two specimens, A and B, were tested. For equal leg angles, specimens A and B were also sampled from each of the two legs but the coupons are numbered only sequentially. Table 9.4 presents the yield and ultimate stresses for each specimen, as well as the average for the direction and angle leg. The ratio between the average longitudinal and transversal stresses, both yield and ultimate, L/T_{Fy} and L/T_{Fu} respectively, are also presented in Table 9.4. Figure 9.10 shows a typical stress-strain curve of an ASTM subsize coupon.

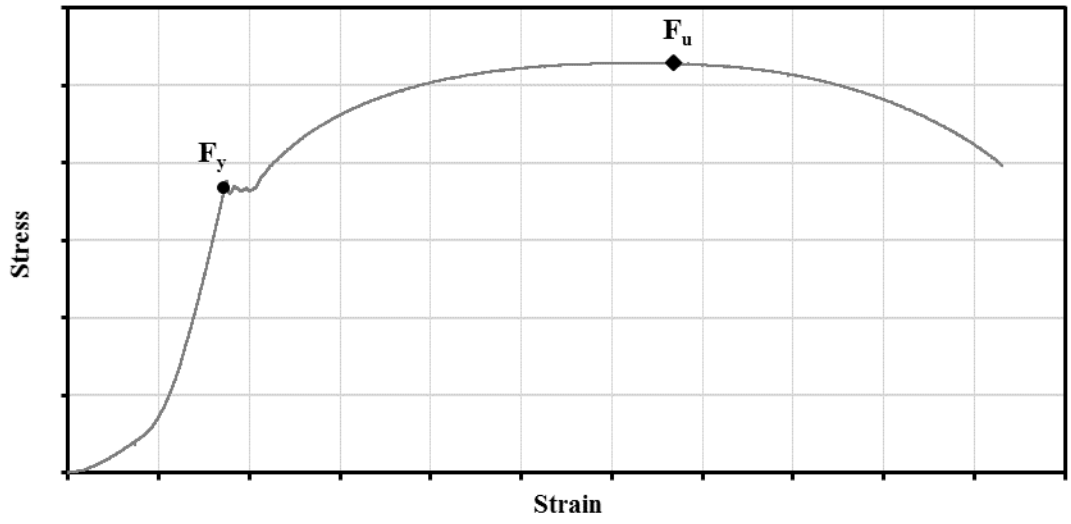


Figure 9.10. Typical stress-strain curve of ASTM Subsize and Strips specimens

Table 9.4. Material data for ASTM Subsize specimens

Direction	Specimen A		Specimen B		Average		L/T $_{Fy}$	L/T $_{Fu}$
	F_y	F_u	F_y	F_u	F_y	F_u		
	MPa	MPa	MPa	MPa	MPa	MPa		
L4x4x5/16 (TC19)								
Longitudinal 1	401	541	397	543	399	542	1.039	1.025
Transversal 1	391	535	376	523	384	529		
Longitudinal 2	393	533	388	535	390	534	1.021	1.021
Transversal 2	386	525	378	522	382	523		
L4x6x3/8 (TC1)								
Longitudinal 4"	375	545	377	543	376	544	0.989	1.004
Transversal 4"	379	541	380	543	380	542		
Longitudinal 6"	367	540	377	543	372	541	1.000	1.000
Transversal 6"	370	540	375	542	372	541		
L6x8x1/2 B (TC4 & TC16)								
Longitudinal 6"	342	507	347	507	345	507	0.989	0.990
Transversal 6"	347	512	352	513	350	512		
Longitudinal 8"	349	513	356	522	353	518	0.986	0.989
Transversal 8"	358	525	358	523	358	524		
L6x4x3/4 A (TC13 & TC14)								
Longitudinal 6"	350	532	352	537	351	535	1.000	0.985
Transversal 6"	352	543	350	544	351	543		
Longitudinal 8"	350	535	350	544	350	540	0.994	0.998
Transversal 8"	351	542	353	541	352	541		
						Average	1.002	1.001
						SD	0.0188	0.0146
						COV	2%	1%

This material investigation showed that no significant differences exist between the transversal and longitudinal results for either the yield or ultimate stress properties. The average ratio for the yield and ultimate stress remain near 1.0. Some variation is observed, with a COV between 2 and 1%, but no general trend can be drawn. Therefore, it can be concluded that strength properties obtained in the direction of rolling can be safely used for the direction perpendicular to rolling.

9.3.4 Results of tensile tests on strips coupons

Additional tensile tests were performed on strip coupons taken from the four angle batches that were used to perform the tensile tests on the ASTM subsize coupons. These tests were motivated by the fact that yielding of the 2L-TS angles of the PR connections develops in localized portions of the leg width and it was necessary to verify if the properties determined near the mid-width of the angle legs were representative of the properties at locations of the plastic hinges forming in the angle legs.

As mentioned in section 3.7, the angle legs were discretized into 12.7 mm (1/2") wide coupons with a small reduced section to evaluate the variation in yield and ultimate tensile stress properties across the angle legs. For each leg, the number of coupons varied depending on the available width of the flat portion of the leg. The coupons were identified based on their position relative to the fillet of the angles, starting with the coupon located the closest from the fillet: coupon number 1 for the beam leg and coupon number A for column leg.

For some of the larger angle sizes, the cumulated width of the material lost during cutting because of width of the saw blade resulted into some coupons being too small to be adequately machined with their reduced cross-section for testing. This occurred for angles L6x8x1/2B (TC4 & TC16) for which coupons 1, A and B could not be fabricated, and for angles L6x8x3/4A (TC13 & TC14) for which coupons 1 and A were not produced. In each test, the yield and ultimate stress properties were obtained using the procedure described for the ASTM subsize specimens. Table 9.5 presents those stresses, as well as the specimen location on the angle section.

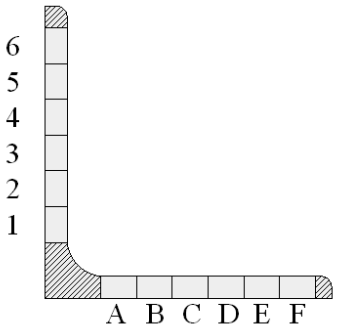
Figure 9.11 to 9.14 present the yield stress distributions across the angle legs for every angle batch tested. In the figures, the yield stress values have been normalized with respect to the average $F_{y,0.2\%}$ values obtained from the first series of tensile tests that were performed on ASTM standard coupons in the direction of rolling (Table 9.3). These reference values are designated as $F_{y,Standard}$ in Figures 9.11 to 9.14. For all angles, the yield stress ratios are close to 1.0 for the strip coupons taken near the center the angle legs. This correlation was expected because the coupons for the first series of tensile tests were sampled at the mid-width of the angle legs.

The yield stress values from the strip coupons near the fillet are compared to the $F_{y\ 0.2\%}$ yield stress obtained from the Standard ASTM coupons ($F_{y\text{-}Standard}$). These ratios are shown along the length of

each leg in Figures 9.11 to 9.14. Generally, these ratios remain within 2% from the values obtained from the series of tensile tests, except for the L4x6x3/8 (TC1) angle shown in Figure 9.12. For this angle, the first coupon strip was up to 15.8% larger than the Standard coupon yield stress. The figures also show that the $F_{y\text{-}Strip}/F_{y\text{-}Standard}$ ratios remain close to 1.0 for the strips located more than 25 mm from the edge of the legs. For the strips located with that 25 mm distance from the edge, the $F_{y\text{-}Strip}/F_{y\text{-}Standard}$ gradually increase to reach values of up to approximately 1.05. Therefore, the yield stress at the edge of the angles is generally larger, likely due to the rolling and/or cooling process used in the angle fabrication. The standard deviation within an angle leg remained below 2%, except for the L4x6x3/8 (TC1) that showed larger variations. The generally small standard deviation indicates a relatively constant yield stress along the leg. The variability in F_y revealed by the tests on the strip coupons thus remains relatively small. Based on the test performed, this variation is small and can be neglected in design. The standard deviation observed within each angle leg for the ultimate stress F_u remained below 2.5%, even for the L4x6x3/8 (TC1) specimens that showed larger variations with the yield stress. Again, the variability in F_u revealed by the strip coupon tests remains relatively small and can therefore be neglected in design.

Table 9.5. Material data from Strip coupons

Specimen	F_y MPa	F_u MPa	Specimen location on angle section
			L4x4x5/16 (TC19)
1	371	506	
2	369	505	
3	375	506	
4	374	504	
5	376	504	
6	372	495	
Average	373	503	
SD	2.64	4.18	
COV	0.71%	0.83%	
A	370	505	
B	371	508	
C	374	506	
D	381	504	
E	384	506	
F	384	508	
Average	377	506	
SD	6.44	1.60	
COV	1.71%	0.32%	
			L4x6x3/8 (TC1)
1	417	554	
2	375	529	
3	371	532	
4	373	525	
5	390	535	
6	415	544	
A	435	560	
Average	397	540	
SD	25.66	13.21	
COV	6.47%	2.45%	
B	402	542	
C	387	536	
D	379	522	
E	364	527	
F	368	528	
G	374	533	
H	375	526	
I	387	537	
J	395	537	
Average	381	532	
SD	12.53	6.56	
COV	3.29%	1.23%	



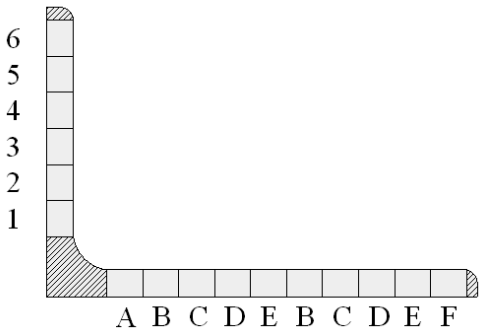


Table 9.5. Material data from Strip coupons (Continuing)

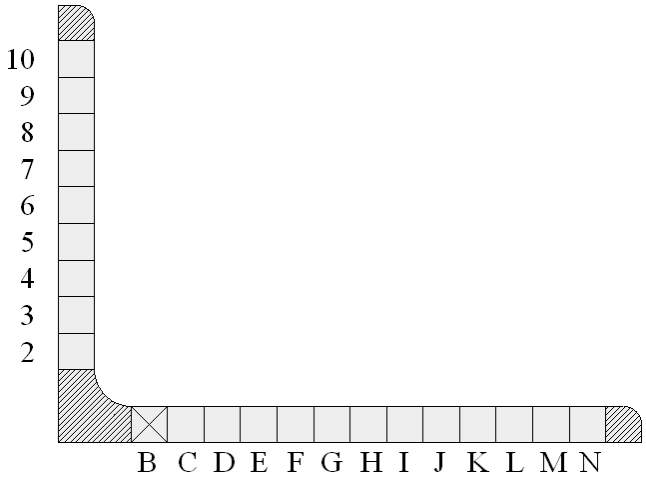
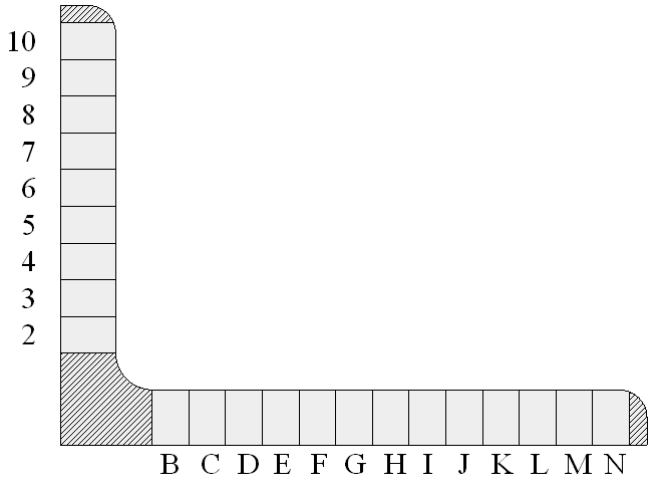
Specimen	F_y MPa	F_u MPa	Specimen location on angle section
L6x8x1/2 B (TC4 & TC16)			
2	351	506	
3	342	497	
4	350	509	
5	352	511	
6	350	508	
7	357	511	
8	359	510	
9	358	508	
10	361	512	
Average	353	508	
SD	5.96	4.53	
COV	1.69%	0.89%	
C	347	506	
D	344	507	
E	340	500	
F	343	501	
G	342	500	
H	343	496	
I	346	500	
J	343	494	
K	347	498	
L	350	504	
M	353	506	
N	361	508	
Average	347	502	
SD	5.81	4.52	
COV	1.68%	0.90%	

Table 9.5. Material data from Strip coupons (End)

Specimen	F_y MPa	F_u MPa	Specimen location on angle section
L6x8x3/4 A (TC13 & TC14)			
2	347	522	
3	345	521	
4	346	524	
5	344	521	
6	343	526	
7	344	524	
8	345	523	
9	342	508	
10	361	523	
Average	346	521	
SD	5.70	5.24	
COV	1.65%	1.01%	
B	339	514	
C	332	511	
D	336	513	
E	339	517	
F	338	513	
G	338	507	
H	339	512	
I	335	510	
J	334	509	
K	334	514	
L	338	514	
M	349	517	
N	356	511	
Average	339	512	
SD	6.56	2.90	
COV	1.93%	0.57%	



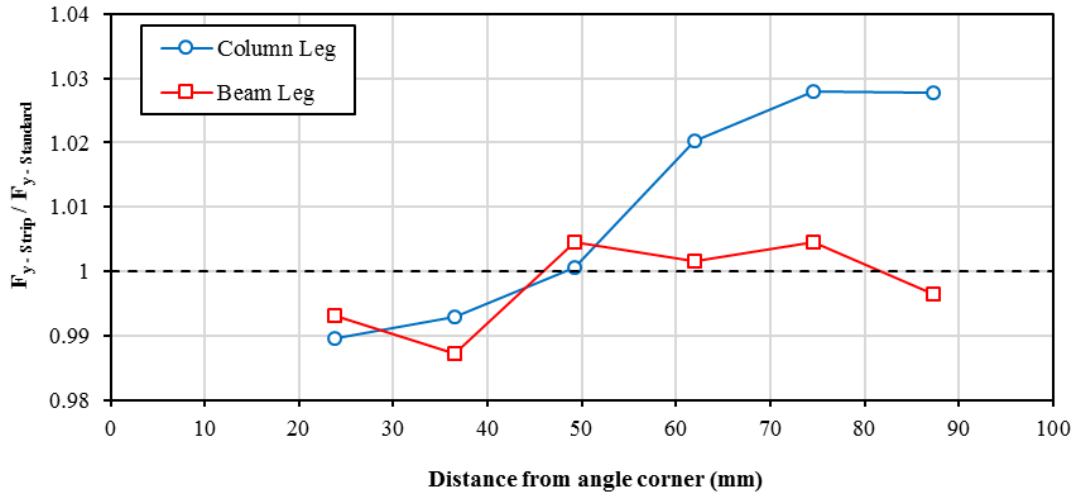


Figure 9.11. Yield stress distribution along angle legs for the L4x4x5/16 (TC19) angles.

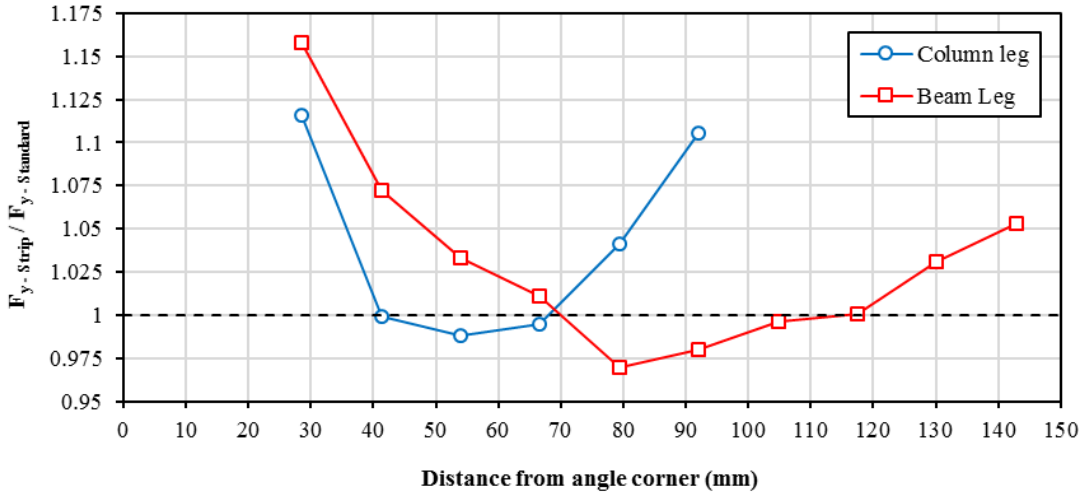


Figure 9.12. Yield stress distribution along angle legs for the L4x6x3/8 (TC1)

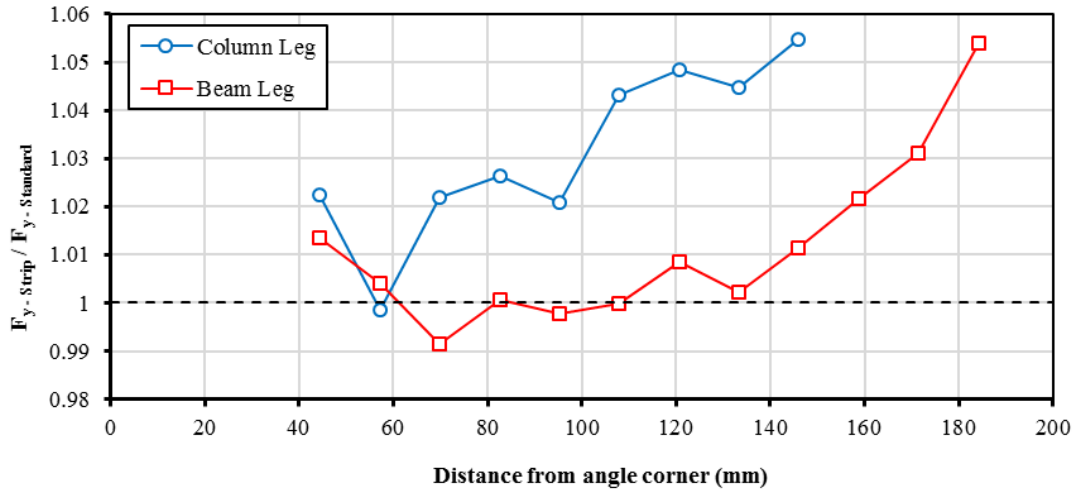


Figure 9.13. Yield stress distribution along angle legs for the L6x8x1/2 B (TC4 & TC16)

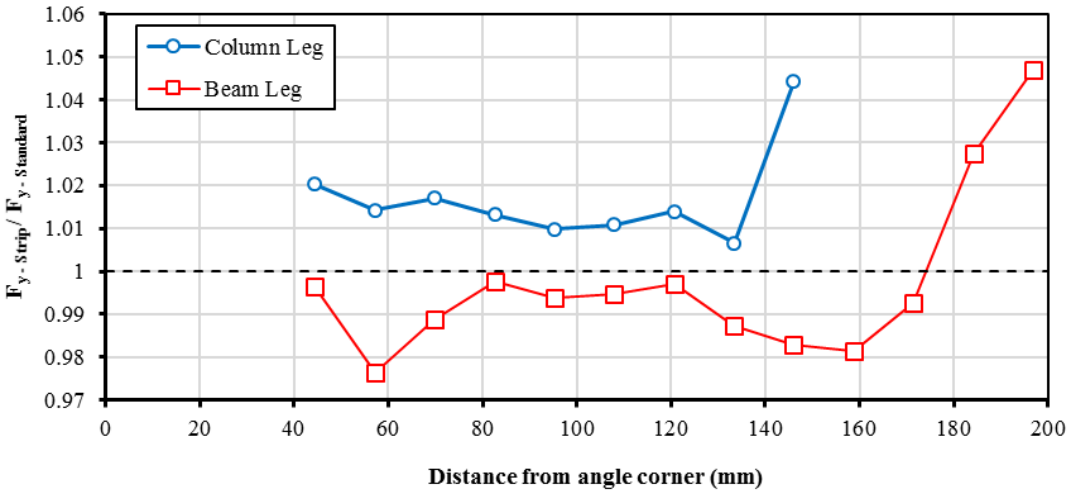


Figure 9.14. Yield stress distribution along angle legs for the L6x8x3/4 A (TC13 & TC14)

9.3.5 Conclusions on the angle material testing

The following conclusions can be drawn from the experimental investigations performed on the angle material:

1. For unequal leg angles, the average yield stress of the column (shorter) leg is generally higher by up to 2% compared to the average yield stress measured in the beam legs;
2. The ratio between the average static yield stress $F_{y\ -\ Static\ avg.}$ and the $F_{y,0.2\%}$ yield stress values averaged 97% with a COV of 0.9%.
3. The measured values of $F_{y,0.2\%}$ varied between 1.17 and 0.97 times the nominal stress of 345 MPa. On average, this ratio is equal to 1.06 with a COV of 4.5%.
4. No significant differences were observed between the yield and ultimate stress properties measured in the longitudinal (parallel to rolling) and transversal directions;
5. The yield stress measured within 25 mm from the edge of the angle legs was generally higher, by approximately 5%, compared to the values measured over the remaining of the leg width. Overall, the variation in the yield and ultimate stress within an angle leg is small and can be neglected in design.

9.4 General discussion on the hypotheses and limitations of the research project

This doctoral research project presents extensive experimental programs performed to characterize the nonlinear behaviour of bolted angle beam-column connections in the gravity frame. A mathematical model is proposed to define the hysteretic force-displacement behaviour of bolted angle components. This model can then be integrated in a component-based modeling approach to numerically represent the moment-rotation behaviour of bolted angle connections. A design procedure is then proposed to enhance the reserve capacity of the gravity framing system without amplifying the brace connection design load. In an effort to thoroughly assess the influence of enhanced gravity connections in the seismic behaviour of Type CC buildings, some limitations regarding the connection modeling and the design procedure were applied on the scope of the project. This doctoral project should be considered as a first step towards a logical methodology to consider the reserve capacity in seismic design.

9.4.1 Limitations of the connection modeling

9.4.1.1 Modeling of the concrete slab

Typical beam-column connections should include the effect of the concrete slab in its moment-rotation behaviour. However, the presence of slab was not included in the beam-column connection experimental program, which rather focused on the behaviour of bolted angles as a connection component. The numerical modeling performed to validate the design procedure with a design example then tried to reproduce the experimental results.

However, the concrete slab could be modeled in the component-based model used to represent the connections. Indeed, fibers can be added to the section above the top angle, to which is assigned a material representing the force-displacement behaviour of the slab. The maximum moment reached in the connection under positive rotation, when the concrete slab is compressed against the column flange, may be larger than the top angle compressive strength. However, as indicated in Figure 9.15, the positive moment capacity is reduced after a certain rotation θ^{+}_{max} because of the concrete

crushing against the column. The material used in the component-based model should include this behaviour.

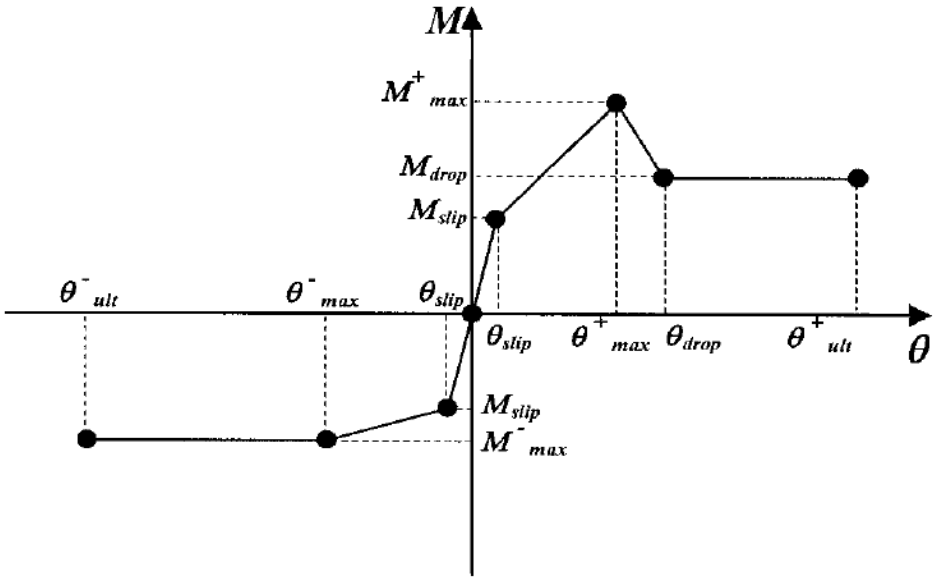


Figure 9.15. Envelope response of a connection with a concrete slab (Liu and Astaneh 2004).

Furthermore, in the double web angle models, the influence of the slab could be beneficial as it brings the neutral axis towards the upper flange of the beam. Therefore, the contribution of the web angle would likely be increased.

9.4.1.2 Modeling of the column panel zone

Furthermore, in typical beam-column connections, the column panel zone should also experience significant shear deformations. However, the column width was modeled with rigid extensions in the numerical modeling. This assumption is nevertheless coherent with the experimental tests where the moment-rotation behaviour of connection was measured at the column flange.

The panel zone shear deformation can be integrated in the numerical modeling by introducing *Joint2D* elements in the numerical model. This element, schematized in Figure 9.16, attaches each beam and column to the panel zone with rotational springs. Individual rotational stiffnesses can be assigned to each spring to represent the shear deformations of the panel zone. Adding this element into the numerical model could introduce further flexibility in the gravity system and modify the

design process. The *zerolengthsection* element representing the connection would be located between the end of the beam and Node 1 or 3 illustrated in Figure 9.16.

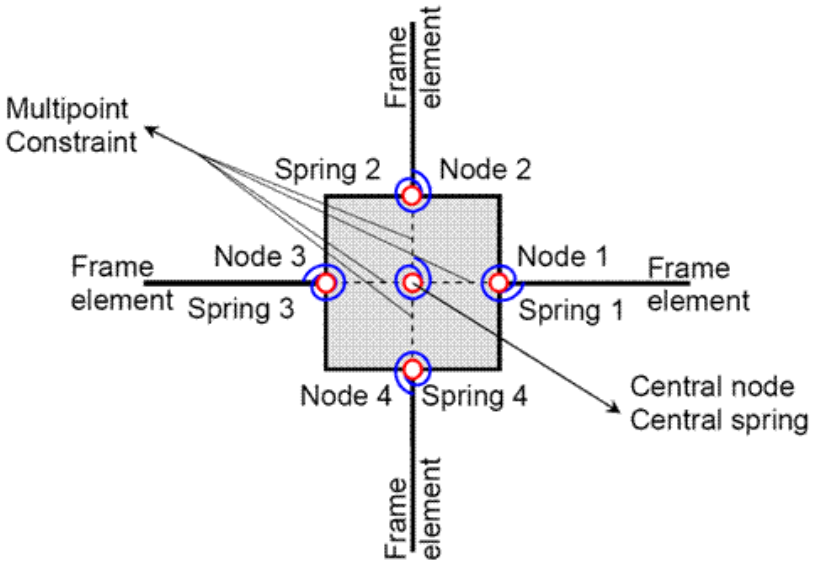


Figure 9.16. *Joint2D* element definition (Mazzoni et al. 2006).

9.4.1.3 Modeling of the gravity shear

The experimental program on the bolted angle connections showed that the gravity shear influenced the moment-rotation response of the connection. However, the experimental tests performed could not allow to establish a relationship between the shear load in the connection and its influence on the moment-rotation behaviour. Furthermore, during the numerical modeling, fiber sections were used to represent the connection. The fiber section formulation only allows the assignment of one material for each fiber, which corresponds to the force-displacement response of the angle component. Modeling the interaction between the shear load and axial load of each fiber would likely require the creation of another type of section. For this reason, the shear-moment interaction has not been included in the numerical modeling.

The vertical displacement of the connection has also been limited by aggregating the fiber section with a stiff elastic element. This modeling simplification was taken since the vertical displacements measured during the experimental program remained small. The additional moment caused by the vertical deformation of the connection and the axial load in the beams are thus also assumed negligible.

9.4.1.4 Modeling of the bolt slip

In the beam-column connection model, bolt slip was not included. This behaviour may reduce the connection stiffness and influence the design procedure. To include the slip, a material can be created by modeling in series the bolted-angle model and the bolt slip model, as pictured in Figure 9.17a. The bolt slip material is presented in Figure 9.17b, as proposed by Shen and Astaneh (2000). The load P_{slip} corresponds to the friction between the elements and the slip displacement δ_{slip} corresponds to the cumulative gap between the bolt and the fastened elements.

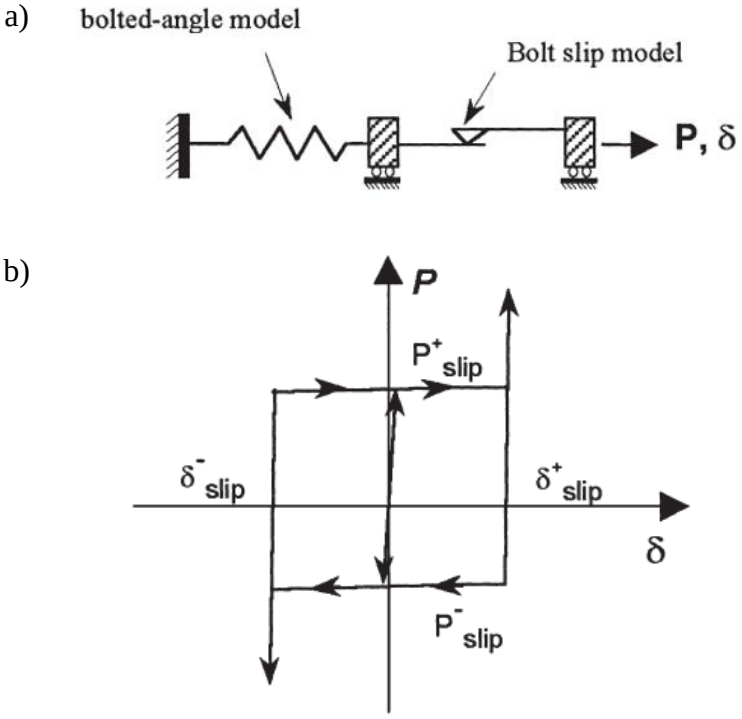


Figure 9.17. a) Modeling of fiber material in series; b) bolt slip model (Shen and Astaneh 2000).

9.4.2 Limitations of the design procedure

This doctoral project aimed at evaluating the possible contribution of the gravity framing system to the seismic robustness of SFRSs of the Conventional Construction category using enhanced beam-column connections. Several parameters can influence the contribution of gravity system to the lateral resistance and the most promising avenue was identified as the development and characterization of a double web bolted angle (2L) gravity beam-column connection enhanced with top and seat angles aiming at improving the building reserve capacity. This doctoral project was

thus limited to the influence of enhanced gravity connections. Furthermore, the connection design guidelines proposed in Chapter 8 aimed to reduce the required brace connection strength of type CC buildings with chevron brace configurations.

The enhanced connections of the proposed design procedure increase the building collapse prevention in its post-failure state. The design procedure for the connections thus allows failure of the SFRS by reducing the required brace connection strength. This design method varies from the typical approaches since failure of an element and significant changes in the building behaviour is tolerated. As illustrated in the design example presented in section 8.3, the presence of enhanced connections is beneficial to the collapse prevention and safety performance of the building. Further numerical studies are recommended with a wider range of building to assess the validity of the Type CC restrictions such as the height limit of 15 m or the amplified seismic loads above this limit.

The numerical validation of the design example was performed with the designed enhanced connections and with pinned connections in the gravity frame. The pinned connections represent the general assumption taken during the design of the SFRS. However, the influence of double web angle only has not been evaluated numerically. The moment-rotation behaviour obtained from the experimental tests on these connections remained quite small, their influence on the lateral stiffness of the building was assumed negligible. However, introducing these connections with the concrete slab effect may influence significantly their contribution to the reserve capacity. Such analysis could be beneficial to assess the influence of the enhanced connections only.

Also, the doctoral research project only focuses on chevron brace configuration buildings. Although this configuration is widely used with Type CC buildings and offers significant reserve capacity after failure of a brace connection, other common configurations such as X-bracing should be investigated. In the design example presented in section 8.3, the reserve capacity created by the long-link EBF (Sizemore 2017, Tremblay 2018) contributes significantly to the residual stiffness of the building after brace failure. Therefore, modifying the brace configuration would also modify the proposed design procedure. A method to evaluate the residual stiffness of other brace configurations could nevertheless be developed and introduced in the proposed procedure instead of the chevron residual stiffness.

Furthermore, the residual stiffness of the chevron braced frames is provided by the mobilization of the beam flexural stiffness. To increase the residual stiffness, the designer could opt to increase the beam size rather than enhance every connection in the building. By increasing the size of the beam, the designer should proceed with caution to avoid failure in the remaining brace connection. Also, this approach does not present as much redundancy as the enhanced connections, which may influence its collapse prevention capacity. Nevertheless, this option may be economically viable but was not studied as it was outside the scope of the research project.

Moreover, other structural elements and behaviour, such as the column base connections and the brace reengagement after failure, may contribute significantly to the reserve capacity of the building and their contribution should be investigated further. The column continuity was included in the design procedure through the simple stiffness equations proposed which calculates the lateral stiffness of the gravity frames as moment frames. However, some discrepancies were observed between the moment distribution in the gravity columns of the numerical model and the expected moment frame distribution. Indeed, the moment distribution in the gravity columns rather follows the pattern observed in a soft-storey mechanism. Therefore, this aspect of the proposed design method could be improved. Furthermore, the design procedure is only valid for brace connection fracture occurring in the first storey. It would be possible to develop the procedure to account for brace connection fracture in the upper storeys. This consideration should however acknowledge the complex dynamic response of the building with a storey significantly more flexible than the others.

CHAPTER 10 CONCLUSION AND RECOMMANDATIONS

10.1 Conclusions

The design process of Type CC SFRSs does not require capacity design and most of the design can be performed quickly based on elastic analysis results, which represents a strong incentive to design engineers for selecting this type of SFRSs. The limited ductility of this system is provided by the inherent ductility of steel and slip in connections to accommodate inelastic deformations and dissipate the seismic energy. The lack of control on the inelastic response and yielding hierarchy can lead to undesirable failure mechanisms such as a soft story or brittle failures in the SFRS. The frame action resulting from the rotational stiffness and strength of gravity beam-column connections can provide additional lateral strength and stiffness to form a reserve capacity system that can significantly enhance the seismic robustness of the structure. Therefore, a connection design that ensures minimum lateral strength, stiffness and ductility from the gravity system can increase considerably the redundancy and seismic collapse capacity of the structure, especially if a failure occurs in the primary SRFS. To evaluate the possible contribution of the gravity framing system to the seismic robustness of Type CC SFRSs using enhanced beam-column connections, analytical and experimental work has been performed. The findings of this work are discussed briefly in the following subsections.

10.1.1 Bolted angle component behaviour

A first experimental program aimed at characterizing the nonlinear behaviour of bolted angle components was conducted. The specific objectives of this program were:

1. **Characterize the influence of geometrical parameters on the angle behaviour:**
    a. Column bolt gauge;
    b. Angle thickness;
2. **Characterize the influence of different loading conditions on the angle behaviour:**
    e. Strain rate of loading;
    f. Static cyclic loading;
    g. Dynamic time-history loading;
    h. Low-cycle fatigue loading;

3. **Characterize the influence of bolt detailing parameters on the angle behaviour:**
    c. The grade of the column bolts (A490 or A325);
    d. The column bolt pretension.

A total of 139 tests were performed on 19 different bolted angle geometries. The results from the monotonic tests were used to determine the parameters of an established power model (Filippou et al. 1983) which can be used to predict the monotonic nonlinear response of the angle. The following conclusions were obtained from this experimental program:

a. Every test exhibited a ductile behaviour characterized by large deformations and a significant tensile capacity. An important part of this tensile capacity was even developed after the angle yielding;
b. An increasing column bolt gauge translated into a more flexible angle, with a smaller tensile capacity, but a larger displacement capacity;
c. An increasing angle thickness implied a stiffer behaviour of the angle, with a larger tensile capacity, but a lesser displacement capacity;
d. The thickness has a larger impact on the angle stiffness than the column leg flexural span.;
e. The bolt head and the angle fillet were unable to offer fixed boundary conditions to the column leg of the angle. However, those boundary conditions tended to act more as fixed as the aspect ratio g_2/t increased.;
f. The static monotonic curve represented a good approximation of the backbone curve for static cyclic tests, although their deformation capacities were reduced compared to the same angle geometry subjected to monotonic loading due to excessive yielding and low-cycle fatigue;
g. The reloading stiffness was similar to the secant stiffness of the angle;

Additionally, testing was performed on the angle material to assess its properties. The following conclusions were made:

a. The average yield stress of the column leg was generally larger by up to 2% compared to the average of the beam leg, due to the rolling and cooling process of those hot-rolled angles;

b. No significant difference between the transversal and longitudinal results for either the yield or ultimate stresses were observed. Therefore, the hot rolling process, the cooling process and the residual stresses in the angles do not affect significantly the isotropic properties of the material; and

In general, the nonlinear behaviour exhibited by bolted angles showed large ductility and resistance, which can translate into a substantial energy-dissipation capacity under seismic loading conditions. However, some previous studies (Azizinamini 1985, Citipitioglu et al 2002, Danesh et al. 2007) mentioned large discrepancies between the angle behaviour observed in full-sized beam-column connections and simple pull tests, as the ones performed in this experimental campaign.

10.1.2 Bolted angle beam-column connection behaviour

To resolve this problem, a second experimental program on full-scale beam-column connections loaded simultaneously in shear and rotational demand has been conducted at École Polytechnique de Montreal to characterize the global nonlinear behaviour of bolted angle connections. More precisely, the second test program had the following specific objectives:

4. **Characterize the influence of top and seat angles on the connection behaviour;**
5. **Characterize the influence of geometrical parameters on the connection behaviour:**
    a. Beam depth of 310 and 410 mm;
    b. Top and seat angles thickness and column gauge; and
    c. Column section.
6. **Characterize the influence of shear loading on the angle behaviour.**

In general, the nonlinear behaviour exhibited by bolted angle connection specimens showed large ductility, which translated into a substantial energy-dissipation capacity under seismic loading conditions. The following conclusions were made:

a. In general, the behaviour of the bolted angles in the connection tests were similar to the angle component pull tests. However, because of the beam leg rotation and the shear loading, larger plastic rotations were observed in the beam leg;
b. The presence of top and seat angles increased significantly the moment capacity of the connection and modified the deformation pattern observed during the test. Indeed, the

connections with top and seat angles failed in the top angle, while the double web angle cracked on the top side of the connection;

c. The negative moment capacity of connections with top and seat angles was larger than the positive one, because of the larger loading of the web angles;
d. Distinct deformation patterns were observed in the specimens loaded with and without a connection shear;
e. In double web angle connections, the presence of shear load created a complex deformation pattern resulting in a highly nonlinear hysteretic behaviour;
f. Every connection tested was able to sustain their design shear load, even after experiencing large rotational demands and plastic deformations;

In general, the nonlinear behaviour exhibited by bolted angle connections showed large ductility, which translated into a substantial energy-dissipation capacity under seismic loading conditions. Furthermore, the addition of top and seat angles allows a significant increase of the connection moment capacity. Therefore, the use of bolted angles for gravity framing connections can be beneficial as their large redundancy combined to their significant energy-dissipation capacity can enhance the reserve capacity of the building and thus mitigate the building collapse Type CC braced frames.

10.1.3 Bolted angle hysteretic behaviour mathematical model

The parameters required to recreate the results of the bolted angle monotonic tests with the *Steel02* material of OpenSees (Mazzoni et al. 2006) were determined. However, some discrepancies between the hysteretic behaviour obtained form the experimental tests and the *Steel02* material of OpenSees (Mazzoni et al. 2006) were identified. To mitigate these divergences, some modifications have been proposed to the mathematical model to increase the model precision to recreate the hysteretic behaviour specific to bolted angles. The input parameters of this proposed mathematical model were determined for each cyclic test of the bolted angle experimental program. Empirical equations based on geometrical and material properties were proposed to recreate the hysteretic behaviour of any bolted angle configuration.

This mathematical model was also implemented in OpenSees as a Uniaxial material (Mazzoni et al. 2006). The hysteretic behaviour obtained in the full-scale beam-column connection

experimental program were accurately recreated with a simple component-based modeling approach.

10.1.4 Enhanced gravity connection design approach

A design approach was proposed to improve the reserve capacity of Type CC buildings using enhanced 2L-TS connections in the gravity frame. Guidelines were proposed to achieve adequate seismic response for steel building structures with Type CC chevron braced frames, while minimizing changes to design procedures of other building components such as gravity beams and columns. Relaxation of the increased brace connection strength requirement was also investigated. A design example of a 3-storey building located in Montreal was performed. This design example was then modeled in OpenSees to assess the dynamic response of the building with enhanced connections. The following conclusions were drawn:

a. The enhanced connections do not have a significant influence on the maximum base shear or the fundamental period of the unfractured building;
b. The component-based model of the connection exhibited a ductile behaviour as expected during the numerical modeling.
c. The presence of enhanced connections reduced the moment developed at the top of the gravity column; and
d. The maximum first storey drift experienced by the models with enhanced connections is smaller than the one experienced by the model with the pinned connections. The maximum storey drift of the building with the enhanced connection was limited to 3%. This storey drift is smaller than the one anticipated during the design process;

10.2 Original contribution

The research work of this Ph.D. project aimed to evaluate the possible contribution of the gravity framing system to the seismic robustness of SFRSs of the Conventional Construction category using enhanced beam-column connections. To fulfill this objective, two experimental programs were conducted, the results were processed to accurately recreate the nonlinear behaviour and a design procedure was proposed. Within the framework of this Ph.D. project, the following original contribution have been made:

1. Characterization of bolted angle hysteretic behaviour through data processing acquired during an extensive experimental program;
2. Development of a mathematical model that can accurately represent the hysteretic behaviour of bolted angle components. This model has been calibrated with experimental results and empirical equations based on angle material and geometrical properties were proposed;
3. Implementation of the mathematical model in the OpenSees framework to model beam-column connections with a component-based approach;
4. Characterization of hysteretic behaviour of bolted angle beam-column connections subjected to simultaneous flexural moment and gravity shear;
5. Development of a design procedure for enhanced gravity connections to improve the building reserve capacity and validation of the design procedure with a design example and numerical modeling.

Results and findings have been submitted for publication in scientific journals specialized in structural engineering and are presented in the thesis. Additionally, research work performed in the course of the Ph.D. project has been published in the following journals and conference proceedings:

1. Davaran, A., Beland, T., Tremblay, R. (2019) “Elastic-plastic analysis of bolted angles usable in steel frame connections”. *Journal of Structural Engineering.* 145(7).
2. Beland, T., Tremblay, R., Sizemore, J., Fahnestock, L. Bradley, C., Hines, E. (2018). “Contribution of beam-column connections with bolted angles in the reserve capacity and full-scale cyclic testing”. *Key Engineering Materials.* 763. pp. 475-484.
3. Beland, T., Tremblay, R., Fahnestock, L., Hines, E., Bradley, C., Sizemore, J., and Davaran, A. (2017). “Hysteretic Behavior Modeling of Beam-Column Connections Made of Bolted Angles Based on Experimental Testing.” *In Proceedings of 3rd Huixian International Forum on Earthquake Engineering for Young Researchers.* Urbana, IL.

4. Beland, T., Sizemore, J., Bradley, C., Tremblay, R., Hines, E., and Fahnestock, L. (2016). "Behavior, Testing and Modeling of Beam-Column Angle Connections." *In Proceedings of 8th International Workshop on Connections in Steel Structures*. Boston, MA.

5. Beland, T., Tremblay, R., and Fahnestock, L. (2015). "Experimental Investigation of the Cyclic Response of Bolted Angles in Gravity Beam-to-Column Connections for Enhanced Seismic Performance." *In Proceedings of 6th International Conferences on Advances in Experimental Structural Engineering & 11th International Workshop on Advanced Smart Materials and Smart Structures Technology*. Urbana, IL.

6. Beland, T., Bradley, C., Nelson, J., Davaran, A., Hines, E., Tremblay, R., and Fahnestock, L. (2014). "Experimental Behavior of Bolted Angles and Beam-to-Column Connections." *In Proceedings of Structures Congress 2014.* American Society of Civil Engineers, Boston, MA. 2405-2416.

7. Davaran, A., Tremblay, R., Beland, T., Fahnestock, L., and Hines, E. (2014). "Experimental Behavior of Low-Ductility Brace Connection Limit States." *In Proceedings of Structures Congress 2014.* American Society of Civil Engineers, Boston, MA. 2429-2441.

8. Fahnestock, L., Hines, E., Tremblay, R., Davaran, A., Sizemore, J., Bradley, C., Nelson, J., and Beland, T. (2014). "Reserve Capacity and Implications for Seismic Collapse Prevention for Low-Ductility Braced Frames in Moderate Seismic Regions." *In Proceedings of Tenth U.S. National Conference on Earthquake Engineering 10NCEE.* Anchorage, AK.

9. Nelson, J., Davaran, A., Beland, T., Bradley, C., Hines, E.M., Tremblay, R., and Fahnestock, L.A. (2014). "Cyclic experimental behavior of angles and applications for connection design and modeling." *In Proceedings of Structures Congress 2014.* American Society of Civil Engineers, Boston, MA. 2381 – 2392.

10.3 Recommendations

10.3.1 Design recommendations

Because of the redundancy in gravity connections, adding top and seat angles to gravity connections can enhance the reserve capacity of the building and mitigate excessive storey drift, soft storey mechanism and building collapse. Numerical validation of the design example showed that enhanced gravity connections offer sufficient lateral capacity in case of brace connection fracture. Therefore, brace connections in the braced frames can be designed for load combinations including seismic loads determined with R_d = 1.5. In this case, the ductile behavior can be supplied by the enhanced gravity system in case of a brace connection failure in the braced frames. However, some guidelines should be followed:

5. The beam and column sections of the gravity frame are designed to resist the gravity load only;
6. The 2L angles must be designed to resist vertical shear from gravity load only, using the design method for regular simple shear connections;
7. In any storey and along each direction, the TS angles used to form the PR connections in the gravity frame must satisfy the following requirements assuming that failure has occurred in one brace connection of all braced frames in that storey:
    a. The PR connections must have sufficient flexural stiffness in the nonlinear range such that the storey shear stiffness of the structure exceeds the negative stiffness from P-delta effects and limit the storey drift to an acceptable value.
    b. The PR connections must have a flexural resistance at the maximum anticipated storey drift such that inelastic rotation will be limited to the PR connections and will not develop in the beams and columns of the of the gravity frame.

10.3.2 Recommendations for future work

10.3.2.1 Bolted angle component behaviour

An experimental program was performed to characterize the influence of a wide range of variables on the nonlinear behaviour of bolted angles. Additional parameters have been identified to allow for a better understanding of the angle behaviour:

1. The flexural span of the column leg did not remain constant across the width of the angle, as the plastic hinge near the bolt head did not develop along the whole angle width. Therefore, a focus should be made in further studies to evaluate the effective width of the angles near the column bolts. A first step towards this evaluation could be to consider the column bolt spacing as a varying parameter.
2. In the bolted angle experimental program, the beam bolt gauge was kept constant. Consequently, the impact of this parameter on the geometrical hardening and the stiffness of the angle could not be evaluated.
3. Even if bolt failure was observed in some cases due to the large prying action and the angle overstrength, the bolts were overdesigned to isolate the behaviour of the angles. Additional testing with a realistic bolt design could provide a more accurate assessment on the realistic failure modes and bolt behaviour of bolted angle connections.
4. Only 12 tests on 2 angle configurations were conducted under low-cycle fatigue loading conditions. Additional tests on different angle geometries could highlight the influence of the geometrical parameters on the low-cycle fatigue behaviour of the angle connections.

10.3.2.2 Bolted angle beam-column connection behaviour

An experimental program has also been conducted on full-scale beam-column connections to characterize the influence of several parameters. Additional parameters have been identified to increase the level of knowledge on these connections:

1. The shear load applied on the connection simultaneously to the rotational demand was kept constant throughout the tests of a specific connection geometry. To further characterize the influence of the shear load, additional tests should be performed on a same connection geometry with different connection shear loading.

2. The connection tested were only attached on the column strong axis. However, in the design example, the connection behaviour was extrapolated to weak axis columns. Further testing on connections to weak axis columns should be performed to assess the influence of this geometrical parameter.
3. The thickness and column gauge of the two top and seat angle geometries tested in this experimental campaign are characterized with a similar g_2/t ratio. The influence of both the thickness and the column gauge individually on the nonlinear behaviour of full-scale connections could provide additional information.
4. The presence of a concrete slab is a common element in gravity beam-column connections. This element was not included in the current study but could provide significant rotational stiffness and strength to the connection when combined with a seat angle. Such composite connections may offer a more economical option than 2L-TS connections. However, the ductility provided by these connections should be evaluated experimentally under combined flexural moment and shear connections.

10.3.2.3 Bolted angle hysteretic behaviour mathematical model

To better represent the hysteretic behaviour of bolted angles and beam-column connections, the following recommendations are proposed:

1. The mathematical model proposed did not include the geometrical hardening observed in flexible angles, as this behaviour was not systematically observed in the cyclic tests. The loading history may influence the geometrical hardening as it was more commonly observed in the monotonic tests. The model could be improved by implementing geometrical hardening. For instance, this implementation could be performed with a procedure similar to the rainflow counting used to determine the damage in the angle.
2. The component-based model used with the proposed mathematical model did not include the effect of shear load on the connection hysteretic moment-rotation behaviour. However, this load influenced the response observed experimentally, especially in 2L connections. The relationship between the shear load and the moment-rotation response could be further investigated.

10.3.2.4 Enhanced gravity connection design approach

1. The proposed design approach does not include the column base connection stiffness. However, this structural element may contribute significantly to the lateral reserve capacity and may increase the lateral stiffness of the first storey. The bolted angle design may thus become more economical if the column base connection stiffness is included in the proposed procedure.
2. The design approach was validated with a single design example. The approach should be applied to a wider range of buildings, with various dimensions, number of storeys and situated in various locations on different soil types to offer a better assessment of the approach.
3. In the numerical model of the design example, several aspects of the buildings were simplified, such as the column base connections and brace-gusset connections. Fore detained numerical modeling would provide a better assessment of the reserve capacity in the building seismic response.
4. The increased brace connection requirement of CSA S16 was investigated when enhanced connections were included in the seismic behaviour. The relaxation of other requirements such as the height restriction of 15 m or the relevance of the additional limitations imposed on buildings taller than 15 m could be investigated.
5. The design approach was developed for chevron brace configurations only. Further work is required to adapt the approach to other configurations, such as X braces, but it could be beneficial to widen the application of the enhanced connections.

BIBLIOGRAPHY

Abdalla, K. M., Drosopoulos, G. A., Stavroulakis, G. E. (2014). "Failure behavior of a top and seat angle bolted steel connection with double web angles." *J. Struct. Eng*., 141(7).

Abolmaali, A., Kukreti, A. R., and Razavi, H. (2003). "Hysteresis behavior of semi-rigid double web angle steel connections." *J. Constr. Steel Res*., 59, 1057–1082.

Abolmaali, A. Kukreti, A. R., Motahari, A., Ghassemieh, M. (2009). "Energy dissipation characteristics of semi-rigid connections." *J. Constr. Steel Res.* 65(5) 1187-1197.

Ackryod, M. H. (1985). *Design of flexibly-connected steel building frames*. Final Research Report (Project No. 133), American Iron and Steel Institute, Washington, D.C.

AISC. (2005). "Seismic provisions for structural steel buildings." *AISC341-05*, Chicago, IL.

AISC. (2016). "Seismic provisions for structural steel buildings." *AISC341-16*, Chicago, IL.

AISC. (2016). "AISC: Market Size and Growth." Retrieved 09-17-2016, 2016, from https://www.aisc.org/content.aspx?id=3800

Adluri, S. M. R., Madugula, M. K. S. (1996). "Flexural buckling of steel angles: Experimental investigation". *J. Struct. Eng.*, 122(3), 309-317.

Anderson, D. (2006). "Design of unbraced multi-storey steel frames." *J. Constr. Steel. Res.* 62(11), 1171-1177.

Ang, K. M., and Morris, G. A. (1984). "Analysis of three-dimensional frames with flexible beam–column connections". *Can. J. Civ. Eng*. 11, 245-254.

Appel, M. E. (2008). *Design of low-ductility chevron braced frames for moderate seismic demands*. M. Sc. Dissertation, Tufts University, Medford, MA.

Ariyaratana, C., and Fahnestock, L. A. (2011). "Evaluation of buckling-restrained braced frame seismic performance considering reserve strength." *Eng. Struct.* 33(1), 77-89.

ASCE7 (2005). "Minimum design loads for buildings and other structures." *American Society of Civil Engineers*, Reston, VA.

ASCE7 (2016). "Minimum design loads and associated criteria for buildings and other structures." *American Society of Civil Engineers*, Reston, VA.

Astaneh-Asl, A., Nader, M. N., Malik, L. (1989). "Cyclic behavior of double angle connections". *J. Struct. Eng.* 115(5). 1101-1118.

Astaneh-Asl, A., and Nader, M. (1990). "Experimental Studies and Design of Steel Tee Shear Connections*." J. Struct. Eng.* 116(10): 2882-2902.

Astaneh-Asl, A. (1999). "Seismic performance and design of bolted steel moment-resisting frames." *Eng. J.-Amer. Inst. Steel Constr.* 36(3): 105-120.

Astaneh-Asl, A., McMullin, K., and Call, S. (1993). "Behavior and Design of Steel Single Plate Shear Connections." *J. Struct. Eng*. 119(8), 2421-2440.

Astaneh-Asl, A., Modjtahedi, D., McMullin, K., Shen, J.-H., D'Amore, E. (1998). "Stability of damaged steel moment frames in Los Angeles." *Eng. Struct*., 20(4), 433-446.

ASTM8 (2000). “Standard test method for tension testing of metallic materials”, ASTM International, West Conshohocken, PA.

ASTM E466 (2015). “Standard practice for conducting force controlled constant amplitude axial fatigue tests of metallic materials”, ASTM International, West Conshohocken, PA.

ASTM E606 (2012). “Standard test method for strain-controlled fatigue testing”, ASTM International, West Conshohocken, PA.

ASTM E739 (2015). “Standard practice for statistical analysis of linear or linearized stress-life (S-N) and strain-life (ε-N) fatigue data”, ASTM International, West Conshohocken, PA.

ASTM E1049 (2017). “Standard practice for cycle counting in fatigue analysis”, ASTM International, West Conshohocken, PA.

Atkinson, G. (2009). “Earthquake time histories compatible with the 2005 National building code of Canada uniform hazard spectrum.” *Can. J. Civ. Eng.* 36(6): 991-1000.

Aviram, A., Stojadinovic, B., and Der Kiureghian, A. (2010). “Performance and Reliability of Exposed Column Base Plate Connections for Steel Moment Resisting Frames.” Pacific Earthquake Engineering Research Center, Berkeley, CA.

Azizinamini, A. (1982). *Monotonic response of semi-rigid steel beam to column connections*. M.S. Dissertation, University of South Carolina, Columbia, SC.

Azizinamini, A. (1985). *Cyclic characteristics of bolted semi-rigid steel beam to column connections*. Ph.D Thesis, University of South Carolina, Columbia, SC.

Azizinamini, A., Radziminski, J. B., (1989), “Static and cyclic performance of semirigid steel beam-to-column connections.”, *J. Struct. Eng.*, 115(12), 2979-2999.

Baker, J.W., Schubert, M., and Faber, M.H. (2008). “On the assessment of robustness.” *Struct. Safety* 30(3): 253-267.

Ballio, G., Calado, L., Castiglioni, C. A. (1997). “Low cycle fatigue behaviour of structural steel members and connections.” *Fatigue Fract. Eng. Mater. Struct.*, 20(8), 1129-1146.

Ban, H., Shi, G., Shi, Y., Wang, Y. (2012). “Residual stress tests of high-strength steel equal angles”. *J. Struct. Eng.*, 138, 1446-1454.

Beland, T., Bradley, C. R., Nelson, J., Sizemore, J. G., Davaran, A., Hines, E. M. Fahnestock, L. A. (2019a). “Experimental parametric characterization of bolted angle connection behavior”. *In Review. Submitted to ASCE Journal of Structural Engineering on April 27 2019.*

Beland, T., Tremblay, R., Hines, E. M., Fahnestock, L. A., (2019b). “Full-scale cyclic testing with shear load of double web with top and seat angle beam-column connections”. *In review. Submitted to ASCE Journal of Structural Engineering on April 27 2019.*

Bernuzzi, C., Calado, L., Castiglioni, C. A. (2000). “Low-cycle fatigue of structural steel components: A method for re-analysis of test data and a design approach based on ductility.” *J. Earthquake Tech.*, 37(4), 47-63.

Bjorhovde, R., Colson, A., Brozzetti, J. (1990). “Classification system for beam-to-column connections.”, *J. Struct. Eng.*, 116(11), 3059-3076.

Braconi, A., Salvatore, W., Tremblay, R., and Bursi, O. S. (2007). "Behaviour and modelling of partial-strength beam-to-column composite joints for seismic applications." *Earthquake Eng. Struct. Dyn.* 36(1), 142-161.

Bradley, C. R. (2019). *Experimental investigation of post-elastic failure mechanisms in low-ductility braced frames and the implications for collapse performance.* M.Sc.A Dissertation. Tufts University. Medford, MA.

Bradley, C. R. (2019). *Design philosophy and parametric collapse performance of low-ductility concentrically braced frames with reserve capacity.* Ph.D Thesis. Tufts University. Medford, MA.

Bradley, C. R., Fahnestock, L. A., Hines, E. M., and Sizemore, J. G. (2017). "Full-scale cyclic testing of low-ductility concentrically braced frames." *J. Struct. Eng.* 143(6): 04017029.

Bruneau, M. (1990). "Preliminary report of structural damage from the Loma Prieta (San Francisco) earthquake of 1989 and pertinence to Canadian structural engineering practice." *Can. J. Civ. Eng.* 17, 198-208.

Brunesi, E., Nascimbene, R., and Rassati, G. (2013). "Evaluation of the Response of Partially Restrained Bolted Beam-to-Column Connection Subjected to Cyclic Pseudo-Static Loads." *Proc. ASCE Structures Congress 2013*, 2310-2321.

Calado, L., De Matteis, G., Landolfo, R. (2000). "Experimental response of top and seat angle semi-rigid steel frame connections". *Mat. And Struct.*, 33(10), 499-510.

Callister, J. T., Pekelnicky, R. G. (2011). "Seismic Evaluation of an existing low ductility braced frame building in California." *Proc. ASCE Structures Congress 2011*, 2756-2767.

Carter, C. J. (2009). *Connections and collapse resistance in R = 3 braced frames.* Ph.D. Thesis, Illinois Institute of Technology, Chicago, IL.

Castonguay, P. X. (2010). *Seismic performance of concentrically braced steel frames of the conventional construction category*. M.Sc.A. Dissertation, Ecole Polytechnique, Montreal (Canada).

Chang, K-C, Lee, G. C. (1987). "Strain rate effect on structural steel under cyclic loading". *J. Eng. Mech.*, 113(9), 1292-1301.

Chasten, C., Lu, L., and Driscoll, G. (1992). "Prying and Shear in End-Plate Connection Design." *J. Struct. Eng.* 118(5): 1295-1311.

Chen, W.F., and Kishi, N. (1989). "Semirigid steel beam-to-column connections - data-base and modeling." *J. Struct. Eng.-ASCE.* 115(1): 105-119.

Chu, X. (2017). *Probabilistic seismic performance assessment of low-ductility concentrically braced frames in East Coast U.S.* Ph.D. Thesis. Lehigh University, Bethlehem, PA.

Citipitioglu, A. M., Haj-Ali, R. M., White, D. W. (2002). "Refined 3D finite element modeling of partially restrained connections including slip." *J. Constr. Steel. Res.*, 58, 995-1013.

Civjan, S. A., Engelhardt, M. D., and Gross, J. L. (2000). "Retrofit of Pre-Northridge Moment-Resisting Connections." *J. Struct. Eng*. 126(4), 445-452.

Civjan, S. A., Engelhardt, M. D., and Gross, J. L. (2001). “Slab Effects in SMRF Retrofit Connection Tests.” *J. Struct. Eng.* 127(3), 230-237.

Chen, W. F., and Kishi, N. (1989). “Semirigid steel beam-to-column connections - data-base and modeling.” *J. Struct. Eng.-ASCE* 115(1), 105-119.

Crocker, J. P., and Chambers, J. J. (2004). “Single plate shear connection response to rotation demands imposed by frames undergoing cyclic lateral displacements.” *J. Struct. Eng.-ASCE* 130(6), 934-941.

CSA-S16-14. (2014). *Design of steel structures*, 8th Edition. Canadian Standards Association, Mississauga, ON.

D'Aronco, M. (2013). *Behaviour of double and triple vertical rows of bolts shear tab connections and weld retrofits.* M.Sc.A. Dissertation, Ecole Polytechnique, Montreal (Canada).

Danesh, F., Pirmoz, A., Daryan, A. S., (2007) “Effect of shear force on the initial stiffness of top and seat angle connections with double web angles.” *J. Constr. Steel. Res.*, 63, 1208-1218.

Davaran, A., Tremblay, R., Beland, T., Fahnestock, L., and Hines, E. (2014). “Experimental Behavior of Low-Ductility Brace Connection Limit States.” In *Structures Congress 2014*. pp. 2429-2441.

Decaen, S. (2015). *Amélioration du comportement sismique des assemblages en cisaillement simple des contreventements concentriqueen X en acier de construction conventionnelle (Type CC).* M.Sc. Dissertation. École Polytechnique de Montréal, Montréal, Canada.

De Stefano, M. Deluca, A., Astaneh-Asl, A. (1994) “Modeling of cyclic moment-rotation response of double-angle connections.” *J. Struct. Eng.* 124(8). 857-867.

Dion, J.A. (1981). *Etude experimentale des assemblages poteau-fondation dans les charpentes d'acier*. M.Sc. Dissertation, Universite Laval (Canada).

Dubina, D., Ciutina, A., and Stratan, A. (2001). “Cyclic tests of double-sided beam-to-column joints.” *J. Struct. Eng.-ASCE*. 127(2), 129-136.

Dumas, M., Beaulieu, D., and Picard, A. (2006). “Characterization equations for steel column base connections.” *Can. J. Civ. Eng.* 33(4): 409-420.

Elkady, A., Lignos, D. G. (2015). “Effect of gravity framing on the overstrength and collapse capacity of steel frame buildings with perimeter special moment frames.” *Earthquake Eng. Struct. Dyn.*, 44(8), 1289–1307.

Elnashai, A., Elghazouli, A. Denesh-Ashtiani, F. (1998). “Response of semirigid steel frames to cyclic and earthquake loads.” *J. Struct. Eng.* 124(7). 765-774.

Ermopoulos, J.C., and Stamatopoulos, G.N. (1996). “Analytical modelling of column-base plates under cyclic loading.” *J. Constr. Steel. Res.* 40(3): 225-238.

European Standard. (1993). *Eurocode 3: Design of steel structures - Part 1-8: Design of joints EN1993-1-8*. Brussels, Belgium.

Faella, C., Piluso, V., Rizzano, G. (1998). “Experimental analysis of bolted connections: Snug versus preloaded bolts”. *J. Struct. Eng.*, 124(7), 765-774.

Fafard, M., Picard, A., and Beaulieu, D. (1990). “Analyse des structures avec joints à rigidité partielle: une approche unifiée.” *Can. J. Civ. Eng.* 17(5): 730-738.

FEMA (1997). Protocol for fabrication, inspection, testing and documentation of beam-column connection tests and other experimental specimens. *Background Document*. F. S. J. Venture. Sacramento, CA, SAC Joint Venture: 41.

FEMA. (2009). *FEMA P695: Quantification of building seismic performance factors*. Washington D.C. p. 421.

Filippou, F. C., Popov, E. P., Bertero, V. V. (1983). “Effects of bond deterioration on hysteretic behavior of reinforced concrete”. *Earthquake Engineering Research Center Report UCB/EERC-83/19*, University of California Berkeley, Berkeley, CA.

Fleischman, R. B., Chasten, C. P., Lu, L.-W., Driscoll, G. C. (1991). “Top-and-seat-angle connections and end-plate connections: Snug vs. fully pretensioned bolts.” A*ISC Eng. J*., 28, 18-28.

Flores, F. X., Charney, F. A., Lopez-Garcia, D. (2014). “Influence of the gravity framing system on the collapse performance of special steel moment frames.” *J. Constr. Steel. Res.*, 101, 351-362.

Flores, F. X., Charney, F. A., Lopez-Garcia, D. (2016). “The influence of gravity column continuity on the seismic performance of special steel moment frame structures.” *J. Constr. Steel. Res.*, 118, 217-230.

Frye, M. J., and Morris, G. A. (1975). “Analysis of Flexibly Connected Steel Frames.” *Can J. Civ. Eng.* 2, 280-291.

Gardner, L., Cruise, R. B. (2009). “Modeling of residual stress in structural stainless steel sections”. *J. Struct. Eng.*, 135(1), 42-53.

Garlock, M. M., Ricles, J. M. Sause, R. (2003). “Cyclic load tests and analysis of bolted top-and-seat angle connections.” *J. Struct. Eng*., 129(12), 1615-1625.

Gélinas, A. (2013). *Étude expérimentale du conportement sismique des assemblages utilisés dans les contreventementss en X en acier*. M.Sc.A. Dissertation. École Polytechnique de Montréal, Montréal, Canada.

Ghindea, M., Catarig, A., Ballok, R. (2015). “Behavior of beam-to-column connections with angles. Part 1-Experimental investigations”. *J. App. Eng. Sci.*, 5(18), 21-28.

Giuffré, A., Pinto, P. E. (1970). “Il comportamento del cemento armato per sollecitazioni cicliche di forte intensita.” *Giornale del Genio Civile.*

Goldberg, J. and Richard, R.H. (1963). “Analysis of nonlinear structures.” *J. of the Struct. Div.*, 89(4), 333-352.

Gong, Y. (2014). “Ultimate tensile deformation and strength capacities of bolted-angle connections.” *J. Constr. Steel. Res*., 100, 50-59.

Green, T., Leon, R., and Rassati, G. (2004). “Bidirectional Tests on Partially Restrained, Composite Beam-to-Column Connections.” *J. Struct. Eng.* 130(2), 320-327.

Gryniuk, M. C. (2008) *Seismic performance of low-ductility chevron braced steel frames in moderate seismic regions*. M.Sc. Dissertation, Tufts University, Medford, MA.

Guilini-Charette, K. (2009). *Effets des mouvements sismiques sur les structures en acier de la catégorie des constructions conventionnelles*. M.Sc.A. Dissertation. Ecole Polytechnique, Montreal, (Canada).

Gupta, A., Krawinkler, H. (2000a). "Behavior of ductile SMRFs at various seismic hazard levels." *J. Struct. Eng*., 126(1), 98-107.

Gupta, A., and Krawinkler, H. (2000b). "Dynamic P-Delta effects for flexible inelastic steel structures." *J. Struct. Eng.* 126(1): 145-154.

Guravich, S. J., Dawe, J. L. (2006). "Simple beam connections in combined shear and tension". *Can. J. Civ. Eng.* 33. 357-372.

Hajjar, J. F., O'Sullivan, D. P., Leon, R. T., Gourley, B. C. (1995). "Evaluation of the damage to the Borax corporate headquarters building as a result of the Northridge earthquake." Technical Report: *Case Studies of Steel Moment Frame Building Performance in the Northridge Earthquake of January 17, 1994*. SAC 95-07.

Hajjar, J. F., Leon, R., Gustafson, M., and Shield, C. (1998). "Seismic Response of Composite Moment-Resisting Connections. II: Behavior." *J. Struct. Eng.* 124(8), 877-885.

Harada, Y., and Morita, K. (2007). "Design of Wide-Flange Section Column-to-Split-Tee Tensile Connection with High-Strength Bolts." *J. Struct. Eng.* 133(3): 335-346.

Heidelbrecht, A. C. (2003). "Overview of seismic provisions of the proposed 2005 edition of the National Building Code of Canada." *Can. J. Civ. Eng.* 30, 241-254.

Hensman, J. S., and Nethercot, D. A. (2001). "Numerical study of unbraced composite frames: generation of data to validate use of the wind moment method of design." *J. Constr. Steel. Res.* 57(7), 791-809.

Hines, E. M., Appel, M. E., Cheever, P. J. (2009). "Collapse performance of low-ductility chevron braced steel frames in moderate seismic regions." *Eng. J. AISC*. 46(3), 149-180.

Hines, E.M., and Fahnestock, L.A. (2010). "Design philosophy for steel structures in moderate seismic regions", *Proc. 9th US National and 10th Canadian Conference on Earthquake Engineering 2010*. Toronto, Canada, July 25-29. 4086-4094.

Hwang, S.-H., Lignos, D. G. (2017). "Effect of modelling assumptions on the earthquake-induced losses and collapse risk of steel-frame buildings with special concentrically braced frames." *J. Struct. Eng*., 143(9).

Jarrett, J. A., Judd, J. P., Charney, F. A. (2015). "Comparative evaluation of innovative and traditional seismic-resisting systems using the FEMA P-58 procedure." *J. Constr. Steel. Res*., 105, 107-118.

Ji, X., Kato, M., Wang, T., Hitaka, T., Nakashima, M. (2009). "Effect of gravity columns on mitigation of drift concentration for braced frames." *J. Struct. Steel. Res*., 65, 2148-2156.

Judd, J. P., Charney, F. A., Pryor, S. E. (2015). "Retrofit of steel-frame buildings using enhanced gravity-frame connections." *Proc. 2nd ATC & SEI Conf. on improving the seismic performance of existing buildings and other structures*, 132-143.

Kanvinde, A., Grilli, D., and Zareian, F. (2012). "Rotational Stiffness of Exposed Column Base Connections: Experiments and Analytical Models." *J. Struct. Eng.* 138(5): 549-560.

Kanvinde, A., Higgins, P., Cooke, R., Perez, J., and Higgins, J. (2014). "Column Base Connections for Hollow Steel Sections: Seismic Performance and Strength Models." *J. Struct. Eng.* 141(7): 04014171.

Kanvinde, A.M., Jordan, S.J., and Cooke, R.J. (2013). "Exposed column base plate connections in moment frames - Simulations and behavioral insights." *J. Constr. Steel. Res.* 84: 82-93.

Kiggins, S., and Uang, C. M. (2006). "Reducing residual drift of buckling-restrained braced frames as a dual system." *Eng. Struct.* 28(11), 1525-1532.

Kim, D. H. (2003). *Seismic performance of PR frames in areas of infrequent seismicity*. Ph.D. Thesis, Georgia Institute of Technology, Atlanta, GA.

Kim, D. H., and Leon, R. (2007). "Seismic Performance of PR Frames in Mid-America Earthquake Region." *J. Struct. Eng.* 133(12), 1808-1820.

Kishi, N., Chen, W.-F. (1990). "Moment-rotation relations of semirigid connections with angles." *J. Struct. Eng.*, 116(7), 1813-1834.

Koduru, S., and Driver, R. (2014). "Generalized Component-Based Model for Shear Tab Connections." *J. Struct. Eng.* 140(2), 04013041.

Komuro, M., Kishi, N., Ahmed, A. (2006). "Elasto-plastic finite element analysis of prying of top and seat-angle connections." From *Advances in engineering structures, mechanics and construction*, Springer, Dordrecht, Netherlands, 289-301.

Kong, Z., Kim, S.-E. (2017) "Moment-rotation behavior of top-and seat-angle connection with double web angles." *J. Constr. Steel. Res.*, 128, 428-439.

Krawinkler, H., Seneviratna, G. D. P. K. (1998). "Pros and cons of a pushover analysis of seismic performance evaluation." *Eng. Struct.*, 20(4), 452-464.

Kukreti, A. R., Abolmaali, A. S. (1999). "Moment-rotation hysteresis behavior of top and seat angle steel frame connections." *J. Struct. Eng.*, 125(8), 810-820.

Kulak, G.L., Fisher, J.W., Struik, J.H.A. (2001). *Guide to design criteria for bolted and riveted joints*. American Institute of Steel Construction, Chicago, IL.

Kunnath, S. K., Heo, Y., Mohle, J. F. (2009). "Nonlinear uniaxial material model for reinforcing steel bars." *J. Struct. Eng.* 135(4), 335-343.

Lanning, J., Uang, C. M. (2014) "Testing and modeling of A36 and stainless steel buckling restrained braces under near-fault loading conditions." *5th Asia Conf. on Earthquake Engineering*, Earthquake Engineering Research Institute, Taipei, Taiwan.

Latour, M., Piluso, V., and Rizzano, G. (2011). "Experimental analysis of innovative dissipative bolted double split tee beam-to-column connections." *Steel Constr.* 4(2): 53-64.

Lee, K., Foutch, D. A. (2002). “Performance evaluation of new steel frame buildings for seismic loads.” *Earthquake Eng. Struct. Dyn*., 31, 653-670.

Lee, S. S., Moon, T. S. (2002). “Moment-rotation model of semi-rigid connections with angles.” *Eng. Struct.* 24(1). 95-107.

Leon, R. T. (1998). “Composite connections.” *Progress Struct. Eng. Mat*., 1(2), 159-169.

Leon, R., Hajjar, J.F., and Gustafson, M. (1998). “Seismic Response of Composite Moment-Resisting Connections.I: Performance.” *J. Struct. Eng.* 124(8): 868-876.

Leon, R. T., and Kim, D. H. (2004). “Seismic performance of older PR frames in areas of infrequent seismicity.” *Proc. 13th World Conf. on Earthquake Eng*.

Liu, J., Astaneh-Asl, A. (2000). “Cyclic testing of simple connections including effects of slab”. *J. Struct. Eng.*, 126(1), 32-39.

Liu, J., and Astaneh-Asl, A. (2004). “Moment-rotation parameters for composite shear tab connections.” *J. Struct. Eng.-ASCE* 130(9), 1371-1380.

Liu, J., Main, J., and Sadek, F. (2012). “Modeling of Double-Angle Shear Connections for the Evaluation of Structural Robustness.” *Proc. 6th Congress on Forensic Eng. 2012,* 1081-1090.

Liu, C., Tan, K. H., Fung, T. C. (2015). “Investigations of nonlinear dynamic performance of top-and-seat with web angle connections subjected to sudden column removal”, *Eng. Struct.,* 99, 449-461.

MacRae, G. (2011). “The Continuous Column Concept - Development and Use.” *Proc. 9th Pacific Conf. on Earthquake Eng.*

MacRae, G., Kimura, Y., and Roeder, C. (2004). “Effect of column stiffness on braced frame seismic behavior.” *J. Struct. Eng*. 130(3), 381-391.

Mander, J. B., Chen, S. S., Pekcan, G. (1994). “Low-cycle fatigue behavior of semi-rigid top-and-seat angle connections.” *AISC Eng. J*., 31, 111-122.

Mander, J. B., Pekcan, G., Chen, S. S. (1995). “Low-cycle variable amplitude fatigue modeling of top-and-seat angle connections.” *AISC Eng. J.*, 32, 54-62.

Mander, T., Magenes, L., and Anderson, T. 2014. Steel Shear Tab Connection Performance at Large Rotations during Blast Loading. In *Structures Congress 2014*. pp. 246-257.

Marosi, M. (2011). *Behaviour of Single and Double Row Bolted Shear Tab Connections and Weld Retrofits.* M.Eng. Dissertation, McGill University (Canada).

Matsuishi, M. Endo, T. (1968). *Fatigue of metals subjected to varying stress.* Japan Society of Mechanical Engineers, Fukuoka, Japan.

Matthews, J., Arjomandi, K. (2017). “Improved ductility of bolted double-angle shear connections.” *Pract. Period. Struct. Des. Constr.,* 22(3).

Mazzoni, S., McKenna, F., Scott, M. H., Fenves, G. L. (2006). *OpenSees command language manual*. Pacific Earthquake Engineering Research Center, University of California Berkeley, Berkeley, CA.

McKenna, F. (1997). *Object-oriented finite element programming: Frameworks for analysis, algorithms and parallel computing.* Ph.D. Thesis, University of California, Berkeley (USA).

McKenna, F., Fenves, G. L. (2016). *Open System for Earthquake Engineering Simulation (OpenSees).* [Software]. Pacific Earthquake Engineering Research Center (PEER), University of California, Berkeley (USA). Available from: http://opensees.berkeley.edu/

McKenna, F., Fenves, G. L., Filippou, F. C. (2010). *OpenSees Menegotto-Pinto Steel Model with Filippou Isotropic Hardening: Steel02.cpp.* [Software Programming]. Pacific Earthquake Engineering Research Center (PEER), University of California, Berkeley (USA). Available from : http://opensees.berkeley.edu/WebSVN/filedetails.php?repname=OpenSees &path=%2Ftrunk%2FSRC%2Fmaterial%2Funiaxial%2FSteel02.cpp.

Menegotto, M., Pinto, P. E. (1973). "Method of analysis for cyclically loaded R.C. plane frames including changes in geometry and non-elastic behaviour of elements under combined normal force and bending". *IABSE reports of the working commissions*. Zurich, Switzerland.

Miner, M. A. (1945). "Cumulative damage in fatigue". *J. Appl. Mech.*, 12, 159-163.

Mitchell, D., Adams, J., DeVall, R.H., Lo, R.C., and Weichert, D. (1986). "Lessons from the 1985 Mexican earthquake." *Can. J. Civ. Eng.* 13, 535-557.

Mitchell, D., Tinawi, R., and Redwood, R. G., (1990a). "Damage to buildings due to the 1989 Loma Prieta earthquake – a Canadian code perspective." *Can. J. Civ. Eng.* 17, 813-834.

Mitchell, D., Tinawi, R., and Law, T. (1990b). "Damage caused by the November 25, 1988, Saguenay earthquake". *Can. J. Civ. Eng.* 17, 338-365.

Mitchell, D., Tremblay, R., Karacabeyli, E., Paultre, P., Saatcioglu, M., and Anderson, D.L. (2003). "Seismic force modification factors for the proposed 2005 edition of the National Building Code of Canada." *Can. J. Civ. Eng.* 30, 308-327.

Mitchell, D., Paultre, P. Tinawi, R., Saatcioglu, M., Tremblay, R., Elwood, K., Adams, J., and DeVall, R. (2010). "Evolution of seismic design provisions in the National building code of Canada." *Can. J. Civ. Eng.* 37, 1157-1170.

Mohsenzadeh, V., Wiebe, L. (2018). "Effect of beam-column connection fixity and gravity framing on the seismic collapse risk of special concentrically braced frames." *Soil Dynamics and Earthquake Eng.* 115 (2018), 685-697.

Morris, G. (1989). "Connections in steel structures: behaviour, strength and design." *Can. J. Civ. Eng*. 16, 785-786.

Morris, G. A., and Packer, J. A. (1987). "Beam-to-column connections in steel frames." *Can. J. Civ. Eng.* 14, 68-76.

Može, P., Cajot, L.-G., Sinur, F., Rejec, K., Beg, D. (2014). "Residual stress distribution of large steel equal leg angles". *Eng. Struct.*, 71, 35-47.

Nakashima, M., Inoue, K., and Tada, M. (1998). "Classification of damage to steel buildings observed in the 1995 Hyogoken-Nanbu earthquake." *Eng. Struct.* 20(4-6): 10.

NBCC. (2015). *National Building code of Canada*, 14th Edition. National Research Council of Canada, Ottawa, ON.

Nethercot, D. A., Li, T. Q., Ahmed, B. (1988). "Unified classification system for beam-to-column connections". *J. Constr. Steel Res.*, 45(1), 39-65.

Oosterhof, S. A., Driver, R. G., (2012). "Performance of steel shear connections under combined moment, shear and tension." *Proc. Structures Congress 2012*. 146-157.

Orakcal, K., Massone, L. M., Wallace, J. W. (2006). "Analytical modeling of reinforced concrete walls for prediction flexural and coupled-shear-flexural responses." *Pacific Earthquake Engineering Research Center, PEER Report 2006/07*, University of California Berkeley, Berkeley, CA.

O'Sullivan, D. P., Hajjar, J. F., Leon, R. T. (1998). "Repairs to mid-rise steel frame damaged in Northridge Earthquake." *J. Perform. Constr. Facilities*, 12(4), 213-220.

Pirmoz, A., Daryan, A. S., Mazaheri, A., Darbandi, H. E. (2008). "Behavior of bolted angle connections subjected to combined shear force and moment". *J. Constr. Steel Res.*, 64, 436-446.

Pirmoz, A., Danesh, F. (2009). "The seat angle role on moment-rotation response of bolted angles connections." *Electron. J. Struct. Eng*. 1-9.

Pirmoz, A. Khoei, A. S., Mohammadrezapour, E., Daryan, A. S. (2009). "Moment-rotation behavior of bolted top-seat angle connections." *J. Constr. Steel. Res.*, 65, 973-984.

Radziminski, J. B., Bradburn, J. H. (1984) "Experimental investigation of semi-rigid steel beam-column connections". *Proc. 8th World Conference on Earthquake Engineering,* 169-176.

Rahgozar, M. A., Humar, J. L. (1998). "Accounting for overstrength in seismic design of steel structures." *J. Can. Civ. Eng.*, 25, 1-15.

Ramberg, W. Osgood, W. R. (1943). Description of stress-strain curves by three parameters. Washington, *National advisory committee for aeronautics*. 902.

Richard, J. (2009) *Étude du comportement sismique de bâtiments industriels avec systèmes de contreventement en acier de faible ductilité.* M. Sc.A Dissertation, École Polytechnique Montreal, Montreal, Canada.

Richard, R.M., and Abbott, B.J. (1975). "Versatile Elastic-Plastic Stress-Strain Formula." *J. Eng. Mech. Div.*, 101(4), 511-515.

Ricles, J. Yura, J. (1983). "Strength of double-row bolted-web connections." *J. Struct. Eng.* 109(1). 126-142.

Sadek, F., Main, J., Lew, H., Robert, S., and Chiarito, V. (2009). "Testing and Analysis of Steel Beam-Column Assemblies under Column Removal Scenarios." In *Structures Congress 2009*. pp. 1-10.

Sahoo, D. R., and Chao, S. (2015). "Stiffness-Based Design for Mitigation of Residual Displacements of Buckling-Restrained Braced Frames." *J. Struct. Eng.* 141(9), 04014229.

Shen, J., Astaneh-Asl, A. (1999). "Hysteretic behavior of bolted-angle connections.", *J. Constr. Steel. Res.*, 51, 201-218.

Shen, J., Astaneh-Asl, A. (2000). “Hysteretic model of bolted-angle connections.”, *J. Constr. Steel. Res.*, 54, 317-343.

Shen, J., Rou, W., Akbas, B., Seker, O., Uckan, E. (2015). “Near-collapse behavior of steel buildings with non-ductile concentrically braced frames.” *J. Const. Steel. Res.* 113, 101-114.

Sizemore, J. G., Fahnestock, L. A., Hines, E. M. (2019). “Seismic performance assessment of low-ductility concentrically braced frames.” *J. Struct. Eng.* 145(4).

Sizemore, J. (2017). *Inelastic behavior and seismic collapse prevention performance of low-ductility steel braced frames.* Ph.D. Thesis. University of Illinois at Urbana-Champaign. Urbana, IL.

Sizemore, J., Davaran, A., Fahnestock, L., Tremblay, R., and Hines, E. (2014). “Seismic Behavior of Low-Ductility Concentrically-Braced Frames.” *Proc. ASCE Structures Congress 2014*. 2369-2380.

Sizemore, J. G., Fahnestock, L. A., Hines, E. M., Bradley, C. R. (2017) “Parametric study of low-ductility concentrically braced frames under cyclic static loading.” *J. Struct. Eng.*, 143(6).

Soroushian, P., Choi, K.-B. (1987). “Steel mechanical properties at different strain rates”. *J. Struct. Eng.*, 113(4), 663-672.

Stafford-Smith, B., Coull, A. (1991). *Tall building structures: Analysis and design*. Wiley-Interscience, New York, NY. 552 p.

Stoakes, C. D., Fahnestock, L. A. (2011). “Cyclic flexural testing of concentrically braced frame beam-column connections.” *J. Struct. Eng.*, 137, 739-747.

Swanson, J. A., Gao, X. (2000). “Strength determination of heavy clip-angle connection components.” *Proc. 4th Int. Workshop on Connections in Steen Struct*, Roanoke, Virginia, US. pp 234-243.

Tremblay, R., Filiatrault, A., Bruneau, M., Nakashima, M., Prion, H.G.L., and DeVall, R. (1996). “Seismic design of steel buildings: lessons from the 1995 Hyogo-ken Nanbu earthquake.” *Can. J. of Civ. Eng.* 23(3): 727-756.

Tremblay, R., Filiatrault, A., Timler, P., and Bruneau, M. (1995). “Performance of steel structures during the 1994 Northridge earthquake.” *Can. J. of Civ. Eng.*22(2): 338-360.

Tremblay, R., Mitchell, D., and Tinawi, R. (2013). “Damage to industrial structures due to the 27 February 2010 Chile earthquake.” *Can. J. of Civ. Eng.* 40(8): 735-749.

Tremblay, R., Stiemer, S.F. (1994). “Back-up stiffness for improving the stability of multi-storey braced frames under seismic loading.” *Proc. 1994 Annual Task Group Technical Session, Struct. Stability Res. Council.*

Tremblay, R. (2018). “An inverted V-braced frame system exhibiting bilinear response for seismic stability under long duration subduction earthquakes.” [Powerpoint presentation]. *9th Int. Conf. on Behaviour of Steel Struct. in Seismic Areas (STESSA 2018). From*

https://www.scnz.org/site/scnz/images/Documents/STESSA/Keynote/STESSA%202018%20-%20Tremblay%20Keynote.pdf

Tsai, K., and Popov, E. (1990). "Cyclic Behavior of End-Plate Moment Connections." *J. Struct. Eng.* 116(11): 2917-2930.

Tsai, K.C., Wu, S., and Popov, E.P. (1995). "Experimental performance of seismic steel beam-column moment joints." *J. Struct. Eng.* 121(6): 925-931.

Tyas, A., Warren, J.A., Stoddart, E.P., Davison, J.B., Tait, S.J., and Huang, Y. 2012. A methodology for combined rotation-extension testing of simple steel beam to column joints at high rates of loading. *Exp. Mech.* 52(8): 1097-1109.

Uriz, P., Mahin, S. A. (2008). "Toward earthquake-resistant design of concentrically braced steel-frame structures." *Pacific Earthquake Engineering Research Center, PEER Report 2008/08*, University of California Berkeley, Berkeley, CA.

Veletsos, A.S., and Newmark, N.M. (1964). *Design procedures for shock isolation systems of underground protective structures. Volume 3: Response spectra of single-degree-of-freedom elastic and inelastic systems*. Defense Documentation Center for Scientific and Technical Information, Alexandria, VA.

Wakabayashi, M., Nakamura, T, Iwai, S, Hayashi, Y. (1984). "Effects of strain rate on the behavior of structural members subjected to earthquake force". *Proc. 8th World Conf. on Earthquake Engineering*, 491–498.

Wang, X.L., Yin, Z.Z., Shen, S.Z., and Li, Q.F. (2006). "Experimental research on stiffness of semi-rigid connection in beam-column and effect on steel frame ductility." *Science Press Beijing*, Beijing.

Weigand, J., and Berman, J. (2014). "Integrity of Steel Single Plate Shear Connections Subjected to Simulated Column Removal." *J. Struct. Eng.* 140(5), 04013114.

Whittaker, A. S., Uang, C. M., and Bertero, V. V. (1989). "Experimental Behavior of Dual Steel System." *J. Struct. Eng.* 115(1), 183-200.

Wilson, W. M., and Moore, H. F. (1917). "Tests to determine the rigidity of riveted joints of steel structures." *University of Illinois Bulletin* 15(14), 60.

Xie, Q. (2008). "Dual system design of steel frames incorporating Buckling-restrained braces." *Proc. 14th World Conf. on Earthquake Engineering*.

Yang, B., Tan, K. H. (2013). "Robustness of bolted-angle connections against progressive collapse: Mechanical modelling of bolted-angle connection under tension." *Eng. Struct.*, 57, 153-168.

Yang, J.-G., Kim, J.-W., and Lee, H.-D. (2014). "Experimental tests for the evaluation of the energy dissipation capacity of a double split tee connection with SMA bolts." *Int J Steel Struct*. 14(4): 723-730.

Zareian, F., and Kanvinde, A. (2013). "Effect of Column-Base Flexibility on the Seismic Response and Safety of Steel Moment-Resisting Frames." *Earthquake Spectra*. 29(4): 1537-1559.

Zhang, X., and Ricles, J. (2006). “Seismic Behavior of Reduced Beam Section Moment Connections to Deep Columns.” *J. Struct. Eng.* 132(3), 358-367.

APPENDIX A ANGLE COMPONENT TEST SUMMARY

This Appendix presents a summary of the experimental results of each test performed on the bolted angles. These results have been discussed in Article 1, presented in Chapter 4. In this Appendix, each test is presented individually on a page where the following information are presented:

- Test identification;
- Type of loading protocol applied;
- Failure mode observed;
- Angle geometrical properties;
- Material properties;
- Bolt properties;
- Key response parameters;
- Force-displacement response;
- Test pictures.

This Appendix aims at providing as much information as possible on the tests performed to allow the use of these experimental results in future studies.

Test TC1-1

Type Monotonic Static

Loading Rate: 100 με/s

Failure mode: Beam

Geometry:

g_{column}	64	mm
t	9.5	mm
g_{beam}	57	mm
φ_{bolt}	19.1	mm
k	22.2	mm
g_2	25.4	mm
g_2/t	2.67	

Materials:

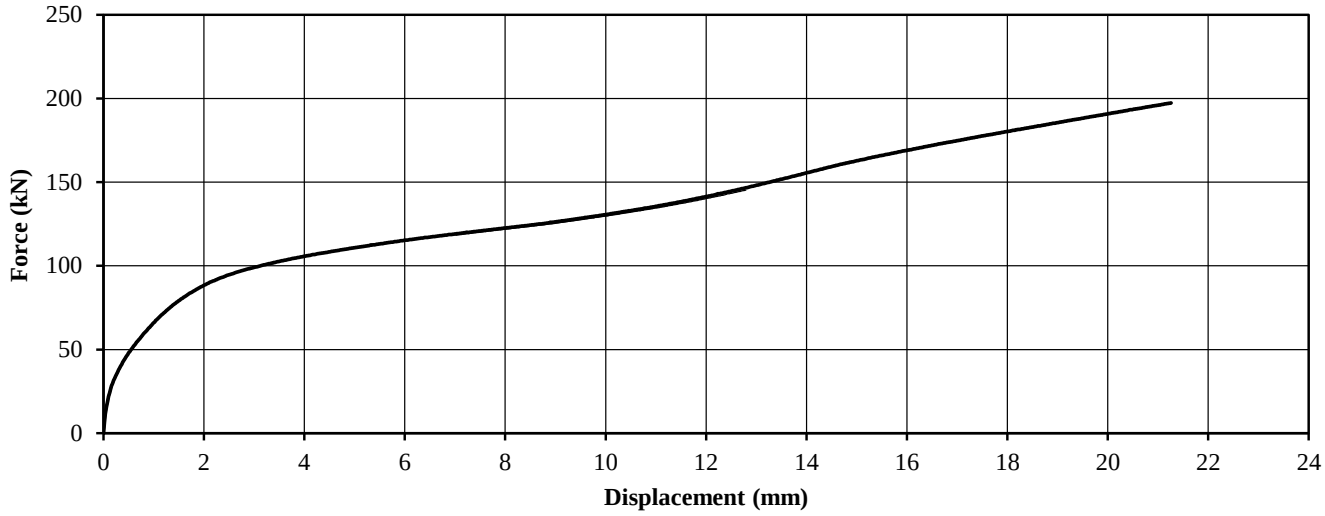
Angle	A36	
F_y	375	MPa
F_u	537	MPa
ε_u	0.2372	
Bolt	A325	
Column bolts	400	lbf-ft
Plate bolts	400	lbf-ft

Key response parameters:

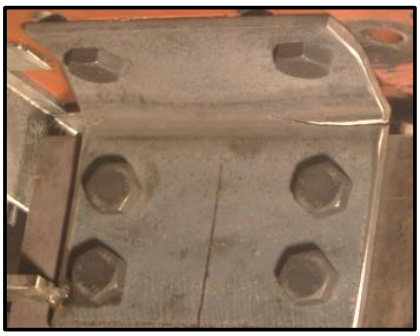
$K_{Plastic}$	3.9	kN/mm
$K_{Softening}$	-	kN/mm
$K_{Hardening}$	6.3	kN/mm

	F (kN)	Δ (mm)
Initial	-	-
Plastic	114	5.8
Softening	-	-
Hardening	133	10.3
Max. Force	197	21.3
Ultimate	197	21.3

Force-displacement

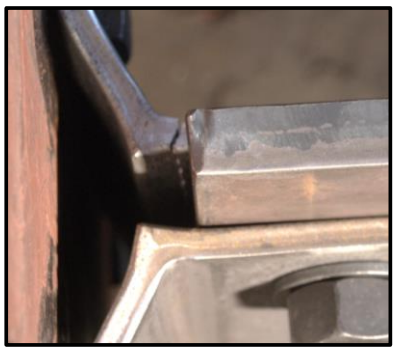












Test TC1-2

Type Monotonic Static

Loading Rate: 600 με/s

Failure mode: Column

Geometry:

g_{column}	64	mm
t	9.5	mm
g_{beam}	57	mm
φ_{bolt}	19.1	mm
k	22.2	mm
g_2	25.4	mm
g_2/t	2.67	

Materials:

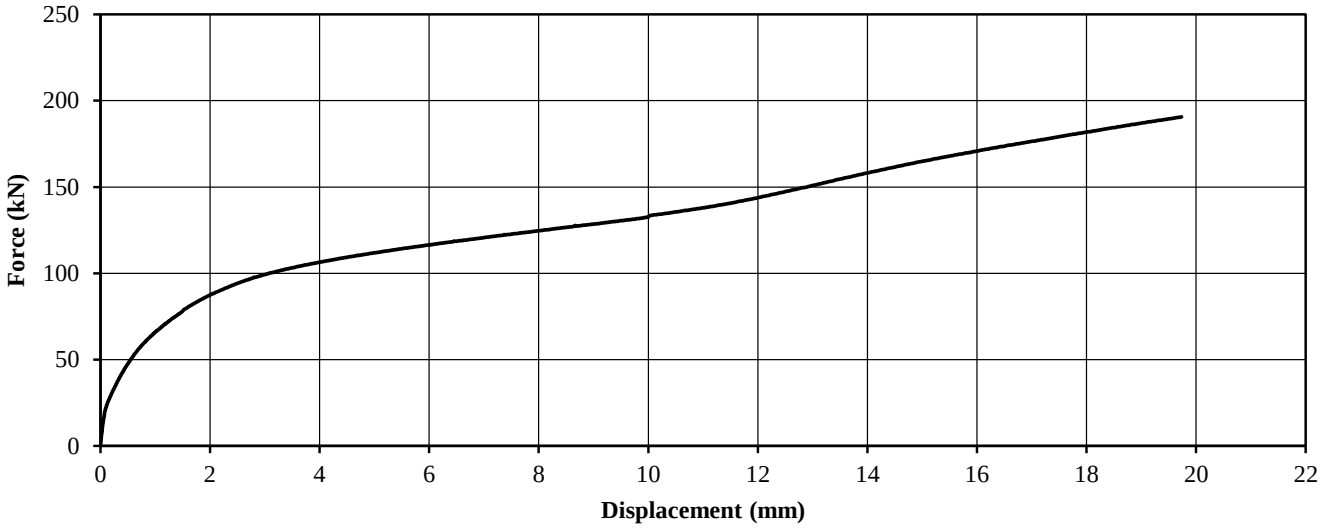
Angle	A36	
F_y	375	MPa
F_u	537	MPa
ε_u	0.2372	
Bolt	A325	
Column bolts	400	lbf-ft
Plate bolts	400	lbf-ft

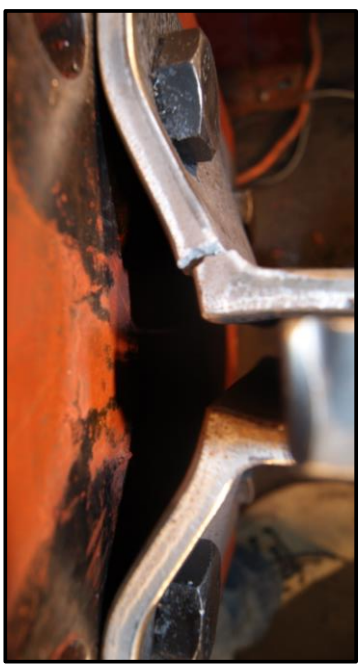
Key response parameters:

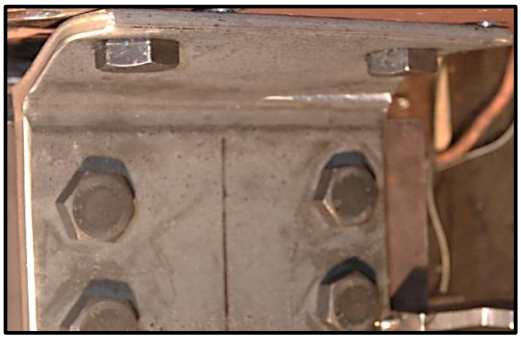
$K_{Plastic}$	4.0	kN/mm
$K_{Softening}$	-	kN/mm
$K_{Hardening}$	5.9	kN/mm

	F (kN)	Δ (mm)
Initial	21.6	0.100
Plastic	118	6.3
Softening	-	-
Hardening	136	10.9
Max. Force	191	19.7
Ultimate	191	19.7

Force-displacement













Test TC1-3

Type Monotonic Dynamic

Loading Rate: 750000 με/s

Failure mode: Column/Net Section

Key response parameters:

$K_{Plastic}$	4.5	kN/mm
$K_{Softening}$	-	kN/mm
$K_{Hardening}$	6.5	kN/mm

Geometry:

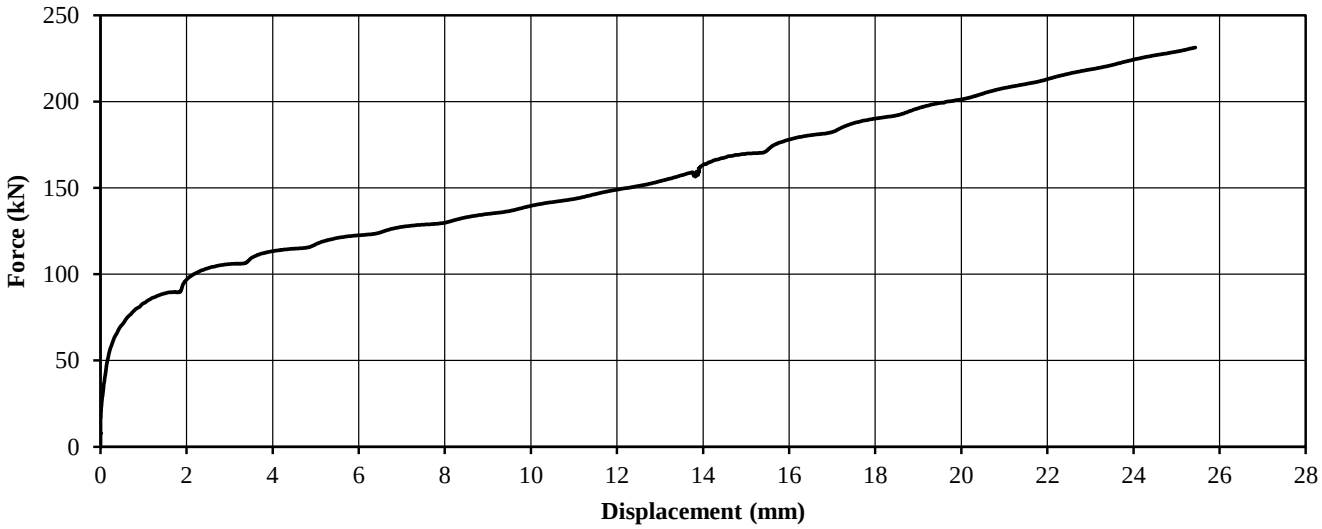
g_{column}	64	mm
t	9.5	mm
g_{beam}	57	mm
φ_{bolt}	19.1	mm
k	22.2	mm
g_2	25.4	mm
g_2/t	2.67	

Materials:

Angle	A36	
F_y	375	MPa
F_u	537	MPa
ε_u	0.2372	
Bolt	A325	
Column bolts	400	lbf-ft
Plate bolts	400	lbf-ft

	F (kN)	Δ (mm)
Initial	19.3	0.008
Plastic	111	6.3
Softening	-	-
Hardening	114	11.0
Max. Force	231	25.4
Ultimate	231	25.4

Force-displacement





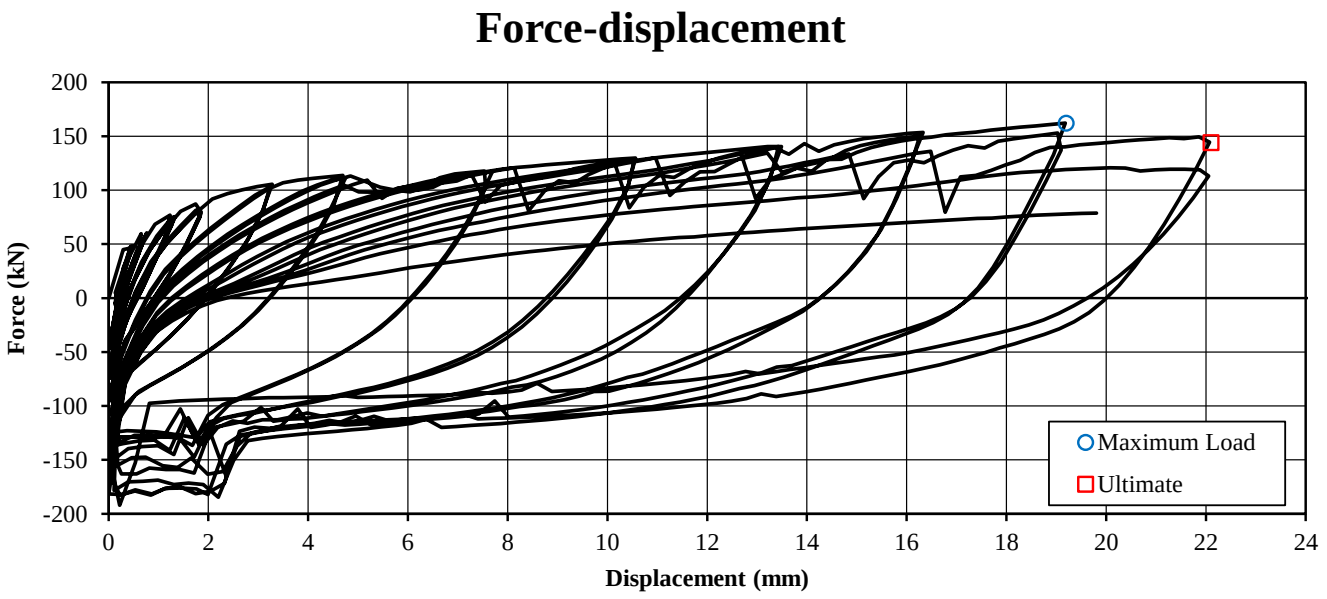
Test TC1-4

Type Cyclic W310 **Failure mode:** Beam/Column/Net Setion

Geometry:		
g_{column}	64	mm
t	9.5	mm
g_{beam}	57	mm
φ_{bolt}	19.1	mm
k	22.2	mm
g_2	25.4	mm
g_2/t	2.67	

Materials:		
Angle	A36	
F_y	375	MPa
F_u	537	MPa
ε_u	0.2372	
Bolt	A325	
Column bolts	400	lbf-ft
Plate bolts	400	lbf-ft

Key response parameters:		
F_{Max}	162	kN
Δ_{FMax}	19.2	mm
$Drift_{FMax}$	7	%
$F_{Ultimate}$	114	kN
$\Delta_{Ultimate}$	22.1	mm
$Drift_{Ultimate}$	8	%

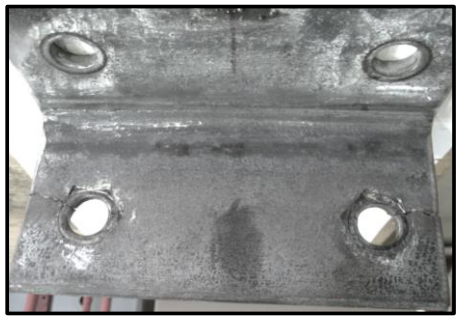












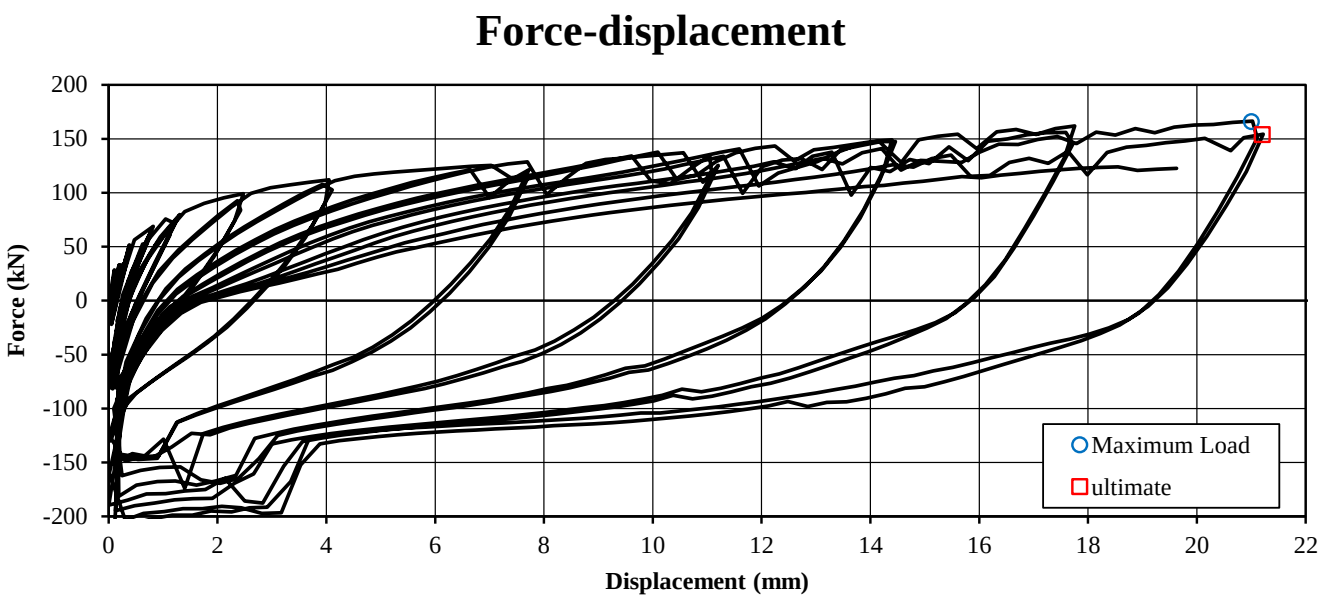
Test TC1-5

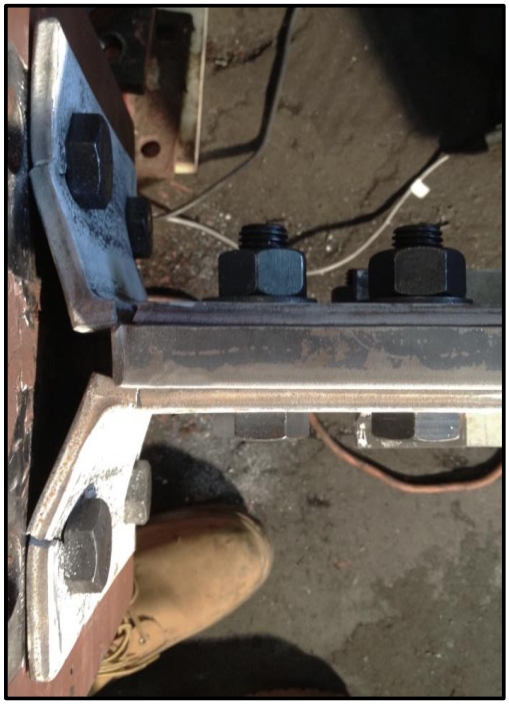
Type Cyclic W410 **Failure mode:** Beam/Net Section

Geometry:		
g_{column}	64	mm
t	9.5	mm
g_{beam}	57	mm
φ_{bolt}	19.1	mm
k	22.2	mm
g_2	25.4	mm
g_2/t	2.67	

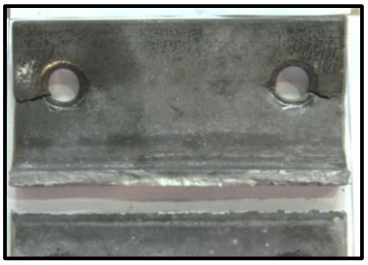
Materials:		
Angle	A36	
F_y	375	MPa
F_u	537	MPa
ε_u	0.2372	
Bolt	A325	
Column bolts	400	lbf-ft
Plate bolts	400	lbf-ft

Key response parameters:		
F_{Max}	166	kN
Δ_{FMax}	21.0	mm
$Drift_{FMax}$	7	%
$F_{Ultimate}$	154	kN
$\Delta_{Ultimate}$	21.2	mm
$Drift_{Ultimate}$	7	%













Test TC1-6

Type Snug-Thight

Failure mode: Beam

Key response parameters:

$K_{Plastic}$	5.0	kN/mm
$K_{Softening}$	-	kN/mm
$K_{Hardening}$	-	kN/mm

Geometry:

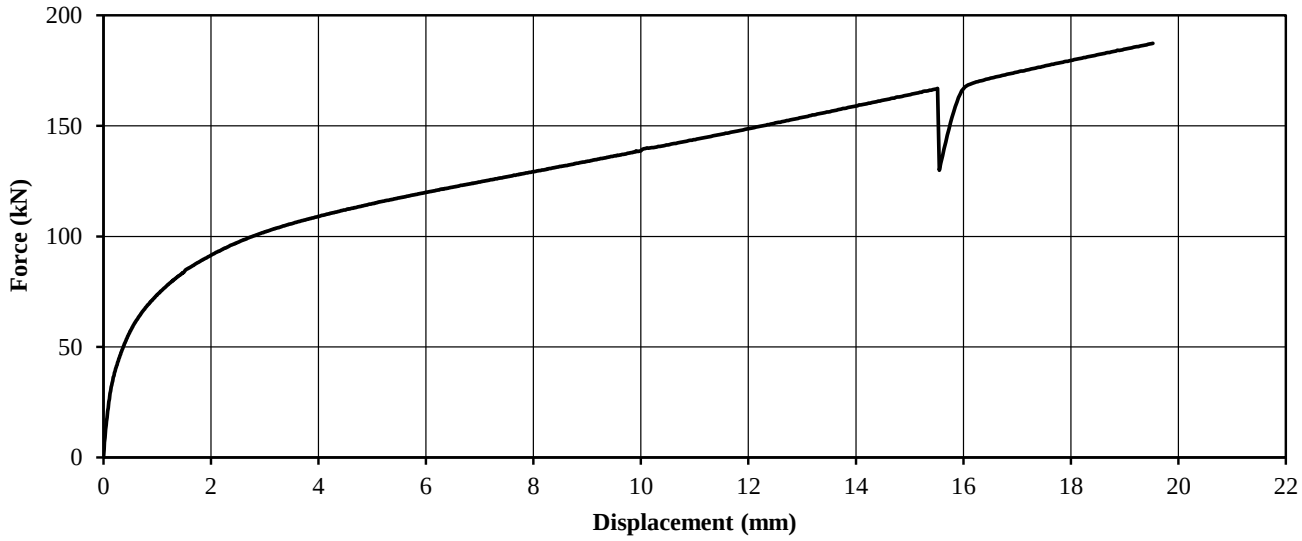
g_{column}	64	mm
t	9.5	mm
g_{beam}	57	mm
φ_{bolt}	19.1	mm
k	22.2	mm
g_2	25.4	mm
g_2/t	2.67	

Materials:

Angle	A36	
F_y	375	MPa
F_u	537	MPa
ε_u	0.2372	
Bolt	A325	
Column bolts	Snug-Thight	
Plate bolts	400	lbf-ft

	F (kN)	Δ (mm)
Initial	-	-
Plastic	111	4.4
Softening	-	-
Hardening	-	-
Max. Force	187	19.5
Ultimate	187	19.5

Force-displacement













Test TC1-7

Type Time-History **Failure mode:** Beam/Column/Net Section

Geometry:

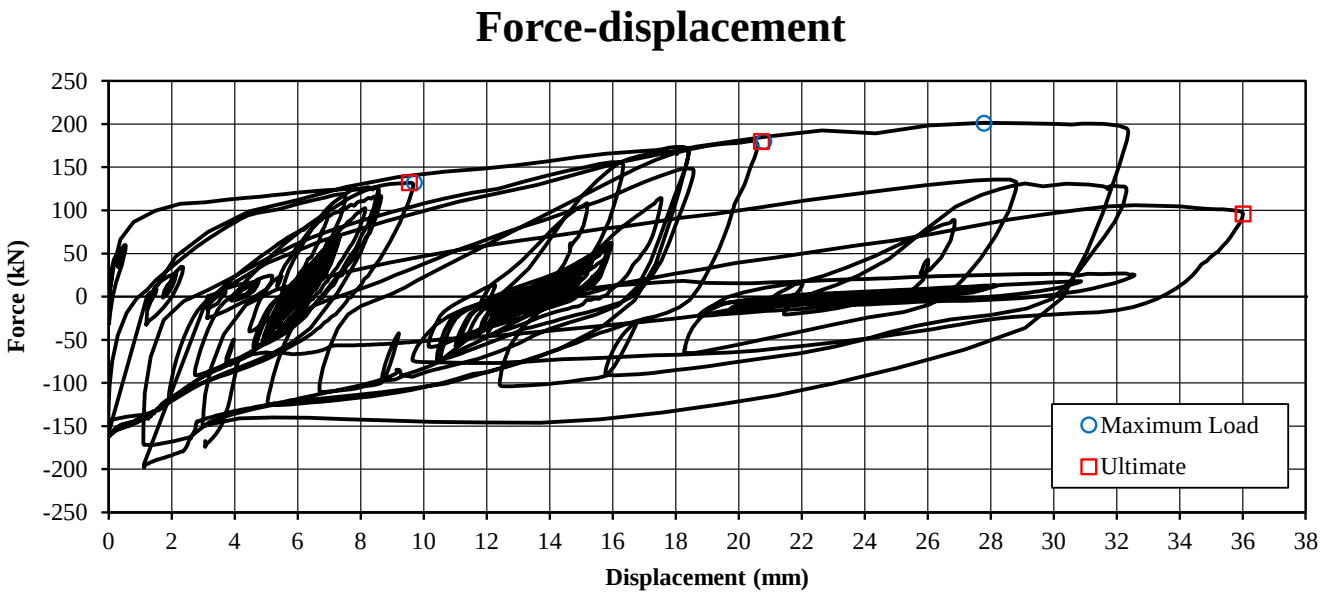
g_{column}	64	mm
t	9.5	mm
g_{beam}	57	mm
φ_{bolt}	19.1	mm
k	22.2	mm
g_2	25.4	mm
g_2/t	2.67	

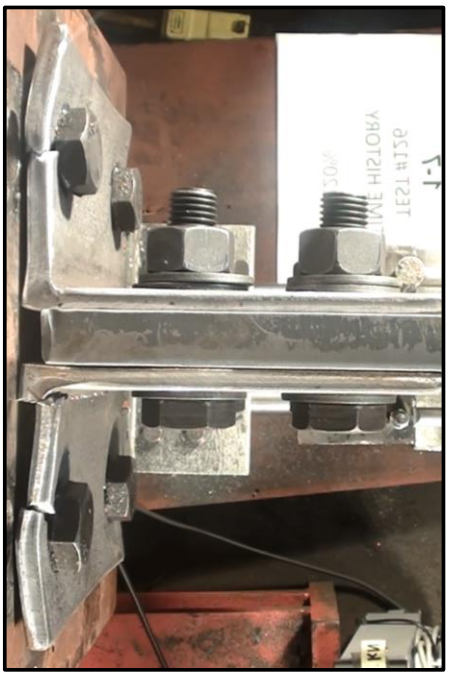
Materials:

Angle	A36	
F_y	375	MPa
F_u	537	MPa
ε_u	0.2372	
Bolt	A325	
Column bolts	400	lbf-ft
Plate bolts	400	lbf-ft

Key response parameters:

Signal factor	65%	130%	220%
Δ_0	0.0	1.2	3.1
$F_{F\ Max}$	132	180	201
$\Delta_{F\ Max}$	9.7	20.8	27.8
$F_{Ultimate}$	132	180	96
$\Delta_{Ultimate}$	9.6	20.7	36.0













Test TC2-1

Type Monotonic Static

Loading Rate: 100 με/s

Failure mode: Column

Key response parameters:

$K_{Plastic}$	4.6	kN/mm
$K_{Softening}$	-	kN/mm
$K_{Hardening}$	5.5	kN/mm

Geometry:

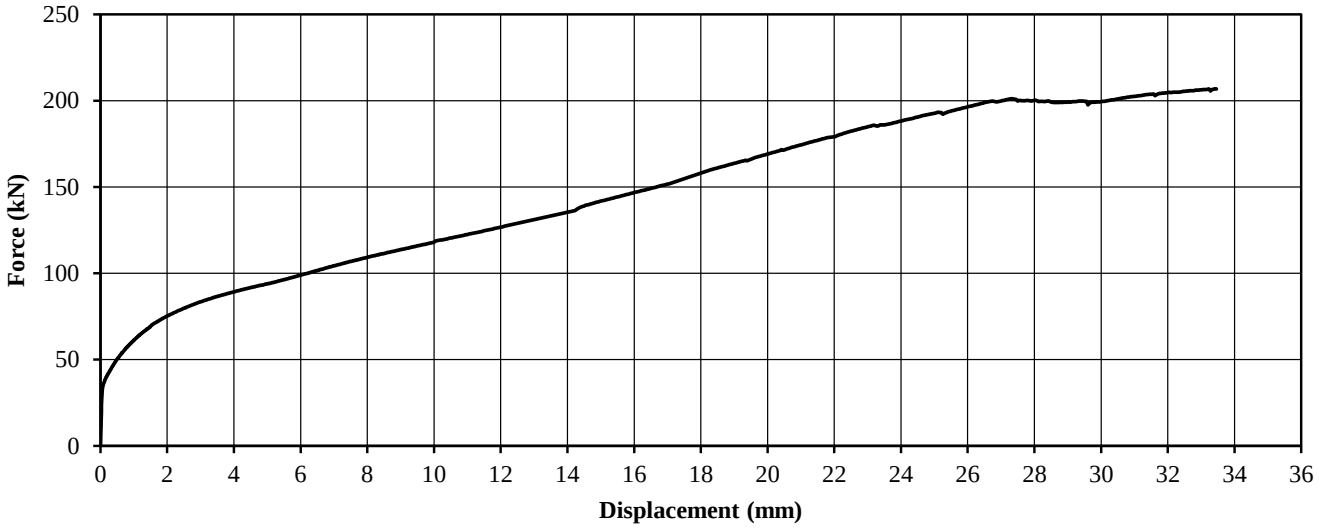
g_{column}	76	mm
t	9.5	mm
g_{beam}	57	mm
φ_{bolt}	19.1	mm
k	22.2	mm
g_2	38.1	mm
g_2/t	4.00	

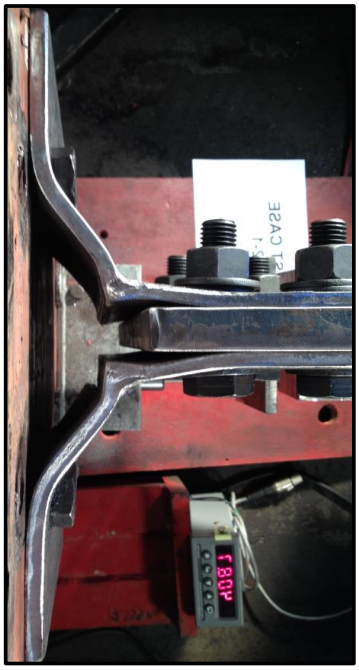
Materials:

Angle	A36	
F_y	370	MPa
F_u	518	MPa
ε_u	0.2420	
Bolt	A325	
Column bolts	400	lbf-ft
Plate bolts	400	lbf-ft

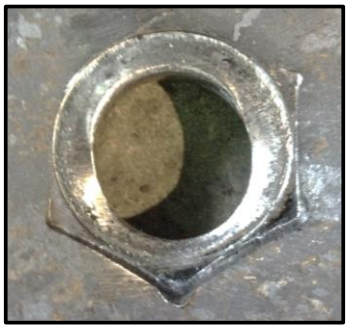
	F (kN)	Δ (mm)
Initial	35	0.070
Plastic	92	4.5
Softening	-	-
Hardening	132	13.3
Max. Force	207	33.5
Ultimate	207	33.5

Force-displacement













Test TC2-2

Type Monotonic Static

Loading Rate: 600 με/s

Failure mode: Column

Geometry:

g_{column}	76	mm
t	9.5	mm
g_{beam}	57	mm
φ_{bolt}	19.1	mm
k	22.2	mm
g_2	38.1	mm
g_2/t	4.00	

Materials:

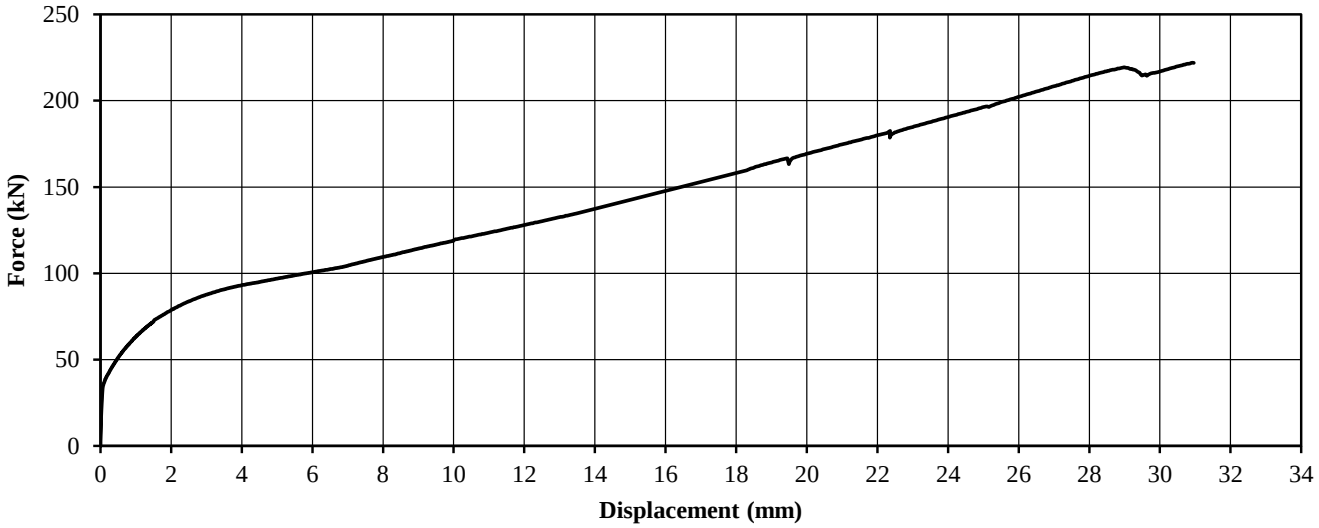
Angle	A36	
F_y	370	MPa
F_u	518	MPa
ε_u	0.2420	
Bolt	A325	
Column bolts	400	lbf-ft
Plate bolts	400	lbf-ft

Key response parameters:

$K_{Plastic}$	4.0	kN/mm
$K_{Softening}$	-	kN/mm
$K_{Hardening}$	5.2	kN/mm

	F (kN)	Δ (mm)
Initial	35	0.064
Plastic	94	4.4
Softening	-	-
Hardening	116	9.7
Max. Force	208	26.9
Ultimate	209	26.9

Force-displacement













Test TC2-3

Type Monotonic Dynamic

Loading Rate: 750000 με/s

Failure mode: Column/Bolt

Key response parameters:

$K_{Plastic}$	4.8	kN/mm
$K_{Softening}$	-	kN/mm
$K_{Hardening}$	6.2	kN/mm

Geometry:

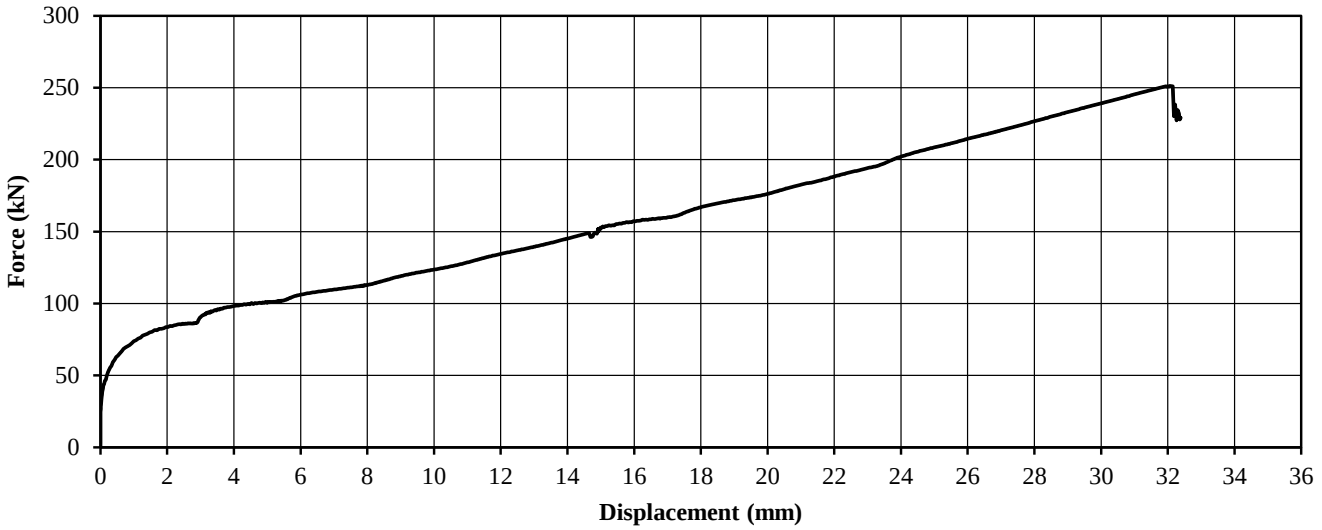
g_{column}	76	mm
t	9.5	mm
g_{beam}	57	mm
φ_{bolt}	19.1	mm
k	22.2	mm
g_2	38.1	mm
g_2/t	4.00	

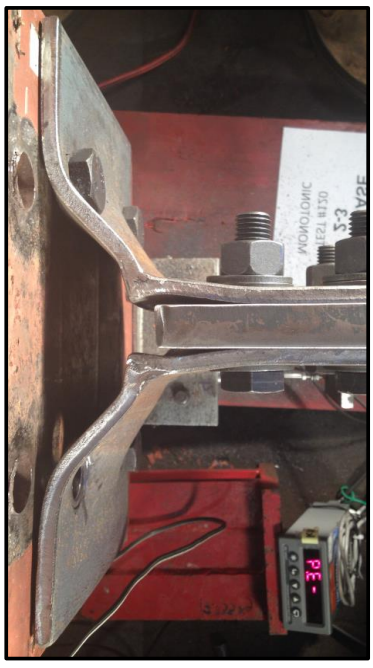
Materials:

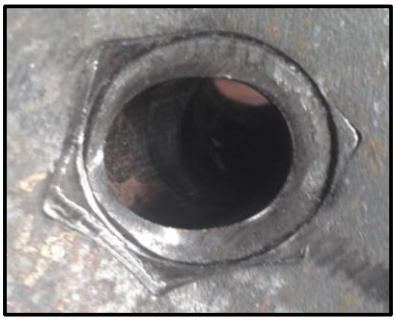
Angle	A36	
F_y	370	MPa
F_u	518	MPa
ε_u	0.2420	
Bolt	A325	
Column bolts	400	lbf-ft
Plate bolts	400	lbf-ft

	F (kN)	Δ (mm)
Initial	37	0.004
Plastic	91	3.0
Softening	-	-
Hardening	159	17.0
Max. Force	251	32.2
Ultimate	229	32.4

Force-displacement













Test TC2-4

Type Snug-Thight

Loading Rate: 100 με/s

Failure mode: Column

Geometry:

g_{column}	76	mm
t	9.5	mm
g_{beam}	57	mm
φ_{bolt}	19.1	mm
k	22.2	mm
g_2	38.1	mm
g_2/t	4.00	

Materials:

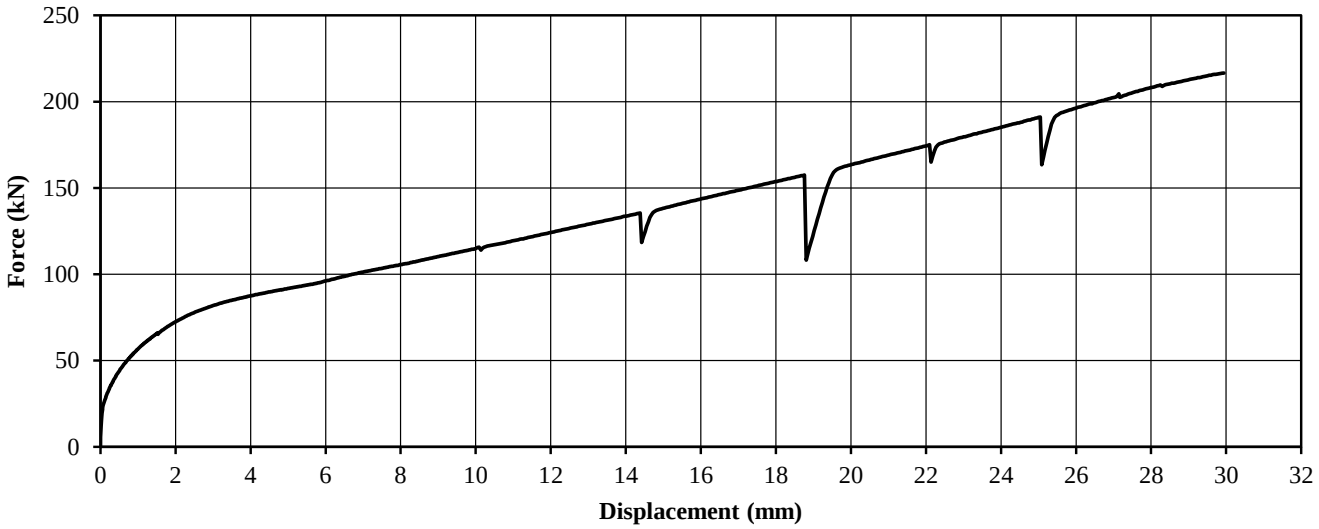
Angle	A36	
F_y	370	MPa
F_u	518	MPa
ε_u	0.2420	
Bolt	A325	
Column bolts	Snug-Thight	
Plate bolts	400	lbf-ft

Key response parameters:

$K_{Plastic}$	4.6	kN/mm
$K_{Softening}$	-	kN/mm
$K_{Hardening}$	5	kN/mm

	F (kN)	Δ (mm)
Initial	29	0.139
Plastic	84	3.3
Softening	-	-
Hardening	122	11.6
Max. Force	217	29.9
Ultimate	217	29.9

Force-displacement





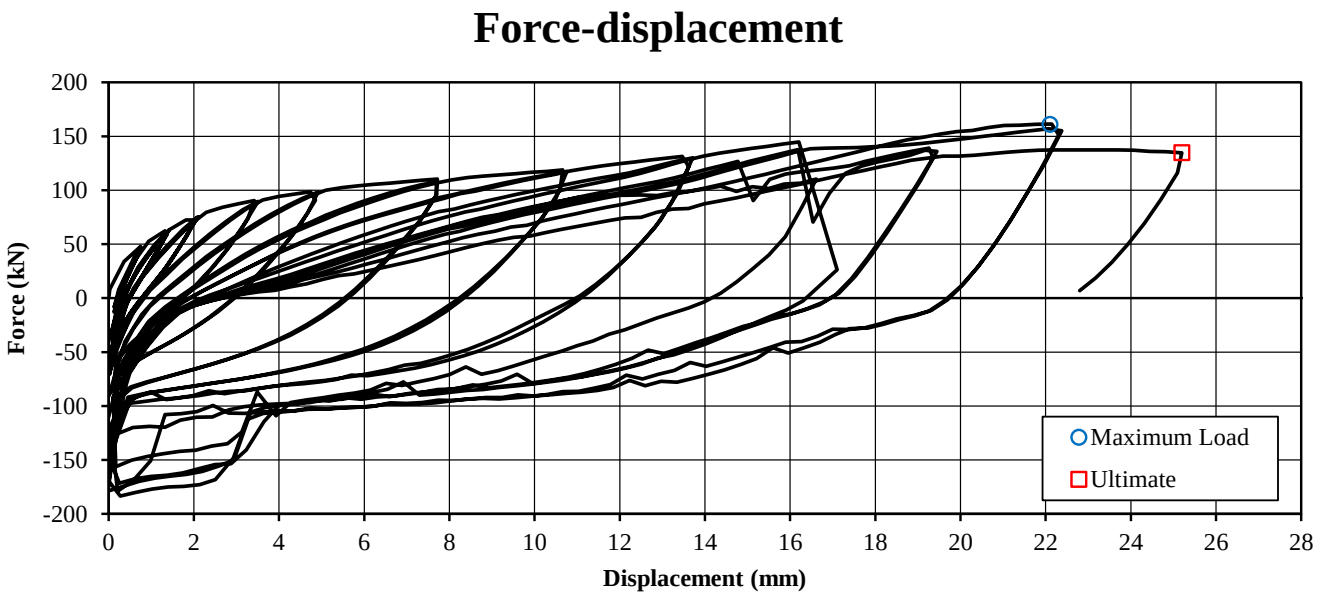
Test TC2-5

Type Cyclic W310 **Failure mode:** Beam

Geometry:		
g_{column}	76	mm
t	9.5	mm
g_{beam}	57	mm
φ_{bolt}	19.1	mm
k	22.2	mm
g_2	38.1	mm
g_2/t	4.00	

Materials:		
Angle	A36	
F_y	370	MPa
F_u	518	MPa
ε_u	0.2420	
Bolt	A325	
Column bolts	400	lbf-ft
Plate bolts	400	lbf-ft

Key response parameters:		
F_{Max}	161	kN
Δ_{FMax}	22.1	mm
$Drift_{FMax}$	8	%
$F_{Ultimate}$	135	kN
$\Delta_{Ultimate}$	25.2	mm
$Drift_{Ultimate}$	9	%













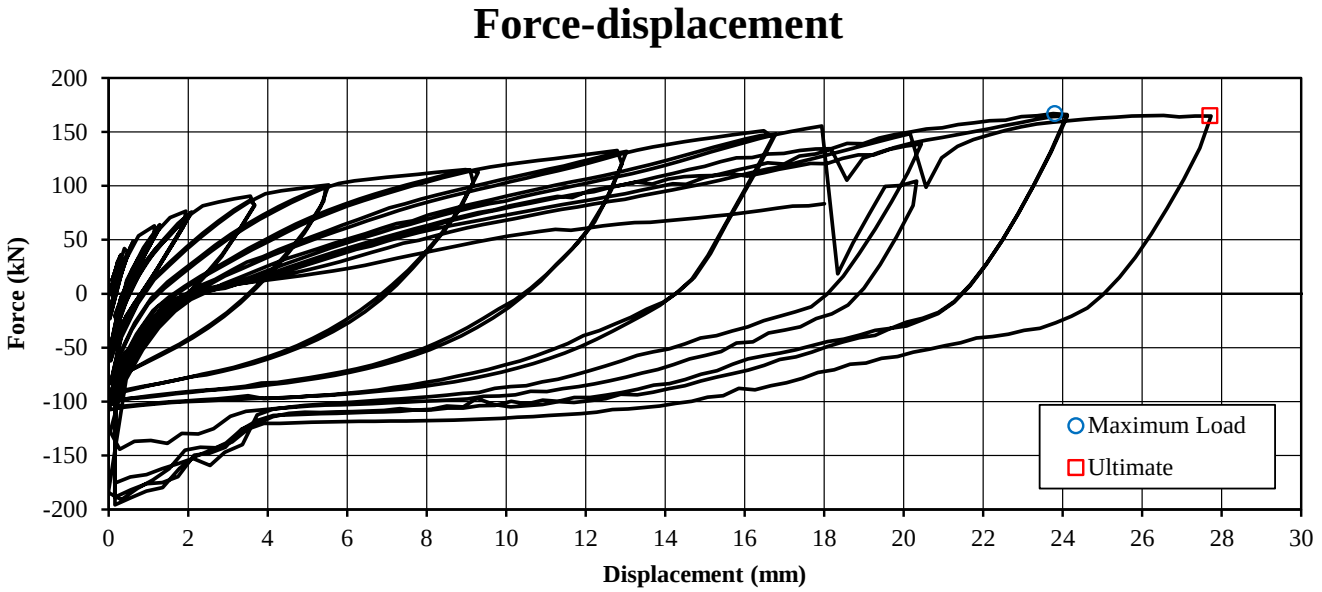
Test TC2-6

Type Cyclic W410 **Failure mode:** Beam

Geometry:		
g_{column}	76	mm
t	9.5	mm
g_{beam}	57	mm
φ_{bolt}	19.1	mm
k	22.2	mm
g_2	38.1	mm
g_2/t	4.00	

Materials:		
Angle	A36	
F_y	370	MPa
F_u	518	MPa
ε_u	0.2420	
Bolt	A325	
Column bolts	400	lbf-ft
Plate bolts	400	lbf-ft

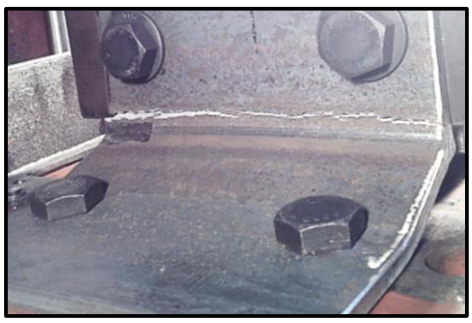
Key response parameters:		
F_{Max}	167	kN
Δ_{FMax}	23.8	mm
$Drift_{FMax}$	7	%
$F_{Ultimate}$	165	kN
$\Delta_{Ultimate}$	27.7	mm
$Drift_{Ultimate}$	8	%













Test TC2-7

Type Time-History **Failure mode:** Beam

Geometry:

g_{column}	76	mm
t	9.5	mm
g_{beam}	57	mm
φ_{bolt}	19.1	mm
k	22.2	mm
g_2	38.1	mm
g_2/t	4.00	

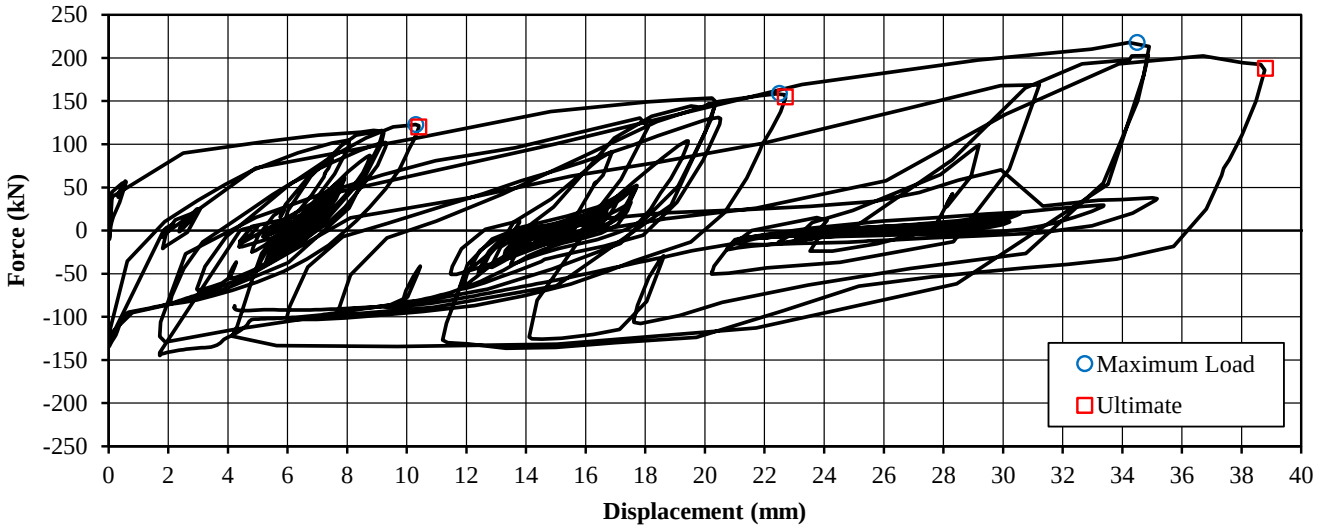
Materials:

Angle	A36	
F_y	370	MPa
F_u	518	MPa
ε_u	0.2420	
Bolt	A325	
Column bolts	400	lbf-ft
Plate bolts	400	lbf-ft

Key response parameters:

Signal factor	70%	140%	230%
Δ_0	0.0	1.8	4.4
$F_{F\ Max}$	123	159	218
$\Delta_{F\ Max}$	10.3	22.5	34.5
$F_{Ultimate}$	120	155	188
$\Delta_{ultimate}$	10.4	22.7	38.8

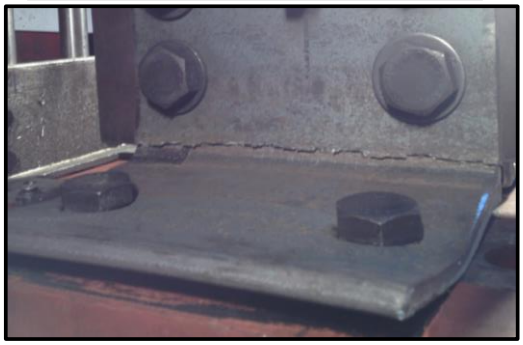
Force-displacement













Test TC3-1

Type Monotonic Static

Loading Rate: 100 με/s

Failure mode: Beam

Geometry:

g_{column}	64	mm
t	12.7	mm
g_{beam}	76	mm
φ_{bolt}	25.4	mm
k	25.4	mm
g_2	17.5	mm
g_2/t	1.38	

Materials:

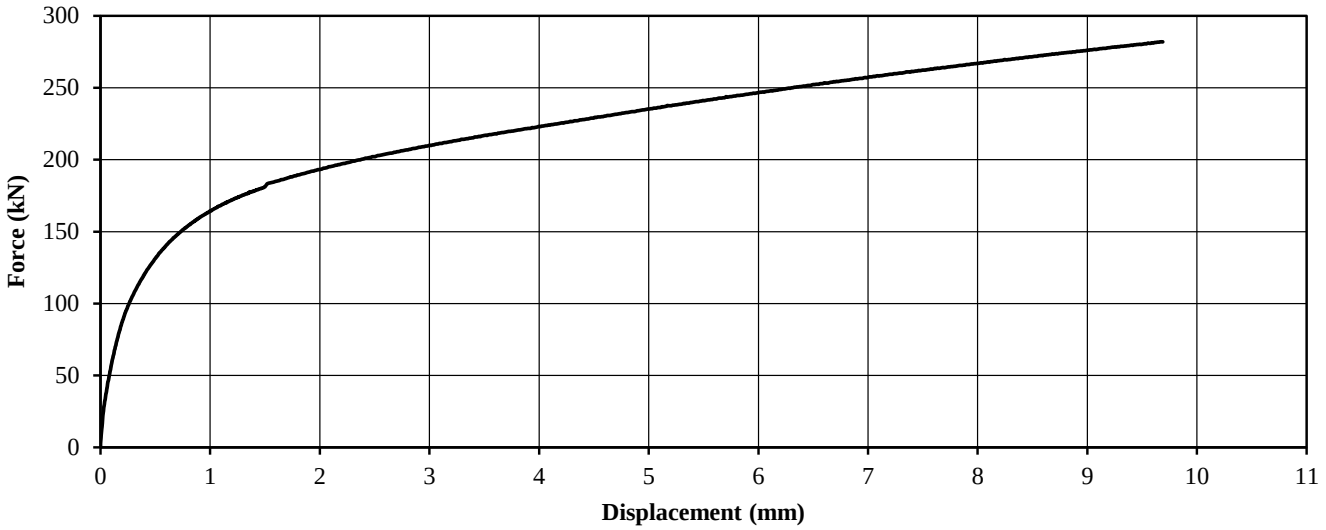
Angle	A36	
F_y	358	MPa
F_u	506	MPa
ε_u	0.2512	
Bolt	A490	
Column bolts	1000	lbf-ft
Plate bolts	1000	lbf-ft

Points of interest:

$K_{Plastic}$	13.0	kN/mm
$K_{Softening}$	9.7	kN/mm
$K_{Hardening}$	-	kN/mm

	F (kN)	Δ (mm)
Initial	-	-
Plastic	206	2.5
Softening	251	6.0
Hardening	-	-
Max. Force	324	13.4
Ultimate	324	13.4

Force-displacement





Test TC3-2

Type Monotonic Static

Loading Rate: 600 με/s

Failure mode: Beam

Geometry:

g_{column}	64	mm
t	12.7	mm
g_{beam}	76	mm
φ_{bolt}	25.4	mm
k	25.4	mm
g_2	17.5	mm
g_2/t	1.38	

Materials:

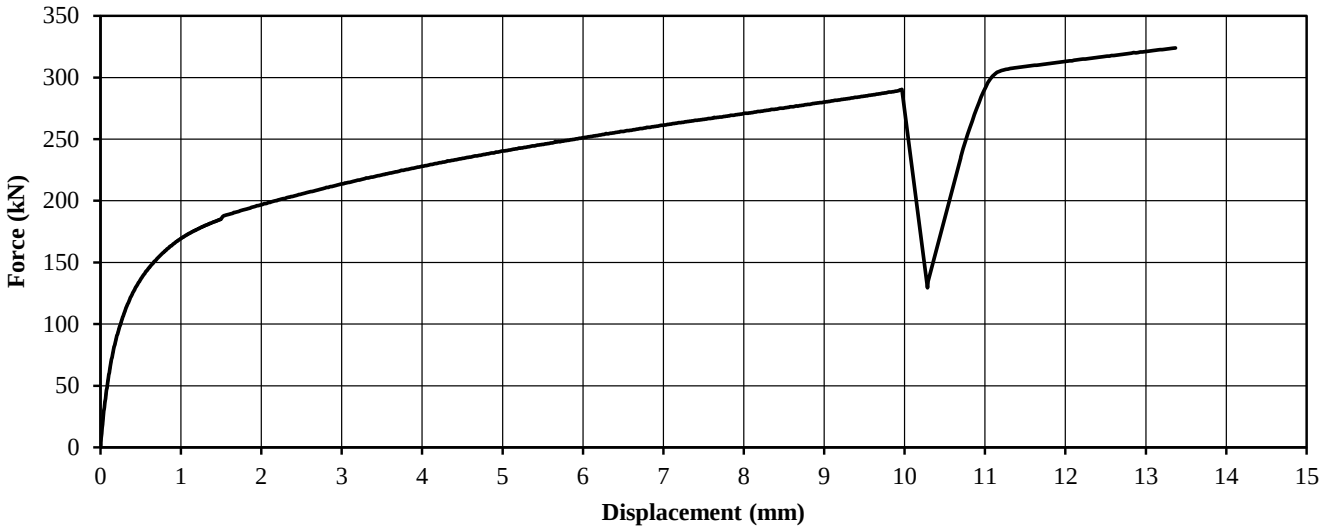
Angle	A36	
F_y	358	MPa
F_u	506	MPa
ε_u	0.2512	
Bolt	A490	
Column bolts	1000	lbf-ft
Plate bolts	1000	lbf-ft

Points of interest:

$K_{Plastic}$	13.0	kN/mm
$K_{Softening}$	9.7	kN/mm
$K_{Hardening}$	-	kN/mm

	F (kN)	Δ (mm)
Initial	-	-
Plastic	206	2.5
Softening	251	6.0
Hardening	-	-
Max. Force	324	13.4
Ultimate	324	13.4

Force-displacement









Test TC3-3

Type Monotonic Static

Loading Rate: 750000 με/s

Failure mode: Beam

Geometry:

g_{column}	64	mm
t	12.7	mm
g_{beam}	76	mm
φ_{bolt}	25.4	mm
k	25.4	mm
g_2	17.5	mm
g_2/t	1.38	

Materials:

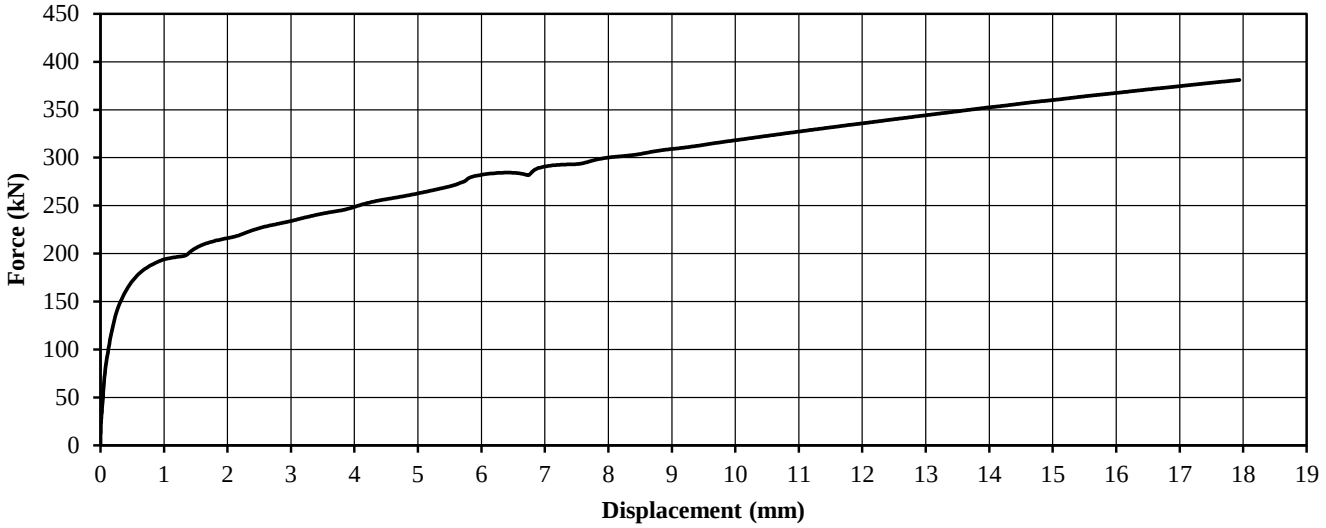
Angle	A36	
F_y	358	MPa
F_u	506	MPa
ε_u	0.2512	
Bolt	A490	
Column bolts	1000	lbf-ft
Plate bolts	1000	lbf-ft

Points of interest:

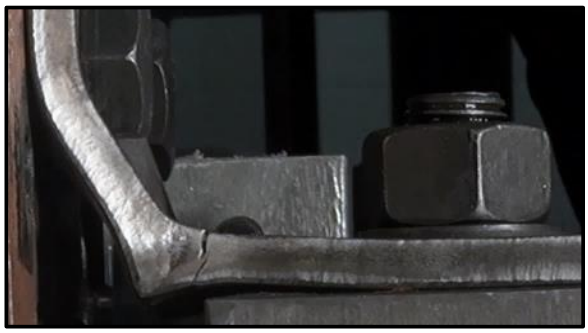
$K_{Plastic}$	15.4	kN/mm
$K_{Softening}$	8.2	kN/mm
$K_{Hardening}$	-	kN/mm

	F (kN)	Δ (mm)
Initial	-	-
Plastic	213	1.8
Softening	296	7.2
Hardening	-	-
Max. Force	381	17.9
Ultimate	381	17.9

Force-displacement









Test TC3-4

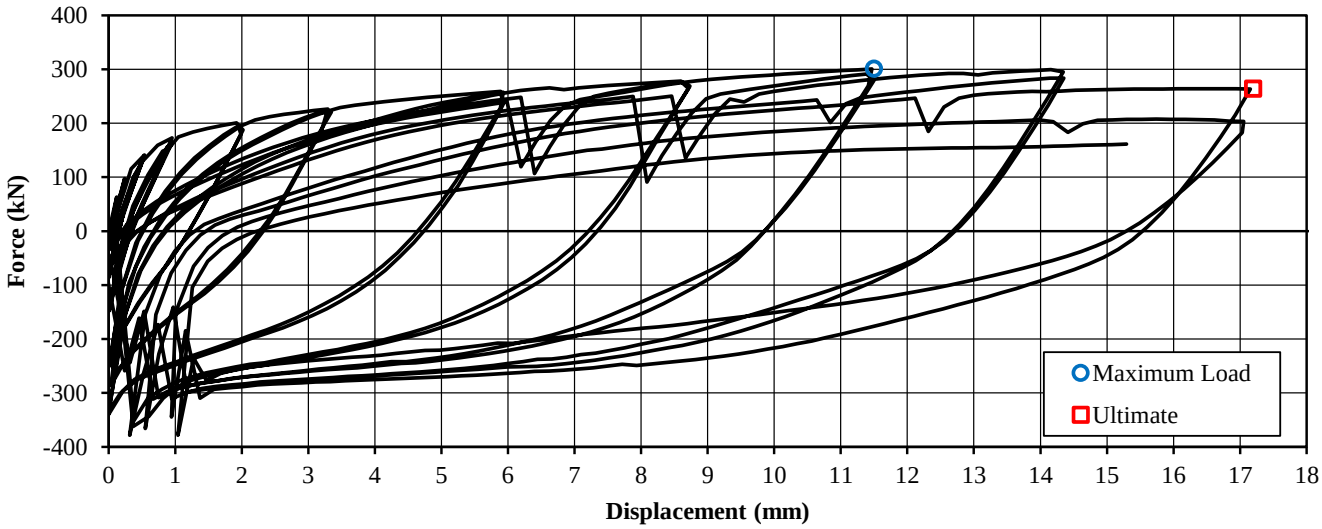
Type Cyclic W310 **Failure mode:** Beam/Net Section

Geometry:		
g_{column}	64	mm
t	12.7	mm
g_{beam}	76	mm
φ_{bolt}	25.4	mm
k	25.4	mm
g_2	17.5	mm
g_2/t	1.38	

Materials:		
Angle	A36	
F_y	358	MPa
F_u	506	MPa
ε_u	0.2512	
Bolt	A490	
Column bolts	1000	lbf-ft
Plate bolts	1000	lbf-ft

Points of interest:		
F_{Max}	301	kN
Δ_{FMax}	11.5	mm
$Drift_{FMax}$	5	%
$F_{Ultimate}$	264	kN
$\Delta_{Ultimate}$	17.2	mm
$Drift_{Ultimate}$	7	%

Force-displacement







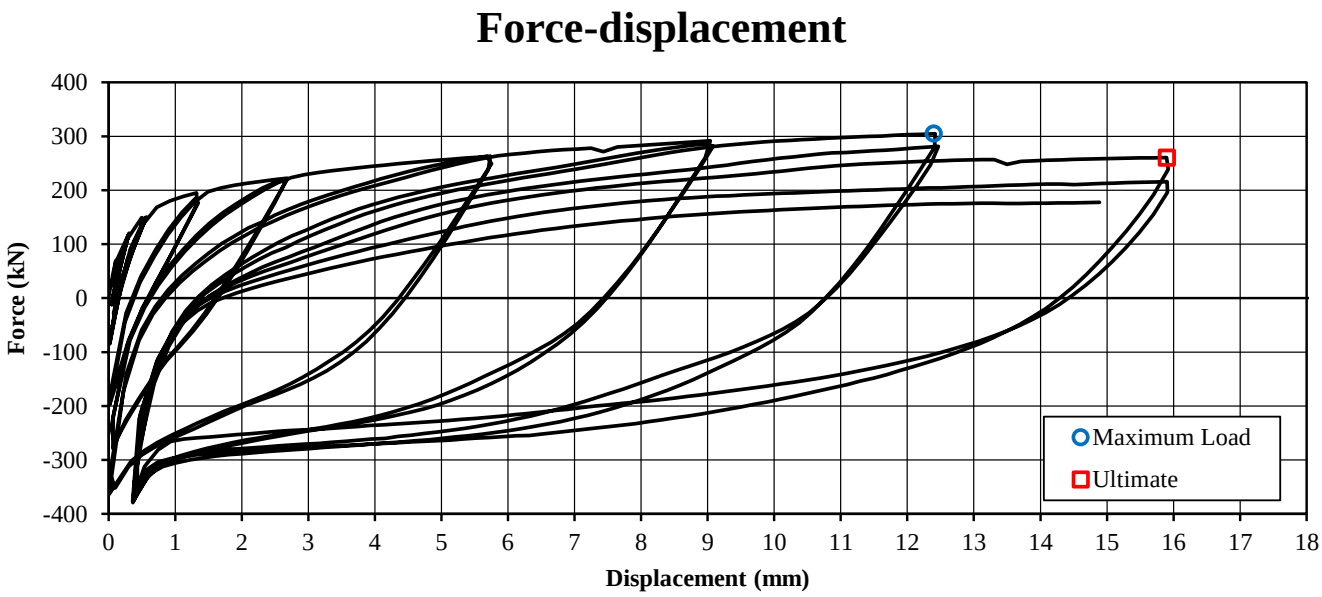
Test TC3-5

Type Cyclic W410 **Failure mode:** Beam/Net Section

Geometry:		
g_{column}	64	mm
t	12.7	mm
g_{beam}	76	mm
φ_{bolt}	25.4	mm
k	25.4	mm
g_2	17.5	mm
g_2/t	1.38	

Materials:		
Angle	A36	
F_y	358	MPa
F_u	506	MPa
ε_u	0.2512	
Bolt	A490	
Column bolts	1000	lbf-ft
Plate bolts	1000	lbf-ft

Points of interest:		
F_{Max}	305	kN
Δ_{FMax}	12.4	mm
$Drift_{FMax}$	5	%
$F_{Ultimate}$	260	kN
$\Delta_{Ultimate}$	15.9	mm
$Drift_{Ultimate}$	7	%









Test TC3-6

Type Time-History **Failure mode:** Beam/Net Section

Geometry:

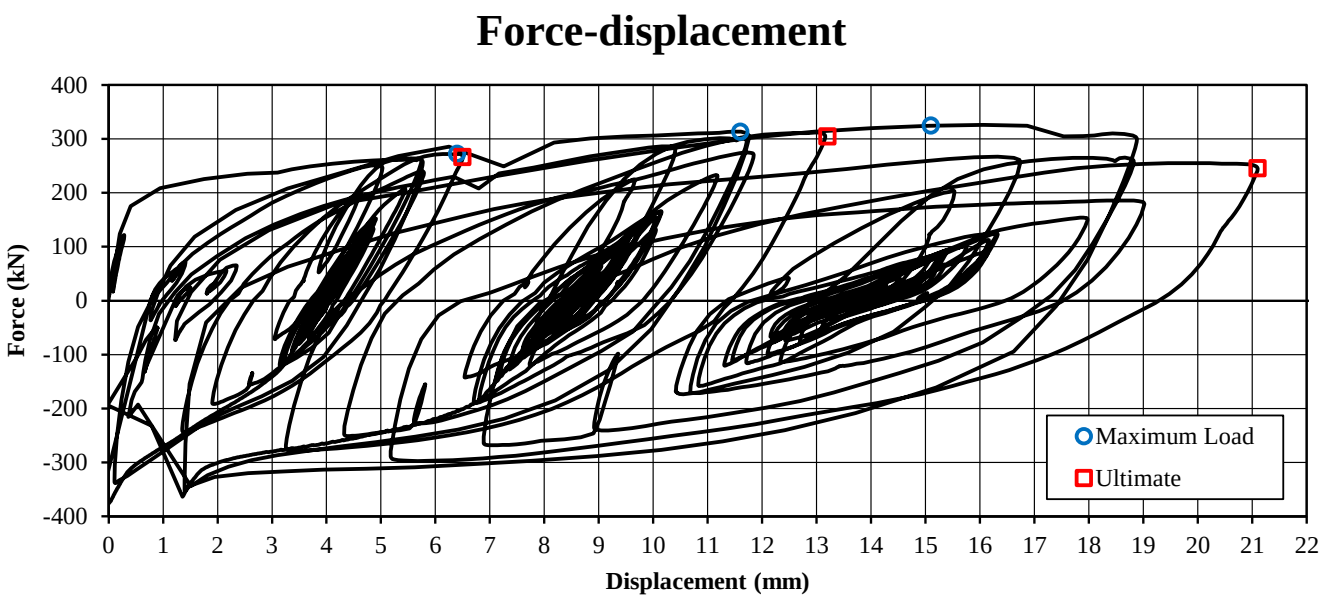
g_{column}	64	mm
t	12.7	mm
g_{beam}	76	mm
φ_{bolt}	25.4	mm
k	25.4	mm
g_2	17.5	mm
g_2/t	1.38	

Materials:

Angle	A36	
F_y	358	MPa
F_u	506	MPa
ε_u	0.2512	
Bolt	A490	
Column bolts	1000	lbf-ft
Plate bolts	1000	lbf-ft

Points of interest:

Signal factor	66%	125%	200%
Δ_0	0.0	0.8	1.2
$F_{F\ Max}$	272	313	324
$\Delta_{F\ Max}$	6.4	11.6	15.1
$F_{Ultimate}$	266	304	245
$\Delta_{ultimate}$	6.5	13.2	21.1







Test TC4-1

Type Monotonic Static

Loading Rate: 100 με/s

Failure mode: Column

Key response parameters:

$K_{Plastic}$	6.7	kN/mm
$K_{Softening}$	-	kN/mm
$K_{Hardening}$	7.9	kN/mm

Geometry:

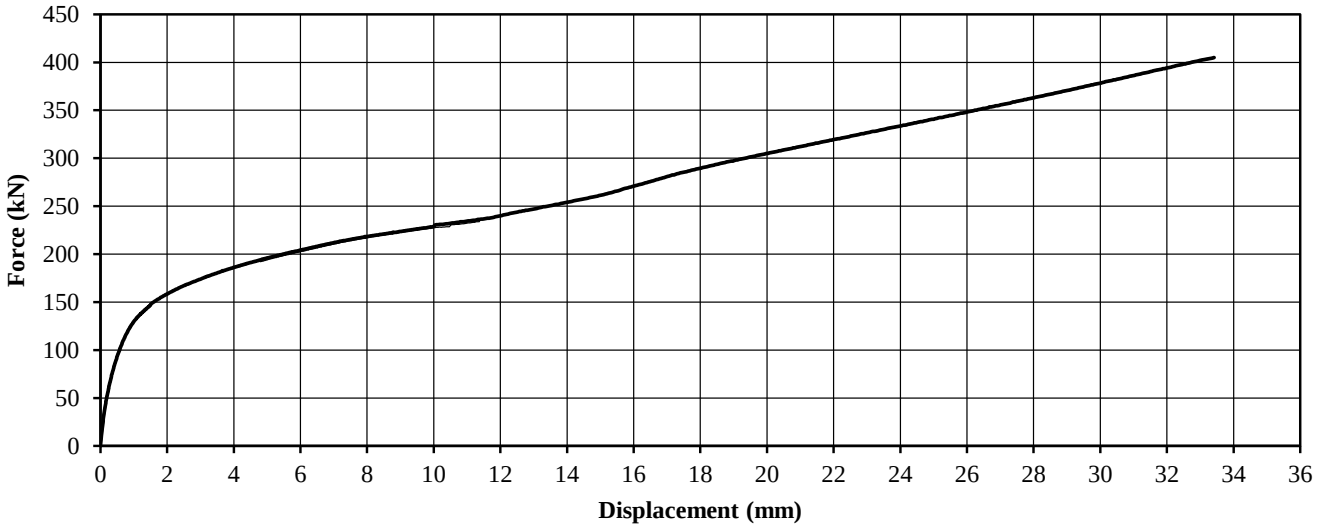
g_{column}	76	mm
t	12.7	mm
g_{beam}	76	mm
φ_{bolt}	25.4	mm
k	25.4	mm
g_2	30.2	mm
g_2/t	2.38	

Materials:

Angle	A36	
F_y	342	MPa
F_u	499	MPa
ε_u	0.2620	
Bolt	A490	
Column bolts	1000	lbf-ft
Plate bolts	1000	lbf-ft

	F (kN)	Δ (mm)
Initial	-	-
Plastic	197	5.1
Softening	-	-
Hardening	258	14.3
Max. Force	405	33.4
Ultimate	405	33.4

Force-displacement













Test TC4-2

Type Monotonic Static

Loading Rate: 600 με/s

Failure mode: Column/Beam

Key response parameters:

$K_{Plastic}$	6.9	kN/mm
$K_{Softening}$	-	kN/mm
$K_{Hardening}$	8.0	kN/mm

Geometry:

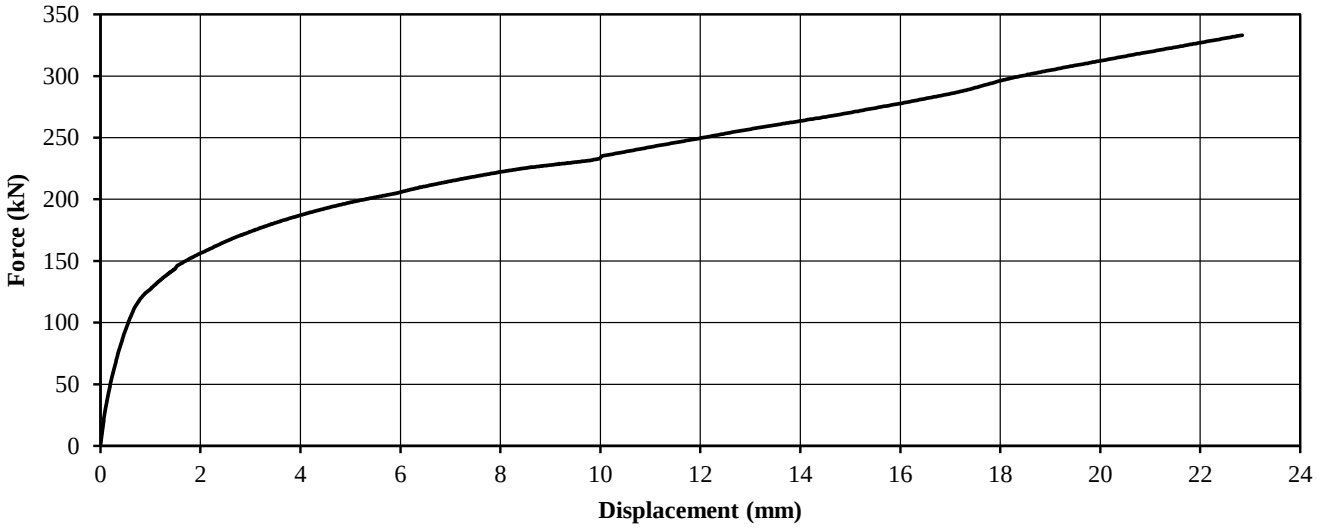
g_{column}	76	mm
t	12.7	mm
g_{beam}	76	mm
φ_{bolt}	25.4	mm
k	25.4	mm
g_2	30.2	mm
g_2/t	2.38	

Materials:

Angle	A36	
Fy	342	MPa
F_u	499	MPa
ε_u	0.2620	
Bolt	A490	
Column bolts	1000	lbf-ft
Plate bolts	1000	lbf-ft

	F (kN)	Δ (mm)
Initial	-	-
Plastic	202	5.6
Softening	-	-
Hardening	242	11.4
Max. Force	333	22.8
Ultimate	333	22.8

Force-displacement













Test TC4-3

Type Monotonic Static

Loading Rate: 750000 με/s

Failure mode: Column

Key response parameters:

$K_{Plastic}$	7.5	kN/mm
$K_{Softening}$	-	kN/mm
$K_{Hardening}$	8.0	kN/mm

Geometry:

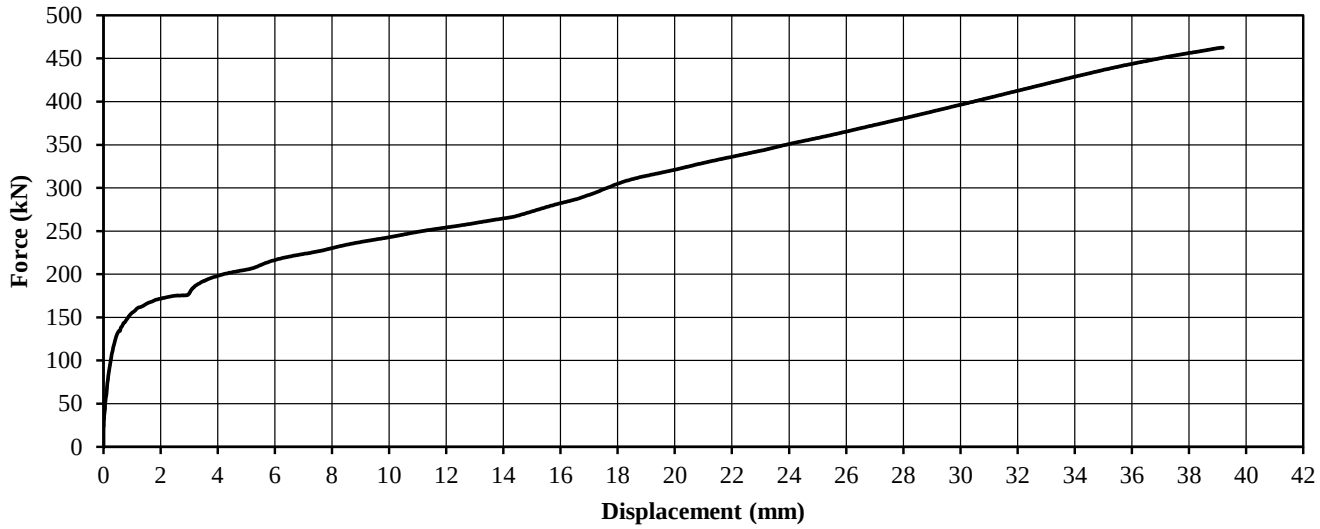
g_{column}	76	mm
t	12.7	mm
g_{beam}	76	mm
φ_{bolt}	25.4	mm
k	25.4	mm
g_2	30.2	mm
g_2/t	2.38	

Materials:

Angle	A36	
Fy	342	MPa
F_u	499	MPa
ε_u	0.2620	
Bolt	A490	
Column bolts	1000	lbf-ft
Plate bolts	1000	lbf-ft

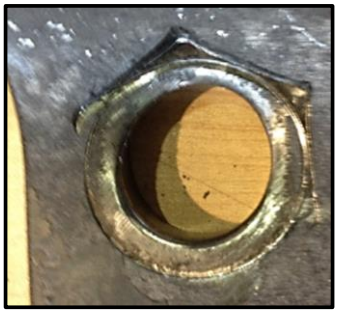
	F (kN)	Δ (mm)
Initial	26	0.016
Plastic	191	3.4
Softening	-	-
Hardening	271	14.1
Max. Force	463	39.2
Ultimate	463	39.2

Force-displacement













Test TC4-4

Type Snug-Thight

Loading Rate: 100 με/s

Failure mode: Column/Net Section

Key response parameters:

$K_{Plastic}$	7.3	kN/mm
$K_{Softening}$	-	kN/mm
$K_{Hardening}$	10.3	kN/mm

Geometry:

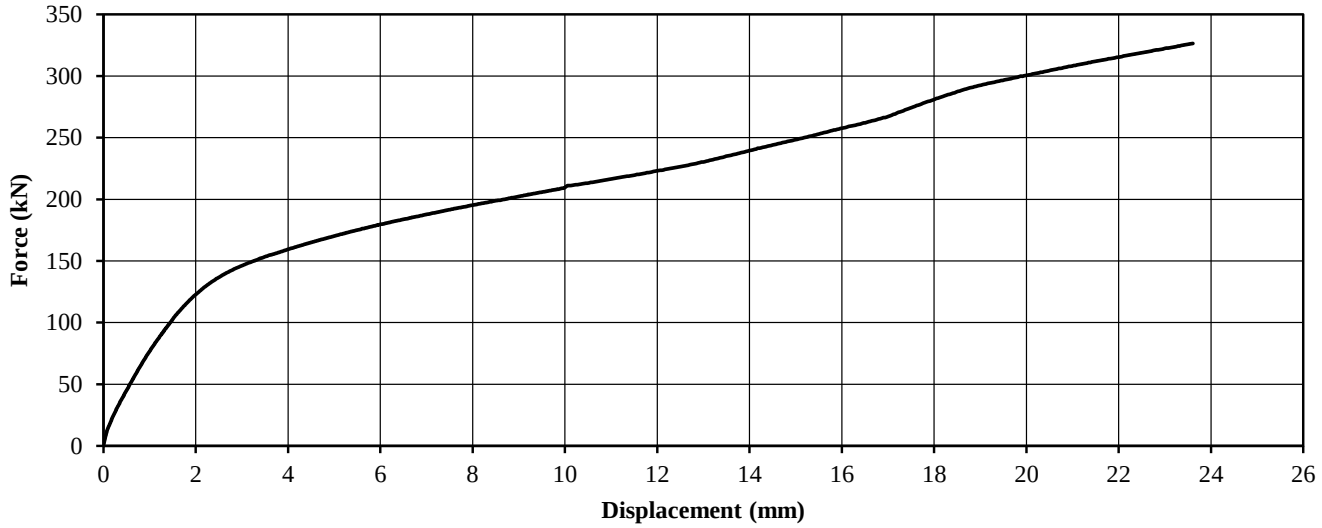
g_{column}	76	mm
t	12.7	mm
g_{beam}	76	mm
φ_{bolt}	25.4	mm
k	25.4	mm
g_2	30.2	mm
g_2/t	2.38	

Materials:

Angle	A36	
Fy	342	MPa
F_u	499	MPa
ε_u	0.2620	
Bolt	A490	
Column bolts	Snug-Thight	
Plate bolts	1000	lbf-ft

	F (kN)	Δ (mm)
Initial	-	-
Plastic	176	5.6
Softening	-	-
Hardening	235	13.7
Max. Force	326	23.6
Ultimate	326	23.6

Force-displacement













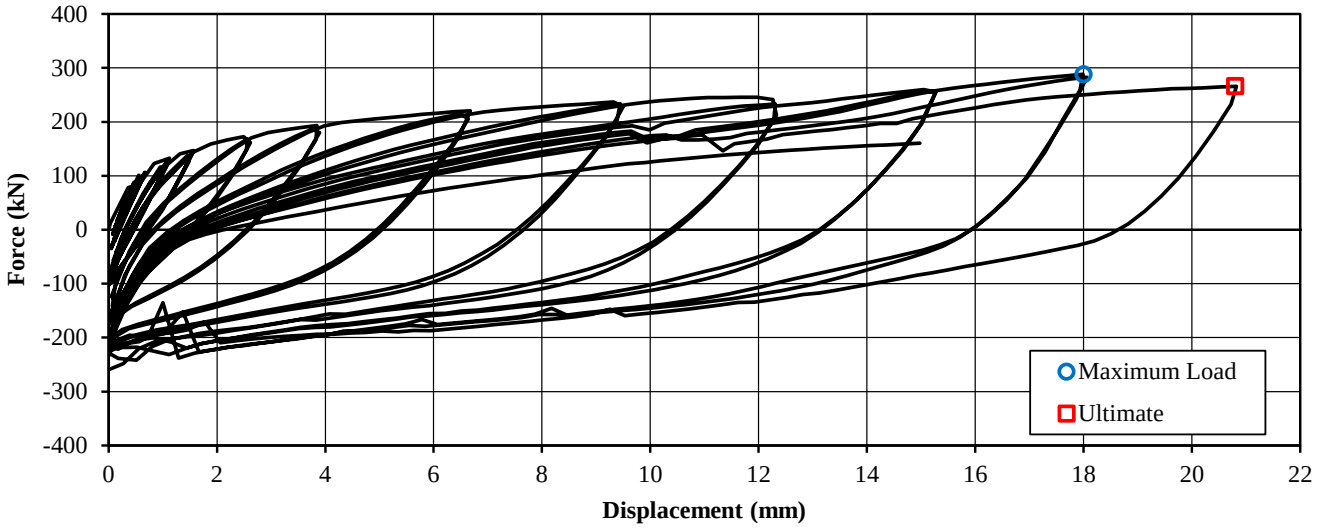
Test TC4-5

Type Cyclic W310 **Failure mode:** Beam

Geometry:		
g_{column}	76	mm
t	12.7	mm
g_{beam}	76	mm
φ_{bolt}	25.4	mm
k	25.4	mm
g_2	30.2	mm
g_2/t	2.38	

Materials:		
Angle	A36	
Fy	342	MPa
F_u	499	MPa
ε_u	0.2620	
Bolt	A490	
Column bolts	1000	lbf-ft
Plate bolts	1000	lbf-ft

Key response parameters:		
F_{Max}	288	kN
Δ_{FMax}	18.0	mm
$Drift_{FMax}$	7	%
$F_{Ultimate}$	266	kN
$\Delta_{Ultimate}$	20.8	mm
$Drift_{Ultimate}$	8	%





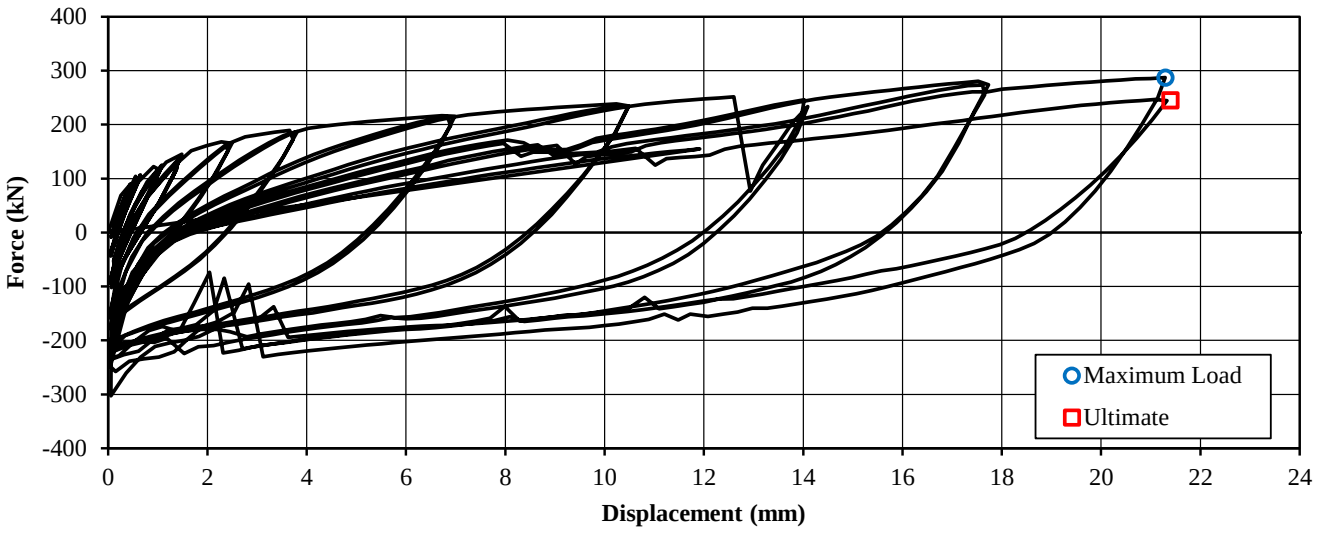
Test TC4-6

Type Cyclic W410 **Failure mode:** Beam

Geometry:		
g_{column}	76	mm
t	12.7	mm
g_{beam}	76	mm
φ_{bolt}	25.4	mm
k	25.4	mm
g_2	30.2	mm
g_2/t	2.38	

Materials:		
Angle	A36	
Fy	342	MPa
F_u	499	MPa
ε_u	0.2620	
Bolt	A490	
Column bolts	1000	lbf-ft
Plate bolts	1000	lbf-ft

Key response parameters:		
F_{Max}	287	kN
Δ_{FMax}	21.3	mm
$Drift_{FMax}$	7	%
$F_{Ultimate}$	245	kN
$\Delta_{Ultimate}$	21.4	mm
$Drift_{Ultimate}$	7	%





Test TC4-7

Type Time-History **Failure mode:** -

Geometry:

g_{column}	76	mm
t	12.7	mm
g_{beam}	76	mm
φ_{bolt}	25.4	mm
k	25.4	mm
g_2	30.2	mm
g_2/t	2.38	

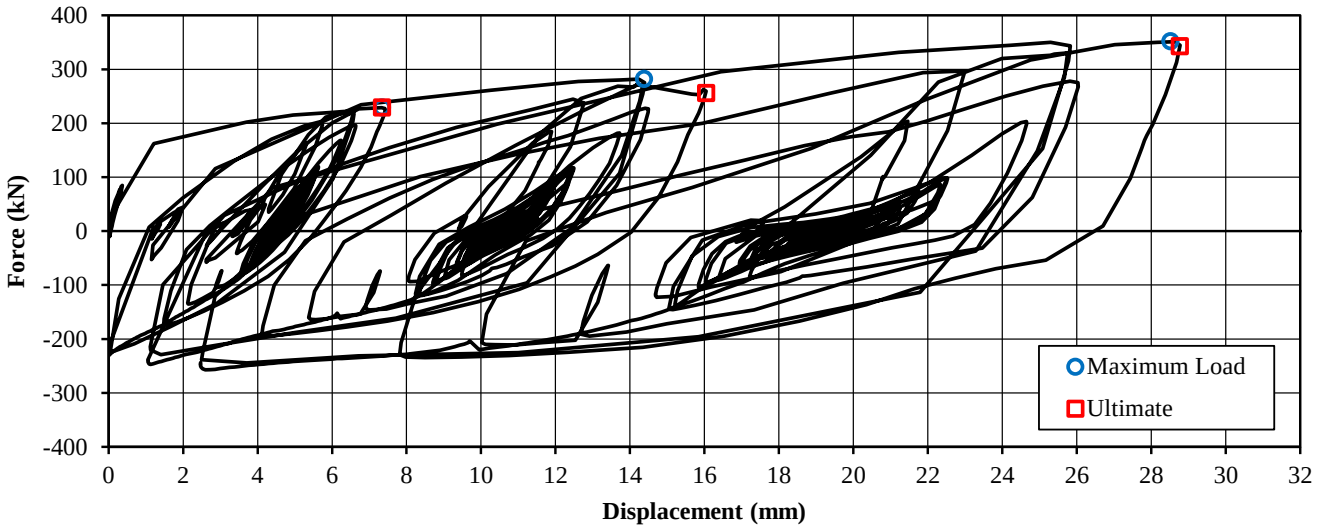
Materials:

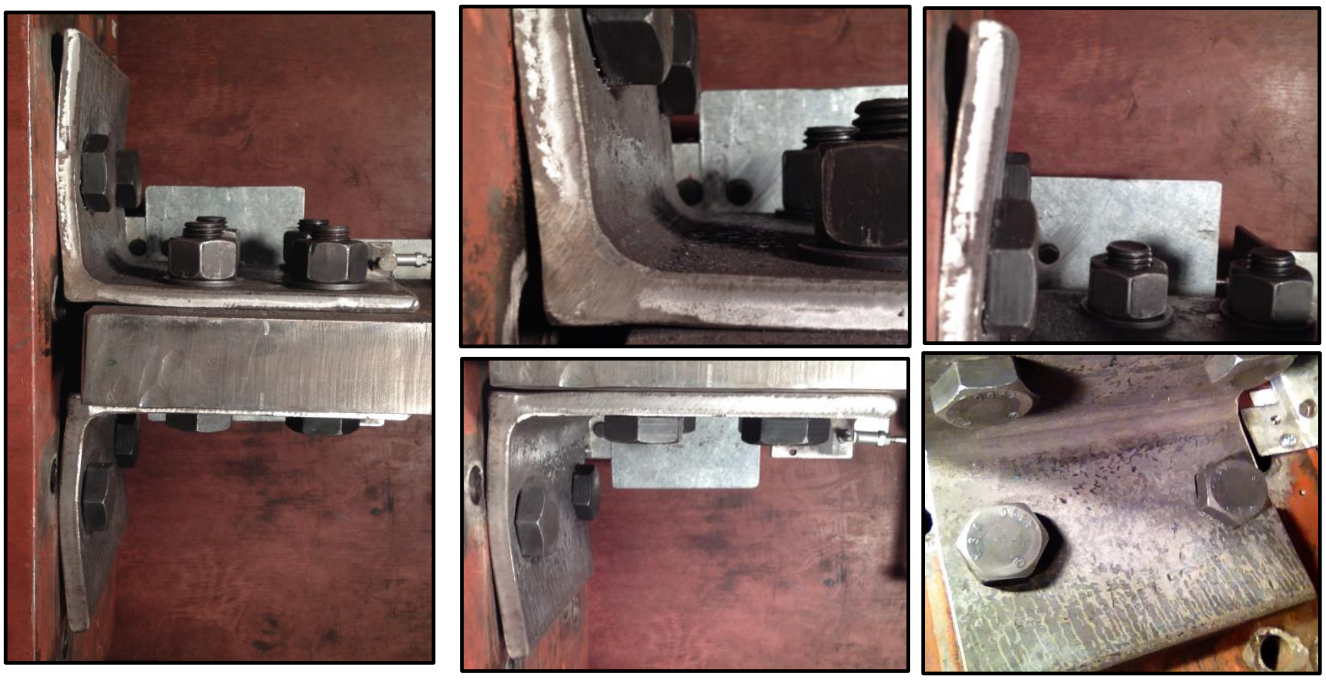
Angle	A36	
Fy	342	MPa
F_u	499	MPa
ε_u	0.2620	
Bolt	A490	
Column bolts	1000	lbf-ft
Plate bolts	1000	lbf-ft

Key response parameters:

Signal factor	50%	100%	175%
Δ_0	0.0	1.2	2.6
$F_{F\ Max}$	229	282	352
$\Delta_{F\ Max}$	7.3	14.4	28.5
$F_{Ultimate}$	229	256	342
$\Delta_{ultimate}$	7.3	16.1	28.8

Force-displacement





Test TC5-1

Type Monotonic Static

Loading Rate: 100 με/s

Failure mode: Bolt

Geometry:

g_{column}	76	mm
t	15.875	mm
g_{beam}	76	mm
φ_{bolt}	25.4	mm
k	28.575	mm
g_2	27.0	mm
g_2/t	1.70	

Materials:

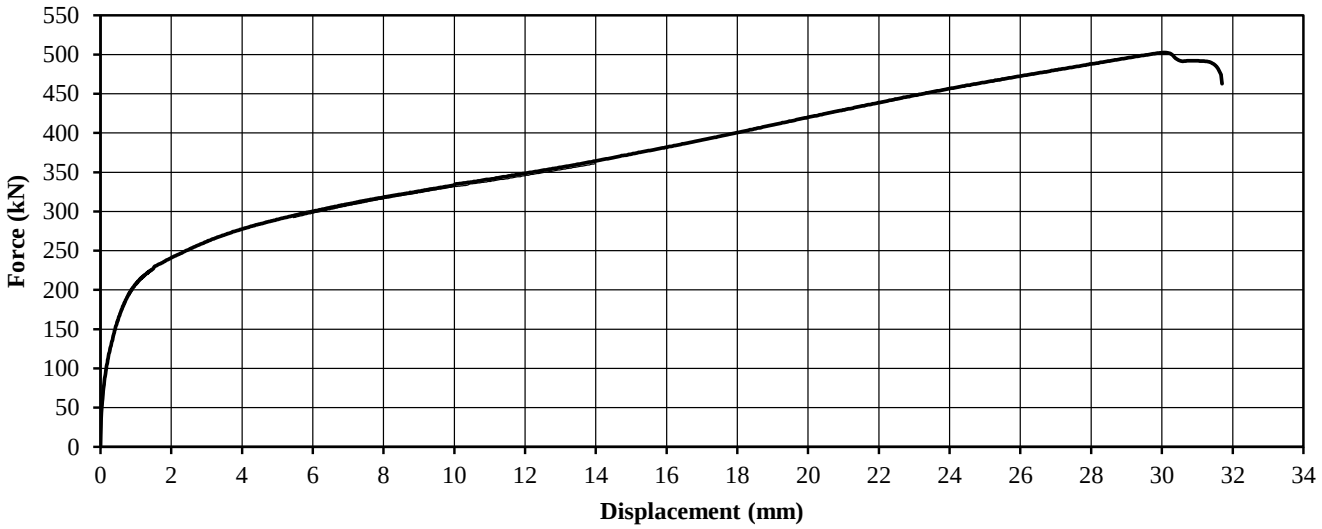
Angle	A36	
F_y	355	MPa
F_u	476	MPa
ε_u	0.2675	
Bolt	A490	
Column bolts	1000	lbf-ft
Plate bolts	1000	lbf-ft

Key response parameters:

$K_{Plastic}$	9.7	kN/mm
$K_{Softening}$	7.5	kN/mm
$K_{Hardening}$	9.4	kN/mm

	F (kN)	Δ (mm)
Initial	-	-
Plastic	278	4.0
Softening	326	9.0
Hardening	364	14.0
Max. Force	503	30.2
Ultimate	463	31.7

Force-displacement













Test TC5-2

Type Monotonic Static

Loading Rate: 600 με/s

Failure mode: Bolt

Geometry:

g_{column}	76	mm
t	15.875	mm
g_{beam}	76	mm
φ_{bolt}	25.4	mm
k	28.575	mm
g_2	27.0	mm
g_2/t	1.70	

Materials:

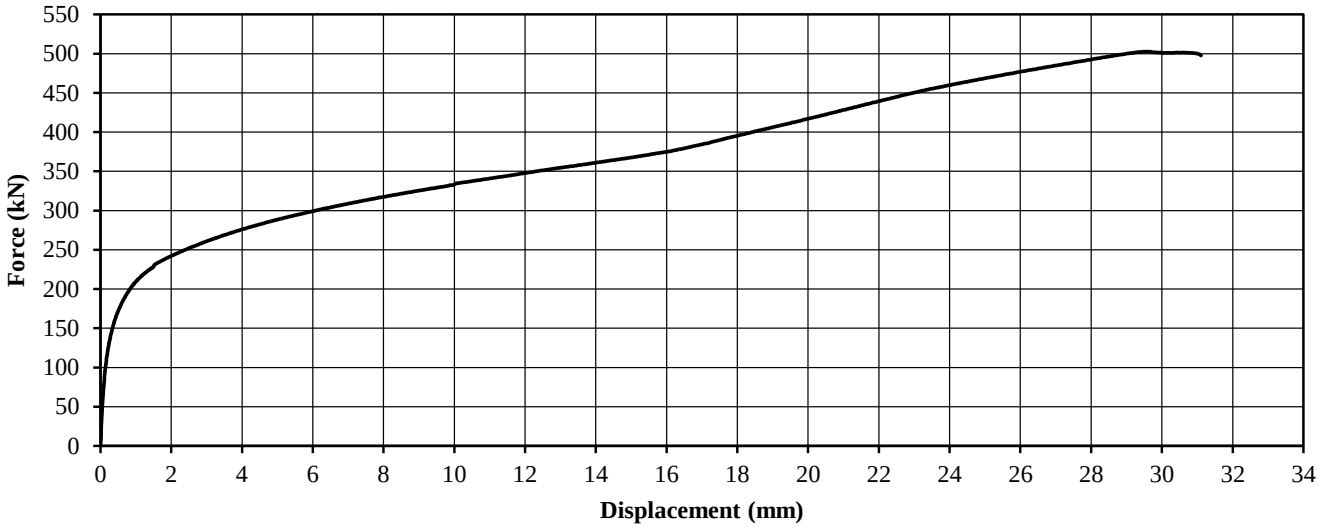
Angle	A36	
F_y	355	MPa
F_u	476	MPa
ε_u	0.2675	
Bolt	A490	
Column bolts	1000	lbf-ft
Plate bolts	1000	lbf-ft

Key response parameters:

$K_{Plastic}$	11.0	kN/mm
$K_{Softening}$	7.1	kN/mm
$K_{Hardening}$	10.5	kN/mm

	F (kN)	Δ (mm)
Initial	-	-
Plastic	263	3.1
Softening	323	8.6
Hardening	376	16.1
Max. Force	502	29.6
Ultimate	498	31.1

Force-displacement













Test TC5-3

Type Monotonic Static

Loading Rate: 750000 με/s

Failure mode: Bolt

Geometry:

g_{column}	76	mm
t	15.875	mm
g_{beam}	76	mm
φ_{bolt}	25.4	mm
k	28.575	mm
g_2	27.0	mm
g_2/t	1.70	

Materials:

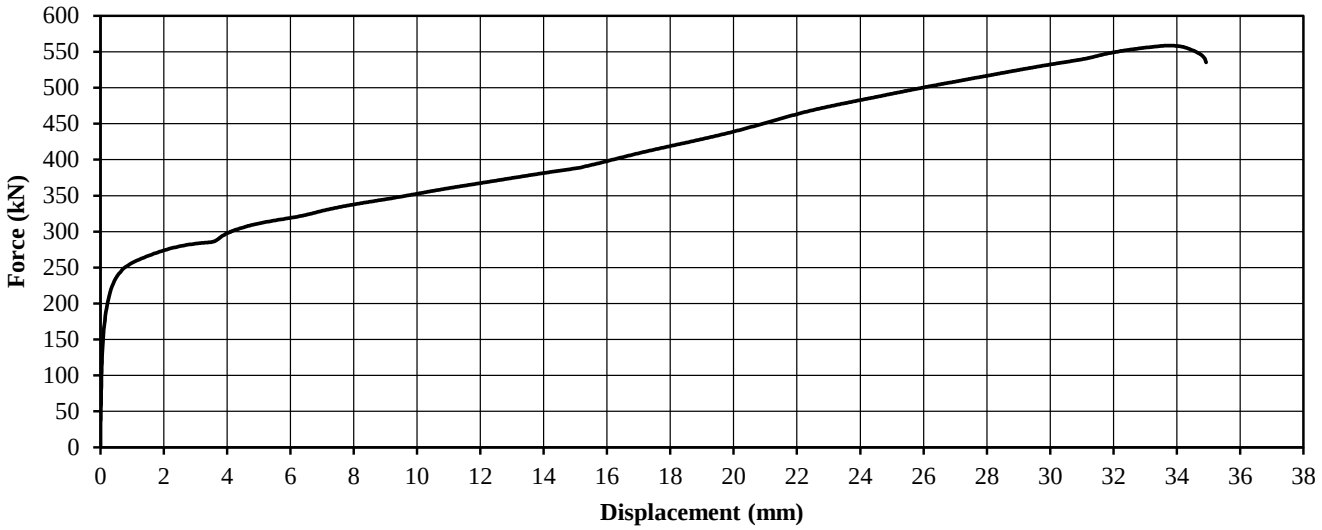
Angle	A36	
F_y	355	MPa
F_u	476	MPa
ε_u	0.2675	
Bolt	A490	
Column bolts	1000	lbf-ft
Plate bolts	1000	lbf-ft

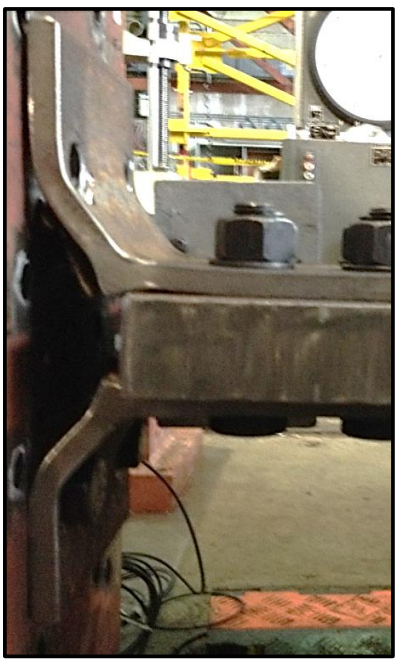
Key response parameters:

$K_{Plastic}$	10.1	kN/mm
$K_{Softening}$	7.3	kN/mm
$K_{Hardening}$	10.0	kN/mm

	F (kN)	Δ (mm)
Initial	-	-
Plastic	270	1.8
Softening	351	9.7
Hardening	385	14.4
Max. Force	559	33.8
Ultimate	535	34.9

Force-displacement













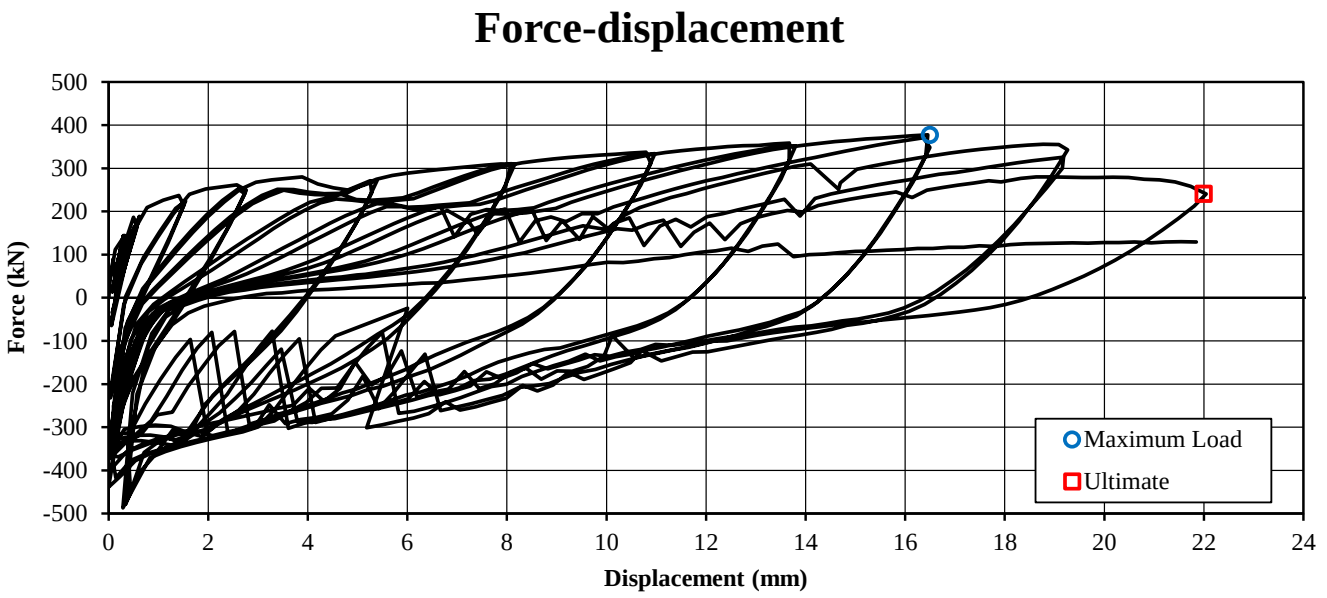
Test TC5-4

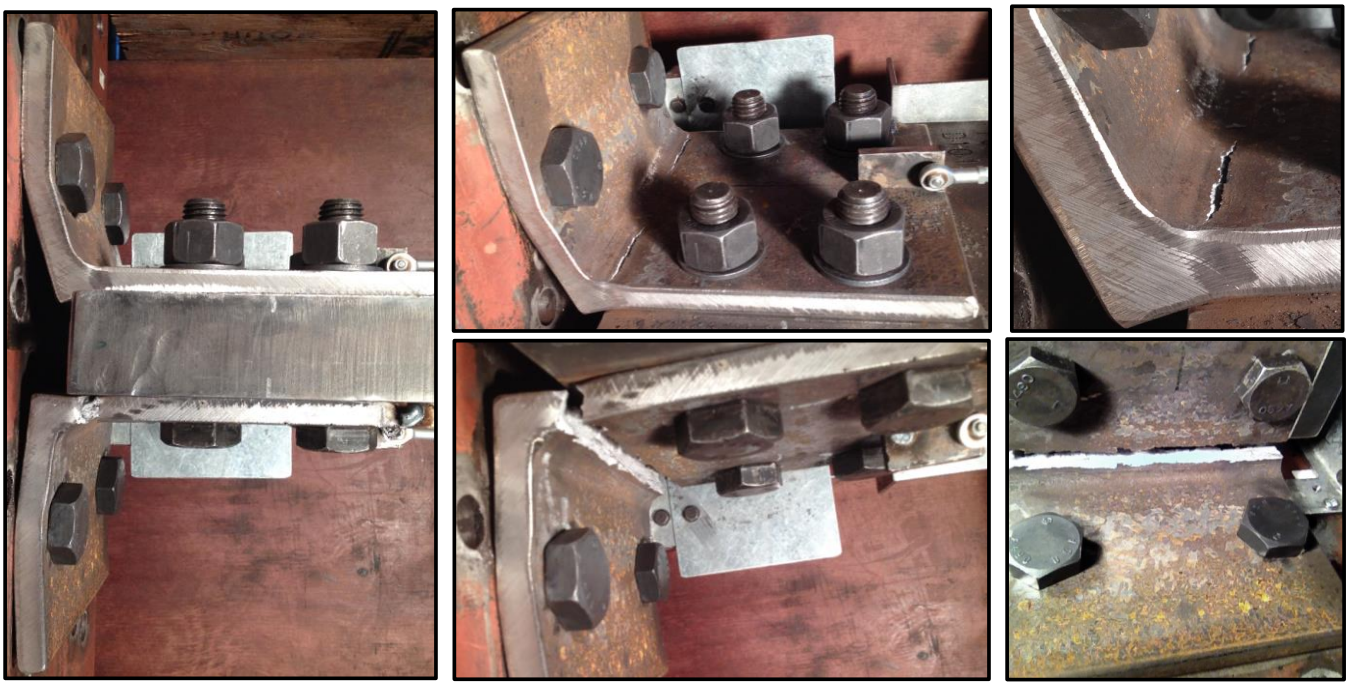
Type Cyclic W310 **Failure mode:** Beam

Geometry:		
g_{column}	76	mm
t	15.875	mm
g_{beam}	76	mm
φ_{bolt}	25.4	mm
k	28.575	mm
g_2	27.0	mm
g_2/t	1.70	

Materials:		
Angle	A36	
F_y	355	MPa
F_u	476	MPa
ε_u	0.2675	
Bolt	A490	
Column bolts	1000	lbf-ft
Plate bolts	1000	lbf-ft

Key response parameters:		
F_{Max}	377	kN
Δ_{FMax}	16.5	mm
$Drift_{FMax}$	7	%
$F_{Ultimate}$	241	kN
$\Delta_{Ultimate}$	22.0	mm
$Drift_{Ultimate}$	9	%





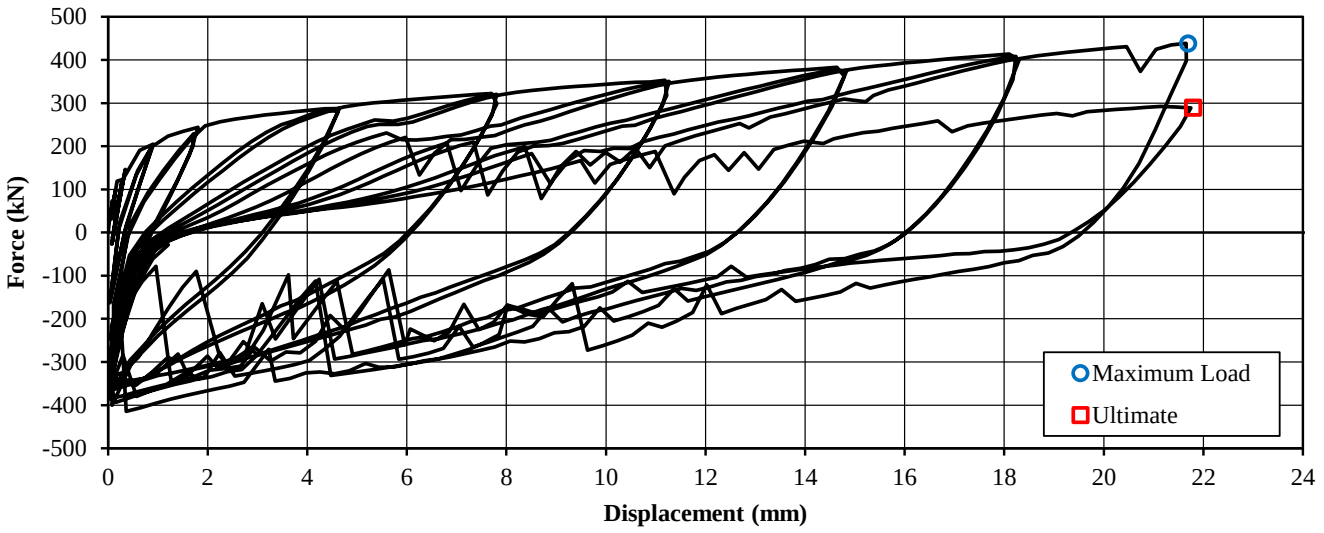
Test TC5-5

Type Cyclic W410 **Failure mode:** Beam

Geometry:		
g_{column}	76	mm
t	15.875	mm
g_{beam}	76	mm
φ_{bolt}	25.4	mm
k	28.575	mm
g_2	27.0	mm
g_2/t	1.70	

Materials:		
Angle	A36	
F_y	355	MPa
F_u	476	MPa
ε_u	0.2675	
Bolt	A490	
Column bolts	1000	lbf-ft
Plate bolts	1000	lbf-ft

Key response parameters:		
F_{Max}	438	kN
Δ_{FMax}	21.7	mm
$Drift_{FMax}$	8	%
$F_{Ultimate}$	289	kN
$\Delta_{Ultimate}$	21.8	mm
$Drift_{Ultimate}$	8	%





Test TC5-6

Type Time-History **Failure mode:** Beam

Geometry:

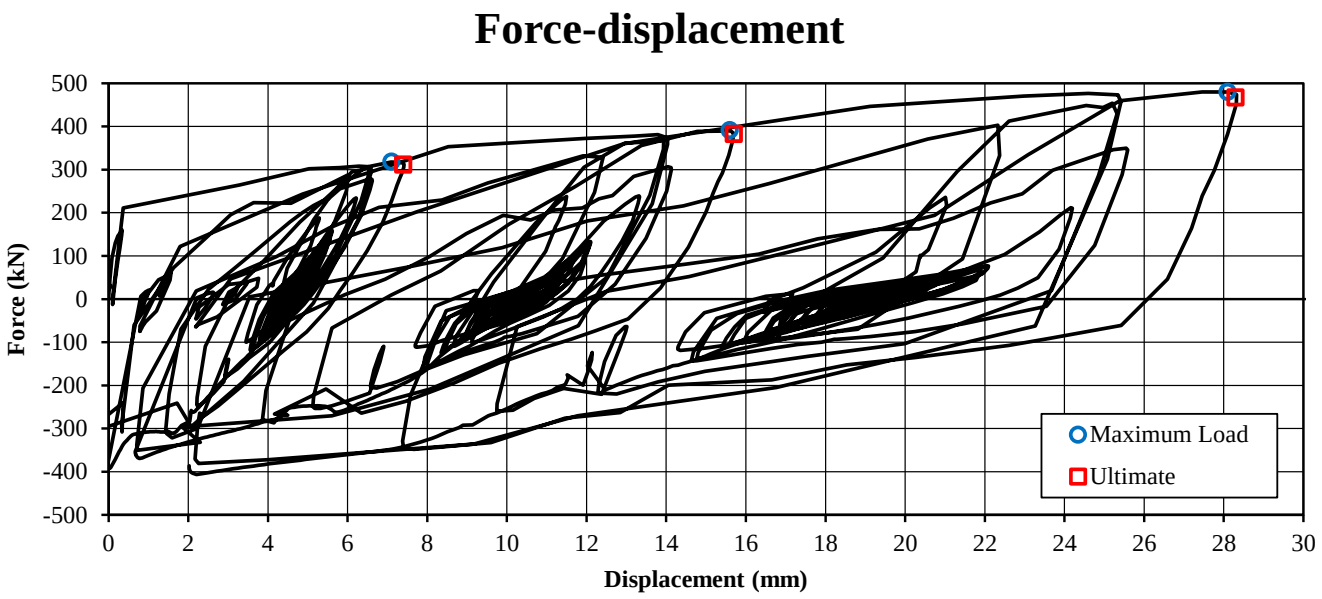
g_{column}	76	mm
t	15.875	mm
g_{beam}	76	mm
φ_{bolt}	25.4	mm
k	28.575	mm
g_2	27.0	mm
g_2/t	1.70	

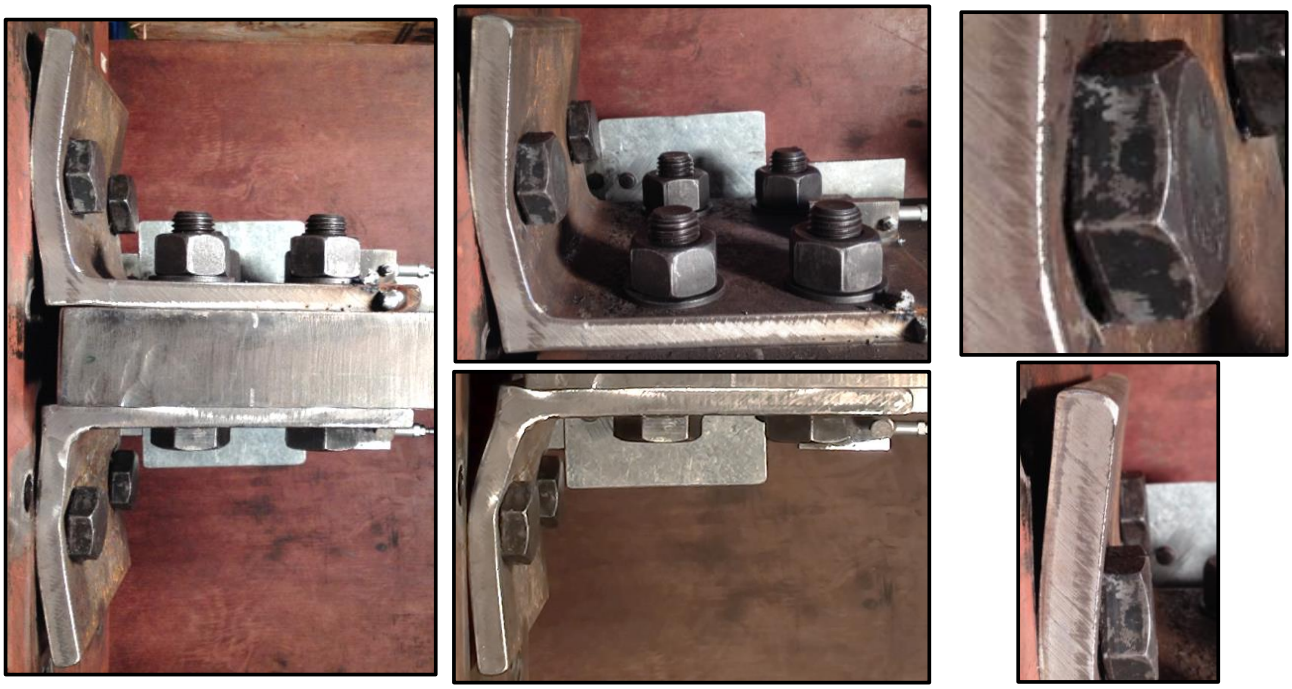
Materials:

Angle	A36	
F_y	355	MPa
F_u	476	MPa
ε_u	0.2675	
Bolt	A490	
Column bolts	1000	lbf-ft
Plate bolts	1000	lbf-ft

Key response parameters:

Signal factor	50%	100%	175%
Δ_0	0.0	0.8	2.2
$F_{F\ Max}$	318	391	480
$\Delta_{F\ Max}$	7.1	15.6	28.1
$F_{Ultimate}$	311	382	467
$\Delta_{ultimate}$	7.4	15.7	28.3





Test TC6-1

Type Monotonic Static

Loading Rate: 100 με/s

Failure mode: Bolt

Geometry:

g_{column}	76	mm
t	19.05	mm
g_{beam}	76	mm
φ_{bolt}	25.4	mm
k	31.75	mm
g_2	23.8	mm
g_2/t	1.25	

Materials:

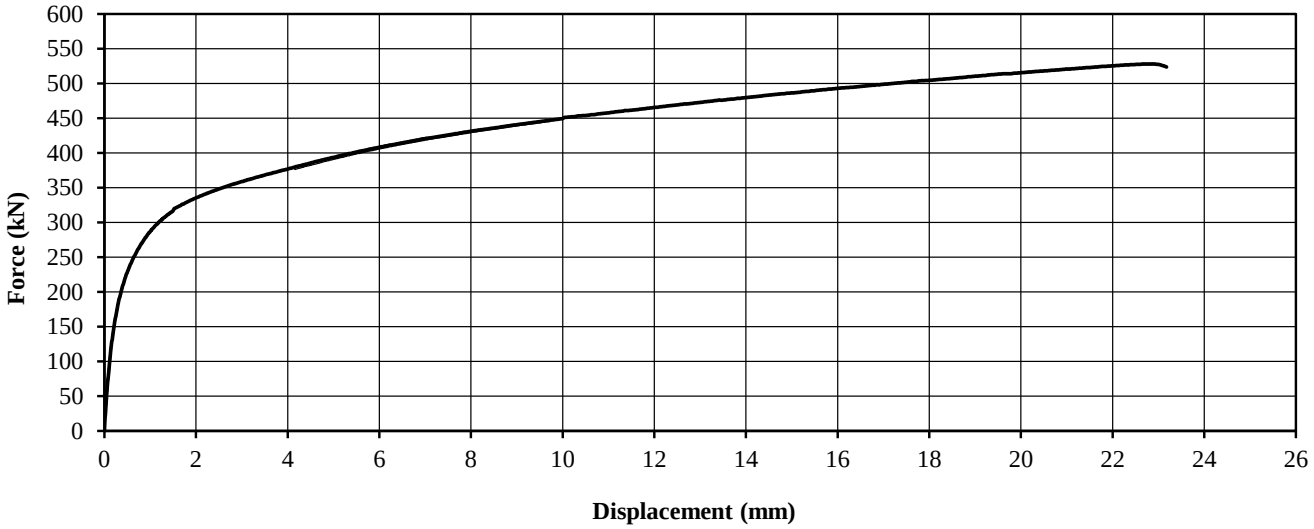
Angle	A36	
F_y	370	MPa
F_u	485	MPa
ε_u	0.2633	
Bolt	A490	
Column bolts	1000	lbf-ft
Plate bolts	1000	lbf-ft

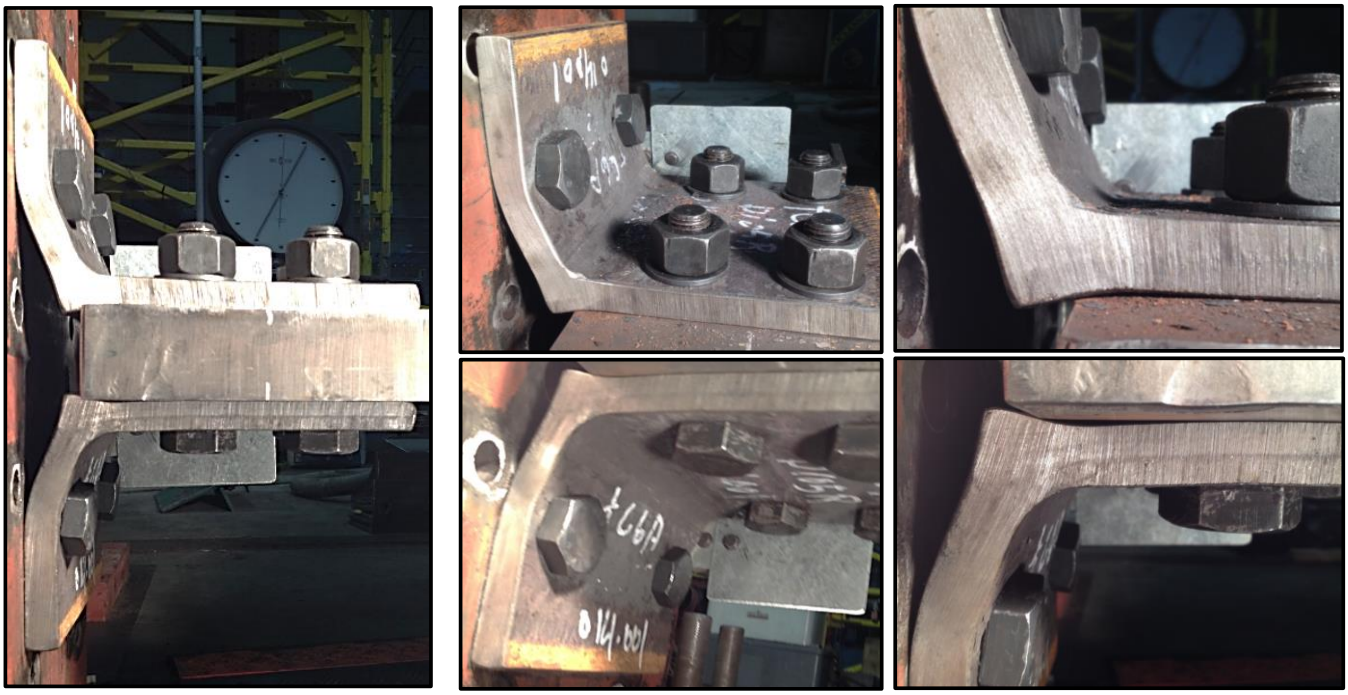
Key response parameters:

$K_{Plastic}$	14.1	kN/mm
$K_{Softening}$	5.9	kN/mm
$K_{Hardening}$	-	kN/mm

	F (kN)	Δ (mm)
Initial	-	-
Plastic	370	3.6
Softening	455	9.6
Hardening	-	-
Max. Force	528	22.8
Ultimate	524	23.2

Force-displacement





The test was stopped when the curve showed bolt failure signs, but prior to bolt fracture for security reasons.

Test TC6-2

Type Monotonic Static

Loading Rate: 600 με/s

Failure mode: Bolt

Geometry:

g_{column}	76	mm
t	19.05	mm
g_{beam}	76	mm
φ_{bolt}	25.4	mm
k	31.75	mm
g_2	23.8	mm
g_2/t	1.25	

Materials:

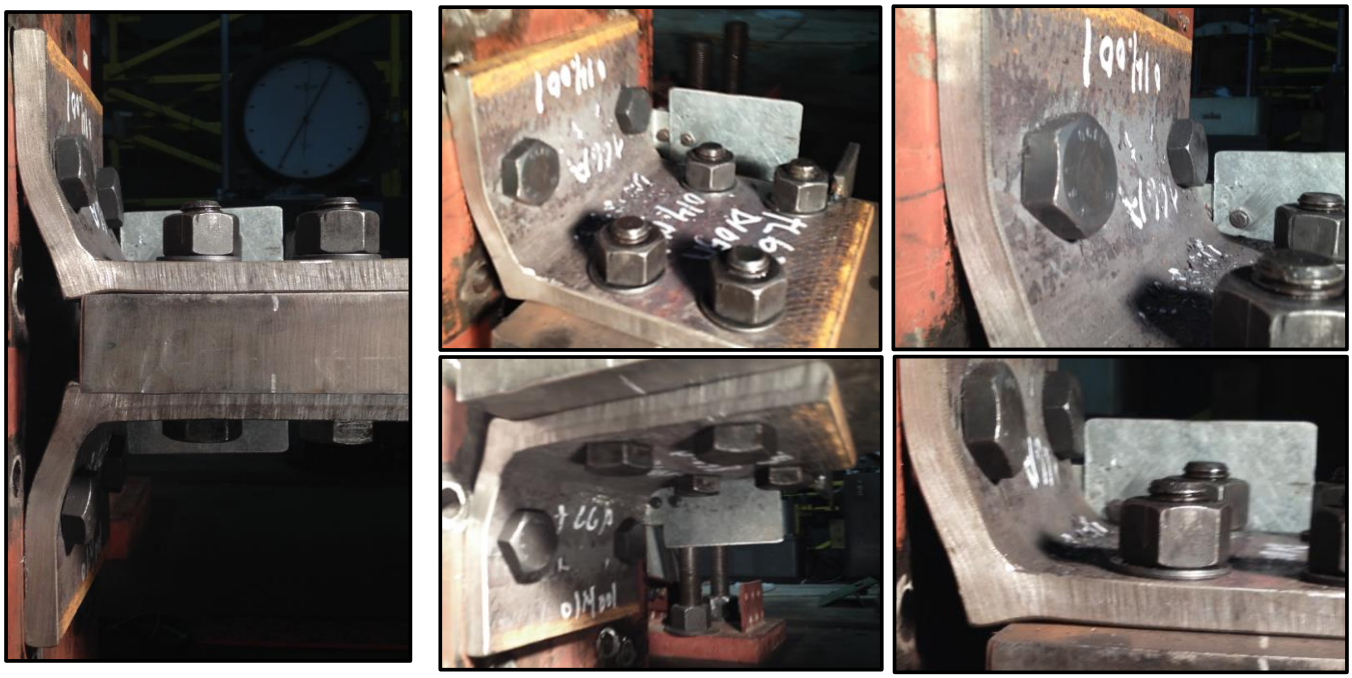
Angle	A36	
F_y	370	MPa
F_u	485	MPa
ε_u	0.2633	
Bolt	A490	
Column bolts	1000	lbf-ft
Plate bolts	1000	lbf-ft

Key response parameters:

$K_{Plastic}$	17.2	kN/mm
$K_{Softening}$	6.3	kN/mm
$K_{Hardening}$	-	kN/mm

	F (kN)	Δ (mm)
Initial	-	-
Plastic	343	2.6
Softening	444	8.5
Hardening	-	-
Max. Force	541	25.4
Ultimate	539	25.7





The test was stopped when the curve showed bolt failure signs, but prior to bolt fracture for security reasons.

Test TC6-3

Type Monotonic Static

Loading Rate: 750000 με/s

Failure mode: Bolt

Geometry:

g_{column}	76	mm
t	19.05	mm
g_{beam}	76	mm
φ_{bolt}	25.4	mm
k	31.75	mm
g_2	23.8	mm
g_2/t	1.25	

Materials:

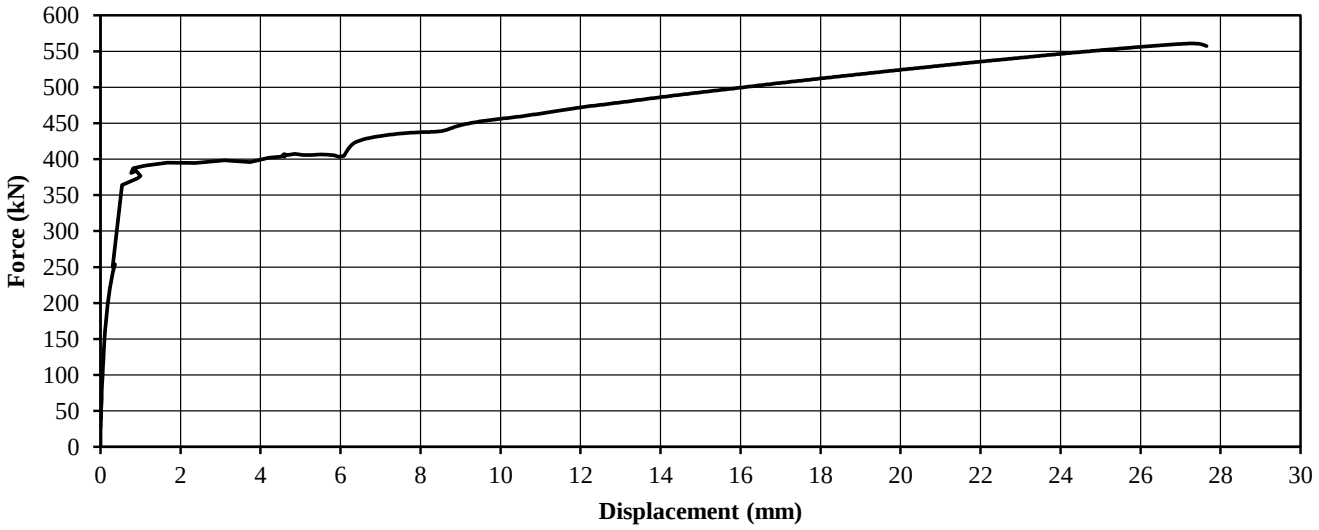
Angle	A36	
F_y	370	MPa
F_u	485	MPa
ε_u	0.2633	
Bolt	A490	
Column bolts	1000	lbf-ft
Plate bolts	1000	lbf-ft

Key response parameters:

$K_{Plastic}$	8.2	kN/mm
$K_{Softening}$	5.3	kN/mm
$K_{Hardening}$	-	kN/mm

	F (kN)	Δ (mm)
Initial	-	-
Plastic	398	3.1
Softening	502	15.7
Hardening	-	-
Max. Force	561	27.1
Ultimate	557	27.6

Force-displacement





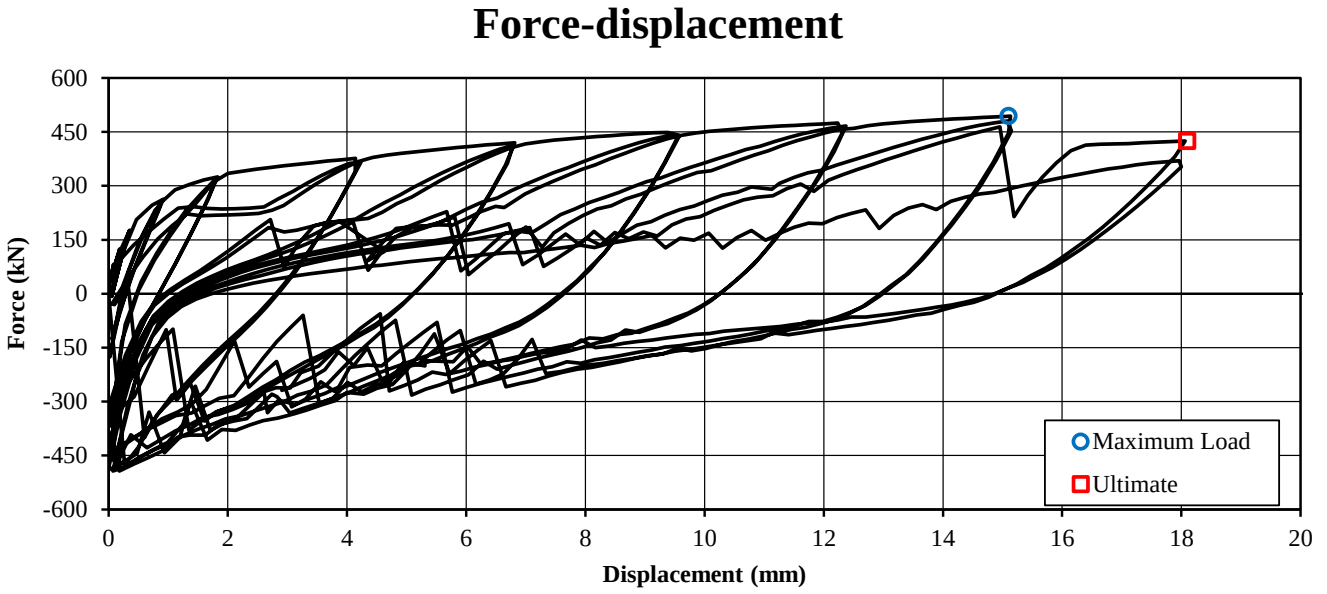
Test TC6-4

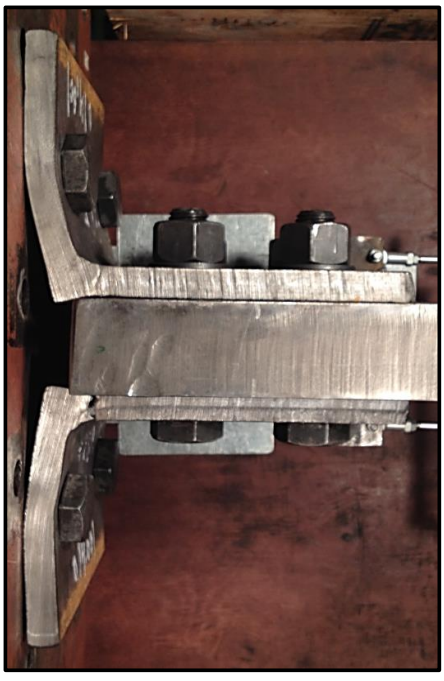
Type Cyclic W310 **Failure mode:** Beam

Geometry:		
g_{column}	76	mm
t	19.05	mm
g_{beam}	76	mm
φ_{bolt}	25.4	mm
k	31.75	mm
g_2	23.8	mm
g_2/t	1.25	

Materials:		
Angle	A36	
F_y	370	MPa
F_u	485	MPa
ε_u	0.2633	
Bolt	A490	
Column bolts	1000	lbf-ft
Plate bolts	1000	lbf-ft

Key response parameters:		
F_{Max}	494	kN
Δ_{FMax}	15.1	mm
$Drift_{FMax}$	7	%
$F_{Ultimate}$	424	kN
$\Delta_{Ultimate}$	18.1	mm
$Drift_{Ultimate}$	8	%













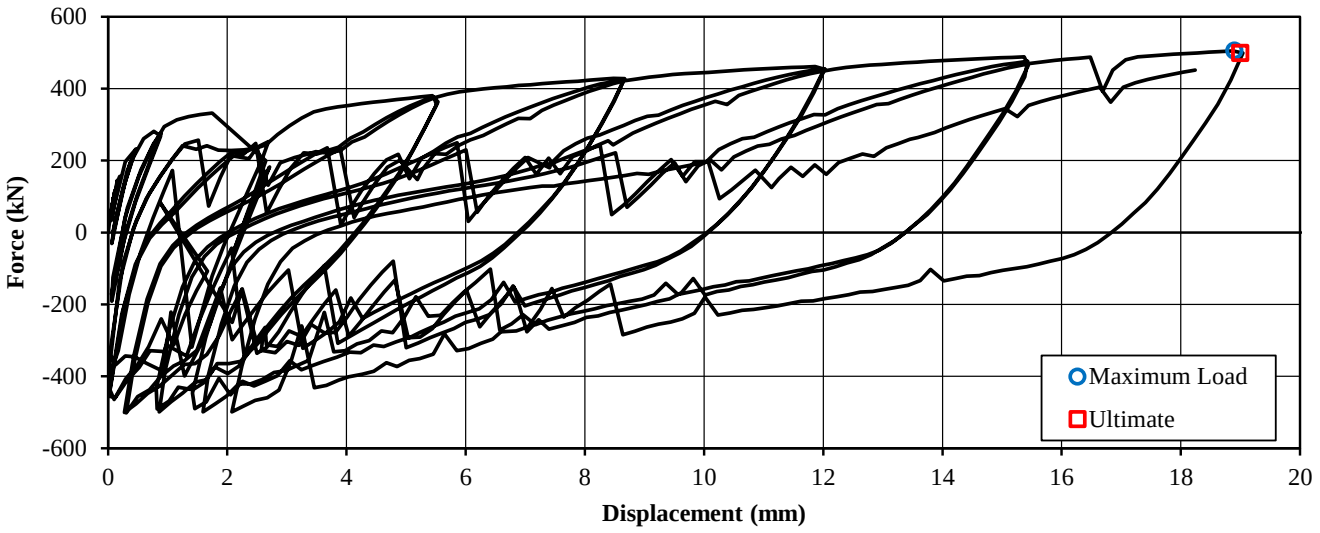
Test TC6-5

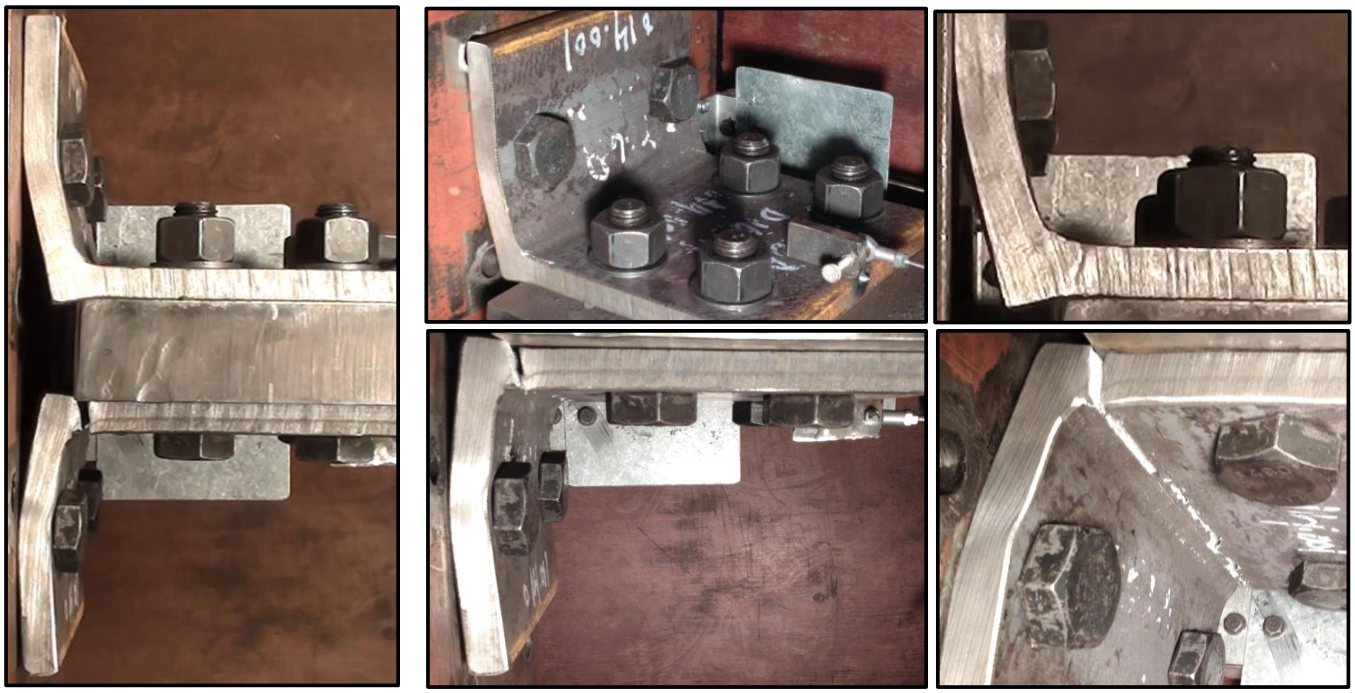
Type Cyclic W410 **Failure mode:** Beam

Geometry:		
g_{column}	76	mm
t	19.05	mm
g_{beam}	76	mm
φ_{bolt}	25.4	mm
k	31.75	mm
g_2	23.8	mm
g_2/t	1.25	

Materials:		
Angle	A36	
F_y	370	MPa
F_u	485	MPa
ε_u	0.2633	
Bolt	A490	
Column bolts	1000	lbf-ft
Plate bolts	1000	lbf-ft

Key response parameters:		
F_{Max}	505	kN
Δ_{FMax}	18.9	mm
$Drift_{FMax}$	8	%
$F_{Ultimate}$	499	kN
$\Delta_{Ultimate}$	19	mm
$Drift_{Ultimate}$	8	%





Test TC6-6

Type Time-History **Failure mode:** Beam

Geometry:

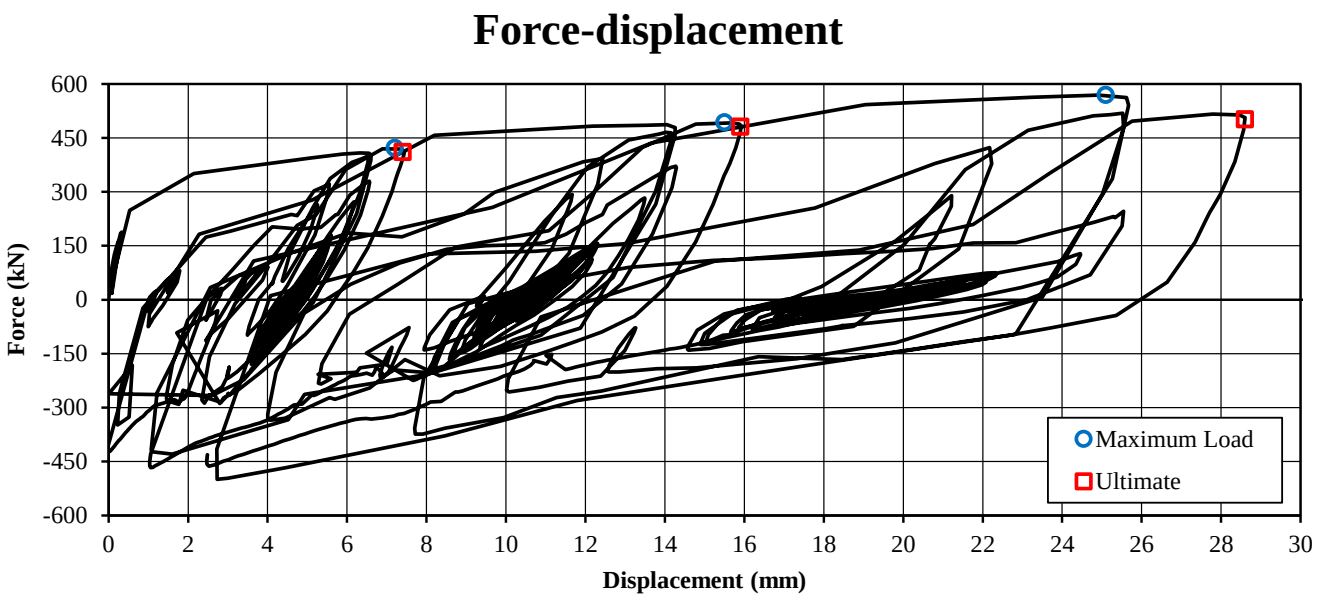
g_{column}	76	mm
t	19.05	mm
g_{beam}	76	mm
φ_{bolt}	25.4	mm
k	31.75	mm
g_2	23.8	mm
g_2/t	1.25	

Materials:

Angle	A36	
F_y	370	MPa
F_u	485	MPa
ε_u	0.2633	
Bolt	A490	
Column bolts	1000	lbf-ft
Plate bolts	1000	lbf-ft

Key response parameters:

Signal factor	50%	100%	175%
Δ_0	0.0	1.0	2.5
$F_{F\ Max}$	422	493	569
$\Delta_{F\ Max}$	7.2	15.5	25.1
$F_{Ultimate}$	410	481	501
$\Delta_{ultimate}$	7.4	15.9	28.6





Test TC7-1

Type Monotonic Static

Loading Rate: 100 με/s

Failure mode: Column

Geometry:

g_{column}	89	mm
t	9.525	mm
g_{beam}	57	mm
φ_{bolt}	19.1	mm
k	22.225	mm
g_2	50.8	mm
g_2/t	5.33	

Materials:

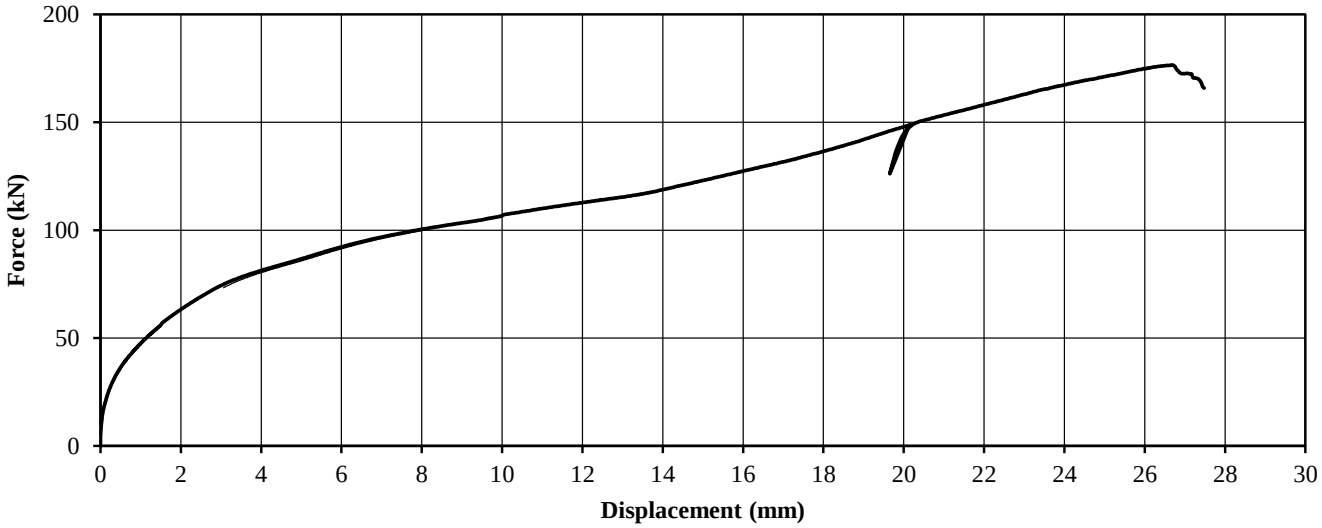
Angle	A36	
F_y	396	MPa
F_u	566	MPa
ε_u	0.2286	
Bolt	A325	
Column bolts	400	lbf-ft
Plate bolts	400	lbf-ft

Key response parameters:

$K_{Plastic}$	3.2	kN/mm
$K_{Softening}$	-	kN/mm
$K_{Hardening}$	5.2	kN/mm

	F (kN)	Δ (mm)
Initial	12.6	0.030
Plastic	95	6.5
Softening	-	-
Hardening	122	15.2
Max. Force	177	26.7
Ultimate	166	27.5

Force-displacement













Test TC7-2

Type Monotonic Static

Loading Rate: 600 με/s

Failure mode: Column/Net Section

Geometry:

g_{column}	89	mm
t	9.525	mm
g_{beam}	57	mm
φ_{bolt}	19.1	mm
k	22.225	mm
g_2	50.8	mm
g_2/t	5.33	

Materials:

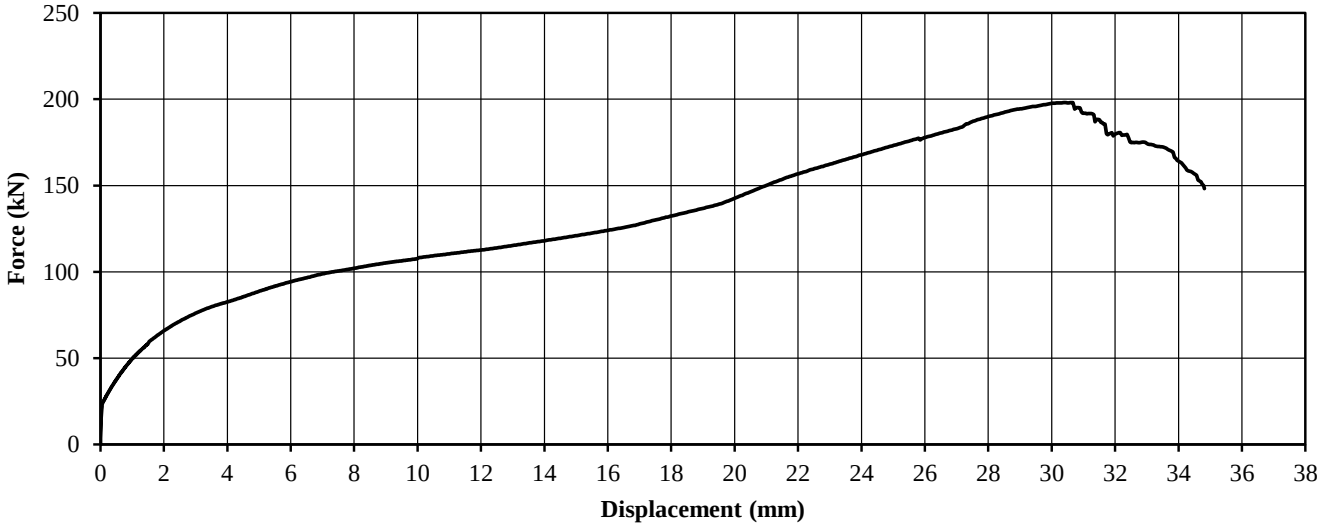
Angle	A36	
F_y	396	MPa
F_u	566	MPa
ε_u	0.2286	
Bolt	A325	
Column bolts	400	lbf-ft
Plate bolts	400	lbf-ft

Key response parameters:

$K_{Plastic}$	2.9	kN/mm
$K_{Softening}$	-	kN/mm
$K_{Hardening}$	5.9	kN/mm

	F (kN)	Δ (mm)
Initial	23	0.044
Plastic	98	6.8
Softening	-	-
Hardening	129	17.4
Max. Force	198	30.1
Ultimate	148	34.8

Force-displacement





Test TC7-3

Type Monotonic Static

Loading Rate: 750000 με/s

Failure mode: Column

Geometry:

g_{column}	89	mm
t	9.525	mm
g_{beam}	57	mm
φ_{bolt}	19.1	mm
k	22.225	mm
g_2	50.8	mm
g_2/t	5.33	

Materials:

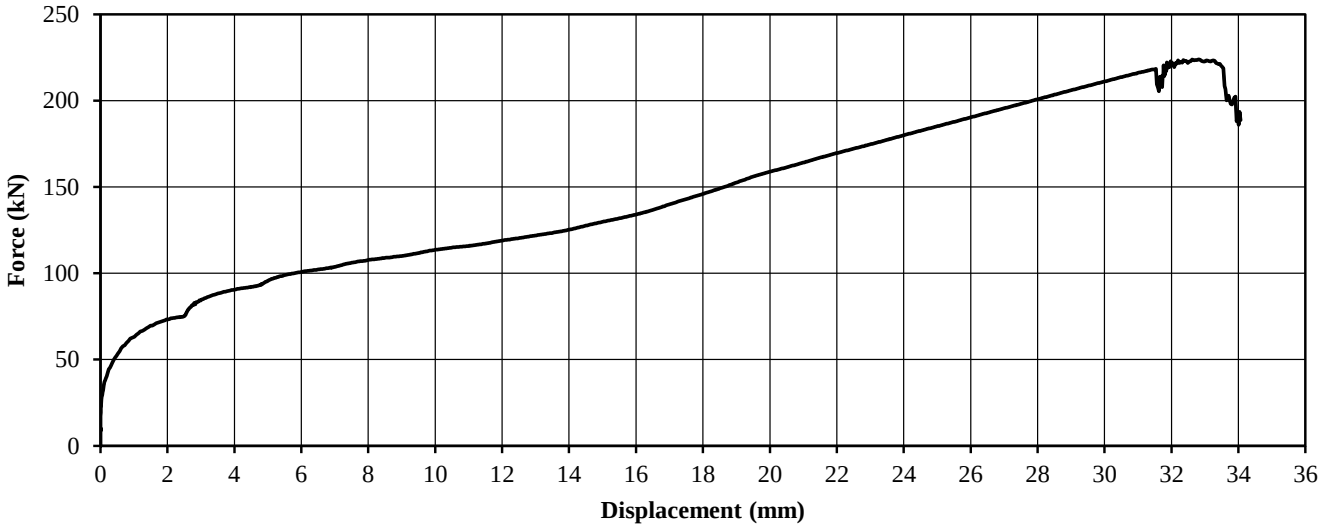
Angle	A36	
F_y	396	MPa
F_u	566	MPa
ε_u	0.2286	
Bolt	A325	
Column bolts	400	lbf-ft
Plate bolts	400	lbf-ft

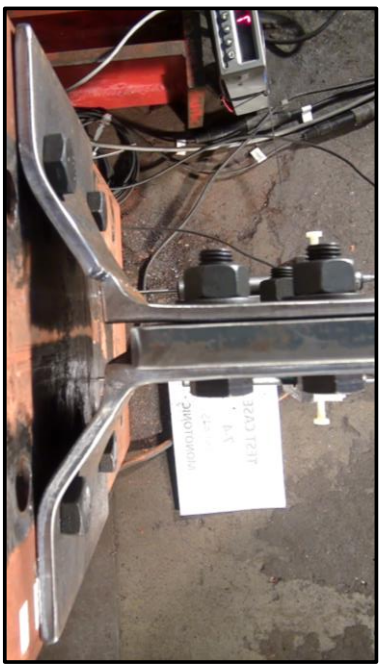
Key response parameters:

$K_{Plastic}$	3.5	kN/mm
$K_{Softening}$	-	kN/mm
$K_{Hardening}$	5.4	kN/mm

	F (kN)	Δ (mm)
Initial	23	0.002
Plastic	91	4.2
Softening	-	-
Hardening	125	13.9
Max. Force	224	33.1
Ultimate	189	34.1

Force-displacement













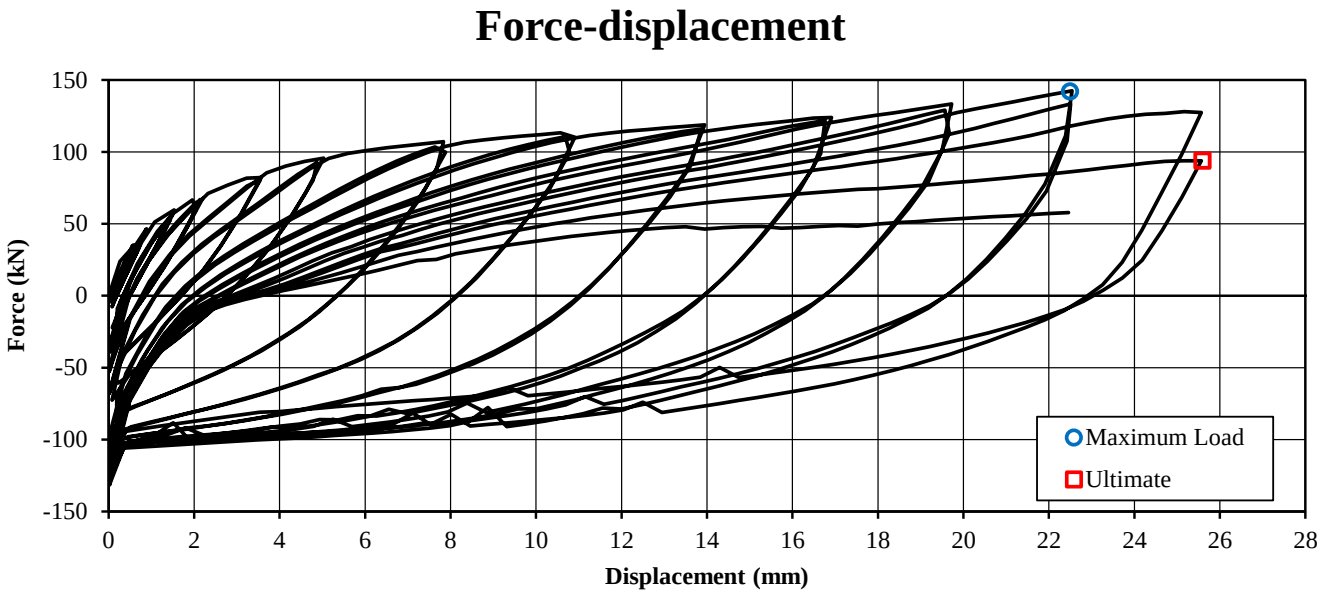
Test TC7-4

Type Cyclic W310 **Failure mode:** Column/Net Section

Geometry:		
g_{column}	89	mm
t	9.525	mm
g_{beam}	57	mm
φ_{bolt}	19.1	mm
k	22.225	mm
g_2	50.8	mm
g_2/t	5.33	

Materials:		
Angle	A36	
F_y	396	MPa
F_u	566	MPa
ε_u	0.2286	
Bolt	A325	
Column bolts	400	lbf-ft
Plate bolts	400	lbf-ft

Key response parameters:		
F_{Max}	142	kN
Δ_{FMax}	22.5	mm
$Drift_{FMax}$	8	%
$F_{Ultimate}$	94	kN
$\Delta_{Ultimate}$	25.6	mm
$Drift_{Ultimate}$	9	%

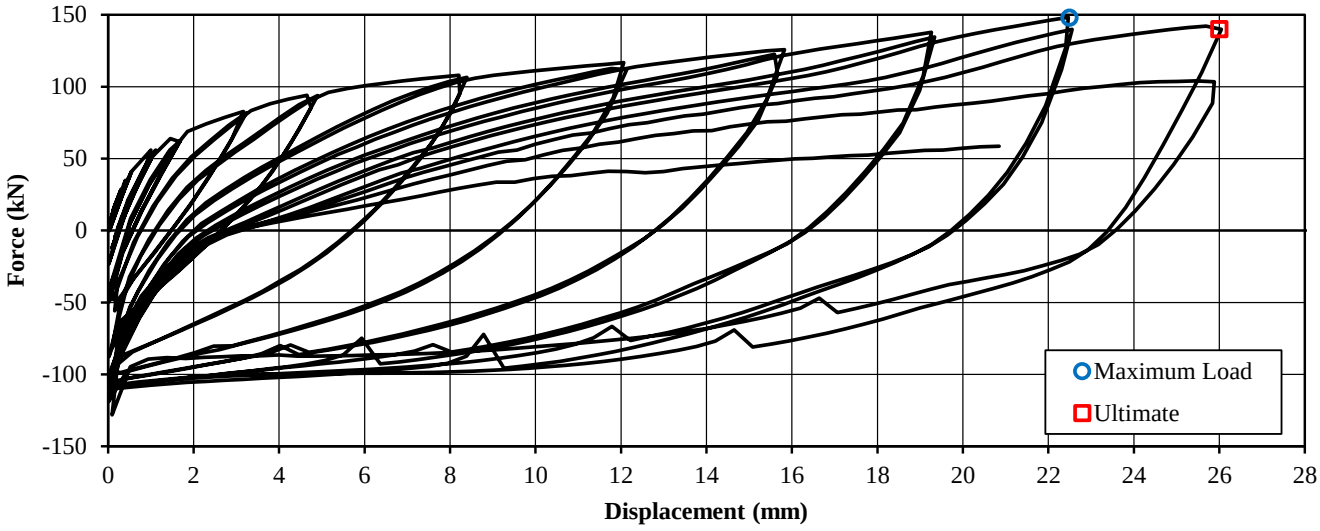




Test TC7-5

Type Cyclic W410 **Failure mode:** Column/Net Section

Geometry:			Materials:			Key response parameters:		
g_{column}	89	mm	**Angle**	A36		F_{Max}	148	kN
t	9.525	mm	F_y	396	MPa	Δ_{FMax}	22.5	mm
g_{beam}	57	mm	F_u	566	MPa	$Drift_{FMax}$	7	%
φ_{bolt}	19.1	mm	ε_u	0.2286		$F_{Ultimate}$	140	kN
k	22.225	mm	**Bolt**	A325		$\Delta_{Ultimate}$	26.0	mm
g_2	50.8	mm	**Column bolts**	400	lbf-ft	$Drift_{Ultimate}$	8	%
g_2/t	5.33		**Plate bolts**	400	lbf-ft			





Test TC7-6

Type Time-History **Failure mode:** Column/Net Section

Geometry:

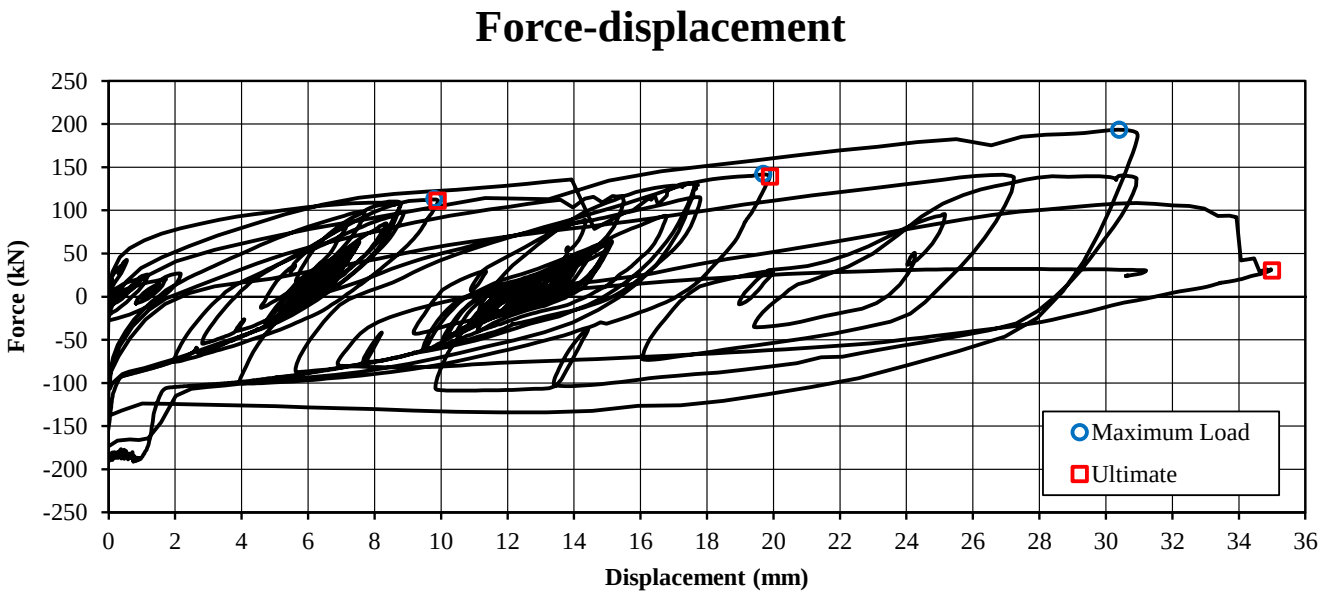
g_{column}	89	mm
t	9.525	mm
g_{beam}	57	mm
φ_{bolt}	19.1	mm
k	22.225	mm
g_2	50.8	mm
g_2/t	5.33	

Materials:

Angle	A36	
F_y	396	MPa
F_u	566	MPa
ε_u	0.2286	
Bolt	A325	
Column bolts	400	lbf-ft
Plate bolts	400	lbf-ft

Key response parameters:

Signal factor	100%	200%	350%
Δ_0	0.0	1.6	2.4
$F_{F\ Max}$	113	142	193
$\Delta_{F\ Max}$	9.8	19.7	30.4
$F_{Ultimate}$	111	139	30
$\Delta_{Ultimate}$	9.9	19.9	35.0





Test TC8-1

Type Monotonic Static

Loading Rate: 100 με/s

Failure mode: Column

Geometry:

g_{column}	102	mm
t	9.525	mm
g_{beam}	57	mm
φ_{bolt}	19.1	mm
k	22.225	mm
g_2	63.5	mm
g_2/t	6.67	

Materials:

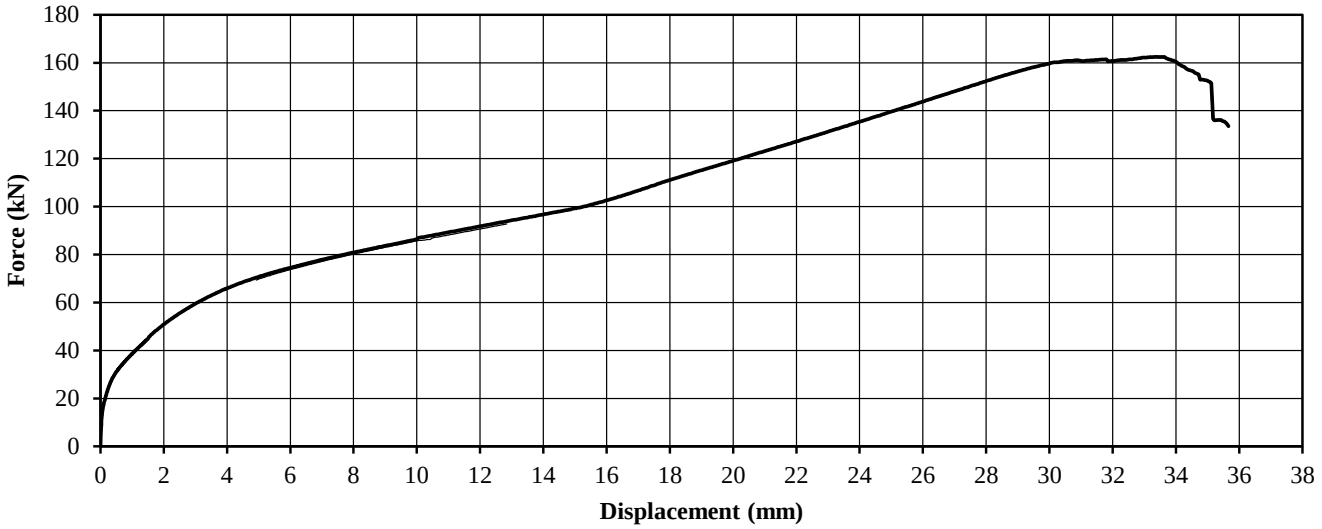
Angle	A36	
F_y	396	MPa
F_u	566	MPa
ε_u	0.2286	
Bolt	A325	
Column bolts	400	lbf-ft
Plate bolts	400	lbf-ft

Key response parameters:

$K_{Plastic}$	2.8	kN/mm
$K_{Softening}$	-	kN/mm
$K_{Hardening}$	4.1	kN/mm

	F (kN)	Δ (mm)
Initial	16	0.063
Plastic	74	5.8
Softening	-	-
Hardening	101	15.6
Max. Force	162	33.6
Ultimate	134	35.7

Force-displacement





Test TC8-2

Type Monotonic Static

Loading Rate: 600 με/s

Failure mode: Column

Geometry:

g_{column}	102	mm
t	9.525	mm
g_{beam}	57	mm
φ_{bolt}	19.1	mm
k	22.225	mm
g_2	63.5	mm
g_2/t	6.67	

Materials:

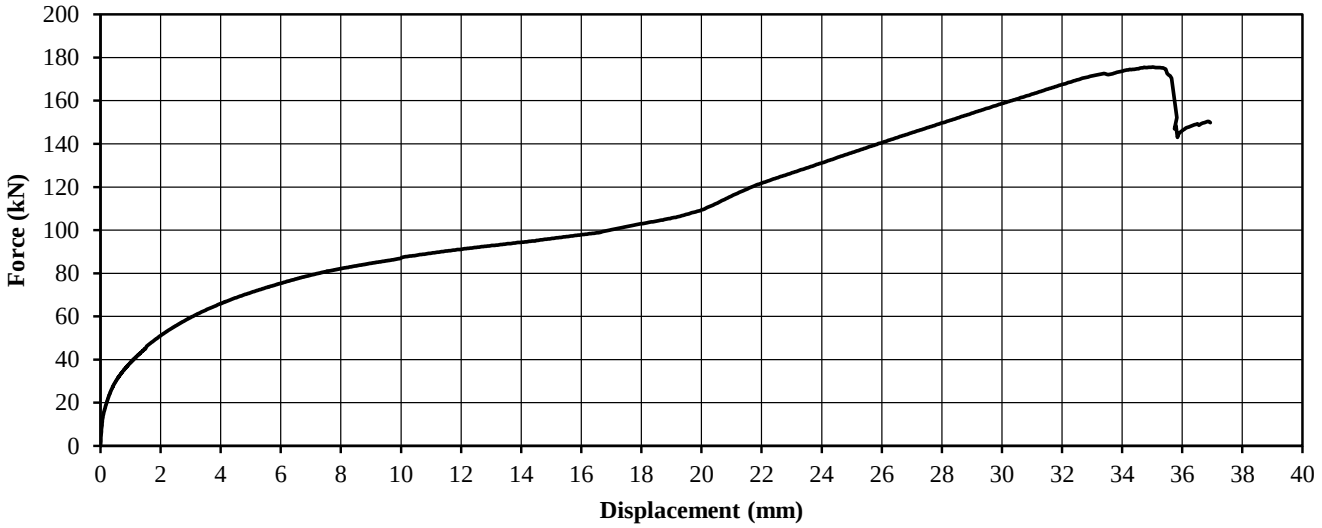
Angle	A36	
F_y	396	MPa
F_u	566	MPa
ε_u	0.2286	
Bolt	A325	
Column bolts	400	lbf-ft
Plate bolts	400	lbf-ft

Key response parameters:

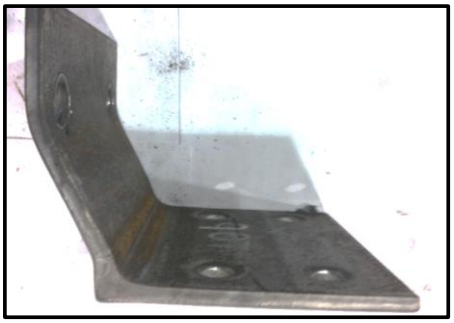
$K_{Plastic}$	2.9	kN/mm
$K_{Softening}$	1.68	kN/mm
$K_{Hardening}$	4.7	kN/mm

	F (kN)	Δ (mm)
Initial	13	0.083
Plastic	76	6.0
Softening	88	10.5
Hardening	100	17.4
Max. Force	176	35.4
Ultimate	150	36.9

Force-displacement













Test TC8-3

Type Monotonic Static

Loading Rate: 750000 με/s

Failure mode: Column

Geometry:

g_{column}	102	mm
t	9.525	mm
g_{beam}	57	mm
φ_{bolt}	19.1	mm
k	22.225	mm
g_2	63.5	mm
g_2/t	6.67	

Materials:

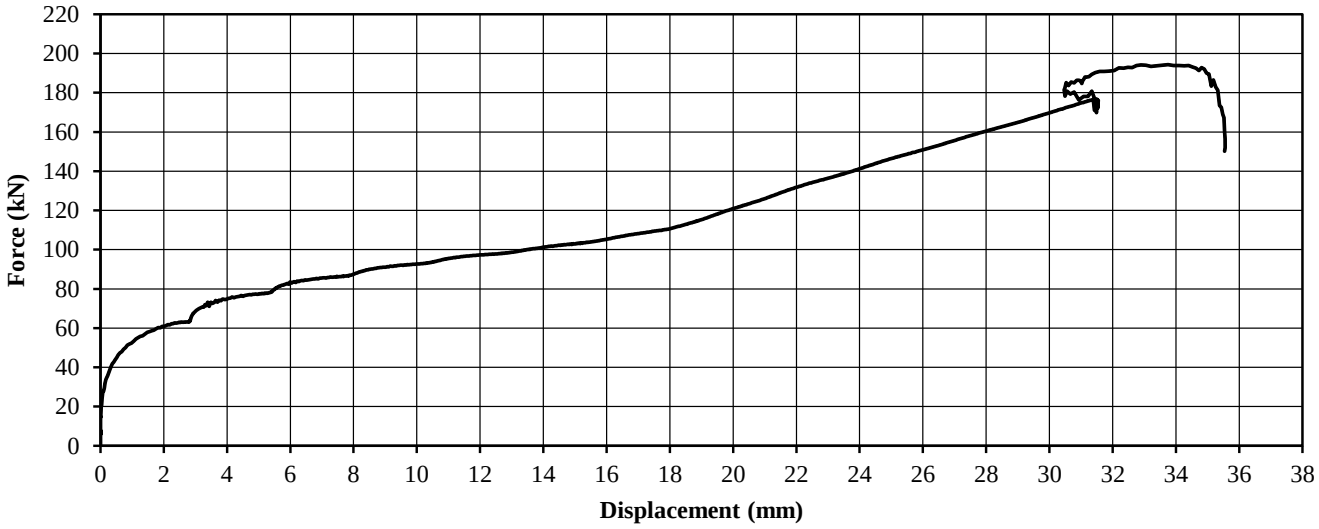
Angle	A36	
F_y	396	MPa
F_u	566	MPa
ε_u	0.2286	
Bolt	A325	
Column bolts	400	lbf-ft
Plate bolts	400	lbf-ft

Key response parameters:

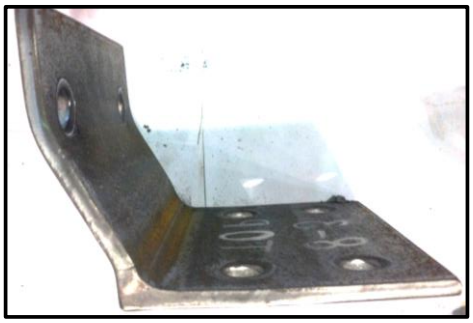
$K_{Plastic}$	2.2	kN/mm
$K_{Softening}$	-	kN/mm
$K_{Hardening}$	4.8	kN/mm

	F (kN)	Δ (mm)
Initial	27	0.049
Plastic	85	6.8
Softening	-	-
Hardening	108	16.9
Max. Force	194	33.6
Ultimate	157	35.6

Force-displacement

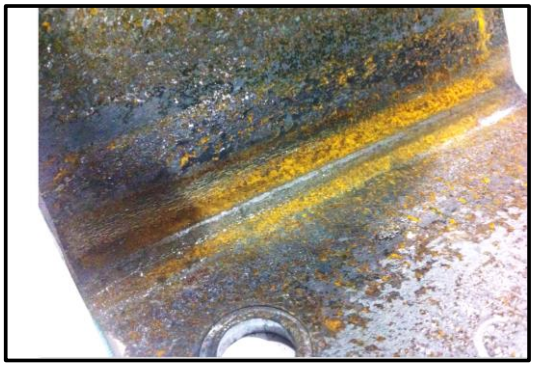








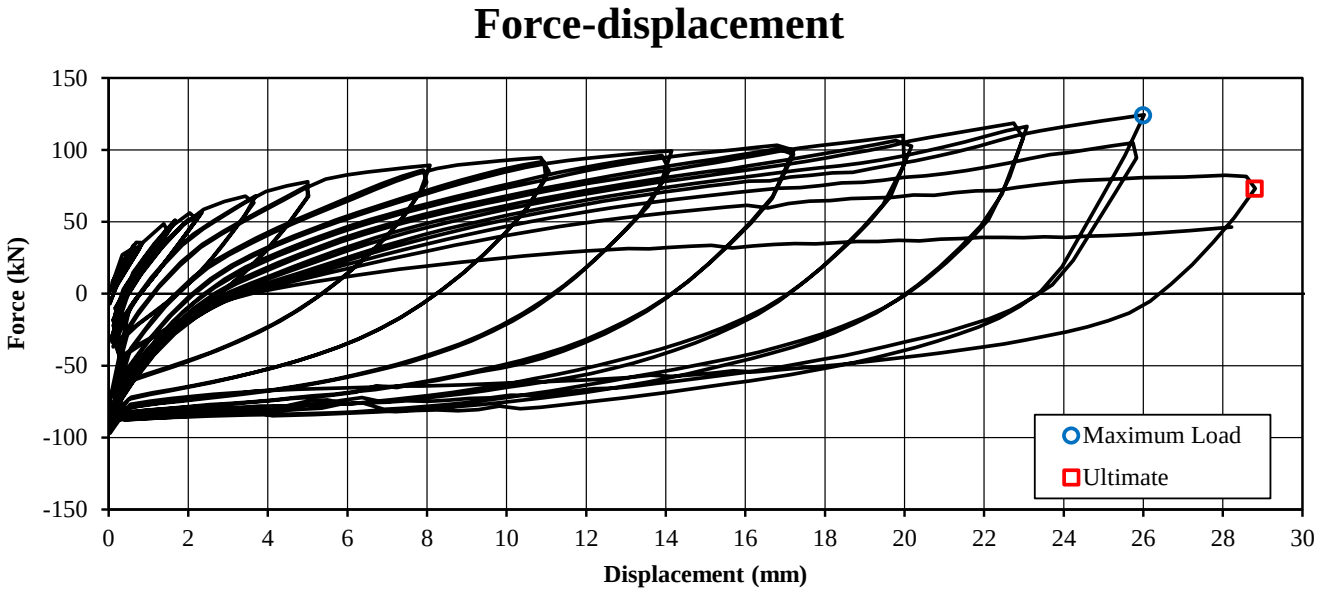




Test TC8-4

Type Cyclic W310 **Failure mode:** Column/Net Section

Geometry:			Materials:			Key response parameters:		
g_{column}	102	mm	**Angle**	A36		F_{Max}	124	kN
t	9.525	mm	F_y	396	MPa	Δ_{FMax}	26.0	mm
g_{beam}	57	mm	F_u	566	MPa	$Drift_{FMax}$	9	%
φ_{bolt}	19.1	mm	ε_u	0.2286		$F_{Ultimate}$	73	kN
k	22.225	mm	**Bolt**	A325		$\Delta_{Ultimate}$	28.8	mm
g_2	63.5	mm	**Column bolts**	400	lbf-ft	$Drift_{Ultimate}$	10	%
g_2/t	6.67		**Plate bolts**	400	lbf-ft			





Test TC8-5

Type Time-History **Failure mode:** Column/Net Section

Geometry:

g_{column}	102	mm
t	9.525	mm
g_{beam}	57	mm
φ_{bolt}	19.1	mm
k	22.225	mm
g_2	63.5	mm
g_2/t	6.67	

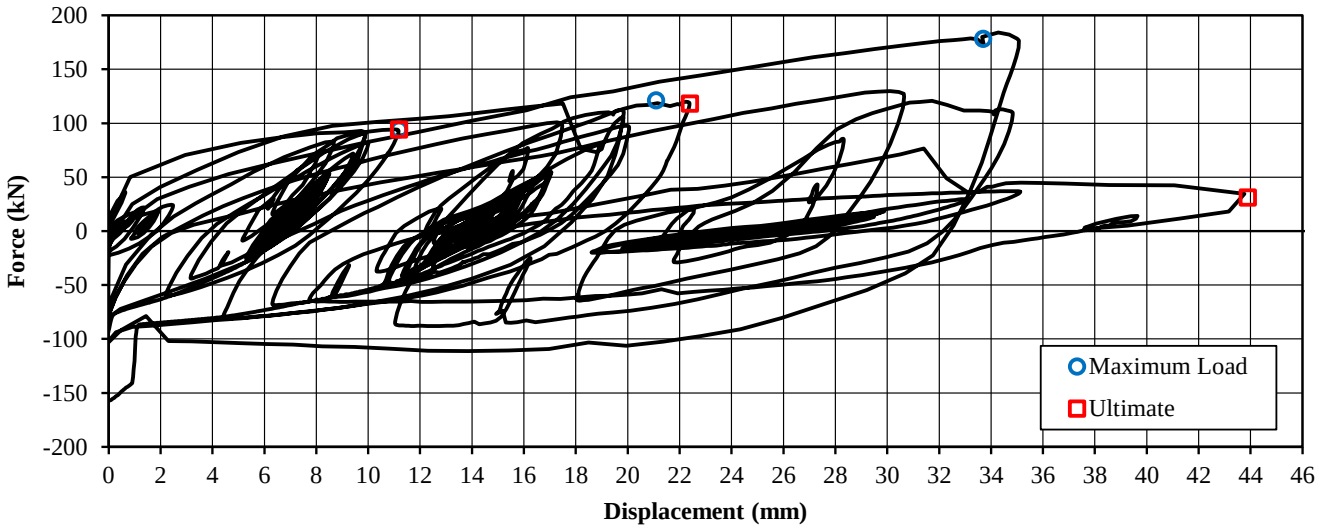
Materials:

Angle	A36	
F_y	396	MPa
F_u	566	MPa
ε_u	0.2286	
Bolt	A325	
Column bolts	400	lbf-ft
Plate bolts	400	lbf-ft

Key response parameters:

Signal factor	100%	200%	350%
Δ_0	0.0	2.0	3.0
$F_{F\ Max}$	94	121	178
$\Delta_{F\ Max}$	11.2	21.1	33.7
$F_{Ultimate}$	94	118	31
$\Delta_{Ultimate}$	11.2	22.4	43.9

Force-displacement





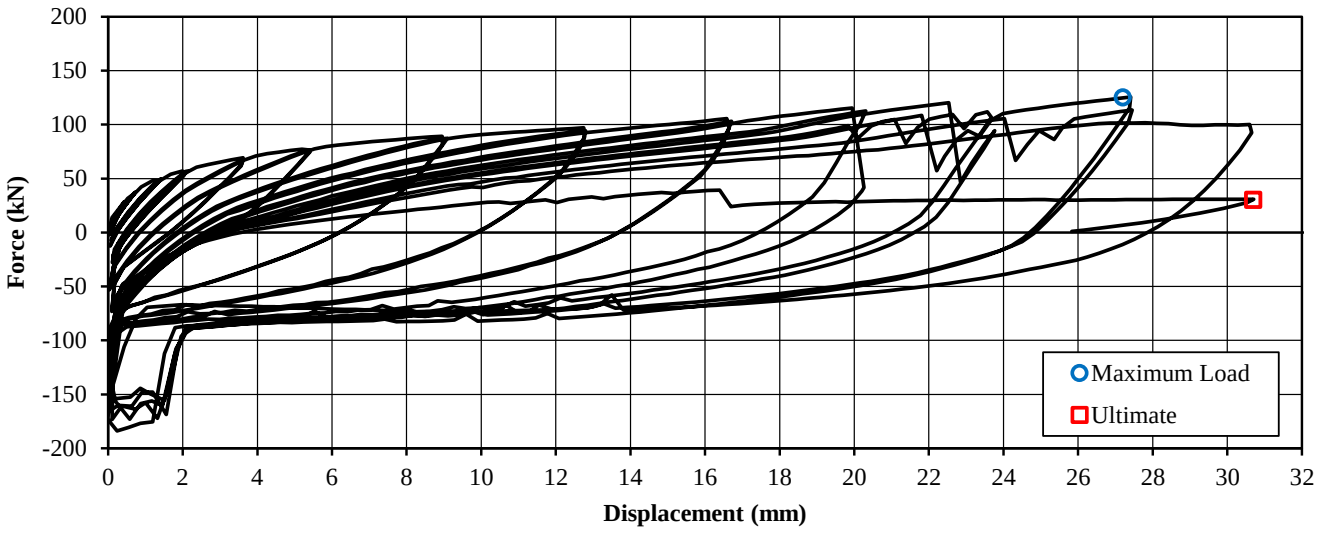
Test TC8-6

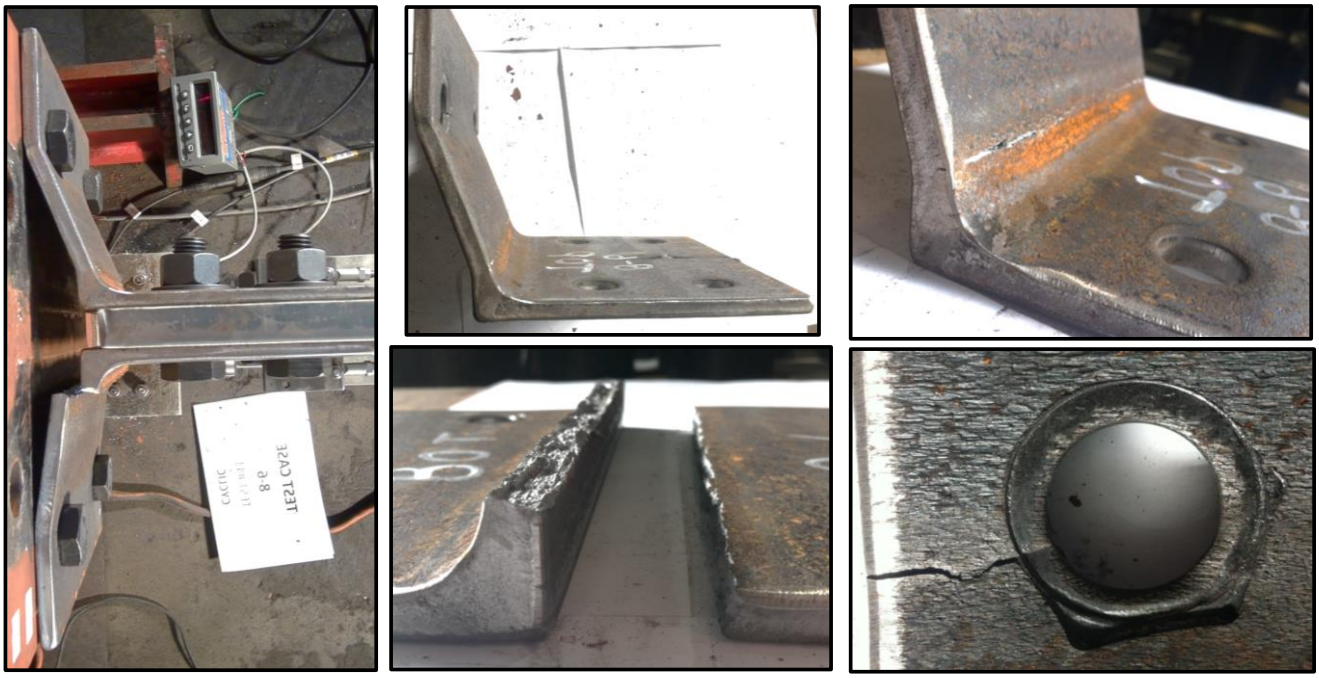
Type Cyclic W410 **Failure mode:** Column/Net Section

Geometry:		
g_{column}	102	mm
t	9.525	mm
g_{beam}	57	mm
φ_{bolt}	19.1	mm
k	22.225	mm
g_2	63.5	mm
g_2/t	6.67	

Materials:		
Angle	A36	
F_y	396	MPa
F_u	566	MPa
ε_u	0.2286	
Bolt	A325	
Column bolts	400	lbf-ft
Plate bolts	400	lbf-ft

Key response parameters:		
F_{Max}	125	kN
Δ_{FMax}	27.2	mm
$Drift_{FMax}$	8	%
$F_{Ultimate}$	30	kN
$\Delta_{Ultimate}$	30.7	mm
$Drift_{Ultimate}$	9	%





Test TC9-1

Type Monotonic Static

Loading Rate: 100 με/s

Failure mode: Beam/Net Section

Key response parameters:

$K_{Plastic}$	4.3	kN/mm
$K_{Softening}$	-	kN/mm
$K_{Hardening}$	7.2	kN/mm

Geometry:

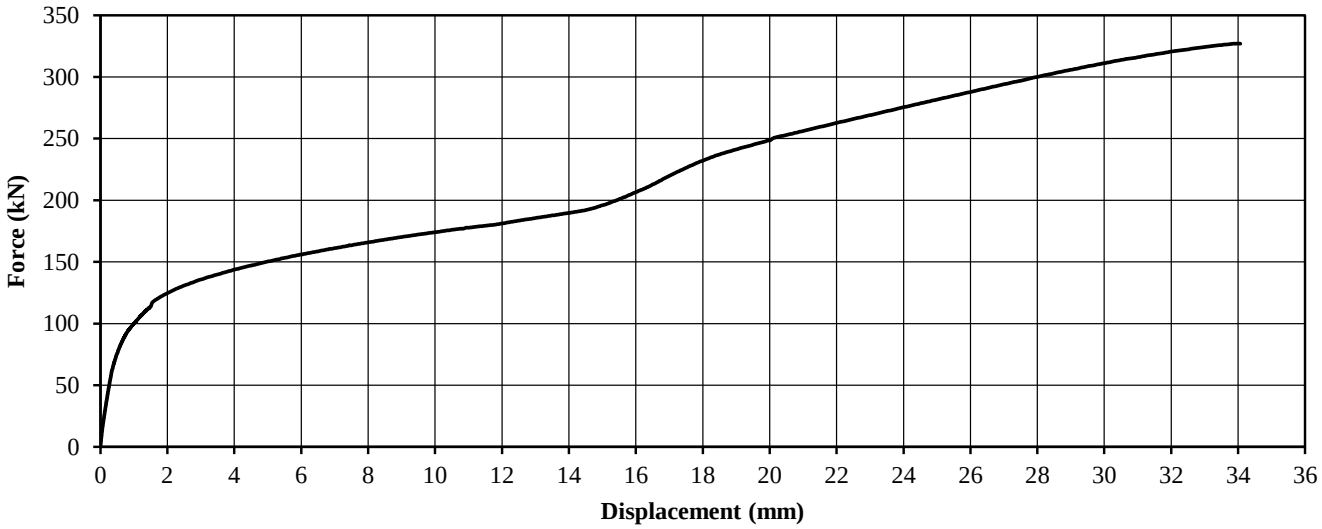
g_{column}	89	mm
t	12.7	mm
g_{beam}	76	mm
φ_{bolt}	25.4	mm
k	25.4	mm
g_2	42.9	mm
g_2/t	3.38	

Materials:

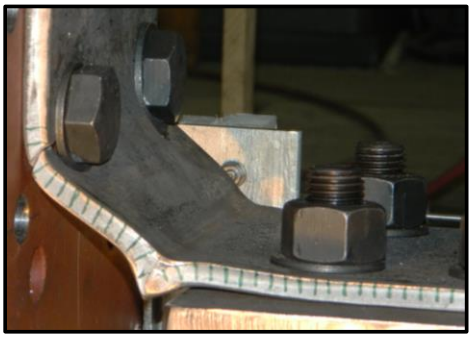
Angle	A36	
F_y	363	MPa
F_u	520	MPa
ε_u	0.2515	
Bolt	A490	
Column bolts	1000	lbf-ft
Plate bolts	1000	lbf-ft

	F (kN)	Δ (mm)
Initial	-	-
Plastic	153	5.5
Softening	-	-
Hardening	177	11.0
Max. Force	327	34.1
Ultimate	327	34.1

Force-displacement













Test TC9-2

Type Monotonic Static

Loading Rate: 600 με/s

Failure mode: Column/Beam

Geometry:

g_{column}	89	mm
t	12.700	mm
g_{beam}	76	mm
φ_{bolt}	25.4	mm
k	25.400	mm
g_2	42.9	mm
g_2/t	3.38	

Materials:

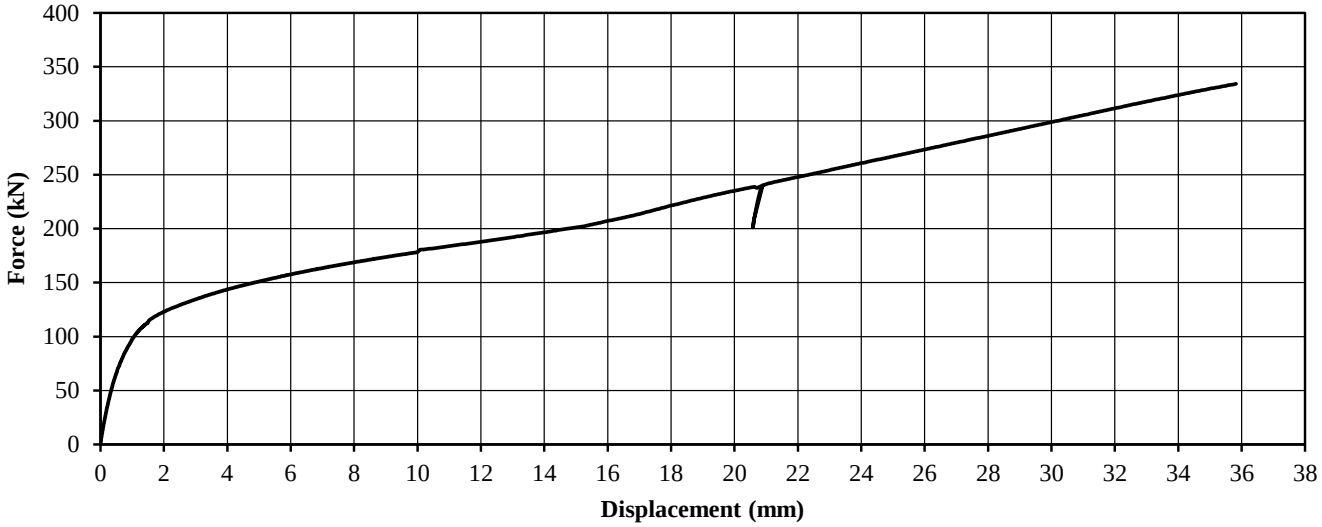
Angle	A36	
F_y	363	MPa
F_u	520	MPa
ε_u	0.2515	
Bolt	A490	
Column bolts	1000	lbf-ft
Plate bolts	1000	lbf-ft

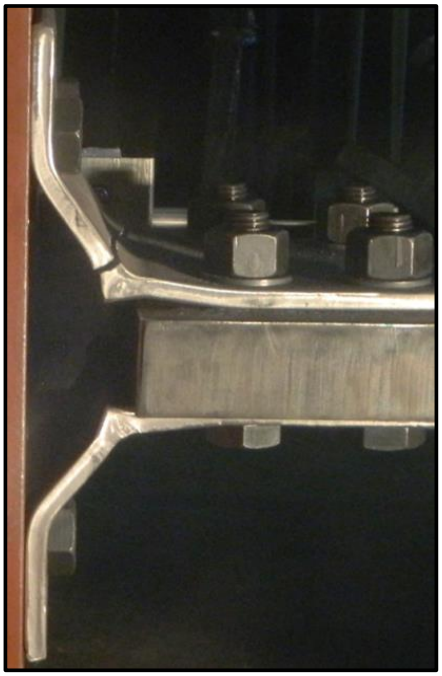
Key response parameters:

$K_{Plastic}$	4.9	kN/mm
$K_{Softening}$	-	kN/mm
$K_{Hardening}$	6.8	kN/mm

	F (kN)	Δ (mm)
Initial	-	-
Plastic	157	5.8
Softening	-	-
Hardening	208	16.4
Max. Force	334	35.8
Ultimate	334	35.8

Force-displacement













Test TC9-3

Type Monotonic Dynamic

Loading Rate: 750000 με/s

Failure mode: Column/Net Section

Key response parameters:

$K_{Plastic}$	5.0	kN/mm
$K_{Softening}$	-	kN/mm
$K_{Hardening}$	7.1	kN/mm

Geometry:

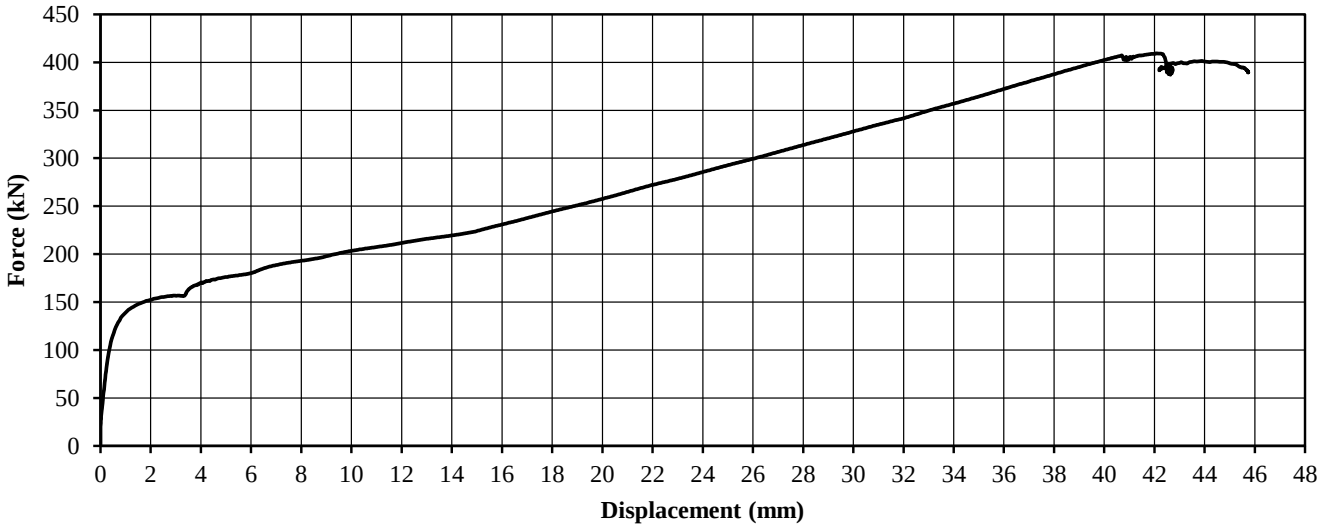
g_{column}	89	mm
t	12.700	mm
g_{beam}	76	mm
φ_{bolt}	25.4	mm
k	25.400	mm
g_2	42.9	mm
g_2/t	3.38	

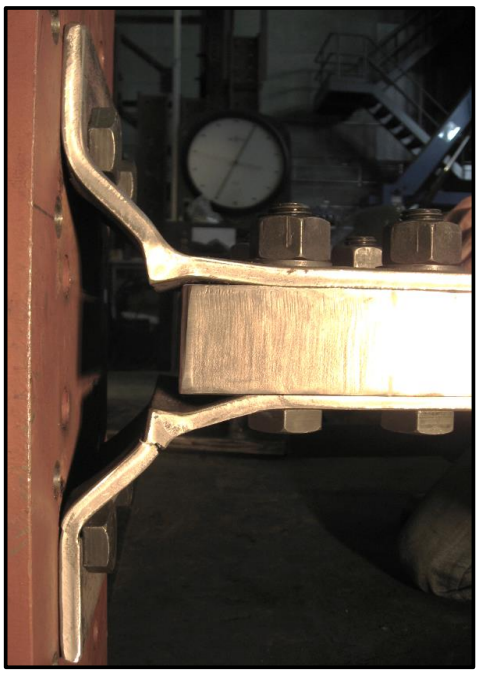
Materials:

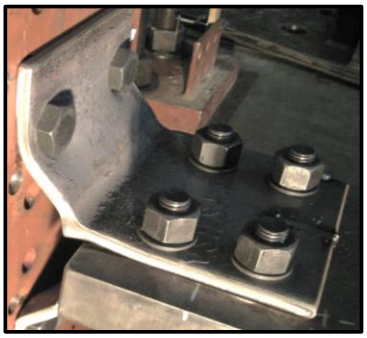
Angle	A36	
F_y	363	MPa
F_u	520	MPa
ε_u	0.2515	
Bolt	A490	
Column bolts	1000	lbf-ft
Plate bolts	1000	lbf-ft

	F (kN)	Δ (mm)
Initial	20	0.007
Plastic	167	3.7
Softening	-	-
Hardening	228	15.8
Max. Force	409	40.9
Ultimate	389	45.7

Force-displacement













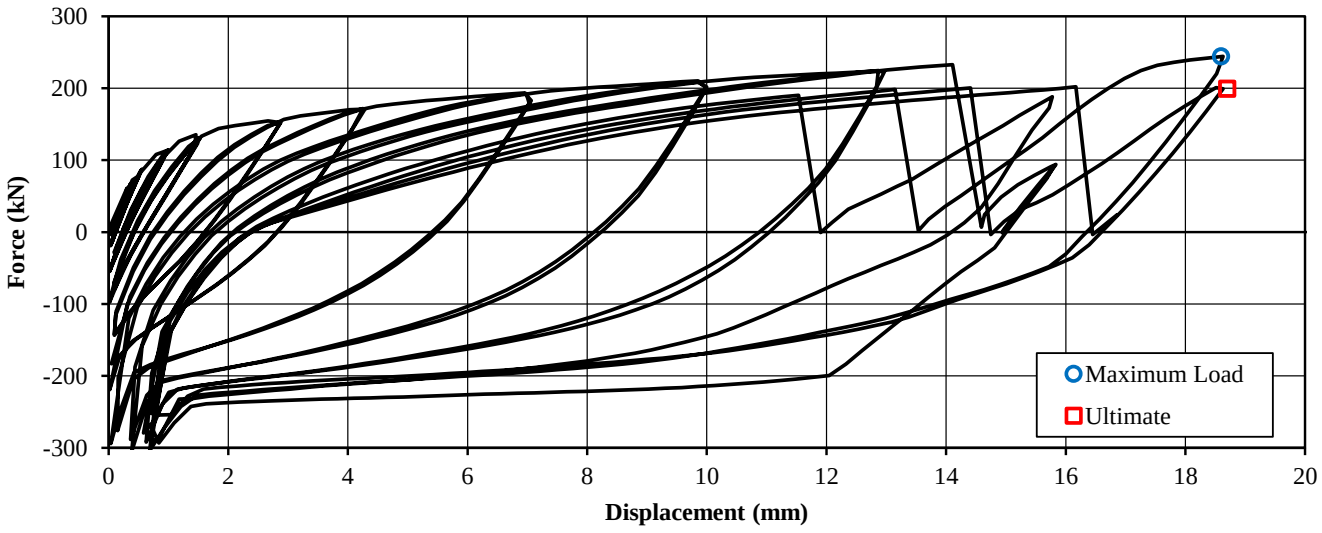
Test TC9-4

Type Cyclic W310 **Failure mode:** Net Section

Geometry:		
g_{column}	89	mm
t	12.700	mm
g_{beam}	76	mm
φ_{bolt}	25.4	mm
k	25.400	mm
g_2	42.9	mm
g_2/t	3.38	

Materials:		
Angle	A36	
F_y	363	MPa
F_u	520	MPa
ε_u	0.2515	
Bolt	A490	
Column bolts	1000	
Plate bolts	1000	lbf-ft

Key response parameters:		
F_{Max}	244	kN
Δ_{FMax}	18.6	mm
$Drift_{FMax}$	8	%
$F_{Ultimate}$	199	kN
$\Delta_{Ultimate}$	18.7	mm
$Drift_{Ultimate}$	8	%





Note: The shocks created by bolt slip caused the loss of a captor. Therefore, the test was terminated before failure of the angles.

Test TC9-5

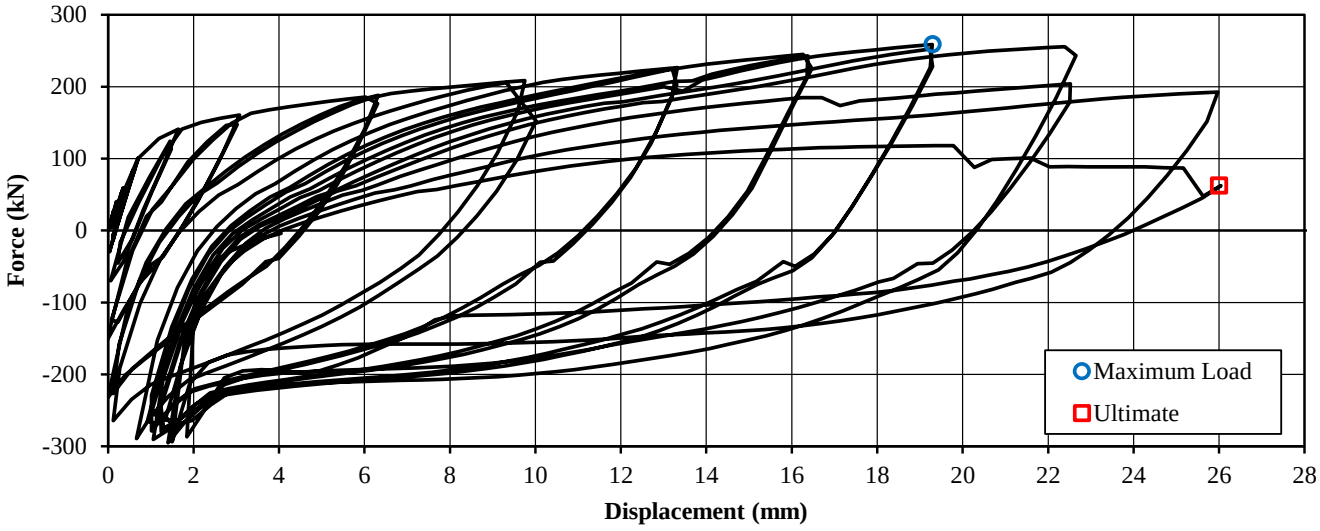
Type Cyclic W410 **Failure mode:** Column/Net Section

Geometry:		
g_{column}	89	mm
t	12.700	mm
g_{beam}	76	mm
φ_{bolt}	25.4	mm
k	25.400	mm
g_2	42.9	mm
g_2/t	3.38	

Materials:		
Angle	A36	
F_y	363	MPa
F_u	520	MPa
ε_u	0.2515	
Bolt	A490	
Column bolts	1000	lbf-ft
Plate bolts	1000	lbf-ft

Key response parameters:		
F_{Max}	259	kN
Δ_{FMax}	19.3	mm
$Drift_{FMax}$	7	%
$F_{Ultimate}$	62.5	kN
$\Delta_{Ultimate}$	26.0	mm
$Drift_{Ultimate}$	9	%

Force-displacement













Test TC9-6

Type Monotonic Snug-thight

Loading Rate: 100 με/s

Failure mode: Column

Key response parameters:

$K_{Plastic}$	6.6	kN/mm
$K_{Softening}$	-	kN/mm
$K_{Hardening}$	-	kN/mm

Geometry:

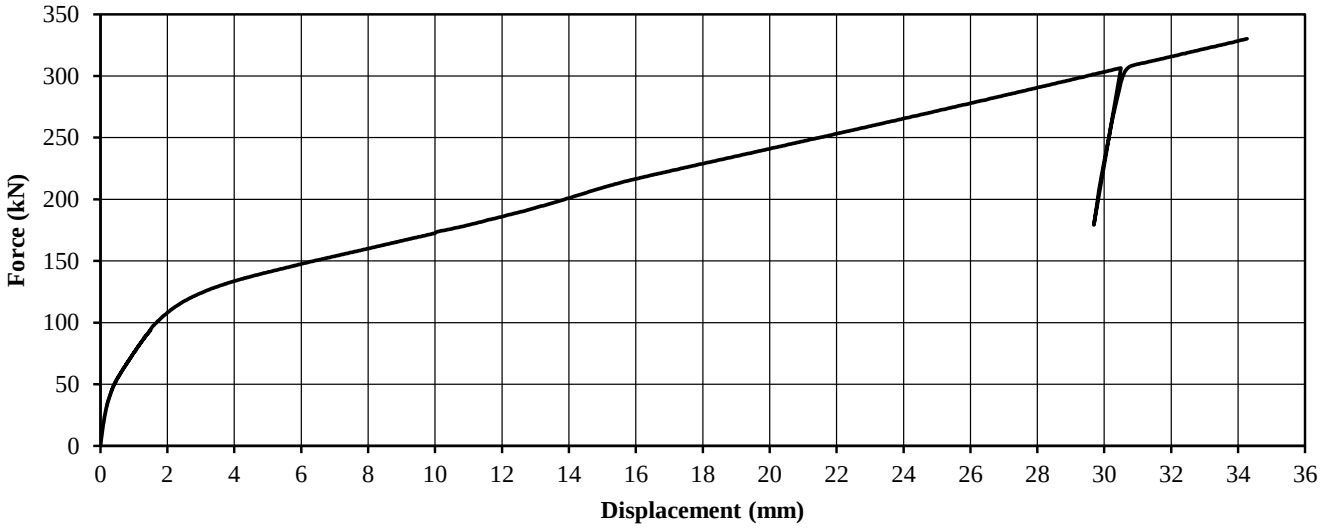
g_{column}	89	mm
t	12.700	mm
g_{beam}	76	mm
φ_{bolt}	25.4	mm
k	25.400	mm
g_2	42.9	mm
g_2/t	3.38	

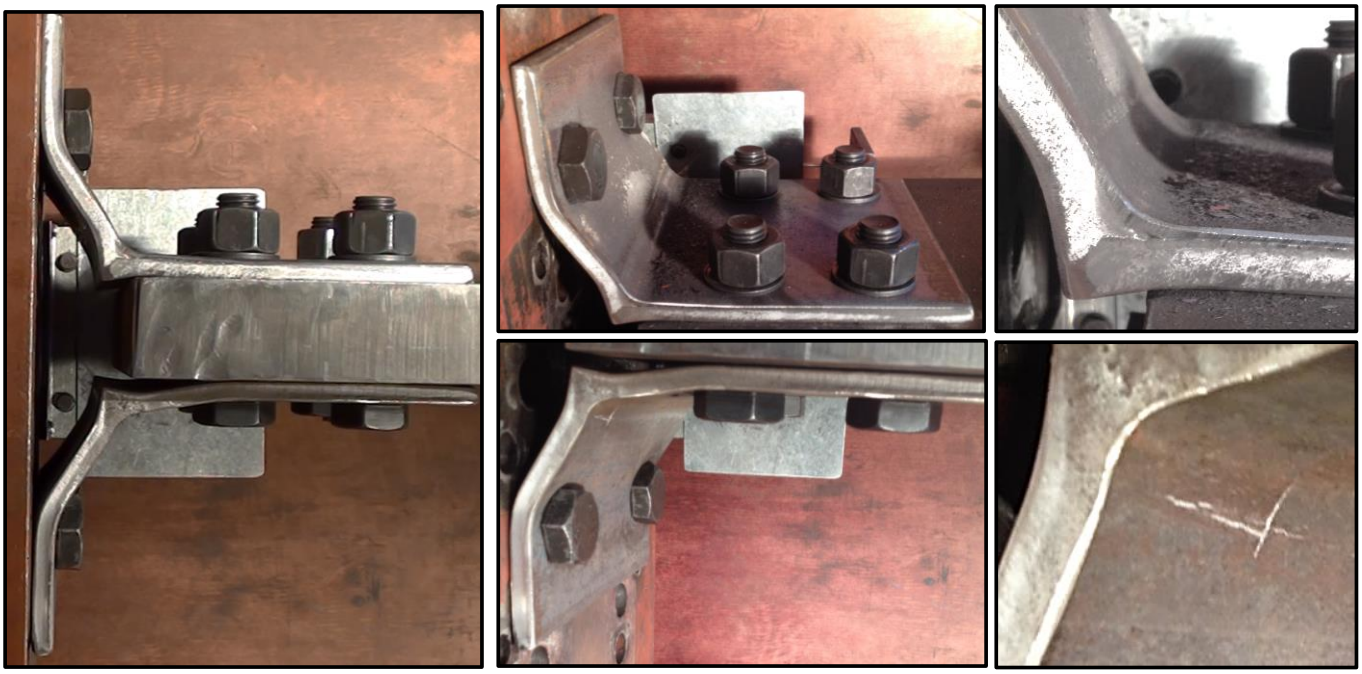
Materials:

Angle	A36	
F_y	363	MPa
F_u	520	MPa
ε_u	0.2515	
Bolt	A490	
Column bolts	0	lbf-ft
Plate bolts	1000	lbf-ft

	F (kN)	Δ (mm)
Initial	26	0.139
Plastic	141	5.0
Softening	-	-
Hardening	-	-
Max. Force	330	34.3
Ultimate	330	34.3

Force-displacement





Test TC9-7

Type Monotonic A325

Loading Rate: 100 με/s

Failure mode: Beam

Geometry:

g_{column}	89	mm
t	12.700	mm
g_{beam}	76	mm
φ_{bolt}	25.4	mm
k	25.400	mm
g_2	42.9	mm
g_2/t	3.38	

Materials:

Angle	A36	
F_y	363	MPa
F_u	520	MPa
ε_u	0.2515	
Bolt	A325	
Column bolts	1000	lbf-ft
Plate bolts	1000	lbf-ft

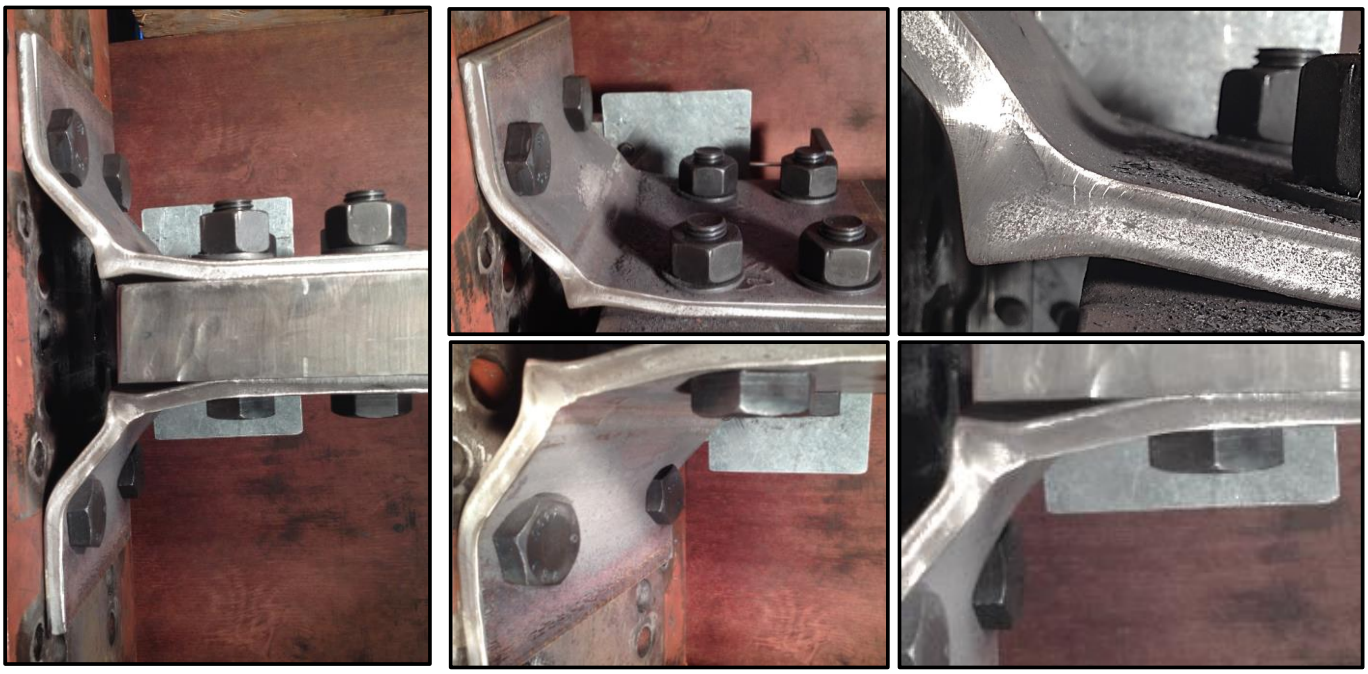
Key response parameters:

$K_{Plastic}$	5.9	kN/mm
$K_{Softening}$	-	kN/mm
$K_{Hardening}$	6	kN/mm

	6.6	Δ (mm)
Initial	-	-
Plastic	161	4.6
Softening	-	-
Hardening	210	12.9
Max. Force	422	43.5
Ultimate	422	43.5

Force-displacement





Test TC9-8

Type Time-History **Failure mode:** Column/Net Section

Geometry:

g_{column}	89	mm
t	12.700	mm
g_{beam}	76	mm
φ_{bolt}	25.4	mm
k	25.400	mm
g_2	42.9	mm
g_2/t	3.38	

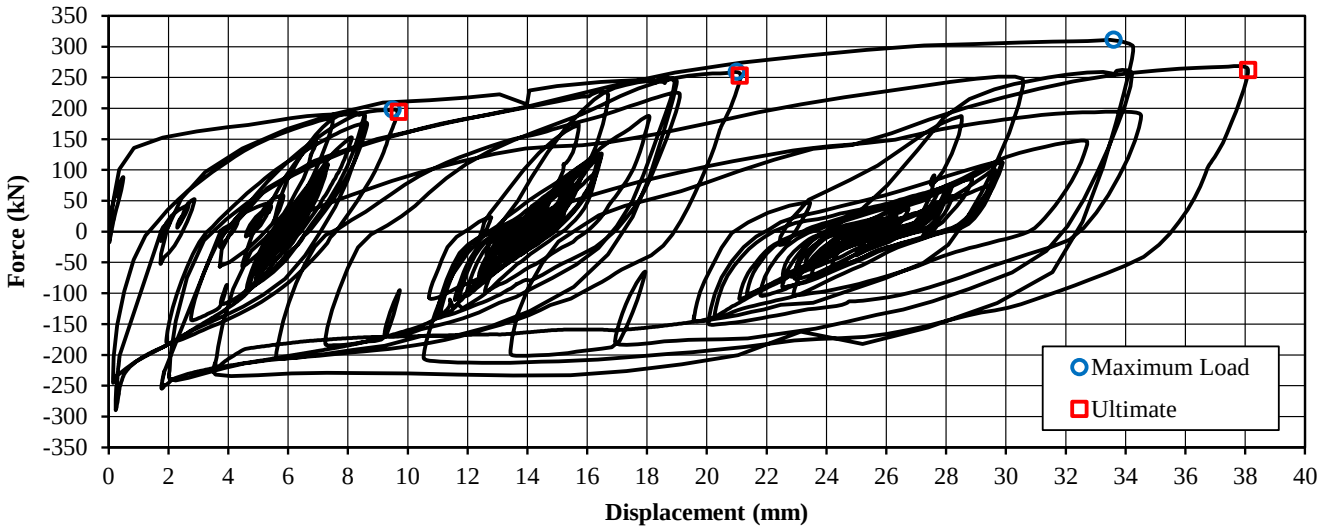
Materials:

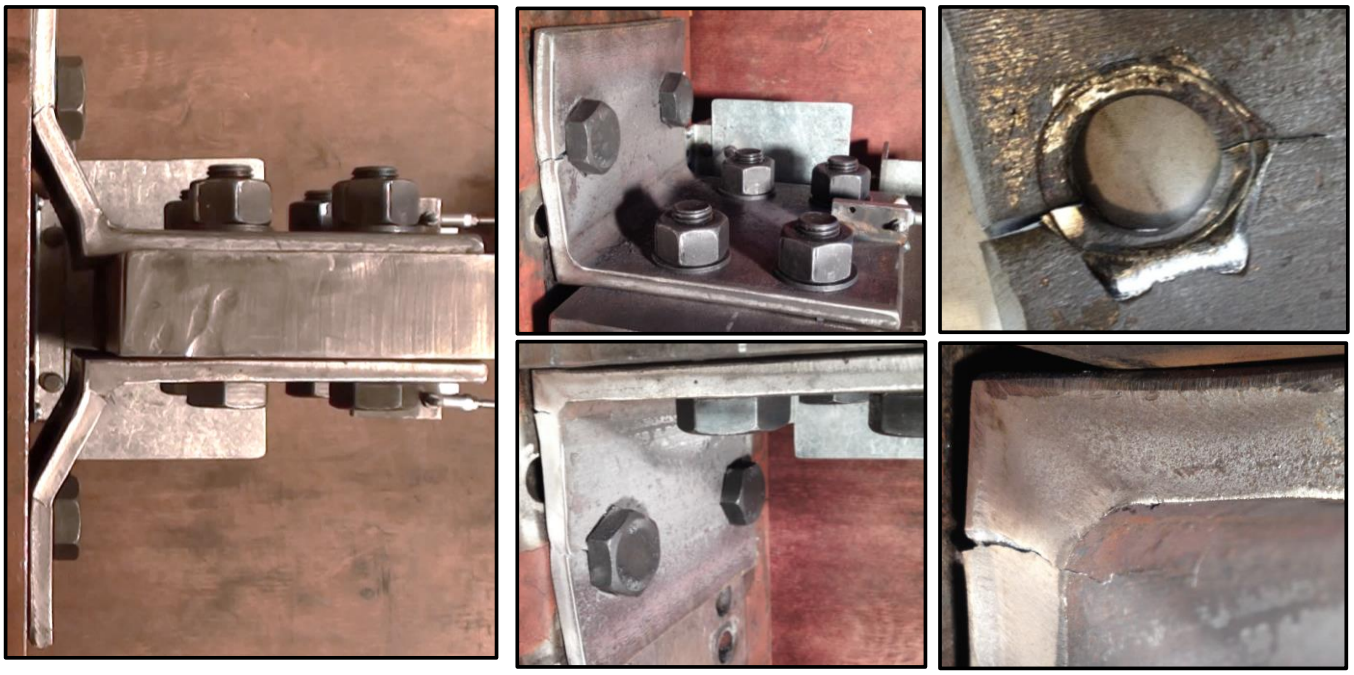
Angle	A36	
F_y	363	MPa
F_u	520	MPa
ε_u	0.2515	
Bolt	A490	
Column bolts	1000	lbf-ft
Plate bolts	1000	lbf-ft

Key response parameters:

Signal factor	65%	130%	230%
Δ_0	0.0	1.7	3.7
$F_{F\ Max}$	198	259	311
$\Delta_{F\ Max}$	9.5	21.0	33.6
$F_{Ultimate}$	194	253	262
$\Delta_{ultimate}$	9.7	21.1	38.1

Force-displacement





Test TC9-9

Type Fatigue **Failure mode:** Column/Net Section

Geometry:

g_{column}	89	mm
t	12.700	mm
g_{beam}	76	mm
φ_{bolt}	25.4	mm
k	25.400	mm
g_2	42.9	mm
g_2/t	3.38	

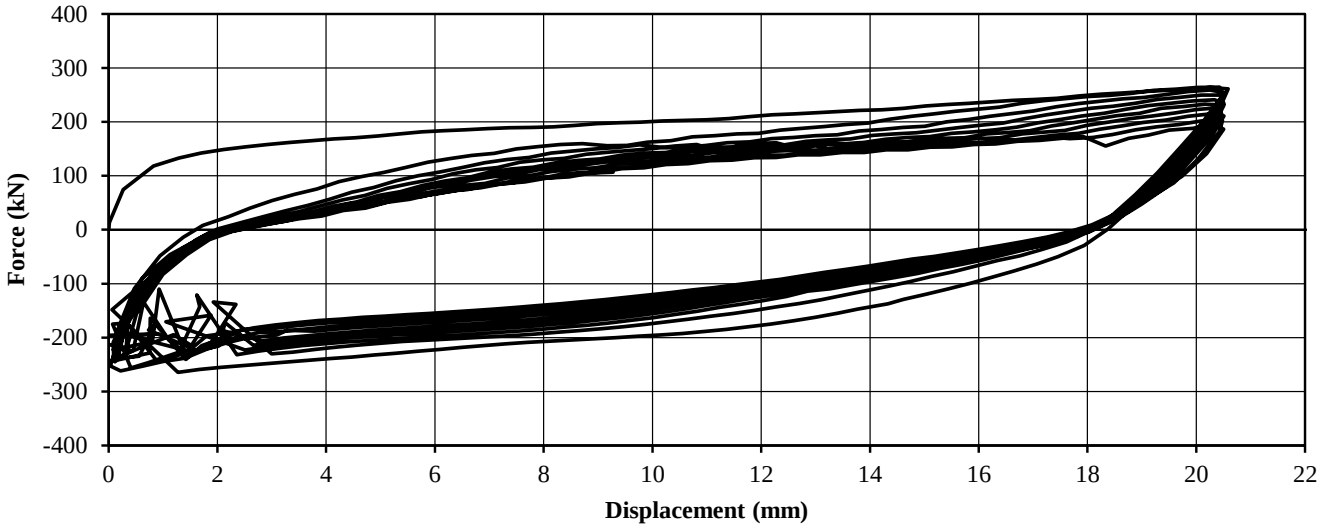
Materials:

Angle	A36	
F_y	363	MPa
F_u	520	MPa
ε_u	0.2515	
Bolt	A490	
Column bolts	1000	lbf-ft
Plate bolts	1000	lbf-ft

Key response parameters:

$\Delta_{Amplitude}$	20.5	mm
F_{Max}	264	kN
Cycles	12	

Force-displacement





Test TC9-10

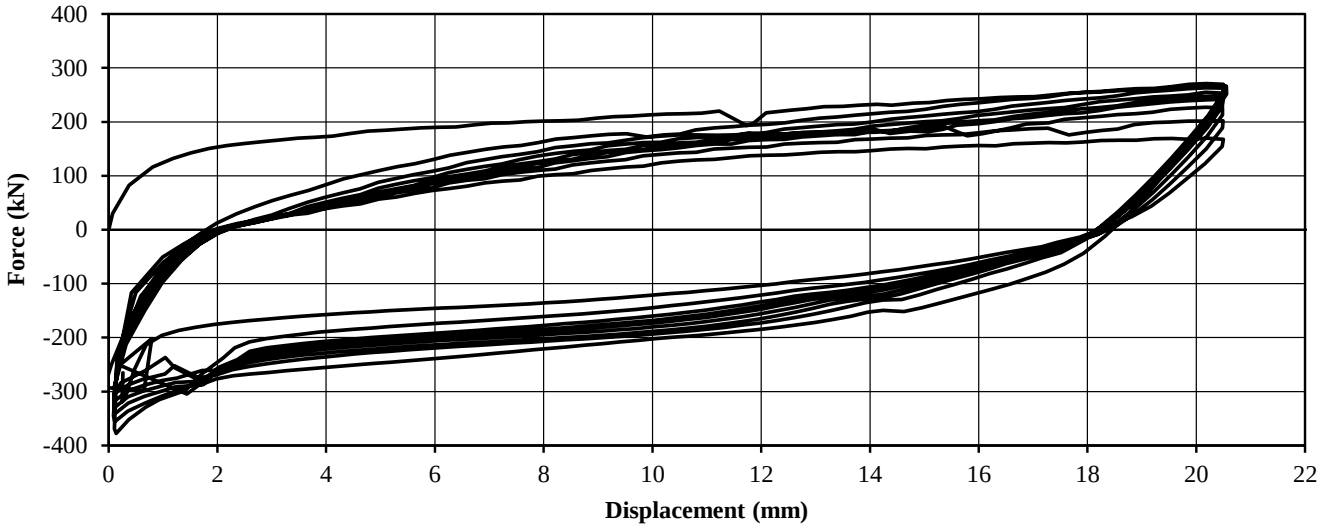
Type Fatigue **Failure mode:** Column/Net Section

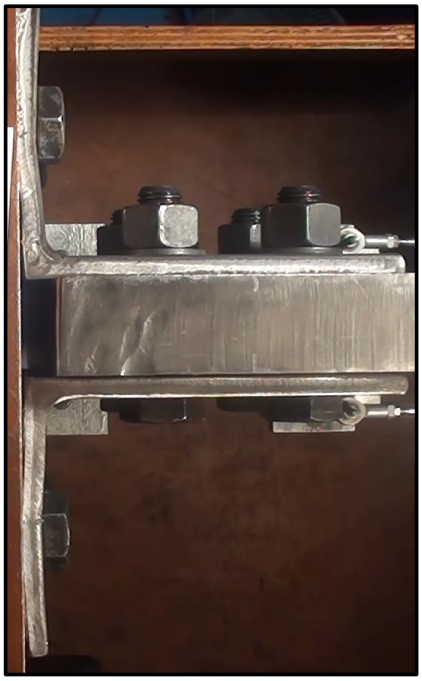
Geometry:		
g_{column}	89	mm
t	12.700	mm
g_{beam}	76	mm
φ_{bolt}	25.4	mm
k	25.400	mm
g_2	42.9	mm
g_2/t	3.38	

Materials:		
Angle	A36	
F_y	363	MPa
F_u	520	MPa
ε_u	0.2515	
Bolt	A325	
Column bolts	1000	lbf-ft
Plate bolts	1000	lbf-ft

Key response parameters:		
$\Delta_{Amplitude}$	20.5	mm
F_{Max}	271	kN
Cycles	8	

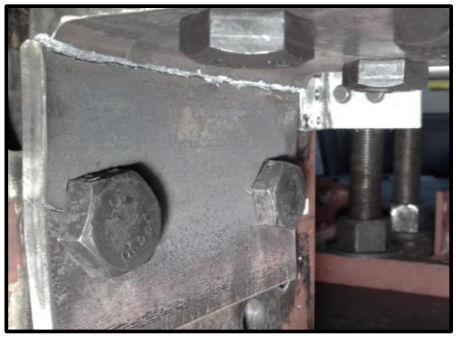
Force-displacement













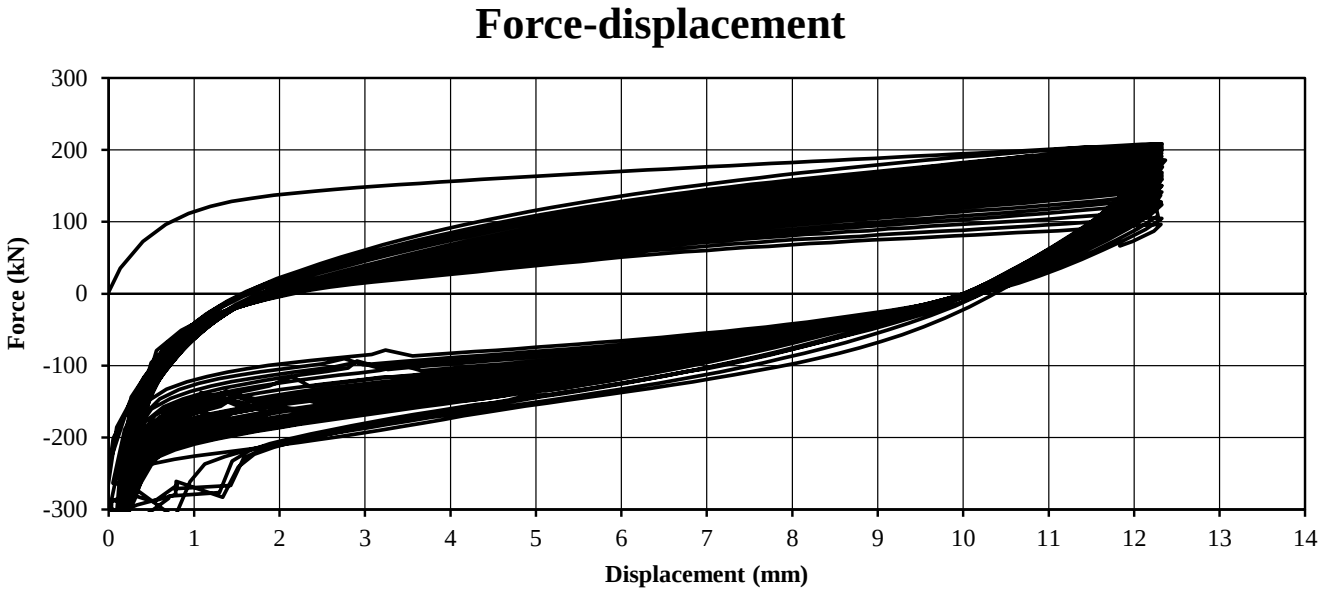
Test TC9-11

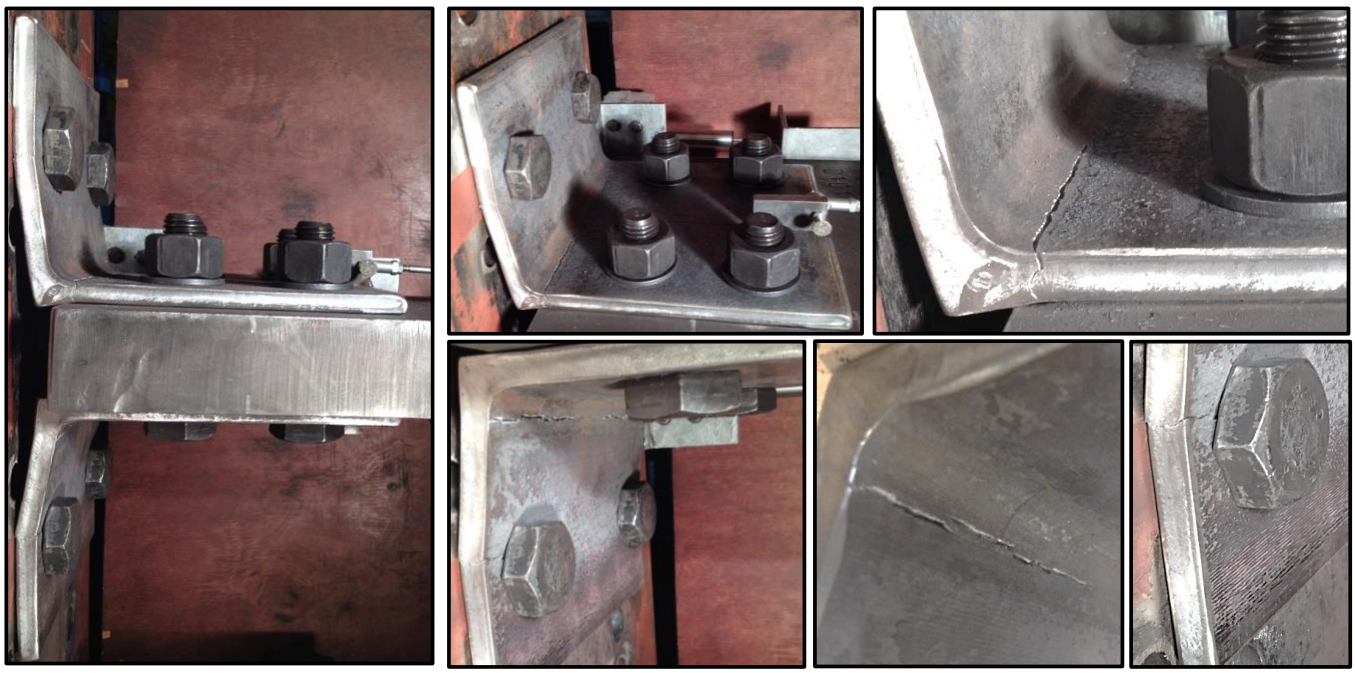
Type Fatigue **Failure mode:** Column/Beam/Net Section

Geometry:		
g_{column}	89	mm
t	12.700	mm
g_{beam}	76	mm
φ_{bolt}	25.4	mm
k	25.400	mm
g_2	42.9	mm
g_2/t	3.38	

Materials:		
Angle	A36	
F_y	363	MPa
F_u	520	MPa
ε_u	0.2515	
Bolt	A490	
Column bolts	1000	lbf-ft
Plate bolts	1000	lbf-ft

Key response parameters:		
$\Delta_{Amplitude}$	12.3	mm
F_{Max}	208	kN
Cycles	41	





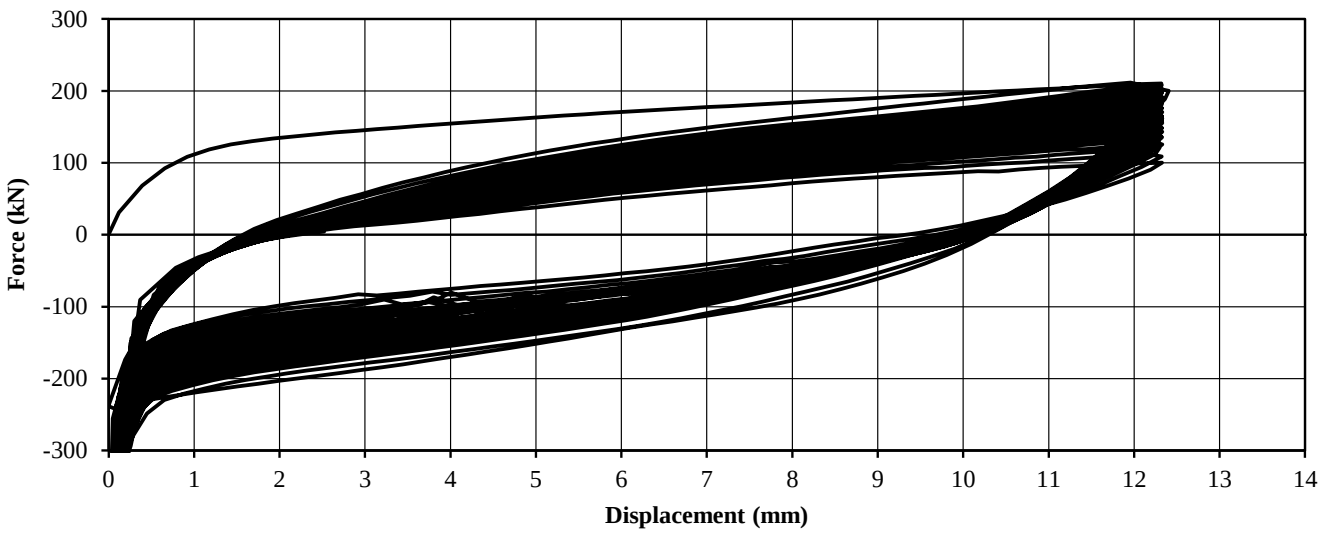
Test TC9-12

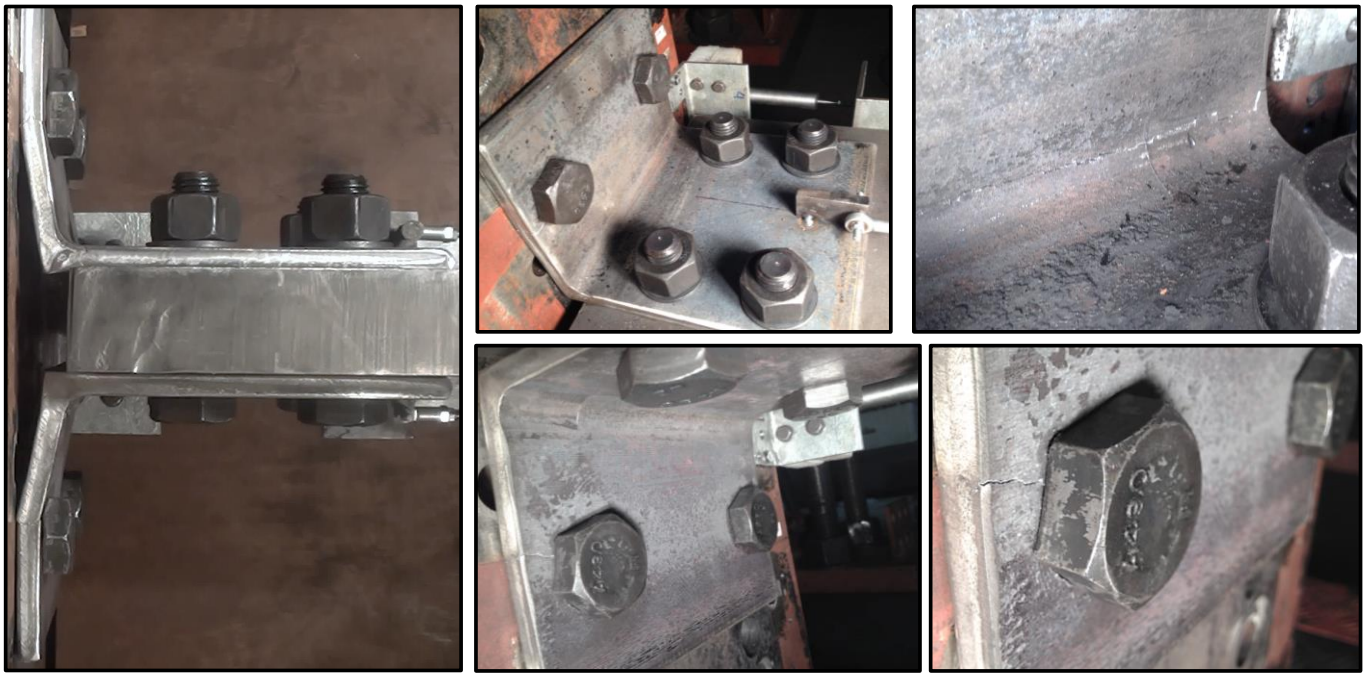
Type Fatigue **Failure mode:** Column/Net Section

Geometry:		
g_{column}	89	mm
t	12.700	mm
g_{beam}	76	mm
φ_{bolt}	25.4	mm
k	25.400	mm
g_2	42.9	mm
g_2/t	3.38	

Materials:		
Angle	A36	
F_y	363	MPa
F_u	520	MPa
ε_u	0.2515	
Bolt	A490	
Column bolts	1000	lbf-ft
Plate bolts	1000	lbf-ft

Key response parameters:		
$\Delta_{Amplitude}$	12.3	mm
F_{Max}	211	kN
Cycles	44	



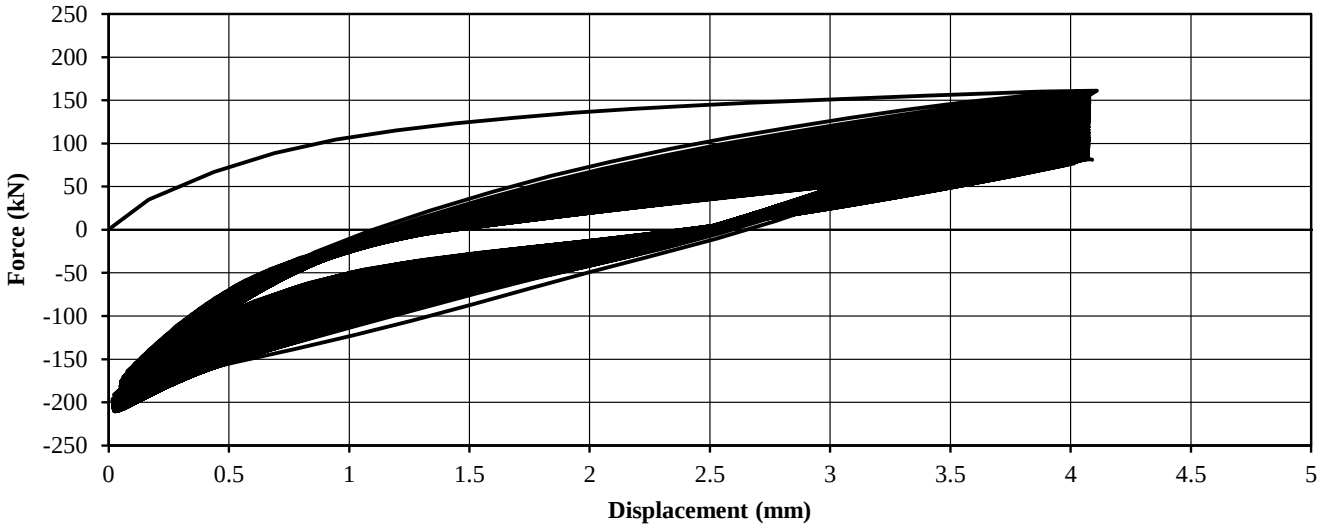


Test TC9-13

Type Fatigue **Failure mode:** Column

Geometry:			Materials:			Key response parameters:		
g_{column}	89	mm	**Angle**	A36		$\Delta_{Amplitude}$	4.1	mm
t	12.700	mm	F_y	363	MPa	F_{Max}	160	kN
g_{beam}	76	mm	F_u	520	MPa	**Cycles**	424	
φ_{bolt}	25.4	mm	ε_u	0.2515				
k	25.400	mm	**Bolt**	A325				
g_2	42.9	mm	**Column bolts**	1000	lbf-ft			
g_2/t	3.38		**Plate bolts**	1000	lbf-ft			

Force-displacement



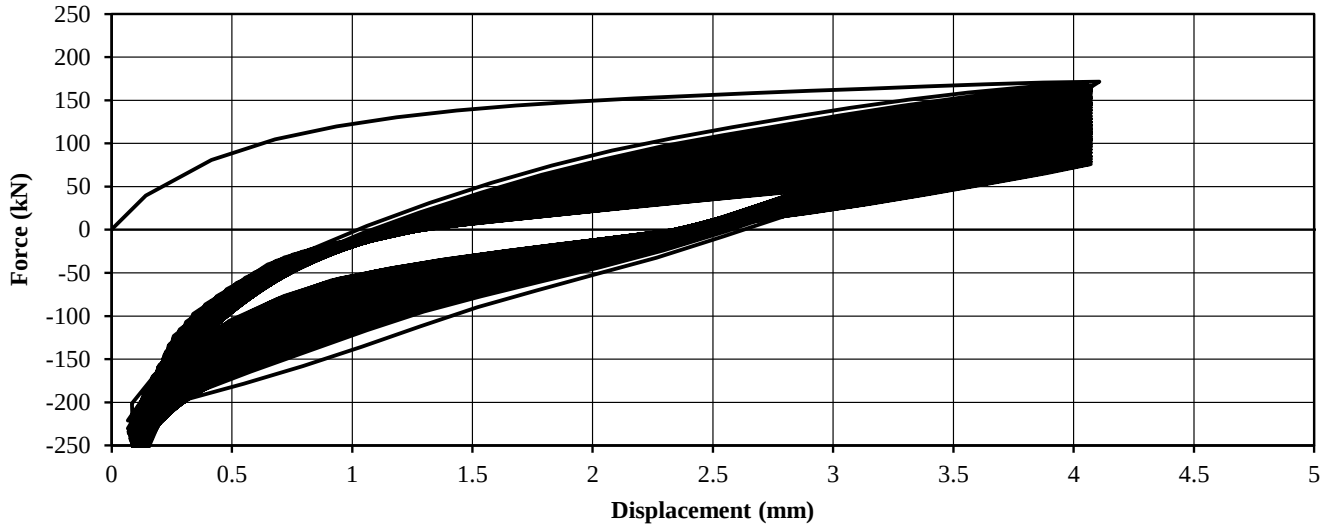


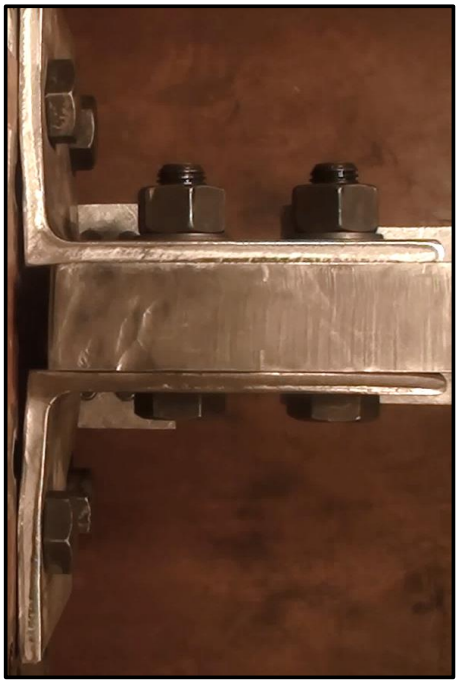
Test TC9-14

Type Fatigue **Failure mode:** Column

Geometry:			Materials:			Key response parameters:		
g_{column}	89	mm	**Angle**	A36		$\Delta_{Amplitude}$	4.1	mm
t	12.700	mm	F_y	363	MPa	F_{Max}	171	kN
g_{beam}	76	mm	F_u	520	MPa	**Cycles**	360	
φ_{bolt}	25.4	mm	ε_u	0.2515				
k	25.400	mm	**Bolt**	A490				
g_2	42.9	mm	**Column bolts**	1000	lbf-ft			
g_2/t	3.38		**Plate bolts**	1000	lbf-ft			

Force-displacement













Test TC10-1

Type Monotonic Static

Loading Rate: 100 με/s

Failure mode: Beam

Geometry:

g_{column}	102	mm
t	12.7	mm
g_{beam}	76	mm
φ_{bolt}	25.4	mm
k	25.4	mm
g_2	55.6	mm
g_2/t	4.38	

Materials:

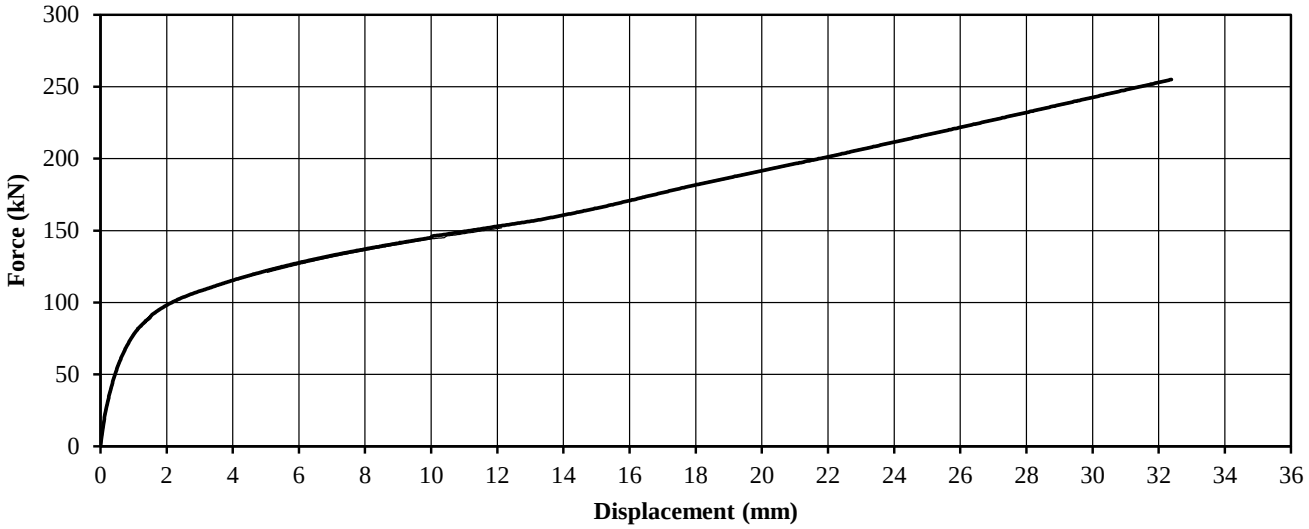
Angle	A36	
F_y	363	MPa
F_u	520	MPa
ε_u	0.2515	
Bolt	A490	
Column bolts	1000	lbf-ft
Plate bolts	1000	lbf-ft

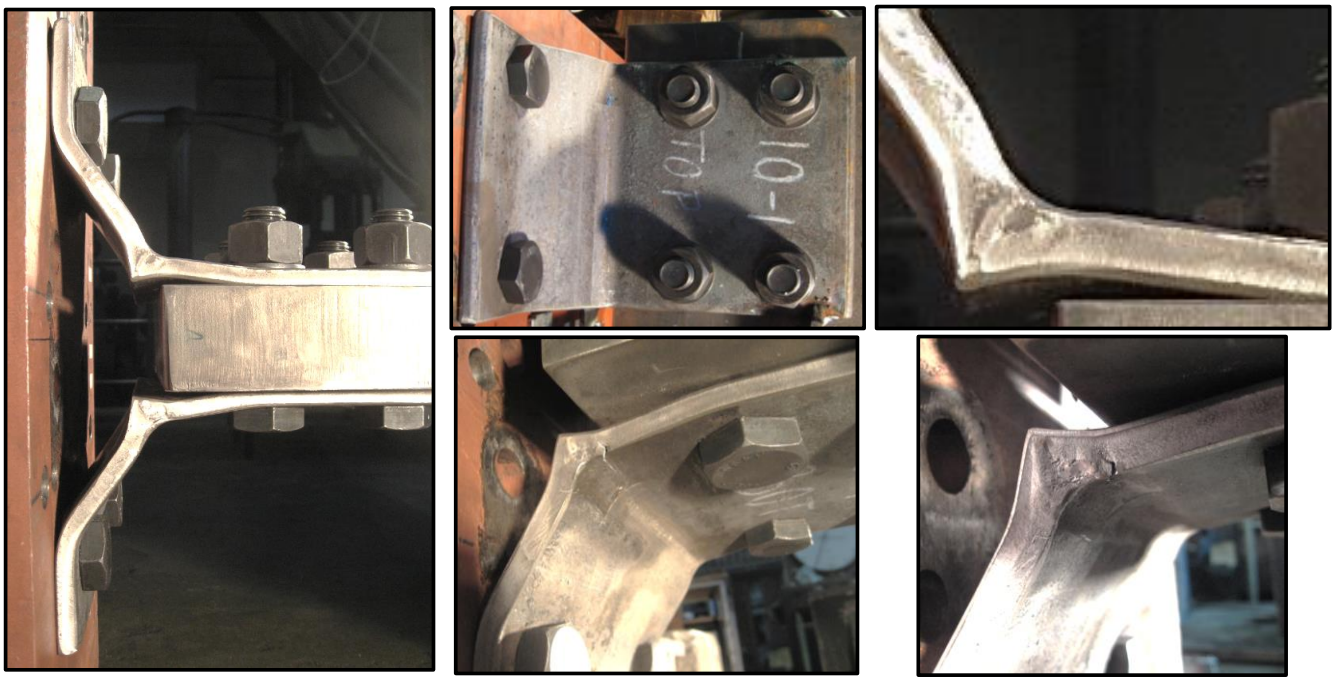
Key response parameters:

$K_{Plastic}$	4.2	kN/mm
$K_{Softening}$	-	kN/mm
$K_{Hardening}$	5.0	kN/mm

	F (kN)	Δ (mm)
Initial	-	-
Plastic	127	5.9
Softening	-	-
Hardening	160	13.6
Max. Force	255	32.4
Ultimate	255	32.4

Force-displacement





Test TC10-2

Type Monotonic Static

Loading Rate: 600 με/s

Failure mode: Column

Geometry:

g_{column}	102	mm
t	12.700	mm
g_{beam}	76	mm
φ_{bolt}	25.4	mm
k	25.400	mm
g_2	55.6	mm
g_2/t	4.38	

Materials:

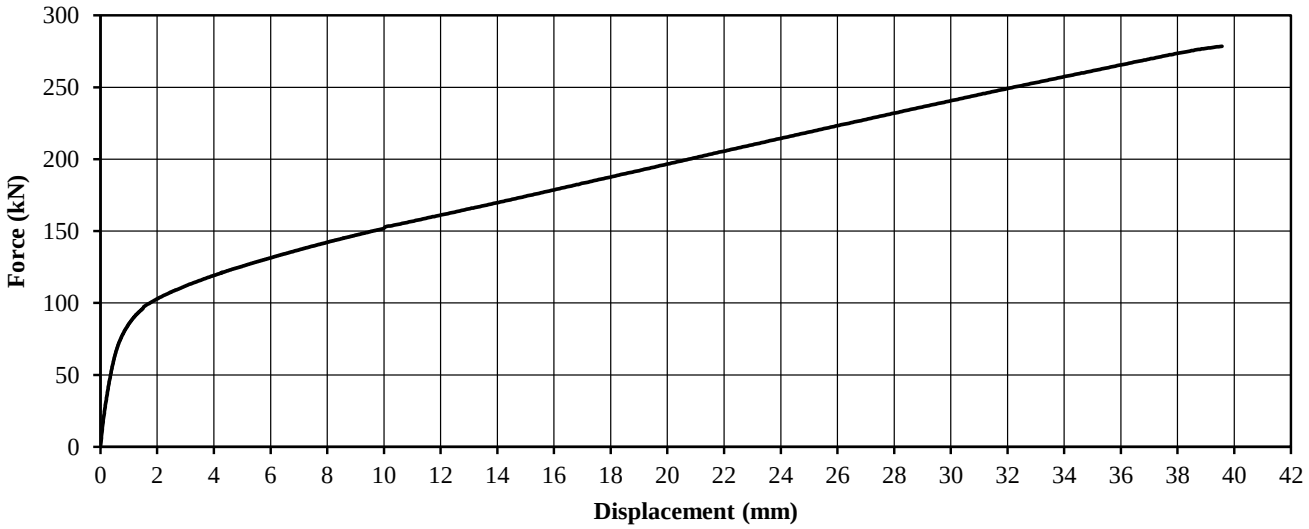
Angle	A36	
F_y	363	MPa
F_u	520	MPa
ε_u	0.2515	
Bolt	A490	
Column bolts	1000	lbf-ft
Plate bolts	1000	lbf-ft

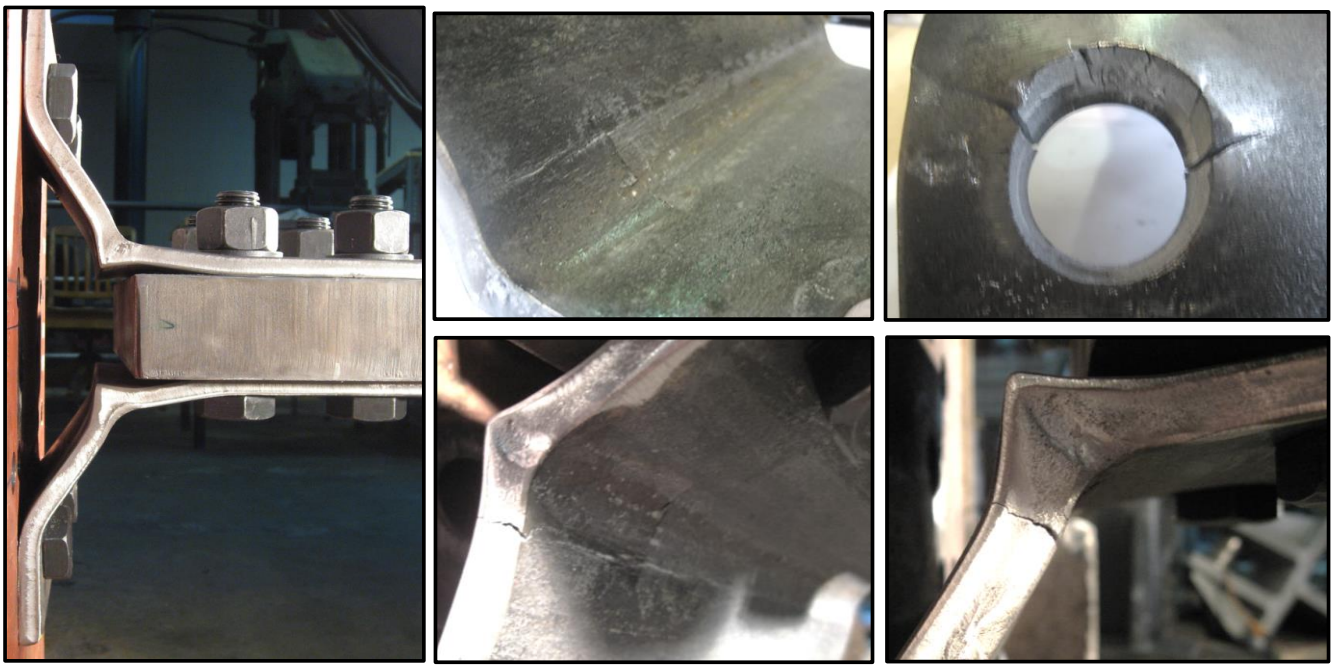
Key response parameters:

$K_{Plastic}$	4.6	kN/mm
$K_{Softening}$	-	kN/mm
$K_{Hardening}$	-	kN/mm

	F (kN)	Δ (mm)
Initial	-	-
Plastic	125	5.0
Softening	-	-
Hardening	-	-
Max. Force	278	39.6
Ultimate	278	39.6

Force-displacement





Test TC10-3

Type Monotonic Static

Loading Rate: 750000 με/s

Failure mode: Column/Net Section

Geometry:

g_{column}	102	mm
t	12.700	mm
g_{beam}	76	mm
φ_{bolt}	25.4	mm
k	25.400	mm
g_2	55.6	mm
g_2/t	4.38	

Materials:

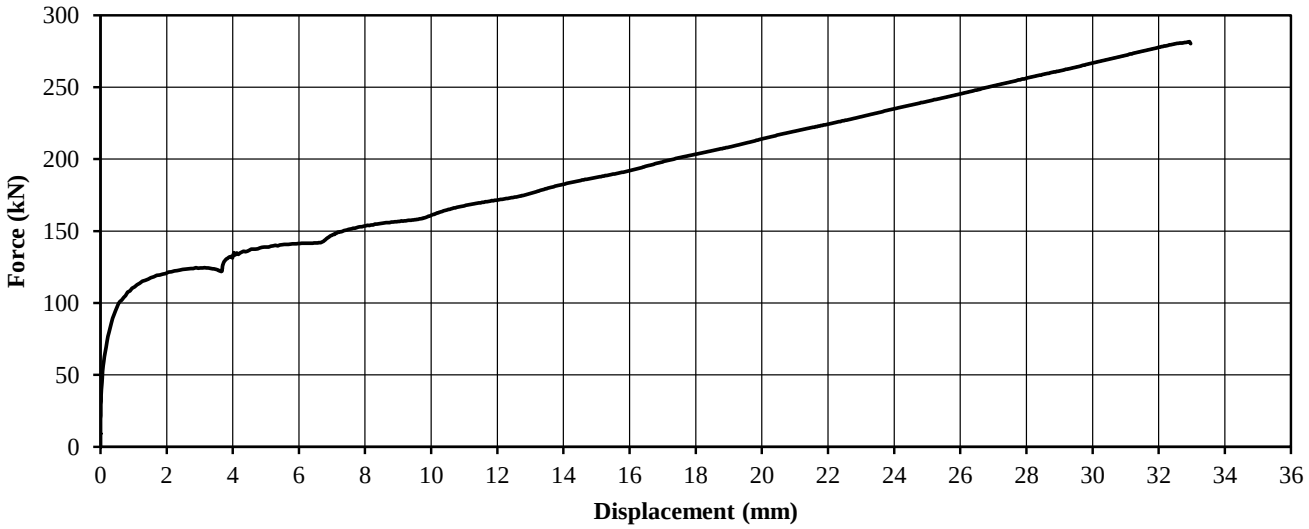
Angle	A36	
F_y	363	MPa
F_u	520	MPa
ε_u	0.2515	
Bolt	A490	
Column bolts	1000	lbf-ft
Plate bolts	1000	lbf-ft

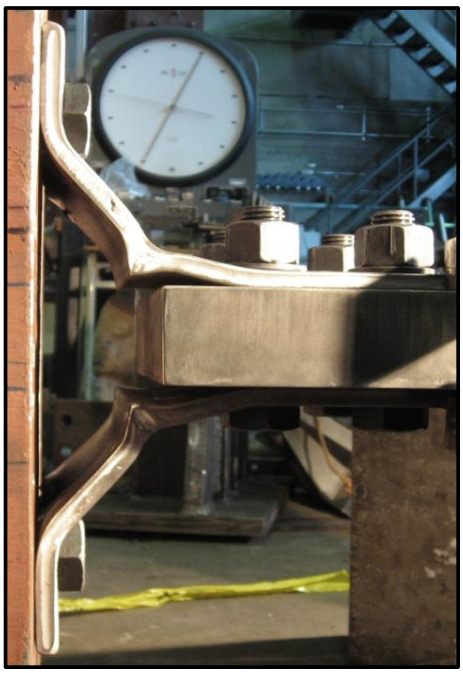
Key response parameters:

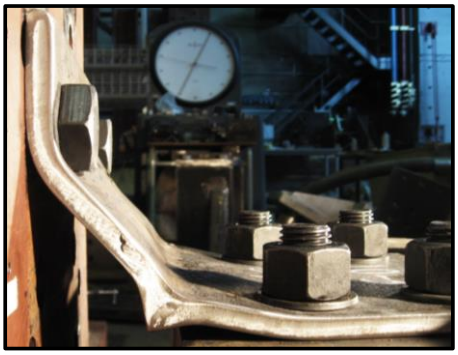
$K_{Plastic}$	4.9	kN/mm
$K_{Softening}$	-	kN/mm
$K_{Hardening}$	5.3	kN/mm

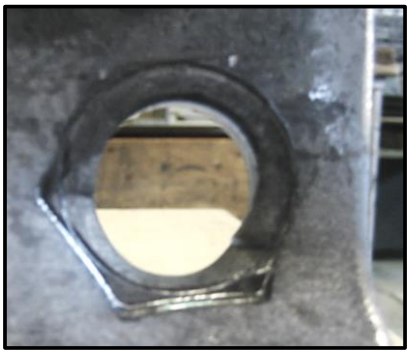
	F (kN)	Δ (mm)
Initial	30	0.028
Plastic	123	2.5
Softening	-	-
Hardening	159	9.7
Max. Force	282	32.9
Ultimate	280	33.0

Force-displacement

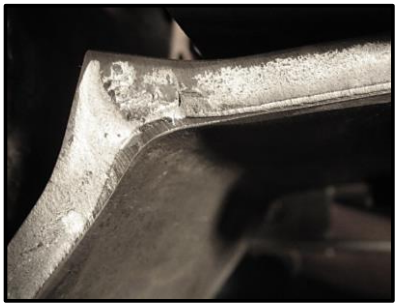












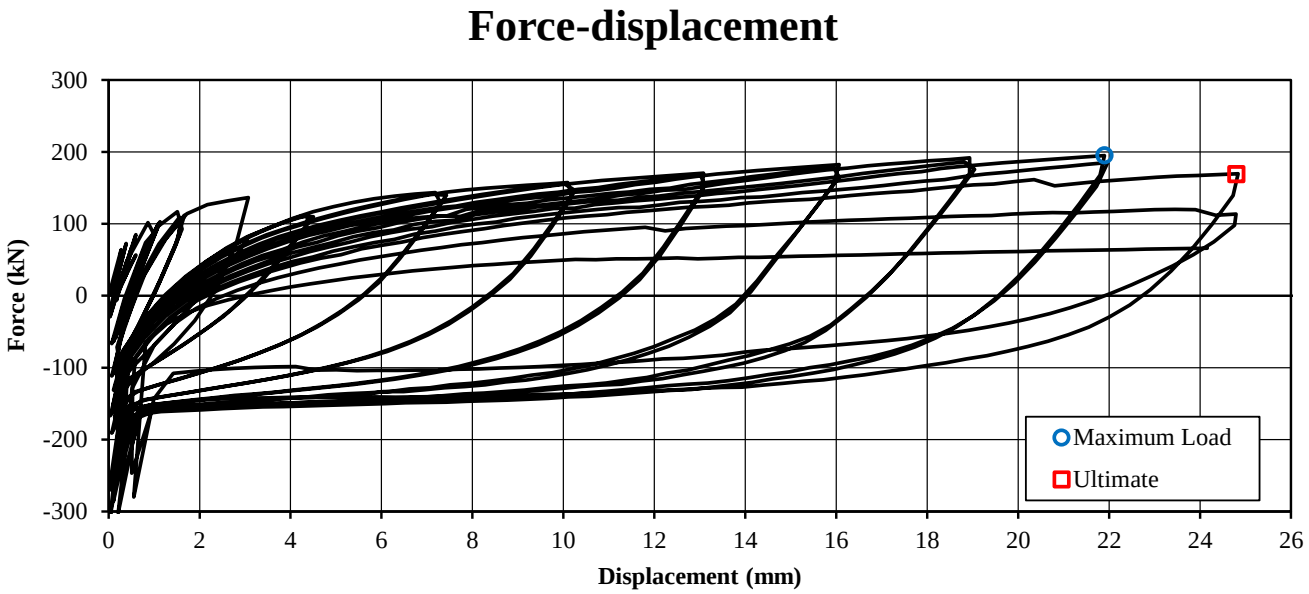
Test TC10-4

Type Cyclic W310 **Failure mode:** Column/Net Section

Geometry:		
g_{column}	102	mm
t	12.700	mm
g_{beam}	76	mm
φ_{bolt}	25.4	mm
k	25.400	mm
g_2	55.6	mm
g_2/t	4.38	

Materials:		
Angle	A36	
F_y	363	MPa
F_u	520	MPa
ε_u	0.2515	
Bolt	A490	
Column bolts	1000	lbf-ft
Plate bolts	1000	lbf-ft

Key response parameters:		
F_{Max}	195	kN
Δ_{FMax}	21.9	mm
$Drift_{FMax}$	8	%
$F_{Ultimate}$	169	kN
$\Delta_{Ultimate}$	24.8	mm
$Drift_{Ultimate}$	9	%

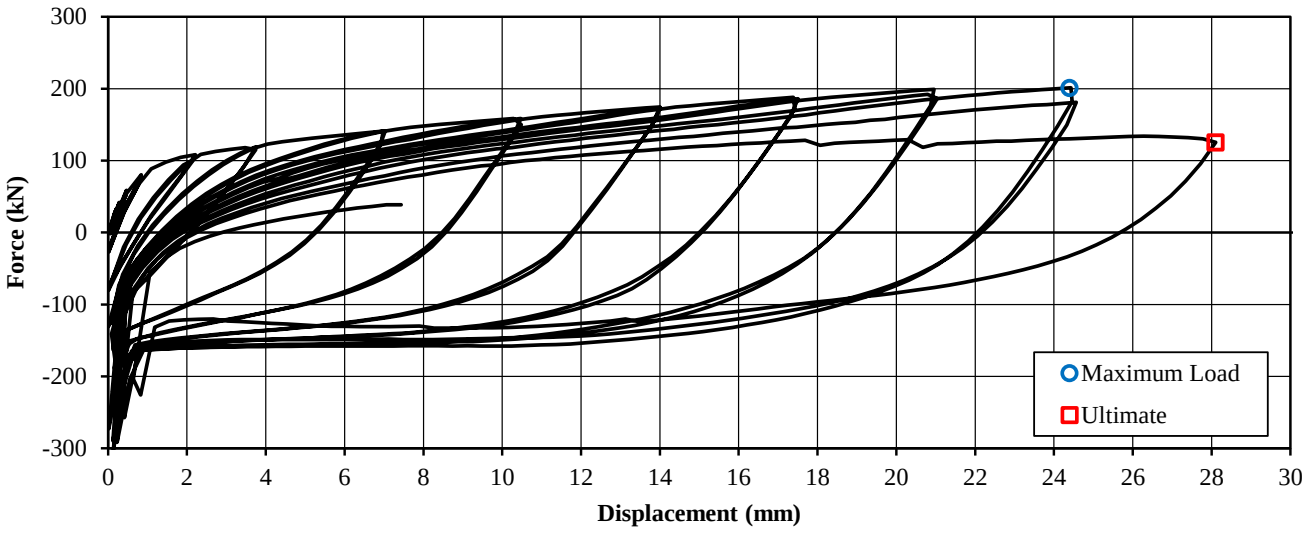




Test TC10-5

Type Cyclic W410 **Failure mode:** Column/Net Section

Geometry:			Materials:			Key response parameters:		
g_{column}	102	mm	**Angle**	A36		F_{Max}	201	kN
t	12.700	mm	F_y	363	MPa	Δ_{FMax}	24.4	mm
g_{beam}	76	mm	F_u	520	MPa	$Drift_{FMax}$	8	%
φ_{bolt}	25.4	mm	ε_u	0.2515		$F_{Ultimate}$	125	kN
k	25.400	mm	**Bolt**	A490		$\Delta_{Ultimate}$	28.1	mm
g_2	55.6	mm	**Column bolts**	1000	lbf-ft	$Drift_{Ultimate}$	9	%
g_2/t	4.38		**Plate bolts**	1000	lbf-ft			













Test TC10-6

Type Monotonic Static

Loading Rate: 600 με/s

Failure mode: Column/Net Section

Geometry:

g_{column}	102	mm
t	12.700	mm
g_{beam}	76	mm
φ_{bolt}	25.4	mm
k	25.400	mm
g_2	55.6	mm
g_2/t	4.38	

Materials:

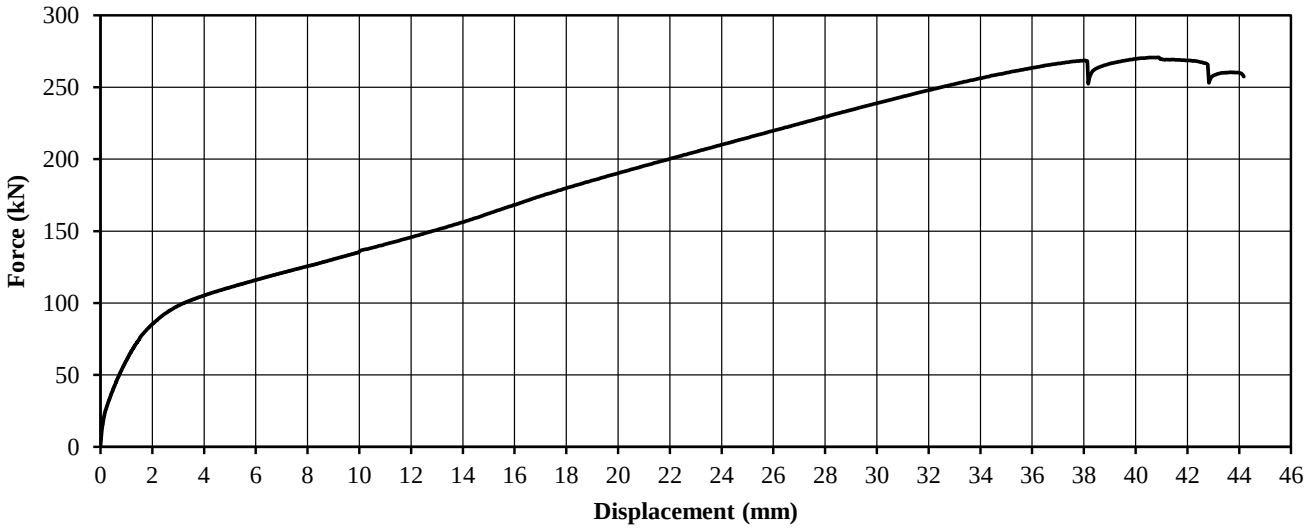
Angle	A36	
F_y	363	MPa
F_u	520	MPa
ε_u	0.2515	
Bolt	A490	
Column bolts	Snug-Thight	
Plate bolts	1000	lbf-ft

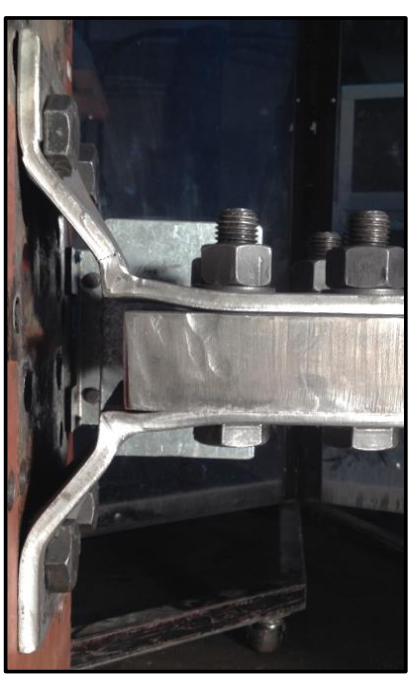
Key response parameters:

$K_{Plastic}$	5.3	kN/mm
$K_{Softening}$	-	kN/mm
$K_{Hardening}$	-	kN/mm

	F (kN)	Δ (mm)
Initial	34	0.168
Plastic	111	4.9
Softening	-	-
Hardening	-	-
Max. Force	271	40.9
Ultimate	257	44.2

Force-displacement













Test TC10-7

Type Monotonic Static

Loading Rate: 600 με/s

Failure mode: Column

Geometry:

g_{column}	102	mm
t	12.700	mm
g_{beam}	76	mm
φ_{bolt}	25.4	mm
k	25.400	mm
g_2	55.6	mm
g_2/t	4.38	

Materials:

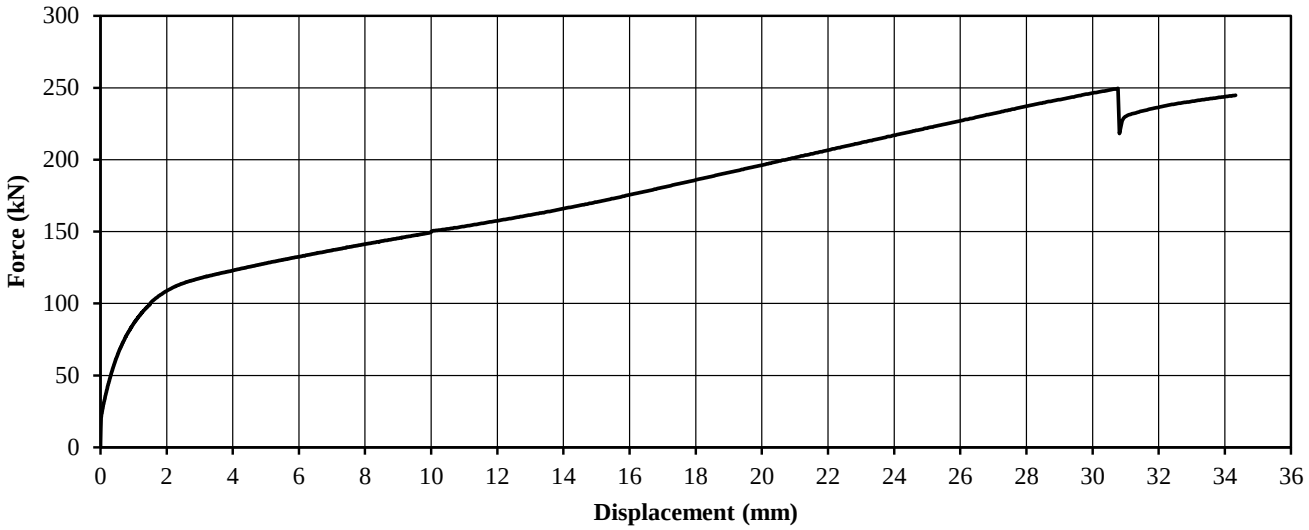
Angle	A36	
F_y	363	MPa
F_u	520	MPa
ε_u	0.2515	
Bolt	A325	
Column bolts	1000	lbf-ft
Plate bolts	1000	lbf-ft

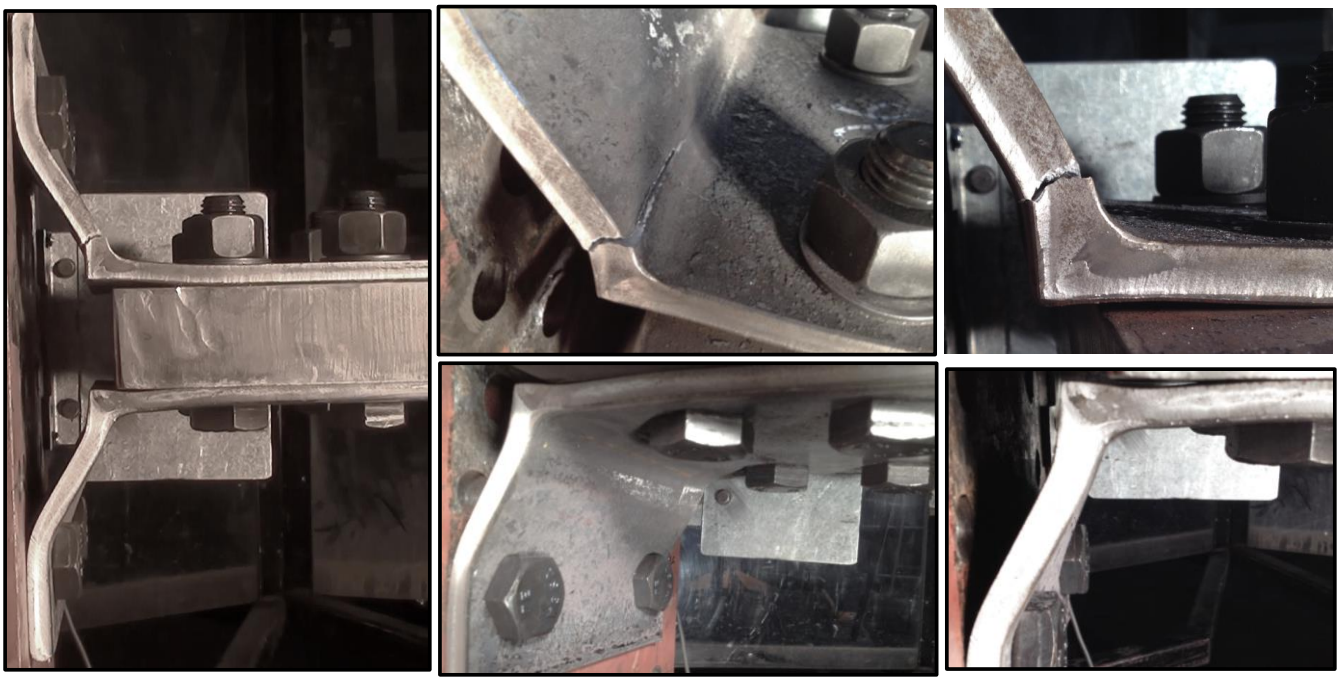
Key response parameters:

$K_{Plastic}$	4.2	kN/mm
$K_{Softening}$	-	kN/mm
$K_{Hardening}$	5.1	kN/mm

	F (kN)	Δ (mm)
Initial	21	0.009
Plastic	127	4.8
Softening	-	-
Hardening	167	14.2
Max. Force	250	30.7
Ultimate	245	34.3

Force-displacement





Test TC10-8

Type Time-History **Failure mode:** Column/Net Section

Geometry:

g_{column}	102	mm
t	12.700	mm
g_{beam}	76	mm
φ_{bolt}	25.4	mm
k	25.400	mm
g_2	55.6	mm
g_2/t	4.38	

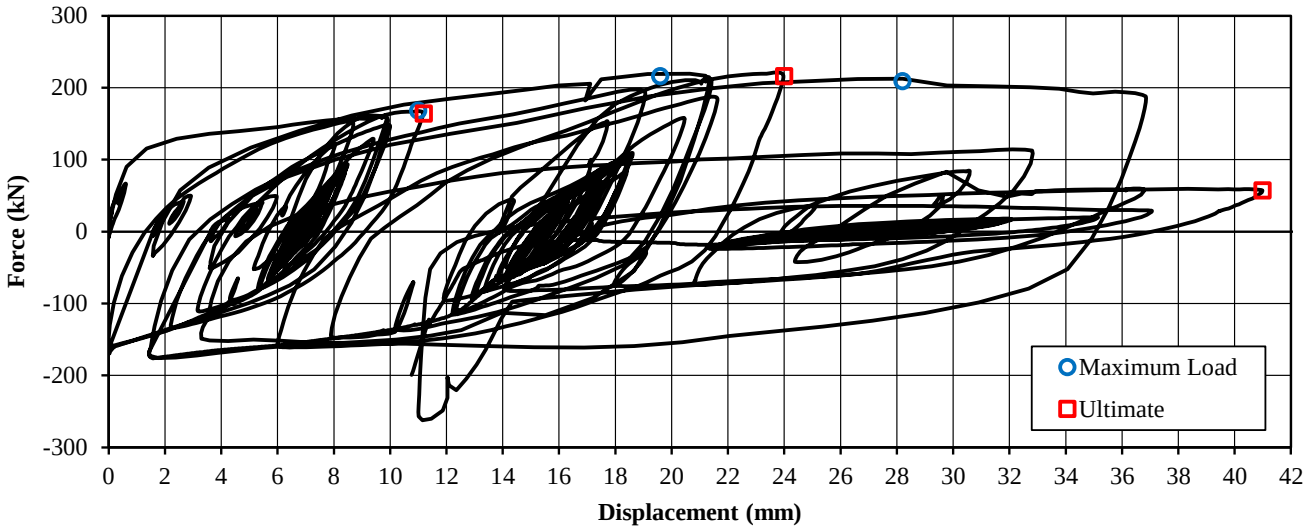
Materials:

Angle	A36	
F_y	363	MPa
F_u	520	MPa
ε_u	0.2515	
Bolt	A490	
Column bolts	1000	lbf-ft
Plate bolts	1000	lbf-ft

Key response parameters:

Signal factor	75%	150%	250%
Δ_0	0.0	1.6	3.6
$F_{F\ Max}$	168	216	209
$\Delta_{F\ Max}$	11.0	19.6	28.2
$F_{Ultimate}$	164	216	57
$\Delta_{Ultimate}$	11.2	24.0	41.0

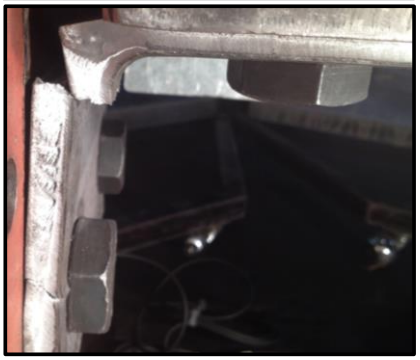
Force-displacement













Test TC11-1

Type Monotonic Static

Loading Rate: 100 με/s

Failure mode: Beam

Geometry:

g_{column}	89	mm
t	15.875	mm
g_{beam}	76	mm
φ_{bolt}	25.4	mm
k	28.575	mm
g_2	39.7	mm
g_2/t	2.50	

Materials:

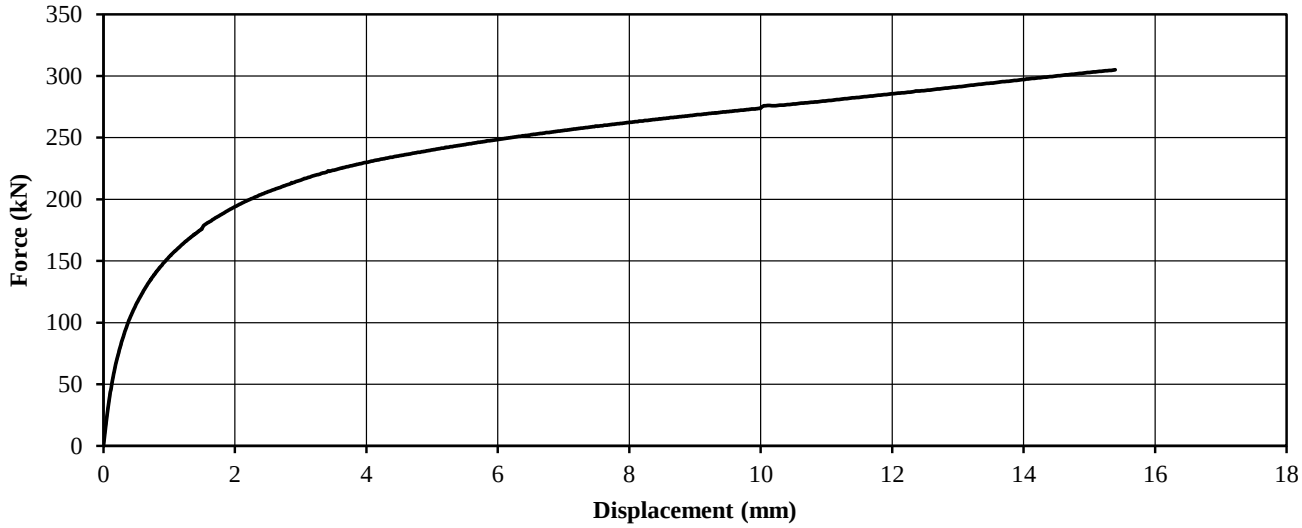
Angle	A36	
F_y	360	MPa
F_u	473	MPa
ε_u	0.2712	
Bolt	A490	
Column bolts	1000	lbf-ft
Plate bolts	1000	lbf-ft

Key response parameters:

$K_{Plastic}$	7.0	kN/mm
$K_{Softening}$	5.7	kN/mm
$K_{Hardening}$	-	kN/mm

	F (kN)	Δ (mm)
Initial	-	-
Plastic	244	5.4
Softening	266	8.5
Hardening	-	-
Max. Force	305	15.4
Ultimate	305	15.4

Force-displacement





Test TC11-2

Type Monotonic Dynamic

Loading Rate: 750000 με/s

Failure mode: Beam

Geometry:

g_{column}	89	mm
t	15.875	mm
g_{beam}	76	mm
φ_{bolt}	25.4	mm
k	28.575	mm
g_2	39.7	mm
g_2/t	2.50	

Materials:

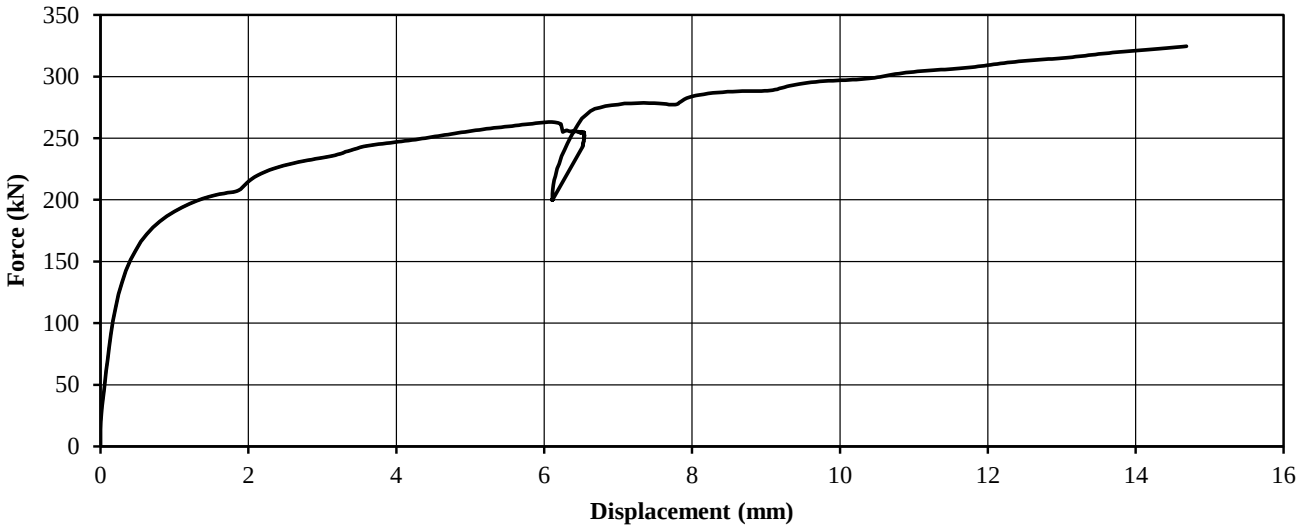
Angle	A36	
F_y	360	MPa
F_u	473	MPa
ε_u	0.2712	
Bolt	A490	
Column bolts	1000	lbf-ft
Plate bolts	1000	lbf-ft

Key response parameters:

$K_{Plastic}$	9.5	kN/mm
$K_{Softening}$	6.4	kN/mm
$K_{Hardening}$	-	kN/mm

	F (kN)	Δ (mm)
Initial	-	-
Plastic	238	3.3
Softening	286	8.3
Hardening	-	-
Max. Force	325	14.7
Ultimate	325	14.7

Force-displacement

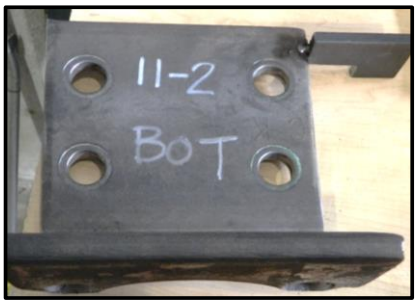












Test TC11-3

Type Monotonic Static

Loading Rate: 600 με/s

Failure mode: Beam

Geometry:

g_{column}	89	mm
t	15.875	mm
g_{beam}	76	mm
φ_{bolt}	25.4	mm
k	28.575	mm
g_2	39.7	mm
g_2/t	2.50	

Materials:

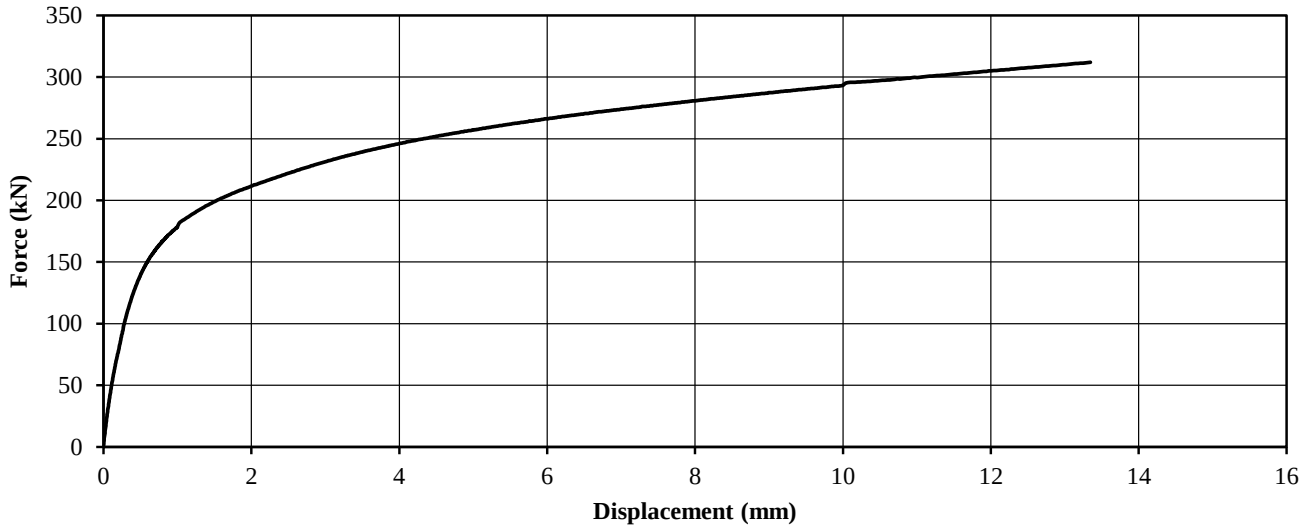
Angle	A36	
F_y	360	MPa
F_u	473	MPa
ε_u	0.2712	
Bolt	A490	
Column bolts	1000	lbf-ft
Plate bolts	1000	lbf-ft

Key response parameters:

$K_{Plastic}$	8.6	kN/mm
$K_{Softening}$	5.9	kN/mm
$K_{Hardening}$	-	kN/mm

	F (kN)	Δ (mm)
Initial	-	-
Plastic	249	4.3
Softening	282	8.1
Hardening	-	-
Max. Force	312	13.3
Ultimate	312	13.3

Force-displacement



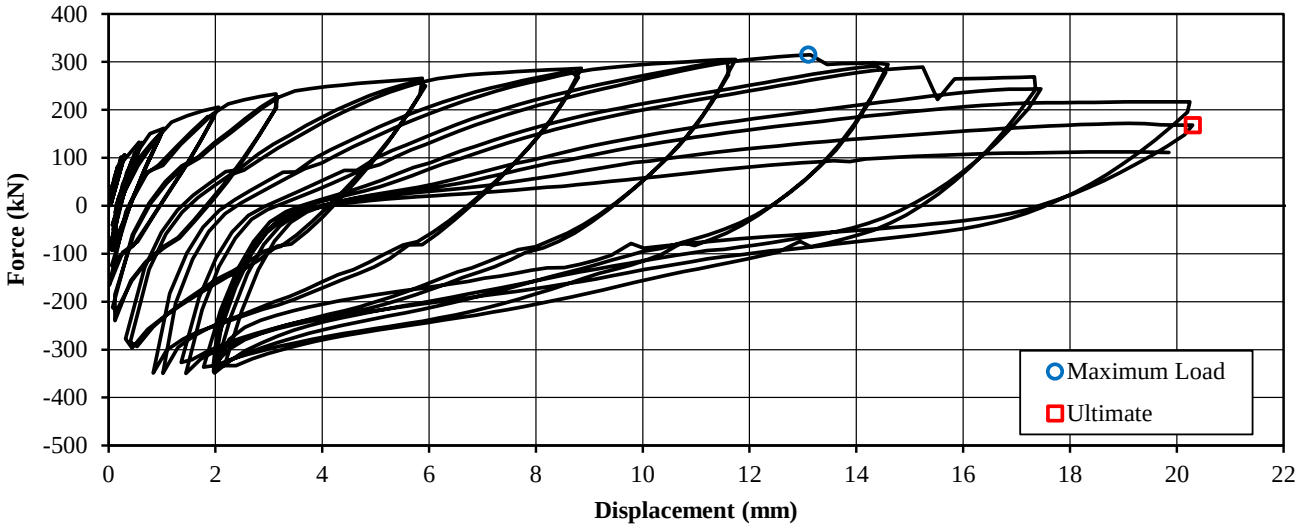


Test TC11-4

Type Cyclic W310 **Failure mode:** Beam/Net Section

Geometry:			Materials:			Points of interest:		
g_{column}	89	mm	**Angle**	A36		F_{Max}	315	kN
t	15.875	mm	F_y	360	MPa	Δ_{FMax}	13.1	mm
g_{beam}	76	mm	F_u	473	MPa	$Drift_{FMax}$	6	%
φ_{bolt}	25.4	mm	ε_u	0.2712		$F_{Ultimate}$	168	kN
k	28.575	mm	**Bolt**	A490		$\Delta_{Ultimate}$	20.3	mm
g_2	39.7	mm	**Column bolts**	1000	lbf-ft	$Drift_{Ultimate}$	8	%
g_2/t	2.50		**Plate bolts**	1000	lbf-ft			

Force-displacement





Test TC11-5

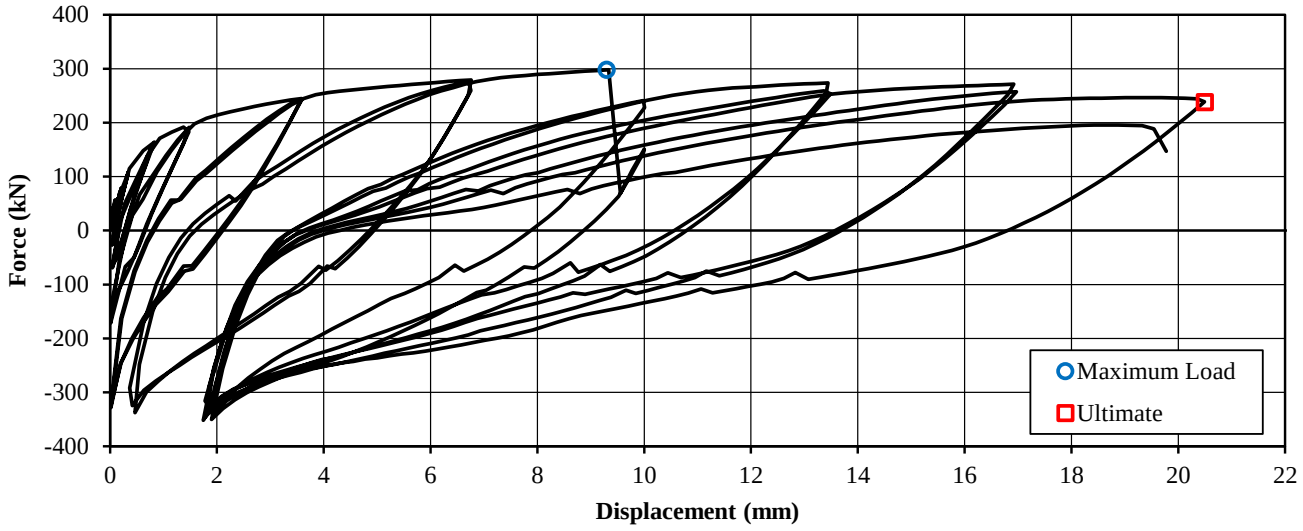
Type Cyclic W410 **Failure mode:** Beam

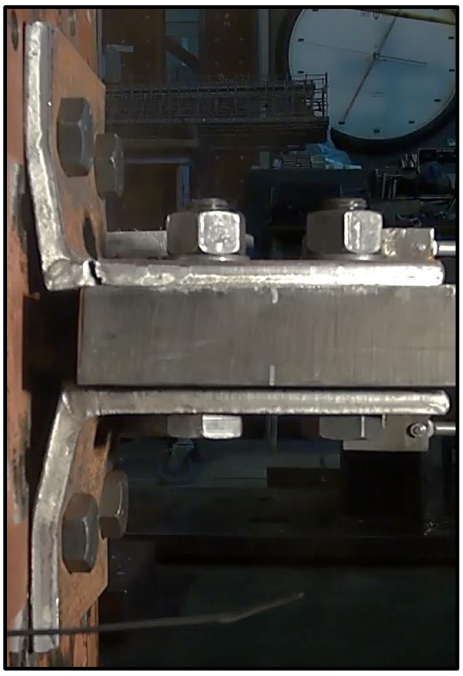
Geometry:		
g_{column}	89	mm
t	15.875	mm
g_{beam}	76	mm
φ_{bolt}	25.4	mm
k	28.575	mm
g_2	39.7	mm
g_2/t	2.50	

Materials:		
Angle	A36	
F_y	360	MPa
F_u	473	MPa
ε_u	0.2712	
Bolt	A490	
Column bolts	1000	lbf-ft
Plate bolts	1000	lbf-ft

Points of interest:		
F_{Max}	298	kN
Δ_{FMax}	9.3	mm
$Drift_{FMax}$	5	%
$F_{Ultimate}$	238	kN
$\Delta_{Ultimate}$	20.5	mm
$Drift_{Ultimate}$	8	%

Force-displacement













Test TC11-6

Type Snug-Thight

Loading Rate: 100 με/s
Failure mode: Column

Key response parameters:

$K_{Plastic}$	8.2	kN/mm
$K_{Softening}$	-	kN/mm
$K_{Hardening}$	9.8	kN/mm

Geometry:

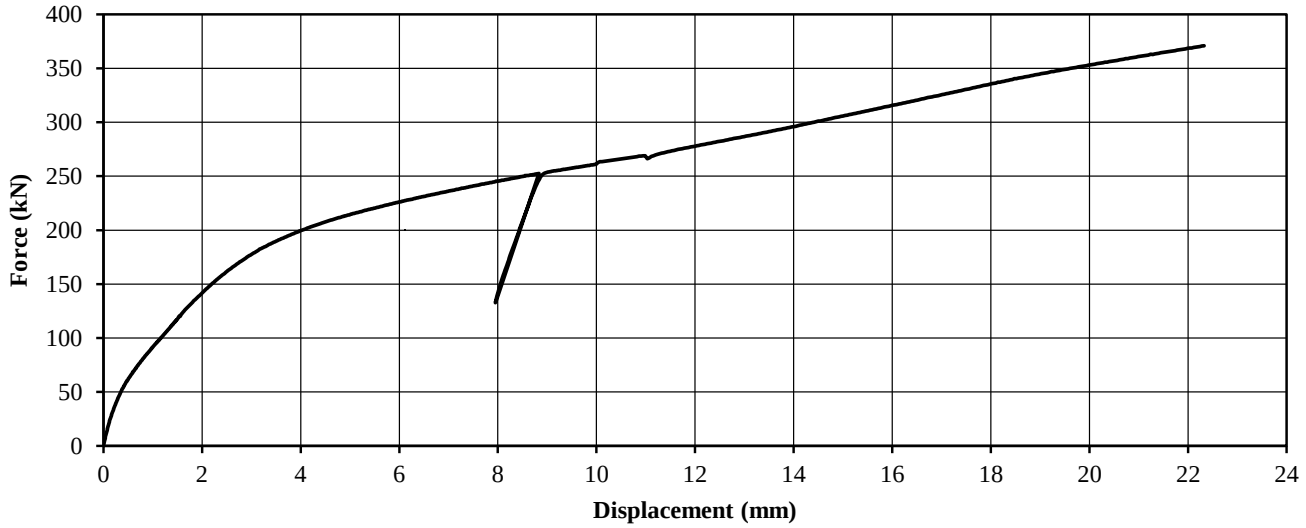
g_{column}	89	mm
t	15.875	mm
g_{beam}	76	mm
φ_{bolt}	25.4	mm
k	28.575	mm
g_2	39.7	mm
g_2/t	2.50	

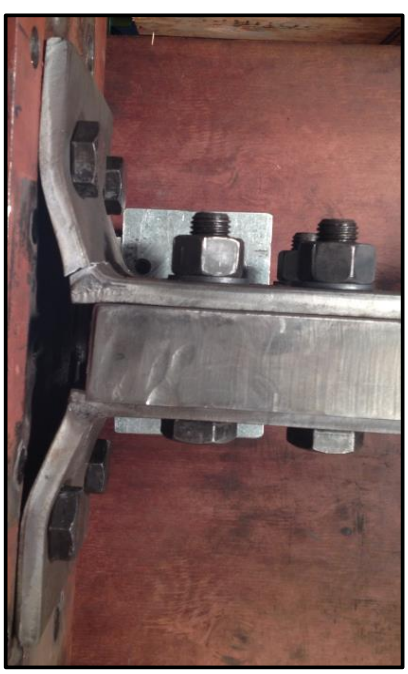
Materials:

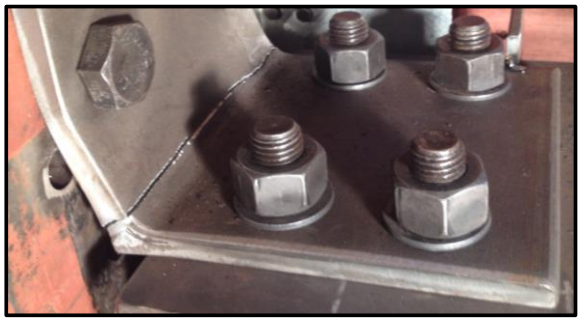
Angle	A36	
F_y	360	MPa
F_u	473	MPa
ε_u	0.2712	
Bolt	A490	
Column bolts	Snug-Thight	
Plate bolts	1000	lbf-ft

	F (kN)	Δ (mm)
Initial	60	0.470
Plastic	228	6.2
Softening	-	-
Hardening	271	11.5
Max. Force	371	22.3
Ultimate	371	22.3

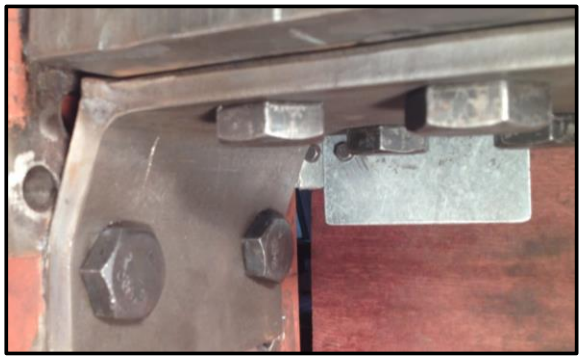
Force-displacement













Test TC11-7

Type A325

Loading Rate: 600 με/s

Failure mode: Column

Geometry:

g_{column}	89	mm
t	15.875	mm
g_{beam}	76	mm
φ_{bolt}	25.4	mm
k	28.575	mm
g_2	39.7	mm
g_2/t	2.50	

Materials:

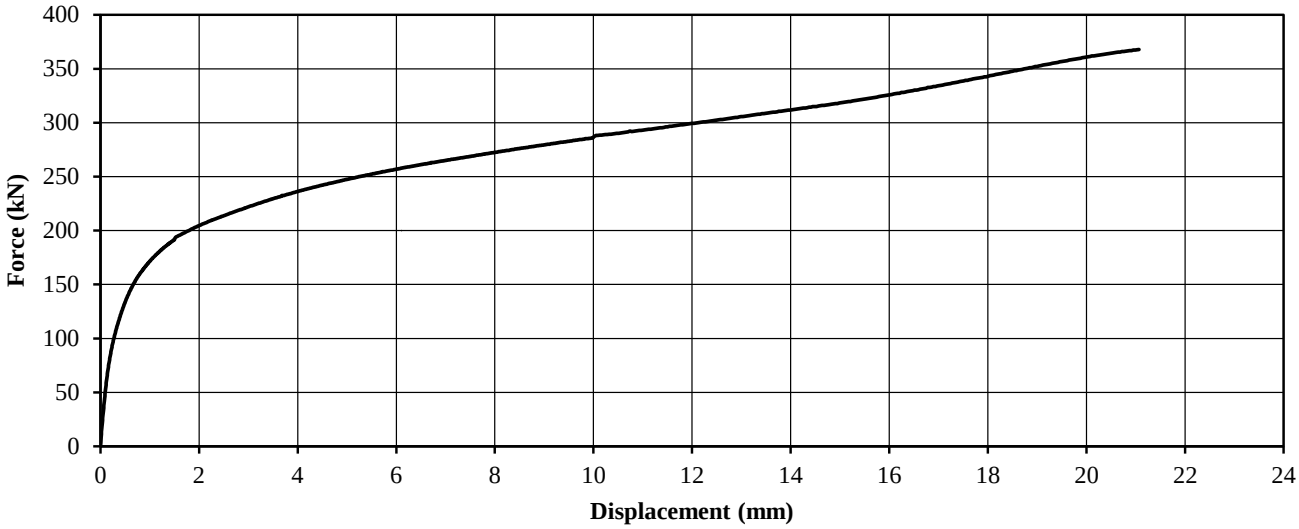
Angle	A36	
F_y	360	MPa
F_u	473	MPa
ε_u	0.2712	
Bolt	A325	
Column bolts	1000	lbf-ft
Plate bolts	1000	lbf-ft

Key response parameters:

$K_{Plastic}$	8.2	kN/mm
$K_{Softening}$	6.4	kN/mm
$K_{Hardening}$	9.1	kN/mm

	F (kN)	Δ (mm)
Initial	-	-
Plastic	249	5.2
Softening	278	8.7
Hardening	327	16.2
Max. Force	368	21.1
Ultimate	368	21.1

Force-displacement





Test TC11-8

Type Time-History **Failure mode:** Column/Net Section

Geometry:

g_{column}	89	mm
t	15.875	mm
g_{beam}	76	mm
φ_{bolt}	25.4	mm
k	28.575	mm
g_2	39.7	mm
g_2/t	2.50	

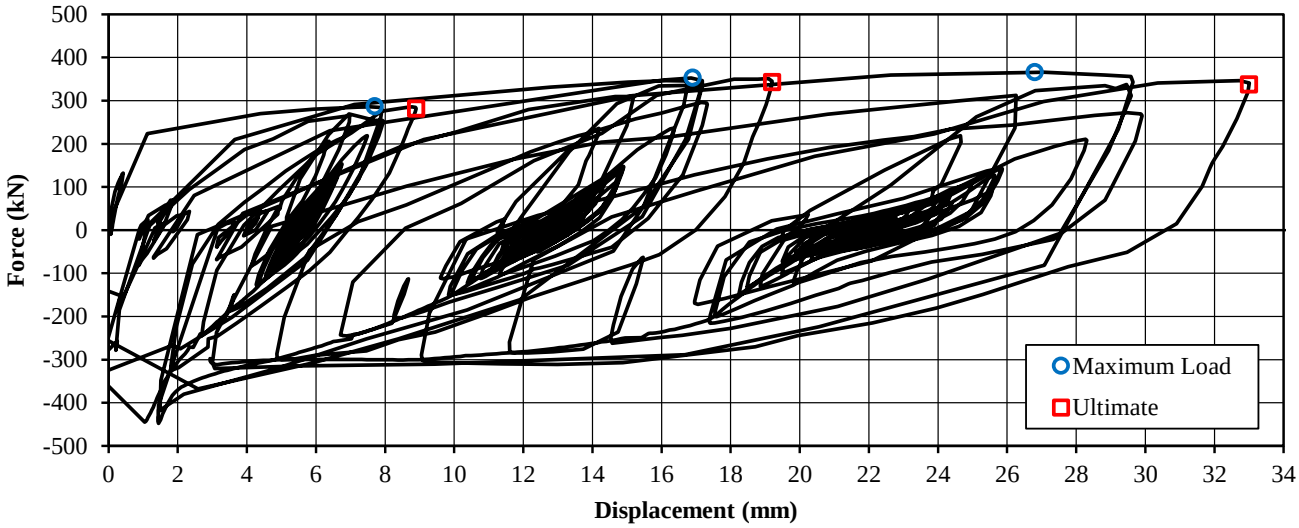
Materials:

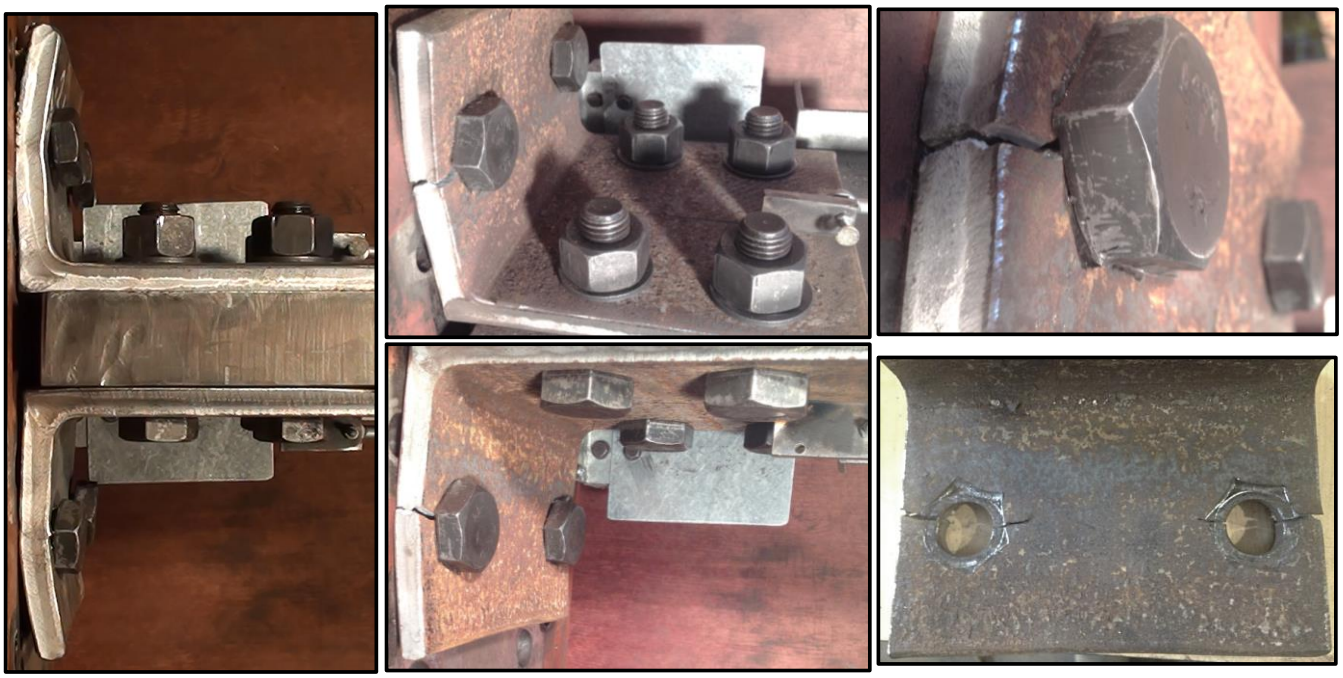
Angle	A36	
F_y	360	MPa
F_u	473	MPa
ε_u	0.2712	
Bolt	A490	
Column bolts	1000	lbf-ft
Plate bolts	1000	lbf-ft

Points of interest:

Signal factor	60%	120%	200%
Δ_0	0.0	0.9	3.1
$F_{F\ Max}$	287	353	366
$\Delta_{F\ Max}$	7.7	16.9	26.8
$F_{Ultimate}$	281	343	337
$\Delta_{Ultimate}$	8.9	19.2	33.0

Force-displacement





Test TC12-1

Type Monotonic Static

Loading Rate: 100 με/s

Failure mode: Column

Geometry:

g_{column}	102	mm
t	15.875	mm
g_{beam}	76	mm
φ_{bolt}	25.4	mm
k	28.575	mm
g_2	52.4	mm
g_2/t	3.30	

Materials:

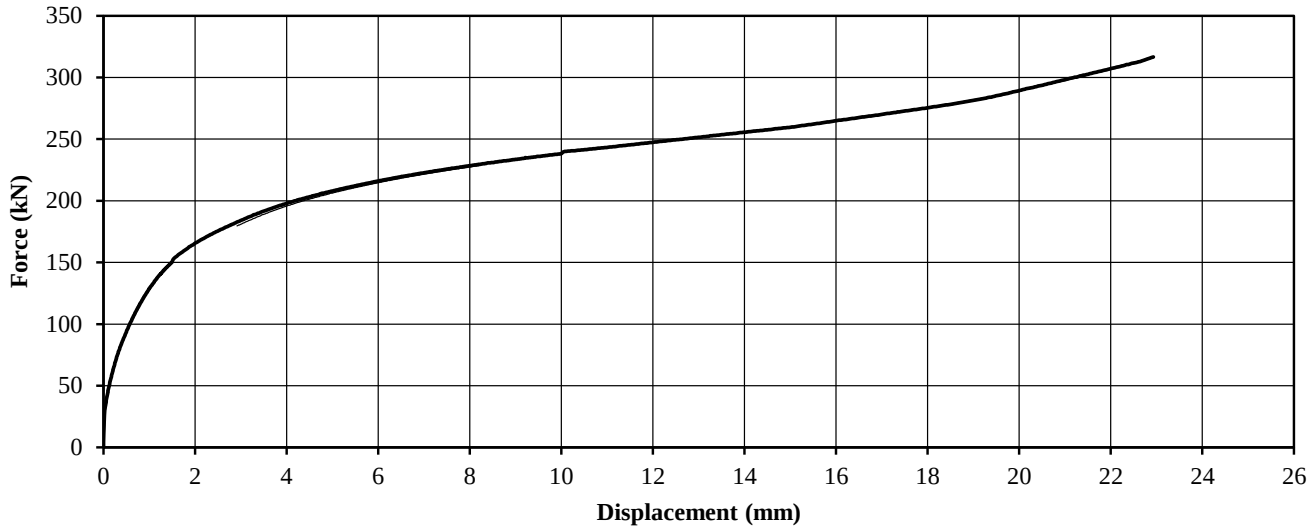
Angle	A36	
F_y	360	MPa
F_u	473	MPa
ε_u	0.2712	
Bolt	A490	
Column bolts	1000	lbf-ft
Plate bolts	1000	lbf-ft

Key response parameters:

$K_{Plastic}$	6.1	kN/mm
$K_{Softening}$	4.2	kN/mm
$K_{Hardening}$	8.8	kN/mm

	F (kN)	Δ (mm)
Initial	30	0.020
Plastic	212	5.5
Softening	238	9.7
Hardening	274	18.2
Max. Force	317	22.9
Ultimate	317	22.9

Force-displacement





Test TC12-2

Type Monotonic Static

Loading Rate: 600 με/s

Failure mode: Column/Beam

Geometry:

g_{column}	102	mm
t	15.875	mm
g_{beam}	76	mm
φ_{bolt}	25.4	mm
k	28.575	mm
g_2	52.4	mm
g_2/t	3.30	

Materials:

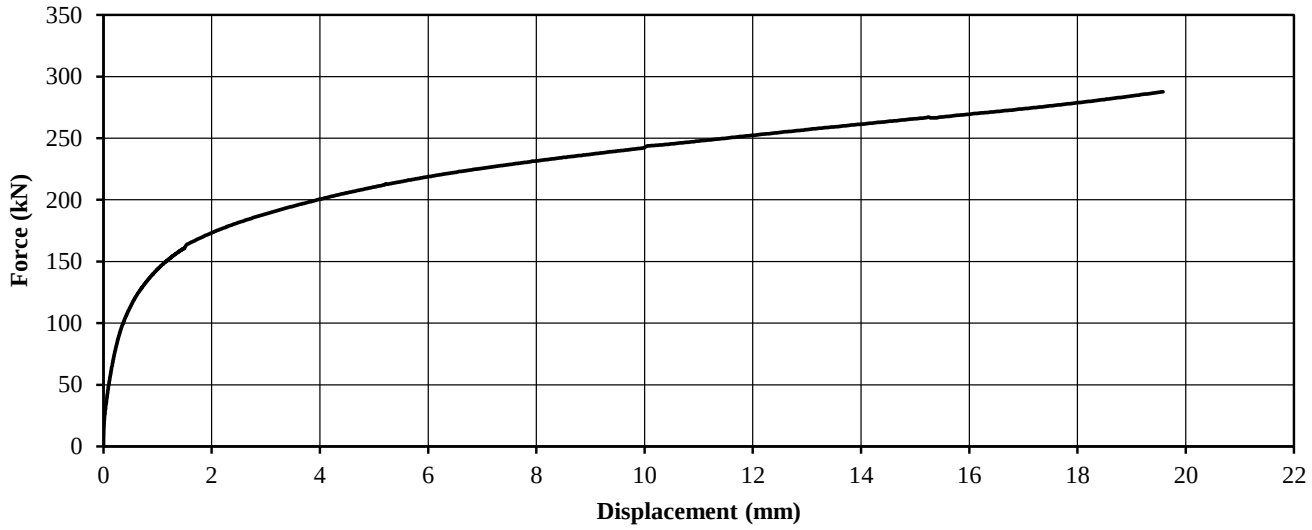
Angle	A36	
F_y	360	MPa
F_u	473	MPa
ε_u	0.2712	
Bolt	A490	
Column bolts	1000	lbf-ft
Plate bolts	1000	lbf-ft

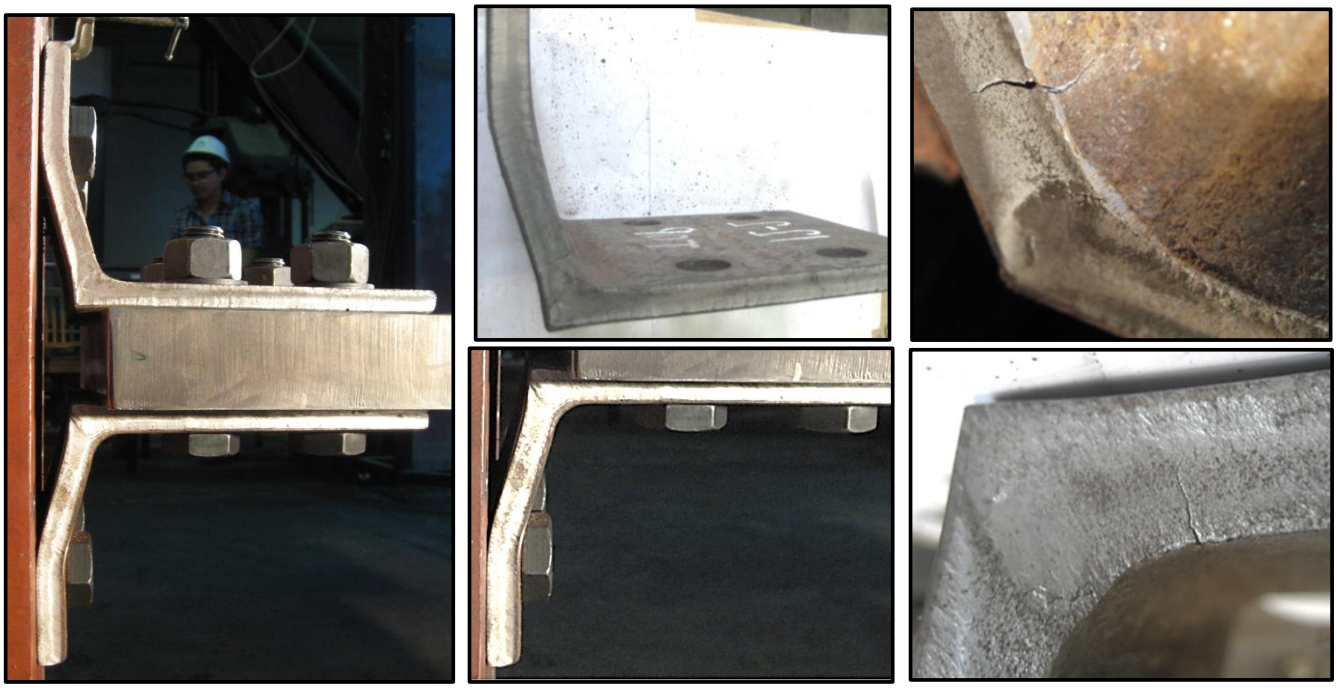
Key response parameters:

$K_{Plastic}$	5.9	kN/mm
$K_{Softening}$	4.3	kN/mm
$K_{Hardening}$	5.3	kN/mm

	F (kN)	Δ (mm)
Initial	20	0.006
Plastic	219	6.0
Softening	248	10.9
Hardening	272	16.5
Max. Force	288	19.6
Ultimate	288	19.6

Force-displacement





Test TC12-3

Type Monotonic Dynamic

Loading Rate: 750000 με/s

Failure mode: Column/Beam/Net Section

Key response parameters:

$K_{Plastic}$	7.5	kN/mm
$K_{Softening}$	4.9	kN/mm
$K_{Hardening}$	6.0	kN/mm

Geometry:

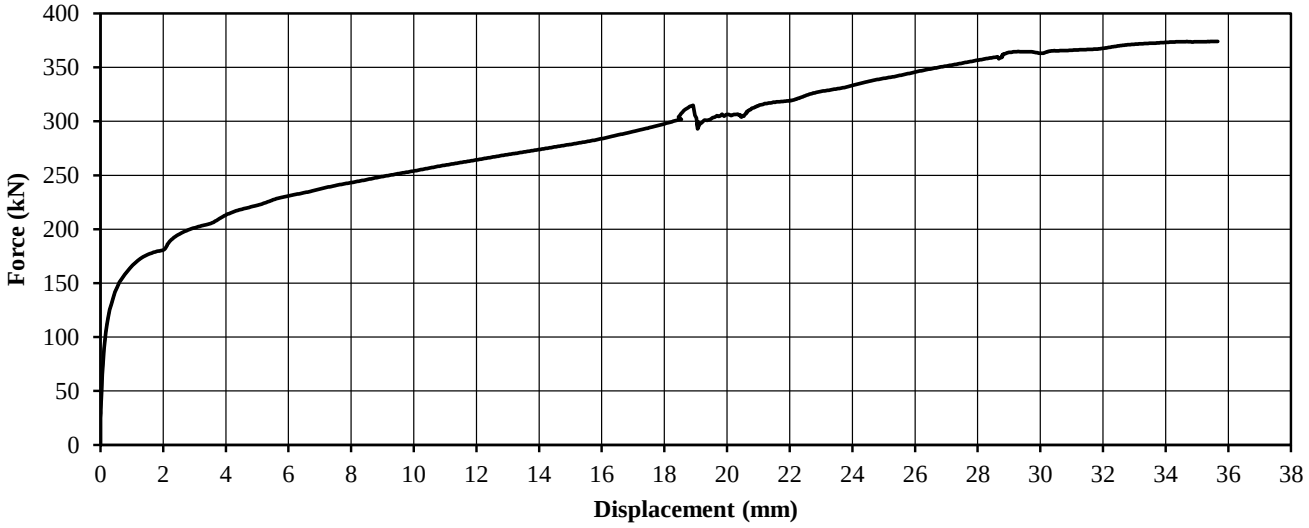
g_{column}	102	mm
t	15.875	mm
g_{beam}	76	mm
φ_{bolt}	25.4	mm
k	28.575	mm
g_2	52.4	mm
g_2/t	3.30	

Materials:

Angle	A36	
F_y	360	MPa
F_u	473	MPa
ε_u	0.2712	
Bolt	A490	
Column bolts	1000	lbf-ft
Plate bolts	1000	lbf-ft

	F (kN)	Δ (mm)
Initial	25	0.004
Plastic	204	3.4
Softening	256	10.3
Hardening	279	15.1
Max. Force	374	35.5
Ultimate	374	35.7

Force-displacement





Test TC12-4

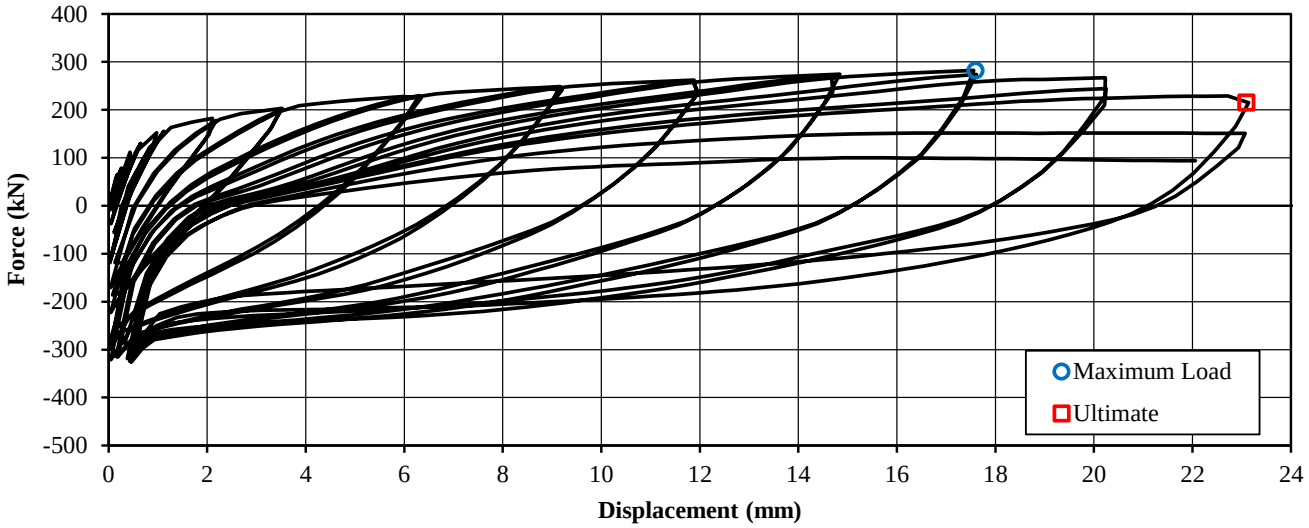
Type Cyclic W310 **Failure mode:** Column/Net Section

Geometry:		
g_{column}	102	mm
t	15.875	mm
g_{beam}	76	mm
φ_{bolt}	25.4	mm
k	28.575	mm
g_2	52.4	mm
g_2/t	3.30	

Materials:		
Angle	A36	
F_y	360	MPa
F_u	473	MPa
ε_u	0.2712	
Bolt	A490	
Column bolts	1000	lbf-ft
Plate bolts	1000	lbf-ft

Key response parameters:		
F_{Max}	282	kN
Δ_{FMax}	17.6	mm
$Drift_{FMax}$	7	%
$F_{Ultimate}$	215	kN
$\Delta_{Ultimate}$	23.1	mm
$Drift_{Ultimate}$	9	%

Force-displacement



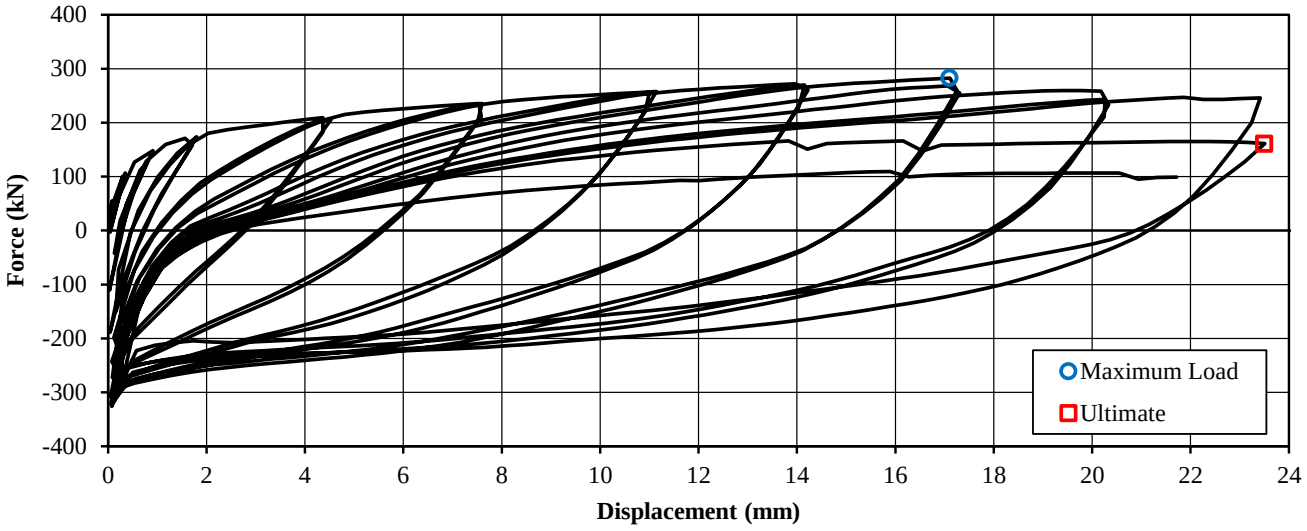


Test TC12-5

Type Cyclic W410 **Failure mode:** Column/Net Section

Geometry:			Materials:			Key response parameters:		
g_{column}	102	mm	**Angle**	A36		F_{Max}	283	kN
t	15.875	mm	F_y	360	MPa	Δ_{FMax}	17.1	mm
g_{beam}	76	mm	F_u	473	MPa	$Drift_{FMax}$	7	%
φ_{bolt}	25.4	mm	ε_u	0.2712		$F_{Ultimate}$	161	kN
k	28.575	mm	**Bolt**	A490		$\Delta_{Ultimate}$	23.5	mm
g_2	52.4	mm	**Column bolts**	1000	lbf-ft	$Drift_{Ultimate}$	9	%
g_2/t	3.30		**Plate bolts**	1000	lbf-ft			

Force-displacement





Test TC12-6

Type Snug-Thight

Loading Rate: 100 με/s

Failure mode: Beam

Key response parameters:

$K_{Plastic}$	7.2	kN/mm
$K_{Softening}$	5.7	kN/mm
$K_{Hardening}$	-	kN/mm

Geometry:

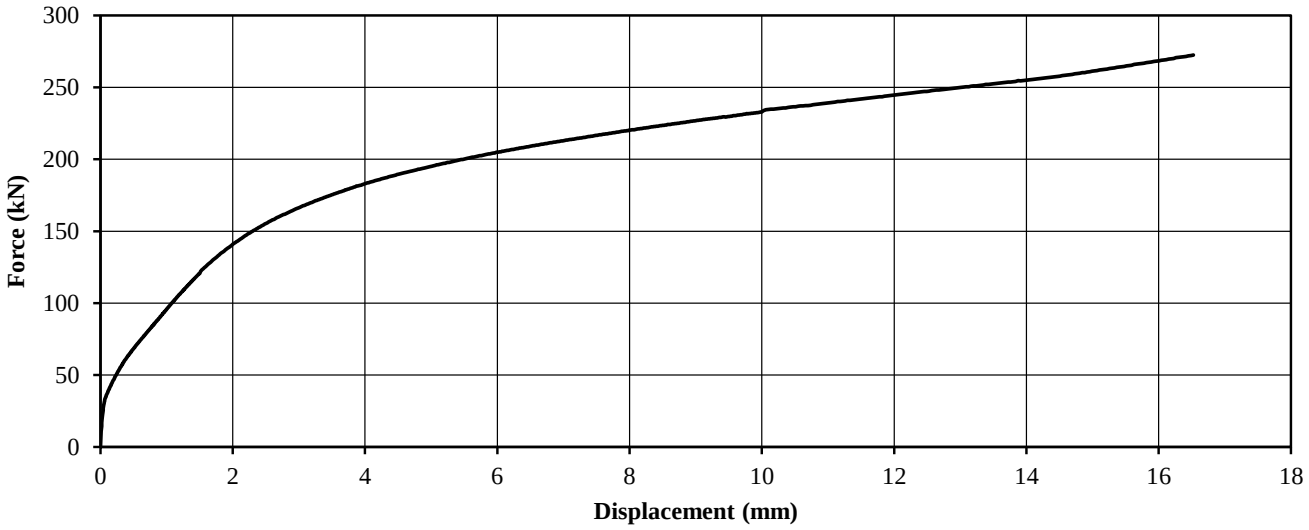
g_{column}	102	mm
t	15.875	mm
g_{beam}	76	mm
φ_{bolt}	25.4	mm
k	28.575	mm
g_2	52.4	mm
g_2/t	3.30	

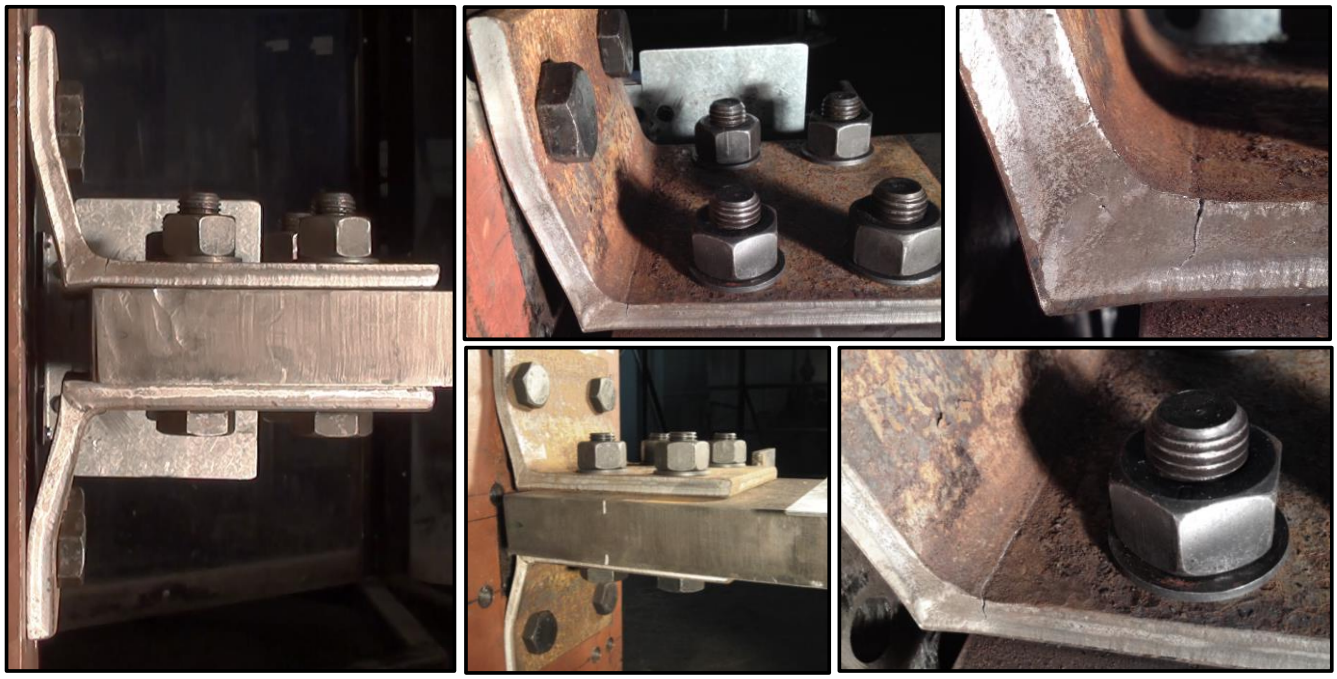
Materials:

Angle	A36	
F_y	360	MPa
F_u	473	MPa
ε_u	0.2712	
Bolt	A490	
Column bolts	0	lbf-ft
Plate bolts	1000	lbf-ft

	F (kN)	Δ (mm)
Initial	30	0.053
Plastic	205	6.0
Softening	231	9.6
Hardening	-	-
Max. Force	272	16.5
Ultimate	272	16.5

Force-displacement





Test TC12-7

Type A325

Loading Rate: 100 με/s

Failure mode: Column

Geometry:

g_{column}	102	mm
t	15.875	mm
g_{beam}	76	mm
φ_{bolt}	25.4	mm
k	28.575	mm
g_2	52.4	mm
g_2/t	3.30	

Materials:

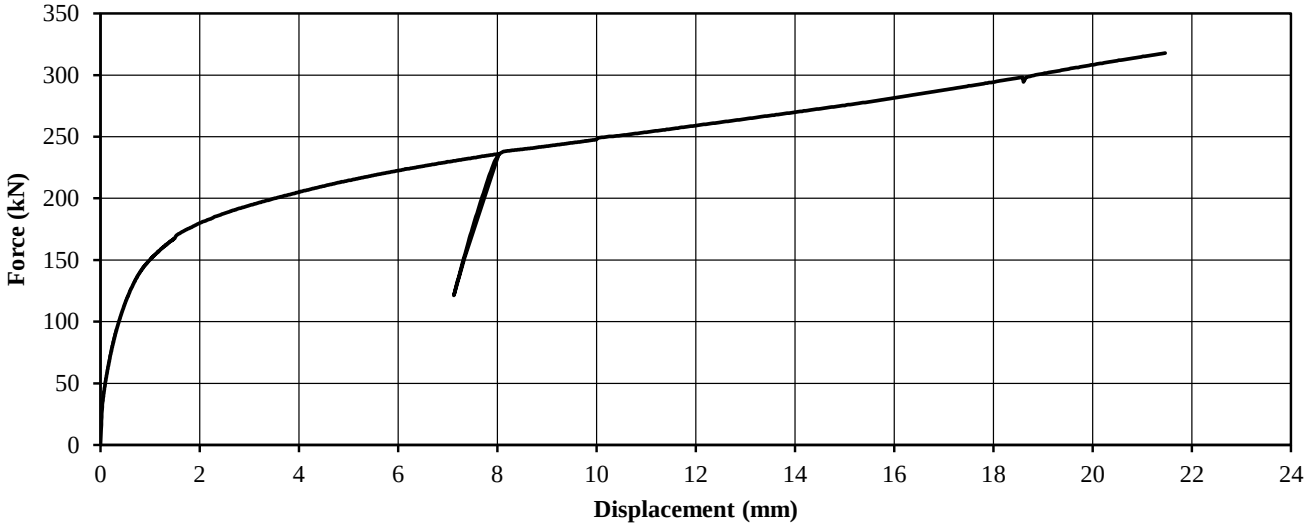
Angle	A36	
F_y	360	MPa
F_u	473	MPa
ε_u	0.2712	
Bolt	A325	
Column bolts	1000	lbf-ft
Plate bolts	1000	lbf-ft

Key response parameters:

$K_{Plastic}$	7.5	kN/mm
$K_{Softening}$	5.5	kN/mm
$K_{Hardening}$	6.7	kN/mm

	F (kN)	Δ (mm)
Initial	36	0.046
Plastic	207	4.2
Softening	241	8.8
Hardening	281	16.0
Max. Force	318	21.5
Ultimate	318	21.5

Force-displacement





Test TC12-8

Type Time-History **Failure mode:** Beam/Net Section

Geometry:

g_{column}	102	mm
t	15.875	mm
g_{beam}	76	mm
φ_{bolt}	25.4	mm
k	28.575	mm
g_2	52.4	mm
g_2/t	3.30	

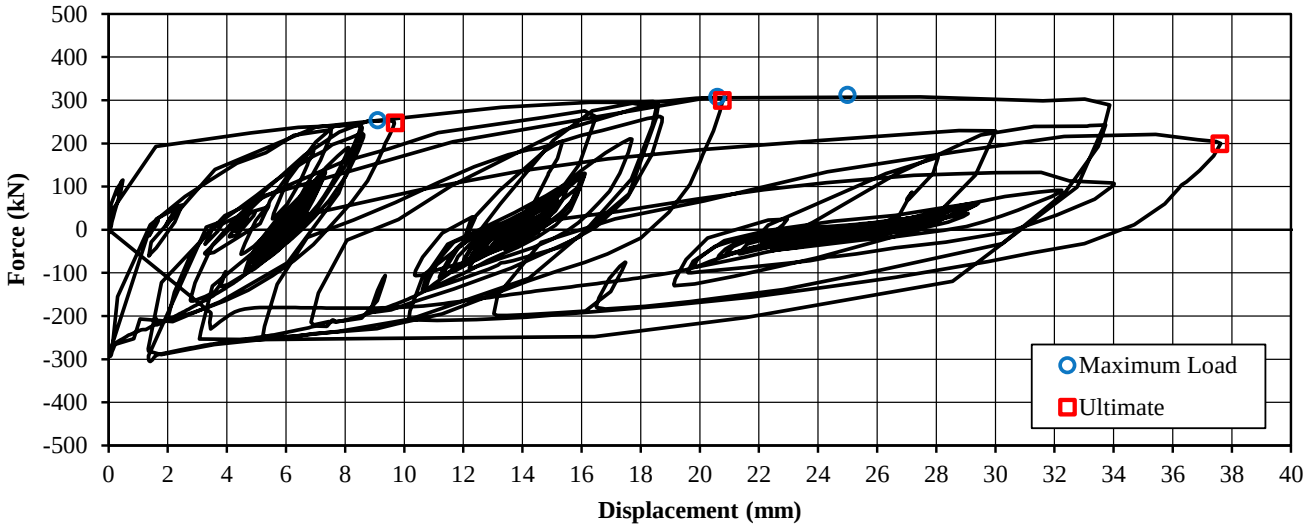
Materials:

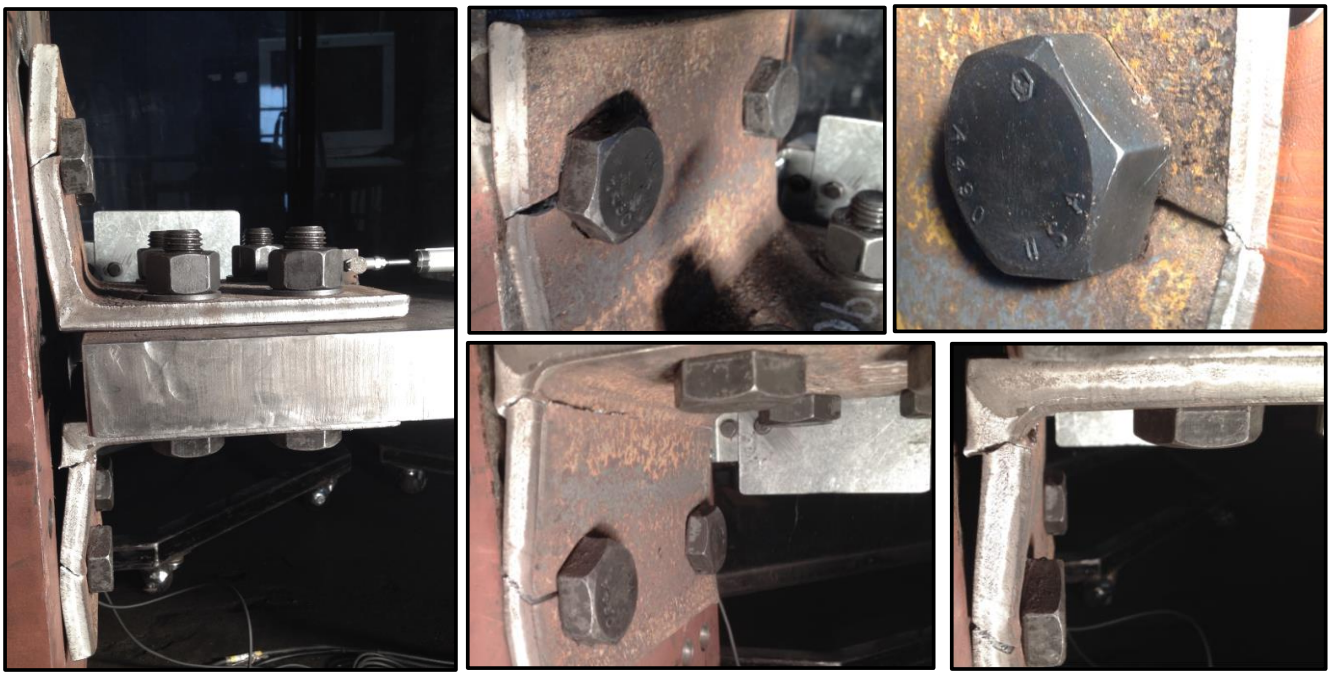
Angle	A36	
F_y	360	MPa
F_u	473	MPa
ε_u	0.2712	
Bolt	A490	
Column bolts	1000	lbf-ft
Plate bolts	1000	lbf-ft

Key response parameters:

Signal factor	65%	130%	230%
Δ_0	0.0	1.4	3.3
$F_{F\ Max}$	253	307	312
$\Delta_{F\ Max}$	9.1	20.6	25.0
$F_{Ultimate}$	247	299	199
$\Delta_{Ultimate}$	9.7	20.8	37.6

Force-displacement





Test TC13-1

Type Monotonic Static

Loading Rate: 100 με/s

Failure mode: Bolt

Geometry:

g_{column}	89	mm
t	19.05	mm
g_{beam}	76	mm
φ_{bolt}	25.4	mm
k	31.75	mm
g_2	36.5	mm
g_2/t	1.92	

Materials:

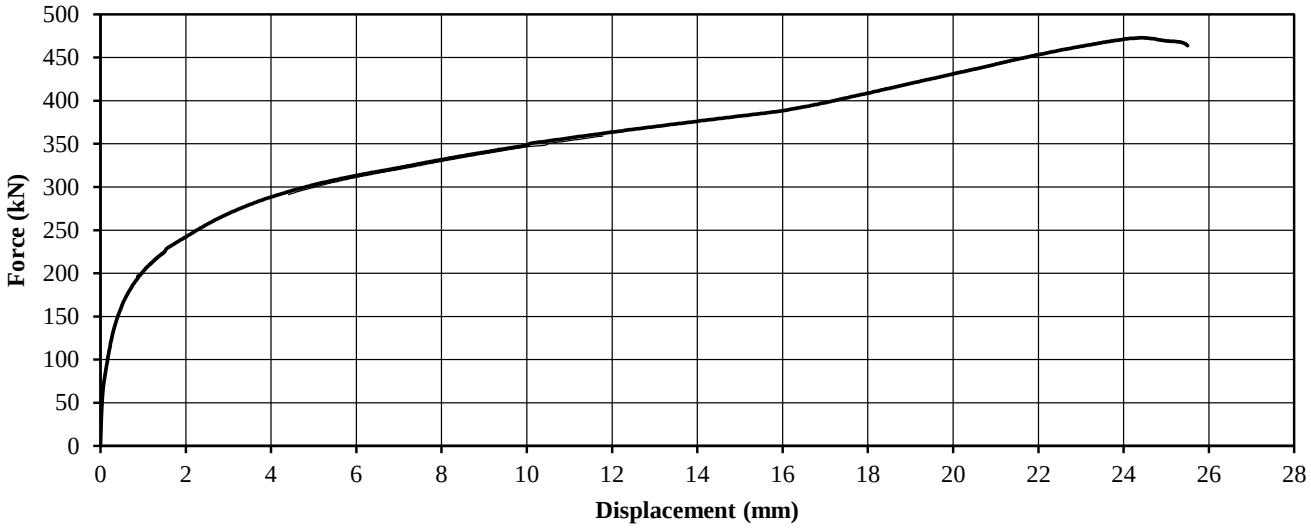
Angle	A36	
F_y	340	MPa
F_u	516	MPa
ε_u	0.2592	
Bolt	A490	
Column bolts	1000	lbf-ft
Plate bolts	1000	lbf-ft

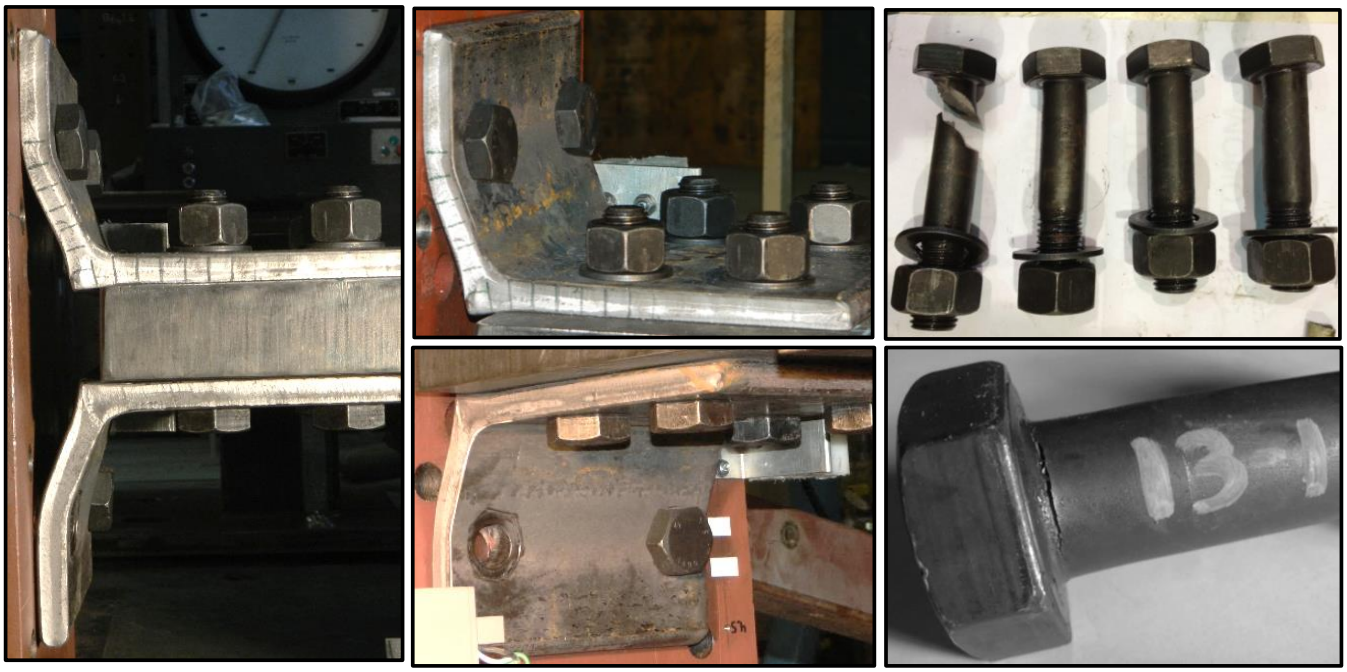
Key response parameters:

$K_{Plastic}$	9.9	kN/mm
$K_{Softening}$	6.4	kN/mm
$K_{Hardening}$	11.0	kN/mm

	F (kN)	Δ (mm)
Initial	73	0.077
Plastic	291	4.2
Softening	354	10.6
Hardening	392	16.4
Max. Force	473	24.6
Ultimate	464	25.5

Force-displacement





Test TC13-2

Type Monotonic Static

Loading Rate: 600 με/s

Failure mode: Beam/Net Section

Geometry:

g_{column}	89	mm
t	19.050	mm
g_{beam}	76	mm
φ_{bolt}	25.4	mm
k	31.750	mm
g_2	36.5	mm
g_2/t	1.92	

Materials:

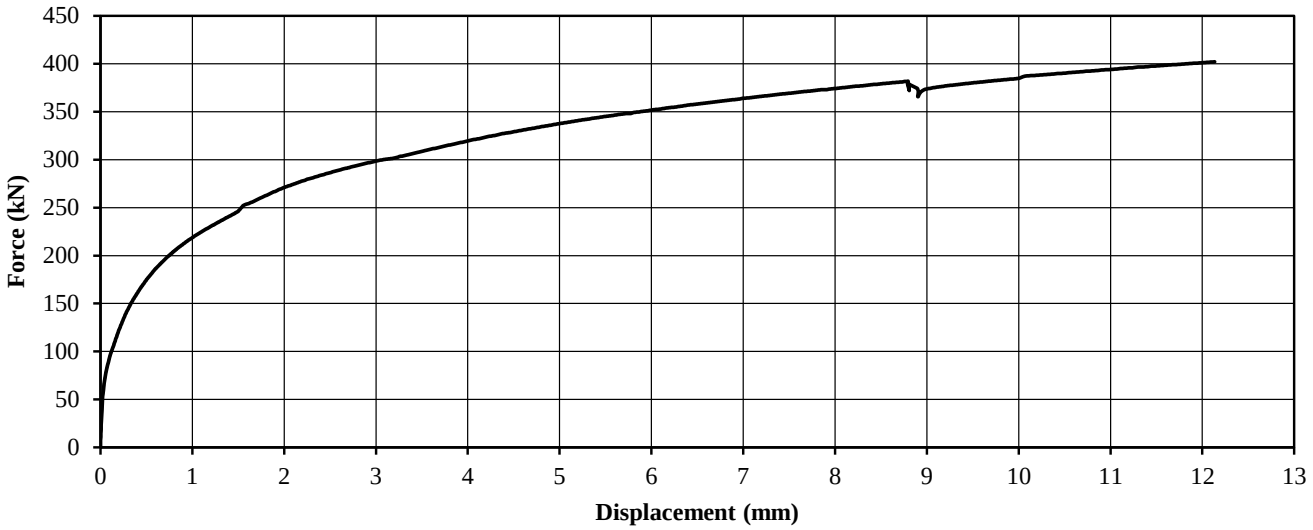
Angle	A36	
F_y	340	MPa
F_u	516	MPa
ε_u	0.2592	
Bolt	A490	
Column bolts	1000	lbf-ft
Plate bolts	1000	lbf-ft

Key response parameters:

$K_{Plastic}$	11.9	kN/mm
$K_{Softening}$	7.3	kN/mm
$K_{Hardening}$	-	kN/mm

	F (kN)	Δ (mm)
Initial	78	0.059
Plastic	337	5.0
Softening	367	7.5
Hardening	-	-
Max. Force	402	12.1
Ultimate	402	12.1

Force-displacement





Test TC13-3

Type Monotonic Static

Loading Rate: 750000 με/s

Failure mode: Beam

Geometry:

g_{column}	89	mm
t	19.050	mm
g_{beam}	76	mm
φ_{bolt}	25.4	mm
k	31.750	mm
g_2	36.5	mm
g_2/t	1.92	

Materials:

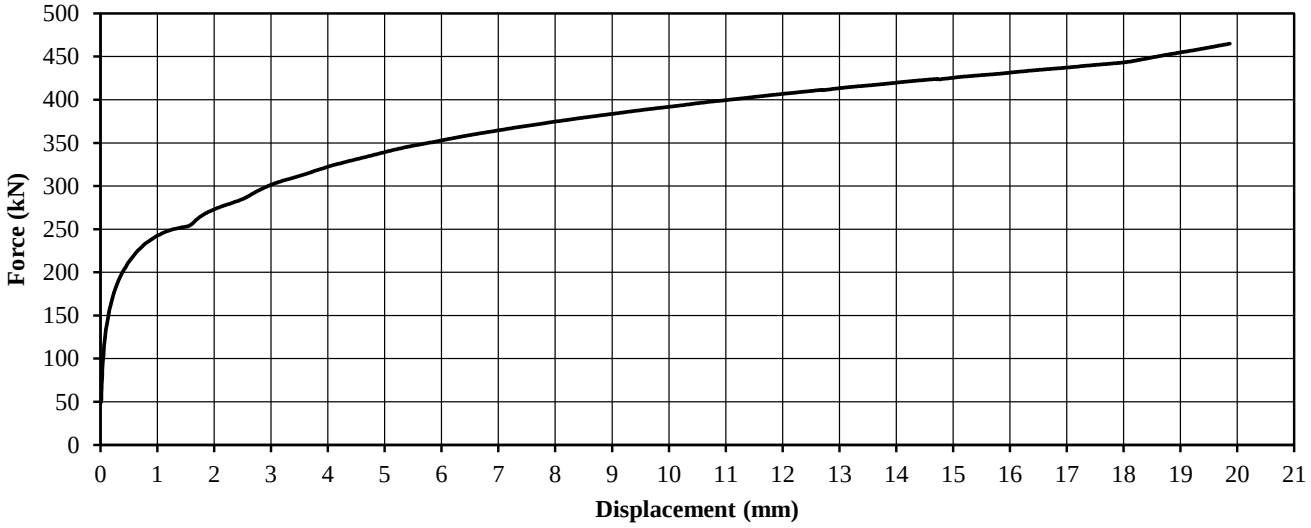
Angle	A36	
F_y	340	MPa
F_u	516	MPa
ε_u	0.2592	
Bolt	A490	
Column bolts	1000	lbf-ft
Plate bolts	1000	lbf-ft

Key response parameters:

$K_{Plastic}$	13.1	kN/mm
$K_{Softening}$	6.3	kN/mm
$K_{Hardening}$	11.4	kN/mm

	F (kN)	Δ (mm)
Initial	115	0.065
Plastic	326	4.2
Softening	385	8.7
Hardening	443	18.0
Max. Force	465	19.9
Ultimate	465	19.9

Force-displacement





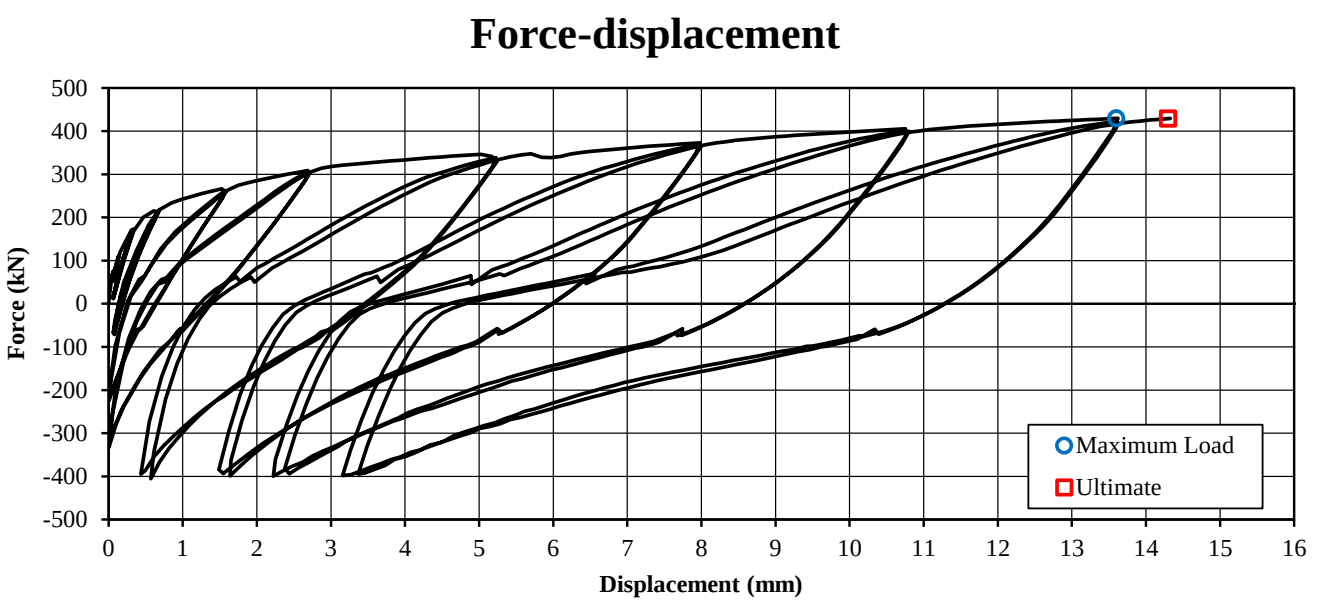
Test TC13-4

Type Cyclic W310 **Failure mode:** Beam

Geometry:		
g_{column}	89	mm
t	19.050	mm
g_{beam}	76	mm
φ_{bolt}	25.4	mm
k	31.750	mm
g_2	36.5	mm
g_2/t	1.92	

Materials:		
Angle	A36	
F_y	340	MPa
F_u	516	MPa
ε_u	0.2592	
Bolt	A490	
Column bolts	1000	lbf-ft
Plate bolts	1000	lbf-ft

Key response parameters:		
F_{Max}	430	kN
Δ_{FMax}	13.6	mm
$Drift_{FMax}$	6	%
$F_{Ultimate}$	429	kN
$\Delta_{Ultimate}$	14.3	mm
$Drift_{Ultimate}$	7	%





Test TC13-5

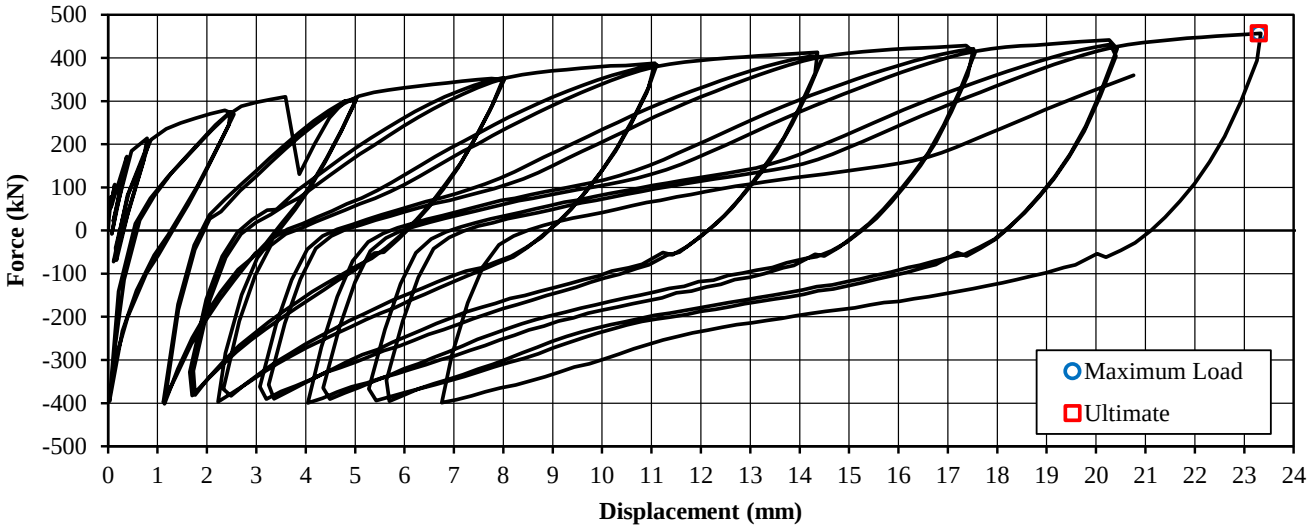
Type Cyclic W410 **Failure mode:** Column/Beam/Net Section

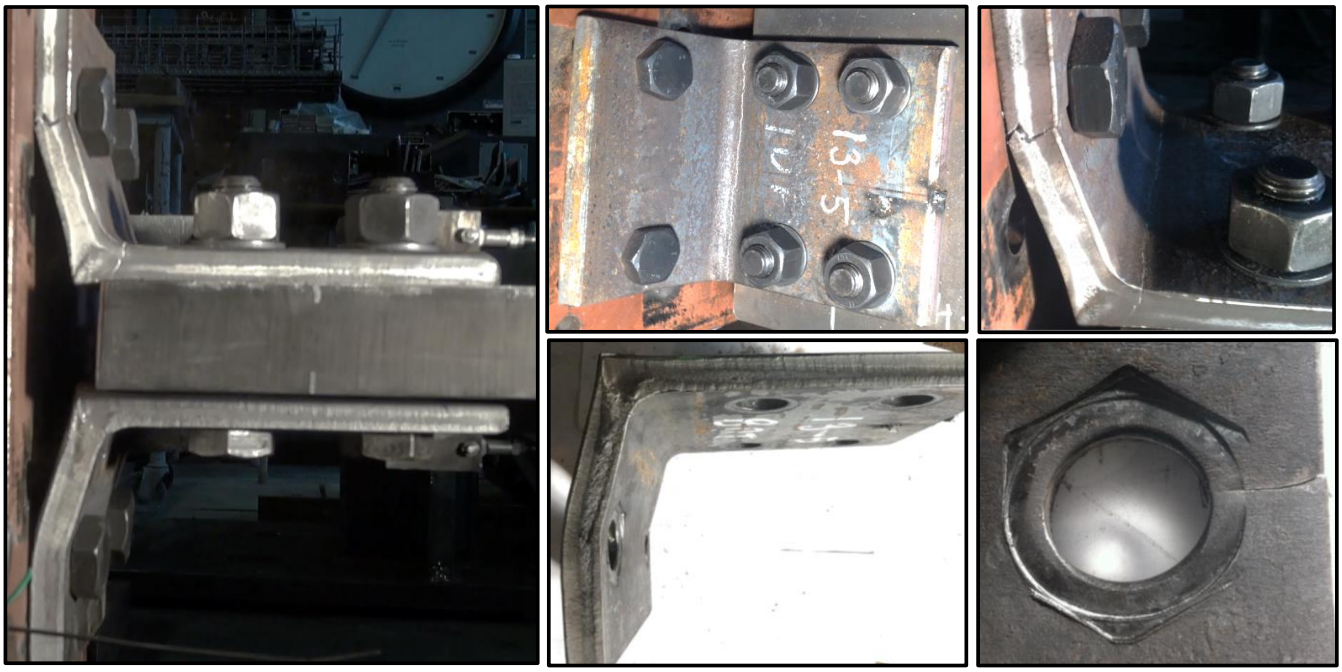
Geometry:		
g_{column}	89	mm
t	19.050	mm
g_{beam}	76	mm
φ_{bolt}	25.4	mm
k	31.750	mm
g_2	36.5	mm
g_2/t	1.92	

Materials:		
Angle	A36	
F_y	340	MPa
F_u	516	MPa
ε_u	0.2592	
Bolt	A490	
Column bolts	1000	lbf-ft
Plate bolts	1000	lbf-ft

Key response parameters:		
F_{Max}	457	kN
Δ_{FMax}	23.3	mm
$Drift_{FMax}$	10	%
$F_{Ultimate}$	457	kN
$\Delta_{Ultimate}$	23.3	mm
$Drift_{Ultimate}$	10	%

Force-displacement





Test TC13-6

Type Time-History **Failure mode:** Net Section

Geometry:

g_{column}	89	mm
t	19.050	mm
g_{beam}	76	mm
φ_{bolt}	25.4	mm
k	31.750	mm
g_2	36.5	mm
g_2/t	1.92	

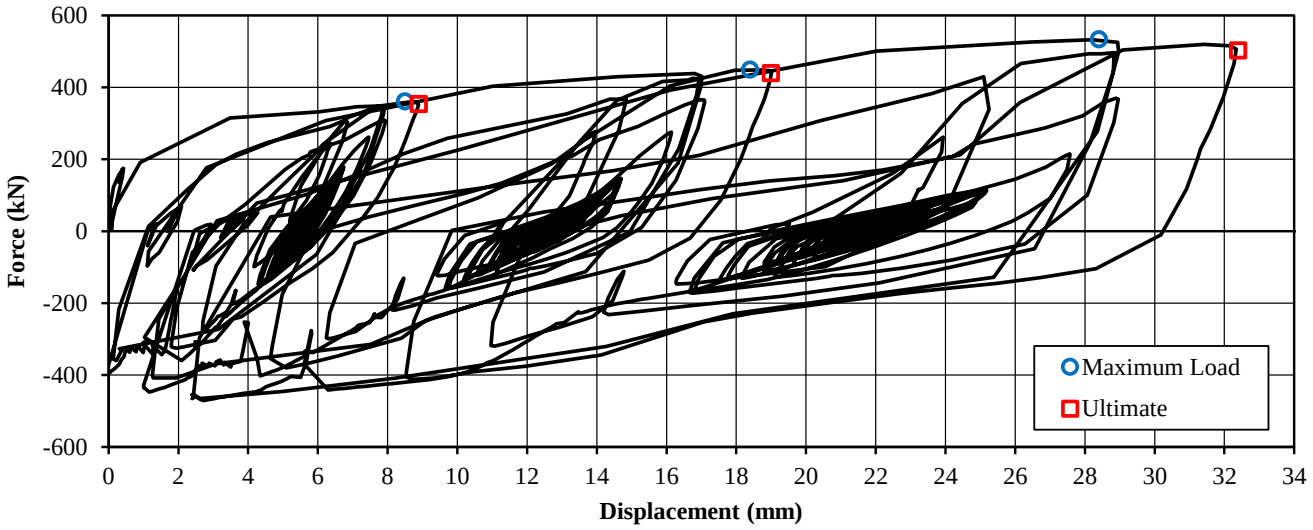
Materials:

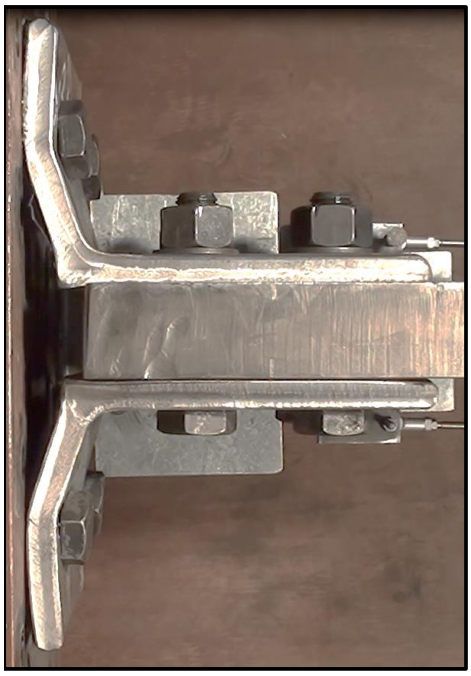
Angle	A36	
F_y	340	MPa
F_u	516	MPa
ε_u	0.2592	
Bolt	A490	
Column bolts	1000	lbf-ft
Plate bolts	1000	lbf-ft

Key response parameters:

Signal factor	60%	120%	200%
Δ_0	0.0	1.1	2.4
$F_{F\ Max}$	360	449	533
$\Delta_{F\ Max}$	8.5	18.4	28.4
$F_{Ultimate}$	353	439	502
$\Delta_{Ultimate}$	8.9	19.0	32.4

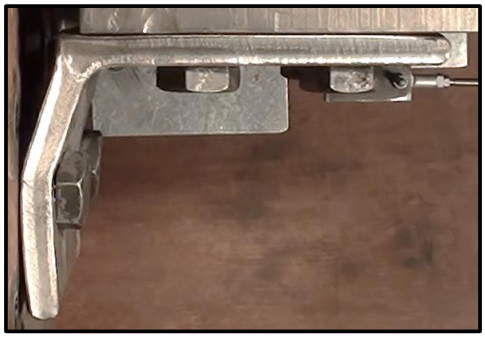
Force-displacement

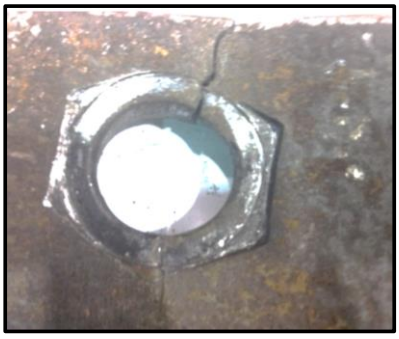












Test TC14-1

Type Monotonic Static

Loading Rate: 100 με/s

Failure mode: Beam

Geometry:

g_{column}	102	mm
t	19.05	mm
g_{beam}	76	mm
φ_{bolt}	25.4	mm
k	31.75	mm
g_2	49.2	mm
g_2/t	2.58	

Materials:

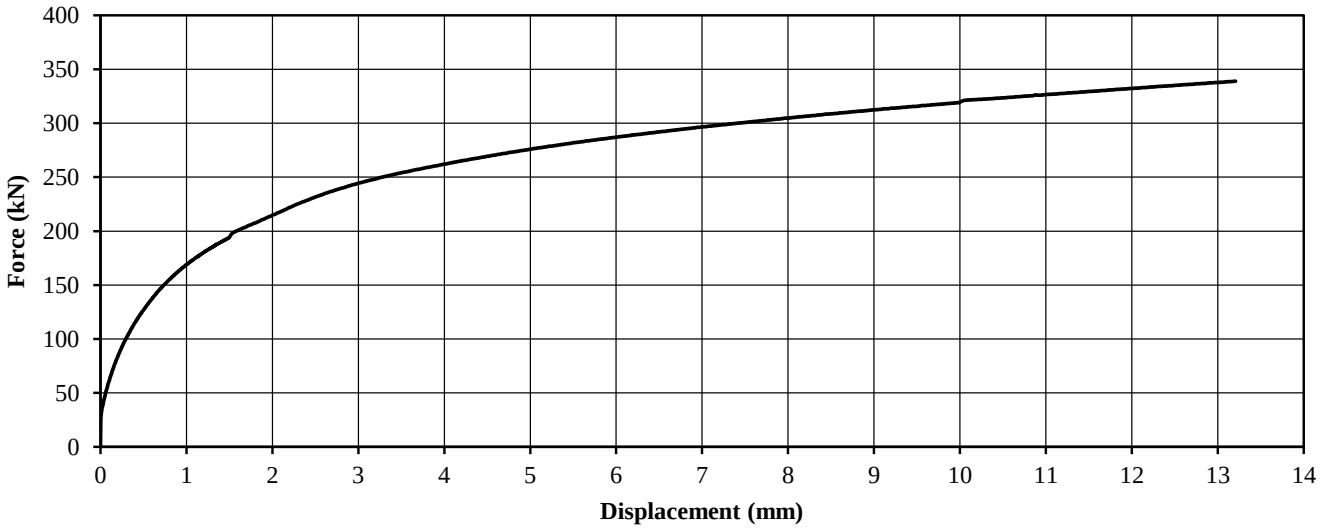
Angle	A36	
F_y	340	MPa
F_u	516	MPa
ε_u	0.2592	
Bolt	A490	
Column bolts	1000	lbf-ft
Plate bolts	1000	lbf-ft

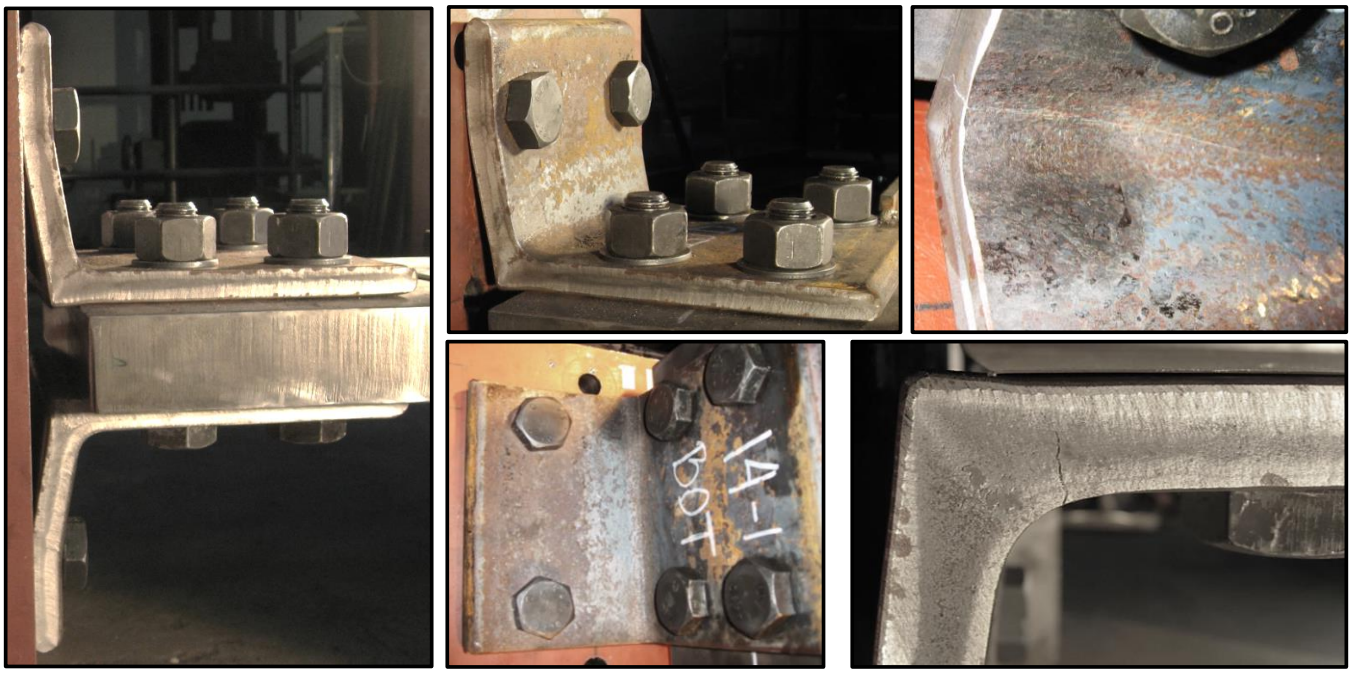
Key response parameters:

$K_{Plastic}$	9.9	kN/mm
$K_{Softening}$	6.9	kN/mm
$K_{Hardening}$	-	kN/mm

	F (kN)	Δ (mm)
Initial	-	-
Plastic	281	5.5
Softening	303	7.7
Hardening	-	-
Max. Force	339	13.2
Ultimate	339	13.2

Force-displacement





Test TC14-2

Type Monotonic Static

Loading Rate: 600 με/s

Failure mode: Beam

Geometry:

g_{column}	102	mm
t	19.05	mm
g_{beam}	76	mm
φ_{bolt}	25.4	mm
k	31.750	mm
g_2	49.2	mm
g_2/t	2.58	

Materials:

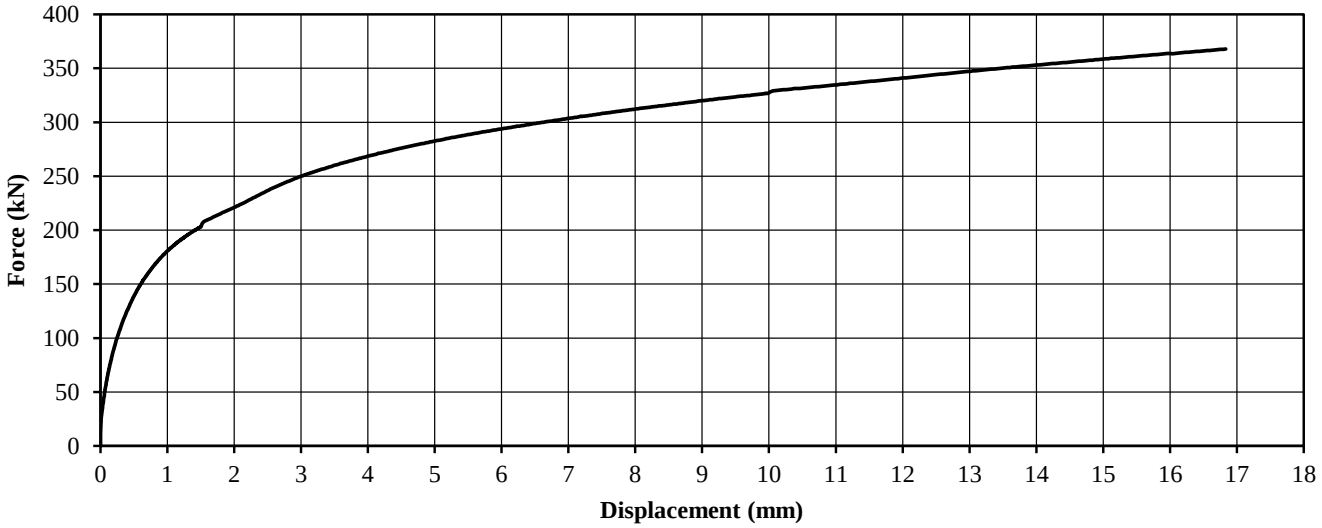
Angle	A36	
F_y	340	MPa
F_u	516	MPa
ε_u	0.2592	
Bolt	A490	
Column bolts	1000	lbf-ft
Plate bolts	1000	lbf-ft

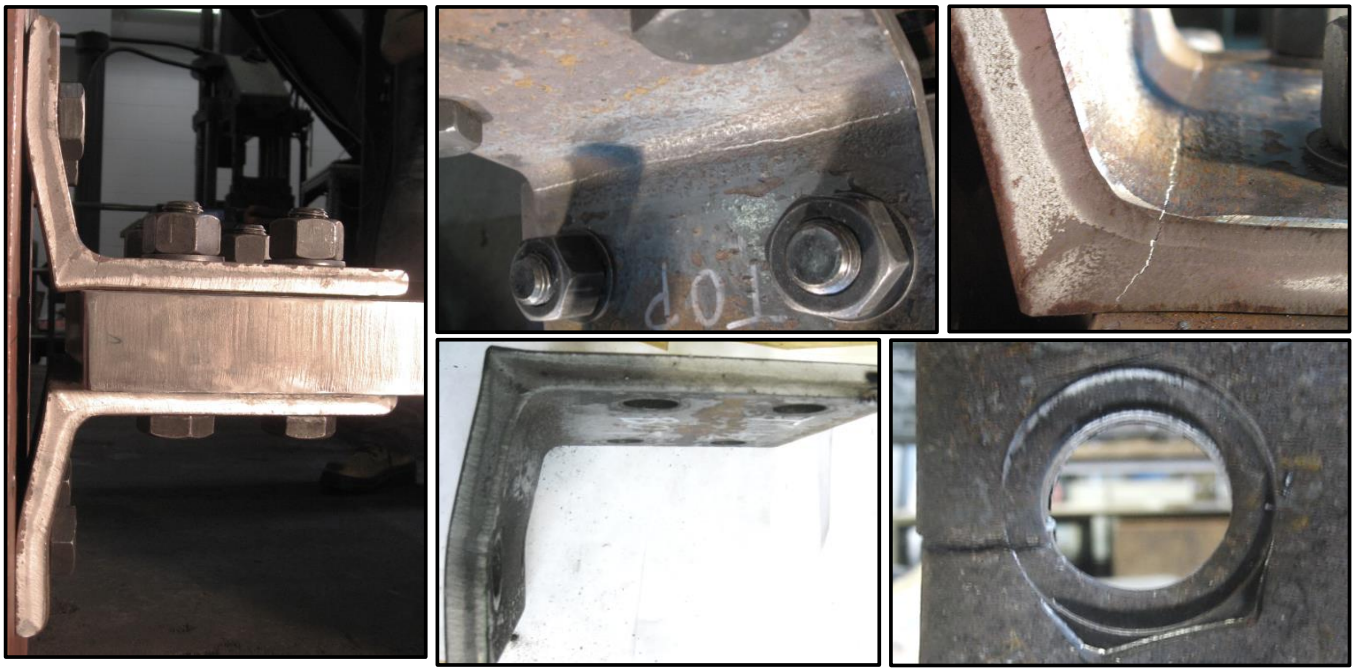
Key response parameters:

$K_{Plastic}$	9.5	kN/mm
$K_{Softening}$	6.1	kN/mm
$K_{Hardening}$	-	kN/mm

	F (kN)	Δ (mm)
Initial	25	0.010
Plastic	286	5.3
Softening	323	9.1
Hardening	-	-
Max. Force	368	16.8
Ultimate	368	16.8

Force-displacement





Test TC14-3

Type Monotonic Dynamic

Loading Rate: 750000 με/s

Failure mode: Column/Net Section

Geometry:

g_{column}	102	mm
t	19.05	mm
g_{beam}	76	mm
φ_{bolt}	25.4	mm
k	31.750	mm
g_2	49.2	mm
g_2/t	2.58	

Materials:

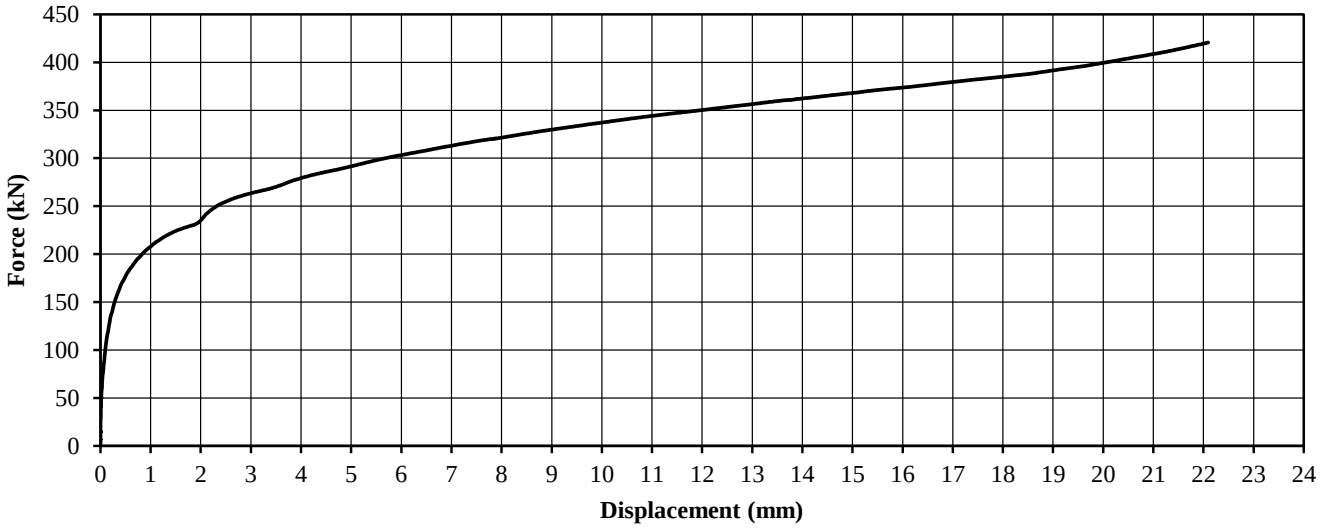
Angle	A36	
F_y	340	MPa
F_u	516	MPa
ε_u	0.2592	
Bolt	A490	
Column bolts	1000	lbf-ft
Plate bolts	1000	lbf-ft

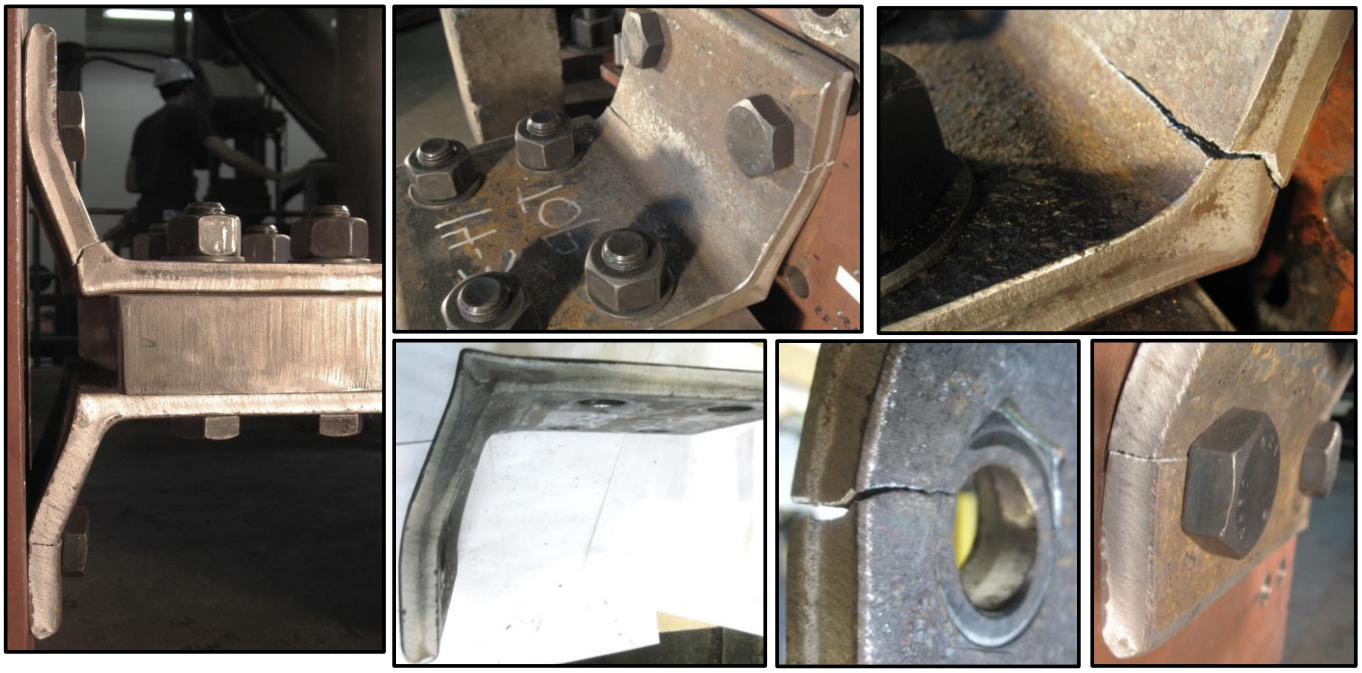
Key response parameters:

$K_{Plastic}$	12.6	kN/mm
$K_{Softening}$	5.8	kN/mm
$K_{Hardening}$	10.0	kN/mm

	F (kN)	Δ (mm)
Initial	30	0.008
Plastic	261	2.9
Softening	329	8.2
Hardening	394	19.5
Max. Force	421	22.1
Ultimate	421	22.1

Force-displacement





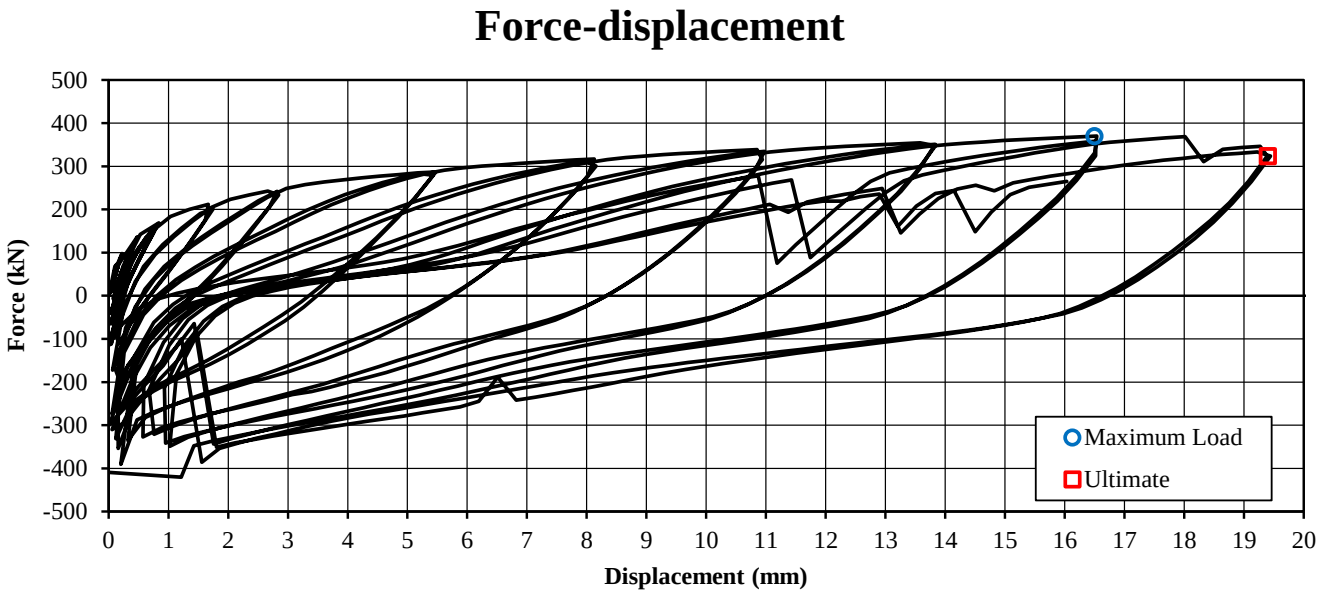
Test TC14-4

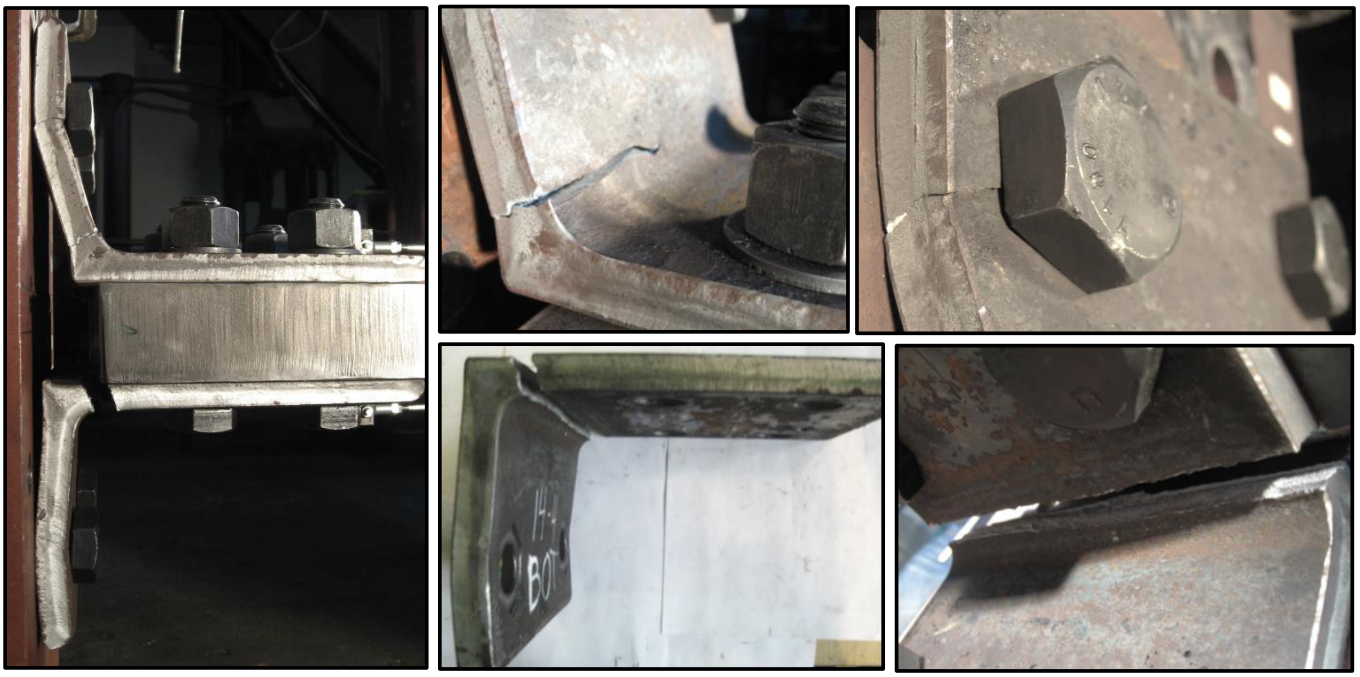
Type Cyclic W310 **Failure mode:** Beam/Column/Net Section

Geometry:		
g_{column}	102	mm
t	19.05	mm
g_{beam}	76	mm
φ_{bolt}	25.4	mm
k	31.750	mm
g_2	49.2	mm
g_2/t	2.58	

Materials:		
Angle	A36	
F_y	340	MPa
F_u	516	MPa
ε_u	0.2592	
Bolt	A490	
Column bolts	1000	lbf-ft
Plate bolts	1000	lbf-ft

Key response parameters:		
F_{Max}	370	kN
Δ_{FMax}	16.5	mm
$Drift_{FMax}$	7	%
$F_{Ultimate}$	323	kN
$\Delta_{Ultimate}$	19.4	mm
$Drift_{Ultimate}$	8	%





Test TC14-5

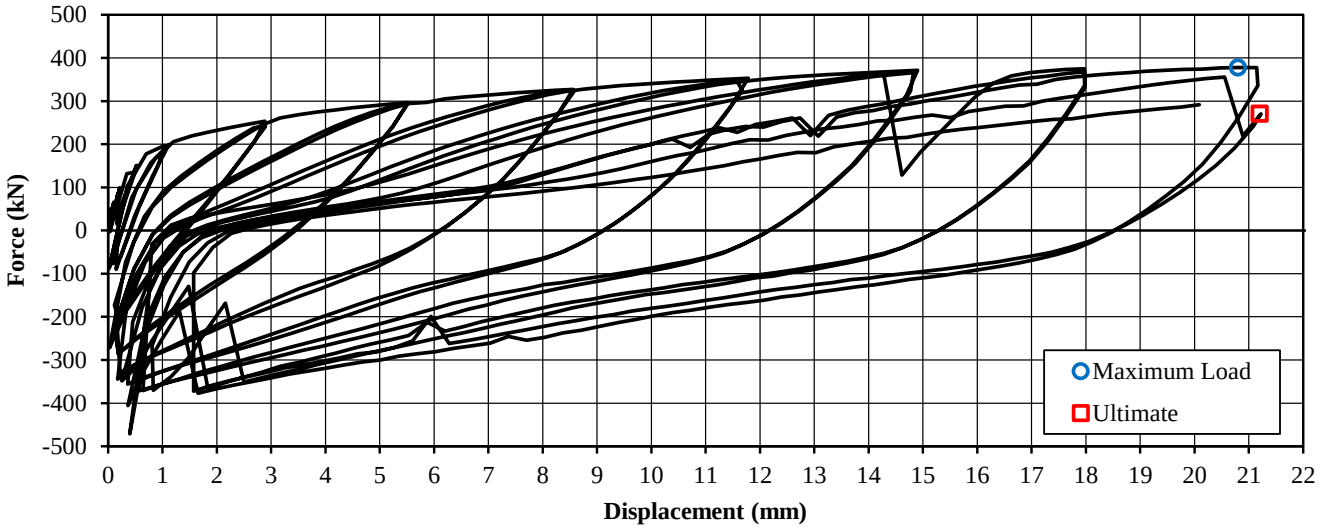
Type Cyclic W410 **Failure mode:** Column/Net Section

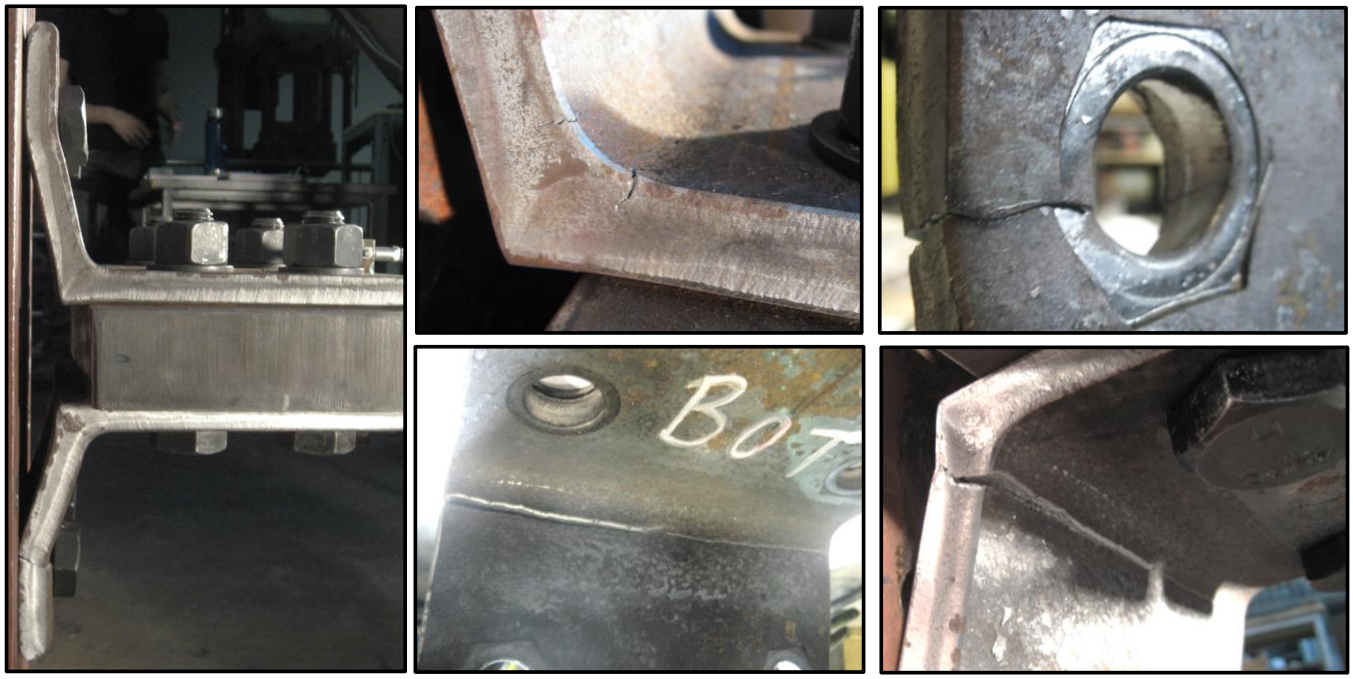
Geometry:		
g_{column}	102	mm
t	19.05	mm
g_{beam}	76	mm
φ_{bolt}	25.4	mm
k	31.750	mm
g_2	49.2	mm
g_2/t	2.58	

Materials:		
Angle	A36	
F_y	340	MPa
F_u	516	MPa
ε_u	0.2592	
Bolt	A490	
Column bolts	1000	lbf-ft
Plate bolts	1000	lbf-ft

Key response parameters:		
F_{Max}	378	kN
Δ_{FMax}	20.8	mm
$Drift_{FMax}$	9	%
$F_{Ultimate}$	271	kN
$\Delta_{Ultimate}$	21.2	mm
$Drift_{Ultimate}$	9	%

Force-displacement





Test TC14-6

Type Time-History **Failure mode:** Column/Net Section

Geometry:

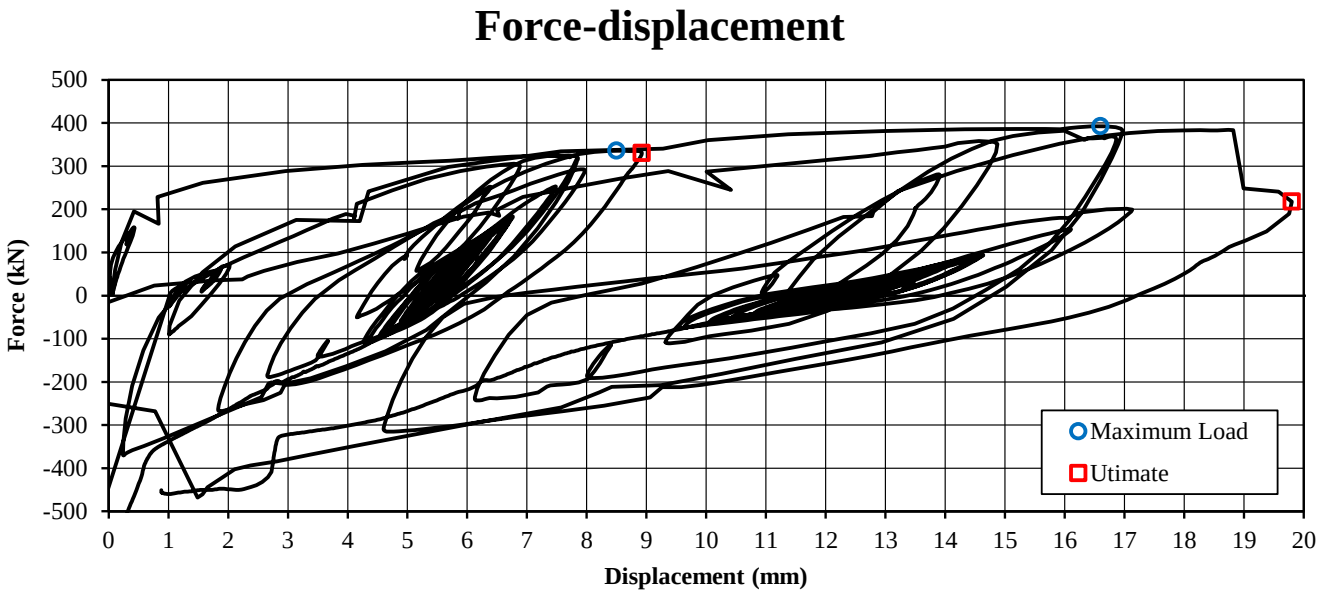
g_{column}	102	mm
t	19.05	mm
g_{beam}	76	mm
φ_{bolt}	25.4	mm
k	31.750	mm
g_2	49.2	mm
g_2/t	2.58	

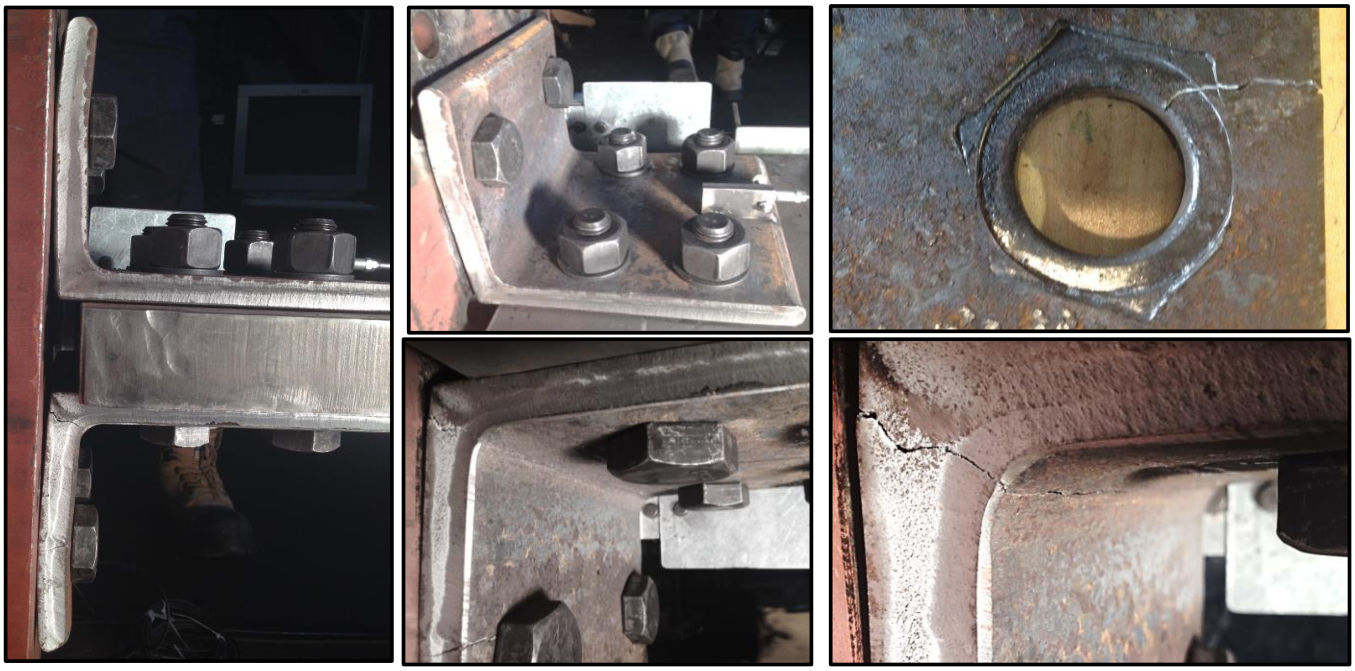
Materials:

Angle	A36	
F_y	340	MPa
F_u	516	MPa
ε_u	0.2592	
Bolt	A490	
Column bolts	1000	lbf-ft
Plate bolts	1000	lbf-ft

Key response parameters:

Signal factor	60%	120%	-
Δ_0	0.0	1.0	-
$F_{F\ Max}$	336	392	-
$\Delta_{F\ Max}$	8.5	16.6	-
$F_{Ultimate}$	330	218	-
$\Delta_{Ultimate}$	8.9	19.8	-





Test TC14-7

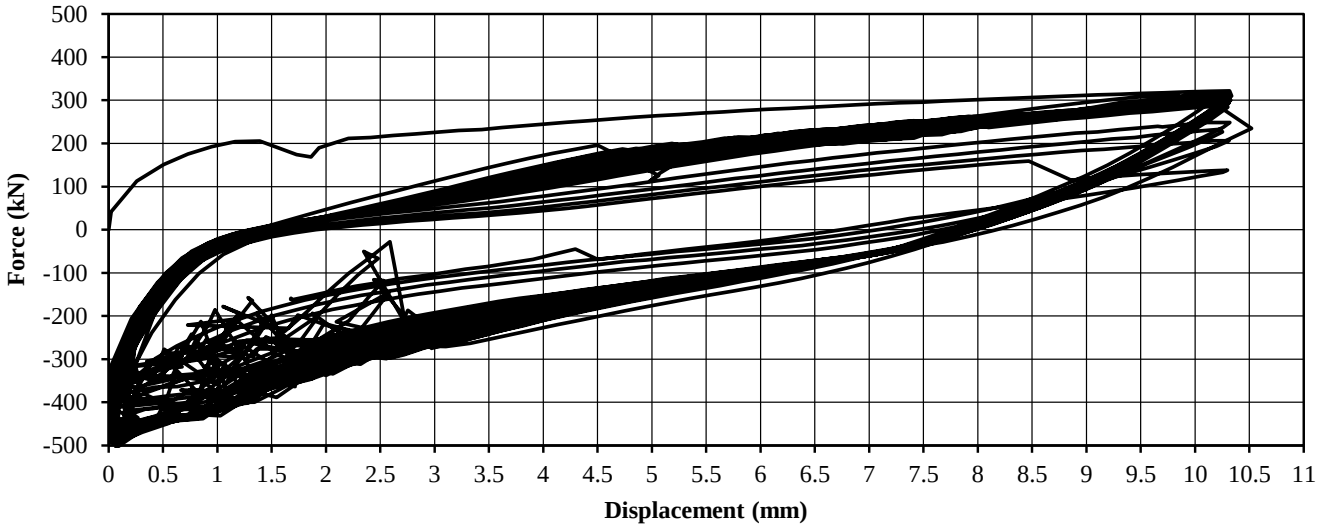
Type Fatigue **Failure mode:** Beam/Net Section

Geometry:		
g_{column}	102	mm
t	19.050	mm
g_{beam}	76	mm
φ_{bolt}	25.4	mm
k	31.750	mm
g_2	49.2	mm
g_2/t	2.58	

Materials:		
Angle	A36	
F_y	340	MPa
F_u	516	MPa
ε_u	0.2592	
Bolt	A490	
Column bolts	1000	lbf-ft
Plate bolts	1000	lbf-ft

Key response parameters:		
$\Delta_{Amplitude}$	10.3	mm
F_{Max}	322	kN
Cycles	44	

Force-displacement





Test TC14-8

Type Fatigue **Failure mode:** Beam/Net Section

Geometry:

g_{column}	102	mm
t	19.050	mm
g_{beam}	76	mm
φ_{bolt}	25.4	mm
k	31.750	mm
g_2	49.2	mm
g_2/t	2.58	

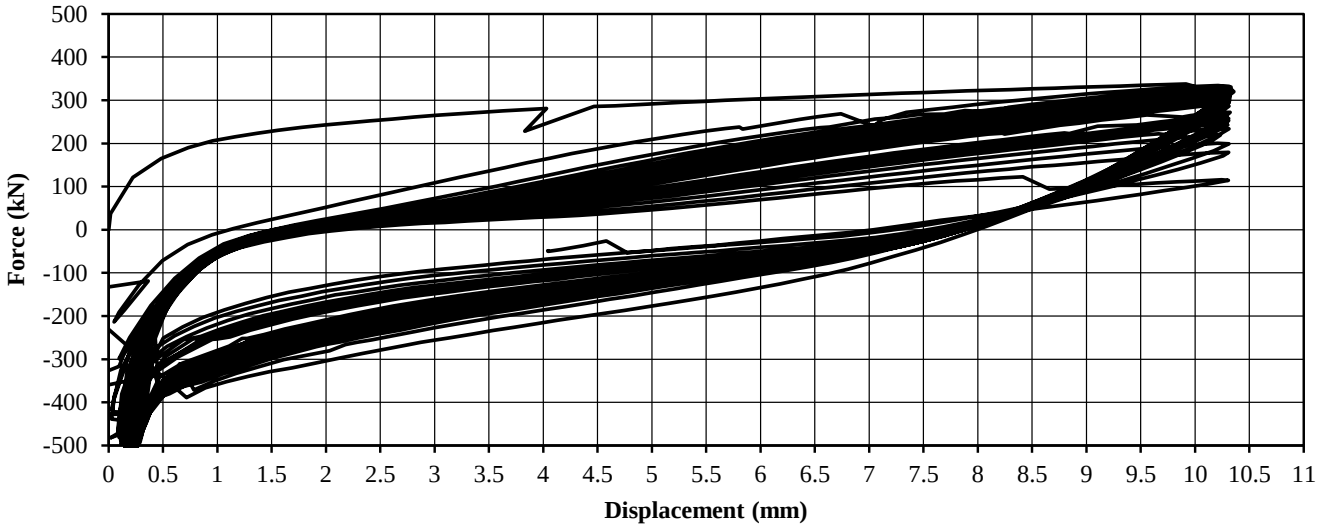
Materials:

Angle	A36	
F_y	340	MPa
F_u	516	MPa
ε_u	0.2592	
Bolt	A490	
Column bolts	1000	lbf-ft
Plate bolts	1000	lbf-ft

Key response parameters:

$\Delta_{Amplitude}$	10.3	mm
F_{Max}	335	kN
Cycles	46	

Force-displacement



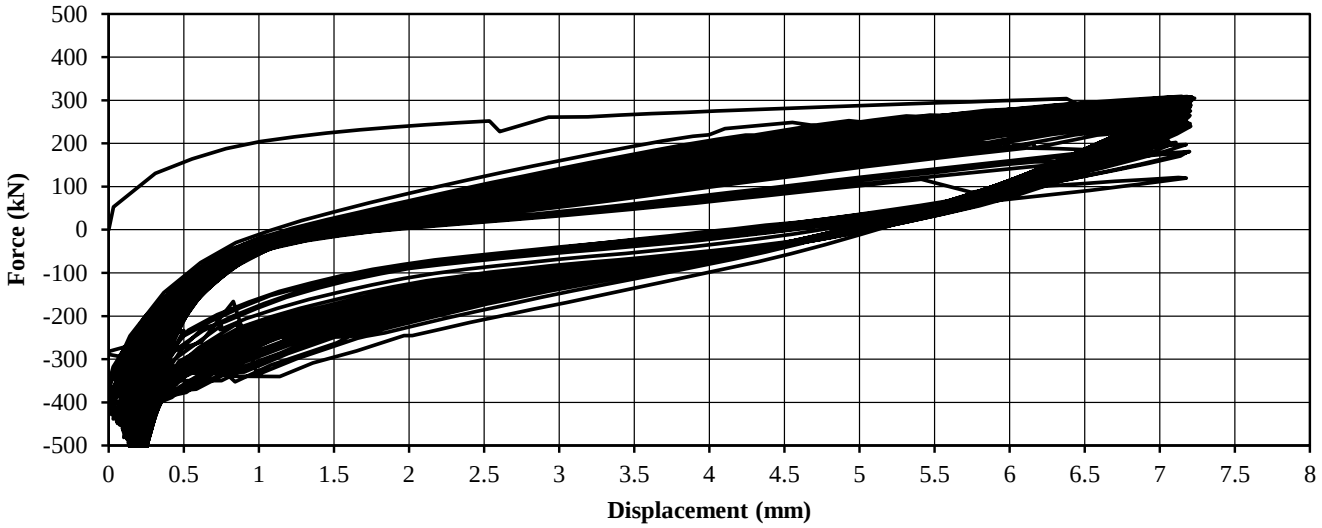


Test TC14-9

Type Fatigue **Failure mode:** Beam

Geometry:			Materials:			Key response parameters:		
g_{column}	102	mm	**Angle**	A36		$\Delta_{Amplitude}$	7.2	mm
t	19.050	mm	F_y	340	MPa	F_{Max}	309	kN
g_{beam}	76	mm	F_u	516	MPa	**Cycles**	81	
φ_{bolt}	25.4	mm	ε_u	0.2592				
k	31.750	mm	**Bolt**	A490				
g_2	49.2	mm	**Column bolts**	1000	lbf-ft			
g_2/t	2.58		**Plate bolts**	1000	lbf-ft			

Force-displacement





Test TC14-10

Type Fatigue **Failure mode:** Beam

Geometry:

g_{column}	102	mm
t	19.050	mm
g_{beam}	76	mm
φ_{bolt}	25.4	mm
k	31.750	mm
g_2	49.2	mm
g_2/t	2.58	

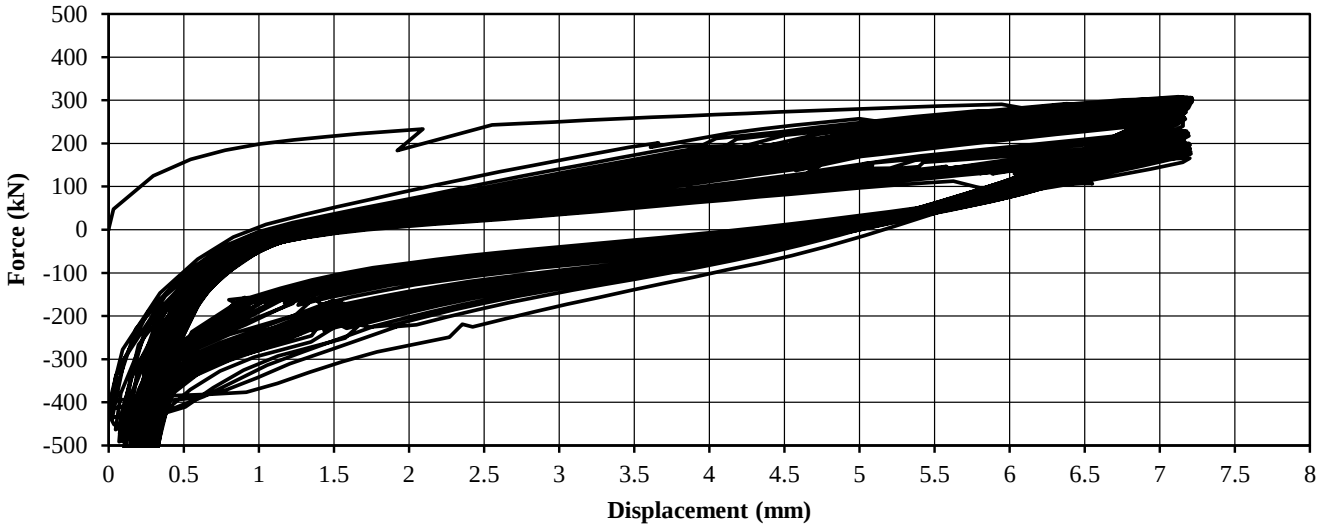
Materials:

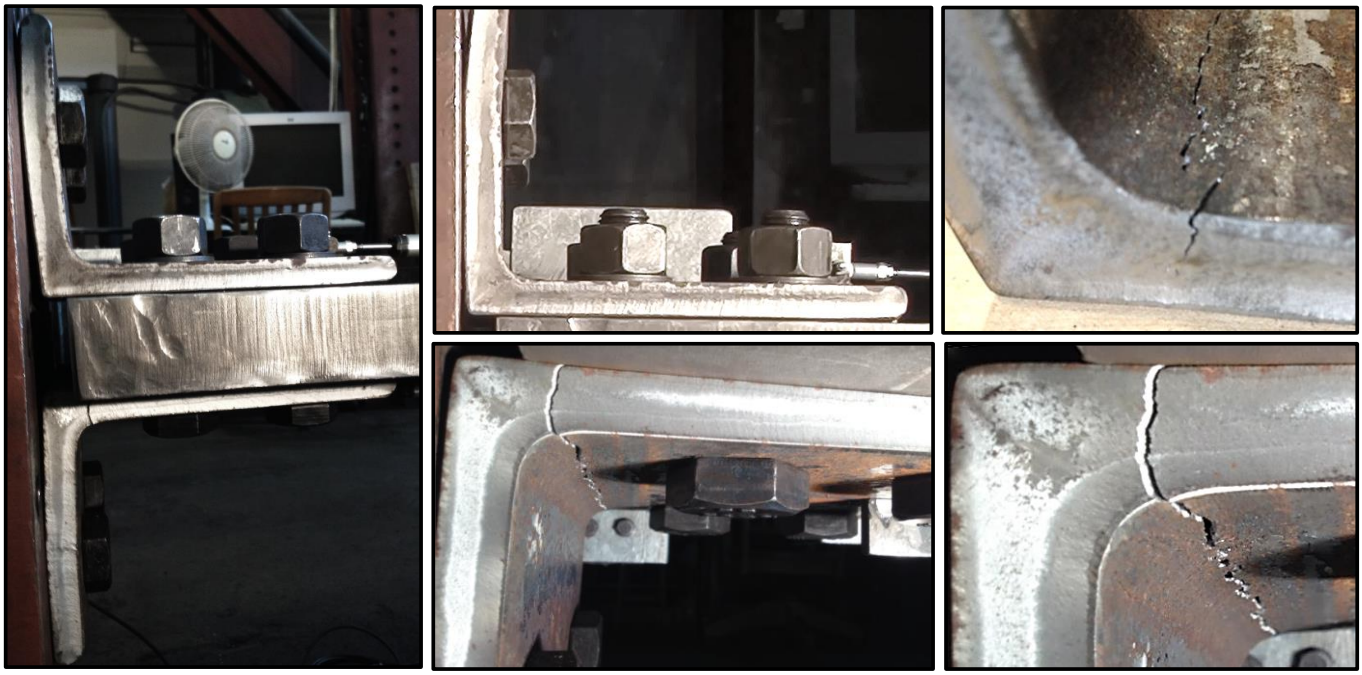
Angle	A36	
F_y	340	MPa
F_u	516	MPa
ε_u	0.2592	
Bolt	A490	
Column bolts	1000	lbf-ft
Plate bolts	1000	lbf-ft

Key response parameters:

$\Delta_{Amplitude}$	7.2	mm
F_{Max}	303	kN
Cycles	81	

Force-displacement



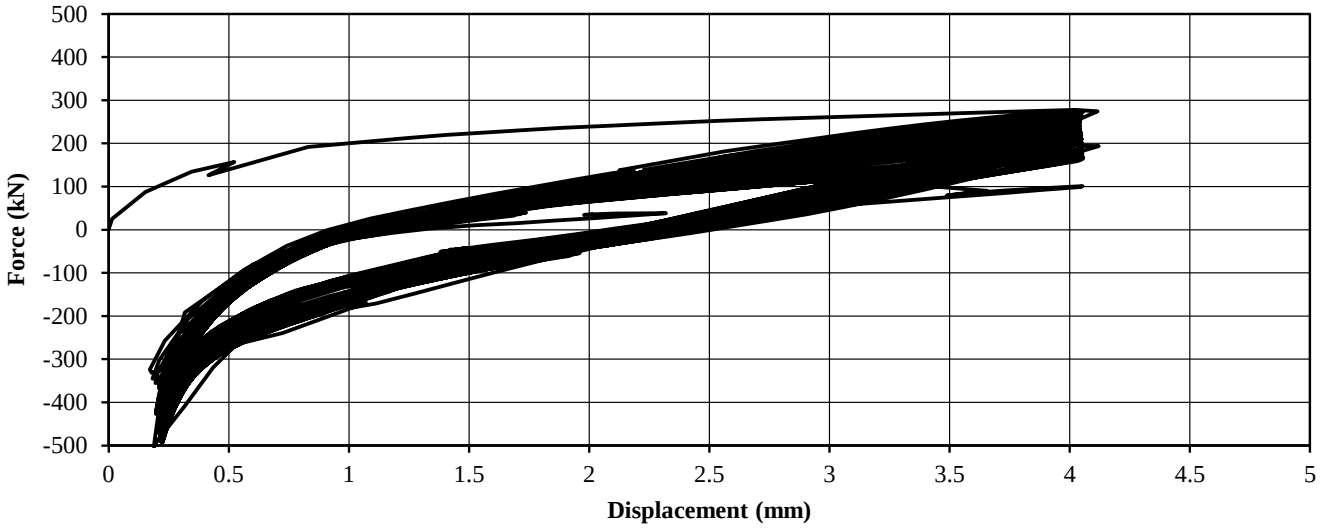


Test TC14-11

Type Fatigue **Failure mode:** Beam

Geometry:			Materials:			Key response parameters:		
g_{column}	102	mm	**Angle**	A36		$\Delta_{Amplitude}$	4.1	mm
t	19.050	mm	F_y	340	MPa	F_{Max}	275	kN
g_{beam}	76	mm	F_u	516	MPa	**Cycles**	259	
φ_{bolt}	25.4	mm	ε_u	0.2592				
k	31.750	mm	**Bolt**	A490				
g_2	49.2	mm	**Column bolts**	1000	lbf-ft			
g_2/t	2.58		**Plate bolts**	1000	lbf-ft			

Force-displacement





Test TC14-12

Type Fatigue **Failure mode:** Beam

Geometry:

g_{column}	102	mm
t	19.050	mm
g_{beam}	76	mm
φ_{bolt}	25.4	mm
k	31.750	mm
g_2	49.2	mm
g_2/t	2.58	

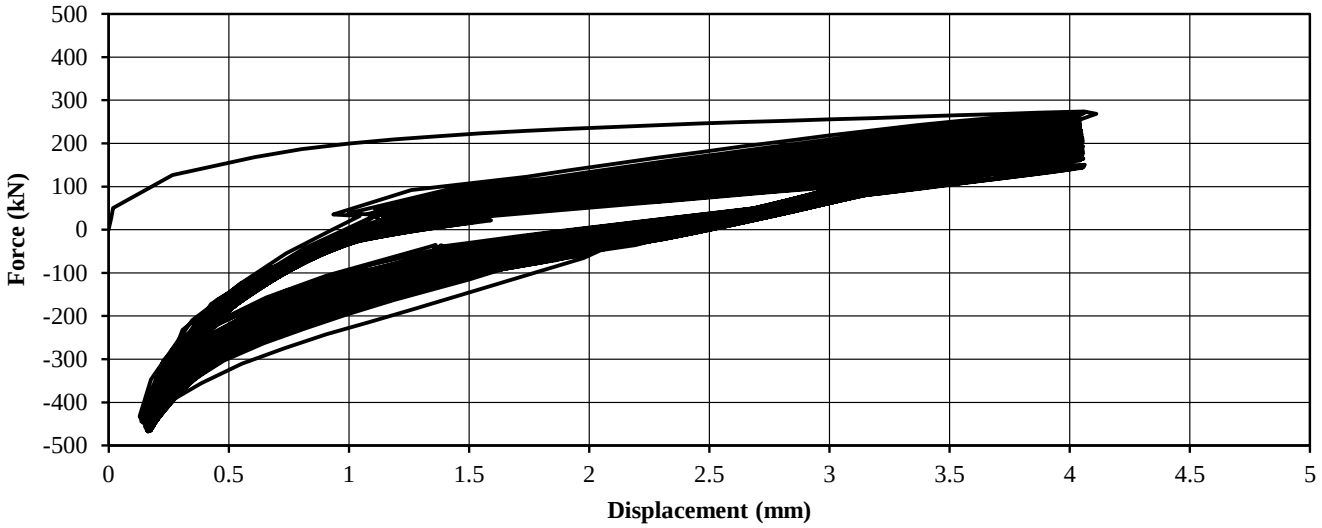
Materials:

Angle	A36	
F_y	340	MPa
F_u	516	MPa
ε_u	0.2592	
Bolt	A490	
Column bolts	1000	lbf-ft
Plate bolts	1000	lbf-ft

Key response parameters:

$\Delta_{Amplitude}$	4.1	mm
F_{Max}	271	kN
Cycles	322	

Force-displacement





Test TC15-1

Type Monotonic Static

Loading Rate: 100 με/s

Failure mode: Column

Geometry:

g_{column}	114	mm
t	9.525	mm
g_{beam}	57	mm
φ_{bolt}	19.1	mm
k	22.225	mm
g_2	76.2	mm
g_2/t	8.00	

Materials:

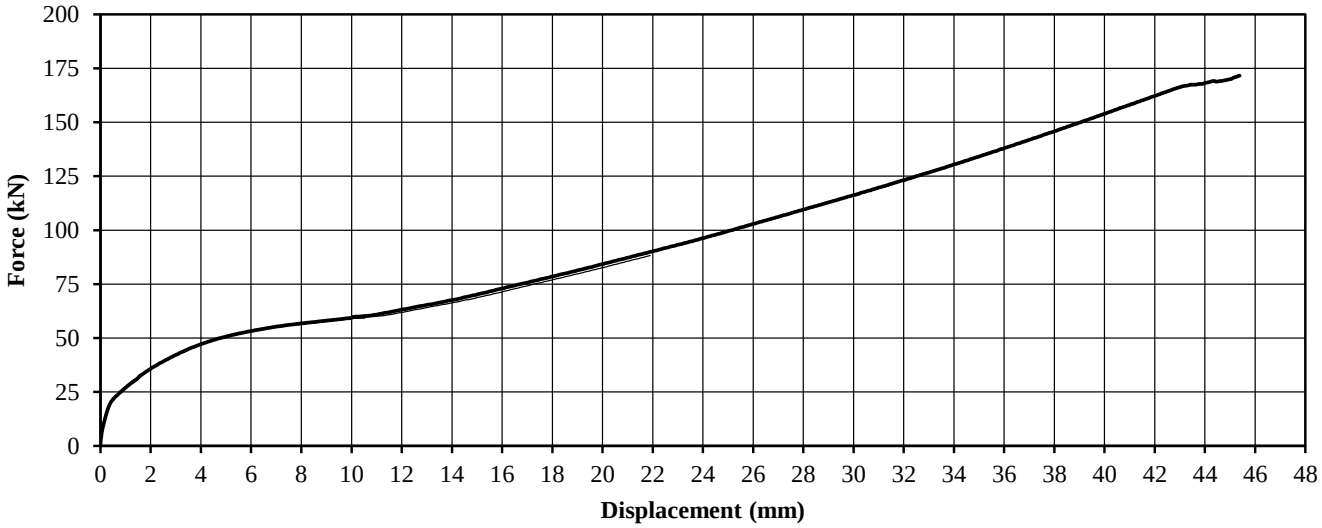
Angle	A36	
F_y	570	MPa
F_u	518	MPa
ε_u	0.2420	
Bolt	A325	
Column bolts	400	lbf-ft
Plate bolts	400	lbf-ft

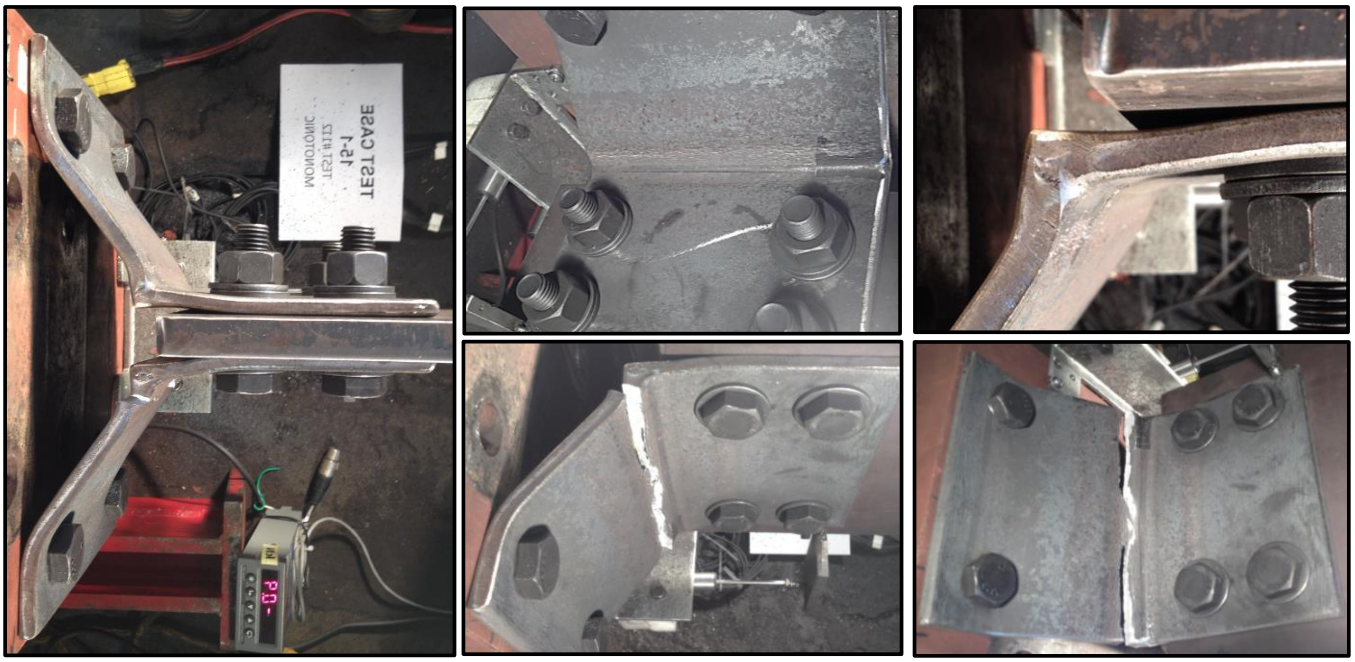
Key response parameters:

$K_{Plastic}$	1.6	kN/mm
$K_{Softening}$	-	kN/mm
$K_{Hardening}$	3.5	kN/mm

	F (kN)	Δ (mm)
Initial	20	0.401
Plastic	55	6.9
Softening	-	-
Hardening	71	16.9
Max. Force	172	45.4
Ultimate	172	45.4

Force-displacement





Test TC15-2

Type Monotonic Static

Loading Rate: 600 με/s

Failure mode: Column

Geometry:

g_{column}	114	mm
t	9.525	mm
g_{beam}	57	mm
φ_{bolt}	19.1	mm
k	22.225	mm
g_2	76.2	mm
g_2/t	8.00	

Materials:

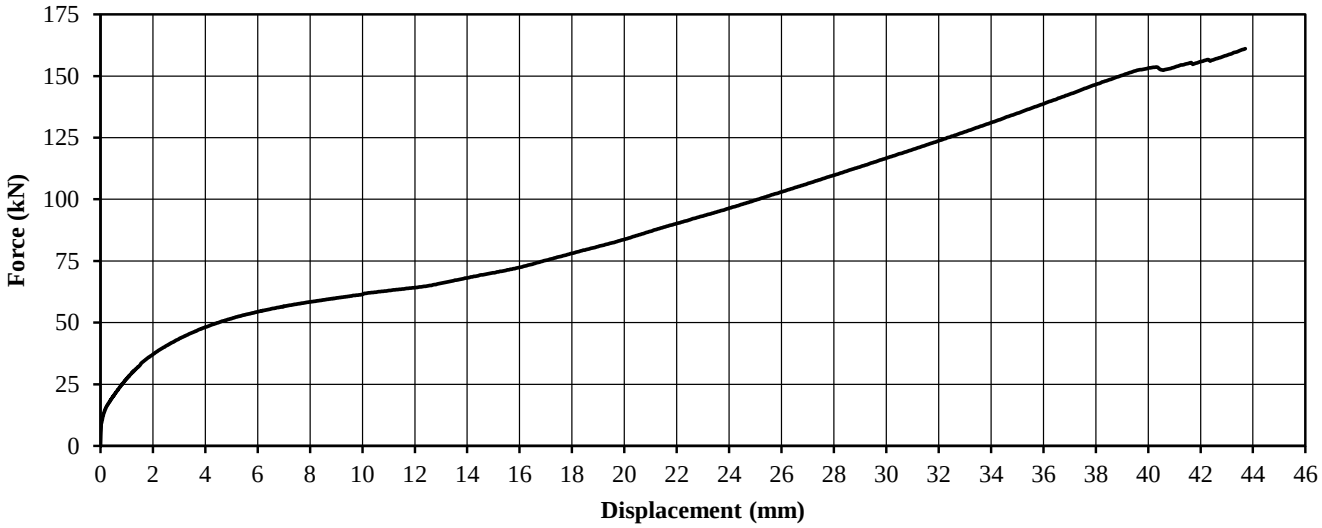
Angle	A36	
F_y	570	MPa
F_u	518	MPa
ε_u	0.2420	
Bolt	A325	
Column bolts	400	lbf-ft
Plate bolts	400	lbf-ft

Key response parameters:

$K_{Plastic}$	1.6	kN/mm
$K_{Softening}$	-	kN/mm
$K_{Hardening}$	3.3	kN/mm

	F (kN)	Δ (mm)
Initial	11	0.069
Plastic	56	6.7
Softening	-	-
Hardening	71	16.2
Max. Force	161	43.7
Ultimate	161	43.7

Force-displacement





Test TC15-3

Type Monotonic Static

Loading Rate: 750000 με/s

Failure mode: Column

Geometry:

g_{column}	114	mm
t	9.525	mm
g_{beam}	57	mm
φ_{bolt}	19.1	mm
k	22.225	mm
g_2	76.2	mm
g_2/t	8.00	

Materials:

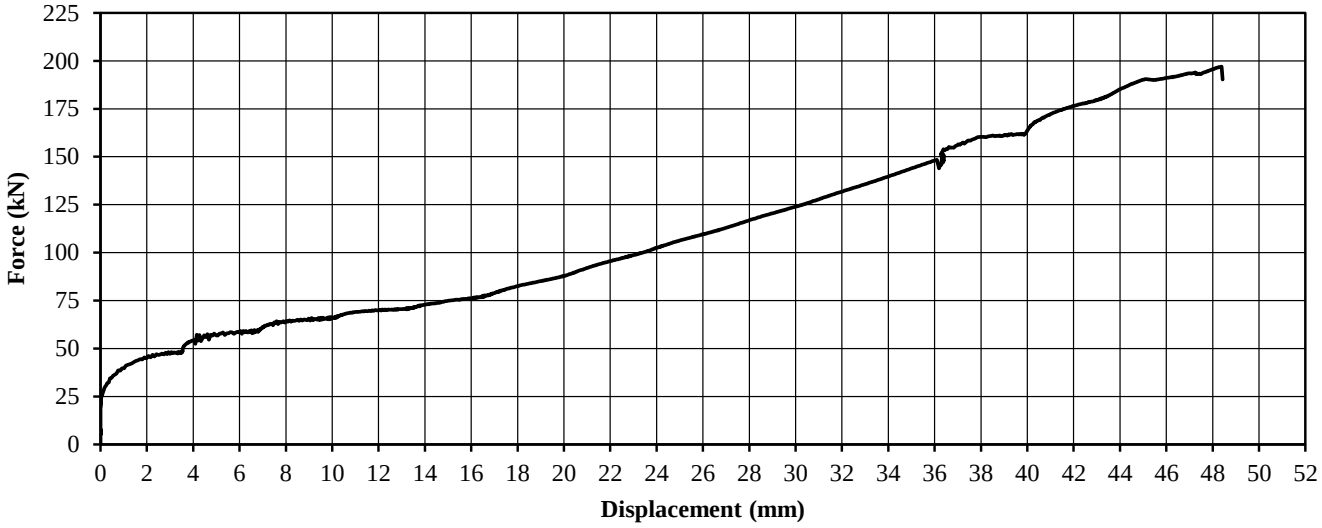
Angle	A36	
F_y	570	MPa
F_u	518	MPa
ε_u	0.2420	
Bolt	A325	
Column bolts	400	lbf-ft
Plate bolts	400	lbf-ft

Key response parameters:

$K_{Plastic}$	2.2	kN/mm
$K_{Softening}$	-	kN/mm
$K_{Hardening}$	3.8	kN/mm

	F (kN)	Δ (mm)
Initial	25	0.005
Plastic	48	2.8
Softening	-	-
Hardening	82	18.7
Max. Force	197	48.4
Ultimate	190	48.4

Force-displacement





Test TC15-4

Type Snug-Thight

Loading Rate: 100 με/s

Failure mode: Column

Key response parameters:

$K_{Plastic}$	2.1	kN/mm
$K_{Softening}$	-	kN/mm
$K_{Hardening}$	3.3	kN/mm

Geometry:

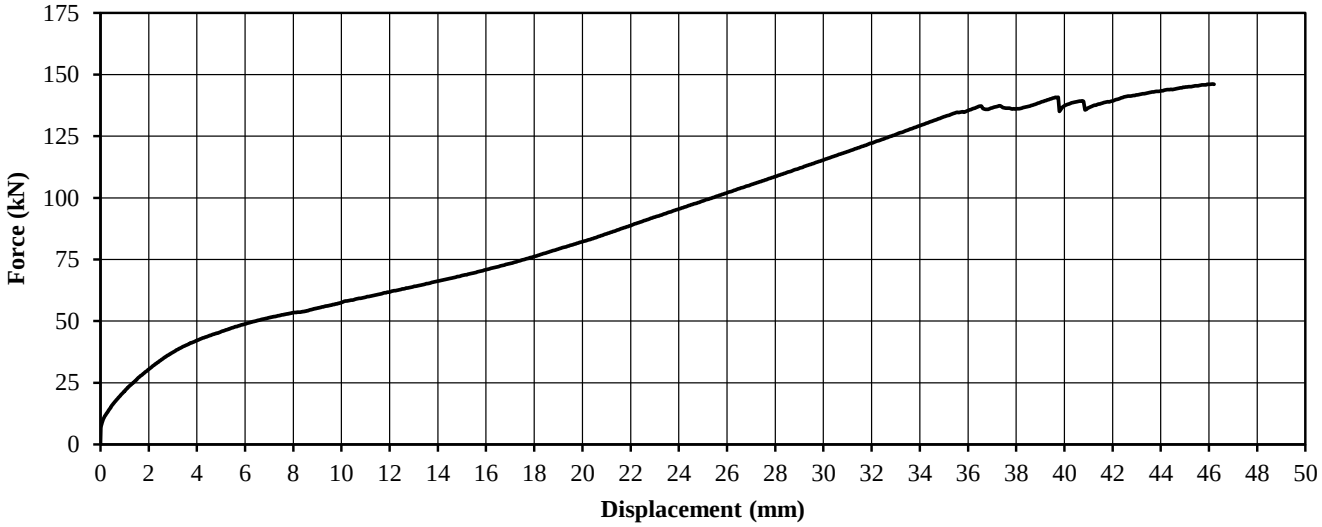
g_{column}	114	mm
t	9.525	mm
g_{beam}	57	mm
φ_{bolt}	19.1	mm
k	22.225	mm
g_2	76.2	mm
g_2/t	8.00	

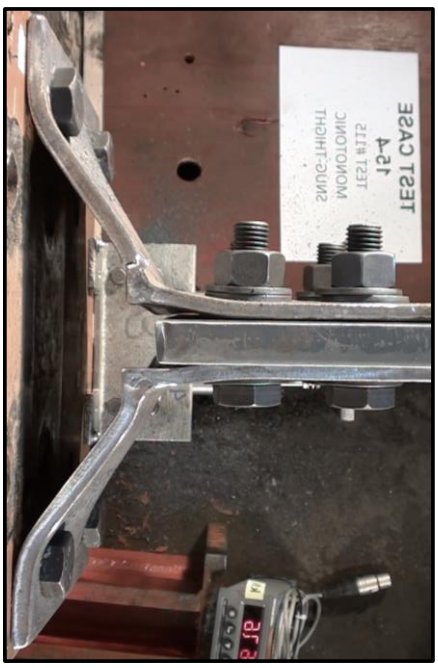
Materials:

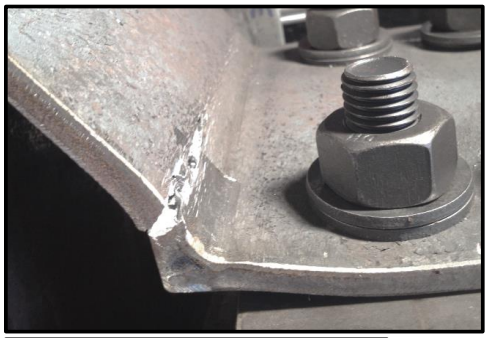
Angle	A36	
F_y	570	MPa
F_u	518	MPa
ε_u	0.2420	
Bolt	A325	
Column bolts	Snug-Thight	
Plate bolts	400	lbf-ft

	F (kN)	Δ (mm)
Initial	10	0.067
Plastic	50	6.5
Softening	-	-
Hardening	73	17.4
Max. Force	146	46.2
Ultimate	146	46.2

Force-displacement











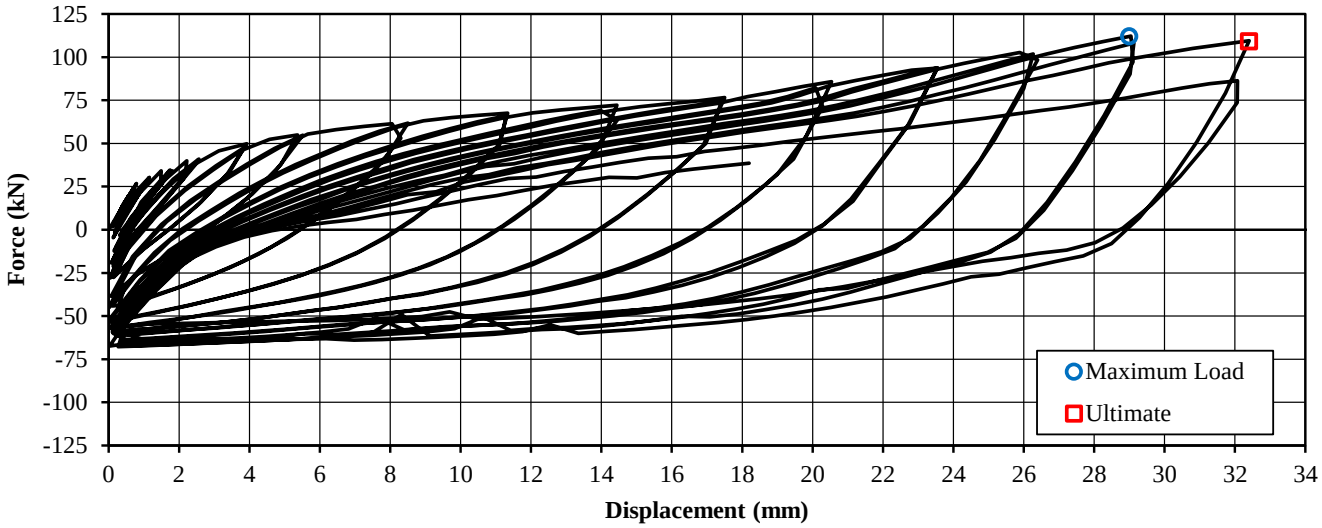


Test TC15-5

Type Cyclic W310 **Failure mode:** Column

Geometry:			Materials:			Key response parameters:		
g_{column}	114	mm	**Angle**	A36		F_{Max}	112	kN
t	9.525	mm	F_y	570	MPa	Δ_{FMax}	29.0	mm
g_{beam}	57	mm	F_u	518	MPa	$Drift_{FMax}$	10	%
φ_{bolt}	19.1	mm	ε_u	0.2420		$F_{Ultimate}$	109	kN
k	22.225	mm	**Bolt**	A325		$\Delta_{Ultimate}$	32.4	mm
g_2	76.2	mm	**Column bolts**	400	lbf-ft	$Drift_{Ultimate}$	11	%
g_2/t	8.00		**Plate bolts**	400	lbf-ft			

Force-displacement





Test TC15-6

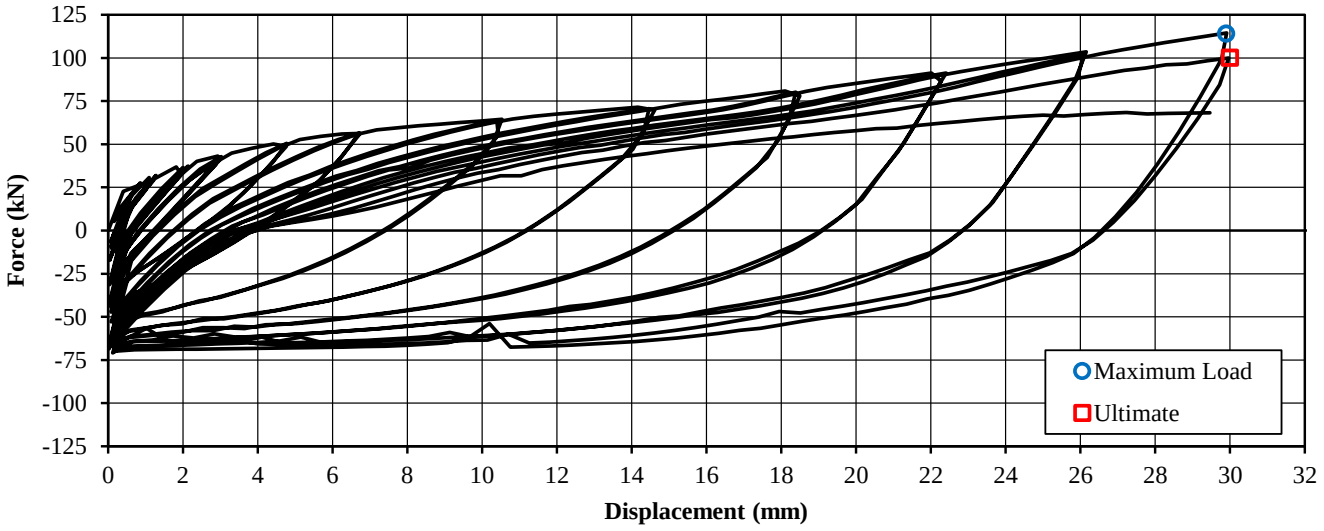
Type Cyclic W410 **Failure mode:** Column

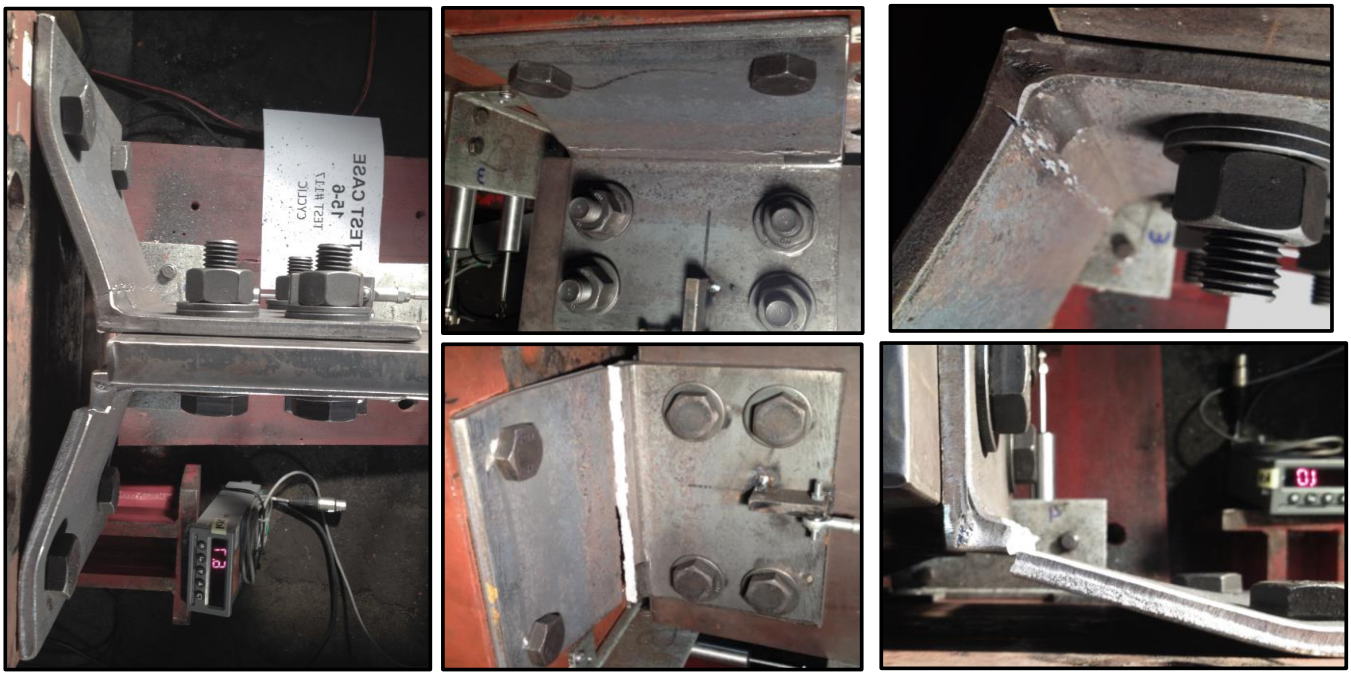
Geometry:		
g_{column}	114	mm
t	9.525	mm
g_{beam}	57	mm
φ_{bolt}	19.1	mm
k	22.225	mm
g_2	76.2	mm
g_2/t	8.00	

Materials:		
Angle	A36	
F_y	570	MPa
F_u	518	MPa
ε_u	0.2420	
Bolt	A325	
Column bolts	400	lbf-ft
Plate bolts	400	lbf-ft

Key response parameters:		
F_{Max}	114	kN
Δ_{FMax}	29.9	mm
$Drift_{FMax}$	8	%
$F_{Ultimate}$	100	kN
$\Delta_{Ultimate}$	30	mm
$Drift_{Ultimate}$	8	%

Force-displacement





Test TC15-7

Type Time-History **Failure mode:** Column

Geometry:

g_{column}	114	mm
t	9.525	mm
g_{beam}	57	mm
φ_{bolt}	19.1	mm
k	22.225	mm
g_2	76.2	mm
g_2/t	8.00	

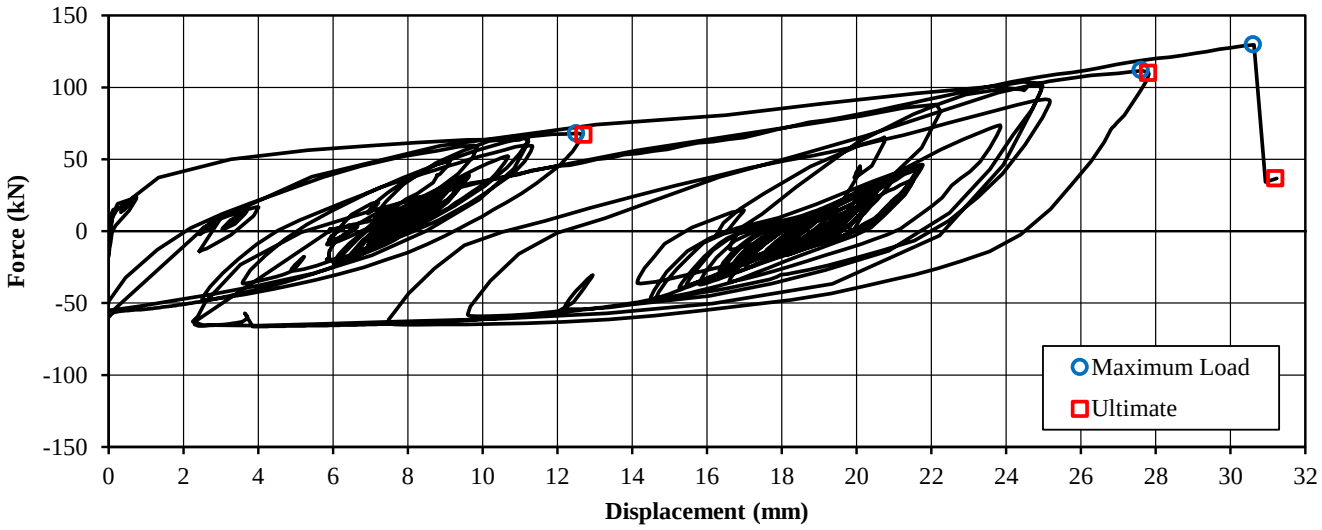
Materials:

Angle	A36	
F_y	570	MPa
F_u	518	MPa
ε_u	0.2420	
Bolt	A325	
Column bolts	400	lbf-ft
Plate bolts	400	lbf-ft

Key response parameters:

Signal factor	85%	170%	285%
Δ_0	0.0	2.4	5.9
$F_{F\ Max}$	68	112	130
$\Delta_{F\ Max}$	12.5	27.6	30.6
$F_{Ultimate}$	67	110	37
$\Delta_{Ultimate}$	12.7	27.8	31.2

Force-displacement





Test TC16-1

Type Monotonic Static

Loading Rate: 100 με/s

Failure mode: Column

Geometry:

g_{column}	114	mm
t	12.7	mm
g_{beam}	76	mm
φ_{bolt}	25.4	mm
k	25.4	mm
g_2	68.3	mm
g_2/t	5.38	

Materials:

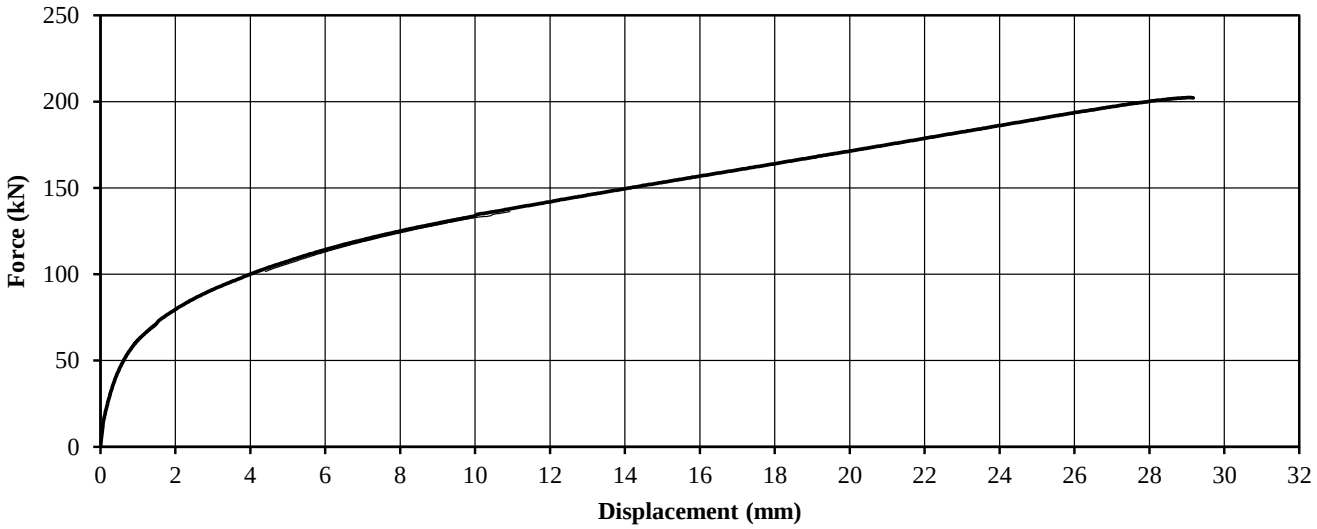
Angle	A36	
F_y	343	MPa
F_u	500	MPa
ε_u	0.2620	
Bolt	A490	
Column bolts	1000	lbf-ft
Plate bolts	1000	lbf-ft

Key response parameters:

$K_{Plastic}$	4.0	kN/mm
$K_{Softening}$	-	kN/mm
$K_{Hardening}$	-	kN/mm

	F (kN)	Δ (mm)
Initial	-	-
Plastic	122	6.3
Softening	-	-
Hardening	-	-
Max. Force	202	29.1
Ultimate	202	29.1

Force-displacement





Test TC16-2

Type Monotonic Static

Loading Rate: 600 με/s

Failure mode: Column

Geometry:

g_{column}	114	mm
t	12.700	mm
g_{beam}	76	mm
φ_{bolt}	25.4	mm
k	25.400	mm
g_2	68.3	mm
g_2/t	5.38	

Materials:

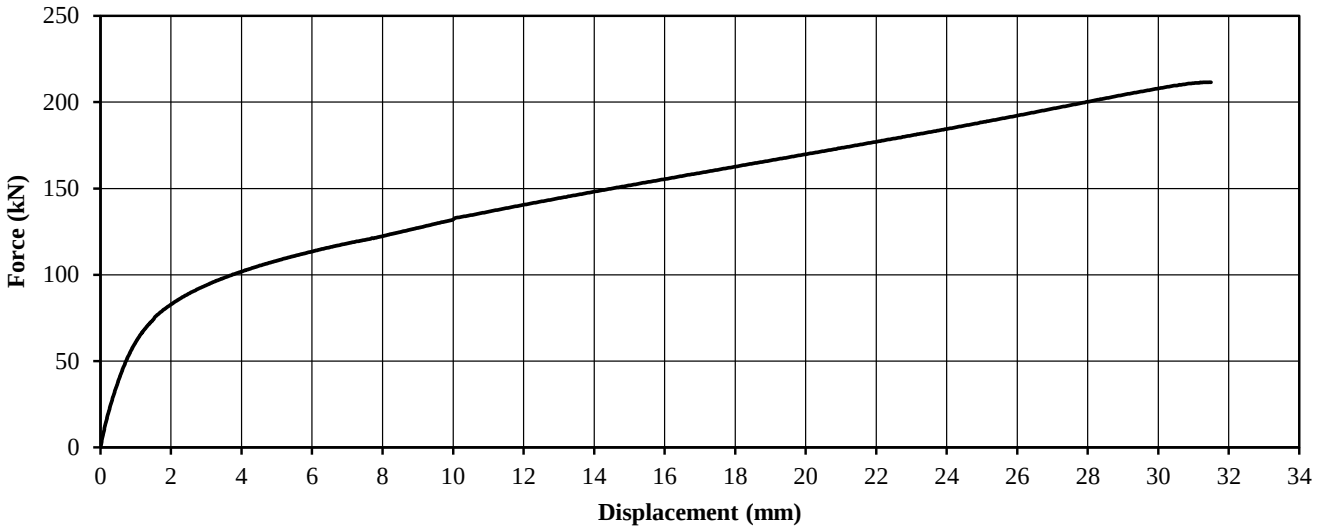
Angle	A36	
F_y	343	MPa
F_u	500	MPa
ε_u	0.2620	
Bolt	A490	
Column bolts	1000	lbf-ft
Plate bolts	1000	lbf-ft

Key response parameters:

$K_{Plastic}$	4.0	kN/mm
$K_{Softening}$	-	kN/mm
$K_{Hardening}$	-	kN/mm

	F (kN)	Δ (mm)
Initial	-	-
Plastic	120	7.4
Softening	-	-
Hardening	-	-
Max. Force	212	31.5
Ultimate	212	31.5

Force-displacement





Test TC16-3

Type Monotonic Dynamic

Loading Rate: 750000 με/s

Failure mode: Column

Key response parameters:

$K_{Plastic}$	4.3	kN/mm
$K_{Softening}$	-	kN/mm
$K_{Hardening}$	4.6	kN/mm

Geometry:

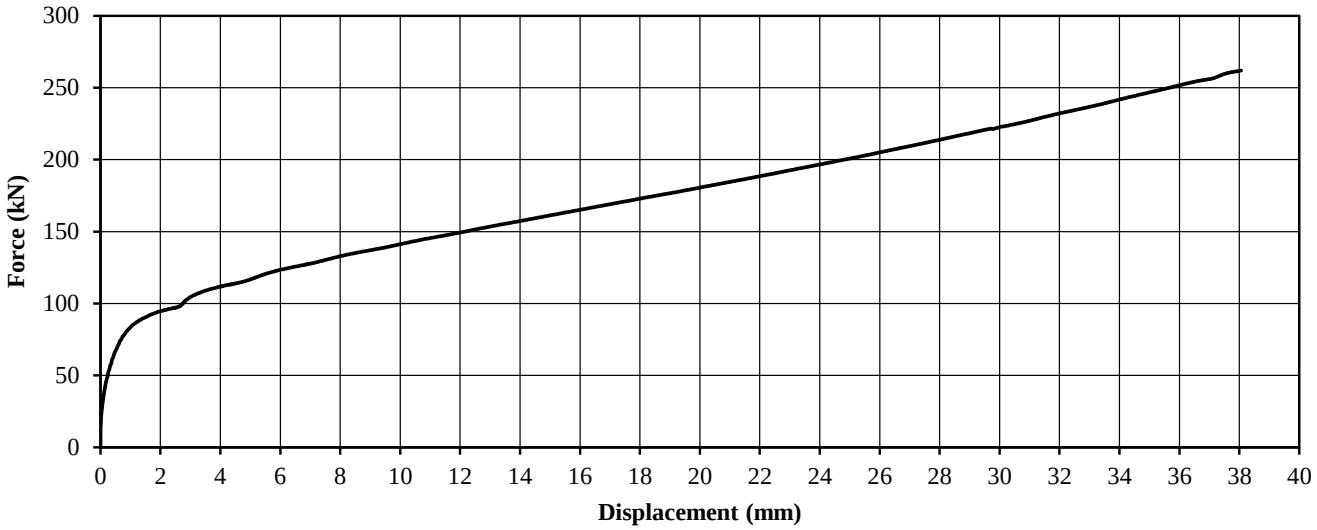
g_{column}	114	mm
t	12.700	mm
g_{beam}	76	mm
φ_{bolt}	25.4	mm
k	25.400	mm
g_2	68.3	mm
g_2/t	5.38	

Materials:

Angle	A36	
F_y	343	MPa
F_u	500	MPa
ε_u	0.2620	
Bolt	A490	
Column bolts	1000	lbf-ft
Plate bolts	1000	lbf-ft

	F (kN)	Δ (mm)
Initial	-	-
Plastic	112	4.0
Softening	-	-
Hardening	216	28.4
Max. Force	262	38.1
Ultimate	262	38.1

Force-displacement





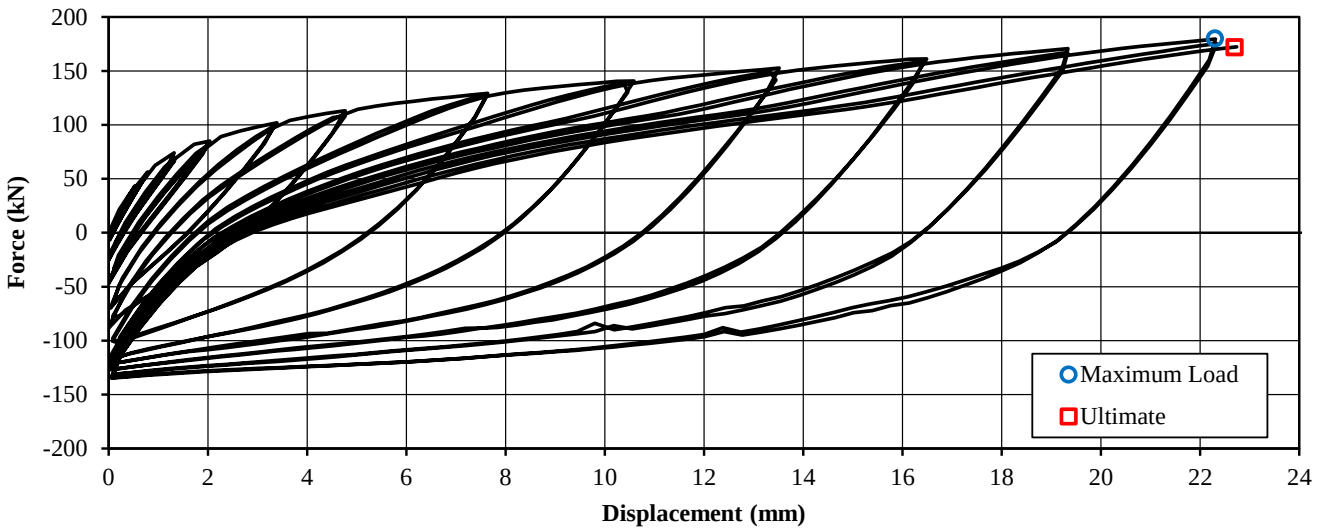
Test TC16-4

Type Cyclic W310 **Failure mode:** Column

Geometry:		
g_{column}	114	mm
t	12.700	mm
g_{beam}	76	mm
φ_{bolt}	25.4	mm
k	25.400	mm
g_2	68.3	mm
g_2/t	5.38	

Materials:		
Angle	A36	
F_y	343	MPa
F_u	500	MPa
ε_u	0.2620	
Bolt	A490	
Column bolts	1000	lbf-ft
Plate bolts	1000	lbf-ft

Key response parameters:		
F_{Max}	180	kN
Δ_{FMax}	22.3	mm
$Drift_{FMax}$	8	%
$F_{Ultimate}$	172	kN
$\Delta_{Ultimate}$	22.7	mm
$Drift_{Ultimate}$	8	%



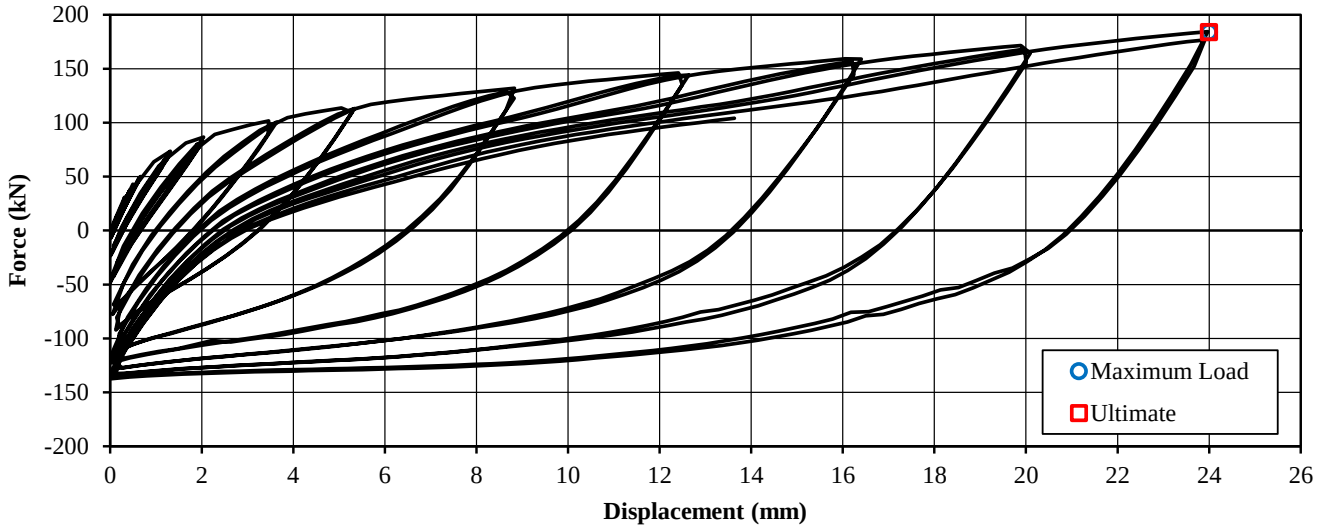


Test TC16-5

Type Cyclic W410 **Failure mode:** Column

Geometry:			Materials:			Key response parameters:		
g_{column}	114	mm	**Angle**	A36		F_{Max}	184	kN
t	12.700	mm	F_y	343	MPa	Δ_{FMax}	24.0	mm
g_{beam}	76	mm	F_u	500	MPa	$Drift_{FMax}$	7	%
φ_{bolt}	25.4	mm	ε_u	0.2620		$F_{Ultimate}$	184	kN
k	25.400	mm	**Bolt**	A490		$\Delta_{Ultimate}$	24.0	mm
g_2	68.3	mm	**Column bolts**	1000	lbf-ft	$Drift_{Ultimate}$	7	%
g_2/t	5.38		**Plate bolts**	1000	lbf-ft			

Force-displacement





Test TC16-6

Type Time-History **Failure mode:** Column

Geometry:

g_{column}	114	mm
t	12.700	mm
g_{beam}	76	mm
φ_{bolt}	25.4	mm
k	25.400	mm
g_2	68.3	mm
g_2/t	5.38	

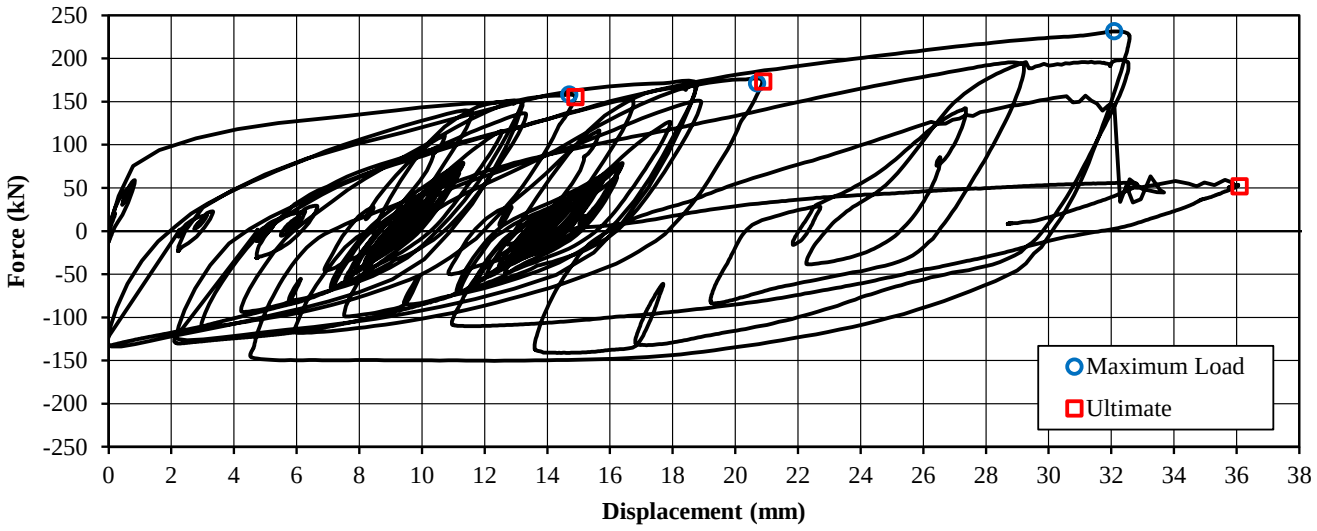
Materials:

Angle	A36	
F_y	343	MPa
F_u	500	MPa
ε_u	0.2620	
Bolt	A490	
Column bolts	1000	lbf-ft
Plate bolts	1000	lbf-ft

Key response parameters:

Signal factor	100%	125%	210%
Δ_0	0.0	2.1	4.7
$F_{F\ Max}$	158	171	231
$\Delta_{F\ Max}$	14.7	20.7	32.1
$F_{Ultimate}$	155	173	52
$\Delta_{ultimate}$	14.9	20.9	36.1

Force-displacement





Test TC16-7

Type Snug-Thight

Loading Rate: 100 με/s

Failure mode: Column

Geometry:

g_{column}	114	mm
t	12.700	mm
g_{beam}	76	mm
φ_{bolt}	25.4	mm
k	25.400	mm
g_2	68.3	mm
g_2/t	5.38	

Materials:

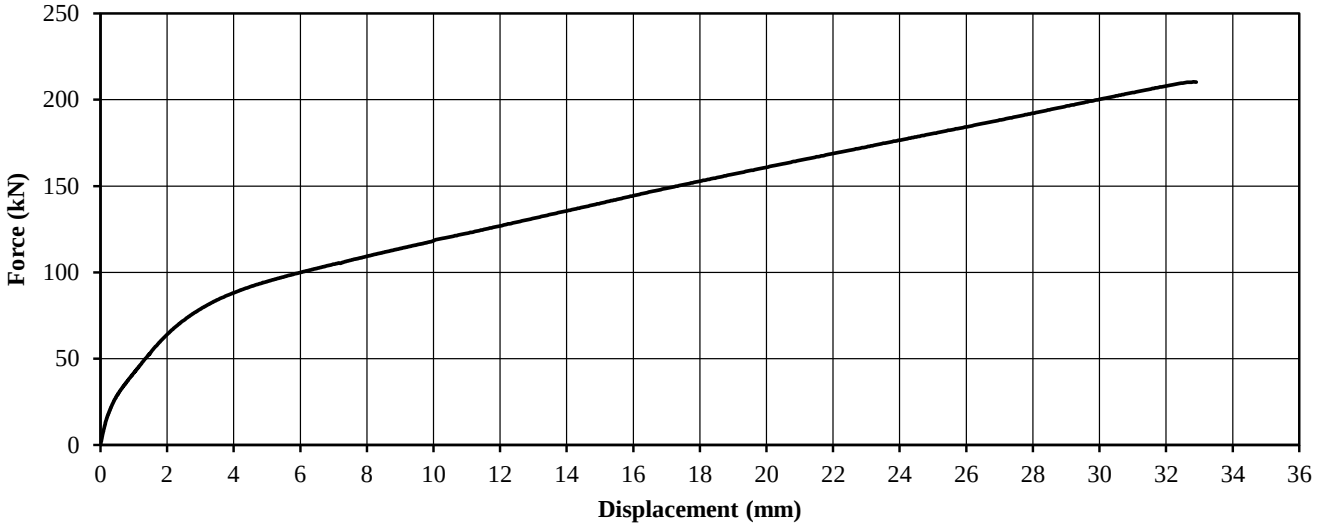
Angle	A36	
F_y	343	MPa
F_u	500	MPa
ε_u	0.2620	
Bolt	A490	
Column bolts	Snug-Thight	
Plate bolts	1000	lbf-ft

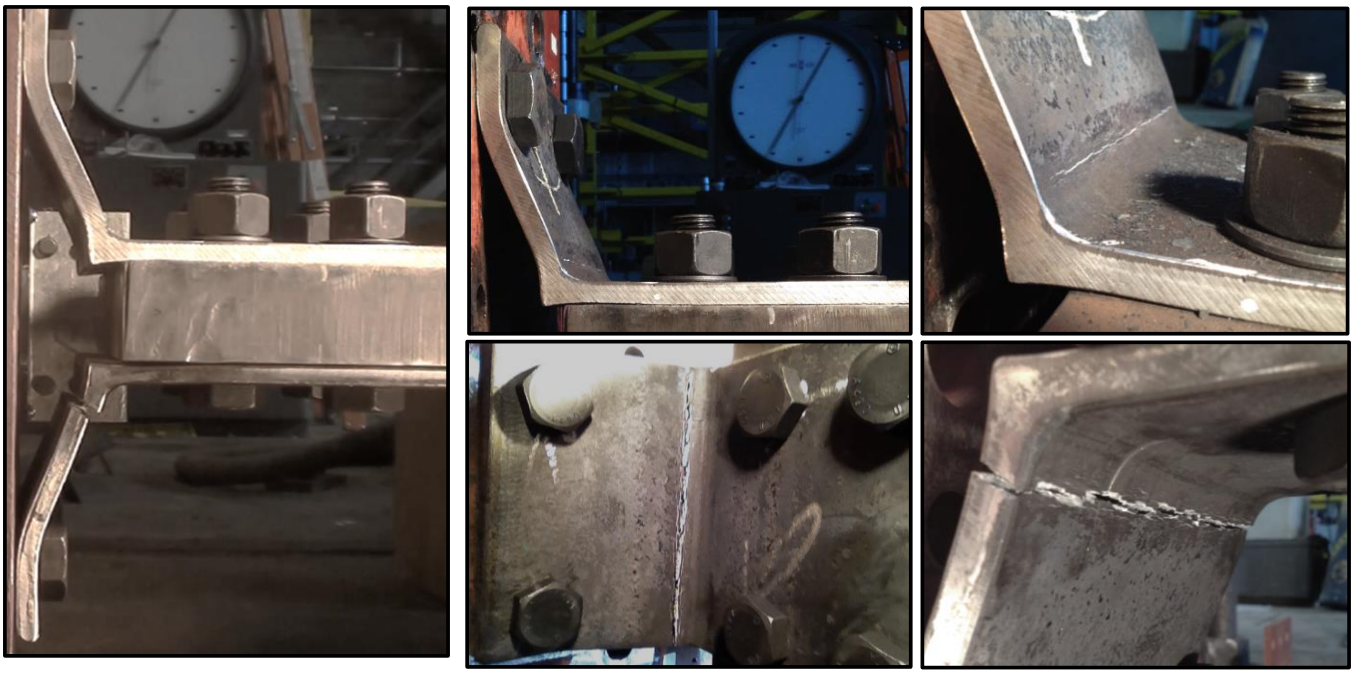
Key response parameters:

$K_{Plastic}$	4.2	kN/mm
$K_{Softening}$	-	kN/mm
$K_{Hardening}$	-	kN/mm

	F (kN)	Δ (mm)
Initial	-	-
Plastic	101	6.2
Softening	-	-
Hardening	-	-
Max. Force	210	32.9
Ultimate	210	32.9

Force-displacement





Test TC17-1

Type Monotonic Static

Loading Rate: 100 με/s

Failure mode: Column

Geometry:

g_{column}	114	mm
t	15.875	mm
g_{beam}	76	mm
φ_{bolt}	25.4	mm
k	28.575	mm
g_2	65.1	mm
g_2/t	4.10	

Materials:

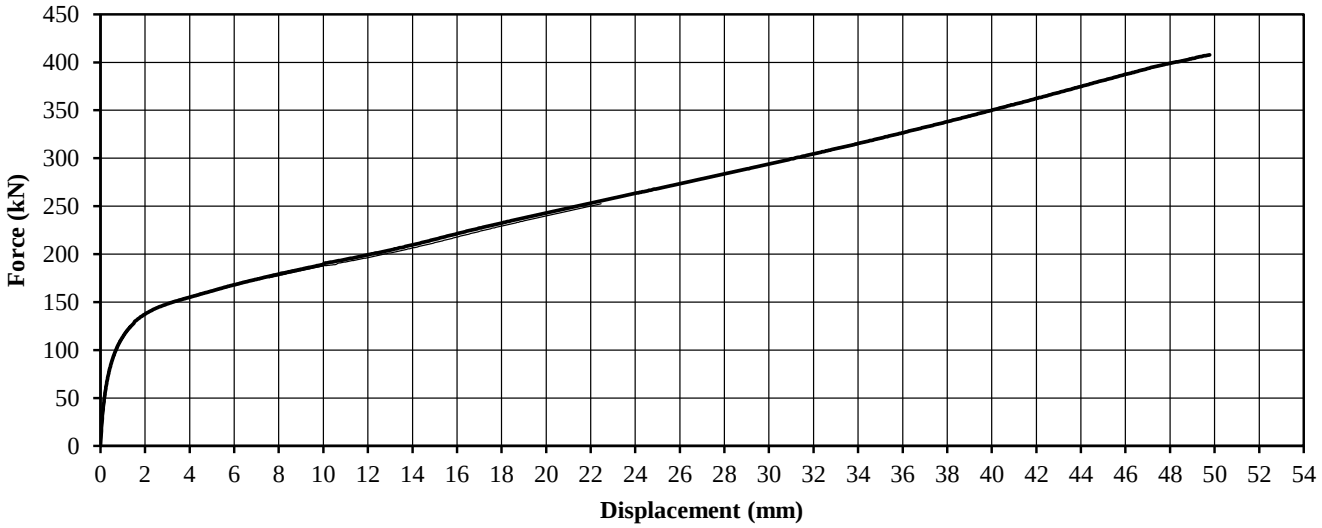
Angle	A36	
F_y	355	MPa
F_u	476	MPa
ε_u	0.2675	
Bolt	A490	
Column bolts	1000	lbf-ft
Plate bolts	1000	lbf-ft

Key response parameters:

$K_{Plastic}$	5.5	kN/mm
$K_{Softening}$	-	kN/mm
$K_{Hardening}$	-	kN/mm

	F (kN)	Δ (mm)
Initial	-	-
Plastic	161	4.9
Softening	-	-
Hardening	-	-
Max. Force	408	49.8
Ultimate	408	49.8

Force-displacement





Test TC17-2

Type Monotonic Static

Loading Rate: 600 με/s

Failure mode: Column

Geometry:

g_{column}	114	mm
t	15.875	mm
g_{beam}	76	mm
φ_{bolt}	25.4	mm
k	28.575	mm
g_2	65.1	mm
g_2/t	4.10	

Materials:

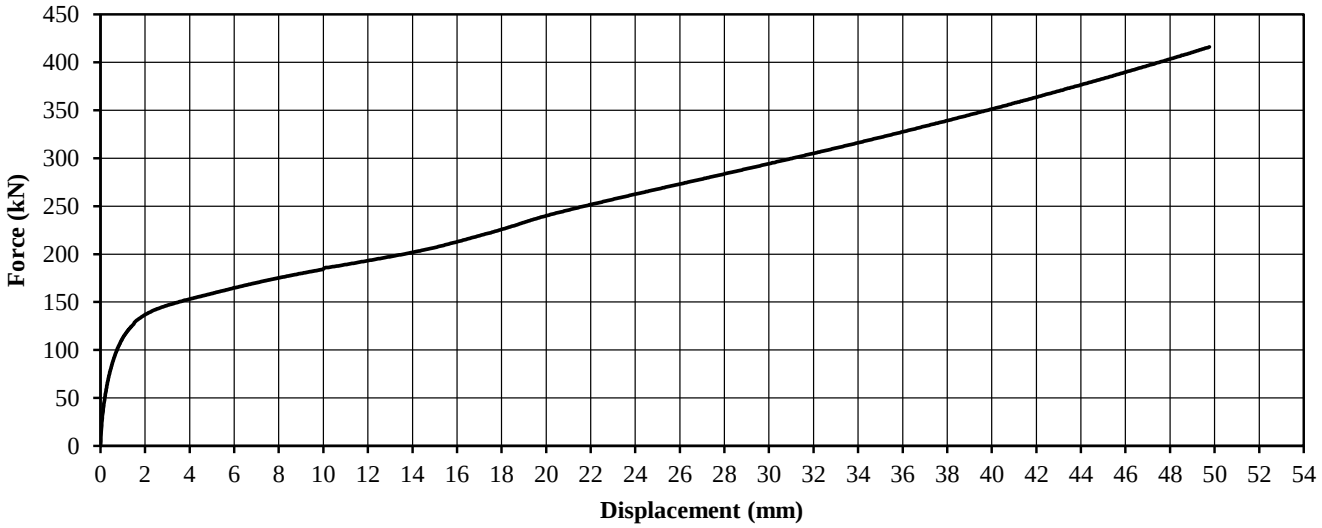
Angle	A36	
F_y	355	MPa
F_u	476	MPa
ε_u	0.2675	
Bolt	A490	
Column bolts	1000	lbf-ft
Plate bolts	1000	lbf-ft

Key response parameters:

$K_{Plastic}$	4.8	kN/mm
$K_{Softening}$	-	kN/mm
$K_{Hardening}$	5.9	kN/mm

	F (kN)	Δ (mm)
Initial	-	-
Plastic	159	5.0
Softening	-	-
Hardening	215	16.8
Max. Force	416	49.8
Ultimate	416	49.8

Force-displacement





Test TC17-3

Type Monotonic Dynamic

Loading Rate: 750000 με/s

Failure mode: Column

Key response parameters:

$K_{Plastic}$	4.9	kN/mm
$K_{Softening}$	-	kN/mm
$K_{Hardening}$	6.1	kN/mm

Geometry:

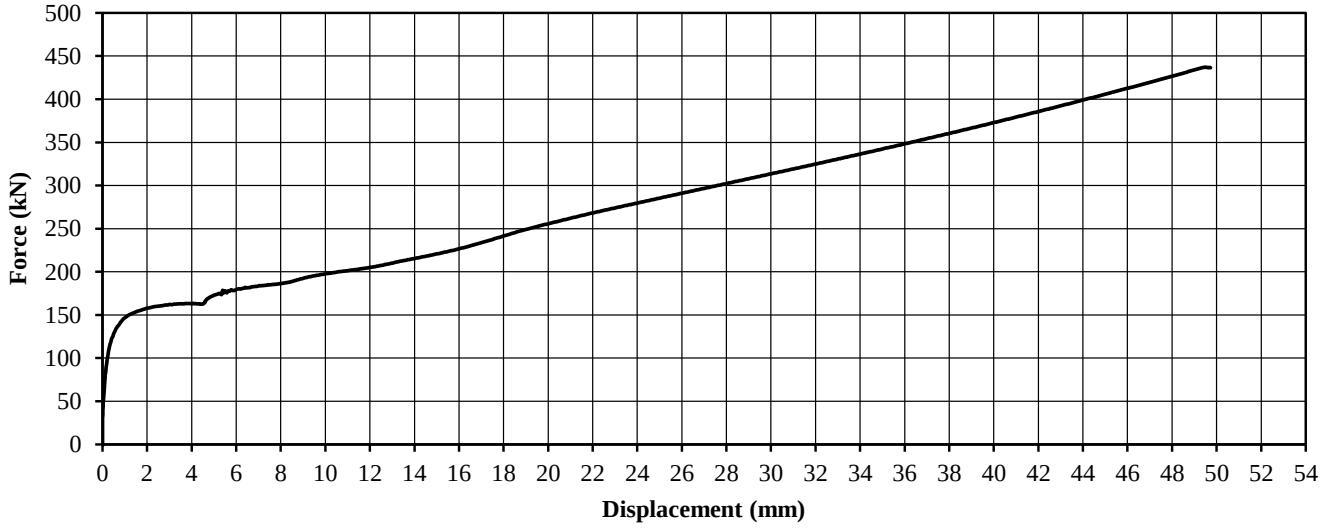
g_{column}	114	mm
t	15.875	mm
g_{beam}	76	mm
φ_{bolt}	25.4	mm
k	28.575	mm
g_2	65.1	mm
g_2/t	4.10	

Materials:

Angle	A36	
F_y	355	MPa
F_u	476	MPa
ε_u	0.2675	
Bolt	A490	
Column bolts	1000	lbf-ft
Plate bolts	1000	lbf-ft

	F (kN)	Δ (mm)
Initial	-	-
Plastic	159	2.2
Softening	-	-
Hardening	227	16.1
Max. Force	437	49.7
Ultimate	437	49.7

Force-displacement

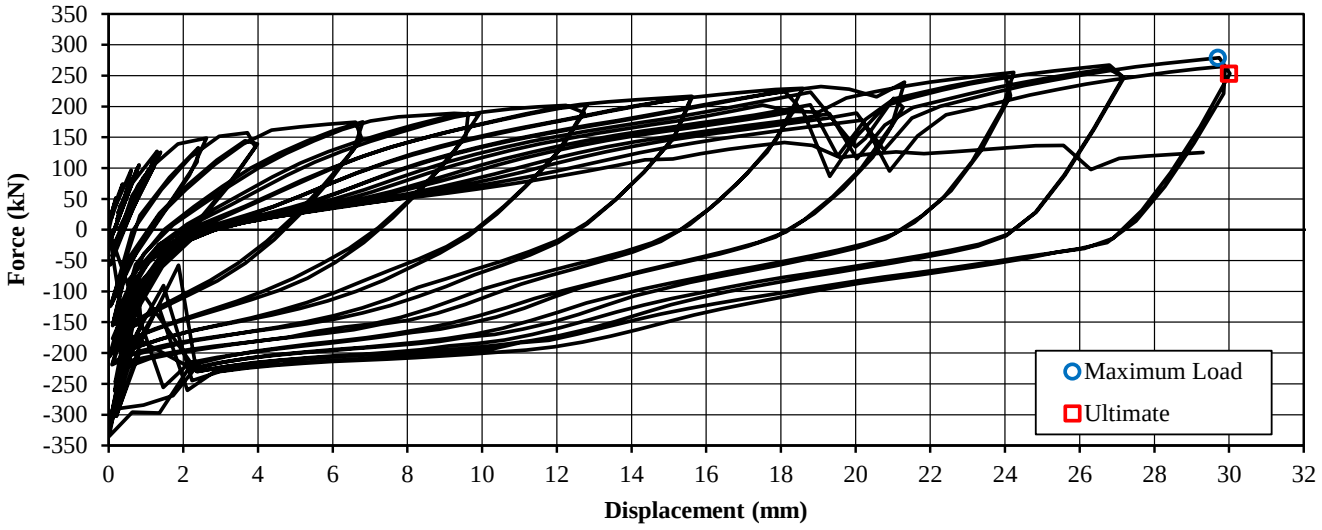




Test TC17-4

Type Cyclic W310 **Failure mode:** Column

Geometry:			Materials:			Key response parameters:		
g_{column}	114	mm	**Angle**	A36		F_{Max}	279	kN
t	15.875	mm	F_y	355	MPa	Δ_{FMax}	29.7	mm
g_{beam}	76	mm	F_u	476	MPa	$Drift_{FMax}$	11	%
φ_{bolt}	25.4	mm	ε_u	0.2675		$F_{Ultimate}$	253	kN
k	28.575	mm	**Bolt**	A490		$\Delta_{Ultimate}$	30.0	mm
g_2	65.1	mm	**Column bolts**	1000	lbf-ft	$Drift_{Ultimate}$	11	%
g_2/t	4.10		**Plate bolts**	1000	lbf-ft			

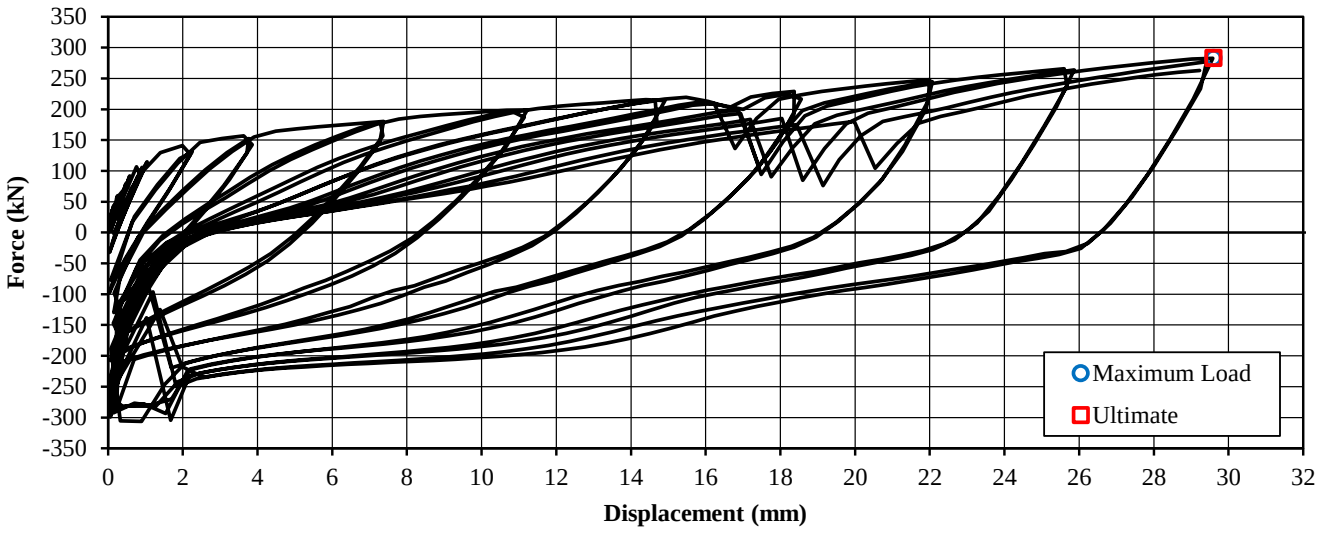




Test TC17-5

Type Cyclic W410 **Failure mode:** Column

Geometry:			Materials:			Key response parameters:		
g_{column}	114	mm	**Angle**	A36		F_{Max}	283	kN
t	15.875	mm	F_y	355	MPa	Δ_{FMax}	29.6	mm
g_{beam}	76	mm	F_u	476	MPa	$Drift_{FMax}$	9	%
φ_{bolt}	25.4	mm	ε_u	0.2675		$F_{Ultimate}$	283	kN
k	28.575	mm	**Bolt**	A490		$\Delta_{Ultimate}$	29.6	mm
g_2	65.1	mm	**Column bolts**	1000	lbf-ft	$Drift_{Ultimate}$	9	%
g_2/t	4.10		**Plate bolts**	1000	lbf-ft			





Test TC18-1

Type Monotonic Static

Loading Rate: 100 με/s

Failure mode: Bolt

Geometry:

g_{column}	114	mm
t	19.05	mm
g_{beam}	76	mm
φ_{bolt}	25.4	mm
k	31.75	mm
g_2	61.9	mm
g_2/t	3.25	

Materials:

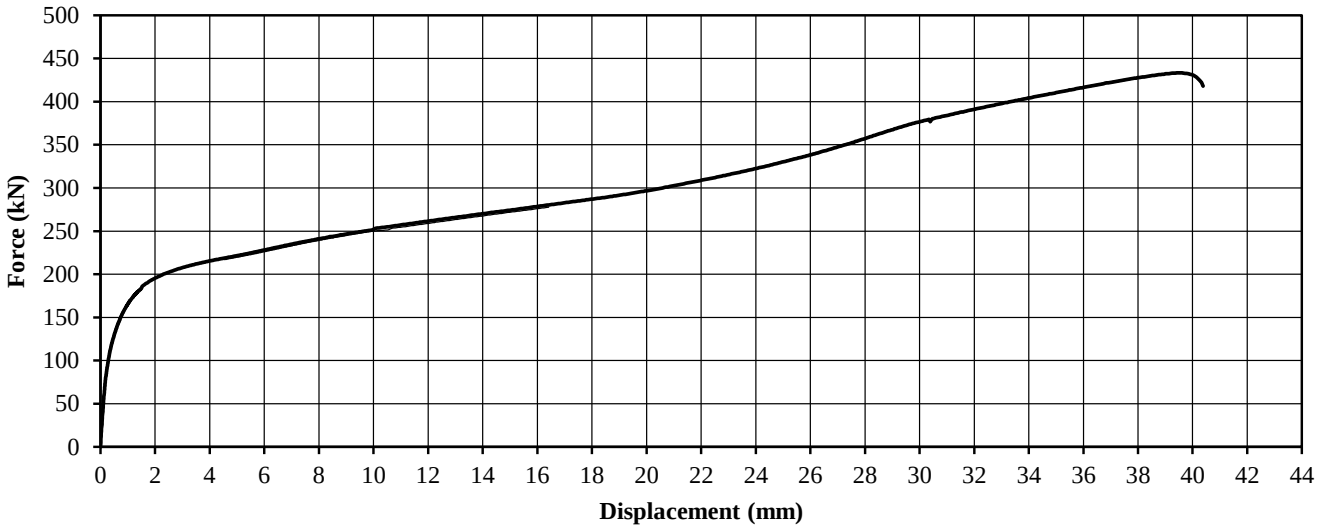
Angle	A36	
F_y	370	MPa
F_u	485	MPa
ε_u	0.2633	
Bolt	A490	
Column bolts	1000	lbf-ft
Plate bolts	1000	lbf-ft

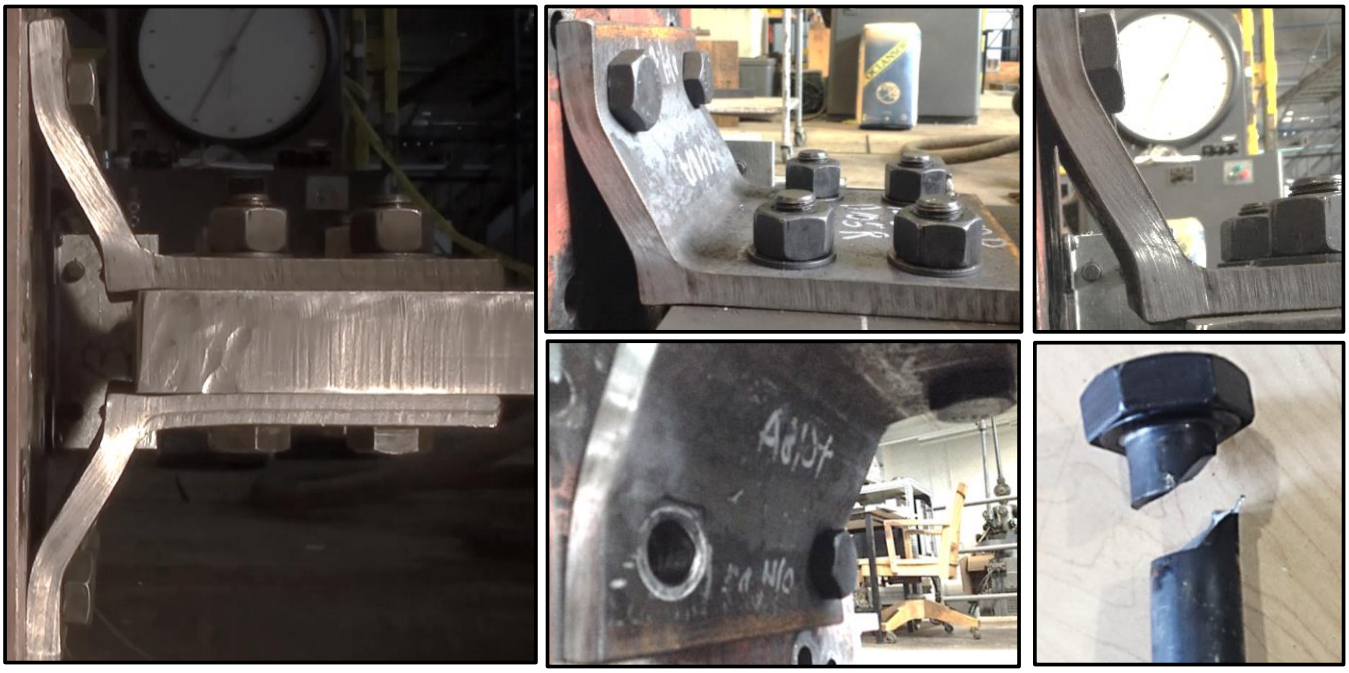
Key response parameters:

$K_{Plastic}$	5.8	kN/mm
$K_{Softening}$	4.4	kN/mm
$K_{Hardening}$	7.4	kN/mm

	F (kN)	Δ (mm)
Initial	-	-
Plastic	220	4.8
Softening	258	-
Hardening	294	11.3
Max. Force	433	39.4
Ultimate	418	40.4

Force-displacement





Test TC18-2

Type Monotonic Static

Loading Rate: 600 με/s

Failure mode: Bolt

Geometry:

g_{column}	114	mm
t	19.050	mm
g_{beam}	76	mm
φ_{bolt}	25.4	mm
k	31.750	mm
g_2	61.9	mm
g_2/t	3.25	

Materials:

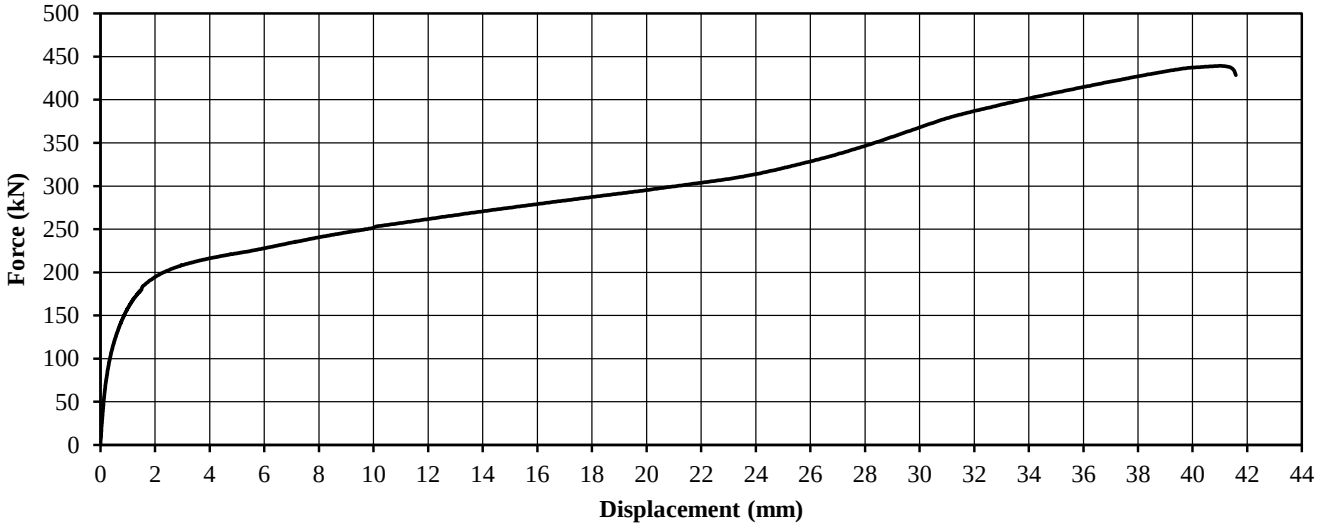
Angle	A36	
F_y	370	MPa
F_u	485	MPa
ε_u	0.2633	
Bolt	A490	
Column bolts	1000	lbf-ft
Plate bolts	1000	lbf-ft

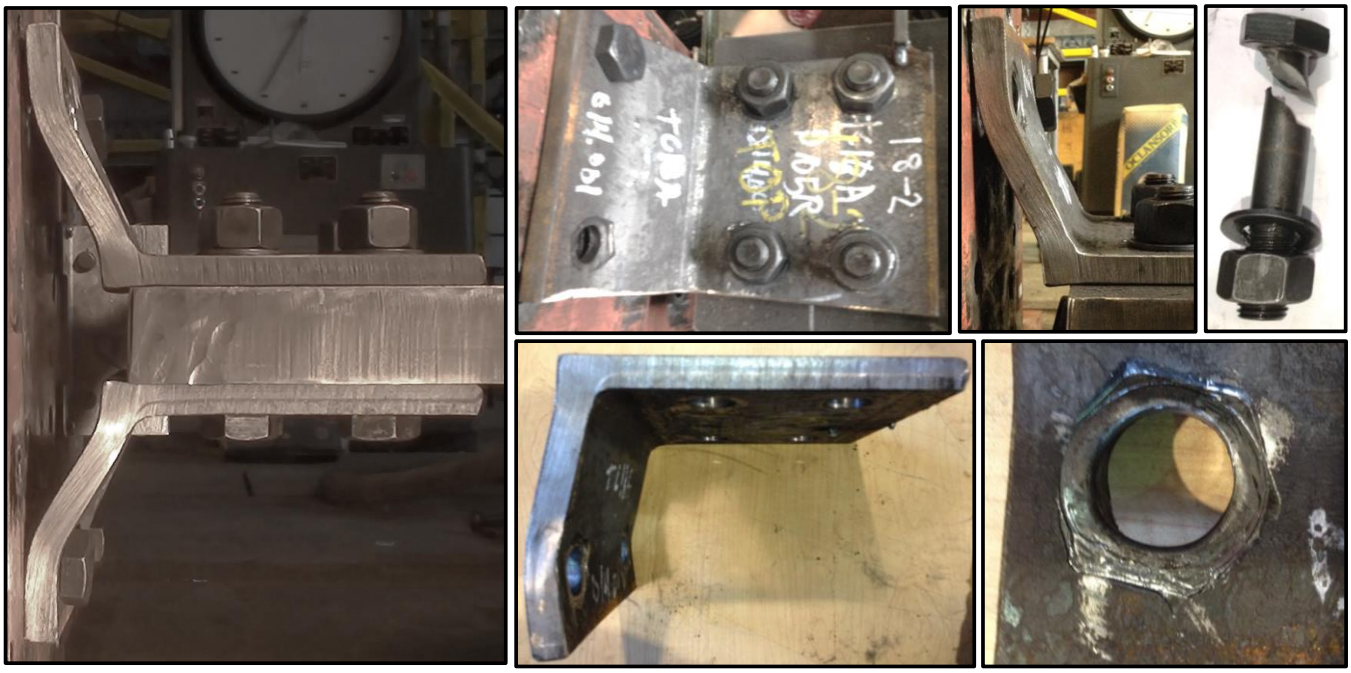
Key response parameters:

$K_{Plastic}$	6.0	kN/mm
$K_{Softening}$	4.3	kN/mm
$K_{Hardening}$	8.6	kN/mm

	F (kN)	Δ (mm)
Initial	-	-
Plastic	222	4.9
Softening	257	10.9
Hardening	313	23.9
Max. Force	439	40.9
Ultimate	429	41.6

Force-displacement





Test TC18-3

Type Monotonic Dynamic

Loading Rate: 750000 με/s

Failure mode: Bolt

Geometry:

g_{column}	114	mm
t	19.050	mm
g_{beam}	76	mm
φ_{bolt}	25.4	mm
k	31.750	mm
g_2	61.9	mm
g_2/t	3.25	

Materials:

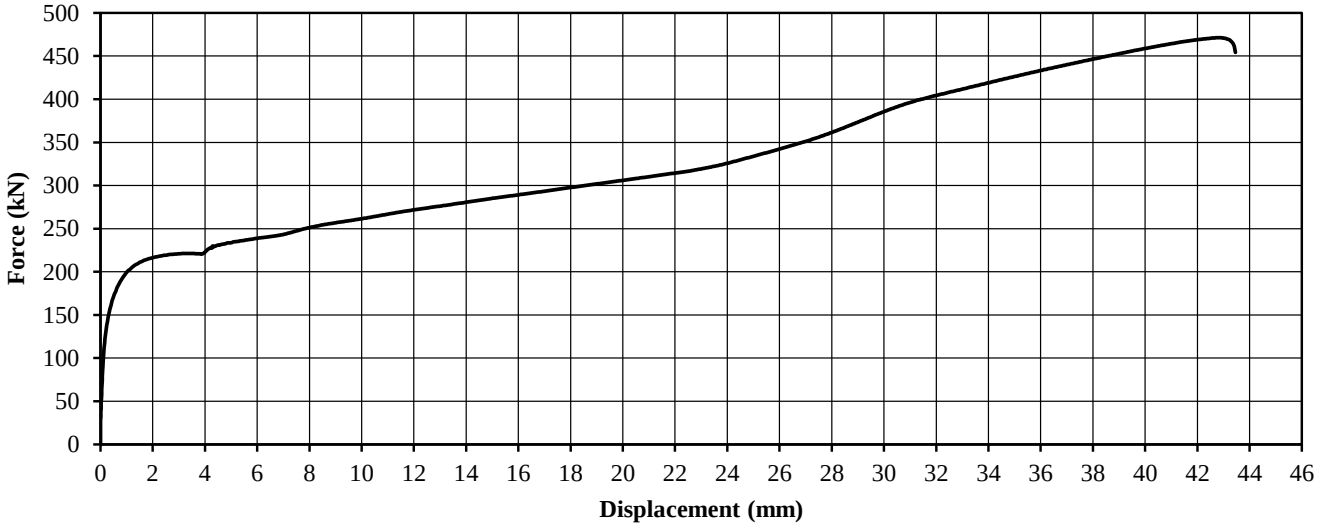
Angle	A36	
F_y	370	MPa
F_u	485	MPa
ε_u	0.2633	
Bolt	A490	
Column bolts	1000	lbf-ft
Plate bolts	1000	lbf-ft

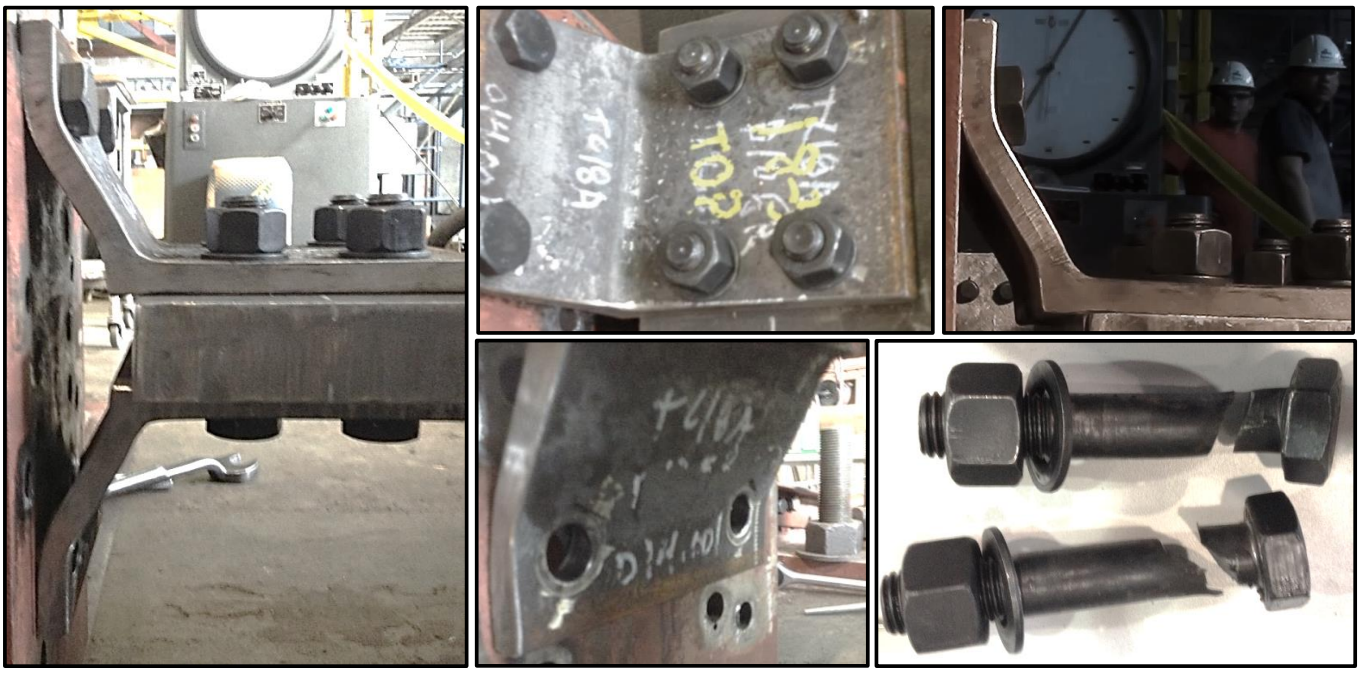
Key response parameters:

$K_{Plastic}$	5.4	kN/mm
$K_{Softening}$	4.4	kN/mm
$K_{Hardening}$	8.6	kN/mm

	F (kN)	Δ (mm)
Initial	-	-
Plastic	220	2.6
Softening	275	12.8
Hardening	320	22.8
Max. Force	471	42.8
Ultimate	454	43.5

Force-displacement



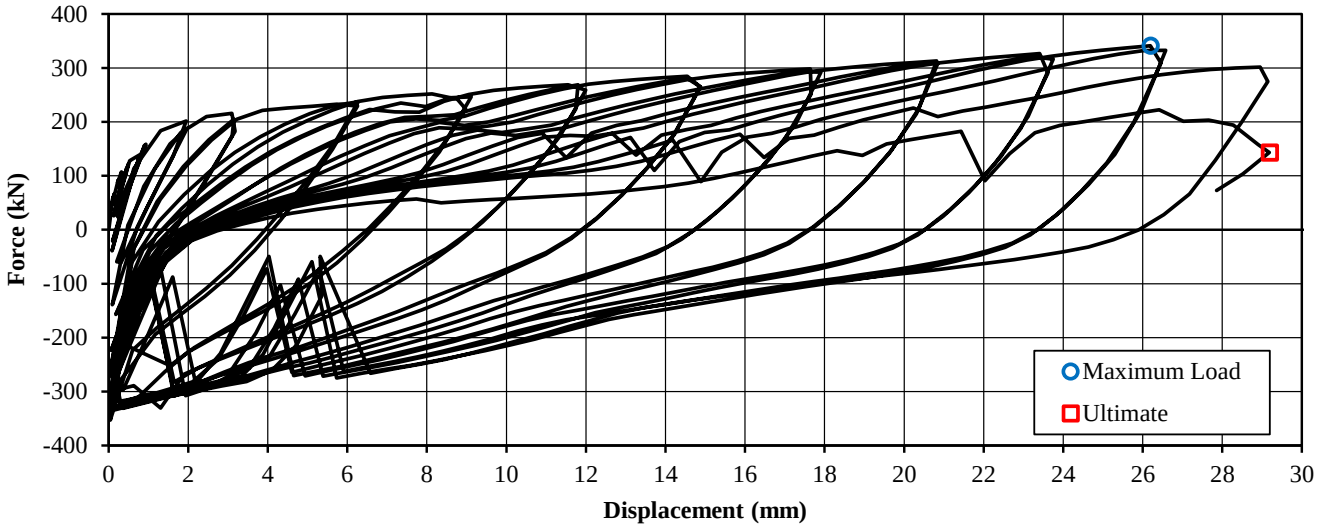


Test TC18-4

Type Cyclic W310 **Failure mode:** Column

Geometry:			Materials:			Key response parameters:		
g_{column}	114	mm	**Angle**	A36		F_{Max}	341	kN
t	19.050	mm	F_y	370	MPa	Δ_{FMax}	26.2	mm
g_{beam}	76	mm	F_u	485	MPa	$Drift_{FMax}$	10	%
φ_{bolt}	25.4	mm	ε_u	0.2633		$F_{Ultimate}$	143	kN
k	31.750	mm	**Bolt**	A490		$\Delta_{Ultimate}$	29.2	mm
g_2	61.9	mm	**Column bolts**	1000	lbf-ft	$Drift_{Ultimate}$	11	%
g_2/t	3.25		**Plate bolts**	1000	lbf-ft			

Force-displacement



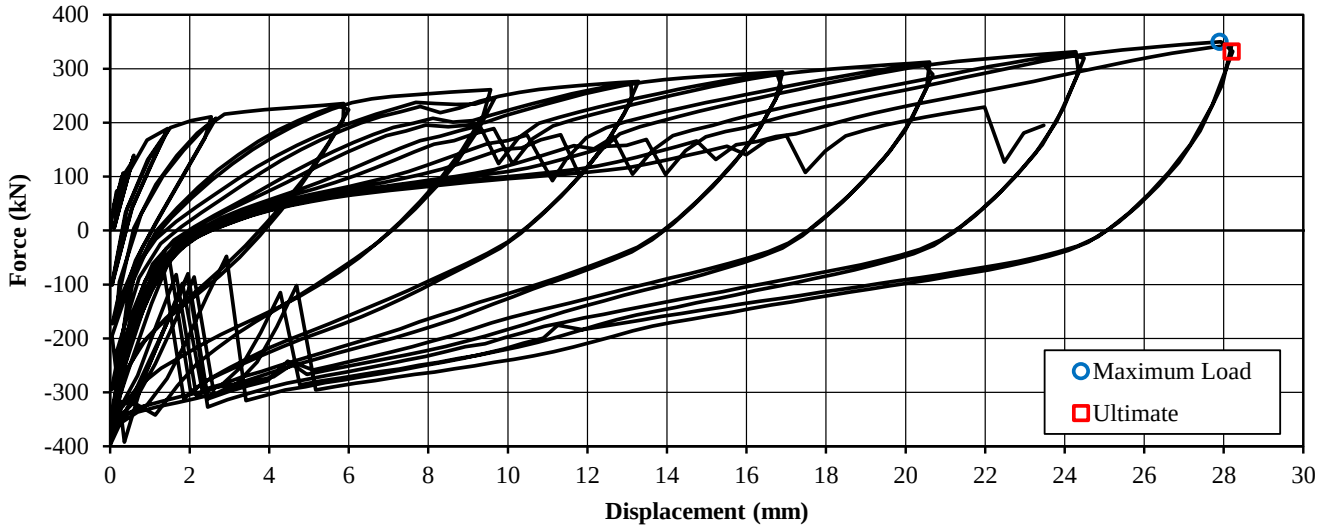


Test TC18-5

Type Cyclic W410 **Failure mode:** Column

Geometry:			Materials:			Key response parameters:		
g_{column}	114	mm	**Angle**	A36		F_{Max}	350	kN
t	19.050	mm	F_y	370	MPa	Δ_{FMax}	27.9	mm
g_{beam}	76	mm	F_u	485	MPa	$Drift_{FMax}$	9	%
φ_{bolt}	25.4	mm	ε_u	0.2633		$F_{Ultimate}$	332	kN
k	31.750	mm	**Bolt**	A490		$\Delta_{Ultimate}$	28.2	mm
g_2	61.9	mm	**Column bolts**	1000	lbf-ft	$Drift_{Ultimate}$	9	%
g_2/t	3.25		**Plate bolts**	1000	lbf-ft			

Force-displacement





Test TC18-6

Type Time-History **Failure mode:** Bolt

Geometry:

g_{column}	114	mm
t	19.050	mm
g_{beam}	76	mm
φ_{bolt}	25.4	mm
k	31.750	mm
g_2	61.9	mm
g_2/t	3.25	

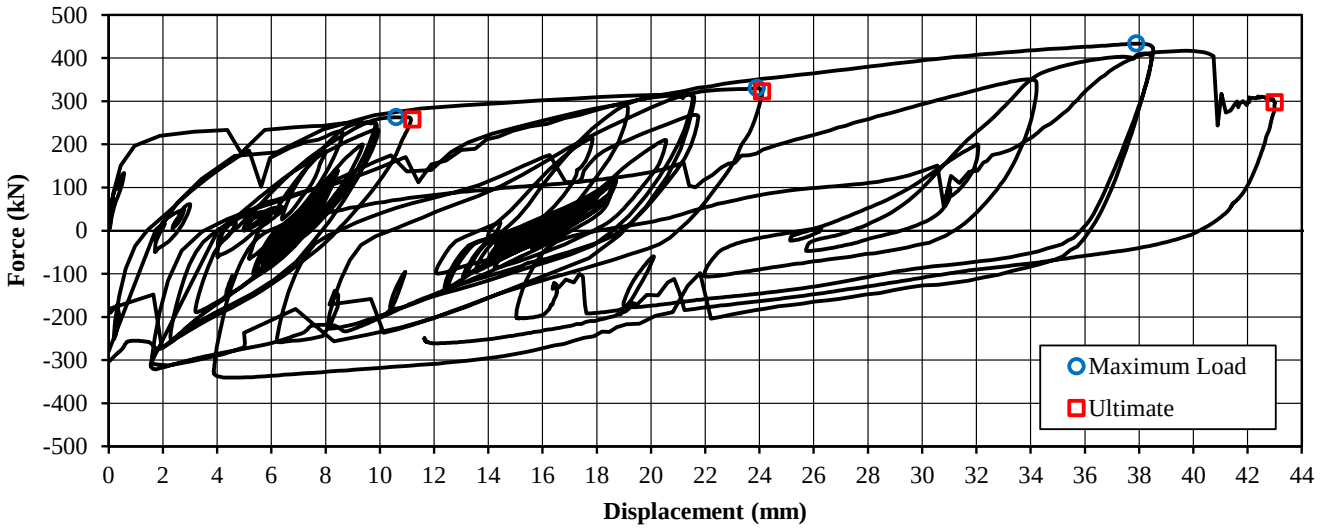
Materials:

Angle	A36	
F_y	370	MPa
F_u	485	MPa
ε_u	0.2633	
Bolt	A490	
Column bolts	1000	lbf-ft
Plate bolts	1000	lbf-ft

Key response parameters:

Signal factor	75%	150%	260%
Δ_0	0.0	1.7	4.0
$F_{F\ Max}$	263	330	433
$\Delta_{F\ Max}$	10.6	23.9	37.9
$F_{Ultimate}$	257	322	297
$\Delta_{ultimate}$	11.2	24.1	43.0

Force-displacement





Test TC19-1

Type Monotonic Static

Loading Rate: 100 με/s

Failure mode: Column

Geometry:

g_{column}	64	mm
t	7.94	mm
g_{beam}	57	mm
φ_{bolt}	19.1	mm
k	17.5	mm
g_2	30.2	mm
g_2/t	3.80	

Materials:

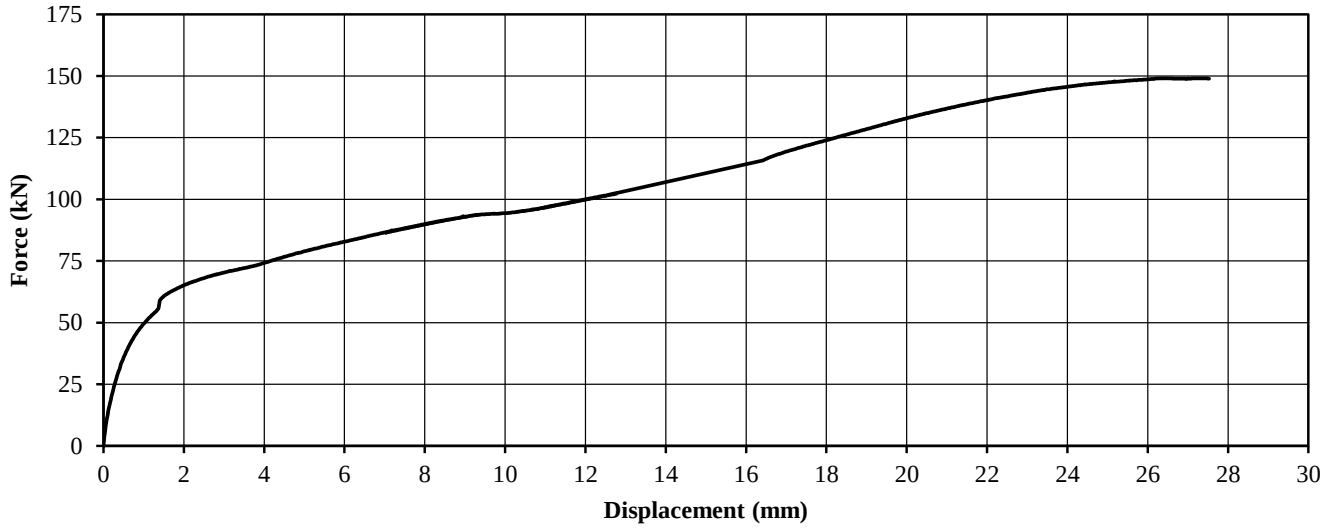
Angle	A36	
F_y	373	MPa
F_u	507	MPa
ε_u	0.2415	
Bolt	A325	
Column bolts	400	lbf-ft
Plate bolts	400	lbf-ft

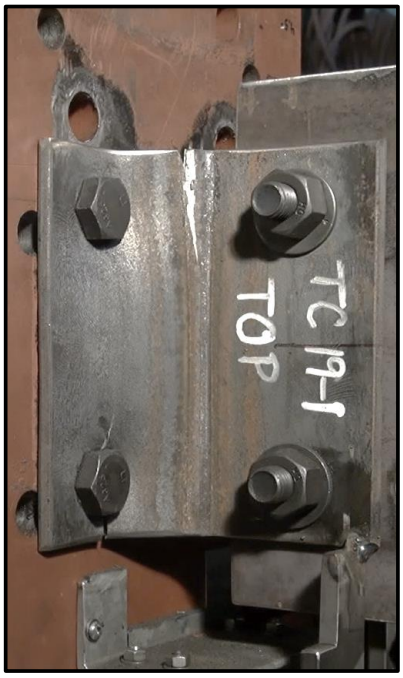
Key response parameters:

$K_{Plastic}$	3.0	kN/mm
$K_{Softening}$	-	kN/mm
$K_{Hardening}$	4.1	kN/mm

	F (kN)	Δ (mm)
Initial	-	-
Plastic	78	4.8
Softening	-	-
Hardening	101	12.4
Max. Force	149	27.5
Ultimate	149	27.5

Force-displacement











Test TC19-2

Type Monotonic Static

Loading Rate: 600 με/s

Failure mode: Column

Geometry:

g_{column}	64	mm
t	7.938	mm
g_{beam}	57	mm
φ_{bolt}	19.1	mm
k	17.475	mm
g_2	30.2	mm
g_2/t	3.80	

Materials:

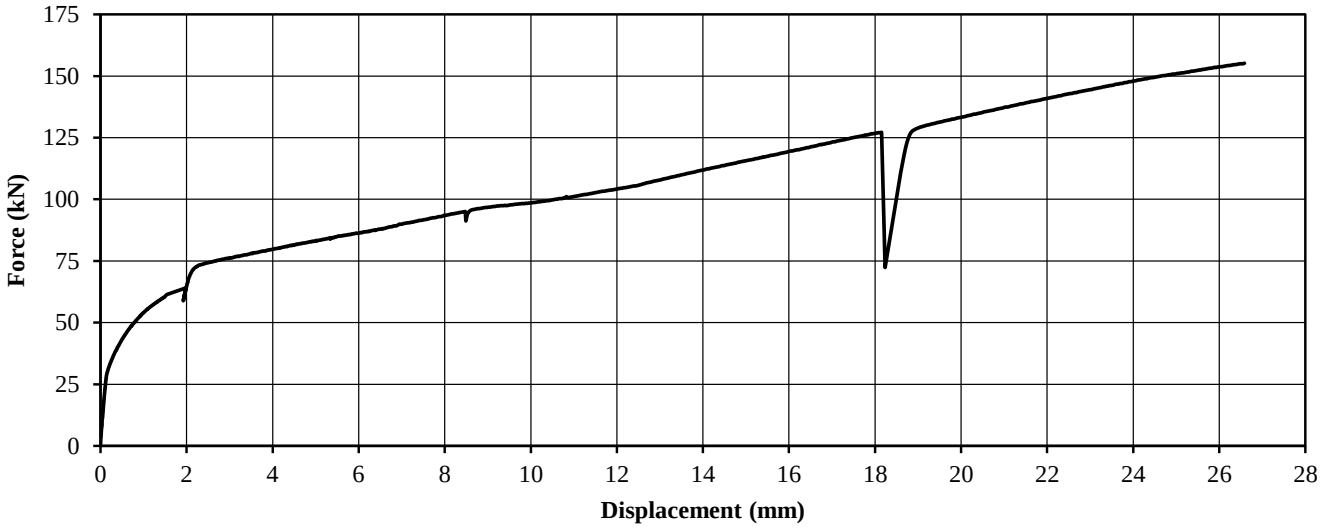
Angle	A36	
F_y	373	MPa
F_u	507	MPa
ε_u	0.2415	
Bolt	A325	
Column bolts	400	lbf-ft
Plate bolts	400	lbf-ft

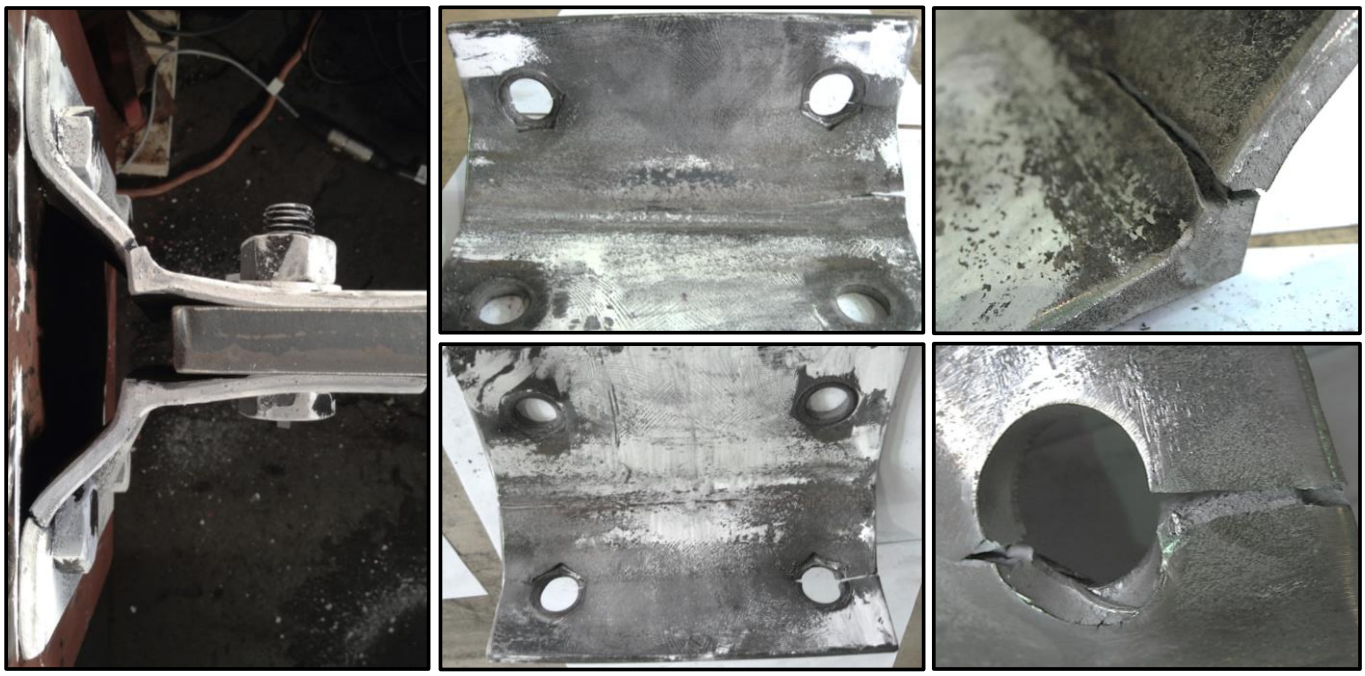
Key response parameters:

$K_{Plastic}$	3.0	kN/mm
$K_{Softening}$	-	kN/mm
$K_{Hardening}$	3.8	kN/mm

	F (kN)	Δ (mm)
Initial	30	0.143
Plastic	81	4.2
Softening	-	-
Hardening	104	12.0
Max. Force	155	26.6
Ultimate	155	26.6

Force-displacement





Test TC19-3

Type Monotonic Dynamic

Loading Rate: 750000 με/s

Failure mode: Column

Geometry:

g_{column}	64	mm
t	7.938	mm
g_{beam}	57	mm
φ_{bolt}	19.1	mm
k	17.475	mm
g_2	30.2	mm
g_2/t	3.80	

Materials:

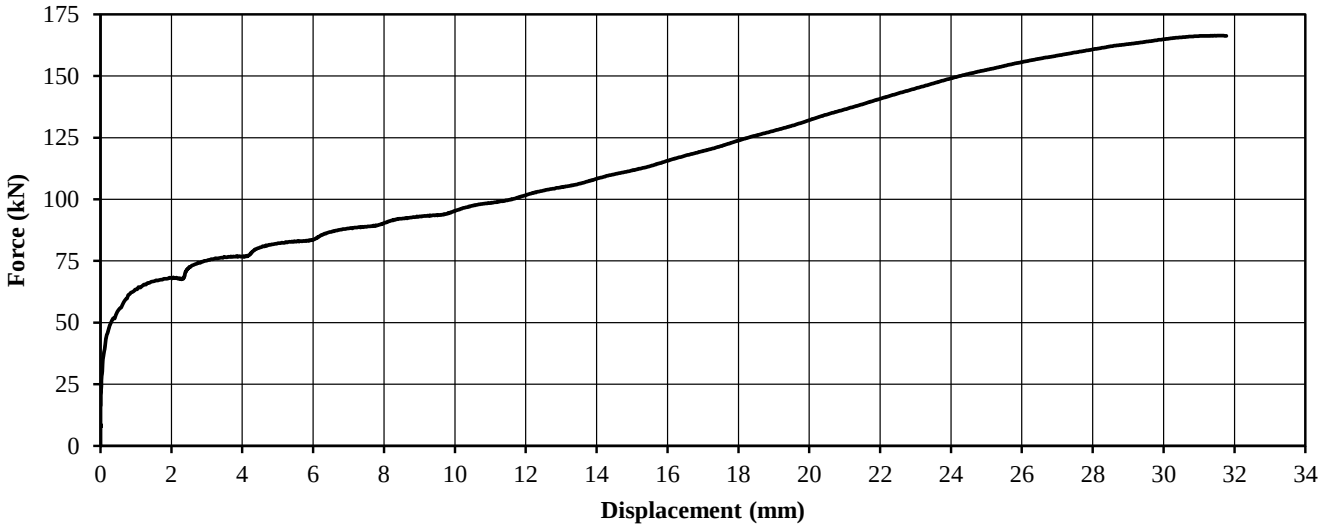
Angle	A36	
F_y	373	MPa
F_u	507	MPa
ε_u	0.2415	
Bolt	A325	
Column bolts	400	lbf-ft
Plate bolts	400	lbf-ft

Key response parameters:

$K_{Plastic}$	3.0	kN/mm
$K_{Softening}$	-	kN/mm
$K_{Hardening}$	4.2	kN/mm

	F (kN)	Δ (mm)
Initial	21	0.012
Plastic	73	2.6
Softening	-	-
Hardening	108	14.3
Max. Force	166	31.8
Ultimate	166	31.8

Force-displacement

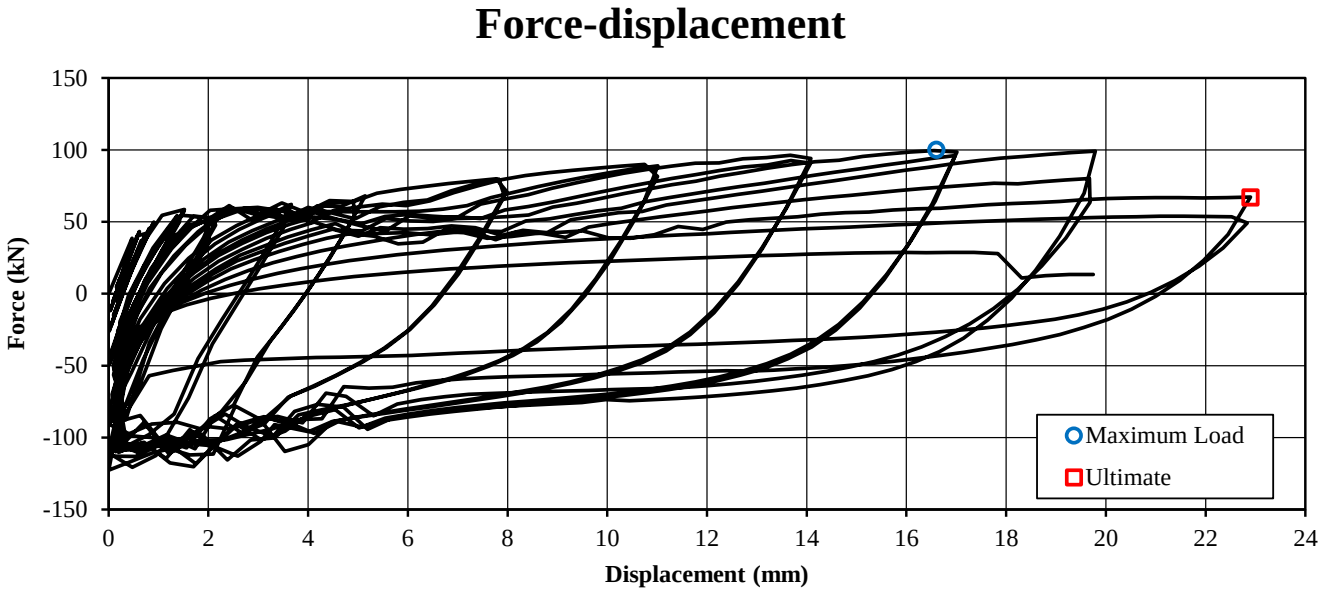




Test TC19-4

Type Cyclic W310 **Failure mode:** Column

Geometry:			Materials:			Key response parameters:		
g_{column}	64	mm	**Angle**	A36		F_{Max}	100	kN
t	7.938	mm	F_y	373	MPa	Δ_{FMax}	16.6	mm
g_{beam}	57	mm	F_u	507	MPa	$Drift_{FMax}$	6	%
φ_{bolt}	19.1	mm	ε_u	0.2415		$F_{Ultimate}$	67	kN
k	17.475	mm	**Bolt**	A325		$\Delta_{Ultimate}$	22.9	mm
g_2	30.2	mm	**Column bolts**	400	lbf-ft	$Drift_{Ultimate}$	8	%
g_2/t	3.80		**Plate bolts**	400	lbf-ft			

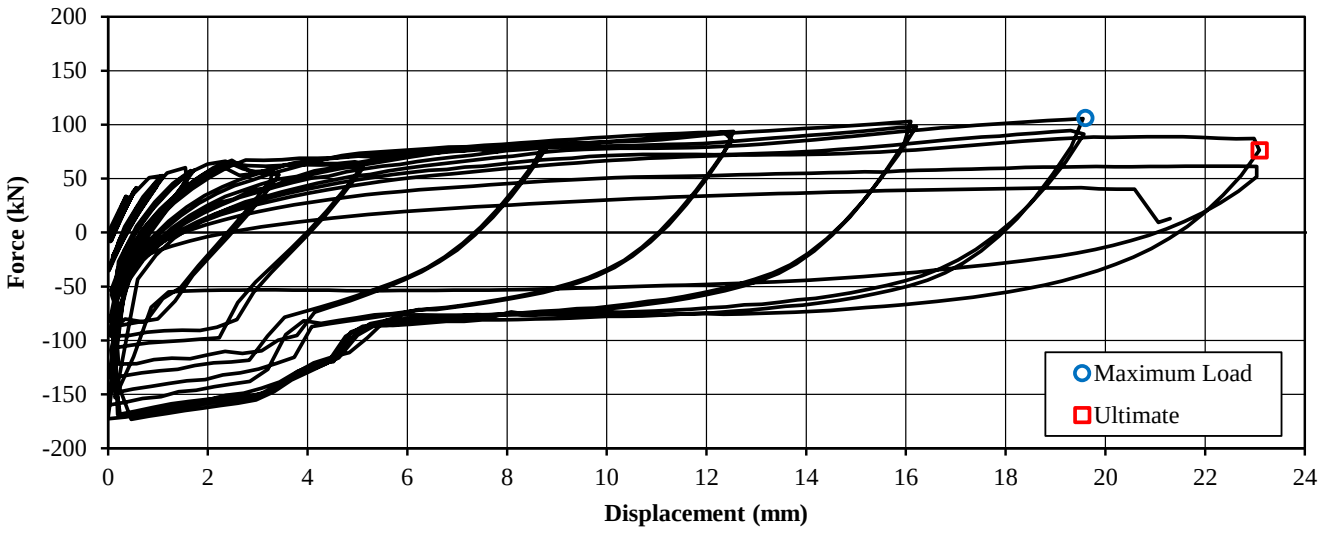




Test TC19-5

Type Cyclic W410 **Failure mode:** Column/Beam

Geometry:			Materials:			Key response parameters:		
g_{column}	64	mm	**Angle**	A36		F_{Max}	106	kN
t	7.938	mm	F_y	373	MPa	Δ_{FMax}	19.6	mm
g_{beam}	57	mm	F_u	507	MPa	$Drift_{FMax}$	6	%
φ_{bolt}	19.1	mm	ε_u	0.2415		$F_{Ultimate}$	76	kN
k	17.475	mm	**Bolt**	A325		$\Delta_{Ultimate}$	23.1	mm
g_2	30.2	mm	**Column bolts**	400	lbf-ft	$Drift_{Ultimate}$	7	%
g_2/t	3.80		**Plate bolts**	400	lbf-ft			





Test TC19-6

Type Snug-Thight

Loading Rate: 100 με/s

Failure mode: Column

Key response parameters:

$K_{Plastic}$	3.8	kN/mm
$K_{Softening}$	-	kN/mm
$K_{Hardening}$	-	kN/mm

Geometry:

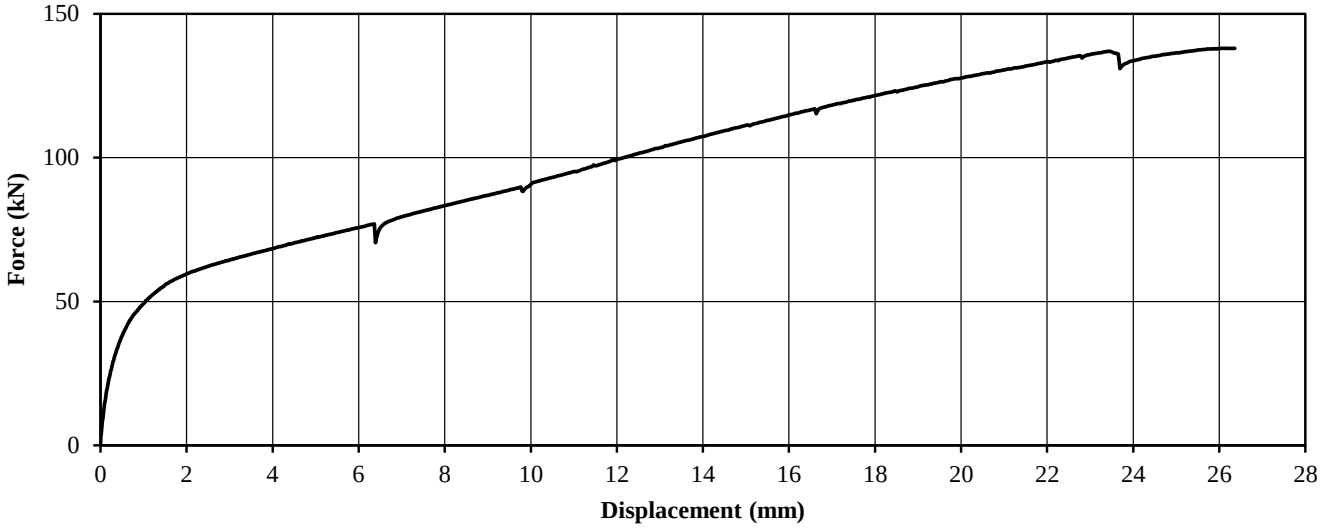
g_{column}	64	mm
t	7.938	mm
g_{beam}	57	mm
φ_{bolt}	19.1	mm
k	17.475	mm
g_2	30.2	mm
g_2/t	3.80	

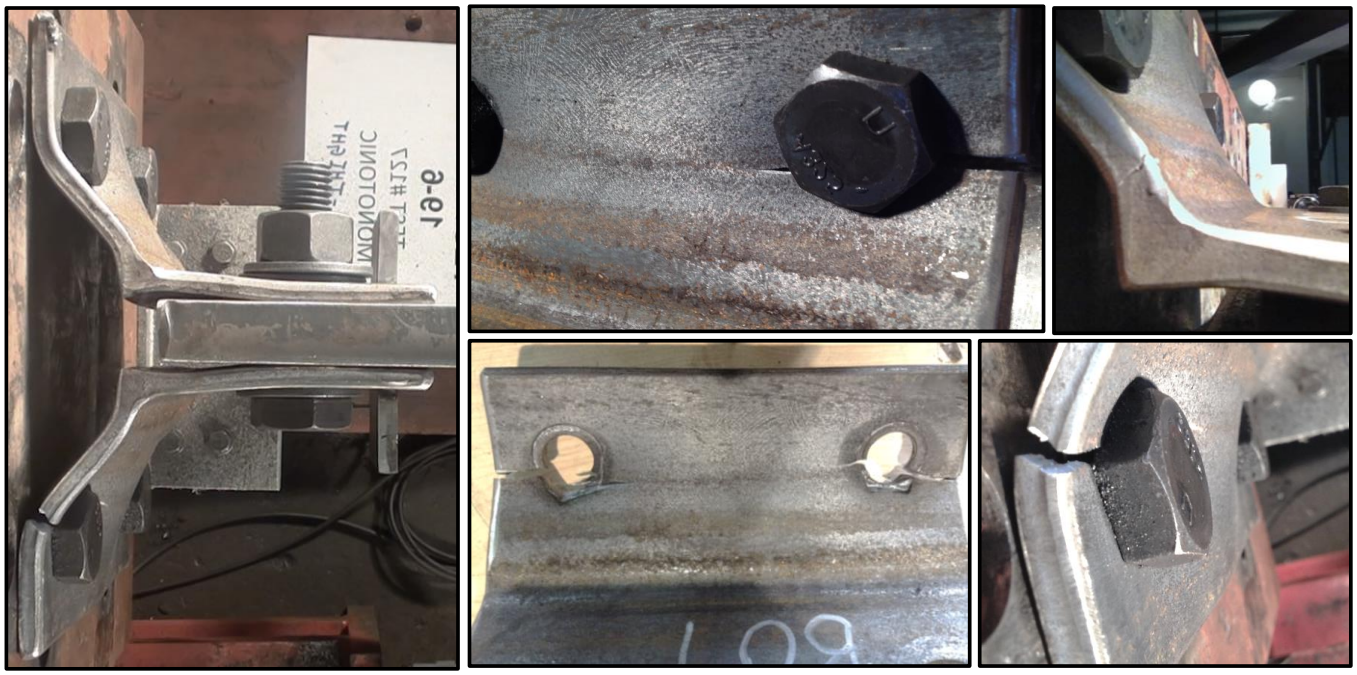
Materials:

Angle	A36	
F_y	373	MPa
F_u	507	MPa
ε_u	0.2415	
Bolt	A325	
Column bolts	Snug-Thight	
Plate bolts	400	lbf-ft

	F (kN)	Δ (mm)
Initial	-	-
Plastic	65	3.1
Softening	-	-
Hardening	-	-
Max. Force	138	26.4
Ultimate	138	26.4

Force-displacement





Test TC19-7

Type Time-History **Failure mode:** Column

Geometry:

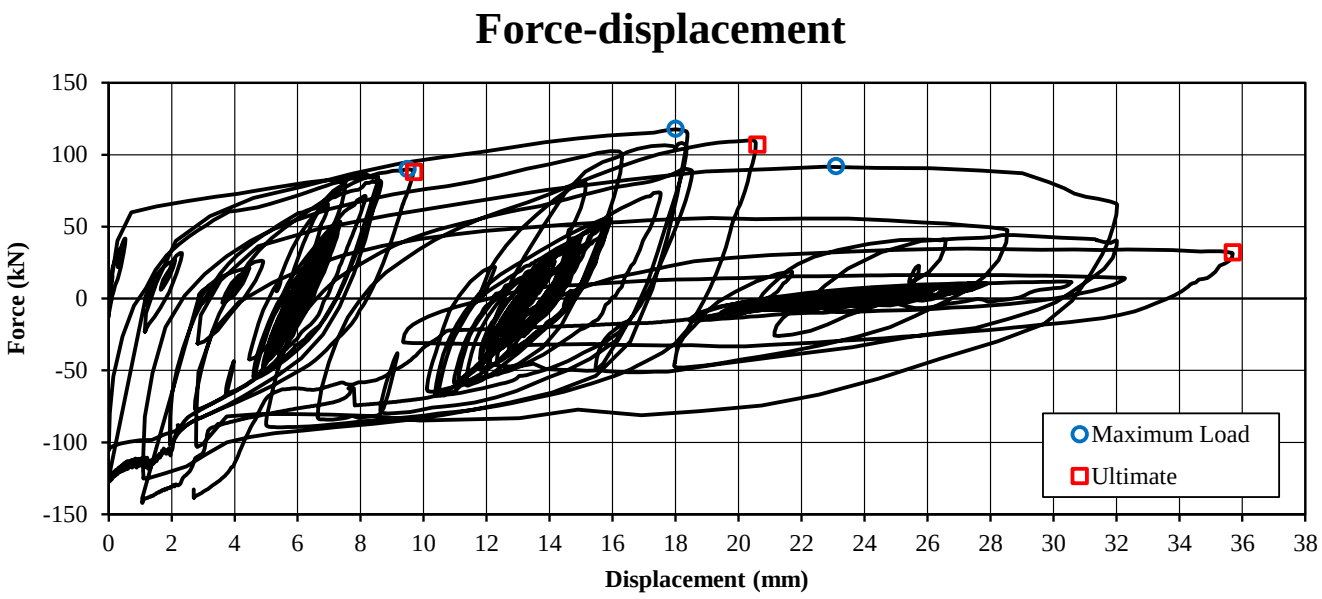
g_{column}	64	mm
t	7.938	mm
g_{beam}	57	mm
φ_{bolt}	19.1	mm
k	17.475	mm
g_2	30.2	mm
g_2/t	3.80	

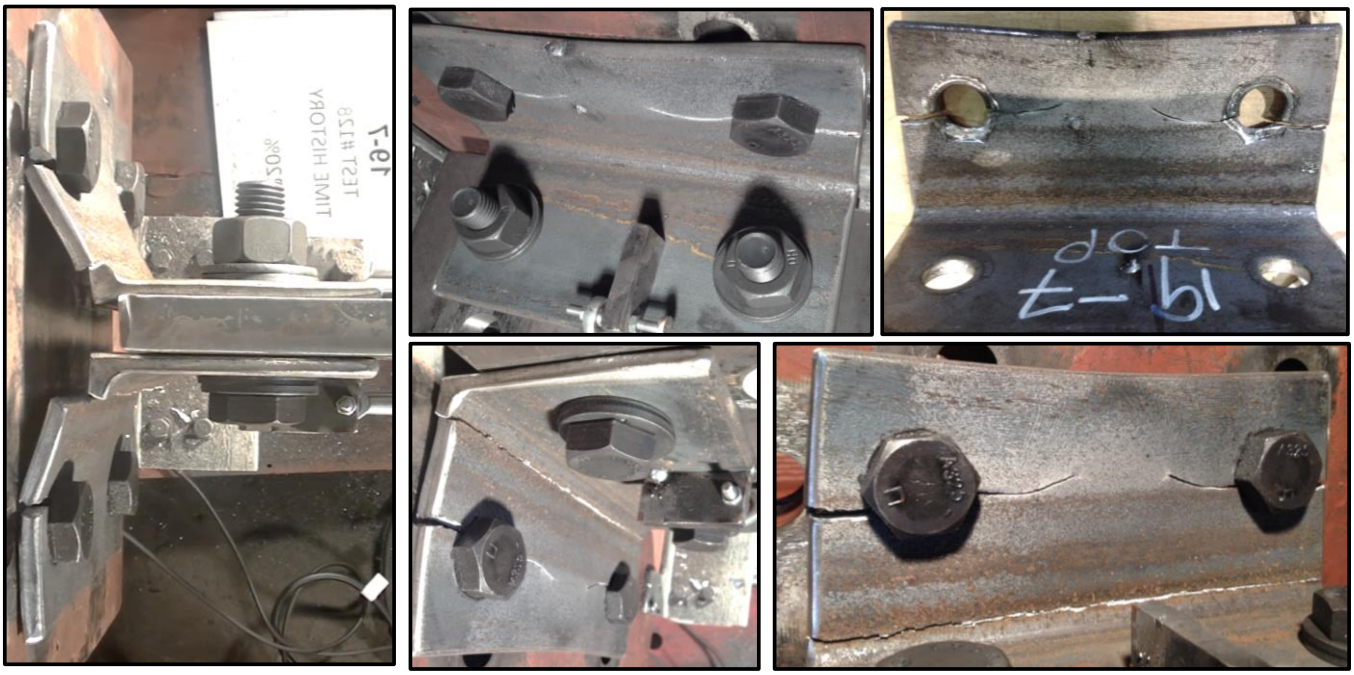
Materials:

Angle	A36	
F_y	373	MPa
F_u	507	MPa
ε_u	0.2415	
Bolt	A325	
Column bolts	400	lbf-ft
Plate bolts	400	lbf-ft

Key response parameters:

Signal factor	65%	130%	200%
Δ_0	0.0	1.2	2.8
$F_{F\ Max}$	90	118	92
$\Delta_{F\ Max}$	9.5	18.0	23.1
$F_{Ultimate}$	88	107	32
$\Delta_{ultimate}$	9.7	20.6	35.7





APPENDIX B FULL-SCALE CONNECTION TESTING RESULTS

This Appendix presents a summary of the experimental results of each test performed on the full-scale connections made of bolted angles. These results have been discussed in Articles 2 and 3, presented in Chapters 5 and 6 for the connections made of double web angles and of top and seat with double web angles respectively. In this Appendix, each test is presented individually on a page where the following information are presented:

- Test identification;
- Beam and column connections;
- Type of loading protocol and values of shear load applied;
- Angle geometrical properties for the top and seat angles and the web angles;
- Angle material properties;
- Maximum displacements measured at the top and bottom angles;
- Failure mode observed;
- Moment-rotation response;
- Test pictures.

This Appendix aims at providing as much information as possible on the tests performed to allow the use of these experimental results in future studies.

SPECIMEN 1A

DISCARDED

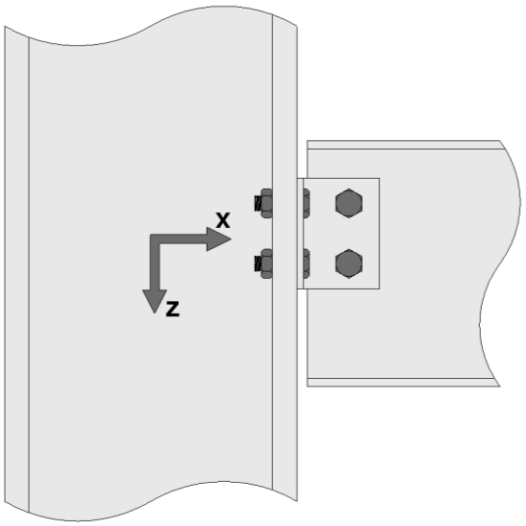
Beam	W310 x 39	
Column	W360 x 347	
Loading Type	Cyclic	
Constant shear	94.3	kN
Shear excursions	-	

Top & Seat Angles

Size	N/A	
Steel Grade	-	
F_y	-	
F_u	-	
ε_u	-	

Web Angles

Size	L4 x 4 x 5/16	
Steel Grade	A36	
F_y	373	MPa
F_u	507	MPa
ε_u	0.2415	
Length	140	mm

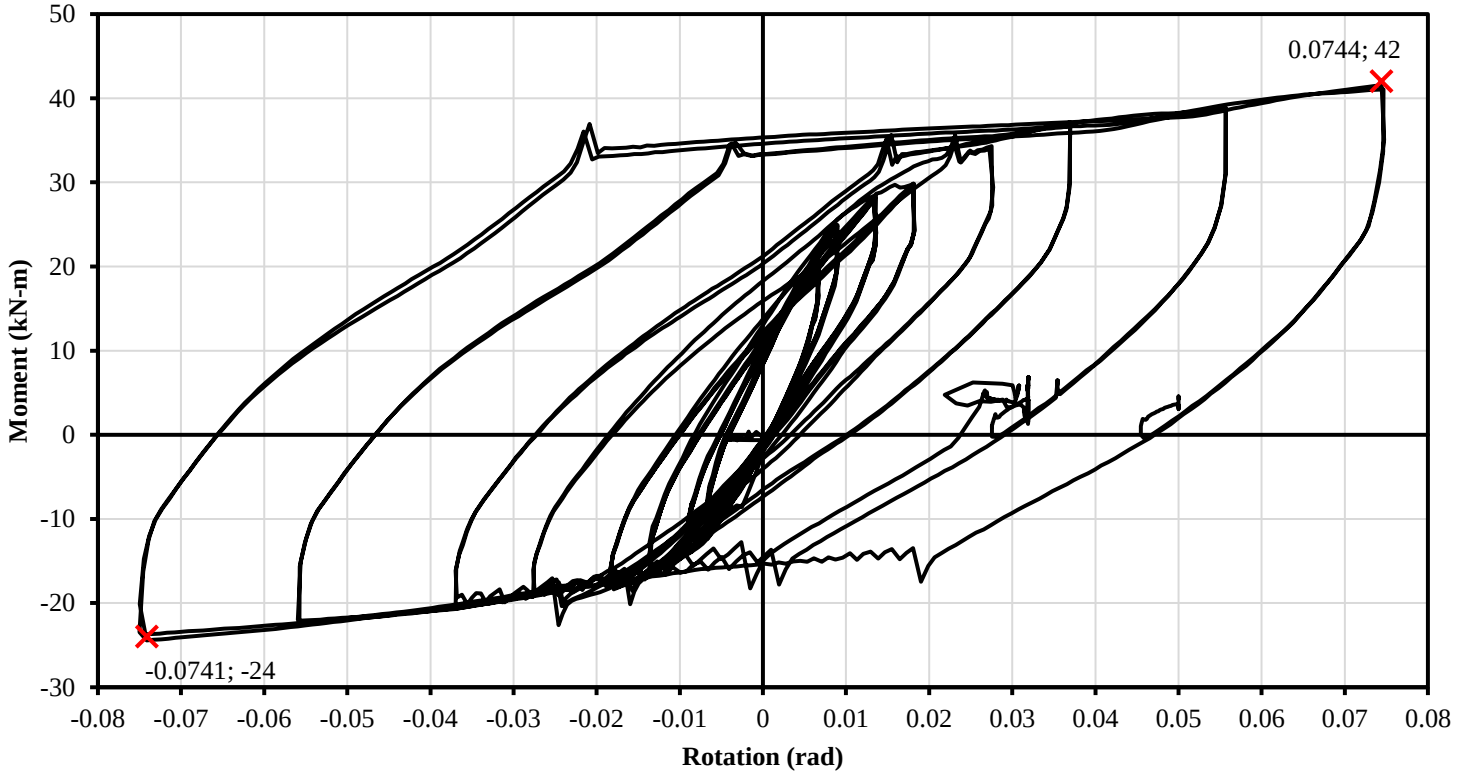


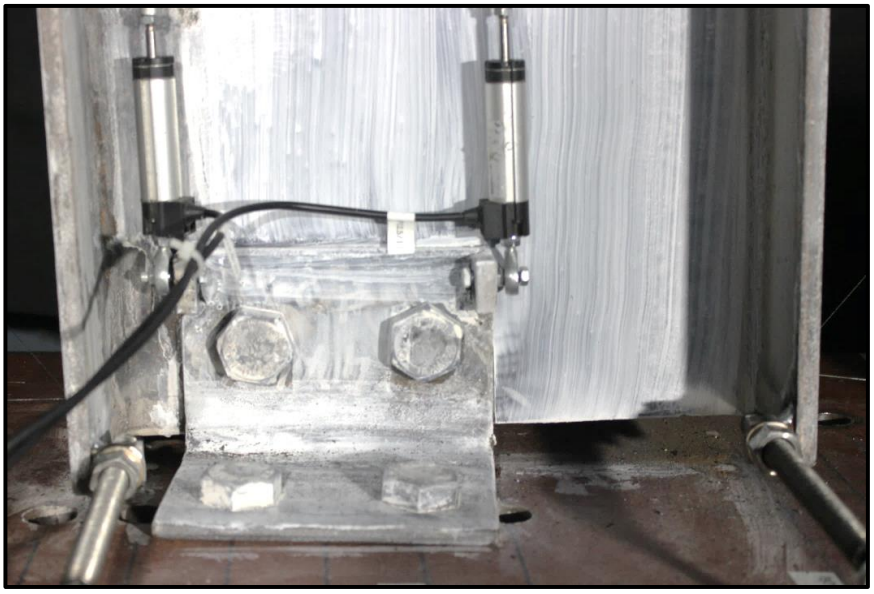
$\Delta_{X\ max\ Top\ +}$	16.4	mm
$\Delta_{Z\ max\ Top\ +}$	0.0	mm
$\Delta_{X\ max\ Top\ -}$	-4.2	mm
$\Delta_{Z\ max\ Top\ -}$	-12.9	mm
$\Delta_{X\ max\ Bottom\ +}$	19.3	mm
$\Delta_{Z\ max\ Bottom\ +}$	0.0	mm
$\Delta_{X\ max\ Bottom\ -}$	-9.9	mm
$\Delta_{Z\ max\ Bottom\ -}$	-12.1	mm

Note: The displacements were measured at the center of the beam flanges.

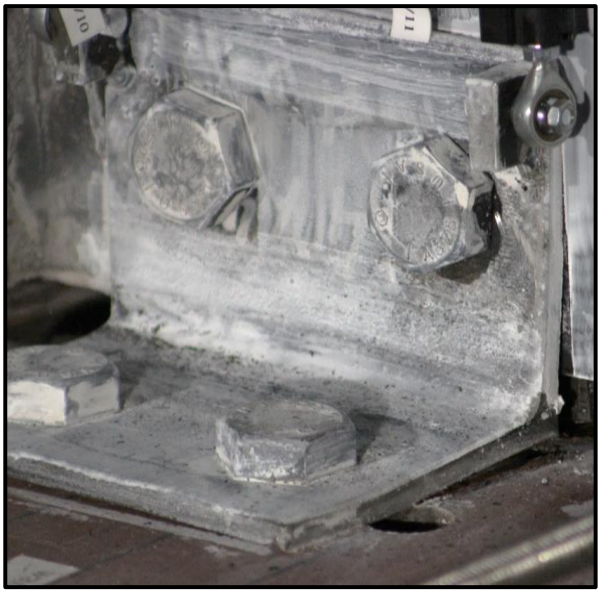
Failure Mode The test was stopped before fracture occured

Moment-Rotation





Connection at end of test



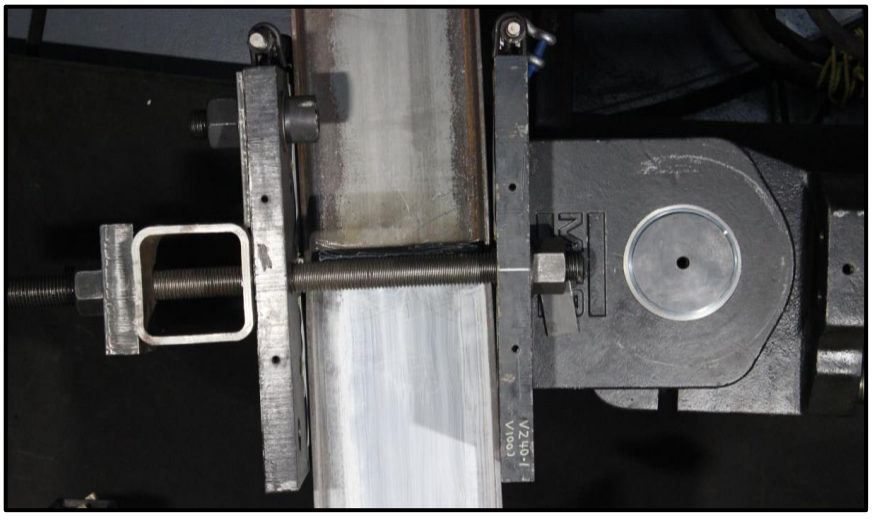
Bottom side at the end of test



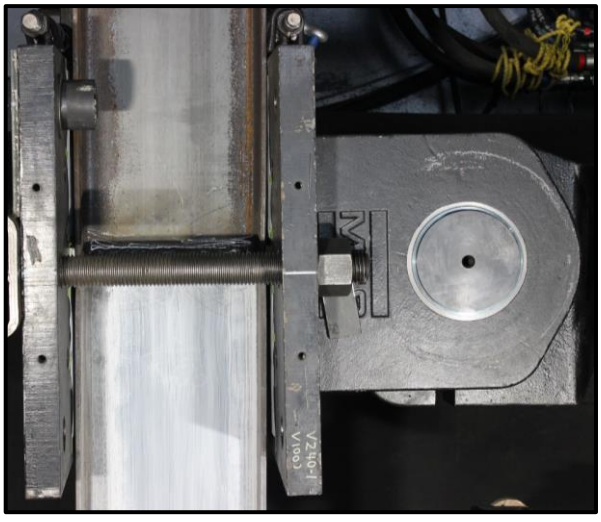
Close-up of the Bottom side of the web angles



Top side of the web angles



Lack of rotation in the actuator hinge due to friction (positive rotation)



Lack of rotation in the hinge (negative rotation)

SPECIMEN 1B

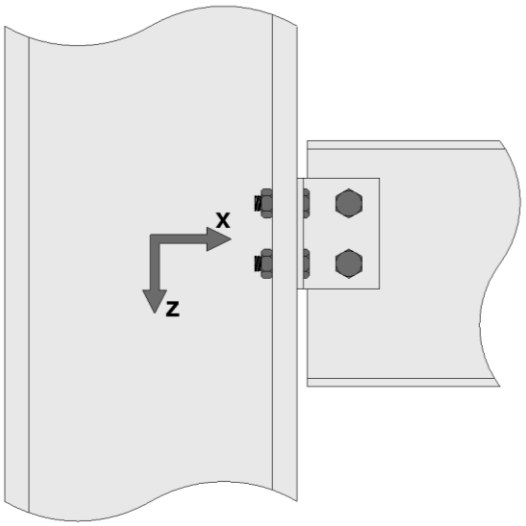
Beam	W310 x 39	
Column	W360 x 347	
Loading Type	Cyclic	
Constant shear	94.3	kN
Shear excursions	-	

Top & Seat Angles

Size	N/A	
Steel Grade	-	
F_y	-	
F_u	-	
ε_u	-	

Web Angles

Size	L4 x 4 x 5/16	
Steel Grade	A36	
F_y	373	MPa
F_u	507	MPa
ε_u	0.2415	
Length	140	mm

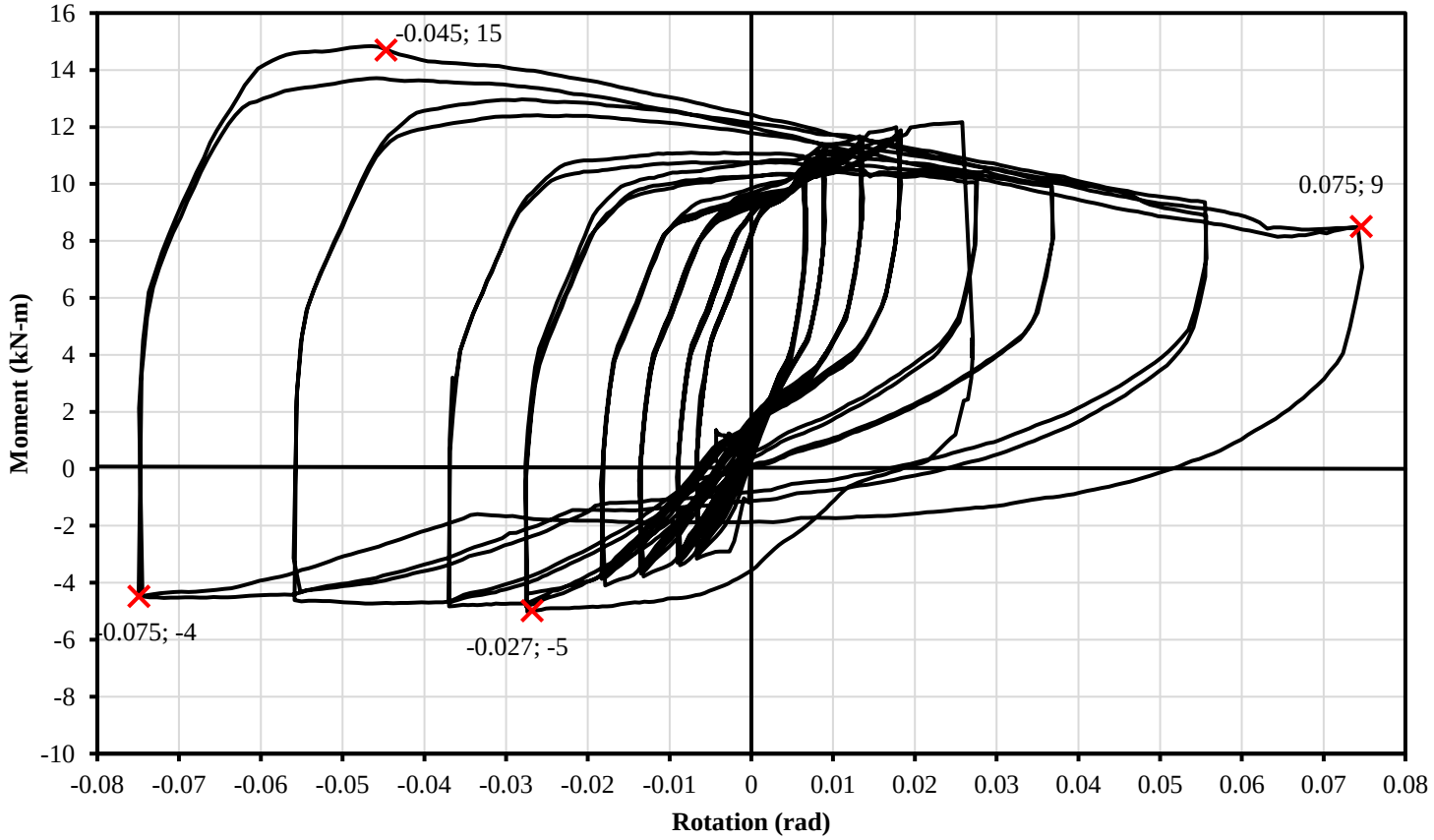


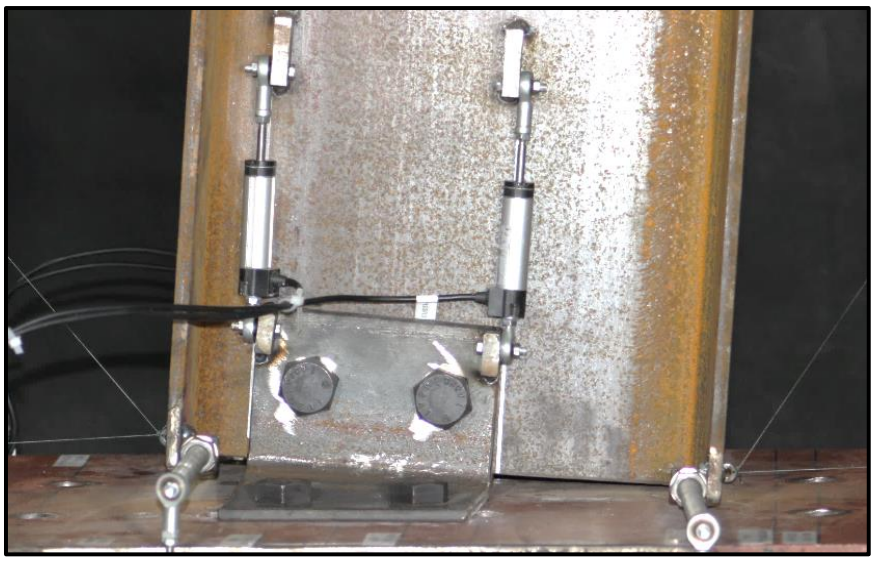
$\Delta_{X\ max\ Top\ +}$	16.63	mm
$\Delta_{Z\ max\ Top\ +}$	-0.01	mm
$\Delta_{X\ max\ Top\ -}$	-3.34	mm
$\Delta_{Z\ max\ Top\ -}$	-10.70	mm
$\Delta_{X\ max\ Bottom\ +}$	20.04	mm
$\Delta_{Z\ max\ Bottom\ +}$	0.05	mm
$\Delta_{X\ max\ Bottom\ -}$	-9.58	mm
$\Delta_{Z\ max\ Bottom\ -}$	-9.36	mm

Note: The displacements were measured at the center of the beam flanges.

Failure Mode the maximum stroke of the top actuator was reached before angle fracture occured

Moment-Rotation

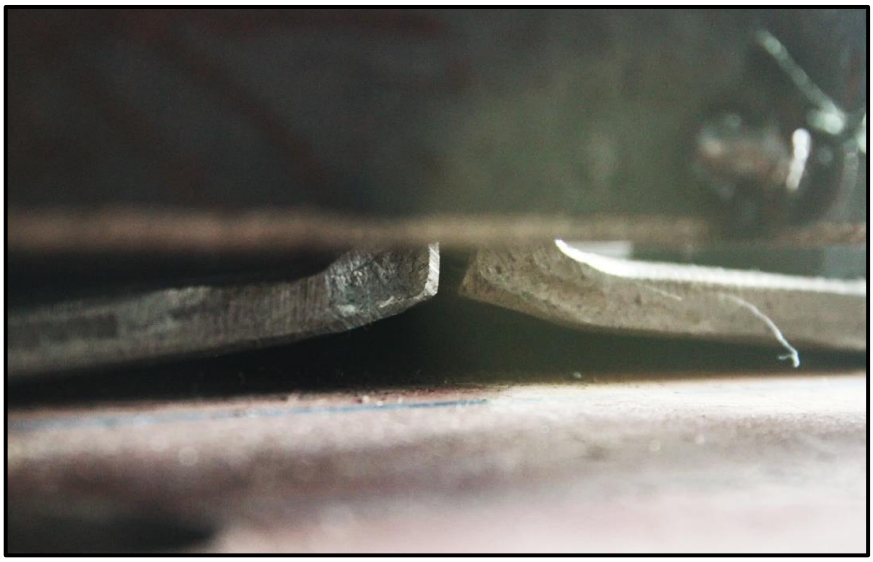




Connection at end of test



Bottom side of web angles at the end of test



Top side of the web angle fillet pushed under the beam web



Top side profile of the web angles



Local yielding of beam web at the top side of angle web position



Shear deformation of web angles

SPECIMEN 1C

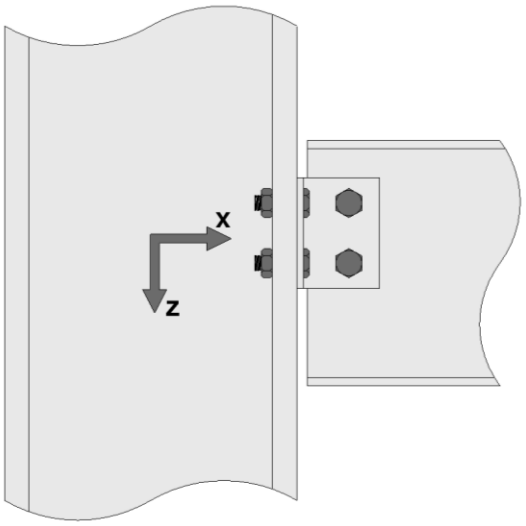
Beam	W310 x 39	
Column	W360 x 347	
Loading Type	Cyclic + Shear Excursions	
Constant shear	94.3	kN
Shear excursions	152.0	kN

Top & Seat Angles

Size	N/A	
Steel Grade	-	
F_y	-	
F_u	-	
ε_u	-	

Web Angles

Size	L4 x 4 x 5/16	
Steel Grade	A36	
F_y	373	MPa
F_u	507	MPa
ε_u	0.2415	
Length	140	mm

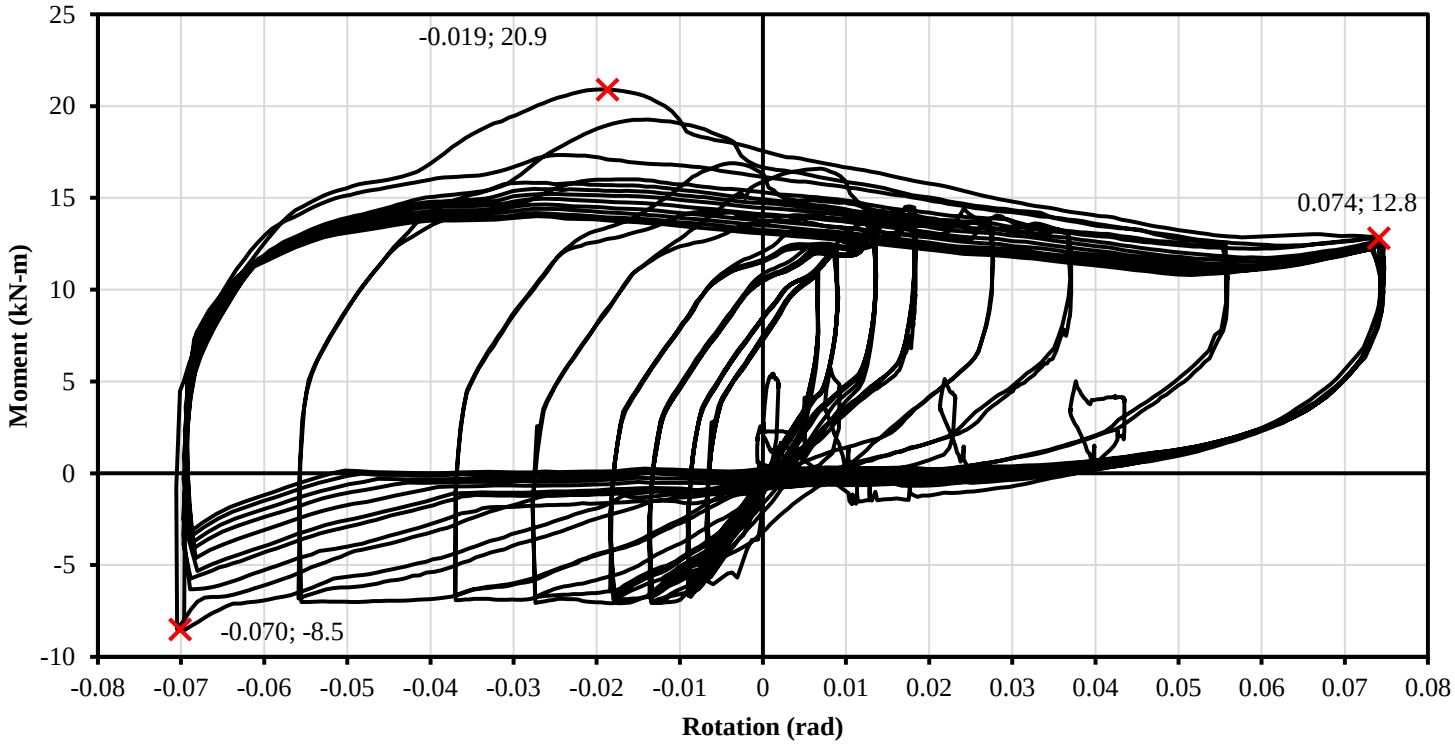


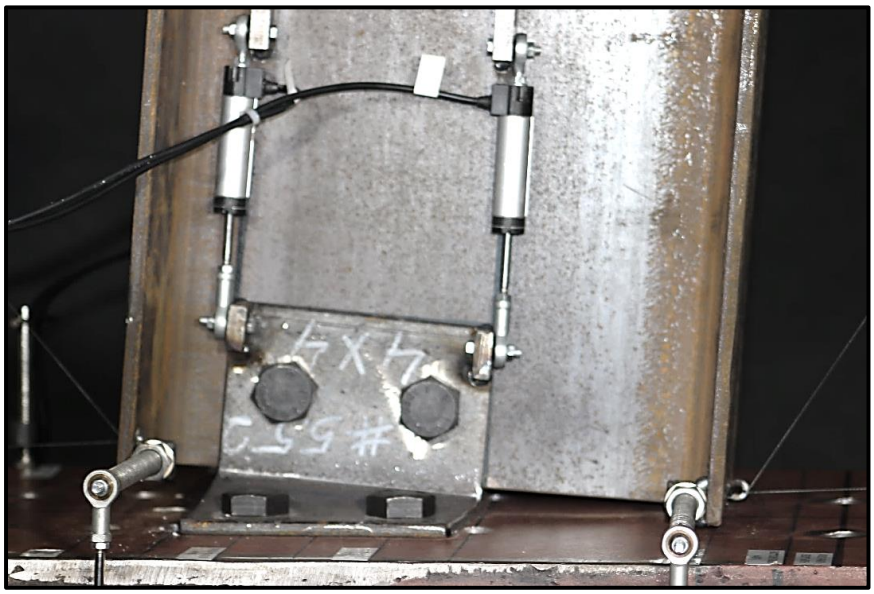
$\Delta_{X\ max\ Top\ +}$	15.56	mm
$\Delta_{Z\ max\ Top\ +}$	-0.47	mm
$\Delta_{X\ max\ Top\ -}$	-3.84	mm
$\Delta_{Z\ max\ Top\ -}$	-13.77	mm
$\Delta_{X\ max\ Bottom\ +}$	21.29	mm
$\Delta_{Z\ max\ Bottom\ +}$	-0.52	mm
$\Delta_{X\ max\ Bottom\ -}$	-8.93	mm
$\Delta_{Z\ max\ Bottom\ -}$	-12.82	mm

Note: The displacements were measured at the center of the beam flanges.

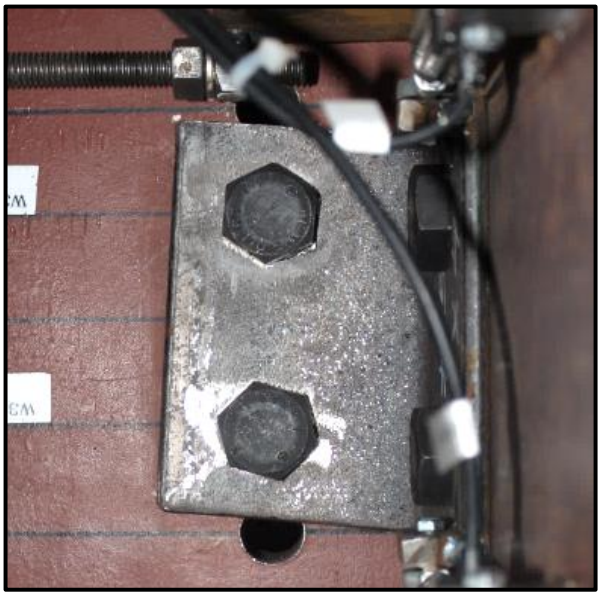
Failure Mode The top actuator maximum stroke was reached before angle fracture occured. Fatigue cycles at the last amplitude were performed to initiate fracture. Tearing of the colun leg of the south web angle was observed.

Moment-Rotation





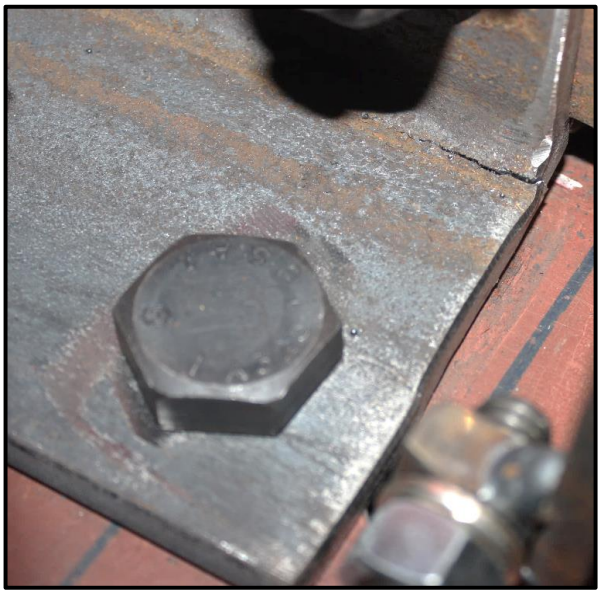
Connection at end of test



Shear deformation of the north web angle



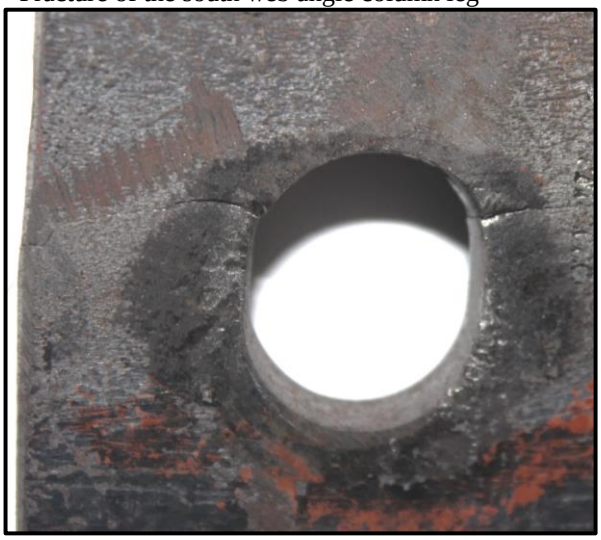
Top side of the web angle fillet pushed under the beam web



Fracture of the south web angle column leg



Local yielding of beam web at the top side of angle web position



Net section frature on column leg

SPECIMEN 1D

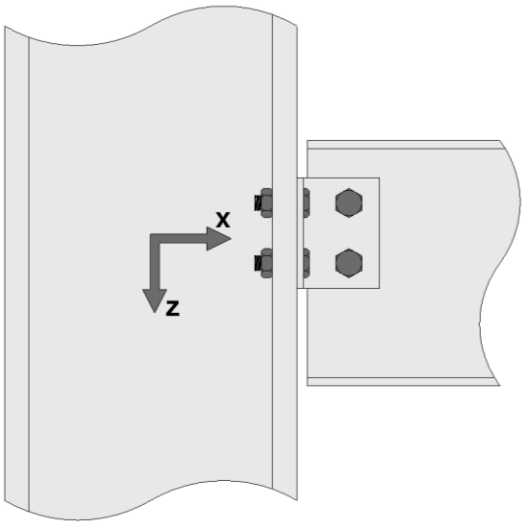
Beam	W310 x 39	
Column	W360 x 347	
Loading Type	Cyclic Only, No Shear	
Constant shear	-	kN
Shear excursions	-	kN

Top & Seat Angles

Size	N/A	
Steel Grade	-	
F_y	-	
F_u	-	
ε_u	-	

Web Angles

Size	L4 x 4 x 5/16	
Steel Grade	A36	
F_y	373	MPa
F_u	507	MPa
ε_u	0.2415	
Length	140	mm

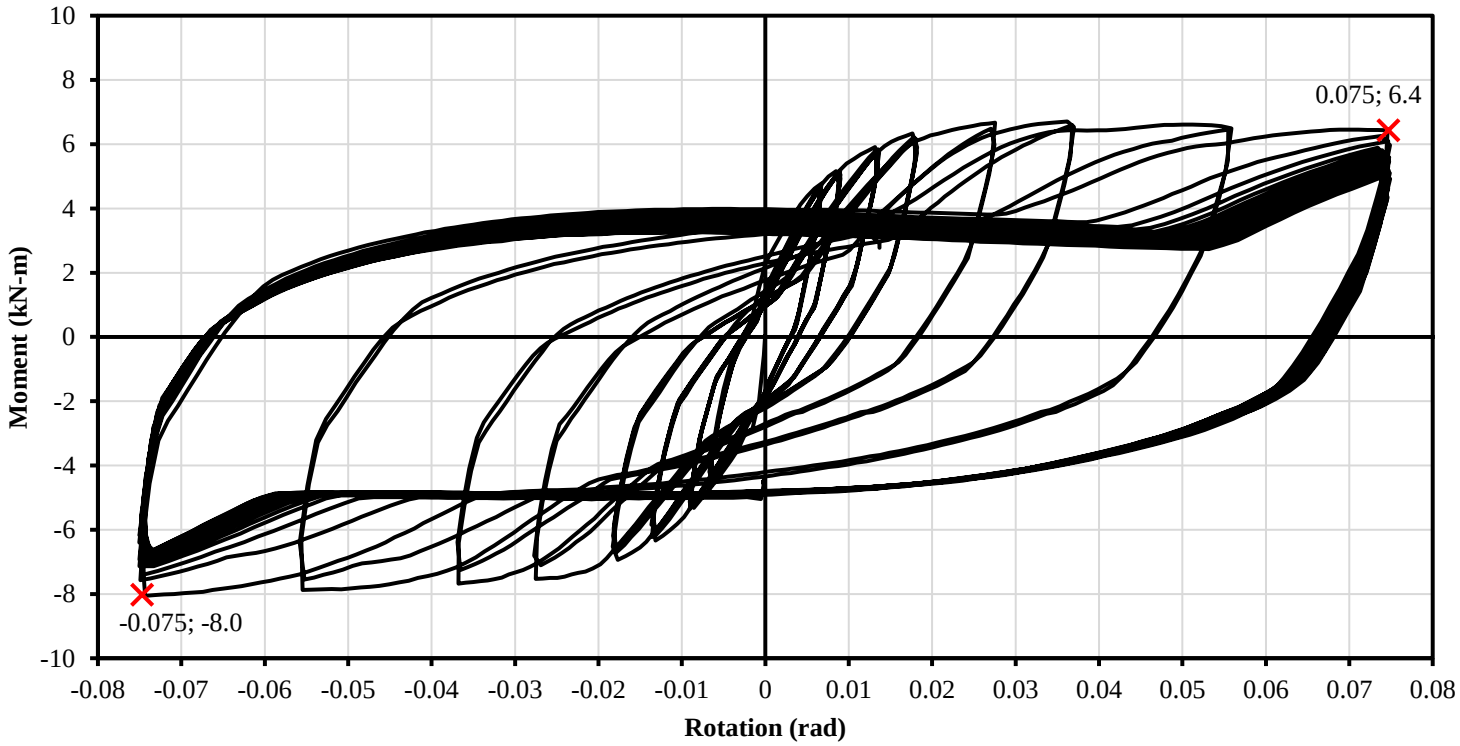


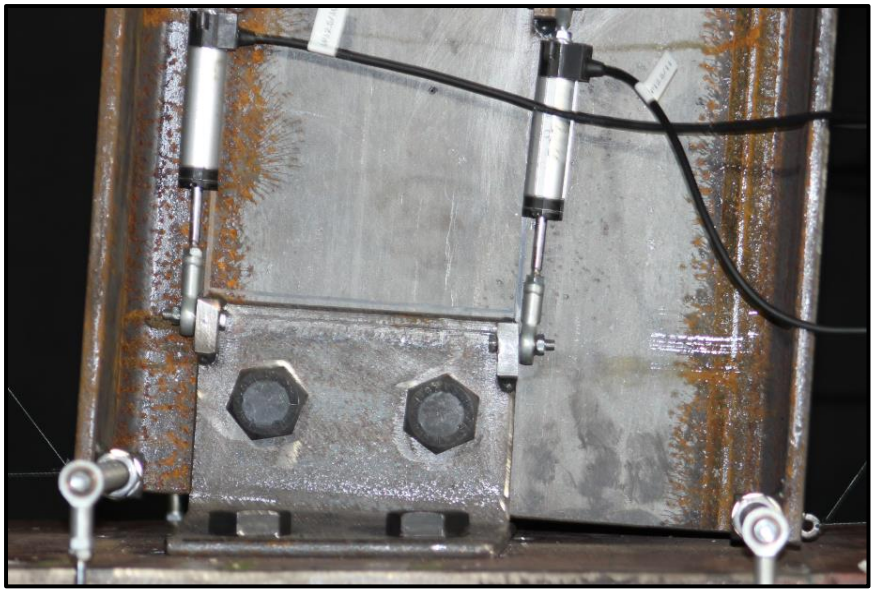
$\Delta_{X\ max\ Top\ +}$	13.95	mm
$\Delta_{Z\ max\ Top\ +}$	1.20	mm
$\Delta_{X\ max\ Top\ -}$	-4.59	mm
$\Delta_{Z\ max\ Top\ -}$	-1.68	mm
$\Delta_{X\ max\ Bottom\ +}$	20.64	mm
$\Delta_{Z\ max\ Bottom\ +}$	2.08	mm
$\Delta_{X\ max\ Bottom\ -}$	-11.44	mm
$\Delta_{Z\ max\ Bottom\ -}$	-0.87	mm

Note: The displacements were measured at the center of the beam flanges.

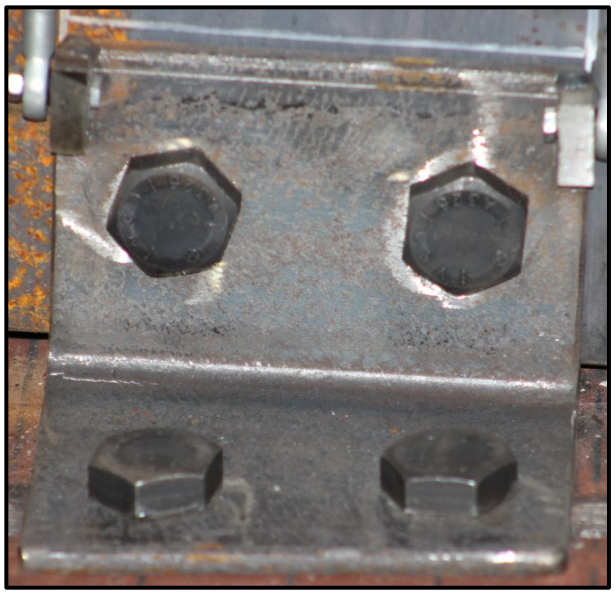
Failure Mode The top actuator maximum stroke was reached before angle fracture occured. Fatigue cycles at the last amplitude were performed to initiate fracture. Tearing of the colun leg of the south web angle was observed.

Moment-Rotation





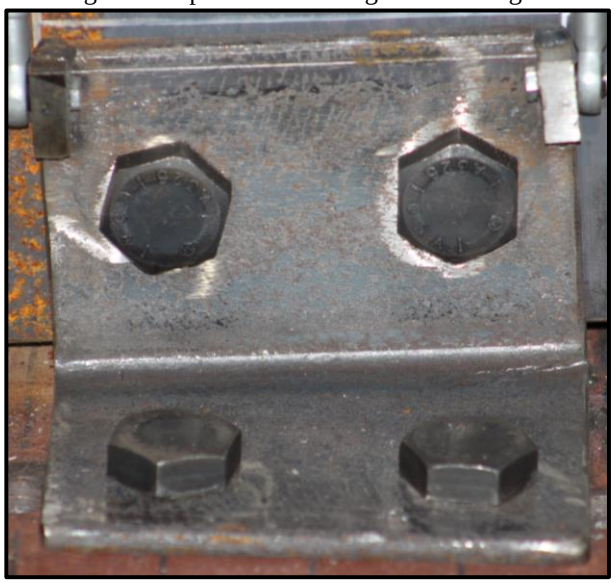
Connection at end of test



Cracking at the top of the north angle column leg



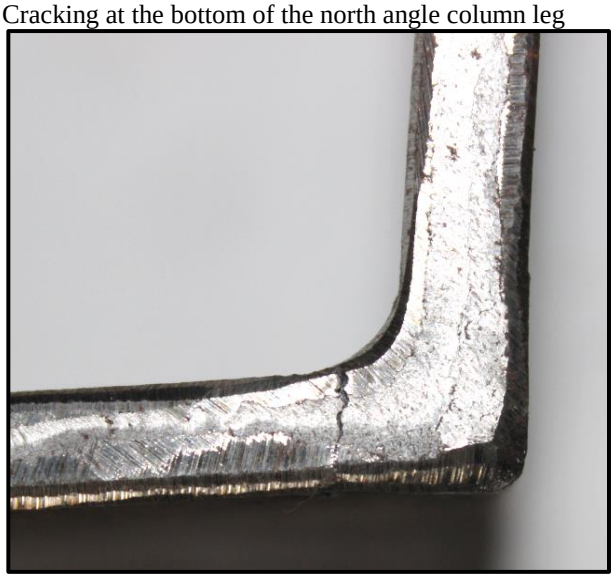
Net section fracture near the column leg holes



Cracking at the bottom of the north angle column leg



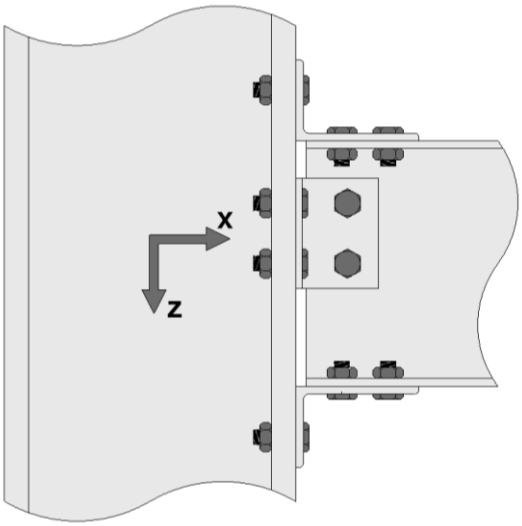
Cracking at the bottom of the south angle column leg



Close up of the bottom side of the south angle

SPECIMEN 2A

Beam	W310 x 39	
Column	W360 x 347	
Loading Type	Cyclic	
Constant shear	94.3	kN
Shear excursions	-	



Top & Seat Angles

Size	L6 x 4 x 3/8	
Steel Grade	A36	
F_y	375	MPa
F_u	537	MPa
ε_u	0.2372	

$\Delta_{X\ max\ Top\ +}$	16.41	mm
$\Delta_{Z\ max\ Top\ +}$	2.23	mm
$\Delta_{X\ max\ Top\ -}$	-0.14	mm
$\Delta_{Z\ max\ Top\ -}$	-3.18	mm
$\Delta_{X\ max\ Bottom\ +}$	15.11	mm
$\Delta_{Z\ max\ Bottom\ +}$	-0.07	mm
$\Delta_{X\ max\ Bottom\ -}$	-0.09	mm
$\Delta_{Z\ max\ Bottom\ -}$	-9.79	mm

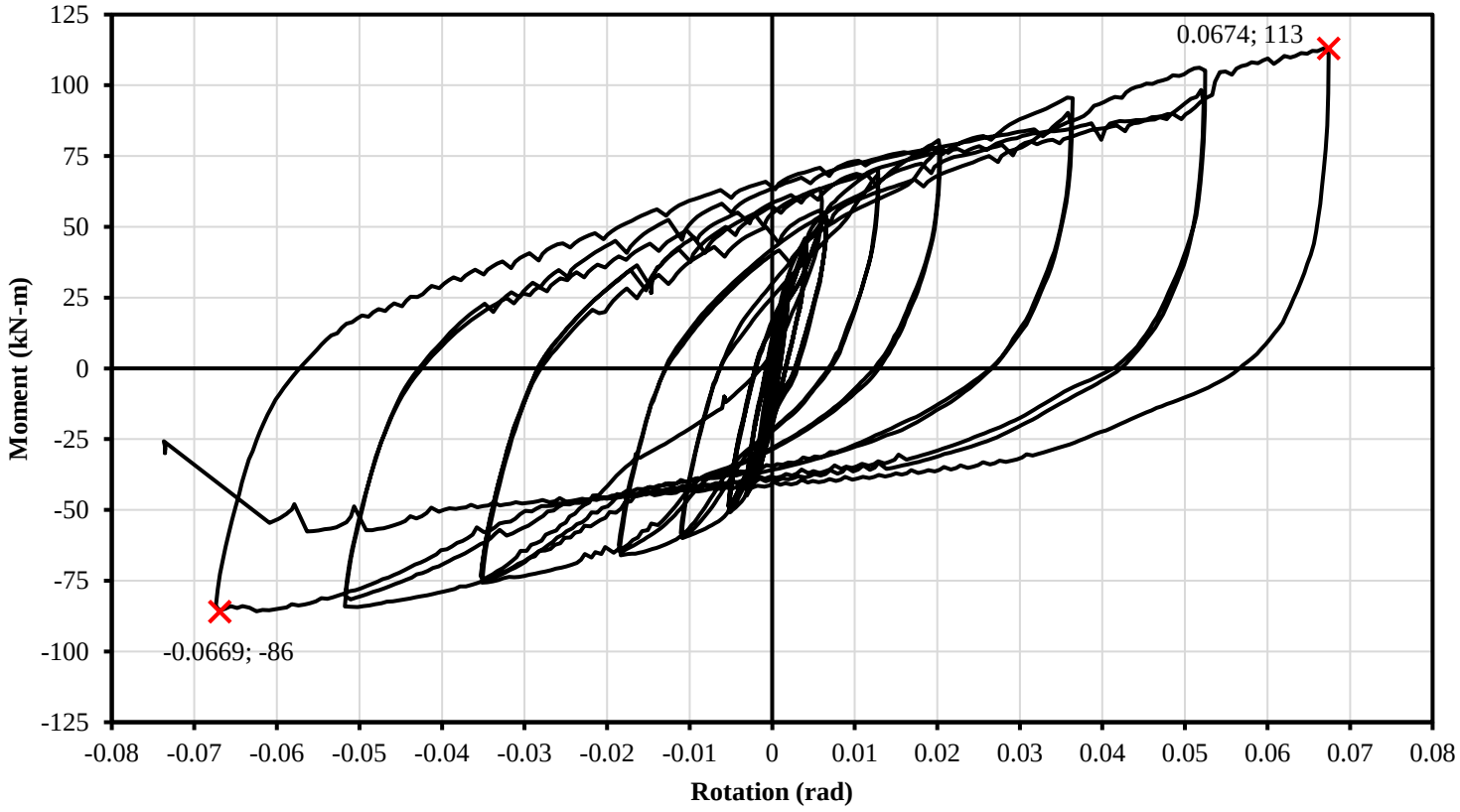
Web Angles

Size	L4 x 4 x 5/16	
Steel Grade	A36	
F_y	373	MPa
F_u	507	MPa
ε_u	0.2415	
Length	140	mm

Note: The displacements were measured at the center of the top and seat angle fillet.

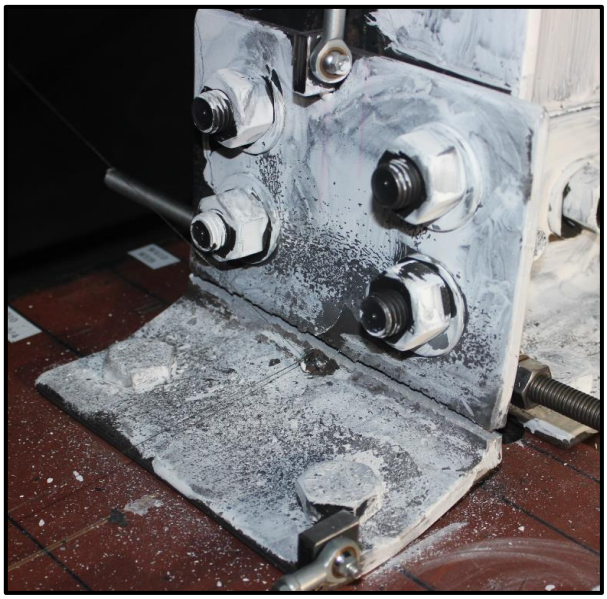
Failure Mode Beam leg fracture of the top angle

Moment-Rotation





Connection at fracture



Top angle at fracture



Web angle deformation at fracture



Bottom angle at fracture



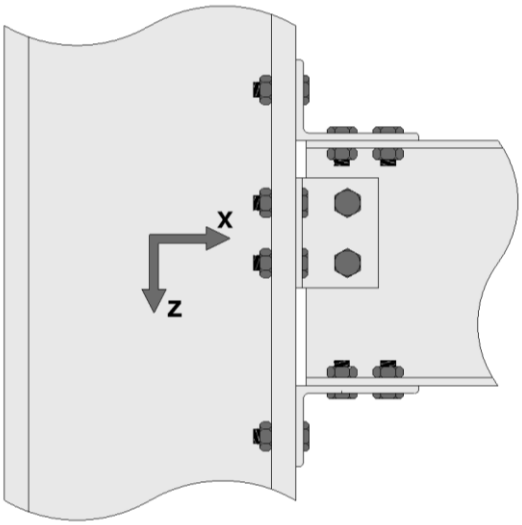
Close-up of the top angle beam leg fracture



Top side of web angles

SPECIMEN 2B

Beam	W310 x 39	
Column	W360 x 347	
Loading Type	Cyclic + Shear Excursions	
Constant shear	94.3	kN
Shear excursions	152.0	kN



Top & Seat Angles

Size	L6 x 4 x 3/8	
Steel Grade	A36	
F_y	375	MPa
F_u	537	MPa
ε_u	0.2372	

$\Delta_{X\ max\ Top\ +}$	17.1	mm
$\Delta_{Z\ max\ Top\ +}$	2.29	mm
$\Delta_{X\ max\ Top\ -}$	-0.13	mm
$\Delta_{Z\ max\ Top\ -}$	-3.77	mm
$\Delta_{X\ max\ Bottom\ +}$	13.35	mm
$\Delta_{Z\ max\ Bottom\ +}$	0.00	mm
$\Delta_{X\ max\ Bottom\ -}$	-0.21	mm
$\Delta_{Z\ max\ Bottom\ -}$	-8.74	mm

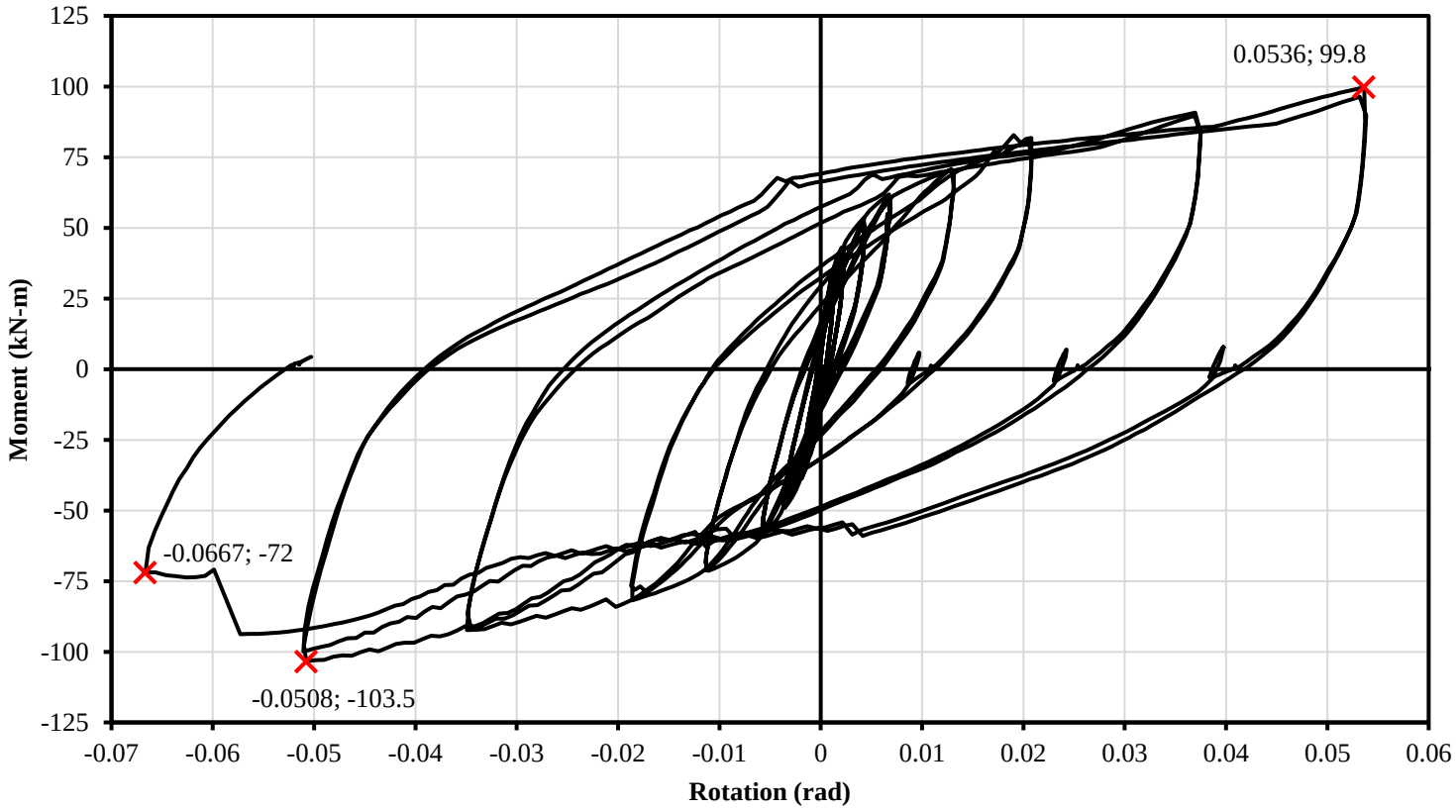
Web Angles

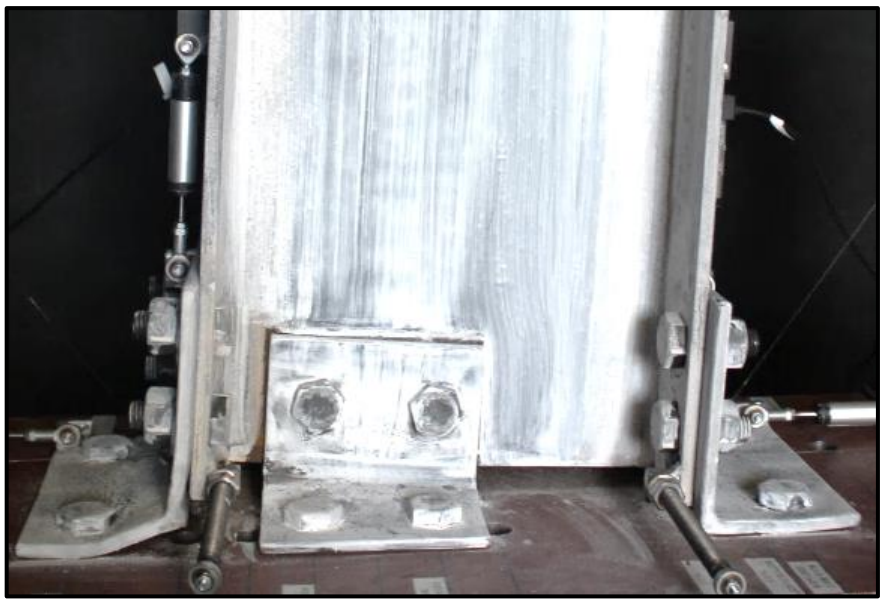
Size	L4 x 4 x 5/16	
Steel Grade	A36	
F_y	373	MPa
F_u	507	MPa
ε_u	0.2415	
Length	140	mm

Note: The displacements were measured at the center of the top and seat angle fillet.

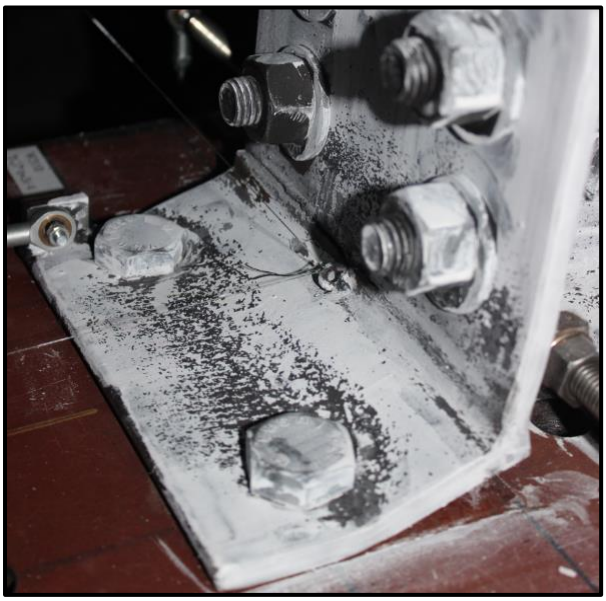
Failure Mode Beam leg fracture of the top angle

Moment-Rotation





Connection at fracture



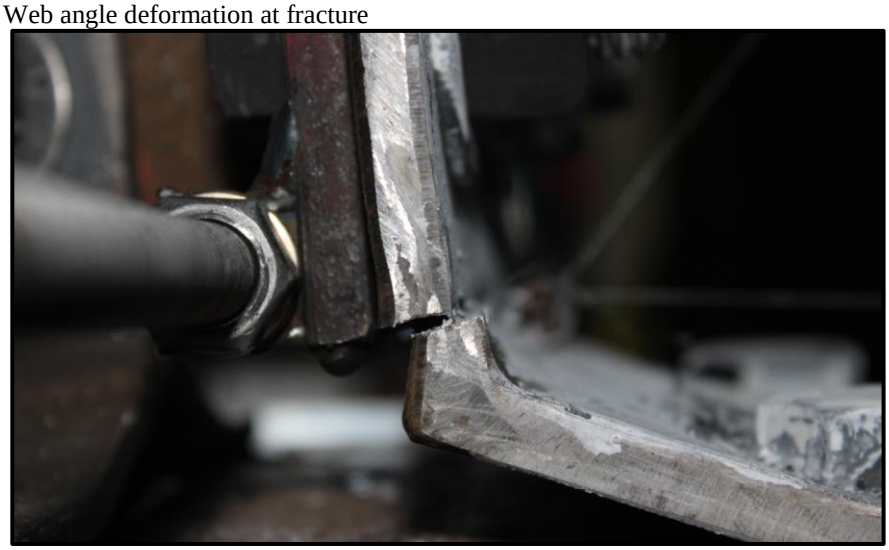
Top angle at fracture



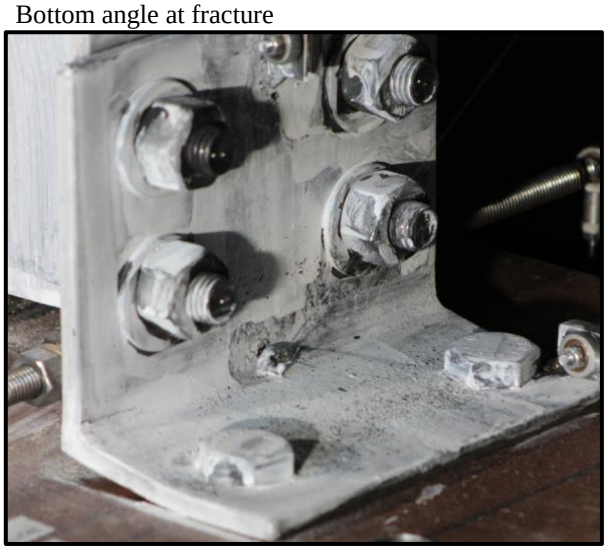
Web angle deformation at fracture



Bottom angle at fracture



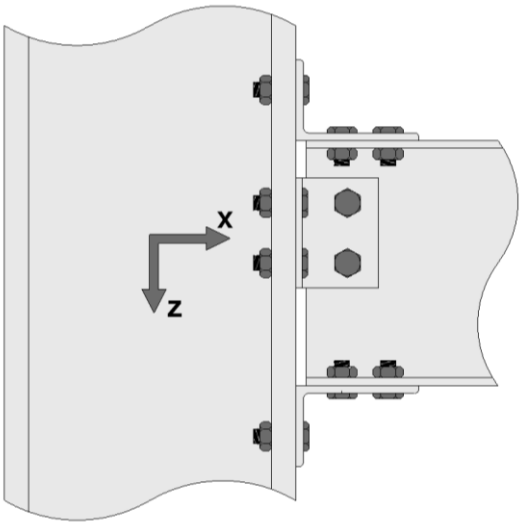
Close-up of top angle beam leg fracture



Crack initiation in bottom angle under positive rotation

SPECIMEN 2C

Beam	W310 x 39	
Column	W360 x 347	
Loading Type	Cyclic, No Shear	
Constant shear	-	kN
Shear excursions	-	kN



Top & Seat Angles

Size	L6 x 4 x 3/8	
Steel Grade	A36	
F_y	375	MPa
F_u	537	MPa
ε_u	0.2372	

$\Delta_{X\ max\ Top\ +}$	13.29	mm
$\Delta_{Z\ max\ Top\ +}$	2.56	mm
$\Delta_{X\ max\ Top\ -}$	-0.23	mm
$\Delta_{Z\ max\ Top\ -}$	-1.06	mm
$\Delta_{X\ max\ Bottom\ +}$	14.76	mm
$\Delta_{Z\ max\ Bottom\ +}$	0.78	mm
$\Delta_{X\ max\ Bottom\ -}$	-0.10	mm
$\Delta_{Z\ max\ Bottom\ -}$	-4.01	mm

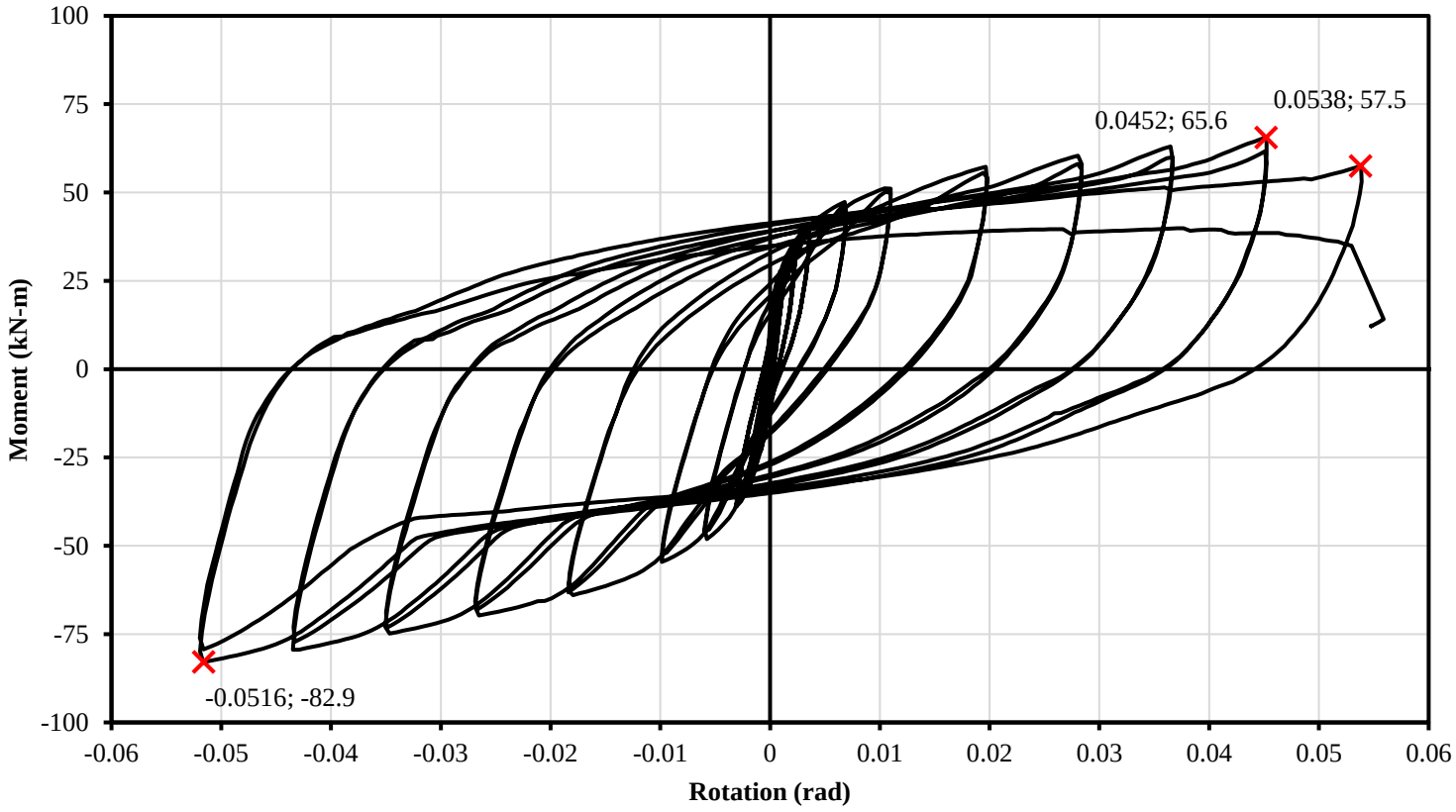
Web Angles

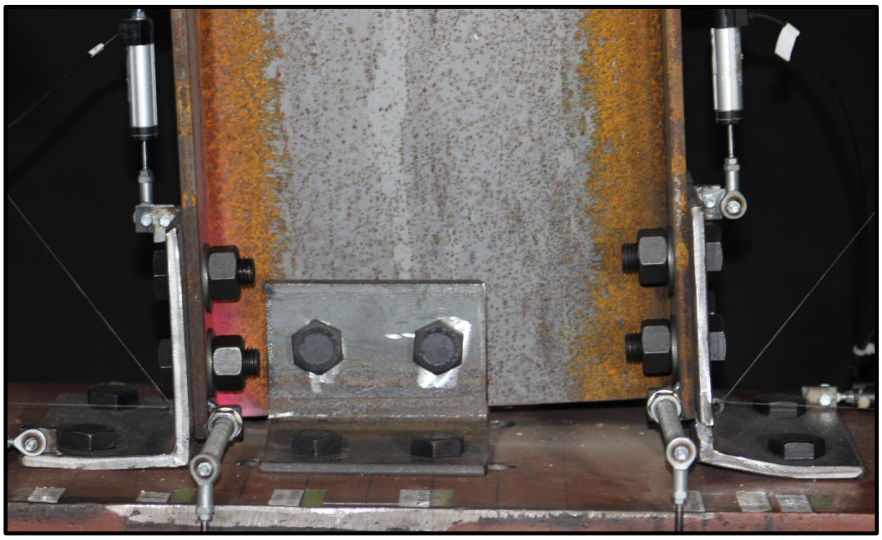
Size	L4 x 4 x 5/16	
Steel Grade	A36	
F_y	373	MPa
F_u	507	MPa
ε_u	0.2415	
Length	140	mm

Note: The displacements were measured at the center of the top and seat angle fillet.

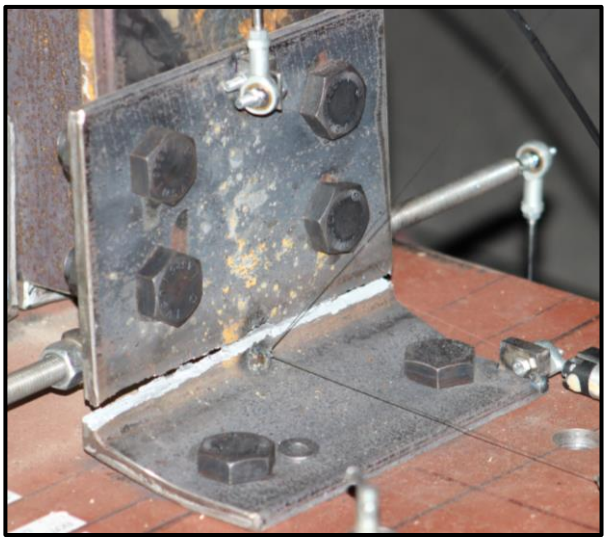
Failure Mode Beam leg fracture of the bottom angle

Moment-Rotation

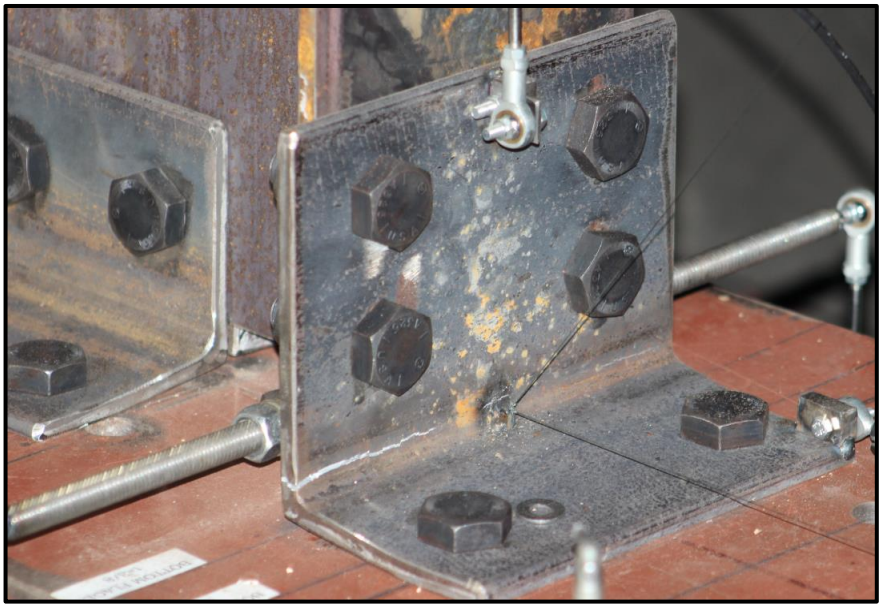




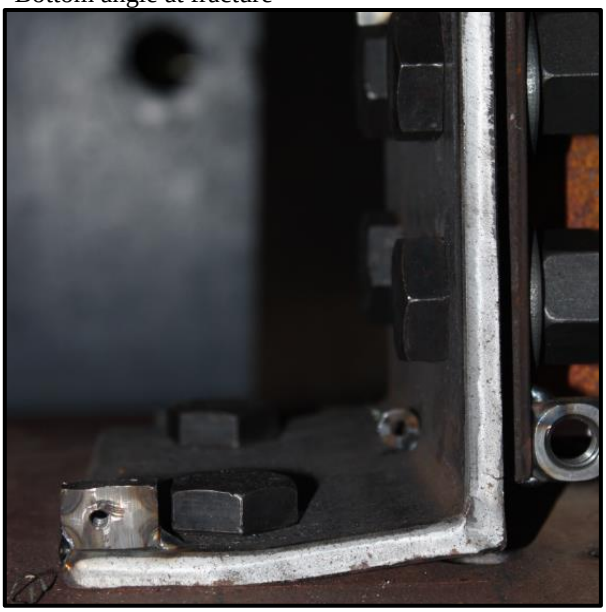
Connection at fracture



Bottom angle at fracture



Bottom angle crack initiation prior to fracture

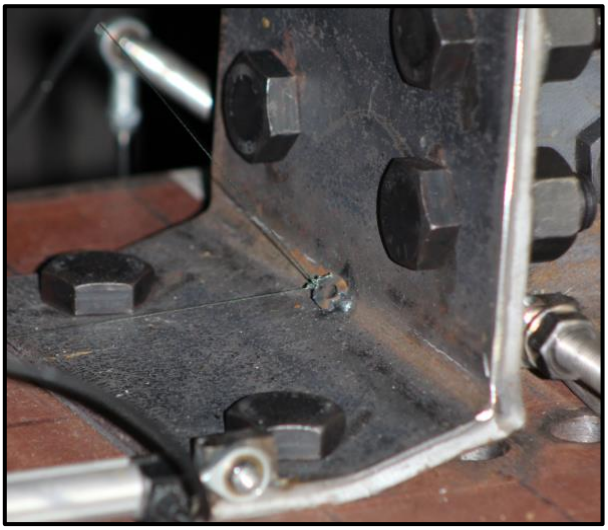


Top angle at fracture





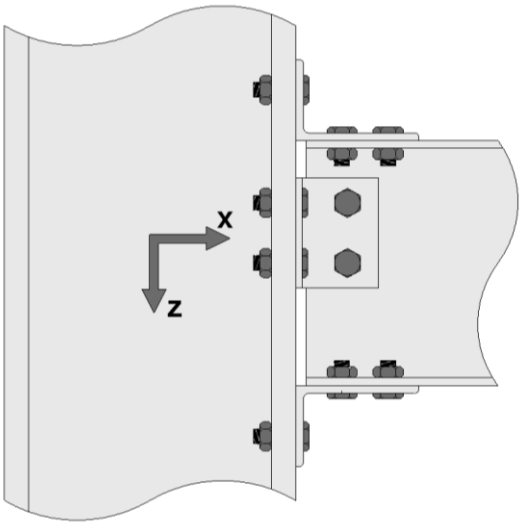
Close-ups of top angle cracking



Crack initiation in top angle under negative rotation

SPECIMEN 2D

Beam	W310 x 39	
Column	W360 x 347	
Loading Type	Cyclic Near fault protocol (-)	
Constant shear	94.3	kN
Shear excursions	-	kN



Top & Seat Angles

Size	L6 x 4 x 3/8	
Steel Grade	A36	
F_y	375	MPa
F_u	537	MPa
ε_u	0.2372	

$\Delta_{X\ max\ Top\ +}$	19.66	mm
$\Delta_{Z\ max\ Top\ +}$	2.50	mm
$\Delta_{X\ max\ Top\ -}$	-0.03	mm
$\Delta_{Z\ max\ Top\ -}$	-2.15	mm
$\Delta_{X\ max\ Bottom\ +}$	9.84	mm
$\Delta_{Z\ max\ Bottom\ +}$	0.03	mm
$\Delta_{X\ max\ Bottom\ -}$	-0.10	mm
$\Delta_{Z\ max\ Bottom\ -}$	-6.38	mm

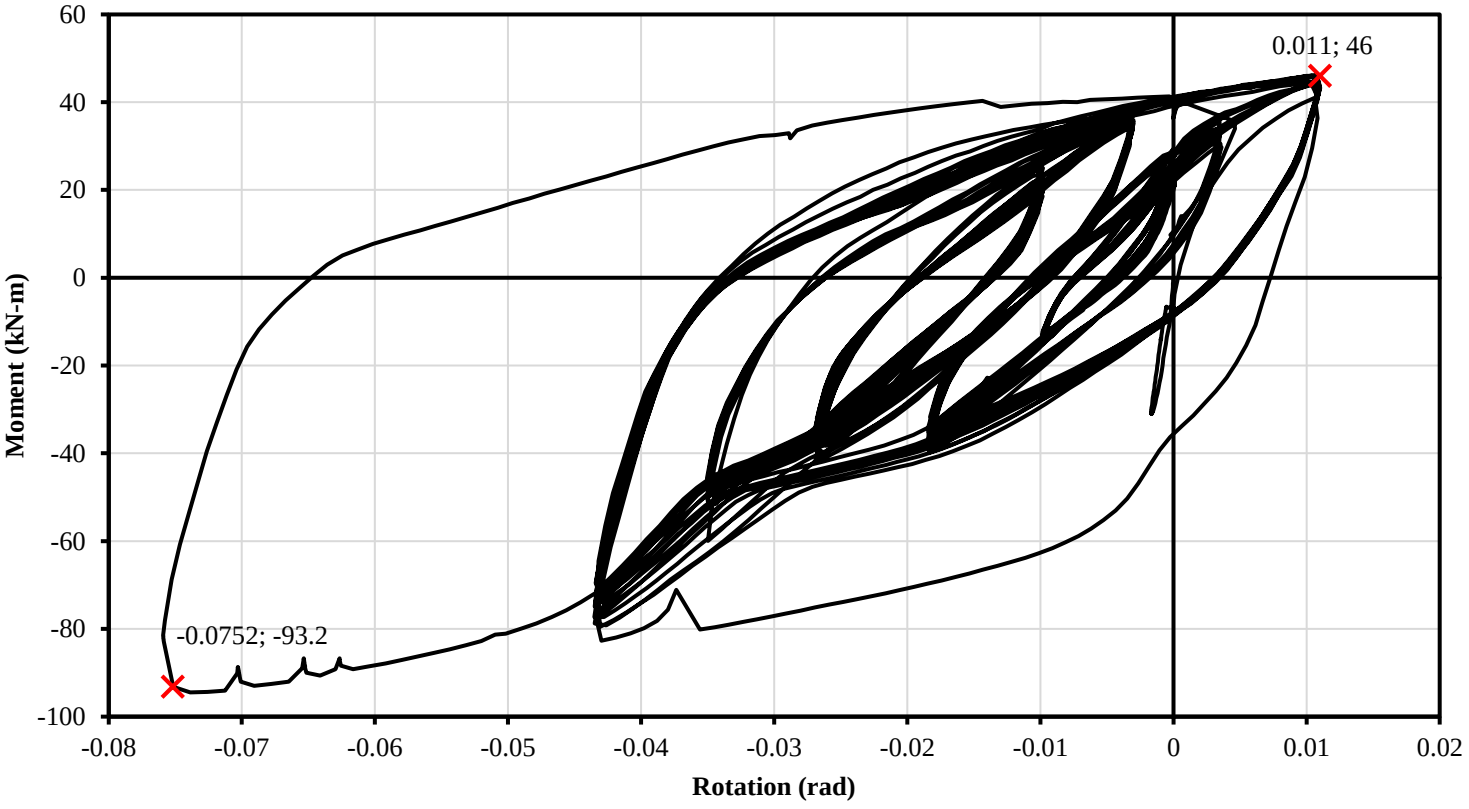
Web Angles

Size	L4 x 4 x 5/16	
Steel Grade	A36	
F_y	373	MPa
F_u	507	MPa
ε_u	0.2415	
Length	140	mm

Note: The displacements were measured at the center of the top and seat angle fillet.

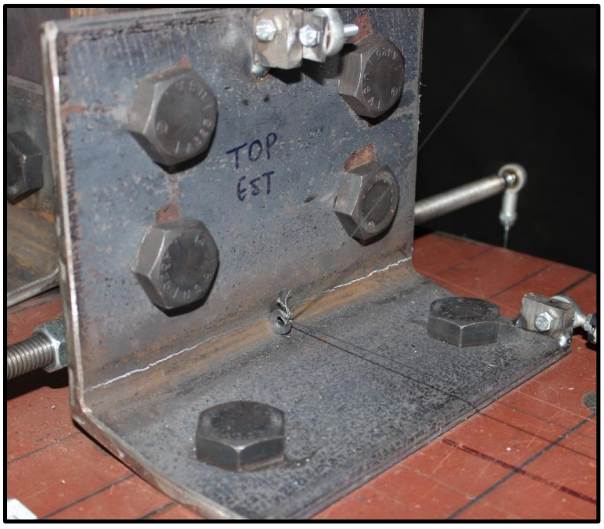
Failure Mode Beam leg fracture of the top angle

Moment-Rotation

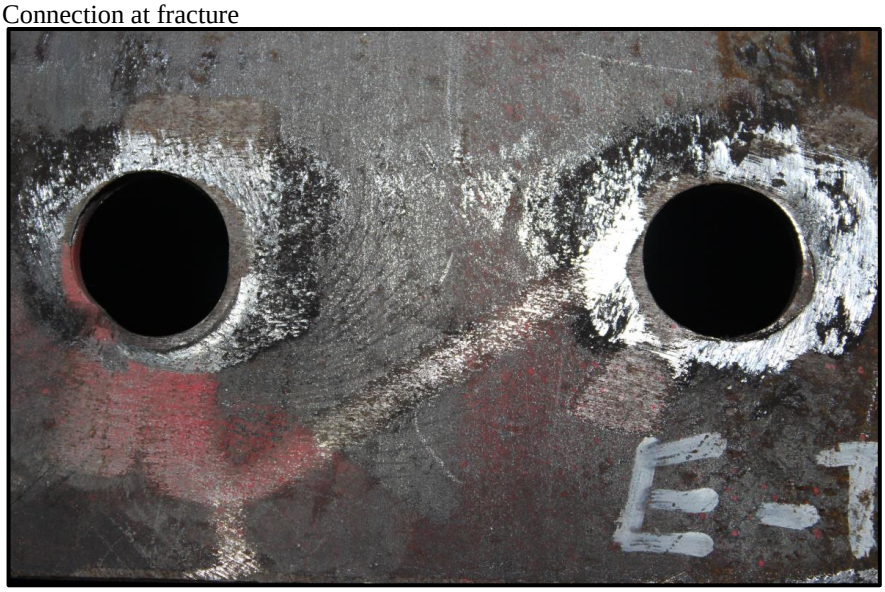




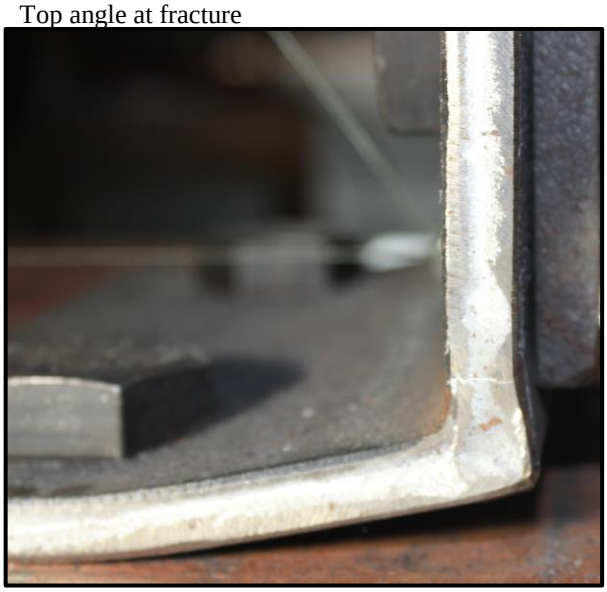
Connection at fracture



Top angle at fracture



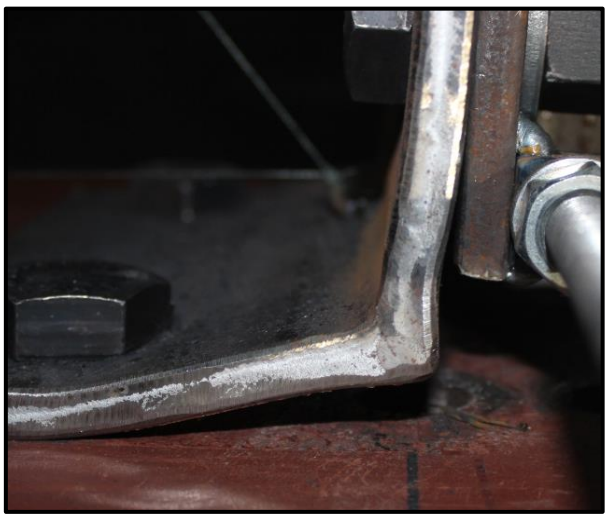
Web angle deformation at fracture



Bottom angle crack initiation and fillet deformation



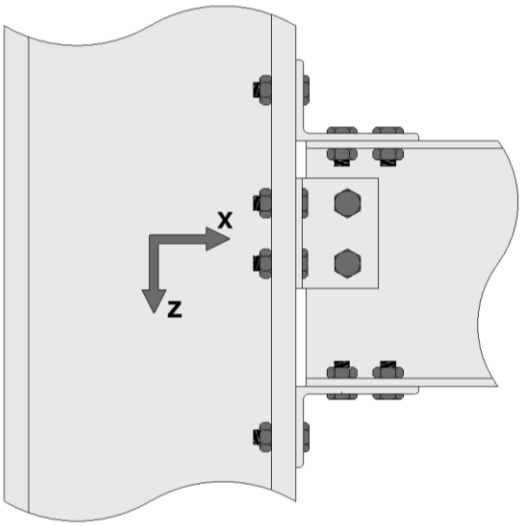
Beam web hole elongation & beam bottom flange deformation



Top angle deformation under negative rotation

SPECIMEN 3A

Beam	W310 x 39	
Column	W360 x 347	
Loading Type	Cyclic	
Constant shear	94.3	kN
Shear excursions	-	



Top & Seat Angles

Size	L8 x 6 x 3/4	
Steel Grade	A36	
F_y	340	MPa
F_u	516	MPa
ε_u	0.2592	

$\Delta_{X\ max\ Top\ +}$	19.55	mm
$\Delta_{Z\ max\ Top\ +}$	3.17	mm
$\Delta_{X\ max\ Top\ -}$	-0.19	mm
$\Delta_{Z\ max\ Top\ -}$	-2.41	mm
$\Delta_{X\ max\ Bottom\ +}$	16.06	mm
$\Delta_{Z\ max\ Bottom\ +}$	-0.07	mm
$\Delta_{X\ max\ Bottom\ -}$	-0.15	mm
$\Delta_{Z\ max\ Bottom\ -}$	-9.30	mm

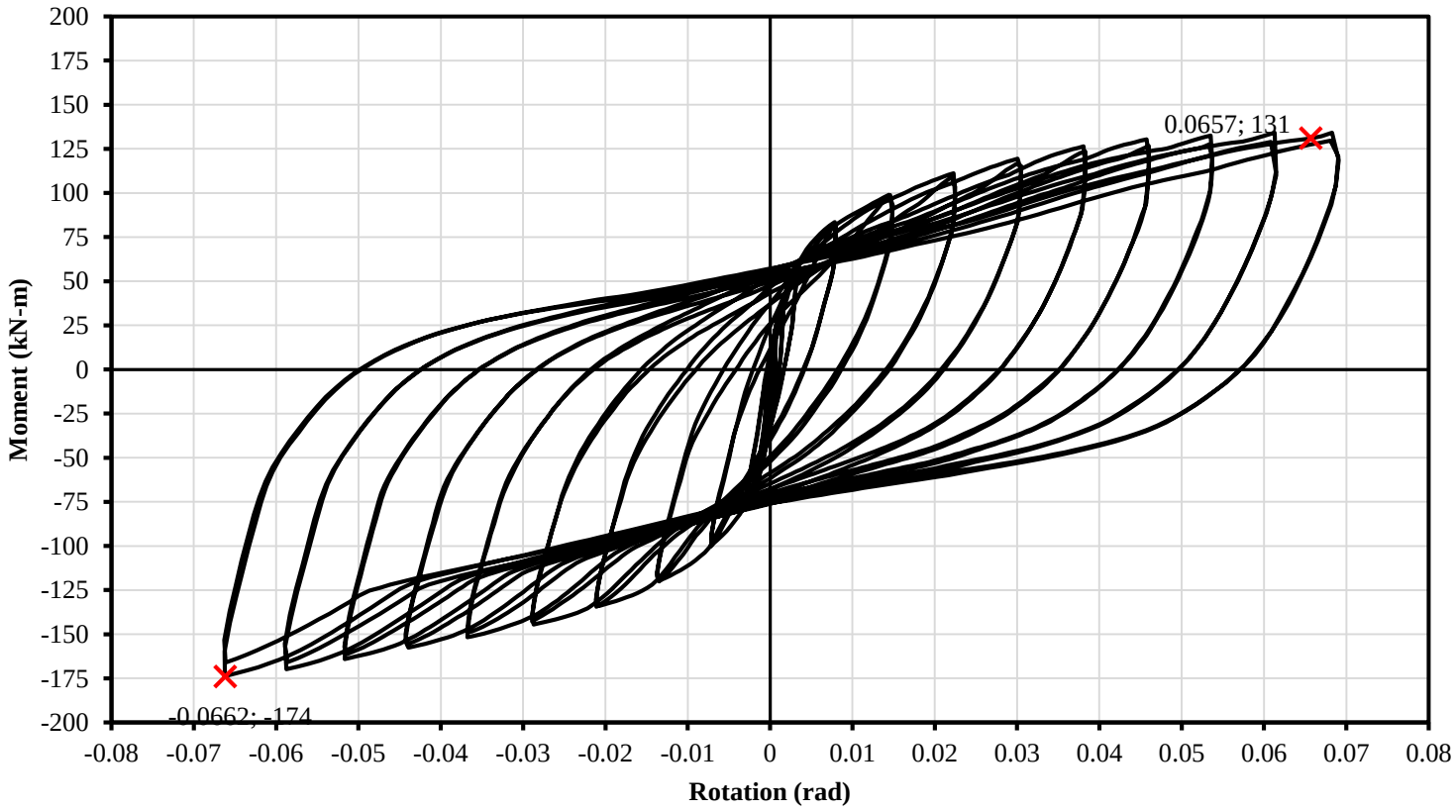
Web Angles

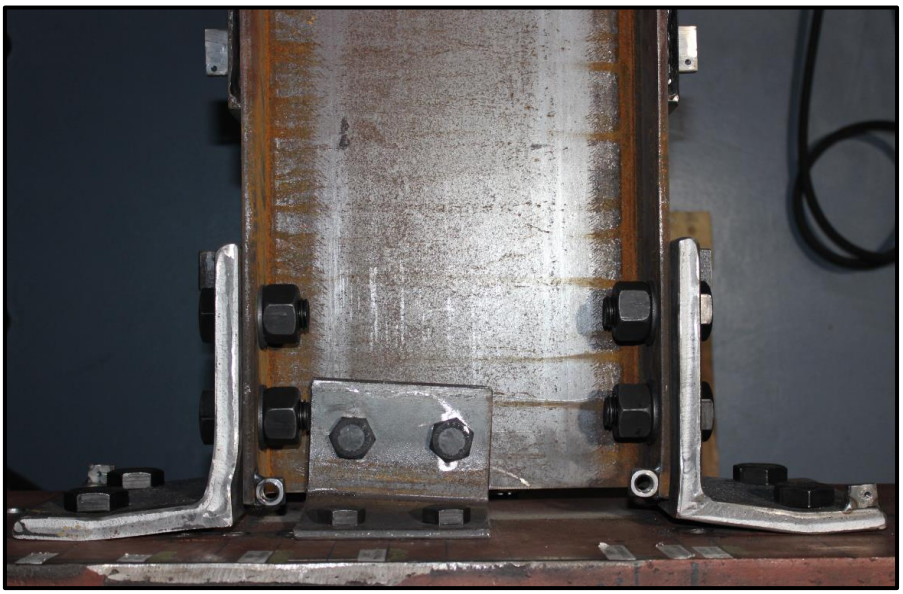
Size	L4 x 4 x 5/16	
Steel Grade	A36	
F_y	373	MPa
F_u	507	MPa
ε_u	0.2415	
Length	140	mm

Note: The displacements were measured at the center of the top and seat angle fillet.

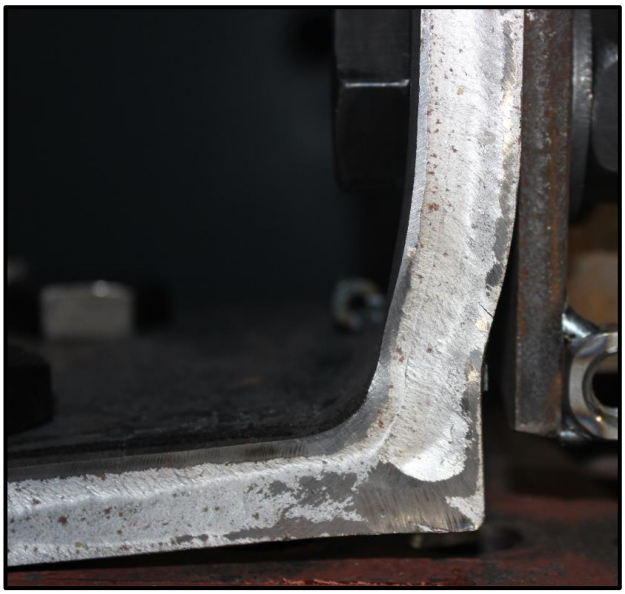
Failure Mode Beam leg fracture of the top angle

Moment-Rotation

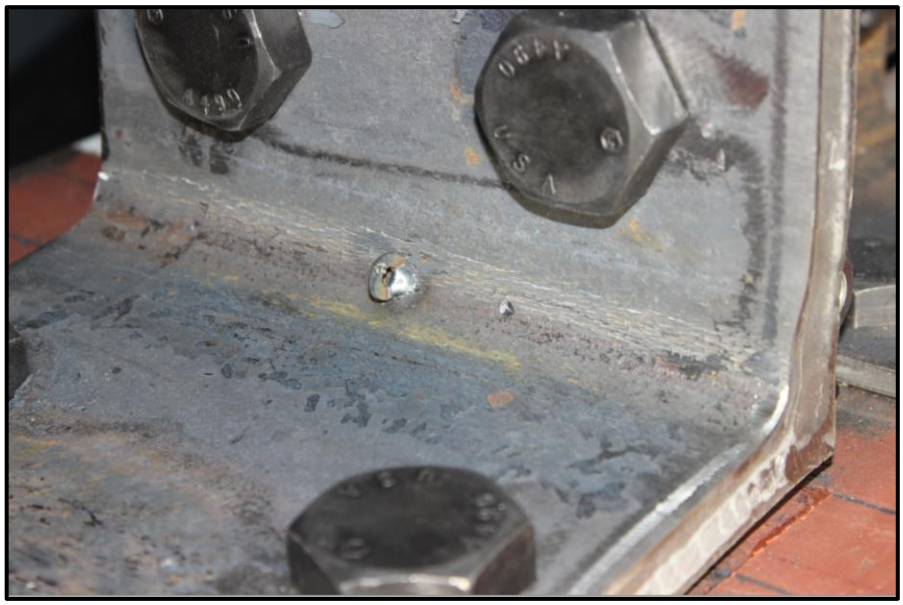




Connection at fracture



Top angle beam leg shear deformation



Top angle beam leg cracking at fracture



Top angle beam leg fracture



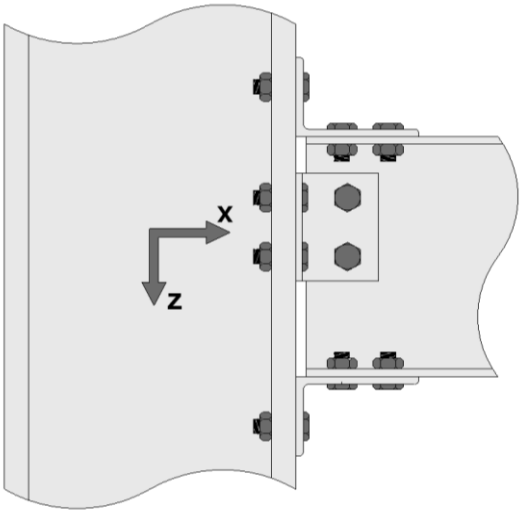
Close-up of the web angle deformation



Seat angle column leg deformation

SPECIMEN 3B

Beam	W310 x 39	
Column	W360 x 347	
Loading Type	Cyclic + Shear Excursions	
Constant shear	94.3	kN
Shear excursions	152.0	kN



Top & Seat Angles

Size	L8 x 6 x 3/4	
Steel Grade	A36	
F_y	340	MPa
F_u	516	MPa
ε_u	0.2592	

$\Delta_{X\ max\ Top\ +}$	19.46	mm
$\Delta_{Z\ max\ Top\ +}$	2.75	mm
$\Delta_{X\ max\ Top\ -}$	-0.07	mm
$\Delta_{Z\ max\ Top\ -}$	-4.03	mm
$\Delta_{X\ max\ Bottom\ +}$	16.62	mm
$\Delta_{Z\ max\ Bottom\ +}$	0.00	mm
$\Delta_{X\ max\ Bottom\ -}$	-0.06	mm
$\Delta_{Z\ max\ Bottom\ -}$	-8.14	mm

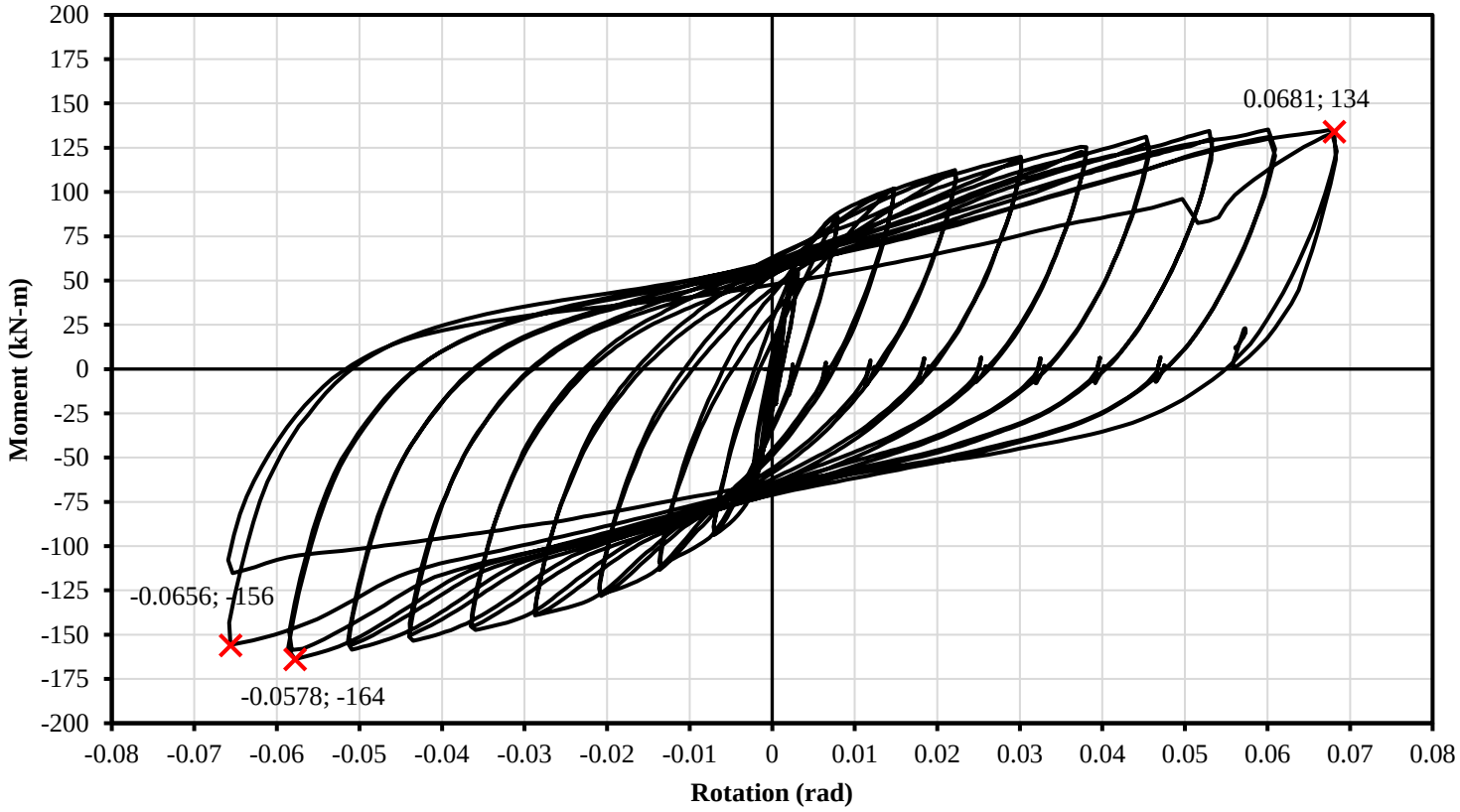
Web Angles

Size	L4 x 4 x 5/16	
Steel Grade	A36	
F_y	373	MPa
F_u	507	MPa
ε_u	0.2415	
Length	140	mm

Note: The displacements were measured at the center of the top and seat angle fillet.

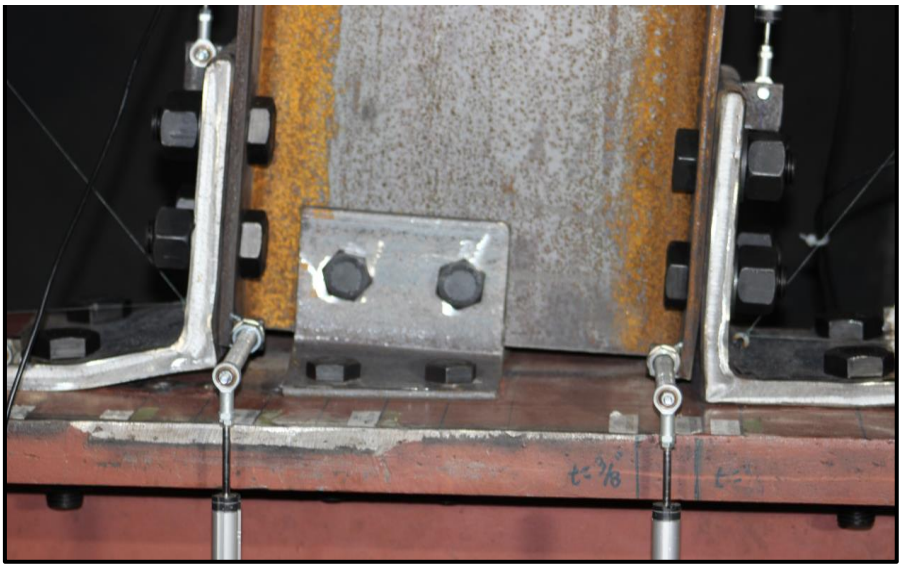
Failure Mode Beam leg fracture of the top angle

Moment-Rotation

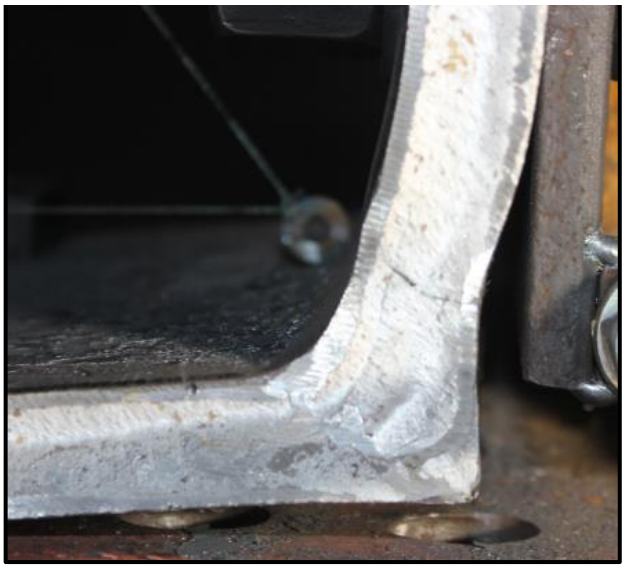




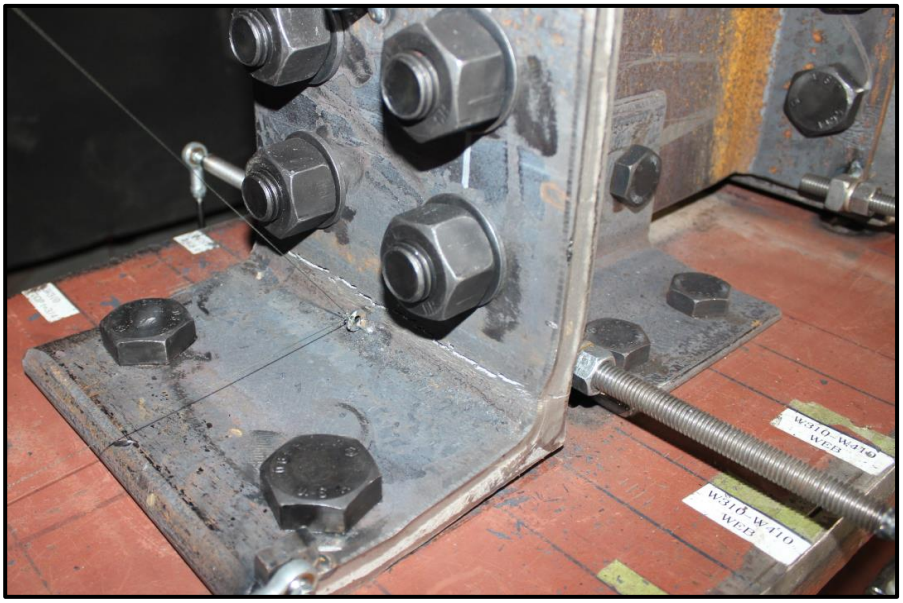




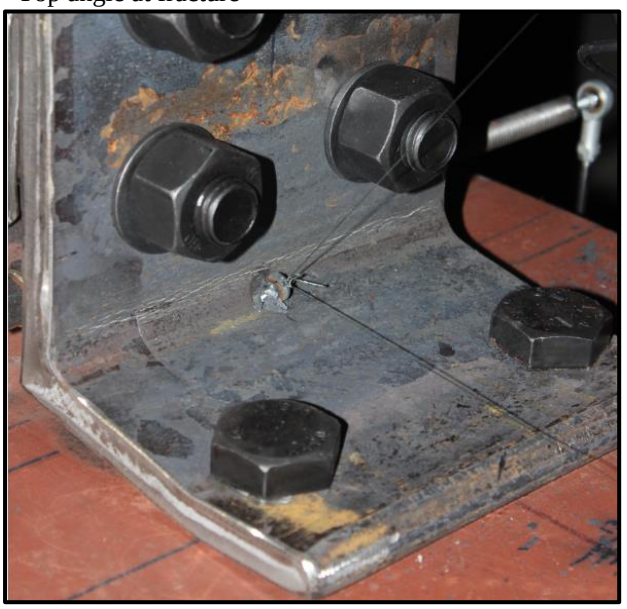
Connection at fracture



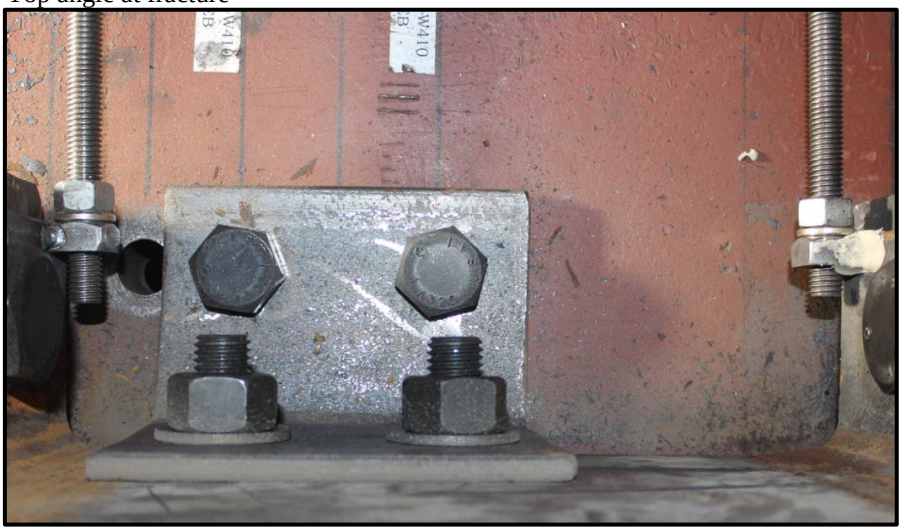
Top angle at fracture



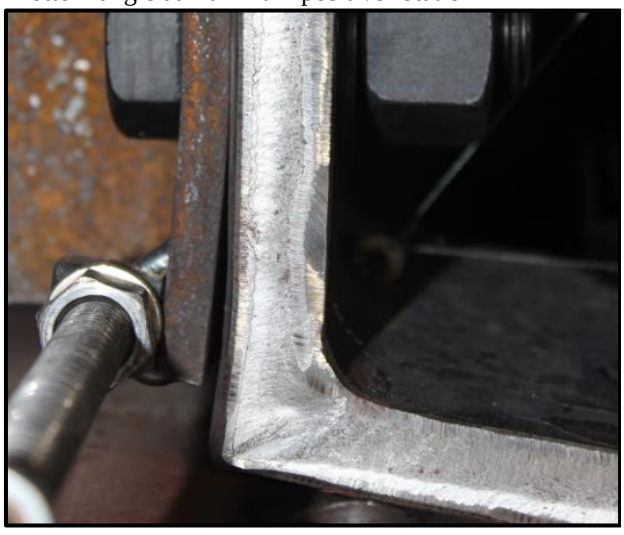
Top angle at fracture



Bottom angle at maximum positive rotation



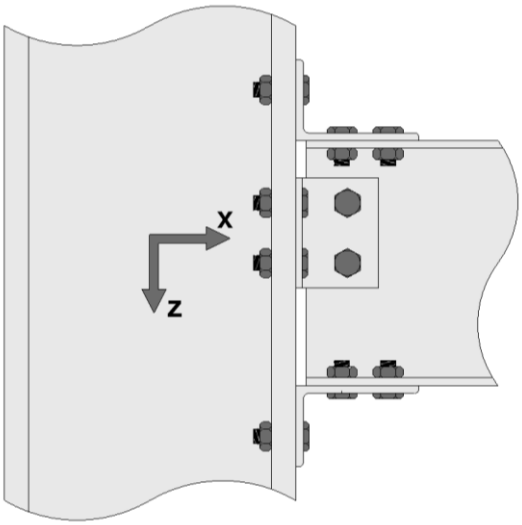
Web angle deformation at fracture



Bottom beam flange local deformation

SPECIMEN 3C

Beam	W310 x 39	
Column	W360 x 347	
Loading Type	Cyclic, No Shear	
Constant shear	-	kN
Shear excursions	-	kN



Top & Seat Angles

Size	L8 x 6 x 3/4	
Steel Grade	A36	
F_y	340	MPa
F_u	516	MPa
ε_u	0.2592	

$\Delta_{X\ max\ Top\ +}$	18.15	mm
$\Delta_{Z\ max\ Top\ +}$	3.66	mm
$\Delta_{X\ max\ Top\ -}$	-0.16	mm
$\Delta_{Z\ max\ Top\ -}$	-1.19	mm
$\Delta_{X\ max\ Bottom\ +}$	17.58	mm
$\Delta_{Z\ max\ Bottom\ +}$	1.49	mm
$\Delta_{X\ max\ Bottom\ -}$	-0.21	mm
$\Delta_{Z\ max\ Bottom\ -}$	-4.28	mm

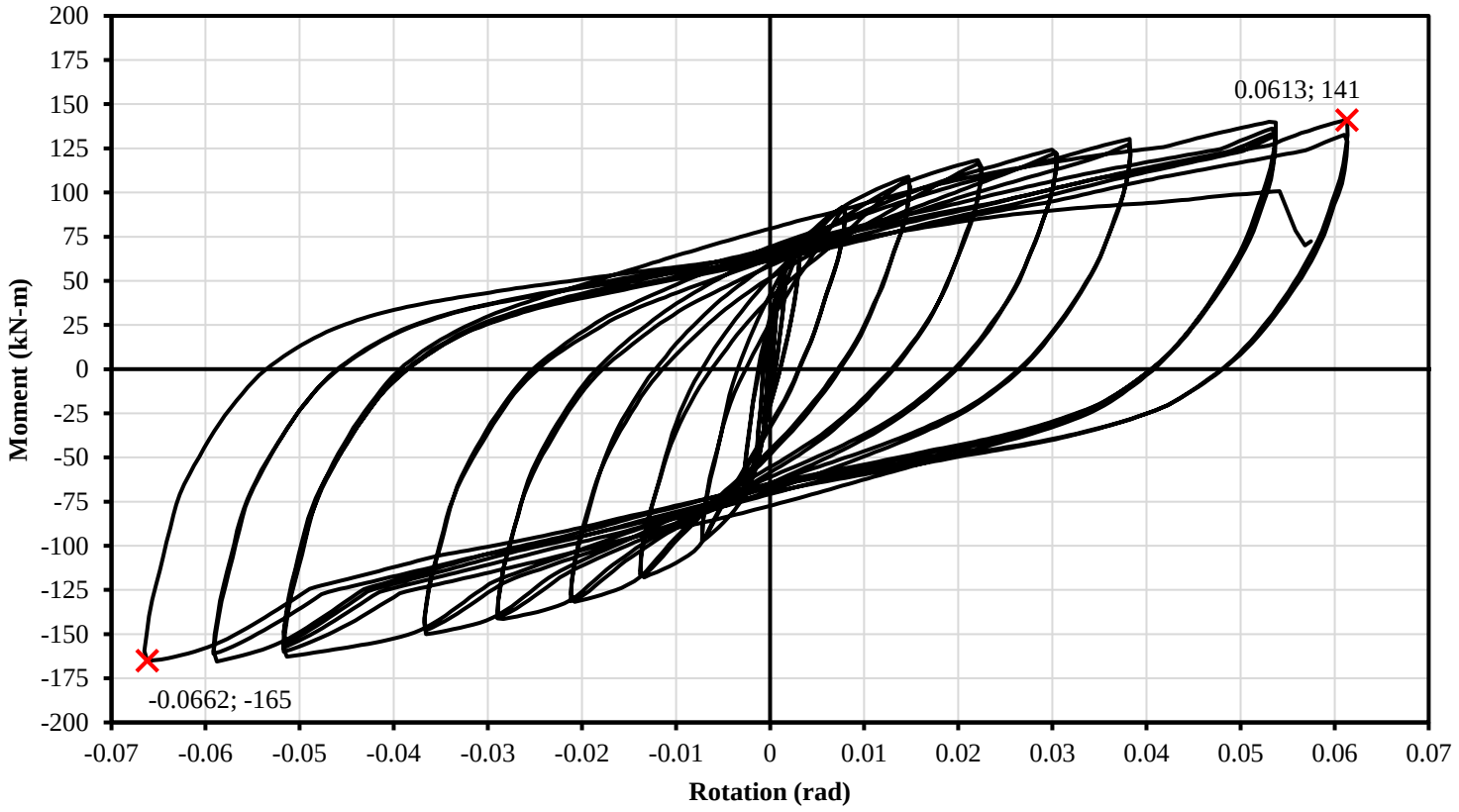
Web Angles

Size	L4 x 4 x 5/16	
Steel Grade	A36	
F_y	373	MPa
F_u	507	MPa
ε_u	0.2415	
Length	140	mm

Note: The displacements were measured at the center of the top and seat angle fillet.

Failure Mode Beam leg fracture of the bottom angle

Moment-Rotation





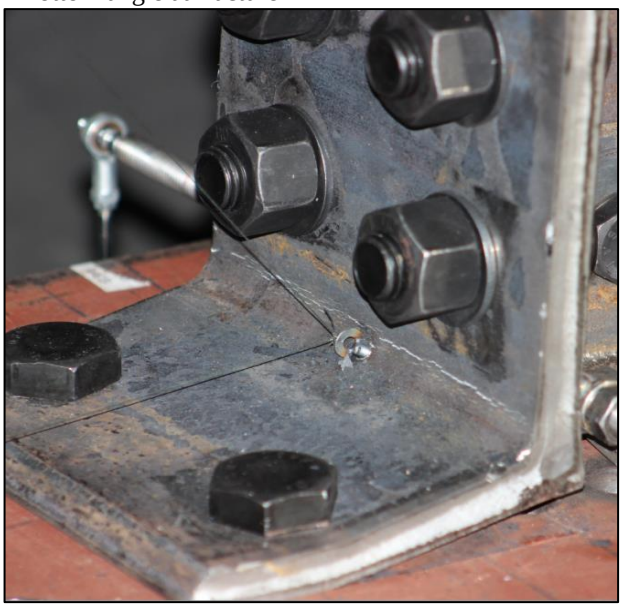
Connection at fracture



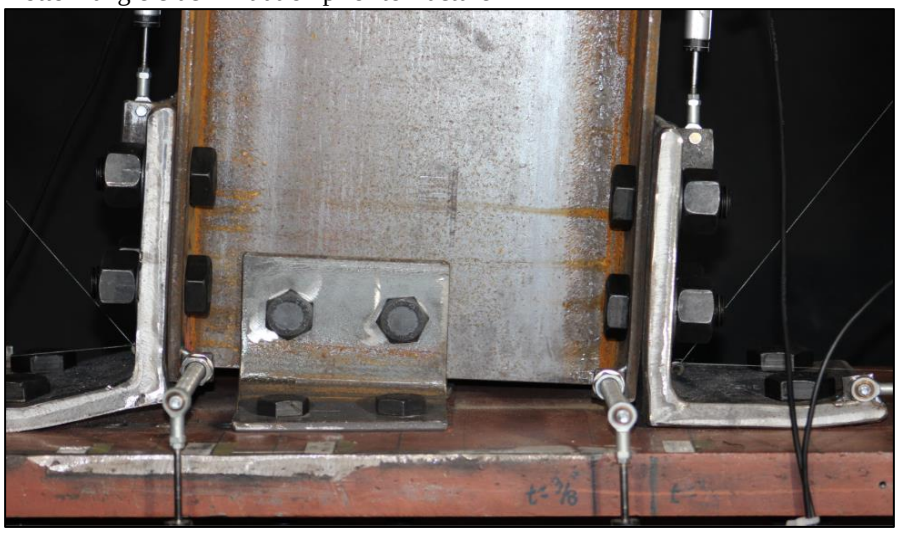
Bottom angle at fracture



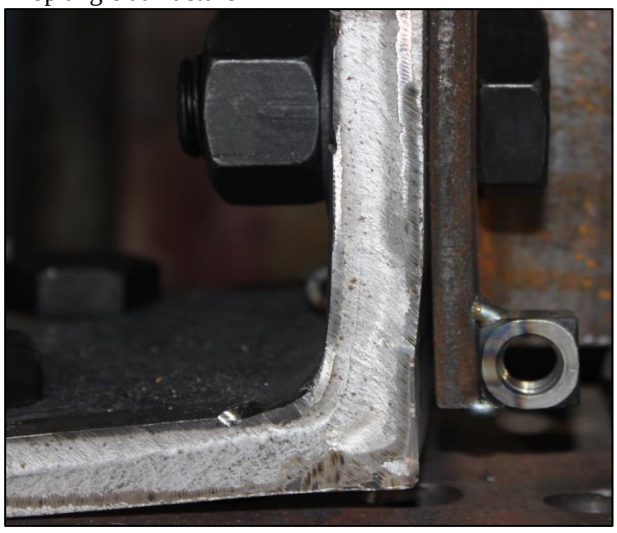
Bottom angle crack initiation prior to fracture



Top angle at fracture



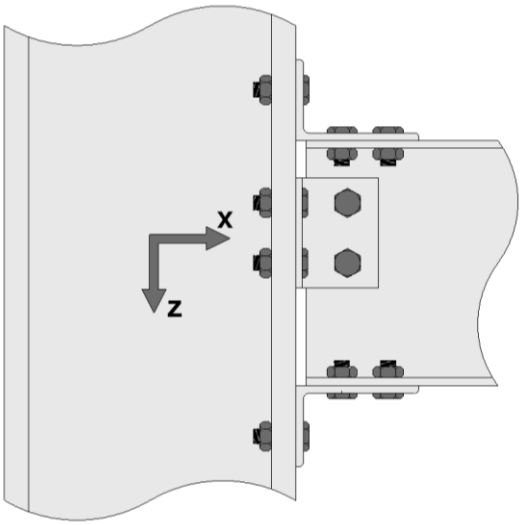
Connection deformation under negative bending



Top angle plastic hinging

SPECIMEN 3D

Beam	W310 x 39	
Column	W250x67	
Loading Type	Cyclic	
Constant shear	94.3	kN
Shear excursions	-	kN



Top & Seat Angles

Size	L8 x 6 x 3/4	
Steel Grade	A36	
F_y	340	MPa
F_u	516	MPa
ε_u	0.2592	

$\Delta_{X\ max\ Top\ +}$	22.35	mm
$\Delta_{Z\ max\ Top\ +}$	1.40	mm
$\Delta_{X\ max\ Top\ -}$	-0.69	mm
$\Delta_{Z\ max\ Top\ -}$	-4.39	mm
$\Delta_{X\ max\ Bottom\ +}$	19.74	mm
$\Delta_{Z\ max\ Bottom\ +}$	-0.08	mm
$\Delta_{X\ max\ Bottom\ -}$	-0.62	mm
$\Delta_{Z\ max\ Bottom\ -}$	-9.43	mm

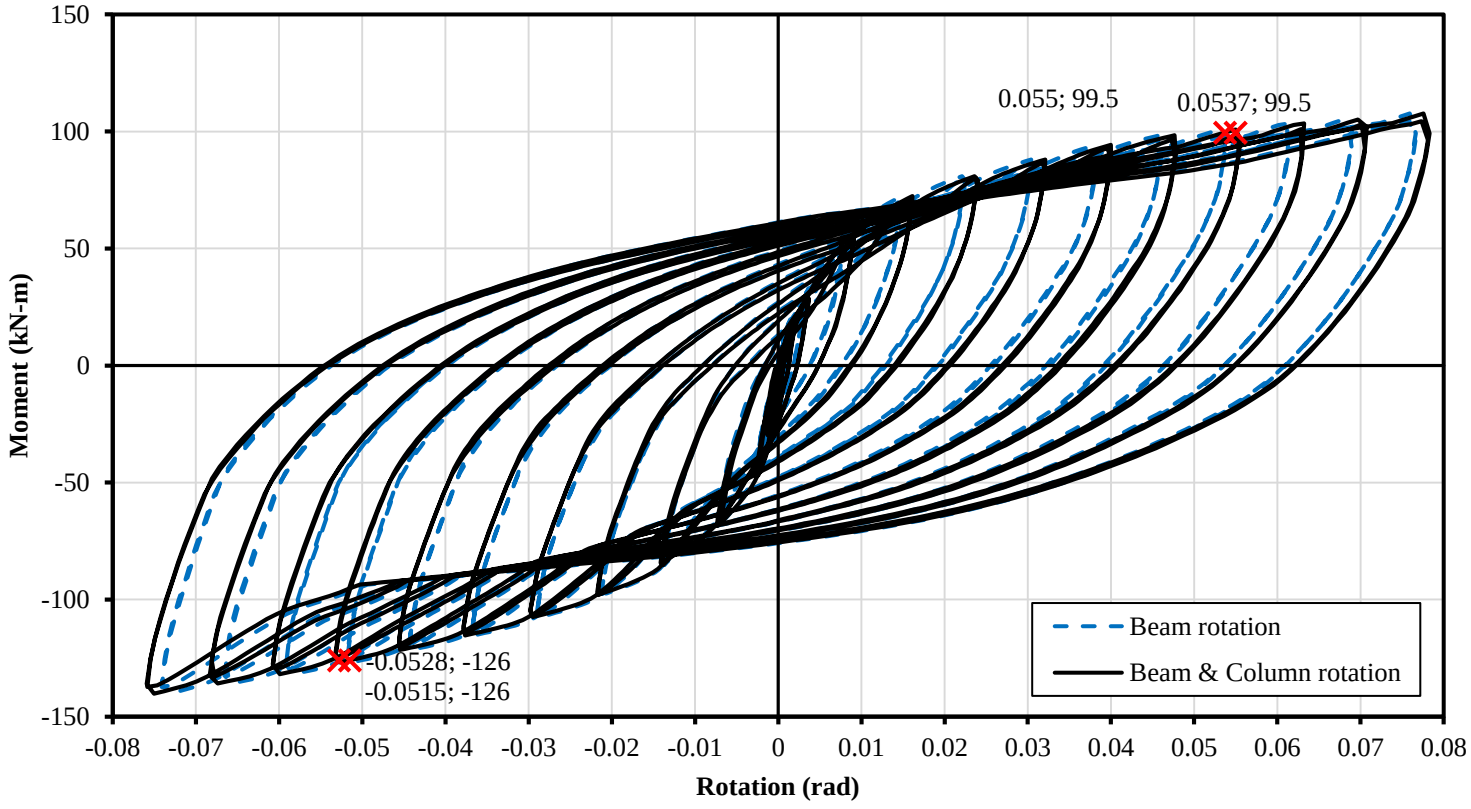
Web Angles

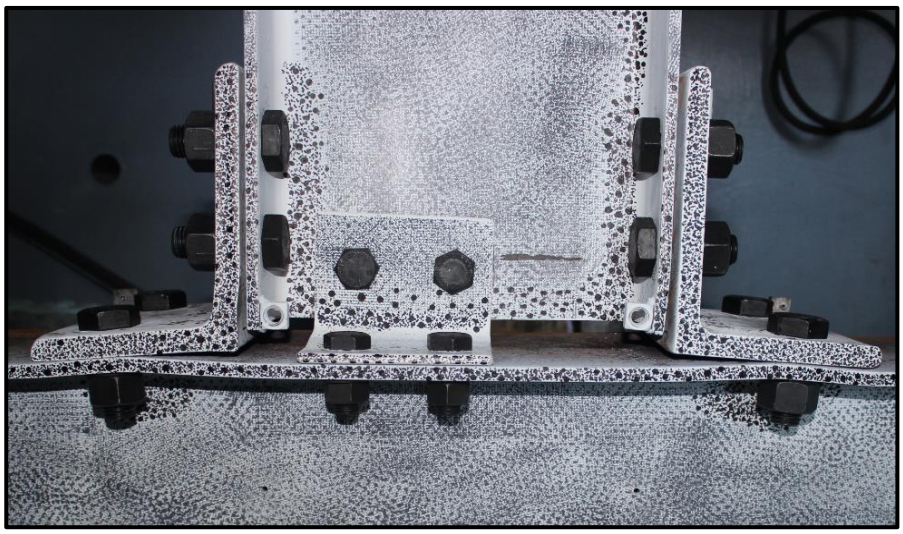
Size	L4 x 4 x 5/16	
Steel Grade	A36	
F_y	373	MPa
F_u	507	MPa
ε_u	0.2415	
Length	140	mm

Note: The displacements were measured at the center of the top and seat angle fillet.

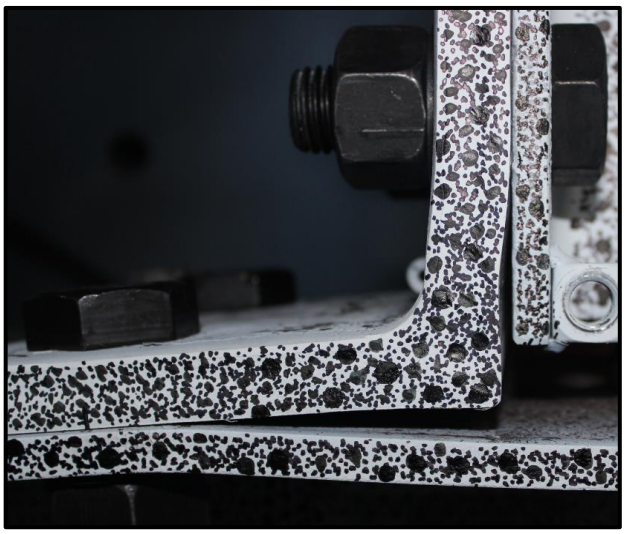
Failure Mode Beam leg fracture of the top angle

Moment-Rotation





Connection at fracture

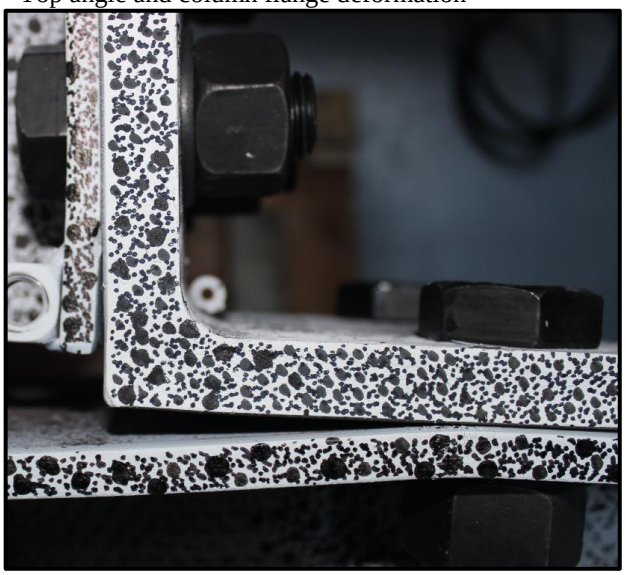


Top angle and column flange deformation





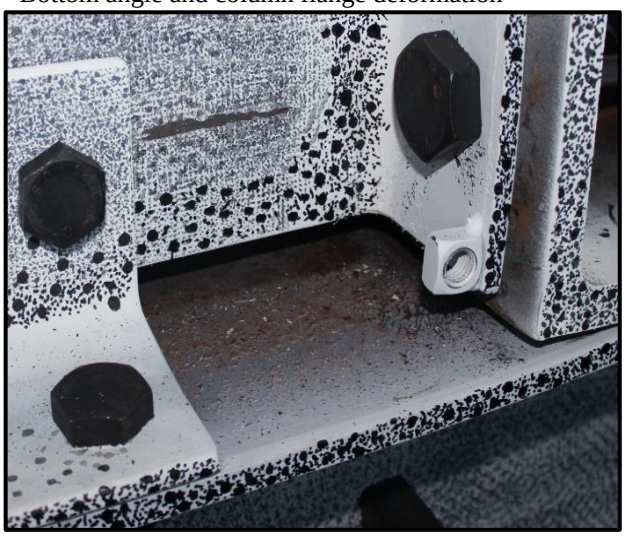
Top angle beam leg fracture



Bottom angle and column flange deformation



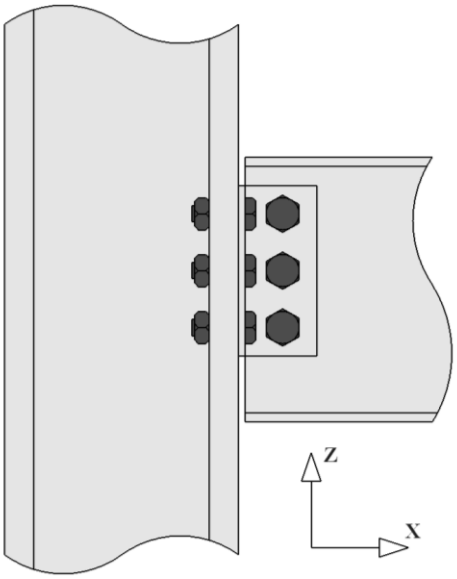
Column flange deformation near the top angle bolts



Beam web yielding near the web angle bolts

SPECIMEN 4A

Beam	W410 x 67	
Column	W360 x 347	
Loading Type	Cyclic	
Constant shear	282.9	kN
Shear excursions	-	



Top & Seat Angles

Size	N/A	
Steel Grade	-	
F_y	-	
F_u	-	
ε_u	-	

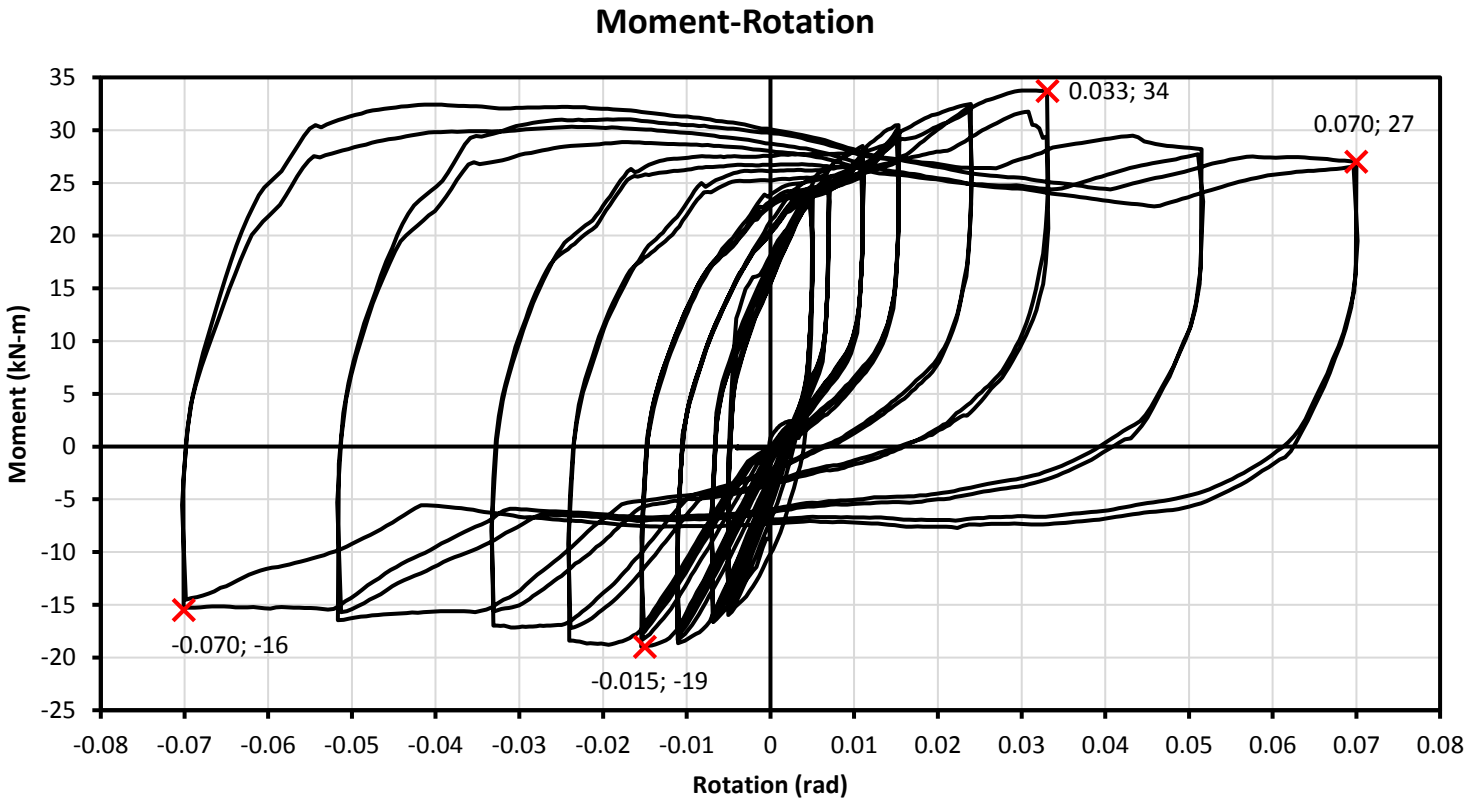
$\Delta_{X\ max\ Top\ +}$	22.36	mm
$\Delta_{Z\ max\ Top\ +}$	0.00	mm
$\Delta_{X\ max\ Top\ -}$	-4.01	mm
$\Delta_{Z\ max\ Top\ -}$	-15.44	mm
$\Delta_{X\ max\ Bottom\ +}$	24.97	mm
$\Delta_{Z\ max\ Bottom\ +}$	0.00	mm
$\Delta_{X\ max\ Bottom\ -}$	-9.81	mm
$\Delta_{Z\ max\ Bottom\ -}$	-14.12	mm

Web Angles

Size	L4 x 4 x 5/16	
Steel Grade	A36	
F_y	373	MPa
F_u	507	MPa
ε_u	0.2415	
Length	216	mm

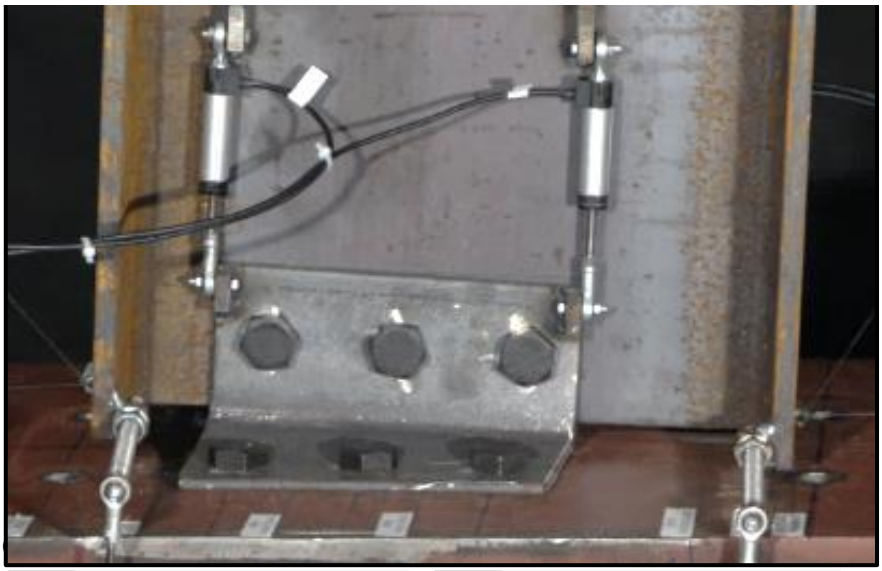
Note: The displacements were measured at the center of the beam flanges.

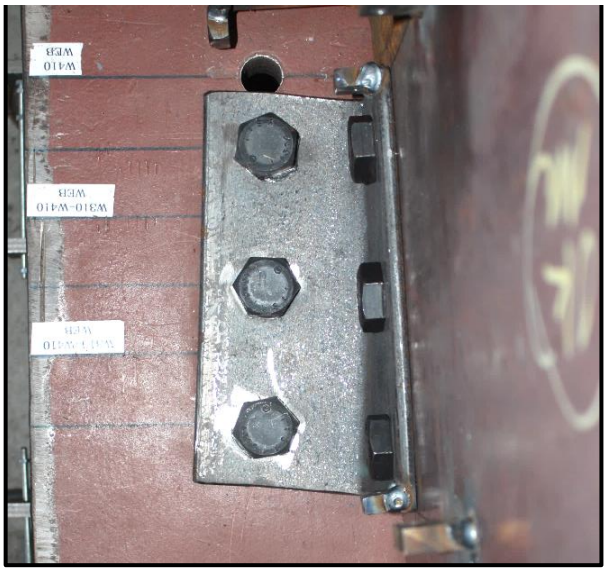
Failure Mode Beam leg fracture on the top side of the north angle

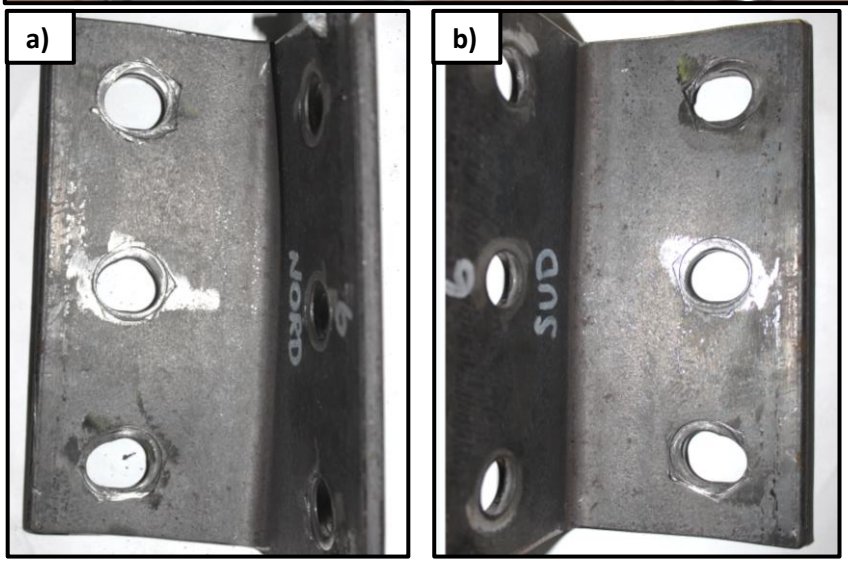








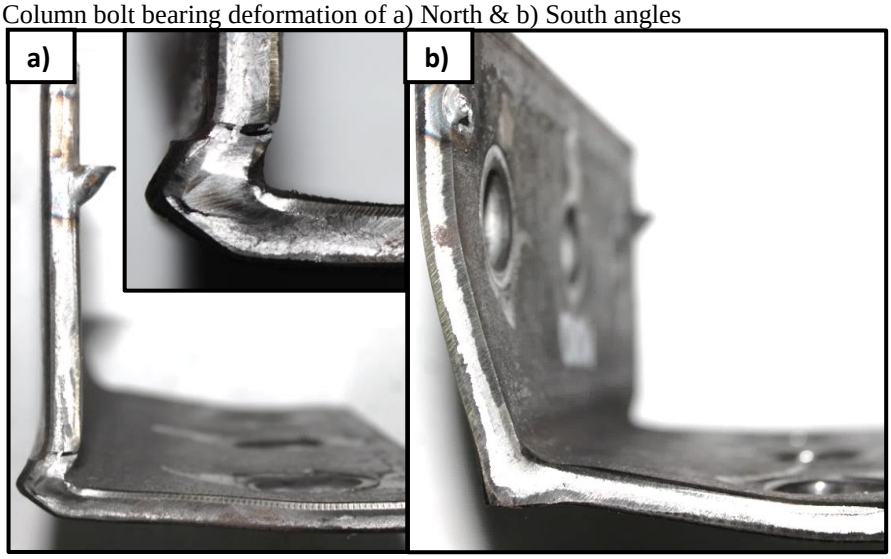




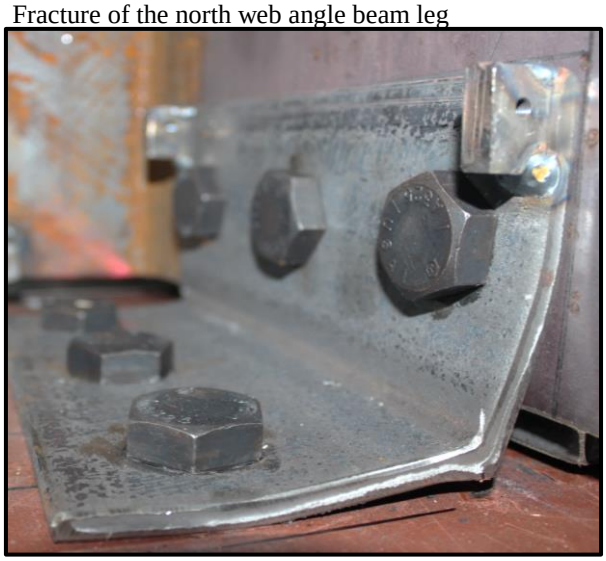
Column bolt bearing deformation of a) North & b) South angles



Fracture of the north web angle beam leg



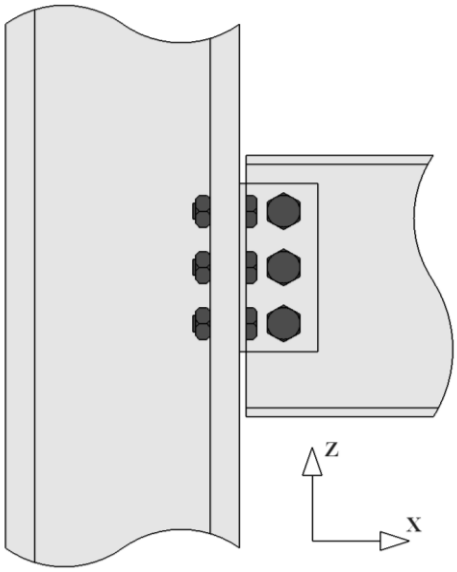
Profile of north web angle on a) top side and b) bottom side



Bottom side of web angle pull out from beam web

SPECIMEN 4B

Beam	W410 x 67	
Column	W360 x 347	
Loading Type	Cyclic + Shear Excursions	
Constant shear	282.9	kN
Shear excursions	456.0	kN



Top & Seat Angles

Size	N/A	
Steel Grade	-	
F_y	-	
F_u	-	
ε_u	-	

$\Delta_{X\ max\ Top\ +}$	21.97	mm
$\Delta_{Z\ max\ Top\ +}$	-0.17	mm
$\Delta_{X\ max\ Top\ -}$	-4.34	mm
$\Delta_{Z\ max\ Top\ -}$	-18.58	mm
$\Delta_{X\ max\ Bottom\ +}$	24.67	mm
$\Delta_{Z\ max\ Bottom\ +}$	0.02	mm
$\Delta_{X\ max\ Bottom\ -}$	-9.87	mm
$\Delta_{Z\ max\ Bottom\ -}$	-16.85	mm

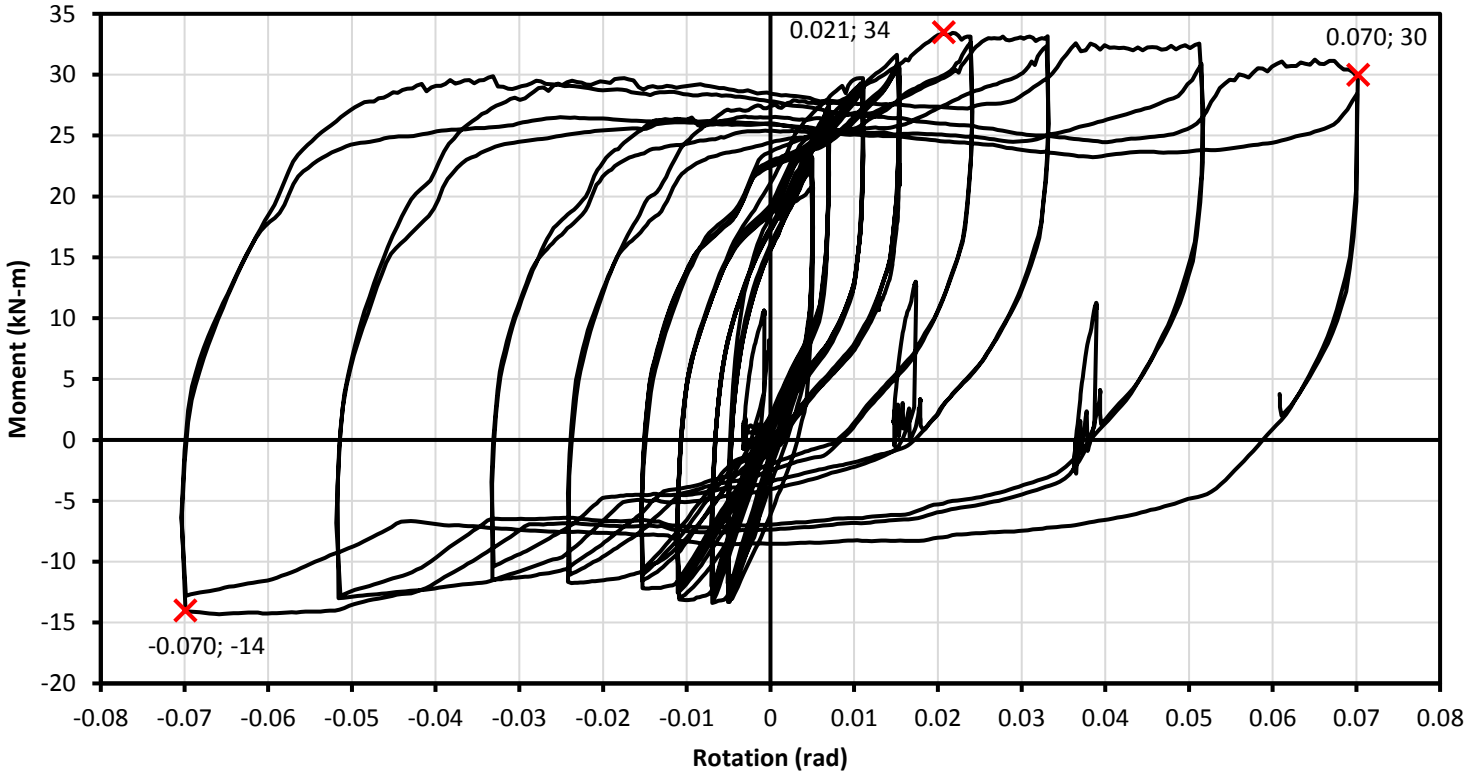
Web Angles

Size	L4 x 4 x 5/16	
Steel Grade	A36	
F_y	373	MPa
F_u	507	MPa
ε_u	0.2415	
Length	216	mm

Note: The displacements were measured at the center of the beam flanges.

Failure Mode Beam leg fracture on the top side of the north angle

Moment-Rotation

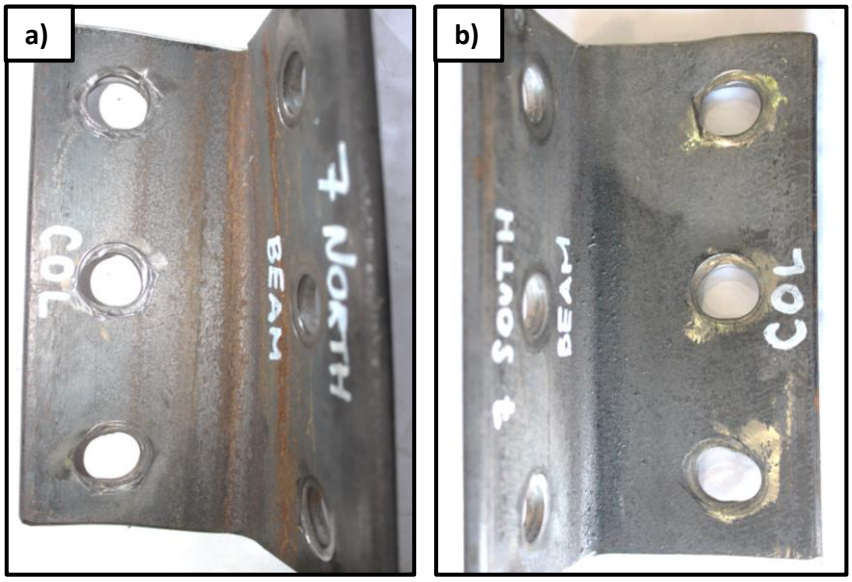




Connection at end of test



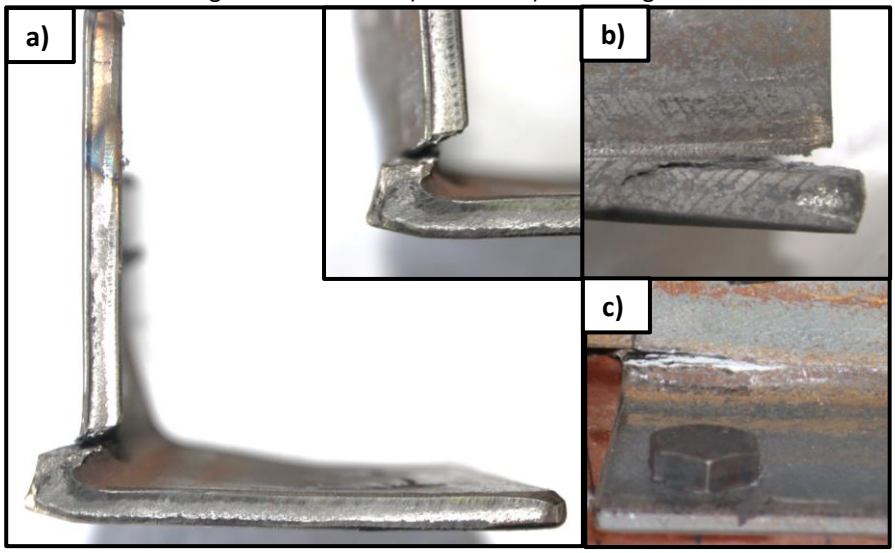
Shear deformation of the north web angle



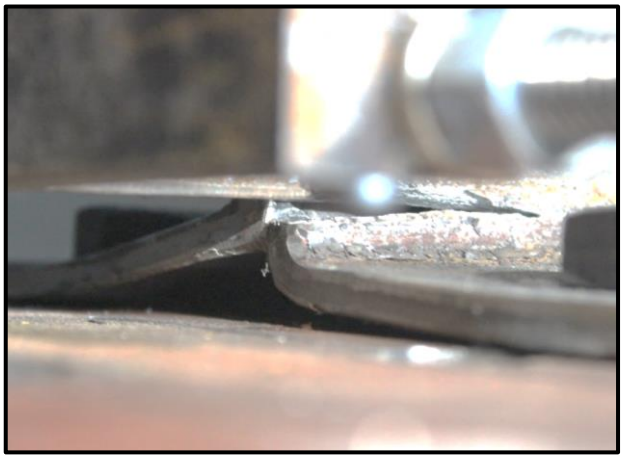
Column bolt bearing deformation of a) North & b) South angles



Bottom side of web angle pulling out from beam web



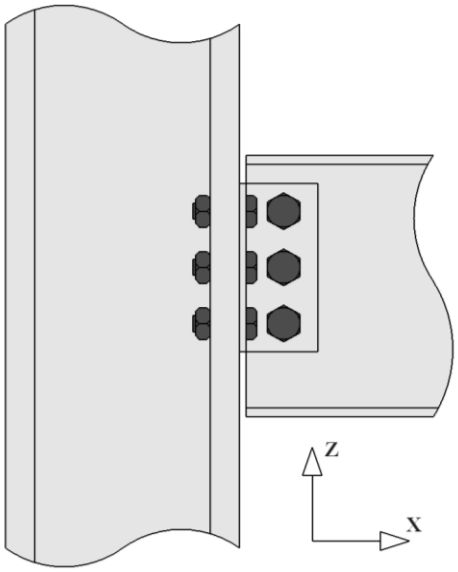
a) Top side profile of web angle & fracture on b) beam web side c) outer side



Top side of web angle fillet pushed under the beam web

SPECIMEN 4C

Beam	W410 x 67	
Column	W360 x 347	
Loading Type	Cyclic only, No shear	
Constant shear	-	kN
Shear excursions	-	kN



Top & Seat Angles

Size	N/A	
Steel Grade	-	
F_y	-	
F_u	-	
ε_u	-	

$\Delta_{X\ max\ Top\ +}$	19.78	mm
$\Delta_{Z\ max\ Top\ +}$	1.70	mm
$\Delta_{X\ max\ Top\ -}$	-6.57	mm
$\Delta_{Z\ max\ Top\ -}$	-2.88	mm
$\Delta_{X\ max\ Bottom\ +}$	24.18	mm
$\Delta_{Z\ max\ Bottom\ +}$	3.00	mm
$\Delta_{X\ max\ Bottom\ -}$	-10.91	mm
$\Delta_{Z\ max\ Bottom\ -}$	-1.59	mm

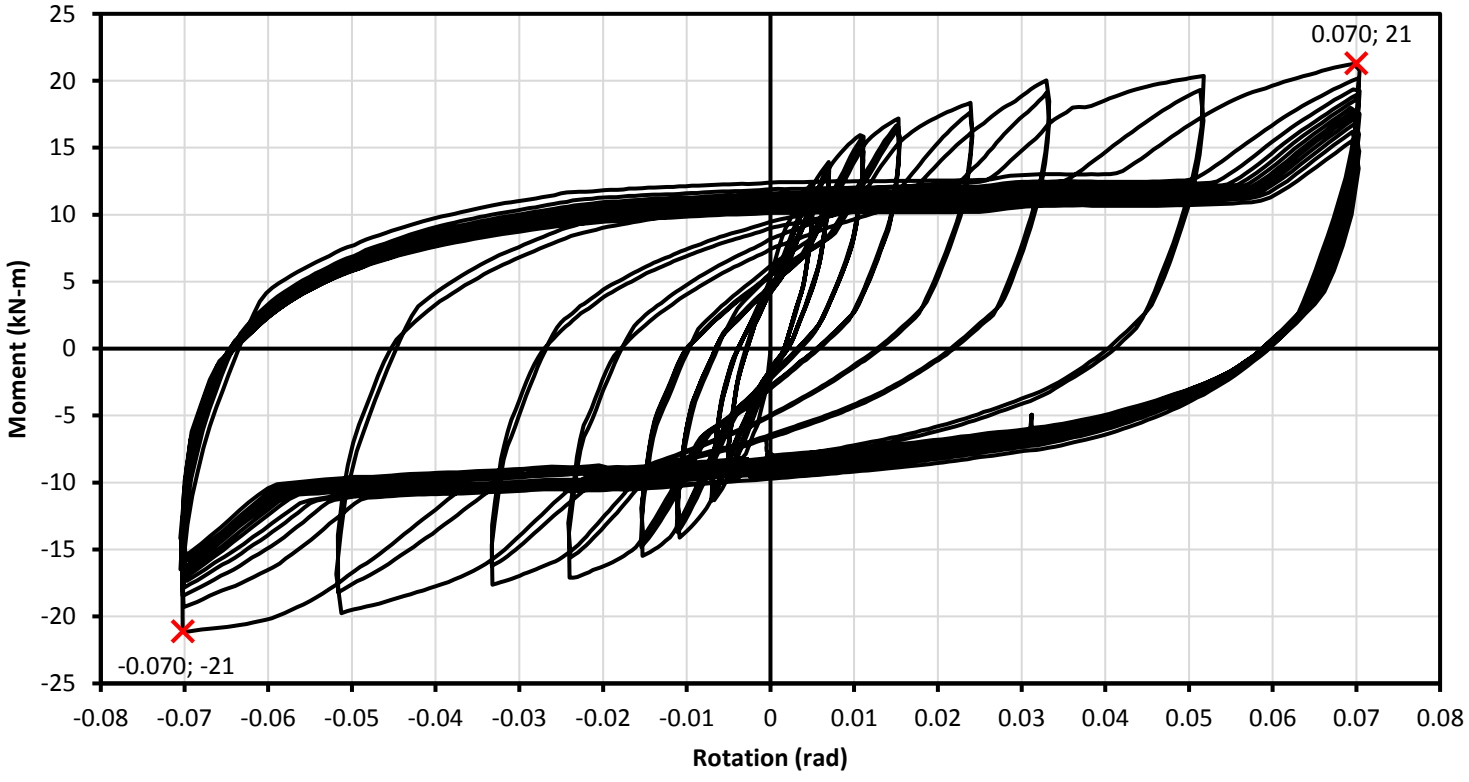
Web Angles

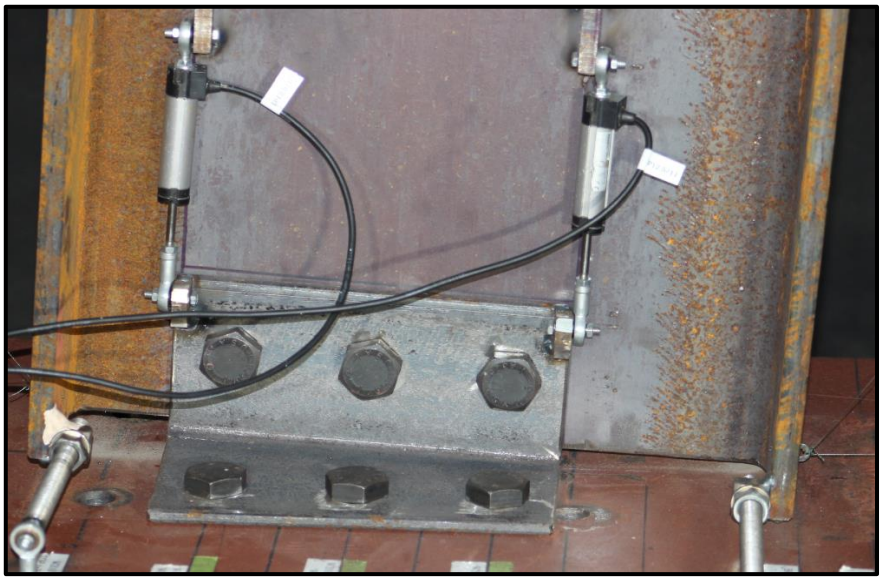
Size	L4 x 4 x 5/16	
Steel Grade	A36	
F_y	373	MPa
F_u	507	MPa
ε_u	0.2415	
Length	216	mm

Note: The displacements were measured at the center of the beam flanges.

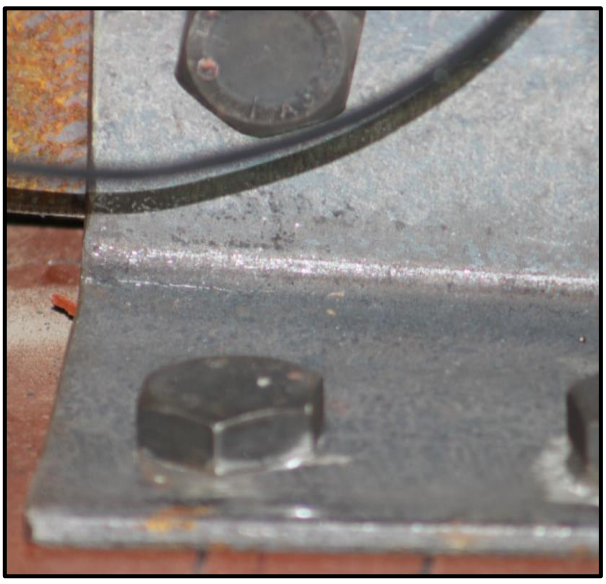
Failure Mode Beam leg fracture on the top side of the north angle

Moment-Rotation

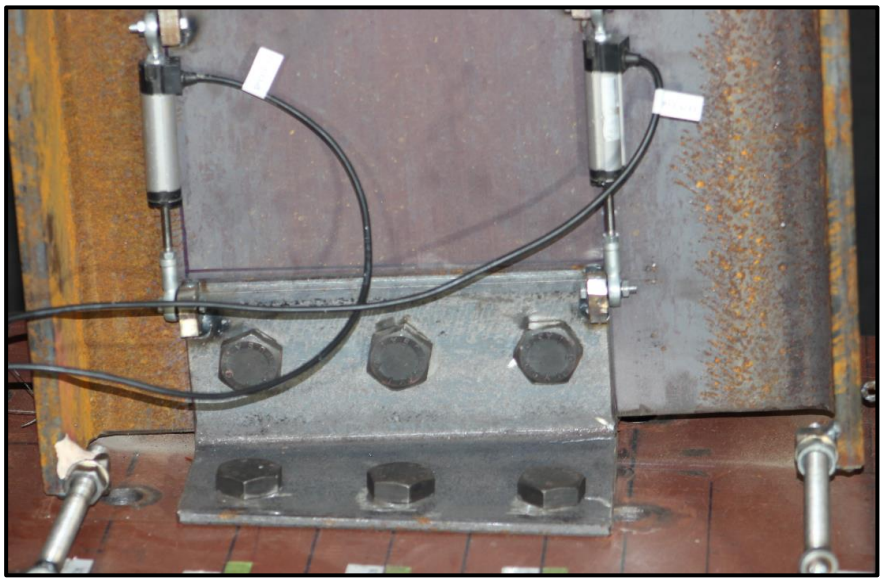




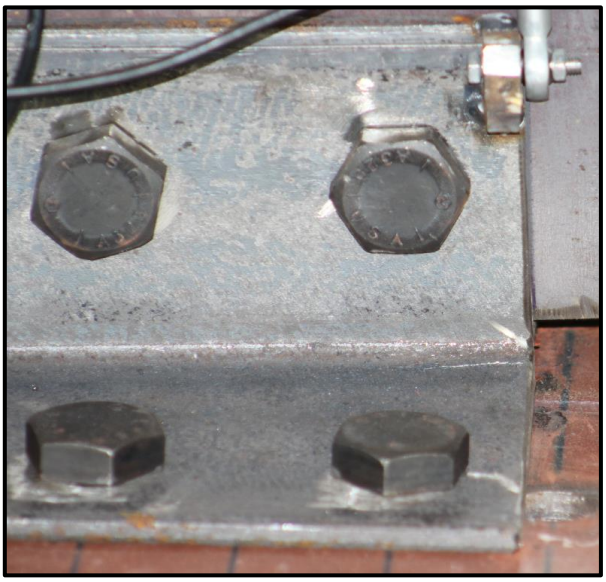
Connection at maximum negative rotation



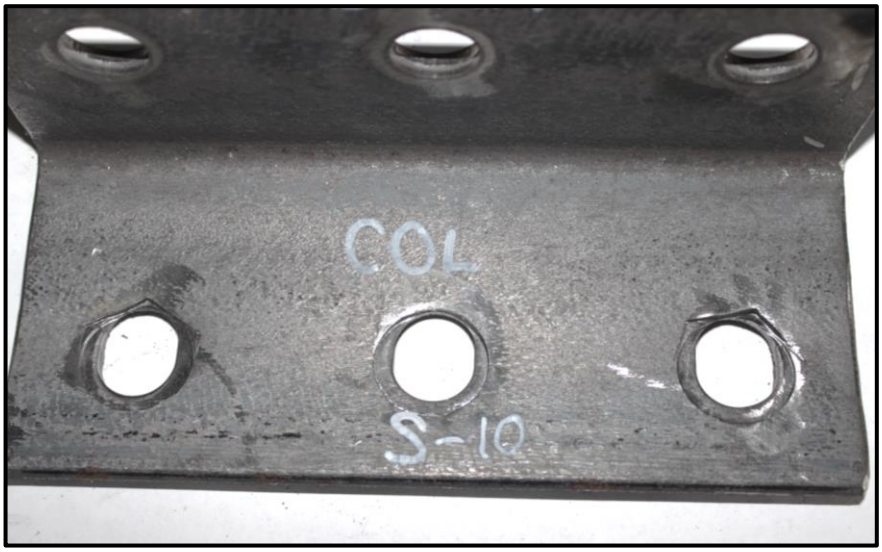
Fracture of north angle top side in negative rotation



Connection at maximum positive rotation



Fracture of north angle bottom side in positive rotation



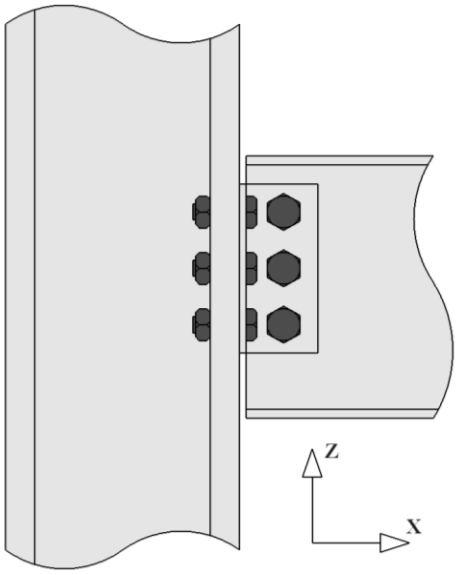
Column bolt hole bearing deformation



Net section fracture near column bolt holes

SPECIMEN 4D

Beam	W410 x 67	
Column	W360 x 347	
Loading Type	Cyclic Near Fault Protocol (-)	
Constant shear	282.9	kN
Shear excursions	-	kN



Top & Seat Angles

Size	N/A	
Steel Grade	-	
F_y	-	
F_u	-	
ε_u	-	

$\Delta_{X\ max\ Top\ +}$	22.27	mm
$\Delta_{Z\ max\ Top\ +}$	0.00	mm
$\Delta_{X\ max\ Top\ -}$	-2.04	mm
$\Delta_{Z\ max\ Top\ -}$	-15.43	mm
$\Delta_{X\ max\ Bottom\ +}$	8.63	mm
$\Delta_{Z\ max\ Bottom\ +}$	0.00	mm
$\Delta_{X\ max\ Bottom\ -}$	-11.39	mm
$\Delta_{Z\ max\ Bottom\ -}$	-14.40	mm

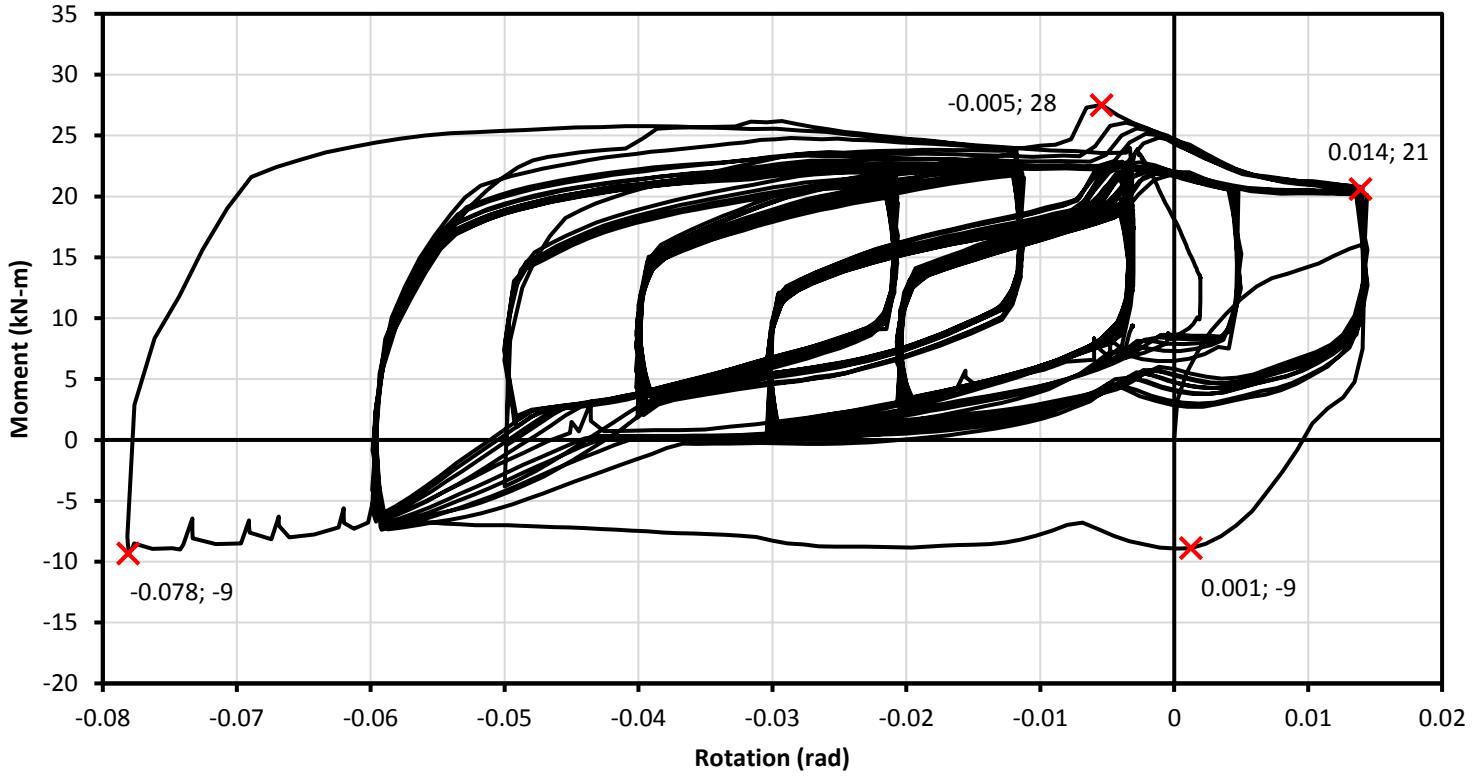
Web Angles

Size	L4 x 4 x 5/16	
Steel Grade	A36	
F_y	373	MPa
F_u	507	MPa
ε_u	0.2415	
Length	216	mm

Note: The displacements were measured at the center of the beam flanges.

Failure Mode The setup limits were reached before fracture

Moment-Rotation





Connection at end of test



Bottom side of web angle pulling out from beam web



Web angle shear deformation



Top side of web angle fillet pushed under the beam web



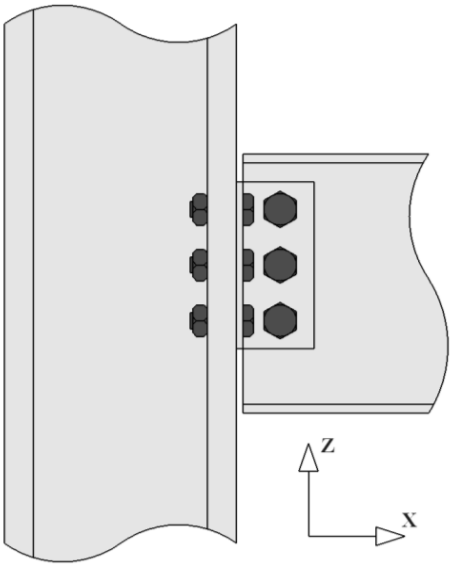
Beam web local yielding caused by the top side angle rotation



Column hole bearing deformations

SPECIMEN 4E

Beam	W410 x 67	
Column	W360 x 347	
Loading Type	Cyclic Near Fault Protocol (+)	
Constant shear	282.9	kN
Shear excursions	-	kN



Top & Seat Angles

Size	N/A	
Steel Grade	-	
F_y	-	
F_u	-	
ε_u	-	

$\Delta_{X\ max\ Top\ +}$	9.12	mm
$\Delta_{Z\ max\ Top\ +}$	0.00	mm
$\Delta_{X\ max\ Top\ -}$	-5.96	mm
$\Delta_{Z\ max\ Top\ -}$	-11.42	mm
$\Delta_{X\ max\ Bottom\ +}$	21.77	mm
$\Delta_{Z\ max\ Bottom\ +}$	0.00	mm
$\Delta_{X\ max\ Bottom\ -}$	-3.37	mm
$\Delta_{Z\ max\ Bottom\ -}$	-11.91	mm

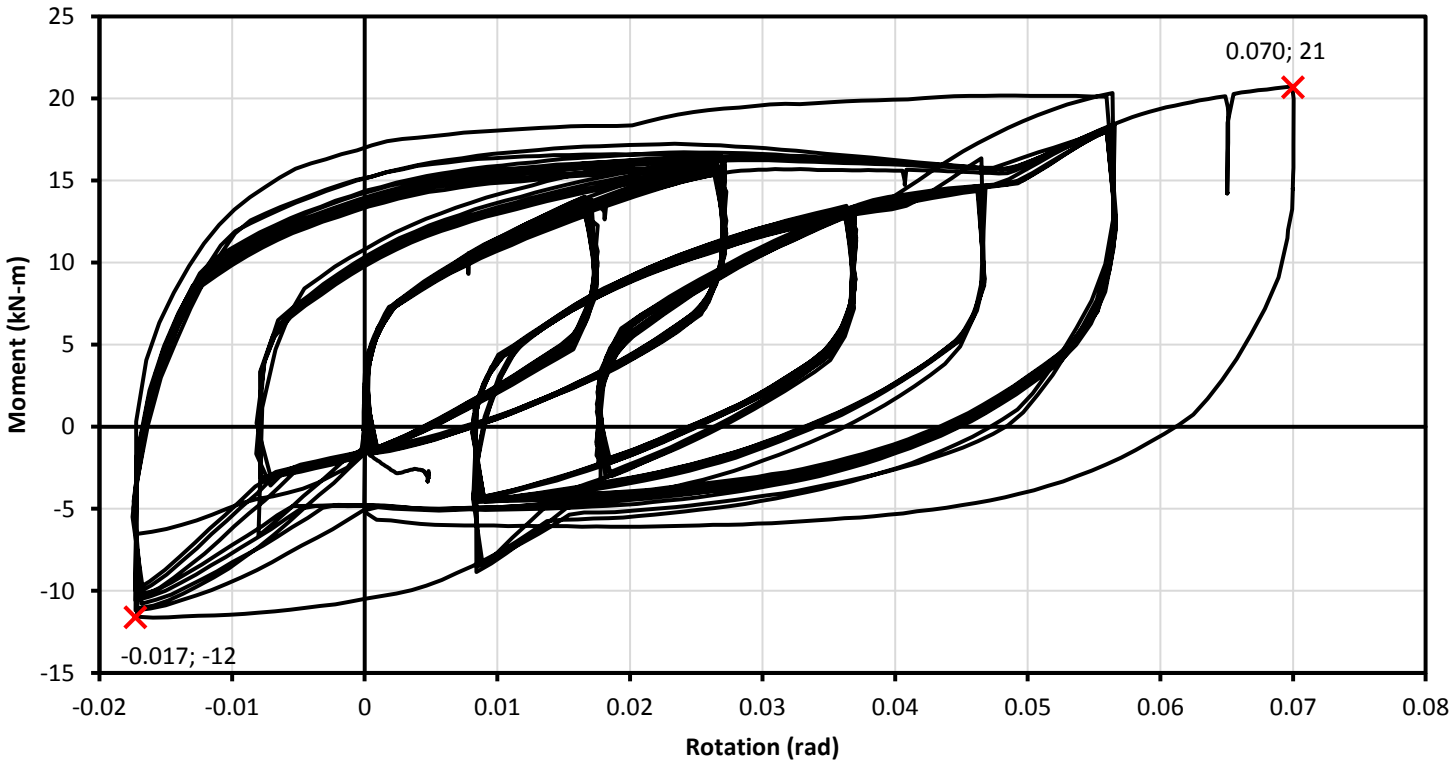
Web Angles

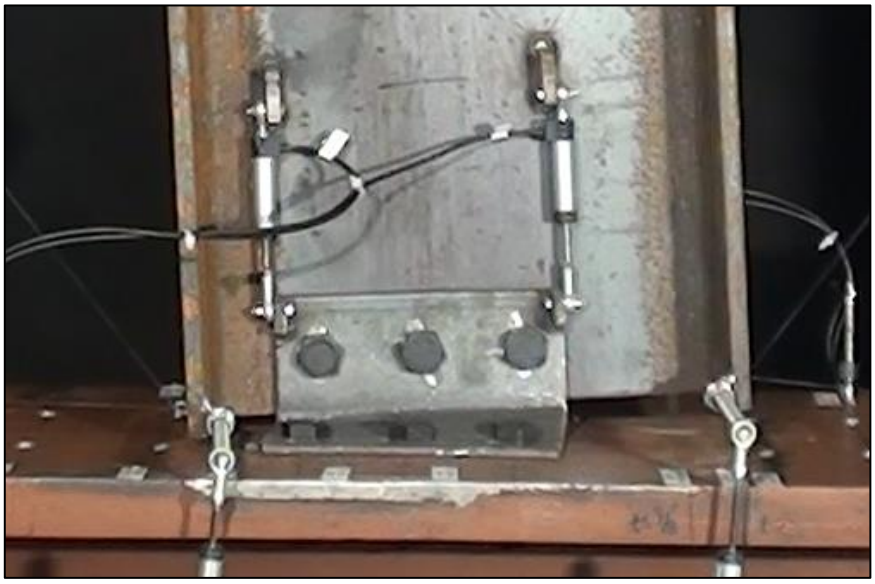
Size	L4 x 4 x 5/16	
Steel Grade	A36	
F_y	373	MPa
F_u	507	MPa
ε_u	0.2415	
Length	216	mm

Note: The displacements were measured at the center of the beam flanges.

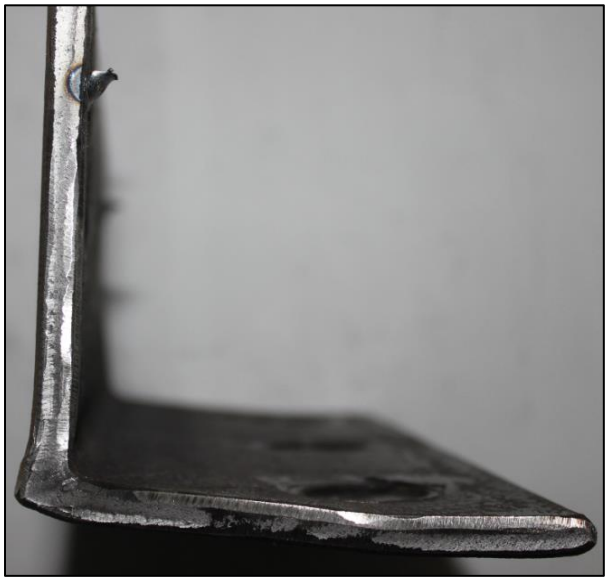
Failure Mode The setup limits were reached before fracture

Moment-Rotation

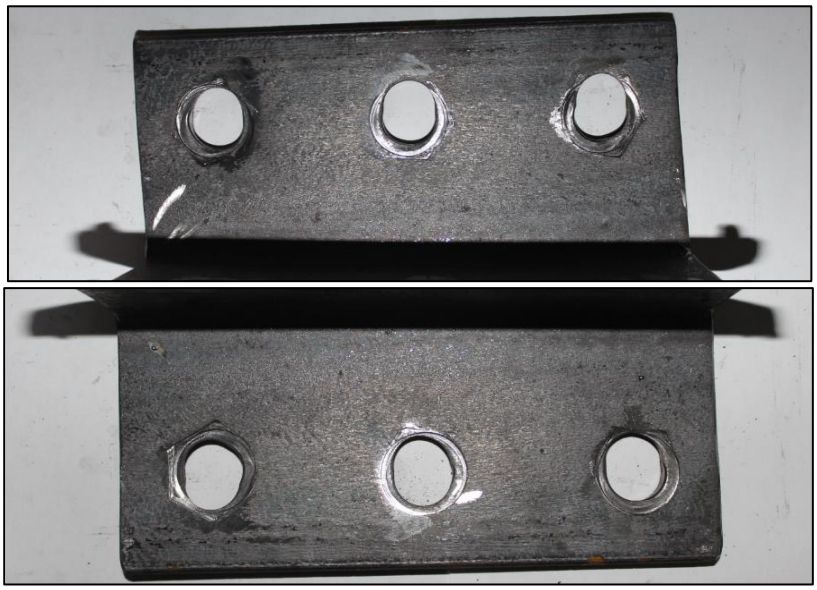




Connection at end of test



Top side deformation of web angles



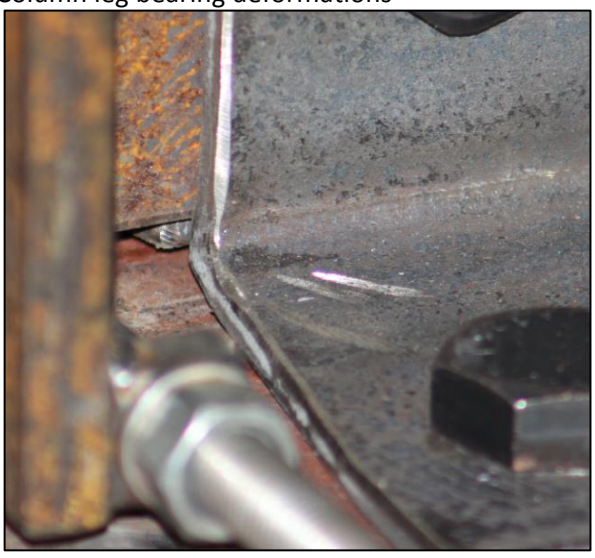
Web angle shear deformations



Column leg bearing deformations



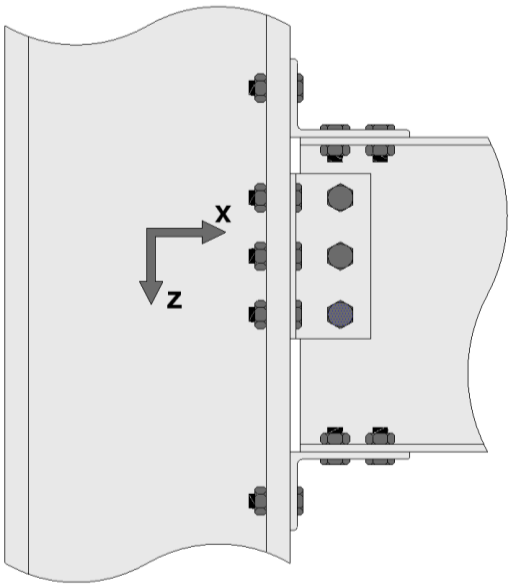
Bottom side of web angle pulling out from beam web



Top side of web angle fillet pushed under the beam web

SPECIMEN 5A

Beam	W410 x 67	
Column	W360 x 347	
Loading Type	Cyclic	
Constant shear	282.9	kN
Shear excursions	-	kN



Top & Seat Angles

Size	L6 x 4 x 3/8	
Steel Grade	A36	
F_y	370	
F_u	518	
ε_u	0.2420	

$\Delta_{X\ max\ Top\ +}$	12.91	mm
$\Delta_{Z\ max\ Top\ +}$	-0.16	mm
$\Delta_{X\ max\ Top\ -}$	0.00	mm
$\Delta_{Z\ max\ Top\ -}$	-2.62	mm
$\Delta_{X\ max\ Bottom\ +}$	12.98	mm
$\Delta_{Z\ max\ Bottom\ +}$	-0.35	mm
$\Delta_{X\ max\ Bottom\ -}$	-0.34	mm
$\Delta_{Z\ max\ Bottom\ -}$	-7.68	mm

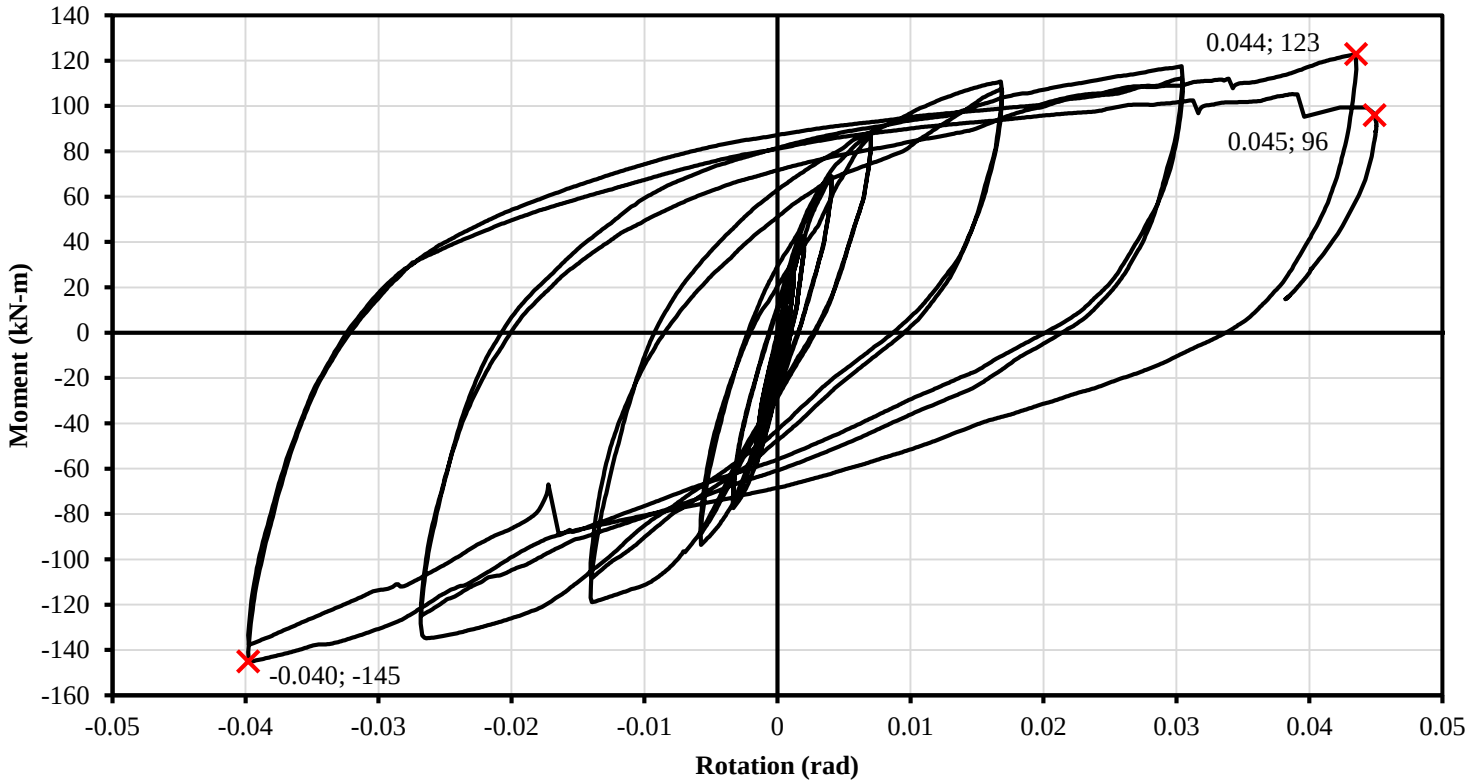
Web Angles

Size	L4 x 4 x 5/16	
Steel Grade	A36	
F_y	373	MPa
F_u	507	MPa
ε_u	0.2415	
Length	216	mm

Note: The displacements were measured at the center of the top and seat angle fillet.

Failure Mode Beam leg cracking of the seat angle

Moment-Rotation

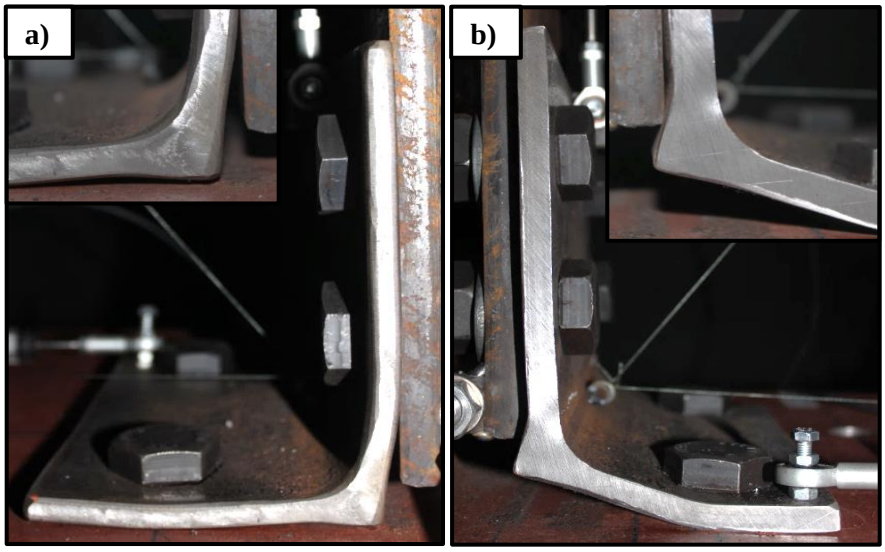




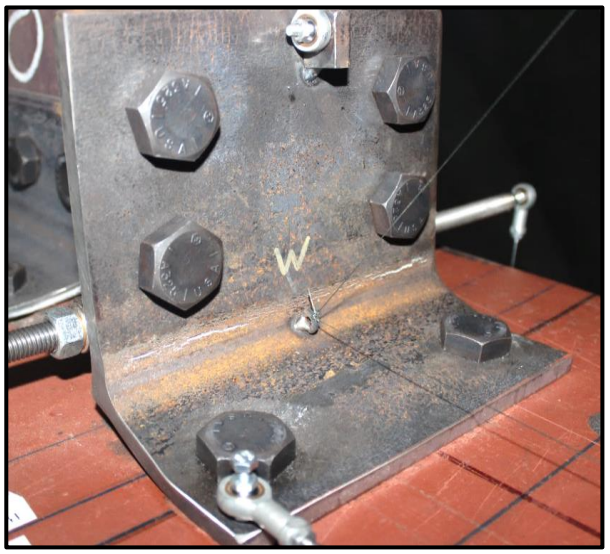
Connection at end of test



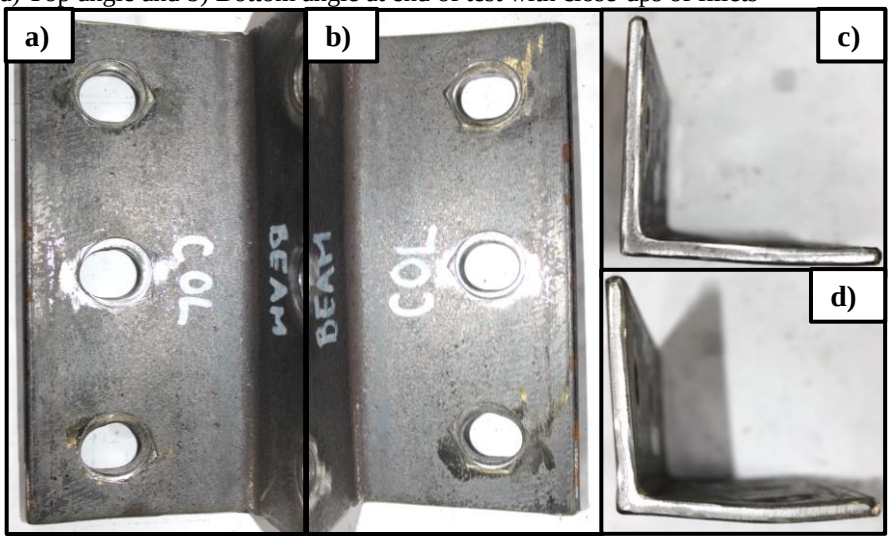
Shear deformation of the north web angle



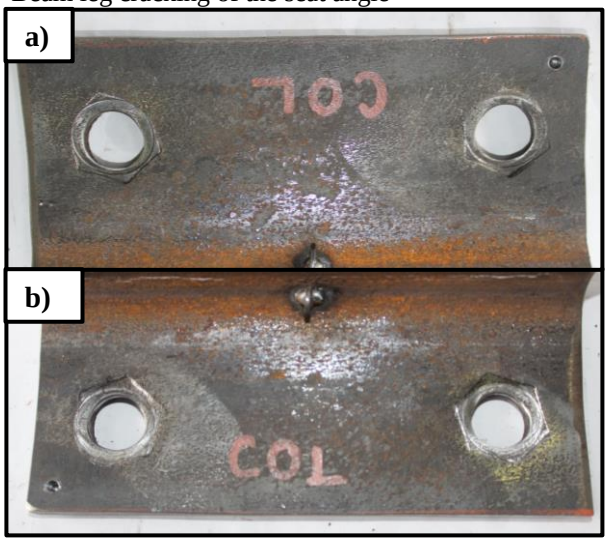
a) Top angle and b) Bottom angle at end of test with close-ups of fillets



Beam leg cracking of the seat angle



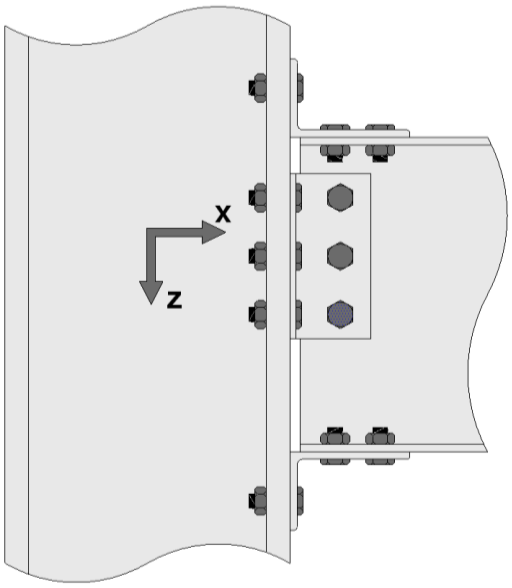
Column bolt bearing deformation of a) North & b) South web angles & profiles of web angles on c) top side and d) bottom side



Column bolt bearing deformation of a) Top and b) Bottom angles

SPECIMEN 5B

Beam	W410 x 67	
Column	W360 x 347	
Loading Type	Cyclic + Shear Excursions	
Constant shear	282.9	kN
Shear excursions	456.0	kN



Top & Seat Angles

Size	L6 x 4 x 3/8	
Steel Grade	A36	
F_y	370	
F_u	518	
ε_u	0.2420	

$\Delta_{X\ max\ Top\ +}$	15.41	mm
$\Delta_{Z\ max\ Top\ +}$	-0.27	mm
$\Delta_{X\ max\ Top\ -}$	-0.37	mm
$\Delta_{Z\ max\ Top\ -}$	-3.83	mm
$\Delta_{X\ max\ Bottom\ +}$	13.17	mm
$\Delta_{Z\ max\ Bottom\ +}$	-0.21	mm
$\Delta_{X\ max\ Bottom\ -}$	-0.47	mm
$\Delta_{Z\ max\ Bottom\ -}$	-9.93	mm

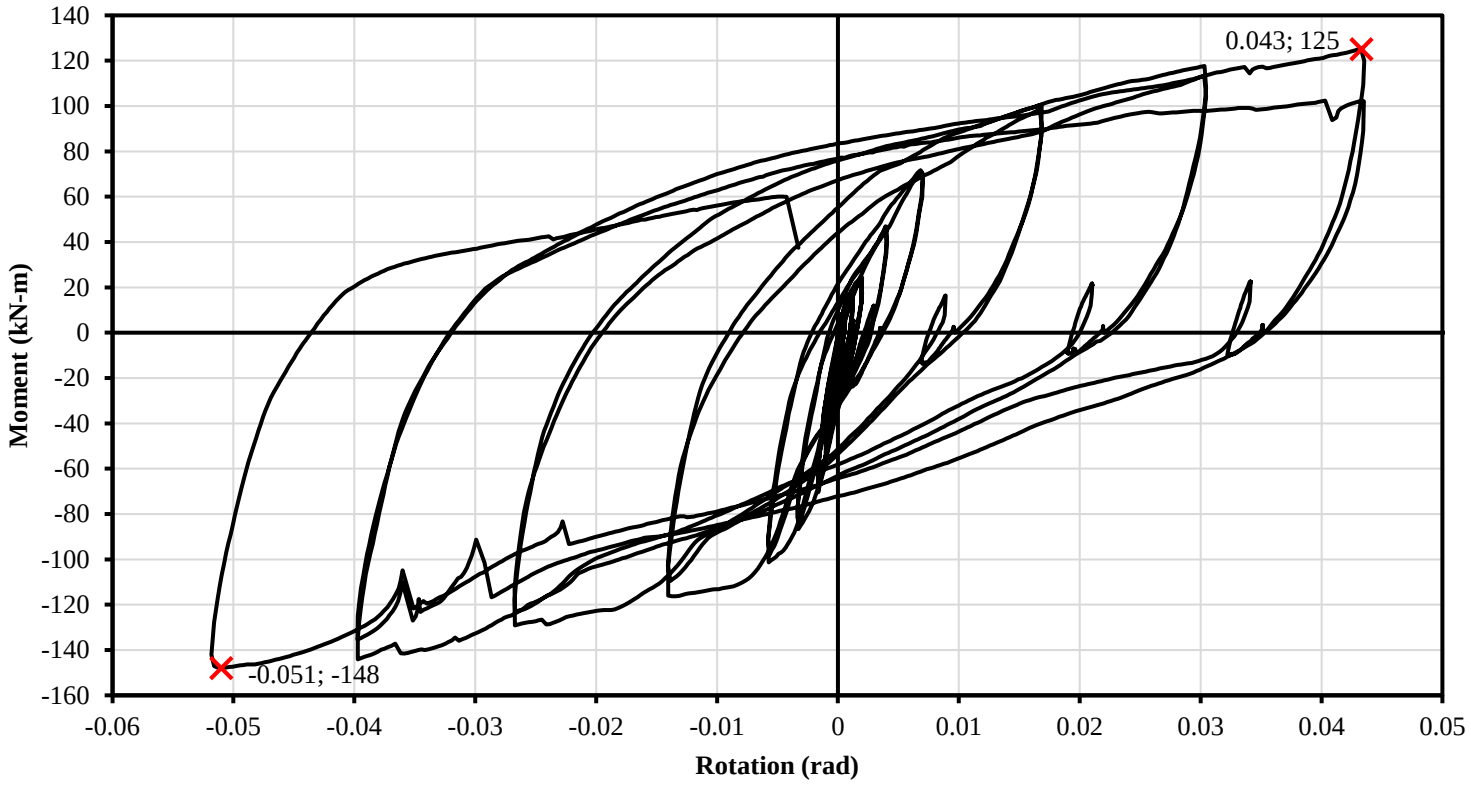
Web Angles

Size	L4 x 4 x 5/16	
Steel Grade	A36	
F_y	373	MPa
F_u	507	MPa
ε_u	0.2415	
Length	216	mm

Note: The displacements were measured at the center of the top and seat angle fillet.

Failure Mode Beam leg fracture of the seat angle

Moment-Rotation





Connection at end of test



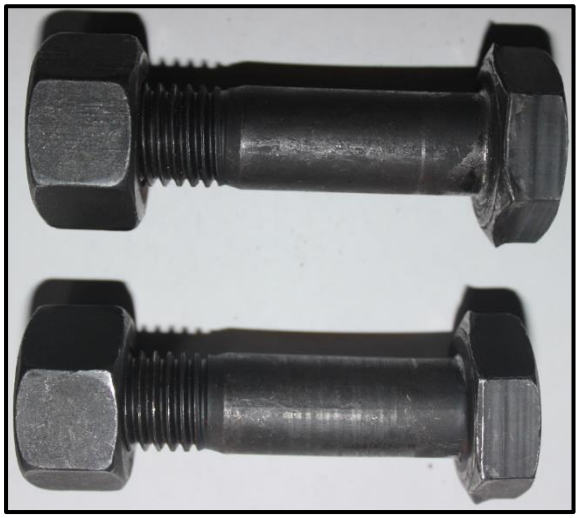
Seat angle fracture in the beam leg

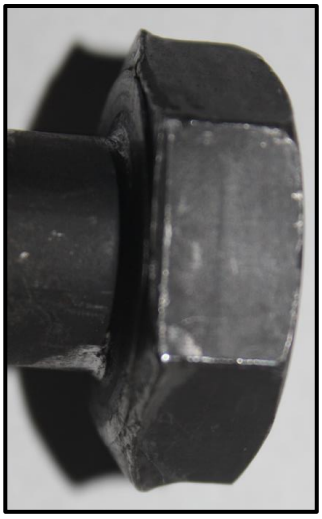


Shear deformation of web angle column legs

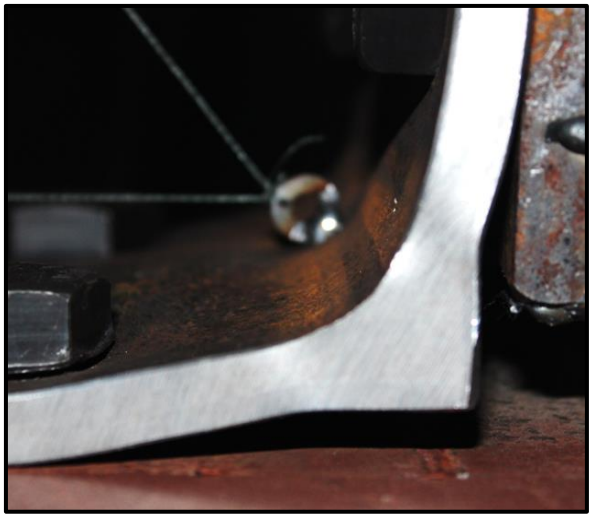


Beam leg cracking of the top angle





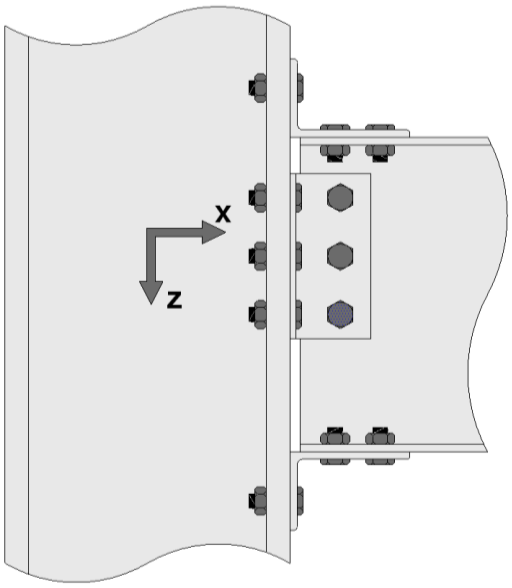
Seast column bolt deformation near the head



Top angle deformation under negative rotation

SPECIMEN 5C

Beam	W410 x 67	
Column	W360 x 347	
Loading Type	Cyclic, No Shear	
Constant shear	-	kN
Shear excursions	-	kN



Top & Seat Angles

Size	L6 x 4 x 3/8	
Steel Grade	A36	
F_y	370	
F_u	518	
ε_u	0.2420	

$\Delta_{X\ max\ Top\ +}$	14.19	mm
$\Delta_{Z\ max\ Top\ +}$	2.37	mm
$\Delta_{X\ max\ Top\ -}$	-0.49	mm
$\Delta_{Z\ max\ Top\ -}$	-0.21	mm
$\Delta_{X\ max\ Bottom\ +}$	13.15	mm
$\Delta_{Z\ max\ Bottom\ +}$	0.30	mm
$\Delta_{X\ max\ Bottom\ -}$	-0.19	mm
$\Delta_{Z\ max\ Bottom\ -}$	-3.19	mm

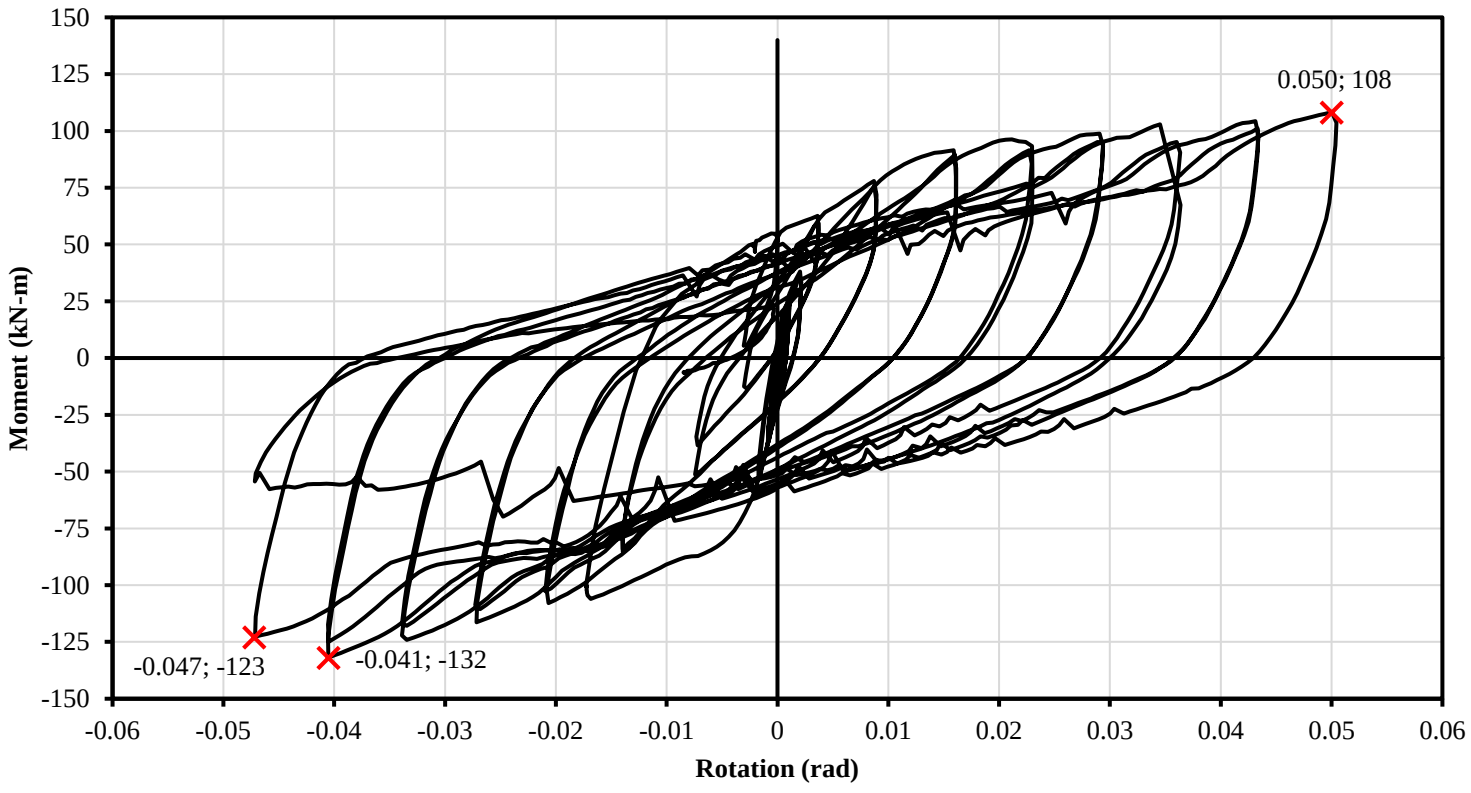
Web Angles

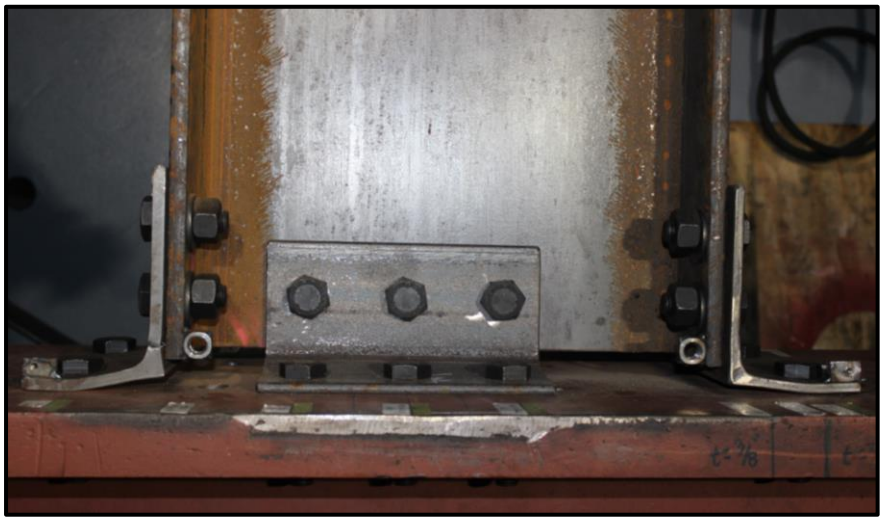
Size	L4 x 4 x 5/16	
Steel Grade	A36	
F_y	373	MPa
F_u	507	MPa
ε_u	0.2415	
Length	216	mm

Note: The displacements were measured at the center of the top and seat angle fillet.

Failure Mode Beam leg cracking of the seat angle

Moment-Rotation





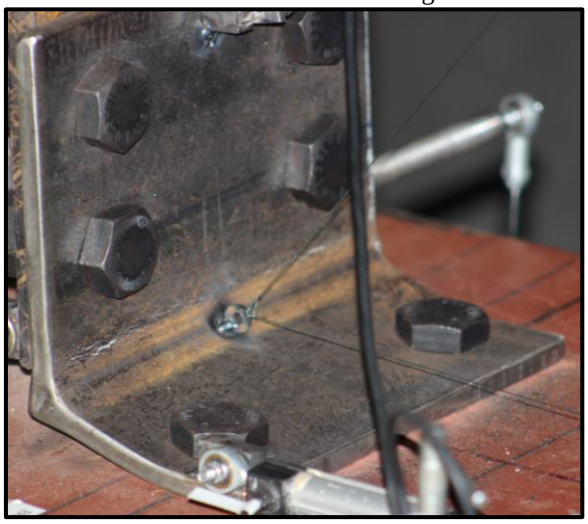
Connection at end of test



Shear deformation of the north web angle



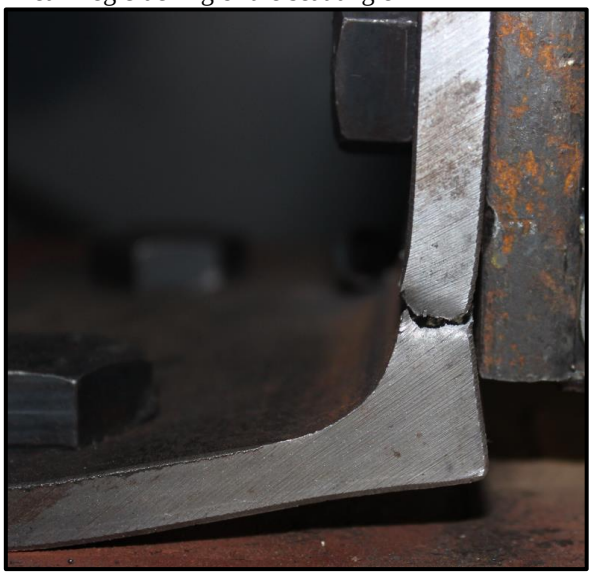
No significant shear deformation in web angles



Beam leg cracking of the seat angle



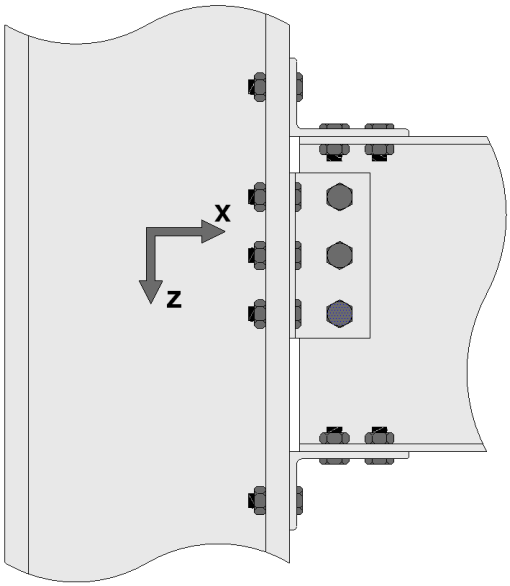
Top angle hole deformation of the column leg



Column bolt bearing deformation of a) Top and

SPECIMEN 6A

Beam	W410 x 67	
Column	W360 x 347	
Loading Type	Cyclic	
Constant shear	282.9	kN
Shear excursions	-	



Top & Seat Angles

Size	L8 x 6 x 3/4	
Steel Grade	A36	
F_y	340	MPa
F_u	516	MPa
ε_u	0.2592	

$\Delta_{X\ max\ Top\ +}$	17.26	mm
$\Delta_{Z\ max\ Top\ +}$	0.68	mm
$\Delta_{X\ max\ Top\ -}$	-0.18	mm
$\Delta_{Z\ max\ Top\ -}$	-3.73	mm
$\Delta_{X\ max\ Bottom\ +}$	13.10	mm
$\Delta_{Z\ max\ Bottom\ +}$	-0.11	mm
$\Delta_{X\ max\ Bottom\ -}$	-0.25	mm
$\Delta_{Z\ max\ Bottom\ -}$	-8.89	mm

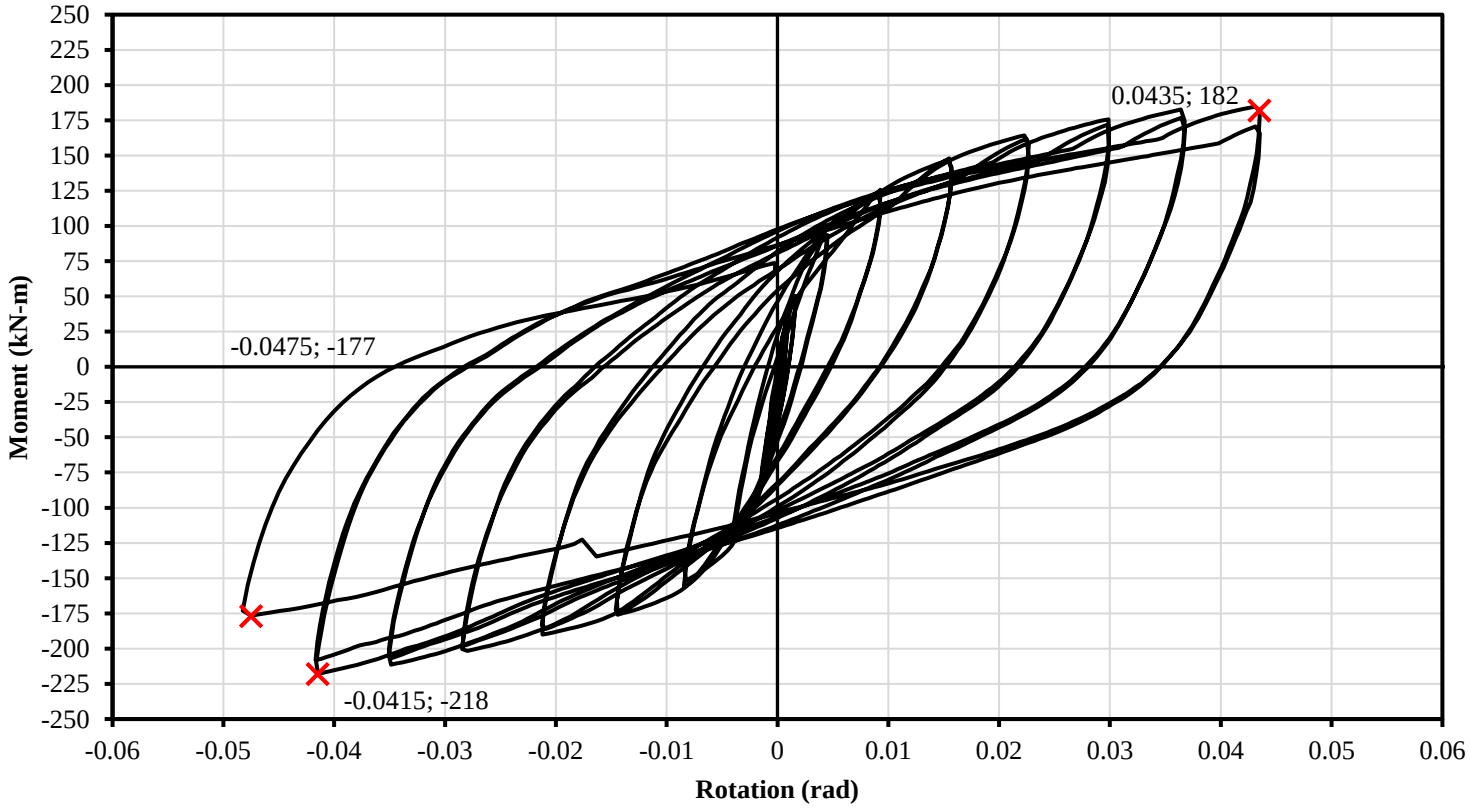
Web Angles

Size	L4 x 4 x 5/16	
Steel Grade	A36	
F_y	373	MPa
F_u	507	MPa
ε_u	0.2415	
Length	216	mm

Note: The displacements were measured at the center of the top and seat angle fillet.

Failure Mode Beam leg fracture of the top angle

Moment-Rotation





Connection at fracture



Top angle at fracture



Web angle deformation at fracture



Bottom angle at fracture



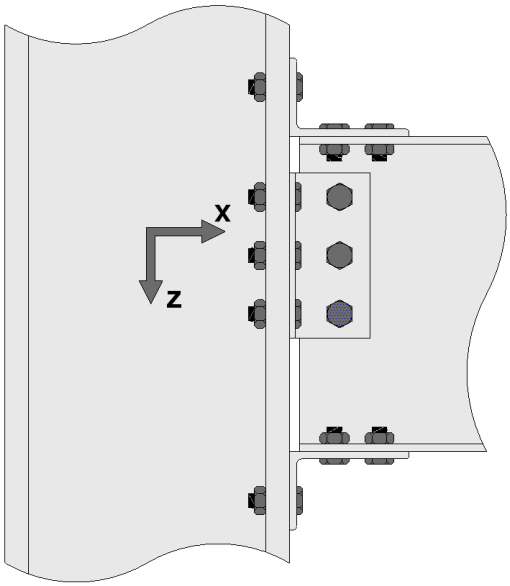
Close-up of the top angle beam leg fracture



Close-up of bottom angle cracking

SPECIMEN 6B

Beam	W410 x 67	
Column	W360 x 347	
Loading Type	Cyclic + Shear Excursions	
Constant shear	282.9	kN
Shear excursions	456.0	kN



Top & Seat Angles

Size	L8 x 6 x 3/4	
Steel Grade	A36	
F_y	340	MPa
F_u	516	MPa
ε_u	0.2592	

$\Delta_{X\ max\ Top\ +}$	19.41	mm
$\Delta_{Z\ max\ Top\ +}$	0.07	mm
$\Delta_{X\ max\ Top\ -}$	-0.19	mm
$\Delta_{Z\ max\ Top\ -}$	-4.43	mm
$\Delta_{X\ max\ Bottom\ +}$	14.55	mm
$\Delta_{Z\ max\ Bottom\ +}$	-0.15	mm
$\Delta_{X\ max\ Bottom\ -}$	-0.27	mm
$\Delta_{Z\ max\ Bottom\ -}$	-8.86	mm

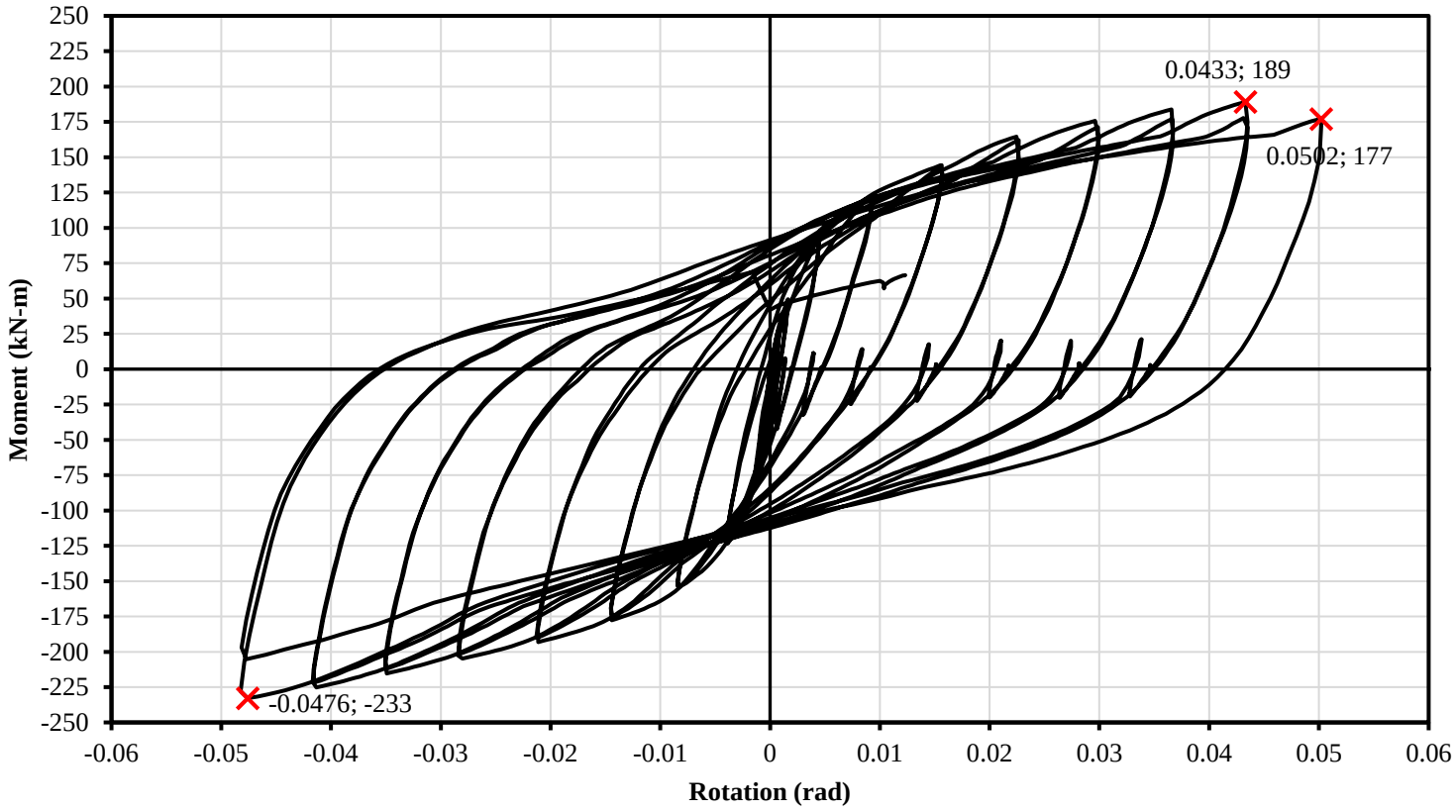
Web Angles

Size	L4 x 4 x 5/16	
Steel Grade	A36	
F_y	373	MPa
F_u	507	MPa
ε_u	0.2415	
Length	216	mm

Note: The displacements were measured at the center of the top and seat angle fillet.

Failure Mode Beam leg fracture of the top angle

Moment-Rotation





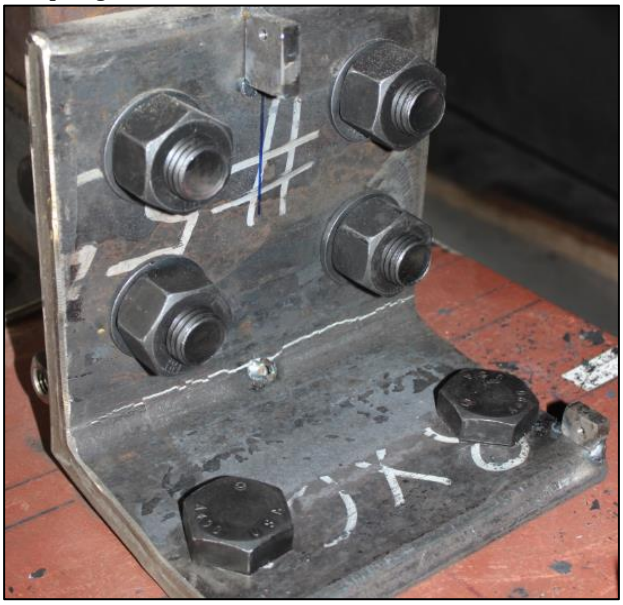
Connection at fracture



Top angle at fracture



Web angle deformation at fracture



Bottom angle at fracture





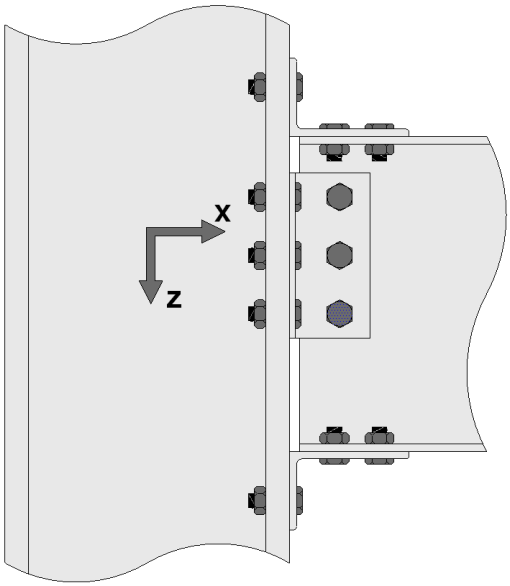
Close-up of top angle beam leg fracture and plastic hinging



Close-up of bottom angle fracture

SPECIMEN 6C

Beam	W410 x 67	
Column	W360 x 347	
Loading Type	Cyclic, No Shear	
Constant shear	-	kN
Shear excursions	-	kN



Top & Seat Angles

Size	L8 x 6 x 3/4	
Steel Grade	A36	
F_y	340	MPa
F_u	516	MPa
ε_u	0.2592	

$\Delta_{X\ max\ Top\ +}$	13.92	mm
$\Delta_{Z\ max\ Top\ +}$	4.55	mm
$\Delta_{X\ max\ Top\ -}$	-0.18	mm
$\Delta_{Z\ max\ Top\ -}$	-0.16	mm
$\Delta_{X\ max\ Bottom\ +}$	15.97	mm
$\Delta_{Z\ max\ Bottom\ +}$	0.88	mm
$\Delta_{X\ max\ Bottom\ -}$	-0.24	mm
$\Delta_{Z\ max\ Bottom\ -}$	-3.19	mm

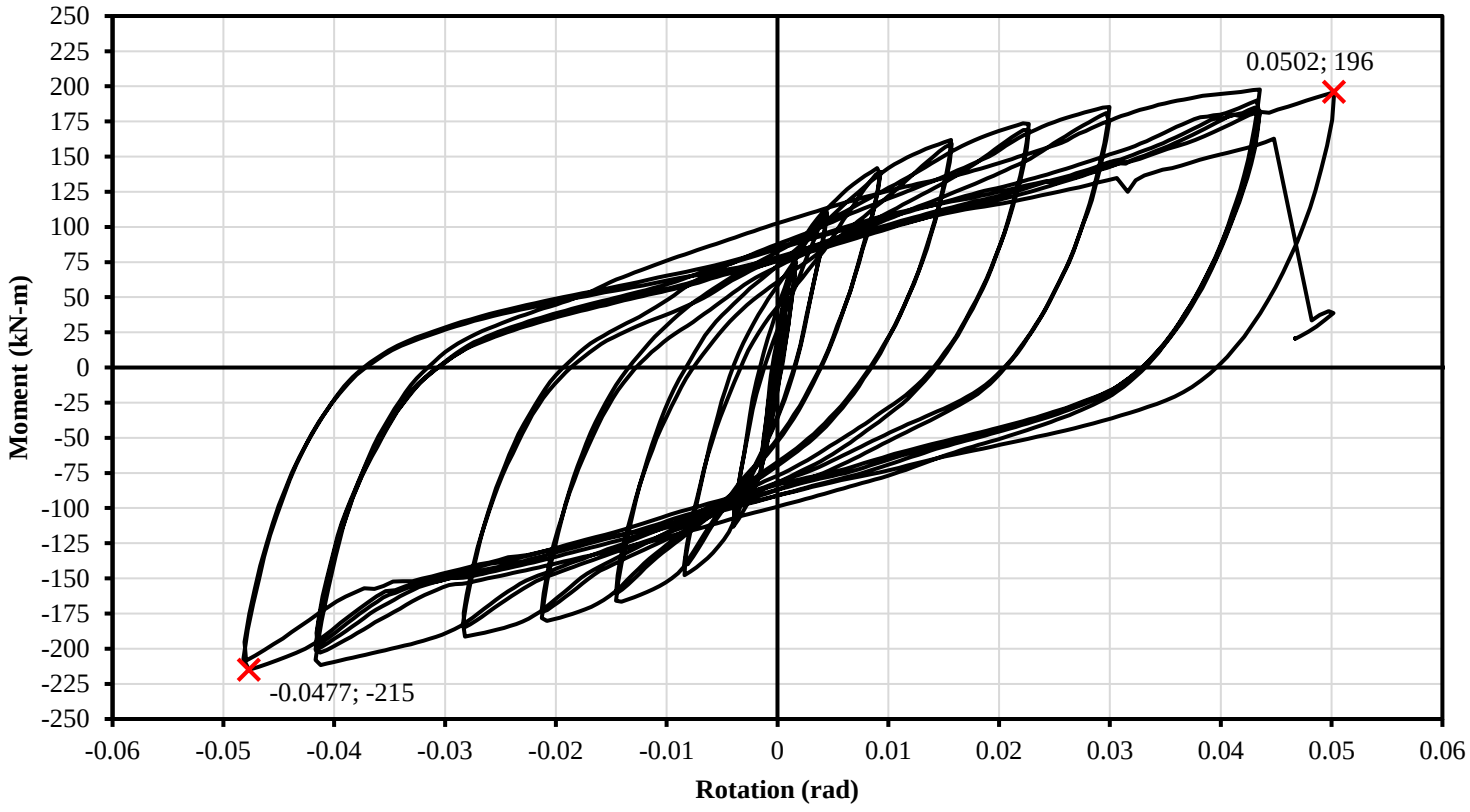
Web Angles

Size	L4 x 4 x 5/16	
Steel Grade	A36	
F_y	373	MPa
F_u	507	MPa
ε_u	0.2415	
Length	216	mm

Note: The displacements were measured at the center of the top and seat angle fillet.

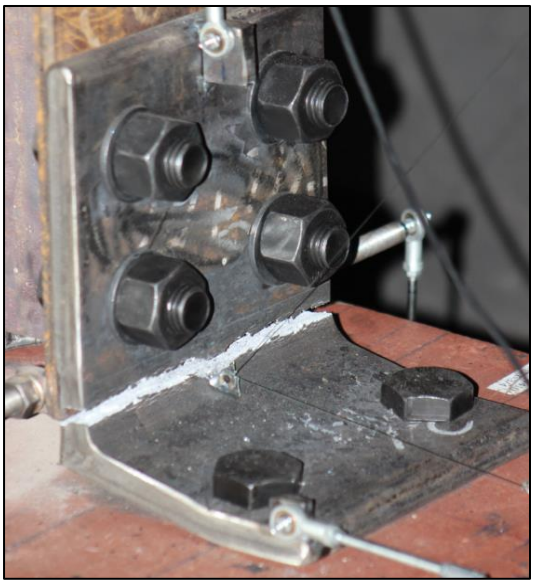
Failure Mode Beam leg fracture of the bottom angle

Moment-Rotation





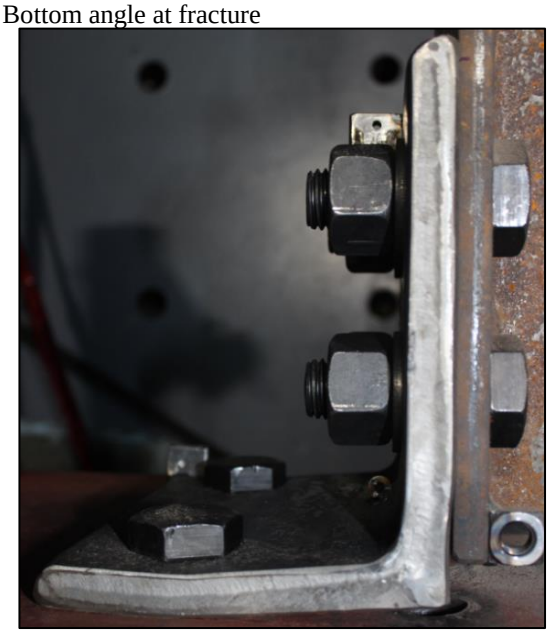
Connection at fracture



Bottom angle at fracture



No significant web angle deformation



Top angle at fracture



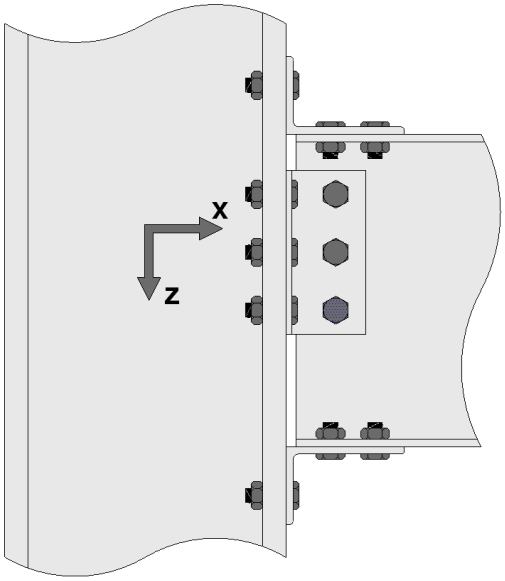
Close-ups of bottom angle cracking



Top angle plastic hinging near fillet close-up

SPECIMEN 6D

Beam	W410 x 67	
Column	W250x67	
Loading Type	Cyclic	
Constant shear	282.9	kN
Shear excursions	-	kN



Top & Seat Angles

Size	L8 x 6 x 3/4	
Steel Grade	A36	
F_y	340	MPa
F_u	516	MPa
ε_u	0.2592	

$\Delta_{X\ max\ Top\ +}$	23.96	mm
$\Delta_{Z\ max\ Top\ +}$	-1.91	mm
$\Delta_{X\ max\ Top\ -}$	-1.22	mm
$\Delta_{Z\ max\ Top\ -}$	-8.31	mm
$\Delta_{X\ max\ Bottom\ +}$	23.03	mm
$\Delta_{Z\ max\ Bottom\ +}$	-1.95	mm
$\Delta_{X\ max\ Bottom\ -}$	-1.19	mm
$\Delta_{Z\ max\ Bottom\ -}$	-10.96	mm

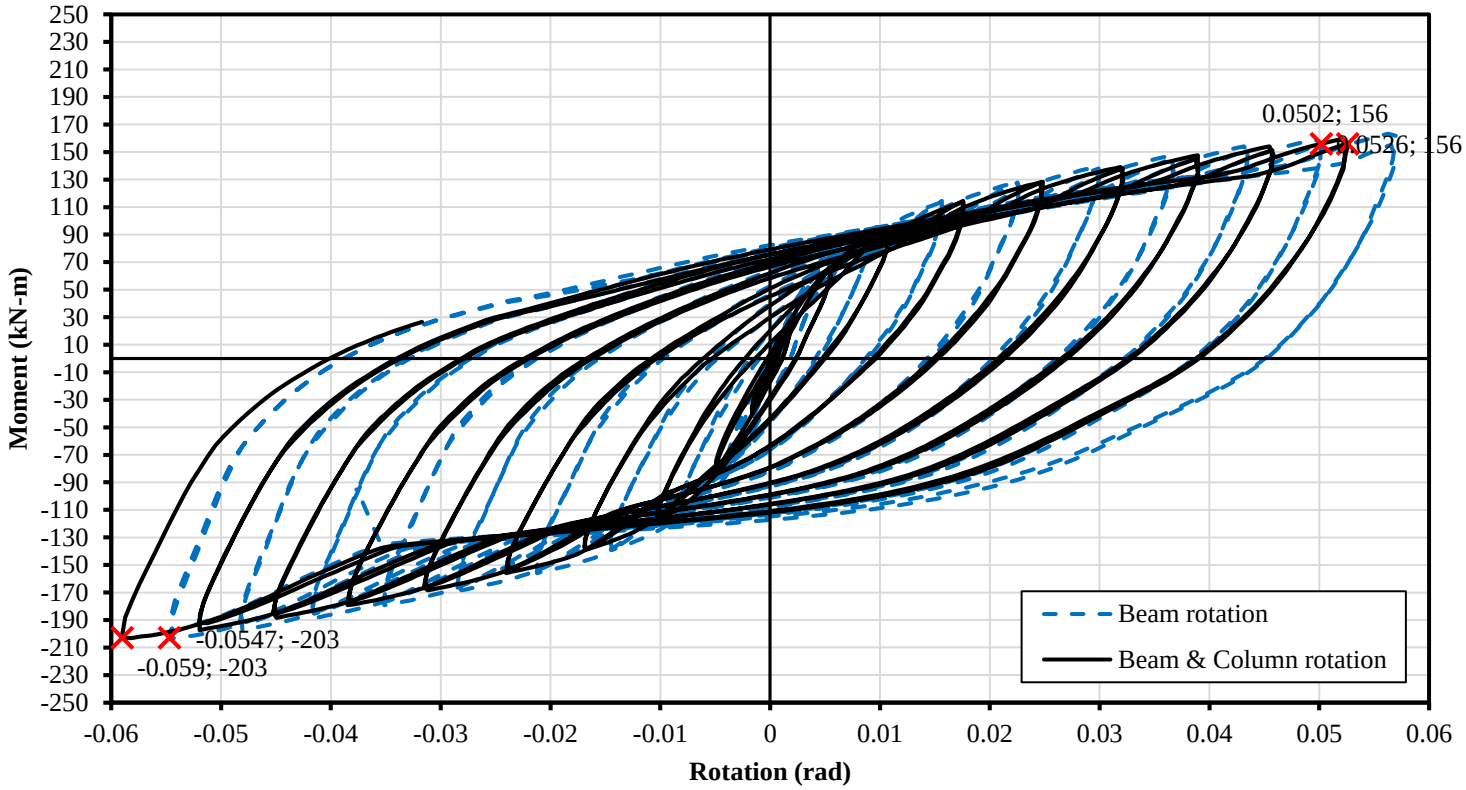
Web Angles

Size	L4 x 4 x 5/16	
Steel Grade	A36	
F_y	373	MPa
F_u	507	MPa
ε_u	0.2415	
Length	216	mm

Note: The displacements were measured at the center of the top and seat angle fillet.

Failure Mode Beam leg fracture of the top angle

Moment-Rotation

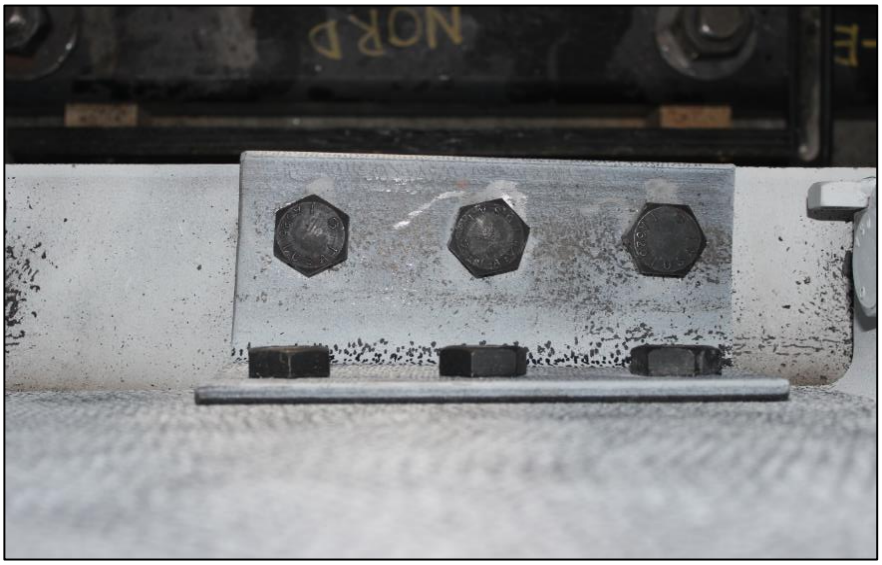




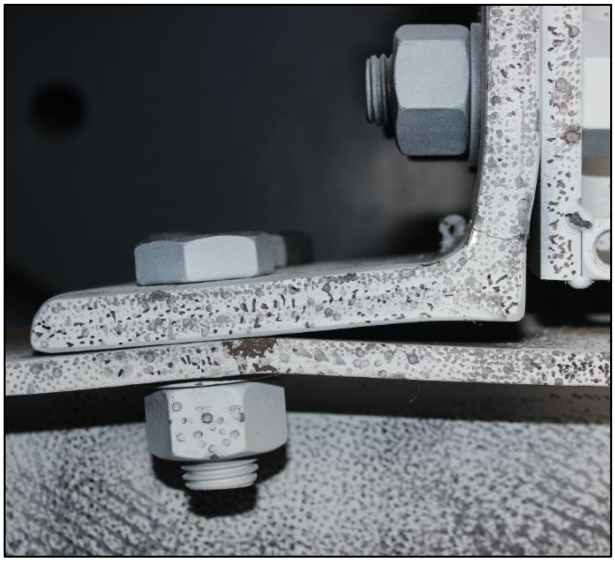
Connection at fracture



Top angle at fracture



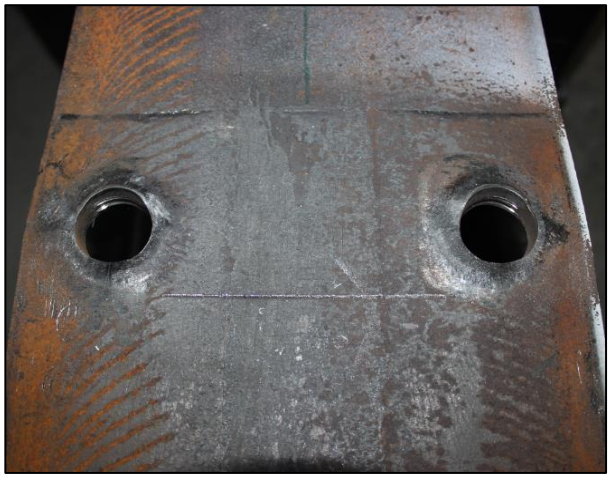
Web angle deformation at fracture



Bottom angle crack initiation



Column flange local deformation



Column flange hole bearing at top angle

APPENDIX C STEELANGLES UNIAXIAL MATERIAL CODE

This Appendix presents the code programmed in C++ and compiled in the OpenSees framework to integrade the *SteelAngles* uniaxial material in the software. This code is composed of two documents:

1. The header file: steelAngles.h; and
2. The *SteelAngles* module: steelAngles.cpp.

HEADER FILE: steelAngles.h

C:\Users\Thierry\Desktop\steelAngles.h 1

```
/* ****************************************************************** **
**    OpenSees - Open System for Earthquake Engineering Simulation    **
**          Pacific Earthquake Engineering Research Center             **
**                                                                     **
**                                                                     **
** (C) Copyright 1999, The Regents of the University of California    **
** All Rights Reserved.                                                **
**                                                                     **
** Commercial use of this program without express permission of the   **
** University of California, Berkeley, is strictly prohibited.  See   **
** file 'COPYRIGHT'  in main directory for information on usage and   **
** redistribution,  and for a DISCLAIMER OF ALL WARRANTIES.            **
**                                                                     **
** ****************************************************************** */

/*-------------------------------------------------------------------- ||
||Revision: 1.2                                                        ||
|| Date: 2019-06-23                                                    ||
|| Source:                                                             ||
|| Written: Thierry Beland                                             ||
|| Description: This file contains the class implementation of         ||
|| SteelAnglesmaterial explained in Beland et al. (2019)               ||
||-------------------------------------------------------------------- */

#ifndef SteelAngles_h
#define SteelAngles_h

#include <UniaxialMaterial.h>

class SteelAngles : public UniaxialMaterial {

public:
    SteelAngles(int tag, double Fy, double E, double b, double FyN, double EN,
      double bN,
        double R0, double cR1, double cR2, double a1, double a2, double a3,
          double a4, double s1, double s2, double s3, double s4, double S,
          double N);

    SteelAngles(int tag, double Fy, double E, double b, double FyN, double EN,
      double bN,
        double R0, double cR1, double cR2, double a1, double a2, double a3,
          double a4, double s1, double s2, double s3, double s4);

    SteelAngles(void);
    ~SteelAngles(void);
    //virtual ~SteelAngles();

    const char *getClassType(void) const { return "SteelAngles"; };

```

```
45      double getInitialTangent(void);
46      UniaxialMaterial *getCopy(void);
47
48      int setTrialStrain(double strain, double strainRate = 0.0);
49      double getStrain(void);
50      double getStress(void);
51      double getTangent(void);
52
53      int commitState(void);
54      int revertToLastCommit(void);
55      int revertToStart(void);
56
57      int sendSelf(int commitTag, Channel &theChannel);
58      int recvSelf(int commitTag, Channel &theChannel,
59          FEM_ObjectBroker &theBroker);
60
61      void Print(OPS_Stream &s, int flag = 0);
62
63  protected:
64
65  private:
66      // matpar : STEEL FIXED PROPERTIES
67      double Fy;   //  = matpar(1)  : yield stress
68      double E;    //  = matpar(2)  : initial stiffness
69      double b;    //  = matpar(3)  : hardening ratio (Esh/E0)
70      double FyN;  //  = matpar(4)  : yield stress
71      double EN;   //  = matpar(5)  : initial stiffness
72      double bN;   //  = matpar(6)  : hardening ratio (Esh/E0)
73      double R0;   //  = matpar(7)  : exp transition elastic-plastic
74      double cR1;  //  = matpar(8)  : coefficient for changing R0 to R
75      double cR2;  //  = matpar(9)  : coefficient for changing R0 to R
76      double a1;   //  = matpar(10) : coefficient for isotropic hardening in
          compression
77      double a2;   //  = matpar(11) : coefficient for isotropic hardening in
          compression
78      double a3;   //  = matpar(12) : coefficient for isotropic hardening in
          tension
79      double a4;   //  = matpar(13) : coefficient for isotropic hardening in
          tension
80      double s1;   //  = matpar(14) : coefficient for secant stiffness behaviour
          in compression
81      double s2;   //  = matpar(15) : coefficient for secant stiffness behaviour
          in compression
82      double s3;   //  = matpar(16) : coefficient for secant stiffness behaviour
          in tension
83      double s4;   //  = matpar(17) : coefficient for secant stiffness behaviour
          in tension
84      double S;
85      double N;
```

```
 86
 87       // hstvP : STEEL HISTORY VARIABLES
 88      double epsminP; //  = hstvP(1) : max eps in compression
 89      double epsmaxP; //  = hstvP(2) : max eps in tension
 90      double sigminP; //  = hstvP(1) : max sig in compression
 91      double sigmaxP; //  = hstvP(2) : max sig in tension
 92      double epsplP;  //  = hstvP(3) : plastic excursion
 93      double epss0P;  //  = hstvP(4) : eps at asymptotes intersection
 94      double sigs0P;  //  = hstvP(5) : sig at asymptotes intersection
 95      double epsr_RP;  //  = hstvP(6) : eps at last inversion point
 96      double epsr_UP;  //  = hstvP(6) : eps at last inversion point
 97      double sigr_RP;  //  = hstvP(6) : eps at last inversion point
 98      double sigr_UP;  //  = hstvP(6) : eps at last inversion point
 99      double epsrP;
100      double sigrP;  //  = hstvP(7) : sig at last inversion point
101      double epssTP;  //  = hstvP(6) : eps at target point
102      double sigsTP;  //  = hstvP(7) : sig at target point
103      int    konP;    //  = hstvP(8) : index for loading/unloading
104      double bSecP;   //  = hstvP(8) : secant stiffness
105      double RP;      //  = hstvP(8) : elastic-plastic transition parameter
106      double DIP;
107                      // hstv : STEEL HISTORY VARIABLES
108      double epsP;  //  = strain at previous converged step
109      double sigP;  //  = stress at previous converged step
110      double eP;    //   stiffness modulus at last converged step;
111      double bSec;
112      double R;
113      double DI;
114
115      double e_R;
116      double e_U;
117      double e_RP;
118      double e_UP;
119
120      double epsmin;
121      double epsmax;
122      double sigmin;
123      double sigmax;
124      double sigsT;
125      double epssT;
126
127      double epspl;
128      double epss0;
129      double sigs0;
130      double epsr_R;
131      double epsr_U;
132      double sigr_R;
133      double sigr_U;
134      double sigr;
```

```
135      double epsr;
136
137      double epsyHP;
138      double epsyH;
139      double sigs0HP;
140      double sigs0H;
141
142      int kon;
143      double sig;
144      double e;
145      double eps;   //  = strain at current step
146      int Coffin_Manson;
147      double b2;
148      double b1;
149      double E1;
150      double b1P;
151      double b2P;
152      double E1P;
153      double R2;
154      double R2P;
155
156      double epsr_1;
157      double sigr_1;
158      double epsr_2;
159      double sigr_2;
160      double epsr_3;
161      double sigr_3;
162      double epss0_1;
163      double sigs0_1;
164      double epss0_2;
165      double sigs0_2;
166      double epss0_3;
167      double sigs0_3;
168
169      double epsr_1P;
170      double sigr_1P;
171      double epsr_2P;
172      double sigr_2P;
173      double epsr_3P;
174      double sigr_3P;
175      double epss0_1P;
176      double sigs0_1P;
177      double epss0_2P;
178      double sigs0_2P;
179      double epss0_3P;
180      double sigs0_3P;
181
182      int Partial_Excursion;
183
```

```
184     //parameters for damage calculation
185     double A;
186     double B;
187     double C;
188     double D;
189     double X;
190     double Y;
191     int SSC;
192     int Next_Peak;
193     int Step;
194
195     double AP;
196     double BP;
197     double CP;
198     double DP;
199     double XP;
200     double YP;
201     int SSCP;
202     int Next_PeakP;
203     int StepP;
204     void Uriz_Damage_Calculator(double epsP);
205
206 };
207
208 #endif
```

MAIN CODE FILE: steelAngles.cpp

C:\Users\Thierry\Desktop\steelAngles.cpp 1

```
/* ****************************************************************** **
**    OpenSees - Open System for Earthquake Engineering Simulation    **
**          Pacific Earthquake Engineering Research Center            **
**                                                                    **
**                                                                    **
** (C) Copyright 1999, The Regents of the University of California    **
** All Rights Reserved.                                               **
**                                                                    **
** Commercial use of this program without express permission of the   **
** University of California, Berkeley, is strictly prohibited.  See   **
** file 'COPYRIGHT'  in main directory for information on usage and   **
** redistribution,  and for a DISCLAIMER OF ALL WARRANTIES.           **
**                                                                    **
** ****************************************************************** */

/*-------------------------------------------------------------------||
||Revision: 1.2                                                       ||
|| Date: 2019-06-23                                                   ||
|| Source:                                                            ||
|| Written: Thierry Beland                                            ||
|| Description: This file contains the class implementation of        ||
|| SteelAnglesmaterial explained in Beland et al. (2019)              ||
||-------------------------------------------------------------------*/

#include <math.h>
#include <stdlib.h>
#include <SteelAngles.h>
#include <OPS_Globals.h>
#include <float.h>
#include <Channel.h>

#include <elementAPI.h>
#include <OPS_Globals.h>
#define OPS_Export
#include <Matrix.h>
#include <Vector.h>
#include <Information.h>

static int numSteelAngles = 0;

OPS_Export void *OPS_SteelAngles(void) {

    // print out some KUDO's
    if (numSteelAngles == 0) {
        opserr << "SteelAngles unaxial material - Written by Beland et al. -
          Use at your Own Peril\n";
        numSteelAngles = 1;
    }

```

```
49      // Pointer to a uniaxial material that will be returned
50      UniaxialMaterial *theMaterial = 0;
51
52      int    iData[1];
53      double dData[19];
54      int numData = 1;
55
56      if (OPS_GetIntInput(&numData, iData) != 0) {
57          opserr << "WARNING invalid uniaxialMaterial SteelAngles tag" << endln;
58          return 0;
59      }
60
61      numData = OPS_GetNumRemainingInputArgs();
62
63      if (numData != 19 && numData != 17) {
64          opserr << "Invalid #args, want: uniaxialMaterial SteelAngles " <<
              iData[0] << " fy? E? b? <R0? cR1? cR2? <a1? a2? a3? a4?>>" << endln;
65          return 0;
66      }
67
68      else if (numData == 19) {
69          if (OPS_GetDoubleInput(&numData, dData) != 0) {
70              opserr << "Invalid arggs: uniaxialMaterial SteelAngles " << iData
                  [0] << " fy? E? b? <R0? cR1? cR2? <a1? a2? a3? a4?>>" << endln;
71              return 0;
72          }
73
74          // Parsing was successful, allocate the material
75          theMaterial = new SteelAngles(iData[0], dData[0], dData[1], dData[2],
              dData[3], dData[4], dData[5], dData[6], dData[7], dData[8], dData
              [9],
76              dData[10], dData[11], dData[12], dData[13], dData[14], dData[15],
                  dData[16], dData[17], dData[18]);
77      }
78      else if (numData == 17) {
79          if (OPS_GetDoubleInput(&numData, dData) != 0) {
80              opserr << "Invalid arggs: uniaxialMaterial SteelAngles " << iData
                  [0] << " fy? E? b? <R0? cR1? cR2? <a1? a2? a3? a4?>>" << endln;
81              return 0;
82          }
83
84          // Parsing was successful, allocate the material
85          theMaterial = new SteelAngles(iData[0], dData[0], dData[1], dData[2],
              dData[3], dData[4], dData[5], dData[6], dData[7], dData[8], dData
              [9],
86              dData[10], dData[11], dData[12], dData[13], dData[14], dData[15],
                  dData[16]);
87      }
88
```

C:\Users\Thierry\Desktop\steelAngles.cpp 3

```
89      if (theMaterial == 0) {
90          opserr << "WARNING could not create uniaxialMaterial of type
              SteelAngles Material\n";
91          return 0;
92      }
93      return theMaterial;
94  }
95
96
97  SteelAngles::SteelAngles(int tag, double _Fy, double _E, double _b, double
      _FyN, double _EN, double _bN, double _R0, double _cR1, double _cR2,
98      double _a1, double _a2, double _a3, double _a4, double _s1, double _s2,
          double _s3, double _s4, double _S, double _N) :
99
100     UniaxialMaterial(tag, MAT_TAG_SteelAngles), Fy(_Fy), E(_E), b(_b), FyN
          (_FyN), EN(_EN), bN(_bN), R0(_R0), cR1(_cR1), cR2(_cR2),
101     a1(_a1), a2(_a2), a3(_a3), a4(_a4), s1(_s1), s2(_s2), s3(_s3), s4(_s4), S
          (_S), N(_N) {
102
103     //Loading History parameters
104     epsmaxP = 0.0;
105     sigmaxP = 0.0;
106     epsminP = 0.0;
107     sigminP = 0.0;
108     epsr_RP = 0.0;
109     sigr_RP = 0.0;
110     epsr_UP = 0.0;
111     sigr_UP = 0.0;
112     DIP = 0.0;
113
114     //Current excursion parameters
115     konP = 0;
116     epss0P = Fy / E;
117     sigs0P = Fy;
118     epsrP = 0.0;
119     sigrP = 0.0;
120     sigsTP = 0.0;
121     epssTP = 0.0;
122     epsr_1P = 0.0;
123     sigr_1P = 0.0;
124     epsr_2P = 0.0;
125     sigr_2P = 0.0;
126     epsr_3P = 0.0;
127     sigr_3P = 0.0;
128     epss0_1P = 0.0;
129     sigs0_1P = 0.0;
130     epss0_2P = 0.0;
131     sigs0_2P = 0.0;
132     epss0_3P = Fy / E;
```

```
133     sigs0_3P = Fy;
134
135     b1P = b;
136     b2P = 0.0;
137     bSecP = 0.0;
138     E1P = E;
139     RP = R0;
140     R2P = 20.0;
141
142     epsP = 0.0;
143     sigP = 0.0;
144     eP = E;
145
146     A = 0.0;
147     B = 0.0;
148     C = 0.0;
149     D = 0.0;
150     X = 0.0;
151     Y = 0.0;
152     SSC = 0;
153     Next_Peak = 1;
154     Step = 1;
155
156     AP = 0.0;
157     BP = 0.0;
158     CP = 0.0;
159     DP = 0.0;
160     XP = 0.0;
161     YP = 0.0;
162     SSCP = 0;
163     Next_PeakP = 1;
164     StepP = 1;
165
166     if (S != 0.0 && N != 0.0) { Coffin_Manson = 1; } else { Coffin_Manson =
          0; }
167
168     //Loading History parameters
169     epsmax = epsmaxP;
170     sigmax = sigmaxP;
171     epsmin = epsminP;
172     sigmin = sigminP;
173     epsr_R = epsr_RP;
174     sigr_R = sigr_RP;
175     epsr_U = epsr_UP;
176     sigr_U = sigr_UP;
177     DI = DIP;
178
179     //Current excursion parameters
180     kon = konP;
```

```
181      epss0 = epss0P;
182      sigs0 = sigs0P;
183      epsr = epsrP;
184      sigr = sigrP;
185      sigsT = sigsTP;
186      epssT = epssTP;
187      epsr_1 = epsr_1P;
188      sigr_1 = sigr_1P;
189      epsr_2 = epsr_2P;
190      sigr_2 = sigr_2P;
191      epsr_3 = epsr_3P;
192      sigr_3 = sigr_3P;
193      epss0_1 = epss0_1P;
194      sigs0_1 = sigs0_1P;
195      epss0_2 = epss0_2P;
196      sigs0_2 = sigs0_2P;
197      epss0_3 = epss0_3P;
198      sigs0_3 = sigs0_3P;
199
200      b1 = b1P;
201      b2 = b2P;
202      bSec = bSecP;
203      E1 = E1P;
204      R = RP;
205      R2 = R2P;
206
207      eps = 0.0;
208      sig = 0.0;
209      e = E;
210
211      A = 0.0;
212      B = 0.0;
213      C = 0.0;
214      D = 0.0;
215      X = 0.0;
216      Y = 0.0;
217      SSC = 0;
218      Next_Peak = 1;
219      Step = 1;
220
221      AP = 0.0;
222      BP = 0.0;
223      CP = 0.0;
224      DP = 0.0;
225      XP = 0.0;
226      YP = 0.0;
227      SSCP = 0;
228      Next_PeakP = 1;
229      StepP = 1;
```

```
230
231 }
232
233 SteelAngles::SteelAngles(int tag, double _Fy, double _E, double _b, double
      _FyN, double _EN, double _bN, double _R0, double _cR1, double _cR2,
234     double _a1, double _a2, double _a3, double _a4, double _s1, double _s2,
        double _s3, double _s4) :
235     UniaxialMaterial(tag, MAT_TAG_SteelAngles), Fy(_Fy), E(_E), b(_b), FyN
        (_FyN), EN(_EN), bN(_bN), R0(_R0), cR1(_cR1), cR2(_cR2),
236     a1(_a1), a2(_a2), a3(_a3), a4(_a4), s1(_s1), s2(_s2), s3(_s3), s4(_s4) {
237
238     //Loading History parameters
239     epsmaxP = 0.0;
240     sigmaxP = 0.0;
241     epsminP = 0.0;
242     sigminP = 0.0;
243     epsr_RP = 0.0;
244     sigr_RP = 0.0;
245     epsr_UP = 0.0;
246     sigr_UP = 0.0;
247     DIP = 0.0;
248
249     //Current excursion parameters
250     konP = 0;
251     epss0P = Fy / E;
252     sigs0P = Fy;
253     epsrP = 0.0;
254     sigrP = 0.0;
255     sigsTP = 0.0;
256     epssTP = 0.0;
257     epsr_1P = 0.0;
258     sigr_1P = 0.0;
259     epsr_2P = 0.0;
260     sigr_2P = 0.0;
261     epsr_3P = 0.0;
262     sigr_3P = 0.0;
263     epss0_1P = 0.0;
264     sigs0_1P = 0.0;
265     epss0_2P = 0.0;
266     sigs0_2P = 0.0;
267     epss0_3P = Fy / E;
268     sigs0_3P = Fy;
269
270     b1P = b;
271     b2P = 0.0;
272     bSecP = 0.0;
273     E1P = E;
274     RP = R0;
275     R2P = 20.0;
```

```
276
277     epsP = 0.0;
278     sigP = 0.0;
279     eP = E;
280
281     S = 0.0;
282     N = 0.0;
283     Coffin_Manson = 0;
284
285     //Loading History parameters
286     epsmax = epsmaxP;
287     sigmax = sigmaxP;
288     epsmin = epsminP;
289     sigmin = sigminP;
290     epsr_R = epsr_RP;
291     sigr_R = sigr_RP;
292     epsr_U = epsr_UP;
293     sigr_U = sigr_UP;
294     DI = DIP;
295
296     //Current excursion parameters
297     kon = konP;
298     epss0 = epss0P;
299     sigs0 = sigs0P;
300     epsr = epsrP;
301     sigr = sigrP;
302     sigsT = sigsTP;
303     epssT = epssTP;
304     epsr_1 = epsr_1P;
305     sigr_1 = sigr_1P;
306     epsr_2 = epsr_2P;
307     sigr_2 = sigr_2P;
308     epsr_3 = epsr_3P;
309     sigr_3 = sigr_3P;
310     epss0_1 = epss0_1P;
311     sigs0_1 = sigs0_1P;
312     epss0_2 = epss0_2P;
313     sigs0_2 = sigs0_2P;
314     epss0_3 = epss0_3P;
315     sigs0_3 = sigs0_3P;
316
317     b1 = b1P;
318     b2 = b2P;
319     bSec = bSecP;
320     E1 = E1P;
321     R = RP;
322     R2 = R2P;
323
324     eps = 0.0;
```

```
325     sig = 0.0;
326     e = E;
327
328     A = 0.0;
329     B = 0.0;
330     C = 0.0;
331     D = 0.0;
332     X = 0.0;
333     Y = 0.0;
334     SSC = 0;
335     Next_Peak = 1;
336     Step = 1;
337
338     AP = 0.0;
339     BP = 0.0;
340     CP = 0.0;
341     DP = 0.0;
342     XP = 0.0;
343     YP = 0.0;
344     SSCP = 0;
345     Next_PeakP = 1;
346     StepP = 1;
347 }
348 // Blank constructor
349 SteelAngles::SteelAngles(void) : UniaxialMaterial(0, MAT_TAG_SteelAngles) {
350     konP = 0;
351 }
352 //Destructor
353 SteelAngles::~SteelAngles(void) {
354 }
355
356 UniaxialMaterial*SteelAngles::getCopy(void) {
357
358     SteelAngles *theCopy = new SteelAngles(this->getTag(), Fy, E, b, FyN, EN,
          bN, R0, cR1, cR2, a1, a2, a3, a4, s1, s2, s3, s4, S, N);
359
360     theCopy->epsminP = epsminP;
361     theCopy->epsmaxP = epsmaxP;
362     theCopy->sigminP = sigminP;
363     theCopy->sigmaxP = sigmaxP;
364     theCopy->epss0P = epss0P;
365     theCopy->sigs0P = sigs0P;
366     theCopy->epsrP = epsrP;
367     theCopy->sigrP = sigrP;
368     theCopy->sigsTP = sigsTP;
369     theCopy->epssTP = epssTP;
370     theCopy->epsr_RP = epsr_RP;
371     theCopy->epsr_UP = epsr_UP;
372     theCopy->sigr_RP = sigr_RP;
```

```
373      theCopy->sigr_UP = sigr_UP;
374      theCopy->konP = konP;
375      theCopy->bSecP = bSecP;
376      theCopy->RP = RP;
377      theCopy->DIP = DIP;
378      theCopy->eP = eP;
379      theCopy->sigP = sigP;
380      theCopy->epsP = epsP;
381      theCopy->b1P = b1P;
382      theCopy->E1P = E1P;
383      theCopy->R2P = R2P;
384      theCopy->Coffin_Manson = Coffin_Manson;
385
386      theCopy->epsmin = epsmin;
387      theCopy->epsmax = epsmax;
388      theCopy->sigmin = sigmin;
389      theCopy->sigmax = sigmax;
390      theCopy->epss0 = epss0;
391      theCopy->sigs0 = sigs0;
392      theCopy->epsr = epsr;
393      theCopy->sigr = sigr;
394      theCopy->sigsT = sigsT;
395      theCopy->epssT = epssT;
396      theCopy->epsr_R = epsr_R;
397      theCopy->epsr_U = epsr_U;
398      theCopy->sigr_R = sigr_R;
399      theCopy->sigr_U = sigr_U;
400      theCopy->kon = kon;
401      theCopy->bSec = bSec;
402      theCopy->R = R;
403      theCopy->DI = DI;
404      theCopy->e = e;
405      theCopy->sig = sig;
406      theCopy->eps = eps;
407      theCopy->b1 = b1;
408      theCopy->E1 = E1;
409      theCopy->R2 = R2;
410
411      return theCopy;
412  }
413
414  int SteelAngles::setTrialStrain(double trialStrain, double strainRate) {
415
416      double epsy = Fy / E;
417      double epsyN = FyN / EN;
418
419      eps = trialStrain;
420
421      double deps = eps - epsP;
```

```
422     //Loading History parameters
423     epsmax = epsmaxP;
424     sigmax = sigmaxP;
425     epsmin = epsminP;
426     sigmin = sigminP;
427     epsr_R = epsr_RP;
428     sigr_R = sigr_RP;
429     epsr_U = epsr_UP;
430     sigr_U = sigr_UP;
431     DI = DIP;
432
433     //Current excursion parameters
434     epss0 = epss0P;
435     sigs0 = sigs0P;
436     epsr = epsrP;
437     sigr = sigrP;
438     sigsT = sigsTP;
439     epssT = epssTP;
440
441     epsr_1 = epsr_1P;
442     sigr_1 = sigr_1P;
443     epsr_2 = epsr_2P;
444     sigr_2 = sigr_2P;
445     epsr_3 = epsr_3P;
446     sigr_3 = sigr_3P;
447     epss0_1 = epss0_1P;
448     sigs0_1 = sigs0_1P;
449     epss0_2 = epss0_2P;
450     sigs0_2 = sigs0_2P;
451     epss0_3 = epss0_3P;
452     sigs0_3 = sigs0_3P;
453
454     b1 = b1P;
455     b2 = b2P;
456     bSec = bSecP;
457     E1 = E1P;
458     R = RP;
459     R2 = R2P;
460
461     // Set the portion of the curve where the increment is located
462     // kon = internal parameter defining which set of equation to use
463     if (deps > 0.0) {
464
465         kon = 0;    // Loading phase
466     }
467     else if (deps < 0.0) {
468
469         kon = 1;    // Unloading phase
470     }
```

```
471     else if (deps == 0.0) {
472         kon = konP;                     // No increment, we remain with the
              same excursion type
473     }
474
475     //------------------------------------------------------------------------
          ------------------------------------------------------------\\
476 // IN CASE OF LOAD REVERSAL:
477 // - update the minimum or maximum previous strain (epsmin or epsmax) and
      stress (sigmin or sigmax)
478 // - store the last load reversal point (epsr, sigr)
479 // - calculate the stress and strain (sigs0 and epss0) at the new intersection
       between elastic and secant siffness asymptote
480 //   The constants s1 & s2 (compression) or s3 & s4 (tension) control the
      shift in the intersection stress
481 // - calculate the target stress and strain (sigsT and epssT) considering the
      strain hardening
482 //   The constants a1 & a2 (compression) or a3 & a4 (tension) control the
      shift in the target stress
483 // - determine the secant stiffness asymptote (bSec)
484 // - determine the elastic-plastic form parameter (R) of the new excursion
485 //   The constants Cr1 and Cr2 determine how the maximum strain experienced
      modify the R parameter
486 // - determine the new cummulative damage D of the angles (Miner Law, with S
      and N parameters)
487 //------------------------------------------------------------------------
      ------------------------------------------------------------\\
488
489     if (kon != konP) {
490         // DEFINE LOAD REVERSAL
491         int Load_Reversal = 0;
492         if (kon == 0) {
493             if (epsP < epsmin) { ;  epsmin = epsP;  sigmin = sigP; };
                        // Update the minimum previous strain (epsmin) and stress
                (sigmin)
494             epsr_R = epsP;
495             sigr_R = sigP;
496             e_U = eP;
497             epsr = epsP;
                        // Store the last load reversal strain (epsr)
498             sigr = sigP;
                        // Store the last load reversal stress (sigr)
499             Load_Reversal = 1;
500         }
501         if (kon == 1) {
502             ;//End of a positive excursion, entering a negative excursion
503             if (epsP > epsmax) { ;  epsmax = epsP;  sigmax = sigP; };
                        // Update the maximum previous strain (epsmax) and stress
                (sigmax)
```

```
504             epsr_U = epsP;
505             sigr_U = sigP;
506             e_R = eP;
507             epsr = epsP;
                       // Store the last load reversal strain (epsr)
508             sigr = sigP;
                       // Store the last load reversal stress (sigr)
509             Load_Reversal = 1;
510         }
511         double xi = fabs((epsmax - epsmin) / (epsy - epsyN));
512         R = R0*(1.0 - (cR1*xi) / (cR2 + xi));
                   // determine the elastic-plastic form parameter (R) of the new
              excursion
513
        //R2 = R0*(1.0 + (cR2*xi));
514
        // DEFINE LOW-CYCLE FATIGUE DAMAGE ACCORDING TO COFFIN-MANSON
515         if (Coffin_Manson == 1 && Load_Reversal == 1) {
516             this->Uriz_Damage_Calculator(epsP);
517             //if (DI >= 1) { DI = 1.0; }
518         }
519         else { DI = 0; }
520         double damage = 1.0 - 0.5*pow(DI, 2.0);
521         if (damage <= 0.00001) { damage = 0.00001; }
522         // DEFINE POINTS CHARACTERIZING A POSITIVE EXCURSION
523         // - Define the target point (epssT, sigsT) based on the cyclic
              degradation a3 & a4 (tension) and the maximum (epsmax) previous
              strain
524         // - Define the intersection point (epss0, sigs0) for de excursion
              (depends if backbone or reloading)
525         // - Define the secant stiffness bSec for de excursion (depends if
              backbone or reloading)
526
527         if (kon == 0) {
528
529             b1 = b;
530             E1 = E;
531
532             //Power 1
533             double d1S = xi / s4;
534             sigs0_1 = Fy * (s3 * pow(d1S, 0.8))*damage;
535             epss0_1 = epsr + ((sigs0_1 - (sigr)) / (E));
536             sigr_1 = sigr;
537             epsr_1 = epsr;
538
539             //Power 2
540             double d1 = xi / a4;
541             double shift = Fy* (a3 * pow(d1, 0.8));
542
```

```
543             double epssTrat = fabs(epsmax / epsy);
544             double dum5 = 1.0 + pow((epssTrat), R0);
545             double dum6 = pow((dum5), (1.0 / R0));
546             double sigsTrat = b1*(epssTrat)+(1.0 - b1)*(epssTrat) / (dum6);
547             sigsT = (sigsTrat*Fy + shift)*damage;
548             epssT = epsmax + (shift*damage / E);
549             //R2 = 20.0;
550             if (epssT == epss0_1) { bSec = 0.0;
551             } else { bSec = ((sigsT - sigs0_1) / (epssT - epss0_1)) / (E); }
552
553             if (bSec == 0.0) { b2 = 0.0;
554             } else { b2 = b1 / bSec; }
555
556             epsr_2 = epsr;
557             sigr_2 = sigs0_1 - bSec*E1*(epss0_1 - epsr);
558
559             //Power 3
560             epss0_3 = epsy*damage + shift*damage/E;
561             sigs0_3= (Fy + shift)*damage;
562             epsr_3 = epssT;
563             sigr_3 = sigsT - b*E*epssT*damage;
564
565         }
566         if (kon == 1) {
567
568             b1 = bN;
569             E1 = EN;
570
571             //Power 1
572             double d1S = xi / s2;
573             sigs0_1 = FyN * (s1 * pow(d1S, 0.8))*damage;
574             epss0_1 = epsr + ((sigs0_1 - (sigr)) / (EN));
575             sigr_1 = sigr;
576             epsr_1 = epsr;
577
578             //Power 2
579             double d1 = xi / a2;
580             double shift = FyN* (a1 * pow(d1, 0.8));
581
582             double epssTrat = fabs(epsmin / epsyN);
583             double dum5 = 1.0 + pow((epssTrat), R0);
584             double dum6 = pow((dum5), (1.0 / R0));
585             double sigsTrat = b1*(epssTrat)+(1.0 - b1)*(epssTrat) / (dum6);
586             sigsT = (sigsTrat*FyN + shift)*damage;
587             epssT = epsmin + (shift / EN);
588             //R2 = 20.0;
589             if (sigsT >= FyN) { ;
590             sigsT = FyN*damage;
591             epssT = epsyN*damage ; }
```

```
592
593             if (epssT == epss0_1) { bSec = 0.0;
594             }   else { bSec = ((sigsT - sigs0_1) / (epssT - epss0_1)) /
                  (EN); }
595
596             if (bSec == 0.0) {  b2 = 0.0;
597             }   else { b2 = b1 / bSec; }
598
599             epsr_2 = epsr;
600             sigr_2 = sigs0_1 - bSec*E1*(epss0_1 - epsr);
601
602             //Power 3
603             epss0_3 = epsyN*damage + shift*damage / EN;
604             sigs0_3 = (FyN + shift)*damage;
605             epsr_3 = epssT;
606             sigr_3 = sigsT - bN*EN*epssT*damage;
607
608         };
609     };
610     //Power 1
611     double sig_1 = 0.0;
612     double e_1 = 0.0;
613     if (epss0_1 != epsr_1) {
614         double epsrat_1 = fabs((eps - epsr_1) / (epss0_1 - epsr_1));
615         double dum1_1 = 1.0 + pow(epsrat_1, R);
616         double dum2_1 = pow(dum1_1, (1.0 / R));
617         double sigrat_1 = (1.0 - b1 - bSec)*epsrat_1 / (dum2_1);
618         sig_1 = sigrat_1*(sigs0_1 - sigr_1);
619
620         double dum1_e1 = 1.0 + pow(epsrat_1, R);
621         double dum2_e1 = pow(dum1_e1, ((1.0 / R)));
622         double dum3_e1 = 1.0 - b1 - bSec;
623         e_1 = dum3_e1 / (dum2_e1*dum1_e1);
624     }
625     //Power 2
626     double sig_2 = 0.0;
627     double e_2 = 0.0;
628     if (epssT != epsr_2) {
629         double epsrat_2 = fabs((eps - epsr_2) / (epssT - epsr_2));
630         double dum1_2 = 1.0 + pow(epsrat_2, R2);
631         double dum2_2 = pow(dum1_2, (1.0 / R2));
632         double sigrat_2 = (1.0 - b2)*epsrat_2 / (dum2_2);
633         sig_2 = sigrat_2*(sigsT - sigr_2);
634
635         double dum1_e2 = 1.0 + pow(epsrat_2, R2);
636         double dum2_e2 = pow(dum1_e2, ((1.0 / R2)));
637         double dum3_e2 = 1.0 - b2;
638         e_2 = (bSec)*dum3_e2 / (dum1_e2*dum2_e2);
639     }
```

```
640     //Power 3
641     double sig_3 = 0.0;
642     double e_3 = 0.0;
643     if ((kon == 0 && eps >= epssT) || (kon == 1 && eps <= epssT)) {
644         double epsrat_3 = (eps / epss0_3);
645         double dum1_3 = 1.0 + pow(fabs(epsrat_3), R);
646         double dum2_3 = pow(dum1_3, (1.0 / R));
647         double sigrat_3 = (1.0 - b1)*epsrat_3 / (dum2_3);
648         sig_3 = sigrat_3*sigs0_3 - sigr_3;
649 
650         double dum1_e3 = 1.0 + pow(fabs(epsrat_3), R);
651         double dum2_e3 = pow(dum1_e3, ((1.0 / R)));
652         double dum3_e3 = 1.0 - b1;
653         e_3 = dum3_e3 / (dum1_e3*dum2_e3);
654     }
655 
656     //Linear
657     double sig_L = b1*E1*(eps - epsr);
658 
659     double e_L = (b1);
660 
661     sig = sig_1 + sig_2 + sig_3 + sig_L + sigr;
662     e = fabs(e_1 + e_2 + e_3 + e_L)*E1;
663 
664     return 0;
665 };
666 
667 double SteelAngles::getInitialTangent(void) {
668     return E;
669 }
670 
671 double SteelAngles::getStrain(void) {
672     return eps;
673 };
674 
675 double SteelAngles::getStress(void) {
676     return sig;
677 };
678 
679 double SteelAngles::getTangent(void) {
680     return e;
681 }
682 
683 int SteelAngles::commitState(void) {
684     epsmaxP = epsmax;
685     sigmaxP = sigmax;
686     epsminP = epsmin;
687     sigminP = sigmin;
688     epsr_RP = epsr_R;
```

```
689      sigr_RP = sigr_R;
690      epsr_UP = epsr_U;
691      sigr_UP = sigr_U;
692      DIP = DI;
693
694      //Current excursion parameters
695      konP = kon;
696      epss0P = epss0;
697      sigs0P = sigs0;
698      epsrP = epsr;
699      sigrP = sigr;
700      sigsTP = sigsT;
701      epssTP = epssT;
702
703      epsr_1P = epsr_1;
704      sigr_1P = sigr_1;
705      epsr_2P = epsr_2;
706      sigr_2P = sigr_2;
707      epsr_3P = epsr_3;
708      sigr_3P =  sigr_3;
709      epss0_1P = epss0_1;
710      sigs0_1P = sigs0_1;
711      epss0_2P = epss0_2;
712      sigs0_2P = sigs0_2;
713      epss0_3P = epss0_3;
714      sigs0_3P = sigs0_3;
715
716      b1P = b1;
717      b2P = b2;
718      bSecP = bSec;
719      E1P = E1;
720      RP = R;
721      R2P = R2;
722
723
724      AP = A;
725      BP = B;
726      CP = C;
727      DP = D;
728      XP = X;
729      YP = Y;
730      SSCP = SSC;
731      Next_PeakP = Next_Peak;
732      StepP = Step;
733
734      epsP = eps;
735      sigP = sig;
736      eP = e;
737      return 0;
```

```
738 };
739
740 int SteelAngles::revertToLastCommit(void) {
741
742     //Loading History parameters
743     epsmax = epsmaxP;
744     sigmax = sigmaxP;
745     epsmin = epsminP;
746     sigmin = sigminP;
747     epsr_R = epsr_RP;
748     sigr_R = sigr_RP;
749     epsr_U = epsr_UP;
750     sigr_U = sigr_UP;
751     DI = DIP;
752
753     //Current excursion parameters
754     kon = konP;
755     epss0 = epss0P;
756     sigs0 = sigs0P;
757     epsr = epsrP;
758     sigr = sigrP;
759     sigsT = sigsTP;
760     epssT = epssTP;
761
762     epsr_1 = epsr_1P;
763     sigr_1 = sigr_1P;
764     epsr_2 = epsr_2P;
765     sigr_2 = sigr_2P;
766     epsr_3 = epsr_3P;
767     sigr_3 = sigr_3P;
768     epss0_1 = epss0_1P;
769     sigs0_1 = sigs0_1P;
770     epss0_2 = epss0_2P;
771     sigs0_2 = sigs0_2P;
772     epss0_3 = epss0_3P;
773     sigs0_3 = sigs0_3P;
774
775     b1 = b1P;
776     b2 = b2P;
777     bSec = bSecP;
778     E1 = E1P;
779     R = RP;
780     R2 = R2P;
781
782     eps = epsP;
783     sig = sigP;
784     e = eP;
785
786     A = AP;
```

```
787      B = BP;
788      C = CP;
789      D = DP;
790      X = XP;
791      Y = YP;
792      SSC = SSCP;
793      Next_Peak = Next_PeakP;
794      Step = StepP;
795
796      return 0;
797  };
798
799  int SteelAngles::revertToStart(void) {
800      //Loading History parameters
801      epsmaxP = 0.0;
802      sigmaxP = 0.0;
803      epsminP = 0.0;
804      sigminP = 0.0;
805      epsr_RP = 0.0;
806      sigr_RP = 0.0;
807      epsr_UP = 0.0;
808      sigr_UP = 0.0;
809      DIP = 0.0;
810
811      //Current excursion parameters
812      konP = 0;
813      epss0P = Fy/E;
814      sigs0P = Fy;
815      epsrP = 0.0;
816      sigrP = 0.0;
817      sigsTP = 0.0;
818      epssTP = 0.0;
819
820      epsr_1P = 0.0;
821      sigr_1P = 0.0;
822      epsr_2P = 0.0;
823      sigr_2P = 0.0;
824      epsr_3P = 0.0;
825      sigr_3P = 0.0;
826      epss0_1P = 0.0;
827      sigs0_1P = 0.0;
828      epss0_2P = 0.0;
829      sigs0_2P = 0.0;
830      epss0_3P = Fy / E;
831      sigs0_3P = Fy;
832
833      b1P = b;
834      b2P = 0.0;
835      bSecP = 0.0;
```

```
836     E1P = E;
837     RP = R0;
838     R2P = 20.0;
839
840     epsP = 0.0;
841     sigP = 0.0;
842     eP = E;
843
844     A = 0.0;
845     B = 0.0;
846     C = 0.0;
847     D = 0.0;
848     X = 0.0;
849     Y = 0.0;
850     SSC = 0;
851     Next_Peak = 1;
852     Step = 1;
853
854     AP = 0.0;
855     BP = 0.0;
856     CP = 0.0;
857     DP = 0.0;
858     XP = 0.0;
859     YP = 0.0;
860     SSCP = 0;
861     Next_PeakP = 1;
862     StepP = 1;
863     if (S == 0) {
864         Coffin_Manson = 0;
865     }
866     else { Coffin_Manson = 1; }
867
868     //Loading History parameters
869     epsmax = epsmaxP;
870     sigmax = sigmaxP;
871     epsmin = epsminP;
872     sigmin = sigminP;
873     epsr_R = epsr_RP;
874     sigr_R = sigr_RP;
875     epsr_U = epsr_UP;
876     sigr_U = sigr_UP;
877     DI = DIP;
878
879     //Current excursion parameters
880     kon = konP;
881     epss0 = epss0P;
882     sigs0 = sigs0P;
883     epsr = epsrP;
884     sigr = sigrP;
```

```
885      sigsT = sigsTP;
886      epssT = epssTP;
887
888      epsr_1 = epsr_1P;
889      sigr_1 = sigr_1P;
890      epsr_2 = epsr_2P;
891      sigr_2 = sigr_2P;
892      epsr_3 = epsr_3P;
893      sigr_3 = sigr_3P;
894      epss0_1 = epss0_1P;
895      sigs0_1 = sigs0_1P;
896      epss0_2 = epss0_2P;
897      sigs0_2 = sigs0_2P;
898      epss0_3 = epss0_3P;
899      sigs0_3 = sigs0_3P;
900
901      b1 = b1P;
902      b2 = b2P;
903      bSec = bSecP;
904      E1 = E1P;
905      R = RP;
906      R2 = R2P;
907
908      eps = 0.0;
909      sig = 0.0;
910      e = E;
911
912      return 0;
913  };
914
915  int SteelAngles::sendSelf(int commitTag, Channel &theChannel) {
916
917      static Vector data(67);
918
919      //Backbone behavior & input parameters
920      data(0) = this->getTag();
921      data(1) = Fy;
922      data(2) = E;
923      data(3) = b;
924      data(4) = FyN;
925      data(5) = EN;
926      data(6) = bN;
927      data(7) = R0;
928      data(8) = cR1;
929      data(9) = cR2;
930      data(10) = a1;
931      data(11) = a2;
932      data(12) = a3;
933      data(13) = a4;
```

```
934       data(14) = s1;
935       data(15) = s2;
936       data(16) = s3;
937       data(17) = s4;
938       data(18) = S;
939       data(19) = N;
940       data(20) = Coffin_Manson;
941
942       //Loading History parameters
943       data(21) = epsmaxP;
944       data(22) = sigmaxP;
945       data(23) = epsminP;
946       data(24) = sigminP;
947       data(25) = epsr_RP;
948       data(26) = sigr_RP;
949       data(27) = epsr_UP;
950       data(28) = sigr_UP;
951       data(29) = DIP;
952
953       //Current excursion parameters
954       data(30) = konP;
955       data(31) = epss0P;
956       data(32) = sigs0P;
957       data(33) = epsrP;
958       data(34) = sigrP;
959       data(35) = epssTP;
960       data(36) = sigsTP;
961       data(37) = epsr_1P;
962       data(38) = sigr_1P;
963       data(39) = epsr_2P;
964       data(40) = sigr_2P;
965       data(41) = epsr_3P;
966       data(42) = sigr_3P;
967       data(43) = epss0_1P;
968       data(44) = sigs0_1P;
969       data(45) = epss0_2P;
970       data(46) = sigs0_2P;
971       data(47) = epss0_3P;
972       data(48) = sigs0_3P;
973
974       data(49) = b1P;
975       data(50) = b2P;
976       data(51) = bSecP;
977       data(52) = E1P;
978       data(53) = RP;
979       data(54) = R2P;
980
981       data(55) = epsP;
982       data(56) = sigP;
```

```
 983      data(57) = eP;
 984
 985      //URIZ DAMAGE PARAMETERS
 986      data(58) = AP;
 987      data(59) = BP;
 988      data(60) = CP;
 989      data(61) = DP;
 990      data(62) = XP;
 991      data(63) = YP;
 992      data(64) = SSCP;
 993      data(65) = Next_PeakP;
 994      data(66) = StepP;
 995
 996      if (theChannel.sendVector(this->getDbTag(), commitTag, data) < 0) {
 997          opserr << "SteelAngles::sendSelf() - failed to sendSelf\n";
 998          return -1;
 999      };
1000      return 0;
1001  };
1002
1003  int SteelAngles::recvSelf(int commitTag, Channel &theChannel, FEM_ObjectBroker
        &theBroker) {
1004      static Vector data(67);
1005
1006      if (theChannel.recvVector(this->getDbTag(), commitTag, data) < 0) {
1007          opserr << "SteelAngles::recvSelf() - failed to recvSelf\n";
1008          return -1;
1009      };
1010
1011      this->setTag(data(0));
1012      Fy = data(1);
1013      E = data(2);
1014      b = data(3);
1015      FyN = data(4);
1016      EN = data(5);
1017      bN = data(6);
1018      R0 = data(7);
1019      cR1 = data(8);
1020      cR2 = data(9);
1021      a1 = data(10);
1022      a2 = data(11);
1023      a3 = data(12);
1024      a4 = data(13);
1025      s1 = data(14);
1026      s2 = data(15);
1027      s3 = data(16);
1028      s4 = data(17);
1029      S = data(18);
1030      N = data(19);
```

```
1031      Coffin_Manson = data(20);
1032
1033      //Loading History parameters
1034      epsmaxP = data(21);
1035      sigmaxP = data(22);
1036      epsminP = data(23);
1037      sigminP = data(24);
1038      epsr_RP = data(25);
1039      sigr_RP = data(26);
1040      epsr_UP = data(27);
1041      sigr_UP = data(28);
1042      DIP = data(29);
1043      //Current excursion parameters
1044      konP = data(30);
1045      epss0P = data(31);
1046      sigs0P = data(32);
1047      epsrP = data(33);
1048      sigrP = data(34);
1049      epssTP = data(35);
1050      sigsTP = data(36);
1051      epsr_1P = data(37);
1052      sigr_1P = data(38);
1053      epsr_2P = data(39);
1054      sigr_2P = data(40);
1055      epsr_3P = data(41);
1056      sigr_3P = data(42);
1057      epss0_1P = data(43);
1058      sigs0_1P = data(44);
1059      epss0_2P = data(45);
1060      sigs0_2P = data(46);
1061      epss0_3P = data(47);
1062      sigs0_3P = data(48);
1063
1064      b1P = data(49);
1065      b2P = data(50);
1066      bSecP = data(51);
1067      E1P = data(52);
1068      RP = data(53);
1069      R2P = data(54);
1070
1071      epsP = data(55);
1072      sigP = data(56);
1073      eP = data(57);
1074
1075      //URIZ DAMAGE PARAMETERS
1076      AP = data(58);
1077      BP = data(59);
1078      CP = data(60);
1079      DP = data(61);
```

```
1080      XP = data(62);
1081      YP = data(63);
1082      SSCP = data(64);
1083      Next_PeakP = data(65);
1084      StepP = data(66);
1085
1086      return 0;
1087  };
1088
1089  void SteelAngles::Print(OPS_Stream &s, int flag) {
1090      s << "SteelAngles:(strain, stress, tangent) " << eps << " " << sig << " " ↵
            << e << endln;
1091  };
1092
1093  void SteelAngles::Uriz_Damage_Calculator(double epsP) {
1094
1095      A = AP;
1096      B = BP;
1097      C = CP;
1098      D = DP;
1099      X = XP;
1100      Y = YP;
1101      SSC = SSCP;
1102      Next_Peak = Next_PeakP;
1103      Step = StepP;
1104      DI = DIP;
1105
1106      double epsyD = N;
1107
1108      if (Next_Peak == 1) {
1109          A = epsP; SSC = 0;
1110          Next_Peak = 2;
1111          Step = 1;
1112      } else if (Next_Peak == 2) {
1113          B = epsP;
1114          Next_Peak = 3;
1115          Step = 2;
1116      } else if (Next_Peak == 3) {
1117          C = epsP;
1118          Step = 3;
1119      } else if (Next_Peak == 4) {
1120          D = epsP;
1121          Step = 4;
1122      };
1123
1124      if (Step == 3) {
1125          Y = fabs(B - A);
1126          X = fabs(C - A);
1127
```

```
1128          if (X > Y) {
1129              double dumD1 = pow(S, -1);
1130              double dumD2 = log(Y / epsyD);
1131              double dumD3 = pow(10.0, dumD1*dumD2);
1132              DI = DIP + 0.5 / dumD3;
1133
1134              A = B;
1135              B = C;
1136              Next_Peak = 3;
1137          }
1138          else if (Y >= X) {
1139              SSC = SSC + 1;
1140              Next_Peak = 4;
1141          };
1142      };
1143
1144      if (Step == 4) {
1145          Y = fabs(C - B);
1146          X = fabs(D - C);
1147
1148          if (X > Y) {
1149              double dumD1 = pow(S, -1);
1150              double dumD2 = log(Y / epsyD);
1151              double dumD3 = pow(10.0, dumD1*dumD2);
1152              DI = DIP + 1.0 / dumD3;
1153
1154              B = D;
1155              Next_Peak = 3;
1156              SSC = 0;
1157          }
1158          else if (Y >= X) {
1159              SSC = SSC + 1;
1160              Step = 5;
1161          };
1162      };
1163
1164      if (Step == 5) {
1165          if (SSC == 2) {
1166              double dumD1 = pow(S, -1);
1167              double dumD2 = log(X / epsyD);
1168              double dumD3 = pow(10.0, dumD1*dumD2);
1169              DI = DIP + 1.0 / dumD3;
1170
1171              B = D;
1172              Next_Peak = 3;
1173              SSC = 0;
1174          };
1175      };
1176  };
```